Transactions of the ASME®

Technical Editor, LEWIS T. WHEELER (1997)

Department of Mechanical Engineering,
University of Houston,
Houston, TX 77204-4792

APPLIED MECHANICS DIVISION

Chairman, WILLIAM S. SARIC
Secretary, THOMAS A. CRUSE
Associate Technical Editors,
R. ABEYARATNE (1994)
T. R. AKYLAS (1994)
S. A. BERGER (1994)
R. M. BOWEN (1993)
S. K. DATTA (1995)
G. J. DVORAK (1995)
M. E. FOURNEY (1993)
R. L. HUSTON (1993)
D. J. INMAN (1995)
S. LICHTER (1995)
X. MARKENSCOFF (1994)
R. M. McMEEKING (1993)
A. K. NOOR (1993)
D. M. PARKS (1995)
J. N. REDDY (1995)
J. W. RUDNICKI (1994)
W. N. SHARPE, JR. (1993)
C. F. SHIH (1995)
P. D. SPANOS (1994)
F. Y. M. WAN (1994)

BOARD ON COMMUNICATIONS

Chairman and Vice-President
R. D. ROCKE

Members-at-Large
T. BARLOW, W. BEGELL, T. F. CONRY
T. DEAR, J. KITTO, R. MATES
W. MORGAN, E. M. PATTON
S. PATULSKI, R. E. REDER
A. VAN DER SLUYS, F. M. WHITE

OFFICERS OF THE ASME
President, J. A. FALCON
Exec. Director
D. L. BELDEN
Treasurer
ROBERT A. BENNETT

PUBLISHING STAFF
Mng. Dir., Publ.,
CHARLES W. BEARDSLEY
Managing Editor,
CORNELIA MONAHAN
Production Editor,
JUDITH SIERANT
Production Assistant,
MARISOL ANDINO

Transactions of the ASME, Journal of Applied Mechanics (ISSN 0021-8936) is published quarterly (Mar., June, Sept., Dec.) for $165.00 per year by The American Society of Mechanical Engineers, 345 East 47th Street, New York, NY 10017. Second class postage paid at New York, NY and additional mailing office. POSTMASTER: Send address changes to Transactions of the ASME, Journal of Applied Mechanics, c/o THE AMERICAN SOCIETY OF MECHANICAL ENGINEERS, 22 Law Drive, Box 2300, *Fairfield, NJ 07007-2300.*

CHANGES OF ADDRESS must be received at Society headquarters seven weeks before they are to be effective. Please send old label and new address.

PRICES: To members, $40.00, annually: to nonmembers, $165.00. Add $24.00 for postage to countries outside the United States and Canada.

STATEMENT from By-Laws. The Society shall not be responsible for statements or opinions advanced in papers or . . . printed in its publications (B7.1, Par. 3).

COPYRIGHT © 1993 by The American Society of Mechanical Engineers. Authorization to photocopy material for internal or personal use under circumstances not falling within the fair use provisions of the Copyright Act is granted by ASME to libraries and other users registered with the *Copyright Clearance Center (CCC) Transactional Reporting* Service provided that the base fee of $3.00 per article is paid directly to CCC, 27 Congress St., Salem, MA 01970. Request for special permission or bulk copying should be addressed to Reprints/Permission Department.

INDEXED by Applied Mechanics Reviews and Engineering Information, Inc. Canadian Goods & Services Tax Registration #126148048

Journal of Applied Mechanics

Published Quarterly by The American Society of Mechanical Engineers

VOLUME 60 • NUMBER 1 • MARCH 1993

TECHNICAL PAPERS

1 A Study of Combined Asymmetric and Cavitated Bifurcations in Neo-Hookean Material Under Symmetric Dead Loading
Hang-sheng Hou

8 Effective Mechanical Properties of Composites at Finite Deformations
N. Fares

15 On the Conditions to Prevent Plastic Shakedown of Structures: Part I—Theory
C. Polizzotto

20 On the Conditions to Prevent Plastic Shakedown of Structures: Part II—The Plastic Shakedown Limit Load
C. Polizzotto

26 Complex Modes and Solvability of Nonclassical Linear Systems
T. K. Caughey and F. Ma

29 A Simple Representation of the J-Integral and Some Estimates of Elastic Stress Intensity Factors
V. A. Lubarda

33 Hollow Circular Cylindrical Inclusion at the Surface of a Half-Space
H. Hasegawa, V.-G. Lee, and T. Mura

41 Exact Elasticity Solution for Laminated Anisotropic Cylindrical Shells
K. Bhaskar and T. K. Varadan

48 A Continuum Theory of a Lubrication Problem With Solid Particles
F. Dai and M. M. Khonsari

59 Gravity-Driven Flows of Smooth, Inelastic Disks Between Parallel Bumpy Boundaries
M. Babić

65 An Inviscid Analysis in Polar Coordinates of Flow Between Two Flat Plates
D. N. Contractor

70 Comparison of Crystal Plasticity and Isotropic Hardening Predictions for Metal-Matrix Composites
A. Needleman and V. Tvergaard

77 Statistical Properties of Residual Stresses and Intergranular Fracture in Ceramic Materials
M. Ortiz and S. Suresh

85 Predicting Wear for Metal Surfaces in Sliding Contact Using a Low-Cycle Fatigue Wear Model
B. S. Hockenhull, E. M. Kopalinsky, and P. L. B. Oxley

93 Photoelastic Determination of Stress Intensity Factor of an Interfacial Crack in a Bi-material
Hua Lu and F. P. Chiang

101 Nonlinear Response of Graphite-Epoxy Wide Columns Subject to Eccentric Load
O. H. Griffin, Jr., E. R. Johnson, and M. D. Sensmeier

109 A Geometrically Nonlinear Theory of Elastic Plates
D. H. Hodges, A. R. Atigan, and D. A. Danielson

117 Correction of Joint Stiffnesses and Constraints for Finite Element Models in Structural Dynamics
J. E. Mottershead and S. Weixun

123 Identification of Nonlinear Dynamic Systems Using Neural Networks
S. F. Masri, A. G. Chassiakos, and T. K. Caughey

134 Vibrations of Sectorial Plates Having Corner Stress Singularities
A. W. Leissa, O. G. McGee, and C. S. Huang

141 Stochastic Dynamics of Nonlinear Systems Driven by Non-normal Delta-Correlated Processes
M. Di Paola and G. Falsone

149 Random Vibrations of Externally Damped Viscoelastic Timoshenko Beams With General Boundary Conditions
M. P. Singh and A. S. Abdelnaser

157 Axisymmetric Bending of Generally Laminated Cylindrical Shells
V. Birman

163 Application of Dressler Theory to Weir Flow
A. S. Ramamurthy and Ngoc-Diep Vo

167 Chaotic Vibrations of Beams: Numerical Solution of Partial Differential Equations
N. S. Abhyankar, E. K. Hall, II, and S. V. Hanagud

175 An Analysis of Crack Trapping by Residual Stresses in Brittle Solids
A. F. Bower and M. Ortiz

183 General Crack-Tip Fields for Stationary and Steadily Growing Interface Cracks in Anisotropic Bimaterials
X. Deng

190 A Simple Continuum Model of Creep in a Fiber Composite Beam
J. T. Evans

195 Buckling of Thick Orthotropic Cylindrical Shells Under External Pressure
G. A. Kardomateas

(Contents continued on Inside Back Cover)

Downloaded 04 May 2010 to 171.66.16.49. Redistribution subject to ASME license or copyright; see http://www.asme.org/terms/Terms_Use.cfm

CONTENTS (CONTINUED)

BRIEF NOTES

Stress Concentration due to Interaction Between Two Imperfectly Bonded Fibers in a Continuous Fiber Composite — 203
D. Kouris

A Superposition Method for One-Dimensional Axially Symmetric Elastic Waves — 206
Z. Xiangzhou

Transverse Vibration of Solid Circular Plates Continuous Over Multiple Concentric Annular Supports — 208
K. M. Liew and K. Y. Lam

A Bilinear Variational Principle Governing Longitudinal Vibration of Rods With Frequency-Dependent Material Damping — 210
G. A. Lesieutre

Elastic-Plastic Tip Field for a Stationary Crack in a Reinforced Thin Sheet — 211
P. Ståhle

An Approximate Solution of a Coupled Differential Equation With Variable Parameter — 214
L. Cveticanin

Response of a Fiber Composite Laminate to a Time-Varying Surface Line Load — 217
E. R. Green

Evaluation of a Complex Stress Intensity Factor of Interface Cracks: A Perturbation Approach — 221
C. Y. Hui and Y. C. Chen

Dynamic Crack Propagation in a Linearly Viscous Body — 223
S. J. Fariborz

Shear Flow Over a Periodically Heated Plate — 225
C. Y. Wang

227 Initiation of an Interface Crack Under Mixed-Mode Loading
P. A. Foltyn and K. Ravi-Chandar

229 Boundary Layer Phenomena in Large Deflection, Small Strain Plate Theory
L. J. Berg

232 On the Approximation of a Deflection Curve by Force Actuators
K. Natarajan, G. A. Dumont, and M. S. Davies

235 Further Results on Iterative Approaches to the Determination of the Response of Nonclassically Damped Systems
F. E. Udwadia

239 On the Interaction of Torsion and Bending in Rotating Shafts
C. Nataraj

241 Negativism: A Nonlinear Version
T. M. Atanackovic and Dj. S. Djukic

244 Compound Infinitesimal Mechanisms
E. N. Kuznetsov

246 A Beam Theory for Laminated Composites and Application to Torsion Problems
B. V. Sankar

249 Fjortoft's Theorem for a Parallel Flow With a Free Surface
J. P. McHugh

DISCUSSIONS

251 **Effect of Accuracy Loss in Classical Shell Theory, by V. Berdichevsky and V. Misyura—Discussion by R. Schmidt**

252 **On Cauchy's Mean Rotation, by Z. S. Zheng and K. C. Hwang—Discussion by R. Rosel**

253 **The Complementary Potentials of Elasticity, Extremal Properties, and Associated Functionals, by G. Wempner—Discussion by W. T. Koiter**

BOOK REVIEWS

255 ***Three-Dimensional Elastic Bodies in Rolling Contact*, by J. J. Kalker . . .** Reviewed by **K. L. Johnson**

ANNOUNCEMENTS AND SPECIAL NOTES

47 IUTAM Symposium on Computational Mechanics of Materials—Announcement

58 Books Received by the Office of the Technical Editor

69 Symposium on Material Instabilities—Call for Papers

174 Change of Address Form

194 Twelfth U.S. National Congress of Applied Mechanics—Announcement

250 Call for Proposals to Host a IUTAM Symposium in 1996 or 1997

256 Worldwide Mechanics Meetings List

258 Information for Authors

Downloaded 04 May 2010 to 171.66.16.49. Redistribution subject to ASME license or copyright; see http://www.asme.org/terms/Terms_Use.cfm

A Study of Combined Asymmetric and Cavitated Bifurcations in Neo-Hookean Material Under Symmetric Dead Loading

Hang-sheng Hou
Department of Mechanical Engineering,
Massachusetts Institute of Technology,
Cambridge, MA 02139

A study is given of the deformations of an incompressible body composed of a neo-Hookean material subjected to a uniform, spherically symmetric, tensile dead load. It is based on the energy minimization method using a constructed kinematically admissible deformation field. It brings together the pure homogeneous asymmetric deformations explored by Rivlin (1948, 1974) and the spherically symmetric cavitated deformations analyzed by Ball (1982) in one setting, and, in addition, it allows nonsymmetric cavitated deformations to compete for a minimum. Many solutions are found and their stabilities examined; especially, the stabilities of the aforementioned asymmetric and cavitated solutions are reassessed in this work, which shows that a cavitated deformation which is stable against the virtual displacements in the spherical form may lose its stability against a wider class of virtual displacements involving nonspherical forms.

1 Introduction

In this work, we study the deformations of an incompressible unit solid sphere in response to a radially applied, uniformly distributed, dead load p at its outer surface; this solid sphere is composed of a neo-Hookean material characterized by the stored energy function $W = (\mu/2)(\lambda_1^2 + \lambda_2^2 + \lambda_3^2 - 3)$, where μ is the infinitesimal shear modulus and $\lambda_1, \lambda_2, \lambda_3$ are principal stretches. One deformation this incompressible body can undergo is the *fundamental* deformation in which the body remains undeformed and the stress state is uniform and hydrostatic. However, certain other deformations can bifurcate from this fundamental deformation when the applied stress is sufficiently large. One such bifurcated deformation, first analyzed by Rivlin (1948, 1974), is that the body adopts an *asymmetric* configuration in which a sphere in the undeformed state becomes a prolate or an oblate ellipsoid in the deformed configuration. Specifically, Rivlin considered the pure homogeneous deformations of a cube of neo-Hookean material subjected to three pairs of equal and opposite uniform tension, each of magnitude p. He found that when $p < 3 \times 4^{-1/3}\mu$, there is only a fundamental solution; when $3 \times 4^{-1/3}\mu < p < 2\mu$, there exist a fundamental solution and, apart from a cyclic permutation, two oblate asymmetric solutions; when $p > 2\mu$, there exist a fundamental solution and, apart from a cyclic permutation, an oblate and a prolate asymmetric solutions. Another bifurcated deformation, investigated by Ball (1982) in the framework of radial deformations, is the *cavitated* deformation in which the body develops a concentric cavity, i.e., a solid sphere in the undeformed configuration is mapped onto a spherical shell. Specifically, Ball considered a solid sphere subjected to a radially applied uniform tension p. For a neo-Hookean material, he found that when $p < (5/2)\mu$ there is a fundamental solution, while when $p > (5/2)\mu$, there exist a fundamental solution and a cavitated solution. These two types of bifurcations have been carried out independently of each other, and in particular, the stability was assessed with respect to each framework separately.

Asymmetric and cavitated deformations of this sort may exist in a general homogeneous, isotropic, incompressible elastic material as well. For asymmetric deformations, the analyses have been carried out extensively. Ball and Schaeffer (1983) analyzed this problem for a class of incompressible materials characterized by the elastic potential $W(\lambda_1, \lambda_2, \lambda_3) = \phi(\lambda_1) + \phi(\lambda_2) + \phi(\lambda_3)$. Kearsley 1986) and MacSithigh (1986) looked into the analogous plane stress problem for a thin sheet of Mooney-Rivlin material. A more general treatment has been accomplished by Chen (1987, 1988). The occurrence of asymmetric deformations was indicated in an early experiment by Treloar (1948). For cavitated deformations, Ball's study (1982) is complete in the case of incompressible hyperelastic materials. The experimental evidence of the formation of an internal cavity in a solid material body was reported under many circumstances, e.g., Gent and Lindley (1958); Ashby, Blunt, and Bannister (1989). All of those theoretical studies again have

Contributed by the Applied Mechanics Division of THE AMERICAN SOCIETY OF MECHANICAL ENGINEERS for publication in the ASME JOURNAL OF APPLIED MECHANICS.

Discussion on this paper should be addressed to the Technical Editor, Professor Lewis T. Wheeler, Department of Mechanical Engineering, University of Houston, Houston, TX 77204-4792, and will be accepted until four months after final publication of the paper itself in the ASME JOURNAL OF APPLIED MECHANICS.

Manuscript received by the ASME Applied Mechanics Division, Aug. 12, 1991; final revision, Dec. 17, 1991. Associate Technical Editor: R. M. Bowen.

Copyright © 1993 by ASME
Downloaded 03 May 2010 to 171.66.16.245. Redistribution subject to ASME license or copyright; see http://www.asme.org/terms/Terms_Use.cfm

been carried out in the absence of any connection between the two types of deformations. In a recent paper (Abeyaratne and Hou, 1991), those two different bifurcations in incompressible hyperelastic materials were compared by an energetic approach and their relationships were determined. In particular, it is established that if there exists a stable cavitated deformation at a load p, then necessarily there exists a stable asymmetric deformation with less energy at that same load. The neo-Hookean material served as a specific example there.

In this work, we confine our attention to investigating the combined asymmetric and cavitated deformations in one framework for a neo-Hookean material. Specifically, we consider a particular class of kinematically admissible deformations which includes the aforementioned asymmetric and cavitated deformations as special cases. This allows us to investigate the stability in a much broader sense that the stability of cavitated deformations will be judged by perturbations against asymmetric virtual displacements and vice versa; moreover, it examines the possible occurrence of nonsymmetric cavitated deformations under symmetric dead load tractions.

In Section 2, we construct a class of kinematically admissible deformations based on a simple and tractable presumed form and the condition of incompressibility; this class of deformations is fully characterized by three parameters. We then determine these unknown parameters by minimizing the total potential energy associated with the class of deformations for a given value of the applied load. In Section 3, two special cases of this class of deformations, obtained by Rivlin (1948, 1974) and Ball (1982), respectively, are given, both representing the exact solutions to the field equations. Section 4 studies this class of kinematically admissible deformations restricted to the axisymmetric deformations containing two parameters. In this case, many solutions are found and their stabilities examined. Some cavitated solutions, which are found to be stable in the spherical deformation, lose their stabilities as a consequence of the widening of the virtual displacement field. Stable nonspherical cavitated solutions corresponding to the occurrence of a prolate ellipsoidal cavity are found. In Section 5, we seek the solutions and examine their stabilities for the class of deformations with all three parameters. The widening of the deformation field in this case does not give rise to any new equilibrium states; however, the stability of the solutions has been affected. All prolate-type of solutions including nonspherical cavitated solutions are found to be unstable.

2 Deformations

Let $\mathbf{x}$ and $\mathbf{y}$, with corresponding Cartesian components (x_1, x_2, x_3) and (y_1, y_2, y_3), denote the positions of a typical material point in the undeformed and deformed configurations, respectively. We study the deformations of a solid sphere of neo-Hookean material, occupying a domain $\Omega = \{\mathbf{x}: |\mathbf{x}| = R < 1\}$, in response to a uniform, radial, nominal tension p applied at its outer surface. Since solving nonlinear field equations rarely lends itself to tractable solutions, we approach this problem by constructing a class of kinematically admissible deformations $\mathfrak{D}$ in which a particle at $\mathbf{x}$ moves to $\mathbf{y}$ obeying the particular pattern

$$y_1 = \psi_1(R)x_1, \quad y_2 = \psi_2(R)x_2, \quad y_3 = \psi_3(R)x_3, \tag{1}$$

where $R^2 = x_1^2 + x_2^2 + x_3^2$ and, without loss of generality, we require that the functions $\psi_1(R)$, $\psi_2(R)$, $\psi_3(R) > 0$ for all R in (0, 1). The deformation gradient is defined as

$$\mathbf{F} = \frac{\partial \mathbf{y}}{\partial \mathbf{x}}, \tag{2}$$

and the incompressibility requires that all deformations be isochoric, i.e., $\det\mathbf{F} = 1$, which, in conjunction with (1) and (2), leads to

$$\psi_1\psi_2\psi_3 + R\psi_1\psi_2\psi_3' + x_1^2\psi_2(\psi_1'\psi_3 - \psi_1\psi_3')/R + x_2^2\psi_1(\psi_2'\psi_3 - \psi_2\psi_3')/R = 1. \tag{3}$$

Equation (3) holds at all points in the body if and only if the following three equations hold at each $R \in (0, 1)$:

$$\psi_1'\psi_3 - \psi_1\psi_3' = 0, \quad \psi_2'\psi_3 - \psi_2\psi_3' = 0, \quad \psi_1\psi_2\psi_3 + R\psi_1\psi_2\psi_3' = 1. \tag{4}$$

On solving these three equations, we obtain

$$\psi_1(R) = \alpha_2^{-1}\alpha_3^{-1}\psi(R), \quad \psi_2(R) = \alpha_2\psi(R), \quad \psi_3(R) = \alpha_3\psi(R), \tag{5}$$

where

$$\psi(R) = (1 + \beta^3/R^3)^{1/3}, \tag{6}$$

and β, α_2, and α_3 are unknown constants resulting from integration, with $\beta > 0$, $\alpha_2 > 0$ and $\alpha_3 > 0$ which follow from the positiveness of $\psi_1(R)$, $\psi_2(R)$, and $\psi_3(R)$. Therefore, all deformations in $\mathfrak{D}$ are completely characterized by three parameters β, α_2, and α_3. The expressions (1), (5) and (6) can be rearranged into the form

$$\alpha_2^2\alpha_3^2y_1^2 + \alpha_2^{-2}y_2^2 + \alpha_3^{-2}y_3^2 = (R^3 + \beta^3)^{2/3}, \tag{7}$$

so that, in general, this deformation field carries a spherical surface in the undeformed configuration into an ellipsoidal one, and in particular, the origin is mapped into an ellipsoidal cavity. It is notable from (7) that β represents a measure of cavity size and α_2, α_3 depict the aspect ratios or the departure from spherical symmetry.

The total potential energy is expressed as

$$U_0 = \int_\Omega W dV - \oint_{\partial\Omega} p\mathbf{n}\cdot(\mathbf{y} - \mathbf{x})dS, \tag{8}$$

where the first term represents the stored elastic strain energy and the second term is the dead load potential with $\partial\Omega$ as the boundary of Ω and $\mathbf{n}$ the unit outward normal on $\partial\Omega$. The stored energy function W associated with all deformations in $\mathfrak{D}$ is obtained as

$$\begin{aligned} W &= (\mu/2)(\lambda_1^2 + \lambda_2^2 + \lambda_3^2 - 3) = (\mu/2)[\mathrm{tr}(\mathbf{F}\mathbf{F}^T) - 3] \\ &= (\mu/2)[\psi^2(\alpha_2^{-2}\alpha_3^{-2} + \alpha_2^2 + \alpha_3^2) \\ &\quad + R^{-2}(\psi^{-4} - \psi^2)(x_1^2\alpha_2^{-2}\alpha_3^{-2} + \alpha_2^2x_2^2 + \alpha_3^2x_3^2) - 3]. \end{aligned} \tag{9}$$

With the aid of a spherical coordinate system, evaluating (8), normalizing and dropping constant terms, we obtain the total potential energy associated with $\mathfrak{D}$

$$\begin{aligned} U_{\mathfrak{D}}(\beta, \alpha_2, \alpha_3) &= (1/2)(\alpha_2^{-2}\alpha_3^{-2} + \alpha_2^2 + \alpha_3^2)(1 + 2\beta^3)(1 + \beta^3)^{-1/3} \\ &\quad - \sigma(1 + \beta^3)^{1/3}(\alpha_2^{-1}\alpha_3^{-1} + \alpha_2 + \alpha_3), \end{aligned} \tag{10}$$

where $U_{\mathfrak{D}}$ is the total potential energy normalized by the factor $4\pi\mu/3$, and $\sigma = p/\mu$ is the normalized load.

A kinematically admissible deformation characterizes an equilibrium configuration only if it renders the total potential energy stationary. An equilibrium state is said to be stable if it corresponds to a local minimum of the total potential energy. In this work, since not all isochoric deformations are accounted for, an equilibrium configuration or state may not necessarily be an exact solution to the field equations of equilibrium. Inasmuch as the energy comparison is restricted to a special class of isochoric deformations, the notion of stability is thereby confined to that class of deformations. The task at hand now is to seek the values of the parameters $\beta \geq 0$, $\alpha_2 > 0$ and $\alpha_3 > 0$ which minimize $U_{\mathfrak{D}}$.

3 Two Special Cases

Certain special choices of the parameters in $\mathfrak{D}$ may result in exact solutions. One such case, explored by Rivlin (1948, 1974), is the pure homogeneous asymmetric solution, and the other case, examined by Ball (1982), is the spherically symmetric cavitated solution.

Downloaded 03 May 2010 to 171.66.16.245. Redistribution subject to ASME license or copyright; see http://www.asme.org/terms/Terms_Use.cfm

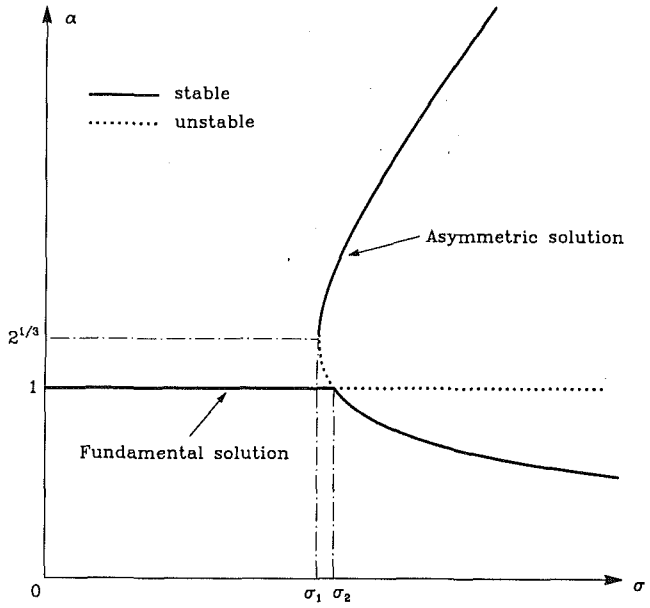


Fig. 1 Solutions in $\mathfrak{R}_1$

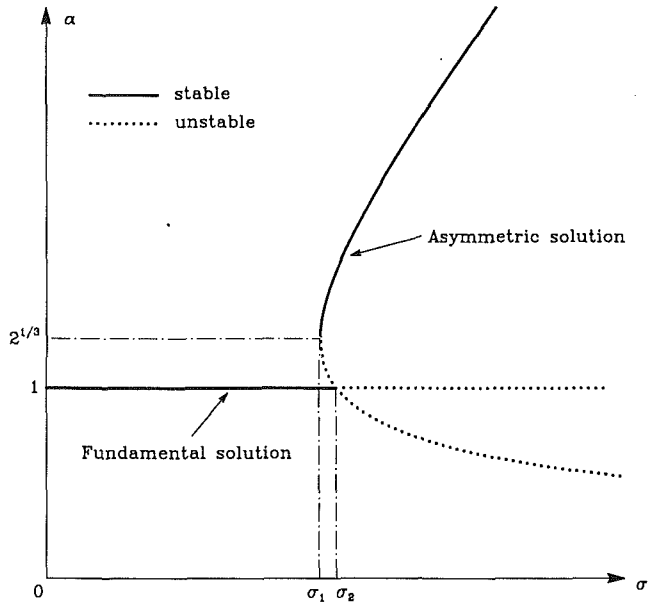


Fig. 2 Solutions in $\mathfrak{R}_2$

3.1 Asymmetric Deformations: Rivlin's Analysis. Consider a subset of deformations $\mathfrak{R}_1$ obtained by setting $\beta = 0$ and $\alpha_2 = \alpha_3 = \alpha$ in $\mathfrak{D}$. By (1), (5), and (6), this subset represents axisymmetric, pure homogeneous asymmetric deformations of the form

$$y_1 = \alpha^{-2}x_1, \quad y_2 = \alpha x_2, \quad y_3 = \alpha x_3. \tag{11}$$

Let $U_{\mathfrak{R}1}(\alpha)$ be the restriction of $U_{\mathfrak{D}}(\beta, \alpha_2, \alpha_3)$ to $\mathfrak{R}_1$, then the total potential is

$$U_{\mathfrak{R}1}(\alpha) = U_{\mathfrak{D}}(0, \alpha, \alpha) = (1/2)(\alpha^{-4} + 2\alpha^2) - \sigma(\alpha^{-2} + 2\alpha) \text{ for } \alpha > 0. \tag{12}$$

The stationary points of (12) are found by solving

$$\frac{dU_{\mathfrak{R}1}}{d\alpha} = 2\left(1 - \frac{1}{\alpha^3}\right)\left(\frac{1}{\alpha^2} + \alpha - \sigma\right) = 0, \tag{13}$$

which leads to two solutions: the fundamental solution

$$\alpha = 1, \tag{14}$$

and the asymmetric solution

$$\sigma = \alpha^{-2} + \alpha, \ \alpha > 0. \tag{15}$$

Corresponding to the two roots of (15), there are two asymmetric solutions whenever $\sigma > \sigma_1 \equiv 3 \times 4^{-1/3} \approx 1.88988$. When $\sigma_1 < \sigma < \sigma_2 \equiv 2$, both roots exceed unity, which describe two asymmetric deformations carrying the sphere into two oblate ellipsoids, while when $\sigma > \sigma_2$ they represent two ellipsoids with one oblate ($\alpha > 1$) and the other prolate ($\alpha < 1$); see Fig. 1.

The second derivative at the fundamental solution is

$$\frac{d^2U_{\mathfrak{R}1}}{d\alpha^2} = 6(2 - \sigma). \tag{16}$$

Therefore the fundamental deformation is stable against pure homogeneous virtual displacements of the form (11) when $\sigma < 2$ and it is unstable when $\sigma > 2$. Similarly at the asymmetric solution we find

$$\frac{d^2U_{\mathfrak{R}1}}{d\alpha^2} = 2\left(1 - \frac{1}{\alpha^3}\right)\left(1 - \frac{2}{\alpha^3}\right). \tag{17}$$

Therefore the asymmetric deformation is stable when $(\alpha - 1)(\alpha - 2^{1/3}) > 0$ and unstable when $(\alpha - 1)(\alpha - 2^{1/3}) < 0$; see Fig. 1, where the solid portion of the curves represents stable configurations and the dotted portion corresponds to unstable ones. In summary, when $\sigma < \sigma_1$, there is a stable fundamental solution. When $\sigma_1 < \sigma < \sigma_2$, there are a stable fundamental solution, a stable oblate asymmetric solution ($\alpha > 2^{1/3}$) and an unstable oblate asymmetric solution ($1 < \alpha < 2^{1/3}$). When $\sigma > \sigma_2$, there are an unstable fundamental solution, a stable oblate asymmetric solution ($\alpha > 2^{1/3}$) and a stable prolate asymmetric solution ($0 < \alpha < 1$).

Now we consider another subset $\mathfrak{R}_2$ obtained by setting $\beta = 0$ but without further restriction on α_2 and α_3 in $\mathfrak{D}$. Clearly $\mathfrak{R}_2 \supset \mathfrak{R}_1$, and $\mathfrak{R}_2$ consists of a two-parameter family of pure homogeneous deformations:

$$y_1 = \alpha_2^{-1}\alpha_3^{-1}x_1, \quad y_2 = \alpha_2 x_2, \quad y_3 = \alpha_3 x_3. \tag{18}$$

Following the same procedure as above, one can conclude that, apart from a cyclic permutation, all equilibrium states in $\mathfrak{R}_2$ are in fact identical with those in $\mathfrak{R}_1$. However, the stability of these equilibrium configurations is now being judged with respect to virtual displacements of the form (18) rather than the more restricted form in $\mathfrak{R}_1$. One can show that in this case the prolate asymmetric deformations are unstable while the conclusions on oblate asymmetric deformations remain unchanged. Thus, as shown in Fig. 2, an asymmetric equilibrium state is stable against pure homogeneous virtual displacements of the form (18) when $\alpha > 2^{1/3}$ and otherwise it is unstable. Further details of this analysis may be found in Rivlin (1948, 1974).

3.2 Cavitated Deformations: Ball's Analysis. Next we consider a subset $\mathfrak{B}$, obtained by setting $\alpha_2 = \alpha_3 = 1$ in $\mathfrak{D}$. In this case, all deformations in $\mathfrak{B}$ are of a spherical form:

$$y_1 = \psi(R)x_1, \quad y_2 = \psi(R)x_2, \quad y_3 = \psi(R)x_3, \tag{19}$$

where $\psi(R)$ is given by (6) and particularly β represents the cavity radius. The corresponding total potential is

$$U_{\mathfrak{B}}(\beta) = U_{\mathfrak{D}}(\beta, 1, 1) = (3/2)(1 + 2\beta^3)(1 + \beta^3)^{-1/3} - 3\sigma(1 + \beta^3)^{1/3}, \ \beta \geq 0, \tag{20}$$

and the stationary points are found from:

$$U'_{\mathfrak{B}}(\beta) = 3\beta^2(1 + \beta^3)^{-2/3}[(5 + 4\beta^3)(1 + \beta^3)^{-2/3}/2 - \sigma] = 0, \tag{21}$$

which yields two equilibrium solutions: the fundamental solution

$$\beta = 0, \tag{22}$$

and the cavitated solution

Downloaded 03 May 2010 to 171.66.16.245. Redistribution subject to ASME license or copyright; see http://www.asme.org/terms/Terms_Use.cfm

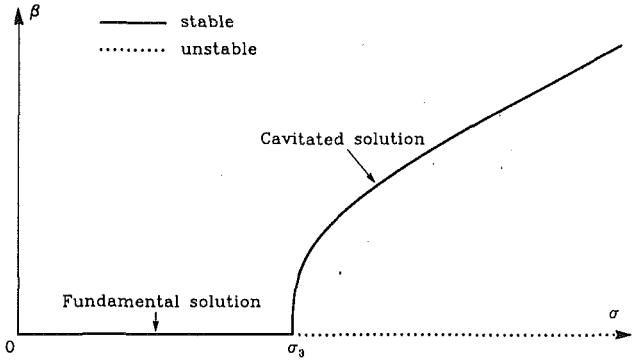


Fig. 3 Solutions in $\mathcal{B}$

$$\sigma = (5+4\beta^3)(1+\beta^3)^{-2/3}/2,\ \beta>0. \tag{23}$$

The cavitated solution corresponding to (23) exists only when $\sigma > \sigma_3 \equiv 5/2$; see Fig. 3.

The second derivative at the fundamental solution vanishes and the third one is

$$\frac{d^3U_{\mathcal{B}}}{d\beta^3} = 6\left(\frac{5}{2}-\sigma\right). \tag{24}$$

Thus, the fundamental deformation is stable against spherical virtual displacements when $\sigma < 5/2$ and it is unstable when $\sigma > 5/2$. The second derivative at the cavitated solution $\beta > 0$ is

$$\frac{d^2U_{\mathcal{B}}}{d\beta^2} = 3\beta^4\frac{1+2\beta^3}{(1+\beta^3)^{7/3}} > 0, \tag{25}$$

which shows that the cavitated deformation is stable against spherical virtual displacements whenever it exists ($\sigma > 5/2$). Figure 3 depicts the above results, with the solid portion of the curves corresponding to stable configurations and the dotted portion denoting unstable ones.

4 Axisymmetric Deformations

4.1 Equilibrium Configurations. In this section, we confine our attention to a subset $\mathcal{A}$ consisting of axisymmetric deformations in $\mathcal{D}$ with $\alpha_2 = \alpha_3 = \alpha$:

$$y_1 = \alpha^{-2}\psi(R)x_1,\quad y_2 = \alpha\psi(R)x_2,\quad y_3 = \alpha\psi(R)x_3, \tag{26}$$

where ψ is given by (6). The total potential is

$$\begin{aligned} U_{\mathcal{A}}(\beta,\alpha) &= U_{\mathcal{D}}(\beta,\alpha,\alpha)\\ &= (\alpha^{-4}+2\alpha^2)(1+2\beta^3)(1+\beta^3)^{-1/3}/2\\ &\quad -\sigma(\alpha^{-2}+2\alpha)(1+\beta^3)^{1/3}. \end{aligned} \tag{27}$$

The stationary points of $U_{\mathcal{A}}$ are found by solving the following pair of equations:

$$\begin{aligned} \frac{\partial U_{\mathcal{A}}}{\partial\beta} &= \frac{\beta^2}{(1+\beta^3)^{2/3}}\left[\left(\frac{1}{\alpha^4}+2\alpha^2\right)\frac{5+4\beta^3}{2(1+\beta^3)^{2/3}} - \sigma\left(\frac{1}{\alpha^2}+2\alpha\right)\right] = 0,\\ \frac{\partial U_{\mathcal{A}}}{\partial\alpha} &= 2(1+\beta^3)^{1/3}\left(1-\frac{1}{\alpha^3}\right)\left[\left(\frac{1}{\alpha^2}+\alpha\right)\frac{1+2\beta^3}{(1+\beta^3)^{2/3}} - \sigma\right] = 0. \end{aligned} \tag{28}$$

Each of the above equations contains two options; thus effectively we have four pairs of equations to solve and they lead to

(1) fundamental solution:

$$\beta = 0,\ \alpha = 1; \tag{29}$$

(2) asymmetric solution:

$$\beta = 0,\ \alpha^{-2}+\alpha-\sigma = 0; \tag{30}$$

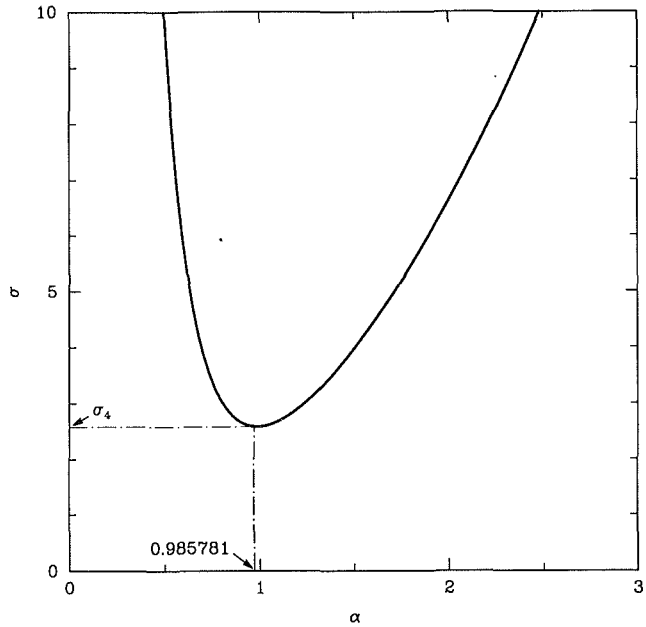


Fig. 4 A graph of σ versus α as given by (34)

(3) cavitated solution:

$$(5+4\beta^3)(1+\beta^3)^{-2/3}/2-\sigma = 0,\ \alpha = 1; \tag{31}$$

(4) nonspherical cavitated solution:

$$\begin{aligned} &(\alpha^{-4}+2\alpha^2)(5+4\beta^3)(1+\beta^3)^{-2/3}/2 - \sigma(\alpha^{-2}+2\alpha) = 0,\\ &(\alpha^{-2}+\alpha)(1+2\beta^3)(1+\beta^3)^{-2/3} - \sigma = 0. \end{aligned} \tag{32}$$

The first three provide the same solutions as those found in the analyses by Ball and Rivlin; here they are obtained simultaneously in one setting. The pair of Eqs. (32) describing nonspherical cavitated solutions can be cast into another equivalent form:

$$\beta^3 = \alpha^{-3}(2\alpha^6-2\alpha^3+1)/4, \tag{33}$$

$$\sigma = 2^{1/3}\alpha^{-3}(2\alpha^6+1)(\alpha^3+1)(2\alpha^6+2\alpha^3+1)^{-2/3}. \tag{34}$$

Given σ, Eq. (34) is to be solved for $\alpha > 0$ and then (33) gives the corresponding value of β. An analysis of Eq. (34) shows that it has two roots $\alpha > 0$ (see Fig. 4) if $\sigma > \sigma_4 \approx 2.58346$ and, corresponding to each α, Eq. (33) will assign a value to β. Therefore, Eqs. (33) and (34) give two distinct roots when $\sigma > \sigma_4$ with each one describing the formation of an ellipsoidal cavity.

4.2 Stability. If the matrix of second partial derivatives, often called the Hessian matrix, is positive definite at a stationary point, then that point represents a local minimum. If the Hessian matrix is singular at a stationary point, we proceed by examining the Taylor expansion of $U_{\mathcal{A}}$ in the vicinity of that point.

The Taylor expansion about the fundamental solution $\beta = 0$, $\alpha = 1$ gives

$$U_{\mathcal{A}} = 3/2-3\sigma+(5/2-\sigma)\beta^3+3(2-\sigma)(\alpha-1)^2+h.o.t. \tag{35}$$

Therefore the fundamental solution corresponds to a minimum when $\sigma < \sigma_2 \equiv 2$.

At the homogeneous asymmetric solution, the Taylor expansion around $\beta = 0$, $\alpha = a$, where a is a root of $(30)_2$, gives

$$\begin{aligned} U_{\mathcal{A}} = &-a^{-4}(2a^6+6a^3+1)/2+(a^{-4}/2)(2a^6-2a^3+1)\beta^3\\ &+a^{-6}(a^3-2)(a^3-1)(\alpha-a)^2+h.o.t., \end{aligned} \tag{36}$$

from which we conclude that the asymmetric solution corresponds to a minimum if the root $\alpha = a$ satisfies $a < 1$ or $a > 2^{1/3}$. Figure 1 describes the fundamental and asymmetric

Downloaded 03 May 2010 to 171.66.16.245. Redistribution subject to ASME license or copyright; see http://www.asme.org/terms/Terms_Use.cfm

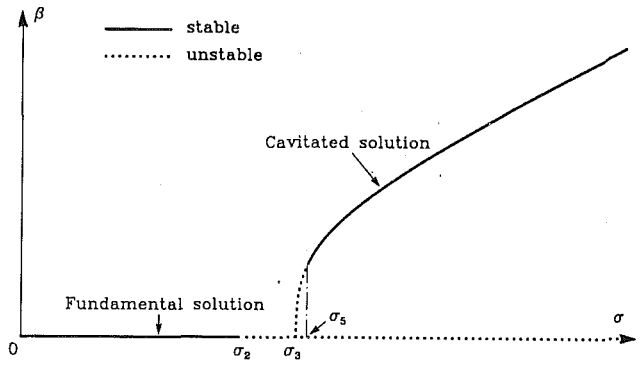


Fig. 5 Cavitated solution revised: a stable cavitated solution in spherical deformations may be unstable against a broader class of virtual displacements.

solutions with stable solutions characterized by solid curves and unstable ones by dotted curves.

At the cavitated solution $\beta = \rho$, $\alpha = 1$, where ρ is the root of $(31)_1$, the second derivative of $U_{\mathcal{A}}$ are

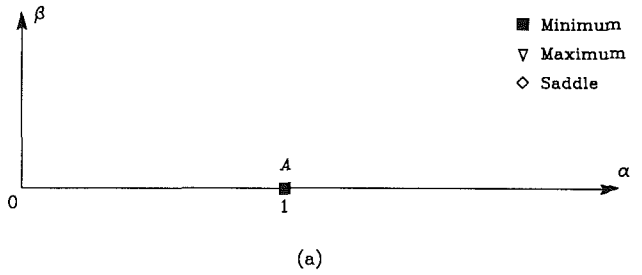
$$\frac{\partial^2 U_{\mathcal{A}}}{\partial \beta^2} = 3\rho^4 \frac{1+2\rho^3}{(1+\rho^3)^{7/3}}, \quad \frac{\partial^2 U_{\mathcal{A}}}{\partial \alpha^2} = 3\frac{4\rho^3-1}{(1+\rho^3)^{1/3}}, \quad \frac{\partial^2 U_{\mathcal{A}}}{\partial \beta \partial \alpha} = 0. \tag{37}$$

This solution represents a stable configuration if for a given value of σ, the cavitated solution $\beta = \rho$ satisfies $\rho > 4^{1/3}$ which occurs when $\sigma > \sigma_5 \equiv 6/5 \times 10^{1/3} \approx 2.58532$. Figure 5 describes the fundamental and cavitated solutions with stable solutions characterized by solid curves and unstable ones by dotted curves. It is interesting to compare Fig. 3 with Fig. 5 and to observe that the cavitated solution corresponding to a load σ in the range (σ_3, σ_5) which was found to be stable against spherical virtual displacements in $\mathcal{B}$ is now found to be unstable against the wider class of the virtual displacements in $\mathcal{A}$. In a recent paper, James and Spector (1991) showed that, for a large class of compressible materials, the cavitated solutions, which are stable in spherically symmetric deformations, are in fact unstable relative to the formation of filamentary voids.

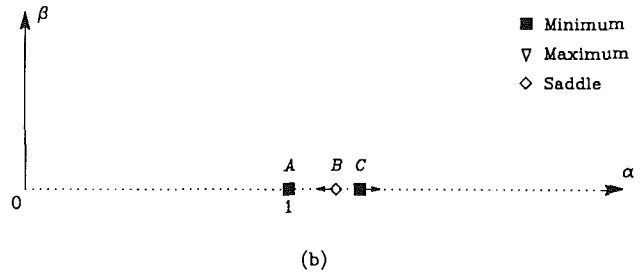
Finally we turn to the nonspherical cavitated solution. The Hessian matrix is positive definite if and only if

$$(1-a)(16a^{21}+8a^{18}-28a^{12}+12a^9+2a^6-4a^3-3)>0, \tag{38}$$

where $\alpha = a$ is a root of (34). The inequality (38) holds when $a_0 < a < 1$, where $a_0 \approx 0.985781$. Therefore the nonspherical cavitated solution $\alpha = a$ with β given by (33) is stable when $a_0 < a < 1$ which corresponds to a load σ in the range $\sigma_4 < \sigma < \sigma_5$. This stable configuration describes the occurrence of a prolate ellipsoidal cavity.

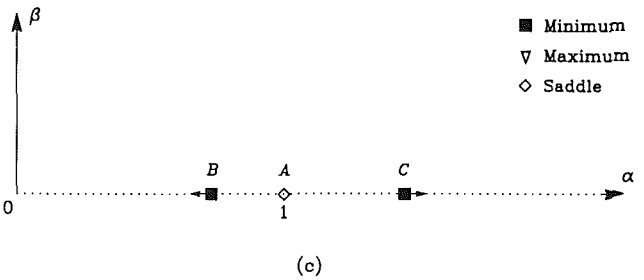


(a)

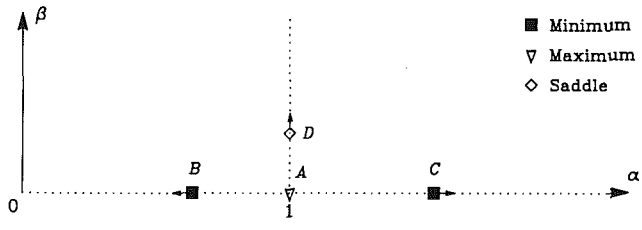


(b)

Fig. (*a*) $0 < \sigma < \sigma_1$; (*b*) $\sigma_1 < \sigma < \sigma_2$

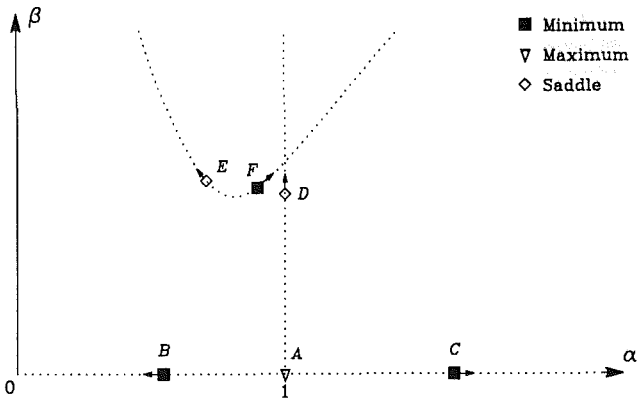


(c)

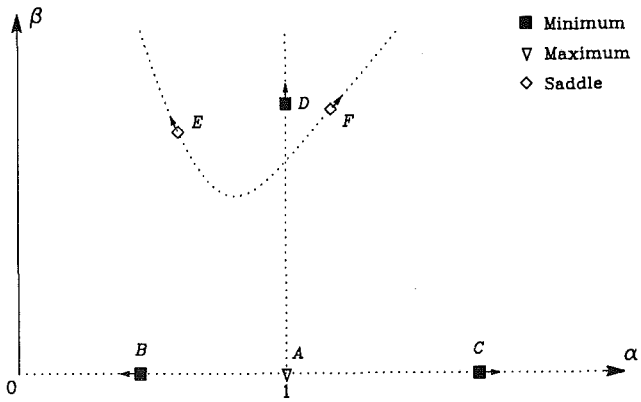


(d)

Fig. (*c*) $\sigma_2 < \sigma < \sigma_3$; (*d*) $\sigma_3 < \sigma < \sigma_4$



(e)



(f)

Fig. (*e*) $\sigma_4 < \sigma < \sigma_5$; (*f*) $\sigma_5 < \sigma$

Fig. 6 Stable and unstable equilibrium states

Downloaded 03 May 2010 to 171.66.16.245. Redistribution subject to ASME license or copyright; see http://www.asme.org/terms/Terms_Use.cfm

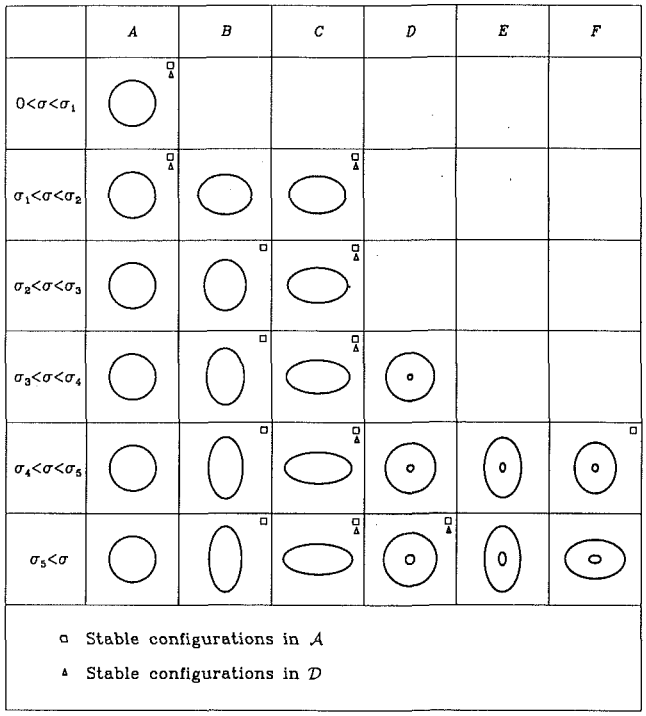


Fig. 7 Schematic representation of all equilibrium configurations with squares denoting stable ones in $\mathcal{A}$ and triangles denoting stable ones in $\mathcal{D}$, where $\sigma_1 \approx 1.89$, $\sigma_2 = 2$, $\sigma_3 = 2.5$, $\sigma_4 \approx 2.583$, $\sigma_5 \approx 2.585$

The above results are summarized in Fig. 6(*a*)-(*f*), where the stationary points (α, β) of $U_{\mathcal{A}}$ are shown. Each figure is drawn for a different range of the applied stress σ and an arrow denotes the moving direction of a stationary point (α, β) as the load σ increases; dotted curves are solution loci and they appear whenever any solutions on them come into existence. Local minima correspond to stable configurations. Figure 7 shows schematically the corresponding equilibrium shapes occupied by the deformed body (which was spherical in the undeformed configuration); all shapes are axisymmetric with respect to the vertical axis. Each row in Fig. 7 gives the equilibrium states available for that range of the applied load, and the columns are labeled by letters corresponding to those in Fig. 6, with stable configurations marked by squares. When $0 < \sigma < \sigma_1$, the only configuration is the fundamental one and it is stable. When $\sigma_1 < \sigma < \sigma_2$, there exist a stable fundamental solution, an unstable and a stable oblate asymmetric solutions. When $\sigma_2 < \sigma < \sigma_3$, there are an unstable fundamental solution, a stable prolate and a stable oblate asymmetric solutions. When $\sigma_3 < \sigma < \sigma_4$, there exist an unstable fundamental solution, a stable prolate and a stable oblate asymmetric solutions, and an unstable cavitated solution. When $\sigma_4 < \sigma < \sigma_5$, there exist an unstable fundamental solution, a stable prolate and a stable oblate asymmetric solutions, an unstable cavitated solution, an unstable and a stable prolate nonspherical cavitated solutions. When $\sigma_5 < \sigma$, there exist an unstable fundamental solution, a stable prolate and a stable oblate asymmetric solutions, a stable cavitated solution, an unstable prolate and an unstable oblate nonspherical cavitated solutions.

5 Three-Parameter Deformations

5.1 Equilibrium Configurations. Finally we consider all deformations in $\mathcal{D}$ with the corresponding total potential given by (10). The stationary points of $U_{\mathcal{D}}$ are found by solving the equations

$$\frac{\partial U_{\mathcal{D}}}{\partial \beta} = \frac{\beta^2}{(1+\beta^3)^{2/3}}\left[\left(\frac{1}{\alpha_2^2\alpha_3^2}+\alpha_2^2+\alpha_3^2\right)\frac{5+4\beta^3}{2(1+\beta^3)^{2/3}} - \sigma\left(\frac{1}{\alpha_2\alpha_3}+\alpha_2+\alpha_3\right)\right] = 0,$$

$$\frac{\partial U_{\mathcal{D}}}{\partial \alpha_2} = (1+\beta^3)^{1/3}\left(1-\frac{1}{\alpha_2^2\alpha_3}\right)\left[\left(\alpha_2+\frac{1}{\alpha_2\alpha_3}\right)\frac{1+2\beta^3}{(1+\beta^3)^{2/3}} - \sigma\right] = 0,$$

$$\frac{\partial U_{\mathcal{D}}}{\partial \alpha_3} = (1+\beta^3)^{1/3}\left(1-\frac{1}{\alpha_2\alpha_3^2}\right)\left[\left(\alpha_3+\frac{1}{\alpha_2\alpha_3}\right)\frac{1+2\beta^3}{(1+\beta^3)^{2/3}} - \sigma\right] = 0, \tag{39}$$

for β, α_2, α_3. Again each equation has two options; therefore there are eight triplets of equations to solve. However, out of these eight combinations, four can be ignored because they simply give cyclic permutations and imply $\alpha_2 = \alpha_3$. The remaining four pairs of equations are identical with those four pairs obtained in the previous section for axisymmetric deformations. Thus, apart from a cyclic permutation, two sets of deformations in $\mathcal{A}$ and $\mathcal{D}$ result in the same equilibrium states given by (29)-(32) with $\alpha_2 = \alpha_3 = \alpha$. In what follows, we examine the stability in the same order as in the axisymmetric case.

5.2 Stability. At the fundamental solution, the Taylor expansion about $\beta = 0$, $\alpha_2 = \alpha_3 = 1$ yields

$$U_{\mathcal{D}} = 3/2 - 3\sigma + (5/2-\sigma)\beta^3 + (2-\sigma)[(\alpha_2-1)^2 + (\alpha_2-1)(\alpha_3-1) + (\alpha_3-1)^2] + h.o.t. \tag{40}$$

Therefore the fundamental solution is stable when $\sigma < \sigma_2 \equiv 2$.

At the asymmetric solution $\beta = 0$, $\alpha_2 = \alpha_3 = a$, the Taylor expansion gives

$$U_{\mathcal{D}} = -(a^{-4}/2 + 3a^{-1} + a^2) + (a^{-4}/2)(2a^6 - 2a^3 + 1)\beta^3 + (a^{-6}/2)(1-a^3)^2(\alpha_2-a)^2 + a^{-6}(1-a^3)(\alpha_2-a)(\alpha_3-a) + (a^{-6}/2)(1-a^3)^2(\alpha_3-a)^2 + h.o.t. \tag{41}$$

Therefore the asymmetric solution is stable if $\alpha_2 = \alpha_3 = \alpha = a$ satisfies $a > 2^{1/3}$ which corresponds to the load $\sigma > \sigma_1$. Note that this widening of the virtual displacement field eliminates the prolate-type of asymmetric solutions from stable solutions.

At the cavitated solution $\beta = \rho$, $\alpha_2 = \alpha_3 = 1$, the second derivatives are

$$\frac{\partial^2 U_{\mathcal{D}}}{\partial \beta^2} = 3\rho^4\frac{1+2\rho^3}{(1+\rho^3)^{7/3}},\quad \frac{\partial^2 U_{\mathcal{D}}}{\partial \alpha_2^2} = \frac{\partial^2 U_{\mathcal{D}}}{\partial \alpha_3^2} = \frac{4\rho^3-1}{(1+\rho^3)^{1/3}},$$
$$\frac{\partial^2 U_{\mathcal{D}}}{\partial \beta \partial \alpha_2} = \frac{\partial^2 U_{\mathcal{D}}}{\partial \beta \partial \alpha_3} = 0.\quad \frac{\partial^2 U_{\mathcal{D}}}{\partial \alpha_2 \partial \alpha_3} = \frac{4\rho^3-1}{2(1+\rho^3)^{1/3}}. \tag{42}$$

Therefore the cavitated solution represents a stable configuration if for a given value of σ, $\beta = \rho$ satisfies $\rho > 4^{1/3}$ which occurs when $\sigma > \sigma_5$, the same as that in the axisymmetric case.

At the nonspherical cavitated solution $\alpha_2 = \alpha_3 = \alpha = a$ with β given by (33), the condition for positive definiteness of the Hessian matrix reduces to the following inequalities:

$$a^3 - 2 > 0, \text{ and } 8a^{15} + 12a^{12} + 8a^9 - 12a^6 - 10a^3 - 3 < 0. \tag{43}$$

An examination of the above inequalities concludes that they are never satisfied. Thus, the widening of the virtual displacement field renders the prolate nonspherical cavitated solutions found stable in the axisymmetric case unstable.

From the above analysis, we see that although no new equilibrium states emerge in response to the widening of the deformation field, the stability of the solutions, however, has been affected. All prolate-type of solutions in $\mathcal{D}$ are unstable.

Downloaded 03 May 2010 to 171.66.16.245. Redistribution subject to ASME license or copyright; see http://www.asme.org/terms/Terms_Use.cfm

All equilibrium configurations are schematically shown in Fig. 7 where the stable ones are denoted by triangles. When $0 < \sigma < \sigma_1$, there is a stable fundamental solution; when $\sigma_1 < \sigma < \sigma_2$, there exist a stable fundamental solution and a stable oblate asymmetric solution; when $\sigma_2 < \sigma < \sigma_5$, there only exists a stable oblate asymmetric solution; when $\sigma > \sigma_5$, there exist a stable oblate asymmetric solution and a stable cavitated solution.

Acknowledgment

This work is based on a topic in a Ph.D. thesis. The author wishes to express his sincere appreciation of Prof. Rohan Abeyaratne for his advice and guidance. The partial support of the U.S. Army Research Office is gratefully acknowledged. The computer code *Mathematica* (Wolfram, 1988) facilitated the symbolical and numerical manipulations.

References

Abeyaratne, R., and Hou, H. S., 1991, "On the Occurrence of the Cavitation Instability Relative to the Asymmetric Instability Under Symmetric Dead Load Conditions," *Quarterly Journal of Mechanics and Applied Mathematics*, Vol. 44, pp. 429–450.

Ashby, M. F., Blunt, F. J., and Bannister, M., 1989, "Flow Characteristics of Highly Constrained Metal Wires," *Acta Metallurgica*, Vol. 37, pp. 1847–1857.

Ball, J. M., 1982, "Discontinuous Equilibrium Solutions and Cavitation in Nonlinear Elasticity," *Philosophical Transactions of the Royal Society of London*, Vol. A306, pp. 557–611.

Ball, J. M., and Schaeffer, D. G., 1983, "Bifurcation and Stability of Homogeneous Equilibrium Configurations of an Elastic Body Under Dead-Load Tractions," *Mathematical Proceedings of the Cambridge Philosophical Society*, Vol. 94, pp. 315–339.

Chen, Y. C., 1988, "Stability of Pure Homogeneous Deformations of an Elastic Plate with Fixed Edges," *Quarterly Journal of Mechanics and Applied Mathematics*, Vol. 41, pp. 249–264.

Chen, Y. C., 1987, "Stability of Homogeneous Deformations of an Incompressible Elastic Body Under Dead-Load Surface Tractions," *Journal of Elasticity*, Vol. 17, pp. 223–248.

Gent, A. N., and Lindley, P. B., 1958, "Internal Rupture of Bonded Cylinders in Tension," *Proceedings of the Royal Society of London*, Vol. A249, pp. 195–205.

James, R. D., and Spector, S. J., 1991, "The Formation of Filamentary Voids in Solids," *Journal of the Mechanics and Physics of Solids*, Vol. 39, pp. 783–813.

Kearsley, E. A., 1986, "Asymmetric Stretching of a Symmetrically Loaded Elastic Sheet," *International Journal of Solids and Structures*, Vol. 22, pp. 111–119.

MacSithigh, G. P., 1986, "Energy-Minimal Finite Deformations of a Symmetrically Loaded Elastic Sheet," *Quarterly Journal of Mechanics and Applied Mathematics*, Vol. 39, pp. 111–123.

Rivlin, R. S., 1974, "Stability of Pure Homogeneous Deformation of an Elastic Cube Under Dead Loading," *Quarterly of Applied Mathematics*, Vol. 32, pp. 265–271.

Rivlin, R. S., 1948, "Large Elastic Deformations of Isotropic Materials, II. Some Uniqueness Theorems for Pure Homogeneous Deformation," *Philosophical Transactions of the Royal Society of London*, Vol. A240, pp. 491–508.

Treloar, L. R. G., 1948, "Stresses and Birefringence in Rubber Subjected to General Homogeneous Strain," *Proceedings of the Physical Society London*, Vol. 60, pp. 135–144.

Wolfram, S., 1988, *Mathematica*, Addison-Wesley.

Downloaded 03 May 2010 to 171.66.16.245. Redistribution subject to ASME license or copyright; see http://www.asme.org/terms/Terms_Use.cfm

Effective Mechanical Properties of Composites at Finite Deformations

N. Fares
Civil Engineering Department,
Polytechnic University,
Brooklyn, NY 11201

A new representation theorem for the deformation gradient rate in the presence of cracks and kinematic constraints is presented. This representation theorem uses an extension of the concept of transformation strains to finite deformations. Based on the representation theorem the overall concentration factor was decomposed into contributions from the opening and sliding of cracks and from material nonhomogeneities. Also, inelastic deformations at the microscale were related to those at the macroscale through elastic concentration factors, where it was found that some of the elastic deformation at the microscale may contribute to the macroscale inelastic deformations.

Introduction

This paper considers some theoretical principles concerning the determination of the effective mechanical properties of composites at finite deformations. Various simple models for the linear elastic properties of composites have been proposed; e.g., Voigt and Reuss models, the Budiansky-Hill-Kroner self-consistent method (Hill, 1965; Budiansky, 1965), and the Mori-Tanaka method (1973). These methods have also been extended to elasto-plastic properties with infinitesimal and finite deformation formulations. In particular, the self-consistent method has been applied to infinitesimal deformation elasto-plasticity by Hutchinson (1970) and by Berveiller and Zaoui (1979) and to finite elastic-plastic deformations by Iwakuma and Nemat-Nasser (1984). Extensions of the self-consistent method to multiple inclusion interactions and infinitesimal deformations have been discussed by Berveiller and Zaoui (1984), Berveiller et al. (1987), and Fassi-Fehri et al. (1989) and to finite deformations by Lipinski and Berveiller (1989).

The determination of the effective properties of a composite having multiple phases is directly related to the determination of concentration factors (Hill, 1963). Concentration factors relate either the overall deformations or the overall stresses to local ones. The self-consistent and Mori-Tanaka methods may be viewed as methods which approximate the actual phase concentration factors with those of particularly chosen inclusion problems. In the process of determining concentration factors, the response of a representative volume to homogeneous stresses or deformations may be considered. Due to the possible statistical nature of microheterogeneity, various realizations of representative volumes may be required (i.e., an "ensemble" average may be needed).

Several approaches may be used to obtain the response of particular representative volumes. The finite element method (Teply and Dvorak, 1988) as well as Fourier analysis (Nemat-Nasser et al., 1982) have been used to obtain the response of representative volumes with periodic structure. An alternative approach relies on integral representation theorems with the use of Green's functions (Dederichs and Zeller, 1973; Willis, 1977; Kroner, 1977; Lipinski and Berveiller, 1989; Walker et al., 1989; Fassi-Fehri et al., 1989). The use of representation theorems in computational mechanics is well known. One numerical technique based on representation theorems is the boundary element method (BEM). The BEM has been successfully used to study elastic and inelastic problems in small deformation theories (e.g., Banerjee and Butterfield, 1981) and has recently been extended to large deformation problems (Chandra and Mukherjee, 1983; Okada et al., 1989, 1990).

This paper presents a derivation of a representation theorem applicable to finite deformation problems in regions which may contain cracks as well as phases subject to kinematical constraints such as incompressibility or perfect rigidity. The representation theorem will be based on extending the concept of transformation strains to finite deformations and will emphasize the significance of a generalized Eshelby tensor in such formulations. A formal structure of the finite deformation effective properties of an elastically or inelastically deforming medium will be obtained based on the use of concentration factors. The representation theorem is then use to delineate the effect of cracks and material nonhomogeneities on concentration factors. Also, a discussion of the role of concentration factors in relating inelastic deformations at the microscale with those at the macroscale will be presented. In this paper, the macroscale variables refer to the observed values of those variables when the composite is modeled as a homogeneous medium, while the microscale variables refers to the local values of those variables when the heterogeneity of the composite is retained (e.g., Hill 1972, 1984, 1985).

Contributed by the Applied Mechanics Division of THE AMERICAN SOCIETY OF MECHANICAL ENGINEERS for publication in the ASME JOURNAL OF APPLIED MECHANICS.

Discussion on this paper should be addressed to the Technical Editor, Professor Lewis T. Wheeler, Department of Mechanical Engineering, University of Houston, Houston, TX 77204-4792, and will be accepted until four months after final publication of the paper itself in the ASME JOURNAL OF APPLIED MECHANICS.

Manuscript received by the ASME Applied Mechanics Division, May 14, 1991; final revision, Oct. 15, 1991. Associate Technical Editor: S. K. Datta.

Copyright © 1993 by ASME
Downloaded 03 May 2010 to 171.66.16.245. Redistribution subject to ASME license or copyright; see http://www.asme.org/terms/Terms_Use.cfm

General Theory

1 Basic Concepts. In the discussions, the same fixed Cartesian frame locating points in both the reference and deformed configurations will be used. Vectors and tensors will be boldfaced and components of those will be written in normal type and indexed. The position vector to a material point in the reference and current configurations will be noted by $\mathbf{X}$ and $\mathbf{x}$, respectively. The average quantity of a given tensor $\mathbf{Z}$ over the reference volume will be denoted by $\langle \mathbf{Z} \rangle$. Also, the summation convention for repeated indices, comma notation for partial differentiation with respect to position, and an overhead dot to denote a material time derivative will be used.

A Lagrangian description is chosen and hence all material point field variables, including the current position vector $\mathbf{x}$ and velocity vector $\mathbf{v}$, are expressed as a function of the reference configuration position vector. Consequently, spatial derivatives are with respect to the reference configuration. An Eulerian formulation may be obtained by instantaneously choosing the reference configuration as the current one and by relating the associated field variables.

Following Hill (1972, 1985), the nominal stress and deformation gradient rates denoted by $\dot{\mathbf{S}}$ and $\dot{\mathbf{F}}$, respectively, will be chosen as the conjugate variables. This is because whenever $\dot{\mathbf{S}}$ and $\dot{\mathbf{F}}$ are self-equilibrated and self-compatible, respectively, the following results hold (Hill, 1972, 1985): The reference volume averages of $\dot{\mathbf{S}}$ and $\dot{\mathbf{F}}$ are uniquely determined from their boundary values; the reference volume average of their product is equal to the product of their respective averages when the boundary values of either $\dot{\mathbf{S}}$ or $\dot{\mathbf{F}}$ are uniform. Accordingly, this choice of conjugate variables has been adopted in the constitutive description of polycrystals by Asaro (1979) and Iwakuma and Nemat-Nasser (1984). When the reference configuration instantaneously coincides with the current one, we have

$$\mathbf{S} = \boldsymbol{\sigma} \tag{1}$$

$$\dot{\mathbf{S}} = \dot{\boldsymbol{\sigma}} + \mathrm{tr}(\mathbf{L})\boldsymbol{\sigma} - \mathbf{L} \cdot \boldsymbol{\sigma} \tag{2}$$

$$\dot{\mathbf{F}} = \mathbf{L} \tag{3}$$

where $\boldsymbol{\sigma}$ is Cauchy's stress, $\mathbf{L}$ is the velocity gradient, tr( ) is the trace operator, and the components of $\mathbf{L} \cdot \boldsymbol{\sigma}$ are given by $L_{ik}\sigma_{ki}$.

An incremental constitutive relation between $\dot{\mathbf{S}}$ and $\dot{\mathbf{F}}$ may be specified by

$$\dot{\mathbf{S}}^T = \mathbf{K} : \dot{\mathbf{F}} \Leftrightarrow \dot{S}_{ji} = K_{ijkl}\dot{F}_{kl} \tag{4}$$

where the superscript T means the transpose and $\mathbf{K}$ may vary with position and may depend on the current state as monitored by the current value of the nominal stress, deformation gradient, deformation gradient rate, and any number of internal variables. The tensor $\mathbf{K}$ is Lagrangian in its outer indices and Eulerian in its inner indices and will be referred to as the stiffness tensor. Thus, in order for the constitutive relation (4) to be objective, the specification of $\mathbf{K}$ has to be such that it evolves with the deformation as an Eulerian objective tensor in its inner indices. In practice, the tensor $\mathbf{K}$ may be deduced from objective constitutive relations specified in terms of more convenient objective stress rate and deformation rate measures such as the second Piolla-Kirchoff stress rate and Green-Lagrange strain rate and rewritten in the form of Eq. (4) through the use of kinematic relations. Such manipulations have been done by Iwakuma and Nemat-Nasser (1984) in order to obtain the $\mathbf{K}$ appropriate to single crystal plasticity. In general, $\mathbf{K}$ is not symmetric with respect to interchange of any of its indices.

Relation (4) assumes that the nominal stress rate may be fully determined from the deformation gradient rate and the current state. This assumption does not apply when the deformation is subject to local kinematic constraints. For example, the mean stress cannot be determined when the medium is incompressible, and no components of the stress rate can be determined from the deformation gradient rate if the material is perfectly rigid. Note that even though a subregion of a representative volume may be subject to local constraints, a relation of the form (4) may still apply between the average nominal stress rate $\langle \dot{\mathbf{S}} \rangle$ and the average deformation gradient rate $\langle \dot{\mathbf{F}} \rangle$. For example, it should be possible to obtain the effective stiffness of a deformable medium containing rigid inclusions. In the presence of local constraints, relation (4) has to be modified as follows:

$$\dot{\mathbf{S}}^T = \mathbf{K} : \dot{\mathbf{F}} + \sum_{i=1}^{n \le 6} q^{(i)} \dot{\mathbf{S}}^{*(i)T} \tag{5}$$

where each $\dot{\mathbf{S}}^{(i)*T}$ are specified in terms of the current state and $q^{(i)}$ are scalars which cannot be determined from the kinematics. Each $\dot{\mathbf{S}}^{(i)*T}$ is an independent stress mode which corresponds to a separate local kinematic constraint. At most six kinematic constraints may be specified and occur when the material is perfectly rigid. In that case, the deformation gradient rate consists of a pure rate of rotation and $\mathbf{K}$ only accounts for these.

In studying the effective properties of a composite medium it is convenient to introduce the concept of comparison medium. A comparison medium is specified by a stiffness $\mathbf{K}^0$ which may be nonuniformly defined over the representative volume but which does not depend on the deformation gradient rate. Unlike the stiffness defined in Eqs. (4) and (5), $\mathbf{K}^0$ is defined such that

$$\dot{\mathbf{S}}^T = \dot{\mathbf{F}} : \mathbf{K}^0. \tag{6}$$

Furthermore, $\mathbf{K}^{0\text{-}1}$ is assumed to exist such that $\mathbf{K}^{0\text{-}1} : \mathbf{K}^0 = \mathbf{I}$ where $\mathbf{I}$ is the fourth-order identity tensor, and that for any choice of $\Delta\dot{\mathbf{F}} \neq \mathbf{0}$, $\mathbf{K}^0$ be such that:

$$\Delta\dot{\mathbf{F}} : \mathbf{K}^0 : \Delta\dot{\mathbf{F}} > \mathbf{0} \Leftrightarrow \Delta\dot{\mathbf{S}}^T : \Delta\dot{\mathbf{F}} > 0. \tag{7}$$

The need for the above restrictions on $\mathbf{K}^0$ will be explained later. It is to be noted, however, that a representative volume having a stiffness $\mathbf{K}^0$ satisfying the above restrictions will have a unique solution for $\dot{\mathbf{S}}$ and $\dot{\mathbf{F}}$ under a uniformly applied deformation gradient rate. However, the restrictions on $\mathbf{K}^0$ are not all necessary for the existence of such a unique solution. An extensive discussion of the uniqueness of solutions on this type of problem is given by Hill (1985). In some instances, the representative volume may be partitioned into phases such that the mechanical properties in each phase are initially uniform. Such is the case in a fibrous composite medium where the properties in each of the fibers and matrix are initially uniform. However, even when initially uniform phases can be identified, nonhomogeneous elastic and/or inelastic finite deformations may lead to a nonuniform instantaneous stiffness within the phases. Thus, a natural choice of a uniform $\mathbf{K}^0$ may not be apparent. If a uniform $\mathbf{K}^0$ is desired, a convenient choice may be the transpose of the initial instantaneous elastic stiffness of the matrix phase.

The concept which is to be associated with a comparison stiffness $\mathbf{K}^0$ is that of a transformation deformation gradient rate denoted by $\dot{\mathbf{F}}^{tr}$. This is an extension of transformation strain or eigenstrain introduced by Eshelby in small deformation theories.

Let $\dot{\mathbf{S}}$ and $\dot{\mathbf{F}}$ be the actual nominal stress and deformation gradient rates at a given point having a constitutive description of the form given by relation (5). $\dot{\mathbf{S}}^{pol}$ is then defined as

$$\dot{\mathbf{S}}^{polT} = \dot{\mathbf{S}}^T - \mathbf{K}^0 : \dot{\mathbf{F}}. \tag{8}$$

The tensor analogous to $\dot{\mathbf{S}}^{pol}$ in small deformation theories is known as the polarization stress in the composites research literature (e.g., Willis, 1977) and as the moment density tensor in the geophysical literature (e.g., Rice, 1980). $\dot{\mathbf{F}}^{tr}$ is then defined as

$$\dot{\mathbf{S}}^{polT} = -\mathbf{K}^0 : \dot{\mathbf{F}}^{tr} \Leftrightarrow \dot{\mathbf{F}}^{tr} = -\mathbf{K}^{0\text{-}1} : \dot{\mathbf{S}}^{polT}. \tag{9}$$

Downloaded 03 May 2010 to 171.66.16.245. Redistribution subject to ASME license or copyright; see http://www.asme.org/terms/Terms_Use.cfm

Note that the definition of $\dot{\mathbf{F}}^{tr}$ requires the existence of $\mathbf{K}^{0-1}$ which is a prerequisite for the choice of $\mathbf{K}^0$. Substituting Eq. (9) into Eq. (8) and rearranging we obtain

$$\dot{\mathbf{S}}^T = \mathbf{K}^0 : (\dot{\mathbf{F}} - \dot{\mathbf{F}}^{tr}) \tag{10a}$$

and

$$\mathbf{K}^0 : (\dot{\mathbf{F}} - \dot{\mathbf{F}}^{tr}) = \mathbf{K} : \dot{\mathbf{F}} + \sum_{i=1}^{n\le 6} q^{(i)} \dot{\mathbf{S}}^{*(i)T}. \tag{10b}$$

Since $\mathbf{K}^0$ is invertible, Eq. (10) can then be solved for $\dot{\mathbf{F}}^{tr}$:

$$\dot{\mathbf{F}}^{tr} = (\mathbf{I} - \mathbf{K}^{0-1} : \mathbf{K}) : \dot{\mathbf{F}} - \sum_{i=1}^{n\le 6} (q^{(i)} \mathbf{K}^{0-1} : \dot{\mathbf{S}}^{*(i)T}). \tag{11}$$

It is emphasized that $\dot{\mathbf{F}}^{tr}$ is not part of the kinematics and thus does not affect the deformation gradient or its rate. $\dot{\mathbf{F}}^{tr}$ is simply a convenient field variable which is used to measure the difference between the actual stress rate and the one predicted by the comparison medium. The physical interpretation of transformation strains discussed by Eshelby for infinitesimal deformations may be similarly pursued in the present case of finite deformations using $\dot{\mathbf{F}}^{tr}$. $\Delta\mathbf{F}^{tr}$ may be interpreted as an a priori deformation gradient that needs to be imposed on a given material element in order to kinematically fit the location and shape it presently occupies at the current state of stress.

In the present discussion of effective properties, the possibility of cracks occurring in the representative volume is allowed. A crack is an internal planar or curved surface defined over the reference configuration across which a displacement and/or velocity discontinuity may occur. By convention, one face of a crack will be called the positive side and the other one called the negative side. Collectively, the positive and negative faces of the cracks will be denoted by A_c^+ and A_c^-, respectively. The corresponding unit normals to the crack faces pointing away from the cracks will be denoted by $\mathbf{N}^+$ and $\mathbf{N}^-$. Tractions are required to be continuous across crack surfaces. This allows for pressurized, frictional, and traction-free cracks but excludes the possibility of having only one face of a given crack being loaded. Thus the following relations are obtained:

$$\Delta\mathbf{v} = \mathbf{v}|_{A_c^+} - \mathbf{v}|_{A_c^-} \neq \mathbf{0} \quad \text{on } A_c \text{ (in general)} \tag{12}$$

$$\mathbf{N}^+ \cdot \mathbf{S} + \mathbf{N}^- \cdot \dot{\mathbf{S}} = \mathbf{0} \qquad \text{on } A_c. \tag{13}$$

It is noted that in a finite deformation analysis, a crack may become a cavity. However, in the present Lagrangian description the crack is always a specified surface over the reference configuration.

It is possible to treat cracks as surfaces over which Dirac singular transformation gradient rates $\dot{\mathbf{F}}^{tr}$ may occur. Such a point of view has been adopted in some small deformation geophysical studies (e.g., Rice, 1980). Similarly, in small deformation studies of the effective properties of materials containing cracks, transformation strains were used to study elliptical and circular cracks as limiting cases of ellipsoidal cavities (Walsh, 1969; Laws, 1977; Laws et al., 1983). In this study, cracks will be directly considered whereas cavities will be assumed to be accounted for by transformation strains. Finally, it is noted that the comparison medium will be assumed not to contain any cracks.

2 Representation Theorem. The derivation of representation theorems requires the use of Green's functions. These functions are usually obtained by solving certain linear boundary value problems. Since the governing equations in terms of the velocity for the actual material may be nonlinear, the Green's functions derived will be relative to the comparison medium. Let $\mathbf{G}^k$, $\overline{\mathbf{G}}^k$, and $\overline{\overline{\mathbf{G}}}^k$ be the velocity, deformation gradient rate, and nominal stress rate of a comparison medium so that

$$\overline{\mathbf{G}}^k = \mathbf{G}^k \nabla \Leftrightarrow \overline{G}^k_{ij} = G^k_{i,j} \tag{14}$$

$$\overline{\overline{\mathbf{G}}}^{kT} = \overline{\mathbf{G}}^k : \mathbf{K}^0 \Leftrightarrow \overline{\overline{G}}^k_{ji} = K^0_{rsij} \overline{G}^k_{rs} \tag{15}$$

$$\nabla \cdot \overline{\overline{\mathbf{G}}}^k(\mathbf{X},\mathbf{X}') = -\mathbf{e}^k \delta^D(\mathbf{X} - \mathbf{X}') \Leftrightarrow \overline{\overline{G}}^k_{ij,i} = -\delta_{kj} \delta^D(X_s - X_s') \tag{16}$$

either $\mathbf{G}^k = 0$ on all the boundary of the representative volume (17*a*)

or $\mathbf{N} \cdot \overline{\overline{\mathbf{G}}}^k = 0$ on all the boundary of the representative volume (17*b*)

where $\mathbf{e}^k$ is a unit vector in the direction of the positive "k" coordinate axis, δ^D is Dirac's delta, δ_{kl} is Kronecker's delta, $\mathbf{X}'$ is any point inside the representative volume, and $\mathbf{N}$ is a unit normal to the outer boundary pointing outside the representative volume. The Green's functions correspond to the response of the comparison medium under an applied unit point force. Note that since $\mathbf{K}^0$ is chosen to be independent of the deformation gradient rate, the boundary value problem described by Eqs. (14) to (17) is linear. In addition, due to the restriction given by Eq. (7), the boundary value problem is elliptic and admits a unique solution defined everywhere except at $\mathbf{X} = \mathbf{X}'$ where a singularity exists. Loss of ellipticity of the governing equations is related to localization phenomena and loss of stability. The relation between the structure of Green's functions and loss of stability was first noted by Iwakuma and Nemat-Nasser (1984) in the context of a uniformly stressed polycrystal.

The representative volume may be subject to either a uniform deformation gradient rate or to a uniform nominal stress rate. Accordingly, boundary conditions (17*a*) and (17*b*) will be chosen respectively. When the representative volume is unbounded, both conditions (17*a*) and (17*b*) apply at infinity. When the comparison medium is homogeneous and the representative volume is unbounded, the Green's functions are easier to obtain and are invariant under the simultaneous translation of $\mathbf{X}$ and $\mathbf{X}'$. For example, for uniform $\mathbf{K}^0$ and boundaries at infinity,

$$\mathbf{G}^k(\mathbf{X},\mathbf{X}') = \mathbf{G}^k(\mathbf{X} - \mathbf{X}', \mathbf{0}). \tag{18}$$

The derivation of the representation theorem is now outlined. Using Eqs. (10) and (15) the following relation is obtained:

$$\overline{\mathbf{G}}^k : \mathbf{K}^0 : \dot{\mathbf{F}} = \overline{\overline{\mathbf{G}}}^{kT} : \dot{\mathbf{F}} = \overline{\mathbf{G}}^k : (\dot{\mathbf{S}}^T + \mathbf{K}^0 : \dot{\mathbf{F}}^{tr}). \tag{19}$$

By noting that whenever $\dot{\mathbf{S}}^{(1)}$ is in equilibrium and $\dot{\mathbf{F}}^{(2)}$ is compatible, there is the following identity:

$$\dot{\mathbf{S}}^{T(1)} : \dot{\mathbf{F}}^{(2)} = \nabla \cdot (\dot{\mathbf{S}}^{T(1)} \cdot \mathbf{v}^{(2)}) - (\nabla \cdot \dot{\mathbf{S}}^{(1)}) \cdot \mathbf{v}^{(2)} = \nabla \cdot (\dot{\mathbf{S}}^{T(1)} \cdot \mathbf{v}^{(2)}). \tag{20}$$

Equation (19) is then transformed to

$$\nabla \cdot (\overline{\overline{\mathbf{G}}}^k \cdot \mathbf{v}) = \nabla \cdot (\dot{\mathbf{S}} \cdot \mathbf{G}^k) + \overline{\overline{\mathbf{G}}}^k : \dot{\mathbf{F}}^{trT}. \tag{21}$$

Equation (21) is defined everywhere inside the representative volume except at point $\mathbf{X} = \mathbf{X}'$ where the Green's functions are singular. Let V_ϵ be a small sphere of radius ϵ surrounding the point $\mathbf{X}'$. Equation (21) can be integrated over the representative volume V excluding the region V_ϵ, then by using the divergence theorem, Eqs. (12) and (13) and the remark that the comparison medium does not contain any cracks the following relations are obtained:

$$\int_A \mathbf{N} \cdot \overline{\overline{\mathbf{G}}}^k \cdot \mathbf{v} dA - \int_{A_\epsilon} \mathbf{N} \cdot \overline{\overline{\mathbf{G}}}^k \cdot \mathbf{v} dA - \int_{A_c} \mathbf{N}^+ \cdot \overline{\overline{\mathbf{G}}}^k \cdot \Delta\mathbf{v} dA = \int_A \mathbf{N} \cdot \dot{\mathbf{S}} \cdot \mathbf{G}^k dA - \int_{A_\epsilon} \mathbf{N} \cdot \dot{\mathbf{S}} \cdot \mathbf{G}^k dA + \int_{V - V_\epsilon} \overline{\overline{\mathbf{G}}}^k : \dot{\mathbf{F}}^{trT} dV \tag{22}$$

where A is the outer boundary of the representative volume. By noting relation (16) of the Green's function, considering

Downloaded 03 May 2010 to 171.66.16.245. Redistribution subject to ASME license or copyright; see http://www.asme.org/terms/Terms_Use.cfm

the level of singularity of $\mathbf{G}^k$, and taking the limit as ϵ tends to zero, the following is obtained:

$$\int_{A_\epsilon} \mathbf{N}\cdot\overline{\overline{\mathbf{G}}}^k\cdot\mathbf{v}dA = \mathbf{e}^k\cdot\mathbf{v}(\mathbf{X}',t) \tag{23}$$

$$\int_{A_\epsilon} \mathbf{N}\cdot\dot{\mathbf{S}}\cdot\mathbf{G}^k dA = 0. \tag{24}$$

Substitution of Eqs. (23) and (24) in (22) results in

$$\mathbf{e}^k\cdot\mathbf{v}(\mathbf{X}',t) = \int_A \mathbf{N}\cdot\overline{\overline{\mathbf{G}}}^k\cdot\mathbf{v}dA - \int_A \mathbf{N}\cdot\dot{\mathbf{S}}\cdot\mathbf{G}^k dA - \int_{A_c} \mathbf{N}^+\cdot\overline{\overline{\mathbf{G}}}^k\cdot\Delta\mathbf{v}dA - \int_{V-V_\epsilon} \overline{\overline{\mathbf{G}}}^k:\dot{\mathbf{F}}^{\mathrm{tr}T}dV. \tag{25}$$

When $\dot{\mathbf{F}}^{\mathrm{tr}} = 0$ and $\Delta\mathbf{v} = 0$, Eq. (25) should give us the response $\mathbf{v}^0$ of the comparison medium under the particular boundary conditions of the problem, thus

$$\mathbf{e}^k\cdot\mathbf{v}^0(\mathbf{X}',t) = \int_A \mathbf{N}\cdot\overline{\overline{\mathbf{G}}}^k\cdot\mathbf{v}dA - \int_A \mathbf{N}\cdot\dot{\mathbf{S}}\cdot\mathbf{G}^k dA \tag{26}$$

$$\mathbf{e}^k\cdot\mathbf{v}(\mathbf{X}',t) = \mathbf{e}^k\cdot\mathbf{v}^0(\mathbf{X}',t) - \int_{A_c} \mathbf{N}^+\cdot\overline{\overline{\mathbf{G}}}^k\cdot\Delta\mathbf{v}dA - \int_{V-V_\epsilon} \overline{\overline{\mathbf{G}}}^k:\dot{\mathbf{F}}^{\mathrm{tr}T}dV. \tag{27}$$

$\boldsymbol{\Gamma}$ is then defined with components given by

$$\Gamma_{kij} = \overline{\overline{G}}^k_{ij}. \tag{28}$$

Using $\boldsymbol{\Gamma}$, Eq. (27) becomes

$$\mathbf{v}(\mathbf{X}',t) = \mathbf{v}^0(\mathbf{X}',t) - \int_{A_c} \boldsymbol{\Gamma}:(\mathbf{N}^+\otimes\Delta\mathbf{v})dA - \int_{V-V_\epsilon} \boldsymbol{\Gamma}:\dot{\mathbf{F}}^{\mathrm{tr}T}dV \tag{29}$$

where $\otimes$ denotes a tensor product. This is then a representation theorem for the velocity in a Lagrangian finite deformation analysis of a region containing cracks and arbitrary material properties. This expression for the velocity is applicable assuming the transformation deformation gradient rate $\dot{\mathbf{F}}^{\mathrm{tr}}$ and the velocity discontinuity $\Delta\mathbf{v}$ across the crack faces can be determined. When the deformations are infinitesimal, the Green's function $\boldsymbol{\Gamma}$ is symmetric and we may use the symmetric part of the operands of $\boldsymbol{\Gamma}$. This leads to the known representation theorem that is used in seismology (e.g., Rice, 1980, rate form of equations 2.14 and 2.17).

The next step is to take the gradient of Eq. (29) in order to obtain the deformation gradient rate. For convenience of notation, $\mathbf{X}$ and $\mathbf{X}'$ are interchanged to obtain

$$\dot{\mathbf{F}}(\mathbf{X},t) = \dot{\mathbf{F}}^0(\mathbf{X},t) - \left(\int_{A_c} \boldsymbol{\Gamma}:(\mathbf{N}^+\otimes\Delta\mathbf{v})dA\right)\nabla - \left(\int_{V-V_\epsilon} \boldsymbol{\Gamma}:\dot{\mathbf{F}}^{\mathrm{tr}T}dV\right)\nabla. \tag{30}$$

The gradient operator in Eq. (30) may commute with the integration operator of the first bracketed term whenever the point $\mathbf{X}$ is not on any crack. When the point $\mathbf{X}$ approaches any crack surface, a careful limiting operation has to be considered for the particular crack involved. In the context of small deformation theory, this has been discussed by Fares and Li (1989). The gradient operator may not commute with the integration operator of the second bracketed term because V_ϵ depends on $\mathbf{X}$ and because the singularity of $\boldsymbol{\Gamma}$ is such that even with ϵ tending to zero, a convected term is obtained. Thus,

$$\left(\int_{V-V_\epsilon} \boldsymbol{\Gamma}:\dot{\mathbf{F}}^{\mathrm{tr}T}dV\right)\nabla = \int_{V-V_\epsilon} \boldsymbol{\Gamma}\nabla:\dot{\mathbf{F}}^{\mathrm{tr}T}dV - \mathbf{S}^{\mathrm{Esh}}:\dot{\mathbf{F}}^{\mathrm{tr}} \tag{31}$$

where $(\boldsymbol{\Gamma}\nabla)_{klmn} = \Gamma_{kmn,l}$ and $\mathbf{S}^{\mathrm{Esh}}$ is a fourth-order tensor which will be called the generalized Eshelby tensor for a sphere. Substituting Eq. (31) in (30) and assuming the point $\mathbf{X}$ does not lie on any crack but may approach one arbitrarily close, the following is obtained:

$$\dot{\mathbf{F}} = \dot{\mathbf{F}}^0 - \int_{A_c} \boldsymbol{\Gamma}\nabla:(\mathbf{N}^+\otimes\Delta\mathbf{v})dA - \int_{V-V_\epsilon} \boldsymbol{\Gamma}\nabla:\dot{\mathbf{F}}^{\mathrm{tr}T}dV + \mathbf{S}^{\mathrm{Esh}}:\dot{\mathbf{F}}^{\mathrm{tr}} \tag{32}$$

where $\dot{\mathbf{F}}^0$ is the deformation gradient rate response of the comparison medium. A term analogous to $\mathbf{S}^{\mathrm{Esh}}:\dot{\mathbf{F}}^{\mathrm{tr}}$ has sometimes been omitted in representation theorems discussed in recent works related to effective properties studies. This omission had already been recognized and corrected by Bui (1978) in research related to the boundary element method (BEM) with infinitesimal deformations in connection with elastoplastic formulations. In his paper, Bui shows that for a spherical inclusion in an isotropic infinite medium undergoing infinitesimal deformations, the term analogous to the second integral in Eq. (32) is identically zero. Hence, the strain in such inclusions is uniform and differs from that of a medium not containing an inclusion because of the Eshelby term. This result conforms with Eshelby's prior well-known result. It is noted that the generalized Eshelby tensor for a sphere only depends on the Green's function and hence only depends on the stiffness of the comparison medium. This generalized Eshelby tensor may be calculated by determining the convected term in Eq. (31).

Assume that a uniform deformation gradient rate $\dot{\mathbf{F}}^h$ is specified on the boundaries and consequently choose boundary condition (17*a*) for the Green's functions. Then for any given distribution of $\Delta\mathbf{v}$ on the crack faces and any given distribution of $\dot{\mathbf{F}}^{\mathrm{tr}}$ inside the representative volume, Eq. (32) defines a self-compatible deformation gradient rate $\dot{\mathbf{F}}$ except for velocity discontinuities $\Delta\mathbf{v}$ on the crack faces and is such that the boundary values of $\dot{\mathbf{F}}$ are given by $\dot{\mathbf{F}}^h$. Furthermore, the stress rate obtained using Eq. (10*a*) is self-equilibrated. Thus, $\dot{\mathbf{F}}^{\mathrm{tr}}$ and $\Delta\mathbf{v}$ are chosen such that the stress rate obtained from (10*a*) correctly matches the required constitutive relation (10*b*) and such that specified boundary conditions are satisfied on the crack faces. If the constitutive Eq. (10*b*) involves stress components $\dot{\mathbf{S}}^{(i)*T}$ which are due to kinematic constraints, then some or all of the associated scalar variables $q^{(i)}$ are additional unknown fields which have to be determined such that $\dot{\mathbf{F}}$ in addition satisfies the kinematic constraint relations. Assuming there are no cracks and no kinematic constraints inside the representative volume, then Eq. (11) may be substituted in (32) to give an integral equation for $\dot{\mathbf{F}}$:

$$\dot{\mathbf{F}} = \dot{\mathbf{F}}^0 - \int_{V-V_\epsilon} \boldsymbol{\Gamma}\nabla:[(\mathbf{I}-\mathbf{K}^{0\text{-}1}:\mathbf{K}):\dot{\mathbf{F}}]^T dV + \mathbf{S}^{\mathrm{Esh}}:(\mathbf{I}-\mathbf{K}^{0\text{-}1}:\mathbf{K}):\dot{\mathbf{F}}. \tag{33}$$

This integral equation is analogous to that presented by Lipinski and Berveiller (1989) in large deformation studies and to those presented by Dederichs and Zeller (1973) and Kroner (1977) in small deformation studies. In that regard, the Born approximation, whereby a formal solution of Eq. (33) is written as an infinite series of iterated integrals, also applies (Dederichs and Zeller, 1973; Kroner, 1977; Lipinski and Berveiller, 1989).

The representation theorem (32) may itself be the basis of a numerical scheme. The fields $\dot{\mathbf{F}}^{\mathrm{tr}}$, $\Delta\mathbf{v}$, and $q^{(i)}$ may be par-

Downloaded 03 May 2010 to 171.66.16.245. Redistribution subject to ASME license or copyright; see http://www.asme.org/terms/Terms_Use.cfm

ameterized over the representative volume, the crack faces, and the subregions where kinematic constraints apply, respectively. The parameterization may take the form of nodal interpolation following the known procedures of finite and boundary element methods. However, it is noted that no compatibility conditions are required on $\dot{\mathbf{F}}^{tr}$ since $\dot{\mathbf{F}}^{tr}$ is not part of the kinematics. For example, a piecewise constant distribution of $\dot{\mathbf{F}}^{tr}$ may be assumed. The next step is to use Eqs. (32) and (10*a*) to obtain self-compatible and self-equilibrated deformation gradient and nominal stress rates, respectively, throughout the representative volume. By approximately satisfying the constitutive relation (10*b*), specified boundary conditions on the crack faces and kinematic constraints in the applicable subregions, one then attempts to determine the unknown fields $\dot{\mathbf{F}}^{tr}$, $\Delta\mathbf{v}$, and $q^{(i)}$. The approximation of these conditions may take the form of some weighted residual statement in general or collocation at particular locations in the representative volume and on the crack faces in particular. Of course this is just an outline of a numerical scheme and the implementation details are important but are beyond the scope of this paper.

3 Concentration Factors and Effective Properties. *3.1 Crack-Free Composite.* Similar to infinitesimal deformation theories, when a uniform deformation gradient rate $\dot{\mathbf{F}}^h$ is applied on the boundary of a representative volume (RV) with volume V, a concentration factor $\mathbf{A}$ is required so that

$$\dot{\mathbf{F}} = \mathbf{A}:\dot{\mathbf{F}}^h = \mathbf{A}:\langle\dot{\mathbf{F}}\rangle \Leftrightarrow \dot{F}_{ij} = A_{ijkl}\dot{F}^h_{kl} = A_{ijkl}\langle\dot{F}_{kl}\rangle. \quad (34)$$

The effective stiffness of the RV is defined by the relation

$$\langle\dot{\mathbf{S}}^T\rangle = \mathbf{K}^{eff}:\langle\dot{\mathbf{F}}\rangle = \mathbf{K}^{eff}:\dot{\mathbf{F}}^h. \quad (35)$$

Using Eqs. (34) and (35), it can be deduced that

$$\mathbf{K}^{eff} = \langle\mathbf{K}:\mathbf{A}\rangle. \quad (36)$$

Similarly, when a uniform nominal stress rate $\dot{\mathbf{S}}^h$ is applied to the RV, and assuming $\mathbf{M} = \mathbf{K}^{-1}$ exists, then

$$\dot{\mathbf{S}} = \mathbf{B}:\dot{\mathbf{S}}^h = \mathbf{B}:\langle\dot{\mathbf{S}}\rangle \quad (37)$$

$$\langle\dot{\mathbf{F}}\rangle = \mathbf{M}^{eff}:\langle\dot{\mathbf{S}}^T\rangle = \mathbf{M}^{eff}:\dot{\mathbf{S}}^{hT} \quad (38)$$

$$\mathbf{M}^{eff} = \langle\mathbf{M}:\mathbf{B}\rangle. \quad (39)$$

The concentration factors $\mathbf{A}$ and $\mathbf{B}$ may in general depend on $\dot{\mathbf{F}}^h$ and $\dot{\mathbf{S}}^h$, respectively. The concentration factors have to be obtained from the response of the RV to all possible applied uniform boundary conditions. The effective response of the composite to a particular deformation or stress history may be obtained from the response of all possible RV realizations and in practice to a particular RV under the particular loading history. Thus all field quantities involved in the response of a representative volume of a composite may be viewed as internal variables in a constitutive description of the effective properties of that composite. The representation theorems may then serve as a guide for formulating micromechanically based constitutive relations for composites.

3.2 Composite With Cracks. When the composite contains cracks, the reference volume average of the deformation gradient rate is not uniquely determined from the velocity field measured on the boundary. The observed deformation gradient rate $\dot{\mathbf{F}}^{observed}$ is then given by

$$\dot{\mathbf{F}}^{observed} = \frac{1}{V}\int_A \mathbf{v}\otimes\mathbf{N}dA = \langle\dot{\mathbf{F}}\rangle - \dot{\mathbf{F}}^{crack} \quad (40a)$$

$$\dot{\mathbf{F}}^{crack} = \frac{1}{V}\int_{A_c} \Delta\mathbf{v}\otimes\mathbf{N}^+ dV \quad (40b)$$

When a uniform deformation gradient rate $\dot{\mathbf{F}}^h$ is applied on the boundary of the RV, then $\dot{\mathbf{F}}^{observed} = \dot{\mathbf{F}}^h$. Equation (40*a*) follows from a simple application of the divergence theorem and the postulate that observed quantities are those that are fully determined from field quantities measured on the boundary. By contrast, when condition (13) applies, the reference volume average of the nominal stress rate is still uniquely determined from the boundary nominal traction rate through the following relation (Hill, 1985):

$$\dot{\mathbf{S}}^{observed} = \langle\dot{\mathbf{S}}\rangle = \frac{1}{V}\int_A \mathbf{X}\otimes(\mathbf{N}\cdot\dot{\mathbf{S}})dA. \quad (41)$$

Equation (41) also follows from a simple application of the divergence theorem and by making use of Eq. (13). Under a uniformly applied deformation gradient rate $\dot{\mathbf{F}}^h$, Eqs. (34) to (36) still apply with $\langle\dot{\mathbf{F}}\rangle$ everywhere replaced by $\dot{\mathbf{F}}^{observed}$. In that case, cracks affect the effective stiffness through their influence on the determination of the concentration factor $\mathbf{A}$. When a uniform nominal stress rate $\dot{\mathbf{S}}^h$ is applied, $\langle\dot{\mathbf{F}}\rangle$ in Eq. (38) again has to be replaced by $\dot{\mathbf{F}}^{observed}$. In this case, additional concentration factors have to be defined by

$$\Delta\mathbf{v} = \mathbf{B}^{crack}:\dot{\mathbf{S}}^{hT} \quad (42)$$

$$\dot{\mathbf{F}}^{crack} = \mathbf{M}^{crack}:\dot{\mathbf{S}}^{hT} \quad (43)$$

where

$$M^{crack}_{ijkl} = \frac{1}{V}\int_{A_c} B^{crack}_{ilk}N^+_j dV. \quad (44)$$

The effective compliance $\mathbf{M}^{eff}$ is then given by

$$\mathbf{M}^{eff} = \langle\mathbf{M}:\mathbf{B}\rangle - \mathbf{M}^{crack}. \quad (45)$$

Therefore, when the nominal stress rate $\dot{\mathbf{S}}^h$ is specified over the boundary, cracks influence the effective compliance implicitly through the concentration factor $\mathbf{B}$ as well as directly through $\mathbf{M}^{crack}$.

3.3 Relation Between Various Concentration Factors. Assume that a uniform deformation gradient rate $\dot{\mathbf{F}}^h$ is applied. Various additional concentration factors may be then defined. These concentration factors denoted by $\mathbf{A}^0$, $\mathbf{A}^{tr}$, and $\mathbf{A}^{cr}$ relate the uniformly applied deformation gradient rate $\dot{\mathbf{F}}^h$ to $\dot{\mathbf{F}}^0$, $\dot{\mathbf{F}}^{tr}$, and $\Delta\mathbf{v}$, respectively,

$$\dot{\mathbf{F}}^0 = \mathbf{A}^0:\dot{\mathbf{F}}^h \quad (46)$$

$$\dot{\mathbf{F}}^{tr} = \mathbf{A}^{tr}:\dot{\mathbf{F}}^h \quad (47)$$

$$\Delta\mathbf{v} = \mathbf{A}^{cr}:\dot{\mathbf{F}}^h. \quad (48)$$

It is noted that $\mathbf{A}^0$ is the identity operator when the comparison medium is homogeneous. When the stiffness $\mathbf{K}$ does not depend on the deformation gradient rate, when there are no kinematic constraints and when the boundary conditions on the crack faces are either independent or depend linearly on the deformation gradient rate, then superposition may be used to generate the concentration factors defined in Eqs. (46) to (48). In particular, Eq. (48) requires the determination of the crack face opening and sliding velocities as a function of applied $\dot{\mathbf{F}}^h$. Substituting Eqs. (34), (46), to (48) into Eq. (32) we obtain

$$\mathbf{A} = \mathbf{A}^0 - \int_{A_c} \mathbf{\Gamma}\nabla\cdot(\mathbf{N}^+\otimes\mathbf{A}^{cr})dA - \int_{V-V_\epsilon} \mathbf{\Gamma}\nabla:\mathbf{A}^{trT}dV + \mathbf{S}^{Esch}:\mathbf{A}^{tr} \quad (49)$$

where the transpose on $\mathbf{A}^{tr}$ is with respect to interchange of the first two indices. Equation (49) is a relation between the various concentration factors and shows the contribution of material nonhomogeneities and cracks to the overall concentration factor $\mathbf{A}$. It is also noted that the effect of kinematic constraints is implicitly accounted for in the determination of $\mathbf{A}^{tr}$ as can be seen from Eq. (11).

3.4 Effect of Kinematic Constraints. Kinematic constraints may in some cases lead to an indeterminancy in the

Downloaded 03 May 2010 to 171.66.16.245. Redistribution subject to ASME license or copyright; see http://www.asme.org/terms/Terms_Use.cfm

resulting reference volume average of the nominal stress rate from the boundary values of $\dot{\mathbf{F}}^h$. In those cases, not all boundary values of $\dot{\mathbf{F}}^h$ may be specified. For example, in a medium composed only of incompressible phases, it is inconsistent to specify $\dot{\mathbf{F}}^h$ having a net rate of volumetric change. In such cases, either there is no solution for the boundary value problem specified over the representative volume or the solution for the nominal stress rate is not unique. When $\dot{\mathbf{F}}^h$ may not be arbitrarily specified over the boundary, Eq. (35) must then be replaced by

$$\langle \dot{\mathbf{S}} \rangle^T = \mathbf{K}^{\text{eff}*} : \dot{\mathbf{F}}^h - \sum_{i=1}^{m \le n} \mathbf{Q}^{(i)} \tag{50}$$

$$\mathbf{Q}^{(i)} = \langle q^{(i)} \dot{\mathbf{S}}^{*(i)T} \rangle \tag{51}$$

where $q^{(i)}$ only includes those modes which may not be determined from a consistent specification of $\dot{\mathbf{F}}^h$. Thus, a kinematic constraint at the microscale may in some cases be transmitted to the macroscale effective properties.

4 Relation Between the Micro and Macro Inelastic Deformations. In the context of studying the transition from the micro to the macro or effective behavior, the relation between micro observed inelastic deformations and the macro inferred ones is now examined. Assume that an inelastic constitutive relation is partially specified as

$$\dot{\mathbf{S}}^T = \mathbf{K}^{\text{elastic}} : \dot{\mathbf{F}}^e \tag{52}$$

$$\dot{\mathbf{F}} = \dot{\mathbf{F}}^{\text{inelastic}} + \dot{\mathbf{F}}^e, \tag{53}$$

where $\mathbf{K}^{\text{elastic}}$ is a stiffness which does not depend on the deformation gradient rate and $\dot{\mathbf{F}}^{\text{inelastic}}$ and $\dot{\mathbf{F}}^e$ do not have to be separately self-compatible. The additive decomposition assumed in Eq. (53) may be justified when the reference configuration is chosen as the current one so that the deformation gradient rate equals the velocity gradient (Hill, 1966; Hill and Rice, 1972; Nemat-Nasser, 1982). Let $\dot{\mathbf{S}}^{(a)}$ be self-equilibrated and $\dot{\mathbf{F}}^{(b)}$ be self-compatible such that $\dot{\mathbf{S}}^{(a)} = \dot{\mathbf{S}}^h$ on the boundary. Then Hill (1972, 1985) has shown that

$$\langle \dot{\mathbf{S}}^{(a)T} : \dot{\mathbf{F}}^{(b)} \rangle = \langle \dot{\mathbf{S}}^{(a)T} \rangle : \langle \dot{\mathbf{F}}^{(b)} \rangle = \dot{\mathbf{S}}^{hT} : \langle \dot{\mathbf{F}}^{(b)} \rangle. \tag{54}$$

Let $\dot{\mathbf{F}}^{(1)}$ and $\dot{\mathbf{F}}^{(2)e}$ be the deformation gradient rates obtained in the representative volume when the region responds inelastically and purely elastically, respectively. A purely elastic response means that $\dot{\mathbf{F}}^{\text{inelastic}}$ is uniformly zero in constitutive Eqs. (52) and (53). Then, for any self-equilibrated nominal stress rate $\dot{\mathbf{S}}$,

$$\langle \dot{\mathbf{S}}^T : (\dot{\mathbf{F}}^{(1)} - \dot{\mathbf{F}}^{(2)e}) \rangle = \dot{\mathbf{S}}^{hT} : (\langle \dot{\mathbf{F}}^{(1)} \rangle - \langle \dot{\mathbf{F}}^{(2)e} \rangle). \tag{55}$$

In general, $\dot{\mathbf{F}}^{(1)e} \neq \dot{\mathbf{F}}^{(2)e}$, since the nominal stress rate distributions in these two problems are expected to be different because of possible stress redistributions occurring with inelastic deformations. This also implies that $\dot{\mathbf{F}}^{(1)\text{inelastic}} \neq (\dot{\mathbf{F}}^{(1)} - \dot{\mathbf{F}}^{(2)e})$ in general. However, it is noted that $\langle \dot{\mathbf{F}}^{(1)} \rangle$ and $\langle \dot{\mathbf{F}}^{(2)e} \rangle$ are the average responses of the material responding inelastically and purely elastically. Hence, $(\langle \dot{\mathbf{F}}^{(1)} \rangle - \langle \dot{\mathbf{F}}^{(2)e} \rangle)$ may be interpreted as the effective inelastic deformation gradient rate which will denoted by $\dot{\mathbf{F}}^{\text{macro-inelastic}}$. Let $\dot{\mathbf{S}} = \dot{\mathbf{S}}^{(1)}$, then substitution in Eq. (55) gives

$$\dot{\mathbf{S}}^{hT} : \dot{\mathbf{F}}^{\text{macro-inelastic}} = \langle \dot{\mathbf{S}}^{(1)T} : \dot{\mathbf{F}}^{(1)} \rangle - \langle \dot{\mathbf{S}}^{(1)T} : \dot{\mathbf{F}}^{(2)e} \rangle. \tag{56}$$

Since $\dot{\mathbf{S}}^{(1)}$ and $\dot{\mathbf{S}}^{(2)}$ are self-equilibrated, and $\dot{\mathbf{F}}^{(1)}$, $\dot{\mathbf{F}}^{(2)e}$ share the same constitutive relation (52), we have

$$\langle \dot{\mathbf{S}}^{(1)T} : \dot{\mathbf{F}}^{(1)} \rangle = \dot{\mathbf{S}}^{hT} : \langle (\dot{\mathbf{F}}^{(1)} \rangle = \langle \dot{\mathbf{S}}^{(2)T} : \dot{\mathbf{F}}^{(1)} \rangle \tag{57}$$

$$\langle \dot{\mathbf{S}}^{(1)T} : \dot{\mathbf{F}}^{(2)e} \rangle = \langle \dot{\mathbf{F}}^{(2)eT} : \mathbf{K}^{\text{elastic}} : \dot{\mathbf{F}}^{(1)e} \rangle = \langle \dot{\mathbf{S}}^{(2^*)T} : \dot{\mathbf{F}}^{(1)e} \rangle \tag{58}$$

where

$$\dot{\mathbf{S}}^{(2^*)T} = \dot{\mathbf{F}}^{(2)eT} : \mathbf{K}^{\text{elastic}}. \tag{59}$$

It is noted that $\dot{\mathbf{S}}^{(2^*)} \neq \dot{\mathbf{S}}^{(2)}$, since $\mathbf{K}^{\text{elastic}}$ is in general not symmetric with respect to the interchange of the first two with the last two indices. However, $\dot{\mathbf{S}}^{(2^*)}$ is fully determined from the purely elastic solution. Therefore, it is useful to define the concentration factors $\mathbf{B}^e$ and $\mathbf{B}^{e^*}$ derived from the purely elastic solutions as

$$\dot{\mathbf{S}}^{(2)T} = \dot{\mathbf{S}}^{hT} : \mathbf{B}^e \tag{60}$$

$$\dot{\mathbf{S}}^{(2^*)T} = \dot{\mathbf{S}}^{hT} : \mathbf{B}^{e^*}. \tag{61}$$

Substitution of Eq. (53) in (57), Eqs. (57) and (58) in (56), and the use of the concentration factors defined in Eqs. (60) and (61) gives

$$\dot{\mathbf{S}}^{hT} : \dot{\mathbf{F}}^{\text{macro-inelastic}} = \dot{\mathbf{S}}^{hT} : [\langle \mathbf{B}^e : \dot{\mathbf{F}}^{(1)\text{inelastic}} \rangle + \langle (\mathbf{B}^e - \mathbf{B}^{e^*}) : \dot{\mathbf{F}}^{(1)e} \rangle]. \tag{62}$$

Dropping the subscript (1) from the deformation gradient rate of the inelastic solution and noting that Eq. (62) holds for any $\dot{\mathbf{S}}^h$, the following relation is obtained:

$$\dot{\mathbf{F}}^{\text{macro-inelastic}} = \langle \mathbf{B}^e : \dot{\mathbf{F}}^{\text{inelastic}} \rangle + \langle (\mathbf{B}^e - \mathbf{B}^{e^*}) : \dot{\mathbf{F}}^e \rangle. \tag{63}$$

Thus, Eq. (63) states that the macro-inelastic deformation gradient rate is due to two contributions. The first contribution is from the micro-inelastic deformation gradient rate weighted by the elastic concentration factor. The second contribution is from the micro-elastic deformation gradient rate and occurs because the elastic stiffness is not in general symmetric. When the deformations are infinitesimal, $\mathbf{S}$ is $\boldsymbol{\sigma}$ and $\mathbf{K}^{\text{elastic}}$ is symmetric, which implies $\mathbf{B}^e - \mathbf{B}^{e^*} = \mathbf{0}$. Then, by taking the symmetric part of (63) we obtain

$$\dot{\boldsymbol{\epsilon}}^{\text{macro-inelastic}} = \langle \mathbf{B}^e : \dot{\boldsymbol{\epsilon}}^{\text{inelastic}} \rangle. \tag{64}$$

The above result (Eq. 64) indicates that the macroscopic inelastic deformations (e.g., "plastic" deformations) are not generally the resultant of local inelastic deformations (e.g., the sum of strains due to individual slippage on slip surfaces) but have to be weighted by the *elastic* concentration factor. The above result has been recently reported and emphasized by Dvorak (1989, equation (2.46)) and has been reported earlier by Rice and Hill (1972) in the context of plasticity.

Conclusions

Some basic theoretical results related to the determination of effective properties of composites at finite deformation have been presented. These results are based on a new representation theorem for the deformation gradient rate in the presence of cracks and kinematic constraints. This representation theorem used an extension of the concept of transformation strains to finite deformations. Based on the representation theorem, several results were obtained. Among these results, the contribution of the crack opening and sliding was shown to contribute to the deformation gradient rate concentration factor through an expression involving the Green's function. Also, the role of elastic concentration factors in relating inelastic deformations at the microscale with those at the macroscale was emphasized and it was found that some of the elastic deformation at the microscale contributes to the macroscale inelastic deformations.

Acknowledgments

This work was supported by the office of Naval Research. The author is indebted to Prof. George Dvorak for useful discussions.

References

Asaro, R. J., 1979, "Geometrical Effects in the Inhomogeneous Deformation of Ductile Single Crystals," *Acta Metall.*, Vol. 27, pp. 445.

Banerjee, P. K., and Butterfield, R., 1981, *Boundary Element Methods in Engineering Science*, McGraw-Hill, New York.

Downloaded 03 May 2010 to 171.66.16.245. Redistribution subject to ASME license or copyright; see http://www.asme.org/terms/Terms_Use.cfm

Berveiller, M., Fassi-Fehri, O., and Hihi, A., 1987, "The Problem of Two Plastic and Heterogeneous Inclusions in an Anisotropic Medium," *Int. J. Engng. Sci.*, Vol. 25, No. 6, pp. 691–709.

Berveiller, M., and Zaoui, A., 1979, "An Extension of the Self-Consistent Scheme to Plastically-Flowing Polycrystals," *J. Mech. Phys. Solids*, Vol. 26, pp. 325–344.

Berveiller, M., and Zaoui, A., 1984, "Modeling of the Plastic Behavior of Inhomogeneous Media," *Jour. Engng. Matl. Tech.*, Vol. 106, pp. 295–298.

Budiansky, B., 1965, "On the Elastic Moduli of Some Heterogeneous Materials," *J. Mech. Phys. Solids*, Vol. 13, pp. 223–227.

Bui, H. D., 1978, "Some Remarks About the Formulation of Three-Dimensional Thermoelastoplastic Problems by Integral Equations," *Int. J. Solids Structures*, Vol. 14, pp. 935–939.

Chandra, A., and Mukherjee, S., 1983, "Applications of the Boundary Element Method to Large Strain Large Deformation Problems of Viscoplasticity," *J. Strain Anal.*, Vol. 18, pp. 261–270.

Dederichs, P. H., and Zeller, R., 1973, "Variational Treatment of the Elastic Constants of Disordered Materials," *Z. Physik*, Vol. 259, pp. 103–116.

Dvorak, G. J., 1989, "Plasticity Theories for Fibrous Composite Materials," *Metal Matrix Composites, Vol. 2: Mechanisms and Properties*, R. K. Everett and R. J. Arsenault, eds., Academic Press, Boston.

Fares, N., and Li, V. C., 1989, "3-D Boundary Element Method for Cracks in a Plate," *Intl. J. Numer. Meth. Eng.*, Vol. 28, pp. 1703–1713.

Fassi-Fehri, O., Hihi, A., and Berveiller, M., 1989, "Multiple Site Self Consistent Scheme," *Int. J. Engng. Sci.*, Vol. 27, No. 5, pp. 495–502.

Hill, R., 1963, "Elastic Properties of Reinforced Solids: Some Theoretical Principles," *J. Mech. Phys. Solids*, Vol. 11, pp. 357–372.

Hill, R., 1965, "A Self-Consistent Mechanics of Composite Materials," *J. Mech. Phys. Solids*, Vol. 13, pp. 213–222.

Hill, R., 1966, "Generalized Constitutive Relations for Incremental Deformation of Metal Crystals by Multislip," *J. Mech. Phys. Solids*, Vol. 14, pp. 95–102.

Hill, R., 1972, "On Constitutive Macro-Variables for Heterogeneous Solids at Finite Strain," *Proc. Royal Soc. London*, Vol. A326, pp. 131–147.

Hill, R., 1984, "On Macroscopic Effects of Heterogeneity in Elastoplastic Media at Finite Strain," *Math. Proc. Camb. Phil. Soc.*, Vol. 95, pp. 481–494.

Hill, R., 1985, "On the Micro-to-Macro Transition in Constitutive Analyses of Elastoplastic Response at Finite Strain," *Math. Proc. Camb. Phil. Soc.*, Vol. 98, pp. 579–590.

Hill, R., and Rice, J. R., 1972, "Constitutive Analysis of Elastic-Plastic Crystals at Arbitrary Strain," *J. Mech. Phys. Solids*, Vol. 20, pp. 401–413.

Hutchinson, J. W., 1970, "Elastic-Plastic Behavior of Polycrystalline Metals and Composites," *Proc. Roy. Soc. London*, Vol. A319, pp. 347.

Iwakuma, T., and Nemat-Nasser, S., 1984, "Finite Elastic-Plastic Deformation of Polycrystalline Metals," *Proc. Roy. Soc. Lond.*, Vol. A394, pp. 87–119.

Kroner, E., 1977, "Bounds for Effective Elastic Moduli of Disordered Materials," *J. Mech. Phys. Solids*, Vol. 25, pp. 137–155.

Laws, N., 1977, "A Note on Interaction Energies Associated with Cracks in Anisotropic Media," *Phil. Mag.*, Vol. 36, pp. 367.

Laws, N., Dvorak, G. J., and Hejazi, M., 1983, "Stiffness Changes in Unidirectional Composites Caused by Crack Systems," *Mech. of Mater.*, Vol. 2, pp. 123–137.

Lipinski, P., and Berveiller, M., 1989, "Elastoplasticity of Micro-Inhomogeneous Metals at Large Strains," *Int. Jour. Plasticity*, Vol. 5, pp. 149–172.

Mori, T., and Tanaka, K., 1973, "Average Stress in Matrix and Average Elastic Energy of Materials with Misfitting Inclusions," *Acta. Metal.*, Vol. 21, pp. 571.

Nemat-Nasser, S., 1982, "On Finite Deformation Elasto-Plasticity," *Int. J. Solids Structures*, Vol. 18, No. 10, pp. 857–872.

Nemat-Nasser, S., Iwakuma, T., and Hejazi, M., 1982, "On Composites with Periodic Structure," *Mech. of Mat.*, Vol. 1, pp. 239–267.

Okada, H., Rajiyah, H., and Atluri, S. N., 1989, "Some Recent Developments in Finite-Strain Elastoplasticity Using the Field-Boundary Element Method," *Comp. Struct.*, Vol. 30, pp. 275–288.

Okada, H., Rajiyah, H., and Atluri, S. N., 1990, "A Full Tangent Stiffness Field-Boundary-Element Formulation for Geometric and Material Non-Linear Problems of Solid Mechanics," *Int. Jour. Numer. Meth. Engng.*, Vol. 29, pp. 15–35.

Rice, J. R., 1980, "The Mechanics of Earthquake Rupture," *Physics of the Earth's Interior*, A. M. Dziewonski and E. Boshi, eds., pp. 555–649.

Teply, J. L., and Dvorak, G. J., 1988, "Bounds on Overall Instantaneous Properties of Elastic-Plastic Composites," *J. Mech. Phys. Solids*, Vol. 36, No. 1, pp. 29–58.

Walker, K. P., Jordan, E. H., and Freed, A. D., 1989, "Nonlinear Mesomechanics of Composites With Periodic Microstructure: First Report," NASA Technical Memorandum 102051.

Walker, K. P., Jordan, E. H., and Freed, A. D., 1989, "Equivalence of Green's Function and the Fourier Series Representation of Composites with Periodic Microstructure," *Micromechanics and Inhomogeneity*, The Toshio-Mura Anniversary Volume, Springer-Verlag, New York, pp. 535–558.

Walsh, J. B., 1969, "New Analysis of Attenuation in Partially Melted Rocks," *J. Geophys. Res.*, Vol. 74, pp. 4333.

Willis, J. R., 1977, "Bounds and Self-Consistent Estimates for the Overall Properties of Anisotropic Composites," *J. Mech. Phys. Solids*, Vol. 25, pp.185–202.

Downloaded 03 May 2010 to 171.66.16.245. Redistribution subject to ASME license or copyright; see http://www.asme.org/terms/Terms_Use.cfm

Castrenze Polizzotto
Dipartimento di Ingegneria Stutturale
& Geotecnica, DISEG,
Università di Palermo,
Viale delle Scienze,
I-90128 Palermo, Italy

On the Conditions to Prevent Plastic Shakedown of Structures: Part I—Theory[1]

For a structure of elastic perfectly plastic material subjected to a given cyclic (mechanical and/or kinematical) load and to a steady (mechanical) load, the conditions are established in which plastic shakedown cannot occur whatever the steady load, and thus the structure is safe against the alternating plasticity collapse. Static and kinematic theorems, analogous to those of classical shakedown theory, are presented.

Introduction

It is a well-known fact (see, e.g., Frederich and Armstrong, 1966; Martin, 1975; Zarka and Casier, 1979) that a perfectly plastic material structure subjected to a combination of cyclic and steady loads shows a transient (short-term) response first, then a steady-state (long-term) response, the latter being independent of the initial conditions and having some periodicity features, namely the stresses σ and the plastic strain rates $\dot{\epsilon}^p$ are periodic with the same period Δt as the loads. The steady-state response is characterized by its own plastic accumulation mechanism, that is a plastic strain rate cycle resulting in a compatible plastic strain field $\Delta\epsilon^p$ (ratchet strain). According to the type of plastic accumulation mechanism, three types of steady-state responses are usually distinguished, namely:

(*i*) *Elastic shakedown* (often simply "shakedown"): the plastic accumulation mechanism is a trivial one, i.e., $\dot{\epsilon}^p$ vanishes identically and thus the structure responds elastically to the loads.

(*ii*) *Plastic shakedown:* the plastic accumulation mechanism is a nontrivial one, but $\Delta\epsilon^p = \mathbf{0}$ in the volume V of the body, that is the plastic strains are alternating in the cycle (alternating plasticity collapse).

(*iii*) *Ratchetting:* the ratchet strain is nonvanishing, i.e., $\Delta\epsilon^p \neq \mathbf{0}$, at least somewhere in V, causing the plastic strain to progressively increase (incremental plastic collapse).

For design purpose, criteria for a priori recognizing the type of steady-state response, without the necessity of performing a step-by-step full analysis, are of paramount importance. The classical Bleich-Melan and Koiter-Neal-Symonds theorems provide criteria to recognize whether elastic shakedown occurs or not under a specified loading (Koiter, 1960; Martin, 1975; Gokhfeld and Cherniavsky, 1980; König, 1987; Symonds and Neal, 1951). Analogous criteria for plastic shakedown and ratchetting, as satisfactory as those for elastic shakedown, are not available in the literature. Ponter and Karadeniz (1985) used heuristic arguments to formulate criteria for plastic shakedown, applicable only to particular structural and loading situations. Generalizations of the latter criteria to a wider range of applicability were proposed by Polizzotto (1989).

The purpose of the present paper is to address and to discuss the conditions for a structure subjected to loads resulting from the combination of a cyclic (mechanical and/or kinematical) load and a steady (mechanical) load not to be in a plastic shakedown state and thus not to suffer alternating plastic strains. To this aim, one has to notice that, for any specified cyclic load, the structure can be forced to finally operate in a shakedown condition by suitably distributing a steady mechanical load throughout the structure's volume, and whether this condition is an elastic shakedown condition or a plastic shakedown one only depends on the acting cyclic load value. The particular cyclic load value that separates elastic from plastic shakedown constitutes what can be called "plastic shakedown limit load." This means that: either ratchetting or elastic shakedown—but not plastic shakedown—are to be expected for smaller cyclic load values, and either ratchetting or plastic shakedown—but not elastic shakedown—are to be expected for higher cyclic load values.

Since the notion of plastic shakedown limit load for a perfectly plastic material structure may undoubtedly be useful for design purposes, the provision of a firm rational basis to it is an important research issue. This goal can be achieved by means of dual theorems analogous to those of classical shakedown theory, as shown in this paper. Gokhfeld and Cherniavsky (1980) and König (1982a, b) provided theorems to establish the conditions in which plastic shakedown cannot occur for loads varying within a given range; the latter results will be re-obtained here as particular cases within a more general loading context.

After some preliminary definitions, static and kinematic theorems will be proved for a specified cyclic load, as well as for loads varying within a given domain. Vectors and tensors

[1]This paper is dedicated to the memory of Professor Jan A. König.

Contributed by the Applied Mechanics Division of THE AMERICAN SOCIETY OF MECHANICAL ENGINEERS for publication in the ASME JOURNAL OF APPLIED MECHANICS.

Discussion on this paper should be addressed to the Technical Editor, Professor Lewis T. Wheeler, Department of Mechanical Engineering, University of Houston, Houston, TX 77204-4792, and will be accepted until four months after final publication of the paper itself in the ASME JOURNAL OF APPLIED MECHANICS.

Manuscript received by the ASME Applied Mechanics Division, Nov. 30, 1990; final revision, Sept. 20, 1991. Associate Technical Editor: R. M. McMeeking.

Copyright © 1993 by ASME
Downloaded 03 May 2010 to 171.66.16.245. Redistribution subject to ASME license or copyright; see http://www.asme.org/terms/Terms_Use.cfm

will be denoted by boldface symbols. The scalar product between two tensors is denoted by a colon. The symbol : = denotes equality by definition.

Preliminaries and Problem Position

An elastic-perfectly plastic material structure, of domain V and boundary surface ∂V, referred to a Cartesian orthogonal coordinate system $\mathbf{x} = (x_1, x_2, x_3)$, is subjected to external actions like body forces in V, tractions on the free boundary $\partial_t V \subset \partial V$, imposed (e.g., thermal) strains in V and imposed displacements on $\partial_u V$, $(\partial_u V \cup \partial_t V = \partial V)$. All these actions are collectively denoted by the symbol P and represented as

$$P(t) = P^c(t) + P^0, \quad 0 \le t \le \Delta t, \quad P^0 \in \mathcal{P}^0 \tag{1}$$

meaning that the load is a combination of a cyclically variable mechanical and/or kinematical load $P^c(t)$ and a time-independent (or steady) mechanical load P^0 belonging to the set $\mathcal{P}^0$. The hypothesis is here made that the latter set $\mathcal{P}^0$ collects all the loads below the plastic collapse limit values (but on occasion it may be narrower). Inertia and viscous forces are assumed negligible, just as negligible is the influence of temperature variations over the material constitutive laws. The classical infinitesimal displacement theory is applicable.

Let $\boldsymbol{\sigma}^c(\mathbf{x}, t)$ and $\boldsymbol{\sigma}^0(\mathbf{x})$ denote the purely elastic stress response of the structure to $P^c(t)$ and P^0, respectively. Referring to the steady-state response produced by the combined load (1) with a specified $P^0 \in \mathcal{P}^0$, let $\boldsymbol{\sigma}$ and $\dot{\boldsymbol{\epsilon}}^p$ be the corresponding actual stresses and plastic strain rates. The classical shakedown theorems provide means for assessing whether elastic shakedown occurs or not under this varying load. Here, for greater easiness, the latter theorems are briefly reminded.

The Bleich-Melan theorem as applied to a combined cyclic/steady load considers statically admissible stress states, each of which consists in a stress field $\hat{\boldsymbol{\sigma}} = \boldsymbol{\sigma}^c + \mathbf{s}$, superposition of the elastic stress response to the cyclic load with a time-independent stress field $\mathbf{s}$ in equilibrium with the steady load. This $\hat{\boldsymbol{\sigma}}$ will be hereafter referred to as post-transient (PT) stresses. Thus one has the following theorem.

Static Elastic Shakedown Theorem. A necessary and sufficient condition for elastic shakedown to occur under the combined cyclic/steady load $P(t) = P^c(t) + P^0$, $0 \le t \le \Delta t$, is that a time-independent stress field $\mathbf{s}$, in equilibrium with P^0, may be found such that the corresponding PT stresses $\hat{\boldsymbol{\sigma}} = \boldsymbol{\sigma}^c + \mathbf{s}$ nowhere violate yield, i.e.,

$$\phi(\hat{\boldsymbol{\sigma}}) \le 0 \text{ in } V \times (0, \Delta t) \tag{2}$$

where $\phi(\boldsymbol{\sigma})$ is the relevant yield function.

The Koiter-Neal-Symonds theorem, as applied to a combined cyclic/steady load, considers kinematically admissible strain rate cycles, each of which consists in a plastic strain-rate field, $\dot{\mathbf{e}}^p(\mathbf{x}, t)$, $0 \le t \le \Delta t$, resulting in a compatible ratchet strain $\Delta\mathbf{e}(\mathbf{x})$. Such a plastic strain-rate field was called "kinematically admissible plastic strain cycle" by Koiter (1960), but hereafter will be referred to as plastic accumulation mechanism (PAM). The set of all PAM's will be denoted by $\mathfrak{M}$. Thus, one can state the following theorem:

Kinematic Elastic Nonshakedown Theorem. A necessary and sufficient condition for elastic shakedown not to occur under the combined cyclic/steady load $P(t) = P^c(t) + P^0$, $0 \le t \le \Delta t$, is that a PAM, $\dot{\mathbf{e}}^p \in \mathfrak{M}$, may be found such as to satisfy the energy unbalance condition:

$$\int_0^{\Delta t} \int_V [D(\dot{\mathbf{e}}^p) - \boldsymbol{\sigma}^c : \dot{\mathbf{e}}^p] dV dt - \int_V \boldsymbol{\sigma}^0 : \Delta\mathbf{e}^p dV < 0 \tag{3}$$

where D is the relevant plastic dissipation function.

By definition, a structure subjected to combined cyclic/steady loads $P(t) = P^c(t) + P^0$, with $P^c(t)$ assigned and $P^0 \in \mathcal{P}^0$, is *safe* against the alternating plasticity collapse when plastic shakedown cannot occur whatever the steady load $P^0 \in \mathcal{P}^0$; conversely, the structure is *unsafe* against the alternating plasticity collapse when there exists at least one steady load $P^0 \in \mathcal{P}^0$ such that the combined load causes plastic shakedown. A plastic shakedown limit load can thus be envisaged as the cyclic load for which the structure is still safe, but in a limit state characterized by an impending alternating plasticity collapse, provided that the limit cyclic load acts in combination with a suitable ("neutralizing") steady load.

Theorems will be provided in the next Sections to discriminate safe and unsafe situations. The simple adjectives "safe" and "unsafe" as referred to the structure, or even to the cyclic load $P^c(t)$ applied upon it, will be used with the same sense here above.

Static Theorems

A central theorem can be established to recognize whether a structure is safe. This theorem is similar to the Bleich-Melan "static" theorem, but makes use of arbitrary time-independent stress fields instead of self-equilibrated ones.

Theorem 1

For a Structure to be Safe. A necessary and sufficient condition in order that a structure subjected to a given cyclic load $P^c(t)$, $0 \le t \le \Delta t$, be safe is that there exists some time-independent stress field, $\mathbf{s}$, such that the related PT stress field, $\hat{\boldsymbol{\sigma}} = \boldsymbol{\sigma}^c + \mathbf{s}$, nowhere violates yield, i.e.,

$$\phi(\hat{\boldsymbol{\sigma}}) \le 0 \text{ in } V \times (0, \Delta t). \tag{4}$$

Proof of the Necessity. Applying upon the structure a steady load, $P^0 \in \mathcal{P}^0$, in combination with the given $P^c(t)$, produces a steady-state structural response with actual plastic strain rates $\dot{\boldsymbol{\epsilon}}^p$ and ratchet strain $\Delta\boldsymbol{\epsilon}^p$. The work L^0 done by P^0 in a complete cycle is

$$L^0 = L^0[\boldsymbol{\sigma}^0] := \int_V \boldsymbol{\sigma}^0 : \Delta\boldsymbol{\epsilon}^p dV \tag{5}$$

where $\boldsymbol{\sigma}^0$ is the elastic stress response to P^0. L^0 turns out to be positive for higher values both of P^0 and $-P^0$, which implies that there must exist some range of loads P^0 for all of which $L^0 = 0$, hence $\partial L^0/\partial\boldsymbol{\sigma}^0 = \Delta\boldsymbol{\epsilon}^p = \mathbf{0}$ in V. That means that for a given $P^c(t)$, there always exists a suitably distributed load P^0 such that the combined load leads the structure to a shakedown condition, either plastic or elastic, but is actually elastic in the present case in which the structure is assumed safe. Thus, due to the Bleich-Melan theorem, there exists a time-independent stress field, $\mathbf{s}$, in equilibrium with the above P^0, such that (4) is satisfied.

Proof of the Sufficiency. By hypothesis, a time-independent stress field $\mathbf{s}$ can be found such as to satisfy Eq. (4) as a strict inequality, i.e.,

$$\phi(\hat{\boldsymbol{\sigma}}) < 0 \text{ in } V \times (0, \Delta t), \tag{6}$$

where $\hat{\boldsymbol{\sigma}} = \boldsymbol{\sigma}^c + \mathbf{s}$. Since $\mathbf{s}$ satisfying (6) is not unique, the Bleich-Melan theorem enables one to state that there exists a subset $\mathcal{P}_S^0 \subset \mathcal{P}^0$ associated with the given cyclic load and such that the combined loads $P^c(t) + P^0$, with $P^0 \in \mathcal{P}_S^0$, all produce elastic shakedown. Any other steady load $P^0 \in \mathcal{P}^0$, but $P^0 \notin \mathcal{P}_S^0$, acting in combination with $P^c(t)$, will cause inadaptation (i.e., lack of elastic shakedown). Let $\boldsymbol{\sigma}$ and $\dot{\boldsymbol{\epsilon}}^p$ be the stresses and plastic strain rates in the resulting steady-state response. Since the stresses $\hat{\boldsymbol{\sigma}}$ of (6) also read

$$\hat{\boldsymbol{\sigma}} = \boldsymbol{\sigma}^c + \mathbf{s} = \boldsymbol{\sigma}^c + \boldsymbol{\sigma}^0 + \mathbf{s}' \tag{7}$$

where $\boldsymbol{\sigma}^0$ is the elastic stress response to the above P^0 and $\mathbf{s}' \equiv \mathbf{s} - \boldsymbol{\sigma}^0$ is in equilibrium with some nonvanishing load, for Drucker's postulate one can write

Downloaded 03 May 2010 to 171.66.16.245. Redistribution subject to ASME license or copyright; see http://www.asme.org/terms/Terms_Use.cfm

$$(\hat{\sigma}-\sigma):\dot{\epsilon}^p=(\mathbf{s}'-\sigma^R):\dot{\epsilon}^p\le 0 \text{ in } V\times(0,\Delta t) \tag{8}$$

where $\sigma^R = \sigma - (\sigma^c + \sigma^0)$ is the actual residual stress and, furthermore, the equality sign holds only if $\dot{\epsilon}^p = \mathbf{0}$. An integration of (8) over $V \times (0, \Delta t)$ then yields

$$\int_V \mathbf{s}':\Delta\epsilon^p dV-\int_0^{\Delta t}\int_V \sigma^R:\dot{\epsilon}^p dV dt<0, \tag{9}$$

as $\dot{\epsilon}^p$ cannot be identically vanishing. Making use of the equality

$$\dot{\epsilon}^p \doteq \dot{\epsilon}^R - \mathbf{A}:\dot{\sigma}^R \tag{10}$$

where $\dot{\epsilon}^R$ is the total (compatible) strain rate associated with $\dot{\epsilon}^p$ and $\mathbf{A}$ is the elastic compliance fourth-order tensor (with its usual symmetry properties), the second integral of the l.h.s. of (9) transforms as

$$\int_0^{\Delta t}\int_V \sigma^R:\dot{\epsilon}^p dV dt=\int_0^{\Delta t}\int_V \sigma^R:\dot{\epsilon}^R dV dt-\int_0^{\Delta t}\int_V \sigma^R:\mathbf{A}:\dot{\sigma}^R dV dt$$

$$=\int_0^{\Delta t}\int_V \sigma^R:\dot{\epsilon}^R dV dt-\frac{1}{2}\int_V \sigma^R:\mathbf{A}:\sigma^R dV\Big|_0^{\Delta t}=0, \tag{11}$$

as both last integral terms of (11) vanish, due to the virtual work principle and, respectively, the periodicity of σ^R. Thus, (9) finally reads

$$\int_V \mathbf{s}':\Delta\epsilon^p dV<0, \tag{12}$$

and the latter inequality enables one to state that the ratchet strain $\Delta\epsilon^p$ cannot be identically vanishing, that is, ratchetting must occur under the combined load $P(t) = P^c(t) + P^0$, whatever $P^0 \in \mathcal{P}^0$, but $P^0 \notin \mathcal{P}^0_S$. The conclusion is that, on the assumption of (6), plastic shakedown cannot occur whatever the steady load $P^0 \in \mathcal{P}^0$ in combination with the given cyclic load, hence the structure is safe. A customary reasoning path basing on perturbation considerations (Koiter, 1960) may be employed here to prove that the latter conclusion holds true also when (6) is weakened as (4). QED.

An obvious alternative form of Theorem 1 is Theorem 2.

Theorem 2.

For a Structure to be Safe—Alternative Statement. A necessary and sufficient condition in order that a structure subjected to a cyclic load be safe is that there exists some steady load—not necessary different from zero—such that elastic shakedown occurs under the combined cyclic/steady load.

In most cases of practice, the cyclic load path is a (closed) piecewise linear curve of the load space with corner loads P_1^B, $P_2^B, \ldots, P_m^B$, the basic loads. Let $\sigma_r^B(\mathbf{x})$ be the elastic stress responses to the basic loads P_r^B, $(r = 1, 2, \ldots, m)$. Like the Bleich-Melan theorem (see, e.g., Polizzotto, 1982; König, 1987), Theorem 1 then takes on the simpler form of Theorem 3.

Theorem 3.

For a Structure to be Safe—Piecewise Linear Load Path. A necessary and sufficient condition in order that a structure subjected to a cyclic load with a piecewise load path and basic loads, P_r^B $(r = 1, 2, \ldots, m)$, be safe is that there exists a time-independent stress field $\mathbf{s}$ such that each of the PT stress fields, $\hat{\sigma}_r^B = \sigma_r^B + \mathbf{s}$, obtained by superposing this $\mathbf{s}$ to the elastic stress responses to the P_r^B, σ_r^B, does not violate yield, i.e.,

$$\phi(\hat{\sigma}_r^B)\le 0 \text{ in } V,\ r=1,2,\ldots,m. \tag{13}$$

Proof. A piecewise linear load path can always be envisaged as a load history jumping from a basic load to the subsequent one with dwell periods $\theta_r = t_r - t_{r-1}$ at P_r^B with $\theta_1 + \theta_2 + \cdots + \theta_m = \Delta t$ and jumping times t_r. Such a load history can thus be represented as

$$P^c(t)=\sum_{r=1}^{m}\mu_r(t)P_r^B \tag{14}$$

with the coefficients μ_r defined as

$$\mu_r(t)=\delta_{rq} \text{ for } t\in(t_{q-1},t_q),\quad r,q\in(1,m) \tag{15}$$

where δ_{rq} is the Kronecker symbol, and analogously, the elastic stress response to (14) is

$$\sigma^c(\mathbf{x},t)=\sum_{r=1}^{m}\mu_r(t)\sigma_r^B(\mathbf{x}). \tag{16}$$

It can be easily recognized that Theorem 1, as applied to the cyclic load (14), identifies with Theorem 3. QED.

Often in practice the loads are allowed to vary arbitrarily within a given domain, Π, such that any closed load path of Π constitutes a potentially active cyclic load for the structure. Under these load conditions, the structure is safe if it is safe for every individual load path in Π; conversely, it is unsafe, if it is unsafe in respect to at least one cyclic load path of Π.

Without loss of generality Π can be assumed convex and of polyhedral shape with corner loads $P_1^B, P_2^B, \ldots, P_m^B$ (basic loads). The load path $P_1^B \to P_2^B \to \cdots \to P_m^B$, hereafter referred to as the enveloping cyclic load, can obviously be represented by (14) and (15), and the related elastic stress response is hence given by (16). Obviously, if the structure is safe for this enveloping cyclic load, in virtue of the convexity of ϕ, it is so also for any other cyclic load within Π. As a result, Theorem 3 is valid also in the present case, provided the piecewise linear load path therein involved coincides with the enveloping cyclic load of Π. More explicitly, when making reference to any load domain Π, one can state:

Theorem 4.

For a Structure to be Safe—Load Varying Within a Given Domain. A necessary and sufficient condition, in order that a structure subjected to loads varying within a given domain Π be safe, is that it is safe with respect to the enveloping cyclic load of Π.

The latter theorem substantially coincides with one previously proposed by König (1982a, b) through different arguments.

Kinematic Theorems

Another central theorem can also be established to characterize an unsafe structure. This theorem is similar to the Koiter-Neal-Symonds "kinematic" theorem, but instead of general PAM's, $\dot{\mathbf{e}}^p \in \mathfrak{M}$, it utilizes a subset $\tilde{\mathfrak{M}} \subset \mathfrak{M}$, containing PAM's characterized by zero ratchet strain, i.e., $\Delta\mathbf{e}^p = \mathbf{0}$ in V.

Theorem 5.

For a Structure to be Unsafe. A necessary and sufficient condition, in order that a structure subjected to a given cyclic load $P^c(t)$, $0 \le t \le \Delta t$, be unsafe, is that there exist some zero-ratchet-strain PAM, $\dot{\mathbf{e}}^p \in \tilde{\mathfrak{M}}$, such as to satisfy the following energy unbalance condition:

$$E[\dot{\mathbf{e}}^p]:=\int_0^{\Delta t}\int_V [D(\dot{\mathbf{e}}^p)-\sigma^c:\dot{\mathbf{e}}^p]dV dt<0. \tag{18}$$

Proof of the Necessity. By hypothesis, the structure subjected to $P^c(t)$ is unsafe. For contradiction, let (18) be negated by assuming $E[\dot{\mathbf{e}}^p] \ge 0$ for all $\dot{\mathbf{e}}^p \in \tilde{\mathfrak{M}}$. This implies that $E[\dot{\mathbf{e}}^p]$ possesses a (vanishing) minimum value in $\tilde{\mathfrak{M}}$ in correspondence of the trivial PAM $\dot{\mathbf{e}}^p \equiv \mathbf{0}$, and thus the problem

Downloaded 03 May 2010 to 171.66.16.245. Redistribution subject to ASME license or copyright; see http://www.asme.org/terms/Terms_Use.cfm

$$\min_{(\mathbf{e}^p)} E[\dot{\mathbf{e}}^p] \text{ s.t. } \dot{\mathbf{e}}^p \in \tilde{\mathfrak{N}}, \tag{19}$$

with "s.t." standing for "subject to," has a solution. As a result, the Euler-Lagrange equations related to (19) have a solution too. Applying the classical Lagrange multiplier method, the relevant augmented functional reads

$$E_a := \int_0^{\Delta t} \int_V [D(\dot{\mathbf{e}}^p) - \boldsymbol{\sigma}^c : \dot{\mathbf{e}}^p] dV dt - \int_V \mathbf{s} : \Delta \mathbf{e}^p dV \tag{20}$$

where $\mathbf{s}$ is a time-independent tensor-valued Lagrange multiplier function. The first variation of (20) is

$$\delta E_a = \int_0^{\Delta t} \int_V \delta \dot{\mathbf{e}}^p : \left[\frac{\partial D}{\partial \dot{\mathbf{e}}^p} - (\boldsymbol{\sigma}^c + \mathbf{s}) \right] dV dt - \int_V \delta \mathbf{s} : \Delta \mathbf{e}^p dV \tag{21}$$

such that the desired Euler-Lagrange equations read

$$\hat{\boldsymbol{\sigma}} := \boldsymbol{\sigma}^c + \mathbf{s} = \frac{\partial D}{\partial \dot{\mathbf{e}}^p} \text{ in } V \times (0, \Delta t), \tag{22}$$

besides the a priori condition $\Delta \mathbf{e}^p = 0$ in V. Equation (22) states that the stresses $\hat{\boldsymbol{\sigma}}$ (superposition of the elastic stresses $\boldsymbol{\sigma}^c$ with some time-independent stresses $\mathbf{s}$), can be qualified as PT stresses which, being derived from the dissipation function $D(\dot{\mathbf{e}}^p)$, satisfy the yield condition (4). Thus, due to Theorem 1, the structure is safe, contrary to the initial hypothesis. As a consequence, a PAM $\dot{\mathbf{e}}^p \in \tilde{\mathfrak{N}}$ satisfying (18) must exist—and the problem (19) has no solution.

Proof of the Sufficiency. By hypothesis, a PAM $\dot{\mathbf{e}}^p \in \tilde{\mathfrak{N}}$ exists which satisfies (18). By absurdity, let the structure be safe. Due to Theorem 1, a time-independent stress field $\mathbf{s}$ must exist, such as the resulting PT stresses $\hat{\boldsymbol{\sigma}} = \boldsymbol{\sigma}^c + \mathbf{s}$ satisfy (4). Thus, the maximum plastic work theorem enables one to write

$$D(\dot{\mathbf{e}}^p) - \hat{\boldsymbol{\sigma}} : \dot{\mathbf{e}}^p \geq 0 \text{ in } V \times (0, \Delta t); \tag{23}$$

then, after an integration over $V \times (0, \Delta t)$ and taking in account the zero-ratchet-strain condition, one has

$$\int_0^{\Delta t} \int_V [D(\dot{\mathbf{e}}^p) - \boldsymbol{\sigma}^c : \dot{\mathbf{e}}^p] dV dt \geq 0, \tag{24}$$

which contradicts the initial hypothesis. Therefore, the structure cannot be safe. QED.

Theorem 5 can be restated in a simpler form in case of piecewise linear load paths like those considered for Theorem 3. To this purpose, discrete-form PAM's are introduced, each of which consists of a discrete set of m plastic strain fields, $\mathbf{e}_1^p(\mathbf{x})$, such that $\mathbf{e}_1^p(\mathbf{x}) + \mathbf{e}_2^p(\mathbf{x}) + \cdots + \mathbf{e}_m^p(\mathbf{x}) = \mathbf{0}$ in V. The class $\tilde{\mathfrak{N}}_d$ of the latter PAM's is a subset of $\tilde{\mathfrak{N}}$, $\tilde{\mathfrak{N}}_d \subset \tilde{\mathfrak{N}}$, as in fact, with the symbols introduced with Theorem 3, one can write for every PAM in $\tilde{\mathfrak{N}}_d$:

$$\dot{\mathbf{e}}^p(\mathbf{x}, t) = \sum_{r=1}^{m} \theta_r^{-1} \mu_r(t) \mathbf{e}_r^p(\mathbf{x}), \; 0 \leq t \leq \Delta t \tag{25}$$

which represents a PAM of $\tilde{\mathfrak{N}}$ because the relevant ratchet strain vanishes. In fact, recalling (15), one has

$$\Delta \mathbf{e}^p = \sum_{r=1}^{m} \mathbf{e}_r^p \theta_r^{-1} \sum_{q=1}^{m} \int_{t_{q-1}}^{t_q} \mu_r(t) dt = \sum_{r=1}^{m} \mathbf{e}_r^p \theta_r^{-1} \sum_{q=1}^{m} \theta_q \delta_{rq}$$
$$= \sum_{r=1}^{m} \mathbf{e}_r^p = \mathbf{0} \text{ in } V. \tag{26}$$

The following theorem is the kinematic counterpart of Theorem 3.

Theorem 6.

For a Structure to be Unsafe—Piecewise Linear Load Path. A necessary and sufficient condition, in order that a structure subjected to a cyclic load with a piecewise linear path and basic loads P_r^B, $(r = 1, 2, \ldots, m)$, be unsafe, is that there exists a discrete-form zero-ratchet-strain PAM, $\mathbf{e}_r^p \in \tilde{\mathfrak{N}}_d$, such that

$$E_d[\mathbf{e}_r^p] = \sum_{r=1}^{m} \int_V [D(\mathbf{e}_r^p) - \boldsymbol{\sigma}_r^B : \mathbf{e}_r^p] dV < 0. \tag{27}$$

Proof. For the necessity part, the structure is assumed unsafe. Thus, due to Theorem 5, a zero-ratchet-strain PAM, $\dot{\mathbf{e}}^p \in \tilde{\mathfrak{N}}$, satisfying (18) exists. Since the cyclic load is one described by (14)–(16), the inequality (18) reads

$$\sum_{r=1}^{m} \int_V \left[\int_{t_{r-1}}^{t_r} D(\dot{\mathbf{e}}^p) dt - \boldsymbol{\sigma}_r^B : \mathbf{e}_r^p \right] dV < 0 \tag{28}$$

where

$$\mathbf{e}_r^p := \int_{t_{r-1}}^{t_r} \dot{\mathbf{e}}^p dt \quad \text{for all } r \in (1, m). \tag{29}$$

But, as it can be easily proved,

$$D(\mathbf{e}_r^p) \leq \int_{t_{r-1}}^{t_r} D(\dot{\mathbf{e}}^p) dt \quad \text{for all } r \in (1, m), \tag{30}$$

so the inequality (28) implies the validity of (27). As for the sufficiency part of the proof, let a discrete-form PAM, $\mathbf{e}_r^p \in \tilde{\mathfrak{N}}_d$, satisfying (27), exist. Inequality (27) is recognized as having the shape taken by (18), when written for the particular PAM (25) generated by this $\mathbf{e}_r^p \in \tilde{\mathfrak{N}}_d$. As a consequence, due to Theorem 5, the structure is unsafe. QED.

Theorem 6 holds good also in the case of loads varying in a domain Π as considered for Theorem 4, provided the piecewise linear load path of Theorem 6 is substituted by the enveloping load path of Π. With reference to any load domain Π, one can state the following.

Theorem 7.

For a Structure to be Unsafe—Load Varying Within a Given Domain. A necessary and sufficient condition, in order that a structure subjected to loads varying within a given domain Π be unsafe, is that it is unsafe under the enveloping cyclic load of Π.

An immediate consequence of Theorem 5 is the following.

Theorem 8.

For a Structure to be Safe. A necessary and sufficient condition for a structure subjected to a given cyclic load $P^c(t)$, $0 \leq t \leq \Delta t$, to be safe is that the inequality $E[\dot{\mathbf{e}}^p] \geq 0$ be satisfied for all $\dot{\mathbf{e}}^p \in \tilde{\mathfrak{N}}$—and thus the minimization problem (19) possesses a solution.

Indeed, the above statement is a negation of Theorem 5. Obviously, on negation of Theorem 6, Theorem 8 in turn takes on a simpler form in which $E[\dot{\mathbf{e}}^p]$ is substituted by $E_d[\mathbf{e}_r^p]$ with $\mathbf{e}_r^p \in \tilde{\mathfrak{N}}_d$. In the latter form, Theorem 8 substantially coincides with a theorem given by König (1982) with reference to loads varying within a given domain.

Conclusion

For a structure of elastic-perfectly plastic material subjected to combined loads, each being the superposition of a given cyclic load with a steady (mechanical) load, the conditions have been here assessed, under which plastic shakedown cannot occur and thus the structure does not suffer alternating plasticity. Two central theorems have been proved which characterize the structure's condition of safety or unsafety with respect to the alternating plasticity collapse. These theorems are fully similar to those of classical shakedown theory; more precisely, the static theorem makes use of time-independent

Downloaded 03 May 2010 to 171.66.16.245. Redistribution subject to ASME license or copyright; see http://www.asme.org/terms/Terms_Use.cfm

stress fields instead of self-equilibrated ones and the kinematic theorem makes use of zero-ratchet strain-rate cycles instead of simple kinematically admissible ones. The cases of piecewise linear cyclic load path and of loads varying within a given (polyhedral) domain have also been considered in which the above theorems take on time discretized forms.

The above theorems, which include the particular cases of previous theorems by König, will be employed in Part II of this paper and is aimed at the assessment of the plastic shakedown limit load together with the related structure's limit state.

Though the safety condition established here appears to be a concept weaker than that related to elastic shakedown, nevertheless the fact that it can be given a firm rational basis fully similar to that of the classical elastic shakedown theory represents a worthwhile result on its own.

Acknowledgement

This paper has been completed with the financial support of the Consiglio Nazionale delle Ricerche, C.N.R., Italy.

References

Frederich, C. O., and Armstrong, P. J., 1966, "Convergent Internal Stresses and Steady Cyclic State of Stresses, *J. Strain Analysis*, Vol. 1, p. 154.

Gokhfeld, D. A., and Cherniavsky, D. F., 1980, *Limit Analysis of Structures at Thermal Cycling*, Sijthoff and Noordhoff, Alphen aan der Rijn, The Netherlands.

Koiter, W. T., 1960, "General Theorems for Elastic-Plastic Solids," *Progress in Solid Mechanics*, Vol. 1, J. N. Sneddon and R. Hill, eds., North Holland, Amsterdam, pp. 167–221.

König, J. A., 1982a, "On Upper Bounds to Shakedown Loads," *ZAMM*, Vol. 52, pp. 421–428.

König, J. A., 1982b, "On Some Recent Developments in the Shakedown Theory," *Advances in Mechanics*, Vol. 5, pp. 237–258.

König, J. A., 1987, *Shakedown of Elastic-Plastic Structures*, PWN—Polish Scientific Publishers, Warsaw.

Martin, J. B., 1975, *Plasticity: Fundamentals and General Results*, The MIT Press, Cambridge, MA.

Polizzotto, C., 1982, "A Unified Treatment of Shakedown Theory and Related Bounding Techniques," *S.M. Archives*, Vol. 7, pp. 19–75.

Polizzotto, C., 1989, "Simplified Methods of Structural Analysis for Cyclic Plasticity," Final Report RA1-0116(I), Commission of European Communities, Brussels, and Dipartimento di Ingegneria Strutturale & Geotecnica, University of Palermo, Palermo.

Polizzotto, C., Borino, G., and Fuschi, P., 1990, "On the Steady State Response of Elastic Perfectly Plastic Solids to Cyclic Loads," *Inelastic Solids and Structures*, M. Kleiber and J. A. König, eds., Pineridge Press, Swansea, pp. 473–488.

Ponter, A. R. S., 1983, "Shakedown and Ratchetting Below the Creep Range," Report EUR 8702 EN, Commission of European Communities, Brussels.

Ponter, A. R. S., and Karadeniz, S., 1985a, "An Extended Shakedown Theory for Structures That Suffer Cyclic Thermal Loadings: Part 1—Theory," ASME Journal of Applied Mechanics, Vol. 52, pp. 877–882.

Ponter, A. R. S., and Karadeniz, S., 1985b, "An Extended Shakedown Theory for Structures That Suffer Cyclic Thermal Loadings: Part 2—Applications," ASME Journal of Applied Mechanics, Vol. 52, pp. 883–889.

Symonds, P. S., and Neal, B. G., 1951, "Recent Progress in the Plastic Methods of Structural Analysis," *J. of the Franklin Institute*, Vol. 252, pp. 383–492.

Zarka, J., and Casier, J., 1979, "Cyclic Loading on Elastic-Plastic Structures," *Mechanics Today*, S. Nemat-Nasser, ed., Pergamon Press, Oxford, pp. 93–198.

Downloaded 03 May 2010 to 171.66.16.245. Redistribution subject to ASME license or copyright; see http://www.asme.org/terms/Terms_Use.cfm

On the Conditions to Prevent Plastic Shakedown of Structures: Part II—The Plastic Shakedown Limit Load[1]

Castrenze Polizzotto
Dipartimento di Ingegneria Strutturale & Geotecnica, DISEG, Università di Palermo, Viale delle Scienze, I-90128, Italy

Following the results of a companion paper, the concept of plastic shakedown limit load is introduced for an elastic-perfectly plastic material structure subjected to combined cyclic (mechanical and/or kinematical) loads and steady (mechanical) load. Static and kinematic approaches are available for the computation of this load, in perfect analogy with the classic (elastic) shakedown limit load. The plastic shakedown limit state of the structure being in an impending alternating plasticity collapse is studied and a number of interesting features of it are pointed out.

Introduction

A previous companion paper (Polizzotto, 1993) has been devoted to the assessment of the conditions in which a structure of elastic-perfectly plastic material and subjected to combined cyclic/steady loads is safe against the alternating plasticity collapse. This goal has been achieved by establishing two central theorems, namely the static and kinematic theorems, fully similar to those of the classical (elastic) shakedown theory, that is the Bleich-Melan theorem and the Koiter-Neal-Symonds theorem (see, e.g., Koiter, 1960; Martin, 1975; Gokhefeld and Cherniavsky, 1980; König, 1983; Symonds and Neal, 1951). The static theorem states the conditions in which the structure is safe, and the kinematic one states those in which the structure is unsafe.

The present paper is devoted to the assessment of the plastic shakedown limit load, that is that cyclic load value which, acting in combination with some "neutralizing" steady load, leads the structure to a limit state of impeding alternating plasticity. This limit load can be determined by means of lower and upper bound theorems, which are derived from the above two central theorems, respectively, in perfect analogy with the elastic shakedown limit load. Also, the structure's plastic shakedown limit state will be investigated and a number of interesting properties of it will be pointed out.

After a brief summary of the above central theorems, methods to compute the plastic shakedown limit load will be presented and discussed together with the related plastic shakedown limit state of the structure. The same tensor notation, as in Part I of this paper, will be used.

The Static and Kinematic Theorems

Let an elastic-perfectly plastic material structure of domain V and boundary surface ∂V, referred to a Cartesian orthogonal coordinate system $\mathbf{x} = (x_1, x_2, x_3)$, be loaded by external actions as body forces in V, tractions on the free boundary $\partial_t V \subset \partial V$, imposed strains in V, and imposed displacements on the constrained boundary $\partial_u V \subset \partial V (\partial_t V \cup \partial_u V = \partial V)$. Let all these actions be collectively denoted as

$$P(t) = P^c(t) + P^0,\ 0 \le t \le \Delta t,\ P^0 \in \mathcal{P}^0 \tag{1}$$

where $P^c(t)$ denotes a quasi-static cyclically variable (mechanical and/or kinematical) load and P^0 a steady (mechanical) load in the set $\mathcal{P}^0$. The latter set is here assumed to include all the loads below the plastic collapse limit values (but on occasion it may be a narrower one). The hypotheses of infinitesimal displacements and of temperature-independent material data are adopted.

A structure subjected to a specified cyclic load $P^c(t)$ can be classified as "safe" or "unsafe" according to the type of steady-state responses produced by $P^c(t)$ acting in combination with the steady loads $P^0 \in \mathcal{P}^0$. Namely, it is safe if plastic shakedown (i.e., alternating plasticity) does not occur whatever the steady load $P^0 \in \mathcal{P}^0$, whereas it is unsafe if plastic shakedown actually occurs for at least one $P^0 \in \mathcal{P}^0$. On the basis of the latter definitions two central theorems were established in the companion paper to a priori recognize whether the structure is safe or unsafe. For later use, these two theorems are reminded here. In the following, $\sigma^c(\mathbf{x}, t)$ and $\sigma^0(\mathbf{x})$ denote the elastic stress responses of the body to $P^c(t)$ and P^0, respectively. Also, $\dot{\mathbf{e}}^p(\mathbf{x}, t)$ denotes a plastic accumulation mechanism (PAM) (or plastic strain cycle) and $\Delta \mathbf{e}^p(\mathbf{x}) = \int_0^{\Delta t} \dot{\mathbf{e}}^p dt$ is the related ratchet strain field.

Static Theorem. A necessary and sufficient condition for

[1]This paper is dedicated to the memory of Professor Jan A. Konig.

Contributed by the Applied Mechanics Division of THE AMERICAN SOCIETY OF MECHANICAL ENGINEERS for publication in the ASME JOURNAL OF APPLIED MECHANICS.

Discussion on this paper should be addressed to the Technical Editor, Professor Lewis T. Wheeler, Department of Mechanical Engineering, University of Houston, Houston, TX 77204-4792, and will be accepted until four months after final publication of the paper itself in the ASME JOURNAL OF APPLIED MECHANICS.

Manuscript received by the ASME Applied Mechanics Division, Nov. 30, 1990; final revision, Sept. 20, 1991. Associate Technical Editor: R. M. McMeeking.

Copyright © 1993 by ASME
Downloaded 03 May 2010 to 171.66.16.245. Redistribution subject to ASME license or copyright; see http://www.asme.org/terms/Terms_Use.cfm

a structure subjected to a specified cyclic load to be safe is that there exists some time-independent stress field $\mathbf{s}$ such that the "post-transient" (PT) stress field $\hat{\boldsymbol{\sigma}} = \boldsymbol{\sigma}^c + \mathbf{s}$ (superposition of $\mathbf{s}$ with the elastic stress response to $P^c(t)$, $\boldsymbol{\sigma}^c(\mathbf{x}, t)$, nowhere violates yield, i.e.,

$$\phi(\hat{\boldsymbol{\sigma}}) \leq 0 \text{ in } V \times (0, \Delta t) \tag{2}$$

where $\phi(\hat{\boldsymbol{\sigma}})$ is the plastic yielding function.

Kinematic Theorem. A necessary and sufficient condition, in order that a structure subjected to a specified cyclic load be unsafe, is that there exists a plastic accumulation mechanism (PAM), $\dot{\boldsymbol{\epsilon}}^p(\mathbf{x}, t)$, resulting in a vanishing ratchet strain field, $\Delta \boldsymbol{\epsilon}^p = \mathbf{0}$ in V, such as to satisfy the energy unbalance condition, i.e.,

$$E[\dot{\boldsymbol{\epsilon}}^p] := \int_0^{\Delta t} \int_V [D(\dot{\boldsymbol{\epsilon}}^p) - \boldsymbol{\sigma}^c : \dot{\boldsymbol{\epsilon}}^p] dV\, dt < 0 \tag{3}$$

where $D(\dot{\boldsymbol{\epsilon}}^p)$ is the plastic dissipation function.

The above theorems are reported as Theorems 1 and 5, respectively, in Part I of this paper. As shown in the latter paper, the two aforementioned theorems take on discrete forms in the case of piecewise linear load path or of loads varying within a specified polyhedral region of the load space.

The Plastic Shakedown Limit Load Multiplier

Let the structure be loaded be a cyclic load $P^c(t) = \beta \overline{P}^c(t)$, where $\overline{P}^c(t)$ is assigned for $0 \leq t \leq \Delta t$, as well as by a steady load $P^0 \in \mathcal{P}^0$. The plastic shakedown limit load, $\beta^* \overline{P}^c(t)$, is the cyclic load that, acting in combination with some "neutralizing" steady load, leads the structure to a limit state of impending alternating plasticity. Lower and upper bounds to β^* can be obtained by the following two theorems.

Lower Bound Theorem. If a structure subjected to a cyclic load $\beta \overline{P}^c(t)$ is safe, then β cannot be greater than β^*.

Proof. Due to the static theorem, a time-independent stress field $\mathbf{s}$ exists such that the PT stress, $\hat{\boldsymbol{\sigma}} = \boldsymbol{\sigma}^c + \mathbf{s}$, does not violate yield, i.e., $\phi(\hat{\boldsymbol{\sigma}}) \leq 0$ in $V \times (0, \Delta t)$. Let $\dot{\boldsymbol{\epsilon}}^p(\mathbf{x}, t)$ describe the impending alternating plasticity collapse related to $\beta^* \overline{P}^c(t)$ acting together with some $P^0 \in \mathcal{P}^0$. By Drucker's postulate, one can write

$$(\boldsymbol{\sigma} - \hat{\boldsymbol{\sigma}}) : \dot{\boldsymbol{\epsilon}}^p \geq 0 \quad \text{in } V \times (0, \Delta t) \tag{4}$$

where $\boldsymbol{\sigma}$ is the actual stress in the limit state. Since $\boldsymbol{\sigma} = \beta^* \overline{\boldsymbol{\sigma}}^c + \boldsymbol{\sigma}^0 + \boldsymbol{\sigma}^R$, with $\boldsymbol{\sigma}^R$ being the actual residual stress, an integration of (4) over $V \times (0, \Delta t)$ gives

$$(\beta^* - \beta) \int_0^{\Delta t} \int_V \overline{\boldsymbol{\sigma}}^c : \dot{\boldsymbol{\epsilon}}^p dV\, dt + \int_V (\boldsymbol{\sigma}^0 - \mathbf{s}) : \Delta \boldsymbol{\epsilon}^p dV + \int_0^{\Delta t} \int_V \boldsymbol{\sigma}^R : \dot{\boldsymbol{\epsilon}}^p dV dt \geq 0. \tag{5}$$

In view of the facts that $\Delta \boldsymbol{\epsilon}^p = \mathbf{0}$ in V, that the last integral in (5) vanishes (see (11) of the twin paper) and that the integral multiplying $\beta^* - \beta$ in (5) is positive, Eq. (5) states that $\beta^* \geq \beta$. QED.

Upper Bound Theorem. If $\dot{\boldsymbol{\epsilon}}^p(\mathbf{x}, t)$ is a PAM with zero ratchet strain, $\Delta \boldsymbol{\epsilon}^p = \mathbf{0}$ in V, the following inequality holds:

$$\int_0^{\Delta t} \int_V D(\dot{\boldsymbol{\epsilon}}^p) dV\, dt \Big/ \int_0^{\Delta t} \int_V \overline{\boldsymbol{\sigma}}^c : \dot{\boldsymbol{\epsilon}}^p dV\, dt \geq \beta^*. \tag{6}$$

Proof. In virtue of the lower bound theorem, the structure subjected to $\beta \overline{P}^c(t)$ with $\beta \leq \beta^*$ is safe. Thus, as a consequence of the kinematic theorem, one has that $E[\dot{\boldsymbol{\epsilon}}^p] \geq 0$. That is

$$\int_0^{\Delta t} \int_V D(\dot{\boldsymbol{\epsilon}}^p) dV\, dt \geq \beta \int_0^{\Delta t} \int_V \overline{\boldsymbol{\sigma}}^c : \dot{\boldsymbol{\epsilon}}^p dV\, dt \tag{7}$$

for all $\beta \leq \beta^*$ and for all PAM's with zero ratchet strain, i.e., $\Delta \boldsymbol{\epsilon}^p = \mathbf{0}$ in V. Since inequality (7), for $\beta = \beta^*$, coincides with (6), the theorem is proved. QED.

The plastic shakedown limit load multiplier, β^* can thus be determined either by a static approach, or a kinematic approach, that is, respectively,

$$\beta^* = \max_{(\beta,\, \mathbf{s})} \beta \text{ s.t. } \phi(\beta \overline{\boldsymbol{\sigma}}^c + \mathbf{s}) \leq 0 \text{ in } V \times (0, \Delta t) \tag{8}$$

$$\beta^* = \min_{(\dot{\boldsymbol{\epsilon}}^p)} \int_0^{\Delta t} \int_V D(\dot{\boldsymbol{\epsilon}}^p) dV\, dt \text{ s.t. } \begin{cases} \Delta \boldsymbol{\epsilon}^p = \displaystyle\int_0^{\Delta t} \dot{\boldsymbol{\epsilon}}^p dt = \mathbf{0} \text{ in } V \\ \displaystyle\int_0^{\Delta t} \int_V \overline{\boldsymbol{\sigma}}^c : \dot{\boldsymbol{\epsilon}}^p dV\, dt = 1 \end{cases} \tag{9}$$

where "s.t." stands for "subject to".

The two problems above are dual of each other as in fact it can be shown through the related Euler-Lagrange equations. The latter equations are easily found by the Lagrange multiplier method. Referring for instance to (8), let one consider the related augmented functional

$$L := -\beta + \int_0^{\Delta t} \int_V \dot{l}\, \phi(\beta \overline{\boldsymbol{\sigma}}^c + \mathbf{s}) dV\, dt, \tag{10}$$

where $\dot{l}(\mathbf{x}, t) \geq 0$ is the relevant multiplier, and let one take the first variation δL, i.e.,

$$\delta L = \delta \beta \left(-1 + \int_0^{\Delta t} \int_V \dot{l}\, \frac{\partial \phi}{\partial \hat{\boldsymbol{\sigma}}} dV\, dt \right) + \int_V \delta \mathbf{s} : \left(\int_0^{\Delta t} \dot{l}\, \frac{\partial \phi}{\partial \hat{\boldsymbol{\sigma}}} dt \right) dV + \int_0^{\Delta t} \int_V \delta \dot{l}\, \phi(\hat{\boldsymbol{\sigma}}) dV\, dt, \tag{11}$$

where $\hat{\boldsymbol{\sigma}} := \beta \overline{\boldsymbol{\sigma}}^c + \mathbf{s}$. Thus, the desired Euler-Lagrange equations read

$$\phi(\hat{\boldsymbol{\sigma}}) \leq 0, \ \dot{l} \geq 0, \ \dot{l}\, \phi(\hat{\boldsymbol{\sigma}}) = 0 \text{ all in } V \times (0, \Delta t) \tag{12a}$$

$$\hat{\boldsymbol{\sigma}} = \beta \overline{\boldsymbol{\sigma}}^c + \mathbf{s}, \ \dot{\boldsymbol{\epsilon}}^p = \dot{l}\, \frac{\partial \phi}{\partial \hat{\boldsymbol{\sigma}}} \text{ all in } V \times (0, \Delta t) \tag{12b}$$

$$\Delta \boldsymbol{\epsilon}^p = \int_0^{\Delta t} \dot{\boldsymbol{\epsilon}}^p dt = \mathbf{0} \text{ in } V \tag{12c}$$

$$\int_0^{\Delta t} \int_V \overline{\boldsymbol{\sigma}}^c : \dot{\boldsymbol{\epsilon}}^p dV\, dt = 1. \tag{12d}$$

On applying a dualization procedure to (12), one can prove that problem (8) transforms into (9), but this point is missed for brevity.

As a consequence of the convexity of ϕ and D, Eqs. (12*a–d*) are not only necessary, but are also sufficient conditions for problems (8) and (9). For brevity, this point is not discussed in detail here.

The solution to (12*a–d*) exhibits uniqueness features which are worth being noticed. Let there exist, by hypothesis, two solutions respectively denoted by primed and doubly primed symbols. Then, Drucker's postulate yields

$$(\hat{\boldsymbol{\sigma}}' - \hat{\boldsymbol{\sigma}}'') : (\dot{\boldsymbol{\epsilon}}^{p\prime} - \dot{\boldsymbol{\epsilon}}^{p\prime\prime}) = (\mathbf{s}' - \mathbf{s}'') : (\dot{\boldsymbol{\epsilon}}^{p\prime} - \dot{\boldsymbol{\epsilon}}^{p\prime\prime}) \geq 0 \text{ in } V \times (0, \Delta t) \tag{13}$$

and the latter inequality, after an integration over $(0, \Delta t)$ and in virtue of (12*c*), becomes

$$\int_0^{\Delta t} (\hat{\boldsymbol{\sigma}}' - \hat{\boldsymbol{\sigma}}'') : (\dot{\boldsymbol{\epsilon}}^{p\prime} - \dot{\boldsymbol{\epsilon}}^{p\prime\prime}) dt = 0 \text{ in } V. \tag{14}$$

This means that (13) must be satisfied as an equality, i.e.,

$$(\hat{\boldsymbol{\sigma}}' - \hat{\boldsymbol{\sigma}}'') : (\dot{\boldsymbol{\epsilon}}^{p\prime} - \dot{\boldsymbol{\epsilon}}^{p\prime\prime}) = (\mathbf{s}' - \mathbf{s}'') : (\dot{\boldsymbol{\epsilon}}^{p\prime} - \dot{\boldsymbol{\epsilon}}^{p\prime\prime}) = 0 \text{ in } V \times (0, \Delta t). \tag{15}$$

In the case that ϕ is smooth (as it has been assumed here), the identity (15) implies that in the region $V_F \subseteq V$ where the yield condition is actually attained somewhere in the cycle, the so-

Downloaded 03 May 2010 to 171.66.16.245. Redistribution subject to ASME license or copyright; see http://www.asme.org/terms/Terms_Use.cfm

lution is unique, that is $\mathbf{s}' = \mathbf{s}'' = \mathbf{s}$, $\dot{\mathbf{e}}^{p\prime} = \dot{\mathbf{e}}^{p\prime\prime} = \dot{\mathbf{e}}^{p}$, whereas in the region V_S, ($V_S \cup V_F = V$) where the yield condition is not attained, i.e., $\phi(\hat{\sigma}) < 0$ for all $t \in (0, \Delta t)$, one has $\dot{\mathbf{e}}^{p\prime} = \dot{\mathbf{e}}^{p\prime\prime} = \mathbf{0}$, such that $\mathbf{s}'$ and $\mathbf{s}''$ may differ from each other. The same results hold good also when ϕ exhibits corners or flat regions in which case $\dot{\mathbf{e}}^{p}$ may exhibit some indeterminancy degree in the V_F region, but with a uniquely determined plastic dissipation. For simplicity's sake, the latter point is not discussed here in detail, and the V_F region—where the yield condition is actually attained within the cycle according to Eqs. (12*a*)—will be regarded as the region where the solution is uniquely determined.

In case of a cyclic load with a (closed) piecewise linear path, problems (8) and (9) take on time discrete forms. Let $\overline{P}_r^B$, ($r = 1,2, \ldots, m$) be the reference basic loads and let $\overline{\sigma}_r^B$ be the related elastic stress responses; also, let $\mathbf{e}_r^p$, ($r = 1,2, \ldots, m$) denote a set of plastic strain fields. Problems (8) and (9) can in this case be rewritten as

$$\beta^* = \max_{(\beta,\ \mathbf{s})} \beta \text{ s.t. } \phi(\beta\overline{\sigma}_r^B + \mathbf{s}) \le 0 \text{ in } V, \text{ all } r \in (1, m) \tag{16}$$

$$\beta^* = \min_{(\mathbf{e}_r^p)} \sum_{r=1}^{m} \int_V D(\mathbf{e}_r^p) dV \text{ s.t. } \begin{cases} \sum_{r=1}^{m} \mathbf{e}_r^p = \mathbf{0} \text{ in } V \\ \sum_{r=1}^{m} \int_V \overline{\sigma}_r^B : \mathbf{e}_r^p dV = 1. \end{cases} \tag{17}$$

Obviously, these problems are consequences of time discrete forms of the lower and upper bound theorems which can be proved easily to hold, but this point is skipped here for simplicity. Problems (16) and (17) are also valid in case of loads varying within a specified polyhedral domain with reference to the related basic loads $\overline{P}_r^B$.

The Plastic Shakedown Limit State

Equations (12*a–d*) describe the plastic shakedown limit state, that is the state in which the structure finds itself when loaded by the combined load $\beta^*\overline{P}^c(t) + P^0$ with $P^0 \in \mathcal{P}_N^0 \subset \mathcal{P}^0$. The subset $\mathcal{P}_N^0$ collects the "neutralizing" loads P^0, determined as the loads equilibrated by the stresses $\mathbf{s}$ pertaining to the solution to (12*a–d*). In view of the uniqueness features of the latter solution, the actual stresses of the limit state can be given the following representation:

$$\hat{\sigma} = \begin{cases} \beta^*\overline{\sigma}^c + \mathbf{s}^* & \text{in } V_F \quad (18a) \\ \beta^*\overline{\sigma}^c + \mathbf{s}^* + \mathbf{t} & \text{in } V_S \quad (18b) \end{cases}$$

where $\mathbf{s}^*$ denotes the uniquely determined $\mathbf{s}$ field in V_F as well as a suitable continuation of it in V_S; whereas $\mathbf{t}$ denotes stresses equilibrating some additional steady load P_a^0 applied upon V_S. Thus, if P^{0*} is the load equilibrated by $\mathbf{s}^*$, i.e., the reference neutralizing load, the entire set of neutralizing loads is obtained as $P^0 = P^{0*} + P_a^0$ where P_a^0 can vary within some range, determined by the condition that the stresses (18*b*) do not attain the yield condition in V_S. On changing P_a^0 within the latter range the structure's plastic shakedown limit state remains unaltered for all, except the stresses $\mathbf{t}$ in V_S. In other words, on application of a steady load P_a^0 upon V_S, such that $P^0 + P_a^0 \in \mathcal{P}_N^0$, V_F remains in the same limit state of impending alternating plasticity as without P_a^0, whereas V_S continues to behave elastically but in a different stress state. This is the insensitivity property of the steady-state response to steady loads applied upon V_S, exhibited by a structure in a condition of plastic shakedown, as previously found by Polizzotto et al. (1989).

The stresses $\hat{\sigma} = \hat{\sigma}^* = \beta^*\overline{\sigma}^c + \mathbf{s}^*$ of (18*a*) are uniquely determined. At every point in V_F they constitute a stress path which results from shifting the elastic stress path $\beta^*\overline{\sigma}^c$ by $\mathbf{s}^*$ such as to settle, in a balanced (or neutral) configuration with respect to the yield surface $\phi = 0$, with the feature that the gradient vectors $\mathbf{q} = \partial\phi/\partial\hat{\sigma}$ evaluated at the "critical" stress points (i.e., where $\phi = 0$) form a set of linearly and positively dependent vectors, as shown by (12*c*) rewritten as

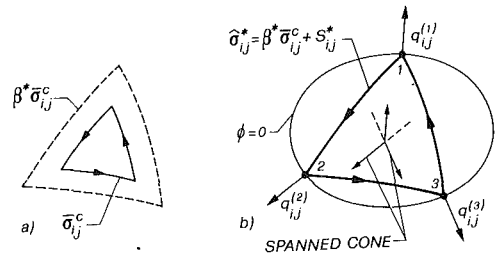


Fig. 1

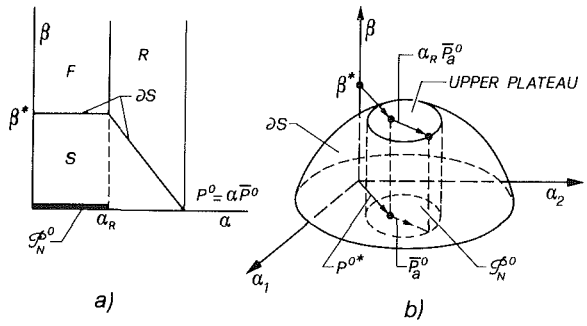


Fig. 2

$$\int_0^{\Delta t} \mathbf{q}\, \dot{l}\, dt = \mathbf{0} \text{ in } V_F, \tag{19}$$

where $\dot{l} \ge 0$ is not identically vanishing in V_F (but $\dot{l} \equiv 0$ in V_S). In general, the critical stress points are a discrete set of isolated points, so that (19) reads

$$\sum_{\nu=1}^{N} \mathbf{q}_\nu l_\nu = \mathbf{0} \text{ in } V_F. \tag{20}$$

The neutral configuration of the stress path $\hat{\sigma}$ with respect to $\phi = 0$ is thus dictated by the following Kuhn-Tucker condition: at every point in V_F, the vectors $\mathbf{q}_\nu = \partial\phi/\partial\hat{\sigma}_\nu$ evaluated at the critical stress points $\hat{\sigma}_\nu$, and drawn from the stress space origin, span a convex hypercone whose halves must contain at least one of the $\mathbf{q}_\nu$, hence $N \ge 2$. This property, illustrated in Fig. 1, was shown by Polizzotto (1989) to be a feature of the structural behavior in the condition of plastic shakedown even under higher cyclic loads.

Since the stress field $\mathbf{s}$ of problem (8) is in equilibrium with some steady load P^0, this same problem can be viewed as the one for the search of the/a $P^0 \in \mathcal{P}^0$ such as to maximize the elastic shakedown load multiplier, $\beta_S(P^0)$, associated with the combined cyclic/steady load $\beta\overline{P}^c(t) + P^0$, namely

$$\beta^* = \max_{(P^0)} \beta_S(P^0) \text{ s.t. } P^0 \in \mathcal{P}^0, \text{ where} \tag{21}$$

$$\beta_S(P^0) = \max_{(\beta,\ \mathbf{s})} \beta \text{ s.t. } \begin{cases} \phi(\beta\overline{\sigma}^c + \mathbf{s}) \le 0 \text{ in } V \times (0, \Delta t) \\ \text{equilibrium conds. on } \mathbf{s} \text{ with } P^0 \\ \text{(fixed).} \end{cases} \tag{22}$$

Problem (22) provides the equation $\beta = \beta_S(P^0)$ of the elastic shakedown interaction surface ∂S—the boundary of the elastic shakedown (convex) region S of the load space $\mathbb{R}^+ \times \mathcal{P}^0 = \{\beta \ge 0, P^0 \in \mathcal{P}^0\}$, see Fig. 2(*a*, *b*). There is, in general, a set $\mathcal{P}_N^0 \subset \mathcal{P}^0$ of maximizing loads P^0 in (21)—that is, the set of neutralizing loads differing from one another only for their components applied upon V_S. Every load $P^0 \in \mathcal{P}_N^0$ makes the elastic stress path $\beta\overline{\sigma}^c$ to homothetically expand (or shrink) at most—with β suitably increasing (or decreasing)—while shift-

Downloaded 03 May 2010 to 171.66.16.245. Redistribution subject to ASME license or copyright; see http://www.asme.org/terms/Terms_Use.cfm

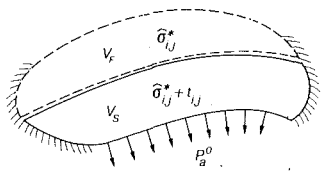


Fig. 3

ing to a neutral configuration with respect to the yield surface $\phi = 0$ within the V_F region. This neutralization effect upon the elastic stress path due to the available steady load identifies with the analogous effect produced by kinematic hardening, a material constitutive behavior known to prevent ratchetting (Zarka and Casier, 1979; Gokhfeld and Cherniavsky, 1980; Ponter, 1983). However, whereas kinematic hardening excludes the occurrence of ratchetting in all load cases, the available steady load produces the same effect only for P^0 within some subset, which depends on β but coincides with $\mathcal{P}^0_N$ for $\beta = \beta^*$.

The pairs (β^*, P^0) with $P^0 \in \mathcal{P}^0_N$ are load points filling an upper plateau of the interaction surface ∂S, as sketched in Fig. 2(a, b). This flat portion of ∂S is representative of the insensitivity of the plastic shakedown limit state to steady loads applied upon V_S. The loads $P^0 \in \partial\mathcal{P}^0_N$ ($\partial\mathcal{P}^0_N$ is the boundary of $\mathcal{P}^0_N$), correspond to the boundary of the upper plateau, and can be evaluated as elastic shakedown limit loads. To this purpose, reminding (18a, b) and setting $P^0 = P^{0*} + \alpha\overline{P}^0_a$, where $\overline{P}^0_a$ is fixed to define a load direction drawn from P^{0*} over the upper plateau, one has to solve the problem

$$\alpha_R = \max_{(\alpha,\ \mathbf{t})} \alpha \text{ s.t. } \begin{cases} \phi(\hat{\boldsymbol{\sigma}}^*) \le 0 \text{ in } V_F \times (0,\ \Delta t) \\ \phi(\hat{\boldsymbol{\sigma}}^* + \mathbf{t}) \le 0 \text{ in } V_S \times (0,\ \Delta t) \\ \text{Equilibrium conds. on } \mathbf{t} \text{ with } \alpha\overline{P}^0_a, \end{cases} \tag{23}$$

where $\hat{\boldsymbol{\sigma}}^* = \beta^*\overline{\boldsymbol{\sigma}}^c + \mathbf{s}^*$. Since both $\hat{\boldsymbol{\sigma}}^*$ and V_F shown above remain fixed as α changes, problem (23) simplifies to

$$\alpha_R = \max_{(\alpha,\ \mathbf{t})} \alpha \text{ s.t. } \begin{cases} \phi(\hat{\boldsymbol{\sigma}}^* + \mathbf{t}) \le \mathbf{0} \text{ in } V_S \times (0,\ \Delta t) \\ \text{Equilibrium conds. on } \mathbf{t} \text{ with } \alpha\overline{P}^0_a. \end{cases} \tag{24}$$

The latter problem is recognized as an elastic shakedown limit load problem for the body V_S left after removal of V_F from V, see Fig. 3. Indeed, $\hat{\boldsymbol{\sigma}}^*$ can be always interpreted as the elastic stress response of V_S to actions applied upon it (including actions at points of the interface between V_S and V_F). Obviously, whenever the body V_S turns out to be a free body, one has $\alpha_R = 0$ and the upper plateau reduces to a single point. Problem (24) reproposes Ponter's method (Ponter, 1983; Ponter and Karadeniz, 1985), which is based on heuristic arguments and aimed at the approximate determination of the border line between the plastic shakedown zone and the ratchetting one in the (α, β)-plane (generalized Bree diagram) for cyclically hardening materials. This method was subsequently modified by Polizzotto (1989) to obtain exact results for perfectly plastic material structures and for all $\beta \ge 0$, but for $\beta = \beta^*$, the Ponter's method and the modified one coincide with each other. The increasing of α to α_R leads the body V_S to a limit state of impending ratchetting. The application of Ponter's method requires one to previously evaluate β^*, $\mathbf{s}^*$, and V_F through the solution of either (8) or (9) or (12).

Remarks on Computational Aspects and Examples

The computational aspects are mainly related to the evaluation of β^* through the solution of problems (8) or (9). It is worth noting that problem (8) is mathematically simpler than the analogous problem for determining the elastic shakedown multiplier $\beta_S(P^0)$ through the static approach (22)—for the stresses $\mathbf{s}$ here are free-stress variables instead of equilibrium stresses. Obviously, every numerical procedure adopted in practice for computing $\beta_S(P^0)$ can also be employed for β^*, including those procedures which lead to linear programming calculations (see e.g., Gokhfeld and Cherniavsky, 1980; König, 1987, Save et al., 1989), but no equilibrium constraints on $\mathbf{s}$ are required here. Problem (9) is, on the contrary, less simple than the analogous problem for determining $\beta_S(P^0)$ through the kinematic approach due to the presence in (9) of the additional zero-ratchet strain constraint. However, methods like that envisaged by Karadeniz and Ponter (1984) to compute $\beta_S(P^0)$ through a linear programming upper bound approach can be extended to the direct computation of β^*.

It is not the aim of the present paper to discuss in detail numerical procedures for computing β^*, but it is appropriate to mention here the notable simplicity with which problem (8) can be solved in the commonest case of a yield function of the form $\phi = f(\boldsymbol{\sigma}) - \sigma_y$ with $f(\boldsymbol{\sigma}) \ge 0$ homogeneous of degree one. In fact, under this hypothesis the constraint inequality of (8) reads

$$\phi(\beta\overline{\boldsymbol{\sigma}}^c + \mathbf{s}) = \beta f(\overline{\boldsymbol{\sigma}}^c + \bar{\mathbf{s}}) - \sigma_y \le 0 \text{ in } V \times (0,\ \Delta t) \tag{25}$$

where σ_y is the material yield stress and $\bar{\mathbf{s}}$ is an arbitrary stress field like $\mathbf{s} = \beta\bar{\mathbf{s}}$. Then let z be the peak value of $f(\overline{\boldsymbol{\sigma}}^c + \bar{\mathbf{s}})$ in the cycle, i.e., $z = \max_{0 \le t \le \Delta t} f(\overline{\boldsymbol{\sigma}}^c + \bar{\mathbf{s}})$ and let z be minimized with respect to $\bar{\mathbf{s}}$ at every $\mathbf{x}$ in V, namely

$$z^* = \min_{(\bar{s})} z \text{ s.t. } f(\overline{\boldsymbol{\sigma}}^c + \bar{\mathbf{s}}) \le z,\ 0 \le t \le \Delta t. \tag{26}$$

Solving problem (26) amounts to finding a suitable transfer stress, say $\bar{\mathbf{s}}^*$, such that the stress path $\overline{\boldsymbol{\sigma}}^c + \bar{\mathbf{s}}^*$ finds itself in a neutral configuration with respect to the potential surface $f(\overline{\boldsymbol{\sigma}}^c + \bar{\mathbf{s}}^*) = z^*$ or, in other words, the shifted stress path touches the above potential surface, at least, at two critical stress points such as to satisfy Eq. (19) or Eq. (20). Often in practice the cyclic stress path $\overline{\boldsymbol{\sigma}}^c$ is a straight segment of the stress space whose neutral configuration is identified as that in which the segment's midpoint coincides with the stress origin (provided that $f(\boldsymbol{\sigma})$ is an even function). In any case, the neutral configuration of the cyclic stress path at a point $\mathbf{x}$ is fully independent of any other point in V, such that problem (26) can be solved separately for the different points of V. Once (26) has been solved for all points in V, β^* is easily found as the maximum β value such that, by Eq. (25), $\beta \le \sigma_y/z^*$, that is,

$$\beta^* = \min_{(V)} \sigma_y/z^*, \tag{27}$$

and the region V_F identifies with the portion of V where the ratio σ_y/z^* takes on its absolute minimum value β^*. The field $\mathbf{s}^* = \beta^*\bar{\mathbf{s}}^*$ turns out to be in equilibrium with some (steady) load $P^{0*} \in \mathcal{P}^0_N$, such that β^* coincides with the elastic shakedown multiplier for the load $\overline{P}^c$ acting together with this P^{0*}, i.e., $\beta^* = \beta_S(P^{0*})$.

The computation of β^* through (8) or (9) provides full information about the plastic shakedown limit state. The extent of the upper plateau (relevant for design purposes) can be exactly evaluated by Ponter's method in its particular shape taken on for $\beta = \beta^*$ (Ponter, 1983; Ponter and Karadeniz, 1985a, b). Hereafter, a few simple examples are reported as an illustration of the conceptual procedure.

(a) *Symmetric Three-Bar Structure.* Fig. 4(a). Three equal bars of cross-section area a are connected to a rigid block. The latter is subjected to a steady load $\alpha\overline{P}^0$ with $\overline{P}^0 = 3a\sigma_y$ = plastic limit load, and the bars suffer cycles of temperature variations $T_i(t)$ as depicted by Fig. 4(b). Let one denote the maximum elastic thermal stress by $\sigma_t := \alpha_T E\vartheta$, with α_T = thermal expansion coefficient, E = Young modulus, and ϑ = maximum temperature variation. The elastic thermal stresses in the bars are: $\sigma^c_3 = -\sigma^c_1 = \mu\sigma_t$, $\sigma^c_2 = 0$, $0 \le \mu \le 1$. The Bree-like diagram is depicted in Fig. 4(c), from which it tran-

Downloaded 03 May 2010 to 171.66.16.245. Redistribution subject to ASME license or copyright; see http://www.asme.org/terms/Terms_Use.cfm

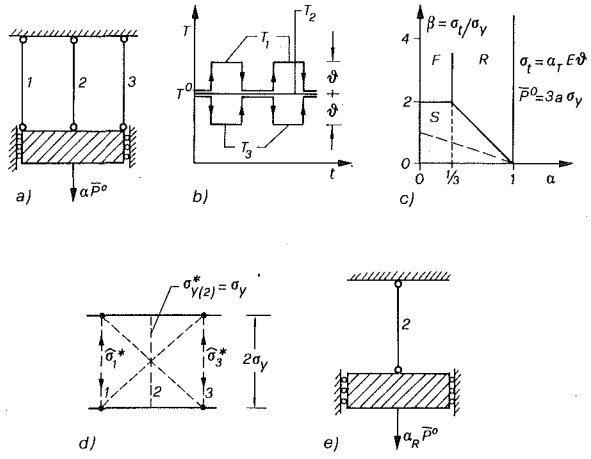


Fig. 4

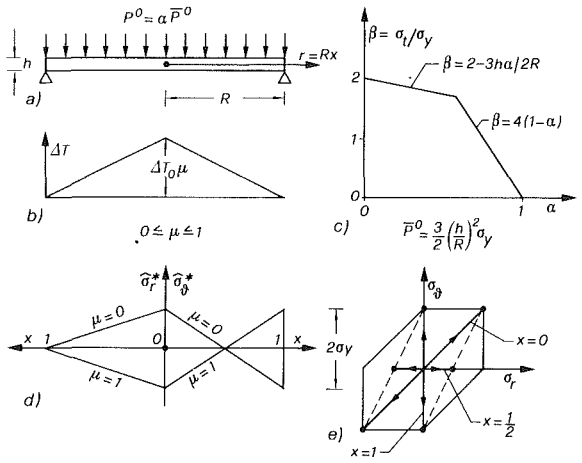


Fig. 6

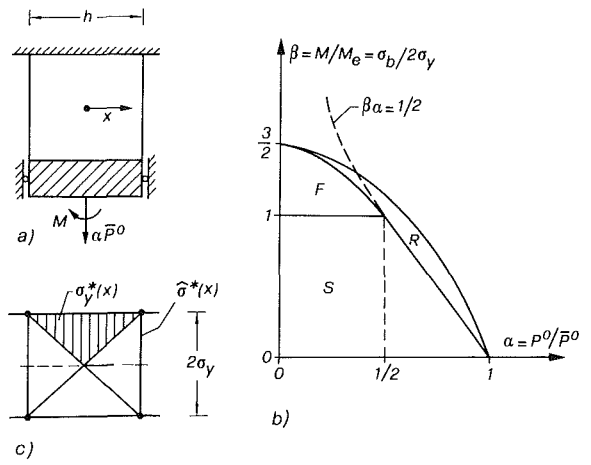


Fig. 5

spires that $\beta^* = 2$. Only bars 1 and 3 attain yield during the cycle, as illustrated in Fig. 4(d) where the reference neutral-configuration PT stresses $\hat{\sigma}_i^*$, ($i = 1, 2, 3$), are depicted. The $\hat{\sigma}_i^*$ are obtained from σ_i^c by means of the transfer self-stress $s_1^* = -s_3^* = \sigma_t/2$, $s_2^* = 0$. The region V_S is thus formed by the stress-free bar 2 alone (Fig. 4(e)). The load $P_a^0 = \alpha_R \overline{P}^0$ corresponding to the extreme of the upper plateau $\beta = \beta^*$ can be obtained as the limit load of V_S in Fig. 4(e), taking into account that the available yield stress $\sigma_{y(2)}^* = \sigma_y$, namely $P_a^0 = a\sigma_y$. Thus, $\alpha_R = a\sigma_y/3a\sigma_y = 1/3$ in accordance with Fig. 4(c).

(b) *Beam Segment.* Fig. 5(a). A beam segment of rectangular cross-section $1 \times h$ is subjected to a cyclic bending moment $M = \mu C$ with $C > 0$ and $-1 \le \mu \le 1$, as well as a steady axial force $P^0 = \alpha \overline{P}^0$, $\overline{P}^0 = h\sigma_y$ = axial yield force. The elastic stress response to M is $\sigma^c = \mu x \sigma_b/h$, where $\sigma_b = 12C/h^2$ = max elastic stress variation. The Bree-like diagram is reported in Fig. 5(b) where $M_e = h^2\sigma_y/6$ = elastic bending moment. The neutral-configuration PT stresses $\hat{\sigma}^*(x) \equiv \sigma^c(x)$ are depicted in Fig. 5(c), from where it transpires that yield is attained during the cycle only at the outer fibers of the beam. Therefore, the region V_S coincides with V and the available yield stress σ_y^* is represented by the shaded triangle. Thus, $P_a^0 = h\sigma_y/2$ and $\alpha_R = P_a^0/\overline{P}^0 = 1/2$, which is in agreement with Fig. 5(b).

(c) *Circular Plate.* Fig. 6(a). A circular plate of constant thickness h and radius R is subjected to a cyclic linear radial temperature variation $\Delta T = \Delta T_0(1-x)\mu$, where $x = r/R$ and $0 \le \mu \le 1$, as well as to a lateral uniform pressure $P^0 = \alpha \overline{P}^0$, $\overline{P}^0 = 3h^2\sigma_y/2R^2$ = plastic limit pressure. The elastic stress response to the cyclic load is (Ponter, 1983; Cocks, 1984): $\sigma_r^c = -\mu\sigma_t(1-x)$ (radial stress), $\sigma_\theta^c = -\mu\sigma_t(1-2x)$ (circumferential stress), where $\sigma_t = E\alpha_T\Delta T_0/3$ = max thermal stress, α_T = coefficient of thermal expansion, and E = Young modulus. The Bree-like diagram of Fig. 6(c), found by Ponter (1983) taking into account the effects of the shear stress and the Tresca yield condition, shows that no upper plateau exists and thus alternating plasticity can occur only under thermal loading for $\beta = \beta^* = 2$, where $\beta = \sigma_t/\sigma_y$. The neutral-configuration PT stresses derivable from the elastic stresses by superposition of the transfer self-stresses $s_r^* = \mu\sigma_t(1-x)/2$, $s_\theta^* = \mu\sigma_t(1-2x)/2$, are depicted in Figs. 6(d, e), from where it transpires that the yield condition is attained only at the outer circumference and at the plate center. Thus, the V_S structure coincides with the entire plate, but with a transversal cylindrical hole of infinitesimal radius at the center, and with no supports. Obviously, as already noted by Ponter (1983) through similar arguments, this V_S plate is unable to resist any transversal pressure.

Discussion and Conclusion

For a structure subjected to combined cyclic/steady loads, the notion of plastic shakedown limit load play a significant role in the understanding of the structural behavior, analogous to that played by the well-known elastic shakedown limit load for a structure subjected to a cyclic load. For design purposes, the latter load is certainly more stringent than the former one, because it sharply specifies the load range in which any form of incremental collapse, either ratchetting or alternating plasticity, is escaped. The plastic shakedown limit load also provides useful information for design purposes, for it specifies the cyclic load value below which plastic shakedown, i.e., alternating plasticity, cannot occur whatever the steady load in combination with the cyclic load. In spite of the link existing between the plastic and elastic shakedown limit loads (the former coincides with the maximum value of the latter on changing the steady load), it is surprising enough that both of them are grounded on substantially the same rational basis in which criteria, like the Bleich-Melan and the Koiter-Neal-Symonds theorems, are available for a priori assessing safe and unsafe structural situations. The underlining concepts are perhaps not yet fully clarified, and further thinking is required to this aim.

The computation of the plastic shakedown limit load, achievable by either static or kinematic approaches, does not present any difficulties, and it may be viewed as a by-product of a computer program devoted to elastic shakedown analysis

Downloaded 03 May 2010 to 171.66.16.245. Redistribution subject to ASME license or copyright; see http://www.asme.org/terms/Terms_Use.cfm

with: (i) no equilibrium constraints on the time-independent stress variables as for the static approach and (ii) the additional zero-ratchet-strain constraint on the plastic strain rates variables as for the kinematic approach. In the commonest case of a yield function homogeneous of degree one, the evaluation of the limit load by the static approach is shown to be extremely simple, for it only consists in operations to be performed locally at every point, or element, of the body.

The plastic shakedown limit state of the structure being in condition of impending alternating plasticity exhibits a number of interesting features. The latter features represent, though within a narrower context, a fully rational confirmation and improvement of heuristic but significant concepts previously envisaged by Ponter (1983) and Ponter and Karadeniz (1985a, b) in regard to the behavior of a structure in conditions of plastic shakedown. That is, the body can be decomposed into two regions V_F and $V_S - V_F$ being in the plastic shakedown limit state and V_S in an elastic shakedown state, with insensitivity properties with respect to steady loads applied upon V_S until V_S is led to a limit state of impending ratchetting, which can be determined applying Ponter's method. The region V_F, that must be known in order to apply Ponter's method, results from the solution to the plastic shakedown limit load problem.

Obviously, the picture here above would change somewhat, or even remarkably, in the case of more realistic hardening materials. This point will be addressed in a future paper. The guiding idea followed here is that there exists a number of intriguing problems of solid mechanics for elastic-perfectly plastic material and cyclic loading which are still open (e.g., criteria for plastic shakedown or ratchetting, analogous to the elastic shakedown ones), and their study and understanding is hoped for before addressing more complicated problems. The present two-paper study is believed to contribute to this direction.

Acknowledgment

This paper has been completed with the financial support of the Consiglio Nazionale delle Ricerche, CNR, of Italy.

References

Cocks, A. C. F., 1984, "Lower Bound Shakedown Analysis of a Simply Supported Plate Carrying a Uniformly Distributed Load and Subjected to a Cyclic Thermal Loading," *Int. J. Mech. Sci.*, Vol. 52, No. 9/19, pp. 471–475.

Gokhfeld, D. A., and Cherniavsky, D. F., 1980, *Limit Analysis of Structures at Thermal Cycling*, Sijthoff and Noordhoff, Alphen and der Rijn, The Netherlands.

Karadeniz, S., and Ponter, A. R. S., 1984, "A Linear Programming Upper Bound Approach to the Shakedown Limit of Thin Shells Subjected to Variable Thermal Loading," *J. Strain Analysis*, Vol. 19, No. 4, pp. 221–230.

Koiter, W. T., 1960, "General Theorems for Elastic-Plastic Solids," *Progress in Solid Mechanics*, Vol. 1, J. N. Sneddon, and R. Hill, eds., North-Holland, Amsterdam, pp. 167–221.

König, J. A., 1982a, "On Upper Bounds to Shakedown Loads," *ZAMM*, Vol. 52, pp. 421–428.

König, J. A., 1982b, "On Some Recent Developments in the Shakedown Theory," *Advances in Mechanics*, Vol. 5, pp. 237–258.

König, J. A., 1987, *Shakedown of Elastic-Plastic Structures*, PWN—Polish Scientific Publishers, Warsaw.

Martin, J. B., 1975, *Plasticity: Fundamentals and General Results*, The MIT Press, Cambridge, MA.

Polizzotto, C., 1989, "Simplified Methods of Structural Analysis for Cyclic Plasticity," Final Report RA1-0116(I), Commission of European Communities, Brussels, and Dipartimento di Ingegneria Strutturale & Geotecnica, University of Palermo, Palermo.

Polizzotto, C., 1993, "On the Conditions to Prevent Plastic Shakedown of Structures: Part I—Theory," ASME JOURNAL OF APPLIED MECHANICS, Vol. 60, pp. 15–19.

Polizzotto, B., Borino, G., and Fuschi, P., 1990, "On The Steady State Response of Elastic Perfectly Plastic Solids to Cyclic Loads," *Inelastic Solids and Structures*, ed. by M. Kleiber and J. A. König, Pineridge Press, Swansea, pp. 473–488.

Ponter, A. R. S., 1983, "Shakedown and Ratchetting Below the Creep Range," Report EUR 8702 EN, Commission of European Communities, Brussels.

Ponter, A. R. S., and Karadeniz, S., 1985a, "An Extended Shakedown Theory for Structures That Suffer Cyclic Thermal Loadings: Part 1—Theory," ASME JOURNAL OF APPLIED MECHANICS, Vol. 52, pp. 877–882.

Ponter, A. R. S., and Karadeniz, S., 1985b, "An Extended Shakedown Theory for Structures That Suffer Cyclic Thermal Loadings: Part 2—Applications," ASME JOURNAL OF APPLIED MECHANICS, Vol. 52, pp. 883–889.

Save, M., De Saxce, G., and Borkoski, A., 1989, "Computation of Shakedown Loads, Feasibility Study," Report Faculté Polytechnique de Mons, Mons, Belgium.

Symonds, P. S., and Neal, B. G., 1951, "Recent Progress in the Plastic Methods of Structural Analysis," *J. of the Franklin Institute*, Vol. 252, pp. 383–492.

Zarka, J., and Casier, J., 1979, "Cyclic Loading on Elastic-Plastic Structures," *Mechanics Today*, S. Nemat-Nasser, ed., Pergamon Press, Oxford, pp. 93–198.

Downloaded 03 May 2010 to 171.66.16.245. Redistribution subject to ASME license or copyright; see http://www.asme.org/terms/Terms_Use.cfm

T. K. Caughey
Professor of Applied Mechanics
and Mechanical Engineering,
Division of Engineering and
Applied Science,
California Institute of Technology,
Pasadena, CA 91125

F. Ma
Associate Professor of Applied Mechanics,
Department of Mechanical Engineering,
University of California,
Berkeley, CA 94720
Mem. ASME

Complex Modes and Solvability of Nonclassical Linear Systems

The purpose of this article is to give necessary and sufficient conditions under which nonclassical linear systems can be decoupled or become solvable.

1 Introduction

The equation of motion of an n-degree-of-freedom linear system under external excitation can be written as

$$\mathbf{M}\ddot{x}+\mathbf{C}\dot{x}+\mathbf{K}x=f(t), \tag{1}$$

where the mass matrix $\mathbf{M}$, the damping matrix $\mathbf{C}$, and the stiffness matrix $\mathbf{K}$ are of order $n \times n$. The displacement $x(t)$ and external excitation $f(t)$ are n-dimensional vectors. For classical systems, it is assumed that $\mathbf{M}$ is symmetric and positive definite, and that $\mathbf{C}$, $\mathbf{K}$ are symmetric and positive semi-definite. These assumptions are not arbitrary, but in fact have solid footing in the theory of Lagrangian dynamics. In the last several decades, classical systems have constituted a subject of intense investigation in vibrations and structures.

The use of modern control devices, however, can easily lead to equations for which $\mathbf{M}$, $\mathbf{C}$, $\mathbf{K}$ do not have any symmetry or definiteness properties. The asymmetry of $\mathbf{C}$ and $\mathbf{K}$ is sometimes addressed in the context of gyroscopic and follower forces, and an example for the asymmetry of $\mathbf{M}$ is given, for instance, by Soom and Kim (1983). Linear systems governed by equations for which $\mathbf{M}$, $\mathbf{C}$, $\mathbf{K}$ lack any specific symmetry or definiteness will be termed nonclassical systems. These systems arise especially frequently in the emerging area of microdynamics. Several authors have considered nonclassical systems. In particular, Inman (1983) has studied nonclassical systems for which $\mathbf{M}$, $\mathbf{C}$, $\mathbf{K}$ can be transformed to symmetric forms simultaneously by a similarity transformation. Such nonclassical systems are said to be symmetrizable. The study of symmetrizability probably represents the first serious attempt in the investigation of nonclassical linear systems. Nonclassical systems will be encountered more frequently in the future as microdevices need to be designed with higher precision. An organized course of investigation of general nonclassical systems, nevertheless, has not been reported in the open literature.

This article sets out to explore some basic properties of nonclassical structures. The purpose is to give necessary and sufficient conditions under which a nonclassical system can be decoupled, or becomes solvable in n-space.

2 Results and Discussion

Consider a linear system governed by Eq. (1). This system can be decoupled if and only if there exist two nonsingular matrices $\mathbf{U}$ and $\mathbf{V}$ such that $\mathbf{UMV}$, $\mathbf{UCV}$, $\mathbf{UKV}$ are diagonal matrices. Two square matrices $\mathbf{A}$ and $\mathbf{B}$, related by $\mathbf{B} = \mathbf{UAV}$ for some nonsingular matrices $\mathbf{U}$, $\mathbf{V}$, are said to be connected by an equivalence transformation. An equivalence transformation between $\mathbf{A}$ and $\mathbf{B}$ preserves the rank of the matrices. If $\mathbf{U} = \mathbf{V}^{-1}$, the equivalence transformation is called a similarity transformation. In the event that $\mathbf{U} = \mathbf{V}^T$, the equivalence transformation is a congruence transformation. A congruence transformation is also a similarity transformation if $\mathbf{V}$ is an orthogonal matrix. Equivalence transformations that are neither similarity nor congruence are rarely used in structural analysis. In addition, congruence transformations cannot be used to advantage on nonclassical systems, whose coefficient matrices lack symmetry. It therefore appears legitimate to confine this study to decoupling by similarity transformations. Unless stated otherwise, it will be understood that systems are to be decoupled by similarity transformations.

If (1) represents a classical system, Caughey and O'Kelly (1965) have shown that it can be decoupled by a congruence transformation if and only if the matrices $\mathbf{M}^{-1}\mathbf{C}$ and $\mathbf{M}^{-1}\mathbf{K}$ commute in multiplication. The diagonalizing matrix is real in this case, and the system possesses a full set of classical normal modes. Ahmadian and Inman (1984) extended the above result to nonclassical symmetrizable systems with the use of similarity transformations. If a general nonclassical system represented by Eq. (1) can be decoupled at all, it is likely that the diagonalizing matrix is complex. However, each column of the diagonalizing matrix is still an independent eigenvector of dimension n, which may therefore be called a mode. Thus a nonclassical structure can be decoupled if and only if it pos-

Contributed by the Applied Mechanics Division of THE AMERICAN SOCIETY OF MECHANICAL ENGINEERS for publication in the ASME JOURNAL OF APPLIED MECHANICS.

Discussion on this paper should be addressed to the Technical Editor, Prof. Lewis T. Wheeler, Department of Mechanical Engineering, University of Houston, Houston, TX 77204-4792, and will be accepted until four months after final publication of the paper itself in the ASME JOURNAL OF APPLIED MECHANICS.

Manuscript received by the ASME Applied Mechanics Division, June 26, 1991; final revision, Dec. 11, 1991. Associate Technical Editor: D. J. Inman.

Copyright © 1993 by ASME
Downloaded 03 May 2010 to 171.66.16.245. Redistribution subject to ASME license or copyright; see http://www.asme.org/terms/Terms_Use.cfm

sesses n independent complex modes in n-space. Note that the above development is different from the practice of converting system (1) into the state-variable formulation, which leads to $2n$ complex modal vectors each of dimension $2n$. In fact, this article focuses on the condition under which the nonclassical system (1) possesses independent complex modes in n-space. If system (1) does not have independent modes or, equivalently, it cannot be decoupled, then the focus is on whether it is solvable in n-space.

A square matrix of order n is diagonalizable if and only if it has n linearly independent eigenvectors. Consider a family of square matrices of order n, each of which is diagonalizable. The simultaneous diagonalization of all members of the family by the same diagonalizing matrix is addressed in the following statement (Horn and Johnson, 1985).

Lemma 1. A family of matrices can be simultaneously diagonalized if and only if each of its members is diagonalizable and any two members commute in multiplication.

If the above assertion is applied to a nonclassical system, a necessary and sufficient condition for the simultaneous diagonalization of the **M**, **C**, **K** matrices can be readily obtained.

Theorem 1. The nonclassical system (1) can be decoupled if and only if the coefficient matrices **M**, **C**, **K** are diagonalizable and pairwise commutative.

That means if each of **M**, **C**, **K** is diagonalizable, and $\mathbf{MC} = \mathbf{CM}$, $\mathbf{MK} = \mathbf{KM}$, $\mathbf{CK} = \mathbf{KC}$, then system (1) possesses n complex modes. When the inverse of **M** exists, the following statement is valid.

Corollary. The nonclassical system (1) possesses n independent modes if and only if $\mathbf{M}^{-1}\mathbf{C}$, $\mathbf{M}^{-1}\mathbf{K}$ are diagonalizable and commutative.

The above corollary contains the results established by Caughey and O'Kelly (1965), and by Ahmadian and Inman (1984), as special cases. In the event that the nonclassical system (1) is symmetrizable, or that it becomes classical, it is straightforward to show that a real matrix can be chosen to diagonalize **M**, **C**, **K** simultaneously. The modes in this case may then be called classical normal modes.

Example 1. Consider a two-degree-of-freedom nonclassical system governed by Eq. (1), with $\mathbf{M} = \mathbf{I}$, and

$$\mathbf{C} = \begin{bmatrix} 1 & 1 \\ -2 & 3 \end{bmatrix}, \tag{2}$$

$$\mathbf{K} = \begin{bmatrix} -7 & 4 \\ -8 & 1 \end{bmatrix}. \tag{3}$$

It can be shown that the system is not symmetrizable. Since $\mathbf{CK} = \mathbf{KC}$, the system can be decoupled, and the diagonalizing matrix is

$$\mathbf{S} = \begin{bmatrix} 1 & 1 \\ 1+i & 1-i \end{bmatrix}. \tag{4}$$

If a nonclassical system can be decoupled, it is of course solvable in n-space. Conceivably, most nonclassical systems do not possess complex modes, and they cannot be decoupled. However, they may still be solvable in n-space. Solvability in n-space requires that **M**, **C**, **K** be simultaneously reduced to upper triangular forms. It is useful to recall that any square matrix can be upper triangularized. As discussed by Ma and Caughey (1981), simultaneous triangularization of a family of matrices is based upon the concept of Lie groups.

A family of square matrices of order n constitutes a Lie algebra if, for all **A**, **B** in **L**, the commutator product $[\mathbf{A}, \mathbf{B}] = \mathbf{AB} - \mathbf{BA}$ belongs to **L**. The notation $\mathbf{L}(\mathbf{A}_1, \mathbf{A}_2, \ldots, \mathbf{A}_p)$ is employed to denote the Lie algebra generated by the matrices $\mathbf{A}_1, \mathbf{A}_2, \ldots, \mathbf{A}_p$. A Lie algebra **L** is associated with its derived sequence, defined inductively as follows:

$$\mathbf{L}^{(0)} = \mathbf{L}, \tag{5}$$

$$\mathbf{L}^{(n+1)} = \{[\mathbf{S}, \mathbf{T}] : \mathbf{S}, \mathbf{T} \text{ in } \mathbf{L}^{(n)}\}, \; n \geq 0. \tag{6}$$

L is solvable if $\mathbf{L}^{(n)} = \{0\}$ for some n. The class of solvable Lie algebra includes the class of pairwise commutative matrices, when $\mathbf{L}^{(1)} = \{0\}$. An interesting property for solvability is the following statement (Sagle and Walde, 1973).

Lemma 2. A matrix Lie algebra **L** is solvable if and only if there exists a nonsingular matrix **S** such that $\mathbf{S}^{-1}\mathbf{AS}$ is upper triangular for all **A** in the Lie algebra.

It is likely that the triangularizing matrix **S** is complex. A constructive proof of the above assertion is provided by Sagle and Walde (1973). When the above assertion is applied to a nonclassical system, a necessary and sufficient condition for the simultaneous triangularization of **M**, **C**, **K** can be easily obtained.

Theorem 2. The nonclassical system (1) is solvable if and only if the coefficient matrices **M**, **C**, **K** generate a solvable Lie algebra.

In addition, if $\mathbf{L}^{(1)}(\mathbf{M}, \mathbf{C}, \mathbf{K}) = \{0\}$ and **M**, **C**, **K** are diagonalizable, then system (1) can be decoupled. When the inverse of **M** exists, it can be stated as a corollary that system (1) is solvable if and only if $\mathbf{M}^{-1}\mathbf{C}$ and $\mathbf{M}^{-1}\mathbf{K}$ generate a solvable Lie algebra. For a classical system, the triangularizing matrix can be chosen to be real.

Example 2. Consider a two-degree-of-freedom structure, with

$$\mathbf{M} = \begin{bmatrix} 2 & -1 \\ 1 & 0 \end{bmatrix}, \tag{7}$$

$$\mathbf{C} = \begin{bmatrix} 1 & 0 \\ 1 & 0 \end{bmatrix}, \tag{8}$$

$$\mathbf{K} = \begin{bmatrix} 1 & -1 \\ 0 & 0 \end{bmatrix}. \tag{9}$$

It is easy to see that the Lie algebra generated by **M**, **C**, **K** is

$$\mathbf{L}(\mathbf{M}, \mathbf{C}, \mathbf{K}) = \{0, \mathbf{M}, \mathbf{C}, \mathbf{K}, \mathbf{A}, -\mathbf{A}\}, \tag{10}$$

where

$$\mathbf{A} = \begin{bmatrix} -1 & 1 \\ -1 & 1 \end{bmatrix}. \tag{11}$$

In addition, $\mathbf{L}^{(0)} = \mathbf{L}$, $\mathbf{L}^{(1)} = \{0, \mathbf{A}, -\mathbf{A}\}$, and $\mathbf{L}^{(2)} = \{0\}$. Hence, $\mathbf{L}(\mathbf{M}, \mathbf{C}, \mathbf{K})$ is solvable, and

$$\mathbf{S} = \begin{bmatrix} 1 & 1 \\ 1 & 0 \end{bmatrix} \tag{12}$$

upper triangularizes the system. We have

$$\mathbf{S}^{-1}\mathbf{MS} = \begin{bmatrix} 1 & 1 \\ 0 & 1 \end{bmatrix}, \tag{13}$$

$$\mathbf{S}^{-1}\mathbf{CS} = \begin{bmatrix} 1 & 1 \\ 0 & 0 \end{bmatrix}, \tag{14}$$

$$\mathbf{S}^{-1}\mathbf{KS} = \begin{bmatrix} 0 & 0 \\ 0 & 1 \end{bmatrix}. \tag{15}$$

Let $x = \mathbf{S}q$. The equation of motion becomes

$$\begin{bmatrix} \ddot{q}_1 + \ddot{q}_2 + \dot{q}_1 + \dot{q}_2 \\ \ddot{q}_2 + q_2 \end{bmatrix} = \begin{bmatrix} f_2(t) \\ f_1(t) - f_2(t) \end{bmatrix}, \tag{16}$$

which leads to

$$\ddot{q}_1 + \dot{q}_1 + \dot{q}_2 - q_2 = 2f_2(t) - f_1(t), \tag{17}$$

$$\ddot{q}_2 + q_2 = f_1(t) - f_2(t). \tag{18}$$

3 Conclusions

Linear structures whose coefficient matrices do not satisfy the classical assumptions of symmetry and definiteness arise

Downloaded 03 May 2010 to 171.66.16.245. Redistribution subject to ASME license or copyright; see http://www.asme.org/terms/Terms_Use.cfm

frequently in modern applications. It has been found that a necessary and sufficient condition under which a nonclassical system can be decoupled is for the coefficient matrices **M**, **C**, **K** to be diagonalizable and pairwise commutative. Even if a nonclassical linear system of dimension n cannot be decoupled, it may still be solvable in n-space. A necessary and sufficient condition under which a nonclassical system is solvable is for the coefficient matrices **M**, **C**, **K** to generate a solvable Lie algebra. The above statements extend previous results on classical normal modes. Two examples have been used to illustrate the theory herein expounded.

Acknowledgment

This research has been supported in part by the National Science Foundation under Grant No. MSS-8657619. Opinions, findings, and conclusions expressed in this paper are those of the authors and do not necessarily reflect the views of the National Science Foundation.

References

Ahmadian, M., and Inman, D. J., 1984, "Classical Normal Modes in Asymmetric Nonconservative Dynamic Systems," *AIAA Journal*, Vol. 22, pp. 1012–1015.

Caughey, T. K., and O'Kelly, M. E. J., 1965, "Classical Normal Modes in Damped Linear Dynamic Systems," ASME JOURNAL OF APPLIED MECHANICS, Vol. 32, pp. 583–588.

Horn, R. A., and Johnson, C. R., 1985, *Matrix Analysis*, Cambridge University Press, Cambridge, p. 52.

Inman, D. J., 1983, "Dynamics of Asymmetric Nonconservative Systems," ASME JOURNAL OF APPLIED MECHANICS, Vol. 50, pp. 199–203.

Ma, F., and Caughey, T. K., 1981, "On the Stability of Linear and Nonlinear Stochastic Transformations," *Int. J. Control*, Vol. 34, pp. 501–511.

Sagle, A. A., and Walde, R. E., 1973, *Introduction to Lie Groups and Lie Algebras*, Academic Press, New York, p. 211.

Soom, A., and Kim, C., 1983, "Roughness-Induced Dynamic Loading at Dry and Boundary-Lubricated Sliding Contacts," *ASME Journal of Tribology*, Vol. 105, pp. 514–517.

Downloaded 03 May 2010 to 171.66.16.245. Redistribution subject to ASME license or copyright; see http://www.asme.org/terms/Terms_Use.cfm

V. A. Lubarda
Department of Mechanical Engineering,
University of Montenegro,
81000 Podgorica, Yugoslavia

A Simple Representation of the J-Integral and Some Estimates of Elastic Stress Intensity Factors

Precise estimates of the elastic stress intensity factors for the Griffith and edge cracks are made by using one convenient representation of the J-integral and asymptotic crack-tip fields, without recourse to the solutions of corresponding boundary value problems.

1 Introduction

We show here that for various two-dimensional elastic crack problems the energy release rate, or J-integral, has a simple representation $J = \sigma A/l$, where σ is a representative measure of applied stress, A is the area defined by the deformed crack faces, and l is the crack length. This directly follows from the M-integral conservation law, although in some cases it can be deduced by more elementary means. Utilizing the crack-opening displacements from the universal, asymptotic crack-tip field, rather than from the specific boundary value problem, we then obtain an estimate of the elastic stress intensity factor, which is for an edge crack only seven percent higher than the true value. By a simple modification, an exact estimate is obtained for the stress intensity of the Griffith crack and an improved estimate, with the error less than three percent, for the edge crack.

2 J Representation

In the case of plane infinitesimal deformation of a homogeneous linearly elastic material, one of the conservation laws introduced by Knowles and Sternberg (1972) states that for any closed contour C within a simply connected region, the following (M) integral vanishes:

$$M(C) = \int_C (Wn_i x_i - T_i u_{i,k} x_k) dC. \tag{1}$$

Here, $W = 1/2\sigma_{ij}\epsilon_{ij}$ is the elastic strain energy density, n_i is the unit normal to C, $T_i = \sigma_{ij}n_j$ the traction, and u_i displacement, all expressed in rectangular Cartesian coordinates, x_1 and x_2. No body forces are considered, so that the equilibrium equations reduce to $\sigma_{ij,j} = 0$. If the region enclosed by C is not simply connected, but contains a cavity, then $M(C) \neq 0$ and Budiansky and Rice (1973) have shown that the value of M is the energy release rate associated with a self-similar expansion of a traction-free cavity. The conservation law $M = 0$ was used by Freund (1978) to determine elastic stress intensity factors for various crack problems, without solving the corresponding elastic boundary value problems. The main characteristics which a problem must have in order for the approach to be useful are discussed in his paper, and they are utilized here.

Consider a two-dimensional infinite medium and a straight crack of length l loaded by uniform compressive stress σ on its two faces (Fig. 1), which is by a superposition equivalent to Griffith crack. Introduce a closed contour C as shown, which consists of two infinitesimal circles Γ_0 around the crack tips, an infinitely large circle Γ_∞, straight segments $\Gamma^\pm$ along the crack faces, and remaining parts $\Gamma_0^\pm$ joining Γ_∞ to one part of Γ_0. The contributions to $M(C)$ from the last two parts cancel each other, $M(\Gamma_0^+ + \Gamma_0^-) = 0$, and the contribution from Γ_∞ is also zero because the applied loads on crack faces are self-equilibrating and stresses decrease faster than $O(r^{-1})$, where r is the radius of large circle (Freund, 1978). Thus, the only

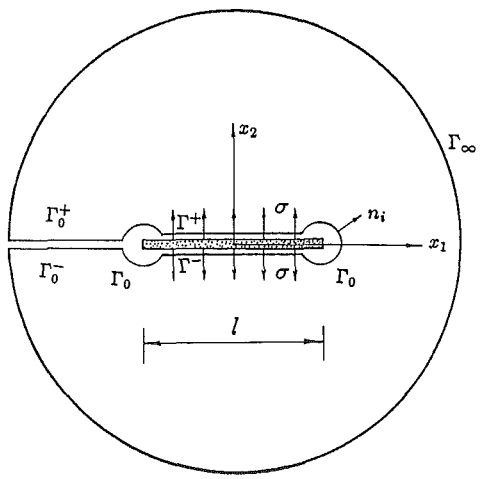


Fig. 1 Closed contour defining simply connected region for which the M integral vanishes. Crack of length l is loaded on its faces by compressive stress σ.

Contributed by the Applied Mechanics Division of THE AMERICAN SOCIETY OF MECHANICAL ENGINEERS for publication in the ASME JOURNAL OF APPLIED MECHANICS.

Discussion on this paper should be addressed to the Technical Editor, Professor Lewis T. Wheeler, Department of Mechanical Engineering, University of Houston, Houston, TX 77204-4792, and will be accepted until four months after final publication of the paper itself in the ASME JOURNAL OF APPLIED MECHANICS.

Manuscript received by the ASME Applied Mechanics Division, Apr. 19, 1991; final revision, Dec. 30, 1992. Associate Technical Editor: C. F. Shih.

Copyright © 1993 by ASME
Downloaded 03 May 2010 to 171.66.16.245. Redistribution subject to ASME license or copyright; see http://www.asme.org/terms/Terms_Use.cfm

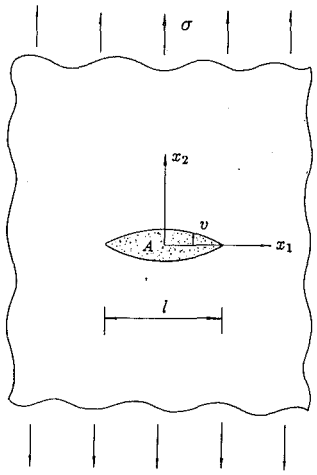


Fig. 2 Deformed configuration of the Griffith crack of length l; v is the crack opening displacement, and A the area within deformed crack faces

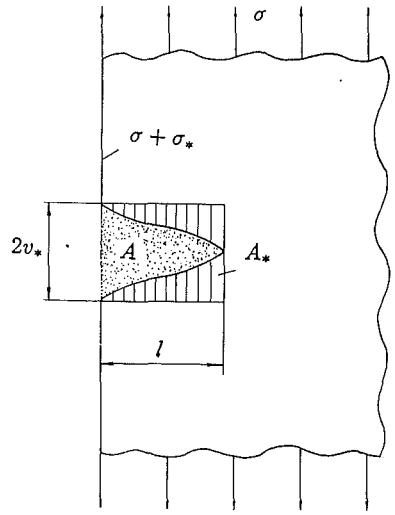


Fig. 3(*a*) Deformed configuration of edge crack of length l; A is the area within deformed crack faces, while quantities denoted by * appear in formula (6)

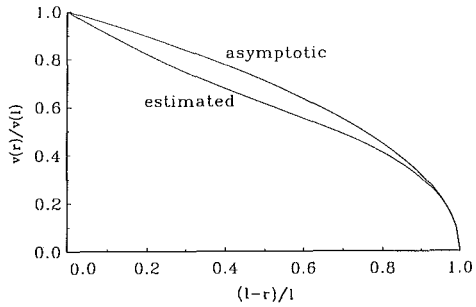


Fig. 3(*b*) Asymptotic and estimated shapes of the crack-opening displacement $v(r)$

contributions that remain are from Γ_0 and $\Gamma^{\pm}$. The contribution from Γ_0 is easily seen to be lJ, where

$$J=\int_{\Gamma_0}(Wn_1-T_iu_{i,1})d\Gamma_0 \tag{2}$$

is Rice's J integral (Rice 1968a, b), while each crack face gives

$$\sigma\int_{-l/2}^{l/2}x_1dv=-\sigma\int_{-l/2}^{l/2}vdx_1=-\sigma\frac{A}{2}, \tag{3}$$

where $A/2$ is half of the area enclosed by deformed crack faces (Fig. 2). Partial integration was utilized above, together with the boundary conditions at the crack tips $v(\pm l/2)=0$, where $v=u_2(x_1, 0)$ denotes lateral displacement (opening) of the crack faces. Hence, from $M=0$, we have $lJ-\sigma A=0$, and therefore

$$J=\frac{\sigma A}{l}. \tag{4}$$

Note that since there is no length scale other than l, A is proportional to l^2 and for the Griffith crack, J is a linear function of l.

For example, if we assume the opening profile of the crack to be an ellipse $v=v_0(1-4x_1^2/l^2)^{1/2}$, we have $A=\pi l/2v_0$ and (4) gives $J=\pi/2\ \sigma v_0$. Substituting $v_0=[(1-\nu)/2\mu]\ \sigma l$ from the exact solution of the Griffith crack (see, for example, Rice 1968a), we recover the well-known relationship between J and l

$$J=kl,\quad k=\frac{1-\nu}{4\mu}\pi\sigma^2 \tag{5}$$

ν being Poisson's ratio and μ the shear modulus.

In retrospect, expression (4) can be directly obtained in the following manner. If Ω is the potential energy, i.e., the strain energy minus the load potential ($\Omega=1/2\ \sigma A-\sigma A=-1/2\ \sigma A$), the energy release rate or J is, by definition, $J=-\partial\Omega/\partial l=1/2\ \sigma dA/dl$. Hence, since A is proportional to l^2, (4) follows. Or, equivalently, let us close the crack in Fig. 2, i.e., apply on its deformed faces uniform gradually increasing tension up to amount σ. The faces will come together and the state of stress will be uniform throughout the body. The corresponding work done is $1/2\sigma A$. This must be equal to the strain energy release in the reverse process of cracking the body by Griffith crack of length l, which is $1/2Jl$ (where J plays a role of the crack extension force), hence (4).

The same expression holds for the edge crack (Fig. 3(a)). Due to less material constraint, one expects A in this case to be bigger than half of the area within the opened Griffith crack, and therefore a higher energy release rate is associated with the edge crack. An additional interesting relationship can be obtained from the M integral by locating the coordinate system at the crack tip, so that there is no contribution from the small circle surrounding the tip, but there is from the edge of the semi-infinite medium. It turns out that the stress deviation along this edge, from the uniform value, obeys the relationship

$$\int_{-\infty}^{\infty}\sigma_*^2dx_2=\frac{4\mu}{1-\nu}\frac{\sigma A_*}{l}, \tag{6}$$

where $A_*=2v_*l-A$ is the shaded area in Fig. 3(a).

3 An Estimate of the Elastic Stress Intensity Factor

Since J is equal to the energy release rate associated with co-planar crack growth, it is related to the plane strain mode I stress intensity factor K_I through

$$J=\frac{1-\nu}{2\mu}K_I^2. \tag{7}$$

Combining this with (4) gives

$$K_I^2=\frac{2\mu}{1-\nu}\frac{\sigma A}{l}. \tag{8}$$

This can be used to make an estimate of K_I without recourse to the solution of the Griffith or edge crack boundary value

Downloaded 03 May 2010 to 171.66.16.245. Redistribution subject to ASME license or copyright; see http://www.asme.org/terms/Terms_Use.cfm

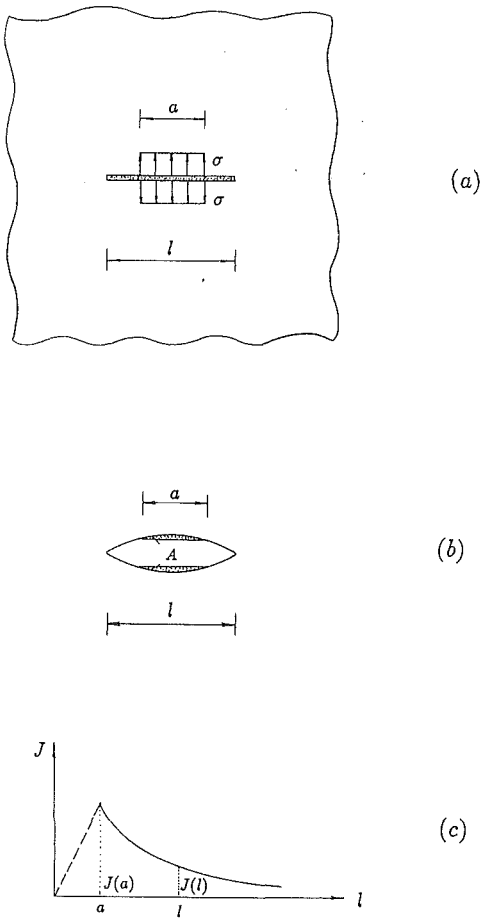


Fig. 4(*a*) Crack of length *l* compressed by σ over the part of length *a*; (*b*) its deformed configuration indicating the area *A* which appears in formula (4); (*c*) qualitative change of the corresponding *J* integral with crack length

problems, by using the crack opening displacement from the universal, asymptotic elastic crack-tip field, which is (Rice, 1968a)

$$v=\sqrt{\frac{2}{\pi}}\frac{1-\nu}{\mu}K_I\sqrt{r}. \tag{9}$$

For example, for the edge crack of length l, this gives

$$A=2\int_0^l v dr=\frac{8}{3\sqrt{2\pi}}\frac{1-\nu}{\mu}K_I l\sqrt{\pi l}, \tag{10}$$

and by substitution into (8),

$$K_I=1.2\sigma\sqrt{\pi l}. \tag{11}$$

This is only seven percent higher than the value obtained from the exact solution, giving $1.1215\sigma\sqrt{\pi l}$ (with a possible numerical error of at most one unit in the last digit, Koiter 1965). Applied to the Griffith crack, (11) is an overestimate of 20 percent, since deviation of the asymptotic field displacement from the true one is more pronounced. However, we can improve this estimate by adjusting the asymptotic expression (9) to meet the symmetry requirement and vanishing slope of the deformed Griffith crack faces at $r = l/2$. An obvious modification to satisfy $v'(l/2) = 0$ is obtained by multiplying (9) with $\sqrt{1-r/l}$, i.e.,

$$v(r)=\sqrt{\frac{2}{\pi}}\frac{1-\nu}{\mu}K_I\sqrt{r\left(1-\frac{r}{l}\right)}. \tag{12}$$

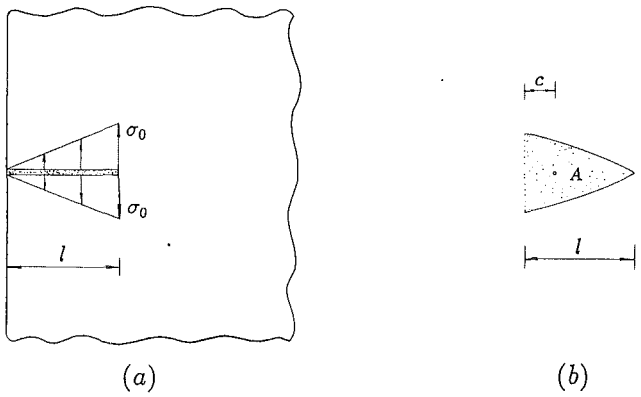


Fig. 5(*a*) Edge crack under triangular loading; (*b*) its deformed configuration; *c* defines the centroid of the crack opening area *A*

This clearly tends to the asymptotic expression (9) as $r \to 0$. Therefore,

$$A=4\int_0^{l/2} v(r)dr=\frac{1-\nu}{2\mu}K_I l\sqrt{\pi l/2}, \tag{13}$$

and from (8) we obtain the exact value for the stress intensity factor of the Griffith crack $K_I = \sigma\sqrt{\pi l/2}$. This exact estimate is a consequence of the fact that (12) turns out to be an ellipsoidal shape, which the complete solution of the Griffith crack boundary value problem indeed confirms.

Similarly, an improved estimate can be made for the edge crack, by modifying the asymptotic expression (9) to allow for an inflection point of the deformed faces, which is on physical ground expected to occur somewhere along the edge crack. Denoting a position of this point by $r = a$, we multiply (9) by $\sqrt{1-r/l(1-r/3a)}$, for then

$$v(r)=\sqrt{\frac{2}{\pi}}\frac{1-\nu}{\mu}K_I\sqrt{r\left[1-\frac{r}{l}\left(1-\frac{r}{3a}\right)\right]} \tag{14}$$

satisfies $v''(a) = 0$. Also, as $r \to 0$, this reduces to (9). By taking $a = l/3$ (so that $v(l)$ given by (14) and (9) coincide (Fig. 3(*b*)), we obtain $K_I = 1.091\,\sigma\sqrt{\pi l}$, which is 2.7 percent lower than the true value. For $a = 0.3l$ (14) gives $K_I = 1.1216\,\sigma\sqrt{\pi l}$, which is essentially equal to Koiter's value. Nonetheless, (14) is only an approximation to the true crack-opening displacement function $v(r)$, given in Koiter's (1956) paper by its Melin's transform (Eq. (72), with $\kappa_0 = 0$ in (91) and (85)), from which it can be extracted by the inverse transform and numerical procedure. There is also integral equations solution by Sneddon and Das (1971), with a performed numerical evaluation of $v(r)$. The plot in Fig. 1 of their paper clearly indicates the inflection point of the deformed crack faces, although their value for the maximum displacement $2\sigma l(1-\nu^2)/E$ is too small, and would only correspond to maximum opening displacement of the Griffith crack. The value reported in Tada et al. (1973), p. 8.1, is proportional to 2.915, which is about 5.8 percent smaller than the value 3.086, predicted by the estimated shape (14) in the case $a = l/3$.

4 Additional Examples

We give two more crack configurations for which a formula of type (4) holds. The derivation proceeds in a straightforward manner by applying the *M* integral. For the case in Fig. 4(*a*), with partially loaded crack faces, the area *A* appearing in (4) is shown in Fig. 4(*b*). For the edge crack and triangular loading, as in Fig. 5(*a*), the representative stress appearing in formula (4) is $\sigma = \sigma_0 2c/l$, where *c* defines the centroid of the crack opening area *A*.

Downloaded 03 May 2010 to 171.66.16.245. Redistribution subject to ASME license or copyright; see http://www.asme.org/terms/Terms_Use.cfm

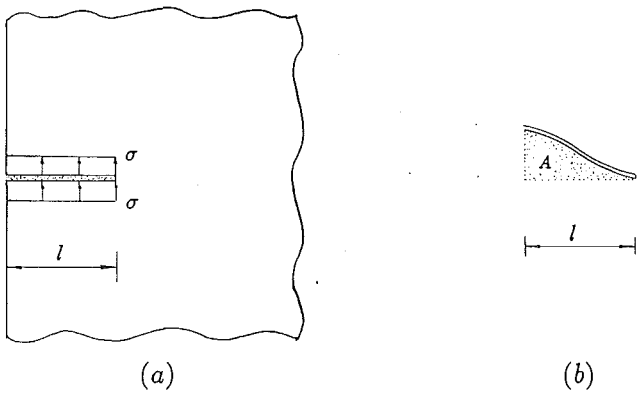


Fig. 6(*a*) Antisymmetric loading of the edge crack; (*b*) deformed faces and the area *A* appearing in formula (17)

A comment should perhaps be made regarding the case in Fig. 4(*a*). The associated potential energy is $\Omega = -1/2\sigma A_*$, where $A_* = A + 2av(a, l)$ is the area of the opened crack below the load σ. Hence, from $J = -\partial\Omega/\partial l$ we have by integration

$$\frac{1}{2}(A_* - A_0) = \int_a^l J(l')dl', \tag{15}$$

where A_0 denotes the area within opened Griffith crack of length a. In view of (4), therefore,

$$\frac{1}{2}J(l)l - \frac{1}{2}J(a)a = \int_a^l J(l')dl' - \sigma a v(a, l), \tag{16}$$

indicating a deviation of $J(l)$ from linearity in l (due to the second term on the right-hand side). The qualitative plot of $J = J(l)$ is shown in Fig. 4(*c*). As l becomes large, much bigger than a, $J(l)$ tends to zero, as less and less energy release rate is associated with further crack growth. Indeed, from the complete solution of this problem (Tada et al., 1973, p. 5.12), $J(l) = 4/\pi^2\, kl\, (\sin^{-1} a/l)^2$, with k given in (5).

Lastly, we give a J representation for the case of the antisymmetric crack loading, shown for example for the edge crack in Fig. 6(*a*). The only difference in the procedure of applying the M integral to this configuration is that there is a contribution to M from the large circle (Γ_∞), due to a concentrated tangential force of amount $2\sigma l$ acting on the edge of the half space. This is (Freund, 1978) $M(\Gamma_\infty) = [(1-\nu)/2\mu]\,(2\sigma l)^2/\pi$, and therefore

$$J = 2\left(\frac{\sigma A}{l} - \frac{1-\nu}{\mu}\frac{\sigma^2 l}{\pi}\right), \tag{17}$$

where A is the area shown in Fig. 6(*b*). Since the antisymmetric loading in Fig. 6(*a*) gives rise to mode II stress intensity factor (K_{II}), while symmetric loading and formula (4) corresponds to mode I, (17) can be used in a superposition procedure to decouple two modes of a mixed-mode loading, as in uniform compression on one of the crack faces. If the loading is by a concentrated tangential force P at the left end of the crack face, it follows that

$$K_I = \frac{\pi}{\sqrt{\pi^2 - 4}}\frac{P}{\sqrt{\pi l}}, \quad K_{II} = \frac{2}{\sqrt{\pi^2 - 4}}\frac{P}{\sqrt{\pi l}} \tag{18}$$

with the face angle determined from $K_{II}/K_I = 2/\pi$.

Acknowledgments

This work was supported by the U.S.-Yugoslav Joint Fund for Scientific and Technological Corporation, in cooperation with the NSF under Grant JF-991.

References

Budiansky, B., and Rice, J. R., 1973, "Conservation Laws and Energy-Release Rates," ASME JOURNAL OF APPLIED MECHANICS, Vol. 40, pp. 201–203.

Freund, L. B., 1978, "Stress Intensity Factor Calculations Based on a Conservation Integral," *Int. J. Solids Structures*, Vol. 14, pp. 241–250.

Knowles, J. K., and Sternberg, E., 1972, "On a Class of Conservation Laws in Linearized and Finite Elastostatics," *Arch. Rational Mechan. Anal.*, Vol. 25, pp. 187–211.

Koiter, W. T., 1956, "On the Flexural Rigidity of a Beam Weakened by Transverse Saw-Cuts," *Proc. Kon. Ned. Ak. Wet. B*, Vol. 59, pp. 354–374.

Koiter, W. T., 1965, discussion, "Rectangular Tensile Sheet with Symmetric Edge Cracks," ASME JOURNAL OF APPLIED MECHANICS, Vol. 32, p. 237.

Rice, J. R., 1968a, "Mathematical Analysis in the Mechanics of Fracture," *Fracture*, Vol. III, H. Liebowitz, ed., pp. 191–311, Academic Press, New York.

Rice, J. R., 1968b, "A Path Independent Integral and the Approximate Analysis of Strain Concentration by Notches and Cracks," ASME JOURNAL OF APPLIED MECHANICS, Vol. 35, pp. 379–386.

Sneddon, I. N., and Das, S. D., 1971, "The Stress Intensity Factor at the Tip of an Edge Crack in an Elastic Half-Plane," *Int. J. Engng. Sci.*, Vol. 9, pp. 25–36.

Tada, H., Paris, P., and Irwin, G. R., 1973, *The Stress Analysis of Cracks Handbook*, Del Research Corporation, Hellertown.

Downloaded 03 May 2010 to 171.66.16.245. Redistribution subject to ASME license or copyright; see http://www.asme.org/terms/Terms_Use.cfm

Hisao Hasegawa
Professor,
Department of Mechanical Engineering,
Meiji University,
Tama-Ku, Kawasaki, 214 Japan

Ven-Gen Lee
Graduate Student.

Toshio Mura
Professor,
Fellow ASME.

Department of Civil Engineering,
Northwestern University,
Evanston, IL 60208

Hollow Circular Cylindrical Inclusion at the Surface of a Half-Space

Exact solutions are presented in closed form for the axisymmetric stresses and displacement fields caused by a solid or hollow circular cylindrical inclusion in the present of uniform eigenstrain in a half space. The elastic fields for interior and exterior points are expressed by one analytical form. The strain energy is also obtained in closed forms.

1 Introduction

The elastic fields due to an inclusion in an elastic half-space has been a subject of numerous investigations, chiefly because of their relevance to the analysis and design of geotechnical structures. The problem of an ellipsoidal inclusion with uniform dilatational eigenstrains in a half-space was solved by Seo and Mura (1979). Mindlin and Cheng (1950) treated the case of thermoelastic stress fields in the semi-infinite solid when a uniform dilatational thermal expansion is given inside a spherical inclusion. Youngdahl and Sternberg (1966) investigated the stress concentration around a cylindrical hole in a semi-infinite elastic body. Their solution is in integral form deduced from the Papkovich stress functions by means of a specially adapted integral-transform technique. Luk and Keer (1979) used Hankle integral transforms and the technique of superposition to solve the axially symmetric elastostatic problem of a half-space containing a partially embedded axially loaded rigid cylindrical rod. Numerical results were obtained. Chiu (1978, 1980) derived the elastic fields in a half-space with a cuboidal zone by using the full space solution of two cuboids with specified initial strain and by relieving the stress acting normal to their plane of symmetry. Yu and Sanday (1990) used an alternate method for deriving the axisymmetric elastic fields in the half-space with an isotropic spheriodal inclusion. Their new approach involved the application of Hankle transformation method for the solution of prismatic dislocation loops and Eshelby's solution for ellipsoidal inclusions. Their solutions were expressed by higher derivatives of harmonic and biharmonic potentials.

The solution for a finite body can be obtained from the solution of an infinite body by applying to the boundary plane equal and opposite normal and shear stresses in order to satisfy the traction-free surface condition. The present paper established the closed-form solutions for the axisymmetric elastic fields caused by a solid or hollow circular cylindrical inclusion with uniform eigenstrain prescribed in a half-space. The strain energy in the cylindrical inclusion is also obtained.

2 Definition of the Problem

A semi-infinite domain is defined by $z \geq 0$, and its surface $z = 0$ is free from external tractions. The analysis considers a single, solid, cylindrical inclusion of radius c or a hollow inclusion with inner and outer radii c_1 and c_2, respectively. The distance from the free surface ($z = 0$) to the upper boundary of inclusion is b_1, to the lower boundary of inclusion is b_2, as shown in Fig. 1. The objective of the analysis is to express the elastic field when the eigenstrain ϵ_z^* is given for interior points of inclusion Ω in the half-space as follows:

(1) for a solid cylindrical inclusion embedded in a half-space,

$$\epsilon_z^* = \epsilon_0\{H(z-b_1) - H(z-b_2)\}\{1 - H(r-c)\} \text{ and} \quad (1)$$

(2) for an hollow cylindrical inclusion embedded in a half space,

$$\epsilon_z^* = \epsilon_0\{H(z-b_1) - H(z-b_2)\}\{H(r-c_1) - H(r-c_2)\} \quad (2)$$

where $H(\ )$ is a Heaviside step function and ϵ_0 is the magnitude of the eigenstrain.

It is well known that the displacement $u_i(r, z)$ due to the eigenstrain $\epsilon_{ij}^*(r, z)$ satisfies the fundamental equations

Contributed by the Applied Mechanics Division of THE AMERICAN SOCIETY OF MECHANICAL ENGINEERS for publication in the ASME JOURNAL OF APPLIED MECHANICS.

Discussion on this paper should be addressed to the Technical Editor, Professor Lewis T. Wheeler, Department of Mechanical Engineering, University of Houston, Houston, TX 77204-4792, and will be accepted until four months after final publication of the paper itself in the ASME JOURNAL OF APPLIED MECHANICS.

Manuscript received by the ASME Applied Mechanics Division, May 2, 1991; final revision, Dec. 30, 1991. Associate Technical Editor: R. M. Bowen.

Copyright © 1993 by ASME
Downloaded 03 May 2010 to 171.66.16.245. Redistribution subject to ASME license or copyright; see http://www.asme.org/terms/Terms_Use.cfm

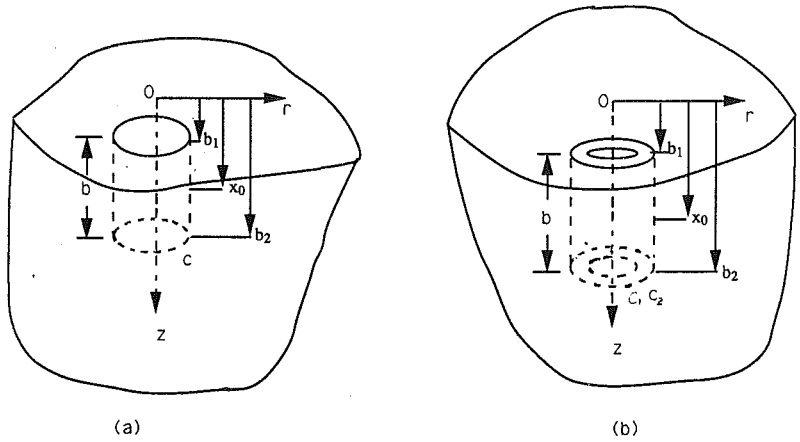


Fig. 1 Cylindrical coordinate system of a half-space with a cylindrical inclusion; (*a*) solid cylindrical inclusion, (*b*) hollow cylindrical inclusion

$$\mu\left(\nabla^2-\frac{1}{r^2}\right)u_i+\mu\delta_{3i}\frac{u_i}{r^2}+(\lambda+2\mu)\mathrm{grad}_i\mathrm{div}U+F_i=f_i \quad (3)$$

with

$$f_1=\frac{2\mu}{r}\frac{\partial}{\partial r}[r(\epsilon_r^*-\epsilon_\theta^*)]+\lambda\frac{\partial}{\partial r}(\epsilon_r^*+\epsilon_z^*)+(\lambda+2\mu)\frac{\partial}{\partial r}\epsilon_\theta^*+\mu\frac{\partial}{\partial z}\gamma_{rz}^*,$$

$$f_2=\mu\left(\frac{\partial}{\partial r}\gamma_{r\theta}^*+\frac{\partial}{\partial z}\gamma_{z\theta}^*+\frac{2}{r}\gamma_{r\theta}^*\right),$$

$$f_3=\lambda\frac{\partial}{\partial z}(\epsilon_r^*+\epsilon_\theta^*)+(\lambda+2\mu)\frac{\partial}{\partial z}\epsilon_z^*+\frac{\mu}{r}\frac{\partial}{\partial r}(r\gamma_{rz}^*) \quad (4)$$

where $F_i(r, z)$ are body forces, U is a displacement vector with the components u_i, λ and μ are the Lame's constants, δ_{ij} is the Kronecker delta, and $\gamma_{ij}^* = 2\epsilon_{ij}^*$, $(i \neq j)$.

The boundary conditions for the free surface are

$$\sigma_z=\tau_{zr}=\tau_{z\theta}=0 \quad z=0,\ 0\le r<\infty. \quad (5)$$

3 Green's function

The Green's function used here is defined as a solution to the problem of an elastic half-space satisfying the boundary conditions (5) and subjected to the axisymmetric body forces

$$F_i=\frac{1}{2\pi r}\delta(r-a)\delta(z-h) \quad (6)$$

distributing on a circle ($r = a$, $z = h$) as shown in Fig. 2. The Green's function defined above can be expressed as follows:

(1) For a radial body force F_1,

$$2\mu u_1=\frac{2}{\pi(1-\nu)}\int_0^\infty\int_0^\infty\alpha\overline{F_1}\left\{\frac{2(1-\nu)}{\alpha^2+\beta^2}-\frac{\alpha^2}{(\alpha^2+\beta^2)^2}\right\}\times J_1(\alpha r)\cos(\beta z)d\alpha d\beta+\int_0^\infty(1-2\nu-\alpha z)\overline{P_1}J_1(\alpha r)e^{-\alpha z}d\alpha,$$

$$2\mu u_2=0,$$

$$2\mu u_3=\frac{-2}{\pi(1-\nu)}\int_0^\infty\int_0^\infty\overline{F_1}\frac{\alpha^2\beta}{(\alpha^2+\beta^2)^2}J_0(\alpha r)\sin(\beta z)d\alpha d\beta-\int_0^\infty\{2(1-\nu)+\alpha z\}\overline{P_1}J_0(\alpha r)e^{-\alpha z}d\alpha. \quad (7)$$

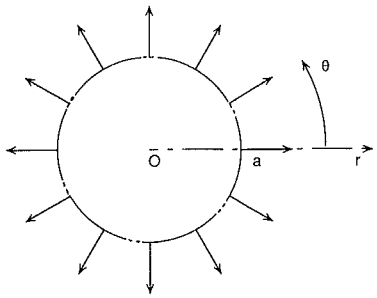


Fig. 2(*a*) A radial force

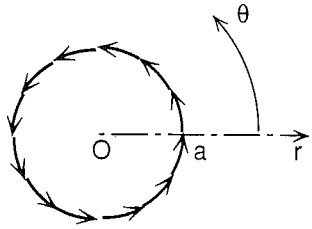


Fig. 2(*b*) A torsional force

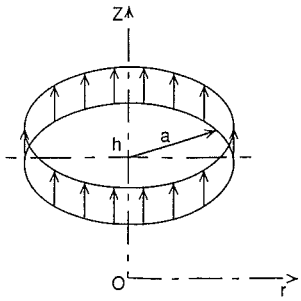


Fig. 2(*c*) An axial force

Fig. 2 The body force acting on a circle

(2) For a torsional body force F_2,

$$2\mu u_2=\frac{4}{\pi}\int_0^\infty\int_0^\infty\overline{F_2}\frac{\alpha}{\alpha^2+\beta^2}J_1(\alpha r)\cos(\beta z)d\alpha d\beta,$$

$$2\mu u_1=2\mu u_3=0. \quad (8)$$

(3) For an axial body force F_3,

Downloaded 03 May 2010 to 171.66.16.245. Redistribution subject to ASME license or copyright; see http://www.asme.org/terms/Terms_Use.cfm

$$2\mu u_1=\frac{2}{\pi(1-\nu)}\int_0^\infty\int_0^\infty \overline{F_3}\,\frac{\alpha^2\beta}{(\alpha^2+\beta^2)^2}J_1(\alpha r)\sin(\beta z)\,d\alpha d\beta - \int_0^\infty \{2(1-\nu)-\alpha z\}\overline{P_3}J_1(\alpha r)e^{-\alpha z}d\alpha,$$

$$2\mu u_2=0,$$

$$2\mu u_3=\frac{2}{\pi(1-\nu)}\int_0^\infty\int_0^\infty \alpha\overline{F_3}\left\{\frac{2(1-\nu)}{\alpha^2+\beta^2}-\frac{\beta^2}{(\alpha^2+\beta^2)^2}\right\} \times J_0(\alpha r)\cos(\beta z)\,d\alpha d\beta+\int_0^\infty (1-2\nu+\alpha z)\overline{P_3}J_0(\alpha r)e^{-\alpha z}d\alpha, \quad (9)$$

with

$$\overline{F_i}=\frac{1}{2\pi}J_n(\alpha a)\cos(\beta h), \quad (10a)$$

where $n = 1$ for $i = 1$ and 2, and $n = 0$ for $i = 3$, and

$$\overline{P_1}=\frac{2}{\pi(1-\nu)}\int_0^\infty \alpha\overline{F_1}\left\{\frac{1-\nu}{\alpha^2+\beta^2}-\frac{\alpha^2}{(\alpha^2+\beta^2)^2}\right\}d\beta,$$

$$\overline{P_3}=\frac{2}{\pi(1-\nu)}\int_0^\infty \alpha\overline{F_3}\left\{\frac{1-\nu}{\alpha^2+\beta^2}-\frac{\beta^2}{(\alpha^2+\beta^2)^2}\right\}d\beta. \quad (10b)$$

Expressions for stresses are obtained from the displacements shown above and from Hooke's law.

4 Stresses and Displacements due to Eigenstrain

The stress and displacement fields caused by a cylindrical inclusion can be obtained from

$$\begin{Bmatrix}u_i\\ \sigma_{ij}\end{Bmatrix}=-\int_\Omega \begin{Bmatrix}u_i^k(r,\,z,\,a,\,h)\\ \sigma_{ij}^k(r,\,z,\,a,\,h)\end{Bmatrix} f_k(a,\,h)\,d\Omega-\begin{Bmatrix}0\\ \overset{*}{\sigma}_{ij}\end{Bmatrix}. \quad (11)$$

Here, u_i^k denotes the displacement component in the i-direction at a point (r, z) when a unit ring force in the k-direction acts along a circle (a, h) of radius a. Here, u_i^k and σ_{ij}^k are the Green's functions mentioned above and Ω is the region of inclusion and $\overset{*}{\sigma}_{ij}$ is

$$\overset{*}{\sigma}_{ij}=\begin{Bmatrix}2\mu\overset{*}{\epsilon}_{ij}+\delta_{ij}\lambda\overset{*}{\epsilon}_{kk}, & (\text{in }\Omega)\\ 0, & (\text{outside of }\Omega)\end{Bmatrix}. \quad (12)$$

From (4), (7), (8), (9), and (11), we obtain

$$\begin{Bmatrix}u_i\\ \sigma_{ij}\end{Bmatrix}=-\int_\Omega\left[\lambda\begin{Bmatrix}u_i^1\\ \sigma_{ij}^1\end{Bmatrix}\frac{\partial\overset{*}{\epsilon}_z}{\partial a}+(\lambda+2\mu)\begin{Bmatrix}u_i^3\\ \sigma_{ij}^3\end{Bmatrix}\frac{\partial\overset{*}{\epsilon}_z}{\partial h}\right]d\Omega-\begin{Bmatrix}0\\ \overset{*}{\sigma}_{ij}\end{Bmatrix}. \quad (13)$$

4.1 Displacement.

From (7) and (13), we have

$$u_i=2\pi c\lambda\epsilon_0\int_{b_1}^{b_2}u_1^1(r,\,z,\,c,\,h)\,dh - 2\pi(\lambda+2\mu)\epsilon_0\int_0^c\{u_i^3(r,\,z,\,a,\,b_1)-u_i^3(r,\,z,\,a,\,b_2)\}\,a\,da. \quad (14)$$

The integrals in (14) can be performed by the use of integral formulas (Erdelyi, 1954; Eason and et al., 1955) and we obtain

$$2\mu u_j=\frac{4\pi\mu c\epsilon_0}{1-2\nu}\sum_{n=1}^{2}(-1)^n\left[\sum_{i=1}^{2}\{\nu\overline{u}_j^1+(1-\nu)\overline{u}_j^3\} + \nu\overline{\overline{u}}_j^1+(1-\nu)\overline{\overline{u}}_j^3\right] \quad (15)$$

with

$$\overline{u}_1^1=\frac{(-1)^i z_i}{D}\left\{2(1-\nu)Q_{1/2}(x_i)+\frac{1-2\nu}{2cr}[(c^2+r^2)Q_{-1/2}(x_i) - (c-r)^2k_i\Pi(p,\,k_i)]\right\},$$

$$\overline{u}_1^3=\frac{z_i}{D}Q_{1/2}(x_i),$$

$$\overline{u}_3^1=\frac{(-1)^i}{D}\left\{rG_2(x_1)+\frac{c^2-r^2-z_i^2}{2c}Q_{-1/2}(x_i)\right\},$$

$$\overline{u}_3^3=\frac{1}{D}\left\{(3-4\nu)rG_2(x_i)+\frac{(3-4\nu)(c^2-r^2)-z_i^2}{2c}Q_{-1/2}(x_i) + (1-2\nu)\frac{c-r}{c+r}\frac{z_i^2}{c}k_i\Pi(p,\,k_i) - (1-2\nu)\frac{\pi\sqrt{cr}\,|z_i|}{c}[1+SGN(c-r)]\right\},$$

$$\overline{\overline{u}}_1^1=-\frac{\nu(1-2\nu)}{Dcr}\{-z_2(c-r)^2k_2\Pi(p,\,k_2) + z_2(c^2+r^2)Q_{-1/2}(x_2)+\frac{2}{D}\{b_n-\nu(3-2\nu)z_2\}Q_{1/2}(x_2),$$

$$\overline{\overline{u}}_1^3=-\frac{1}{D}\left\{\frac{(1-\nu)(1-2\nu)}{cr}[(c-r)^2z_2k_2\Pi(p,\,k_2) - z_2(c^2+r^2)Q_{-1/2}(x_2)]+[-2(2-\nu)(1-2\nu)z + 2(1-\nu)(1+2\nu)b_n]Q_{1/2}(x_2)+\frac{b_nzz_2}{cr}\frac{1}{x_2^2-1}G_1(x_2)\right\},$$

$$\overline{\overline{u}}_3^1=\frac{2}{D}\left\{-4\nu(1-\nu)rG_2(x_2)-\frac{b_nz}{2r}\left[Q_{1/2}(x_2)-\frac{x_2-r/c}{x_2^2-1}G_1(x_2)\right] - (1-\nu)(1-2\nu)\pi b_n\frac{\sqrt{cr}}{c}[1+SGN(c-r)] + (1-2\nu)\frac{c-r}{c+r}\frac{z_2}{c}k_2\Pi(p,\,k_2)[(1-\nu)b_n-\nu z]\right] + \frac{1}{c}[(1-\nu)b_nz_2+\nu zz_2-2\nu(1-\nu)(c^2-r^2)]Q_{-1/2}(x_2)\right\},$$

$$\overline{\overline{u}}_3^3=\frac{1}{D}\left\{(1-2\nu)^2r\left[2G_2(x_2)+\frac{c^2-r^2}{cr}Q_{-1/2}(x_2)\right] - (1-2\nu)\frac{z_2^2}{c}\left[2\nu\frac{c-r}{c+r}k_2\Pi(p,\,k_2)+Q_{-1/2}(x_2)\right] + 2\nu(1-2\nu)\frac{\pi\sqrt{cr}z_2}{c}\{1+SGN(c-r)\} + \frac{b_nz}{r}\left[Q_{1/2}(x_2)-\frac{x_2-r/c}{x_2^2-1}G_1(x_2)\right]\right\}, \quad (16)$$

with

$$D=8\pi^2\sqrt{cr}(1-\nu)$$

$$z_1=z-b_n,\ z_2=z+b_n,\ x_i=\frac{r^2+c^2+z_i^2}{2cr},$$

$$p=\frac{4cr}{(c+r)^2},\ k_i^2=\frac{4cr}{(c+r)^2+z_i^2},$$

$$G_1(x_i)=x_iQ_{1/2}(x_i)-Q_{-1/2}(x_i),$$

$$G_2(x_i)=x_iQ_{-1/2}(x_i)-Q_{1/2}(x_i), \quad (17)$$

where $Q_n(x_i)$ is a Legendre function of the second kind of the order n and $SGN(c-r)$ is $+1$, 0 or -1 according to positive, zero, or negative value of $(c-r)$. $\Pi(p, k_i)$ is a complete elliptic integral of the third kind. The same details of the integration technique are given in the Appendix.

Downloaded 03 May 2010 to 171.66.16.245. Redistribution subject to ASME license or copyright; see http://www.asme.org/terms/Terms_Use.cfm

4.2 Stresses. From (7) and (13) we have

$$\sigma_{ij}=2\pi c\lambda\epsilon_0\int_{b_1}^{b_2}\sigma_{ij}^1(r,\,z,\,c,\,h)dh-2\pi(\lambda+2\mu)\epsilon_0 \times\int_0^c\{\sigma_{ij}^3(r,\,z,\,a,\,b_1)-\sigma_{ij}^3(r,\,z,\,a,\,b_2)\}ada-\sigma_{ij}^*. \quad (18)$$

By similar considerations as indicated above for the displacements and the Hooke's law, the stresses can be derived from (18) as follows:

$$\sigma_{pq}=\frac{4\pi\mu c\epsilon_0}{1-2\nu}\sum_{n=1}^{2}(-1)^n\left[\sum_{i=1}^{2}\{\nu\bar{\sigma}_{pq}^1+(1-\nu)\bar{\sigma}_{pq}^3\}+\nu\bar{\bar{\sigma}}_{pq}^1+(1-\nu)\bar{\bar{\sigma}}_{pq}^3\right] \quad (19)$$

where

$$\bar{\sigma}_r^1=\frac{(-1)^iz_i}{2Dc}\left\{\left[1-\frac{(1-2\nu)c^2}{r^2}\right]Q_{-1/2}(x_i)-\frac{(3-4\nu)c}{r}Q_{1/2}(x_i) -\frac{c}{r}\frac{x_i-r/c}{x_i^2-1}G_1(x_i)+\left[2(1-\nu)\frac{c-r}{c+r}+(1-2\nu)\frac{(c-r)^2}{r^2}\right]k_i\Pi(p,\,k_i)\right\},$$

$$\bar{\sigma}_\theta^1=\frac{(-1)^iz_i}{2Dc}\left\{\left[1+\frac{(1-2\nu)c^2}{r^2}\right]Q_{-1/2}(x_i)+\frac{4(1-\nu)c}{r}Q_{1/2}(x_i) +\left[2\nu\frac{c-r}{c+r}-(1-2\nu)\frac{(c-r)^2}{r^2}\right]k_i\Pi(p,\,k_i)\right\},$$

$$\bar{\sigma}_z^1=\frac{(-1)^iz_i}{2Dc}\left\{-\frac{c}{r}\left[Q_{1/2}(x_i)-\frac{x_i-r/c}{x_i^2-1}G_1(x_i)\right] +2\nu\left[Q_{-1/2}(x_i)+\frac{c-r}{c+r}k_i\Pi(p,\,k_i)\right]\right\},$$

$$\bar{\tau}_{rz}^1=\frac{(-1)^i}{2D}\left\{2(1-2\nu)Q_{1/2}(x_i)+\frac{1}{x_i^2-1}\frac{z_i^2}{cr}G_1(x_i)\right\},$$

$$\bar{\sigma}_r^3=\frac{z_i}{2Dc}\left\{-\frac{c}{r}\left[Q_{1/2}(x_i)+\frac{x_i-r/c}{x_i^2-1}G_1(x_i)\right] +2\nu\left[Q_{-1/2}(x_i)+\frac{c-r}{c+r}k_i\Pi(p,\,k_i)\right]\right\},$$

$$\bar{\sigma}_\theta^3=\frac{z_i}{Dc}\left\{\frac{c}{r}Q_{1/2}(x_i)+\nu\left[Q_{-1/2}(x_i)+\frac{c-r}{c+r}k_i\Pi(p,\,k_i)\right]\right\},$$

$$\bar{\sigma}_z^3=\frac{z_i}{2Dc}\left\{-\frac{c}{r}\left[Q_{1/2}(x_i)-\frac{x_i-r/c}{x_i^2-1}G_1(x_i)\right] +2(1-\nu)\left[Q_{-1/2}(x_i)+\frac{c-r}{c+r}k_i\Pi(p,\,k_i)\right]\right\},$$

$$\bar{\tau}_{rz}^3=\frac{-1}{2D}\left\{2(1-2\nu)Q_{1/2}(x_i)-\frac{1}{x_i^2-1}\frac{z_i^2}{cr}G_1(x_i)\right\},$$

$$\bar{\bar{\sigma}}_r^1=\frac{1}{Dc}\left\{-\left[2\nu-\nu(1-2\nu)\frac{c^2+r^2}{r^2}\right]z_2Q_{-1/2}(x_2) -\left[2\nu\frac{c-r}{c+r}+\nu(1-2\nu)\frac{(c-r)^2}{r^2}\right]z_2k_2\Pi(p,\,k_2) +\frac{2\nu c}{r}[2z+(1-2\nu)z_2]Q_{1/2}(x_2) -\frac{c}{r}\left[(b_n-4b_n\nu+2\nu z)Q_{1/2}(x_2)+(b_n-2\nu z)\frac{x_2-r/c}{x_2^2-1}G_1(x_2)\right] -\frac{b_nzz_2}{2r^2}\frac{1}{x_2^2-1}\left[3Q_{-1/2}(x_2)+\frac{r}{c}Q_{1/2}(x_2) -\frac{4}{x_2^2-1}\left(G_1(x_2)+\frac{r}{c}G_2(x_2)\right)+2G_1(x_2)\right]\right\},$$

$$\bar{\bar{\sigma}}_\theta^1=\frac{2}{Dc}\left\{-z_2\nu\left[2\nu\frac{c-r}{c+r}-(1-2\nu)\frac{(c-r)^2}{2r^2}\right]k_2\Pi(p,\,k_2) -\frac{\nu z_2}{2}\left[(1+2\nu)+(1-2\nu)\frac{c^2}{r^2}\right]Q_{-1/2}(x_2) +[(1-\nu)b_n-2\nu z-\nu(1-2\nu)z_2]\frac{c}{r}Q_{1/2}(x_2) +\frac{b_nc}{r}\left[\frac{zz_2}{2cr}-\nu(x_2-r/c)\right]\frac{1}{x_2^2-1}G_1(x_2)\right\},$$

$$\bar{\bar{\sigma}}_z^1=\frac{1}{Dc}\left\{\frac{(b_n+2\nu z)c}{r}\left[Q_{1/2}(x_2)-\frac{x_2-r/c}{x_2^2-1}G_1(x_2)\right] -2\nu z_2\left[Q_{-1/2}(x_2)+\frac{c-r}{c+r}k_2\Pi(p,\,k_2)\right]+\frac{b_nzz_2}{2r^2}\frac{1}{x_2^2-1} \times\left[3Q_{-1/2}(x_2)+\frac{r}{c}Q_{1/2}(x_2)-\frac{4}{x_2^2-1}\left(G_1(x_2)+\frac{r}{c}G_2(x_2)\right)\right]\right\},$$

$$\bar{\bar{\tau}}_{rz}^1=\frac{z}{Dcr}\left\{\frac{b_n-2\nu z_2}{x_2^2-1}G_1(x_2) -\frac{b_n}{x_2^2-1}\left[\frac{z_2^2}{2cr}Q_{1/2}(x_2)-\frac{2}{x_2^2-1}\frac{z_2^2}{cr}G_2(x_2)\right]\right\},$$

$$\bar{\bar{\sigma}}_r^3=\frac{2}{Dr}\left\{-\frac{b_nzz_2}{c^2(x_2^2-1)^2}G_2(x_2)+\left[\frac{b_nzz_2}{4cr}\frac{3}{x_2^2-1} +\frac{(1-2\nu)rz_2}{c}\left(\frac{1+\nu}{2}-\frac{1-\nu}{2}\frac{c^2}{r^2}\right)\right]Q_{-1/2}(x_2) +\left[\frac{b_nzz_2}{4c^2}\frac{1}{x_2^2-1}-\frac{(1-2\nu)(3-2\nu)}{2}z+\nu(1-2\nu)b_n\right]Q_{1/2}(x_2) +\frac{(1-2\nu)rz_2}{c}\times\left[\frac{c-r}{c+r}+(1-\nu)\frac{(c-r)^2}{2r^2}\right]k_2\Pi(p,\,k_2)+\frac{1}{x_2^2-1} \times\left[\frac{b_nzz_2}{2cr}\left(1-\frac{2}{x_2^2-1}\right)-\frac{(1-2\nu)z-2b_n}{2}(x_2-r/c)\right]G_1(x_2)\right\},$$

$$\bar{\bar{\sigma}}_\theta^3=-\frac{2}{Dr}\left\{\frac{1}{x_2^2-1}\left[\frac{b_nzz_2}{2cr}-b\nu(x_2-r/c)\right]G_1(x_2) -(1-2\nu)\frac{z_2}{2c}\left[2\nu r+(1-\nu)\frac{c^2+r^2}{r}\right]Q_{-1/2}(x_2) +\frac{z_2}{2c}(c-r)(1-2\nu)\left[-\frac{2\nu r}{c+r}+(1-\nu)\frac{c-r}{r}\right]k_2\Pi(p,\,k_2) +[-(1-2\nu)(2-\nu)z+b_n(1+2\nu-2\nu^2)]Q_{1/2}(x_2)\right\}$$

$$\bar{\bar{\sigma}}_z^3=-\frac{z}{Dr}\left\{-\frac{1}{x_2^2-1}\left[\frac{2b_nz_2}{cr}\frac{1}{x_2^2-1}+(1-2\nu)(x_2-r/c)\right]G_1(x_2)\right.$$

Downloaded 03 May 2010 to 171.66.16.245. Redistribution subject to ASME license or copyright; see http://www.asme.org/terms/Terms_Use.cfm

$$-\frac{2b_nz_2}{(x_2^2-1)^2c^2}G_2(x_2)+\frac{3b_nz_2}{2cr}\frac{1}{x_2^2-1}Q_{-1/2}(x_2)$$
$$+\left[\frac{b_nz_2}{x_2^2-1}\frac{1}{2c^2}+(1-2\nu)\right]Q_{1/2}(x_2)\Bigg\},$$

$$\bar{\bar{\tau}}^3_{rz}=\frac{1}{D}\left\{\frac{1}{x_2^2-1}\frac{(1-2\nu)zz_2-b_n(z+z_2)}{cr}G_1(x_2)\right.$$
$$-\frac{2b_nzz_2^2}{(x_2^2-1)^2}\frac{1}{c^2r^2}G_2(x_2)$$
$$\left.+\left[\frac{b_nzz_2^2}{x_2^2-1}\frac{1}{2c^2r^2}+2(1-2\nu)\right]Q_{1/2}(x_2)\right\}. \quad (20)$$

5 A Hollow Cylindrical Inclusion Embedded in the Half-Space

The stresses and displacements caused by a hollow circular cylindrical inclusion are easily obtained by using the results shown previously for a solid cylindrical inclusion.

The eigenstrain distribution in a hollow cylindrical inclusion shown in Eq. (2) can be rearranged as

$$\epsilon_z^*=\sum_{m=1}^{2}(-1)^m\epsilon_0\{H(z-b_1)-H(z-b_2)\}\{1-H(r-c_m)\}. \quad (21)$$

From (1) and (21), it is observed that the stress and displacement fields caused by the hollow cylindrical inclusion can be obtained by a simple superposition of the field caused by two solid cylindrical inclusions with radius c_1 and c_2, respectively, and are expressed as follows:

$$2\mu u_j=\sum_{m=1}^{2}(-1)^m\left\{\frac{4\pi\mu c_m\epsilon_0}{1-2\nu}\sum_{n=1}^{2}(-1)^n\left[\sum_{i=1}^{2}\{\nu\bar{u}_j^1+(1-\nu)\bar{u}_j^3\}\right.\right.$$
$$\left.\left.+\nu\bar{\bar{u}}_j^1+(1-\nu)\bar{\bar{u}}_j^3\right]\right\},$$
$$\sigma_{pq}=\sum_{m=1}^{2}(-1)^m\left\{\frac{4\pi\mu c_m\epsilon_0}{1-2\nu}\sum_{n=1}^{2}(-1)^n\left[\sum_{i=1}^{2}\{\nu\bar{\sigma}_{pq}^1+(1-\nu)\bar{\sigma}_{pq}^3\}\right.\right.$$
$$\left.\left.+\nu\bar{\bar{\sigma}}_{pq}^1+(1-\nu)\bar{\bar{\sigma}}_{pq}^3\right]\right\} \quad (22)$$

where $\bar{u}_j^k$, $\bar{\bar{u}}_j^k$, $\bar{\sigma}_{pq}^k$, and $\bar{\bar{\sigma}}_{pq}^k$ are the same as (16) and (20) with parameters (r, z, c_m, b_n).

6 Strain Energy for a Solid Cylindrical Inclusion

We consider the eigenstrains ϵ_{ij}^* are just prescribed in Ω, where Ω is the subdomain of χ. The elastic strain energy is (Mura, 1982)

$$W^*=\frac{1}{2}\int_\chi\sigma_{ij}e_{ij}d\chi \quad (23a)$$

where $e_{ij}=\epsilon_{ij}-\epsilon_{ij}^*$ and $\epsilon_{ij}=1/2(u_{i,j}+u_{j,i})$. Integrating by parts, we obtain from Eq. (23a)

$$W^*=-\frac{1}{2}\int_\Omega\sigma_{ij}\epsilon_{ij}^*d\chi=-\frac{1}{2}\int_\Omega\sigma_z\epsilon_z^*d\chi \quad (23b)$$

where σ_{ij} is the stress caused by ϵ_{ij}^*.

From (1), (18), and (23), we have

$$W^*=-\frac{1}{2}\int_\Omega\sigma_z\epsilon_z^*d\chi=-\pi\epsilon_0\int_0^c\int_{b_1}^{b_2}\sigma_z r dr dz$$
$$=\frac{\mu\epsilon_0^2c}{3(1-\nu)(1-2\nu)}\sum_{n=1}^{2}(-1)^n\{\nu(W_1+W_2)$$
$$+(1-\nu)(W_3-W_4)\} \quad (24)$$

where

$$W_1=2(1+2\nu)c^2+3b_n^2\{Q_{1/2}(y_1)+Q_{-1/2}(y_1)\}$$
$$-(1+2\nu)\{(c^2+3b_n^2)Q_{-1/2}(y_1)+(b_n^2-c^2)Q_{1/2}(y_1)\}$$
$$W_2=-16\nu c^2+8\nu\left\{\left(\frac{b_n^2}{2}-c^2\right)Q_{1/2}(y_1)+\left(\frac{3b_n^2}{2}+2c^2\right)Q_{-1/2}(y_1)\right.$$
$$\left.-(b_n^2-c^2)Q_{1/2}(y_2)-(3b_n^2+c^2)Q_{-1/2}(y_2)\right\}$$
$$-3(1+\nu)b_n^2\{Q_{1/2}(y_1)+Q_{-1/2}(y_1)-2[Q_{1/2}(y_2)$$
$$+Q_{-1/2}(y_2)]\}-3b_n^2Q_{1/2}(y_2),$$
$$W_3=2(3-2\nu)c^2+(3-2\nu)\{(c^2+3b_n^2)Q_{-1/2}(y_2)$$
$$+(b_n^2-c^2)Q_{1/2}(y_2)\}-3b_n^2\{Q_{1/2}(y_2)+Q_{-1/2}(y_2)\}$$
$$+2(3-2\nu)c^2\{Q_{1/2}(y_1)-Q_{-1/2}(y_1)\}+b_n^2\{\nu Q_{1/2}(y_1)$$
$$-3(1-\nu)Q_{-1/2}(y_1)\},$$
$$W_4=\frac{b_n^2}{2}\{Q_{1/2}(y_1)+Q_{-1/2}(y_1)\}$$
$$-2(1-\nu)b_n^2\{Q_{1/2}(y_2)+Q_{-1/2}(y_2)\}$$
$$+b_n^2Q_{1/2}(y_2)-(1-2\nu)\times\left\{\left(\frac{3b_n^2}{2}+2c^2\right)Q_{-1/2}(y_1)\right.$$
$$-\left(2c^2-\frac{b_n^2}{2}\right)Q_{1/2}(y_1)+2(c^2-b_n^2)Q_{1/2}(y_2)$$
$$\left.-2(3b_n^2+c^2)Q_{-1/2}(y_2)\right\} \quad (25)$$

with

$$y_1=1+\frac{1}{2}\left(\frac{b_n}{c}\right)^2,\quad y_2=1+2\left(\frac{b_n}{c}\right)^2. \quad (26)$$

7 Discussion and Results

Numerical calculations for stresses and displacements have been performed for a solid cylindrical inclusion to show the distribution. The Poisson's ratio of the material is assumed to be 0.3. The center of the inclusion is at depth x_0 from the surface ($z = 0$) of the isotropic half space and b is the length of inclusion.

Figures 3 and 4 illustrate the distribution of displacement. Figure 3 shows the effect of inclusion depth (x_0) on displace-

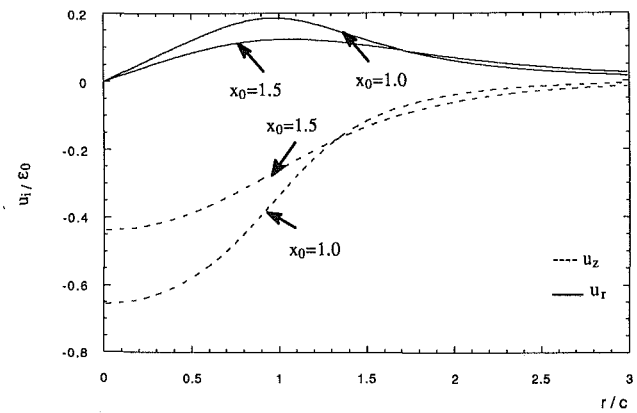


Fig. 3 Effect of the inclusion depth (x_0) on the surface displacement with b = 1

Downloaded 03 May 2010 to 171.66.16.245. Redistribution subject to ASME license or copyright; see http://www.asme.org/terms/Terms_Use.cfm

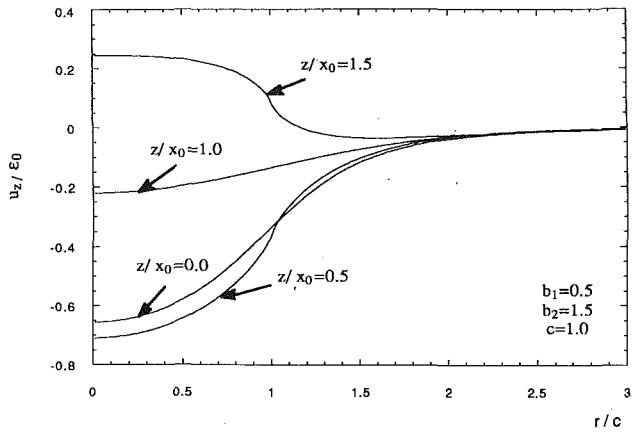


Fig. 4 Variation of u_z along the r-direction

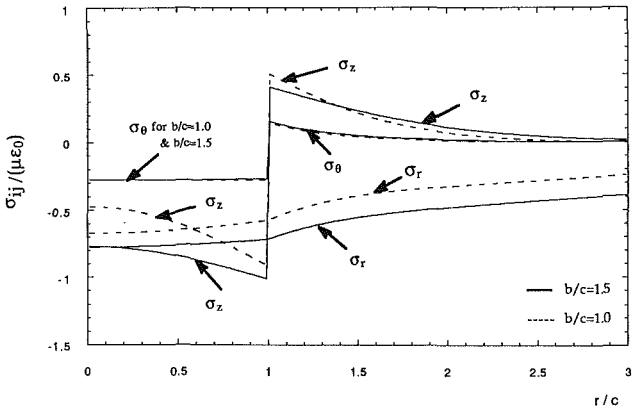


Fig. 5 Comparison of stresses on the bottom of inclusion for two inclusion size ratio b/c

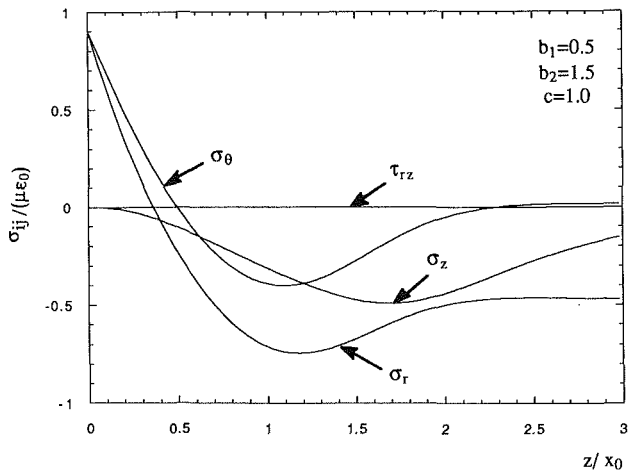


Fig. 6 Variation of stresses along the z-axis (r = 0)

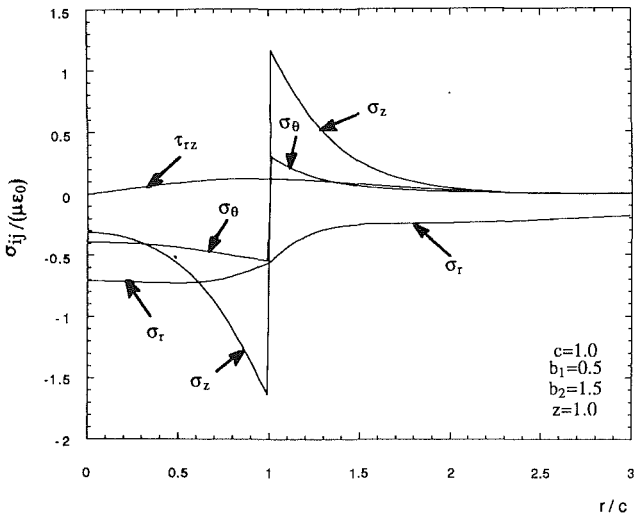


Fig. 7 Variation of stresses along the r-direction on the central plane of inclusion

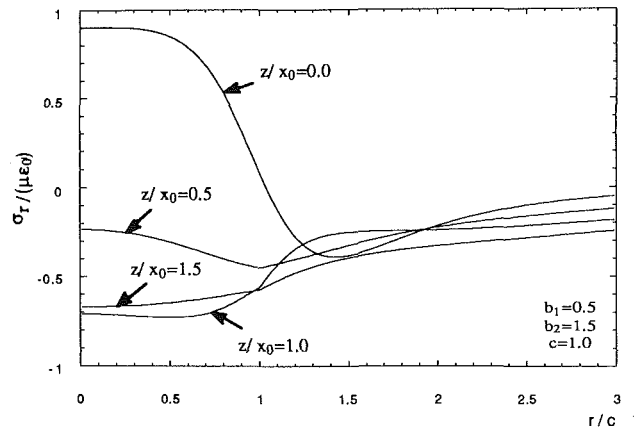


Fig. 8 Variation of σ_r along the r-direction on a different depth z/x_0

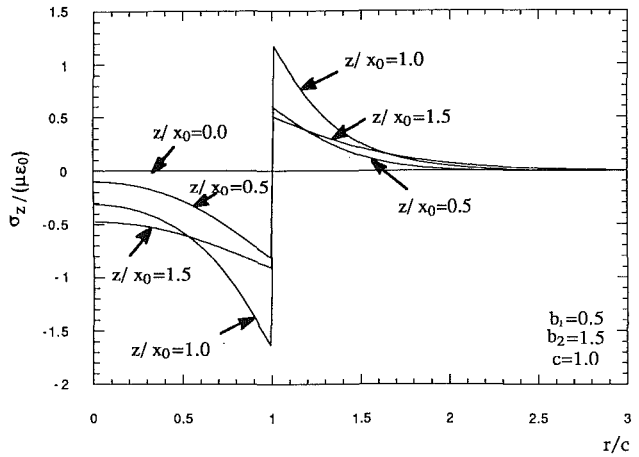


Fig. 9 Variation of σ_z along the r-direction on a different depth z/x_0

ment on the free surface with $b = 1.0$. It is evident that as x_0 becomes larger, the influence on the surface decreases. Figure 4 shows the vertical displacement u_z with different geometric aspect ration z/x_0 where the inclusion is located at $b_1 = 0.5$ and $b_2 = 1.5$.

Figures 5–9 show the distribution of stresses due to inclusion when b_1 is kept to be 0.5 and c is equal to 1. Figure 5 shows the comparison of stresses along r-axis on the bottom of inclusion with different slender ration b/c(b/c = 1.0 and b/c = 1.5). Normal stresses are compressive at interior points, σ_z and σ_θ change to tension at exterior points. It is observed that the magnitude of σ_θ is independent of b/c and is uniform at interior points. σ_z has the largest value among the stress component. From Fig. 6 we know all the normal stresses are continuous across the boundary of inclusion. Figure 7 illustrates the variation of stresses along the r-axis on the central plane of inclusion. The stress distributions are not uniform. Figures

Downloaded 03 May 2010 to 171.66.16.245. Redistribution subject to ASME license or copyright; see http://www.asme.org/terms/Terms_Use.cfm

8 and 9 show the variation of σ_z and σ_r along the r-axis on a different depth. σ_r has the largest value on the surface but decreases fast when it approaches the inclusion boundary. At interior points, the maximum value occurs on the central plane of inclusion for both components.

An application of this solution may be to the three-phase problem of inclusions, where the interface between the matrix and fibers are different materials from the matrix and the fibers. In other words, the fibers are coated by other materials.

Acknowledgment

This research was supported by AFOSR F49620-92-J-0319.

References

Chiu, Y. P., 1978, "On the Stress Field and Surface Deformation in a Half-Space with a Cuboidal Zone in which Initial Strains Are Uniform," ASME JOURNAL OF APPLIED MECHANICS, Vol. 45, pp. 302–306.

Chiu, Y. P., 1980, "On the Internal Stresses in a Half Plane and a Layer Containing Localized Inelastic Strains or Inclusions," ASME JOURNAL OF APPLIED MECHANICS, Vol. 47, pp. 313–318.

Eason, G., Noble, B., and Sneddon, I. N., 1955, "On Certain Integrals of Lipschitz-Hankel Type Involving Products of Bessel Functions," *Philosophical Transactions of the Royal Society of London*, Vol. A247, pp. 529–551.

Erdelyi, A., 1954, *Tables of Integral Transforms*, Vols. 1 and 2, McGraw-Hill, New York.

Hasegawa, H., 1976, "Axisymmetric Body Force Problems of an Elastic Half Space," *Bulletin of the JSME*, Vol. 19, pp. 1262–1269.

Hasegawa, H., 1984, "Green's Functions for Axisymmetric Body Force Problems of an Elastic Half Space and Their Application," *Bulletin of the JSME*, Vol. 27, pp. 1829–1835.

Luk, V. K., and Keer, L. M., 1979, "Stress Analysis For An Elastic Half Space Containing An Axially-Loaded Rigid Cylindrical Rod," *International Journal of Solids And Structures*, Vol. 15, pp. 805–827.

Mindlin, R. D., and Cheng, D. H., 1950, "Thermoelastic Stress in The Semi-Infinite Solid," *Journal of Applied Physics*, Vol. 21, pp. 931–933.

Mura, T., 1982, *Micromechanics of Defects in Solids*, Martinus-Nihjoff.

Seo, K., and Mura, T., 1979, "The Elastic Field in a Half Space Due to Ellipsoidal Inclusions with Uniform Dilatational Eigenstrains," ASME JOURNAL OF APPLIED MECHANICS, Vol. 46, pp. 568–572.

Youngdahl, C. K., and Sternberg, E., 1966, "Three-Dimensional Stress Concentration Around a Cylindrical Hole in a Semi-Infinite Elastic Body," ASME JOURNAL OF APPLIED MECHANICS, Series E, Vol. 33, pp. 855–865.

Yu, H. Y., and Sanday, S. C., 1990, "Axisymmetric Inclusion in a Half Space," ASME JOURNAL OF APPLIED MECHANICS, Vol. 57, pp. 74–77.

APPENDIX

(a) The following integral formulas are used to evaluate the integrals appear in this paper:

$$\int_0^\infty J_1(\alpha a)J_0(\alpha r)e^{-\alpha z i}d\alpha=\frac{1}{2\sqrt{ar}}\left\{\sqrt{\frac{r}{a}}\,[1+\operatorname{sgn}(a-r)]-\frac{z_i}{\pi a}\left[Q_{-1/2}(x_i)+\frac{a-r}{a+r}\,k_i\Pi(p,\,k_i)\right]\right\} \quad \text{(A1)}$$

$$\int_0^\infty \alpha J_1(\alpha a)J_0(\alpha r)e^{-\alpha z i}d\alpha=\frac{1}{2\pi r\sqrt{ar}}\left\{Q_{1/2}(x_i)-\frac{x_i-\frac{r}{a}}{x_i^2-1}\,G_1(x_i)\right\} \quad \text{(A2)}$$

$$\int_0^\infty J_1(\alpha a)J_1(\alpha r)e^{-\alpha z i}d\alpha=\frac{1}{\pi\sqrt{ar}}\,Q_{1/2}(x_i) \quad \text{(A3)}$$

$$\int_0^\infty \alpha J_1(\alpha a)J_1(\alpha r)e^{-\alpha z i}d\alpha=-\frac{1}{2\pi\sqrt{ar}}\,\frac{z_i}{ar}\,\frac{1}{x_i^2-1}\,[x_iQ_{1/2}(x_i)-Q_{-1/2}(x_i)] \quad \text{(A4)}$$

$$\int_0^\infty J_1(\alpha a)J_0(\alpha r)d\alpha=\begin{cases}0, & r>a\\ \dfrac{1}{2a}, & r=a\\ \dfrac{1}{a}, & r<a\end{cases}=q_1 \quad \text{(A5)}$$

$$\int_0^\infty \frac{1}{\alpha}J_1(\alpha a)J_1(\alpha r)d\alpha=\begin{cases}\dfrac{r}{2a}, & a\ge r>0\\ \dfrac{a}{2r}, & r\ge a>0\end{cases}=q_2 \quad \text{(A6)}$$

$$\int_0^\infty \frac{1}{\alpha}J_1(\alpha a)J_1(\alpha r)e^{-\alpha z i}d\alpha=q_2+\frac{1}{4\pi ar\sqrt{ar}}\,[z_i(a-r)^2k_i\Pi(p,\,k_i)-2arz_iQ_{1/2}(x_i)-z_i(a^2+r^2)Q_{-1/2}(x_i)] \quad \text{(A7)}$$

$$\int_0^\infty \frac{1}{\alpha}J_1(\alpha a)J_0(\alpha r)e^{-\alpha z i}d\alpha=-q_1z_i+\frac{1}{\pi}\sqrt{\frac{r}{a}}\left[\frac{a-r}{a+r}\,\frac{z_i^2}{2ar}\,k_i\Pi(p,\,k_i)+G_2(x_i)+\frac{a^2-r^2}{2ar}\,Q_{-1/2}(x_i)\right] \quad \text{(A8)}$$

$$\int_0^\infty \alpha^2J_1(\alpha a)J_0(\alpha r)e^{-\alpha z i}d\alpha=\frac{1}{4\pi\sqrt{ar}}\,\frac{z}{ar^2}\,\frac{1}{x_i^2-1}\left\{3Q_{-1/2}(x_i)+\frac{r}{a}\,Q_{1/2}(x_i)-\frac{4}{x_i^2-1}\left[G_1(x_i)+\frac{r}{a}\,G_2(x_i)\right]\right\} \quad \text{(A9)}$$

$$\int_0^\infty \alpha^2J_1(\alpha a)J_1(\alpha r)e^{-\alpha z_i}d\alpha=\frac{1}{2\pi\sqrt{ar}}\,\frac{1}{ar}\,\frac{1}{x_i^2-1}\times\left\{G_1(x_i)-\frac{z_i^2}{2ar}\,Q_{1/2}(x_i)+\frac{2z_i^2}{ar(x_i^2-1)}\,G_2(x_i)\right\}. \quad \text{(A10)}$$

(b) Green's function for stresses are shown as follows:

(1) For $\bar{F}_1$,

$$\sigma_r=\frac{2}{\pi(1-\nu)}\int_0^\infty\int_0^\infty \alpha\bar{F}_1\left\{\left[\frac{1-\nu}{\alpha^2+\beta^2}+\frac{\beta^2}{(\alpha^2+\beta^2)^2}\right]\frac{\partial J_1(\alpha r)}{\partial r}+\frac{\nu}{r}\,\frac{J_1(\alpha r)}{\alpha^2+\beta^2}\right\}\cos(\beta z)\,d\alpha d\beta+\int_0^\infty\left\{\alpha(1-\alpha z)J_0(\alpha r)-(1-2\nu-\alpha z)\,\frac{J_1(\alpha r)}{r}\right\}\bar{p}_1e^{-\alpha z}d\alpha,$$

$$\sigma_\theta=\frac{2}{\pi(1-\nu)}\int_0^\infty\int_0^\infty \alpha\bar{F}_1\left\{\left[\frac{1-\nu}{\alpha^2+\beta^2}+\frac{\beta^2}{(\alpha^2+\beta^2)^2}\right]\frac{J_1(\alpha r)}{r}+\frac{\nu}{\alpha^2+\beta^2}\,\frac{\partial J_1(\alpha r)}{\partial r}\right\}\cos(\beta z)\,d\alpha d\beta+\int_0^\infty\left\{2\nu\alpha J_0(\alpha r)+(1-2\nu-\alpha z)\,\frac{J_1(\alpha r)}{r}\right\}\bar{p}_1e^{-\alpha z}d\alpha,$$

$$\sigma_z=\frac{2}{\pi(1-\nu)}\int_0^\infty\int_0^\infty \alpha^2\bar{F}_1J_0(\alpha r)\left\{\frac{\alpha^2}{(\alpha^2+\beta^2)^2}-\frac{1-\nu}{\alpha^2+\beta^2}\right\}\cos(\beta z)\,d\alpha d\beta+\int_0^\infty \alpha(1+\alpha z)J_0(\alpha r)\bar{p}_1e^{-\alpha z}d\alpha,$$

$$\tau_{rz}=\frac{2}{\pi(1-\nu)}\int_0^\infty\int_0^\infty \alpha\beta\bar{F}_1J_1(\alpha r)\left\{\frac{\alpha^2}{(\alpha^2+\beta^2)^2}-\frac{1-\nu}{\alpha^2+\beta^2}\right\}\times\sin(\beta z)\,d\alpha d\beta+z\int_0^\infty \alpha^2J_1(\alpha r)\bar{p}_1e^{-\alpha z}d\alpha. \quad \text{(A11)}$$

Downloaded 03 May 2010 to 171.66.16.245. Redistribution subject to ASME license or copyright; see http://www.asme.org/terms/Terms_Use.cfm

(2) For $\bar{F}_3$,

$$\sigma_r=\frac{-2}{\pi(1-\nu)}\int_0^\infty\int_0^\infty \alpha\beta\bar{F}_3\left\{\frac{\nu}{\alpha^2+\beta^2}J_0(\alpha r)-\frac{\alpha}{(\alpha^2+\beta^2)^2}\frac{\partial J_1(\alpha r)}{\partial r}\right\}\sin(\beta z)\,d\alpha d\beta$$
$$+\int_0^\infty\left\{-\alpha(2-\alpha z)J_0(\alpha r)+\{2(1-\nu)-\alpha z\}\frac{J_1(\alpha r)}{r}\right\}\bar{p}_3e^{-\alpha z}d\alpha,$$

$$\sigma_\theta=\frac{-2}{\pi(1-\nu)}\int_0^\infty\int_0^\infty \alpha\beta\bar{F}_3\left\{\frac{\nu}{\alpha^2+\beta^2}J_0(\alpha r)-\frac{\alpha}{(\alpha^2+\beta^2)^2}\frac{J_1(\alpha r)}{r}\right\}\sin(\beta z)\,d\alpha d\beta$$
$$-\int_0^\infty\left\{2\alpha\nu J_0(\alpha r)+\{2(1-\nu)-\alpha z\}\frac{J_1(\alpha r)}{r}\right\}\bar{p}_3e^{-\alpha z}d\alpha,$$

$$\sigma_z=\frac{-2}{\pi(1-\nu)}\int_0^\infty\int_0^\infty \alpha\beta\bar{F}_3J_0(\alpha r)\left\{\frac{\alpha^2}{(\alpha^2+\beta^2)^2}+\frac{1-\nu}{\alpha^2+\beta^2}\right\}\times\sin(\beta z)\,d\alpha d\beta-z\int_0^\infty\alpha^2J_0(\alpha r)\bar{p}_3e^{-\alpha z}d\alpha,$$

$$\tau_{rz}=\frac{-2}{\pi(1-\nu)}\int_0^\infty\int_0^\infty \alpha^2\bar{F}_3J_1(\alpha r)\left\{\frac{1-\nu}{\alpha^2+\beta^2}-\frac{\beta^2}{(\alpha^2+\beta^2)^2}\right\}\times\cos(\beta z)\,d\alpha d\beta+\int_0^\infty(\alpha-\alpha^2z)J_1(\alpha r)\bar{p}_3e^{-\alpha z}d\alpha. \quad \text{(A12)}$$

Downloaded 03 May 2010 to 171.66.16.245. Redistribution subject to ASME license or copyright; see http://www.asme.org/terms/Terms_Use.cfm

Exact Elasticity Solution for Laminated Anisotropic Cylindrical Shells

K. Bhaskar
Senior Project Officer.

T. K. Varadan
Professor.
Department of Aerospace Engineering,
Indian Institute of Technology,
Madras 600 036, India

An exact three-dimensional elasticity solution is obtained for cylindrical bending of simply-supported laminated anisotropic cylindrical shell strips subjected to transverse loading. Displacements and stresses are presented for different angle-ply layups and radius-to-thickness ratios, so as to serve as useful benchmark results for the assessment of various two-dimensional shell theories. Finally, in the light of these results, the accuracy of the Love-type classical shell theory is examined.

1 Introduction

Plate/shell structures are usually analyzed by employing approximate two-dimensional theories based on either the classical Kirchhoff-Love hypothesis of nondeformable normals, or refinements to it to include the effects of transverse shear deformation and normal stretch. However, to assess the validity of these approximate theories, rigorous analytical solutions based on the exact three-dimensional theory of elasticity should be obtained for some plate/shell problems which are amenable to such analysis. Such benchmark elasticity solutions are very valuable, especially for laminated composite structures wherein the inherent anisotropy and inhomogeneity lead to considerable warping of the normal to the middle surface of the plate or shell, and to abrupt variations of the stresses at the interfaces of the laminate.

A number of elasticity solutions have been available for laminated composite plates. The first problem to be considered was that of cylindrical bending of a simply-supported orthotropic strip under sinusoidal transverse load (Pagano, 1969). Later investigations considered the cases of finite rectangular plates (Pagano, 1970a; Pagano and Hatfield, 1972), off-axis layers (Pagano, 1970b; Noor and Burton, 1990), and localized loading (Pagano and Wang, 1971). Exact solutions for vibration and buckling (Srinivas and Rao, 1970; Kulkarni and Pagano, 1972) have also been obtained. These exact solutions have enabled us to quantify the errors involved in various laminated plate theories (Noor and Burton, 1989).

As far as laminated composite shells are concerned, analysis using theory of elasticity has been of more recent origin compared to that of plates, probably due to the greater complexity of the governing equations. Though a Frobenius' series solution for free vibrations of a laminated orthotropic cylindrical shell was available earlier (Srinivas, 1974), results for cross-ply cylindrical shells undergoing plane-strain deformation due to transverse loading, provided by Ren (1987), mark the beginning of useful benchmark solutions for laminated composite shells. Solution for the more general case of finite-length cylindrical shells under two-dimensional surface loading has been obtained recently (Ren, 1989; Varadan and Bhaskar, 1991). However, all these solutions are confined to shells with orthotropic layups. In this context, the present paper provides a benchmark solution for laminated cylindrical shells with anisotropic layers.

Specifically, the elasticity solution for a simply-supported, infinitely long, transversely loaded cylindrical shell strip with off-axis layers is obtained. This problem is the counterpart of the plate problem treated by Pagano (1970b), but the governing differential equations are more complex than those for the plate, due to the presence of variable coefficients. Results are presented for various angle-ply shells, in tabular form for future reference. Further, significant deviations from plate behavior are indicated. Finally, the accuracy of the classical lamination theory based on Love's first approximation has been studied.

2 The Problem

An infinitely long circular cylindrical shell panel made up of N orthotropic layers is considered. R_o, R_{max}, h and θ_m refer to the mean radius, maximum radius, thickness and angular span, respectively, of the shell. A cylindrical polar coordinate system r-θ-z is used, and the layers are numbered sequentially starting from the innermost layer. The material axes of any layer are not necessarily aligned with the θ and z directions, so that the shell conforms to what is generally designated as a laminated anisotropic shell. The shell is in a state of generalized plane strain with all displacements and stresses invariant in the z direction. It is subjected to a normal traction $q(\theta)$, applied on the outer surface, which can be assumed, without loss of generality, as

$$q(\theta) = q_o \sin s\theta;\ s = m\pi/\theta_m \tag{1}$$

Contributed by the Applied Mechanics Division of The American Society of Mechanical Engineers for publication in the ASME Journal of Applied Mechanics.

Discussion on this paper should be addressed to the Technical Editor, Professor Lewis T. Wheeler, Department of Mechanical Engineering, University of Houston, Houston, TX 77204-4792 and will be accepted until four months after final publication of the paper itself in the ASME Journal of Applied Mechanics.

Manuscript received by the ASME Applied Mechanics Division, May 30, 1991; final revision, Dec. 11, 1991. Associate Technical Editor: J. G. Simmonds.

Copyright © 1993 by ASME
Downloaded 03 May 2010 to 171.66.16.245. Redistribution subject to ASME license or copyright; see http://www.asme.org/terms/Terms_Use.cfm

where m is the number of half-waves in the θ direction.

The governing equations of the boundary value problem, applicable to any layer of the shell, are the equilibrium equations, the constitutive law, and the strain-displacement relations. Denoting differentiation by a subscript comma, these equations are as follows:

$$\sigma_{r,r}+\tau_{r\theta,\theta}/r+(\sigma_r-\sigma_\theta)/r=0$$
$$\tau_{r\theta,r}+\sigma_{\theta,\theta}/r+2\tau_{r\theta}/r=0 \tag{2}$$
$$\tau_{rz,r}+(\tau_{\theta z,\theta}+\tau_{rz})/r=0$$

$$\begin{Bmatrix}\sigma_r\\ \sigma_\theta\\ \sigma_z\\ \tau_{\theta z}\end{Bmatrix}=\begin{bmatrix}C_{11}&C_{12}&C_{14}\\ C_{12}&C_{22}&C_{24}\\ C_{13}&C_{23}&C_{34}\\ C_{14}&C_{24}&C_{44}\end{bmatrix}\begin{Bmatrix}\epsilon_r\\ \epsilon_\theta\\ \gamma_{\theta z}\end{Bmatrix};\ \begin{Bmatrix}\tau_{rz}\\ \tau_{r\theta}\end{Bmatrix}$$
$$=\begin{bmatrix}C_{55}&C_{56}\\ C_{56}&C_{66}\end{bmatrix}\begin{Bmatrix}\gamma_{rz}\\ \gamma_{r\theta}\end{Bmatrix} \tag{3}$$

$$\epsilon_r=u_{r,r};\ \epsilon_\theta=(u_{\theta,\theta}+u_r)/r;\ \gamma_{\theta z}=u_{z,\theta}/r$$
$$\gamma_{rz}=u_{z,r};\ \gamma_{r\theta}=(u_{r,\theta}-u_\theta)/r+u_{\theta,r}. \tag{4}$$

In the above equations, u_r, u_θ, and u_z denote the displacements along the coordinate axes and C_{ij} are the stiffness coefficients of the layer under consideration.

The boundary conditions to be satisfied are those at the longitudinal edges of the shell, as well as those on the lateral surfaces and the different interfaces of the laminate. The longitudinal edges are assumed to be freely supported and the interfaces to be slip-free, so that the boundary conditions can be written as

(i) $u_r=\sigma_\theta=\tau_{\theta z}=0$ at $\theta=0,\ \theta_m$ for all layers (5*a*)

(ii) $\sigma_r=\tau_{rz}=\tau_{r\theta}=0$ at $\bar{r}=\bar{r}_o$ (0) for the first layer; (5*b*)

$\sigma_r=q;\tau_{rz}=\tau_{r\theta}=0$ at $\bar{r}=1$ for the Nth layer.

(iii) $(u_r,u_\theta,u_z,\sigma_r,\tau_{rz},\tau_{r\theta})$ are the same for the ith and $(i+1)$th layers at $\bar{r}=\bar{r}_o(i)$, $i=1$ to $(N-1)$ (5*c*)

where $\bar{r}=r/R_{\max}$, and $\bar{r}_o(i)$ is the value of $\bar{r}$ at the outer surface of the ith layer.

3 Solution

A solution for the boundary value problem, satisfying Eq. (5*a*), is assumed as

$$u_r=R_{\max}\phi_r\sin s\theta;\ (u_\theta,\ u_z)=R_{\max}\cos s\theta\ (\phi_\theta,\phi_z) \tag{6}$$

where ϕ_r, ϕ_θ, and ϕ_z are nondimensional functions of $\bar{r}$.

Substitution of Eqs. (3), (4), and (6) into (2) yields the governing differential equations in terms of ϕ's as

$$[C_{11}(D_2+D_1/\bar{r})-(C_{22}+s^2C_{66})/\bar{r}^2]\phi_r+[-(C_{12}+C_{66})sD_1/\bar{r}+(C_{22}+C_{66})s/\bar{r}^2]\phi_\theta+[-(C_{14}+C_{56})sD_1/\bar{r}+C_{24}s/\bar{r}^2]\phi_z=0 \tag{7a}$$

$$[(C_{66}+C_{12})sD_1/\bar{r})+(C_{22}+C_{66})s/\bar{r}^2]\phi_r+[C_{66}(D_2+D_1/\bar{r})-(C_{22}s^2+C_{66})/\bar{r}^2]\phi_\theta+[C_{56}(D_2+2D_1/\bar{r})-C_{24}s^2/\bar{r}^2]\phi_z=0 \tag{7b}$$

$$[(C_{14}+C_{56})sD_1/\bar{r}+C_{24}s/\bar{r}^2]\phi_r+[C_{56}D_2-s^2C_{24}/\bar{r}^2]\phi_\theta+[C_{55}(D_2+D_1/\bar{r})-s^2C_{44}/\bar{r}^2]\phi_z=0 \tag{7c}$$

where $D_2=d^2/d\bar{r}^2$ and $D_1=d/d\bar{r}$.

Equation (7) is a set of coupled homogeneous ordinary differential equations with variable coefficients. Noting that the differential operators in these equations always occur as D_2, $D_1/\bar{r}$ or $1/\bar{r}^2$ (as in the Euler-Cauchy equation (Wylie and Barrett, 1986)), and that $\bar{r}\neq 0$ at any point in the shell domain, a change of independent variable defined by

$$\bar{r}=e^t \text{ or } t=\ln\bar{r} \tag{8}$$

is used to reduce Eq. (7) to a set of differential equations with constant coefficients. These equations are obtained by multiplying Eqs. (7) by $\bar{r}^2$ and by replacing $(\bar{r}^2D_2)$ and $(\bar{r}D_1)$ by $\bar{D}(\bar{D}-1)$ and $\bar{D}$, respectively, where $\bar{D}=d/dt$. The resulting equations can be written in a concise form as

$$[P(\bar{D})]\{\phi\}=\{0\} \tag{9}$$

where P_{ij}'s are polynomial operators in $\bar{D}$ and $\{\phi\}=[\phi_r\ \phi_\theta\ \phi_z]^T$. Assuming solutions of Eq. (9) in the form

$$\begin{Bmatrix}\phi_r\\ \phi_\theta\\ \phi_z\end{Bmatrix}=\begin{Bmatrix}k_1\\ k_2\\ k_3\end{Bmatrix}e^{\lambda t}, \tag{10}$$

the characteristic equation is given by

$$|P(\lambda)|=0, \tag{11}$$

which yields the following algebraic equation in λ:

$$-A\lambda^6+B\lambda^4+C\lambda^2+D=0 \tag{12}$$

where

$$A=C_{11}(C_{55}C_{66}-C_{56}^2)$$
$$B=s^2C_{55}(C_{11}C_{22}-C_{12}^2)+s^2C_{66}(C_{11}C_{44}-C_{14}^2)+(C_{11}+C_{22}-2s^2C_{12})(C_{55}C_{66}-C_{56}^2)-2s^2C_{56}(C_{11}C_{24}-C_{12}C_{14})$$
$$C=[s^4C_{14}+2s^2(s^2-1)C_{56}](C_{22}C_{14}-C_{12}C_{24})-s^4C_{11}(C_{22}C_{44}-C_{24}^2)+s^4(C_{12}+2C_{66})\times(C_{12}C_{44}-C_{14}C_{24})-C_{22}(s^2-1)^2(C_{55}C_{66}-C_{56}^2)+s^2C_{66}(C_{14}^2+C_{24}^2-C_{11}C_{44}-C_{22}C_{44})$$
$$D=s^2(s^2-1)^2C_{66}(C_{22}C_{44}-C_{24}^2). \tag{13}$$

Equation (12) can be transformed to a third-degree equation given by

$$\gamma^3+d\gamma+f=0 \tag{14}$$

where $\gamma=\lambda^2-B/3A$; $-3dA^2=3CA+B^2$; $-27fA^3=2B^3+9ABC+27DA^2$.

Equation (14) has three distinct real roots if

$$f^2/4+d^3/27<0. \tag{15}$$

For fiber-reinforced laminates, numerical studies by varying material properties and the parameter s show that the inequality (15) is always satisfied. (A similar situation arises during the analysis of laminated plates also (Pagano, 1970a, b). Hence, the three real roots of Eq. (14) are given by

$$\gamma_j=2(-d/3)^{1/2}\cos[\phi/3,\ (\phi+2\pi)/3,\ (\phi+4\pi)/3];\ j=1\text{ to }3 \tag{16}$$

where $\cos\phi=-f\sqrt{27}/2(-d)^{3/2}$.

Depending on the sign of $(\gamma_j+B/3A)$, $\lambda=\pm\sqrt{\gamma_j+B}/3A$ can be real or imaginary. The final solution is obtained from Eq. (10) with suitable manipulation for the case of imaginary roots (Wylie and Barrett, 1986).

The general solution for ϕ_r, ϕ_θ, ϕ_z can be written as

$$\begin{Bmatrix}\phi_r\\ \phi_\theta\\ \phi_z\end{Bmatrix}=\sum_{j=1}^{3}\begin{bmatrix}F_{rj}&S_{rj}\\ F_{\theta j}&S_{\theta j}\\ F_{zj}&S_{zj}\end{bmatrix}\begin{Bmatrix}G_j\\ H_j\end{Bmatrix} \tag{17}$$

Downloaded 03 May 2010 to 171.66.16.245. Redistribution subject to ASME license or copyright; see http://www.asme.org/terms/Terms_Use.cfm

where G_j and H_j are undetermined constants, and

$$\begin{Bmatrix} F_{rj} \\ F_{\theta j} \\ F_{zj} \end{Bmatrix} = \begin{Bmatrix} 1 \\ \bar{k}_2(m_j) \\ \bar{k}_3(m_j) \end{Bmatrix} (\bar{r})^{m_j}; \quad \begin{Bmatrix} S_{rj} \\ S_{\theta j} \\ S_{zj} \end{Bmatrix} = \begin{Bmatrix} 1 \\ \bar{k}_2(-m_j) \\ \bar{k}_3(-m_j) \end{Bmatrix} (\bar{r})^{-m_j}$$

$$\text{if } \gamma_j + B/3A > 0 \quad (18a)$$

$$\begin{Bmatrix} F_{rj} \\ F_{\theta j} \\ F_{zj} \end{Bmatrix} = R\begin{Bmatrix} 1 \\ \bar{k}_2(im_j) \\ \bar{k}_3(im_j) \end{Bmatrix} \cos(m_j \ln \bar{r}) - I\begin{Bmatrix} 0 \\ \bar{k}_2(im_j) \\ \bar{k}_3(im_j) \end{Bmatrix} \sin(m_j \ln \bar{r});$$

$$\begin{Bmatrix} S_{rj} \\ S_{\theta j} \\ S_{zj} \end{Bmatrix} = R\begin{Bmatrix} 1 \\ \bar{k}_2(im_j) \\ \bar{k}_3(im_j) \end{Bmatrix} \sin(m_j \ln \bar{r}) + I\begin{Bmatrix} 0 \\ \bar{k}_2(im_j) \\ \bar{k}_3(im_j) \end{Bmatrix} \cos(m_j \ln \bar{r})$$

$$\text{if } \gamma_j + B/3A < 0 \quad (18b)$$

In Eqs. (18), m_j stands for $|\gamma_j + B/3A|^{1/2}$, $\bar{k}_2(\ )$ and $\bar{k}_3(\ )$ are functions defined in the Appendix, and $R\{k\}$ and $I\{k\}$ denote the real and imaginary portions, respectively, of $\{k\}$. Further, t has been replaced by $\ln \bar{r}$ in all places.

Noting that Eq. (17) gives the values of ϕ's for a particular layer, the solution for a laminate having N layers is obtained in terms of $6N$ undetermined constants, viz., G_{ij}, H_{ij}, $i=1$ to N, $j=1$ to 3. The strains and stresses are then obtained in terms of G_{ij} and H_{ij} from Eqs. (4) and (3), respectively, along with (6) and (17). Finally, the $6N$ conditions of Eqs. (5*b*) and (5*c*) (written in terms of G_{ij} and H_{ij}) yield a system of $6N$ algebraic equations to determine the unknown constants.

The preceding solution fails if the layers of the shell are specially orthotropic, i.e., with their material axes coinciding with the θ, z directions, or if they exhibit isotropy or transverse isotropy with respect to the r-axis. In such cases, due to the absence of the coupling stiffnesses C_{14}, C_{24}, C_{34} and C_{56}, ϕ_z becomes coupled from ϕ_r and ϕ_z in Eqs. (7). Thus, the problem becomes the conventional plane-strain case involving only u_r and u_θ, with Eqs. (7*a*) and (7*b*) as the two governing equations. The solution for such a case can be obtained by following the same methodology as in the generalized plane-strain problem solved above. However, since this special case has already been treated earlier (Ren, 1987, wherein a stress function approach was used), and benchmark results provided for cross-ply laminates, it is not discussed here any further.

4 Classical Lamination Theory (CLT)

The governing equations for a laminated anisotropic cylindrical shell have been presented by Bert et al. (1969) using a classical shell theory based on Love's first approximation. Referring the shell to the conventional shell theory coordinates x, θ, z in the longitudinal, circumferential, and radial directions, respectively, and denoting the corresponding displacements by u, v, w, respectively, the governing equations for the generalized plane strain problem are as follows:

$$\sigma_i = Q_{ij}\epsilon_j, \ i = 1(x),\ 2(\theta),\ 6(x\theta) \quad (19)$$

$$(A_{ij}, B_{ij}, D_{ij}) = \int (1, z, z^2) Q_{ij}\, dz \quad (20)$$

$$\begin{bmatrix} L_1 & L_2 & L_3 \\ L_2 & L_4 & L_5 \\ L_3 & L_5 & L_6 \end{bmatrix} \begin{Bmatrix} u \\ v \\ w \end{Bmatrix} = \begin{Bmatrix} 0 \\ 0 \\ \bar{q} \end{Bmatrix} \quad (21)$$

where

$$L_1 = A_{66}d_y^2$$

$$L_2 = (A_{26} + B_{26}/R_o)d_y^2$$

$$L_3 = A_{26}d_y/R_o - B_{26}d_y^3$$

$$L_4 = (A_{22} + 2B_{22}/R_o + D_{22}/R_o^2)d_y^2$$

$$L_5 = (A_{22} + B_{22}/R_o)d_y/R_o - (B_{22} + D_{22}/R_o)d_y^3$$

$$L_6 = A_{22}/R_o^2 - 2B_{22}d_y^2/R_o + D_{22}d_y^4 \quad (22)$$

and d_y, d_y^2, etc., refer to $d/(R_o d\theta)$, $d^2/(R_o d\theta)^2$, etc., respectively. $\bar{q}$ is the load per unit area of the middle surface of the shell and, for the case of external traction considered here (Eq. (1)),

$$\bar{q} = q_o(1 + h/2R_o)\sin s\theta. \quad (23)$$

For the problem of the simply-supported panel, a Navier-type solution is possible wherein Eq. (21) reduces to a system of algebraic equations to yield u, v, and w. The strains and the in-plane stresses are then obtained using the kinematic relations and the constitutive law.

5 Numerical Results and Discussion

Results are presented for various angle-ply shells as specified here:

(i) a single layered shell with the fibers inclined at an angle α to the longitudinal axis, α being positive clockwise,
(ii) a coupled $(\alpha/-\alpha)$ shell (α for the outer layer and $-\alpha$ for the inner layer),
(iii) a three-layered $(\alpha/-\alpha/\alpha)$ shell, and
(iv) a ten-layered $(\alpha/-\alpha/\alpha/-\alpha/\alpha)_s$ shell.

In these problems, all the layers are of equal thickness and are assumed to be made of square symmetric unidirectional fibrous composite material with the following properties:

$$E_L/E_T = 25;\ G_{LT}/E_T = 0.5;\ G_{TT}/E_T = 0.2;\ \nu_{LT} = \nu_{TT} = 0.25$$

where L is the direction parallel to the fibers and T is the transverse direction. Various values of α ranging from 15 deg to 75 deg have been considered. Geometric and loading parameters are assumed as

$$\theta_m = 1 \text{ radian};\ m = 1.$$

Results are presented in terms of the following normalized maximum displacements/stresses. The notation corresponds to that used with CLT.

$$\bar{w} = 100E_T w/q_o h S^4;\ (\bar{u}, \bar{v}) = (100E_T/q_o h S^3)(u, v);$$

$$(\bar{\sigma}_x, \bar{\sigma}_\theta, \bar{\tau}_{x\theta}) = (\sigma_x, \sigma_\theta, \tau_{x\theta})/q_o S^2$$

$$(\bar{\tau}_{xz}, \bar{\tau}_{\theta z}) = (\tau_{xz}, \tau_{\theta z})/q_o S;\ \bar{\sigma}_z = \sigma_z/q_o;\ S = R_o/h$$

For convenience, a nondimensional transverse coordinate ξ $(= z/h)$, varying from -0.5 at the inner diameter to 0.5 at the outer diameter, is defined.

Results based on exact elasticity are presented in Tables 1–6 and Fig. 1. The nondimensional radial deflection and the six stresses, at ξ locations where they are high, are presented in Tables 1–4 for all the laminates considered here, for values of R_o/h ranging from 4 to 100. Through-the-thickness variation of $\bar{u}$, $\bar{v}$ and the six stresses are presented in Tables 5 and 6 for the two and three-layer shells, respectively, for α = 45 deg and R_o/h = 4, 10. These results are presented in tabular form to facilitate quantitative assessment of the accuracy of different shell theories.

Figure 1 presents the typical thickness-wise variation of the transverse normal stress. It shows that σ_z can reach very high values within the thickness of the shell, especially for thin shells. Such a variation (reported earlier for orthotropic shells (Varadan and Bhaskar, 1991)) is markedly different from that in a laminated plate wherein the maximum value always occurs

Downloaded 03 May 2010 to 171.66.16.245. Redistribution subject to ASME license or copyright; see http://www.asme.org/terms/Terms_Use.cfm

Table 1 Deflections and stresses for α shell—case 1

S	α	$\bar{w}$ (ξ=0)	$\bar{\sigma}_\theta$ (ξ=-1/2)	$\bar{\sigma}_x$ (ξ=-1/2)	$\bar{\tau}_{x\theta}$ (ξ=-1/2)	$\bar{\tau}_{xz}$ (ξ=0)	$\bar{\tau}_{\theta z}$ (ξ=0)	$\bar{\sigma}_z$ (ξ=0)
4	15°	19.48	-0.9019	-1.302	-0.3388	0.2250	0.5851	- 0.1309
	30°	10.90	-0.9452	-1.505	-0.8248	0.4941	0.5776	- 0.1233
	45°	5.808	-1.037	-0.8313	-0.7784	0.4134	0.5628	- 0.1080
	60°	3.759	-1.131	-0.3504	-0.5535	0.2644	0.5490	- 0.0932
	75°	2.932	-1.200	-0.0934	-0.2845	0.1266	0.5400	- 0.0829
10	15°	14.71	-0.7524	-1.120	-0.2953	0.2207	0.5559	- 1.225
	30°	6.849	-0.7598	-1.324	-0.7469	0.5481	0.5545	- 1.221
	45°	2.788	-0.7754	-0.6539	-0.6328	0.4532	0.5516	- 1.212
	60°	1.505	-0.7913	-0.2502	-0.4096	0.2863	0.5487	- 1.202
	75°	1.070	-0.8031	-0.0628	-0.1989	0.1365	0.5466	- 1.196
100	15°	13.51	-0.6868	-1.036	-0.2744	0.2147	0.5367	-16.58
	30°	5.918	-0.6850	-1.229	-0.6994	0.5471	0.5352	-16.53
	45°	2.154	-0.6841	-0.5878	-0.5753	0.4499	0.5343	-16.50
	60°	1.052	-0.6839	-0.2182	-0.3623	0.2832	0.5341	-16.50
	75°	0.701	-0.6839	-0.0536	-0.1727	0.1350	0.5339	-16.49

Table 2 Deflections and stresses for ($\alpha l - \alpha$) shell—case 2

S	α	$\bar{w}$ (ξ=0)	$\bar{\sigma}_\theta$ (ξ=-1/2)	$\bar{\sigma}_x$ (ξ=-1/2)	$\bar{\tau}_{x\theta}$ (ξ=-1/2)	$\bar{\tau}_{xz}$ (ξ=-1/4)	$\bar{\tau}_{\theta z}$ (ξ=-1/4)	$\bar{\sigma}_z$ (ξ=-1/4)
4	15°	20.67	-0.9254	-0.9875	0.2196	-0.0861	0.5095	- 0.4206
	30°	14.77	-1.120	-1.547	0.8027	-0.3001	0.5407	- 0.4332
	45°	8.701	-1.363	-1.039	0.9395	-0.3339	0.5683	- 0.4402
	60°	5.430	-1.484	-0.4484	0.6760	-0.2266	0.5704	- 0.4344
	75°	3.686	-1.425	-0.1093	0.2944	-0.0896	0.5432	- 0.4157
10	15°	15.77	-0.7714	-0.7754	0.1655	-0.0653	0.4434	- 1.228
	30°	11.06	-0.9326	-1.279	0.6620	-0.2597	0.4744	- 1.304
	45°	5.958	-1.127	-0.8653	0.7858	-0.3060	0.5103	- 1.391
	60°	3.293	-1.192	-0.3604	0.5440	-0.2097	0.5200	- 1.414
	75°	1.879	-1.072	-0.0820	0.2133	-0.0805	0.4941	- 1.350
100	15°	14.52	-0.7042	-0.6987	0.1477	-0.0581	0.4080	-12.83
	30°	10.12	-0.8482	-1.160	0.5995	-0.2356	0.4359	-13.70
	45°	5.309	-1.020	-0.7833	0.7115	-0.2797	0.4691	-14.73
	60°	2.821	-1.069	-0.3232	0.4876	-0.1916	0.4785	-15.02
	75°	1.502	-0.9458	-0.0722	0.1858	-0.0730	0.4541	-14.26

on the loaded surface. This phenomenon—of the occurrence of high σ_z due to curvature of the shell—is very significant since a lack of appreciation of this fact can lead to catastrophic delamination failures (Edward et al., 1989).

The variations of the in-surface displacements and stresses, and the transverse shear stresses, are similar to those occurring in laminated plates, and hence are not shown here.

Finally, selected results of CLT are presented in Figs. 2 and 3. Only w and σ_θ are plotted here, since the accuracy of the other two in-surface stresses is not significantly different from that of σ_θ. These figures show that CLT is more accurate for the prediction of stresses than that of the transverse deflection at any value of R_o/h, and that all results uniformly converge to the exact solution as R_o/h increases. From the results of the various cases considered during the present investigation, it has been found that CLT predicts w with less than 12 percent error for $R_o/h \geq 20$, while for stresses the error is less than 12 percent for $R_o/h \geq 10$.

6 Conclusion

A standard elasticity solution for angle-ply cylindrical shells has been presented. The problem considers cylindrical bending due to transverse sinusoidal loading. Results for various radius-to-thickness ratios and stacking sequences have been presented to serve as a benchmark, against which laminated shell theories can be assessed. Finally, the range of applicability of Love's classical shell theory has been studied for the prediction of deflections and the in-surface stresses in a laminated shell.

Downloaded 03 May 2010 to 171.66.16.245. Redistribution subject to ASME license or copyright; see http://www.asme.org/terms/Terms_Use.cfm

Table 3 Deflections and stresses for $(\alpha/-\alpha/\alpha)$ shell—case 3

S	α	$\bar{w}$ (ξ=0)	$\bar{\sigma}_\theta$ (ξ=-1/2)	$\bar{\sigma}_x$ (ξ=-1/2)	$\bar{\tau}_{x\theta}$ (ξ=-1/2)	$\bar{\tau}_{xz}$ (ξ=-1/6)	$\bar{\tau}_{\theta z}$ (ξ=-1/6)	$\bar{\sigma}_z$ (ξ=-1/6)
4	15°	19.99	-0.9086	-1.216	-0.3063	0.1761	0.5644	- 0.3665
	30°	12.58	-0.9929	-1.533	-0.8308	0.3952	0.5289	- 0.3222
	45°	7.319	-1.159	-0.9232	-0.8609	0.3216	0.4806	- 0.2561
	60°	4.631	-1.274	-0.3941	-0.6204	0.2101	0.4666	- 0.2317
	75°	3.209	-1.266	-0.0984	-0.2964	0.1106	0.4997	- 0.2718
10	15°	14.80	-0.7529	-1.103	-0.2888	0.1948	0.5104	- 1.332
	30°	7.196	-0.7653	-1.323	-0.7448	0.4852	0.5013	- 1.304
	45°	3.117	-0.7949	-0.6692	-0.6469	0.3983	0.4902	- 1.268
	60°	1.690	-0.8153	-0.2578	-0.4219	0.2528	0.4876	- 1.259
	75°	1.123	-0.8115	-0.0635	-0.2007	0.1230	0.4959	- 1.284
100	15°	13.51	-0.6867	-1.036	-0.2742	0.1913	0.4786	-14.97
	30°	5.922	-0.6847	-1.229	-0.6994	0.4875	0.4768	-14.92
	45°	2.157	-0.6837	-0.5877	-0.5755	0.4009	0.4758	-14.88
	60°	1.054	-0.6836	-0.2181	-0.3624	0.2524	0.4755	-14.87
	75°	0.702	-0.6835	-0.0536	-0.1728	0.1204	0.4756	-14.88

Table 4 Deflections and stresses for the ten-layered shell—case 4

S	α	$\bar{w}$ (ξ=0)	$\bar{\sigma}_\theta$ (ξ=-1/2)	$\bar{\sigma}_x$ (ξ=-1/2)	$\bar{\tau}_{x\theta}$ (ξ=-1/2)	$\bar{\tau}_{xz}$ (ξ=-0.4)	$\bar{\tau}_{\theta z}$ (ξ=0)	$\bar{\sigma}_z$ (ξ=-0.1)
4	15°	19.74	-0.9018	-1.316	-0.3439	0.1029	0.5853	- 0.2940
	30°	11.03	-0.9097	-1.556	-0.8730	0.2520	0.5840	- 0.2885
	45°	6.092	-0.9763	-0.8180	-0.7884	0.2110	0.5761	- 0.2691
	60°	4.033	-1.080	-0.3407	-0.5553	0.1400	0.5619	- 0.2489
	75°	3.029	-1.171	-0.0915	-0.2870	0.0719	0.5458	- 0.2372
10	15°	14.75	-0.7522	-1.128	-0.2980	0.0868	0.5559	- 1.342
	30°	6.843	-0.7517	-1.337	-0.7588	0.2197	0.5558	- 1.341
	45°	2.814	-0.7604	-0.6503	-0.6348	0.1815	0.5544	- 1.334
	60°	1.541	-0.7792	-0.2481	-0.4107	0.1160	0.5511	- 1.324
	75°	1.083	-0.7976	-0.0625	-0.2005	0.0565	0.5476	- 1.317
100	15°	13.51	-0.6868	-1.037	-0.2746	0.0779	0.5367	-16.08
	30°	5.918	-0.6848	-1.230	-0.7001	0.1986	0.5352	-16.03
	45°	2.154	-0.6838	-0.5880	-0.5758	0.1633	0.5344	-16.01
	60°	1.053	-0.6836	-0.2182	-0.3626	0.1028	0.5341	-16.00
	75°	0.701	-0.6837	-0.0536	-0.1729	0.0490	0.5340	-16.00

Table 5 Distribution of stresses and displacements through thickness of (45 deg/ – 45 deg) shell

S	ξ	$\bar{u}$	$\bar{v}$	$\bar{\sigma}_\theta$	$\bar{\sigma}_x$	$\bar{\tau}_{x\theta}$	$\bar{\tau}_{xz}$	$\bar{\tau}_{\theta z}$	$\bar{\sigma}_z$
4	-1/2	4.37	19.99	-1.36	-1.04	0.94	0	0	0
	-1/4	3.95	15.18	-0.19	-0.06	-0.02	-0.33	0.57	-0.44
	0	3.89	11.17	0.72 -0.75	0.72 -0.75	-0.77 -0.80	-0.02	0.31	0.22
	1/4	3.78	7.12	0.17	0.05	-0.01	0.26	0.46	0.29
	1/2	4.06	2.28	1.09	0.84	0.75	0	0	1.00
10	-1/2	3.73	26.84	-1.13	-0.87	0.79	0	0	0
	-1/4	3.67	22.84	-0.18	-0.06	-0.005	-0.31	0.51	-1.39
	0	3.67	18.95	0.69 -0.69	0.69 -0.69	-0.74 -0.73	-0.007	0.29	-0.36
	1/4	3.66	15.06	0.17	0.06	≃0	0.27	0.46	-0.63
	1/2	3.71	11.05	1.01	0.78	0.71	0	0	1.00

Downloaded 03 May 2010 to 171.66.16.245. Redistribution subject to ASME license or copyright; see http://www.asme.org/terms/Terms_Use.cfm

Table 6 Distribution of stresses and displacements through thickness of (45 deg/ – 45 deg/45 deg) shell

S	ξ	$\bar{u}$	$\bar{v}$	$\bar{\sigma}_\theta$	$\bar{\sigma}_x$	$\bar{\tau}_{x\theta}$	$\bar{\tau}_{xz}$	$\bar{\tau}_{\theta z}$	$\bar{\sigma}_z$
4	-1/2	-2.42	15.84	-1.16	-0.92	-0.86	0	0	0
	-1/3	-2.14	12.86	-0.43	-0.31	-0.26	0.30	0.42	-0.41
	-1/6	-1.69	10.50	0.05 -0.61	0.09 -0.57	0.12 0.58	0.32	0.48	-0.26
	0	-0.02	9.40	-0.02	-0.02	0.02	0.16	0.60	-0.15
	1/6	1.51	8.25	0.51 -0.04	0.48 -0.07	-0.48 -0.10	0.27	0.43	0.27
	1/3	1.84	5.95	0.39	0.29	0.25	0.22	0.32	0.56
	1/2	2.02	3.09	0.92	0.75	0.69	0	0	1.00
10	-1/2	-0.52	13.71	-0.79	-0.67	-0.65	0	0	0
	-1/3	-0.48	12.31	-0.46	-0.39	-0.37	0.27	0.33	-0.98
	-1/6	-0.38	10.99	-0.17 -0.32	-0.14 -0.29	-0.13 0.28	0.40	0.49	-1.27
	0	-0.04	9.92	-0.01	-0.01	0.009	0.32	0.56	-1.24
	1/6	0.28	8.85	0.29 0.18	0.25 0.15	-0.25 0.14	0.37	0.47	-0.72
	1/3	0.37	7.54	0.44	0.37	0.36	0.24	0.30	-0.008
	1/2	0.40	6.15	0.73	0.62	0.60	0	0	1.00

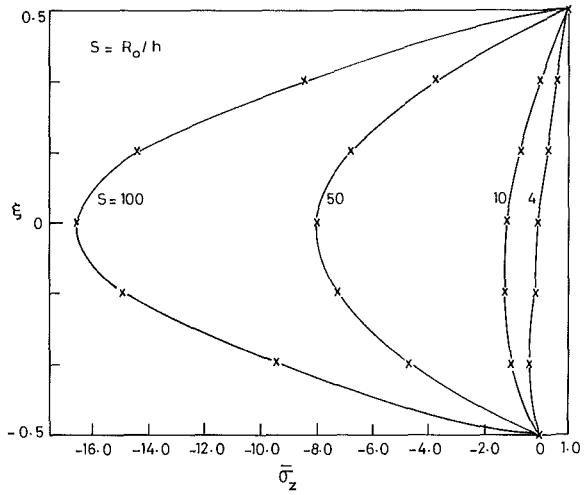


Fig. 1 σ_z in (60 deg/ – 60 deg/60 deg) shell

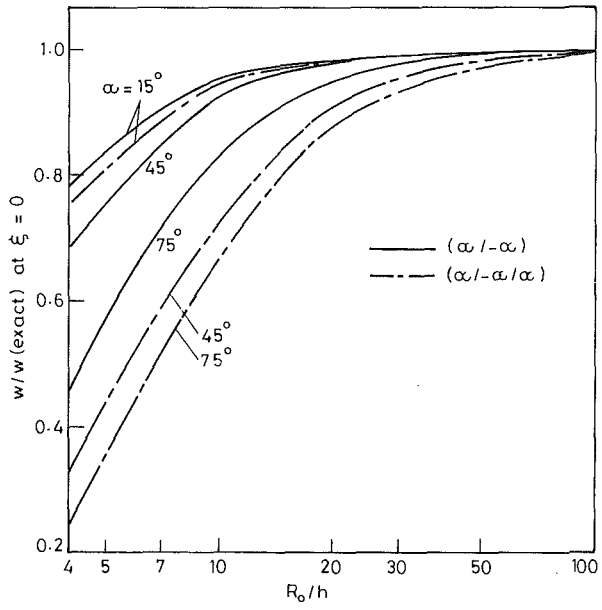


Fig. 2 CLT results—transverse deflection

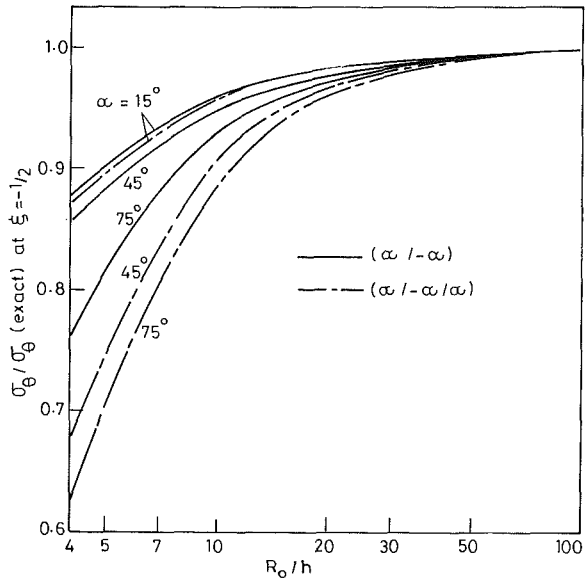


Fig. 3 CLT results—circumferential stress

References

Bert, C. W., Baker, J. L., and Egle, D. M., 1969, "Free Vibrations of Multilayer Anisotropic Cylindrical Shells," *Journal of Composite Materials*, Vol. 3, pp. 480–499.

Edward, K. T., Wilson, R. S., and McLean, S. K., 1989, "Flexure of Simply Curved Composite Shapes," *Composites*, Vol. 20, pp. 527–536.

Kulkarni, S. V., and Pagano, N. J., 1972, "Dynamic Characteristics of Composite Laminates," *Journal of Sound and Vibration*, Vol. 23, pp. 127–143.

Noor, A. K., and Burton, W. S., 1989, "Assessment of Shear Deformation Theories for Multilayered Composite Plates," ASME *Applied Mechanics Reviews*, Vol. 42, pp. 1–13.

Noor, A. K., and Burton, W. S., 1990, "Three-Dimensional Solutions for Antisymmetrically Laminated Anisotropic Plates," ASME JOURNAL OF APPLIED MECHANICS, Vol. 57, pp. 182–188.

Pagano, N. J., 1969, "Exact Solutions for Composite Laminates in Cylindrical Bending," *Journal of Composite Materials*, Vol. 3, pp. 398–411.

Pagano, N. J., 1970a, "Exact Solutions for Rectangular Bidirectional Composites and Sandwich Plates," *Journal of Composite Materials*, Vol. 4, pp. 20–34.

Pagano, N. J., 1970b, "Influence of Shear Coupling in Cylindrical Bending of Anisotropic Laminates," *Journal of Composite Materials*, Vol. 4, pp. 330–343.

Downloaded 03 May 2010 to 171.66.16.245. Redistribution subject to ASME license or copyright; see http://www.asme.org/terms/Terms_Use.cfm

Pagano, N. J., and Wang, A. S. D., 1971, "Further Study of Composite Laminates Under Cylindrical Bending," *Journal of Composite Materials*, Vol. 5, pp. 521–528.

Pagano, N. J., and Hatfield, S. J., 1972, "Elastic Behavior of Multilayered Bidirectional Composites," *AIAA Journal*, Vol. 10, pp. 931–933.

Ren, J. G., 1987, "Exact Solutions for Laminated Cylindrical Shells in Cylindrical Bending," *Composites Science and Technology*, Vol. 29, pp. 169–187.

Ren, J. G., 1989, "Analysis of Simply-Supported Laminated Circular Cylindrical Shell Roofs," *Composite Structures*, Vol. 11, pp. 277–292.

Srinivas, S., and Rao, A. K., 1970, "Bending, Vibration and Buckling of Simply Supported Thick Orthotropic Rectangular Plates and Laminates," *International Journal of Solids and Structures*, Vol. 6, pp. 1463–1481.

Srinivas, S., 1974, "Analysis of Laminated, Composite, Circular Cylindrical Shells With General Boundary Conditions," NASA Technical Report R-412, Washington, D.C.

Varadan, T. K., and Bhaskar, K., 1991, "Bending of Laminated Orthotropic Cylindrical Shells—An Elasticity Approach," *Composite Structures*, Vol. 17, pp. 141–156.

Wylie, C. R., and Barrett, L. C., 1986, *Advanced Engineering Mathematics*, McGraw-Hill, Singapore, pp. 109–112; 232–240.

APPENDIX

The functions $\bar{k}_2(x)$ and $\bar{k}_3(x)$ appearing in Eqs. (18) are given by

$$\bar{k}_2(x) = \bar{A}(x)/\bar{J}(x);\ \bar{k}_3(x) = \bar{B}(x)/\bar{J}(x)$$

where $\bar{A}$, $\bar{B}$, and $\bar{J}$ are functions of x defined as follows:

$$\begin{aligned}\bar{A}(x) = &-C_{11}C_{56}(x^4+x^3)+[C_{11}C_{24}s^2\\ &+C_{56}(C_{22}+s^2C_{66})-s^2(C_{14}+C_{56})(C_{66}+C_{12})]x^2\\ &+[C_{56}(C_{22}+s^2C_{66})+s^2C_{24}(C_{66}+C_{12})\\ &-s^2(C_{22}+C_{66})(C_{14}+C_{56})]x\\ &+C_{24}C_{66}s^2(1-s^2).\end{aligned}$$

$$\begin{aligned}\bar{B}(x) = &\,C_{11}C_{66}x^4+[s^2(C_{12}+C_{66})^2\\ &-C_{11}(s^2C_{22}+C_{66})-C_{66}(C_{22}+s^2C_{66})]x^2\\ &+C_{22}C_{66}(s^2-1)^2.\end{aligned}$$

$$\begin{aligned}\bar{J}(x) = &\,s(C_{14}C_{66}-C_{12}C_{56})x^3+s(C_{22}C_{56}-C_{12}C_{56}-C_{24}C_{66})x^2\\ &+[s^3C_{24}(C_{12}+C_{66})+sC_{56}(C_{22}+C_{66})\\ &-s(C_{14}+C_{56})(s^2C_{22}+C_{66})]x\\ &+C_{24}C_{66}s(1-s^2).\end{aligned}$$

Downloaded 03 May 2010 to 171.66.16.245. Redistribution subject to ASME license or copyright; see http://www.asme.org/terms/Terms_Use.cfm

A Continuum Theory of a Lubrication Problem With Solid Particles

Fuling Dai[1]
Assoc. Mem.

M. M. Khonsari
William Whiteford Faculty Fellow,
Mem. ASME.

Department of Mechanical Engineering,
University of Pittsburgh,
Pittsburgh, PA 15261

The governing equations for a two-dimensional lubrication problem involving the mixture of a Newtonian fluid with solid particles at an arbitrary volume fraction are developed using the theory of interacting continuua (mixture theory). The equations take the interaction between the fluid and the particles into consideration. Provision is made for the possibility of particle slippage at the boundaries. The equations are simplified assuming that the solid volume fraction varies in the sliding direction alone. Equations are solved for the velocity of the fluid phase and that of the solid phase of the mixture flow in the clearance space of an arbitrary shaped bearing. It is shown that the classical pure fluid case can be recovered as a special case of the solutions presented. Extensive numerical solutions are presented to quantify the effect of particulate solid for a number of pertinent performance parameters for both slider and journal bearings. Included in the results are discussions on the influence of particle slippage on the boundaries as well as the role of the interacting body force between the fluid and solid particles.

1 Introduction

This paper is a report of a long-term research project devoted to the understanding of the lubrication characteristics of a mixture of particulate solids embedded in a carrier fluid. Some recent contributions in this field are reported by Khonsari et al. (1988, 1989, 1990). The purpose of such multiphase flow is the development of alternative lubricants for applications under severe operating conditions where conventional liquid lubricants may not be functional. An example of such an application is the stringent requirement for lubrication of mechanical components, such as bearings, in a high-temperature environment. It has been suggested that effective lubrication may be provided by injecting a stream of closely packed particles (e.g., powder) into the surfaces to be lubricated. For such an application, a conventional lubricating oil may be used as a carrier fluid. To predict the behavior of the mixture, we assume that the particulate matter can be modeled as the granular material and that the lubricating oil has the characteristics of a Newtonian fluid. The objective of the present work is to develop the equations governing the behavior of the mixture flow within the context of the lubrication theory and present numerical results.

The prediction of the behavior of the mixture of granular material and fluid is indeed a complex problem. Over the past two decades, a number of publications have appeared that have dealt with the simple shear flow or gravity flow of granular materials as single constituents (cf. Savage's review article, 1984). To the authors' knowledge and within the open literature, not much work, however, has been reported in this area particularly as applied to lubrication problems. A recent theoretical model was developed for the mixture of a granular material in conventional lubricating oil (Dai and Khonsari, 1991). Using the principles of continuum mechanics, perturbation solutions were obtained for the mixture flows of particulate solids embedded in a linearly viscous (Newtonian) fluid. The mixture was assumed to be dragged into the clearance space of an infinitely wide slider bearing. The problem and the solutions were restricted to small solid volume fractions, defined as the ratio of the volume of the solid phase to that of the mixture. The mixture problem, as such, falls into the category of dilute dispersion problems or what Bagnold (1954) classified as the "macroviscous regime," where the fluid viscosity plays a major role.

In the present work, we concentrate on situations in which the solid volume fraction is comparable to that of the fluid. The mechanical interaction of particles and fluid as well as the possibility of particle slippage at moving and stationary boundaries are taken into consideration. Both of these effects were assumed to be absent in the previous study of Dai and Khonsari (1991).

The plan of this paper is as follows. In Section 2 the constitutive equations for the fluid phase, the solid phase, and the mixture are introduced. In Section 3, the governing equations for the mixture within the context of hydrodynamic lubrication

[1]Currently at the Department of Mechanical Engineering, University of California at Berkeley, Berkeley, CA 94720.

Contributed by the Applied Mechanics Division of THE AMERICAN SOCIETY OF MECHANICAL ENGINEERS for publication in the ASME JOURNAL OF APPLIED MECHANICS.

Discussion on this paper should be addressed to the Technical Editor, Professor Lewis T. Wheeler, Department of Mechanical Engineering, University of Houston, Houston, TX 77204-4792, and will be accepted until four months after final publication of the paper itself in the ASME JOURNAL OF APPLIED MECHANICS.

Manuscript received by the ASME Applied Mechanics Division, July 5, 1991; final revision, Jan. 26, 1992. Associate Technical Editor: S. A. Berger.

Copyright © 1993 by ASME
Downloaded 03 May 2010 to 171.66.16.245. Redistribution subject to ASME license or copyright; see http://www.asme.org/terms/Terms_Use.cfm

are presented. In Section 4, equations are solved for the velocity profile of each phase. Also presented in this section are the formulation of some of the performance parameters, such as the friction coefficient and mass flow rates, for a mixture flow in a bearing with an arbitrary shaped film thickness. Several interesting special cases are shown in Section 5. Numerical simulation procedures and applications of the theory to slider and journal bearings are given in the last section.

2 Constitutive Equations and Momentum Equations

2.1 Constitutive Equations. Consider a mixture consisting of a linearly viscous (Newtonian) fluid with an ensemble of granular particles. We shall assume that the individual granules (as opposed to the bulk) are incompressible. Also, we assume that the fluid and the solid phases are continuous, from the continuum mechanics point of view, so that the properties of the mixture may be represented by continuous functions of position. The continuum scale is clearly one which is sufficiently large to contain many elements of both the fluid and solid phases, but remains small in comparison with the length scale of the problem. To quantitatively describe the mass distribution of the particles in the mixture, a continuous function of position, $\nu(\mathbf{x})$ $(0 \le \nu \le 1)$, is introduced as an independent kinematic parameter. This parameter will be referred to as the solid volume fraction and is defined as the ratio of the volume occupied by the particles to the space volume of the mixture at a point in the mixed region, where "a point" should be considered as "a point and its neighborhood." Therefore, specification of ν at a point conceptually implies an average of the solid volume fraction in the neighborhood of that point. Similarly, all other physical quantities associated with the point are averaged in some sense over the neighborhood whose center is at the specified position (cf. Cowin, 1974).

We now turn our attention to the constitutive equations of each phase. Although the liquid lubricant, modeled as a Newtonian fluid, can be assumed incompressible at the pure stage, the mixture may indeed be "compressible" in the sense that the density of the mixture at a given point is dependent upon the volume of the solid particles content. To account for this "compressibility," the constitutive equation for the Newtonian fluid is modified as shown below (cf. Dai and Khonsari, 1991):

$$\pi = -p(\nu)\mathbf{I} + \lambda_f(\nu)(\mathrm{tr}\mathbf{D}_f)\mathbf{I} + 2\mu_f(\nu)\mathbf{D}_f, \quad \text{(no sum on } f\text{)} \tag{1}$$

where $\mathbf{I}$ is the identity tensor, p is the pressure of the fluid phase, λ_f and μ_f are material functions of the fluid phase, and $\mathbf{D}_f$ is the rate of deformation tensor of the fluid phase.

The constitutive equation for the solid phase is based on that of granular materials given by Cowin (1974) and Savage (1979):

$$\sigma = [\beta_0(\nu) + \beta_1(\nu)\mathrm{grad}\ \nu \cdot \mathrm{grad}\ \nu + \beta_2(\nu)\mathrm{tr}\mathbf{D}_s]\mathbf{I} + 2\mu_s(\nu)\mathbf{D}_s + \beta_3(\nu)\mathrm{grad}\ \nu \otimes \mathrm{grad}\ \nu, \quad \text{(no sum on } s\text{)} \tag{2}$$

where β_0 through β_3 and μ_s are material functions and $\mathbf{D}_s$ is the rate-of-deformation tensor of the solid phase. All of the above material functions in Eqs. (1) and (2) are assumed to depend on the solid volume fraction ν.

According to the theory of mixture, the total stress in the mixture $\mathbf{T}$ is the summation of the two partial stresses given by Eqs. (1) and (2)

$$\mathbf{T} = [-p(\nu) + \beta_0(\nu) + \beta_1(\nu)\mathrm{grad}\ \nu \cdot \mathrm{grad}\ \nu + \lambda_f(\nu)\mathrm{tr}\mathbf{D}_f + \beta_2(\nu)\mathrm{tr}\mathbf{D}_s]\mathbf{I} + 2[\mu_f(\nu)\mathbf{D}_f + \mu_s(\nu)\mathbf{D}_s] + \beta_3(\nu)\mathrm{grad}\ \nu \otimes \mathrm{grad}\ \nu. \tag{3}$$

2.2 Restrictions on Material Functions. Two limiting cases of the mixture may be deduced from Eq. (3) for pure fluid ($\nu = 0$) and total solid theoretically made up of granular particles with zero void ($\nu = 1$). When $\nu = 0$, Eq. (3) reduces to the familiar form of that of the incompressible, Newtonian fluid: $\mathbf{T} = -p_p\mathbf{I} + 2\mu\mathbf{D}_f$. The following restrictions required in this case are

$$p(0) = p_p, \quad \mu_f(0) = \mu, \quad \lambda_f(0) = 0, \quad \text{and} \quad \mu_s(0) = \beta_0(0) = \beta_2(0) = 0, \tag{4}$$

where p_p is the hydrodynamic pressure and μ is viscosity of the pure fluid, respectively. Theoretically, when $\nu = 1$, Eq. (3) should reduce to that for granular material flows. There the following restrictions are required:

$$p(1) = \lambda_f(1) = \mu_f(1) = 0. \tag{5}$$

2.3 Balance of Linear Momentum. In the absence of external body forces, the conservation of linear momentum equation for each phase is

$$\mathrm{div}\ \pi + \mathbf{b} = \rho_f \mathbf{a}_f, \tag{6}$$

and

$$\mathrm{div}\ \sigma - \mathbf{b} = \rho_s \mathbf{a}_s, \tag{7}$$

where $\mathbf{a}_f$ and $\mathbf{a}_s$ are the acceleration vectors of the solid and fluid phases, respectively. The parameter $\mathbf{b}$ is the interacting body force vector. It represents the mechanical interaction between the fluid and solid phases as a result of effects of density gradients, drag, and virtual mass. Denoting the velocity vector of the fluid phase by $\mathbf{u}$ and that of the solid phase by $\mathbf{w}$, the general form of this interaction may be written as follows (cf. Homsy et al., 1980):

$$\mathbf{b} = \alpha_1(\nu)\ \mathrm{grad}\ \rho_f + \alpha_2(\nu)\ \mathrm{grad}\ \rho_s + \alpha_3(\nu)(\mathbf{w} - \mathbf{u}) + \alpha_4(\nu) \times \left[\frac{\partial}{\partial t}(\mathbf{w} - \mathbf{u}) + \mathrm{grad}(\mathbf{w} - \mathbf{u}) \cdot (\mathbf{w} - \mathbf{u})\right], \tag{8}$$

where ρ_f and ρ_s are the densities of the fluid phase and solid phase, respectively, in the mixed state, and α_1 through α_4 are assumed to be functions of the solid volume fraction ν. The first two terms of the above equation are the forces due to density gradients, the third term represents the drag force, and the last term reflects the virtual mass effects. These terms are frame indifferent.

3 Governing Equations for Lubrication Problems

Consider a two-dimensional, steady-state lubrication problem corresponding to an infinitely long bearing with an arbitrary film thickness. We can write:

$$u_x = u_x(x,y), \quad u_y = u_y(x,y), \quad u_z = 0,$$

$$w_x = w_x(x,y), \quad w_y = w_y(x,y), \quad w_z = 0.$$

The general governing equations presented in Section 2 can be significantly reduced by using an order-of-magnitude analysis by using the following scales for variables and material functions (cf. Dai and Khonsari, 1991):

$$x \sim L, \quad y \sim h_0, \quad w_x, u_x \sim U, \quad w_y, u_y \sim \frac{Uh_0}{L},$$

$$\lambda_f, \mu_f, u_s, \beta_2 \sim \mu, \quad \beta_1, \beta_3 \sim LU\mu, \quad \beta_0 \sim \frac{U\mu}{L}, \quad p \sim \frac{U\mu}{L}\left(\frac{L}{h_0}\right)^2,$$

where L is the characteristic bearing length in the sliding direction, h_0 is the film thickness at the inlet, and U is the velocity of the sliding surface.

The coefficients α_1 through α_4 appearing in the interacting body force can also be scaled. We assume that the drag force exerted between the fluid and particles is much greater than that of the forces due to the density gradient and the virtual mass. This assumption is motivated by the work of Saffman (1962) on dusty gas in which a similar expression for the drag force was introduced in the momentum equation of the fluid as the dominant interacting body force between the two constituents. Considering the appropriate dimensions, we use the following scales for α_1 through α_4:

Downloaded 03 May 2010 to 171.66.16.245. Redistribution subject to ASME license or copyright; see http://www.asme.org/terms/Terms_Use.cfm

$$\alpha_1,\alpha_2 \sim \frac{U\mu}{L\rho_{s0}}\left(\frac{L}{h_0}\right), \quad \alpha_3 \sim \frac{\mu}{L^2}\left(\frac{L}{h_0}\right)^2, \quad \alpha_4 \sim \frac{\mu}{LU}\left(\frac{L}{h_0}\right),$$

where the scales of order L/h_0 have been chosen for α_1, α_2, and α_4, and the larger scale of order $(L/h_0)^2$ has been incorporated for the drag force term function α_3.

Using the above scales, the momentum Eqs. (6) and (7) reduce to the equations shown below for the fluid phase:

$$\frac{\partial p}{\partial y}=0, \tag{9}$$

$$\frac{\partial p}{\partial x}=\frac{\partial}{\partial y}\left[\mu_f(\nu)\frac{\partial u_x}{\partial y}\right]+\alpha_3(\nu)(w_x-u_x), \tag{10}$$

and for the solid phase:

$$\frac{\partial}{\partial x}\left[\beta_1(\nu)\left(\frac{\partial \nu}{\partial y}\right)^2\right]+\frac{\partial}{\partial y}\left[\mu_s(\nu)\frac{\partial w_x}{\partial y}+\beta_3(\nu)\frac{\partial \nu}{\partial x}\frac{\partial \nu}{\partial y}\right] - \alpha_3(\nu)(w_x-u_x)=0, \tag{11}$$

$$\frac{\partial}{\partial y}\left[\beta_1(\nu)\left(\frac{\partial \nu}{\partial y}\right)^2+\beta_3(\nu)\left(\frac{\partial \nu}{\partial y}\right)^2\right]=0. \tag{12}$$

Equation (9) implies that fluid pressure is constant across the lubricant film thickness which is typical of most lubrication problems. Equation (10) gives the hydrodynamic pressure distribution in the lubricating oil. The first term on the right-hand side reduces to $\partial\tau_{xy}/\partial_y$ for a pure Newtonian fluid, when $\nu = 0$. The second term represents the drag term which is the dominant mechanical interaction between the fluid phase and the solid phase. In the absence of this term and for $\nu = 0$, Eq. (10) can be integrated twice and solved for the pure fluid velocity distribution as a function of the pressure gradient $\partial p/\partial x$. Equation (11) gives the momentum balance in the solid phase between the normal stress in the film thickness direction, the shear stress, the shear equilibrium stress (cf. Savage, 1979), and the drag force of the granular flow. Equation (12) implies that the summation of the normal stress and the normal equilibrium stress of the solid phase in the film thickness direction is uniform. In general, for the mixture flow, Eqs. (10)–(12) are coupled through the interaction term, $\alpha_3(\nu)(w_x - u_x)$, and the solid volume fraction, ν.

Before proceeding to solve these equations, we expand the material functions β_1, β_3, μ_f, μ_s and α_3 in the Taylor's series about ν (cf. Dai and Khonsari, 1991):

$$\beta_1(\nu)=\beta_1^0+\beta_1^1\nu+O(\nu^2), \quad \beta_3(\nu)=\beta_3^0+\beta_3^1\nu+O(\nu^2),$$
$$\mu_f(\nu)=\mu(1-\nu)+O(\nu^2), \quad \mu_s(\nu)=(\mu_s^0+\mu_s^1\nu)\nu+O(\nu^3),$$
$$\alpha_3(\nu)=\alpha^2\nu+O(\nu^2), \tag{13}$$

where β_1^0, β_1^1, β_3^0, β_3^1, μ_s^0, μ_s^1 and α are all constants. We note that in expanding the material functions, the restrictions given by Eqs. (4) and (5) are used.

Substitution of the equations in (13) into Eqs. (9)–(12) yields the following governing equations for the problem at hand:

$$\frac{\partial p}{\partial y}=0, \tag{14}$$

$$\frac{\partial p}{\partial x}-\mu\frac{\partial}{\partial y}\left[(1-\nu)\frac{\partial u_x}{\partial y}\right]-\alpha^2\nu(w_x-u_x)=0, \tag{15}$$

$$\frac{\partial}{\partial x}\left[(\beta_1^0+\beta_1^1\nu)\left(\frac{\partial \nu}{\partial y}\right)^2\right]+\frac{\partial}{\partial y}\left[(\mu_s^0+\mu_s^1\nu)\nu\frac{\partial w_x}{\partial y} + (\beta_3^0+\beta_3^1\nu)\frac{\partial \nu}{\partial x}\frac{\partial \nu}{\partial y}\right]-\alpha^2\nu(w_x-u_x)=0, \tag{16}$$

$$\frac{\partial}{\partial y}\left\{[\beta_1^0+\beta_3^0+(\beta_1^1+\beta_3^1)\nu]\left(\frac{\partial \nu}{\partial y}\right)^2\right\}=0. \tag{17}$$

4 Solutions of the Lubrication Problem

Equations (14)–(17) are coupled nonlinear partial differential equations and in their present form can be solved by numerical methods only. Valuable insight can be gained by referring to the work of Campbell and Brennen (1985) who presented extensive simulations of granular shear flows between two parallel plates. They showed that for what corresponds to the classical no-slip boundary condition, the solid volume fraction is virtually uniform across the gap. Motivated by their work and considering the geometric characteristics of a lubrication film, we hypothesize that the solid volume fraction, ν, remains uniform across the film, i.e., $\nu = \nu(x)$ only. This assumption greatly simplifies the problem as closed-form analytical expressions for both the fluid and the solid velocity distributions will be obtained.

From Eqs. (15) and (16), we obtain the following equation:

$$\frac{\mu(\mu_s^0+\mu_s^1\nu)(1-\nu)}{\alpha^2}\frac{\partial^4 u_x}{\partial y^4}-G(x)\frac{\partial^2 u_x}{\partial y^2}+\frac{dp}{dx}=0, \tag{18}$$

where

$$G(x)=\mu(1-\nu)+(\mu_s^0+\mu_s^1\nu)\nu. \tag{19}$$

Velocity Boundary Conditions. In a hydrodynamic bearing, normally one surface is stationary and one moves at an imposed velocity U. For the problem under consideration, we assume the classical no-slip boundary condition for the fluid phase but make provision for the possibility of solid particle slippage on either the moving or the stationary surface. The above consideration yields the following boundary conditions:

$$u_x|_{y=0}=U, \quad u_x|_{y=h(x)}=0, \quad u_y|_{y=0}=0, \quad u_y|_{y=h(x)}=0,$$
$$w_x|_{y=0}=B_1(x), \quad w_x|_{y=h(x)}=B_2(x), \quad w_y|_{y=0}=0,$$
$$w_y|_{y=h(x)}=\frac{dh(x)}{dx}B_2(x),$$

where the parameter h represents the film gap between the sliding surface and the stationary surface. The form of this function depends on the geometry of the bearing. $B_1^{(x)}$ and $B_2^{(x)}$ are the slip functions of the solid particles on the moving and stationary boundary surfaces, respectively.

Velocity Distributions. Solution of Eq. (18) and application of the above boundary conditions to the result yield the following equation that describes the velocity distribution of the fluid phase:

$$u_x=\frac{1}{G(x)}\left\{\frac{y^2-h(x)y}{2}-\frac{\nu(\mu_s^0+\mu_s^1\nu)^2}{\alpha^2 G(x)}\times\left[1-\frac{e^{\alpha k(x)y}}{1+e^{\alpha k(x)h(x)}}-\frac{e^{-\alpha k(x)y}}{1+e^{-\alpha k(x)h(x)}}\right]\right\}\frac{dp}{dx} - \frac{\nu(\mu_s^0+\mu_s^1\nu)[U-B_1(x)]}{G(x)}\left\{1-\frac{y}{h(x)} - \left[\frac{e^{\alpha k(x)y}}{1+e^{\alpha k(x)h(x)}}-\frac{e^{\alpha k(x)[h(x)-y]}}{1+e^{-\alpha k(x)h(x)}}\right]\frac{1}{1-e^{\alpha k(x)h(x)}}\right\} + \frac{\nu(\mu_s^0+\mu_s^1\nu)B_2(x)}{G(x)}\left\{\frac{y}{h(x)}+\left[\frac{e^{\alpha k(x)[h(x)+y]}}{1+e^{\alpha k(x)h(x)}} - \frac{e^{-\alpha k(x)y}}{1+e^{-\alpha k(x)h(x)}}\right]\frac{1}{1-e^{\alpha k(x)h(x)}}\right\}+U\left[1-\frac{y}{h(x)}\right], \tag{20}$$

where

$$k(x)=\sqrt{\frac{G(x)}{\mu(\mu_s^0+\mu_s^1\nu)(1-\nu)}}.$$

The velocity component of the solid phase, w_x, can be obtained

Downloaded 03 May 2010 to 171.66.16.245. Redistribution subject to ASME license or copyright; see http://www.asme.org/terms/Terms_Use.cfm

by substituting Eq. (20) into Eq. (15). The result is given as follows:

$$w_x=\frac{1}{G(x)}\left\{\frac{y^2-h(x)y}{2}+\frac{\mu(\mu_s^0+\mu_s^1\nu)(1-\nu)}{\alpha^2G(x)}\times\left[1-\frac{e^{\alpha k(x)y}}{1+e^{\alpha k(x)h(x)}}-\frac{e^{-\alpha k(x)y}}{1+e^{-\alpha k(x)h(x)}}\right]\right\}\frac{dp}{dx}-\frac{U-B_1(x)}{G(x)}\left\{\nu(\mu_s^0+\mu_s^1\nu)\left[1-\frac{y}{h(x)}\right]+\frac{\mu(1-\nu)}{1-e^{\alpha k(x)h(x)}}\left[\frac{e^{\alpha k(x)y}}{1+e^{\alpha k(x)h(x)}}-\frac{e^{\alpha k(x)[h(x)-y]}}{1+e^{-\alpha k(x)h(x)}}\right]\right\}+\frac{B_2(x)}{G(x)}\left\{\frac{(\mu_s^0+\mu_s^1\nu)\nu y}{h(x)}-\frac{\mu(1-\nu)}{1-e^{\alpha k(x)h(x)}}\times\left[\frac{e^{\alpha k(x)[h(x)+y]}}{1+e^{\alpha k(x)h(x)}}-\frac{e^{-\alpha k(x)y}}{1+e^{-\alpha k(x)h(x)}}\right]\right\}+U\left[1-\frac{y}{h(x)}\right]. \tag{21}$$

It can be seen, from Eqs. (20) and (21), that the local velocity profiles of the fluid and solid phases are composed of four major terms: the first portion is generated by the pressure gradient (corresponding to Poiseuille flow), the second portion represents the slippage of the granules on the sliding surface, the third portion is related to the particle slippage on the stationary boundary, and the fourth portion is due to the motion of the sliding surface (Couette flow).

Volumetric Flow Rates. Under the steady-state condition, the statements of "conservation of mass" for the fluid and solid phases are given by, respectively:

$$\frac{\partial}{\partial x}[(1-\nu)u_x]+\frac{\partial}{\partial y}[(1-\nu)u_y]=0$$

and

$$\frac{\partial}{\partial x}(\nu w_x)+\frac{\partial}{\partial y}(\nu w_y)=0. \tag{22}$$

Integration of Eqs. $(22)_1$ and $(22)_2$ over y from 0 to h, application of the velocity boundary conditions and use of Leibnitz's integration rule yield:

$$M_s=\int_0^{h(x)}\nu w_x dy \quad \text{and} \quad Q=\int_0^{h(x)}(1-\nu)u_x dy, \tag{23}$$

where M_s is the constant of integration which defines the rate of mass flow of the solid phase and Q is defined as the volumetric flow rate of the fluid phase.

Substituting the velocity distributions of the fluid and solid phases, Eqs. (20) and (21), into Eqs. $(23)_1$ and $(23)_2$, and integrating the resulting equations, we obtain flow rates in terms of the pressure gradient and the slip functions as shown below:

$$Q=-\frac{1-\nu}{G(x)}\left\{\frac{h^3(x)}{12}+\frac{\nu(\mu_s^0+\mu_s^1\nu)^2}{\alpha^2G(x)}\times\left[h(x)-\frac{2}{\alpha k(x)}\frac{1-e^{-\alpha k(x)h(x)}}{1+e^{-\alpha k(x)h(x)}}\right]\right\}\frac{dp}{dx}+\frac{1-\nu}{2}\left\{Uh(x)+\frac{\nu(\mu_s^0+\mu_s^1\nu)[B_1(x)+B_2(x)-U]}{G(x)}\times\left[h(x)-\frac{2}{\alpha k(x)}\frac{1-e^{-\alpha k(x)h(x)}}{1+e^{-\alpha k(x)h(x)}}\right]\right\}, \tag{24}$$

$$M_s=-\frac{\nu}{G(x)}\left\{\frac{h^3(x)}{12}-\frac{\mu(\mu_s^0+\mu_s^1\nu)(1-\nu)}{\alpha^2G(x)}\times\left[h(x)-\frac{2}{\alpha k(x)}\frac{1-e^{-\alpha k(x)h(x)}}{1+e^{-\alpha k(x)h(x)}}\right]\right\}\frac{dp}{dx}+\frac{\nu}{2}\left\{Uh(x)+\frac{B_1(x)+B_2(x)-U}{G(x)}\left[\nu(\mu_s^0+\mu_s^1\nu)h(x)+\frac{2\mu(1-\nu)}{\alpha k(x)}\frac{1-e^{-\alpha k(x)h(x)}}{1+e^{-\alpha k(x)h(x)}}\right]\right\}. \tag{25}$$

Equations (24) and (25) are coupled nonlinear ordinary differential equations. There are four unknowns in the system: ν, p, Q, and M_s. When a ratio of Q to M_s is given, this system can be solved for ν and p through numerical method. The details of the numerical simulation will be given in Section 6.

Shear and Normal Stress in the Mixture. We now turn attention to consider the stresses in the mixture flow. The total stress in the mixture flow is given in Eq. (3). Its matrix form is given as follows:

$$\mathbf{T}=\left\{-p+(\beta_1^0+\beta_1^1\nu)\left[\left(\frac{\partial\nu}{\partial x}\right)^2+\left(\frac{\partial\nu}{\partial y}\right)^2\right]\right\}\times\begin{bmatrix}1&0\\0&1\end{bmatrix}+\mu(1-\nu)\begin{bmatrix}2\frac{\partial u_x}{\partial x}&\frac{\partial u_x}{\partial y}+\frac{\partial u_y}{\partial x}\\ \frac{\partial u_x}{\partial y}+\frac{\partial u_y}{\partial x}&2\frac{\partial u_y}{\partial y}\end{bmatrix}+(\mu_s^0+\mu_s^1\nu)\nu\begin{bmatrix}2\frac{\partial w_x}{\partial x}&\frac{\partial w_x}{\partial y}+\frac{\partial w_y}{\partial x}\\ \frac{\partial w_x}{\partial y}+\frac{\partial w_y}{\partial x}&2\frac{\partial w_y}{\partial y}\end{bmatrix}+(\beta_3^0+\beta_3^1\nu)\begin{bmatrix}\left(\frac{\partial\nu}{\partial x}\right)^2&\frac{\partial\nu}{\partial x}\frac{\partial\nu}{\partial y}\\ \frac{\partial\nu}{\partial x}\frac{\partial\nu}{\partial y}&\left(\frac{\partial\nu}{\partial y}\right)^2\end{bmatrix}. \tag{26}$$

Equation (26) can be simplified considerably by using an order-of-magnitude analysis. Making use of the scales for the material functions, and noting $\nu=\nu(x)$, Eq. (26) reduces to the following equation:

$$\mathbf{T}=-p\begin{bmatrix}1&0\\0&1\end{bmatrix}+\begin{bmatrix}0&\mu(1-\nu)\frac{\partial u_x}{\partial y}+\nu(\mu_s^0+\mu_s^1\nu)\frac{\partial w_x}{\partial y}\\ \mu(1-\nu)\frac{\partial u_x}{\partial y}+\nu(\mu_s^0+\mu_s^1\nu)\frac{\partial w_x}{\partial y}&0\end{bmatrix}+O\left(\frac{h_0}{L}\right).$$

Thus, the normal stress, T_{yy}, and shear stress of the mixture flow, T_{xy}, take the forms

$$T_{yy}=-p, \quad T_{xy}=\frac{2y-h(x)}{2}\frac{dp}{dx}-\frac{UG(x)}{h(x)}+\frac{\nu(\mu_s^0+\mu_s^1\nu)}{h(x)}\times[B_2(x)+U-B_1(x)], \tag{27}$$

where the h_0/L order terms have been neglected.

Downloaded 03 May 2010 to 171.66.16.245. Redistribution subject to ASME license or copyright; see http://www.asme.org/terms/Terms_Use.cfm

The friction force, F_m, the load carrying capacity, W_m, and the friction coefficient, f_m, of the mixture flow are defined as

$$F_m=\int_0^H T_{xy}|_{y=0}dx, \quad W_m=\int_0^H p dx, \quad f_m=\frac{F_m}{W_m}, \tag{28}$$

where H is the bearing length in the sliding direction and

$$T_{xy}|_{y=0}=-\frac{1}{h(x)}\left\{\frac{h^2(x)}{2}\frac{dp}{dx}+UG(x) - \nu(\mu_s^0+\mu_s^1\nu)[B_2(x)+U-B_1(x)]\right\}. \tag{29}$$

5 Special Cases

In this section, we examine a number of interesting special cases that can be recovered from the general equations defined in this paper.

5.1 No-Slip Boundary Conditions. Suppose that the granules do not slip on both the moving and stationary surfaces. In this case, the particles assume the same velocity as the boundaries. Physically, this no-slip boundary condition case would best describe to the situations where particles are small and the boundary surfaces are rough. Setting $B_1 = U$ and $B_2 = 0$, from Eqs. (20), (21), (24), (25), and (29), we find that

$$u_x=\frac{1}{G(x)}\left\{\frac{y^2-h(x)y}{2}-\frac{\nu(\mu_s^0+\mu_s^1\nu)^2}{\alpha^2G(x)}\times\left[1-\frac{e^{\alpha k(x)y}}{1+e^{\alpha k(x)h(x)}}-\frac{e^{-\alpha k(x)y}}{1+e^{-\alpha k(x)h(x)}}\right]\right\}\frac{dp}{dx} + U\left[1-\frac{y}{h(x)}\right], \tag{30}$$

$$w_x=\frac{1}{G(x)}\left\{\frac{y^2-h(x)y}{2}+\frac{\mu(\mu_s^0+\mu_s^1\nu)(1-\nu)}{\alpha^2G(x)}\times\left[1-\frac{e^{\alpha k(x)y}}{1+e^{\alpha k(x)h(x)}}-\frac{e^{-\alpha k(x)y}}{1+e^{-\alpha k(x)h(x)}}\right]\right\}\frac{dp}{dx} + U\left[1-\frac{y}{h(x)}\right], \tag{31}$$

$$Q=-\frac{1-\nu}{G(x)}\left\{\frac{h^3(x)}{12}+\frac{\nu(\mu_s^0+\mu_s^1\nu)^2}{\alpha^2G(x)}\times\left[h(x)-\frac{2}{\alpha k(x)}\frac{1-e^{-\alpha k(x)h(x)}}{1+e^{-\alpha k(x)h(x)}}\right]\right\}\frac{dp}{dx} + \frac{U}{2}h(x)(1-\nu), \tag{32}$$

$$M_s=-\frac{\nu}{G(x)}\left\{\frac{h^3(x)}{12}-\frac{\mu(\mu_s^0+\mu_s^1\nu)(1-\nu)}{\alpha^2G(x)}\times\left[h(x)-\frac{2}{\alpha k(x)}\frac{1-e^{-\alpha k(x)h(x)}}{1+e^{-\alpha k(x)h(x)}}\right]\right\}\frac{dp}{dx} + \frac{U}{2}h(x)\nu, \tag{33}$$

$$T_{xy}|_{y=0}=-\frac{1}{h(x)}\left[\frac{h^2(x)}{2}\frac{dp}{dx}+UG(x)\right]. \tag{34}$$

5.2 Pure Fluid Flow Case. In pure fluid flow case, $\nu = 0$. Therefore, $G(x) = \mu$. Suppressing ν from Eqs. (30)–(34), we can obtain the classical expressions for the pure fluid flow.

5.3 The Case Where $\alpha = 0$. This case physically corresponds to the cases where the mechanical interaction between the fluid phase and the solid phase is negligibly small. Note that

$$\lim_{\alpha\to 0}\frac{1}{\alpha^2}\left[1-\frac{e^{\alpha k(x)y}}{1+e^{\alpha k(x)h(x)}}-\frac{e^{-\alpha k(x)y}}{1+e^{-\alpha k(x)h(x)}}\right] \to -\frac{k^2[y^2-h(x)y]}{2},$$

$$\lim_{\alpha\to 0}\left[\frac{e^{\alpha k(x)[h(x)+y]}}{1+e^{\alpha k(x)h(x)}}-\frac{e^{-\alpha k(x)y}}{1+e^{-\alpha k(x)h(x)}}\right]\frac{1}{e^{\alpha k(x)h(x)}}\to -\frac{y}{h(x)},$$

$$\lim_{\alpha\to 0}\left[\frac{e^{\alpha k(x)y}}{1+e^{\alpha k(x)h(x)}}-\frac{e^{\alpha k(x)[h(x)-y]}}{1+e^{-\alpha k(x)h(x)}}\right]\frac{1}{1-e^{\alpha k(x)h(x)}}\to 1-\frac{y}{h(x)},$$

$$\lim_{\alpha\to 0}\frac{1}{\alpha^2}\left[h(x)-\frac{2}{\alpha k(x)}\frac{1-e^{-\alpha k(x)h(x)}}{1+e^{-\alpha k(x)h(x)}}\right]\to\frac{k^2(x)h^3(x)}{12},$$

$$\lim_{\alpha\to 0}\frac{1}{\alpha}\frac{1-e^{-\alpha k(x)h(x)}}{1+e^{-\alpha k(x)h(x)}}\to\frac{k(x)h(x)}{2}.$$

From Eqs. (20), (21), (24), and (25), we find that

$$u_x=\frac{y^2-h(x)y}{2\mu}\frac{dp}{dx}+U\left[1-\frac{y}{h(x)}\right],$$

$$w_x=B_1(x)\left[1-\frac{y}{h(x)}\right]+B_2(x)\frac{y}{h(x)}, \tag{35}$$

$$Q=-\frac{h^3(x)}{12\mu}\frac{dp}{dx}+\frac{U}{2}h(x)(1-\nu),$$

$$M_s=-\frac{\nu h(x)}{2}[B_1(x)+B_2(x)], \tag{36}$$

and the shear stress at $y = 0$ remains the same as given by Eq. (34).

5.4 The Case Where $\alpha \to \infty$. This case physically corresponds to the situations where the solid particles travel with the fluid at the same velocity (i.e., $u_x = w_x$). Note that

$$\lim_{\alpha\to\infty}\frac{1}{\alpha^2}\left[1-\frac{e^{\alpha k(x)y}}{1+e^{\alpha k(x)h(x)}}-\frac{e^{-\alpha k(x)y}}{1+e^{-\alpha k(x)h(x)}}\right]\to 0,$$

$$\lim_{\alpha\to\infty}\frac{1}{\alpha^2}\left[h(x)-\frac{2}{\alpha k(x)}\frac{1-e^{-\alpha k(x)h(x)}}{1+e^{-\alpha k(x)h(x)}}\right]\to 0,$$

From Eqs. (30)–(34), we obtain:

$$u_x=w_x=\frac{y^2-h(x)y}{2G(x)}\frac{dp}{dx}+U\left[1-\frac{y}{h(x)}\right], \tag{37}$$

$$Q=-\frac{(1-\nu)h^3(x)}{12G(x)}\frac{dp}{dx}+\frac{U}{2}h(x)(1-\nu),$$

$$M_s=-\frac{\nu h^3(x)}{12G(x)}\frac{dp}{dx}+\frac{U}{2}h(x)\nu, \tag{38}$$

$$T_{xy}|_{y=0}=-\frac{h(x)}{2}\frac{dp}{dx}-\frac{UG(x)}{h(x)}. \tag{39}$$

It follows from Eqs. $(38)_1$ and $(38)_2$ that

$$Q_m=-\frac{h^3(x)}{12G(x)}\frac{dp}{dx}+\frac{Uh(x)}{2}, \tag{40}$$

where $Q_m = Q + M_s$. Comparing the above expressions with the classical results for pure Newtonian fluid flow, one can find that Eqs. (37), (39), and (40) can be obtained from the classical results by replacing μ with G.

5.5 Effective Viscosity of Mixture. The definition of function G, Eq. (19), can be rewritten as

$$G(x)=\mu\left[1-\nu\left(1-\frac{\mu_s^0}{\mu}-\frac{\mu_s^1}{\mu}\nu\right)\right].$$

Downloaded 03 May 2010 to 171.66.16.245. Redistribution subject to ASME license or copyright; see http://www.asme.org/terms/Terms_Use.cfm

It is interesting to note that when the solid volume fraction, ν, is a constant and is small enough such that the term ν^2 can be neglected, at $\mu_s^0/\mu = 3.5$, the preceding equation reduces to Einstein's formula for the effective viscosity μ_m of a mixture, i.e., $\mu_m = \mu(1 + 2.5\nu)$.

6 Numerical Solution

6.1 Nondimensionalization. To pursue numerical simulation, the following dimensionless parameters are defined:

$$\bar{x}=\frac{x}{L},\quad \bar{y}=\frac{y}{h_0},\quad \bar{h}(\bar{x})=\frac{h(x)}{h_0},\quad \bar{Q}=\frac{Q}{Uh_0},\quad \bar{M}_s=\frac{M_s}{Uh_0},\quad \bar{H}=\frac{H}{L},$$

$$\bar{B}_1(\bar{x})=\frac{B_1(x)}{U},\quad \bar{B}_2(\bar{x})=\frac{B_2(x)}{U},\quad \bar{G}(\bar{x})=\frac{G(x)}{\mu},$$

$$\bar{k}(\bar{x})=k(x)\sqrt{\mu},\quad \bar{\mu}_s^0=\frac{\mu_s^0}{\mu},\quad \bar{\mu}_s^1=\frac{\mu_s^1}{\mu},\quad \bar{\alpha}=\alpha\frac{h_0}{\sqrt{\mu}},\quad \bar{p}=p\frac{h_0^2}{LU\mu},$$

$$\bar{T}_{xy}=T_{xy}\frac{h_0}{U\mu},\quad \bar{T}_{yy}=T_{yy}\frac{h_0^2}{LU\mu},\quad \bar{u}_x=\frac{u_x}{U},\quad \bar{w}_x=\frac{w_x}{U},$$

$$\bar{F}_m=F_m\frac{h_0}{LU\mu},\quad \bar{W}_m=W_m\frac{h_0^2}{L^2U\mu},$$

where all the characters with an overbar are the dimensionless form of their corresponding parameters.

Equations (24) and (25) can be rewritten in the following dimensionless form:

$$\frac{\bar{Q}}{12}\bar{h}^3(\bar{x})[\nu-\gamma(1-\nu)]+\frac{\bar{h}(\bar{x})\nu}{2\bar{\alpha}}[\bar{B}_1(\bar{x})+\bar{B}_2(\bar{x})-1]$$
$$\times\left\{\frac{\nu(\bar{\mu}_s^0+\bar{\mu}_s^1\nu)^2\bar{h}(\bar{x})}{\bar{\alpha}\bar{G}(\bar{x})}+\frac{1}{\bar{k}(\bar{x})}\left[\frac{(1-\nu)\bar{h}^2(\bar{x})}{6}-\frac{2\nu(\bar{\mu}_s^0+\bar{\mu}_s^1\nu)^2}{\bar{\alpha}^2\bar{G}(\bar{x})}\right]\right.$$
$$\left.\times\frac{1-e^{-\bar{\alpha}\bar{k}(\bar{x})\bar{h}(\bar{x})}}{1+e^{-\bar{\alpha}\bar{k}(\bar{x})\bar{h}(\bar{x})}}\right\}+\frac{\nu(1-\nu)(\bar{\mu}_s^0+\bar{\mu}_s^1\nu)}{\bar{\alpha}^2\bar{G}(\bar{x})}\left[\bar{h}(\bar{x})-\frac{2}{\bar{\alpha}\bar{k}(\bar{x})}\right.$$
$$\left.\times\frac{1-e^{-\bar{\alpha}\bar{k}(\bar{x})\bar{h}(\bar{x})}}{1-e^{-\bar{\alpha}\bar{k}(\bar{x})\bar{h}(\bar{x})}}\right]\left\{\bar{Q}[1-\gamma(\bar{\mu}_s^0+\bar{\mu}_s^1\nu)]-\frac{\bar{h}(\bar{x})\bar{G}(\bar{x})}{2}\right\}=0, \quad (41)$$

and

$$\left\{\frac{\bar{h}^3(\bar{x})}{12}[\gamma(1-\nu)-\nu]+\frac{\nu(1-\nu)(\bar{\mu}_s^0+\bar{\mu}_s^1\nu)[1+\gamma(\bar{\mu}_s^0+\bar{\mu}_s^1\nu)]}{\bar{\alpha}^2\bar{G}(\bar{x})}\right.$$
$$\left.\times\left[\bar{h}(\bar{x})-\frac{2}{\bar{\alpha}\bar{k}(\bar{x})}\frac{1-e^{-\bar{\alpha}\bar{k}(\bar{x})\bar{h}(\bar{x})}}{1+e^{-\bar{\alpha}\bar{k}(\bar{x})\bar{h}(\bar{x})}}\right]\right\}\frac{d\bar{p}}{d\bar{x}}-\frac{\bar{h}(\bar{x})\bar{G}(\bar{x})}{2}$$
$$\times[\gamma(1-\nu)-\nu]-\frac{\nu[\bar{B}_1(\bar{x})+\bar{B}_2(\bar{x})-1]}{2}$$
$$\times\left\{(\bar{\mu}_s^0+\bar{\mu}_s^1\nu)\bar{h}(\bar{x})[\gamma(1-\nu)-\nu]\right.$$
$$\left.-\frac{2(1-\nu)[1+\gamma(\bar{\mu}_s^0+\bar{\mu}_s^1\nu)]}{\bar{\alpha}\bar{k}(\bar{x})}\frac{1-e^{-\bar{\alpha}\bar{k}(\bar{x})\bar{h}(\bar{x})}}{1+e^{-\bar{\alpha}\bar{k}(\bar{x})\bar{h}(\bar{x})}}\right\}=0, \quad (42)$$

where $\gamma = \bar{M}_s/\bar{Q}$.

The pressure boundary conditions in their dimensionless form are given by

$$\bar{p}|_{\bar{x}=0}=\bar{p}_0,\quad \bar{p}|_{\bar{x}=\bar{H}}=\bar{p}_0, \quad (43)$$

where $\bar{p}_0$ is a dimensionless constant. For a slider bearing $\bar{H} = 1$, and in a journal bearing of diameter, D, $\bar{H} = 2\pi$.

The dimensionless forms of the normal stress, shear stress at the boundary, friction force, load-carrying capacity, and friction coefficient of the mixture flow are

$$\bar{T}_{xy}|_{\bar{y}=0}=-\frac{1}{\bar{h}(\bar{x})}\left\{\frac{\bar{h}^2(\bar{x})}{2}\frac{d\bar{p}}{d\bar{x}}\right.$$
$$\left.+\bar{G}(\bar{x})-\nu(\bar{\mu}_s^0+\bar{\mu}_s^1\nu)[\bar{B}_2(\bar{x})-\bar{B}_1(\bar{x})+1]\right\},$$

$$\bar{T}_{yy}=-\bar{p},\quad \bar{F}_m=\int_0^{\bar{H}}\bar{T}_{xy}|_{\bar{y}=0}d\bar{x},$$

$$\bar{W}_m=\int_0^{\bar{H}}\bar{p}d\bar{x},\quad f_m=\frac{\bar{F}_m}{\bar{W}_m}\left(\frac{h_0}{L}\right).$$

6.2 Numerical Simulation. To determine the bearing performance parameters with mixture, first the solid volume fraction ν and pressure distribution $\bar{p}$ must be evaluated. These are governed by Eqs. (41) and (42). For a given ratio of $\bar{M}_s$ and $\bar{Q}$, i.e., γ, Eqs. (41) and (42) can be solved numerically, subject to the pressure boundary conditions, Eq. (43).

To illustrate the procedure adopted in the numerical simulations, we write Eqs. (41) and (42) into the following system:

$$\bar{f}[\nu(\bar{x});\bar{h}(\bar{x}),\bar{B}_1(\bar{x}),\bar{B}_2(\bar{x});\gamma,\bar{Q},\bar{\mu}_s^0,\bar{\mu}_s^1]=0, \quad (44)$$

and

$$\frac{d\bar{p}}{d\bar{x}}=-\frac{\bar{F}_1[\nu(\bar{x});\bar{h}(\bar{x}),\bar{B}_1(\bar{x}),\bar{B}_2(\bar{x});\gamma,\bar{\mu}_s^0,\bar{\mu}_s^1]}{\bar{F}_2[\nu(\bar{x});\bar{h}(\bar{x});\gamma,\bar{\mu}_s^0,\bar{\mu}_s^1]}, \quad (45)$$

where

$$\bar{f}=\frac{\bar{Q}}{12}\bar{h}^3(\bar{x})[\nu-\gamma(1-\nu)]+\frac{\bar{h}(\bar{x})\nu}{2\bar{\alpha}}[\bar{B}_1(\bar{x})+\bar{B}_2(\bar{x})-1]$$
$$\times\left\{\frac{\nu(\bar{\mu}_s^0+\bar{\mu}_s^1\nu)^2\bar{h}(\bar{x})}{\bar{\alpha}\bar{G}(\bar{x})}+\frac{1}{\bar{k}(\bar{x})}\left[\frac{(1-\nu)\bar{h}^2(\bar{x})}{6}-\frac{2\nu(\bar{\mu}_s^0+\bar{\mu}_s^1\nu)^2}{\bar{\alpha}^2\bar{G}(\bar{x})}\right]\right.$$
$$\left.\times\frac{1-e^{-\bar{\alpha}\bar{k}(\bar{x})\bar{h}(\bar{x})}}{1+e^{-\bar{\alpha}\bar{k}(\bar{x})\bar{h}(\bar{x})}}\right\}-\frac{\nu(1-\nu)(\bar{\mu}_s^0+\bar{\mu}_s^1\nu)}{\bar{\alpha}^2\bar{G}(\bar{x})}$$
$$\times\left[\bar{h}(\bar{x})-\frac{2}{\bar{\alpha}\bar{k}(\bar{x})}\frac{1-e^{-\bar{\alpha}\bar{k}(\bar{x})\bar{h}(\bar{x})}}{1+e^{-\bar{\alpha}\bar{k}(\bar{x})\bar{h}(\bar{x})}}\right]$$
$$\times\left\{\bar{Q}[1+\gamma(\bar{\mu}_s^0+\bar{\mu}_s^1\nu)]-\frac{\bar{h}(\bar{x})\bar{G}(\bar{x})}{2}\right\},$$

$$\bar{F}_1=-\frac{\bar{h}(\bar{x})\bar{G}(\bar{x})}{2}[\gamma(1-\nu)-\nu]-\frac{\nu[\bar{B}_1(\bar{x})+\bar{B}_2(\bar{x})-1]}{2}$$
$$\times\left\{\bar{h}(\bar{x})(\bar{\mu}_s^0+\bar{\mu}_s^1\nu)[\gamma(1-\nu)-\nu]-\frac{2(1-\nu)}{\bar{\alpha}\bar{k}(\bar{x})}\right.$$
$$\left.\times[1+\gamma(\bar{\mu}_s^0+\bar{\mu}_s^1\nu)]\frac{1-e^{-\bar{\alpha}\bar{k}(\bar{x})\bar{h}(\bar{x})}}{1+e^{-\bar{\alpha}\bar{k}(\bar{x})\bar{h}(\bar{x})}}\right\},$$

$$\bar{F}_2=\frac{\bar{h}^3(\bar{x})}{12}[\gamma(1-\nu)-\nu]+\frac{\nu(1-\nu)(\bar{\mu}_s^0+\bar{\mu}_s^1\nu)[1+\gamma(\bar{\mu}_s^0+\bar{\mu}_s^1\nu)]}{\bar{\alpha}^2\bar{G}(\bar{x})}$$
$$\times\left[\bar{h}(\bar{x})-\frac{2}{\bar{\alpha}\bar{k}(\bar{x})}\frac{1-e^{-\bar{\alpha}\bar{k}(\bar{x})\bar{h}(\bar{x})}}{1+e^{-\bar{\alpha}\bar{k}(\bar{x})\bar{h}(\bar{x})}}\right].$$

To solve the system of Eqs. (44) and (45), the viscosity coefficients of the solid phase, $\bar{\mu}_s^0$ and $\bar{\mu}_s^1$, the geometry function of the film thickness, $\bar{h}(\bar{x})$, the ratio of the volumetric flow rates, γ, and the slip functions of the solid particles on the moving and stationary boundary surfaces, $\bar{B}_1$ and $\bar{B}_2$, must be specified. The system can be solved by first calculating $\nu(\bar{x})$ from Eq. (44) and then evaluating $\bar{p}(\bar{x})$ from Eq. (45).

Since the boundary conditions at both $\bar{x} = 0$ and $\bar{x} = \bar{H}$ are known, this procedure requires a shooting method. In applying this method, first, a value of $\bar{Q}$ is guessed and $\nu(\bar{x})$ is calculated from Eq. (44). Computed values of $\nu(\bar{x})$ are then

Downloaded 03 May 2010 to 171.66.16.245. Redistribution subject to ASME license or copyright; see http://www.asme.org/terms/Terms_Use.cfm

substituted into Eq. (45) and integrated to evaluate $\bar{p}$. Equation (45) is, next, integrated using a fourth-order Runge-Kutta method subject to the boundary conditions in (43). The starting value for the numerical integration is given by $(43)_1$, $\bar{p}(0) = \bar{p}_0$. The integrated end value of $\bar{p}$, such as $\bar{p}_Q$, is compared with the end condition required by $(43)_2$, namely $\bar{p}(\bar{H}) = \bar{p}_0$. If $|\bar{p}_Q - \bar{p}_0| = \delta > \epsilon$, where ϵ is a prescribed value for error tolerance, the value guessed for $\bar{Q}$ is adjusted and the process is repeated until the condition $|\bar{p}_Q - \bar{p}_0| = \delta \leq \epsilon$ is met. The procedure for adjusting the value of $\bar{Q}$ is described by Dai et al. (1992).

An error tolerance value of $\epsilon = 1 \times 10^{-5}$ was used for all slider bearing simulations and $\epsilon = 1 \times 10^{-6}$ for the journal bearing. Typically 15 iterations on $\bar{Q}$ were needed to achieve convergence with $\epsilon = 1 \times 10^{-5}$ and 20 iterations for $\epsilon = 1 \times 10^{-6}$.

Once the converged values of ν and $\bar{p}$ are determined, the program proceeds to evaluate the velocity distributions of the fluid and the solid phases, the volumetric flow rates, the normal stress and the shear stress of the mixture flow, and the bearing performance parameters.

6.3 Applications. Extensive simulations are presented for two of the most common hydrodynamic bearing geometries, namely the slider and journal bearings. All the simulations presented in this paper pertain to two dimensions—what is commonly referred to as an infinitely long bearing—only.

6.3.1 Slider Bearing. The dimensionless geometric function of the film thickness for a slider bearing is given as follows:

$$\bar{h}(\bar{x}) = 1 - (1 - \bar{h}_2)\bar{x},$$

where $\bar{h}(\bar{x}) = h(x)/h_1$, $\bar{x} = x/H$, $\bar{h}_2 = h_2/h_1$, $H\ (= L)$ is the length of the slider and $h_1\ (= h_0)$ and h_2 are the thickness of the film gap at the inlet and outlet, respectively. In this paper, we use the following specifications for the results to be presented for the slider bearing

$$\frac{h_0}{H} = 0.002, \quad \bar{p}_0 = 0, \quad \bar{\mu}_s^1 = 0.$$

Pressure Profile. Before we proceed to the presentation of the performance parameter of mixture in a slider bearing, we show a typical pressure distribution in the bearing with comparison to the pure fluid case. Shown in Fig. 1 is the pressure distribution in the mixture flow with assumed values for slip functions on both surfaces ($\bar{B}_1 = 0.9$ and $\bar{B}_2 = 0.6$). As shown, the shape of the pressure distribution in the mixture flow is nearly the same as the pure fluid case. The magnitude of the pressure generated in the mixture flow, however, is dependent upon the viscosity coefficient of the solid phase, $\bar{\mu}_s^0$.

Influence of Solid Phase Viscosity Coefficient, $\bar{\mu}_s^0$. Let us now examine the effect of the solid phase viscosity coefficient, $\bar{\mu}_s^0$, on the load-carrying capacity, the shear force and the friction coefficient. The simulation results for a range of γ values are depicted in Figs. 2–4, respectively, assuming that the classical no-slip boundary conditions prevail. Referring to these figures, it is seen that the load-carrying capacity, the shear force, and the friction coefficient tend to increase for larger values of $\bar{\mu}_s^0$. However, the rate of change of friction force with $\bar{\mu}_s^0$ is higher than that of the load-carrying capacity. Therefore, the friction coefficient (Fig. 4) increases as $\bar{\mu}_s^0$ is increased. It is worthwhile to note that for $\bar{\mu}_s^0 < 1$, the friction coefficient of the mixture flow is lower than the pure fluid case for $0 < \gamma \leq 4.5$. Since the friction coefficient is directly related to the bearing power loss, this signifies an improvement in the lubrication effectiveness of the mixture flow. For $\bar{\mu}_s^0 > 1$, the theory predicts a higher friction coefficient (and therefore a larger power loss) in the mixture case as compared to the pure lubricant. Figure 4 shows that regardless of the value

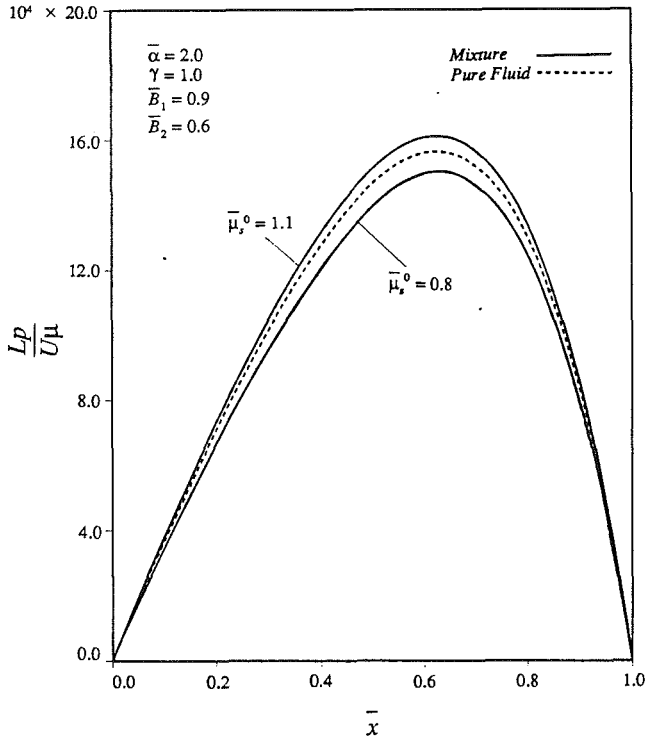


Fig. 1 Pressure distribution in a slider bearing

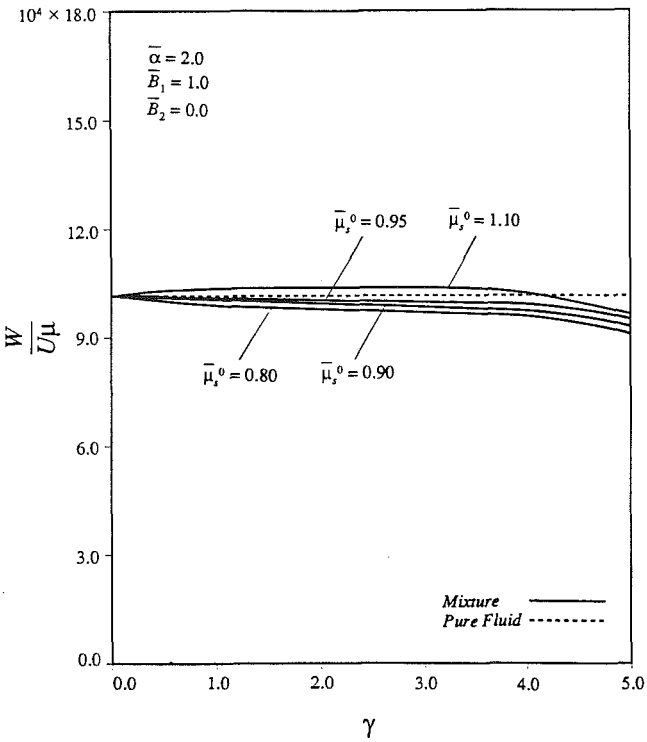


Fig. 2 Effect of solid phase viscosity coefficient $\bar{\mu}_s^0$ on load-carrying capacity in a slider bearing

of $\bar{\mu}_s^0$, the friction coefficient of the mixture flow begins to increase around $\gamma = 4$ where the load-carrying capacity drops (see Fig. 2). Therefore, for practical purposes where a lower friction coefficient is desirable, γ should be kept below this value.

Influence of Interacting Coefficient, $\bar{\alpha}$. Next, the effect of

Downloaded 03 May 2010 to 171.66.16.245. Redistribution subject to ASME license or copyright; see http://www.asme.org/terms/Terms_Use.cfm

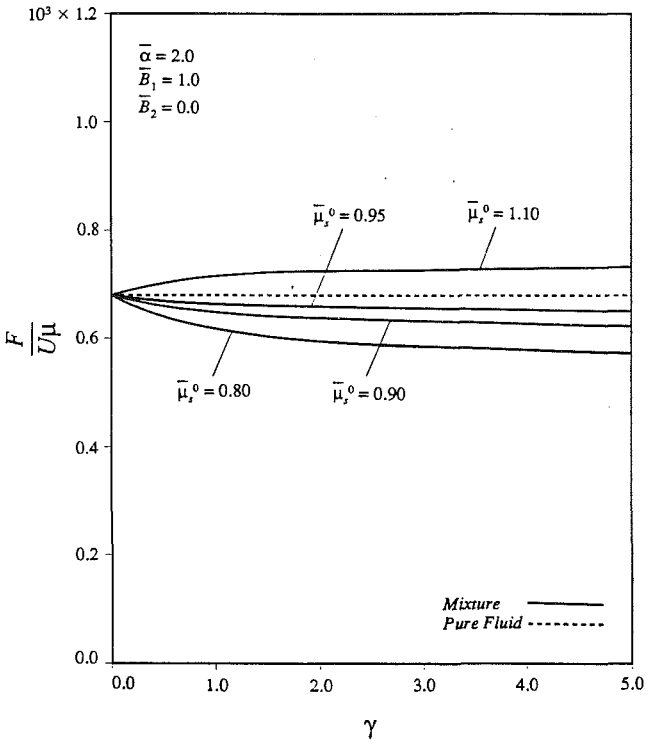


Fig. 3 Effect of solid phase viscosity coefficient $\bar{\mu}_s^0$ on shear force in a slider bearing

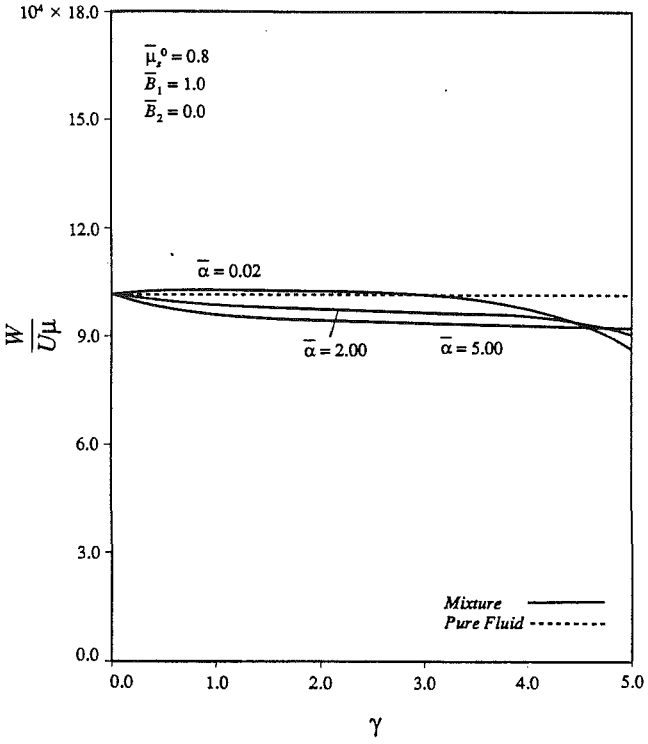


Fig. 5 Effect of interacting coefficient $\bar{\alpha}$ on load-carrying capacity in a slider bearing

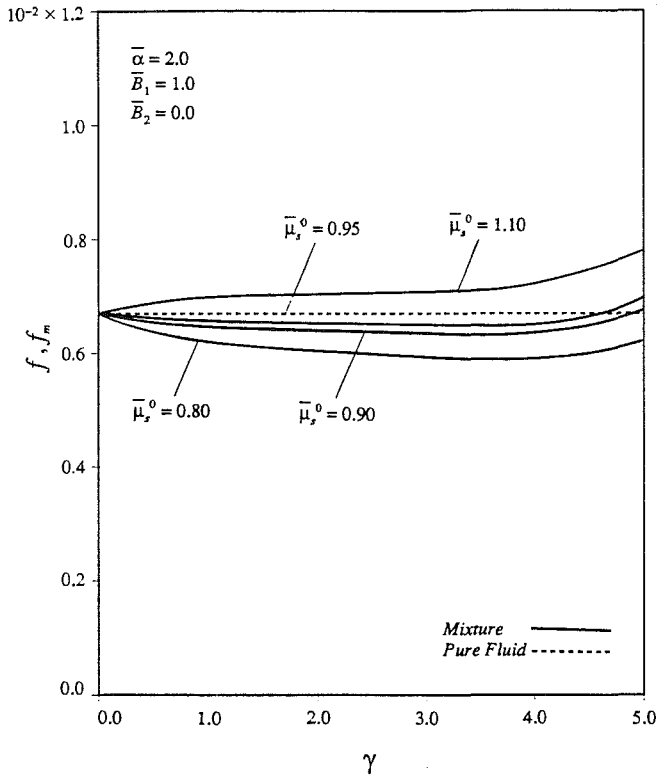


Fig. 4 Effect of solid phase viscosity coefficient $\bar{\mu}_s^0$ on friction coefficient in a slider bearing

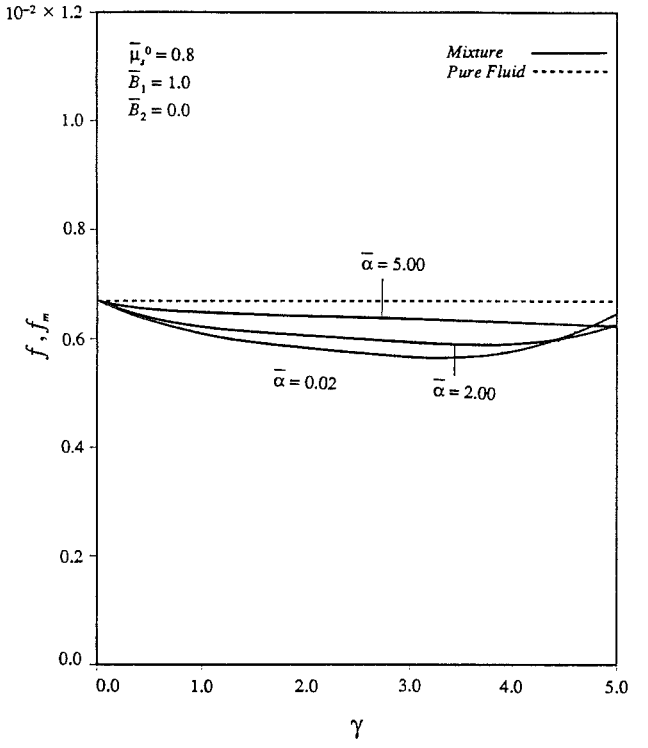


Fig. 6 Effect of interacting coefficient $\bar{\alpha}$ on friction coefficient in a slider bearing

$\bar{\alpha}$ on the load-carrying capacity, again under the no-slip boundary conditions is investigated. For very small values of $\bar{\alpha}$ (= 0.02), i.e., the drag effect is very small and for the ratio of the volumetric flow rates up to roughly $\gamma = 3$, a slight enhancement in the load-carrying capacity is noted (see Fig. 5). Similar results were reported in a separate study which was valid for small values of γ with negligible interaction between the two constituents (cf. Dai and Khonsari, 1991). It is noted that the consideration of the interaction between the fluid and solid phases as characterized by $\bar{\alpha}$ can significantly influence

Downloaded 03 May 2010 to 171.66.16.245. Redistribution subject to ASME license or copyright; see http://www.asme.org/terms/Terms_Use.cfm

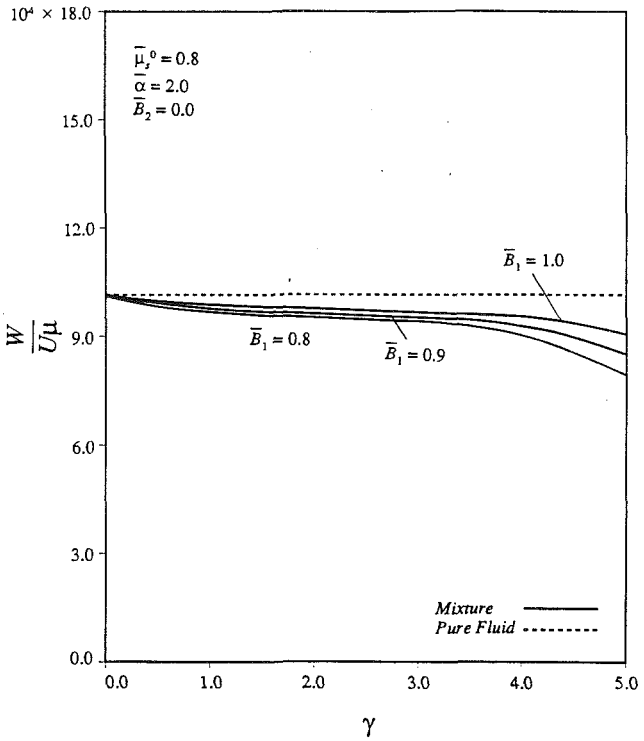


Fig. 7 Effect of solid particle slippage at sliding surface $\bar{B}_1$ on load-carrying capacity in a slider bearing

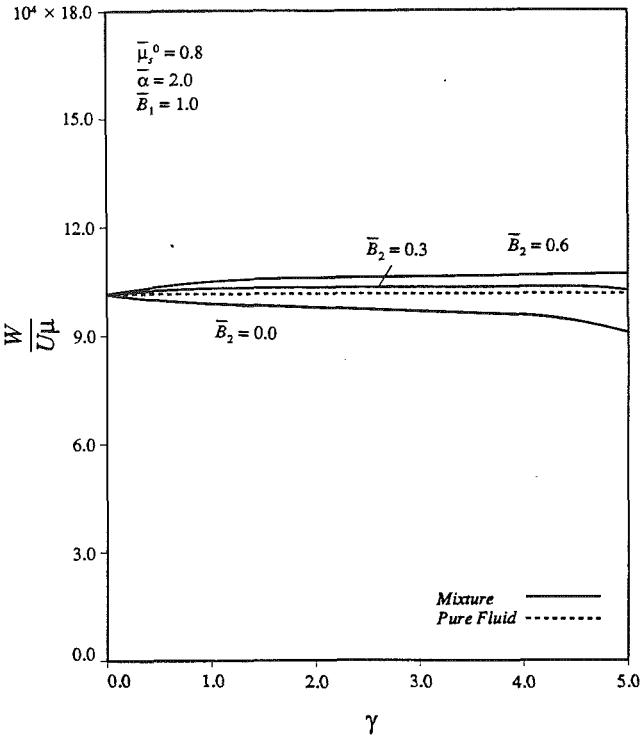


Fig. 9 Effect of solid particle slippage at stationary surface $\bar{B}_2$ on load-carrying capacity in a slider bearing

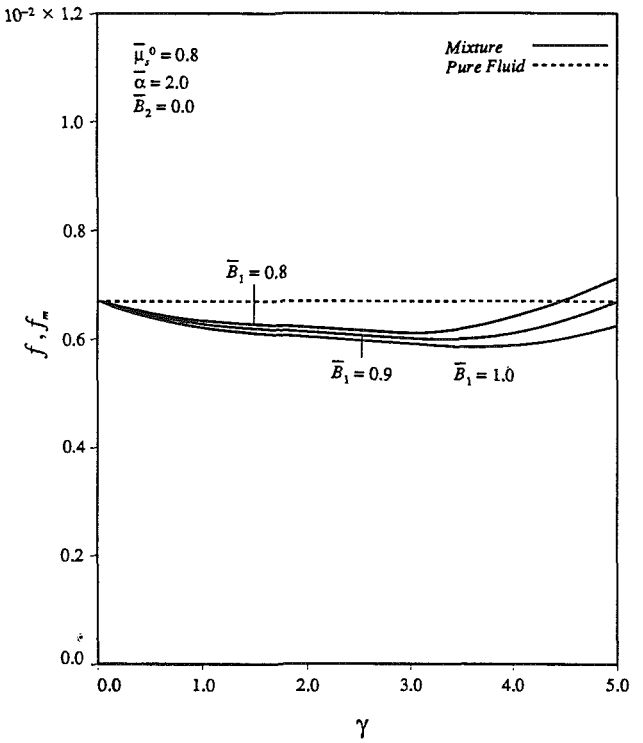


Fig. 8 Effect of solid particle slippage at sliding surface $\bar{B}_1$ on friction coefficient in a slider bearing

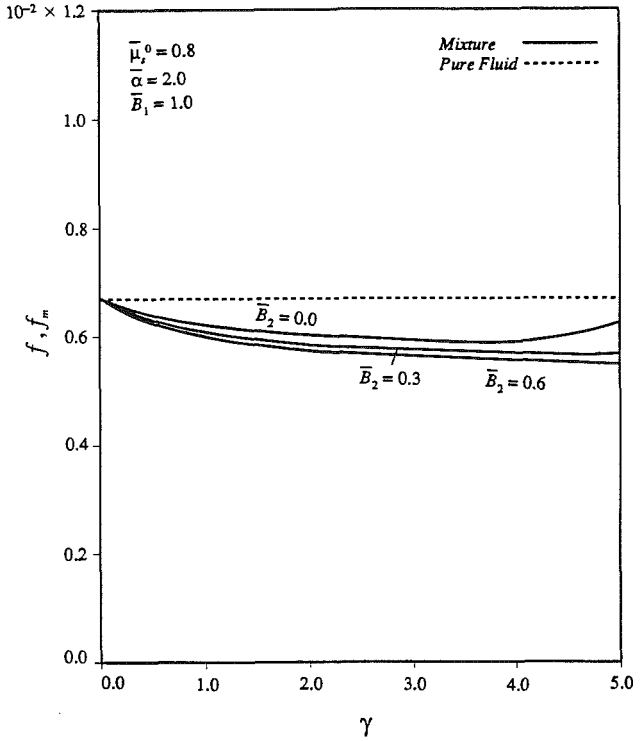


Fig. 10 Effect of solid particle slippage at stationary surface $\bar{B}_2$ on friction coefficient in a slider bearing

the load-carrying capacity and friction coefficient as shown in Figs. 5 and 6, respectively.

Influence of Slip Boundary Conditions. The effect of the solid particle slippage at boundary surfaces on the load-carrying capacity and the friction coefficient are shown in Figs. 7–10. Figures 7 and 8 show the effects of the slippage of the solid particles at the moving surface on the load-carrying capacity and the friction coefficient. Consideration of the particle slippage at the sliding boundary surface leads to a lower load-carrying capacity and a higher friction coefficient. The solid particle slippage on the stationary boundary surface, however,

Downloaded 03 May 2010 to 171.66.16.245. Redistribution subject to ASME license or copyright; see http://www.asme.org/terms/Terms_Use.cfm

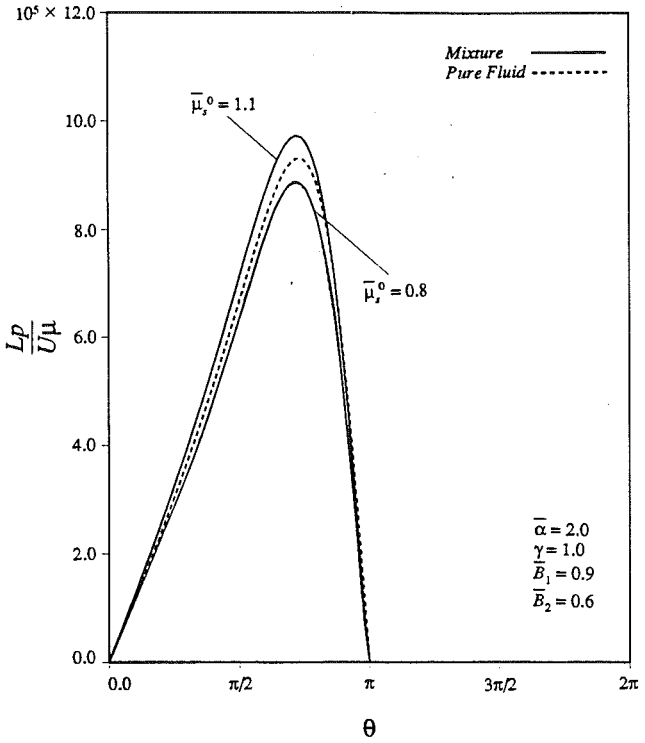


Fig. 11 Pressure distribution in a journal bearing

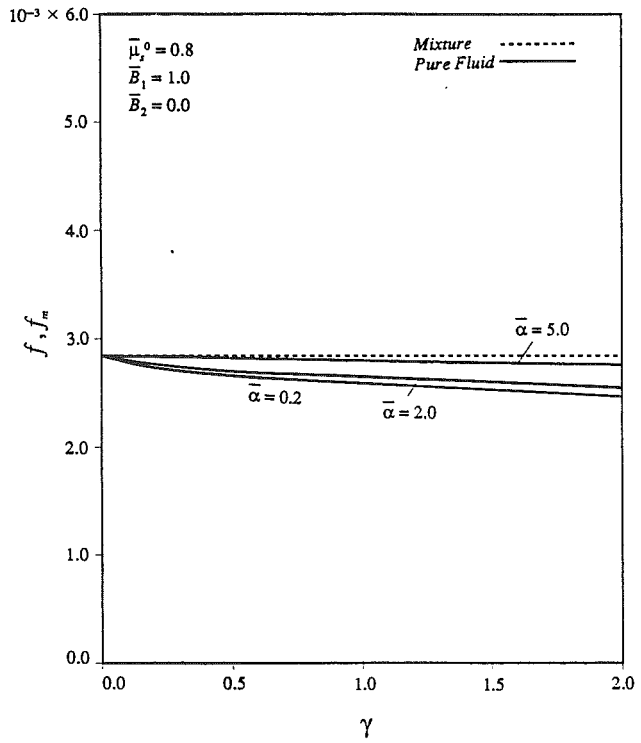


Fig. 13 Effect of interacting coefficient $\bar{\alpha}$ on friction coefficient in a journal bearing

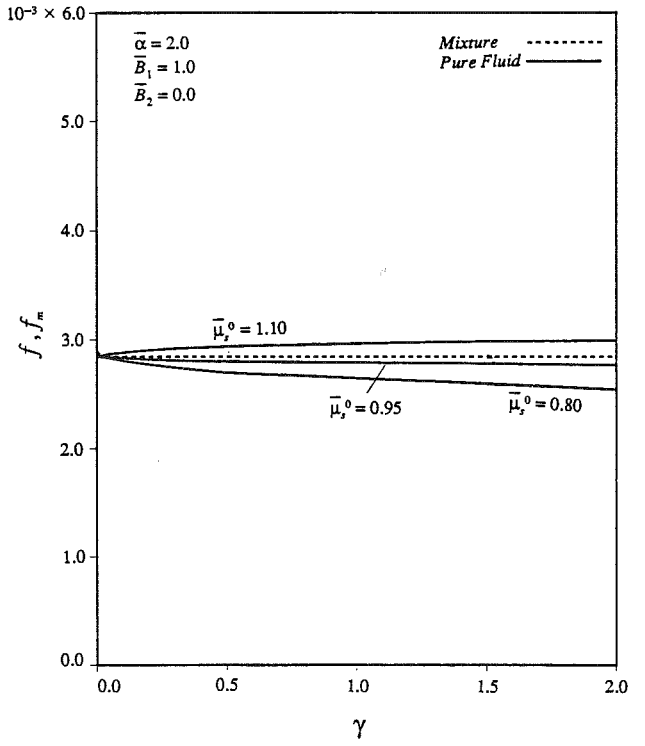


Fig. 12 Effect of solid phase viscosity coefficient $\bar{\mu}_s^0$ on friction coefficient in a journal bearing

increases the load-carrying capacity and decreases the friction coefficient, as shown in Figs. 9 and 10.

6.3.2 Journal Bearing. The dimensionless geometric function of the film thickness in the journal bearing case is given here:

$$\bar{h}(\bar{x}) = 1 + \bar{d}\cos(\bar{x}),$$

where $\bar{h}(\bar{x}) = h(x)/C$, $\bar{x} = x/R = \theta$, $\bar{d} = e/C$, $H = 2\pi R$, $\bar{H} = H/R = 2\pi$, θ is the circumferential coordinate, C ($= h_0$) is the bearing clearance, and R ($= L$) the radius of the journal. The parameter e denotes the eccentricity of the center of the rotating journal from that of the stationary bushing and $\bar{d}$ is defined as the dimensionless eccentricity ratio. For the simulation that follows, it is assumed that

$$\frac{C}{R} = 0.002, \quad \bar{p}_0 = 0, \quad \bar{\mu}_s^1 = 0.$$

The results presented for the journal bearing correspond to the classical assumption of the half-Sommerfeld boundary condition for cavitation, i.e., $\bar{p} = 0$ at $\theta = \pi$ (cf. Cameron, 1967).

Figure 11 shows the pressure distribution of the mixture flow and the pure fluid flow along $\bar{x}$. As in the case of the slider bearing, the magnitude of the pressure in the mixture flow is affected by $\bar{\mu}_s^0$ while the shape remains similar to that of the pure fluid. The effects of the solid phase viscosity coefficient, $\bar{\mu}_s^0$, and the interacting coefficient, $\bar{\alpha}$, on the friction coefficient are presented in Figs. 12 and 13, respectively. Similar trends as in the slider bearing case are also observed in the journal bearing.

Acknowledgments

The authors wish to acknowledge the National Science Foundation, Pittsburgh, Supercomputing Center, and NASA for support of this research at various stages.

References

Bagnold, R. A., 1954, "Experiments of Gravity Free Dispersion of Large Solid Spheres in a Newtonian Fluid Under Shear," *Proceedings of the Royal Society, London*, Vol. A225, p. 49.

Cameron, A., 1967, *The Principles of Lubrication*, John Wiley and Sons, New York.

Campbell, C. S., and Brennen, C. E., 1985, "Computer Simulation of Granular Shear Flows," *J. Fluid Mech.*, Vol. 151, p. 167.

Cowin, S. C., 1974, "A Theory for the Flow of Granular Materials," *Powder Technol.*, Vol. 9, p. 61.

Dai, F., and Khonsari, M. M., 1991, "On the Solution of a Lubrication

Downloaded 03 May 2010 to 171.66.16.245. Redistribution subject to ASME license or copyright; see http://www.asme.org/terms/Terms_Use.cfm

Problem with Particulate Solids," *Int. J. Engng. Sci.*, Vol. 29, No. 9, p. 1019.

Dai, F., Rajagopal, K. R., and Wineman, A. S., 1992, "Non-Uniform Extension of a Non-Linear Viscoelastic Slab," *Int. J. of Solids and Structures*, Vol. 29, No. 7, p. 911.

Homsy, G. M., El-Kaissy, M. M., and Didwania, A., 1980, "Instability Waves and the Origin of Bubbles in Fluidized Beds—II," *Int. J. Multiphase Flow*, Vol. 6, p. 305.

Khonsari, M. M., and Esfahanian, V., 1985, "Thermohydrodynamic Analysis of Solid-Liquid Lubricated Journal Bearings," ASME *Journal of Tribology*, Vol. 110, p. 367.

Khonsari, M. M., Wang, S., and Qi, Y., 1989, "A Theory of Liquid-Solid Lubrication in Elastohydrodynamic Regime," ASME *Journal of Tribology*, Vol. 111, p. 440.

Khonsari, M. M., Wang, S., and Qi, Y., 1990, "A Theory of Thermo-Elastohydrodynamic Lubrication for Liquid-Solid Lubricated Cylinders," ASME *Journal of Tribology*, Vol. 112, p. 259.

Saffman, P. G., 1962, "On the Stability of Laminar Flow of a Dusty Gas," *J. Fluid Mech.*, Vol. 13, p. 120.

Savage, S. B., 1979, "Gravity Flow of Cohesionless Granular Materials in Chutes and Channels," *J. Fluid Mech.*, Vol. 92, p. 53.

Savage, S. B., 1984, "The Mechanics of Rapid Granular Flows," *Adv. Appl. Mech.*, Vol. 24, p. 289.

Downloaded 03 May 2010 to 171.66.16.245. Redistribution subject to ASME license or copyright; see http://www.asme.org/terms/Terms_Use.cfm

Gravity-Driven Flows of Smooth, Inelastic Disks Between Parallel Bumpy Boundaries

M. Babić[1]
Department of Civil and Environmental Engineering, Clarkson University, Potsdam, NY 13676

The problem of a steady gravity-driven granular flow of identical, smooth, slightly inelastic, circular disks between parallel bumpy boundaries is analyzed. The balance laws, constitutive equations and boundary conditions obtained by the kinetic theory (Richman and Chou, 1988) are utilized. Both collisional and transport contributions to the fluxes of momentum and fluctuation energy are considered. The problem is reduced to a system of coupled differential equations governing the transverse variations of granular temperature, shear stress, and solid fraction with the appropriate boundary conditions. The numerical procedure is developed using a variation of shooting method in order to simultaneously satisfy all of the boundary conditions. The particle flux (discharge) calculated using the present theory compares favorably with the data from numerical simulations and air table experiments reported by Sanders et al. (1988).

1 Introduction

Flow of granular materials occurs in many industrial processes involving the rapid transport of bulk materials such as coal, oil shale rubble, ore, and pharmaceuticals, as well as in many geophysical phenomena such as landslides, debris flows, rock falls, snow avalanches, sediment transport, ice jams, etc. Granular materials are discrete systems that can be viewed as a continuum only upon suitable statistical averaging. Macroscopic behavior of the system is then described by differential forms of mass, momentum, and energy conservation laws. The closure of this system requires constitutive equations for the stress tensor, energy flux, and the rate of energy dissipation.

A number of theories has been developed for the rapid granular flows in which the dominant interactions between particles are instantaneous binary collisions. The most detailed development of theory extends the methods from the kinetic theory of dense gases (Chapman and Cowling, 1970) to include the dissipation of energy in inelastic collisions. These theories are based on an approximate solution of the evolution equation for the particle velocity distribution function. Theories developed in this manner include those of Jenkins and Savage (1983), Lun et al. (1984), and Jenkins and Richman (1985a) for systems of smooth, slightly inelastic spheres and Jenkins and Richman (1985b) for rough, slightly inelastic disks. A simplified averaging technique based on a delta function approximation for the fluctuation velocity distribution function has been employed by Shen and Ackermann (1982) for rough spheres and Shen and Ackermann (1984) for rough disks. Improvements introduced by Pasquarell et al. (1988) for disks and Pasquarell and Babić (1990) for spheres have brought these theories in a close agreement with the more sophisticated kinetic theories mentioned above. Babić and Shen (1989) have incorporated effects of the particle transport (kinetic stresses) for disks and spheres.

These theories have all been applied to homogeneous shear flows which are characterized by an uniform velocity gradient, fluctuation energy, and density. The computed stresses were tested against both experiments and numerical simulations. Experiments on steady shearing flows of idealized granular materials have been carried out by Bagnold (1954), Savage and Sayed (1984), Hanes and Inman (1985), and Craig et al. (1987). Particle-tracking numerical simulations of rapid plane flows have been carried out by Campbell and Brennen (1985a) for Couette flow of hard disks, Campbell and Brennen (1985b) for chute flow of hard disks, Campbell and Gong (1986) for simple shear of hard disks, Campbell (1989) for simple shear flow of hard spheres, Walton and Braun (1985) and Babić et al. (1990) for simple shear flow of deformable disks, and Walton and Braun (1987) for simple shear flow of deformable, smooth spheres.

While the comparison of theory with simple shear simulations was remarkable, there was much more difficulty in comparison of theory with shear cell experiments, principally because of significant boundary effects. Generally, slip at the boundary occurs and the apparent shear rate associated with the cell is different from the actual shear rate experienced by contained granular material. The magnitude of slip, actual

[1] Presently at the Department of Civil Engineering and Geological Sciences, University of Notre Dame, Notre Dame, IN 46556.

Contributed by the Applied Mechanics Division of The American Society of Mechanical Engineers for publication in the ASME Journal of Applied Mechanics.

Discussion on this paper should be addressed to the Technical Editor, Professor Leon M. Keer, The Technological Institute, Northwestern University, Evanston, IL 60208, and will be accepted until four months after final publication of the paper itself in the ASME Journal of Applied Mechanics.

Manuscript received by the ASME Applied Mechanics Division, June 4, 1990; final revision, Nov. 8, 1991. Associate Technical Editor: J. T. C. Liu.

Copyright © 1993 by ASME
Downloaded 03 May 2010 to 171.66.16.245. Redistribution subject to ASME license or copyright; see http://www.asme.org/terms/Terms_Use.cfm

shear rate and measured stresses are strongly affected by geometry and roughness of the boundary. This has prompted a strong research activity to complete the mathematical formulation of the problem by derivation of boundary conditions that are as detailed as the derivations of constitutive equations of the flow. Hui et al. (1984) have obtained boundary conditions that complement a phenomenological theory by Haff (1983). Their boundary condition contain several unknown parameters related to the roughness of the boundary. In addition, the effect of slip on the energetics at the boundary was ignored. In the spirit of kinetic theories for granular flows, Jenkins and Richman (1986) have obtained expressions for the rate at which linear momentum and energy are supplied to the flow disks in collisions with the boundary composed of halves of similar disks attached at equal intervals to a flat wall. Then, at the boundary, these rates of supply are balanced with the corresponding quantities in the flow. Boundary roughness is explicitly considered in terms of the diameter of wall particles and the spacing between them. The rates of momentum and energy supply from the boundary to the flow are proportional to the function χ, which accounts for the effects of excluded area and particle shielding. Jenkins and Richman (1986) assumed that χ is an a priori known function of solid fraction (although such an expression is not available). When this assumption is used in the normal force boundary condition, the solid fraction at the wall is forced to assume a fixed, unique value, independent of the flow conditions and boundary properties. This approach leads to uniqueness of steady solutions to the boundary value problem. The average solid fraction could not be specified arbitrarily but was obtained as a part of the solution, thus implying that for any other average solid fraction a steady flow would not be possible. However, this is inconsistent with the results of numerical simulations of Campbell and Brennen (1985a) where steady solutions could be found for any given average solid fraction. Pasquarell (1987) has applied similar procedure to the gravity flow of disks between parallel bumpy boundaries and also obtained only an unique solution, which was inconsistent with the air table experiments and simulations of Sanders et al. (1988).

In a recent work, Hanes et al. (1988) have modified this approach and eliminated the assumption that led to the paradoxical unique solution. They did not assume that χ is a known function of the solid fraction, but rather treated it as a factor of proportionality between the normal force, tangential force and energy flux at the boundary. In this way, χ becomes a flow property which can be determined a posteriori from the solution of the problem. Applied to the Couette flow, the balance equations and boundary conditions led to an eigenvalue relationship between the flow thickness and the ratio of shear to normal force. The profiles of temperature, mean velocity, and solid fraction can be determined using this eigenvalue relationship, and the steady solutions are possible for any specified average solid fraction. The obtained results are in a very good agreement with numerical simulations of Louge et al. (1990), Richman and Chou (1988) improved this solution by considering more accurate velocity distribution function and the transport contributions to momentum and energy fluxes, while in Hanes et al. (1988) only collisional contributions were considered. In a similar manner Richman and Marciniec (1990) obtained an approximate steady solution of the gravity driven granular chute flows of smooth, inelastic spheres down bumpy inclines.

In this paper, the problem of a steady gravity driven flow of identical, smooth, nearly elastic circular disks between parallel bumpy boundaries is solved. Steady solutions can be obtained for any specified average solid fraction. However, because of the fact that shear force varies across the cross-section due to the weight of the flowing material, the problem is mathematically more complex and requires a numerical solution.

2 Theoretical Formulation

The kinetic theory for the rapid granular flows developed by Jenkins and Richman (1985a) provides a system of transport equations for the mean density ρ; the mean velocity $\mathbf{u}$, about which the actual particle velocities fluctuate; and the granular temperature T, which is a measure of the kinetic energy per unit mass associated with velocity fluctuations. The mean density ρ is equal to the product of the particle mass m and the mean number of disks per unit area n, or, equivalently, to the product of the mean solid fraction (concentration) ν and the particle density ρ_s. The balance equation for the mass is

$$\dot{\rho} + \rho \nabla \cdot \mathbf{u} = 0, \tag{1}$$

where an overdot indicates the time derivative following the mean motion. The balance equation for the linear momentum is

$$\rho \dot{\mathbf{u}} = \nabla \cdot \mathbf{P} + \rho \mathbf{g}, \tag{2}$$

where $\mathbf{P}$ is the stress tensor and $\mathbf{g}$ is the body force per unit mass. The balance equation for the fluctuation energy is

$$\rho \dot{T} = -\nabla \cdot \mathbf{q} + \mathrm{tr}(\mathbf{P} \cdot \nabla \mathbf{u}) - \gamma, \tag{3}$$

where $\mathbf{q}$ is the flux of fluctuation energy and γ is the rate of energy dissipation in inelastic collisions per unit volume.

These equations are applied to the problem of steady uniform flow of disks between two parallel rough boundaries (Fig. 1).

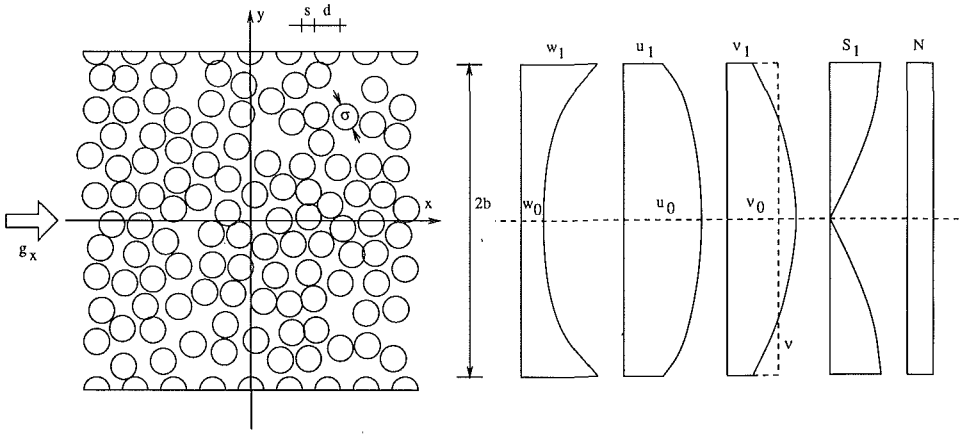


Fig. 1 Gravity driven flow of disks in a channel. Schematic profiles left to right: *w*, *u*, *ν*, *S*, *N*.

Downloaded 03 May 2010 to 171.66.16.245. Redistribution subject to ASME license or copyright; see http://www.asme.org/terms/Terms_Use.cfm

The nominal width of the flow domain is $2b = W - d$. The flow is driven by the gravity component g_x in the x-direction. In the flow, the x-component u of the mean velocity $\mathbf{u}$, the mean density ρ and the granular temperature T are functions of y only. In this case, Eq. (1) is satisfied identically and the x and y-components of Eq. (2) become $dS/dy = \rho g_x$ and $dN/dy = 0$, where $N = -P_{yy}$, $S = -P_{yx}$. The normal force N is constant across the channel width, and the shear force S varies between $S(y=0) = 0$ and $S(y=b) = S_1 = \rho_s g_x \bar{\nu} b$, where $\bar{\nu}$ is the average solid fraction. Energy balance Eq. (3) reduces to

$$\frac{dQ}{dy} + S\frac{du}{dy} + \gamma = 0, \tag{4}$$

where $Q \equiv q_y$. In order to formulate a closed system of equations for the problem, a set of the constitutive equations for S, N, Q, and γ in terms of the mean fields ρ, u, and T is needed. The constitutive equations used in this study are essentially the same as the ones used by Richman and Chou (1988) for an analysis of the Couette flows of disks. The expressions for N, S, Q, and γ are

$$N = 2\rho GFT \tag{5}$$

$$S = -\frac{1}{\sqrt{\pi}}\rho GJ\sigma\sqrt{T}\frac{du}{dy} \tag{6}$$

$$Q = -\frac{2}{\sqrt{\pi}}\rho GM\sigma\sqrt{T}\frac{dT}{dy} \tag{7}$$

$$\gamma = \frac{8}{\sqrt{\pi}}(1-e)\rho G\frac{T^{3/2}}{\sigma}. \tag{8}$$

In the above equations, σ is the particle diameter, e is the coefficient of restitution which is a measure of the energy lost in an inelastic collision, and G, F, J, and M are functions of solid fraction ν given by $G(\nu) = \nu g_o$, $F(\nu) = 1 + 1/2G$, $J(\nu) = 1 + (\pi/8)(1 + 1/G)^2$ and $M(\nu) = 1 + (\pi/4)(3/2 + 1/G)^2$.

Function $g_o(\nu) = (1 - 7\nu/16)/(1-\nu)^2$ is the radial distribution function evaluated at the point of contact. The above approximation for g_o, introduced by Verlet and Levesque (1982), is in an excellent agreement with the results of numerical simulations performed by Hoover and Alder (1967) on systems of hard, elastic disks. Physically, function g_o accounts for the increased probability of collisions at higher concentrations due to the effects of excluded area and particle shielding.

Using (5) in (6), (7), and (8), denoting $w = \sqrt{T}$, one obtains

$$\frac{du}{dy} = -2\sqrt{\pi}\frac{F}{J}\frac{S}{N}\frac{w}{\sigma} \tag{9}$$

$$Q = -\frac{2}{\sqrt{\pi}}\frac{M}{F}N\sigma\frac{dw}{dy} \tag{10}$$

$$\gamma = \frac{4}{\sqrt{\pi}}(1-e)\frac{N}{F}\frac{w}{\sigma}. \tag{11}$$

Substituting (9), (10), and (11) into (4), one obtains

$$\sigma^2\left[\frac{d^2w}{dy^2} - \frac{dw}{dy}\frac{dv}{dy}\frac{d}{dv}\ln(F/M)\right] + \left[\frac{\pi F^2}{JM}\frac{S^2}{N^2} - \frac{2}{M}(1-e)\right]w = 0. \tag{12}$$

From Eq. (5), the gradient of the solid fraction can be expressed as

$$\frac{dv}{dy} = -\frac{2}{w}\frac{dw}{dy}\left[\frac{d}{dv}\ln(\nu GF)\right]^{-1}. \tag{13}$$

Introducing dimensionless variables $W = w/\sqrt{g_x b}$, $U = u/\sqrt{g_x b}$, $S^* = S/S_1$, $\lambda = S_1/N$, $Y = y/b$ and $\beta = b/\sigma$, substituting (13) into (12) and rearranging, one obtains

$$\frac{W''}{W} + H\left(\frac{W'}{W}\right)^2 + \beta^2\left(\frac{\pi F^2}{JM}\lambda^2 S^{*2} - \frac{2}{M}(1-e)\right) = 0 \tag{14}$$

where a prime denotes differentiation with respect to Y, and $H(\nu)$ is given by

$$H(\nu) = 2\frac{d}{dv}\ln(F/M)\left[\frac{d}{dv}\ln(\nu GF)\right]^{-1}. \tag{15}$$

Equation $ds/dy = \rho g_x$ reduces to

$$dS^*/dY = \nu/\bar{\nu}, \tag{16}$$

and Eq. (5) reduces to

$$\nu GF = \frac{\bar{\nu}}{2\lambda W^2}. \tag{17}$$

The derivation presented above follows closely the derivation presented by Richman and Chou (1988), and the resulting Eq. (14) is essentially the same as their Eq. (28). They also showed that function H ranges from $H(0) = 1/2$ $H(1) = 0$. When the transport contributions to the stresses and energy flux are neglected, $G = 0$, $F = 1$, $J = 1 + \pi/8$, $M = 1 + 9\pi/16$ are constants and $H = 0$. In this particular case, Eq. (14) reduces to Eq. (13) of Hanes et al. (1988). In the case of the Couette flow studied by Hanes et al. (1988) and Richman and Chou (1988), S/N is a constant. In the dense limit (Hanes et al., 1988) the corresponding equation for w is linear and decoupled from other mean fields, thus allowing further analytical developments. The present problem, however, consists of a coupled set of differential Eqs. (14) and (16) for W and S^* with a algebraic relation (17) between ν and W. This coupled problem is mathematically considerably more complex.

Before attempting to solve the set of equations obtained above, the boundary conditions have to be formulated first. The boundary consists of a flat wall to which identical half-disks of diameter d are attached and evenly spaced a distance s apart. The boundary conditions at the bumpy wall essentially express the balance of momentum and fluctuation energy at the wall. The balance of momentum at a point on the boundary with unit inward normal $\mathbf{n}$ requires that $\mathbf{M} = -\mathbf{P}\cdot\mathbf{n}$, where $\mathbf{M}$ is the rate of momentum transfer from the boundary to the flow per unit length of the boundary. For the boundary at $y = b$, $n_x = 0$, $n_y = -1$, and x and y-components of the boundary momentum balance become $M_x = P_{yx} = -S_1$ and $M_y = P_{yy} = -N$, respectively. The balance of energy at a point on the boundary with unit inward normal $\mathbf{n}$ requires that $\mathbf{M}\cdot\mathbf{n} - D = \mathbf{Q}\cdot\mathbf{n}$, where D is the rate of energy dissipation in inelastic collisions between the flow particles and the boundary particles per unit length of the boundary, and $\mathbf{v}$ is the slip velocity which is equal to the difference between the velocity of the boundary and the flow velocity at the boundary. For the stationary boundary at $y = b$, $v_x = -u_1$, $v_y = 0$, where $u_1 = u(b)$. Since $\mathbf{q}\cdot\mathbf{n} = -q_y = -Q$, the equation of energy balance at the boundary becomes $S_1 v_1 - D = -Q$.

The expressions for $\mathbf{M}$ and D have been obtained by Richman and Chou (1988) for the case of slightly inelastic boundary collisions. They performed averaging of the change of momentum or energy in a collision over the probable frequency of collisions. The dense limit of these expressions has been used by Hanes et al. (1988) in the Couette flow study. In the present study, the expressions used by Richman and Chou (1988) are utilized. The y-component of $\mathbf{M}$ can be expressed as

$$M_y = -\rho\chi w^2. \tag{18}$$

The x-component of $\mathbf{M}$ can be expressed as

$$M_x = -(2/\pi)^{1/2}\rho\chi w(\theta\csc\theta - \cos\theta) \times \left[u_1 + \bar{\sigma}\frac{du}{dy}\left(1 - \frac{2/3(1 + B\sigma/\bar{\sigma})\sin^2\theta}{\theta\csc\theta - \cos\theta}\right)\right] \tag{19}$$

Downloaded 03 May 2010 to 171.66.16.245. Redistribution subject to ASME license or copyright; see http://www.asme.org/terms/Terms_Use.cfm

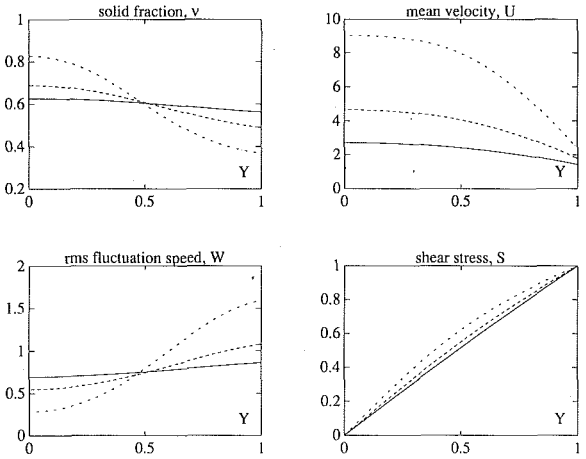


Fig. 2 Profiles of ν, U, W and S for $\bar{\nu}=0.60$, $\epsilon=0.65$, $e=0.95$, $d/\sigma=1$, $s/d=0$. Solid line: $\beta=5$, dashed line: $\beta=10$, dash-dot line: $\beta=20$.

where $\sin\theta=(d+s)/(d+\sigma)$, $\bar{\sigma}=(d+\sigma)/2$, and $B(\nu)=(\pi/8\sqrt{2})(1+1/G)$. The rate of energy dissipation per unit length of the boundary D can be expressed as

$$D=(2/\pi)^{1/2}\theta\csc\theta\,\rho\chi(1-\epsilon)w^3, \tag{20}$$

where ϵ is the coefficient of restitution for a collision between a wall disk and a flow disk. In Eqs. (18), (19), and (20) the function χ accounts for the effects of excluded area and particle shielding on the frequency of boundary collisions. The normal momentum boundary condition yields

$$N=\rho\chi w_1^2, \tag{21}$$

where $w_1=w(b)$. Using (9) is used to eliminate du/dy, and (21) to eliminate χ, the tangential momentum boundary condition yields

$$\frac{u_1}{w_1}=Z\frac{S_1}{N}, \tag{22}$$

where Z is a function of the solid fraction at the boundary ν_1 (through F, J and B) and boundary roughness (through θ and $\bar{\sigma}/\sigma$) given by

$$Z(\nu_1)=\sqrt{\frac{\pi}{2}}\left(\frac{1-(4\sqrt{2}/3)(F/J)(\bar{\sigma}/\sigma)(1+B\sigma/\bar{\sigma})\sin^2\theta)}{\theta\csc\theta-\cos\theta}\right)+2\sqrt{\pi}\frac{F}{J}\frac{\bar{\sigma}}{\sigma}. \tag{23}$$

Finally, employing (10), (22), (20), and (21) in the energy boundary condition yields

$$\frac{W'}{W}(1)=\beta\frac{\sqrt{\pi}}{2}\frac{F}{M}(\lambda^2 Z-\theta\csc\theta(1-\epsilon)). \tag{24}$$

Equation (24) corresponds to Eq. (34) of Richman and Chou (1988). In the dense limit, when transport contributions are neglected, Eq. (24) corresponds to Eq. (22) of Hanes et al. (1988). Equation (24) is the boundary condition on w at the bumpy wall ($y=b$). The boundary condition on S^* at the wall is $S^*(1)=1$. Because of the symmetry, the boundary conditions at the centerline ($Y=0$) are simply: $W'(0)=0$, $\nu'(0)=0$ and therefore $S^*(0)=0$.

3 Solution Procedure

The problem has been reduced to a system of differential Eqs. (14) and (16) with algebraic relation (17) between ν and W. These equations contain the following parameters: the average solid fraction $\bar{\nu}$, the dimensionless half-width β, the ratio of shear to normal stress at the wall λ, boundary geometry parameters d/σ and s/d, and restitution coefficients e and ϵ. If all of these parameters would be arbitrarily fixed, it would not be possible to solve the system (14) and (16) and satisfy all boundary conditions. It therefore follows that one of the parameters is also part of the solution, since only for the particular choice of this parameter (an eigenvalue) can all boundary conditions be satisfied.

In the following solution procedure boundary geometry, restitution coefficients, the average solid fraction and the width of the channel are specified, but the stress ratio λ is treated as an unknown parameter which is a part of the solution. Steady solutions to the problem are found by a trial-and-error search. The trial-and-error procedure is based on a numerical solution of Eqs. (14) and (16) by the Runge-Kutta method. The initial guesses for $W_o=W(0)$ and λ are specified. Functions f_1 and f_2 which measure a deviation from specified boundary conditions at the wall are calculated as

$$f_1(W_o,\lambda)=\frac{W'}{W}(1)-\beta\frac{\sqrt{\pi}}{2}\frac{F}{M}(\lambda^2 Z-\theta\csc\theta(1-\epsilon)) \tag{25}$$

$$f_2(W_o,\lambda)=S^*(1)-1. \tag{26}$$

We are looking for the values of (W_o,λ) for which the implicitly defined, nonlinear functions f_1 and f_2 are both equal to zero. This root finding problem is numerically solved utilizing the IMSL routine DNEQNF. This routine uses a variation of Newton's method (Levenberg-Marquardt algorithm and a finite difference approximation to the Jacobian) to solve a system of nonlinear equations. This algorithm converges to the root in a few iterations provided that an initial guesses for W_o and λ are not too far from correct values. Once the correct values of W_o and λ are obtained, the profiles of W, S^*, and ν are obtained using the final call to the Runge-Kutta solver. The profile of the mean velocity U is then obtained by the numerical integration of (9). Once the profiles of ν and U are known, the mass flux $\dot{m}$ across the channel width can be calculated as

$$\dot{m}=2\int_0^b\rho(y)u(y)dy. \tag{27}$$

The mass flux can be expressed in terms of the dimensionless particle flux q, which is defined as

$$q=\frac{\dot{m}}{2b\rho_s\sqrt{g_x b}}=\int_0^1\nu(Y)U(Y)dY \tag{28}$$

4 Results

Figure 2 shows profiles of $W(Y)$, $S^*(Y)$, $\nu(Y)$, and $U(Y)$, for $\bar{\nu}=0.6$, $e=0.95$, $\epsilon=0.65$, $d/\sigma/=1$, $s/d=0$. It can be seen that W is a monotonically increasing function of Y. The fluctuation energy is higher near the wall than near the centerline, and the energy flows from the wall towards the centerline.

In Figs. 3 and 4, dimensionless particle flux q is plotted versus $\bar{\nu}$ and compared with the data from the air table experiments and numerical simulations reported by Sanders et al. (1988). In Fig. 3, the ratio of the channel width to the particle diameter is 10.3 ($\beta=4.65$). In Fig. 4, the ratio of the channel width to the particle diameter ratio is 6 ($\beta=2.5$). Recall $\beta=[W-d]/2\sigma$. The present theory and experimental data are in a good qualitative agreement. However, theoretically predicted discharge rates are lower then experimental by as much as 30 percent. A discussion of possible reasons for this discrepancy is postpones until the next section.

In Fig. 5, q is plotted versus β for several values of $\bar{\nu}$. The dependence of q on β appears to be approximately linear. As a consequence of this, the boundary "drag coefficient" $S_1/(\rho g_x b q^2)$ is proportional to β^{-2}, i.e., to the square of particle diameter. This result may be of interest for an approximate closure of a phenomenological one-dimensional model.

Downloaded 03 May 2010 to 171.66.16.245. Redistribution subject to ASME license or copyright; see http://www.asme.org/terms/Terms_Use.cfm

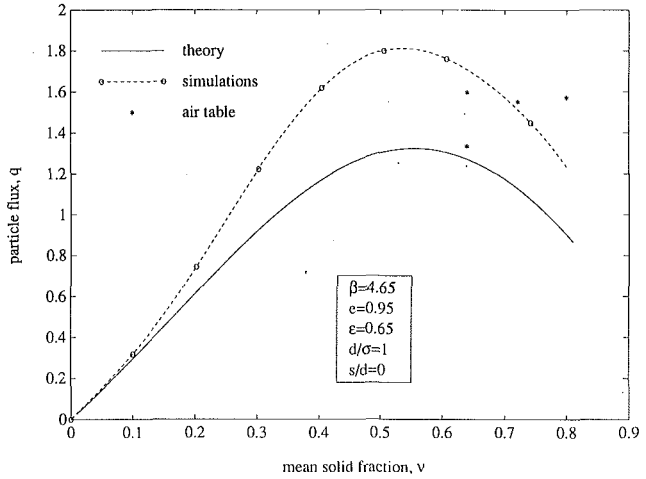


Fig. 3 Dimensionless particle flux q versus average solid fraction $\bar{\nu}$ for $W/\sigma = 10.3$. (Comparison with simulation and experimental data of Sanders et al. (1988).)

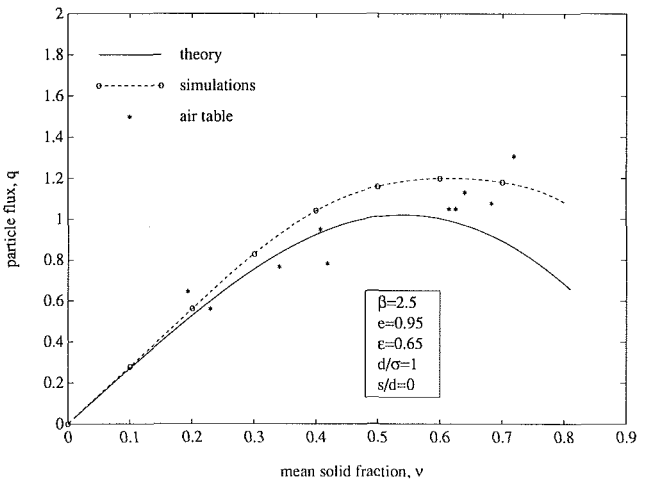


Fig. 4 Dimensionless particle flux q versus average solid fraction $\bar{\nu}$ for $W/\sigma = 6$. (Comparison with simulation and experimental data of Sanders et al. (1988).)

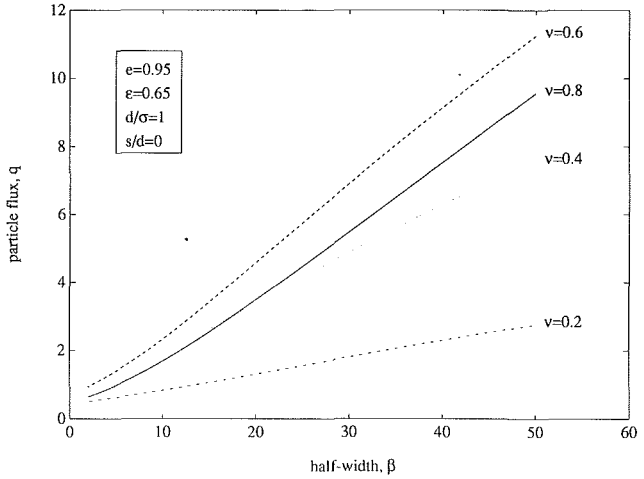


Fig. 5 Dimensionless particle flux q versus dimensionless half-width β

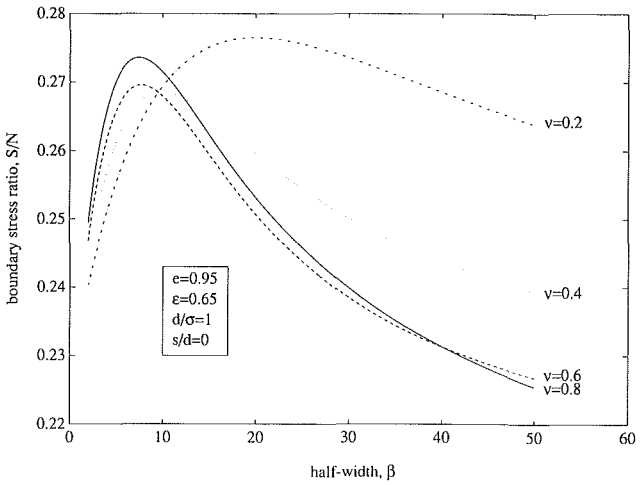


Fig. 6 Shear to normal boundary stress ratio S/N versus dimensionless half-width β

In Fig. 6, the ratio of shear to normal stress at the boundary $\lambda = S_1/N$ is plotted versus β for several values of $\bar{\nu}$. It can be seen that for high values of $\bar{\nu}$, λ exhibits a maximum near $\beta = 8$, while for lower values of $\bar{\nu}$, the maximum shifts towards higher values of β.

The results presented above are obtained for the particular set of parameters $e = 0.95$, $\epsilon = 0.65$, $d/\sigma = 1$ and $s/d = 0$. All of the trends described above do not change for different combinations of parameters.

5 Conclusions

In this paper, the problem of a steady gravity-driven granular flow of identical, smooth, slightly inelastic, circular disks between parallel bumpy boundaries is analyzed. The balance laws, constitutive equations, and boundary conditions obtained by the kinetic theory (Richman and Chou (1988)) are utilized. Both collisional and transport contributions to the fluxes of momentum and fluctuation energy are considered. The problem is reduced to a system of coupled differential equations governing the transverse variations of temperature, shear stress, and solid fraction. Boundary conditions at the bumpy wall essentially express the balance of linear momentum and fluctuation energy. These boundary conditions are manipulated in the same way as in the recent works of Hanes et al. (1988) and Richman and Chou (1988). This approach leads to a range of steady solutions over the full range of solid fractions, unlike the previous approach of Jenkins and Richman (1986) and Pasquarell (1987) which lead to a paradoxical unique solution.

The numerical procedure is developed using a variation of shooting method in order to simultaneously satisfy all of the boundary conditions. The parameters that have to be specified include the dimensionless channel half-width β, average solid fraction $\bar{\nu}$, restitution coefficients e and ϵ, and boundary roughness parameters d/σ and s/d. The results include the profiles of temperature, solid fraction, shear stress, and mean velocity; ratio of the shear to normal stress at the boundary λ; and dimensionless particle flux q.

The dimensionless particle flux q calculated using the present theory is compared with the data from the numerical simulations and air table experiments reported by Sanders et al. (1988). A good qualitative agreement is obtained. Theoretically predicted discharge rates are lower than experimental by as much as 30 percent.

The first reason for discrepancy which comes to mind is the fact that experimental results are obtained with frictional disks (coefficient of friction $\mu = 0.112$), while the theory considers smooth, frictionless disks. The effect of friction can be indirectly deduced by comparing the results of simulations with $\mu = 0.114$ (Sanders et al., 1988) and simulations with $\mu = 0$

Downloaded 03 May 2010 to 171.66.16.245. Redistribution subject to ASME license or copyright; see http://www.asme.org/terms/Terms_Use.cfm

(Babić, 1990). For example, for $\bar{\nu}=0.5$ and $\beta=4.65$, the particle flux from simulations are: for $\mu=0.114$, $q=1.7975$; for $\mu=0$, $q=1.6323$; and the theoretical prediction is $q=1.3029$. Hence, the actual discrepancy between theory for $\mu=0$ and simulations for $\mu=0$ is 25 percent. The difference between simulations for $\mu=0.114$ and $\mu=0$ is 26 percent. The effect of friction can not account for the entire discrepancy between the theoretical solution and the experimental/simulation data.

The other possible source of the discrepancy lies in the fact that constitutive equations and boundary conditions utilized in the present study have been derived for slightly inelastic collisions, i.e., for small values of $1-e$ and $1-\epsilon$, respectively. The results presented in this paper have been obtained for the wall restitution coefficient $\epsilon=0.65$, in order to perform comparison with the experimental data.

Finally, a part of the discrepancy may be due to the fact that even for moderately high solid fractions particles tend to form a densely packed "plug" in the middle of the channel (Sanders et al., 1988). The stresses in the plug can not be described by the constitutive equations used in this study, which are appropriate for the rapidly deforming granular material. In order to tackle the problem of plug formation, one could follow the approach of Jenkins and Askari (1991) and consider two distinct flow regions: (i) the region within the plug, in which the material behaves like a "glassy solid" and (ii) the region between the plug and the wall, in which the material behaves like a granular fluid. The interface between the two regions would occur at the solid fraction corresponding to the phase change transition. Such an extension of the present work will be considered in the future.

Acknowledgments

Helpful comments from Dr. Hayley H. Shen and Dr. Hung Tao Shen are appreciated. This study was supported by the U.S. Army Cold Regions Research and Engineering Laboratory through Contract No. DACA89-87-K-001.

References

Babić, M., 1990, "Discrete Element Modeling of Granular Flows," PhD Thesis, Clarkson University, Potsdam, New York.

Babić, M., and Shen, H. H., 1989, "Simple Mean Free Path Theory for Rapid Granular Flows," *J. Engng. Mech. Div., ASCE*, Vol. 120, pp. 1262–1282.

Babić, M., Shen, H. H., and Shen, H. T., 1990, "The Stress Tensor in Granular Shear Flows of Uniform, Deformable Disks at High Solids Concentrations," *J. Fluid Mech.*, Vol. 219, pp. 81–118.

Bagnold, R. A., 19545, "Experiments on Gravity-Free Dispersion of Large Solid Spheres in a Newtonian Fluid Under Shear," *Proc. Royal Soc. London*, Vol. A225, pp. 49–63.

Campbell, C. S., 1989, "The Stress Tensor for Simple Shear Flows of a Granular Material," *J. Fluid Mech.*, Vol. 203, pp. 449–473.

Campbell, C. S., and Brennen, C. E., 1985a, "Computer Simulation of Granular Shear Flows," *J. Fluid Mech.*, Vol. 151, pp. 167–188.

Campbell, C. S., and Brennen, C. E., 1985b, "Chute Flows of Granular Materials: Some Computer Simulations," ASME JOURNAL OF APPLIED MECHANICS, Vol. 52, pp. 172–178.

Campbell, C. S., and Gong, A., 1986, "The Stress Tensor in a Two-Dimensional Granular Shear Flow," *J. Fluid Mech.*, Vol. 164, pp. 107–125.

Chapman, S., and Cowling, T. G., 1970, *The Mathematical Theory of Non-uniform Gases*, 3rd ed., Cambridge University Press, Cambridge, U.K.

Craig, K., Buckholz, R. H., and Domoto, G., 1987, "The Effects of Shear Surface Boundaries on Stresses for the Rapid Shearing of Dry Metal Powders: An Experimental Study," ASME *Journal of Tribology*, Vol. 109, pp. 232–237.

Haff, P. K., 1983, "Grain Flow as a Fluid-Mechanical Phenomenon," *J. Fluid Mech.*, Vol. 134, pp. 401–430.

Hanes, D. M., and Inman, D. L., 1985, "Observations of Rapidly Flowing Granular Fluid Materials," *J. Fluid Mech.*, Vol. 150, pp. 357–380.

Hanes, D. M., Jenkins, J. T., and Richman, M. W., 1988, "The Thickness of Steady Plane Shear Flows of Circular Disks Driven by Identical Boundaries," ASME JOURNAL OF APPLIED MECHANICS, Vol. 55, pp. 969–974.

Hoover, W. G., and Alder, B. J., 1967, "Studies in Molecular Dynamics: IV—The Pressure, Collision Rate and Their Number Dependence for Hard Disks," *J. Chem. Phys.*, Vol. 46, pp. 686–691.

Hui, K., Haff, P. K., Ungar, J. E., and Jackson, R., 1984, "Boundary Conditions for High-Shear Grain Flows," *J. Fluid Mech.*, Vol. 145, pp. 223–233.

Jenkins, J. T., and Askari, E., 1991, "Boundary Conditions for Granular Flows: Phase Interfaces," *J. Fluid Mech.*, Vol. 223, pp. 497–508.

Jenkins, J. T., and Richman, M. W., 1985a, "Grad's 13-Moment System for a Dense Gas of Inelastic Spheres," *Arch. Rat. Mech. Anal.*, Vol. 87, pp. 355–377.

Jenkins, J. T., and Richman, M. W., 1985b, "Kinetic Theory for Plane Shear Flows of a Dense Gas of Identical, Rough, Inelastic, Circular Disks," *Phys. Fluids*, Vol. 28, pp. 3485–3494.

Jenkins, J. T., and Richman, M. W., 1986, "Boundary Conditions for Plane Flows of Smooth, Nearly Elastic, Circular Disks," *J. Fluid Mech.*, Vol. 171, pp. 53–69.

Jenkins, J. T., and Savage, S. B., 1983, "A Theory for the Rapid Flow of Identical, Smooth, Nearly Elastic, Spherical Particles," *J. Fluid Mech.*, Vol. 130, pp. 187–202.

Louge, M. Y., Jenkins, J. T., and Hopkins, M. A., 1990, "Computer Simulations of Rapid Granular Shear Flows Between Parallel Bumpy Boundaries," *Phys. Fluids A*, Vol. 2, pp. 1042–1044.

Lun, C. K. K., and Savage, S. B., 1987, "A Simple Kinetic Theory for Granular Flow of Rough, Inelastic, Spherical Particles," ASME JOURNAL OF APPLIED MECHANICS, Vol. 54, pp. 47–53.

Lun, C. K. K., Savage, S. B., Jeffrey, D. J., and Chepurney, N., 1984, "Kinetic Theories for Granular Flow: Inelastic Particles in a Couette Flow and Slightly Inelastic Particles in a General Flowfield," *J. Fluid Mech.*, Vol. 140, pp. 223–256.

Pasquarell, G. C., 1987, "Boundary Value Problems for Planar, Smooth, Rapidly Sheared Granular Flows Including Phase Changes," PhD Thesis, Clarkson University, Potsdam, New York.

Pasquarell, G. C., Ackermann, N. L., Shen, H. H., and Hopkins, M. A., 1988, "Collisional Stresses in Granular Flows: Bagnold Revisited," *J. Engng. Mech. Div., ASCE*, Vol. 114, pp. 49–64.

Pasquarell, G. C., and Babić, M., 1990, "On the Form of the Velocity Distribution Function for Rapid Granular Flows," *J. Engng. Mech. Div., ASCE*, Vol. 116, pp. 1261–1275.

Richman, M. W., and Chou, C. S., 1988, "Boundary Effects on Granular Shear Flows of Smooth Disks," *ZAMP*, Vol. 39, pp. 885–901.

Richman, M. W., and Marciniec, R. P., 1990, "Gravity-Driven Granular Flows of Smooth Inelastic Spheres Down Bumpy Inclines," ASME JOURNAL OF APPLIED MECHANICS, Vol. 57, pp. 1036–1043.

Sanders, B. E., Hopkins, M. A., and Ackermann, N. L., 1988, "Physical Experiments and Numerical Simulation of Two Dimensional Chute Flow," *Micromechanics of Granular Materials*, M. Satake and J. T. Jenkins, eds., Elsevier, New York.

Savage, S. B., 1978, "Experiments on Shear Flows of Cohensionless Granular Materials," *Continuum Mechanical and Statistical Approaches in the Mechanics of Granular Material*, S. Cousin and M. Satake, eds., pp. 241–254.

Savage, S. B., and Sayed, M., 1984, "Stresses Developed by Dry Cohensionless Material Sheared in an Annular Shear Cell," *J. Fluid Mech.*, Vol. 142, pp. 453–472.

Shen, H. H., and Ackermann, N. L., 1982, "Constitutive Equations for Fluid-Solid Mixtures," *J. Engng. Mech. Div., ASCE*, Vol. 108, pp. 748–762.

Shen, H. H., and Ackermann, N. L., 1984, "Constitutive Equations for a Simple Shear Flow of Disk Shaped Granular Mixture," *Intl. J. Engng. Sci.*, Vol. 22, pp. 829–843.

Verlet, L., and Levesque, D., 1982, "Integral Equations for Classical Fluids: III—The Hard Discs System," *Molecular Physics*, Vol. 46, pp. 969–980.

Walton, O. R., and Braun, R. L., 1985, "Viscosity, Granular Temperature and Stress Calculations for Shearing Assemblies of Inelastic, Frictional Disks," *J. Rheol.*, Vol. 30, pp. 949–980.

Walton, O. R., and Braun, R. L., 1987, "Stress Calculations for Assemblies of Inelastic Spheres in Uniform Shear," *Acta Mech.*, Vol. 63, pp. 73–86.

Downloaded 03 May 2010 to 171.66.16.245. Redistribution subject to ASME license or copyright; see http://www.asme.org/terms/Terms_Use.cfm

An Inviscid Analysis in Polar Coordinates of Flow Between Two Flat Plates

D. N. Contractor
Department of Civil Engineering
and Engineering Mechanics,
University of Arizona,
Tucson, AZ 85721
Mem. ASME

An inviscid analysis is conducted of two-dimensional flow between a flat plate pivoting about an external point and falling onto another plate at rest. The motion of the fluid between the two plates is analyzed by the simultaneous solution of the unsteady Bernoulli equation, the equation of continuity, and the equation of motion for the plate. Numerical solution of the equations resulted in velocities and pressures along the plate as a function of time. The pressures were integrated to yield forces and moments on the falling plate. The results are compared with the motion of a horizontal flat plate falling vertically onto a rigid stationary flat plate. The two results are similar to one another.

Introduction

An inviscid analysis is made of the fluid between a horizontal flat plate and another plate falling onto it by pivoting about an external point. This kind of motion occurs when glassmakers want to stack glass plates one on top of the other. They either let one plate fall vertically on the other or they line up the edges of the two plates and let the upper plate fall by rotation onto the stationary plate. In either case, the pressure of the air between the two plates slows down the upper plate to such an extent that no damage occurs.

The fluid mechanics of colliding plates has been studied by Yih, 1974. He presented results for plates of different shapes falling vertically and rotating. However, he neglected the angular acceleration of the falling plates in the equation of motion of the plate. Weinbaum et al. (1985) have presented analytic solutions for inviscid flow and for small Reynolds numbers for the fluid between parallel plates with a constant normal force. They dealt with radial flow occurring between the plates and included the inertia of the moving body. Lawrence et al. (1985) followed up the previous paper by presenting boundary layer and exact numerical solutions, for the case of negligible inertia of the moving body. Lawrence and Weinbaum (1988) have analyzed the motion of a flat body moving toward a parallel plane surface in an incompressible fluid both in the presence and absence of an applied force for a nonvanishing initial velocity. Raichlen (1990) has presented a theoretical development of the motion of a two-dimensional rectangular plate falling vertically onto a hard surface.

This paper analyses the inviscid motion of a fluid between a stationary horizontal flat plate and another flat plate rotating about an external point and falling on it. (See Fig. 1.) The motion is studied for small angles, θ, so that $\cos\theta \approx 1$ and $\sin\theta \approx \theta$. As the plate falls, the fluid at radius r_2 is forced out away from the center of rotation and at radius r_1 the fluid flows toward the center. This results in a stagnation point on the stationary plate and a streamline that separates the flow moving away from and toward the center of rotation. The location, r_*, of this dividing streamline is an important outcome of the theory. It does not occur at the center of the plate as it would for a horizontal plate falling vertically. It occurs slightly toward the center of rotation. The problem involves the simultaneous solution of three differential equations: the equation of continuity, the unsteady Bernoulli equation, and the equation of motion for the plate. The nonlinear equations are solved numerically for $\dot{\theta}$, θ and r_* as functions of time. All other parameters of interest are calculated from these parameters, e.g., velocities, pressures, accelerations, forces, and moments.

Equation of Continuity

The two-dimensional equation of continuity in polar coordinates is given as follows:

$$\frac{1}{r}\frac{\partial(ru_r)}{\partial r}+\frac{1}{r}\frac{\partial(u_\theta)}{\partial\theta}=0 \tag{1}$$

when u_r, u_θ, are the velocities in the radial and θ directions.

Thus,

$$\frac{\partial(ru_r)}{\partial r}=\frac{-\partial u_\theta}{\partial\theta}. \tag{2}$$

If we make the assumption that $u_r = f(r, t) \neq f(\theta)$, then the left-hand side of Eq. (2) will also not be a function of θ.

Contributed by the Applied Mechanics Division of THE AMERICAN SOCIETY OF MECHANICAL ENGINEERS for publication in the ASME JOURNAL OF APPLIED MECHANICS.

Discussion on this paper should be addressed to the Technical Editor, Professor Lewis T. Wheeler, Department of Mechanical Engineering, University of Houston, Houston, TX 77204-4792, and will be accepted until four months after final publication of the paper itself in the ASME JOURNAL OF APPLIED MECHANICS.

Manuscript received by the ASME Applied Mechanics Division, Apr. 29, 1991; final revision, Jan. 24, 1992. Associate Technical Editor: K. Sreenivasan.

Copyright © 1993 by ASME
Downloaded 03 May 2010 to 171.66.16.245. Redistribution subject to ASME license or copyright; see http://www.asme.org/terms/Terms_Use.cfm

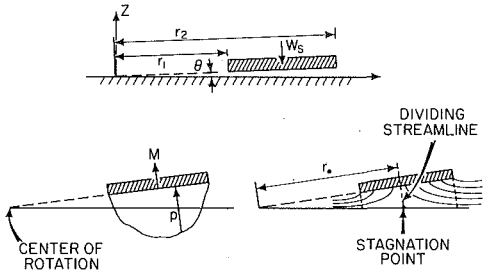


Fig. 1 Definition of problem geometry in polar coordinates

$$\int_0^{\theta_p r} -\partial u_\theta = \int_0^{\theta_p} \frac{\partial (ru_r)}{\partial r}\, d\theta = \frac{\partial (ru_r)}{\partial r} \int_0^{\theta_p} d\theta \tag{3}$$

where θ_p is the inclination of the plate and $\dot{\theta}_p$ is the angular velocity of the plate.

$$-\dot{\theta}_p r = \frac{\partial (ru_r)}{\partial r}\theta_p \tag{4}$$

or

$$\frac{\partial (ru_r)}{\partial r} = \frac{-\dot{\theta}_p}{\theta_p} r \tag{5}$$

$$\int_{ru_r}^{0} d(ru_r) = \int_r^{r_*} -\frac{\dot{\theta}_p}{\theta_p} r\, dr \tag{6}$$

$$u_r = \frac{\dot{\theta}_p}{\theta_p}\left(\frac{r_*^2 - r^2}{2r}\right). \tag{7}$$

The subscripts p and r will be dropped from here on for the sake of simplicity. Thus,

$$u = \frac{\dot{\theta}}{\theta}\left(\frac{r_*^2 - r^2}{2r}\right). \tag{8}$$

Unsteady Bernoulli Equation

The unsteady Bernoulli equation is derived in textbooks of fluid mechanics and is presented here.

$$\int \frac{\partial u}{\partial t} dr + \frac{V^2}{2} + \frac{p}{\rho} + gZ = \text{constant or } F(t) \tag{9}$$

Differentiating Eq. (8), we get

$$\frac{\partial u}{\partial t} = \left(\frac{\ddot{\theta}}{\theta} - \left(\frac{\dot{\theta}}{\theta}\right)^2\right)\left(\frac{r_*^2 - r^2}{2r}\right) + \frac{\dot{\theta}}{\theta}\frac{r_*}{r}\dot{r}_*. \tag{10}$$

Along the stationary plate, $u_\theta = 0$ for all r and hence the total velocity V will be equal to u_r. Along the falling plate, u_θ is equal to $\dot{\theta} r$ and u_r is given by Eq. (8). Thus,

$$V^2 = u_\theta^2 + u_r^2 = (\dot{\theta} r)^2 + \left(\frac{\dot{\theta}}{\theta}\left(\frac{r_*^2 - r^2}{2r}\right)\right)^2. \tag{11}$$

The unsteady Bernoulli equation is applied along the moving plate from the inner edge of the plate r_1 to the location of the dividing streamline r_*.

$$\int_{r_*}^{r_1} \frac{\partial u}{\partial t} dr + \frac{V_1^2}{2} + \frac{p_1}{\rho} + gZ_1 = \frac{p_*}{\rho} + \frac{V_*^2}{2} + gZ_*. \tag{12}$$

In this equation, p_1/ρ is equal to zero, $(z_1 - z_*)$ is small and can be neglected and the first term is evaluated by integrating Eq. (10).

$$\frac{p_*}{\rho} = \left\{\frac{\ddot{\theta}}{\theta} - \left(\frac{\dot{\theta}}{\theta}\right)^2\right\}\left\{\frac{r_*^2}{2}\ln\left(\frac{r_1}{r_*}\right) - \left(\frac{r_1^2 - r_*^2}{4}\right)\right\} + \frac{\dot{\theta}}{\theta} r_* \dot{r}_* \ln\left(\frac{r_1}{r_*}\right) + \frac{1}{2}\left\{\frac{\dot{\theta}}{\theta}\left(\frac{r_*^2 - r_1^2}{2r_1}\right)\right\}^2 + \frac{1}{2}(\dot{\theta})^2 (r_1^2 - r_*^2) \tag{13}$$

Similarly, the unsteady Bernoulli equation can be applied along the moving plate from r_* to the outer edge of the plate r_2.

$$\frac{p_*}{\rho} = \left\{\frac{\ddot{\theta}}{\theta} - \left(\frac{\dot{\theta}}{\theta}\right)^2\right\}\left\{\frac{r_*^2}{2}\ln\left(\frac{r_2}{r_*}\right) - \left(\frac{r_2^2 - r_*^2}{4}\right)\right\} + \frac{\dot{\theta}}{\theta} r_* \dot{r}_* \ln\left(\frac{r_2}{r_*}\right) + \frac{1}{2}\left\{\frac{\dot{\theta}}{\theta}\left(\frac{r_*^2 - r_1^2}{2r_1}\right)\right\}^2 + \frac{1}{2}(\dot{\theta})^2 (r_*^2 - r_*^2) \tag{14}$$

Equating the right-hand sides of Eqs. (13) and (14) results in the differential equation for r_*.

$$\dot{r}_* = \frac{-\theta}{\dot{\theta} r_* \ln\left(\frac{r_1}{r_2}\right)}\left[\left(\frac{\ddot{\theta}}{\theta} - \left(\frac{\dot{\theta}}{\theta}\right)^2\right)\left\{\frac{r_*^2}{2}\ln\left(\frac{r_1}{r_2}\right) + \frac{(r_2^2 - r_1^2)}{4}\right\} + \frac{1}{8}\left(\frac{\dot{\theta}}{\theta}\right)^2\left\{r_*^4\left(\frac{1}{r_1^2} - \frac{1}{r_2^2}\right) + (r_1^2 + r_2^2)\right\} + \frac{(\dot{\theta})^2}{2}(r_1^2 - r_2^2)\right] \tag{15}$$

$$\dot{r}_* = C5\ddot{\theta} + C6 \tag{15a}$$

where

$$C5 = \frac{-1}{\dot{\theta} r_* \ln\left(\frac{r_1}{r_2}\right)}\left\{\frac{r_*^2}{2}\ln\left(\frac{r_1}{r_2}\right) + \left(\frac{r_2^2 - r_1^2}{4}\right)\right\} \tag{15b}$$

and

$$C6 = \frac{-\theta}{\dot{\theta} r_* \ln\left(\frac{r_1}{r_2}\right)}\left[-\left(\frac{\dot{\theta}}{\theta}\right)^2\left\{\frac{r_*^2}{2}\ln\left(\frac{r_1}{r_2}\right) + \frac{r_2^2 - r_1^2}{4}\right)\right\} + \frac{1}{8}\left(\frac{\dot{\theta}}{\theta}\right)^2\left\{r_*^4\left(\frac{1}{r_1^2} - \frac{1}{r_2^2}\right) + (r_1^2 + r_2^2)\right\} + \frac{(\dot{\theta})^2}{2}(r_1^2 - r_2^2)\right]. \tag{15c}$$

The pressure at any radius r can be obtained by applying the unsteady Bernoulli equation between any arbitrary radius r and the outer edge of the plate r_2. Utilizing the same assumptions as those used in the derivation of Eq. (13), we have

$$\frac{p}{\rho} = \frac{V_2^2 - V^2}{2} - \int_{r_2}^{r} \frac{\partial u}{\partial t} dr = \frac{1}{2}\left(\frac{\dot{\theta}}{\theta}\right)^2\left\{\left(\frac{r_*^2 - r_2^2}{2r_2}\right)^2 - \left(\frac{r_*^2 - r^2}{2r}\right)^2\right\} + \frac{(\dot{\theta})^2}{2}(r_2^2 - r^2) - \left(\frac{\ddot{\theta}}{\theta} - \left(\frac{\dot{\theta}}{\theta}\right)^2\right)\left\{\frac{r_*^2}{2}\ln\left(\frac{r}{r_2}\right) - \left(\frac{r^2 - r_2^2}{4}\right)\right\} - \frac{\dot{\theta} r_* \dot{r}_*}{\theta}\ln\left(\frac{r}{r_2}\right). \tag{16}$$

Forces and Moments on Falling Plate

The pressures calculated from Eq. (16) can be integrated along the plate length to give the normal force and the moment about the center of rotation. Thus,

$$F = \int_{r_1}^{r_2} p\, dr \tag{17}$$

and

$$M = \int_{r_1}^{r_2} pr\, dr \tag{18}$$

where F and M are calculated per unit width of the plate.

Since the moment M is used in the equation of motion for the plate, the result of the integration in Eq. (18) is presented as follows:

$$M = C1\left(\frac{\dot{\theta}}{\theta}\right)^2 + C2(\dot{\theta})^2 - C3\left(\frac{\ddot{\theta}}{\theta} - \left(\frac{\dot{\theta}}{\theta}\right)^2\right) - C4\,\dot{r}_* \tag{19}$$

Downloaded 03 May 2010 to 171.66.16.245. Redistribution subject to ASME license or copyright; see http://www.asme.org/terms/Terms_Use.cfm

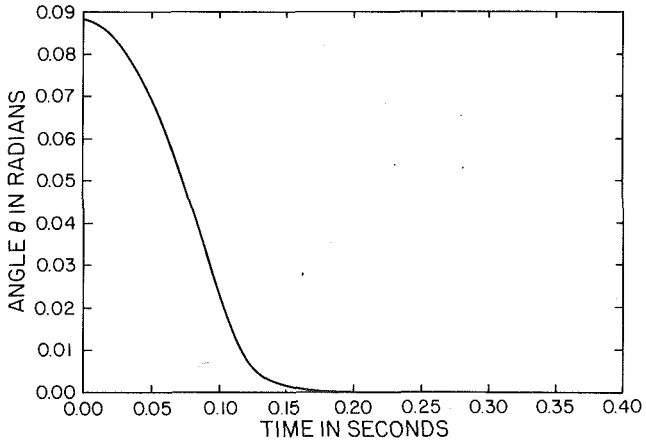


Fig. 2 Variation of angle θ as a function of time

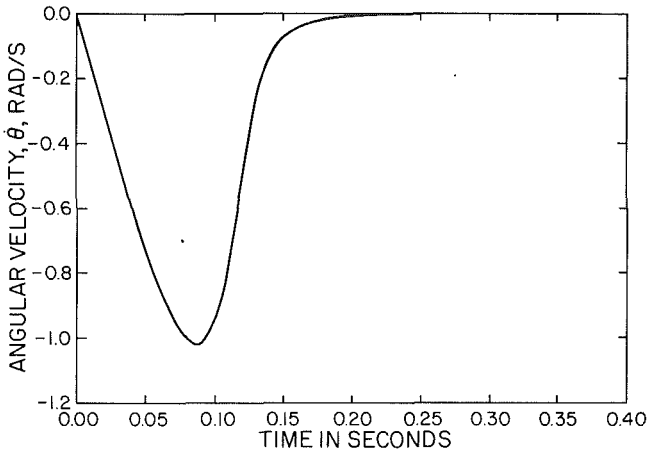


Fig. 3 Variation of angular velocity θ as a function of time

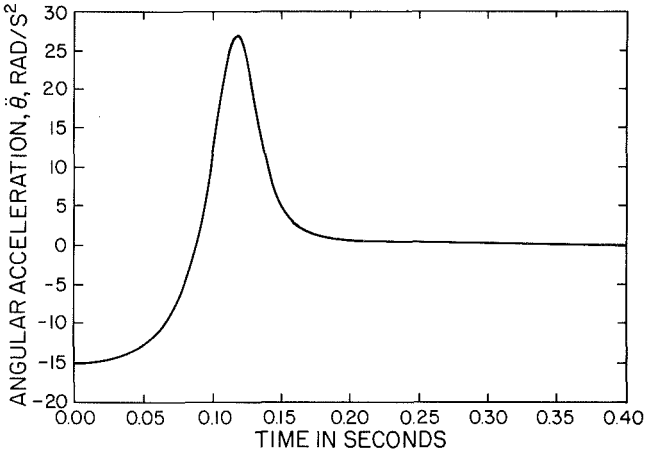


Fig. 4 Variation of angular acceleration θ as a function of time

where

$$C1=\frac{\rho}{2}\left\{\left(\frac{r_*^2-r_2^2}{2r_2}\right)^2\left(\frac{r_2^2-r_1^2}{2}\right)-\frac{1}{4}\left(r_*^4\ln\left(\frac{r_2}{r_1}\right)-r_*^2(r_2^2-r_1^2)+\left(\frac{r_2^4-r_1^4}{4}\right)\right)\right\}$$

$$C2=\frac{\rho}{2}\left\{r_2^2\left(\frac{r_2^2-r_1^2}{2}\right)-\left(\frac{r_2^4-r_1^4}{4}\right)\right\}$$

$$C3=\rho\left\{\frac{r_*^2r_2^2}{2}\left(-\frac{1}{4}-\frac{1}{2}\left(\frac{r_1}{r_2}\right)^2\ln\left(\frac{r_1}{r_2}\right)+\frac{1}{4}\left(\frac{r_1}{r_2}\right)^2\right)-\frac{1}{4}\left(\frac{r_2^4-r_1^4}{4}-r_2^2\left(\frac{r_2^2-r_1^2}{2}\right)\right)\right\}$$

$$C4=\frac{\rho\dot{\theta}r_*r_2^2}{\theta}\left\{-\frac{1}{4}-\frac{1}{2}\left(\frac{r_1}{r_2}\right)^2\ln\left(\frac{r_1}{r_2}\right)+\frac{1}{4}\left(\frac{r_1}{r_2}\right)^2\right\}.$$

Substituting Eq. (15*a*) into Eq. (19), we get

$$M=C1\left(\frac{\dot{\theta}}{\theta}\right)^2+C2(\dot{\theta})^2-C3\left(\frac{\ddot{\theta}}{\theta}-\left(\frac{\dot{\theta}}{\theta}\right)^2\right)-C4(C5\ddot{\theta}+C6). \tag{20}$$

Equation of Motion of Plate

The moment from Eq. (20) acts on the plate in the anticlockwise direction. Let the submerged weight W_s of the plate act at a distance r_{cg} from the center of rotation. A clockwise moment is thus exerted on the plate of magnitude $W_s r_{cg}$. The difference of these moments results in an angular acceleration, $\ddot{\theta}$. Thus,

$$M-W_sr_{cg}=I\ddot{\theta} \tag{21}$$

where I = Polar Moment of Inertia of the plate about the center of rotation.

Substituting Eq. (20) into (21), we get

$$\ddot{\theta}=\frac{\left\{(C1+C3)\left(\frac{\dot{\theta}}{\theta}\right)^2+C2(\dot{\theta})^2-C4C6-W_sr_{cg}\right\}}{\left(I+\frac{C3}{\theta}+C4C5\right)} \tag{22}$$

Equations (15) and (22) are two nonlinear ordinary differential equations that need to be solved simultaneously for θ and r_* as functions of time.

Numerical Solution

Numerical solutions of Eqs. (15) and (22) were obtained on a SUN workstation using appropriate initial conditions. The setup of the equations using software package MATLAB is outlined below. MATLAB has a subroutine ODE23 which can solve a number of simultaneous, first-order differential equations using the Runge-Kutta method.

Initial conditions have to be specified for θ, $\dot{\theta}$ and r_* and the maximum time of simulation has to be provided. The program selects the appropriate time step and solves for θ, $\dot{\theta}$ and r_* as functions of time. Once these variables are known, then all the other parameters, such as accelerations, pressures, forces, and moments can be calculated as a function of time.

The program was run using the following input parameters:

$r_1=0.1938$ m (0.6358 ft); $r_2=0.2758$ m (0.905 ft);

$r_{cg}=0.1379$ m (0.4525 ft); $w_s=38.03$ N (8.55 lbs.);

$\rho=1000$ kg/m^3 (1.94 slugs/cft);

$I=0.3071$ kg-m^2 (0.2265 slug-ft^2).

The initial conditions that were specified were

$\theta=0.0881$ rads; $\dot{\theta}=0$ rads/s; $r_*=0.2758$ m (0.905 ft).

Results and Discussion

Figure 2 represents the variation of θ as a function of time. It can be seen that θ approaches zero asymptotically in approximately 0.2 seconds. An inflection point occurs just prior to 0.1 secs., indicating the location of the maximum velocity.

Figure 3 is a plot of the angular velocity as a function of time. It can be seen that the angular velocity starts at zero, reaches a maximum value and reduces to zero asymptotically. Before the peak, the slope is negative; therefore, the acceleration is negative. After the peak, the slope is positive and therefore the acceleration is positive. This is shown to be so in Fig. 4. Once again, the acceleration approaches zero asymp-

Downloaded 03 May 2010 to 171.66.16.245. Redistribution subject to ASME license or copyright; see http://www.asme.org/terms/Terms_Use.cfm

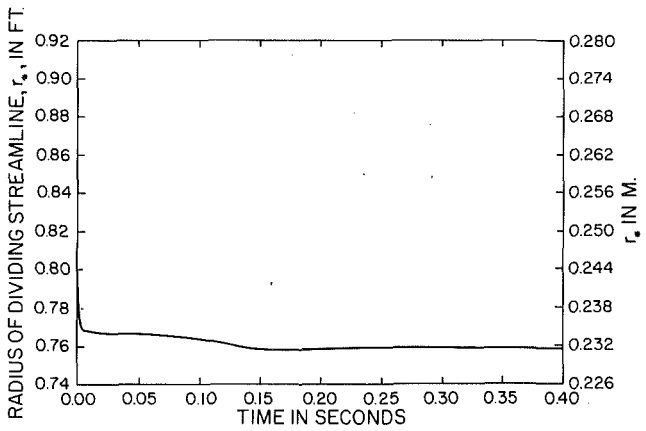


Fig. 5 Variation of location of dividing streamline r_s as a function of time

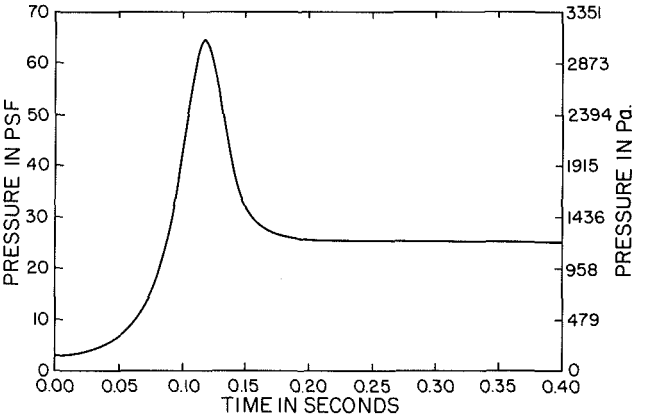


Fig. 6 Variation of pressure at $r=0.2457$ m (0.806 ft) as a function

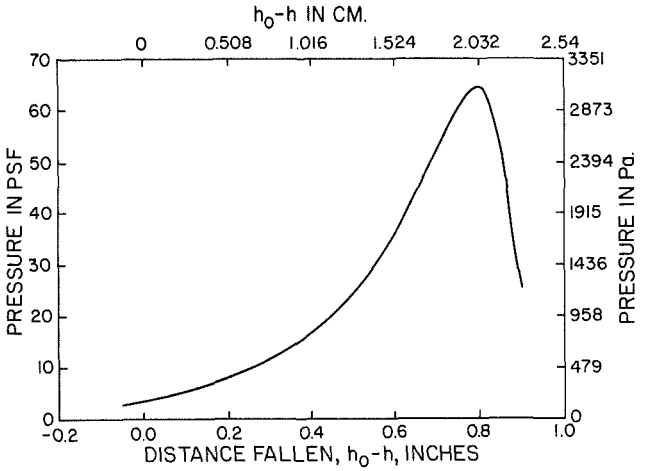


Fig. 7 Variation of pressure at $r=0.2457$ m (0.806 ft) as a function of the distance fallen, $h_o - h$

totically. This is the reason why glass plates falling on each other do not suffer any damage. All three parameters, θ, $\dot{\theta}$, and $\ddot{\theta}$ approach zero values very gradually. Their variation with respect to time before impact is such that high pressures are built up beneath the plate to slow it down and prevent damage. The pressure variation will be shown in later figures.

Figure 5 shows the location of the dividing streamline as a function of time. The variation is only slight and occurs approximately at 46 percent of the plate length away from the inside edge of the plate. This percentage would tend to approach zero as the magnitude of r_1 approaches zero. If the

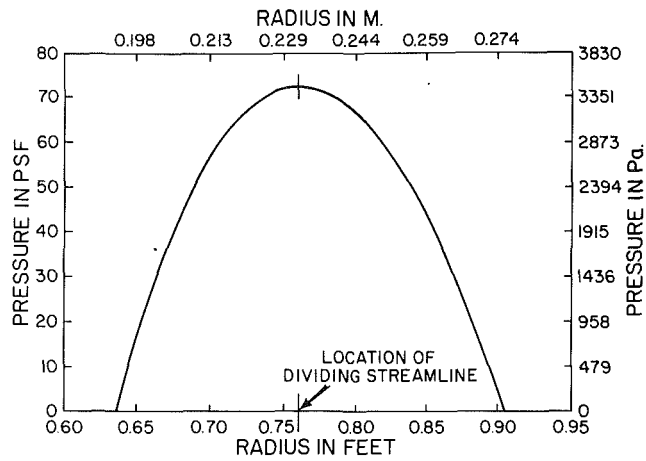


Fig. 8 Pressure distribution across the plate at an instant of time

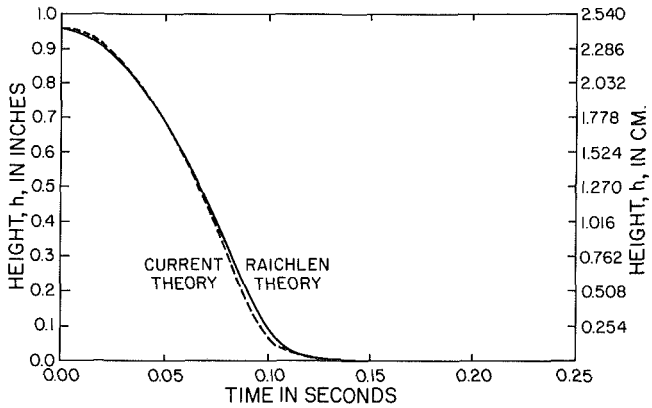


Fig. 9 Variation of height h as a function of time. Comparison of two theories.

two plates are always parallel, the dividing streamline is of course located at 50 percent of the plate length.

Figures 6 and 7 present the variation of the pressure at an arbitrary radius of 0.2457 m (0.806 ft) as a function of time and the drop in height $(h_o - h)$ of the outer edge of the plate. There are a couple of anomalies in these figures that call for an explanation. The first deals with the magnitude of the pressure at $t=0$. The pressure should be zero but shows up as 143.6 Pa (3.0 psf) in Fig. 6. The initial pressure was specified to be zero. However, it can be seen from Fig. 4 that at $t=0^+$ secs., the acceleration $\ddot{\theta}$ is -15 rads/s^2. Substitution of this value of $\ddot{\theta}$ in Eq. (16), gives rise to $p=143.6$ Pa (3.0 psf). The second anomaly is related to the pressure having an asymptotic value of 1.197 kPa (25 psf) at large values of t. The reason for this is related to the fact that the pressure (Eq. (16)) is dependent on the two ratios $\dot{\theta}/\theta$ and $\ddot{\theta}/\theta$. Now, even though θ, $\dot{\theta}$ and $\ddot{\theta}$ approach zero asymptotically, the ratios $\dot{\theta}/\theta$ and $\ddot{\theta}/\theta$ result in nonzero values, leading to an asymptotic pressure of 1.197 kPa (25 psf). Figure 7 shows how the pressure builds up as the drop in height $(h_o - h)$ at radius r_2 increases, reaching a maximum at $h=0.398$ cm (0.157 in.) and then dropping off again. It becomes clear from this diagram why a glass plate slows down during its fall and touches the stationary plate gently. Figure 8 shows the distribution of pressures across the plate at a given instant of time. The distribution is asymmetrical with the maximum pressure occurring four percent of the plate length away from the centerline towards the center of rotation.

The results of this analysis were compared with the results of an inviscid analysis (Raichlen, 1990) of a horizontal plate having the same dimensions falling vertically from the same initial height h_o. Figure 9 shows the decrease in height h as a

Downloaded 03 May 2010 to 171.66.16.245. Redistribution subject to ASME license or copyright; see http://www.asme.org/terms/Terms_Use.cfm

function of time. The points from the current theory fall very close to the points from Raichlen (1990). This shows that the inviscid analysis of a horizontal plate falling vertically is a very good approximation of a physical situation where the plate falls by rotating about an external point. The angular rotation, of course, has to be small.

The inviscid analysis is valid only when the Reynolds number of the flow is large and inertia terms dominate over viscous terms. In Fig. 2, after $t=0.1$ secs. the gap height h will be small and the fluid velocities are also small, resulting in a low Reynolds number. Under these conditions, viscous forces may dominate and the results of the inviscid theory will be incorrect. Results of a viscous theory also may not produce the anomalous pressure for $t>0.2$ secs. shown in Fig. 6.

Conclusions

An inviscid theory has been formulated to analyze the flow between a stationary horizontal plate and another plate that falls on top of it by rotating about an external point. The results of this theory clarify why a glass plate made to fall on another by rotating about one edge does not result in any damage. The pressure distribution along the plate is asymmetrical with the maximum pressure occurring away from the center of the plate and towards the center of rotation. The results of this theory are very similar to the inviscid theory for a horizontal plate falling vertically on a stationary plate. Further work needs to be done to use viscous theory at those times in the flow pattern when the Reynolds number is small and viscous forces begin to dominate.

Acknowledgments

The author is grateful to Bob Taylor, Don Jones, and other personnel of the Naval Civil Engineering Laboratory, Port Hueneme, Calif., for their help and encouragement during the summer of 1990. The author was a participant of the US Navy/ASEE Summer Faculty Research Program that year and is grateful for that opportunity.

References

Lawrence, C. J., Kuang, Y., and Weinbaum, S., 1985, "The Inertial Draining of a Thin Fluid Layer Between Parallel Plates with a Constant Normal Force. Part 2. Boundary Layer and Exact Numerical Solutions," *Journal of Fluid Mechanics*, Vol. 156, pp. 479–484.

Lawrene, C. J., and Weinbaum, S., 1988, "Hydrodynamic Arrest of a Flat Body Moving Toward a Parallel Surface at Arbitrary Reynolds Number," *Journal of Fluid Mechanics*, Vol. 186, pp. 285–304.

Raichlen, F., 1990, Letter report given to Bob Taylor, Code L-42, Naval Civil Engineering Lab., Port Hueneme, CA.

Weinbaum, S., Lawrence, C. J., and Kuang, Y., 1985, "The Inertial Draining of a Thin Fluid Layer Between Parallel Plates with a Constant Normal Force. Part 1. Analytic Solutions: Inviscid and Small But Finite-Reynolds-Number Limits," *Journal of Fluid Mechanics*, Vol. 156, pp. 463–477.

Yih, Chia-Shun, 1974, "Fluid Mechanics of Colliding Plates," *The Physics of Fluids*, Vol. 17, No. 11, pp. 1936–1940.

Downloaded 03 May 2010 to 171.66.16.245. Redistribution subject to ASME license or copyright; see http://www.asme.org/terms/Terms_Use.cfm

Comparison of Crystal Plasticity and Isotropic Hardening Predictions for Metal-Matrix Composites

A. Needleman
Division of Engineering,
Brown University,
Providence, RI 02912
Fellow ASME

V. Tvergaard
Department of Solid Mechanics,
The Technical University of Denmark,
Lyngby, Denmark

In a numerical micromechanical study of the tensile properties of a metal reinforced by short whiskers, the elastic-plastic deformations of the metal are described in terms of crystalline plasticity, using a planar crystal model that allows for either two or three slip systems. Plane strain analyses are carried out for a periodic array of aligned whiskers for whisker volume fractions of 10 percent to 30 percent, and comparison is made with predictions based on a corresponding flow theory of plasticity with isotropic hardening. The predicted trend for composite strengthening with whisker volume fraction is the same for the various matrix material constitutive characterizations. It is found that the crystal model can give rise to shear localization, initiating at the sharp whisker edges. As a consequence of this localization, the stress carrying capacity eventually drops.

1 Introduction

The mechanical properties of metallic materials can be significantly improved by reinforcing with brittle fibers, whiskers, or particulates. Thus, metal-matrix composites exhibit markedly higher stiffness and strength than the matrix alloys, and the metals reinforced by particulates or whiskers still have the advantage of being machinable and workable using conventional processing techniques. On the other hand, the reinforcement also results in poor ductility and low fracture toughness owing to early void formation by debonding of the matrix-fiber interface or fiber breakage (Divecha et al., 1981; McDanels, 1985; Nutt and Needleman, 1987; Zok et al., 1988). To obtain a parametric understanding of the effect of material parameters such as the volume fraction, the shape and the distribution of particles, or the matrix constitutive behavior, numerical micromechanical studies are an important tool.

For whisker reinforced metals a number of computations have been carried out to study the effect of material parameters on the overall tensile properties, assuming a situation of perfect bonding. Thus, Christman et al. (1989) have used an axisymmetric cell-model analysis, representing a periodic array of aligned whiskers, to investigate the uniaxial tensile stress-strain behavior of a 2124 Al-SiC whisker composite. An alternative axisymmetric cell-model analysis by Tvergaard (1990) has shown that an array of transversely staggered whiskers gives a noticeably softer response than an array of transversely aligned whiskers, and this has also been found in a full three-dimensional numerical analysis by Levy and Papazian (1990). Planar models have been used by Chistman et al. (1989) to study the effect of various distributions of whiskers, showing that whiskers clustering tends to reduce the overall stress levels compared to those predicted for a simple periodic array of whiskers. A number of different cell-model analyses have been used by Bao et al. (1991) to study metals reinforced by periodic arrays of particulates, short fibers, or platelets.

A common feature of the studies mentioned above is that the elastic-plastic deformations of the matrix material have been described by a phenomenological flow theory of plasticity with isotropic hardening. However, SiC whiskers have a diameter of about 0.5 μm, and grain sizes could typically be of comparable size or larger, so that anisotropic crystal slip could have a significant influence on the predicted interaction between matrix deformations and whiskers. Therefore, in the present paper the effect of matrix deformations described by crystal plasticity is investigated, and comparison is made with predictions based on isotropic hardening flow theory, using the Taylor factor to relate the two types of constitutive descriptions. A planar model of the metal reinforced by short whiskers is used, and results are obtained for three different volume fractions of whiskers. For simplicity, the matrix material is modeled as a single crystal, allowing for three slip systems, although contact between a few different grains and a short whisker might be as typical. The interaction between

Contributed by the Applied Mechanics Division of THE AMERICAN SOCIETY OF MECHANICAL ENGINEERS for publication in the ASME JOURNAL OF APPLIED MECHANICS.

Discussion on this paper should be addressed to the Technical Editor, Professor Lewis T. Wheeler, Department of Mechanical Engineering, University of Houston, Houston, TX 77204-4792, and will be accepted until four months after final publication of the paper itself in the ASME JOURNAL OF APPLIED MECHANICS.

Manuscript received by the ASME Applied Mechanics Division, Apr. 19, 1991; final revision, Dec. 19, 1991. Associate Technical Editor: R. M. McMeeking.

Copyright © 1993 by ASME
Downloaded 03 May 2010 to 171.66.16.245. Redistribution subject to ASME license or copyright; see http://www.asme.org/terms/Terms_Use.cfm

a number of grains and the reinforcement has been analyzed for a planar model of particulate reinforced materials by McHugh et al. (1989, 1991).

2 Problem Formulation

The finite element analyses are based on a finite strain, convected coordinate formulation, with the initial unstressed state taken as reference. This formulation has been employed extensively in previous finite element analyses (e.g., Needleman (1972), Tvergaard (1976), and Christman et al. (1989)). All field quantities are considered to be functions of convected coordinates, y^i, which serve as particle labels, and time, t. Attention is confined to quasi-static deformations and, with body forces neglected, the rate form of the principle of virtual work is written as

$$\Delta t\int_V [\dot\tau^{ij}\delta E_{ij}+\tau^{ij}\dot u^k_{,i}\delta u_{k,j}]dV=\Delta t\int_S \dot T^i\delta u_i\,dS - \left[\int_V \tau^{ij}\delta E_{ij}\,dV-\int_S T^i\delta\, u_i\,dS\right]. \quad (1)$$

Here, V and S are the volume and surface, respectively, of the body in the reference configuration and $\dot{(\ )}=\partial()/\partial t$ at fixed y^i. The quantities τ^{ij} are the contravariant components of the Kirchhoff stress ($\tau=J\sigma$, where σ is the Cauchy stress and J is the ratio of current to reference volume of a material element) on the deformed convected coordinate net. The second term on the right-hand side is an equilibrium correction term that is used in the numerical procedure to reduce drift from the equilibrium path due to the discrete time step.

The nominal traction components, T^i, and the Lagrangian strain components, E_{ij}, are given by

$$T^i=(\tau^{ij}+\tau^{kj}u^i_{,k})\nu_j \quad (2)$$

$$E_{ij}=\frac{1}{2}(u_{i,j}+u_{j,i}+u^k_{,i}u_{k,j}) \quad (3)$$

where u_j are the components of the displacement vector on base vectors in the reference configuration, $()_{,i}$ denotes covariant differentiation in the reference frame and ν is the surface normal in the reference configuration.

A doubly periodic array of identical cells is subject to plane strain tension, with y^2 being the tensile axis. Each cell contains a single rigid whisker, aligned with the tensile axis, and the cell dimensions are $2w_0$ along the y^1 direction and $2L_0$ along the y^2 direction. Consideration is restricted to deformations for which the straight lines bounding each cell remain straight after deformation (this is a stronger constraint than required by periodicity, since the imposed boundary conditions do not permit a bifurcation from the configuration in which each cell remains rectangular). Furthermore, attention is restricted to deformations that preserve the mirror symmetry of the array so that straight lines connecting the centers of the cells remain straight. With these symmetries, the boundary value problem for the doubly periodic array can be reduced to one for one quadrant of one cell. The boundary conditions for the quadrant analyzed numerically are

$$\dot u^2=0 \quad \dot T^1=0 \quad \text{on} \quad y^2=0 \text{ and } \dot u^1=0 \quad \dot T^2=0 \text{ on } y^1=0^{11} \quad (4)$$

$$\dot u^2=\dot U_2=\dot\epsilon_{\text{ave}}\,(L_0+U_2) \quad \dot T^1=0 \quad \text{on} \quad y^2=L_0 \quad (5)$$

$$\dot u^1=\dot U_1 \quad \dot T^2=0 \quad \text{on} \quad y^1=w_0. \quad (6)$$

Here, $\dot\epsilon_{\text{ave}}$ is a prescribed constant while $\dot U_1$ is determined from the condition that the average lateral traction rate vanishes, i.e.,

$$\int_0^{L_0}\dot T^1 dy^2=0 \quad \text{on} \quad y^1=w_0. \quad (7)$$

The matrix material is assumed to remain perfectly bonded to the rigid whisker so that $u_1=u_2=0$ along the whisker-matrix interface.

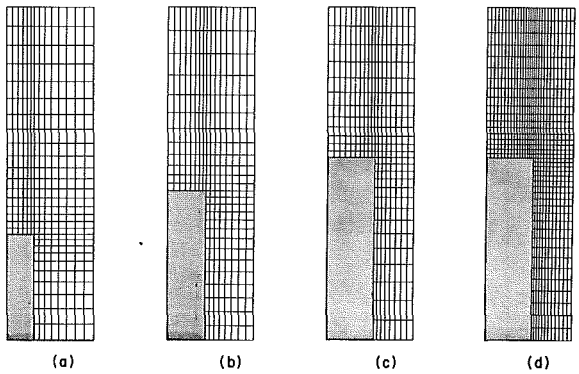


Fig. 1 Finite element meshes; (*a*) 10 percent whisker volume fraction, 332 quadrilateral elements; (*b*) 20 percent whisker volume fraction, 304 quadrilateral elements; (*c*) 30 percent whisker volume fraction, 328 quadrilateral elements; 30 percent whisker volume fraction, 768 quadrilateral elements. Each quadrilateral consists of four "crossed" triangular linear displacement elements.

Fiber volume fractions of 10, 20, and 30 percent are considered. (Because attention is confined to plane strain models, the whisker area fraction and volume fraction coincide). In each case the ratio of whisker length to whisker width is fixed at 4. Also, the cell length to width ratio, L_0/w_0, is taken to be 4. Figure 1, which shows finite element meshes for each whisker volume fraction, illustrates the geometry of the cell quadrant analyzed numerically.

3 Constitutive Relations

The finite deformation framework for crystalline plasticity is that developed in Rice (1971) and Hill and Rice (1972), see also Havner (1982). The numerical calculations are carried out using the planar crystal model of Asaro (1979), as modified in Harren and Asaro (1989) and as used in McHugh et al. (1989, 1991), to allow for three rather than two slips systems. The specific constitutive formulation and numerical implementation follow that in Peirce et al. (1983), where further details can be found. As in Lee (1969), the deformation gradient is written as

$$\mathbf{F}=\mathbf{F}^*\mathbf{F}^p. \quad (8)$$

Elastic deformation and any rigid-body rotation are included in $\mathbf{F}^*$ and the deformation $\mathbf{F}^p$ consists solely of crystallographic slipping along specific slip systems ($\mathbf{s}^{(\alpha)}$, $\mathbf{m}^{(\alpha)}$), where $\mathbf{s}^{(\alpha)}$ is the slip direction and $\mathbf{m}^{(\alpha)}$ is the slip plane normal for slip system α. The three slip systems are specified by $\mathbf{s}^{(\alpha)}=(\cos\theta^{(\alpha)}, \sin\theta^{(\alpha)})$, with $\theta^{(1)}=60$ deg, $\theta^{(2)}=120$ deg and $\theta^{(3)}=180$ deg and with $\theta^{(\alpha)}$ measured from the y^1-axis. For comparison purposes, some calculations are also carried out using two slip systems, $\theta^{(1)}=60$ deg and $\theta^{(2)}=120$ deg.

The vectors $\mathbf{s}^{(\alpha)}$ and $\mathbf{m}^{(\alpha)}$ are regarded as lattice vectors so that they stretch and rotate by

$$\mathbf{s}^{(\alpha)*}=\mathbf{F}^*\cdot\mathbf{s}^{(\alpha)} \quad \mathbf{m}^{(\alpha)*}=\mathbf{m}^{(\alpha)}\cdot\mathbf{F}^{*-1}. \quad (9)$$

From (8), the rate of deformation tensor is

$$\dot{\mathbf{F}}\cdot\mathbf{F}^{-1}=\dot{\mathbf{F}}^*\cdot\mathbf{F}^{*-1}+\mathbf{F}^*\cdot\dot{\mathbf{F}}^p\cdot\mathbf{F}^{p-1}\cdot\mathbf{F}^{*-1} =(\mathbf{D}^*+\mathbf{\Omega}^*)+(\mathbf{D}^p+\mathbf{\Omega}^p). \quad (10)$$

The first term on the right-hand side of (10), $(\mathbf{D}^*+\mathbf{\Omega}^*)$, is the elastic part of the rate of deformation tensor and the second term is the plastic part. The plastic stretching, $\mathbf{D}^p$, and spin tensors, $\mathbf{\Omega}^p$, are given by

$$\mathbf{D}^p=\sum_\alpha\dot\gamma^{(\alpha)}\mathbf{P}^{(\alpha)} \quad \mathbf{\Omega}^p=\sum_\alpha\dot\gamma^{(\alpha)}\mathbf{W}^{(\alpha)} \quad (11)$$

where $\dot\gamma^{(\alpha)}$ is the rate of shearing on slip system α, and

Downloaded 03 May 2010 to 171.66.16.245. Redistribution subject to ASME license or copyright; see http://www.asme.org/terms/Terms_Use.cfm

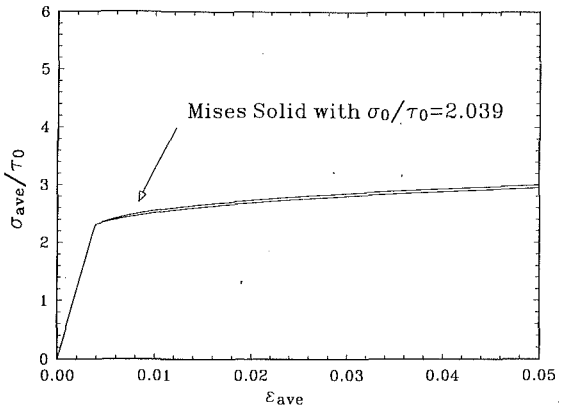


Fig. 2 Stress versus strain in plane-strain tension for a planar single crystal oriented for symmetric double slip, with $\theta^{(1)}=60$ deg and $\theta^{(2)}=120$ deg, and a Mises solid. The crystal material parameters are given by $N=0.1$, $m=0.005$, $\gamma_0=0.01$, $\nu=1/3$, $h_0/\tau_0=10$ and $\tau_0/E=0.001875$. For the Mises solid, $\sigma_0/\tau_0=2/\sin(60)$ and the remaining material parameters are given in the text.

$$\mathbf{P}^{(\alpha)}=\frac{1}{2}\left(\mathbf{s}^{(\alpha)*}\mathbf{m}^{(\alpha)*}+\mathbf{m}^{(\alpha)*}\mathbf{s}^{(\alpha)*}\right)$$

$$\mathbf{W}^{(\alpha)}=\frac{1}{2}\left(\mathbf{s}^{(\alpha)*}\mathbf{m}^{(\alpha)*}-\mathbf{m}^{(\alpha)*}\mathbf{s}^{(\alpha)*}\right). \tag{12}$$

The lattice Jaumann rate of Kirchhoff stress and the elastic rate of stretching are related by

$$\hat{\tau}^*=\mathbf{L}:\mathbf{D}^* \tag{13}$$

where

$$\hat{\tau}^*=\dot{\tau}+\tau\cdot\Omega^*-\Omega^*\cdot\tau. \tag{14}$$

The crystal elasticity is assumed to be unaffected by slip and isotropic, and the elastic strains remain small so that

$$\mathbf{L}=\frac{E}{1+\nu}\left[\mathbf{I}'+\frac{\nu}{1-2\nu}\mathbf{II}\right]. \tag{15}$$

Here, E is Young's modulus, ν is Poisson's ratio, $\mathbf{I}$ is the second order identity tensor, and $\mathbf{I}'$ is the fourth-order identity tensor.

Combining (11) and (13) and, for use in (1), expressing the relation in terms of the material convected rate of Kirchhoff stress, $\dot{\tau}^c$, gives

$$\dot{\tau}^c=\mathbf{L}:\mathbf{D}-\sum_{\alpha}\dot{\gamma}^{(\alpha)}\mathbf{R}^{(\alpha)}-\mathbf{D}\cdot\tau-\tau\cdot\mathbf{D} \tag{16}$$

with

$$\mathbf{R}^{(\alpha)}=\mathbf{L}:\mathbf{P}^{(\alpha)}+\mathbf{W}^{(\alpha)}\cdot\tau-\tau\cdot\mathbf{W}^{(\alpha)} \tag{17}$$

Strain-rate hardening is described by the power-law relation (Hutchinson (1976), Pan and Rice (1983), and Peirce et al. (1983))

$$\dot{\gamma}^{(\alpha)}=\dot{a}\left[\frac{\tau^{(\alpha)}}{g^{(\alpha)}}\right]\left[\left|\frac{\tau^{(\alpha)}}{g^{(\alpha)}}\right|\right]^{(1/m)-1}. \tag{18}$$

Here, $\dot{a}$ is a reference strain rate, m is the strain-rate hardening exponent, $g^{(\alpha)}$ is the slip system hardness, and the slip system resolved shear stress, $\tau^{(\alpha)}$, is given by

$$\tau^{(\alpha)}=\mathbf{s}^{(\alpha)*}\cdot\tau\cdot\mathbf{m}^{(\alpha)*}. \tag{19}$$

The evolution law for the hardness $g^{(\alpha)}$ has the form

$$\dot{g}^{(\alpha)}(\gamma)=\sum_{\beta}h_{\alpha\beta}|\dot{\gamma}^{(\beta)}|\quad g^{(\alpha)}(0)=\tau_0^{(\alpha)}. \tag{20}$$

In (20), $\tau_0^{(\alpha)}$ is the initial flow strength of slip system α and

$$h_{\alpha\beta}=qh(\gamma)+(1-q)h(\gamma)\delta_{\alpha\beta}\quad\gamma=\sum_{\alpha}|\gamma^{(\alpha)}|. \tag{21}$$

In the calculations, $q=1$ is used and the self-hardening function $h(\gamma)$ is specified as

$$h(\gamma)=h_0(\gamma/\gamma_0+1)^{N-1} \tag{22}$$

where h_0 is the initial slip-system hardening rate, γ_0 is a reference strain and N is the strain hardening exponent.

For comparison purposes, some calculations were carried out for an isotropically hardening, elastic-viscoplastic Mises solid for which the flow rule is given by

$$\mathbf{D}^p=\frac{3\dot{\bar{\epsilon}}}{2\bar{\sigma}}\tau' \tag{23}$$

where $\dot{\bar{\epsilon}}$ is the effective plastic strain rate and

$$\tau'=\tau-\sigma_m\mathbf{I}\quad\bar{\sigma}^2=\frac{3}{2}\tau':\tau'\quad\sigma_m=\frac{1}{3}(\tau:\mathbf{I}) \tag{24}$$

$$\dot{\bar{\epsilon}}=\dot{a}\,[\bar{\sigma}/g(\bar{\epsilon})]^{1/m}\,g(\bar{\epsilon})=\sigma_0\,(\bar{\epsilon}/\epsilon_0+1)^N. \tag{25}$$

Here, $\bar{\epsilon}=\int\dot{\bar{\epsilon}}\,dt$ and σ_0 is a reference strength.

Using $\mathbf{D}=\mathbf{D}^e+\mathbf{D}^p$, the flow rule (23) and the elastic moduli (15), the relation between the material convected rate of Kirchhoff stress and the rate of deformation tensor is obtained for use in (1).

Figure 2 shows a comparison between the homogeneous true stress versus logarithmic strain response in plane-strain tension, at an imposed strain rate $\dot{\epsilon}_{ave}=\dot{a}$, for the model crystal and for a Mises solid. For plane-strain tension, the resolved shear stress on slip system 3, $\tau^{(3)}=0$, and the geometry of the model crystal becomes that proposed by Asaro (1979) as a planar model of a face-centered cubic crystal oriented for symmetric double slip. In both cases in Fig. 2, $N=0.1$ and $m=0.005$. Also, $\tau^{(1)}=\tau^{(2)}=\tau_0$, with $\tau_0/E=0.001875$, $h_0/\tau_0=10$, $\gamma_0=0.01$ and $\nu=1/3$. The value of σ_0 for the Mises solid in (25) is taken as $2.039\,\tau_0$, where 2.039 is the plane-strain Taylor factor for $\nu=1/3$, and ϵ_0 is taken as $\gamma_0/2$.

For homogeneous plane-strain tension, the response of the Mises solid essentially coincides with that of the model crystal. In subsequent calculations, unless specifically stated otherwise, $\tau^{(1)}=\tau^{(2)}=\tau^{(3)}=\tau_0$, and all material parameters have the values employed in Fig. 2.

4 Numerical Method and Results

An imposed strain rate $\dot{\epsilon}_{ave}=\dot{a}$ is prescribed and the deformation history is calculated in a linear incremental manner. In order to increase the stable time step, a rate tangent modulus method, as described in Peirce et al. (1983), is used. The finite element discretization is based on linear displacement triangles, with each quadrilateral in the meshes shown in Fig. 1 consisting of four "crossed" triangles. The incremental boundary value problem is solved using a combined finite element-Galerkin method, which is the finite element-Rayleigh-Ritz method of Tvergaard (1976) for circumstances where the stiffness matrix is unsymmetric.

The overall stress-strain response for the three volume fractions considered is shown in Fig. 3. Here, $\epsilon_{ave}=\ln(1+U_2/L_0)$ and

$$\sigma_{ave}=\frac{1}{w_0+U_1}\int_0^{w_0}T^2dy^1. \tag{26}$$

In the early stages of deformation, the response of the composites with the Mises matrix coincides with that of the composites with the single crystal matrix, because the elastic response is identical in both cases and plastic flow is not extensive. Once large-scale plasticity develops, the composite with a Mises matrix has a larger stress, at a given strain. The difference between a composite with the Mises matrix and a corresponding composite with a single crystal matrix increases with increasing whisker volume concentration. Nevertheless, the overall trends for composite strengthening with whisker volume fraction agree, both qualitatively and quantitatively, for the two matrix material characterizations. For example,

Downloaded 03 May 2010 to 171.66.16.245. Redistribution subject to ASME license or copyright; see http://www.asme.org/terms/Terms_Use.cfm

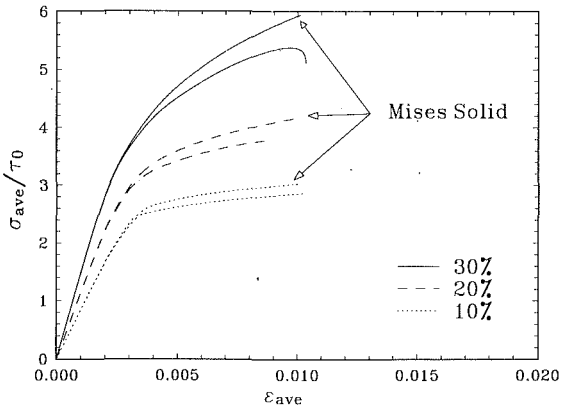


Fig. 3 Effect of whisker volume fraction on overall stress-strain response for two characterizations of the matrix material; a planar single crystal with three slip systems, $\theta^{(1)} = 60$ deg, $\theta^{(2)} = 120$ deg, and $\theta^{(3)} = 180$ deg, and a Mises solid. These calculations are based on the meshes shown in Figs. 1(*a*), 1(*b*), and 1(*c*), and the material parameters are the same as used in Fig. 2.

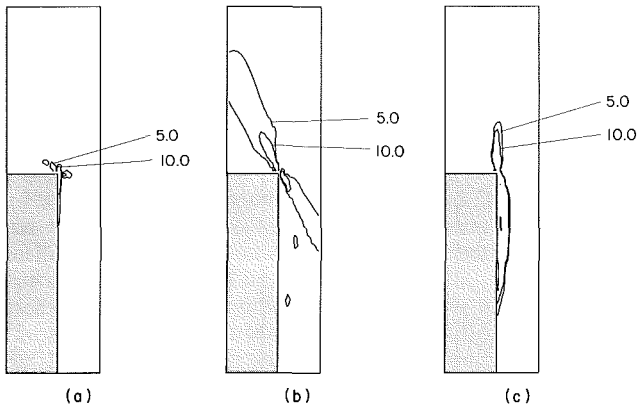


Fig. 4 Contours of constant slip rate magnitude for a 30 percent whisker volume concentration at $\epsilon_{ave} = 0.00666$; (*a*) $|\dot{\gamma}^{(1)}|/\dot{a}$; (*b*) $|\dot{\gamma}^{(2)}|/\dot{a}$; (*c*) $|\dot{\gamma}^{(3)}|/\dot{a}$. These contours are based on a 768 quadrilateral mesh.

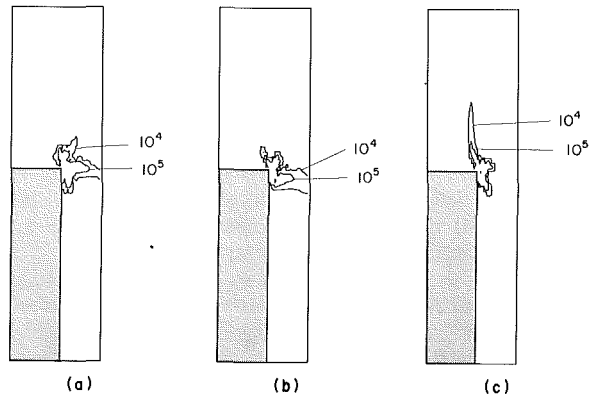


Fig. 5 Contours of constant slip rate magnitude for a 30 percent whisker volume concentration at $\epsilon_{ave} = 0.00818$; (*a*) $|\dot{\gamma}^{(1)}|/\dot{a}$; (*b*) $|\dot{\gamma}^{(2)}|/\dot{a}$; (*c*) $|\dot{\gamma}^{(3)}|/\dot{a}$. These contours are based on a 768 quadrilateral mesh.

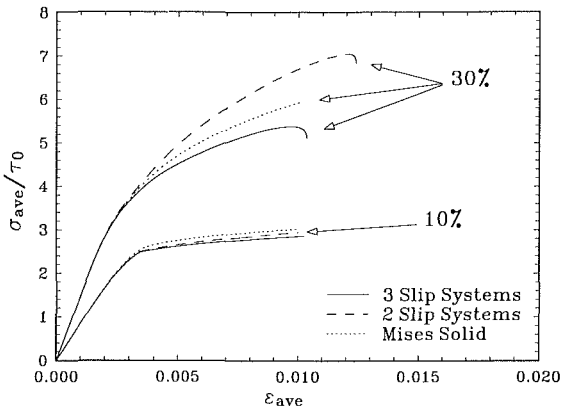


Fig. 6 Comparison of composite stress-strain response based on three matrix characterizations; (i) a single crystal with three slip systems, $\theta^{(1)} = 60$ deg, $\theta^{(2)} = 120$ deg, and $\theta^{(3)} = 180$ deg; (ii) a single crystal with two slip systems $\theta^{(1)} = 60$ deg and $\theta^{(2)} = 120$ deg; and (iii) a Mises solid. These calculations are based on the meshes shown in Figs. 1(*a*), 1(*b*), and 1(*c*), and the material parameters are the same as used in Fig. 2.

with a whisker volume fraction of ten percent, both the crystal model and the isotropic hardening model exhibit a fairly abrupt elastic-plastic transition, similar to that of the matrix material in Fig. 2. With increasing whisker volume fraction, the crystal model and the isotropic hardening model predict that the elastic-plastic transition becomes more gradual in much the same way. For particulate reinforced composites, with up to 16 percent reinforcement, McHugh et al. (1991) found virtually identical overall stress-strain response for calculations based on a Mises constitutive relation and for corresponding calculations using a matrix consisting of a collection of three-slip-system planar grains.

Over the strain range shown in Fig. 3, the rate of composite hardening is quite similar for the two matrix material characterizations at whisker volume fractions of 10 and 20 percent. However, with a 30 percent whisker volume fraction the composite with the planar crystal matrix progressively softens relative to the composite with the Mises matrix. Eventually, the true stress reaches a maximum and subsequently decreases. This is a consequence of the strain concentration at the whisker corner promoting highly localized straining.

Figures 4 and 5 show contours of constant slip rate on each of the three slip systems at two stages of the deformation history for the case with 30 percent whisker volume concentration. The stage shown in Fig. 4 precedes the stress drop signalling localization, while Fig. 5 shows strain rate contours subsequent to localization. Figure 4 shows that there is a band of material, away from the whisker, where the matrix is essentially undergoing single slipping on slip system 2. The general features of the slip rate patterns for the 10 percent and 20 percent cases are similar to those in Fig. 4. Figure 5 shows that the slip rates localize on all three slip systems.

The effect of the third slip system is shown in Fig. 6. Overall stress-strain curves for a matrix material with two slip systems, $\theta^{(1)} = 60$ deg and $\theta^{(2)} = 120$ deg, are compared with the corresponding curves when the matrix material is a Mises solid and when the matrix material is a crystal with three slip systems. These comparisons are shown for both a 10 percent and 30 percent whisker volume concentration. For both volume fractions, the qualitative features of the response are the same for the two cases with single crystal matrix materials. For the 30 percent whisker volume fraction, localization is significantly delayed when there are only two slip systems. Prior to localization, the two-slip system matrix composite gives a stiffer response than does the Mises matrix composite. For the ten percent whisker volume fraction, the composite with the Mises matrix has the stiffest response, although there is little difference between the three cases.

Figure 7 shows the variation in overall stress-strain behavior as the mesh is refined for 20 percent and 30 percent whisker volume concentrations. The onset of the stress drop accompanying localization is very sensitive to the degree of mesh refinement. At least in part this is due to the role of the very high strain concentration at the whisker corner in precipitating

Downloaded 03 May 2010 to 171.66.16.245. Redistribution subject to ASME license or copyright; see http://www.asme.org/terms/Terms_Use.cfm

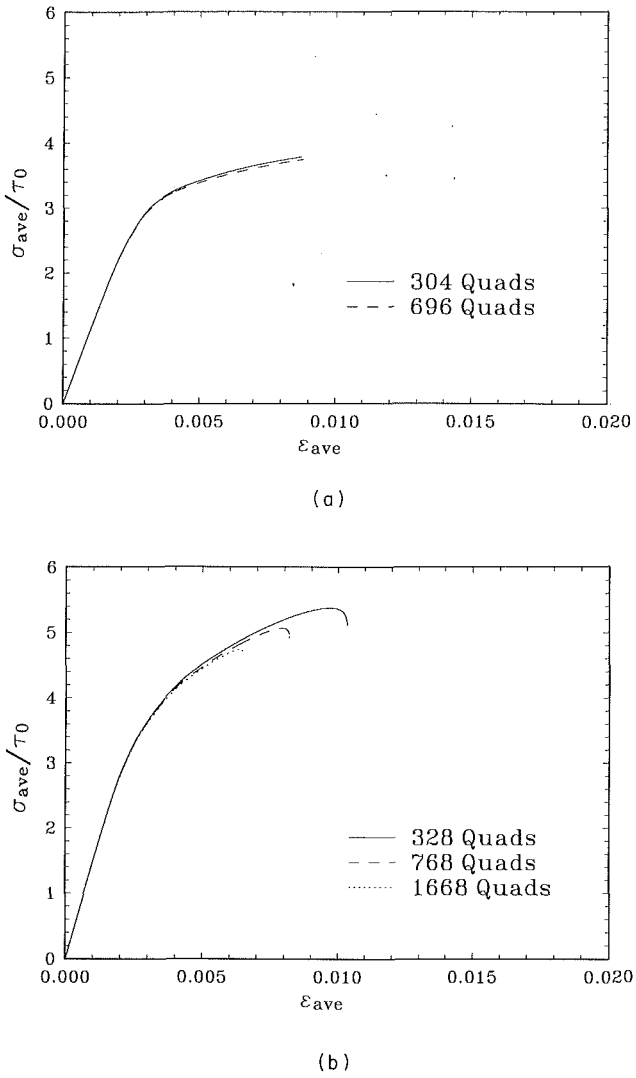


Fig. 7 Effect of mesh resolution on the computed stress-strain response; (*a*) 20 percent whisker volume fraction, (*b*) 30 percent whisker volume fraction

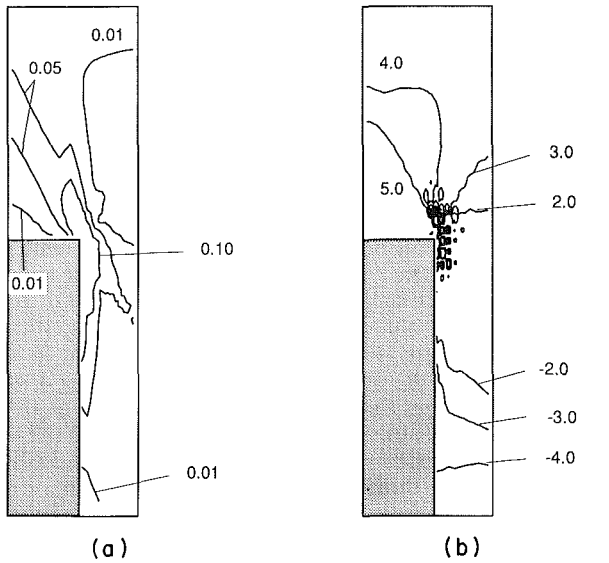


Fig. 8 Contours of constant (*a*) accumulated shear strain, γ, and (*b*) mean normal stress, σ_m/τ_0, for the 30 percent volume fraction composite with a crystal matrix having three slip systems; $\epsilon_{ave} = 0.0103$. These contours are taken from results using the mesh in Fig. 1(*c*).

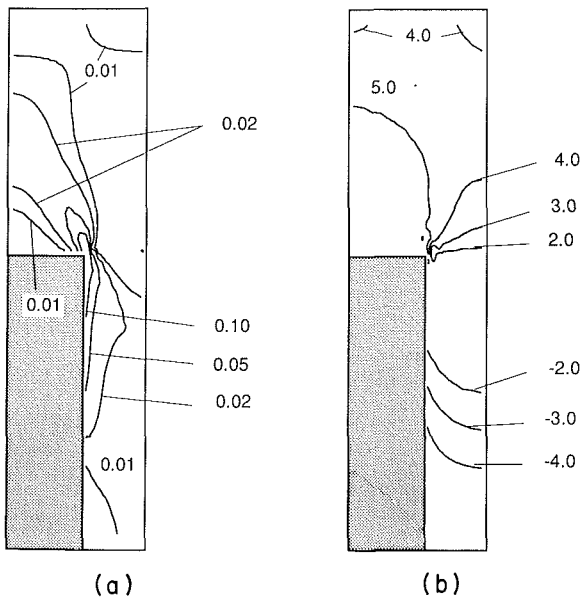


Fig. 9 Contours of constant (*a*) Mises equivalent strain, $\bar{\epsilon}$, and (*b*) mean normal stress, σ_m/τ_0, are shown for a 30 percent volume fraction when the matrix is a Mises solid; $\epsilon_{ave} = 0.0103$. These contours are taken from results using the mesh in Fig. 1(*c*).

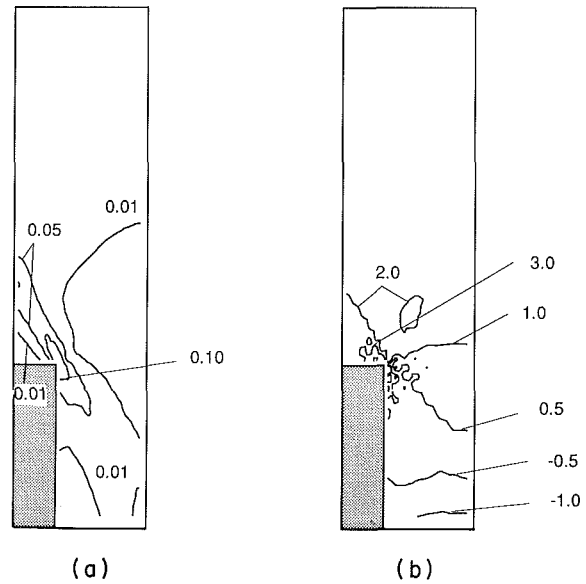


Fig. 10 Contours of constant (*a*) accumulated shear strain, γ, and (*b*) mean normal stress, σ_m/τ_0, for the ten percent volume fraction composite with a crystal matrix having three slip systems; $\epsilon_{ave} = 0.0101$. These contours are taken from results using the mesh in Fig. 1(*a*).

localization. Because strain gradients at the corner are very steep, even the finest mesh used may not adequately resolve field quantities near the corner. Prior to localization or when localization does not occur, as for the 20 percent volume concentration over the strain range considered, there is very good agreement between results based on the various meshes.

Figure 8 shows contours of accumulated shear strain, γ, and mean normal stress, σ_m, for the 30 percent volume fraction composite with a crystal matrix. In Fig. 9, contours of Mises equivalent strain, $\bar{\epsilon}$, and mean normal stress, σ_m, are shown for a 30 percent volume fraction when the matrix is a Mises solid. The effect of the strain localization can be seen by comparing Figs. 8(*a*) and 9(*a*). Nevertheless, the overall strain and mean normal stress distributions in Figs. 8 and 9 are rather similar.

Downloaded 03 May 2010 to 171.66.16.245. Redistribution subject to ASME license or copyright; see http://www.asme.org/terms/Terms_Use.cfm

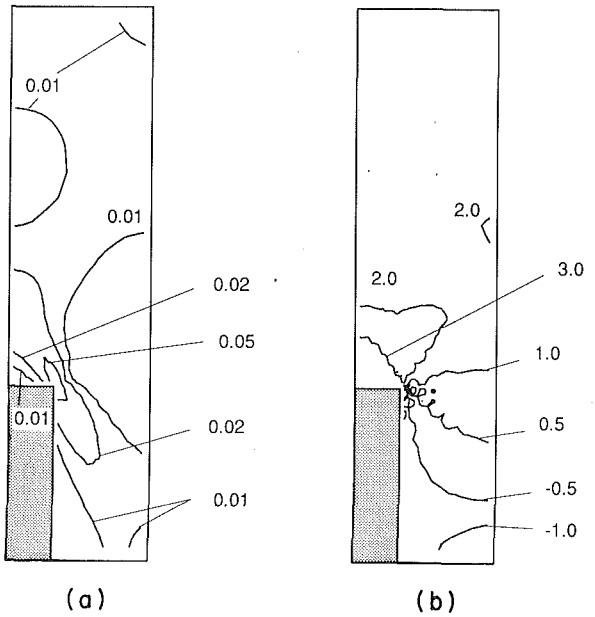


Fig. 11 Contours of constant (*a*) Mises equivalent strain, $\bar{\epsilon}$, and (*b*) mean normal stress, σ_m/τ_0, are shown for a ten percent volume fraction when the matrix is a Mises solid; $\epsilon_{ave} = 0.0104$. These contours are taken from results using the mesh in Fig. 1(*a*).

Figure 10 shows contours of accumulated shear strain, γ, and mean normal stress, σ_m, for the ten percent fraction composite with a crystal matrix. In Fig. 11, contours of Mises equivalent strain $\bar{\epsilon}$, and mean normal stress, σ_m, are shown for a ten percent volume fraction when the matrix is a Mises solid. The strain and mean normal stress distributions in Figs. 10 and 11 are in good agreement, when allowance is made for the fact that the strains in Fig. 10(*a*) are equivalent shear strains, while those plotted in Fig. 11(*a*) are equivalent tensile strains. The differences in local field quantities would lead to different predictions for the initiation of failure by interfacial debonding, as found in Needleman (1992) for debonding at an inclusion with a circular cross-section.

5 Discussion

The present studies for a whisker embedded in a crystal show significant differences between the overall tensile properties predicted by crystal plasticity and those predicted by a phenomenological theory of plasticity with isotropic hardening, even though nearly identical stress-strain curves are predicted by these two material models for an unreinforced tensile test specimen. These differences are more pronounced for the higher volume fraction of whiskers analyzed, and it seems clear that the difference is associated with strongly localized flow induced by the high strain concentrations at the sharp whisker edge. For the lowest volume fraction analyzed the difference is much less in the range considered, since here the strain concentrations at the whisker edge grow less rapidly as a function of the average overall strain, but larger differences are expected at a later stage.

Predictions for the onset of shear band localization in uniformly stretched solids show a strong sensitivity to the constitutive law (Rice, 1977). Thus, it is well known that the classical elastic-plastic solid with isotropic hardening and normality of the plastic flow rule gives no localization at realistic strain levels, whereas rather early localization is predicted for materials that develop a vertex on the yield surface. This is quite significant in the context of the present paper, since the crystal model represents a solid with a vertex on the yield surface (e.g., see localization studies by the double slip model of Asaro, 1979). Even though the material models used in the present paper are rate sensitive, so that strictly speaking a vertex does not exist, the properties relating to localization predictions are still there (see Peirce et al., 1983). This localization gives rise to geometrical softening (Asaro, 1979; Peirce et al., 1983), as the strains grow large inside the bands, and therefore the stress-strain curves predicted here for the 30 percent whisker volume fraction crystal model show a noticeable stress drop at the end. Similar behavior is expected for the composites with 10 percent and 20 percent whisker volume fractions at somewhat larger overall strains.

The deformation patterns in Figs. 8 to 11, including those calculated based on a Mises material characterization, all show a concentration of strain in a fairly well defined band. This concentration of deformation into a band is induced by the geometric constraints, is relatively constitutive relation insensitive, and does not by itself lead to a stress drop. Such a concentration of deformation is not localization in the localization-instability sense used here. For the crystal constitutive relation, it is textural changes leading to geometric softening that induce localization, but other mechanisms can also precipitate localization. For example, matrix cavitation occurs in metal-matrix composites and the softening induced by progressive microrupture promotes localization, with an associated drop in stress carrying capacity (Christman et al., 1991; LLorca et al., 1991).

One of the three slip planes considered in the present analyses is chosen normal to the tensile direction, so that slip on this plane is not active in a homogeneous tensile test specimen (Fig. 2). However, this additional slip system plays a significant role in the strongly nonuniform flow around whiskers, and it is found (Fig. 6) that the stress levels are raised and that the predicted onset of localization is delayed, if only two slip systems are accounted for.

The present numerical studies are based on a planar model of the metal reinforced by short whiskers. An analogous axisymmetric cell-model analysis, with the whiskers represented as circular cylinders, would be significantly complicated by the fact that the crystal slip model does not have axisymmetric properties. Therefore, a full three-dimensional numerical analysis would be required. It is known that solids subject to axisymmetric stress conditions are far more resistant to localization than under plane-strain conditions (Needleman and Rice, 1978). On this basis it is expected that the cell model under axisymmetric stressing would show a much delayed influence of localized straining, but still a noticeably softer response could occur for the whisker embedded in a crystal than for one embedded in an isotropic hardening plastic solid.

Some composite models have made use of dislocation models of hardening, and the issue of whether or not a continuum theory of plasticity is appropriate for a given size of reinforcing particle is still subject to discussion. It is generally assumed that continuum theories apply when the dislocation cell size is small compared to the reinforcement size, and it has been found that the flow strength of Al-matrix composites is quite well explained by continuum plasticity models for a wide spectrum of SiC reinforcements (Christman et al., 1989; Tvergaard, 1990; Levy and Papazian, 1990; Evans et al., 1990). The present analyses represent an intermediate level, where the effect of specific slip plane orientations relative to whisker orientations is considered, without accounting for dislocation issues such as the resistance against bowing between whiskers, etc.

Acknowledgments

A.N. is grateful for support provided by the Office of Naval Research through grant N00014-89-J-3054. Computations reported here were carried out on the Cray YMP at the Pittsburgh Supercomputer Center and on a Stardent GS2000 workstation.

Downloaded 03 May 2010 to 171.66.16.245. Redistribution subject to ASME license or copyright; see http://www.asme.org/terms/Terms_Use.cfm

References

Asaro, R. J., 1979, "Geometrical Effects in the Inhomogeneous Deformation of Ductile Single Crystals," *Acta. Metall.*, Vol. 27, pp. 445–453.

Bao, G., Hutchinson, J. W., and McMeeking, R. M., 1991, "Particle Reinforcement of Ductile Matrices Against Plastic Flow and Creep," *Acta. Metall. Mater.*, Vol. 39, pp. 1871–1882.

Christman, T., LLorca, J., Suresh, S., and Needleman, A., 1991, "The Effect of Superposed Hydrostatic Stress on the Mechanical Responses of Metal-Matrix Composites," *Inelastic Deformation of Composite Materials*, G. Dvorak ed., Springer-Verlag, New York, p. 309.

Christman, T., Needleman, A., and Suresh, S., 1989, "An Experimental and Numerical Study of Deformation in Metal-Matrix Composites," *Acta Metall.*, Vol. 37, pp. 3029–3050 (see also Corrigendum, 1990, *Acta Metall. Mater.*, Vol. 38, p. 879).

Divecha, A. P., Fishman, S. G., and Karmarker, S. D., 1981, "Silicon Carbide Reinforced Aluminum—A Formable Composite," *J. Metals*, Vol. 33, pp. 12–17.

Evans, A. G., Hutchinson, J. W., and McMeeking, R. M., 1990, "Stress-Strain Behavior of Metal Matrix Composites with Discontinuous Reinforcements," Materials Department Report, University of California, Santa Barbara, CA.

Harren, S. V., and Asaro, R. J., 1989, "Nonuniform Deformation in Polycrystals and Aspects of the Validity of the Taylor Model," *J. Mech. Phys. Solids*, Vol. 37, pp. 191–232.

Havner, K. S., 1982, "The Theory of Finite Plastic Deformation of Crystalline Solids," *Mechanics of Solids* (The Rodney Hill 60th Anniversary Volume), H. G. Hopkins and M. J. Sewell eds., Pergamon Press, Oxford, p. 265.

Hill, R., and Rice, J. R., 1972, "Constitutive Analysis of Elastic-Plastic Crystals at Arbitrary Strain," *J. Mech. Phys. Solids.*, Vol. 20, pp. 401–413.

Hutchinson, J. W., 1976, "Bounds and Self-Consistent Estimates for Creep of Polycrystalline Materials," *Proc. Roy. Soc. Lond.*, Vol. A348, pp. 101–127.

Lee, E. H., 1969, "Elastic-Plastic Deformation at Finite Strains," ASME JOURNAL OF APPLIED MECHANICS, Vol. 36, pp. 1–6.

Levy, A., and Papazian, J. M., 1990, "Tensile Properties of Short Fiber Reinforced SiC/Al Composites: Part II Finite Element Analysis," *Metall. Trans.*, Vol. 21A, pp. 411–420.

LLorca, J., Needleman, A., and Suresh, S., 1991, "An Analysis of the Effects of Matrix Void Growth on Deformation and Ductility of Metal-Ceramic Composites," *Acta Metall. Mater.*, Vol. 39, pp. 2317–2335.

McDanels, D. L., 1985, "Analysis of Stress-Strain, Fracture, and Ductility Behavior of Aluminum Matrix Composites Containing Discontinuous Silicon Carbide Reinforcement," *Metall. Trans.*, Vol. 16A, pp. 1105–1115.

McHugh, P. E., Asaro, R. J., and Shih, C. F., 1991, "Computational Modeling of Metal Matrix Composite Materials," *Proceedings of the 1991 TMS Annual Meeting*, to be published.

McHugh, P. E., Varias, A. G., Asaro, R. J., and Shih, C. F., 1989, "Computational Modeling of Microstructures," *Fut. Gen. Comp. Systems*, Vol. 5, pp. 295–318.

Needleman, A., 1972, "A Numerical Study of Necking in Circular, Cylindrical Bars," *J. Mech. Phys. Solids*, Vol. 20, pp. 111–120.

Needleman, A., 1992, "Micromechanical Modeling of Interfacial Decohesion," *Ultramicroscopy*, Vol. 40, pp. 203–214.

Needleman, A., and Rice, J. R., 1978, "Limits to Ductility Set by Plastic Flow Localization," *Mechanics of Sheet Metal Forming*, D. P. Koistinen and N.-M. Wang, eds., p. 237, Plenum Press, New York, p. 237.

Nutt, S. R., and Needleman, A., 1987, "Void Nucleation at Fiber Ends in Al-SiC Composites," *Scripta Metall.*, Vol. 21, pp. 705–710.

Pan, J., and Rice, J. R., 1983, "Rate Sensitivity of Plastic Flow and Its Implications for Yield-Surface Vertices," *Int. J. Solids Struct.*, Vol. 19, pp. 973–987.

Peirce, D., Asaro, R. J., and Needleman, A., 1983, "Material Rate Dependence and Localized Deformation in Crystalline Solids," *Acta Metall.*, Vol. 31, pp. 1951–1976.

Rice, J. R., 1971, "Inelastic Constitutive Relations for Solids: An Internal Variable Theory and Its Application to Metal Plasticity," *J. Mech. Phys. Solids*, Vol. 19, pp. 433–455.

Rice, J. R., 1977, "The Localization of Plastic Deformation," *Theoretical and Applied Mechanics*, W. T. Koiter ed., North-Holland, Amsterdam, p. 207.

Tvergaard, V., 1976, "Effect of Thickness Inhomogeneities in Internally Pressurized Elastic-Plastic Spherical Shells," *J. Mech. Phys. Solids*, Vol. 24, pp. 291–304.

Tvergaard, V., 1990, "Analysis of Tensile Properties for a Whisker Reinforced Metal Matrix Composite," *Acta Metall. Mater.*, Vol. 38, pp. 185–194.

Zok, F., Embury, J. D., Ashby, M. F., and Richmond, O., 1988, "The Influence of Pressure on Damage Evolution and Fracture in Metal-Matrix Composites," *Mechanical and Physical Behavior of Metallic and Ceramic Composites*, S.I. Andersen et al., eds., Risø National Laboratory, Denmark, pp. 517–526.

Downloaded 03 May 2010 to 171.66.16.245. Redistribution subject to ASME license or copyright; see http://www.asme.org/terms/Terms_Use.cfm

Statistical Properties of Residual Stresses and Intergranular Fracture in Ceramic Materials

M. Ortiz
Mem. ASME.

S. Suresh
Mem. ASME.

Division of Engineering,
Brown University,
Providence, RI 02912

The problem addressed in this paper concerns the statistical characterization of the state of residual stress generated in polycrystalline ceramics during cooling from the fabrication temperature. Detailed finite element simulations are carried out for an ensemble of large numbers of randomly oriented, planar hexagonal grains with elastic and thermal expansion anisotropy, and brittle grain interfaces. The calculations show that the distribution of normal and shear tractions induced by thermal contraction mismatch among grains is gaussian and that these tractions are statistically independent random variables. Although the gaussian nature of the distributions remains unaffected by the introduction of elastic anisotropy, the results indicate that elastic anisotropy has a significant effect on the residual stresses for finite departures from isotropy. When the hexagonal grains are randomly distorted, the magnitude and distribution of residual stresses are found to be insignificantly altered. Spontaneous microfracture due to the generation of internal stresses is also simulated in the analysis by allowing for the nucleation and growth of intergranular microcracks when the fracture energy along the grain facets exceeds a certain critical value. When such microcracking is incorporated into the computation, the levels of residual stress are markedly reduced as a consequence of stress dissipation. The dependence of intergranular microcracking on grain size and temperature variation is examined and the predicted trends on material degradation or the complete suppression of microfracture are discussed in the light of available experimental results.

1 Introduction

In noncubic, single-phase polycrystalline aggregates and in multiphase mixtures of ceramic materials, cooling from the processing temperature gives rise to microstructural residual stresses. These internal stresses, induced by the anisotropy of thermal contraction between adjacent grains, can promote spontaneous cracking along grain facets (e.g., Clarke, 1964; Matsuo and Sasaki, 1966; Davidge and Green, 1968; Kuszyk and Bradt, 1973; Cleveland and Bradt, 1978; Evans, 1978; Blendell and Coble, 1982; Yu and Evans, 1985; Fredrich and Wong, 1986). The occurrence of microcracking has been found to depend on the scale of the microstructure in that there exists a critical grain size in single-phase systems below which grain boundary microfracture is essentially suppressed (Matsuo and Sasaki, 1966; Evans, 1978; Rice and Pohanka, 1979). In addition, prior studies have identified the existence of a critical grain size beyond which total loss of material integrity occurs in some ceramic materials (Kuszyk and Bradt, 1973; Rice and Pohanka, 1979). The cooling rate is also known to have an effect on the magnitude of the microstructural stresses and on the extent of microcracking (Blendell and Coble, 1982).

On the basis of a study of residual stresses developed in polycrystalline metals during repeated heating and cooling, Boas and Honeycombe (1946) postulated that microstructural stresses are relatively insensitive to elastic anisotropy. In more recent analyses of intergranular residual stresses in thermally anisotropic, but elastically isotropic, aggregates of planar hexagonal grains, Evans (1978) and Fu and Evans (1985) developed closed-form solutions for the distribution of internal stresses along grain facets. It was shown that a singularity exists for stresses near a grain boundary triple point. By means of a perturbation expansion, Ortiz and Molinari (1988) showed that elastic anisotropy is indeed a second-order effect when deviations from elastic and thermal isotropy are small. They went on to determining analytically some of the statistical properties of the residual stress distribution such as their mean square value. Some caution must be exercised, however, in interpreting these results. It is known that perturbation expansions may not converge pointwise, particularly close to singularities. To ascertain the conditions which develop at triple point junctions, for instance, more detailed analyses of the type conducted by Tvergaard and Hutchinson (1988) are required. These

Contributed by the Applied Mechanics Division of THE AMERICAN SOCIETY OF MECHANICAL ENGINEERS for publication in the ASME JOURNAL OF APPLIED MECHANICS.

Discussion on this paper should be addressed to the Technical Editor, Professor Lewis T. Wheeler, Department of Mechanical Engineering, University of Houston, Houston, TX 77204-4792, and will be accepted until four months after final publication of the paper itself in the ASME JOURNAL OF APPLIED MECHANICS.

Manuscript received by the ASME Applied Mechanics Division, May 14, 1991; final revision, Dec. 3, 1991. Associate Technical Editor: R. M. McMeeking.

Copyright © 1993 by ASME
Downloaded 03 May 2010 to 171.66.16.245. Redistribution subject to ASME license or copyright; see http://www.asme.org/terms/Terms_Use.cfm

investigators analyzed the stress singularities at triple points in planar arrays of hexagonal grains by an asymptotic method and by way of numerical simulation.

More recently, Laws and Lee (1989) have examined the evolution of residual stresses and microfracture in elastically isotropic and thermally anisotropic polycrystalline ceramics, the same case treated analytically by Ortiz and Molinari (1988). Laws and Lee (1989) have computed numerically the residual stress field for arbitrary orientation distributions of the axes of thermal anisotropy. They note that it is necessary to consider a two-dimensional polycrystalline ensemble of at least 200 grains in order to derive accurate predictions of the normal tractions at the midpoint of grain boundary facets.

Most of the analyses available to date on the generation of internal stresses by thermal and/or elastic anisotropy in brittle solids have been prediated upon specific choices of crystallographic orientations for neighboring grains within the polycrystalline ensemble (e.g., Evans, 1978; Fu and Evans, 1985; Tvergaard and Hutchinson, 1988). It is, however, evident that the random distribution of anisotropic grains in ceramic materials can give rise to residual stress patterns which may deviate markedly from those predicted by simple deterministic models. Furthermore, the limited number of grains for which analytical solutions of internal stresses and singularities have been discussed for some select cases of crystallographic anisotropy may not be representative of the trends exhibited by structural ceramics composed of large numbers of grains. Although analytical and numerical solutions of residual stress fields in polycrystalline aggregates consisting of large numbers of grains are beginning to emerge (e.g., Tvergaard and Hutchinson, 1988; Laws and Lee, 1989), the statistical properties of residual stress fields arising from thermal and elastic anisotropy remain largely unexplored.

In the present study, detailed finite element simulations have been carried out with the objective of investigating the statistical properties of the residual stress fields extending over large numbers of randomly oriented grains in single-phase brittle materials. The results provide valuable insights into the dependence of those properties on elastic and thermal anisotropy, grain size, and temperature. Furthermore, the nucleation and growth of grain boundary microcracks due to the development of residual stresses have also been analyzed, and the effects of grain size and thermal excursions on the extent of progressive microfracture have been investigated. In view of the present limitations of computational hardware, large-scale simulations must a fortiriori be based on two-dimensional models. It is expected, however, that many of the trends inferred from the two-dimensional analysis may carry over to the three-dimensional case as well.

2 Problem Formulation and Numerical Modeling

Throughout this study, we idealize a monolithic ceramic as an ensemble of randomly oriented, elastically and thermally anisotropic grains with brittle intergranular interfaces. We neglect any stress redistribution which may occur at high temperatures as a consequence of creep. Envision a process of cooling whereby the solid is brought from its fabrication temperature down to some final conditions, typically room temperature. The cooling is assumed to be slow enough that the temperature remains nearly uniform over the body at all times. During this cooling process, the body develops microstructural residual stresses due to the thermal and elastic anisotropy of grains. Our primary goal in this study is to develop an understanding of the statistical properties of the residual stress and microcrack distributions over large numbers of grains.

2.1 Modeling of Elastic and Thermal Properties. Under the assumptions of the analysis, the response of each grain is characterized by its elastic moduli C_{ijkl} and its thermal expansion coefficients α_{ij}. The components of these tensors on some global cartesian reference frame $\{x_1, x_2, x_3\}$ depend on the orientation of the grain. The dependence on grain orientation can be characterized by introducing a set of axes $\{x_1', x_2', x_3'\}$ attached to the crystalline lattice, Fig. 1. Then, if C'_{ijkl} and α'_{ij} denote the crystal thermal moduli and thermal expansion coefficients, respectively, the global components are given by

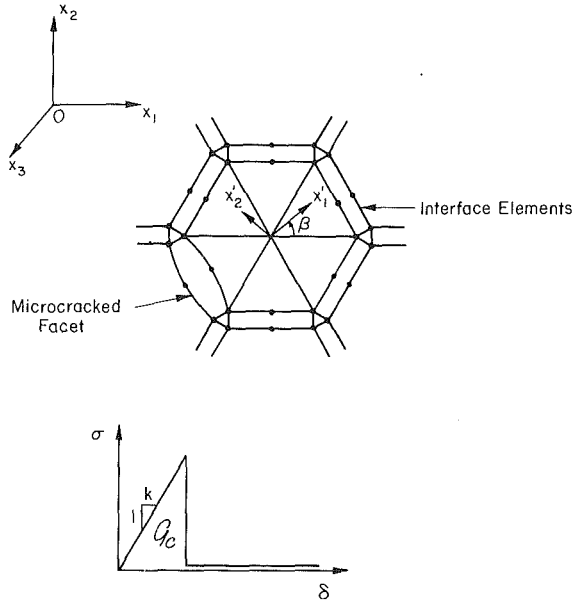


Fig. 1 Finite element model of hexagonal grain, showing connectivity with adjacent grains by means of interface elements. Inset is a schematic of the cohesive law obeyed by the interface elements. Also shown are the global and local grain cartesian axes. $x_3' = x_3$.

$$C_{ijkl} = Q_{im}Q_{jn}Q_{kp}Q_{lq}C'_{mnpq}$$
$$\alpha_{ij} = Q_{im}Q_{jn}\alpha'_{mn} \tag{1}$$

where Q_{ij} is the appropriate transformation tensor. As indicated above, Q_{ij} is taken as a uniformly distributed random variable. With these definitions, the stress-strain relations at the grain level may be expressed as

$$\epsilon'_{ij} = C'_{ijkl}\sigma'_{kl} + \theta\alpha'_{ij} \tag{2}$$

where ϵ'_{ij} and σ'_{ij} denote the components of strain and stress relative to the grain axes, respectively, and θ is the drop in temperature.

We confine our attention to a consideration of the relative roles played by elastic and thermal anisotropy in the generation of residual stresses and microcracking. In particular, we seek to ascertain whether the effect of elastic anisotropy is significant for finite departures from isotropy. To this end, a simple model proposed by Tvergaard and Hutchinson (1988) is employed. In the present notation, this model amounts to taking

$$C'_{ijkl} = \lambda\delta_{ij}\delta_{kl} + \mu(\sigma_{il}\delta_{jk} + \delta_{ik}\delta_{jl}) + (f-1)(\lambda+2\mu)\delta_{1i}\delta_{1j}\delta_{1k}\delta_{1l} + (f^{-1}-1)(\lambda+2\mu)\delta_{2i}\delta_{2j}\delta_{2k}\delta_{2l} \tag{3}$$

where λ and μ are Lamé-like constants and f is an additional material parameter. For $f=1$, the moduli are isotropic. For $f\neq 1$, the crystals become elastically orthotropic, with $\{x_1', x_2', x_3'\}$ as the principal axes of orthotropy. The quantity $\log(f)$ may conveniently be taken as a measure of anisotropy of the crystals.

The moduli (3) are designed for use in two-dimensional calculations, with $x_3 = x_3'$ as the out-of-plane direction. Tvergaard and Hutchinson (1988) noted that (3) does not model the elasticities of any particular ceramic, but that, choosing $f=\sqrt{2}$ gives a ratio of $C'_{1111}/C'_{2222} = 2$, which reflects the typical properties of a number of crystals (Simmons and Wang, 1971).

Downloaded 03 May 2010 to 171.66.16.245. Redistribution subject to ASME license or copyright; see http://www.asme.org/terms/Terms_Use.cfm

We note that the moduli (3) are orthotropic, with x_3' as one of the principal axes of orthotropy. Under these conditions, it is convenient to identify the grain axes with the principal axes of orthotropy. It is further assumed that the thermal expansion tensor α_{ij}' has the same principal axes as the elastic orthotropy, and the principal thermal expansion coefficients are denoted by α_1, α_2, and α_3.

In a two-dimensional setting, the orientations of the grains are defined by a single angle β such that

$$\mathbf{Q}=\begin{pmatrix}\cos\beta & -\sin\beta & 0\\ \sin\beta & \cos\beta & 0\\ 0 & 0 & 1\end{pmatrix}. \tag{4}$$

Throughout our simulations, we have taken β to be a random variable uniformly distributed in the range $[0, \pi]$. In actual finite element computations we have defined the orientations of individual grains using a random number generator.

All calculations presented in this paper are for plane-strain deformation, for which $\epsilon_{33}'=\epsilon_{33}=0$. This condition can be used, in conjunction with the orthotropy of the grains, to reduce (2) to the two-dimensional form

$$\begin{aligned}\epsilon_{11}' &= \left(C_{11\alpha\beta}'-\frac{C_{1133}'C_{33\alpha\beta}'}{C_{3333}'}\right)\sigma_{\alpha\beta}'+\left(\alpha_1-\frac{C_{1133}'}{C_{3333}'}\alpha_3\right)\theta\\ \epsilon_{22}' &= \left(C_{22\alpha\beta}'-\frac{C_{2233}'C_{33\alpha\beta}'}{C_{3333}'}\right)\sigma_{\alpha\beta}'+\left(\alpha_2-\frac{C_{2233}'}{C_{3333}'}\alpha_3\right)\theta\\ 2\epsilon_{12}' &= C_{1212}'\sigma_{12}'.\end{aligned} \tag{5}$$

Some useful insights into the parametric dependencies of the solution can be derived as follows. The parameters which define the model are Young's modulus E, Poisson's ratio ν, the dimensionless elastic anisotropy constant f, the temperature drop θ, the tensile strength of the facets σ_c, and the principal thermal expansion coefficients α_1, α_2, and α_3. However, these latter parameters and the temperature enter the formulation only through the combinations involved in (5).

Introduce the reduced coefficients

$$\alpha_1^*=\alpha_1-\frac{C_{1133}'}{C_{3333}'}\alpha_3,\quad \alpha_2^*=\alpha_2-\frac{C_{2233}'}{C_{3333}'}\alpha_3. \tag{6}$$

By the assumed isotropy of the distribution of grain orientations, it follows that α_1^*, α_2^*, and θ can only enter the solution through the combination $|\alpha_1^*-\alpha_2^*|\theta\equiv\alpha_e\theta$, where the effective thermal expansion coefficient α_e may be taken as a measure of the degree of thermal anisotropy of the grains. For moduli (3), it follows that $C_{1133}'=C_{2233}'=\lambda$, and the effective thermal expansion coefficient reduces to

$$\alpha_e=|\alpha_1-\alpha_2|. \tag{7}$$

We note that $\alpha_e=0$ if the grains are thermally isotropic.

2.2 Computational Model. In order to be able to make statistical inferences regarding the distribution of residual stresses, a large number of grains needs to be included in the analysis. This effectively rules out the possibility of conducting three-dimensional numerical simulations. Even in two dimensions, an idealized description of each individual grain needs to be adopted. In our calculations the polycrystalline ensemble is assumed to be topologically hexagonal (Fig. 1). Each grain is discretized into six four-noded elements, with quadratic displacement interpolation over the grain boundary. In some simulations, we have randomly distorted the grains with a view to studying the sensitivity of the results to grain geometry. This distortion is accomplished by displacing the nodes along random directions by a prescribed distance, typically some fraction of the facet length.

Adjacent grains are held together by means of three-noded surface elements (Fig. 1). These elements allow for quadratic opening displacements. The grain boundaries are assumed to be brittle and to crack according to the cohesive law shown in Fig. 1. This is linear in both the normal and shearing tractions up to a critical value of the former, at which point the strength of the boundary is assumed to drop to zero. The shaded area under the tensile cohesive law in Fig. 1 defines the critical energy release rate G_c in the absence of any shearing. The stiffness k of the interface is chosen to be the same in tension and in shear, and to be much larger than that of the surrounding grains. Under these conditions, the grain boundaries remain essentially undeformed up to decohesion. The cohesive law is enforced on three quadrature points of each surface element. At any given point in the solution, an element can simultaneously contain failed and intact quadrature points. This permits the simulation of partially fractured boundary facets. We also note that microcracks need not remain confined to a facet, but can extend across triple grain junctions into adjacent facets.

The calculations proceed incrementally. At each increment, the temperature is decreased by a prescribed amount. An iteration is then carried out until equilibrium is satisfied and the microcracking process has stabilized.

2.3 Sample Size Requirements. A key consideration in designing the numerical model concerns the number of grains required to accurately predict the various statistics of interest. Imagine that stresses are sampled at n points within the region of the solid under consideration. In calculations, the sampling points coincide with the quadrature points of the element. Denote by $\sigma_{\alpha\beta}^i$ the components of stress at sampling point i. By virtue of the randomness in the orientations of the grains, the pointwise values of the components of stress are themselves random variables of an as yet unknown distribution. By equilibrium, the average stresses

$$\langle\sigma_{\alpha\beta}\rangle=\frac{1}{n}\sum_{i=1}^{n}\sigma_{\alpha\beta}^i \tag{8}$$

must vanish identically. Let

$$\langle\sigma_{\alpha\beta}\sigma_{\gamma\delta}\rangle=\frac{1}{n}\sum_{i=1}^{n}\sigma_{\alpha\beta}^i\sigma_{\gamma\delta}^i \tag{9}$$

be the covariance matrix of the (pointwise) stresses. Analytical expressions for $\langle\sigma_{\alpha\beta}\sigma_{\gamma\delta}\rangle$ were obtained by Ortiz and Molinari (1988) for the case of thermally anisotropic but elastically isotropic solids. By the isotropy of the stress distribution it follows that $\langle\sigma_{\alpha\beta}\sigma_{\gamma\delta}\rangle$ must be an isotropic tensor, i.e., must be of the form

$$\langle\sigma_{\alpha\beta}\sigma_{\gamma\delta}\rangle=(\sigma^2-2\tau^2)\delta_{\alpha\beta}\delta_{\gamma\delta}+\tau^2(\delta_{\alpha\delta}\delta_{\beta\gamma}+\delta_{\alpha\gamma}\delta_{\beta\delta}) \tag{10}$$

where

$$\begin{aligned}\sigma &= \langle\sigma_{11}\sigma_{11}\rangle^{1/2}=\langle\sigma_{22}\sigma_{22}\rangle^{1/2}\\ \tau &= \langle\sigma_{12}\sigma_{12}\rangle^{1/2}\end{aligned} \tag{11}$$

are the standard deviations of the normal and shear tractions, respectively. These quantities provide scalar measures of the magnitude of the residual stresses. A further consequence of the isotropy of the covariance matrix is that $\langle\sigma_{11}\sigma_{12}\rangle=\langle\sigma_{22}\sigma_{12}\rangle=0$, i.e., the normal and shear stress components are uncorrelated pointwise.

The values of σ and τ corresponding to different microstructural realizations also define random variables. In actual simulations, however, only one particular grain arrangement, i.e., one single sample from the overall ensemble of polycrystalline bodies, is analyzed, and σ and τ are computed as in (9). A central question in sampling theory is how representative the parametric estimates so computed are of their respective ensemble averages. In general, the distributions of σ and τ may be expected to become increasingly more concentrated about their means as the size n of the sample (i.e., the number of grains included in the simulation) is increased. Thus, the larger

Downloaded 03 May 2010 to 171.66.16.245. Redistribution subject to ASME license or copyright; see http://www.asme.org/terms/Terms_Use.cfm

the choice of n, the more likely the computed values of σ and τ are to be close to their mean values.

Next, we wish to determine how large n needs to be for the mean and standard deviation of σ and τ to be within acceptable confidence intervals. Simple estimates of sample size requirements may be obtained from standard results of parametric point estimation (see, for example, Mood et al., 1974). Consider a random sample $(X_1, \ldots, X_n)$ of size n of a normally distributed variable X with mean m_1 and standard deviation m_2. Then, the maximum likelihood estimators M_1 and M_2 of m_1 and m_2 are given by the familiar expressions

$$M_1 = \frac{1}{n}\sum_{i=1}^{n} X_i, \quad M_2 = \frac{1}{n}\sum_{i=1}^{n} (X_i - M_1)^2, \tag{12}$$

respectively. Evidently, different finite samples may be expected to yield different values of M_1 and M_2. In fact, the values of M_1 and M_2 so obtained are themselves random variables. A particularly useful result is that, as the size of the sample $n \to \infty$, M_1 and M_2 are asymptotically normally distributed with mean m_1 and m_2, respectively, and variance

$$s_1^2 = m_2/n, \quad s_2^2 = 2m_2^2/n, \tag{13}$$

respectively. These standard deviations coincide with the so-called Cramér-Rao lower bounds (Mood et al., 1974).

Next, we apply these results to the residual stress distribution. As it will become apparent in subsequent discussions, $\sigma_{\alpha\beta}$ turn out to be very nearly normally distributed and uncorrelated. Hence, it follows from the above results that the maximum likelihood estimators (9) of σ and τ are themselves normally distributed with mean

$$m_\sigma = \sigma, \quad m_\tau = \tau \tag{14}$$

and standard deviation

$$s_\sigma^2 = 2\sigma^2/n, \quad s_\tau^2 = 2\tau^2/n. \tag{15}$$

From tables of the normal distribution, it is found that the computed values of σ and τ may be expected to lie in the intervals

$$\begin{aligned} m_\sigma - 1.96 s_\sigma \le \sigma \le m_\sigma + 1.96 s_\sigma \\ m_\tau - 1.96 s_\tau \le \tau \le m_\tau + 1.96 s_\tau, \end{aligned} \tag{16}$$

with 95 percent confidence. The implication of (16) is that, if we wish to obtain computed values of σ and τ within, say, p percent of the averages m_σ and m_τ with 95 percent confidence, then we must have

$$s_\sigma \le 0.51 p m_\sigma \quad s_\tau \le 0.51 p m_\tau. \tag{17}$$

Using (14) and (15), we obtain the condition

$$n \ge 2/(0.51p)^2 \tag{18}$$

If, for instance, we wish to impose a tolerance of ten percent on the results, i.e., $p = 0.1$, then a model containing $n \ge 769$ facets is required. This corresponds to an ensemble of 331 grains, or 4,303 nodal points. If the tolerance is lowered to one percent, then the number of facets must be increased to $n = 76{,}894$—clearly out of the realm of possibility for the present investigation. Throughout our calculations we have used a model containing 469 grains and 1,332 facets. The estimated standard deviations so obtained are within 7.6 percent of their mean values with 95 percent confidence. The finite element mesh comprises 4,146 solid elements and 6,097 nodal points.

3 Results of Numerical Simulations

3.1 Effect of Thermal Anisotropy. Our first simulations are aimed at characterizing the state of residual stress that develops in the linear range, i.e., in the absence of microcracking. By virtue of the linearity of the problem, the residual stresses are then proportional to the temperature drop. We start by considering the case of thermally anisotropic but elastically isotropic grains. This corresponds to taking $f = 1$ in (3). The properties of the material used in the calculations are: $E = 380$ GPa, $\nu = 0.25$, $\alpha_1 = 8.3 \times 10^{-6}$ °C^{-1}, $\alpha_2 = 9.0 \times 10^{-6}$ °C^{-1}, grain size $d = 25$ μm, and temperature drop $\theta = 1000$°C. For these parameters one has $\alpha_e = 0.7 \times 10^{-6}$ °C^{-1} and $\mu = 152$ GPa. These parameters are representative of polycrystalline alumina (e.g., Kingery et al., 1976).

Figures 2(*a-c*) show the histograms of the stress components σ_{11}, σ_{22}, σ_{12} computed at the quadrature points within the elements, as well as gaussian fits obtained through the standard formulas (12). As may be seen, the distributions are strikingly gaussian. The mean stresses are computed to be zero, as befits the self-equilibrated nature of the residual stress field. As expected from the isotropy of the distribution of grain orientations, the correlation between normal and shear stress components is virtually zero. In addition, σ_{11} and σ_{22} must be distributed identically. Under these conditions, the pointwise distribution of the residual stresses is fully described by the parameters σ and τ defined above. These parameters may be thought of as mean-square values of the normal and shear stresses, respectively, and thus arise as natural residual stress measures.

As a test of the adequacy of the mesh size and the resulting traction samples obtained in the simulations, we have repeated the above calculations for a larger mesh of 4326 solid elements and 9373 nodal points. This corresponds to an ensemble of 721 grains containing 2070 facets. The standard deviations computed from the coarser mesh were within five percent of those computed from the finer mesh, which represents a statistically insignificant deviation from the results of the smaller model.

3.2 Effect of Thermal and Elastic Anisotropy. Next, we investigate the effect of elastic anisotropy by setting $f = 1.414$ in the expression (3) for the elastic moduli. This choice of f has been used by Tvergaard and Hutchinson (1988) in their study of stress singularities at triple point junctions, and defines a rather substantial departure from elastic isotropy not unlike those found in some ceramic single crystals (Simmons and Wang, 1971). The resulting residual stress histograms are shown in Fig. 3. It is evident from these results that the gaussian nature of the distributions remains unaffected by the introduction of elastic anisotropy. As in the previous simulation, normal and shear stresses are found to be uncorrelated. However, the computed mean-square stresses are roughly three times larger than those computed under the assumption of elastic isotropy. These results indicate that, whereas thermal anisotropy may indeed be the main effect for small departures from thermal and elastic isotropy, as shown by Ortiz and Molinari (1988) for many actual polycrytalline materials the effect of elastic anisotropy cannot be neglected. All calculations presented in the sequel are for thermally as well as elastically anisotropic grains.

We also note the computed residual stresses are somewhat higher than those measured experimentally (e.g., Blendell and Coble, 1982, see discussions to follow). The assumption of no microcracking in the calculations is a contributing factor to this overshoot in the results. When microcracking is taken into account, the levels of stress are considerably reduced, as demonstrated in subsequent simulations. This underscores the important role played by microcracking as a stress dissipation mechanism.

3.3 Effect of Grain Distortion. The above calculations were carried out on an undistorted mesh, i.e., one in which all the grains are taken to be perfectly hexagonal. The results of the computations, however, are found to be quite insensitive to the degree of distortion of the mesh. If, for instance, the

Downloaded 03 May 2010 to 171.66.16.245. Redistribution subject to ASME license or copyright; see http://www.asme.org/terms/Terms_Use.cfm

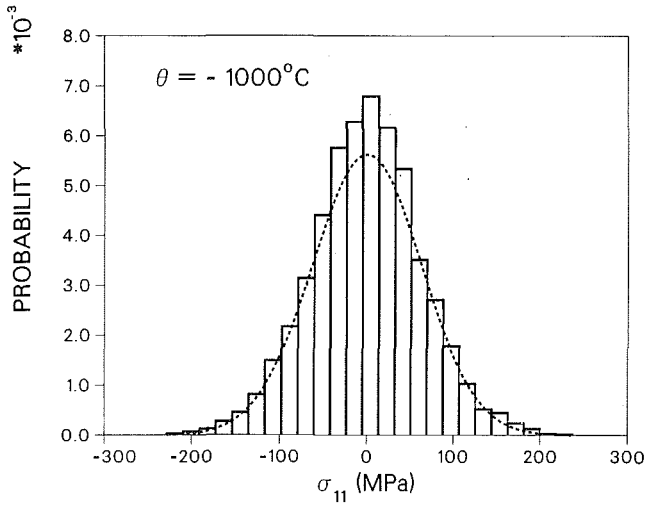


Fig. 2(*a*)

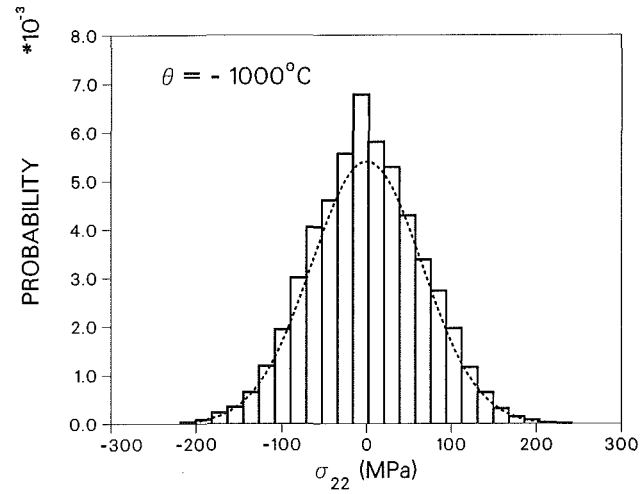


Fig. 2(*b*)

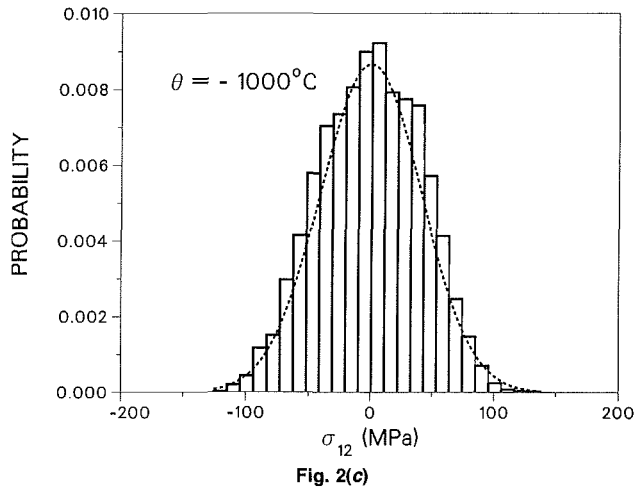


Fig. 2(*c*)

Fig. 2 Distribution of residual stresses induced by thermal anisotropy in the absence of elastic anisotropy and microcracking. Regular hexagonal mesh. Dashed lines represent gaussian fits to the computed distributions.

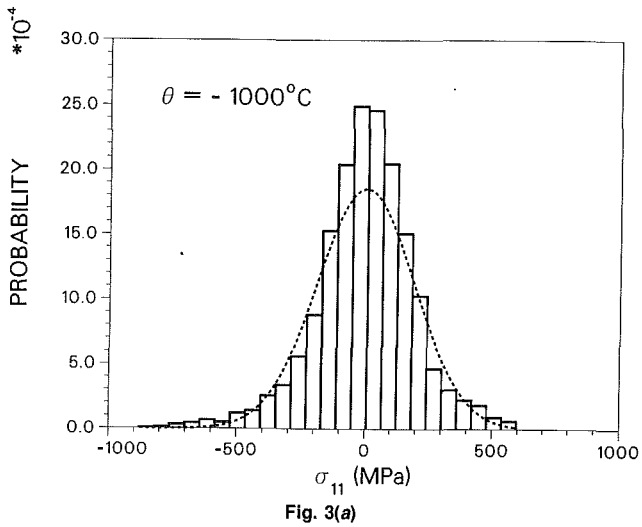


Fig. 3(*a*)

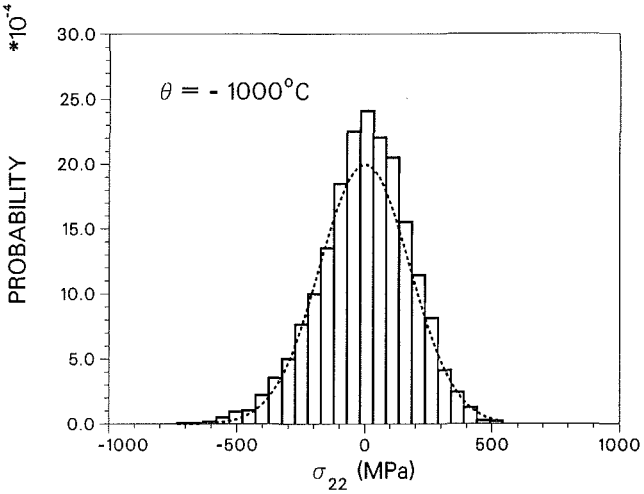


Fig. 3(*b*)

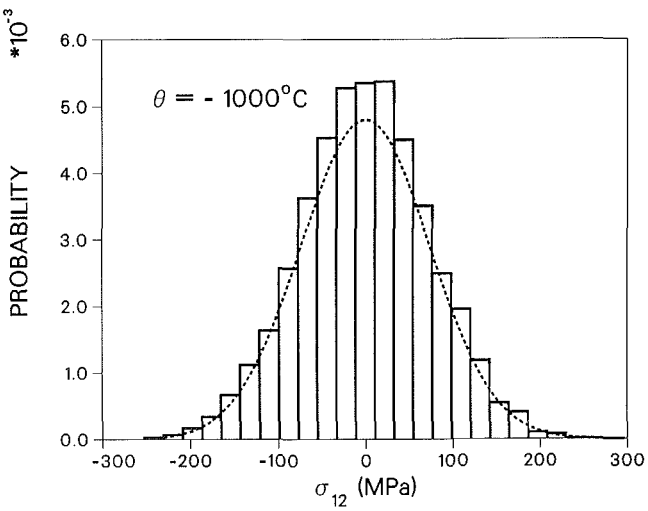


Fig. 3(*c*)

Fig. 3 Distribution of residual stresses induced by thermal and elastic anisotropy in the absence of microcracking. Regular hexagonal mesh. Dashed lines represent gaussian fits to the computed distributions.

nodes defining the grain boundaries are displaced in random directions by one fifth of the facet length, the computed mean-square stresses are within six percent of those corresponding to the undistorted mesh. The histograms of normal and shear stress are also found to be ostensibly similar to those for the regular geometry. All remaining calculations are based on the perfectly hexagonal model.

3.4 Grain Boundary Microcracking. Next, we extend the analysis into the nonlinear range by allowing for the formation of microcracks along grain boundaries. The surface energy γ of the facets which, as discussed in Section 2.2, governs microcrack growth, is taken to be 1 J/m, which is typical of monolithic ceramics. Figure 4 shows the histograms of normal and

Downloaded 03 May 2010 to 171.66.16.245. Redistribution subject to ASME license or copyright; see http://www.asme.org/terms/Terms_Use.cfm

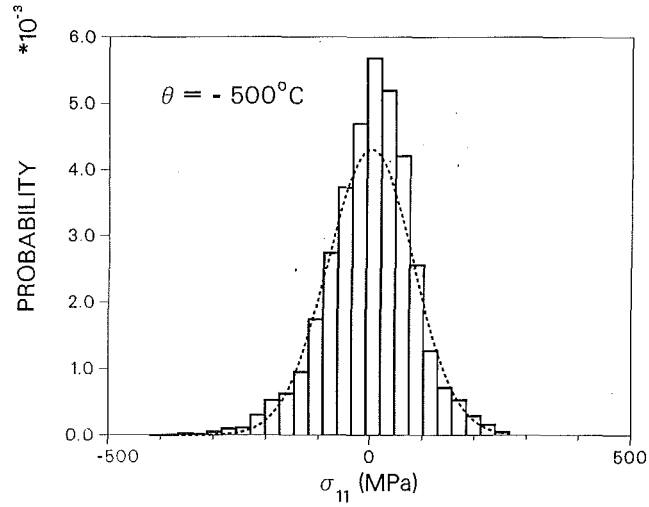


Fig. 4(*a*.1)

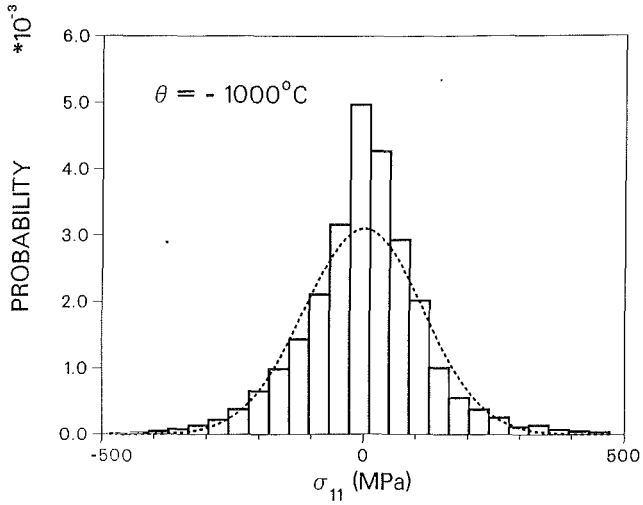


Fig. 4(*b*.1)

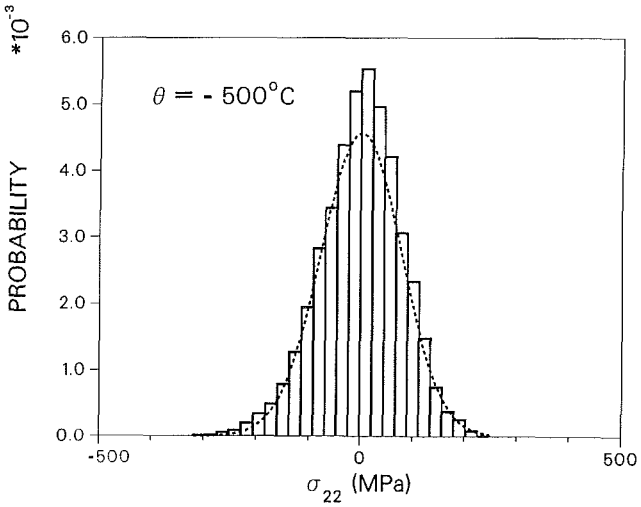


Fig. 4(*a*.2)

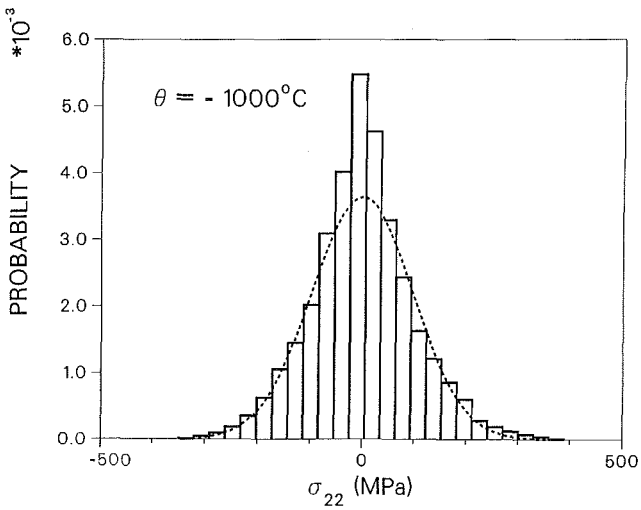


Fig. 4(*b*.2)

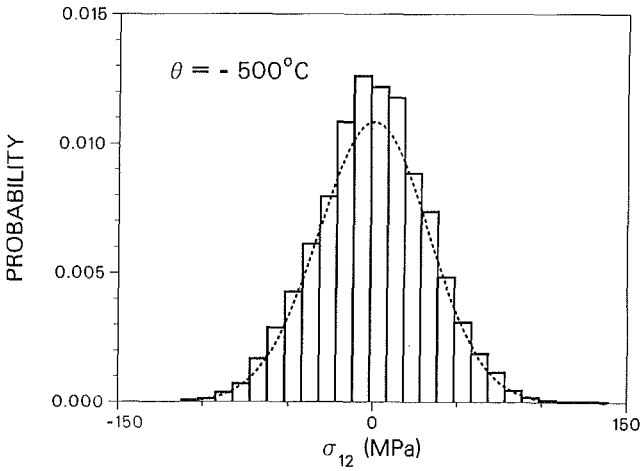


Fig. 4(*a*.3)

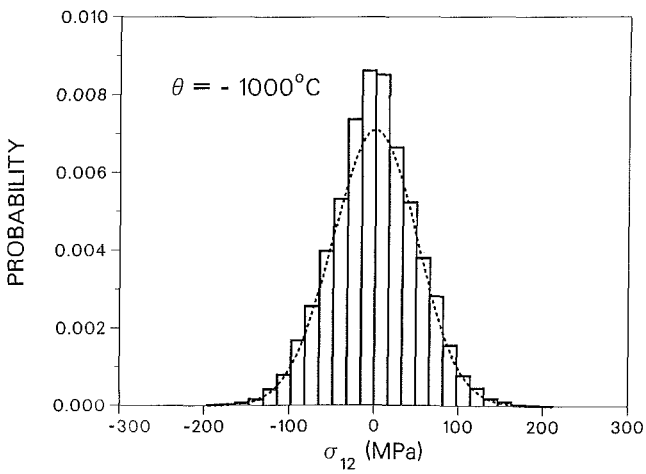


Fig. 4(*b*.3)

Fig. 4 Distribution of residual stresses induced by thermal anisotropy, elastic anisotropy, and microcracking for two different temperature drops. Regular hexagonal mesh. Dashed lines represent gaussian fits to the computed distributions.

Downloaded 03 May 2010 to 171.66.16.245. Redistribution subject to ASME license or copyright; see http://www.asme.org/terms/Terms_Use.cfm

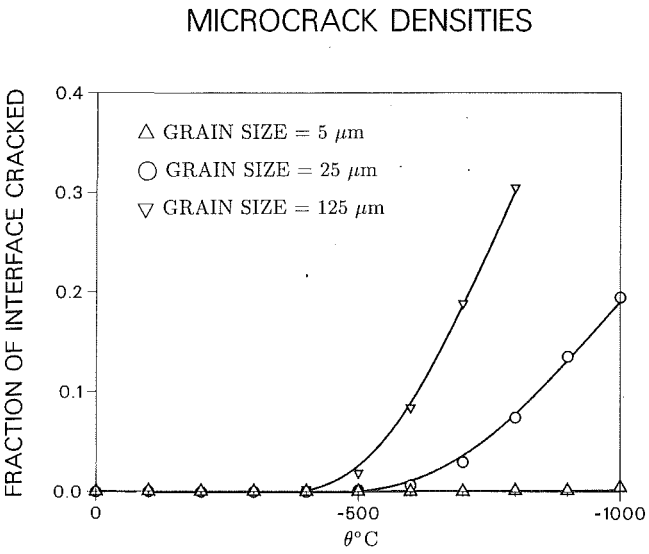


Fig. 5 Dependence of the fraction of cracked intergranular facets on temperature drop for three grain sizes

shear residual stress in a thermally and elastically anisotropic polycrystalline material ($f=1.414$) subjected to temperature reductions of 500°C and 1000°C. It is noted that, because of the varying extent of microcracking, the computed stresses no longer vary linearly with the temperature drop. Thus, the computed mean-square normal and shear stresses are $\sigma=91$ MPa and $\tau=37$ MPa, respectively, for a temperature drop of 500°C and $\sigma=121$ MPa and $\tau=56$ MPa for a temperature drop of 1000°C. As before, the normal and shear stresses are ostensibly normally distributed and nearly uncorrelated. As expected, however, the mean-square residual stresses are sharply reduced from the values predicted for the case where no intergranular fracture is permitted. This result illustrates the important role played by microcracking in reducing the levels of residual stress.

The variation of the fraction of microcracked facets with the temperature drop is plotted in Fig. 5 for grain sizes 5 μm, 25 μm, and 125 μm. Contrary to the simulations discussed in previous sections which are insensitive to grain size effects, here the surface energy of the facets introduces a length scale into the problem, with the consequence that, after microcracking sets in, the results are markedly dependent on grain size.

It is apparent from Fig. 5 that, for a fixed temperature drop, there exists a critical grain size (in the present case, at least 5 μm) below which grain boundary microcracking due to thermal and elastic anisotropy is completely suppressed. This prediction of the model is fully consistent with previous experimental and analytical results (Kuszyk and Bradt, 1973; Evans, 1978; Rice and Pohanka, 1979; Fu and Evans, 1985; Laws and Lee, 1989). For instance, Kuszyk and Bradt (1973) and Evans (1978) detected no appreciable microcracking below a threshold grain size. Also in keeping with the available observational evidence (Kuszyk and Bradt, 1973; Evans, 1978), for the grain size range 15–150 μm the computed extent of microcracking increases rapidly with grain size. Indeed, Rice and Pohanka (1979) have observed considerable microcracking in alumina at grain sizes of about 100 μm. The behavior of very coarse grained systems varies from material to material. For some systems, beyond a certain grain size the rate at which microcracking increases with grain size slows down, probably due to saturation. Other systems spontaneously disintegrate as a result of extensive microfracture (Rice and Pohanka, 1979).

For the coarsest grained material considered in the calculations (grain size = 125 μm), some grains become completely detached following a temperature drop of the order of 800°C, and the calculations have to be stopped. Thus, under the conditions of the analysis, spontaneous disintegration seems to occur prior to microcrack saturation. Whether or not disintegration precedes saturation in the numerical simulations is likely to depend critically on how triple grain joints are modeled and, more specifically, on the precise manner in which microcracks are allowed to propagate through triple points. For instance, if triple points are assumed to act as strong barriers to microcrack growth, then microcracks will tend to remain stably confined within isolated grain facets, and saturation will eventually be attained. Additionally, the two-dimensional nature of the model can be expected to facilitate the full detachment of grains, thus promoting disintegration.

4 Discussion

The finite element simulations conducted in this work provide detailed predictions of the magnitude and statistical distribution of thermal residual stresses in brittle solids. The implications of these results are now examined in the context of available experimental results for polycrystalline aggregates of noncubic ceramic materials.

For polycrystalline aluminum oxide with a grain size range of 50 to 150 μm, Blendell and Coble (1982) measured the internal stresses in the material at 77 K by means of the broadening of spectroscopic R lines following cooling from a temperature of 2150 K at constant cooling rates of 0.1 to 100 K/min. It has been suggested that there exists a freezing temperature below which the internal stresses build up during cooling without stress relaxation; this freezing temperature ($\approx$ 1500 K for alumina) has been postulated to be independent of grain size and cooling rate (Blendell and Coble, 1982). Incorporating thermal and elastic anisotropy and allowing for spontaneous microcracking (and the attendant stress relaxation), the mean-square normal and shear residual stresses computed in the present study are $\sigma\approx 120$ MPa and $\tau\approx 55$ MPa, respectively, for a grain size of 25 μm and a temperature drop of 1000°C. Given that the extent of microcracking increases rapidly with grain size, the level of residual stress at the grain size of 50 μm considered by Blendell and Coble (1982) should be somewhat reduced from the level corresponding to a grain size of 25 μm considered in our calculations. Indeed, the maximum value of residual stresses observed by Blendell and Coble (1982) was in the range 80 to 100 MPa for the conditions investigated. Because measurements of microstructural residual stresses using spectroscopic methods are inherently prone to considerable experimental scatter and uncertainties, the agreement between the computed and measured residual stress levels may be considered satisfactory.

Our estimates of the dependence of microcrack density on the grain size also provide an opportunity for comparisons with experiment. The calculations show that, for alumina with a grain size smaller than 5 μm, essentially no microcracking occurs for a temperature drop of 1000°C. It may then be inferred that thermally induced microfracture is essentially suppressed for fine-grained ceramics. The results of several independent experimental investigations on the threshold for spontaneous microcracking in ceramics are seen to be consistent with the trends predicted by the finite element calculations: (i) Evans (1978) examined the conditions for grain boundary microfracture due to thermal stresses in sintered (lucalox) Al_2O_3 that was annealed at various times to yield a range of grain sizes. For a temperature drop of 1850°C, a threshold for the suppression of microcracking was identified. In transmission electron microscopy observations, no microcracks could be detected below an average grain size of about 80 μm. (ii) Kuszyk and Bradt (1973) and Cleveland and Bradt (1978) investigated the relationship between microcracking and grain size in three pseudobrookite oxides, $MgTi_2O_5$, Fe_2TiO_5,

Downloaded 03 May 2010 to 171.66.16.245. Redistribution subject to ASME license or copyright; see http://www.asme.org/terms/Terms_Use.cfm

and Al_2TiO_5, which have a significantly greater degree of thermal anisotropy than polycrystalline Al_2O_3. For these three oxides, the threshold grain size for the total suppression of intergranular microfracture during cooling was reported to be 5 μm, 3 μm, and 1 μm, respectively (Kuszyk and Bradt, 1973; Cleveland and Bradt, 1978). (iii) In situ observations of intergranular microcracking in notched plates of alumina subjected to cyclic compression at room temperature reveal that the extent of microcracking decreases significantly with decreasing grain size (Suresh and Brockenbrough, 1988). Here microcracking damage in the vicinity of the notch tip and the attendant nucleation of a fatigue crack are strongly influenced by both the residual stresses (arising from thermal and elastic anisotropy) and the imposed cyclic compressive stresses (Suresh, 1991).

There is considerable uncertainty in identifying the conditions that control thermal stress-induced microfracture because of the experimental difficulties in observing the microcracks (especially in fine-grained materials) and the wide variations in compositions and processing conditions used by different investigators. There is general agreement on the existence of a threshold grain size for microcracking and on the deleterious role of coarser grains in exacerbating spontaneous intergranular microfracture during cooling (e.g., Rice and Pohanka, 1979). In keeping with these observations, in our calculations we observe a precipitous increase in the number of cracked facets above a grain size of about 20 μm, and a certain tendency of coarse grained materials to disintegrate beyond a critical temperature drop. This latter effect, however, may be sensitive to details in the modeling of triple points and be promoted by the two-dimensional character of the formulation.

Although the present analyses pertain to a planar array of equi-axed grains, the trends observed in the statistical properties of the residual stresses can be reasonably expected to carry over to three dimensions. Refinements to the analysis should include the consideration of local stress concentrations at multiple grain junctions, the detailed modeling of microcrack growth through those junctions, and the consideration of three-dimensional grain geometries.

Acknowledgments

The authors wish to thank Dr. Lynn Ewart for her help with the finite element modeling. This work has been supported by the Materials Research Group on Micro-Mechanics of Failure-Resistant Materials at Brown University which is funded by the National Science Foundation under grant DMR-9002994. S. S. acknowledges the support of the U.S. Dept. of Energy under grant DE-FG02-84ER-45167.

References

Blendell, J. E., and Coble, R. L., 1982, "Measurement of Stress Due to Thermal Expansion Anisotropy in Al_2O_3," *Journal of the American Ceramic Society*, Vol. 65, No. 3, pp. 174–78.

Boas, W., and Honeycombe, R. W. K., 1946, "The Plastic Deformation of Non-Cubic Metals by Heating and Cooling," *Proceedings of the Royal Society, London*, Vol. A186, No. 1, pp. 57–71.

Clarke, F. J. P., 1964, "Residual Strain and the Fracture Stress-Grain Size Relationship in Brittle Solids," *Acta Metallurgica*, Vol. 12, No. 2, pp. 139–43.

Cleveland, J. J., and Bradt, R. C., 1978, "Grain Size/Microcracking Relations for Pseudo-brookite Oxides," *Journal of the American Ceramic Society*, Vol. 61, No. 11–12, pp. 478–81.

Davidge, R. W., and Green, T. J., 1968, "Strength of Two-Phase Ceramic/Glass Materials," *Journal of Materials Science*, Vol. 3, No. 6, pp. 629–34.

Evans, A. G., 1978, "Microfracture from Thermal Expansion Anisotropy—I. Single Phase Systems," *Acta Metallurgica*, Vol. 26, No. 12, pp. 1845–1853.

Fredrich, J. T., and Wong, T.-F., 1986, "Micromechanics of Thermally Induced Cracking in Three Crustal Rocks," *Journal of Geophysical Research B*, Vol. 91, No. 12, pp. 12,743–12,764.

Fu, Y., and Evans, A. G., 1985, "Some Effects of Microcracks on the Mechanical Properties of Brittle Solids—I. Stress, Strain Relations," *Acta Metallurgica*, Vol. 33, No. 8, pp. 1515–1523.

Kingery, W. D., Bowen, H. K., and Uhlmann, D. R., 1976, *Introduction to Ceramics*, 2nd ed., John Wiley and Sons, New York.

Kuszyk, J. A., and Bradt, R. C., 1973, "Influence of Grain Size on Effects of Thermal Expansion Anisotropy in $MgTi_2O_5$," *Journal of the American Ceramic Society*, Vol. 56, No. 8, pp. 420–23.

Laws, N., and Lee, J. C., 1989, "Microcracking in Polycrystalline Ceramics: Elastic Isotropy and Thermal Anisotropy," *Journal of the Mechanics and Physics of Solids*, Vol. 37, No. 5, pp. 603–618.

Matsuo, Y., and Sasaki, H., 1966, "Effect of Grain Size on Microcracking in Lead Titanate Ceramics," *Journal of the American Ceramic Society*, Vol. 49, No. 4, pp. 229–30.

Mood, A. M., Graybill, F. A., and Boes, D. C., 1974, *Introduction to the Theory of Statistics*, 3rd ed., McGraw-Hill, New York.

Ortiz, M., and Molinari, A., 1988, "Microstructural Residual Stresses in Ceramic Materials," *Journal of the Mechanics and Physics of Solids*, Vol. 36, No. 4, pp. 385–400.

Rice, R. W., and Pohanka, R. C., 1979, "Grain Size Dependence of Spontaneous Cracking in Ceramics," *Journal of the American Ceramic Society*, Vol. 62, No. 11–12, pp. 559–563.

Simmons, G., and Wang, H., 1971, *Single Crystal Elastic Constants and Calculated Aggregate Properties: A Handbook*, 2nd ed., MIT Press, Cambridge, MA.

Suresh, S., 1991, *Fatigue of Materials*, Cambridge University Press, Cambridge, U.K.

Suresh, S., and Brockenbrough, J. R., 1988, "Theory and Experiments of Fracture in Cyclic Compression: Single Phase Ceramics, Transforming Ceramics and Ceramic Composites," *Acta Metallurgica*, Vol. 36, No. 6, pp. 1455–1470.

Tvergaard, V., and Hutchinson, J. W., 1988, "Microcracking in Ceramics Induced by Thermal Expansion or Elastic Anisotropy," *Journal of the American Ceramic Society*, Vol. 71, No. 3, pp. 157–166.

Downloaded 03 May 2010 to 171.66.16.245. Redistribution subject to ASME license or copyright; see http://www.asme.org/terms/Terms_Use.cfm

B. S. Hockenhull[2]
School of Industrial Science,
Cranfield Institute of Technology,
Cranfield, U.K.

E. M. Kopalinsky

P. L. B. Oxley

School of Mechanical and
Manufacturing Engineering,
University of New Youth Wales,
Kensington, N.S.W. 2033,
Australia

Predicting Wear for Metal Surfaces in Sliding Contact Using a Low-Cycle Fatigue Wear Model[1]

The frictional force when a hard surface slides over a relatively soft one is explained as the force needed to push waves of plastically deformed material along the soft surface ahead of asperities on the hard one. Using plastic strain increments determined from the wave model and assuming that wear occurs as a result of low-cycle fatigue, predictions are made of wear which take account of the surface roughness and lubrication conditions and a comparison is made with experimental results. Metallographic results are given which support the assumption that low cycle fatigue is important in causing surface damage and hence wear. These results also show that ironing of the surface by the passage of waves leads to surface damage and wear. It is concluded that in future work account will have to be taken of both low-cycle fatigue and ironing in making wear predictions.

1 Introduction

The genesis of the present work is to be found in two papers by Green (1954, 1955). In these he applied plasticity theory to estimate the forces involved in asperity deformation and obtained slipline field solutions for both strong and weak junctions, with no sliding at the interface of the contacting asperities for the former but with sliding for the latter. Like Bowden and Tabor (1950) and most subsequent workers, Green was firmly committed to the adhesion asperity interaction model and considered the life cycle of a typical asperity interaction to consist of formation, deformation, and fracture. Considering the adhesion model too severe for many practical sliding conditions, Challen and Oxley (1979) have developed a model for the case of a hard surface sliding over a relatively soft one which need not involve fracture. In this the frictional force is explained as the force needed to push waves of plastically deformed material in the soft surface ahead of asperities on the hard surface. It is this wave model which forms the basis of the work considered in this paper. The model is now described.

2 Wave Model

The plane-strain (rigid-perfectly plastic) slipline field and hodograph introduced by Challen and Oxley (1979) to represent the wave formation process are given in Fig. 1. In this the hard asperity is assumed to be rigid so that plastic deformation of only one surface need be considered. The field is similar to Green's field for a weak junction and also to fields used by Collins (1972) in considering rolling contact and by Johnson and Rowe (1968) in representing the wave that can occur ahead of the die in wire drawing. The interface DE between the hard asperity and soft asperity (wave) and the surface EA, which is taken to be stress free, are both assumed to be straight with their directions defined by the angles α and η measured from the sliding direction, which for convenience is represented by the velocity U of the soft material, the hard asperity being assumed to be stationary.

In constructing the slipline field the independent variables

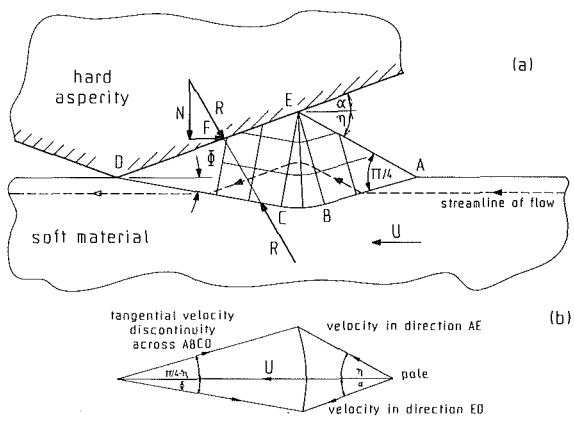


Fig. 1 Wave model: (*a*) slipline field; (*b*) hodograph

[1]This paper was presented at the 1990 ASME Winter Annual Meeting, Dallas, Texas at a session on "Intersections of Tribology and Fracture."

[2]Deceased.

Contributed by the Applied Mechanics Division of THE AMERICAN SOCIETY OF MECHANICAL ENGINEERS for publication in the ASME JOURNAL OF APPLIED MECHANICS.

Discussion on this paper should be addressed to the Technical Editor, Professor Lewis T. Wheeler, Department of Mechanical Engineering, University of Houston, Houston, TX 77204-4792, and will be accepted until four months after final publication of the paper itself in the ASME JOURNAL OF APPLIED MECHANICS.

Manuscript received by the ASME Mechanics Division, Dec. 3, 1990; final revision, Feb. 7, 1992. Associate Technical Editor: L. M. Keer.

Copyright © 1993 by ASME
Downloaded 03 May 2010 to 171.66.16.245. Redistribution subject to ASME license or copyright; see http://www.asme.org/terms/Terms_Use.cfm

are taken to be the slope of the hard asperity, α (surface roughness parameter) and the normalized strength of the interfacial film along DE, f (lubrication parameter). The latter is defined in the usual way as the ratio of the shear strength of the film τ to the shear flow stress of the soft material k (which will be constant for the assumed perfectly plastic material); i.e., $f = \tau/k$, with $0 \le f \le 1$. For the plastic wave process, the straight line joining A and D must be parallel to U to satisfy continuity. Also, the shear force on the soft asperity at the interface must act in the direction DE to oppose motion, with the value of f determining the inclination of the sliplines to DE. These conditions, together with the condition that the sliplines must be inclined at an angle, $1/4\pi$ to the stress free surface EA to satisfy equilibrium, define the slipline field and it follows from geometry that

$$\alpha + \Phi = \frac{1}{2} \arccos f \tag{1}$$

and

$$\eta = \arcsin\{(1-f)^{-1/2} \sin\alpha\} \tag{2}$$

where Φ is the angle between CD and U, and is measured positive as shown in Fig. 1. The hodograph shows that there is a discontinuity in the tangential component of velocity across the boundary slipline $ABCD$ so that material that enters and leaves the field with a velocity U flows in the directions AE and ED in the regions ABE and CDE and along a curved path in the centered fan region BCE, as shown by the typical streamline given in Fig. 1. The range over which the solution can apply is determined from the condition that Φ must be positive so that material can flow into and out of the wave. Taken in conjunction with Eqs. (1) and (2) this gives $\alpha \le \eta \le 1/4\pi$.

It can be shown from the stress analysis of the slipline field (see Challen and Oxley, 1979) that the horizontal and vertical components of the resultant force R (Fig. 1) per unit width are given by

$$F = k\left[\left\{1 + 2\left(\frac{1}{4}\pi + \Phi - \eta\right)\right\}\sin\alpha + \cos(\alpha + 2\Phi)\right]d \tag{3}$$

and

$$N = k\left[\left\{1 + 2\left(\frac{1}{4}\pi + \Phi - \eta\right)\right\}\cos\alpha + \sin(\alpha + 2\Phi)\right]d \tag{4}$$

where d is the length of the interface DE. For a given normal force N, d can be determined from Eq. (4) and substituted in Eq. (3) to give the corresponding frictional force F. The basic laws of friction are therefore satisfied with F proportional to N and independent of the area of the contacting surfaces. From Eqs. (3) and (4) and by substituting for Φ and η from Eqs. (1) and (2) the coefficient of friction $\mu = F/N$ given by the wave model can be expressed as

$$\mu = \frac{A\ \sin\alpha + \cos(\arccos f - \alpha)}{A\ \cos\alpha + \sin(\arccos f - \alpha)} \tag{5}$$

where

$$A = 1 + \frac{1}{2}\pi + \arccos f - 2\alpha - 2\ \arcsin\{(1-f)^{-1/2}\ \sin\alpha\}.$$

Equation (5) shows that for the range of validity of the wave model μ falls in the range $0 \le \mu \le 1$.

Experiments have been made by Challen et al. (1984) to check the wave model and in particular to determine how accurately Eq. (5) predicts μ. In the experiments a hard wedge (model asperity) was indented vertically into the horizontal surface of the softer specimen material with subsequent movement of the specimen relative to the wedge in a direction parallel to its surface and normal to the edge of the wedge. Approximate plane-strain conditions were achieved by clamping the specimen between side plates which also formed the sides of a bath for containing the lubricant where a liquid lubricant was used. The loading system was such that the wedge was free to move up or down during the horizontal movement of the specimen thus allowing a constant vertical force (N in Fig. 1) to be maintained during a test. Challen et al. (1984) have given a detailed description of the test rig used in their experiments. In this the forces were measured using load cells and the wedge and specimen were disengaged at the end of a test using a roller and ramp device. More recently, Black et al. (1988) have improved the rig in two main ways. First they have introduced a hydraulic "quick-stop" device for disengaging the wedge and specimen which allowed far more rapid disengagement thus leaving the deformed material in a state very close to that in the actual test, and second they have used a Kistler dynamometer, which formed part of the specimen assembly, to enable more accurate measurements of the forces to be made.

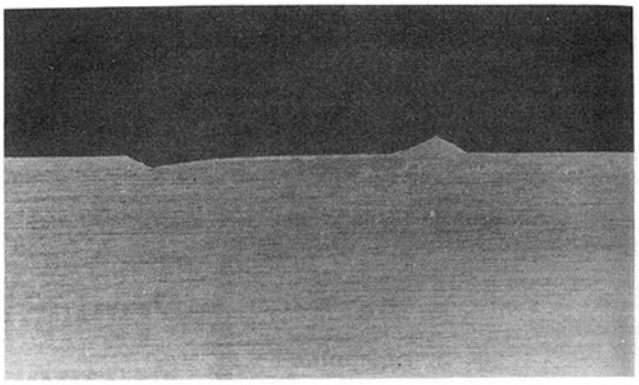


Fig. 2 Photograph showing initial indentation on left and wave being pushed along surface on right: height of wave ≈0.4 mm

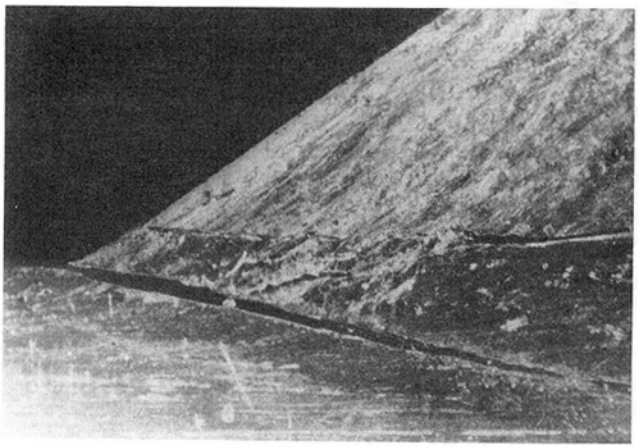


Fig. 3 Photograph showing crack

The results obtained by Challen et al. (1984) showed that when horizontal movement of the specimen occurred after initial indentation the wedge first dug in deeper as the vertical force was transferred to a single face of the wedge and then rose on material plastically deformed by this face. Then depending on the conditions (wedge angle and lubrication condition), either a steady-state wave was pushed along the surface as shown in Fig. 2, or cracks occurred in the deforming material, as shown in Fig. 3, and the process was nonsteady state. For those conditions for which a wave was formed the values of μ were calculated from the measured values of F and N and compared with the values given by Eq. (5) for the corresponding values of α and f. The agreement was found to be excellent for a wide range of α and f values. More recently, Black et

Downloaded 03 May 2010 to 171.66.16.245. Redistribution subject to ASME license or copyright; see http://www.asme.org/terms/Terms_Use.cfm

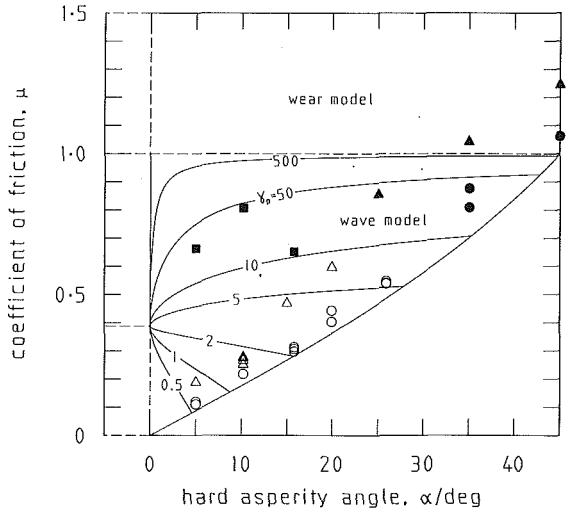


Fig. 4 Experimental results showing when cracking occurred (solid symbols) and when a wave was formed (open symbols) and theoretical results represented as constant γ_p lines

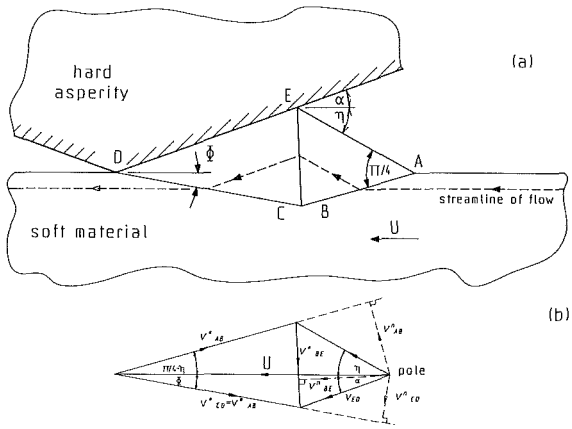


Fig. 5 Simplified wave model for calculating shear strain occurring as material flows through wave: (*a*) pattern of velocity discontinuities; (*b*) hodograph

al. (1988) have confirmed this good agreement for an even wider range of conditions. In considering real asperities as opposed to model asperities, Moalic et al. (1987) have shown that Eq. (5) predicts μ accurately for actual surfaces as long as α is measured from those regions of the asperities on the surface actually in contact during sliding.

The results in Fig. 4 (Challen et al., 1984) show those experimental conditions where cracking occurred (solid symbols) and those where a wave was formed (open symbols). Also given in Fig. 4 are the values of maximum shear strain γ_p (represented by lines of equal γ_p) occurring as material flows through the wave. This strain can be calculated from the slipline field and hodograph given in Fig. 1. However, it can be calculated more conveniently by replacing the centered fan region of Fig. 1 by a tangential velocity discontinuity as shown in Fig. 5. The shear strain occurring in crossing a tangential velocity discontinuity is given by the magnitude of the discontinuity v^* divided by the magnitude of the velocity normal to the discontinuity v^n. Therefore, with reference to Fig. 5,

$$\gamma_p = \frac{v^*_{AB}}{v^n_{AB}} + \frac{v^*_{BE}}{v^n_{BE}} + \frac{v^*_{CD}}{v^n_{CD}}. \tag{6}$$

The values of γ_p given in Fig. 4 were calculated by assuming that in the theoretical wave formation region, defined in Fig. 4 by the bottom line which corresponds to $f = 0$, $\mu = \tan\alpha$ and the line representing $\mu = 1$, a wave will be formed for all values of α and f. Then by using values of Φ and η determined from Eqs. (1) and (2) for given values of α and f to define the hodograph in Fig. 5 the required velocities were found for substitution in Eq. (6).

It can be seen from the results in Fig. 4, for which the specimen material was a cold rolled 5086-H32 aluminum-magnesium alloy, that waves were formed in the experiments by plastic deformation with no macrocracking for $\gamma_p < 10$ but that above this strain cracks occurred. Although the occurrence of a crack in the experiments did not always result in the removal of the deformed material, it is reasonable to assume that, in an actual frictional sliding situation, not many asperity interactions would be needed at the crack site before removal occurred. This form of wear appears to be similar in nature to adhesive wear although it is different in that the asperities need not be welded together at the interface as is the case with the adhesive model. Clearly it represents a severe form of wear. Another severe type of wear considered by Challen and Oxley (1979) in their slipline field analysis of asperity interactions was abrasion. They showed that as the asperity angle α (Fig. 1) is increased a point is reached where material is removed by a chip formation process and therefore that the wear is abrasive in nature.

It is clear that in many engineering applications the wear processes taking place are far less severe than the two processes described above, and that wear will result not from a single event but from surface damage which accumulates as a result of repeated deformation of the contacting surfaces. Taking this view Kraghelsky (1965) has proposed that wear occurs as a result of fatigue while Suh (1973) has proposed a delamination theory of wear in which a wear particle is produced at a certain level of accumulated plastic strain in the surface. In his work Kraghelsky considers that plastic contact in asperity interactions is far less important than elastic contact arguing that even if the initial contact is plastic this soon changes to elastic contact with repeated loading. For this reason, he has concentrated his efforts on explaining wear in terms of cyclic stresses below the elastic limit although he has also considered the case where the stresses are above the elastic limit and the so-called low-cycle fatigue mechanism applies. In contrast to Kraghelsky's contention that asperity contact is usually elastic, Challen et al. (1986) have assumed that it will remain plastic even after the running-in period and have used the wave model of asperity deformation together with a low-cycle fatigue equation to predict wear. This work is now described.

3 Low-Cycle Fatigue Wear Predictions

In their analysis, Challen et al. (1986) limited attention to the case of a hard surface sliding over a soft one with each asperity interaction modeled as in Fig. 1. For fully plastic conditions such as encountered in the wave formation process, it is generally accepted that damage is more closely related to the strain amplitude than to the stress amplitude and that the number of cycles to failure n is given by an equation of the form

$$n = \left(\frac{C}{\epsilon_a}\right)^D \tag{7}$$

where ϵ_a is the plastic strain amplitude and the constant C is related to the monotonic fracture strain for the process and material considered. According to Manson (1965) and others the constant D in Eq. (7) is approximately 2 for a range of materials. The validity of Eq. (7) has been tested mainly under uniaxial conditions of loading and there is little information available for complex stress states similar to that applying in the wave formation process. In the absence of such information, Challen et al. assumed that the number of cycles to

Downloaded 03 May 2010 to 171.66.16.245. Redistribution subject to ASME license or copyright; see http://www.asme.org/terms/Terms_Use.cfm

failure, that is, the number of wave passes required to produce a wear particle, can be determined from the equation

$$n=\left(\frac{C}{\gamma_p}\right)^D \tag{8}$$

which is similar to Eq. (7) but with the shear strain increment γ_p, calculated from Eq. (6), replacing ϵ_a.

In making estimates of wear it is assumed that the asperities on the hard surface are of equal slope α (Fig. 1) and the interfacial film strength f is constant over the surfaces. The strain increment put into the surface with each wave pass is therefore the same for all asperities. For a given shear strain increment γ_p, the number of cycles to failure is given by Eq. (8). Hence, the cumulative plastic strain needed to generate a wear particle is

$$n\gamma_p=\left(\frac{C}{\gamma_p}\right)^D \gamma_p. \tag{9}$$

If $\bar{k}$ is the average shear flow stress of the wearing material during the process of generating a wear particle, then the plastic work required to produce unit volume of worn material is given by

$$\bar{k}n\gamma_p=\bar{k}C^D\gamma_p^{1-D}. \tag{10}$$

This quantity can also be determined from the frictional force F acting on the surfaces and the total volume of material removed V in a sliding distance L, that is,

$$\text{plastic work per unit volume of worn material}=\frac{rFL}{V}, \tag{11}$$

where r is the ratio of plastic to total work. Hence, equating Eqs. (10) and (11),

$$\frac{rFL}{V}=\bar{k}C^D\gamma_p^{1-D},$$

which taking $F = \mu N$ can be rearranged to give

$$\frac{V}{NL}=\frac{r\mu}{\bar{k}C^D\gamma_p^{1-D}}, \tag{12}$$

where N is the normal force acting on the contacting surfaces and μ is the corresponding coefficient of friction.

Whatever the physical basis of Archard's well-known wear equation (1953), it is known that it gives a good fit with experimental wear results. Therefore, to facilitate a comparison of their own wear predictions with experimental results Challen et al. replaced the average shear flow stress $\bar{k}$ in Eq. (12) by the hardness H of the wearing surface so that it could be compared directly with Archard's equation. Tabor (1951) has shown that $H \approx 3Y$ where Y is the uniaxial yield stress which from the shear strain energy yield criterion can be taken for the present case as equal to $3^{1/2}\bar{k}$. Therefore, $\bar{k} = H/(3 \times 3^{1/2})$ and substituting this in Eq. (12) gives

$$V=\frac{9\times 3^{1/2}r\mu}{C^D\gamma_p^{1-D}}\frac{NL}{3H}. \tag{13}$$

From comparison of Eq. (13) with Archard's equation,

$$V=\frac{KNL}{3H}, \tag{14}$$

it can be seen that the wear coefficient K, according to the low cycle fatigue model, is equal to

$$K=\frac{9\times 3^{1/2}r\mu}{C^D\gamma_p^{1-D}}. \tag{15}$$

Experimental wear results are often expressed in terms of K, and in comparing predictions made from the low-cycle fatigue model with experimental results, it is convenient to do this in terms of K.

For given values of C and D, K can be determined from Eq. (15) as r, and μ and γ_p can all be obtained from the slipline field analysis in terms of α and f. The method for determining γ_p has already been described. The method for finding the product $r\mu$ is as follows. Referring to Fig. 1, the expression for r can be written

$$r=\frac{UF-v_{ED}F'}{UF}$$

where F' is the force per unit width acting along the interface, DE, and is given by $F' = f\bar{k}d$, and v_{ED} is the velocity along DE. Therefore, the product $r\mu$ is given by

$$r\mu=\frac{UF-v_{ED}F'}{UF}\frac{F}{N}$$

$$=\frac{UF-v_{ED}F'}{UN}.$$

Substituting from the slipline field analysis for all the terms on the right-hand side of this equation it can be shown that

$$r\mu=\frac{A\sin\alpha+\cos(\arccos f-\alpha)-Bf}{A\cos\alpha+\sin(\arccos f-\alpha)} \tag{16}$$

where A is the same as in Eq. (5) and

$$B=\frac{\sin\left(\frac{1}{2}\arccos f-\alpha\right)}{\sin\left(\frac{1}{2}\arccos f\right)}.$$

Values of the wear coefficient K, calculated in this way from Eq. (15), for a range of values of α and f, are given in Fig. 6. The corresponding values of γ_p found in making these calculations are given in Fig. 7. In the calculations, C was taken as 10 on the basis of the results in Fig. 4, that is, so that when $\gamma_p = 10$, $n = 1$, and D was taken as 2. In considering the results for K it should be noted that the slipline field model used in determining γ_p assumes a rigid-plastic material. Therefore, the results for γ_p can only be taken with a reasonable degree of confidence when γ_p is at least 10 times, say, greater than the elastic strain at the yield point. From Fig. 7 this would mean that for steels, with good lubrication conditions (i.e., small f's) applying, only those results for $\alpha > 0.1$ deg are really applicable. If this limitation is accepted, it can be seen that K is predicted to vary in the range from 10^{-6} to nearly 1 for α and f values in the ranges 0.1 deg to 10 deg and 0 to 0.99, respectively. To account for values of K less than 10^{-6}

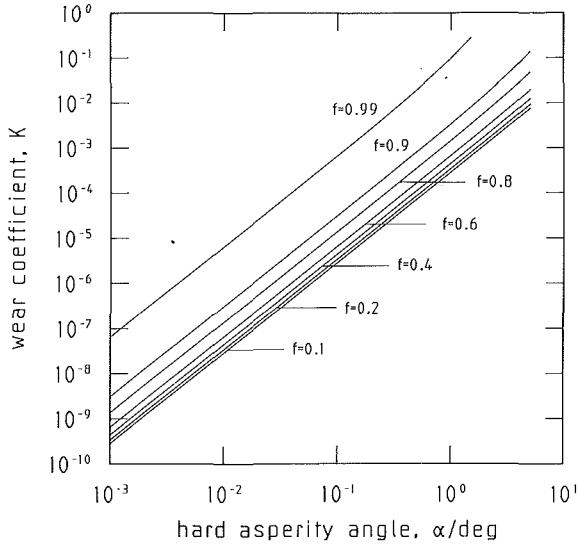


Fig. 6 Variation in K with α and f

Downloaded 03 May 2010 to 171.66.16.245. Redistribution subject to ASME license or copyright; see http://www.asme.org/terms/Terms_Use.cfm

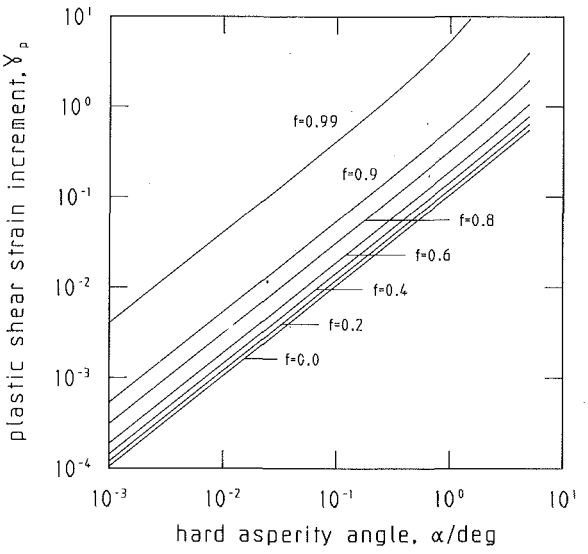


Fig. 7 Variation in γ_p with α and f

it would be necessary to take $\alpha < 0.1$ deg, as shown by the results in Fig. 6, and to assume that the model still gave reliable values of γ_p (Fig. 7), even when this was of the same order of magnitude as the elastic strain. As would be expected, the results show that K increases with increase in α and f.

Challen et al. (1987) have compared predicted values of K determined from the low-cycle fatigue analysis with results from experiments in which, for different surface roughness and lubrication conditions, both K and the friction coefficient μ were measured. Results obtained from Eqs. (15) and (5) for K and μ are given in Figs. 8 and 9, which also give experimental results obtained by Roberts (1985) and Rabinowicz (1977). The theoretical results are represented by lines for constant f values with the crosses on the lines indicating the α values. In the calculations D was again taken as 2 and C as 10. In assigning this value to C no account was taken of the differences in the properties of the materials used in the experiments of Roberts (1985) and Rabinowicz (1977), and of those of Challen et al. (1984), from which the value $C = 10$ was obtained. Nor was account taken of the differences in material properties which might have been expected to result from the different tem-

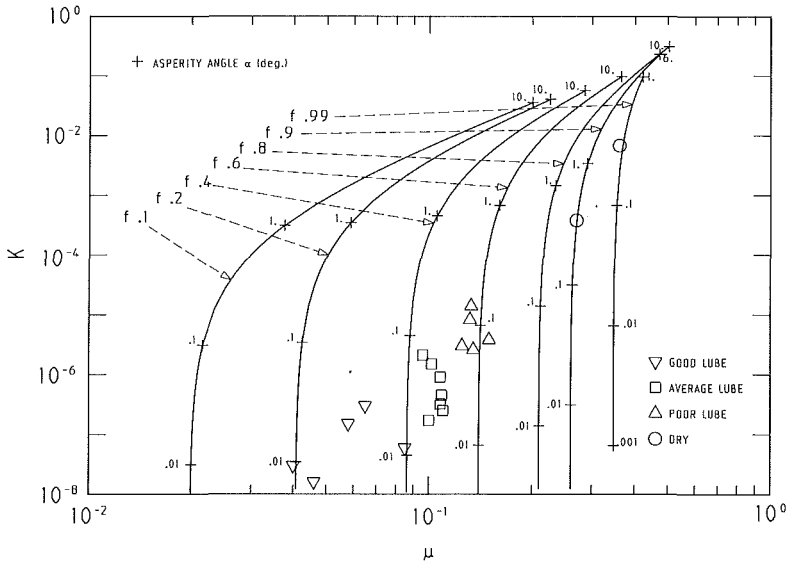


Fig. 8 Theoretical and experimental results for the wear and friction coefficients K and μ; experimental results are those obtained by Roberts (1985)

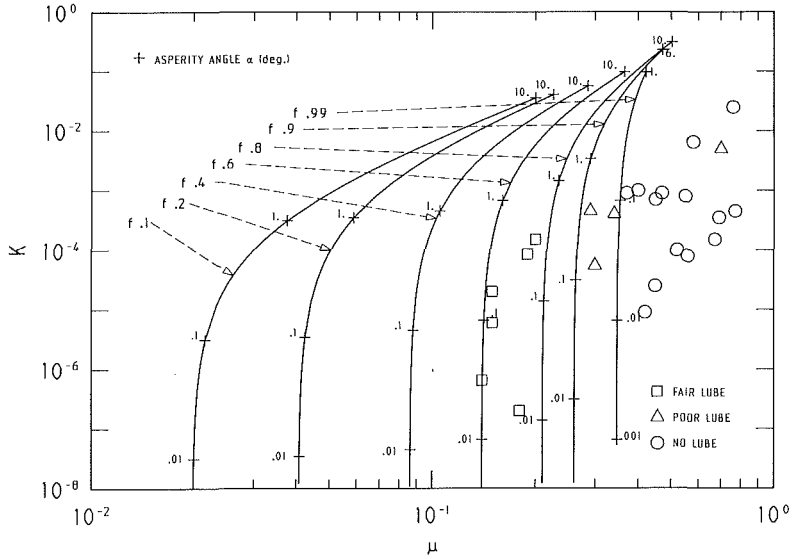


Fig. 9 Theoretical and experimental results for the wear and friction coefficients K and μ; experimental results are those obtained by Rabinowicz (1977)

Downloaded 03 May 2010 to 171.66.16.245. Redistribution subject to ASME license or copyright; see http://www.asme.org/terms/Terms_Use.cfm

peratures and strain rates encountered in the slow-speed wedge tests of Challen et al. and the conventional speed friction and wear tests of Roberts and Rabinowicz. Indeed, at this stage it would be very difficult to take account of these factors. The effect of changing the value of C is mainly to change the values of α at which given values of K and μ occur. As it is difficult to determine α from the data presented by Rabinowicz, and impossible from those presented by Roberts, the selection of C can be seen to be less critical than it might otherwise have been.

From Fig. 8 it can be seen that all of Robert's experimental results fall within the predicted range and that the results for a given lubrication condition fall reasonably close to one of the predicted constant f lines with the corresponding values of f decreasing with improvement in lubrication as would be expected. Of particular interest is the near vertical nature of the constant f lines for lower K values; a prediction which is born out by the experimental results. In this range, therefore, while μ only changes slightly, K can change by several orders of magnitude. This is of course a well-known observation in friction and wear tests. The experimental results of Rabinowicz in Fig. 9 show similar trends to those of Roberts but also include a large number of results lying outside the predicted range. These results, which show surprisingly small K values considering the accompanying high values of μ, cannot be explained in terms of the low-cycle fatigue model and suggest that some other wear mechanism is taking place.

The generally good agreement found between the predictions made from the low-cycle fatigue model and experimental results is encouraging and helps justify the use of this model. However, it is clear that far greater support for the model would be obtained if it could be shown directly that a low-cycle fatigue process is actually taking place during the repeated passage of plastic waves across a surface.

4 Metallographic Investigation of the Surface Damage Resulting From the Repeated Passage of Plastic Waves

In looking for direct evidence of low-cycle fatigue it is appropriate to start by considering the stress cycle undergone by material as it flows through the wave. It can be seen from Eqs. (1) and (2), as noted by Challen et al. (1986), that for small values of α and f the sections AB and CD of the boundary slipline in Fig. 1 will be approximately at 90 deg to each other. This means that the direction of shear on an element face parallel to AB will be reversed as the element crossed CD.

Johnson (1987) has noted that in terms of stresses acting parallel to the surface, this stress cycle can be interpreted as compression at entry to the wave, followed by shear at the midpoint of the wave, followed by tension at exit to the wave. In a recent paper Johnson (1989) has shown that the same nonproportional stress cycle is experienced by near-surface elements beneath a braked wheel (negative traction) with the opposite sequence followed beneath a driven wheel (positive traction). He has concluded that it is this complex, nonproportional stress cycle which is responsible for the distress of surfaces in rolling and sliding contact and has referred to results of biaxial low-cycle fatigue tests made by Kanazawa et al. (1977) which show that the shortest lives were obtained when the two cyclic stress components were 90 deg out of phase as in the rolling/sliding cycle.

Hockenhull et al. (1991) have reported a metallographic study of the damage sustained by a relatively soft surface resulting from the repeated unidirectional pushing of waves along it by a hard wedge. Relatively small wedge angles and good lubrication were used so that the strain cycle experienced by material flowing through the wave was close to the nonproportional cycle described above. The experiments were carried out using the test rig in the modified form described by Black et al. (1988). The test specimens were made from cold rolled 5083-H321 aluminum-magnesium alloy and the wedges from tool steel (Bohler Amutit S). The lubricant used as a mineral oil (Shell Vitrea 100). The wedge angles used were mainly in the range from $\alpha = 3$ deg to 10 deg, although a few tests were made for larger values of α. The normal force N was kept approximately at the same value of $8000N$ throughout the tests.

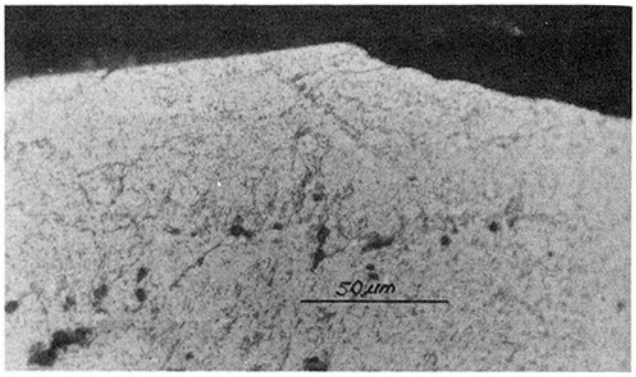


Fig. 10 Section through wave during second pass with $\alpha = 10$ deg

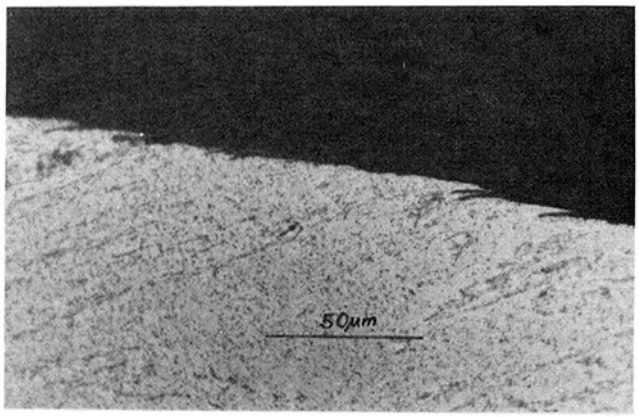


Fig. 11 Section showing free surface during fifth pass with $\alpha = 10$ deg

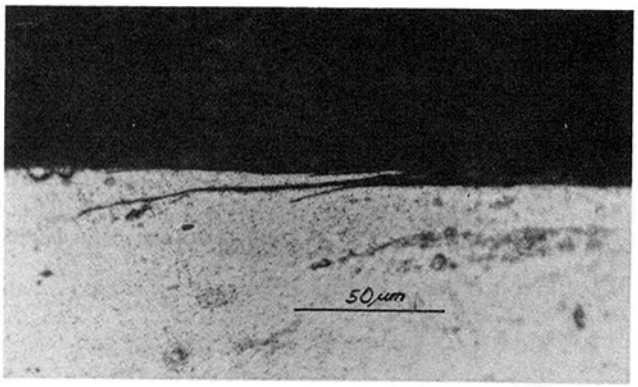


Fig. 12 Section showing surface after passage of sixth wave with $\alpha = 10$ deg

Some typical features of the deformed surface obtained in this way are shown in Figs. 10 to 12 and 14. To give some indication of the relative size of these features it should be noted that the depth of the plastically deformed layer for all of the wedge angles used was approximately 1 mm. The free surface of the wave associated with the second pass (second wave pushed along surface) with a 10 deg wedge is shown in Fig. 10. It can be seen that there are significant undulations in this surface, the most prominent being around 10 microns

Downloaded 03 May 2010 to 171.66.16.245. Redistribution subject to ASME license or copyright; see http://www.asme.org/terms/Terms_Use.cfm

in length measured along the surface and up to 3 microns in depth. Figure 11 shows the free surface for the same conditions after the fifth pass and well-established crack-like features up to 15 microns in length can be seen along this surface. Figure 12 shows the specimen surface after the passage of the sixth wave with a well-developed crack approximately 100 microns in length now existing.

Hockenhull et al. have explained the formation of undulations along the free surface (Fig. 10) in terms of those factors which will vary the ease of plastic flow from point to point along the surface (i.e., grain size, crystallographic orientation, rupture of surface oxide films). In considering the transition from the undulations in the free surface in Fig. 10 to the crack-like features in this surface shown in Fig. 11, they have proposed that this results from the ironing of the surface by the passage of waves. This ironing process can be best understood by reference to the wave model in Fig. 1. From the hodograph it can be seen that material which flows through the wave is retarded, relative to the flow outside the wave, the material nearest the surface suffering the greatest degree of retardation as it has to traverse the longest path. Ironing of the surface layer is clearly demonstrated by the deformed grid in Fig. 13 obtained after a single pass using the technique described by Kopalinsky et al. (1990). Ironing of the undulations would therefore have caused them to lengthen and thin down as shown in Fig. 11 in the same way as for the surface grid elements in Fig. 13. With this mechanism the resulting crack-like features could not extend more deeply into the surface than the undulations from which they were formed. The crack in Fig. 12 has penetrated far more deeply into the surface (≈ 15 microns) than can be explained in this way and it seems that some fatigue mechanism must be invoked to explain this. From the results obtained for the various wedge angles it appears that the tips of the cracks were propagating more or less in the direction of maximum shear stress presumably as a result of the repeated shears. The cracks were therefore extending in a Mode II manner, that is, in a similar way to Stage 1 fatigue cracks. Nearer to the surface the cracks do not follow the maximum shear stress direction as can be seen from Fig. 12 but this simply results from the greater degree of ironing undergone by these earlier stages of the crack.

5 Comparison of Wave Test Results With Low-Cycle Fatigue Equation and Concluding Remarks

In their experiments Hockenhull et al. (1991) found that material was removed from the surface after a relatively small number of passes by the breaking off of the tips of ironed-out tongues of metal as shown in Fig. 14. With increase in the number of passes the surface damage increased to the point

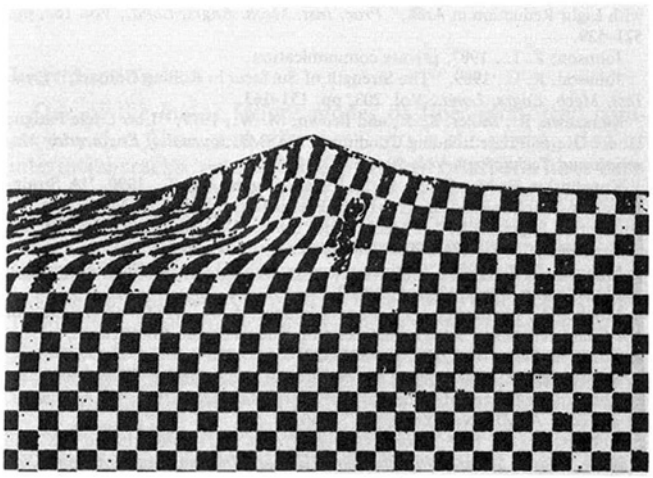


Fig. 13 Deformed grid; grid 0.1 mm sides, $\alpha = 20$ deg

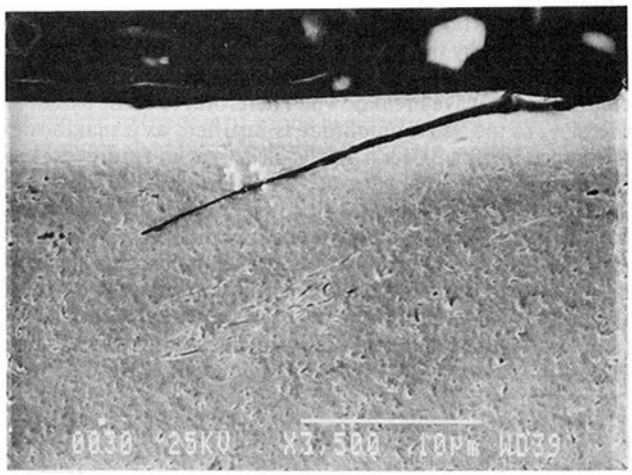


Fig. 14 Section showing surface after passage of eighth wave with $\alpha = 5$ deg

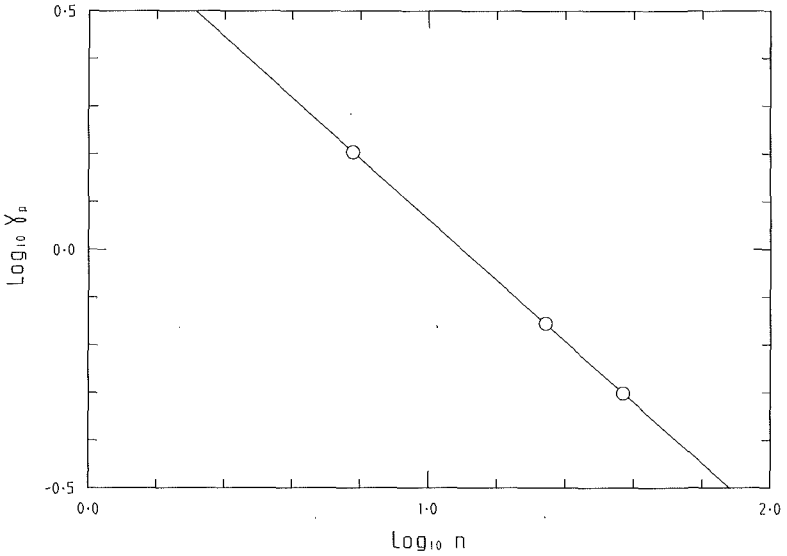


Fig. 15 Experimental low-cycle fatigue results

Downloaded 03 May 2010 to 171.66.16.245. Redistribution subject to ASME license or copyright; see http://www.asme.org/terms/Terms_Use.cfm

where complete breakdown of the wave occurred. Taking this latter event as the criterion of failure, Hockenhull et al. have compared their results with Eq. (8). The number of cycles to failure was found to be 6, 22, and 37 for the wedge angles of 10 deg, 5 deg and 3 deg, respectively. The corresponding values of γ_p calculated from Eq. (6) are 1.6, 0.7, and 0.5. These results are shown plotted in Fig. 15 on the basis of $\log_{10}\gamma_p$ against $\log_{10}n$ and can be seen to give a good fit to a straight line thus supporting a relation of the form given in Eq. (8). The value of D measured from the line is approximately 1.6, which is less than the usually quoted value of 2. However, this latter value is invariably obtained from the results of uniaxial tests and the difference could result from the more complex nature of the strain cycle in wave formation as indicated by the results of Kanazawa et al. (1977). Another problem in comparing the wave test results with low-cycle fatigue test results is to do with the use of γ_p calculated from Eq. (6) as the strain amplitude in Eq. (8). In low-cycle fatigue tests the strain cycle is normally closed, and there is no accumulation of unidirectional strain. In wave formation the strain cycle is not closed and γ_p can be seen to have a unidirectional component which is accumulated in the surface as a result of ironing of the surface. It might, therefore, be thought that it would be more appropriate to take γ_p minus the ironing strain (which can incidentally be calculated in terms of α and f from the geometry of Fig. 5) as the strain amplitude in Eq. (8). If surface damage and ultimate breakdown of the wave resulted entirely from low-cycle fatigue this would certainly be the case. However, as shown by the metallographic results, the ironing process itself also leads to the extension of cracks and thus contributes to wave breakdown. Therefore, to some extent the use of γ_p as the strain amplitude is justified, as it makes some allowance for this. Even so, it is clear that in future work on the prediction of wear, detailed consideration will have to be given to the respective roles of low-cycle fatigue and ironing in producing surface damage and hence wear. It would be expected that this would involve a more sophisticated analysis of the strain occurring in wave formation than that given in the present paper. In this connection the recent paper by Kopalinsky et al. (1990) in which these strains are determined from the analysis of an experimental flow field is of considerable interest.

Acknowledgment

The authors wish to thank the Australian Research Council (ARC) for financial support of the work reported in this paper.

References

Archard, J. F., 1953, "Contact and Rubbing of Flat Surfaces," *J. Appl. Phys.*, Vol. 24, pp. 981–988.

Black, A. J., Kopalinsky, E. M., and Oxley, P. L. B., 1988, "An Investigation of the Different Regimes of Deformation which can Occur when a Hard Wedge Slides Over a Soft Surface: The Influence of Wedge Angle, Lubrication and Prior Plastic Working of Surface," *Wear*, Vol. 123, pp. 97–114.

Bowden, F. P., and Tabor, D., 1950, *The Friction and Lubrication of Solids*, Clarendon Press, Oxford.

Challen, J. M., and Oxley, P. L. B., 1979, "An Explanation of the Different Regimes of Friction and Wear Using Asperity Deformation Models," *Wear*, Vol. 53, pp. 229–243.

Challen, J. M., McLean, L. J., and Oxley, P. L. B., 1984, "Plastic Deformation of a Metal Surface in Sliding Contact with a Hard Wedge: Its Relation to Friction and Wear," *Proc. R. Soc. Lond.*, Vol. A394, pp. 161–181.

Challen, J. M., Oxley, P. L. B., and Hockenhull, B. S., 1986, "Prediction of Archard's Wear Coefficient for Metallic Sliding Friction Assuming a Low Cycle Fatigue Wear Mechanism," *Wear*, Vol. 111, pp. 275–288.

Challen, J. M., Kopalinsky, E. M., and Oxley, P. L. B., 1987, "An Asperity Deformation Model for Relating the Coefficients of Friction and Wear in Sliding Metallic Friction," *Conference on Tribology, C156/87, Inst. Mech. Engrs, Lond.*, pp. 957–964.

Collins, I. F., 1972, "A Simplified Analysis of the Rolling of a Cylinder on a Rigid/Perfectly Plastic Half Space," *Int. J. Mech. Sci.*, Vol. 14, pp. 1–14.

Green, A. P., 1954, "The Plastic Yielding of Metal Junctions Due to Combined Shear and Pressure," *J. Mech. Phys. Solids*, Vol. 2, pp. 197–211.

Green, A. P., 1955, "Friction Between Unlubricated Metals: A Theoretical Analysis of the Junction Model," *Proc. R. Soc. Lond.*, Vol. A228, pp. 191–204.

Hockenhull, B. S., Kopalinsky, E. M., and Oxley, P. L. B., 1991, "An Investigation of the Role of Low Cycle Fatigue in Producing Surface Damage in Sliding Metallic Friction," *Wear*, Vol. 148, pp. 135–146.

Johnson, R. W., and Rowe, G. W., 1968, "Bulge Forming in Strip Drawing with Light Reduction in Area," *Proc. Inst. Mech. Engrs, Lond.*, Vol. 182, pp. 521–529.

Johnson, K. L., 1987, private communication.

Johnson, K. L., 1989, "The Strength of Surfaces in Rolling Contact," *Proc. Inst. Mech. Engrs, Lond.*, Vol. 203, pp. 151–163.

Kanazawa, K., Miller, K. J., and Brown, M. W., 1977, "Low Cycle Fatigue Under Out-of-Phase Loading Conditions," ASME *Journal of Engineering Materials and Technology*, Vol. 99, pp. 222–228.

Kopalinsky, E. M., Oxley, P. L. B., and Young, H. T., 1990, "A Strain-Hardening Slipline Field Analysis of the Plastic Deformation in a Model Asperity Interaction Experiment," *J. Mech. Phys. Solids*, Vol. 38, No. 6, pp. 765–785.

Kraghelsky, I. V., 1965, *Friction and Wear*, Butterworths.

Manson, S. S., 1965, "Fatigue-Complex Subject—Some Simple Approximations," *Exp. Mech.*, Vol. 5, No. 7, pp. 193–226.

Moalic, H., Fitzpatrick, J. A., and Torrance, A. A., 1987, "Correlation of the Characteristics of Rough Surfaces with Their Friction Coefficients," *Proc. Inst. Mech. Engrs*, Vol. 201, pp. 321–329.

Rabinowicz, E., 1977, "The Dependence of the Adhesive Wear Coefficient on the Surface Energy of Adhesion," *Wear of Materials—1977*, W. A. Glaeser, et al., eds., ASME, New York, pp. 36–40.

Roberts, W. H., 1985, "Some Current Trends in Tribology in the U.K. and Europe," *Japan Society of Lubrication Engineers International Tribology Conference*, Tokyo, July 8–10.

Suh, N. P., 1973, "The Delamination Theory of Wear," *Wear*, Vol. 25, pp. 111–124.

Tabor, D., 1951, *The Hardness of Metals*, Clarendon Press, Oxford.

Downloaded 03 May 2010 to 171.66.16.245. Redistribution subject to ASME license or copyright; see http://www.asme.org/terms/Terms_Use.cfm

Hua Lu[1]

F. P. Chiang
Mem. ASME

Laboratory for Experimental
Mechanics Research,
Department of Mechanical Engineering,
State University of New York,
Stony Brook, NY 11790-2300

Photoelastic Determination of Stress Intensity Factor of an Interfacial Crack in a Bi-material

The stress intensity factor of an interfacial crack in a bi-material can be represented by a complex vector whose phase changes as a function of r, *the radial distance from a crack tip. Two photoelasticity approaches are proposed for the determination of both the magnitude and the phase angle of this complex vector. It is shown that within the* K-*dominated zone the complex stress intensity factor can be determined at any* r *and then converted to any other* r. *The case of an interfacial crack under remote tension is used as an example for the illustration of the proposed techniques.*

Introduction

One of the major failure modes of fiber-reinforced composites, thin films, and adhesive joints is the propagation of interfacial cracks. As a result a great deal of efforts have been devoted to the study of interfacial fracture of bi-materials. The basic solution to this problem was formulated by Williams (1959). There have been many discussions on its unusual local characteristics throughout the years. Its validity in a variety of situations has been clarified by Rice (1988) in a recent paper. There have been many definitions of stress intensity factor proposed for the purpose of characterizing the near-tip field of an interfacial crack (e.g., Sih and Rice, 1964; Cherepanov, 1979; Huchinson, Mear, and Rice, 1987; Shih and Asaro, 1988; Rice, 1988). Most of these definitions differ from one another only by a phase factor. In this paper, we shall adopt Rice's definition of the so-called stress intensity factor of classical type (1988).

The motivation for this study stems from the fact that while classical photoelasticity has been extensively utilized in the study of fracture of homogeneous materials, its application to the interfacial fracture of bi-material is rather limited. Recently theoretical and numerical studies of the subject have shed new insight to the problem. And as a result, the classical methods of photoelastic characterization of the stress intensity factor have become inadequate. In this paper a general framework of using photoelasticity for the determination of the stress intensity factor in a bi-material is formulated, and two specific approaches are proposed employing the concept of the stress intensity factor of classical type. As an illustration, the methods are applied to the case of a long bi-material panel with a central crack along the interface loaded in remote tension.

Stress Intensity Factor for Interfacial Cracks

For a bi-material interfacial crack with configuration shown in Fig. 1, linear elastic analysis based on either Williams' eigenfunction expansion approach or Rice's analytical function method gives the same solution. Let material 1 with elastic constants E_1 and ν_1 and material 2 with E_2 and ν_2 occupy the upper and lower half-planes, respectively; and (x_1, x_2) be the

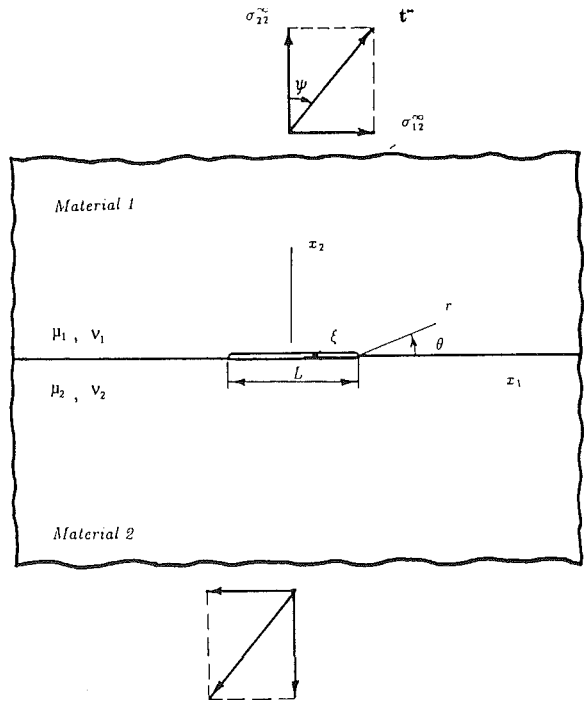


Fig. 1 Schematic of interfacial crack loaded at remote boundary

[1]Currently with the Department of Mechanical Engineering, Ryerson Polytechnical Institute, Toronto, ON M5B 2K3, Canada.

Contributed by the Applied Mechanics Division of THE AMERICAN SOCIETY OF MECHANICAL ENGINEERS for publication in the ASME JOURNAL OF APPLIED MECHANICS.

Discussion on this paper should be addressed to the Technical Editor, Professor Lewis T. Wheeler, Department of Mechanical Engineering, University of Houston, TX 77204-4792, and will be accepted until four months after final publication of the paper itself in the ASME JOURNAL OF APPLIED MECHANICS.

Manuscript received by the ASME Applied Mechanics Division, Aug. 2, 1989; final revision, Jan. 11, 1991. Associate Technical Editor: W. Knauss.

Copyright © 1993 by ASME
Downloaded 03 May 2010 to 171.66.16.245. Redistribution subject to ASME license or copyright; see http://www.asme.org/terms/Terms_Use.cfm

global Cartesian coordinates. The interface is along the x_1-direction and contains a crack between $x_1 = -L/2$ and $x_1 = L/2$ (L is the crack length). The crack faces are assumed stress-free. On the bonded portion of the interface, continuities are assumed for displacement components, strain components ϵ_{12} and ϵ_{22}, and stress components σ_{12} and σ_{22}, whereas σ_{11} is allowed to be discontinuous across the interface (See Sih and Rice, 1964). The linear elastic solutions for the near crack-tip fields obtained under these boundary conditions have closed forms.

Many definitions of the stress intensity factor have been proposed for the purpose of characterizing the crack-tip field. The earliest one is that of Sih and Rice (1964). They defined a complex parameter $\mathbf{k}$ given by:

$$\mathbf{k} = (\sigma_{22}^{\infty} + i\sigma_{12}^{\infty})(1 + 2i\epsilon)L^{-i\epsilon}\frac{\sqrt{L/2\pi}}{\cosh(\pi\epsilon)}, \tag{1}$$

in which σ_{12}^{∞} and σ_{22}^{∞} are stresses on the remote boundary, L is the crack length, and ϵ is the bi-material constant defined as follows:

$$\epsilon = \frac{1}{2\pi}\ln\left\{\frac{\frac{\kappa_1}{\mu_1}+\frac{1}{\mu_2}}{\frac{1}{\mu_1}+\frac{\kappa_2}{\mu_2}}\right\}, \tag{2}$$

where $\kappa_1 = 3 - \nu_1/1 + \nu_1$, $\kappa_2 = 3 - \nu_2/1 + \nu_2$ for plane stress. ν_1, ν_2, and μ_1, μ_2 are Poisson's ratios and shear moduli of materials 1 and 2, respectively.

Huchinson et al. (1987) proposed a slightly different stress intensity factor called $\mathbf{K}$, which differs from $\mathbf{k}$ by a constant as

$$\mathbf{K} = K_1 + iK_2 = \mathbf{k}\sqrt{\pi}\cosh(\pi\epsilon)$$

or

$$\mathbf{K} = (\sigma_{22}^{\infty} + i\sigma_{12}^{\infty})(1 + 2i\epsilon)L^{-i\epsilon}\sqrt{L/2}. \tag{3}$$

But both $\mathbf{k}$ and $\mathbf{K}$ contain a crack length related phase term $L^{-i\epsilon}$ giving rise to a complex dimension. As a result, when one changes the unit of length, not only does the magnitude of complex stress intensity factor, but the phase angle (i.e., the ratio of the real and imaginary components) changes also. This is inconvenient in applications where one may have to switch length units. However, should $L^{-i\epsilon}$ be removed from the definition of the stress intensity factor, it would have to be included in the angular distribution function of the field solution. In such a case, the crack length effect would no longer be uniquely characterized by the stress intensity factor, leading to a situation where cracks with the same stress intensity factor but different length have different near-tip fields.

In 1988, Rice suggested a definition of the stress intensity factor of the so-called "classical type," denoted by $K_I + iK_{II}$, which circumvented these difficulties. Rather than removing the phase term $L^{-i\epsilon}$ from $\mathbf{K}$, another phase term $\hat{r}^{i\epsilon}$ is added, i.e.,

$$K_I + iK_{II} = \mathbf{K}\hat{r}^{i\epsilon}, \tag{4}$$

where $\hat{r}$ is a particular value of radial distance r. The stress intensity factor of the classical type is then given by

$$K_I + iK_{II} = (\sigma_{22}^{\infty} + i\sigma_{12}^{\infty})(1 + 2i\epsilon)\sqrt{L/2}(\hat{r}/L)^{i\epsilon}. \tag{5}$$

Or, with the modulus and phase term separated, it can be expressed as follows:

$$K_I + iK_{II} = \sqrt{\pi L(1+4\epsilon^2)/2}\,|\,\vec{t}^{\infty}\,|\,e^{i(\Psi + \arctan(2\epsilon) + \epsilon\ln\hat{r}/L)}, \tag{6}$$

in which

$$\vec{t} = \sigma_{22}^{\infty} + i\sigma_{12}^{\infty} = |\,\vec{t}^{\infty}\,|\,e^{i\Psi},$$

and

$$\Psi = \arctan\,\sigma_{12}^{\infty}/\sigma_{22}^{\infty}.$$

The stress intensity factor, defined by either Eq. (5) or Eq. (6), fully specifies the effect of load and crack geometry. Furthermore, since its phase term is dimensionless, it is real rather than complex in dimension. $K_I + K_{II}$ is called the classical type because it has the same dimension as its counterpart in homogeneous materials. And when $\epsilon = 0$, it becomes the stress intensity factor for homogeneous materials. K_I and K_{II} may be considered as the intensity of the respective singularity fields in the classical sense.

However, $K_I + iK_{II}$ as a whole differs from its counterpart in certain aspects. First, its real component K_I (or its imaginary component K_{II}) does not by itself reflect the effect of opening (or shearing) load. Indeed, the two singular fields coexist at all mode mixities. Secondly, the value of $K_I + iK_{II}$ depends on where it is defined. As a result, different values of $K_I + iK_{II}$ will have no comparative meaning if they are not all taken at the same $\hat{r}$. Rice (1988) suggested that $\hat{r}$ be taken as some material length, invariant to differences of crack size or other geometric dimensions.

In the following it will be shown that $K_I + iK_{II}$ obtained at one $\hat{r}$ can be converted to that at a different $\hat{r}$. As a result there will be no restriction in the selection of $\hat{r}$ so long as it is within the $K_I + iK_{II}$ dominated zone. This is important in the experimental determination of the stress intensity factor, because very often one needs to take data at different points. For the convenience of the following discussion, some minor modification on the notations are needed. $K_I + iK_{II}$ is used to stand for the stress intensity factor defined at a general r, whereas $\hat{K}_I + i\hat{K}_{II}$ is introduced to represent a specific complex constant defined at a specific r, i.e., $\hat{r}$. While $\hat{K}_I + i\hat{K}_{II}$ is simply a constant similar to the stress intensity factor in homogeneous materials, $K_I + iK_{II}$ is a function of r. Thus,

$$K_I + iK_{II} = \sqrt{\pi L(1+4\epsilon^2)/2}\,|\,\vec{t}^{\infty}\,|\,e^{i(\Psi + \arctan(2\epsilon) + \epsilon\ln r/L)}, \tag{7}$$

and

$$\hat{K}_I + i\hat{K}_{II} = \sqrt{\pi L(1+4\epsilon^2)/2}\,|\,\vec{t}^{\infty}\,|\,e^{i(\Psi + \arctan(2\epsilon) + \epsilon\ln\hat{r}/L)}. \tag{8}$$

And the asymptotic solution for the near crack-tip stress field is

$$\sigma_{ij} = \frac{A}{\sqrt{2\pi r}}(K_I f_{ij}^{(I)}(\epsilon,\theta) + K_{II} f_{ij}^{(II)}(\epsilon,\theta)), \quad i,j = r,\theta, \tag{9}$$

in which r and θ are the polar coordinates centered at the right-hand crack tip as shown in Fig. 1, with θ varying from 0 to π; $A = 1/2\cosh(\pi\epsilon)$ is a constant; ϵ, K_I, and K_{II} are as defined previously. $f_j^{(I)}$ and $f_j^{(II)}$ are functions representing the angular distribution of the stress field. They are derived from the g_{ij} of Shih and Asaro (1988). In polar coordinates,

$$f_{rr}^{(I)} = e^{-\epsilon(\pi-\theta)}\cos\frac{\theta}{2}\left(3 + 2\epsilon\,\sin\,\theta - 2\,\sin^2\frac{\theta}{2}\right) - e^{\epsilon(\pi-\theta)}\,\cos\frac{3\theta}{2},$$

$$f_{rr}^{(II)} = e^{-\epsilon(\pi-\theta)}\sin\frac{\theta}{2}\left(-3 + 2\epsilon\,\sin\,\theta + 2\,\cos^2\frac{\theta}{2}\right) + e^{\epsilon(\pi-\theta)}\sin\frac{3\theta}{2},$$

$$f_{\theta\theta}^{(I)} = e^{-\epsilon(\pi-\theta)}\cos\frac{\theta}{2}\left(1 - 2\epsilon\,\sin\,\theta + 2\,\sin^2\frac{\theta}{2}\right) + e^{\epsilon(\pi-\theta)}\cos\frac{3\theta}{2},$$

$$f_{\theta\theta}^{(II)} = e^{-\epsilon(\pi-\theta)}\sin\frac{\theta}{2}\left(-1 - 2\epsilon\,\sin\,\theta - 2\,\cos^2\frac{\theta}{2}\right) - e^{\epsilon(\pi-\theta)}\sin\frac{3\theta}{2},$$

$$f_{r\theta}^{(I)} = e^{-\epsilon(\pi-\theta)}\sin\frac{\theta}{2}\left(1 - 2\epsilon\,\sin\,\theta - 2\,\cos^2\frac{\theta}{2}\right) + e^{\epsilon(\pi-\theta)}\sin\frac{3\theta}{2},$$

$$f_{r\theta}^{(II)} = e^{-\epsilon(\pi-\theta)}\cos\frac{\theta}{2}\left(1 + 2\epsilon\,\sin\,\theta - 2\,\sin^2\frac{\theta}{2}\right) + e^{\epsilon(\pi-\theta)}\cos\frac{3\theta}{2}.$$

Downloaded 03 May 2010 to 171.66.16.245. Redistribution subject to ASME license or copyright; see http://www.asme.org/terms/Terms_Use.cfm

For a given interfacial crack, the near-tip field is uniquely determined by the complex stress intensity factor, $K_I + iK_{II}$, via Eq. (9). Combining Eq. (7) and (8), one obtains the following relation:

$$K_I + iK_{II} = (\hat{K}_I + i\hat{K}_{II}) e^{i\epsilon \ln r/\hat{r}}. \tag{10}$$

Thus, determining the complex constant $\hat{K}_I + i\hat{K}_{II}$ at $\hat{r}$ is equivalent to determining the complex function $K_I + iK_{II}$ at r. Equation (10) also states that for a given crack-tip field the complex vector $K_I + iK_{II}$ rotates, in the complex plane, by an angle of $\epsilon \ln r/\hat{r}$ as r deviates from $\hat{r}$, while remaining a constant magnitude. Fundamentally, it is this r dependence of the complex function in Eq. (7) that results in the classical Mode I and Mode II singularity fields being coupled together in the bi-material case. Rice (1988) indicated that since ϵ is a small quantity ranging from 0.01 to 0.03 for most engineering bi-materials, the variation of the stress intensity factor of classical type with r is usually weak. However, there are situations where ϵ may be large. In the present study, the bi-material panel has an ϵ equal to 0.08.

In determining the stress intensity factors K_I and K_{II}, either stress, strain, or displacement information at two or more points need to be collected. Of course, these points have to be within the K-dominated zone. In the following two photoelastic methods using isochromatics are proposed for the determination of the stress intensity factor. Stress information at two points along either a circular arc or a radial line are utilized in the calculation. This is done to reduce the computational effort so as to illustrate the procedures. More accurate numerical results would be obtained if more data points are used.

Determination of the Stress Intensity Factor Using Photoelastic Isochromatic Patterns

Photoelastic technique has been very effectively used in the experimental determination of stress intensity factors for two-dimensional and three-dimensional cracked bodies made of homogeneous materials. Among the voluminous relevant works appearing in the literature, most are devoted to the study of a single mode case (either Mode I or Mode II). Only a few papers (e.g., Smith and Smith, 1972; Gdoutos and Theocaris, 1978; Sanford and Dally, 1979) have dealt with the mixed-mode situation. Earlier attempts of using photoelasticity for the determination of stress intensity factors of interfacial cracks were made by Theocaris and Stassinakis (1981) and Gdoutos and Papakaliatakis (1982). The former presented an analysis of the isochromatic fringe patterns generated theoretically according to the then available analytical solution. The later included an application of the technique of caustics to an interfacial crack and the evaluation of the complex stress intensity factor from the resulting shadow spot.

In photoelasticity the maximum shear stress τ_m at a point (r, θ) is obtained through the stress optics law as follows:

$$2\tau_m = \frac{Nf_\sigma}{h}, \tag{11}$$

where N (=0, 1, 2, ...) is the fringe order at the point, f_σ is the material fringe value, and h is the thickness of a specimen. Note that τ_m is related to the polar components of stress by

$$\tau_m = \sqrt{\left(\frac{\sigma_{rr} - \sigma_{\theta\theta}}{2}\right)^2 + \sigma_{r\theta}^2}. \tag{12}$$

By combining Eq. (9) and (12), it can be shown that τ_m is related to K_I and K_{II} by

$$\tau_m^2 = \frac{A^2}{2\pi r}(C_1(\theta)K_I^2 + C_2(\theta)K_{II}^2 + C_3(\theta)K_IK_{II}), \tag{13}$$

where

$$C_1(\theta) = \frac{1}{4}(f_{rr}^{(I)} - f_{\theta\theta}^{(I)})^2 + (f_{r\theta}^{(I)})^2,$$

$$C_2(\theta) = \frac{1}{4}(f_{rr}^{(II)} - f_{\theta\theta}^{(II)})^2 + (f_{r\theta}^{(II)})^2,$$

$$C_3(\theta) = \frac{1}{2}(f_{rr}^{(I)} - f_{\theta\theta}^{(I)})(f_{rr}^{(II)} - f_{\theta\theta}^{(II)}) + 2f_{r\theta}^{(I)}f_{r\theta}^{(II)}.$$

Equation (13) is fundamental to the development of different approaches for the determination of the stress intensity factor. The following are but two examples among many other possible methods.

Approach 1

Use two data points (r, θ_1) and (r, θ_2) located along the same circular arc centred at the crack tip.

Since in this case r is a constant, $K_I + iK_{II}$ at any two points are the same. Thus, one has

$$\tau_{m1}^2 = \frac{A^2}{2\pi r}(C_1(\theta_1)K_I^2 + C_2(\theta_1)K_{II}^2 + C_3(\theta_1)K_IK_{II}), \tag{14}$$

$$\tau_{m2}^2 = \frac{A^2}{2\pi r}(C_1(\theta_2)K_I^2 + C_2(\theta_2)K_{II}^2 + C_3(\theta_2)K_IK_{II}), \tag{15}$$

in which the subscripts 1 and 2 of τ_m and θ refer to points 1 and 2, respectively. C_1, C_2, and C_3 are those defined in Eq. (13). Under the condition that $\tau_{m1}, \tau_{m2} \neq 0$ (the zeroth order fringe, if it exists within the specimen, is usually outside the K-region), Eq. (14) and (15) can be combined to give

$$aK_{II}^2 + bK_IK_{II} + cK_I^2 = 0, \tag{16}$$

in which a, b, and c are coefficients and

$$a = \tau_{m1}^2 C_2(\theta_2) - \tau_{m2}^2 C_2(\theta_1),$$

$$b = \tau_{m1}^2 C_3(\theta_2) - \tau_{m2}^2 C_3(\theta_1),$$

$$c = \tau_{m1}^2 C_1(\theta_2) - \tau_{m2}^2 C_1(\theta_1).$$

Assuming $K_I \neq 0$, Eq. (16) can be rewritten as

$$a\left(\frac{K_{II}}{K_I}\right)^2 + b\left(\frac{K_{II}}{K_I}\right) + c = 0. \tag{17}$$

Once K_{II}/K_I is solved from the quadratic equation, K_I and K_{II} are readily determined by substituting this ratio into either Eq. (14) or (15). In the case that Eq. (14) is used, it yields

$$K_I = \sqrt{\frac{1}{\tau_{m1}}\left(C_1(\theta_1) + C_2(\theta_1)\left(\frac{K_{II}}{K_I}\right)^2 + C_3(\theta_1)\left(\frac{K_{II}}{K_I}\right)\right)}, \tag{18}$$

and

$$K_{II} = K_I\left(\frac{K_{II}}{K_I}\right). \tag{19}$$

Approach 2

Use two data points (r_1, θ) and (r_2, θ) located on the same radial line.

Again, from Eq. (13) one has

$$\tau_{m1}^2 = \frac{A^2}{2\pi r_1}(C_1(\theta)K_I^2(r_1) + C_2(\theta)K_{II}^2(r_1) + C_3(\theta)K_I(r_1)K_{II}(r_1)), \tag{20}$$

and

$$\tau_{m2}^2 = \frac{A^2}{2\pi r_2}(C_1(\theta)K_I^2(r_2) + C_2(\theta)K_{II}^2(r_2) + C_3(\theta)K_I(r_2)K_{II}(r_2)). \tag{21}$$

From Eq. (10),

$$K_I(r_1) + iK_{II}(r_1) = (K_I(r_2) + iK_{II}(r_2))e^{i\epsilon \ln r_2/r_1}, \tag{22}$$

Downloaded 03 May 2010 to 171.66.16.245. Redistribution subject to ASME license or copyright; see http://www.asme.org/terms/Terms_Use.cfm

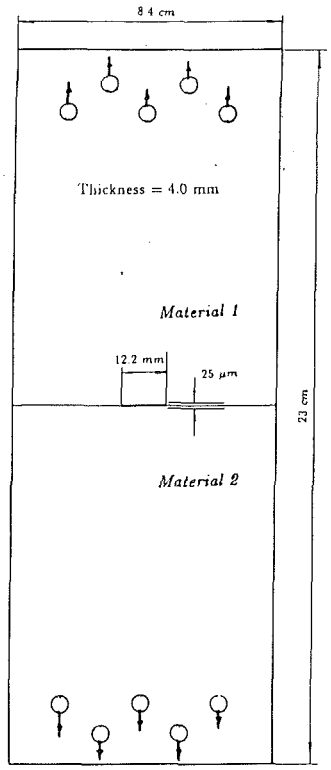
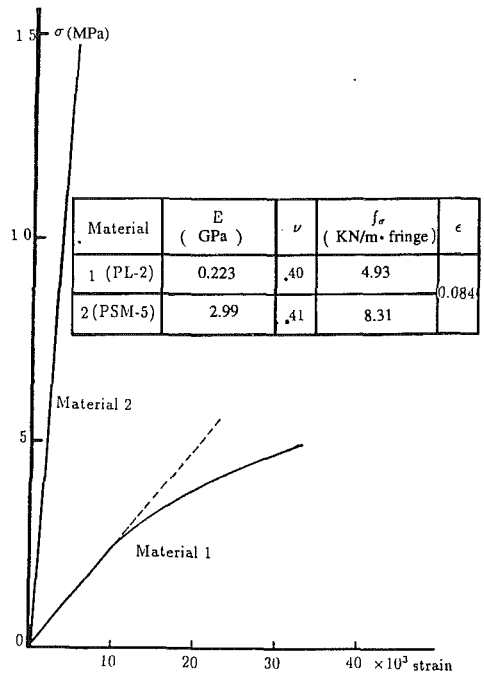


Fig. 2 Configuration of specimen geometry and load in tension test



Material	E (GPa)	ν	f_σ (KN/m·fringe)	ε
1 (PL-2)	0.223	.40	4.93	0.084
2 (PSM-5)	2.99	.41	8.31	

Fig. 3 Calibrated $\epsilon - \sigma$ curves of material 1 and 2 and material constants

or equivalently,

$$\begin{Bmatrix} K_I(r_2) \\ K_{II}(r_2) \end{Bmatrix} = \begin{bmatrix} \cos\phi & -\sin\phi \\ \sin\phi & \cos\phi \end{bmatrix} \begin{Bmatrix} K_I(r_1) \\ K_{II}(r_1) \end{Bmatrix}, \quad (23)$$

in which $\phi = \epsilon \ln r_2/r_1$ represents the phase difference between the complex stress intensity factors at the two points. Substituting Eqs. (23) into Eq. (21) yields

$$\tau_{m2}^2 = \frac{A^2}{2\pi r_2}(C_1' K_I^2(r_1) + C_2' K_{II}^2(r_1) + C_3' K_I(r_1) K_{II}(r_1)), \quad (24)$$

in which

$$C_1' = C_1(\theta)\cos^2\phi + C_2(\theta)\sin^2\phi + \frac{1}{2} C_3(\theta)\sin 2\phi,$$

$$C_2' = C_1(\theta)\sin^2\phi + C_2(\theta)\cos^2\phi - \frac{1}{2} C_3(\theta)\sin 2\phi,$$

$$C_3' = -C_1(\theta)\sin 2\phi + C_2(\theta)\sin 2\phi + C_3(\theta)\cos 2\phi.$$

Following the similar procedure as in Approach 1, an equation in the same form as Eq. (16) is obtained:

$$aK_{II}^2(r_1) + bK_I(r_1)K_{II}(r_1) + cK_I^2(r_1) = 0. \quad (25)$$

Similarly, if $K_I \neq 0$, one has

$$a\left(\frac{K_{II}(r_1)}{K_I(r_1)}\right)^2 + b\left(\frac{K_{II}(r_1)}{K_I(r_1)}\right) + c = 0. \quad (26)$$

The coefficients a, b, and c in Eqs. (25) and (26) are as follows:

$$a = \tau_{m1}^2 r_1 C_2' - \tau_{m2}^2 r_2 C_2,$$

$$b = \tau_{m1}^2 r_1 C_3' - \tau_{m2}^2 r_2 C_3,$$

$$c = \tau_{m1}^2 r_1 C_1' - \tau_{m2}^2 r_2 C_1. \quad (27)$$

Experimental Procedures

The preceding section outlines two approaches for the determination of the stress intensity factor based on photoelasticity. In this section an example of an interfacial crack under remote tension is presented to demonstrate their usage. The general technique for manufacturing photoelastic bi-material plates is described in a previous paper (Chiang, Lu, and Yan, 1989). In the current application, the bi-material plate was made of two kinds of photoelastic resin, PSM-5 and PL-2 (from Measurement Group, Inc.). PL-2 was cast onto a PSM-5 plate with a Teflon foil (about 10 μm in thickness) preattached near the center of the bonding edges. In preparing the casting, PL-2 liquid plastic and PLH-2 hardener were prewarmed to 50°C for an hour to increase their fluidity. They were then cooled to 40°C, and kept at this temperature while being blended together at a ratio of 50:50 by weight. Gentle stirring was essential to avoid air bubbles being trapped into the cast plate. The mixture was then cast onto the prepared edge of the PSM-5 sheet at room temperature. Curing usually takes about 24 hours at room temperature. Calibration of the mechanical and optical properties of both materials as well as the test of the specimen were performed one week after the bi-material plate was manufactured. It was noticed that some residual stresses were created as a result of the manufacturing process. However, they proved to be negligible when the plate was examined in the polariscope prior to testing. The crack formed by the embedded Teflon layer had a width less than 25 μm. The geometry of the specimen is as shown in Fig. 2 and the stress-strain curve, the mechanical and optical properties of both materials as well as the bi-material constant, are given in Fig. 3.

The specimen was loaded in simple tension using a Tinius Oslen digital testing machine. The slowest cross-head speed, 25 mm/min, was chosen to minimize the rate effect. The load was applied in steps at levels of 445 N (100 lb), 667 N (150 lb), and 890 N (200 lb), and the resulting isochromatic fringe pattern were recorded. Figure 4 shows a typical full-field isochromatics in a crossed circular polariscope under a load of 667 N (150 lb). The local detail of the same fringe loops surrounding the crack tip is as depicted in Fig. 5.

Results

From Figs. 4 and 5 it is seen that the isochromatic patterns of an interfacial crack under remote tension bear some resem-

Downloaded 03 May 2010 to 171.66.16.245. Redistribution subject to ASME license or copyright; see http://www.asme.org/terms/Terms_Use.cfm

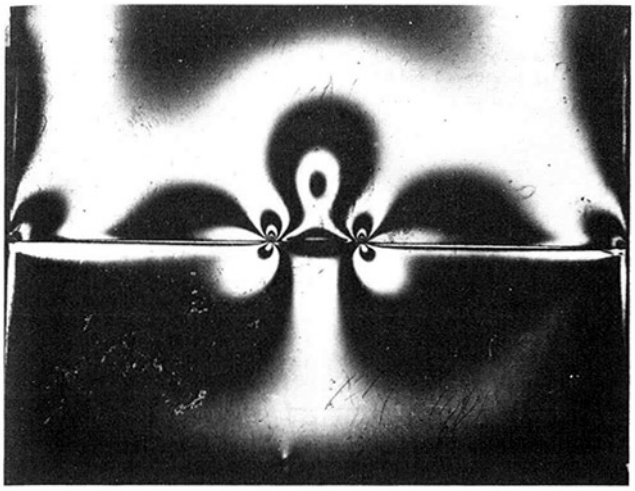


Fig. 4 Full-field isochromatics under remote tension of 150 lb

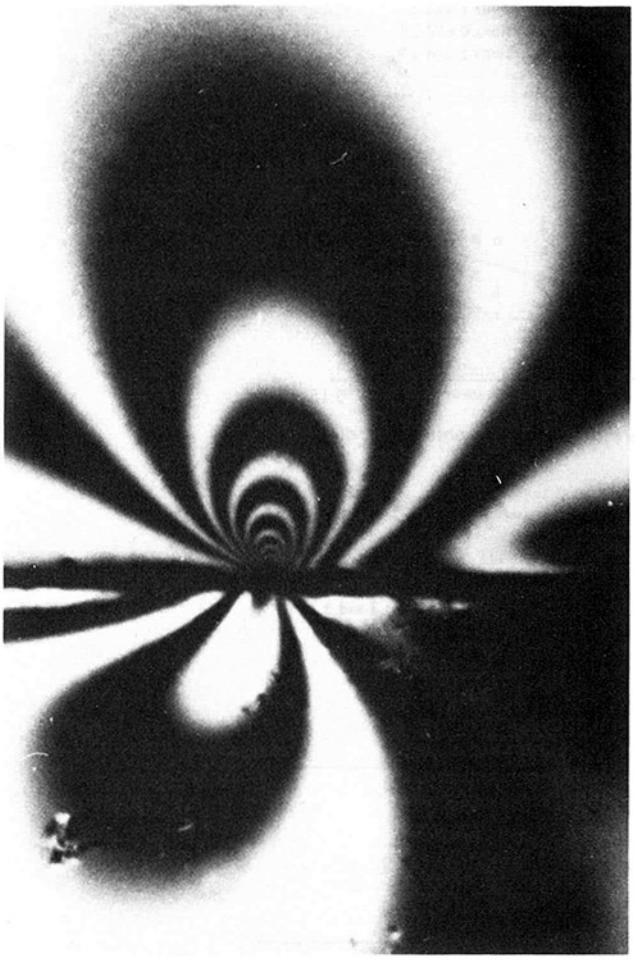


Fig. 5 Enlarged local isochromatic pattern around crack tip

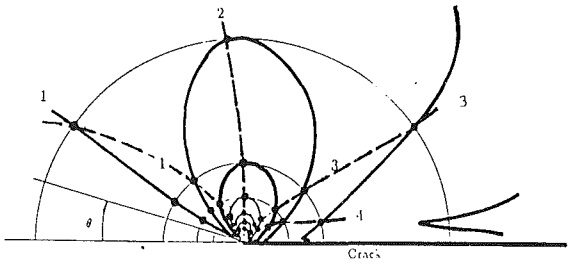


Fig. 6 Arrangement for data points in Approach I

blance to that of a mixed-mode crack in a homogeneous material. But the two are not the same. The difference is manifested in the inclination of the fringe loops around the crack. A fringe loop inclination angle θ_m may be defined as the angular coordinate of the point in a fringe loop whose radial coordinate r is the maximum for all points along the loop. It can be shown in the classical mixed-mode case of homogeneous materials, θ_m is proportional to K_{II}/K_I, the mode mixity, provided that the effects of finite specimen width and the higher order terms of the asymptotic expansion are negligible. Indeed, in some applications (e.g., Smith and Smith, 1972), this angle has been used as a measure of K_{II}/K_I. For a homogeneous material, K_{II}/K_I is constant over the K-dominated region indicating that θ_m must be the same for all fringe loops within the region. This, however, is not the case for interfacial cracks in bimaterials. Theoretically, it is the result of the rotational nature of the stress intensity factor vector (i.e., its phase angle changes as a function of r). Experimentally it manifests itself in the variation of inclination angle θ_m as one crosses from one fringe loop to another. And this is evidenced from the isochromatics depicted in Fig. 5. Curve 2 in Fig. 6 connects the points (r_m, θ_m) for all the fringe loops around the crack tip, and it illustrates in essence the rotation of the stress intensity factor vector or the intrinsic inseparability of the opening and sliding effects of an interfacial crack.

Another interesting experimental result that can be observed directly is the so-called free edge or corner effect of a bimaterial interface. As depicted in Fig. 4, two families of singular fringe loops are seen to emanate from the corners where the interface intercepts the boundary of the specimen. As the load is increased (see Figs. 4, 13, and 14), the two singular fringe families tend to interfere with each other. Furthermore, it may be argued that since the edge effect also occurs at the corners where the crack front intercepts with the free surfaces of the specimen, a tearing (Mode III)-type singularity must exist at these places as well. Thus, it is noted that in a bimaterial plate, the true state of stress near the tip of an interfacial crack may be a mixture of all three modes. The significance of this three dimensionality of the crack-tip stress field needs to be examined in detail if one is to have a comprehensive understanding of the problem.

In extracting the stress intensity factor information from the fringe loops, only the first approach was used. Figure 6 shows the circles around a crack tip used in selecting the data points. The radius of each of these circles was determined in such a way that the circles are tangent to the farthest point of the fringe loops from the crack tip. The data were extracted from the intersections of the circles with the center lines of the fringes. Using the data from each pair of the neighboring points along the same circle a value for the complex stress intensity factor is generated following Approach 1. Having compared all the obtained stress intensity factor values, it was found that the best agreement between the theoretical solution and the experimental result was obtained in an angular region of θ approximately between 90 deg and 130 deg. To illustrate this, four dashed curves were plotted as shown in Fig. 6 including the Curve 2 described previously. Each curve connects data points along different circles. Each two points on same circle but from two neighboring dash line curves composes a pair of data points in the calculation of K_I and K_{II}. The results show that the modulus of $K_I + iK_{II}$ generated from data points along Curve 2 and Curve 3 match fairly well with the theoretical values. And these two curves outline the aforementioned fan-like region. Figures 7, 8, and 9 show the results of the modulus

Downloaded 03 May 2010 to 171.66.16.245. Redistribution subject to ASME license or copyright; see http://www.asme.org/terms/Terms_Use.cfm

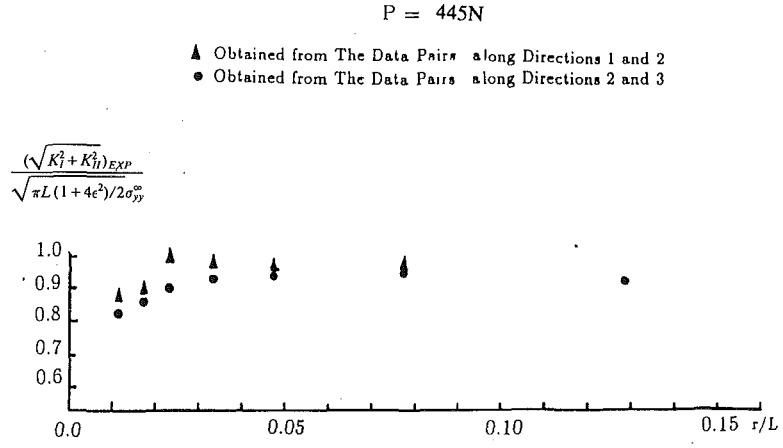


Fig. 7 Modulus of complex stress intensity factors obtained at different r/L for load 445N

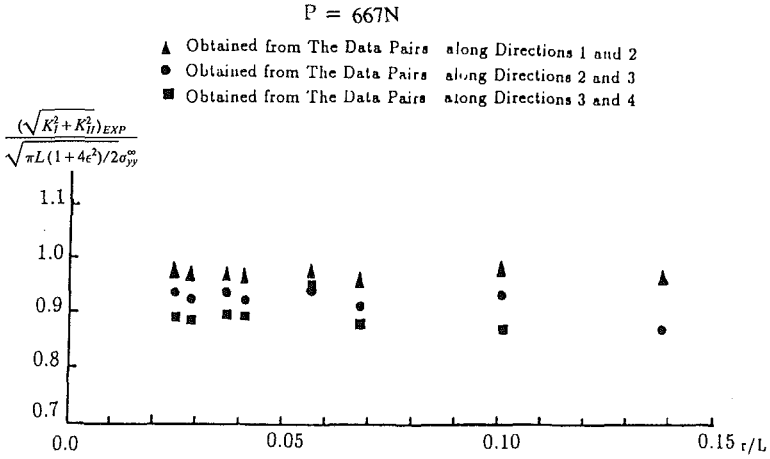


Fig. 8 Modulus of a complex stress intensity factors obtained at different r/L for load 667N

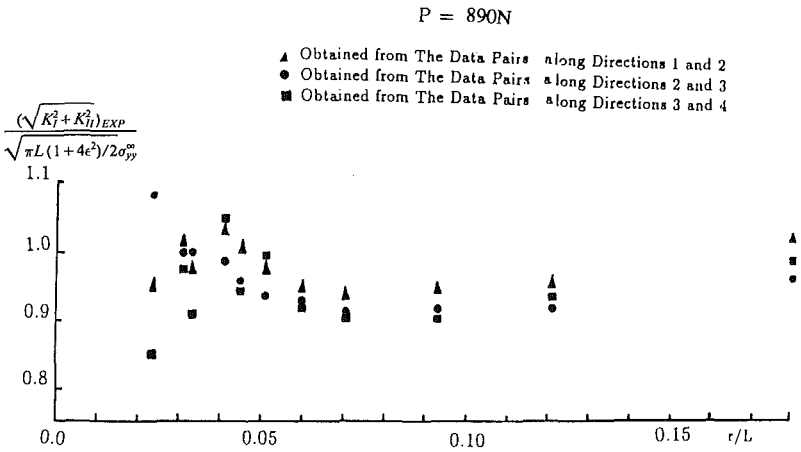


Fig. 9 Modulus of a complex stress intensity factor obtained at different r/L for load 890N

of the complex stress intensity factor vector, i.e., $\sqrt{K_I^2+K_{II}^2}$, under different loads, respectively. The modulus of the stress intensity factor in each case should be constant over the entire K-dominated region as predicted by the theory. And this is essentially true as evidenced by the experimental results shown (data points marked by the circular dots). The larger discrepancy between the experimental and theoretical results outside the fan region may be attributed to several reasons. First, there is a larger inherent uncertainty in the measurement of coordinates, (r, θ), for data points outside this region. It can be seen from the fringe loops that in regions closer to the interface a slight change of θ along a fringe would be accompanied by

Downloaded 03 May 2010 to 171.66.16.245. Redistribution subject to ASME license or copyright; see http://www.asme.org/terms/Terms_Use.cfm

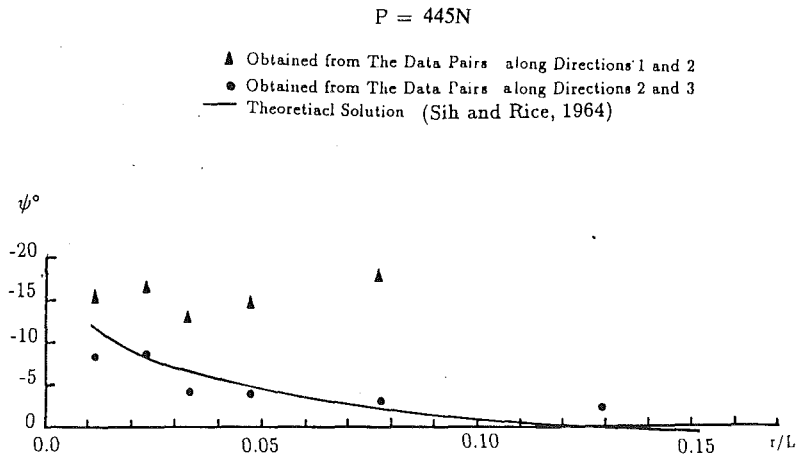


Fig. 10 Variation of phase angle of a complex stress intensity factor with r/L for load 445N

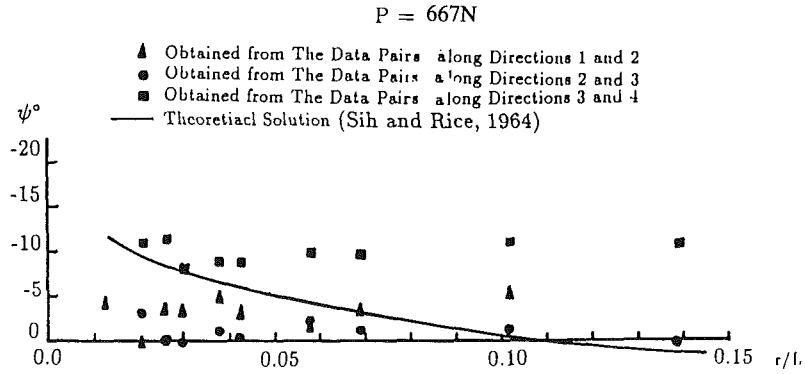


Fig. 11 Variation of phase angle of a complex stress intensity factor with r/L for load 667N

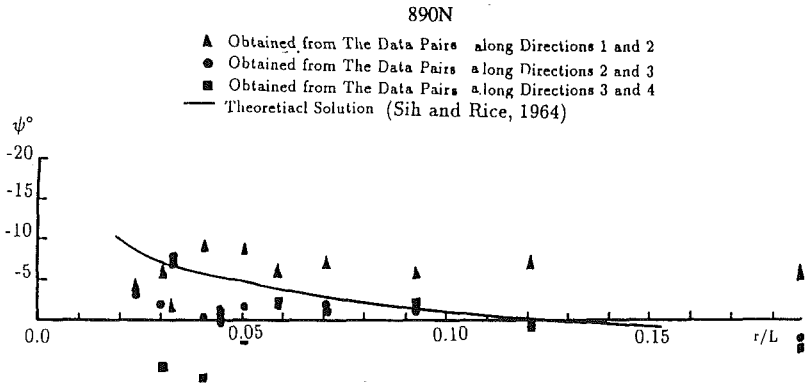


Fig. 12 Variation of phase angle of a complex stress intensity factor with r/L for load 890N

a large variation of r resulting in larger uncertainty. The residual stress due to bonding though small may nevertheless influence the result; and this influence is larger near the interface. For regions very close to the crack tip (r/L less than three percent), the larger discrepancies may be attributed to nonlinear and three-dimensional effects and also to the decreased accuracy of measurements. Within the fan region and for 3 percent $\leq r/L \leq$ 15 percent, the deviation between the experimentally obtained moduli of the stress intensity factors and the theoretical ones is well within 10 percent. However, the deviation of the phase angle (Figs. 10, 11, and 12) is much larger.

Discussion and Conclusion

In this paper a general framework for the determination of complex stress intensity factor for interfacial cracks using photoelasticity is outlined together with two detailed specific approaches. The first utilizes isochromatic values of two data points along a small circle centered at the crack tip and the second employs isochromatic values of two data points along a radial line emanating from the crack tip. To demonstrate the usage, an example is given for an interfacial central crack loaded in remote tension. The resulting isochromatic fringe loops around crack tips show the characteristics of mixed-mode stress field inherent in an interfacial crack. Each loop has a

Downloaded 03 May 2010 to 171.66.16.245. Redistribution subject to ASME license or copyright; see http://www.asme.org/terms/Terms_Use.cfm

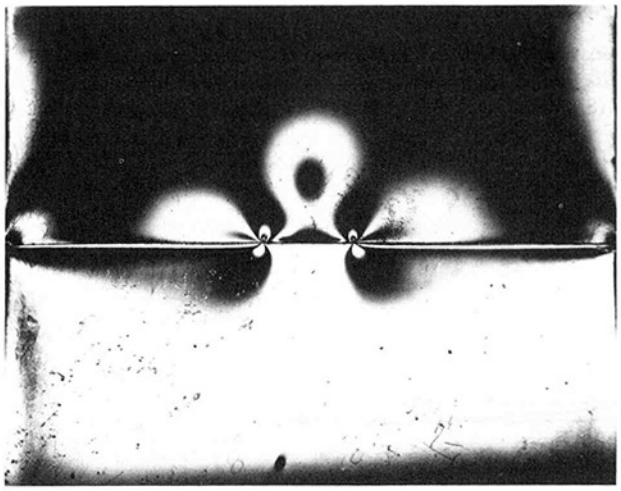


Fig. 13 Full-field isochromatics under remote tension of 445N

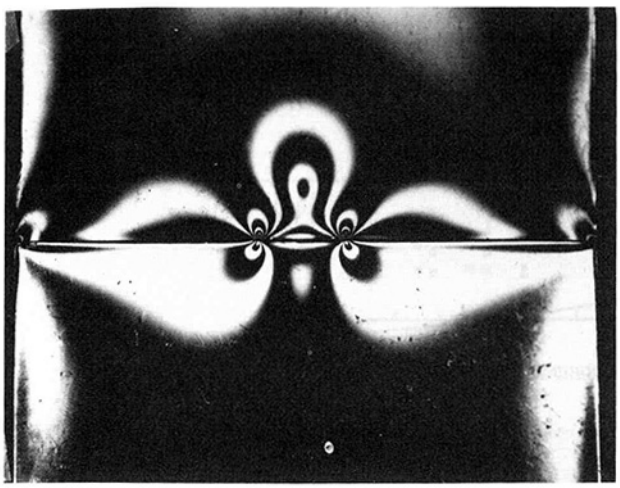


Fig. 14 Full-field isochromatics under remote tension of 800N

different inclination demonstrating the inseparability of these two modes.

Data analysis was carried out using the proposed Approach 1. Results indicate that better agreement with theory is obtained when data are taken within a sector fan with 90 deg ~ 130 deg from the crack tip, and the values of the modulus of the complex stress intensity factor thus determined are within ten percent of that predicted by theory. However, the discrepancies between the phase angles are somewhat larger.

The present frame work of using photoelasticity for the determination of the complex stress intensity factor is based on the asymptotic solution without taking into account the higher order terms. Since data are taken at a finite, though small, distance away from the crack tip, its effect on the accuracy needs to be studied. The present work offers as a basis for future more detailed investigation. Measuring errors can also be reduced by taking advantage of the overdeterministic methods proposed by Sanford and Dally (1979) for homogeneous materials.

Acknowledgment

We thank the Office of Naval Research, Mechanics Division, for sponsoring the work reported here through contract No. N0001482K0566 and the understanding and encouragement of the Scientific Officer, Dr. Yapa Rajapakse. Mr. X. T. Yan contributed to the manufacturing of the model and analysis of the results. The paper was presented at the 3rd ASCE/ASME Mechanics Conference, University of California, San Diego, La Jolla, July 9–12, 1989.

References

Cherepanov, G. P., 1979, *Mechanics of Brittle Fracture* (English Translation), McGraw-Hill, New York, pp. 82–87.

Chiang, F. P., Lu, Hua, and Yan, X. T., 1989, "Photoelastic Analysis of a Crack at Bimaterial Interface," *Proceeding of ICF 7*, Houston, Mar. 20–24, pp. 3063–3072.

Gdoutos, E. E., and Theocaris, P. S., 1978, "A Photoelastic Determination of Mixed Mode Stress Intensity Factors," *Experimental Mechanics*, Vol. 18, No. 3, pp. 87–96.

Huchinson, J. W., Mear, M., and Rice, J. R., 1987, "Crack Paralleling an Interface Between Dissimilar Materials," ASME JOURNAL OF APPLIED MECHANICS, Vol. 54, pp. 828–832.

Rice, J. R., 1988, "Elastic Fracture Mechanics Concepts for Interfacial Cracks," ASME JOURNAL OF APPLIED MECHANICS, Vol. 55, pp. 98–103.

Sanford, R. J., and Dally, J. W., 1979, "A General Method for Determining Mixed-mode Stress Intensity Factors from Isochromatic Fringe Patterns," *Engineering Fracture Mechanics*, Vol. 11, pp. 621–633.

Shih, C. F., and Asaro, R. J., 1988, "Elastic-plastic Analysis of Cracks on Bimaterial Interfaces: Part I—Small Scale Yielding," ASME JOURNAL OF APPLIED MECHANICS, Vol. 55, pp. 299–316.

Sih, G. C., and Rice, J. R., 1964, "The Bending of Plates of Dissimilar Materials With Cracks," ASME JOURNAL OF APPLIED MECHANICS, Vol. 31, pp. 477–482.

Smith, D. G., and Smith, C. W., 1972, "Photoelastic Determination of Mixed-mode Stress-intensity Factors," *Engineering Fracture Mechanics*, Vol. 4, No. 2, pp. 357–366.

Theocaris, P. S., and Stassinakis, C. A., 1981, "Complex Stress Intensity Factors at Tips of Cracks along Interfaces of Dissimilar Media," *Engineering Fracture Mechanics*, Vol. 14, pp. 363–372.

Williams, M. L., 1959, "The Stress around a Fault or Crack in Dissimilar Media," *Bulletin of the Seismological Society of America*, Vol. 49, pp. 199–204.

Downloaded 03 May 2010 to 171.66.16.245. Redistribution subject to ASME license or copyright; see http://www.asme.org/terms/Terms_Use.cfm

O. Hayden Griffin, Jr.
Associate Professor of Engineering Science and Mechanics, Mem. ASME.

Eric R. Johnson
Associate Professor of Aerospace and Ocean Engineering, Mem. ASME.

Virginia Polytechnic Institute and State University, Blacksburg, VA 24061-0219

Mark D. Sensmeier
Engineer-Materials Behavior, GE Aircraft Engines, Cincinnati, OH 45215-6301

Nonlinear Response of Graphite-Epoxy Wide Columns Subject to Eccentric Load

It is shown that including the effects of bend-twist coupling and material nonlinearity on the large displacement flexural response of graphite-epoxy wide columns is necessary to adequately model their response. Results from static tests on $[0_{30}]_T$ and $[(30/0/-30)_5]_s$ laminated specimens under eccentric axial compression are compared to a nonlinear analysis. The analysis is based on a Kantrovich expansion of the displacements in the width coordinate and a finite element representation in the axial coordinate. An incremental, updated Lagrangian formulation and element corotational coordinates are employed. Nonlinear elastic material behavior was measured in a separate set of material characterization tests, and these data are used to compute tangent stiffnesses in the updated configuration.

Introduction

It is forecast that the next generation transport aircraft will utilize advanced composite materials in the primary structure in addition to their current utilization in secondary structural components. An important safety issue is the crashworthiness of the composite fuselage. A crashworthy fuselage structure should be designed to absorb the energy on impact up to speeds of about 12 meters per second such that the passengers are protected from dangerous deceleration magnitudes. From drop test results on metallic transport fuselage sections reported by Fasanella et al. (1984) it can be inferred that a majority of the energy absorbed during a crash is by bending failures of the skin, frame, and stringers. Insufficient data on the large deflection flexural response and failure of composite laminates, that is, data necessary for composite fuselage crash studies, motivated a study by Derian and Hyer (1986).

A drop tower test fixture was designed by Derian and Hyer (1986) to study the dynamic response and failure of rectangular laminated composite plates subjected to eccentric axial loads. The specimens in the study were longer along the load axis than they were wide, the two loaded edges were mounted in hinged supports, and the two unloaded edges were free; i.e., the test conditions approximated wide column behavior for rectangular plates in compression. In this test configuration the bending deformation of the specimen is substantially greater than the compressive deformation, such that a nearly pure flexural response is achieved. An important result from Derian and Hyer's study was that, for laminate layups of practical importance, the static and dynamic failure modes were essentially the same. The experimental results from the static tests reported in this work were obtained with the same fixture used by Derian and Hyer.

The purpose of the present paper is to show the influence of the coupling between bending and twisting of symmetric laminates containing off-axis plies, and material nonlinearity, on the large deflection behavior of these laminates when used as a wide column. These effects were not completely studied in the analysis by Derian and Hyer. A one-dimensional element is developed in this paper that accounts for distortion of the column's cross-section via Kantrovich's method, and has 11 degrees-of-freedom per node. Geometric nonlinearity is represented by an updated Lagrangian formulation in element corotational coordinates. Material nonlinearity is accounted for by computing the tangent stiffnesses in the updated configuration.

Specimens, Apparatus, and Tests

The specimens were made from AS4/3502 graphite-epoxy unidirectional preimpregnated tape by hand layup. A number of symmetric layups from 16 to 32 plies thick were fabricated into panels 61 cm long by 40.6 cm wide.[1] The integrity of the panels was verified by ultrasonic C-scan inspection. Six specimens 58.4 cm long and 5.08 cm wide were cut from each panel. Only the $[0]_{30}$ and the $[(30/0/30)_5]_s$ laminated specimen test results are discussed in this paper. Test results for the other laminates are given in the report by Sensmeier et al. (1988).

Contributed by the Applied Mechanics Division of THE AMERICAN SOCIETY OF MECHANICAL ENGINEERS for publication in the ASME JOURNAL OF APPLIED MECHANICS.

Discussion on this paper should be addressed to the Technical Editor, Professor Lewis T. Wheeler, Department of Mechanical Engineering, University of Houston, Houston, TX 77204-4792, and will be accepted until four months after final publication of the paper itself in the ASME JOURNAL OF APPLIED MECHANICS.

Manuscript received by the ASME Applied Mechanics Division, May 14, 1990; final revision, Oct. 4, 1991. Associate Technical Editor: G. J. Dvorak.

[1] N.B.; all measurements in the experiments were made in U.S. customary units and converted to the SI dimensional unit system for this paper.

Copyright © 1993 by ASME
Downloaded 03 May 2010 to 171.66.16.245. Redistribution subject to ASME license or copyright; see http://www.asme.org/terms/Terms_Use.cfm

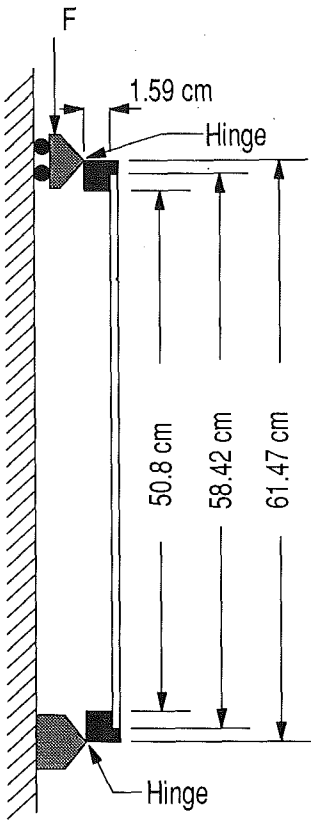


Fig. 1 Schematic of the wide column test configuration

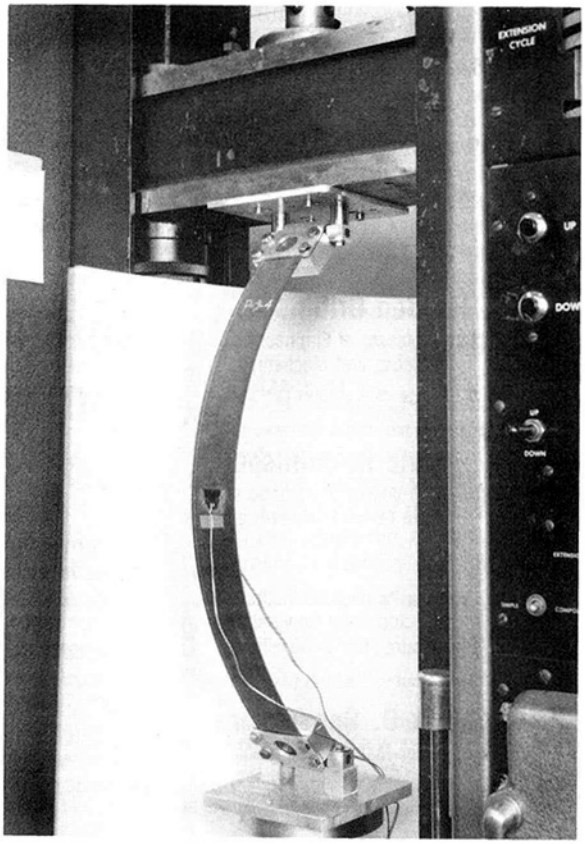


Fig. 2 Photograph of a specimen in a static test

A schematic of the loading configuration is shown in Fig. 1. The specimen was mounted vertically with its ends clamped in blocks that are hinged to supports. The lower support was fixed and the upper support was free to move downward under the action of the vertical force F. The test section of the specimen is 50.8 cm long and the axial load eccentricity is 15.9 mm plus a half of the specimen's thickness. Static tests were conducted on a standard screw-driven load frame, rather than in a drop tower. The drop tower was used in the dynamic tests. A photograph of a specimen in a static test is shown in Fig. 2. The static test configuration allowed the top end of the specimen to translate downward about 33 cm before the hinges contacted the support plates. This distance was sufficient to load most of the laminates to failure. The specimens were tested statically to failure or until hinge contact, whichever came first.

Four data sets were recorded during the static tests. These were the axial load, axial displacement at the loaded end, and axial surface strains on both sides at the center of the specimen. The crosshead speed was set to 5.08 cm per minute, and this rate was used to calculate the end displacement. The load-end shortening curve was plotted on a chart recorder. The strains were recorded on an X-Y plotter, then manually digitized.

Material Characterization Tests

In-plane stress-strain response data were obtained from coupons cut from an 18-ply unidirectional panel fabricated from the AS4/3502 material. Tension, compression, and shear tests were performed in a standard screw-driven load frame under displacement control. The tension coupons were 25.4 cm × 1.27 cm for loading parallel to the fibers (longitudinal), and 25.4 cm × 2.54 cm for loading perpendicular to the fibers (transverse). Longitudinal and transverse strain gages were bonded to the tension coupons. Compression tests were conducted on coupons 3.81 cm long and 1.91 to 2.54 cm wide in an end-loading fixture designed by Gürdal (Gürdal and Starbuck, 1988). Each compression coupon had two back-to-back longitudinal strain gages bonded to the center of it, and a transverse strain gage bonded to one side. An Iosipescu (1967) test was chosen to characterize the shear response. The coupons were 7.62 cm long, 1.90 cm wide, and had a V-notch cut in the center of the two long edges. A 45-deg strain gage rosette was bonded to each shear test coupon. A computerized data acquisition system was used to record the axial force measured by the load cell of the testing machine and to record the signals from the strain gages. From two to five replicate coupons were run for each type of test, and the amount of scatter in the data was small. Further details are given by Sensmeier et al. (1988).

The longitudinal stress-strain response was linear for low strain magnitudes, stiffened for large tensile strains, and softened for large compressive strains. The transverse stress-strain response was linear at low strain magnitudes and softened in both tension and compression for larger magnitudes. The largest tensile strain magnitudes were smaller than the largest compressive strain magnitudes prior to failure in the transverse tests. The shear stress-strain response was linear at low strain magnitudes and softened at larger magnitudes. The Poisson's ratio was found to be fairly constant in the longitudinal tension tests and the data from the longitudinal compression tests were questionable. Hence, a constant value of 0.28 was used for the major Poisson's ratio as determined from the longitudinal tension tests.

The nonlinear behavior of the in-plane moduli were represented by cubic polynomials. To determine the four coefficients in these polynomials, the tangent modulus was determined at the initial, final, and two intermediate strain points. These moduli were determined graphically. Substituting these values into the cubic polynomials yielded four equations which were solved for the unknown coefficients. The moduli polynomials obtained by this method were then integrated to obtain the corresponding fourth-degree polynomials for the stress-strain relation. These stress-strain functions were plotted with the

Downloaded 03 May 2010 to 171.66.16.245. Redistribution subject to ASME license or copyright; see http://www.asme.org/terms/Terms_Use.cfm

Table 1 Coefficients for tangent moduli in Eq. (1)

Material Property	Initial Modulus P_o, GPa	A, GPa	B, TPa	C, TPa	ϵ_{max} Strain Limit	Final Modulus GPa	% Change[a]
E_1 (tension)	136.9	2460.680	-253.05491	42,856.586	0.009	169.74	24
E_1 (compression)	133.8	2204.004	363.38592	104,260.38	-0.007	100.38	-24.9
E_2 (tension)	9.86	-102.9983	59.514708	-16,330.251	0.0055	8.34	-15.2
E_2 (compression)	10.2	98.1836	-1.7242544	28.130491	-0.029	5.24	-48.6
G_{12}	5.63	-45.6213	-17.590931	521.94289	0.025	1.65	-70.7

[a] Change in final modulus relative to initial modulus.

experimental stress-strain data and were found to correlate well. The in-plane moduli polynomials are written in the form

$$P = P_0 + A\epsilon + B\epsilon^2 + C\epsilon^3 \tag{1}$$

in which P denotes one of the in-plane moduli, ϵ is the corresponding strain, P_o is the initial modulus, and A, B, and C are coefficients. The values of these coefficients for each type of material characterization test are given in the Table. In addition, the maximum strain magnitude ϵ_{max} for which these polynomial expressions are applicable are given in the table. A range of 15 to 70 percent change in the final in-plane moduli with respect to their initial values is exhibited by this material, as is shown in the last columns in the table. Although the ply constitutive equations are determined under uniaxial testing conditions, it is assumed that they are applicable to multidimensional states of stress and strain.

Variational Principle

An incremental finite element method is used to analyze the response of the wide column specimens. The displacement of the body for an increment in load is described using an updated Lagrangian formulation and corotational coordinates for an element. It is assumed the load increment is small such that a linearized incremental virtual work functional is sufficient to determine the displacement increments. This functional is given by Horrigmoe and Bergen (1976) for the general case of continuous deformation, and is specialized here to deformations consistent with Kirchhoff's hypotheses for thin plates under wide column loading conditions.

The initial stress-free configuration of a laminated plate element is denoted Γ_o and is referenced to the global cartesian system (x_o, y_o, z_o). The reference surface with area A_o is the middle plane of the laminate defined by $z_o = 0$, with $-h/2 \le z_o \le h/2$, where h is the thickness of the laminate. Axis x_o is parallel to the load axis with $x_o^e \le x_o \le x_o^{e+1}$, where x_o^e and x_o^{e+1} are axial nodal coordinates, and $x_o^{e+1} - x_o^e = L_o$ is the length of the element. Axis y_o is parallel to the width with $-b/2 \le y_o \le b/2$, where b is the width of the plate. The updated configuration of the plate element is denoted Γ_1 and is referenced to the corotating cartesian system (x_1, y_1, z_1). For the wide column problem, the component of the rotation of a line element about the y_o-axis dominates the rotations about other directions. Thus, it is assumed the cartesian frame in Γ_1 is rotated about the y_o-axis through the angle ϕ, such that the direction cosines between the corotational system and the global system are given by

	x_o	y_o	z_o
x_1	$\cos\phi$	0	$\sin\phi$
y_1	0	1	0
z_1	$-\sin\phi$	0	$\cos\phi$.

(2)

The angle ϕ is determined from the displacement of the nodes x_o^e and x_o^{e+1} at $y_o = z_o = 0$. See Fig. 3.

All statical and kinematical variables are referenced to configuration Γ_1. The geometry of configuration Γ_1, and the Cauchy stresses, are assumed to be known under the action of tractions along element edges originally at $x_o = x_o^e$ and $x_o = x_o^{e+1}$. The edges originally at $y_o = \pm b/2$ are traction-free as are the upper and lower surfaces of the laminate. Body forces are neglected. It is assumed that the deformed geometry of the plate element relative to the corotational system is small such that the configuration is adequately approximated by a flat plate in Γ_1 with a rectangular reference surface area A_1 of length L and width b. Although we assume the width of the reference surface doesn't change for purposes of equilibrium, the axial contraction from L_o to L is accounted for in the virtual work expression for equilibrium.

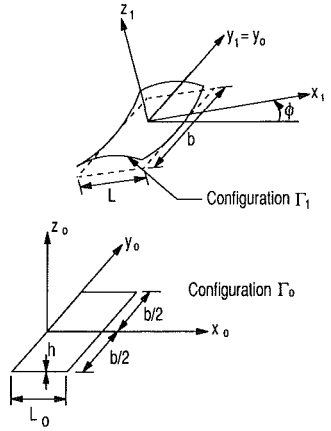


Fig. 3 Original (Γ_o) and current (Γ_1) configurations of a plate element

Consider an increment in the components of the force resultants ΔP_x, ΔP_{xy}, and ΔP_z per unit length, and the moment resultant ΔC_x per unit length, on the x-edges of the element in Γ_1. This increment in external load causes incremental displacements of the reference surface in the x_1-, y_1-, and z_1-directions denoted by $\Delta u(x_1, y_1)$, $\Delta v(x_1, y_1)$, and $\Delta w(x_1, y_1)$, respectively. The associated incremental membrane strains and curvature vectors in terms of the incremental displacements are

$$\begin{aligned}\Delta\epsilon &= [\Delta\epsilon_x,\ \Delta\epsilon_y,\ \Delta\gamma_{xy}]^T \\ &= [\partial\Delta u/\partial x_1,\ \partial\Delta v/\partial y_1,\ \partial\Delta u/\partial y_1 + \partial\Delta v/\partial x_1]^T \\ \Delta\kappa &= [\Delta\kappa_x,\ \Delta\kappa_y,\ \Delta\kappa_{xy}]^T \\ &= [-\partial^2\Delta w/\partial x_1^2,\ -\partial^2\Delta w/\partial y_1^2,\ -2\partial^2\Delta w/\partial x_1\partial y_1]^T\end{aligned} \tag{3}$$

where the superscript T means transpose. The increments in the membrane and bending moment resultants are given in the vector form

$$\begin{aligned}\Delta\mathbf{N} &= [\Delta N_x,\ \Delta N_y,\ \Delta N_{xy}]^T = \int_h [\Delta S_{xx},\ \Delta S_{yy},\ \Delta S_{xy}]^T dz_1 \\ \Delta\mathbf{M} &= [\Delta M_x,\ \Delta M_y,\ \Delta M_{xy}]^T = \int_h [\Delta S_{xx},\ \Delta S_{yy},\ \Delta S_{xy}]^T z_1 dz_1\end{aligned} \tag{4}$$

Downloaded 03 May 2010 to 171.66.16.245. Redistribution subject to ASME license or copyright; see http://www.asme.org/terms/Terms_Use.cfm

where ΔS_{xx}, ΔS_{yy}, and ΔS_{xy} are the increments in the second Piola-Kirchhoff stress components. The membrane resultants are

$$(N_x, N_y, N_{xy}) = \int_h (\sigma_{xx}, \sigma_{yy}, \sigma_{xy}) dz_1 \tag{5}$$

where σ_{xx}, σ_{yy}, and σ_{xy} are the Cauchy stress components in Γ_1. The linearized incremental virtual work functional is

$$\begin{aligned}\int_{A_1} [\delta(\Delta\epsilon)]^T \Delta\mathbf{N} + [\delta(\Delta\kappa)]^T \Delta\mathbf{M}\, dA \\ + \int_{A_1} \{N_x \partial(\Delta w)/\partial x_1\, \delta[\partial(\Delta w)/\partial x_1] \\ + N_y \delta(\Delta w)/\partial y_1\, \delta[\partial(\Delta w)/\partial y_1] \\ + N_{xy} \partial(\Delta w)/\partial x_1\, \delta[\partial(\Delta w)/\partial y_1] \\ + N_{xy} \partial(\Delta w)/\partial y_1\, \delta[\partial(\Delta w)/\partial x_1]\}\, dA \\ + \int_b [\Delta P_x \delta(\Delta u) + \Delta P_{xy} \delta(\Delta v) + \Delta P_z \delta(\Delta w) \\ + \Delta C_x \delta(\partial \Delta w/\partial x_1)]_{x_1=0}^{x_1=L}\, dy_1 = 0\end{aligned} \tag{6}$$

The incremental plate resultants are linearly related to the incremental strains by

$$\begin{Bmatrix} \Delta\mathbf{N} \\ \Delta\mathbf{M} \end{Bmatrix} = \begin{bmatrix} \mathbf{A} & \mathbf{B} \\ \mathbf{B} & \mathbf{D} \end{bmatrix} \begin{Bmatrix} \Delta\epsilon \\ \Delta\kappa \end{Bmatrix} \tag{7}$$

in which formulas for matrices **A**, **B**, and **D** in terms of the in-plane material properties E_1, E_2, ν_{12}, and G_{12} are as given in classical laminated plate theory (Jones, 1975). Since the moduli E_1, E_2, and G_{12} are functions of the state of strain in configuration Γ_1 as given by Eq. (1), the matrices **A**, **B**, and **D** in Eq. (7) are tangent stiffness matrices. It is interesting to note that a symmetric layup can lead to a tangent coupling matrix **B**, because of the nonlinear constitutive behavior and the nonuniform distribution of in-plane strains through the thickness of the laminate.

Displacement Approximation and Element Equations

The method of Kantrovich (Fung, 1965) is used to express the displacements as a power series in the width-wise coordinate y_1, and the finite element method is used to represent the x_1-dependence of the generalized coordinate functions in the Kantrovich expansion. The incremental displacements of the reference surface are assumed to be

$$\begin{aligned}\Delta u(x_1, y_1) &= \Delta U(x_1) + \Delta\eta(x_1) y_1 + \Delta\alpha(x_1) y_1^2 \\ \Delta v(x_1, y_1) &= \Delta V(x_1) + \Delta\omega(x_1) y_1 \\ \Delta w(x_1, y_1) &= \Delta W(x_1) + \Delta\theta(x_1) y_1 + \Delta g(x_1) y_1^2.\end{aligned} \tag{8}$$

For a two-noded element, the generalized coordinate functions ΔU, $\Delta\eta$, $\Delta\alpha$, ΔV, and $\Delta\omega$, are interpolated with linear polynomials, and the generalized coordinate functions Δw, $\Delta\theta$, and Δg are interpolated with Hermite cubic polynomials. Let $\mathbf{h}_1(x_1)$ denote a 1×2 row vector of the linear interpolation functions, and $\mathbf{h}_2(x_1)$ denote a 1×4 row vector of the cubic interpolation functions. Then, the incremental displacements are approximated by

$$\begin{Bmatrix} \Delta u \\ \Delta v \end{Bmatrix} = \mathbf{H}_1(x_1, y_1) \Delta\mathbf{u}_\alpha$$
$$\Delta w = \mathbf{H}_2(x_1, y_1) \Delta\mathbf{u}_\beta \tag{9}$$

in which the interpolation matrices are

$$\mathbf{H}_1(x_1, y_1) = \begin{bmatrix} \mathbf{h}_1(x_1) & y_1\mathbf{h}_1(x_1) & y_1^2\mathbf{h}_1(x_1) & 0 & 0 \\ 0 & 1 & 0 & \mathbf{h}_1(x_1) & y_1\mathbf{h}_1(x_1) \end{bmatrix}$$

$$\mathbf{H}_2(x_1, y_1) = [\mathbf{h}_2 x_1) \;\; y_1\mathbf{h}_2(x_1) \;\; y_1^2\mathbf{h}_2(x_1)]. \tag{10}$$

The 10×1 vector of in-plane nodal displacement increments $\Delta\mathbf{u}_\alpha$, and the 12×1 vector of out-of-plane nodal displacement increments $\Delta\mathbf{u}_\beta$ are

$$\begin{aligned}\Delta\mathbf{u}_\alpha &= [\Delta U_1, \Delta U_2, \Delta\eta_1, \Delta\alpha_1, \Delta\alpha_2, \Delta V_1, \Delta V_2, \Delta\omega_1, \Delta\omega_2]^T \\ \Delta\mathbf{u}_\beta &= [\Delta W_1, -\Delta W_1', \Delta W_2, -\Delta W_2', \Delta\theta_1, -\Delta\theta_1', \Delta\theta_2, \\ &\qquad -\Delta\theta_2', \Delta g_1, -\Delta g_1', \Delta g_2, -\Delta g_2']^T\end{aligned} \tag{11}$$

where subscript 1 refers to the left node, subscript 2 refers to the right node, and prime means derivative with respect to x_1.

Substituting the interpolations (9), (10) into Eqs. (8), and then substituting these results into Eqs. (3) gives

$$\Delta\epsilon = \mathbf{B}_1 \Delta\mathbf{u}_\alpha, \quad \text{and} \quad \Delta\kappa = \mathbf{B}_2 \Delta\mathbf{u}_\beta \tag{12}$$

where the strain matrices are

$$\mathbf{B}_1(x_1, y_1) = \begin{bmatrix} \mathbf{h}_1 & y_1\mathbf{h}_1' & y_1^2\mathbf{h}_1' & 0 & 0 \\ 0 & 0 & 0 & 0 & \mathbf{h}_1 \\ 0 & \mathbf{h}_1 & 2y_1\mathbf{h}_1 & \mathbf{h}_1' & y_1\mathbf{h}_1' \end{bmatrix} \tag{13}$$

$$\mathbf{B}_2(x_1, y_1) = \begin{bmatrix} -\mathbf{h}_2'' & -y_1\mathbf{h}_2'' & -y_1^2\mathbf{h}_2'' \\ 0 & 0 & -2\mathbf{h}_2 \\ 0 & -2\mathbf{h}_2' & -4y_1\mathbf{h}_2' \end{bmatrix} \tag{14}$$

The influence of the initial stresses in the incremental virtual work Eq. (6) requires, in general, a stress accumulation procedure to compute the Cauchy stresses in the updated configuration from the increments of the second Piola-Kirchhoff stresses referred to the previous configuration. For example, see Kleiber (1989). However, for the wide column problem under study here, the influence of the initial resultants N_y and N_{xy} are neglected with respect to the resultant N_x, since the load path is axial. Further, the value of N_x within an element is simply taken to be the projection along the x_1-axis of the element of the applied axial load resultant per unit width (F/b). This is the same procedure used by Yang (1973) for incremental analysis of the elastica by a matrix displacement approach.

The displacement approximations in Eqs. (9) and the strain-displacement Eqs. (12) are substituted into the incremental virtual work functional (6) to get

$$\begin{bmatrix} \mathbf{K}_{\alpha\alpha} & \mathbf{K}_{\alpha\beta} \\ \mathbf{K}_{\beta\alpha} & \mathbf{K}_{\beta\beta} \end{bmatrix} \begin{Bmatrix} \Delta\mathbf{u}_\alpha \\ \Delta\mathbf{u}_\beta \end{Bmatrix} = \begin{Bmatrix} \Delta\mathbf{F}_\alpha \\ \Delta\mathbf{F}_\beta \end{Bmatrix} \tag{15}$$

in which the stiffness submatrices are

$$\begin{aligned}\mathbf{K}_{\alpha\alpha} &= \int_{A_1} \mathbf{B}_1^T \mathbf{A}\, \mathbf{B}_1\, dA \\ \mathbf{K}_{\alpha\beta} = \mathbf{K}_{\beta\alpha}^T &= \int_{A_1} \mathbf{B}_1^T \mathbf{B}\, \mathbf{B}_2\, dA \\ \mathbf{K}_{\beta\beta} &= \int_{A_1} \{\mathbf{B}_2^T \mathbf{D}\, \mathbf{B}_2 + N_x[\partial\mathbf{H}_2/\partial x_1]^T[\partial\mathbf{H}_2/\partial x_1]\}\, dA\end{aligned} \tag{16}$$

and the incremental load vectors are

$$\begin{aligned}\Delta\mathbf{F}_\alpha &= \int_b \mathbf{H}_1^T [\Delta P_x\, \Delta P_{xy}]_{x_1=0}^{x_1=L}\, dy_1 \\ \Delta\mathbf{F}_\beta &= \int_b [\mathbf{H}_2^T \Delta P_z + (\mathbf{H}_2')^T \Delta C_x]_{x_1=0}^{x_1=L}\, dy_1.\end{aligned} \tag{17}$$

Solution Procedure and Modeling Details

The incremental Eqs. (15) for each element are transformed to global coordinate directions using the direction cosines of Eqs. (2) for each element. Then, the element equations in global coordinate directions are assembled in the usual fashion. The nodal displacements are set to zero at the end nodes of the wide column model, except for the axial displacement ΔU_2 at the upper hinge. Instead of prescribing ΔU_2, the increment in

Downloaded 03 May 2010 to 171.66.16.245. Redistribution subject to ASME license or copyright; see http://www.asme.org/terms/Terms_Use.cfm

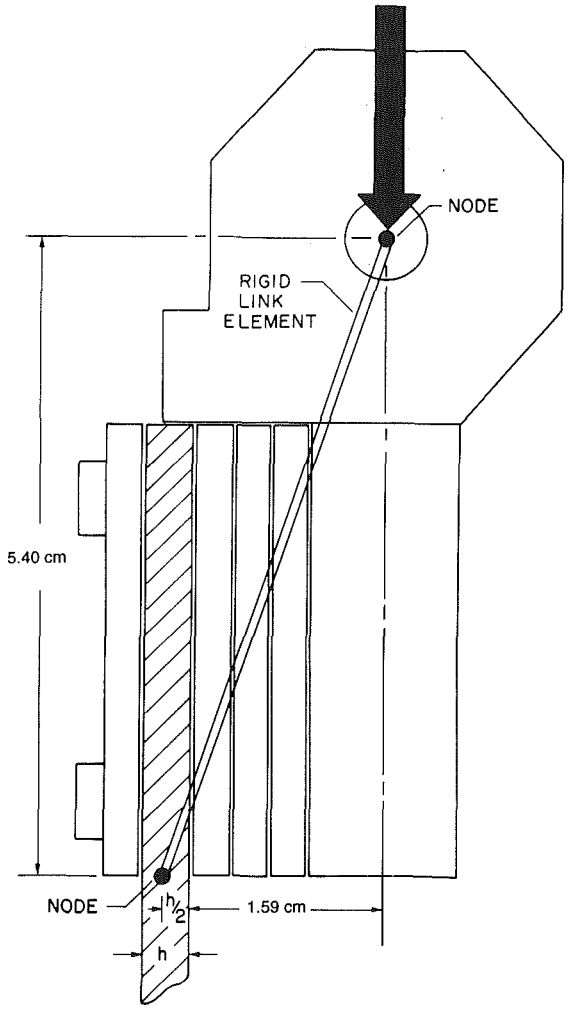


Fig. 4 Geometry and dimensions of hinge support

axial downward load per unit width, ΔP_x, is prescribed at the upper hinge. Forty elements were used to model the 50.8 cm test section and two rigid link elements were used to model the portion of the specimen secured to the leaves of the hinges. The rigid link elements approximate the substantial increase in stiffness to those portions of the specimen's ends bolted to the leaves of the hinges, and also account for the eccentricity of the load with respect to the middle plane of the laminate. (See Fig. 4.)

After the solution for the incremental displacements has been obtained with respect to configuration Γ_1 the new location of the nodes, the new element lengths L, and the new element rotation angles ϕ are computed. The incremental strains are computed from Eqs. (12), and these are added to the old total strains in configuration Γ_1. These new total strains in the old coordinate directions are transformed to the new coordinate directions of the element. The transformed strains are used to calculate the tangent moduli from Eq. (1) and the new tangent stiffness matrices of laminated plate theory in Eqs. (7). The load increment is added to the applied load of configuration Γ_1 to get the new total load. The new total load and the new rotation angles ϕ are used to compute the new initial resultant N_x in each element. The stiffness matrices for the element are computed via Eqs. (16), and the solution process for the incremental displacements is repeated for a new increment in the load.

No iteration of the equations at a fixed value of the load is performed to correct the linearization within a load step. Thus, the load increments are prescribed small enough so that the incremental displacement Δw is less than the thickness of the

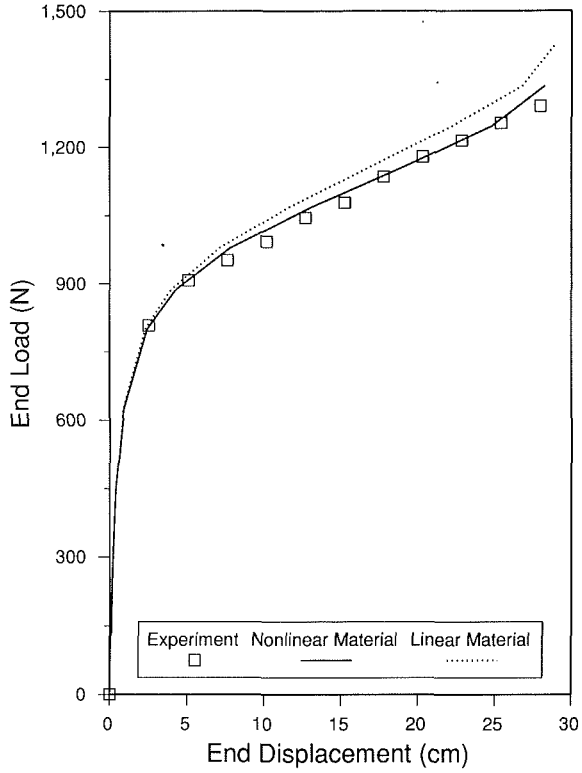


Fig. 5 Load-end shortening for the $[0_{30}]_T$ specimen compared to the generalized cylindrical bending analyses

laminate. For further details of the numerical model, see Sensmeier et al. (1988).

Results and Discussion

To demonstrate the conditions under which the distortion of the cross-section of the wide column laminates are important, the full model is compared to one in which the width-wise degree of freedom $\Delta\eta$, $\Delta\alpha$, $\Delta\omega$, $\Delta\theta$, and Δg in Eqs. (8) were set to zero for all load increments. This implies that the displacements of the laminate are independent of y_1, so that there is no distortion of the rectangular cross-section of the column in its plane and that the out-of-plane distortion is a rigid-body rotation of the section about the y_1-axis. This is called the generalized cylindrical bending model, and, except for the displacement $V(x_1)$ and stiffnesses determined from a plate theory, it is nearly a Bernoulli-Euler beam model of the wide column problem.

To demonstrate the influence of the nonlinear material behavior, analyses were performed for linear material behavior. The linear material models are obtained by setting coefficients A, B, and C to zero in Eq. (1), such that moduli E_1, E_2, and G_{12} are equal to their values at the origin of their respective stress-strain curves.

The generalized cylindrical bending model with and without material nonlinearity, and the width-wise model with and without material nonlinearity are compared to experimental results for the $[0_{30}]_T$ laminate in Figs. 5–8, and for the $[(30/0/-30)_5]_s$ laminate in Figs. 9–12. All the analytical models account for geometric nonlinearity.

The load-end shortening response for the $[0_{30}]_T$ specimen is shown in Fig. 5 compared with the generalized cylindrical bending analysis, and compared to the width-wise model in Fig. 6. The solid lines in both figures represent nonlinear material behavior, and the dashed lines represent linear material behavior. The open square symbols are experimental data. All analyses correlate well with the experimental results, with the full model (width-wise degrees of freedom active and material

Downloaded 03 May 2010 to 171.66.16.245. Redistribution subject to ASME license or copyright; see http://www.asme.org/terms/Terms_Use.cfm

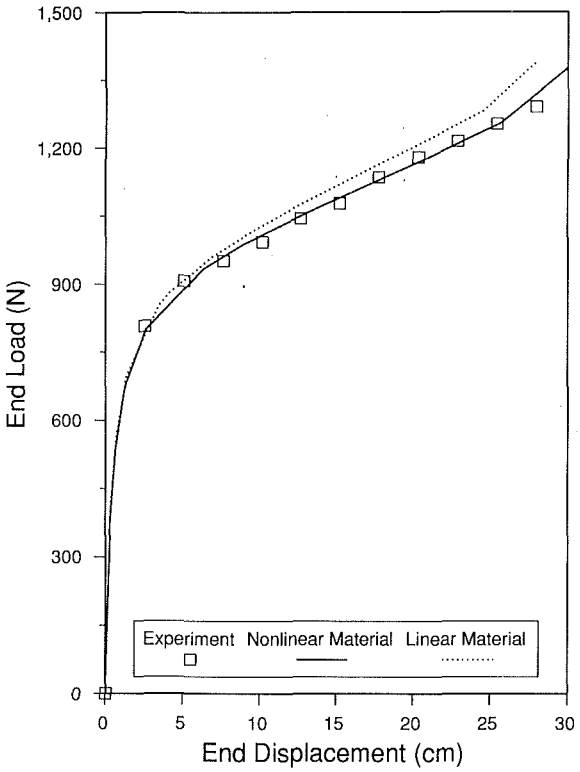


Fig. 6 Load-end shortening for the $[0_{30}]_T$ specimen compared to the analyses including width-wise distortions

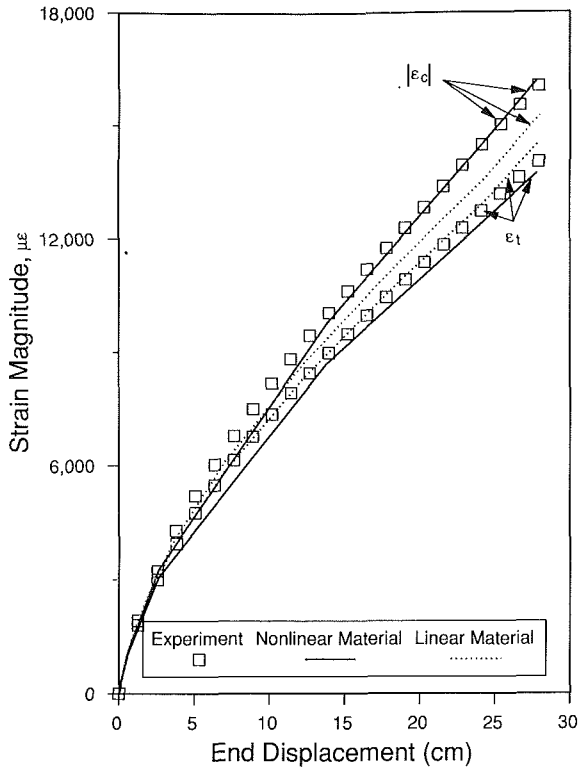


Fig. 8 Back-to-back axial surface strain magnitudes for the $[0_{30}]_T$ specimen compared to the analyses including width-wise distortions

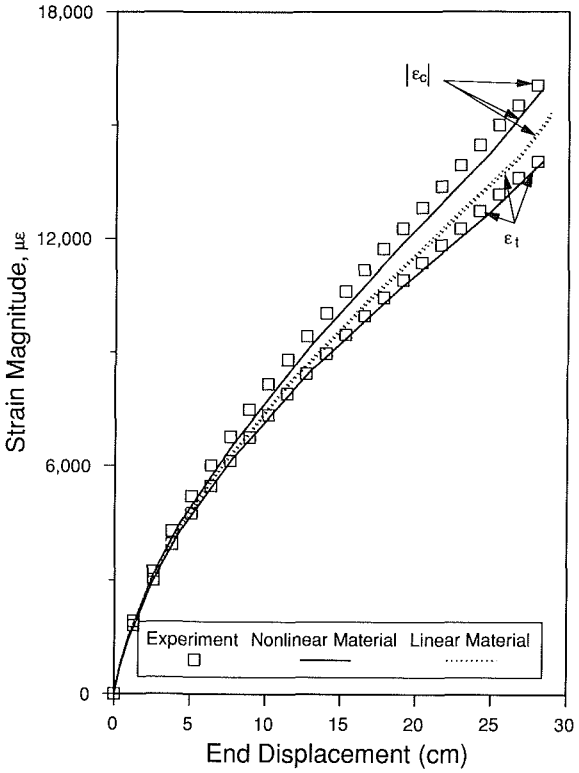


Fig. 7 Back-to-back axial surface strain magnitudes for the $[0_{30}]_T$ specimen compared to the generalized cylindrical bending analyses

nonlinearity) only marginally better. The load versus the magnitudes of the back-to-back axial surface strains measured at the center of the specimen at midspan is shown in Fig. 7 for the generalized cylindrical bending model, and in Fig. 8 for the width-wise model. The tensile side strain results are labeled ϵ_t and the compressive side strain magnitudes are labeled $|\epsilon_c|$ in the figures. The results for the generalized cylindrical bending analysis with linear material behavior (Fig. 7) predict that the magnitudes of the axial surface strains are essentially the same. Since the strains are of opposite sign, the laminate is subject to pure bending. The experimental results and the nonlinear material behavior analyses show that the axial strain magnitudes on the compressive side are larger than on the tensile side. The analyses including the width-wise effects are shown in Fig. 8, and a slight improvement in the correlation between experiment and the material nonlinear analyses is achieved with the width-wise model compared to the generalized cylindrical bending model.

The correlation between experiment and analysis for the $[(30/0/-30)_5]_s$ laminate is shown on load-end shortening plots in Figs. 9 and 10, and the load axial strain magnitude plots in Figs. 11 and 12. It is clear that the generalized cylindrical bending model is far too stiff, and the effect of material nonlinearity is small (Figs. 9 and 11). However, including width-wise effects in the analysis makes a dramatic improvement in the correlation with the experiment as shown in Figs. 10 and 12. Even the analysis without material nonlinearity compares favorably to the experiment when width-wise effects are included, and there is a small improvement in the correlation when material nonlinearity is included in the width-wise model. The full analysis correlates very well with the experiment.

The influence of the off-axis plies is further illustrated in Figs. 13 and 14, which show the relative shapes of the deformed midplane within a cross-section (anticlastic curvature) for a $[(\theta/0/-\theta)_3]_s$ family of laminates. The relative shape is a plot of Δw minus $\Delta W(x_1)$ in Eq. (8) as a function of y_1 for a fixed value of x_1. The relative shapes are shown for the cross-section at quarter span and an end displacement of 18.8 cm. It is clear from the figures that the cross-sectional distortion is greatest for $\theta = 30$ deg where the bend-twist coupling (D_{16}) is the largest, and is least when $\theta = 90$ deg where it is zero. The presence of the bend-twist coupling causes asymmetry in the distortion of the cross-section in its own plane. The cross-sectional distortions predicted from the analysis are limited by the assumed

Downloaded 03 May 2010 to 171.66.16.245. Redistribution subject to ASME license or copyright; see http://www.asme.org/terms/Terms_Use.cfm

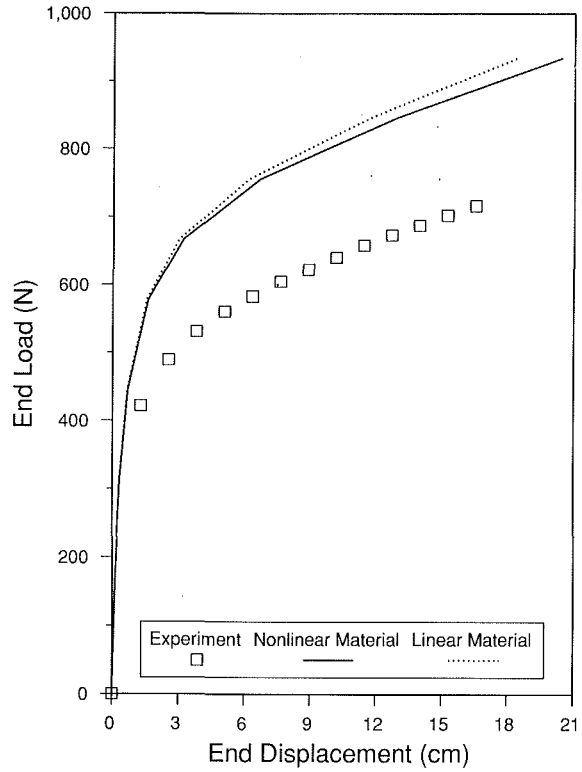


Fig. 9 Load-end shortening for the $[(30/0/-30)_5]_s$ specimen compared to the generalized cylindrical bending analyses

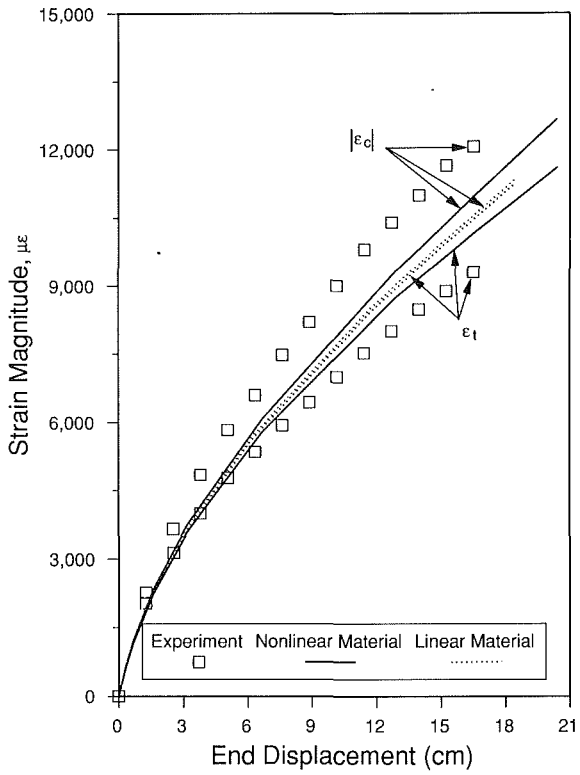


Fig. 11 Back-to-back axial surface strain magnitudes for the $[(30/0/-30)_5]_s$ specimen compared to the generalized cylindrical bending analyses

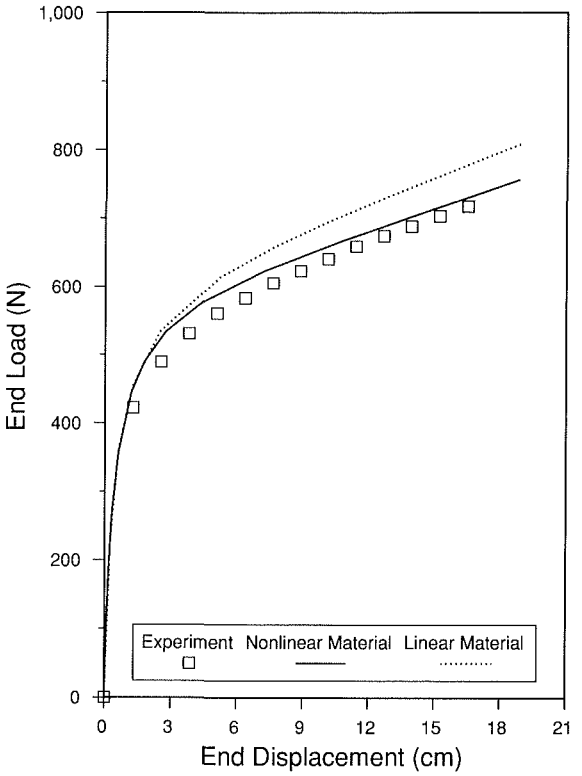


Fig. 10 Load-end shortening for the $[(30/0/-30)_5]_s$ specimen compared to the analyses including width-wise distortions

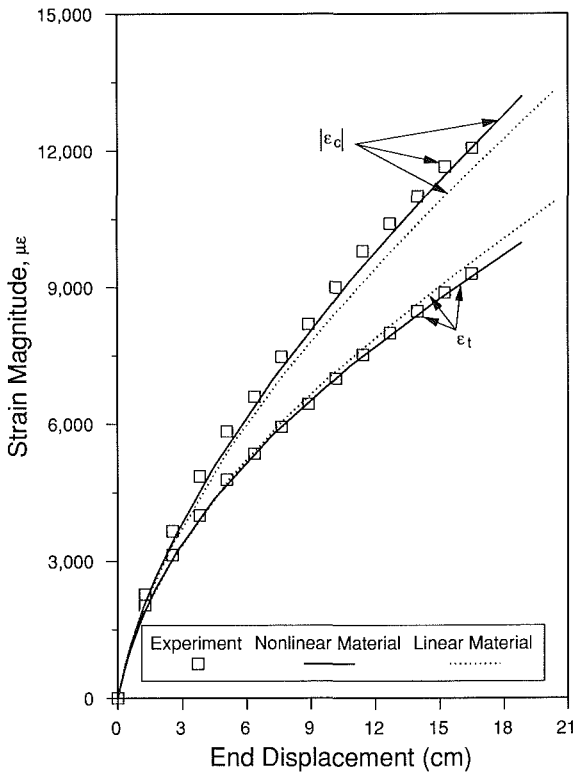


Fig. 12 Back-to-back axial surface strain magnitudes for the $[(30/0/-30)_5]_s$ specimen compared to the analyses including width-wise distortions

dependence of the displacements on the width coordinate y_1 (Eqs. (8)), and the fact that the geometrically nonlinear contributions of initial resultants N_y and N_{xy} were neglected (see Eq. (6)). For balanced and symmetric laminates, Hyer and Bhavani (1984) have shown that geometric nonlinearity tends to suppress the anticlastic curvature effects. However, Hyer and Bhavani do not account for the bend-twist coupling. The suppression of the anticlastic curvature was not observed in the present analysis because of the previously cited assump-

Downloaded 03 May 2010 to 171.66.16.245. Redistribution subject to ASME license or copyright; see http://www.asme.org/terms/Terms_Use.cfm

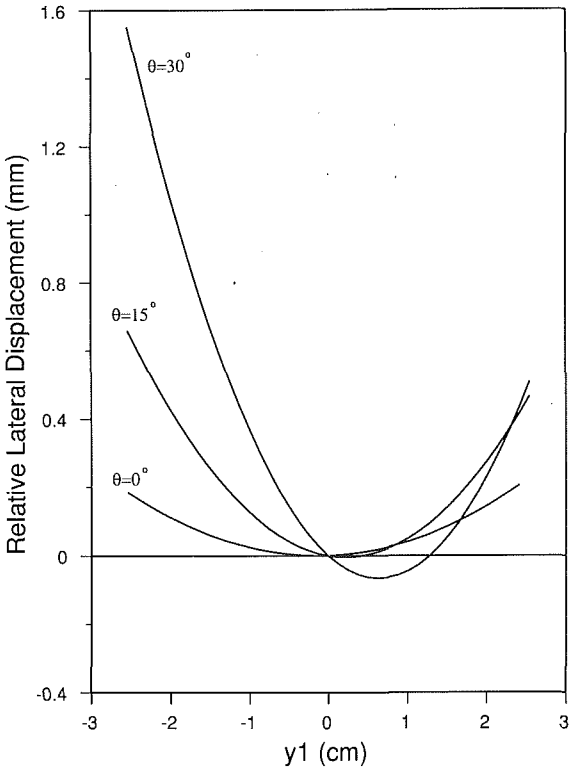


Fig. 13 Relative shapes of the deformed midplane within the cross-section for $[(\theta/0/-\theta)_3]_s$ laminates with $\theta = 0$ deg, 15 deg, and 30 deg

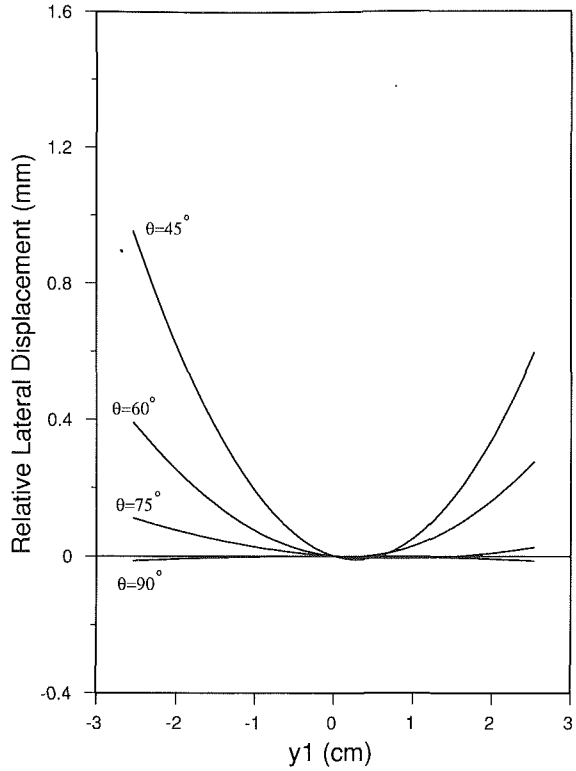


Fig. 14 Relative shapes of the deformed midplane within the cross-section for $[(\theta/0/-\theta)_3]_s$ laminates with $\theta = 45$ deg, 60 deg, 75 deg, and 90 deg

tions. Also, no detailed measurements of the displacements across the width of the specimens were made in the tests to establish whether or not anticlastic curvature is suppressed.

Concluding Remarks

This study demonstrates the importance of including the distortion of the cross-section in its own plane for the analysis of the wide column when off-axis plies are present in the laminate. The presence of off-axis plies couples shear and extension, and for balanced symmetric layups results in bend-twist coupling. Thus, to achieve good correlation with the analysis for the $[(30/0/-30)_5]_s$ laminated specimen it is important to include cross-sectional distortion in the analysis. Whereas, it is less important to include cross-sectional distortion in the analysis of the $[0_{30}]_T$ laminated specimen to achieve good correlation with the experimental results.

The difference in axial strain magnitudes between the tensile and compressive sides of the specimens, which are essentially subject to pure bending in the tests, is a result of material nonlinearity and width-wise deformations. For the $[0_{30}]$ specimen, material nonlinearity is the major reason for the difference in tensile and compressive side strain magnitudes, and including the width-wise distortions of the section only account for a small improvement in the analysis. See Figs. 7 and 8. For the $[(30/0/-30)_5]_s$ specimen, the biaxial state of strain resulting from the width-wise distortion of the section accounts for the majority of difference in the tensile and compressive side strain magnitudes, and material nonlinearity accounts for a smaller portion. (See Figs. 11 and 12.)

Acknowledgment

This research was supported by the NASA Langley Research Center under Grant NAG1-343, the NASA-Virginia Tech Composites Program. The technical monitor was Mr. Huey Carden of the Landing and Impact Dynamics Branch.

References

Derian, E. J., and Hyer, M. W., 1986, "Large Deformation Dynamic Bending of Composite Beams," NASA Contractor Report 4006, Aug.

Fasanella, E. L., Hayduk, R. J., Robinson, M. P., and Widmayer, E., 1984, "Analysis of a Transport Fuselage Section Drop Test," *Research in Structures and Dynamics–1984*, compiled by Robert J. Hayduk and Ahmed K. Noor, NASA Conference Publication 2335, pp. 347–368.

Fung, Y. C., 1965, *Foundations of Solid Mechanics*, Prentice-Hall, Englewood Cliffs, NJ, p. 337.

Gürdal, Z., and Starbuck, J. M., 1988, "Compression Characterization of Unidirectional Composite Materials," *Analytical and Testing Methodologies for Design with Advanced Materials*, G. C. Sih, J. T. Pindera, and S. V. Hoa, eds., Elsevier Science Publishers B. V., pp. 337–347.

Horrigmoe, G., and Bergen, P. G., 1976, "Incremental Variational Principles and Finite Element Models for Nonlinear Problems," *Computer Methods in Applied Mechanics and Engineering*, Vol. 7, pp. 210–217.

Hyer, M. W., and Bhavani, P. C., 1984, "Suppression of Anticlastic Curvature in Isotropic and Composite Plates," *International Journal of Solids and Structures*, Vol. 20, No. 6, pp. 553–570.

Iosipescu, N., 1967, "New Accurate Procedure of Single Shear Testing of Metals," *Journal of Materials*, Vol. 2, No. 3, p. 537.

Jones, Robert M., 1975, *Mechanics of Composite Materials*, Scripta Book Company, Washington, DC, pp. 46, 51, 154, 155.

Kleiber, Michal, 1989, *Incremental Finite Element Modelling in Non-Linear Solid Mechanics* (C. T. F. Ross, translation editor), Ellis Horwood Limited, Chichester, and PWN-Polish Scientific Publishers, Warszawa, pp. 50–52.

Sensmeier, Mark D., Griffin, Jr., O. Hayden, and Johnson, Eric R., 1988, "Static and Dynamic Large Deflection Flexural Response of Graphite-Epoxy Beams," NASA Contractor Report 4118, Mar.

Yang, T. Y., 1973, "Matrix Displacement Solution to Elastica Problems of Beams and Frames," *International Journal of Solids and Structures*, Vol. 9, pp. 829–842.

Downloaded 03 May 2010 to 171.66.16.245. Redistribution subject to ASME license or copyright; see http://www.asme.org/terms/Terms_Use.cfm

A Geometrically Nonlinear Theory of Elastic Plates

Dewey H. Hodges
Professor.

Ali R. Atilgan[1]
Post Doctoral Fellow.

School of Aerospace Engineering,
Georgia Institute of Technology,
Atlanta, GA 30332-0150

D. A. Danielson
Professor,
Mathematics Department,
Naval Postgraduate School,
Monterey, CA

A set of kinematical and intrinsic equilibrium equations are derived for plates undergoing large deflection and rotation but with small strain. The large rotation is handled by means of the general finite rotation *of a frame in which the material points that are originally along a normal line in the undeformed plate undergo only small displacements. The unit vector fixed in this frame, which coincides with the normal when the plate is undeformed, is not in general normal to the deformed plate average surface because of transverse shear. The arbitrarily large displacement and rotation of this frame, which vary over the surface of the plate, are termed global deformation; the small relative displacement is termed warping. It is shown that rotation of the frame about the normal is not zero and that it can be expressed in terms of other global deformation variables. Exact intrinsic virtual strain-displacement relations are derived; based on a reduced two-dimensional strain energy function from which the warping has been systematically eliminated, a set of intrinsic equilibrium equations follow. It is shown that* only five equilibrium equations can be derived *in this manner, because the component of virtual rotation about the normal is not independent. These equilibrium equations contain terms which cannot be obtained without the use of a finite rotation vector which contains three nonzero components. These extra terms correspond to the difference of in-plane shear stress resultants in other theories; this difference is a reactive quantity in the present theory.*

Introduction

This paper focuses on geometrically nonlinear analysis (i.e., small strain with possibly large deflections and rotations) of plates—solids with one small dimension and without initial curvature. We note that if all three dimensions of a flexible body are comparable, and if the body is undergoing small-strain deformation, then the displacement field in addition to rigid-body motion must be small. If, however, one or two dimensions of the body are small relative to the other(s), then even if the strains remain small the body can undergo large deflections.

Previous Work. Whenever a theory is formulated which is independent of any displacement or rotational variables, it is called an "intrinsic" theory. The earliest development of plates of an intrinsic nature is the work of Synge and Chien (1941). Therein, with the aid of series expansions in powers of a small thickness parameter, approximate theories are derived from three-dimensional elasticity. Sanders (1963) refers to this work as being "completely general" but also points out its being discussed and criticized in the literature. A quite recent intrinsic development is the work of Simo et al. (1989a, 1989b). They formulated a shell model in which finite deflections and rotations are taken into account. Their formulation regards the shell as a Cosserat surface, with an extensible director in the latter work, which is used in lieu of enforcing the usual plane stress assumption; thus, three-dimensional constitutive models can be employed, as done by Koiter and Simmonds (1972).

Some intrinsic theories are strictly two dimensional. That is, they provide no information about the three-dimensional behavior of the plate. Furthermore, they may rely on a two-dimensional constitutive law but not consider how to obtain such a law. For example, Reissner (1974) developed linear and nonlinear two-dimensional theories of shells in this manner. This was also the case when Ericksen and Truesdell (1958) formulated elegant theories for thin shells and curved rods without attempting to deduce them from the three-dimensional theory of elasticity. See Naghdi (1972) for an extensive review of this kind of approach, in which the constitutive relations are deliberately left out of consideration because they are unnecessary for the description of strain and the derivation of equilibrium equations. This approach appears to have originated with the Cosserats (1909) and is able to account for transverse shear and normal strains and rotations associated with couple stresses.

Writing plate/shell equations in a compact and concise form, even when finite deflections and rotations are considered, was

[1]Presently Assistant Professor, Mechanics Division, Department of Civil Engineering, Istanbul Technical University, Istanbul, Turkey.

Contributed by the Applied Mechanics Division of The American Society of Mechanical Engineers for publication in the ASME Journal of Applied Mechanics.

Discussion on this paper should be addressed to the Technical Editor, Professor Lewis T. Wheeler, Department of Mechanical Engineering, University of Houston, Houston, TX 77204-4792, and will be accepted until four months after final publication of the paper itself in the ASME Journal of Applied Mechanics.

Manuscript received by the ASME Applied Mechanics Division, Dec. 3, 1990; final revision, Sept. 16, 1991. Associate Technical Editor: L. M. Keer.

Copyright © 1993 by ASME

Downloaded 03 May 2010 to 171.66.16.245. Redistribution subject to ASME license or copyright; see http://www.asme.org/terms/Terms_Use.cfm

first suggested by Reissner (1950). Simmonds and Danielson (1970, 1972) also developed a general theory of shells which allowed large deflections in which the rotation was represented with a finite rotation vector. Other recent developments in shell theory are exemplified by Reissner (1982, 1986), Pietraszkiewicz (1979, 1989), Libai and Simmonds (1983), and Axelrad (1986). All of these more recent works develop the theory in terms of displacement of the reference surface and finite rotation of a frame. For the historical development as well as the state of the art in the development of two-dimensional plate/shell theories until 1972, the reader is referred to the review paper of Koiter and Simmonds (1972). For computational aspects of the problem, the reader should consult works by Noor et al. (1989a, 1989b).

Present Approach. The purpose of the present investigation is to find an appropriate set of equations for geometrically nonlinear two-dimensional plate analysis when the plate undergoes large displacements and rotations. Although the use of finite rotation vectors is rather common in plate/shell analyses, the present work attempts to refine the current understanding of the kinematics of rotation—including the "drilling rotation." A complete analysis of plates and shells includes the treatment of *surface kinematics*, *surface equilibrium*, and *modeling*. The term modeling refers to the determination of an appropriate two-dimensional constitutive law (from three-dimensional theory) and accurate *three-dimensional distributions* of displacement, strain, and stress *throughout the plate* in terms of surface (two-dimensional) deformation quantities. Modeling is an inherently approximate process.

Although the framework derived in this paper can be used to develop a modeling approach, that is not the main focus. The variational-asymptotical method of Berdichevsky (1979) is a viable possibility for modeling. This method allows one to calculate asymptotically correct two-dimensional strain energy and three-dimensional displacement, strain, and stress fields. Atılgan and Hodges (1992) applied this method to certain anisotropic plates. Only two assumptions were made regarding deformation: (1) strain is small compared to unity; (2) the wavelength of the deformation is long relative to the thickness of the plate. The first assumption allows them to treat only *geometrically* nonlinear behavior. The second leads to a hierarchy of approximations to general three-dimensional nonlinear theory, the first approximation being a Kirchhoff-like theory and the second analogous to Reissner-Mindlin theory. Although their analysis is applicable to laminated plates, their strain energy is asymptotically exact only if the plate is homogeneous with monoclinic material symmetry about its midplane. This way, there is no elastic coupling in the three-dimensional strain energy between transverse normal and transverse shear strains or between in-plane and transverse shear strains. Their resulting strain energy is the same as that obtained for nonlinear shell theory by Berdichevsky (1980), when appropriately specialized for homogeneous plates, and is the starting point for the plate deformation analysis herein.

We first develop a displacement field which is valid for any plate. Then we identify relevant two-dimensional intrinsic strain measures. Compatibility equations and global strain-displacement relations are then developed. A description of finite rotation for the plate is adopted which gives new insight into the relationship between drilling rotation and the other kinematical variables. After determining the virtual strain-displacement relations, the nonlinear intrinsic equlibrium equations are found. Finally, these equations are compared with published plate equations.

Three-Dimensional Displacement Field

A plate is a flexible body in which matter is distributed about a planar surface so that one dimension is significantly smaller

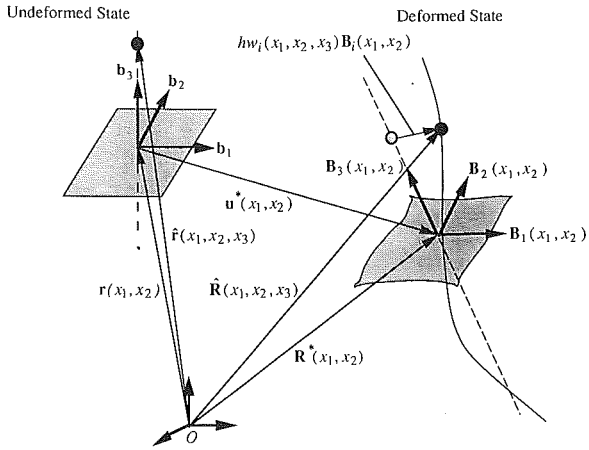


Fig. 1 Schematic of plate deformation

than the other two. Throughout the analysis, Greek indices assume values 1 or 2; Latin indices assume values 1, 2, and 3; and repeated indices are summed over their ranges. In this section, we develop a general expression for the three-dimensional displacement field. This will later lead naturally to a general requirement of equality of the two intrinsic inplane shear strain measures.

Let us introduce Cartesian coordinates x_i so that x_α denotes lengths along orthogonal straight lines in the midsurface of the undeformed plate, and $x_3 = h\zeta$ is the distance of an arbitrary point to the midsurface in the undeformed plate; See Fig. 1. Here h is the thickness of the plate, a constant, and $-1/2 \le \zeta \le 1/2$. Let $\mathbf{b}_i$ denote an orthogonal reference triad along the undeformed coordinate lines. The position vector from a fixed point O to an arbitrary point is

$$\hat{\mathbf{r}}(x_1,x_2,\zeta) = x_\alpha \mathbf{b}_\alpha + h\zeta \mathbf{b}_3 = \mathbf{r}(x_1,x_2) + h\zeta \mathbf{b}_3. \tag{1}$$

Covariant and contravariant undeformed base vectors both reduce to $\mathbf{b}_i$ since the coordinate system is Cartesian. The position vector to the midsurface is also the average position of points along the normal line, at a particular value of x_1 and x_2, so that

$$\mathbf{r} = \int_{-1/2}^{1/2} \hat{\mathbf{r}}\, d\zeta = \langle \hat{\mathbf{r}} \rangle. \tag{2}$$

The angle brackets $\langle\ \rangle$ are used throughout the paper to denote the integral through the thickness.

Now consider the deformed state configuration. The particle which had position vector $\hat{\mathbf{r}}(x_1, x_2, \zeta)$ in the undeformed plate now has position vector $\hat{\mathbf{R}}(x_1, x_2, \zeta)$. We consider the set N of material points along a typical line normal to the undeformed plate, parallel to $\mathbf{b}_3$. During deformation of the plate, N undergoes a displacement which can be described as a small deformation superimposed on a possibly large rigid-body displacement and rotation. The rigid-body displacement and rotation of N vary over the surface of the plate. For the purpose of describing the global deformation in generic terms, we introduce a frame B (kinematically a rigid body) whose position and orientation vary over the plate. At any arbitrary point in the deformed plate, the points belonging to N are seen in B to be displaced only very slightly form a straight line fixed in B. This small displacement is termed warping.

To facilitate a mathematically simple description of the deformation, we introduce another orthonormal triad $\mathbf{B}_i(x_1, x_2)$ fixed in the frame B. We call $\mathbf{B}_i$ the deformed plate triad, whose orientation relative to $\mathbf{b}_i$ can be specified by an arbitrarily large rotation. The orientation of $\mathbf{B}_i$ is coincident with $\mathbf{b}_i$ when the plate is undeformed and must be defined in terms of the plate deformation. Rotation from $\mathbf{b}_i$ to $\mathbf{B}_i$ is described in terms of a matrix $C(x_1, x_2)$ the elements of which, C_{ij}, are the direction cosines

Downloaded 03 May 2010 to 171.66.16.245. Redistribution subject to ASME license or copyright; see http://www.asme.org/terms/Terms_Use.cfm

$$\mathbf{B}_i = C_{ij}\mathbf{b}_j \quad C_{ij} = \mathbf{B}_i \cdot \mathbf{b}_j. \tag{3}$$

Now, we can write the position vector from O to any point in the deformed plate (Fig. 1) as

$$\hat{\mathbf{R}}(x_1,x_2,\zeta) = \mathbf{R}^*(x_1,x_2) + h\zeta\mathbf{B}_3(x_1,x_2) + hw_i(x_1,x_2,\zeta)\mathbf{B}_i(x_1,x_2) \tag{4}$$

where hw_i is the warping displacement field. The displacement field implied by Eq. (4) accounts for all possible deformations, but it is not yet well defined because the warping is measured in a translated and rotated frame B. The position ($\mathbf{R}^*$) and orientation ($\mathbf{B}_i$) of this frame must be defined in order to make the field unique. Thus, it is necessary to identify six dependency relations between $\mathbf{R}^*$ and the triad $\mathbf{B}_i$; in all but one case these relations will lead to equations which the warping must satisfy.

First, in order for Eq. (4) to be analogous to Eq. (1), $\mathbf{R}^*$ is defined as the average position of points parallel to the vector $\mathbf{B}_3$ corresponding to particular values of x_1 and x_2 in the plate.

$$\mathbf{R}^*(x_1,x_2) \triangleq \langle \hat{\mathbf{R}}(x_1,x_2,\zeta) \rangle = \mathbf{r}(x_1,x_2) + \mathbf{u}^*(x_1,x_2) \tag{5}$$

In order for this definition to hold, the warping must satisfy these three equations

$$\langle w_i(x_1,x_2,\zeta) \rangle = 0. \tag{6}$$

Equation (4) is still indeterminate until three additional dependency relations are placed either on $\mathbf{B}_i$ or on $\mathbf{R}^*$. Consider now the inner product of this vector and $\mathbf{B}_\alpha$ one obtains

$$\mathbf{B}_\alpha \cdot \langle \zeta\hat{\mathbf{R}} \rangle = h\langle \zeta w_\alpha \rangle. \tag{7}$$

To set the direction of $\mathbf{B}_3$ so that it is parallel to $\langle \zeta\hat{\mathbf{R}} \rangle$, we simply require the warping to satisfy the two equations

$$\langle \zeta w_\alpha \rangle = 0. \tag{8}$$

Now only one more dependency relation is needed to make Eq. (4) determinant. Recall that the amount of rigid-body translation of the normal line element is determined by the first three relations, Eqs. (6); the direction of $\mathbf{B}_3$ is determined by the fourth and fifth, Eqs. (8). However, the direction of $\mathbf{B}_\alpha$ (i.e., the amount which B must be rotated about $\mathbf{B}_3$) is not yet settled. It is clear that we are free to set this rotation so that

$$\mathbf{B}_1 \cdot \mathbf{R}^*_{,2} = \mathbf{B}_2 \cdot \mathbf{R}^*_{,1} \tag{9}$$

where $(\ )_{,\alpha}$ denotes differentiation with respect to x_α. The corresponding relations which the warping must satisfy, so that these relations hold, are identically satisfied because of Eqs. (6). Now the displacement field is well defined and unique, assuring continuity of deformation. This final relation will be written quite simply in terms of generalized strain measures, defined below.

Note that the triad $\mathbf{B}_i$ is not exactly the same as the triad ($\mathbf{A}_\alpha$, $\mathbf{N}$) used in Reissner (1974), Simmonds and Danielson (1972), and Libai and Simmonds (1983), unless the average surface of the deformed plate is the image of the midsurface of the undeformed plate. Also note that $\mathbf{R}^*$ is the position vector from O to the points of the *average surface of the deformed plate* and is not in general equal to $\hat{\mathbf{R}}(x_1, x_2, 0)$.

Global Deformation Analysis

After identifying the set of intrinsic strain measures which appear in the two-dimensional energy, compatibility equations and plate strain-displacement measures are finally developed in terms of the displacement of the average surface and rotation of B. We then develop a set of relationships that give variations of intrinsic strain measures in terms of virtual displacements, which are independent of the displacement or rotational variables chosen.

Two-Dimensional Strain Measures and Strain Energy. The strain field derived from the above displacement field can be put into very simple form if, similar to the one-dimensional development in Danielson and Hodges (1987), we introduce the generalized (two-dimensional) strain measures analogous to those of Reissner (1974), Simmonds and Danielson (1972), and Libai and Simmonds (1983) such that

$$\mathbf{R}^*_{,\alpha} = \mathbf{B}_\alpha + \epsilon_{\alpha\beta}\mathbf{B}_\beta + 2\gamma^*_{\alpha 3}\mathbf{B}_3 \tag{10}$$

and components of the curvature vectors such that

$$\mathbf{B}_{i,\alpha} = (-K_{\alpha\beta}\mathbf{B}_\beta \times \mathbf{B}_3 + K_{\alpha 3}\mathbf{B}_3) \times \mathbf{B}_i. \tag{11}$$

It is clear from Eq. (10) that the sixth dependency relation, Eq. (9), reduces to

$$\epsilon_{12} = \epsilon_{21}. \tag{12}$$

It is important to note that *no assumptions were made which in any way limit the validity of this condition. It is completely general and valid for all plates.*

Note that $\mathbf{R}^*_1 \times \mathbf{R}^*_2$ is normal to the average surface of the deformed plate and is not in general parallel to $\mathbf{B}_3$ unless the Kirchhoff hypothesis is adopted which constrains $2\gamma^*_{\alpha 3} = 0$. We will henceforth use the term normal to refer to $\mathbf{B}_3$ (although it may only be approximately normal to the deformed plate average surface).

The presence of the warping variable w_i in $\hat{\mathbf{R}}$, while accounting for all possible deformations, creates practical difficulties. Indeed, for one to use a strain field containing w_i is tantamount to using three-dimensional elasticity. To be a true plate theory, the warping must be eliminated. There are several options for elimination of the warping, the most common approaches being based on asymptotical methods. A variety of such methods are referred to in Reissner (1974) and Libai and Simmonds (1983).

For example, the variational asymptotical method of Berdichevsky (1980) was applied to plates by Atılgan and Hodges (1991). Therein, the warping is eliminated in a systematic way. The three-dimensional strain energy per unit volume is expressed in terms of the three-dimensional strain field. The strain field is in turn expressed in terms of ϵ_{11}, $2\epsilon_{12}$, ϵ_{22}, hK_{11}, $h(K_{12} + K_{21})$, hK_{22}, $2\gamma^*_{13}$, and $2\gamma^*_{23}$, each of which is taken to be $O(\epsilon)$. Here ϵ and h/l are the small parameters and l is the wavelength of the deformation pattern. An asymptotical analysis leads to a hierarchical approximation for the two-dimensional strain energy, where the first approximation is classical theory; the energy is $O(\mu\epsilon^2)$ and is independent of the transverse shear strains $2\gamma^*_{\alpha 3}$. Here, μ represents the order of the material constants. Each succeeding approximation is of a higher power of h/l than the last, but no higher powers of ϵ are retained, which is appropriate for geometrically nonlinear theory. They carried out the analysis through the second approximation, where their resulting strain energy is asymptotically correct to $O(\mu\epsilon^2 h^2/l^2)$ for homogeneous monoclinic plates. The transverse shear strain measures turn out to be $O(\epsilon h/l)$.

Rather than repeat that entire analysis here, we will simply state the results in symbolic form and build the present analysis on them. Atılgan and Hodges (1991) showed that the approximate two-dimensional strain energy derived from the above displacement field can be put into very simple form if the reference surface of the deformed plate is shifted. The position of this new surface is denoted by $\mathbf{R}(x_1, x_2)$ where

$$\mathbf{R} = \mathbf{R}^* - 12h\mathbf{B}_3 z(\epsilon_{11}, 2\epsilon_{12}, \epsilon_{22}, K_{11}, K_{12}+K_{21}, K_{22}) \tag{13}$$

and where z is a dimensionless function of $O(\epsilon)$, the form of which is not important in the present context. This also implies a shifted displacement vector such that $\mathbf{R} = \mathbf{r} + \mathbf{u}$. Then, use of a transformed transverse shear strain $2\gamma_{\alpha 3}$ defined as

$$\mathbf{R}_{,\alpha} \cdot \mathbf{R}_3 = 2\gamma_{\alpha 3} \tag{14}$$

allows the asymptotically correct two-dimensional strain energy to be expressed to $O(\mu\epsilon^2 h^2/l^2)$ for homogeneous monoclinic plates independent of the derivatives of the two-

Downloaded 03 May 2010 to 171.66.16.245. Redistribution subject to ASME license or copyright; see http://www.asme.org/terms/Terms_Use.cfm

dimensional strain measures. This new position vector will change ϵ_{11}, $2\epsilon_{12}$, and ϵ_{22} only by terms of order ϵ^2, but the curvature components are unaffected. In Atılgan and Hodges (1991) expressions for the warping and strain fields are given in terms of these measures.

The two-dimensional strain energy function is a quadratic form

$$U = U(\epsilon_{11}, 2\epsilon_{12}, \epsilon_{22}, 2\gamma_{13}, 2\gamma_{23}, K_{11}, K_{12}+K_{21}, K_{22}). \quad (15)$$

This way the plate elastic law can be put into a form so that the conjugate stress resultants denoted by N_{11}, N_{12}, N_{22}, Q_α, M_{11}, M_{12}, and M_{22}, are linear functions of ϵ_{11}, $2\epsilon_{12}$, ϵ_{22}, $2\gamma_{\alpha 3}$, K_{11}, K_{12} + K_{21}, and K_{22}. The quantities N_{11} and N_{22} are the in-plane stretching stress resultants, N_{12} is the in-plane shear stress resultant, Q_α are the transverse shear stress resultants; M_{11} and M_{22} are the bending moment resultants and M_{12} is the twisting moment resultant, all expressed in the $\mathbf{B}_i$ basis. This is physically equivalent to the energy functional suggested in the first two lines of Eq. (34) of Reissner (1986) (these two lines do not consider the effects of laminations which are not parallel to the plane of the undeflected plate).

We note that a materially nonlinear theory would require the retention of higher-order terms in ϵ. This would, in general, introduce terms which involve the difference $K_{12} - K_{21}$. However, these terms do not enter a *geometrically* nonlinear plate theory because they contribute terms to the strain energy that are of higher order than quadratic in ϵ (a more precise statement is given below). Apparently, the difference $K_{12} - K_{21}$ shows up in a *physically linear* theory only by consideration of couple-stress elasticity, such as in Reissner (1972).

Compatibility Equations. It is well known that the 11 quantities ϵ_{11}, $2\epsilon_{12}$, ϵ_{22}, $2\gamma_{\alpha 3}$, $K_{\alpha\beta}$, and $K_{\alpha 3}$ are not independent. First, it is clear that the kinematics of the deformed plate reference surface can be expressed in terms of *at most* six independent quantities: three measures of displacement, say $\mathbf{u}\cdot\mathbf{b}_i$, and three measures of the rotation of B (since the elements of C can be expressed in terms of three independent quantities). In Simmonds and Danielson (1972) and Reissner (1974), appropriate compatibility equations are derived by first enforcing the equalities

$$\mathbf{R}_{,12} = \mathbf{R}_{,21} \quad \mathbf{B}_{i,12} = \mathbf{B}_{i,21}. \quad (16)$$

These two vector equations lead to six independent compatibility equations equivalent to a form of those found in Reissner (1974) specialized for plates. These equations are rewritten here for convenience in the present notation.

First, from the $\mathbf{B}_3$ component of Eq. (16*a*) we obtain

$$(1+\epsilon_{22})K_{12} - (1+\epsilon_{11})K_{21} = 2\gamma_{23,1} - 2\gamma_{13,2} + \epsilon_{12}(K_{22} - K_{11}). \quad (17)$$

Next, from the $\mathbf{B}_\alpha$ components of Eq. (16*a*) we obtain two equations, for α = 1 and 2, respectively,

$$\begin{aligned}(1+\epsilon_{22})K_{13} - \epsilon_{12}K_{23} &= \epsilon_{12,1} - \epsilon_{11,2} - 2\gamma_{13}K_{21} + 2\gamma_{23}K_{11}\\ (1+\epsilon_{11})K_{23} + \epsilon_{12}K_{13} &= \epsilon_{22,1} - \epsilon_{12,2} - 2\gamma_{13}K_{22} + 2\gamma_{23}K_{12}. \quad (18)\end{aligned}$$

Finally, from the three components of Eq. (16*b*) we obtain

$$\begin{aligned}K_{11,2} - K_{21,1} + K_{13}K_{22} - K_{12}K_{23} &= 0\\ K_{22,1} - K_{12,2} + K_{23}K_{11} - K_{21}K_{13} &= 0\\ K_{23,1} - K_{13,2} + K_{11}K_{22} - K_{12}K_{21} &= 0. \quad (19)\end{aligned}$$

Equations (17)–(19) are similar to those of Reissner (1974) when specialized for plates. Equations (18) can also be derived by enforcing $\epsilon_{12,\alpha} = \epsilon_{21,\alpha}$.

There are now 11 quantities which are related by six compatibility equations. This means that these strain measures can be determined in terms of *only five* independent quantities—*not six*.

We have established above that the strain energy is a function only of the sum K_{12} + K_{21}. To take advantage of this, we introduce a twist measure

$$2\kappa_{12} = K_{12} + K_{21}. \quad (20)$$

Now the individual twisting curvatures can be expressed in terms of $2\kappa_{12}$ as

$$\begin{aligned}K_{12} &= \frac{2\gamma_{23,1} - 2\gamma_{13,2} + \epsilon_{12}(K_{22} - K_{11}) + (1+\epsilon_{11})2\kappa_{12}}{2+\epsilon_{11}+\epsilon_{22}}\\ K_{21} &= \frac{2\gamma_{13,2} - 2\gamma_{23,1} + \epsilon_{12}(K_{22} - K_{11}) + (1+\epsilon_{22})2\kappa_{12}}{2+\epsilon_{11}+\epsilon_{22}}. \quad (21)\end{aligned}$$

The difference of these can now be found such that

$$\frac{K_{12} - K_{21}}{2} = \frac{2\gamma_{23,1} - 2\gamma_{13,2} + \epsilon_{12}(K_{22} - K_{11}) + \kappa_{12}(\epsilon_{11} - \epsilon_{22})}{2+\epsilon_{11}+\epsilon_{22}}. \quad (22)$$

This difference is clearly $O(\epsilon h/l^2)$, and one can show that it contributes terms that are $O(\mu\epsilon^3 h^2/l^2)$ to the strain energy. Retention of such terms is inappropriate in a physically linear theory.

Clearly, Eqs. (18) can be solved for the in-plane curvatures K_{13} and K_{23}. Now, using these expressions for K_{13} and K_{23}, along with Eqs. (21), one can rewrite the *three* Eqs. (19) entirely in terms of the *eight* strain measures ϵ_{11}, $2\epsilon_{12}$, ϵ_{22}, $2\gamma_{13}$, $2\gamma_{23}$, K_{11}, $2\kappa_{12}$, and K_{22}. This confirms that *only five independent measures of displacement and rotation are necessary to define these strain measures as we will demonstrate conclusively below by deriving such measures.*

Global Displacement and Rotation Variables. There is no unique choice for the global deformation variables. For this reason, the importance (not to mention the beauty) of an intrinsic formulation is widely appreciated. On the other hand, for the purpose of understanding the displacement field more fully, for actual computational algorithms, and for easy derivation of virtual strain-displacement relations, Hodges (1990), which are needed below for the intrinsic analysis, it is expedient to introduce a suitable set of displacement measures.

The displacement measures we choose are derived by expressing $\mathbf{R}$ in terms of $\mathbf{r}$ plus a displacement vector so that

$$\begin{aligned}\mathbf{R}(x_1,x_2) &= \mathbf{r}(x_1,x_2) + \mathbf{u}(x_1,x_2)\\ &= x_\alpha\mathbf{b}_\alpha + u_i\mathbf{b}_i.\end{aligned} \quad (23)$$

This allows the determination of the strain measures $\epsilon_{\alpha\beta}$ and $2\gamma_{\alpha 3}$ in terms of C and the derivatives of u_i. Introducing column matrices $u = \lfloor u_1\ u_2\ u_3 \rfloor^T$, $e_1 = \lfloor 1\ 0\ 0 \rfloor^T$, $e_2 = \lfloor 0\ 1\ 0 \rfloor^T$, $\gamma_1 = \lfloor \epsilon_{11}\ \epsilon_{12}\ 2\gamma_{13} \rfloor^T$, and $\gamma_2 = \lfloor \epsilon_{21}\ \epsilon_{22}\ 2\gamma_{23} \rfloor^T$, we use Eqs. (10), (13), and (14) to determine

$$e_\alpha + \gamma_\alpha = C(e_\alpha + u_{,\alpha}) \quad (24)$$

where C is the matrix of direction cosines from Eq. (3).

As rotation measures Rodrigues parameters, Kane et al. (1983), allow the compact expression of C. Euler's theorem shows that any rotation can be represented as a rotation of magnitude Θ about a line parallel to a unit vector $\mathbf{e}$. Defining $\rho_i = 2\mathbf{e}\cdot\mathbf{b}_i \tan(\Theta/2)$ and arranging these in a column matrix $\rho = \lfloor \rho_1\ \rho_2\ \rho_3 \rfloor^T$, the matrix C is simply

$$C = \frac{\left(1 - \frac{\rho^T\rho}{4}\right)I - \tilde{\rho} + \frac{\rho\rho^T}{2}}{1 + \frac{\rho^T\rho}{4}} \quad (25)$$

where here and throughout the paper $\tilde{(\ )}$ is the antisymmetric matrix whose elements are $\tilde{(\ )}_{12} = -(\ )_3$, $\tilde{(\ )}_{13} = (\ )_2$, $\tilde{(\ )}_{23} = -(\ )_1$.

However, in the present context it is expedient to work in terms of the direction cosines of $\mathbf{B}_3$ and a rotation about $\mathbf{B}_3$. Clearly this is also a general way to represent finite rotation. Let us denote the Kronecker symbol by δ_{ij}, the direction cosines of $\mathbf{B}_3$ by

Downloaded 03 May 2010 to 171.66.16.245. Redistribution subject to ASME license or copyright; see http://www.asme.org/terms/Terms_Use.cfm

$$\theta_i = C_{3i} - \delta_{3i} \tag{26}$$

and the angle of rotation about $\mathbf{B}_3$ by ϕ_3. Hodges (1987) has shown that the Rodrigues parameters can be uniquely expressed in terms of θ_i and ϕ_3 as

$$\rho_1 = \frac{\rho_3\theta_1 - 2\theta_2}{2+\theta_3}$$

$$\rho_2 = \frac{\rho_3\theta_2 + 2\theta_1}{2+\theta_3}$$

$$\rho_3 = 2\tan\left(\frac{\phi_3}{2}\right). \tag{27}$$

The three rotational parameters θ_i are not independent. They satisfy the constraint

$$\theta_1^2 + \theta_2^2 + (1+\theta_3)^2 = 1. \tag{28}$$

Recall that Eq. (9) affects only the choice of $\mathbf{B}_\alpha$ and reduces to $\epsilon_{12} = \epsilon_{21}$. The above characterization of finite rotation will allow this choice to be easily expressed in terms of ϕ_3.

When Eq. (27) is substituted into Eq. (25), the resulting elements of C can be expressed as functions of θ_i and ϕ_3

$$C_{11} = \frac{(2+\theta_3-\theta_1^2)\cos\phi_3 - \theta_1\theta_2\sin\phi_3}{2+\theta_3}$$

$$C_{12} = \frac{(2+\theta_3-\theta_2^2)\sin\phi_3 - \theta_1\theta_2\cos\phi_3}{2+\theta_3}$$

$$C_{13} = -\theta_1\cos\phi_3 - \theta_2\sin\phi_3$$

$$C_{21} = \frac{-(2+\theta_3-\theta_1^2)\sin\phi_3 - \theta_1\theta_2\cos\phi_3}{2+\theta_3}$$

$$C_{22} = \frac{(2+\theta_3-\theta_2^2)\cos\phi_3 + \theta_1\theta_2\sin\phi_3}{2+\theta_3}$$

$$C_{23} = \theta_1\sin\phi_3 - \theta_2\cos\phi_3$$

$$C_{31} = \theta_1$$

$$C_{32} = \theta_2$$

$$C_{33} = 1+\theta_3. \tag{29}$$

This representation reduces to those of Reissner (1982, 1986) when considering small, finite rotations. There is an apparent singularity in the present scheme when $\theta_3 = -2$ (i.e., when the plate deforms in such a way that $\mathbf{B}_3$ is pointed in the opposite direction of $\mathbf{b}_3$). This should pose no practical problem, however, since θ_1 and $\theta_2 = 0$ for that condition, and none of the kinematical relations become infinite in the limit as $\theta_3 \to -2$.

When these expressions for the direction cosines are substituted into Eq. (24), explicit expressions for the strain measures can be found as

$$1+\epsilon_{11} = \frac{[(2+\theta_3-\theta_1^2)(1+u_{1,1}) - \theta_1\theta_2u_{2,1} - \theta_1u_{3,1}(2+\theta_3)]\cos\phi_3}{1+\theta_3}$$
$$+\frac{[-\theta_1\theta_2(1+u_{1,1}) + (2+\theta_3-\theta_2^2)u_{2,1} - \theta_2u_{3,1}(2+\theta_3)]\sin\phi_3}{2+\theta_3}$$

$$1+\epsilon_{22} = \frac{[-\theta_1\theta_2u_{1,2} + (2+\theta_3-\theta_1^2)(1+u_{2,2}) - \theta_2u_{3,2}(2+\theta_3)]\cos\phi_3}{2+\theta_3}$$
$$-\frac{[(2+\theta_3-\theta_1^2)u_{1,2} - \theta_1\theta_2(1+u_{2,2}) - \theta_1u_{3,2}(2+\theta_3)]\sin\phi_3}{2+\theta_3}$$

$$\epsilon_{12} = \frac{[-\theta_1\theta_2(1+u_{1,1}) + (2+\theta_3-\theta_2^2)u_{2,1} - \theta_2u_{3,1}(2+\theta_3)]\cos\phi_3}{2+\theta_3}$$
$$-\frac{[(2+\theta_3-\theta_1^2)(1+u_{1,1}) - \theta_1\theta_2u_{2,1} - \theta_1u_{3,1}(2+\theta_3)]\sin\phi_3}{2+\theta_3}$$

$$\epsilon_{21} = \frac{[-\theta_1\theta_2(1+u_{2,2}) + (2+\theta_3-\theta_2^2)u_{1,2} - \theta_1u_{3,2}(2+\theta_3)]\cos\phi_3}{2+\theta_3}$$
$$+\frac{[(2+\theta_3-\theta_2^2)(1+u_{2,2}) - \theta_1\theta_2u_{1,2} - \theta_2u_{3,2}(2+\theta_3)]\sin\phi_3}{2+\theta_3} \tag{30}$$

$$2\gamma_{13} = \theta_1(1+u_{1,1}) + \theta_2u_{2,1} + (1+\theta_3)u_{3,1}$$

$$2\gamma_{23} = \theta_1u_{1,2} + \theta_2(1+u_{2,2}) + (1+\theta_3)u_{3,2}.$$

These expressions explicitly depend on $\sin\phi_3$ and $\cos\phi_3$. It is evident that one can choose ϕ_3 so that $\epsilon_{12} = \epsilon_{21}$, yielding

$$\tan\phi_3 = \frac{(2+\theta_3)(u_{2,1} - u_{1,2} + \theta_1u_{3,2} - \theta_2u_{3,1}) - \theta_2^2u_{2,1} + \theta_1^2u_{1,2} + \theta_1\theta_2(u_{2,2} - u_{1,1})}{(2+\theta_3)(2+\theta_3+u_{1,1}+u_{2,2} - \theta_1u_{3,1} - \theta_2u_{3,2}) - \theta_1^2u_{1,1} - \theta_2^2u_{2,2} - \theta_1\theta_2(u_{1,2}+u_{2,1})}. \tag{31}$$

It is now clear that once the functions u_1, u_2, u_3, θ_1, and θ_2 are known, the entire displacement field is determined. Because of this, one should expect that a variational formulation would yield only five equilibrium equations—not six. Indeed, five intrinsic equilibrium equations are derived below from Eq. (15).

For small displacement, we note that the rotation about the normal reduces to

$$\phi_3 = \frac{1}{2}(u_{2,1} - u_{1,2}) \text{ (small deflection, small strain)} \tag{32}$$

as expected.

Although one can now find exact expressions for ϵ_{11}, $2\epsilon_{12}$, ϵ_{22}, $2\gamma_{13}$, and $2\gamma_{23}$ which are independent of ϕ_3, such expressions are rather lengthy and are not given here. Alternatiively, one could leave ϕ_3 in the equations and regard, say, Eq. (31) as a constraint. This would allow the construction of a plate finite element which would be compatible with beam elements which have three rotational degrees-of-freedom at the nodes.

Expressions for the curvatures can also be found in terms of C from Eqs. (11).

$$\tilde{K}_\alpha = -C_{,\alpha}C^T \tag{33}$$

where the column matrices $K_\alpha = \lfloor -K_{\alpha 2}\ K_{\alpha 1}\ K_{\alpha 3} \rfloor^T$. Using the form of C from Eqs. (29), the following expressions for the curvatures result:

$$K_{\alpha 1} = \theta_{1,\alpha}\cos\phi_3 + \theta_{2,\alpha}\sin\phi_3 - \frac{\theta_{3,\alpha}(\theta_1\cos\phi_3 + \theta_2\sin\phi_3)}{2+\theta_3}$$

$$K_{\alpha 2} = -\theta_{1,\alpha}\sin\phi_3 + \theta_{2,\alpha}\cos\phi_3 - \frac{\theta_{3,\alpha}(-\theta_1\sin\phi_3 + \theta_2\cos\phi_3)}{2+\theta_3}$$

$$K_{\alpha 3} = \phi_{3,\alpha} + \frac{\theta_{1,\alpha}\theta_2 - \theta_1\theta_{2,\alpha}}{2+\theta_3} \tag{34}$$

As before, ϕ_3 can be eliminated from these expressions so that all six curvatures can be expressed in terms of five independent quantities. Note that $K_{\alpha 3}$ does not appear in the strain field. It will, however, appear in the equilibrium equations because of its appearance in the virtual strain-displacement relations derived below.

Virtual Strain-Displacement Relations. In order to derive intrinsic equilibrium equations from the strain energy, it is necessary to express the variations of generalized strain meas-

Downloaded 03 May 2010 to 171.66.16.245. Redistribution subject to ASME license or copyright; see http://www.asme.org/terms/Terms_Use.cfm

ures in terms of virtual displacements and virtual rotations.

The variation of the strain energy can be written from Eq. (15) as

$$\delta U=\frac{\partial U}{\partial \epsilon_{11}}\,\delta\epsilon_{11}+\frac{\partial U}{\partial \epsilon_{12}}\,\delta\epsilon_{12}+\frac{\partial U}{\partial \epsilon_{22}}\,\delta\epsilon_{22}+\frac{\partial U}{\partial \gamma_{13}}\,\delta\gamma_{13}+\frac{\partial U}{\partial \gamma_{23}}\,\delta\gamma_{23}+\frac{\partial U}{\partial K_{11}}\,\delta K_{11}+\frac{\partial U}{\partial \kappa_{12}}\,\delta\kappa_{12}+\frac{\partial U}{\partial K_{22}}\,\delta K_{22}. \quad (35)$$

It is obvious now that one must express $\delta\epsilon_{11}, \ldots, \delta K_{22}$, in terms of virtual displacements and rotations in order to obtain the final Euler-Lagrange equations of the energy functional in their intrinsic form. Following Hodges (1990), we introduce measures of virtual displacement and rotation which are "compatible," Kane (1968), with the intrinsic strain measures. For the virtual displacement, we note the form of Eq. (24) and choose

$$\overline{\delta q}=C\delta u. \quad (36)$$

Similarly, for the virtual rotation, we note the form of Eq. (33) and write

$$\widetilde{\overline{\delta\psi}}=-\delta C C^T. \quad (37)$$

The bars indicate that these quantities are not variations of functions. Using these relations it is clear that

$$\delta u=C^T\overline{\delta q} \quad (38)$$

and

$$\delta C=-\widetilde{\overline{\delta\psi}}C. \quad (39)$$

Let us begin with the generalized strain-displacement relationship, Eq. (24). A particular in-plane strain element can be written as

$$\epsilon_{\alpha\beta}=e_\beta^T[C(e_\alpha+u_{,\alpha})-e_\alpha]. \quad (40)$$

Taking a straightforward variation, one obtains

$$\delta\epsilon_{\alpha\beta}=e_\beta^T[\delta C(e_\alpha+u_{,\alpha})+C\delta u_{,\alpha}]. \quad (41)$$

The right-hand side contains $u_{,\alpha}$ and $\delta u_{,\alpha}$ which must be eliminated in order to obtain variations of the strain which are independent of displacement. These are needed to derive intrinsic equilibrium equations.

Premultiplying both sides of Eq. (24) by C^T, making use of Eq. (39), and finally using a property of the tilde operator that, for arbitrary column matrices Y land Z, $\tilde{Y}Z = -\tilde{Z}Y$, one can make the first term in brackets on the right-hand side independent of $u_{,\alpha}$. After all this, one can obtain

$$\begin{aligned}\delta C(e_\alpha+u_{,\alpha})&=\delta CC^T(e_\alpha+\gamma_\alpha)\\&=-\widetilde{\overline{\delta\psi}}(e_\alpha+\gamma_\alpha)\\&=(\widetilde{e_\alpha}+\widetilde{\gamma_\alpha})\overline{\delta\psi}.\end{aligned} \quad (42)$$

An expression for the second term in brackets on the right-hand side of Eq. (41) can now be obtained by differentiating Eq. (38) with respect to x_α and premultiplying by C. This yields

$$C\delta u_{,\alpha}=C(C^T\overline{\delta q})_{,\alpha}=\overline{\delta q}_{,\alpha}-C_{,\alpha}C^T\overline{\delta q}. \quad (43)$$

Now, recalling Eq. (33), one can simplify the second term on the right-hand side so that

$$C\delta u_{,\alpha}=\overline{\delta q}_{,\alpha}+\widetilde{K_\alpha}\overline{\delta q} \quad (44)$$

Substituting Eqs. (42) and (44) into Eq. (41), one can obtain an intrinsic expression for the variation of the in-plane strain components as

$$\delta\epsilon_{\alpha\beta}=e_\beta^T[\overline{\delta q}_{,\alpha}+\widetilde{K_\alpha}\overline{\delta q}+(\widetilde{e_\alpha}+\widetilde{\gamma_\alpha})\overline{\delta\psi}] \quad (45)$$

where $e_\beta^T\,\widetilde{e_\alpha}$ vanishes when $\alpha=\beta$. This equation can be written as four scalar equations

$$\begin{aligned}\delta\epsilon_{11}&=\overline{\delta q}_{1,1}-K_{13}\overline{\delta q}_2+K_{11}\overline{\delta q}_3-2\gamma_{13}\overline{\delta\psi}_1+\epsilon_{12}\overline{\delta\psi}_3\\\delta\epsilon_{12}&=\overline{\delta q}_{2,1}+K_{13}\overline{\delta q}_1+K_{12}\overline{\delta q}_3-2\gamma_{13}\overline{\delta\psi}_2-(1+\epsilon_{11})\overline{\delta\psi}_3\\\delta\epsilon_{21}&=\overline{\delta q}_{1,2}-K_{23}\overline{\delta q}_2+K_{21}\overline{\delta q}_3-2\gamma_{23}\overline{\delta\psi}_1+(1+\epsilon_{22})\overline{\delta\psi}_3\\\delta\epsilon_{22}&=\overline{\delta q}_{2,2}+K_{23}\overline{\delta q}_1+K_{22}\overline{\delta q}_3-2\gamma_{23}\overline{\delta\psi}_2-\epsilon_{12}\overline{\delta\psi}_3.\end{aligned} \quad (46)$$

Now, by virtue of Eq. (12),

$$\delta\epsilon_{12}=\delta\epsilon_{21}. \quad (47)$$

From this, one can solve for the virtual rotation component about $\mathbf{B}_3$ as

$$\overline{\delta\psi}_3=\frac{\overline{\delta q}_{2,1}-\overline{\delta q}_{1,2}+K_{13}\overline{\delta q}_1+K_{23}\overline{\delta q}_2+(K_{12}-K_{21})\overline{\delta q}_3-2\gamma_{13}\overline{\delta\psi}_2+2\gamma_{23}\overline{\delta\psi}_1}{2+\epsilon_{11}+\epsilon_{22}}. \quad (48)$$

It is now possible to write the variations of all strain measures in terms of three virtual displacement and two virtual rotation components as

$$\begin{aligned}\delta\epsilon_{11}&=\overline{\delta q}_{1,1}-K_{13}\overline{\delta q}_2+K_{11}\overline{\delta q}_3-2\gamma_{13}\overline{\delta\psi}_1+\epsilon_{12}\overline{\delta\psi}_3\\\delta\epsilon_{22}&=\overline{\delta q}_{2,2}+K_{23}\overline{\delta q}_1+K_{22}\overline{\delta q}_3-2\gamma_{23}\overline{\delta\psi}_2-\epsilon_{12}\overline{\delta\psi}_3\\2\delta\epsilon_{12}&=\overline{\delta q}_{2,1}+\overline{\delta q}_{1,2}+K_{13}\overline{\delta q}_1-K_{23}\overline{\delta q}_2+(K_{12}+K_{21})\overline{\delta\psi}_3\\&\quad-2\gamma_{13}\overline{\delta\psi}_2-2\gamma_{23}\overline{\delta\psi}_1+(\epsilon_{22}-\epsilon_{11})\overline{\delta\psi}_3\end{aligned} \quad (49)$$

with $\overline{\delta\psi}_3$ taken from Eq. (48).

Let us now consider the transverse shear strains

$$2\gamma_{\alpha3}=e_3^T[C(e_\alpha+u_{,\alpha})-e_\alpha]. \quad (50)$$

Taking a straightforward variation and making use of Eq. (39) with the above tilde identity, one can find the virtual strain-displacement equation for transverse shear strains as follows:

$$2\delta\gamma_{\alpha3}=e_3^T[\overline{\delta q}_{,\alpha}+\widetilde{K_\alpha}\overline{\delta q}+(\widetilde{e_\alpha}+\widetilde{\gamma_\alpha})\overline{\delta\psi}]. \quad (51)$$

Explicit expressions for the variations of the shear strain components are now easily written as

$$2\delta\gamma_{\alpha3}=\overline{\delta q}_{3,\alpha}+\overline{\delta\psi}_\alpha+\epsilon_{\alpha\beta}\overline{\delta\psi}_\beta-K_{\alpha\beta}\overline{\delta q}_\beta. \quad (52)$$

Finally, the variations of the curvatures are found. First, taking the straightforward variation of Eq. (33), one obtains

$$\delta\widetilde{K_\alpha}=-\delta C_{,\alpha}C^T-C_{,\alpha}\delta C^T. \quad (53)$$

In order to eliminate $\delta C_{,\alpha}$, we differentiate Eq. (37) with respect to x_α:

$$\widetilde{\overline{\delta\psi}}_{,\alpha}=-\delta C_{,\alpha}C^T-\delta CC^T_{,\alpha}. \quad (54)$$

In order to eliminate δC, we can use Eq. (39). Then Eq. (53) becomes

$$\delta\widetilde{K_\alpha}=\widetilde{\overline{\delta\psi}}_{,\alpha}+\widetilde{K_\alpha}\widetilde{\overline{\delta\psi}}-\widetilde{\overline{\delta\psi}}\widetilde{K_\alpha}. \quad (55)$$

Using another tilde identity ($\widetilde{YZ}=\tilde{Y}\tilde{Z}-\tilde{Z}\tilde{Y}$) one can find the following virtual strain-displacement relation:

$$\delta K_\alpha=\overline{\delta\psi}_{,\alpha}+\widetilde{K_\alpha}\overline{\delta\psi}. \quad (56)$$

In explicit form

$$\begin{aligned}\delta K_{11}&=\overline{\delta\psi}_{1,1}-K_{13}\overline{\delta\psi}_2+K_{12}\overline{\delta\psi}_3\\\delta K_{22}&=\overline{\delta\psi}_{2,2}+K_{23}\overline{\delta\psi}_1-K_{21}\overline{\delta\psi}_3\\2\delta\kappa_{12}&=\overline{\delta\psi}_{1,2}+\overline{\delta\psi}_{2,1}+K_{13}\overline{\delta\psi}_1-K_{23}\overline{\delta\psi}_2+(K_{22}-K_{11})\overline{\delta\psi}_3,\end{aligned} \quad (57)$$

where $\overline{\delta\psi}_3$ should again be eliminated by using Eq. (48).

Intrinsic Equilibrium Equations

In this section, we will make use of the virtual strain-displacement relations in the variation of the internal strain energy

Downloaded 03 May 2010 to 171.66.16.245. Redistribution subject to ASME license or copyright; see http://www.asme.org/terms/Terms_Use.cfm

in order to derive the intrinsic equilibrium equations. Here we define the generalized forces as

$$\frac{\partial U}{\partial \epsilon_{11}} = N_{11} \qquad \frac{\partial U}{\partial \epsilon_{22}} = N_{22} \qquad \frac{1}{2}\frac{\partial U}{\partial \epsilon_{12}} = N_{12}$$

$$\frac{\partial U}{\partial K_{11}} = M_{11} \qquad \frac{\partial U}{\partial K_{22}} = M_{22} \qquad \frac{1}{2}\frac{\partial U}{\partial \kappa_{12}} = M_{12}$$

$$\frac{1}{2}\frac{\partial U}{\partial \gamma_{13}} = Q_1 \qquad \frac{1}{2}\frac{\partial U}{\partial \gamma_{23}} = Q_2. \tag{58}$$

If the influence of warping on the virtual work of body forces and surface tractions is ignored, body forces and applied tractions over the upper and lower surfaces of the plate can be shown to have virtual work equivalent to that of applied forces and moments distributed over the plate reference surface. The virtual work per unit area can then be written as

$$\overline{\delta W} = \overline{\delta q_i} f_i + \overline{\delta \psi_i} m_i \tag{59}$$

where $\overline{\delta \psi_3}$ is given by Eq. (48). It is now possible to obtain intrinsic equilibrium equations and consistent edge conditions, as in Basar (1987), by use of the principle of virtual work and the virtual strain-displacement relations derived in the previous section. The equilibrium equations are

$$\begin{aligned}
&N_{11,1} + (N_{12} + \mathfrak{N})_{,2} - K_{13}(N_{12} - \mathfrak{N}) \\
&\qquad - K_{23}N_{22} + Q_1 K_{11} + Q_2 K_{21} + f_1 = 0 \\
&N_{22,2} + (N_{12} - \mathfrak{N})_{,1} + K_{23}(N_{12} + \mathfrak{N}) \\
&\qquad + K_{13}N_{11} + Q_1 K_{12} + Q_2 K_{22} + f_2 = 0 \\
&Q_{1,1} + Q_{2,2} - K_{11}N_{11} - K_{22}N_{22} - 2\kappa_{12}N_{12} + (K_{12} - K_{21})\mathfrak{N} + f_3 = 0 \\
&M_{11,1} + M_{12,2} - Q_1(1 + \epsilon_{11}) - Q_2\epsilon_{12} \\
&\qquad + 2\gamma_{13}N_{11} + 2\gamma_{23}(N_{12} + \mathfrak{N}) - M_{12}K_{13} - M_{22}K_{23} + m_1 = 0 \\
&M_{12,1} + M_{22,2} - Q_1\epsilon_{12} - Q_2(1 + \epsilon_{22}) \\
&\qquad + 2\gamma_{13}(N_{12} - \mathfrak{N}) + 2\gamma_{23}N_{22} + M_{11}K_{13} + M_{12}K_{23} + m_2 = 0
\end{aligned} \tag{60}$$

where

$$\begin{aligned}
(2 + \epsilon_{11} + \epsilon_{22})\mathfrak{N} &= (N_{22} - N_{11})\epsilon_{12} + N_{12}(\epsilon_{11} - \epsilon_{22}) \\
&\quad + M_{22}K_{21} - M_{11}K_{12} + M_{12}(K_{11} - K_{22}) + m_3.
\end{aligned} \tag{61}$$

When displacements and rotations are free along an edge, the boundary conditions for a rectangular domain allow for specification of N_{11}, $N_{12} - \mathfrak{N}$, Q_1, M_{11}, and M_{12} on an edge where x_1 = constant; similarly $N_{12} + \mathfrak{N}$, N_{22}, Q_2, M_{12}, and M_{22} can be specified on an edge where x_2 = constant. We note that an applied "drilling moment" m_3, stemming only from tractions on the upper and lower surface of the plate, is hard to physically realize. It is retained in the equations for completeness, however.

The terms containing $\mathfrak{N}$ stem from consistent inclusion of the finite rotation of B although the *nonzero* rotation about $\mathbf{B}_3$ is expressed in terms of other kinematical quantities. Similar terms are found in the shell equations derived by Berdichevsky (1979, 1989) where only five equilibrium equations are derived.

In a mixed formulation, $\mathfrak{N}$ can be shown to be the Lagrange multiplier that enforces Eq. (48). To further understand the nature of $\mathfrak{N}$, one can undertake the following exercize: Specialize the six equilibrium equations of Reissner (1974) for plates, also setting $P_i = 0$ and $\epsilon_{12} = \epsilon_{21}$. The sixth equation then becomes zeroth-order and can be solved for $(N_{21} - N_{12})/2$. This shows that Reissner's $(N_{21} - N_{12})/2$ is the same as our $\mathfrak{N}$, and Reissner's $(N_{21} + N_{12})/2$ is the same as our N_{12}. Finally, substitution of this sixth equation into the other five yields our five equilibrium equations, Eq. (60).

A few investigators have noted an apparent conflict between the symmetry of the stress resultants and the satisfaction of moment equilibrium about the normal; for example, see Kraus (1967). In reality there is no conflict, but one must be careful. We show herein that the triad $\mathbf{B}_i$ can always be chosen so that $\epsilon_{12} = \epsilon_{21}$. If this relation is enforced strongly, there is only one in-plane shear stress resultant, N_{12}, that can be derived from the energy. In that case the physical quantity associated with the antisymmetric part of Reissner's in-plane stress resultants, while it is not available from the constitutive law, is nevertheless available as a reactive quantity from the moment equilibrium equation about the normal. However, it must be stressed that the moment equilibrium equation about the normal is not available from a conventional energy approach, in which virtual displacements and rotations must be independent.

A somewhat analogous situation arises in reducing Timoshenko beam theory to Euler-Bernoulli beam theory. Shear deformation is suppressed, and thus the shear force resultant is no longer available from the constitutive law. It must be determined from the equilibrium equations as the derivative of the bending moment. If the constraint of vanishing shear deformation is further used to eliminate the virtual rotation, the moment equilibrium equation cannot be derived from the energy.

In a somewhat similar vein, not being able to obtain the antisymmetric part of the moment stress resultants from derivatives of the two-dimensional strain energy is a result of the approximate dimensional reduction process in which it was determined that, based on asymptotical arguments and *geometrically* nonlinear three-dimensional elasticity, the antisymmetric term $K_{12} - K_{21}$ does not appear in the two-dimensional strain energy. When the foundation of the theory is broadened so as to include couple-stress considerations, then $K_{12} - K_{21}$ could appear; see Reissner (1972, 1982).

For practical computational schemes, these equilibrium equations need to be supplemented with additional sets of equations. Any approach will require a set of constitutive relations between the stress resultants N_{11}, N_{12}, N_{22}, Q_1, Q_2, M_{11}, M_{12}, and M_{22}, and the strain measures ϵ_{11}, $2\epsilon_{12}$, ϵ_{22}, $2\gamma_{13}$, $2\gamma_{23}$, K_{11}, $2\kappa_{12}$, and K_{22}; an example of such a set is given in Atılgan and Hodges (1991). Finally a set of kinematical equations is needed. The kinematical part of the analysis can be done in two fundamentally different wasy: a purely intrinsic form and a mixed form.

In the intrinsic form we have five equilibrium equations, Eqs. (60); six compatibility equations, Eqs. (17)–(19); and the eight constitutive equations—a total of 19 equations. The 19 unknowns are the eight stress resultants, N_{11}, N_{12}, N_{22}, Q_1, Q_2, M_{11}, M_{12}, and M_{22}; and 11 strain measures ϵ_{11}, $2\epsilon_{12}$, ϵ_{22}, $2\gamma_{13}$, $2\gamma_{23}$, K_{11}, $2\kappa_{12}$, and K_{22}, along with K_{13}, K_{23}, and $K_{12} - K_{21}$. The last three strain measures appear in the equilibrium equations but not in the constitutive law.

In the mixed form we use the same five equilibrium equations and eight constitutive equations. We also need a set of strain-displacement relations between the 11 strain measures ϵ_{11}, $2\epsilon_{12}$, ϵ_{22}, $2\gamma_{13}$, $2\gamma_{23}$, K_{11}, $2\kappa_{12}$, and K_{22}, along with K_{13}, K_{23}, and $K_{12} - K_{21}$, and the five global displacement and rotational variables u_1, u_2, u_3, θ_1, and θ_2. One possible set of such equations is as follows: use five of Eqs. (30), using either ϵ_{12} or ϵ_{21}; use the six Eqs. (34), with Eq. (20). There are also the two other rotational variables θ_3 and ϕ_3 which are governed by Eqs. (28) and (31), respectively. This way there are 26 equations and 26 unknowns. This mixed formualtion is capable of handling boundary conditions on two-dimensional stress resultants and displacement/rotation variables. At least in principle, one could derive a displacement formulation by eliminating all the unknowns except the displacement and rotation variables.

Equations (60) and (61) contain terms which could be disregarded because of the original assumption of small strain. We will not undertake this simplification here, because it is not necessary for using the equations in computational algorithms. Therefore, our equilibrium equations and kinematical

Downloaded 03 May 2010 to 171.66.16.245. Redistribution subject to ASME license or copyright; see http://www.asme.org/terms/Terms_Use.cfm

equations are geometrically exact; all approximations stem from the reduction process used to obtain the two-dimensional constitutive law.

Lest it be thought that the phenomena associated with the drilling rotation not being independent affects only nonlinear problems, Kanok-Nukulchai (1979) developed a linear shell finite element including three rotations at each node. It was shown that unless the constraint expressed in Eq. (32) is enforced on the rotation about the normal, the shell element derived therein fails to converge to the exact solution. This result would appear to confirm the present conclusion concerning the importance of dealing properly with the rotation about the normal.

Conclusions

Governing equations for the small-strain deformation of an elastic plate are derived. Expansion of the displacement field in terms of the normal coordinate is not needed; rather, the warping of the line of material points normal to the plate is determined by Atılgan and Hodges (1991), based on the variational asymptotical method. The two-dimensional strain and curvature measures which remain in the strain energy are the same as those in Berdichevsky (1980). Global strain-displacement relations, compatibility equations, and exact intrinsic virtual strain-displacement (transpositional) relations are derived from these measures. Intrinsic equilibrium equations are then derived from the approximate two-dimensional strain energy function, making use of the transpositional relations. The resulting intrinsic equilibrium and compatibility equations are compared with others in the literature.

The following conclusions are drawn in this paper:

1 A full finite rotation must be permitted so that the displacement field is fully specified. However, the rotation about the normal is not independent, but rather is known in terms of other quantities. Indeed, it can always be chosen, for any plate, so that the two-dimensional in-plane shear strain measures are equal. This way, all the strain measures can be expressed in terms of five independent quantities: three displacement and two rotation measures.

2 Equality of the surface in-plane shear strain measures leads to only five independent virtual displacement and rotation measures in an energy-based development. This implies that only five equilibrium equations are obtainable in a displacement-based variational formulation. Moment equilibrium about the normal is satisfied implicitly. If one does not include the full finite rotation, but rather sets the rotation about the normal equal to zero, the correct equilibrium equations cannot be obtained.

Acknowledgments

The first and second authors were supported by the U.S. Army Aerostructures Directorate, Langley Research Center, under contract NASA Grant NAG-1-1094. The technical monitor is Howard E. Hinnant. The third author was supported by the Naval Postgraduate School Research Program. Technical discussions between the first two authors and V. L. Berdichevsky are gratefully acknowledged. The authors thank J. G. Simmonds and an anonymous reviewer for insightful criticisms.

References

Atılgan, A. R., and Hodges, D. H., 1992, "On the Strain Energy of Laminated Composite Plates," *International Journal of Solids and Structures*, Vol. 24, No. 20, pp. 2527–2543.

Axelrad, E., 1986, *Theory of Flexible Shells*, North-Holland, Amsterdam.

Basar, Y., 1987, "A Consistent Theory of Geometrically Nonlinear Shells with an Independent Rotation Vector," *International Journal of Solids and Structures*, Vol. 23, No. 10, pp. 1401–1415.

Berdichevsky, V. L., 1979, "Variational-Asymptotic Method of Constructing a Theory of Shells," *PMM*, Vol. 43, No. 4, pp. 664–687.

Berdichevsky, V. L., 1980, "Variational-Asymptotic Method of Constructing the Nonlinear Shell Theory," *Theory of Shells*, Ed. by W. T. Koiter and G. K. Mikhailov, eds., North-Holland Publishing Company, Amsterdam, pp. 137–161.

Cosserat, B., and Cosserat, F., 1909, *Théorie des Corps Deformables*, Hermann, Paris.

Danielson, D. A., and Hodges, D. H., 1987, "Nonlinear Beam Kinematics by Decomposition of the Rotation Tensor," ASME JOURNAL OF APPLIED MECHANICS, Vol. 54, No. 2, pp. 258–262.

Ericksen, J. L., and Truesdell, C., 1958, "Exact Theory of Stress and Strain in Rods and Shells," *Archives for Rational Mechanics and Analysis*, Vol. 1, pp. 295–323.

Hodges, D. H., 1987, "Finite Rotation and Nonlinear Beam Kinematics," *Vertica*, Vol. 11, No. 1–2, pp. 297–307.

Hodges, D. H., 1990, "A Mixed Variational Formulation Based On Exact Intrinsic Equations for Dynamics of Moving Beams," *International Journal of Solids and Structures*, Vol. 26, No. 11, pp. 1253–1273.

Kane, T. R., 1968, *Dynamics*, Holt, Rinehart, and Winston, pp. 51–55.

Kane, T. R., Likins, P. W., and Levinson, D. A., 1983, *Spacecraft Dynamics*, McGraw-Hill, New York, Chapter 1.

Kanok-Nukulchai, W., 1979, "A Simple and Efficient Finite Element for General Shell Analysis," *International Journal for Numerical Methods in Engineering*, Vol. 14, pp. 179–200.

Koiter, W. T., and Simmonds, J. G., 1972, "Foundation of Shell Theory," *Proceedings of the 13th International Congress of Applied Mechanics*, Moscow, USSR, pp. 150–176.

Kraus, H., 1967, *Thin Elastic Shells*, John Wiley and Sons, p. 59.

Libai, A., and Simmonds, J. G., 1983, "Nonlinear Elastic Shell Theory," *Advances in Applied Mechanics*, Vol. 23, pp. 271–371.

Naghdi, P. M., 1972, "The Theory of Shells and Plates," *Handbuch der Physik*, Vol. 6 a/2, Springer-Verlag, Berlin, pp. 425–640.

Noor, A. K. Belytschko, T., and Simo, J. C., eds., 1989a, *Analytical and Computational Models of Shells*, ASME, New York.

Noor, A. K., and Burton, S. W., 1989b, "Assessment of Shear Deformation Theories for Multilayered Composite Plates," *Applied Mechanics Reviews*, Vol. 41, No. 1, pp. 1–13.

Pietraszkiewicz, W., 1979, *Finite Rotations and Lagrangian Description in the Nonlinear Theory of Shells*, Polish Scientific Publishers.

Pietraszkiewicz, W., 1989, "Geometrically Nonlinear Theories of Thin Elastic Shells," *Advances in Mechanics*, Vol. 12, pp. 51–130.

Reissner, E., 1950, "On Axisymmetrical Deformations of Thin Shells of Revolution," *Proceedings of the Symposia in Applied Mathematics*, Vol. 3, pp. 27–50.

Reissner, E., 1972, "On Sandwich-Type Plates with Cores Capable of Supporting Moment Stresses," *Acta Mechanica*, Vol. 14, pp. 43–51.

Reissner, E., 1974, "Linear and Nonlinear Theory of Shells," *Thin Shell Structures* (Sechler Anniversary Volume), Y. C. Fung and E. E. Sechler, eds., Prentice-Hall, Englewood Cliffs, NJ, pp. 29–44.

Reissner, E., 1982, "On the Derivation of Two-Dimensional Strain Displacement Relations for Small Finite Deflections of Shear-deformable Plates," ASME JOURNAL OF APPLIED MECHANICS, Vol. 49, pp. 232–234.

Reissner, E., 1986, "On Finite Deflections of Anisotropic Laminated Elastic Plates," *International Journal of Solids and Structures*, Vol. 22, No. 10, pp. 1107–1115.

Sanders, J. L., 1963, "Nonlinear Theories for Thin Shells," *Quarterly of Applied Mathematics*, Vol. 21, pp. 21–36.

Simmonds, J. G., and Danielson, D. A., 1970, "Nonlinear Shell Theory with a Finite Rotation Vector," *Proc. Koninkl. Nederl. Akademie Van Wettenschappen*, Series B, Vol. 73, pp. 460–478.

Simmonds, J. G., and Danielson, D. A., 1972, "Nonlinear Shell Theory with Finite Rotation and Stress-Function Vectors," ASME JOURNAL OF APPLIED MECHANICS, Vol. 39, pp. 1085–1090.

Simo, J. C., and Fox, D. D., 1989a, "On a Stress Resultant Geometrically Exact Shell Model. Part I: Formulation and Optimal Parameterization," *Computer Methods in Applied Mechanics and Engineering*, Vol. 72, pp. 267–304.

Simo, J. C., Fox, D. D., and Rifai, M. S., 1989b, "Geometrically Exact Stress Resultant Shell Models: Formulation and Computational Aspects of the Nonlinear Theory," *Analytical and Computational Models of Shells*, Ed. by A. K. Noor, T. Belytschko, and J. C. Simo, eds., ASME, New York, pp. 161–190.

Synge, J. L., and Chien, W. Z., 1941, "The Intrinsic Theory of Elastic Shells and Plates," *Theodore von Karman Anniversary Volume*, California Institute of Technology, pp. 103–120.

Downloaded 03 May 2010 to 171.66.16.245. Redistribution subject to ASME license or copyright; see http://www.asme.org/terms/Terms_Use.cfm

Correction of Joint Stiffnesses and Constraints for Finite Element Models in Structural Dynamics

John E. Mottershead

Shao Weixun[1]

Department of Mechanical Engineering,
University College of Swansea,
Swansea, SA2 8PP, U.K.

Finite element models are based upon known physical characteristics. But there are two main sources of error, namely (i) ill-defined joints and boundary constraints, and (ii) overstiffening due to the application of shape function discretization. It is difficult to correct an ill-defined constraint without simultaneously compensating (to some unknown degree) for discretization overstiffening. A general approach is proposed whereby the measured eigendata from a physical system are altered to resemble the eigendata of a discrete system with identical (but unknown) constraints. With the effects of discretization overstiffening present in both the adjusted measurements and the model it is straightforward to obtain progressively improved estimates of the constraint stiffnesses by using the least-squares method. The proposed approach may be considered to be equivalent to a model reduction scheme. Specific methods are applied to the correction of a stiffness in the joint of a finite element framework model.

Introduction

The verification of finite element models usually involves the comparison of modal test results with numerical predictions. Although the finite element method has been developed to a high degree of sophistication it is nevertheless often found in practice that considerable discrepancies exist between numerical and test results. Over recent years methods have been formulated for the adjustment of numerical models by the processing of either measured modal data or measured frequency responses. Such methods are based upon the constrained minimization of an objective function by using either Lagrange multipliers (Berman, 1979; Baruch, 1982) or penalty functions (Natke, 1988; Mottershead and Foster, 1991).

It is well known that the task of updating a numerical model by using experimental data is beset with problems. One source of such problems is the unavoidable lack of precision in the measurements. If the statistics of the measurement uncertainty are available then established techniques (Isenberg, 1979) are capable of providing unbiased updated parameters. It is not unusual for certain vibration modes to be absent from the measurements because of the location of the excitation, or transducers, at (or near to) vibration nodes. Such data are said to be incomplete and the processing of incomplete data will generally lead to the estimation of ill-conditioned system matrices (Mottershead and Foster, 1991). Ill-conditioned mass and stiffness matrices formed in this way constitute an incomplete model. The problem of incompleteness can generally be overcome by constraining the updated model such that it varies minimally from the finite element representation.

Further complications arise from inaccuracy associated with the finite element model. In particular we would wish to correct uncertain stiffness in a model which is likely to be inaccurate due to shape function discretization. The uncertain stiffnesses might typically be associated with bolted joints and welds. The inaccuracy associated with shape function discretization is apparent in the eigendata of the model, but regardless of that it is argued in the following section that finite element parameters are physically meaningful. In this paper methods are presented whereby the uncertain stiffnesses are adjusted by using measured data which is altered to account for shape function discretization. Thus the physical meaning which may attributed to the bulk of the finite element model is retained, and the uncertain stiffnesses are improved.

Finite Element Models

Finite elements are based upon material properties (such as E, ν, and ρ) and upon the physical dimensions of the system represented by the model. The distribution of the mass and stiffness properties is determined by the shape functions of the chosen elements. Thus, a carefully produced finite element model with correct boundary conditions will possess mass and stiffness parameters which are physically meaningful. How-

[1]On leave from East China Institute of Metallurgy, Ma An Shan, An Hui, China.

Contributed by the Applied Mechanics Division of THE AMERICAN SOCIETY OF MECHANICAL ENGINEERS for publication in the ASME JOURNAL OF APPLIED MECHANICS.

Discussion on this paper should be addressed to the Technical Editor, Professor Lewis T. Wheeler, Department of Mechanical Engineering, University of Houston, Houston, TX 77204-4792, and will be accepted until four months after final publication of the paper itself in the ASME JOURNAL OF APPLIED MECHANICS.

Manuscript received by the ASME Applied Mechanics Division, Jan. 25, 1991; final revision, Feb. 7, 1992.

Copyright © 1993 by ASME
Downloaded 03 May 2010 to 171.66.16.245. Redistribution subject to ASME license or copyright; see http://www.asme.org/terms/Terms_Use.cfm

ever, the parameters of a second model composed of elements with different shape functions may be equally meaningful but different. Thus it must be concluded that finite element parameters are meaningful but nonunique.

Berman (1984) has pointed out that all discrete models may be considered as linearized, reduced models of continuous systems. This latter observation explains the well-known failure of finite element models to faithfully reproduce the dynamics of a physical system over the entire frequency range of the model. Usually about the first third of the computed natural frequencies and modes shapes may be considered to be accurate enough for design purposes. But this is of no consequence if we are able to generate a model which is large enough to provide accurate predictions in the frequency range of interest.

If the analysis is accurate there will be good agreement with the natural frequencies of the physical structure over the range of the first third of the modes, and there will be no point in updating the model. However, it is often the case that boundary constraints and joints are ill-defined and then discrepancies may occur even at low frequencies. At higher frequencies the lack of agreement arises from two sources; uncertain boundary constraints and model reduction. In finite elements the model reduction is achieved by the application of shape functions for the interpolation of element (internal) displacements from nodal values. We have already referred to this process as shape function discretization which is generally associated with significant overestimation of the higher eigenvalues (or overstiffening of the model).

Ideally we would wish to update boundary constraint stiffnesses in isolation from the influence of shape function discretization. Then we would hope to obtain updated matrices such that the mass and stiffness properties are given according to a known distribution related to the shape functions. Any deviation from shape function distributions would lead to a lack of confidence in the physical meaning of the adjusted parameters.

It is to be expected that a model which has been updated according to the ideal approach would replicate the dynamics of the physical system (with reasonable accuracy) over a range of frequencies covering the first third of the eigenvalues of the model. In the main the updated model would retain the physical meaning of the finite elements and would be improved in those regions of joint and constraint uncertainty.

In the sequel new approaches are presented which are based upon the discretization effects observed in a small discrete model when compared with a much larger system. The large system may be an analytical model or a physical structure, but the small model and large system must have identical constraint stiffnesses which are thought to differ by a small amount from the unknown constraint stiffnesses of the physical system under test. The small model is updated on the basis of measured eigendata from the physical system. The latter eigendata are adjusted prior to processing with the intention of retaining the physical significance of the small model. This is achieved in the updating process by using not only the measured eigendata but also the previously observed discretization effects. The new methods rely upon an assumption that the error which arises from shape function discretization is not significantly affected by small changes in the constraint conditions.

Correction of Joint Stiffnesses and Constraints

The methods are best explained by considering four distinct eigendata systems which may be defined as follows:

(i) measured eigendata $\overline{\mathbf{Q}}((p^2 + p) \times 1)$ at p-frequencies of a physical system with unknown constraint stiffnesses $\overline{\mathbf{x}}(m \times 1)$ which are to be estimated. The eigendata may be arranged in vector form such that, $\mathbf{Q} = (\Lambda_1, \Lambda_2, \ldots, \Lambda_i, \ldots, \Lambda_p, \Phi_1^T, \Phi_2^T, \ldots, \Phi_i^T, \ldots, \Phi_p^T)^T$ where Λ_i and Φ_i represent the ith eigenvalue and eigenvector, respectively.

(ii) eigendata $\hat{\mathbf{Q}}_k((p^2 + p) \times 1)$ obtained on the basis of known constraint stiffnesses $\hat{\mathbf{x}}_k (m \times 1)$ which are thought to provide a close estimate to $\overline{\mathbf{x}}(m \times 1)$. Such eigendata may be obtained from a physical experiment or from a large finite element model $\hat{\mathbf{B}}_k(p \times p)$, where $\mathbf{B} = (-\omega^2\mathbf{M} + \mathbf{K})$ and $\mathbf{M}$ and $\mathbf{K}$ represent mass and stiffness matrices. In the latter case the effects of discretization upon $\hat{\mathbf{Q}}_k((p^2 + p) \times 1)$ are considered to be insignificant in a range of frequencies $n \ll p$.

(iii) eigendata $\hat{\mathbf{P}}_k((n^2 + n) \times 1)$ obtained from a finite element model $\hat{\mathbf{B}}_k(n \times n)$ with constraint stiffnesses $\hat{\mathbf{x}}_k(m \times 1)$ identical to those in (ii) above. The effects of discretization are apparent from a comparison of $\hat{\mathbf{P}}_k((n^2 + n) \times 1)$ with $\hat{\mathbf{Q}}_k((p^2 + p) \times 1)$ over the range of the first n-frequencies. The eigendata vector is given by $\mathbf{P} = (\lambda_1, \lambda_2, \ldots, \lambda_i, \ldots, \lambda_n, \phi_1^T, \phi_2^T, \ldots, \phi_i^T, \ldots, \phi_n^T)^T$, where the ith eigenpair are denoted by λ_i and ϕ_i.

(iv) eigendata $\overline{\mathbf{P}}((n^2 + n) \times 1))$ based on constraint stiffnesses $\overline{\mathbf{x}}(m \times 1)$ (as in (i) above) which are estimated in the context of a small model $\overline{\mathbf{B}}(n \times n)$. The physical significance associated with the parameters of $\overline{\mathbf{B}}(n \times n)$ is retained by adjusting the measured eigendata $\overline{\mathbf{Q}}((p^2 + p) \times 1)$ to resemble $\overline{\mathbf{P}}((n^2 + n) \times 1)$ by including the influence of discretization mentioned in (iii) above.

The objective is to update the estimates $\hat{\mathbf{x}}_k$ so that they more closely approximate to the unknown constraint stiffnesses $\overline{\mathbf{x}}$. The number of unknown constraints is considered to be small in comparison with the dimension of any of the above models.

We will assume that the above eigendata are related through a matrix $\mathbf{A}(\mathbf{x}_k)$ of order $((n^2 + n) \times (p^2 + p))$ such that,

$$\hat{\mathbf{P}}_{k+1} = \hat{\mathbf{P}}_k + \mathbf{A}(\hat{\mathbf{x}}_k)(\overline{\mathbf{Q}} - \hat{\mathbf{Q}}_k) \tag{1}$$

where $\hat{\mathbf{P}}_{k+1}$ is a closer estimate than $\hat{\mathbf{P}}_k$ to the exact eigendata $\overline{\mathbf{P}}$. The vector $\hat{\mathbf{P}}_{k+1}$ then provides the basis for an updated EWLS estimate of $\overline{\mathbf{x}}$ given by

$$\hat{\mathbf{x}}_{k+1} = \hat{\mathbf{x}}_k + \mathbf{R}(\hat{\mathbf{P}}_{k+1} - \hat{\mathbf{P}}_k) \tag{2}$$

$$\text{where } \mathbf{R} = (\mathbf{W}_x + \mathbf{G}^T(\hat{\mathbf{x}}_k)\mathbf{W}_\epsilon\mathbf{G}(\hat{\mathbf{x}}_k))^{-1}\mathbf{G}^T(\hat{\mathbf{x}}_k)\mathbf{W}_\epsilon \tag{3}$$

$$\text{and } \mathbf{G}(\hat{\mathbf{x}}_k) = \left.\frac{\partial \mathbf{P}}{\partial \mathbf{x}^T}\right|_{\mathbf{x}=\hat{\mathbf{x}}_k}. \tag{4}$$

We may consider that after many iterations $\hat{\mathbf{P}}_{k+1}$ contains the measured eigendata which has been modified to closely resemble the eigendata $\overline{\mathbf{P}}$ of a reduced model with identical constraints. The implementation of the general formulation described above is presented as a flow chart in Fig. 1. Generally Eq. (2) may undergo iteration within each step of Eq. (1).

It is of interest to consider what form the matrix $\mathbf{A}(\hat{\mathbf{x}}_k)$ might take. Consider first the case when $\mathbf{W}_x = \mathbf{0}$ and $\mathbf{W}_\epsilon = \mathbf{I}$ such that $\mathbf{R} = \mathbf{G}^+(\hat{\mathbf{x}}_k)$.

$$\text{If } \mathbf{A}(\hat{\mathbf{x}}_k) = \mathbf{G}(\hat{\mathbf{x}}_k)\mathbf{H}^+(\hat{\mathbf{x}}_k) \tag{5}$$

$$\text{where } \mathbf{H}(\hat{\mathbf{x}}_k) = \left.\frac{\partial \mathbf{Q}}{\partial \mathbf{x}^T}\right|_{\mathbf{x}=\hat{\mathbf{x}}_k}, \tag{6}$$

then by combining Eqs. (1) and (5) it is found that

$$\hat{\mathbf{P}}_{k+1} = \hat{\mathbf{P}}_k + \mathbf{G}(\hat{\mathbf{x}}_k)\mathbf{H}^+(\hat{\mathbf{x}}_k)(\overline{\mathbf{Q}} - \hat{\mathbf{Q}}_k). \tag{7}$$

When this result is substituted into Eq. (2) the updated estimate is given by

$$\hat{\mathbf{x}}_{k+1} = \hat{\mathbf{x}}_k + \mathbf{G}^+(\hat{\mathbf{x}}_k)\mathbf{G}(\hat{\mathbf{x}}_k)\mathbf{H}^+(\hat{\mathbf{x}}_k)(\overline{\mathbf{Q}} - \hat{\mathbf{Q}}_k)$$

or when rank(G) = m,

$$\hat{\mathbf{x}}_{k+1} = \hat{\mathbf{x}}_k + \mathbf{H}^+(\hat{\mathbf{x}}_k)(\overline{\mathbf{Q}} - \hat{\mathbf{Q}}_k) \tag{8}$$

which is a least-squares estimate based entirely upon the large model. Assume, for the moment, that $\overline{\mathbf{Q}}$ is obtained from a discrete model $\overline{\mathbf{B}}(n \times n)$ in a simulated problem. It is well known that in such problems the task of updating a perturbed model by using data from an exact model of the same discrete

Downloaded 03 May 2010 to 171.66.16.245. Redistribution subject to ASME license or copyright; see http://www.asme.org/terms/Terms_Use.cfm

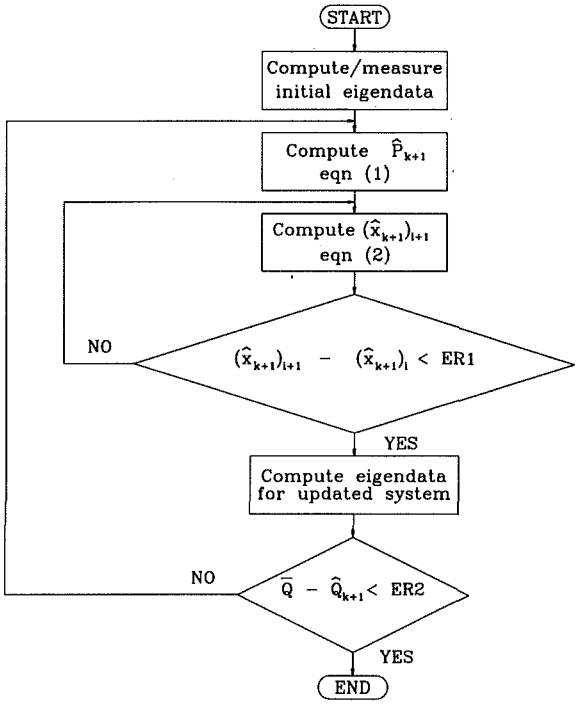


Fig. 1 Flowchart

system is trivial. Thus in the simulated problem we would expect accurate convergence of $\hat{\mathbf{x}}_{k+1}$ following many iterations.

In the realistic problem where model $\hat{\mathbf{B}}_k(n \times n)$ is to be updated on the basis of measured eigendata $\bar{\mathbf{Q}}$ from a physical system, the eigendata sensitivities $\mathbf{H}$ may not be readily available and will certainly be expensive to compute. Then alternative forms of matrix $\mathbf{A}$ should be considered. We will consider the particular case where $\mathbf{A}$ is partitioned as follows:

$$\mathbf{A} = \left[\begin{array}{c|c|c} \mathbf{I}(n \times n) & \mathbf{0} & \mathbf{0}(n \times p^2) \\ \hline \mathbf{0}(n^2 \times p) & \mathbf{N}(n^2 \times np) & \mathbf{0} \end{array}\right] \tag{9}$$

where $\mathbf{N}$ provides shape-function interpolation such that the first n-modes of $\hat{\mathbf{B}}_k(p \times p)$ are defined at the nodal points of the $(n \times n)$ model according to

$$\mathbf{N}[\Phi_1^T, \Phi_2^T, \ldots, \Phi_n^T]^T.$$

It is necessary to perform mass normalization of the interpolated eigenvectors using the $n \times n$ mass matrix.

The meaning of the redefined matrix $\mathbf{A}$ is that the effects of shape function discretization are assumed to be the same in $\hat{\mathbf{B}}_k(p \times p) \xrightarrow{\text{reduce}} \hat{\mathbf{B}}_k(n \times n)$ as in the reduction of the physical system to $\bar{\mathbf{B}}(n \times n)$.

Thus, by combining Eq. (1) and (9) it is found that

$$\begin{Bmatrix} \hat{\lambda}_1 \\ \hat{\lambda}_2 \\ \vdots \\ \hat{\lambda}_n \end{Bmatrix}_{k+1} = \begin{Bmatrix} \hat{\lambda}_1 \\ \hat{\lambda}_2 \\ \vdots \\ \hat{\lambda}_n \end{Bmatrix}_k + \begin{Bmatrix} \bar{\Lambda}_1 - \hat{\Lambda}_1 \\ \bar{\Lambda}_2 - \hat{\Lambda}_2 \\ \vdots \\ \bar{\Lambda}_n - \hat{\Lambda}_n \end{Bmatrix}_k \tag{10}$$

and

$$\begin{Bmatrix} \hat{\phi}_1 \\ \hat{\phi}_2 \\ \vdots \\ \hat{\phi}_n \end{Bmatrix}_{k+1} = \begin{Bmatrix} \hat{\phi}_1 \\ \hat{\phi}_2 \\ \vdots \\ \hat{\phi}_n \end{Bmatrix}_k + \mathbf{N} \begin{Bmatrix} \bar{\Phi}_1 - \hat{\Phi}_1 \\ \bar{\Phi}_2 - \hat{\Phi}_2 \\ \vdots \\ \bar{\Phi}_n - \hat{\Phi}_n \end{Bmatrix}_k . \tag{11}$$

If the estimated constraints $\hat{\mathbf{x}}_{k+1}$ converge closely to $\bar{\mathbf{x}}$ then the assumption above will be valid. The eigendata $\hat{\mathbf{Q}}_k$ may be obtained from a specially contrived experiment involving a system with clearly defined constraints and joints. In this case the outer loop shown in the flow diagram of Fig. 1 is omitted.

Alternatively, $\hat{\mathbf{Q}}_k$ may be obtained from a numerical model which is sufficiently large so that the first n-eigenvalues and eigenvectors are computed with negligible error due to shape function discretization. It should be noted that the accuracy required is very much greater than that required of a finite element model for design purposes. Consequently, $p = \dim(\hat{\mathbf{B}}_k)$ is likely to be very large indeed and certainly larger than the design model. It has been demonstrated above how model updating may be achieved by using a much smaller model. The general approach adopted may be considered to be equivalent to a model reduction scheme.

It is apparent that the general formulation of Eqs. (1)–(4) can be developed to form 3-specific methods as follows:

(i) a method based upon the application of Eq. (8) in a single iterative loop. The matrix $\mathbf{H}^+$ must be recomputed at each pass through the loop by using the first n-frequencies and modes of the large system.

(ii) a method using equations (1), (2), and (5). $\mathbf{H}^+$ must be recomputed at each outer loop and $\mathbf{R}$ recomputed at each inner loop excursion. This method may be applied with equal merit to frequency response function data instead of eigendata as shown here.

(iii) A method using Eqs. (1), (2), and (9). The first n-frequencies and modes must be recomputed at each pass through the outer loop for the construction of $\mathbf{A}$. At each inner loop excursion $\mathbf{R}$ must be recomputed.

With methods (ii) and (iii) the updating is performed upon the small model on the basis of adjusted eigendata. The application of method (i) is likely to result in the updating of a model considerably larger than the design model.

The above methods may be applied in the case of incomplete data when r-eigenvalues and eigenvectors ($r < n$) are considered. It is well known that the eigenvalues are more sensitive than the eigenvectors to changes in $\hat{\mathbf{x}}_k$ and it is thus reasonable to compute an updated estimate according to

$$\hat{\mathbf{x}}_{k+1} = \hat{\mathbf{x}}_k + \mathbf{R} \left\{ \begin{Bmatrix} \hat{\lambda}_1 \\ \hat{\lambda}_2 \\ \vdots \\ \hat{\lambda}_r \end{Bmatrix}_{k+1} - \begin{Bmatrix} \hat{\lambda}_1 \\ \hat{\lambda}_2 \\ \vdots \\ \hat{\lambda}_r \end{Bmatrix}_k \right\} \tag{12}$$

where $(\hat{\lambda}_1, \hat{\lambda}_2, \ldots, \hat{\lambda}_r)_{k+1}^T$ is found from Eq. (10). For the computation of eigendata sensitivities the reader is referred to Rogers (1970) and Fox and Kapoor (1968).

Having described three techniques it remains to apply them in a controlled numerical experiment. We investigate the particular problem of updating an ill-defined joint stiffness in a finite element framework model by using method (iii) above. Finally, the computational requirements of the three approaches are considered.

Numerical Experiments

In the numerical experiments two finite element models of the same frame structure are considered. A frame model comprising 17-elements and 49 degrees-of-freedom is shown in Fig. 2. In Fig. 3 a second model of the same frame with 7 elements and 19 degrees-of-freedom is shown. The members of the frame have rigidities EA = 1 and EI = 1, and mass per unit length $m = 1$. The dimensions of the frame are 4×3 such that in Fig. 2 the elements representing the horizontal and vertical members are each of unit length. The junctions between the elements are rigid connections except in the case where node 1 meets node 2. These nodes are separated by a vertical, translational spring of stiffness $k = 4$. Nodes 1 and 2 are considered to have identical horizontal displacements and identical rotations.

Downloaded 03 May 2010 to 171.66.16.245. Redistribution subject to ASME license or copyright; see http://www.asme.org/terms/Terms_Use.cfm

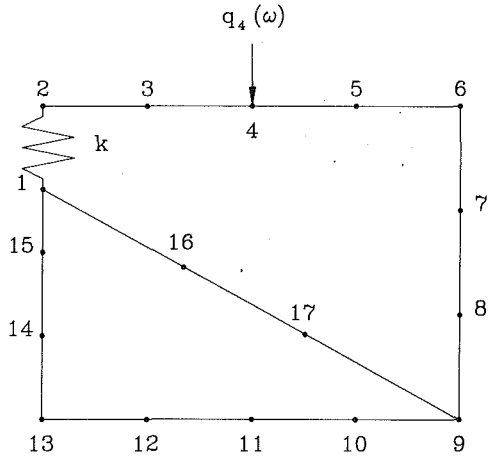


Fig. 2 Frame model—17 elements

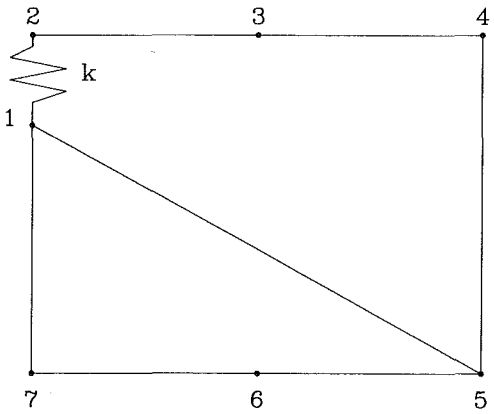


Fig. 3 Frame model—7 elements

The frame, which is freely supported, receives white noise, force excitation in the vertical direction at node 4 of the 17-element model. It is considered that the structural members are well defined by the finite elements but that the discrete spring k is unknown. We aim to update the model shown in Fig. 3 by processing measured eigenvalue data from the 17-element system.

It is considered that the problem described here is realistic. In a physical experiment a discrete model is updated on the basis of data acquired from a continuous system. The above problem is similar in that a discrete model is adjusted using data from another model which more closely represents the dynamics of a continuous structure.

Three numerical experiments are described for updating the discrete system. In the first we consider updating k only, and this is to be achieved in the 7-element model using raw measurement data from the 17-element system. In the second experiment we attempt to compensate for overstiffening (in the 7-element model) due to shape function discretization, by updating not only the discrete stiffness, k, but also the overall stiffness and mass of the system. This necessitates the updating of three parameters which can easily be defined by using the substructuring approach (Natke, 1983). In the final experiment we update k only, by using method (iii) described in the previous section. In all of the numerical experiments k is adjusted on the basis of measured natural frequencies only. Thus, in the third experiment we use the method defined by Eqs. (10), (12), and (3). In all of the numerical experiments an initial estimate of the discrete stiffness was given by $\hat{x}_o = \alpha k$.

Table 1 Table of natural frequencies

Natural Frequency (Hz)		% Error
17-element model ω_{17}	7-element model ω_7	$\frac{\omega_7 - \omega_{17}}{\omega_{17}} \times 100\%$
0.44564491	0.45484632	2
0.46343589	0.46923684	1.25
0.51390197	0.53126238	3.38
0.52025173	0.58882390	13.18
0.60968703	0.65170658	6.9

Table 2 Improved estimates: experiment (i)

α	Improved k	Number of iterations
1	1.24522368	16
0.8	1.24522388	11
0.5	1.24522392	6
0.2	1.24522388	4
0	1.24522392	5

Results

The quality of the 7-element model can be assessed by inspection of the MAC matrix (Allemang and Brown, 1982) which is an indicator of the correlation between the eigenvectors of the two systems. The MAC matrix corresponding to the first 12-nonzero eigenvalues of the two systems is given in the Appendix. Reading from the top left-hand corner it can be seen that the first five numbers on the leading diagonal are greater than 0.9, which indicates reasonable correlation in the first five mode shapes. Beyond the fifth mode, eigenvector correlation is poor owing to shape function discretization. The first five natural frequencies of the two systems are given in Table 1. Of these, the first three are in agreement to within five percent and the fourth mode of the 7-element system is in error to an extent greater than ten percent. In the numerical experiments k is updated by using the first three measured eigenvalues.

In the first numerical experiment we attempt to update the discrete stiffness in the 7-element model by using eigenvalues from the 17-element system. The result is shown in Table 2 where it can be seen that the converged estimate is considerably less than the known value of $k = 4$. With a variety of starting estimates the routine is consistent in locating the same converged estimate (to eight significant figures). It is as a result of discretization over-stiffening that k is consistently under estimated.

In the second experiment we seek optimal scalar factors to be applied to the overall mass and overall stiffness matrices, and these are to be estimated simultaneously with the discrete stiffness. The result is given in Table 3 where it is apparent that the discrete stiffness remains virtually unchanged. This behavior can be explained by inspection of the eigenvalue sensitivities. Table 4 shows that all of the nonzero eigenvalues are more sensitive to changes in the overall mass and stiffness than to changes in k. If the overall stiffness, overall mass and k are updated to simultaneously compensate for both uncertainty in

Downloaded 03 May 2010 to 171.66.16.245. Redistribution subject to ASME license or copyright; see http://www.asme.org/terms/Terms_Use.cfm

the initial value of k and overstiffening due to shape function discretization then it is to be expected that the greatest changes will occur in the overall stiffness and mass. It is apparent that there is nothing to prevent alterations to the overall stiffness and mass in response to observed differences between the measured and modelled eigendata, which is properly due to inaccuracy of the model in representing the stiffness k. In other words there is a built in preference to update the overall mass and stiffness rather than k, which has been found to be responsible for inaccurate estimation of the discrete stiffness.

In the third numerical experiment we apply method (iii) which has been described above. It can be seen from Table 5 that excellent converged estimates were obtained from a variety of starting values. The weights (in Eq. (13)) were $W_x = 10^{-3}$ and $\mathbf{W}_\epsilon = \mathbf{I}$ and the convergence criteria were, for parameters ER1 = 10^{-6}, and for eigenvalues ER2 = 10^{-12}. Method (ii) is capable of providing results of the same quality.

The following comments can be made regarding the computational requirements of the three methods:

In the above example the CPU time required for one loop using method (i) was 0.0614 seconds on an IBM3081 machine. Method (ii) required 0.0736 seconds of CPU time for an outer loop and 0.0108 seconds for an inner loop. Method (iii) required 0.0139 seconds for an outer loop and 0.0108 seconds for an inner loop. It was found that method (iii) generally required a greater number of excursions through the outer loop than method (ii) and when initial estimates $\hat{\mathbf{x}}$ were remote from $\bar{\mathbf{x}}$ method (ii) usually required less CPU time in total than

Table 3 Improved estimates: experiment (ii)

Initial values			Updated values			W_ϵ=I	Number of iterations
K_{11}	k	M_{11}	K_{11}	k	M_{11}	W_x	
1.10700400	0.0	3.51616667	1.08747247	0.14371406	3.51389919	10^2xI	16
1.10700400	2.0	3.51616667	1.08938394	2.03086425	3.57380886	I	11
1.10700400	4.0	3.51616667	1.08478706	3.99931909	3.58863563	I	12
1.10700400	6.0	3.51616667	1.08836794	5.96605371	3.57654156	2xI	14

Table 4 Table of eigenvalue sensitivities

Mode	Sensitivity		
	Overall Stiffness	Stiffness k	Overall Mass
1	0.96996E-01	0.23341E-02	-0.99330E-01
2	0.10551E+00	0.20545E-03	-0.10571E+00
3	0.13479E+00	0.72100E-03	-0.13551E+00
4	0.16637E+00	0.93838E-04	-0.16647E+00
5	0.20360E+00	0.32302E-03	-0.20392E+00
6	0.51534E+00	0.19857E-04	-0.51536E+00
7	0.71529E+00	0.27593E-01	-0.74289E+00
8	0.74505E+00	0.76501E-01	-0.82155E+00
9	0.87094E+00	0.26433E-02	-0.87359E+00
10	0.17936E+01	0.54611E+00	-0.23397E+01
11	0.18031E+01	0.11121E+01	-0.29153E+01
12	0.46129E+01	0.18092E+00	-0.47938E+01
13	0.68573E+01	0.46095E-01	-0.69034E+01
14	0.95676E+01	0.14441E+01	-0.11012E+02
15	0.23101E+02	0.14686E-01	-0.23116E+02
16	0.26693E+02	0.86240E+00	-0.27555E+02

Table 5 Improved estimates: experiment (iii)

Initial k	0.0	2.0	4.0	6.0
Improved k	3.99969387	3.99969785	4.00000000	4.00121516
Number of iterations (outer loop)	16	15	1	20
Max. Number of iterations (inner loop)	20	20	1	20

Downloaded 03 May 2010 to 171.66.16.245. Redistribution subject to ASME license or copyright; see http://www.asme.org/terms/Terms_Use.cfm

method (iii). Conversely, when $\hat{\mathbf{x}}$ was close to $\bar{\mathbf{x}}$ method, (iii) usually provided a more rapid convergence than method (ii).

A further numerical example was considered where the disparity (in terms of degrees-of-freedom) between the large model and the small model was more significant. In this case the number of degrees-of-freedom of the large model was 151 whereas the small model was described by 7 degrees-of-freedom. Using method (i) the CPU time per loop was 0.543 seconds. With method (ii) the outer and inner loop times were 0.551 seconds and 0.002 seconds, respectively. Method (iii) required 0.06 seconds for an outer loop and 0.002 seconds for an inner loop excursion. In all examples considered by the authors, methods (ii) and (iii) required less CPU time in total than method (i).

Conclusions

In the updating of finite element models by using measured vibration data it is necessary to separate the task of correcting ill-defined constraint stiffnesses from that of compensating for overstiffening due to discretization. New iterative methods have been presented which depend upon the availability of (i) a small number of eigenvalues (and eigenvectors) from the system under test and (ii) an estimate of the influence of discretization overstiffening provided by the comparison of the eigendata of a small discrete model with the eigendata from a larger system. Providing that the two systems which offer the assessment of discretization effects have identical constraint stiffnesses, which are reasonably close to the unknown physical constraint conditions, then the new methods are capable of providing improved discrete stiffness estimates largely unaffected by discretization overstiffening. The new methods offer significant computational advantages over existing techniques and may be considered to be equivalent to model reduction schemes. It is argued that the parameters of the updated model are physically meaningful but nonunique.

Acknowledgments

This work is supported by Nuclear Electric plc under contract CON/BC/2076. The authors wish to thank the Board of Directors of Nuclear Electric plc for permission to publish this paper.

References

Allemang, R. J., and Brown, D. L., 1982, "A Correlation Coefficient for Modal Vector Analysis," *Proc. 1st IMAC*, Orlando, FL, pp. 110–116.

Baruch, M., 1982, "Optimal Correction of Mass and Stiffness Matrices Using Measured Modes," *AIAA Journal*, Vol. 20, pp. 1623–1626.

Berman, A., 1979, "Mass Matrix Correction Using an Incomplete Set of Measured Modes," *AIAA Journal*, Vol. 17, pp. 1147–1148.

Berman, A., 1984, "System Identification of Structural Dynamic Modes—Theoretical and Practical Bounds," *AIAA Conf.*, Paper 84-0929.

Fox, R. L., and Kapoor, M. P., 1968, "Rates of Change of Eigenvalues and Eigenvectors," *AIAA Journal*, Vol. 6, pp. 2426–2429.

Isenberg, J., 1979, "Progressing from Least-Squares to Bayesian Estimation," *Proc. of the ASME Winter Annual Meeting*, ASME New York, 79-WA/DSC-16.

Mottershead, J. E., and Foster, C. D., 1991, "On the Treatment of Ill-Conditioning in Spatial Parameter Estimation from Measured Vibration Data," *Mech. Sys. Sig. Proc.*, Vol. 5, No. 2, pp. 139–154.

Natke, H. G., 1983, *Einführung in Theorie und Praxis der Zeitreihen-und Modalanalyse—Identifikation schwingungsföhiger elastomechanischer systeme*, Friedr. Vieweg and Sohn, Braunschweig, Weisbaden, F.R.G.

Natke, H. G., 1988, "Updating Computational Models in the Frequency Domain Based on Measured Data: A Survey," *Prob. Engng. Mech.*, Vol. 3, pp. 28–35.

Rogers, L. C., 1970, "Derivatives of Eigenvalues and Eigenvectors," *AIAA Journal*, Vol. 8, pp. 943–944.

APPENDIX

MAC Matrix

0.956	0.052	0.009	0.000	0.000	0.056	0.055	0.000	0.002	0.127	0.018	0.001
0.041	0.948	0.000	0.000	0.000	0.006	0.001	0.000	0.002	0.073	0.025	0.007
0.002	0.000	0.991	0.000	0.000	0.024	0.001	0.000	0.001	0.003	0.006	0.013
0.000	0.000	0.000	0.951	0.006	0.003	0.001	0.108	0.000	0.000	0.004	0.003
0.000	0.000	0.000	0.001	0.984	0.069	0.002	0.016	0.000	0.019	0.071	0.201
0.000	0.000	0.000	0.000	0.001	0.508	0.004	0.017	0.000	0.004	0.014	0.223
0.000	0.000	0.000	0.000	0.000	0.000	0.517	0.031	0.383	0.074	0.009	0.029
0.000	0.000	0.000	0.000	0.000	0.002	0.002	0.387	0.220	0.008	0.011	0.042
0.000	0.000	0.000	0.000	0.000	0.049	0.246	0.094	0.380	0.107	0.005	0.011
0.000	0.000	0.000	0.000	0.000	0.000	0.014	0.005	0.001	0.443	0.001	0.038
0.000	0.000	0.000	0.000	0.000	0.116	0.012	0.005	0.000	0.001	0.404	0.014
0.000	0.000	0.000	0.000	0.000	0.023	0.000	0.003	0.000	0.000	0.006	0.368

Downloaded 03 May 2010 to 171.66.16.245. Redistribution subject to ASME license or copyright; see http://www.asme.org/terms/Terms_Use.cfm

S. F. Masri
Department of Civil Engineering,
University of Southern California,
Los Angeles, CA 90089
Mem. ASME

A. G. Chassiakos
School of Engineering,
California State University,
Long Beach, CA 90840
Mem. ASME

T. K. Caughey
Division of Engineering,
California Institute of Technology,
Pasadena, CA 91125

Identification of Nonlinear Dynamic Systems Using Neural Networks

A procedure based on the use of artificial neural networks for the identification of nonlinear dynamic systems is developed and applied to the damped Duffing oscillator under deterministic excitation. The "generalization" ability of neural networks is invoked to predict the response of the same nonlinear oscillator under stochastic excitations of differing magnitude. The analogy between the neural network approach and a qualitatively similar nonparametric identification technique previously developed by the authors is illustrated. Some of the computational aspects of identification by neural networks, as well as their fault-tolerant nature, are discussed. It is shown that neural networks provide high-fidelity mathematical models of structure-unknown nonlinear systems encountered in the applied mechanics field.

1 Introduction

1.1 Background. This paper explores the potential of using parallel distributed processing methodologies (artificial neural networks) to identify the internal forces of structure-unknown nonlinear dynamic systems typically encountered in the field of applied mechanics.

The pioneering work in the field of neural networks is usually attributed to McCulloch and Pitts (1943) who developed a simplified model of the neuron (the basic unit of the living brain) consisting of variable resistors and summing amplifiers. Over the intervening years, seminal contributions were made by Hebb (1949), Rosenblat (1962), Widrow (1962), Minsky and Papert (1969), Werbos (1974), Albus (1975), and Grossberg (1976). The interest in the analysis of neural networks was revived in the early 1980's due to the work of Hopfield (1982), and later on to the works of Hinton (1984), Kohonen (1984), McLelland and Rumelhart (1986), and Mead (1989). Introductory background information can be found in some recent publications such as Aleksander and Morton (1990), Khanna (1990), Nelson and Illingworth (1991), Lippman (1987), and Nguyen and Widrow (1990).

Artificial neural network models have several inherent properties which distinguish them from traditional computational models (Lippmann, 1987):

(1) Neural network models do not perform sequential computations as a Von Neuman machine does, but are massively parallel nets of simpler computational elements. Analog VLSI implementation of these networks provides much higher computation rates than sequential machines because of the inherent parallelism.

(2) Because neural networks contain many more processing elements than a sequential machine, and because these elements have primarily local connections, an artificial neural network has a higher degree of robustness or fault tolerance. If a few of the many links in the network are severed, the overall performance will not downgrade dramatically.

(3) Artificial neural networks are systems that have the property of adaptation or learning. Given a system and a set of "training" patterns, the neural network can "learn" about the system by adapting its internal parameters to match the training examples.

The above properties make artificial neural networks the ideal choice in cases in which real-time adaptation and fast processing of large amounts of data are required. For this reason a lot of attention has been paid to artificial neural networks for high-performance speech or image recognition, and recently for applications such as robotics, control, and system identification.

Even though there are numerous studies dealing with all computational aspects of system identification, there is a paucity of publications in the open literature that address the use of artificial neural networks for identifying physical systems encountered in the applied mechanics field. It is this subject that this paper explores.

1.2 Scope. This paper applies a neural network-based identification procedure to a "calibration" problem which incorporates realistic test situations and nonlinear characteristics. Subsequently, a "validation" problem is considered to investigate the range of validity of the neural network identification/prediction procedure.

Section 2 defines the example nonlinear model (Duffing oscillator) characteristics and the deterministic probing signal

Contributed by the Applied Mechanics Division of THE AMERICAN SOCIETY OF MECHANICAL ENGINEERS for publication in the ASME JOURNAL OF APPLIED MECHANICS.

Discussion on this paper should be addressed to the Technical Editor, Professor Lewis T. Wheeler, Department of Mechanical Engineering, University of Houston, Houston, TX 77204-4792, and will be accepted until four months after final publication of the paper itself in the ASME JOURNAL OF APPLIED MECHANICS.

Manuscript received by the ASME Applied Mechanics Division, Apr. 10, 1991; final revision, Nov. 15, 1991. Associate Technical Editor: P. D. Spanos.

 Copyright © 1993 by ASME

Downloaded 03 May 2010 to 171.66.16.245. Redistribution subject to ASME license or copyright; see http://www.asme.org/terms/Terms_Use.cfm

used for identification. The internal forces in the Duffing oscillator are identified through the use of a three-layer, feed-forward neural network. Subsequently, the "generalization" concept of neural networks is invoked to predict the response of the same Duffing oscillator under stochastic excitations of differing magnitude.

Section 3 discusses the analogy between the neural network approach and a qualitatively similar nonparametric identification technique previously developed by the authors. Some of the computational aspects of identification by neural networks, as well as the fault-tolerant nature of the neural network procedure, are also discussed in this section.

2 Identification

2.1 Model Characteristics. The identification procedure under discussion will be outlined in the context of the nonlinear single-degree-of-freedom system illustrated in Fig. 1, in which the (presumably) unknown restoring force acting on the system is $g(y, \dot{y})$. It is assumed that the excitation $u(t)$ and the acceleration $\ddot{y}(t)$ of the system are available from measurements, and that the mass m is known or easily estimated.

The present demonstration example corresponds to the Duffing oscillator with a hardening nonlinearity. The specific parameters used to characterize the system for simulation purposes are shown in Fig. 1. All of the following steps in the identification procedure are predicated on the assumption that the structure of this system (i.e., the nature of the nonlinearity) is unknown.

The equation of motion of the system in Fig. 1,

$$m\ddot{y}(t)+g(y, \dot{y})=u(t), \tag{1}$$

allows the determination of the time history of the restoring force from

$$g(y, \dot{y})=u(t)-m\ddot{y}(t). \tag{2}$$

2.2 Generation of "Experimental" Measurements. Assume that the experimental measurements for $u(t)$ and $\ddot{y}(t)$ are available over a period t_{max}. The corresponding system displacement $y(t)$ and velocity $\dot{y}(t)$ of m can be found by direct measurements or through integration of $\ddot{y}(t)$. If the measurements are taken at discrete times t_k:

$$y_k=y(t_k);\ \ \dot{y}_k=\dot{y}(t_k);\ \ \ddot{y}_k=\ddot{y}(t_k);\ u_k=u(t_k).$$

Then the values $g_k=g(y(t_k), \dot{y}(t_k))$ can be computed from

$$g_k=u_k-m\ddot{y}_k. \tag{3}$$

For the Duffing oscillator used here, the restoring force is

$$g(y, \dot{y})=ay+by^3+c\dot{y}. \tag{4}$$

In the present test, the system parameters had the following values:

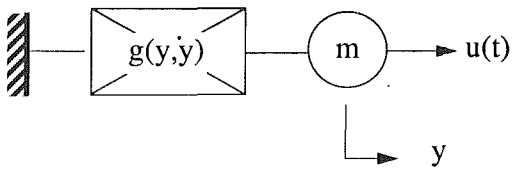
$$m=1,\ \ a=2\pi,\ \ b=10,\ \ c=1.25. \tag{5}$$

The method under consideration imposes no restrictions on the nature of the excitation source to be used as a probing signal. In the present example, the excitation used for training the neural network is a swept sine signal with amplitude $u_0=(2\pi)^2$. The system parameters listed above result in a "small amplitude" period $T\simeq 1$ and $\zeta=0.10$. The swept-sine excitation was characterized by

$$\omega_l/\omega_n=0.9,\ \ \omega_u/\omega_n=1.1 \tag{6}$$

where ω_l and ω_u are the lower and upper limits, respectively, of the swept-sine excitation, and $\omega_n=\sqrt{a/m}$.

The time-history records for the single-degree-of-freedom system excitation, acceleration, velocity, displacement, and the internal force $g(y, \dot{y})$ corresponding to the example nonlinear single-degree-of-freedom system under swept-sine excitation are shown in Fig. 2. The time segment shown corresponds to about 20 natural periods.



(a) Nonlinear System Model

$$g(y, \dot{y}) = a y + b y^3 + c \dot{y}$$

$$a = 2\pi \qquad b=10 \qquad c=1.25$$

(b) Duffing Model Characteristics

Fig. 1 Model of system

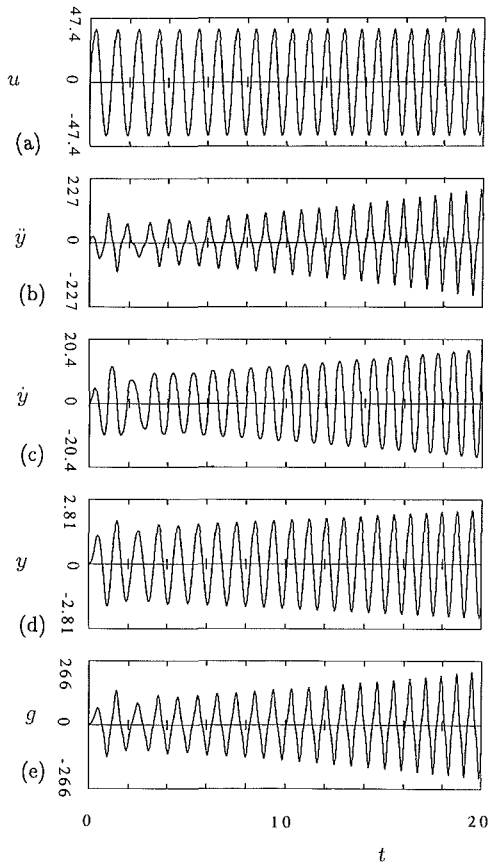


Fig. 2 Time history records of the nonlinear system excitation and response under swept sine excitation used to train the neural network; (a) excitation, (b) acceleration, (c) velocity, (d) displacement, (e) restoring force

2.3 Identification of the Internal Forces in the Duffing Oscillator. The neural identifier is shown in block diagram form in Fig. 3. Inputs to the net are the displacement and velocity measurements, $y(t)$ and $\dot{y}(t)$, and the network output $\hat{g}(y, \dot{y})$ is an approximation of the unknown restoring force $g(y, \dot{y})$. The network shown in Fig. 3 is a three-layer feed-forward net (Narendra and Parthasarathy, 1990), with 2 inputs, 1 output, and 15 and 10 nodes in the first and second hidden layers, respectively. The network topology is represented by the various matrices W^i and bias terms b^i. Let $Y=$

Downloaded 03 May 2010 to 171.66.16.245. Redistribution subject to ASME license or copyright; see http://www.asme.org/terms/Terms_Use.cfm

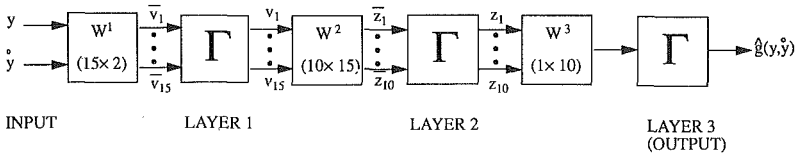


Fig. 3 Multilayer feedforward neural network used to identify the Duffing oscillator

$[y, \dot{y}]^T$ be the input vector, and $\gamma()$ be a (typically sigmoidal) nonlinear function. The output of the network $\hat{g}(y, \dot{y})$ is computed according to the following equations:

$$\left.\begin{aligned} &\bar{v} = W^1 Y + b^1; \quad && v_i = \gamma(\bar{v}_i),\ i = 1, \ldots 15 \\ &\bar{z} = W^2 v + b^2; \quad && z_i = \gamma(\bar{z}_i),\ i = 1, \ldots 10 \\ &\hat{g} = \gamma(W^3 z + b^3) \end{aligned}\right\}. \tag{7}$$

The identification procedure consists of two phases: the network training (or learning) phase and the validation phase.

During the training phase, the network is presented with the sequence of input vectors $\{[y_k, \dot{y}_k]^T\}$ and the sequence $\{g_k\}$ of desired output vectors. Given a set of weights and biases (which initially is chosen randomly), the input vector $\{[y_k, \dot{y}_k]^T\}$ is propagated forward through the net at time t_k and the network output $\hat{g}_k$ is calculated according to the equations above. This $\hat{g}_k$ is compared to the desired output g_k. A performance criterion based on the error between g_k and $\hat{g}_k$ is then evaluated and the weights and biases are adjusted in the direction that will reduce the error. The procedure is repeated until an acceptable value of the error criterion is obtained. Now, given an input vector $[y_k, \dot{y}_k]^T$, the network will produce an output $\hat{g}_k$ close to the desired output g_k. At this stage, the neural net has "learned" the system.

During the validation phase, the network is given other input vector sequences $\{[y_\alpha, \dot{y}_\alpha]^T\}$ not among those used for training. If the training was successful and the network is a good identifier, it should produce an output sequence $\{\hat{g}_\alpha\}$ very close to the actual system output $\{g_\alpha\} = \{g(y_\alpha, \dot{y}_\alpha)\}$.

Figure 4 shows a detailed diagram for some of the nodes in the network used for the problem at hand. It should be noted that no specific guidelines presently exist on how to choose the network topology, the number of layers, and the number of nodes. Many of these decisions are based on experience and depend on the particular application. The network structure presented here was employed after experimentation with networks of different sizes and topologies. Since the net has two inputs, 15 and 10 nodes in the hidden layers, and one output, the total number of the network parameters to be adjusted is 216 (190 weights and 26 bias terms). Initially the network parameters are assigned random values since nothing is known about the optimal parameter set (i.e., the set of weights that will minimize the performance criterion). Training is performed by the back-propagation algorithm using a modified version of the back-propagation program from (McLelland and Rumelhart, 1987). A hyperbolic tangent function was used as the node nonlinearity:

$$\gamma(x) = (1 - e^{-\alpha x})/(1 + e^{-\alpha x}); \quad \alpha > 0. \tag{8}$$

By implementing the identification procedure under discussion, the optimum values of the weight matrices and biases that characterize the neural network were obtained. A discussion on the computational aspects of the identification procedure (convergence rates, training patterns, optimal weight set, etc.) is given in Section 3.2.

The training was performed using the data of Fig. 2: the network inputs were y and $\dot{y}$ and the desired output was the set of values of $g = u - m\ddot{y}$ over the time period from 0.0 to 20.0 sec. After the training was over, the weights and biases were fixed to the values obtained by the back propagation

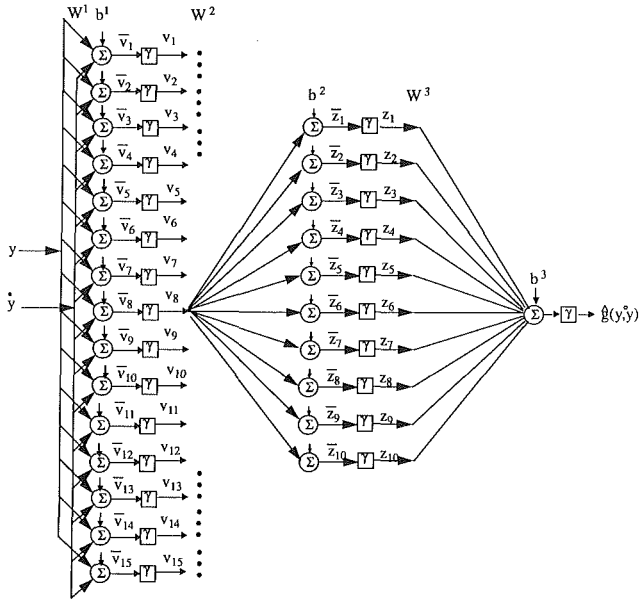


Fig. 4 Detail interconnections among some of the nodes in the multilayer feedforward neural network used to identify the Duffing oscillator

algorithm. From this point on, the network is used to model the unknown restoring force nonlinearity. It is worth pointing out that no extra information about the physical system was given to the net, other than the input/output sequences, and that *no model of the system was assumed* during the learning phase. Several tests of the network's identifying ability were performed:

(1) First, the actual data y and $\dot{y}$ of Fig. 2 were used as inputs to the net. The network output $\hat{g}(y, \dot{y})$ is virtually identical to the plot of $g(y, \dot{y})$ shown in the bottom of Fig. 2. This of course is expected since the network was trained on the basis of these data.

(2) Next, the network was used as a model of the unknown nonlinearity for prediction of the system's responses to various excitations. The predicted responses $\hat{y}$ and $\dot{\hat{y}}$ are obtained by standard time-marching techniques as numerical solutions of the equation of motion

$$m\ddot{\hat{y}} + \hat{g}(\hat{y}, \dot{\hat{y}}) = u(t) \tag{9}$$

which is the same as the system Eq. (1), with $\hat{g}$ replacing the unknown function g. A distinction is made in Eq. (1) and Eq. (9) between y and $\hat{y}$ since the dependent variables in Eq. (9) evolve from the approximating restoring function $\hat{g} = N(\hat{y}, \dot{\hat{y}})$ rather than the exact function $g(y, \dot{y})$ used in Eq. (1). The predicted values of $\hat{y}$ and $\dot{\hat{y}}$ include the effects of the network identification errors as well as error propagation effects associated with the computational scheme (Runge-Kutta) used to obtain the numerical solution of Eq. (9). The time plots of the predicted responses $\hat{y}(t)$, $\dot{\hat{y}}(t)$, when plotted to the same scale used in Fig. 2, are virtually indistinguishable from the plots of the exact responses $y(t)$, $\dot{y}(t)$. For this reason, the time history plots of $\hat{y}(t)$, $\dot{\hat{y}}(t)$ are not shown. The state variable plots of the actual and predicted responses are pre-

Downloaded 03 May 2010 to 171.66.16.245. Redistribution subject to ASME license or copyright; see http://www.asme.org/terms/Terms_Use.cfm

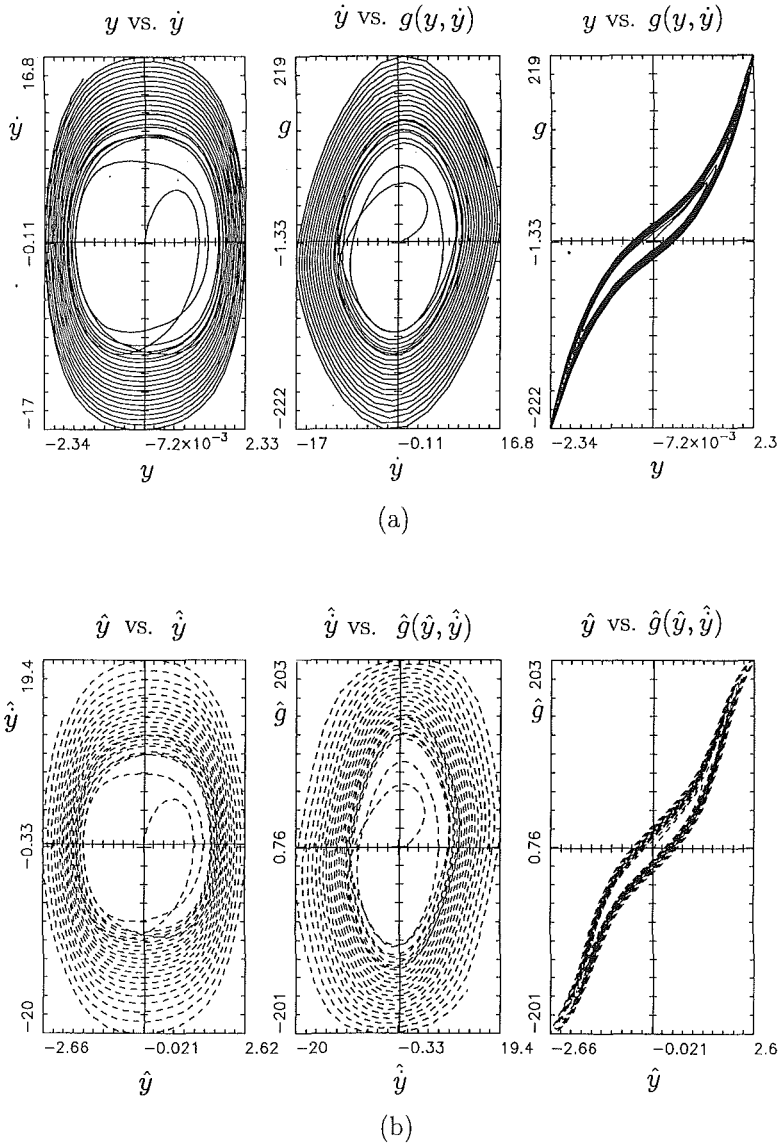


Fig. 5 State variable plots of the nonlinear system under the same swept sine excitation used in Fig. 2; (*a*) response of exact nonlinear system, (*b*) response of the identified neural network

sented in Fig. 5 in which the solid line refers to the exact measurements and the dashed line corresponds to the output of the neural network. The three plots shown in the upper half of Fig. 5 correspond to the exact data of Fig. 2, while the three plots shown in the lower half of Fig. 5 correspond to the predicted responses $\hat{y}(t)$, $\hat{\dot{y}}(t)$, and $\hat{g}(\hat{y}, \hat{\dot{y}})$ numerically computed in the manner discussed above.

Inspection of the plot limits shown in Fig. 5 furnishes a convenient means for gauging the errors in the peak values of the predicted state variables and restoring force. Thus, it is seen that the ranges of "measured" y, $\dot{y}$, and g are $-2.34 \le y \le 2.33$, $-17.0 \le \dot{y} \le 16.8$, and $-222 \le g \le 219$, respectively, while the corresponding bounds for the predicted response $\hat{y}$, $\hat{\dot{y}}$, and $\hat{g}$ are $-2.66 \le \hat{y} \le 2.62$, $-20.0 \le \hat{\dot{y}} \le 19.4$, and $-201 \le \hat{g} \le 203$, respectively. The percentage errors in the peaks of the predicted $\hat{y}$, $\hat{\dot{y}}$, and $\hat{g}$ are ≈ 12, 15, and 14 percent, respectively.

The force-deflection curve shown in Fig. 5(*a*) (i.e., y versus $g(y, \dot{y})$) exhibits the hardening characteristics associated with the nonlinear Duffing oscillator for which the nonlinearity parameter b has a positive sign. Due to the presence of dissipative damping forces, the force-deformation curve encloses a net area proportional to the damping parameter c. Notice from Fig. 5(*b*) that the $\hat{y}$ versus $\hat{g}(\hat{y}, \hat{\dot{y}})$ obtained from the neural network exhibits the same hardening characteristics as well as the damping level of the exact measurements.

(3) Next, the network was tested under random excitation. This is a severe test of the network's modeling ability, since the training was performed under deterministic excitation of limited frequency content (± 10 percent of ω_n). The results of two wide-band random excitation tests are presented in Section 2.4.

2.4 Prediction Using Different Random Excitations. To investigate the validity of the identification results, a different probing signal was used to predict the response of the identified Duffing system. In the present test, wide-band random excitation, with Gaussian distribution, of the form $n(\mu, \sigma)$ where μ is the mean and σ is the standard deviation, was used as an excitation source:

$$u(t) = n(\mu, \sigma), \quad \mu = 0, \quad \sigma = 50. \tag{10}$$

Downloaded 03 May 2010 to 171.66.16.245. Redistribution subject to ASME license or copyright; see http://www.asme.org/terms/Terms_Use.cfm

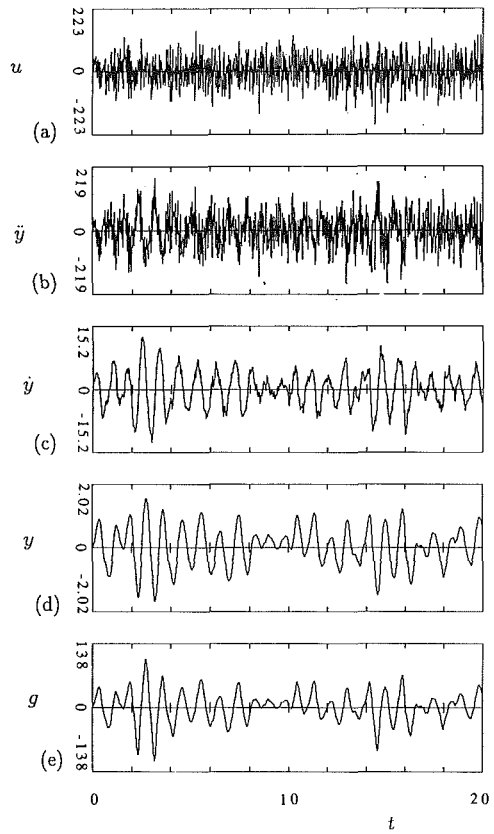


Fig. 6 Time history records of the nonlinear system excitation and response under wide band random excitation; (*a*) excitation, (*b*) acceleration, (*c*) velocity, (*d*) displacement, (*e*) restoring force

Time-history plots of the measured response are shown in Fig. 6 plotted in the same format used for Fig. 2. Here again, the duration of the test is roughly 20 system "periods." Comparison of the time histories of the probing signals $u(t)$ used in the swept-sine test shown in Fig. 2 and the random $u(t)$ used in the new test clearly reveals the difference in amplitude as well as the spectral content of these test signals.

Phase diagrams of the state variables and the restoring force corresponding to the time-history plots of Fig. 6 are shown in Fig. 7(a). These phase-plane plots clearly show the extent of the nonlinear response. Comparison of the three sets of plots in Fig. 5(a) with the corresponding ones in Fig. 7(a) shows that the motion range in this random test is within the bounds reached in the swept-sine test (here $-1.69 \le y \le 1.59$ compared to $-2.34 \le y \le 2.33$ in the swept-sine test). The peak displacement range in the random case is about 0.7 times the corresponding level used for identification (i.e., training the network).

Phase-plane plots are shown in Fig. 7(b) for the response $\hat{y}$ and $\hat{\dot{y}}$ predicted through the solution of the governing differential equation of motion Eq. (9), in conjunction with the identified representation of the restoring force g by the neural network counterpart $\hat{g}$, in the manner discussed in Section 2.3. Comparison of the corresponding sets of plots in Fig. 7(a) and Fig. 7(b) shows that the percentage errors in the peak values of the predicted $\hat{y}$, $\hat{\dot{y}}$, and $\hat{g}(\hat{y}, \hat{\dot{y}})$ are ≈ -4, -2, and -4 percent, respectively.

A comparison in the time domain between the "measured" response and identified response is shown in Fig. 8 in which the solid line refers to the exact measurements and the dashed line corresponds to the output of the neural network. The accuracy of the neural network predictions is so high as to make the two distinct curves in each of the plots practically indistinguishable.

To further demonstrate the range of validity of the identification results, another test using wide-band random excitation was conducted. In this test, the level of excitation was about twice the level shown in Fig. 6. The same steps used to generate Fig. 6, Fig. 7, and Fig. 8 were repeated again in conjunction with this new random excitation.

Phase diagrams of the state variables and the restoring force corresponding to the time history plots of this new random test are shown in Fig. 9(a). These phase-plane plots clearly show the extent of the increased nonlinear response compared to the previous random test. Comparison of the three sets of plots in Fig. 5(a) with the corresponding ones in Fig. 9(a) reveals that the motion range in the new random test significantly exceeds the bounds reached in the swept-sine test. The peak displacement range in this random case is about 1.3 times the corresponding level used for identification (i.e., training the network).

Since the motion range under this random excitation goes significantly beyond the range within which the neural network was trained, substantial errors arise in the prediction of the peak values of the response. Comparison of the corresponding sets of plots in Fig. 9(a) and Fig. 9(b) shows that the percentage errors in the peak values of the predicted $\hat{y}$, $\hat{\dot{y}}$, and $\hat{g}(\hat{y}, \hat{\dot{y}})$ are $\approx +14$, $+9$, and -40 percent, respectively. In other words, the predicted displacement and velocity overshoot the corresponding "measured" values, while the peak value of the predicted restoring force $\hat{g}$ undershoots the measured g by about 40 percent. As pointed out previously, this inaccurate estimate of g is due to the fact that the hardening nature of the Duffing oscillator makes the effective stiffness (and therefore, the restoring force) increase with increasing response levels. The range of displacement used for training the network spanned the range $-2.34 \le y \le 2.33$, $-17.0 \le \dot{y} \le 16.8$, while under random excitation the actual (measured) motion range is $-2.89 \le y \le 2.91$, $-23.3 \le \dot{y} \le 25.3$. Thus, here again the deviation between the measured and predicted response quantities reflect the cumulative effects of (significant) identification errors as well as propagation errors.

A comparison in the time domain between the "measured" response and identified response is shown in Fig. 10 in which the solid line refers to the exact measurements and the dashed line corresponds to the output of the neural network. Except in the peak motion range (which goes beyond the training range), the match between the measured and predicted results is very good. It is worth pointing out that, in spite of the large error in the peak value of $\hat{g}$, the network is capable of delivering a very accurate prediction of the response within about two "periods" after recovering from the overshoot in the range of g used for training (see the comparisons in the displacement and velocity shown in Fig. 10).

3 Discussion

3.1 Similarity to Nonparametric Identification Approaches. Before embarking on a discussion of the neural net computational procedure to identify nonlinear systems, it is worth summarizing the salient features of the authors' approach (Masri and Caughey, 1979). This summary will serve to demonstrate the remarkable qualitative similarities between what the authors' nonparametric identification approach does, and the way neural nets accomplish the identification of nonlinear systems.

The authors' nonparametric identification method, which does not require any information concerning the nature of the underlying nonlinearity,

(1) determines the optimum coefficients of a doubly indexed series in order to analytically construct a surface in three-dimensional space whose topography approximates the data set used for identification, and

Downloaded 03 May 2010 to 171.66.16.245. Redistribution subject to ASME license or copyright; see http://www.asme.org/terms/Terms_Use.cfm

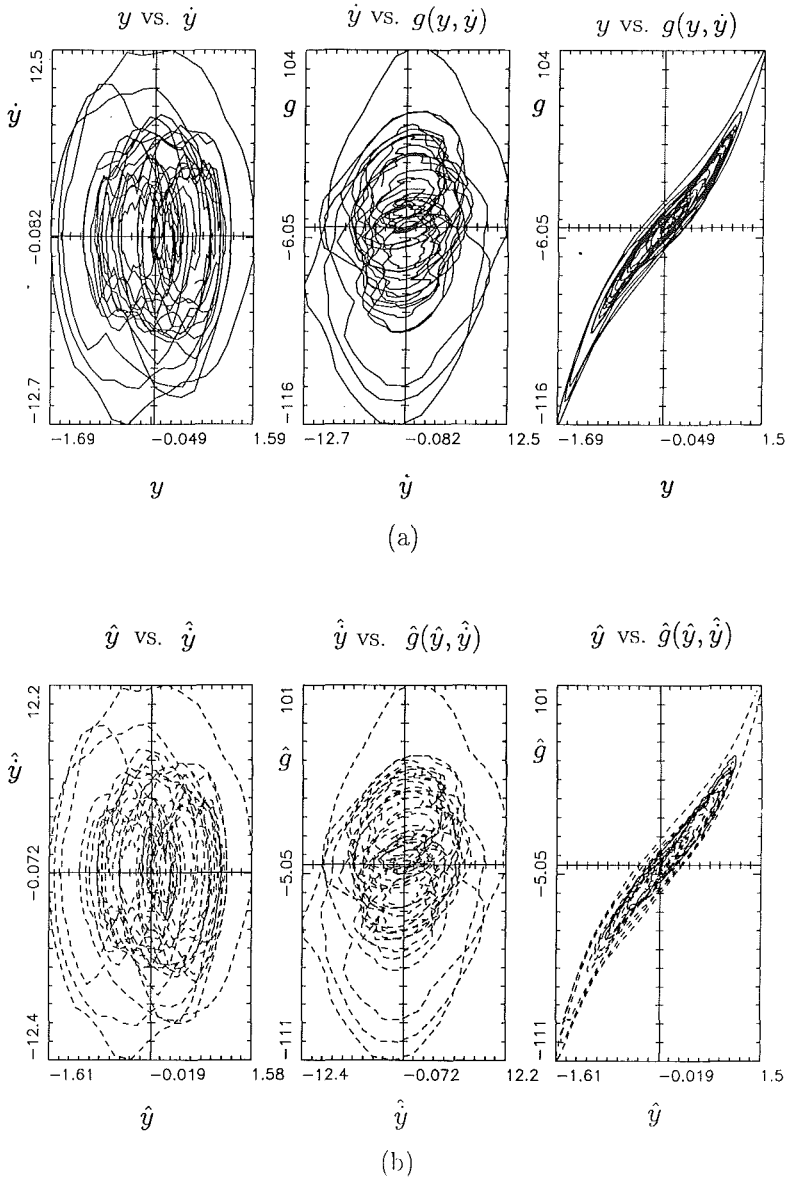


Fig. 7 State variable plots of the nonlinear system under the wide band random excitation used in Fig. 6; (*a*) response of exact nonlinear system, (*b*) response of the identified neural network

(2) uses interpolation techniques to estimate what the restoring force should be when given a new (i.e., not from the data set used for identification) set of coordinates in the state-space of the system.

Figure 11(*a*) shows a three-dimensional representation of the exact system restoring force g as a function of y and $\dot{y}$. The corresponding surface determined by using the aforementioned nonparametric approach is shown in Fig. 11(*b*), and the Chebyshev coefficients used by this approach to approximate the restoring function by the following expression:

$$g(y, \dot{y}) = \sum_{i=0}^{n_1} \sum_{j=0}^{n_2} C_{ij} T_i(y') T_j(\dot{y}'), \tag{11}$$

are shown in Fig. 12 together with the a_{ij} coefficients corresponding to the denormalized power series representation of Eq. (11):

$$g(y, \dot{y}) = \sum_{i=0}^{n_1} \sum_{j=0}^{n_2} a_{ij} y^i \dot{y}^j. \tag{12}$$

On the other hand, if the task of system identification through the use of neural nets is viewed as a curve fitting of the data in a high-dimensional space, then the main concepts in neural nets ("learning" and "generalization") are seen to be very similar to the aforementioned steps: starting with a complex data set obtained from a structure-unknown system, the neural net procedure,

(1) fits a surface in multidimensional space to the data set (the "learning" phase), and
(2) later on uses interpolation techniques at points where the training set does not have data points (the "generalization" phase).

Consequently, both methods accomplish essentially the same qualitative procedure using fundamentally different approaches. The surface $\hat{g}(y, \dot{y})$ obtained by using the neural network approach is shown in Fig. 11(*c*). The three figures are strikingly close to each other. The analogy between the nonparametric identification approach and the neural network

Downloaded 03 May 2010 to 171.66.16.245. Redistribution subject to ASME license or copyright; see http://www.asme.org/terms/Terms_Use.cfm

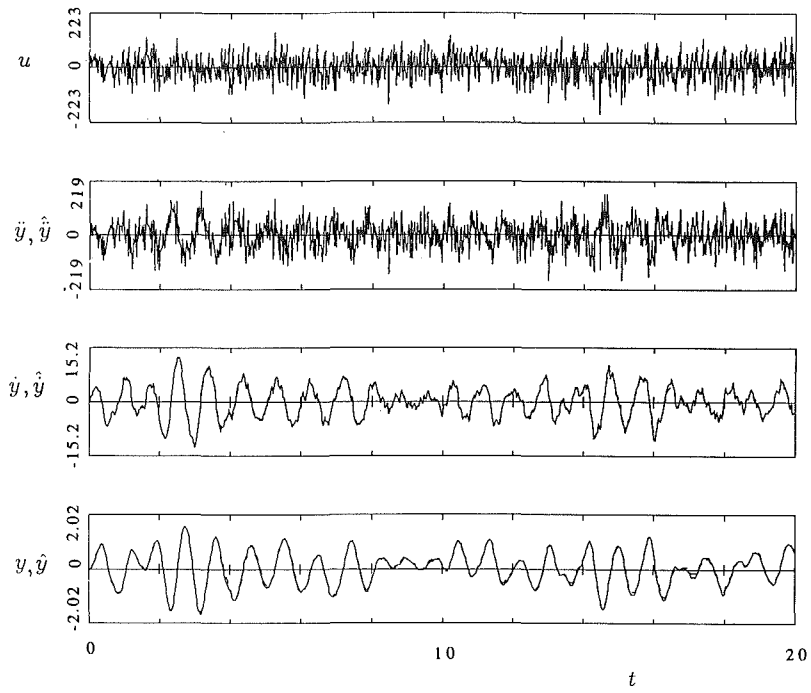


Fig. 8 Comparison between the response time histories of the exact nonlinear system and the identified neural network under wide band random excitation. Each plot shows two separate curves corresponding to the measured and predicted results. Solid line (——) is the exact response; dashed line (···) represents the predictions of the neural net.

procedure in characterizing structure-unknown nonlinear systems is tabulated in Fig. 13.

3.2 Computational Aspects of Identification by Neural Networks. A discussion of the computational aspects of identification by neural networks involves several issues related to:

(1) network size and network topology,
(2) training patterns and training procedures,
(3) number of iterations required for learning and factors affecting convergence, and
(4) meaning of the values of the weights.

Since the theory of artificial neural networks is still in its infancy and few analytical results are available, the answers to most of the questions enumerated above can be given only in a qualitative manner, drawing conclusions from experience and from experimentation with different neural network structures and training procedures.

The network topology plays a significant role in problem solving. It has been well known for quite some time that a net without hidden units cannot implement anything more than very simple logic gate arrangements. Minsky and Pappert (1969) proved that such a network cannot solve the simple *logic exclusive OR* (*XOR*) problem, unless hidden layers are introduced. It is clear that in order to be able to implement complicated logic functions and to be able to solve complex problems, the neural network needs to have one or more hidden layers. The network size is an important factor in the final performance. If the net is too small, then it is not able to store all the training patterns, due to an insufficient number of parameters. On the other hand, if the net is too large, then it does not "generalize": it tends to simply store the training patterns rather than performing interpolation. For the application presented here, it was decided that a neural network with two hidden layers be used, containing 15 nodes in the first hidden layer and 10 nodes in the second (see Fig. 4). This decision was made after extensive experimentation with several net sizes and topologies.

The training patterns were chosen so as to cover an extensive range of input/output values. For the present application, 100 training patterns were used, taken from the system input/output time history, sampled every 0.2 sec. It is seen that this training set is adequate to give a satisfactory network performance. During the learning process two different methods of feeding the training patterns into the net were tried:

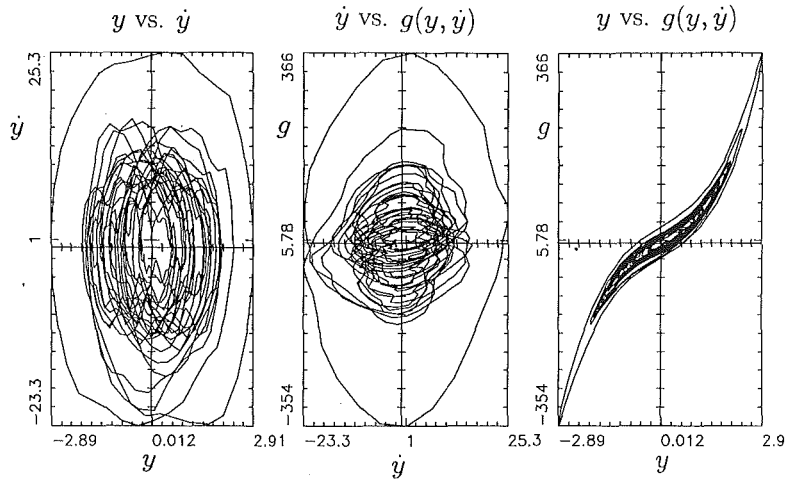
(1) Start with a random set of initial weights and then input the training patterns into the net one by one. For each pattern fed into the net,

(a) perform a forward pass using the initial set of weights,
(b) obtain the network response, and
(c) calculate the error for this particular pattern.

Repeat until all 100 patterns have been fed into the net. Then calculate the total error (over the whole set of 100 training patterns) and use it in the back propagation algorithm to obtain the updated set of weights. The process so far constitutes one iteration. Next repeat the procedure starting with the updated set of weights and keep iterating until an acceptable total error has been achieved or a predefined number of iterations has been reached.

(2) Start again with a random set of initial weights but now use a smaller set of training patterns (e.g., the first ten training patterns). Perform one iteration as described above using only these ten patterns: calculate the error for the ten patterns, back propagate it, and update the set of weights. Keep iterating until an acceptable error has been achieved. Then use this set of weights as the initial weight values for an enlarged training set (e.g., a set containing 20 training patterns: the first ten patterns plus the next ten patterns of the original training set). Now keep iterating and updating the weights using these 20 patterns until an acceptable error value is achieved.

Downloaded 03 May 2010 to 171.66.16.245. Redistribution subject to ASME license or copyright; see http://www.asme.org/terms/Terms_Use.cfm



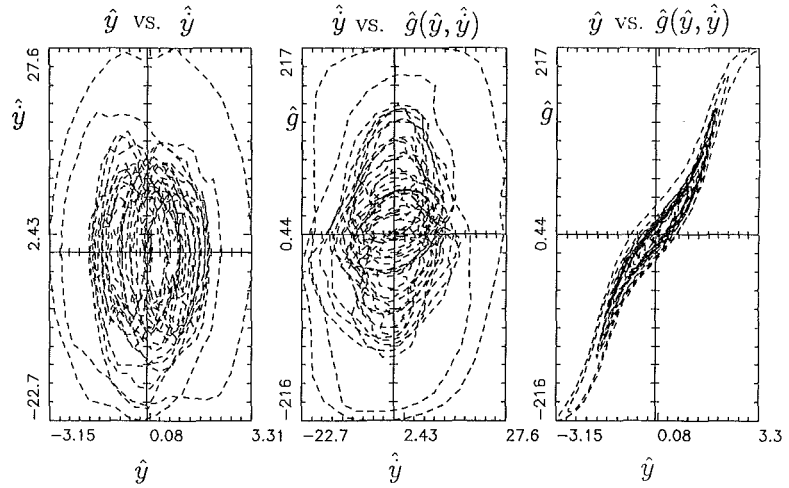


Fig. 9 State variable plots of the nonlinear system under wide band random excitation about twice the level used in Fig. 6; (*a*) response of exact nonlinear system, (*b*) response of the identified neural network

At this point, enlarge the training set by the next ten training pairs and keep repeating the process until all 100 patterns have been processed and an acceptable total error has been achieved or a predefined total number of iterations has been reached.

For the application presented here, both methods were used and were found to be almost equivalent in terms of speed of convergence and magnitude of total error. All the results presented herein correspond to method 1. For more complicated problems with a large number of training patterns, method 1 tends to stop at local minima of the parameter surface more often, and tends to produce higher total errors than method 2. Hence, for a large number of training patterns, method 2 is the method of choice.

During the validation phase, the network is given new patterns (i.e., patterns not contained in the training set) and its response is evaluated. It is noted that the net performs very well as long as the values of the new patterns do not exceed the range used for training (Fig. 6). However, the net loses some of its "generalization" ability if the values of the new patterns exceed the range of values used for training (Fig. 10).

The number of iterations required to achieve a specified error value depends on the net topology and size, the training set, and the training algorithm. For the application at hand, the effect of the learning rate η on the total number of iterations and on the speed of convergence was examined (Fig. 14). Five values of η were tested: $\eta = 0.005$, 0.01, 0.03, 0.04, 0.10. The maximum acceptable error value was set to 0.02 (total error for 100 patterns) and the training algorithm was tested for all five values of η. All training sessions started from the same random values of the initial weight set. It is seen in Fig. 14(*a*) that all five learning curves have similar characteristics: they start from the same total error value and go through a plateau phase during which the error remains almost constant. Then there is a very sudden drop in the error value, an indication that learning has taken place. It is observed, as expected, that a smaller η will give a slower convergence rate (e.g., for $\eta = 0.005$ the plateau phase lasts for about 70 iterations, whereas for $\eta = 0.10$, the plateau phase lasts for only ten iterations). It is also observed that a high η will reduce the error in an oscillatory manner, whereas a small η reduces the error smoothly. The differences in convergence and total error between the various learning rates are also shown in Fig. 14(*b*) for $\eta = 0.005$, 0.01, 0.03, 0.04.

It is of particular interest to observe the behavior of the

Downloaded 03 May 2010 to 171.66.16.245. Redistribution subject to ASME license or copyright; see http://www.asme.org/terms/Terms_Use.cfm

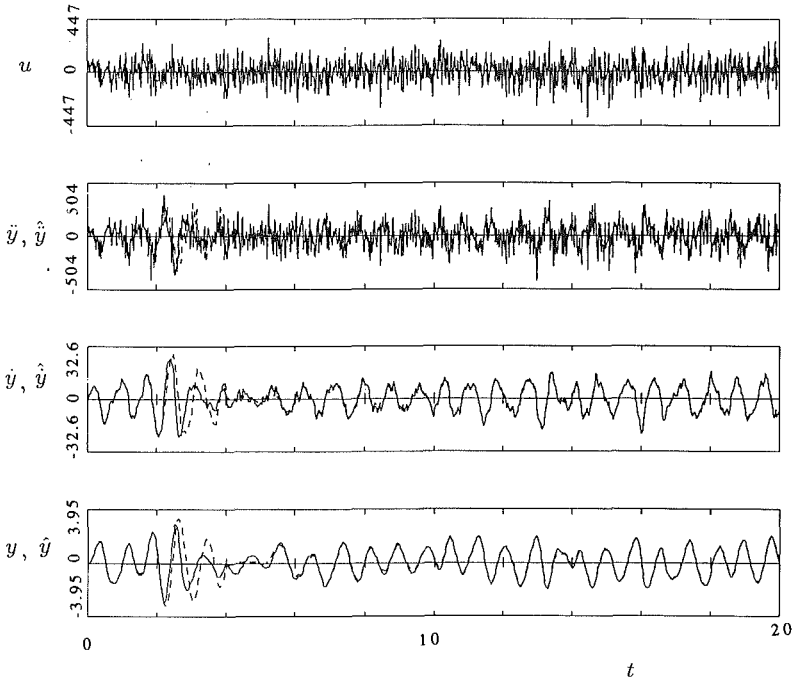


Fig. 10 Comparison between the response time histories of the exact nonlinear system and the identified neural network under wide band random excitation about twice the level used in Fig. 6. Each plot shows two separate curves corresponding to the measured and predicted results. Solid line (——) equals exact response; dashed line (- - -) equals predictions of the neural net.

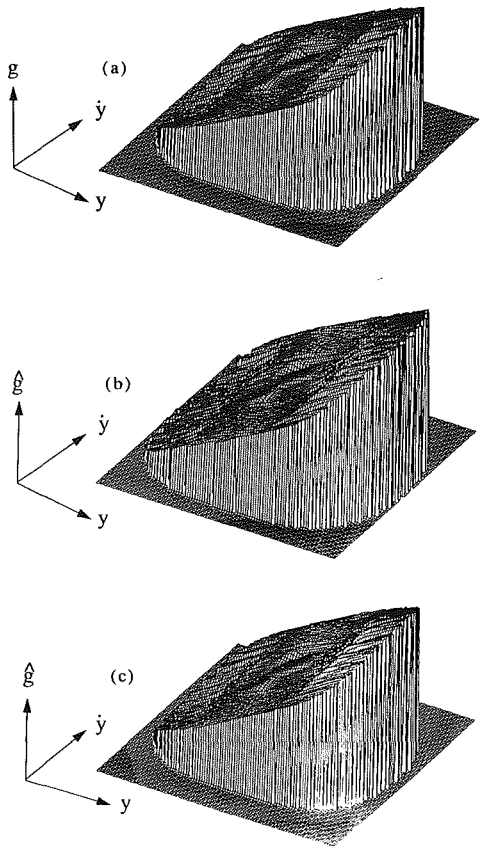


Fig. 11 Three-dimensional representation of the variation of the system restoring force *g* as a function of the system state variables *y* and *ẏ* under the swept sine excitation used in Fig. 2; (*a*) measured *g*, (*b*) estimated *g* using the nonparametric identification approach, (*c*) estimated *g* using the neural net in Fig. 3.

Chebyshev C_{ij} Coefficients

$$g(y,\dot{y}) = \sum_{i=0}^{n_1}\sum_{j=0}^{n_2} C_{ij}T_i(y')T_j(\dot{y}')$$

y_{min} = -2.341D+00 y_{max} = 2.326D+00
$\dot{y}_{min}$ = -1.700D+01 $\dot{y}_{max}$ = 1.678D+01

	$T_0(\dot{y}')$	$T_1(\dot{y}')$
$T_0(y')$	-2.094D+00	2.119D+01
$T_1(y')$	1.855D+02	1.255D-02
$T_2(y')$	3.905D-01	5.033D-01
$T_3(y')$	2.700D+01	-6.941D-02

(a)

Power Series a_{ij} Coefficients

$$g(y,\dot{y}) = \sum_{i=0}^{n_1}\sum_{j=0}^{n_2} a_{ij}y^i\dot{y}^j$$

	$\dot{y}^0$	$\dot{y}^1$
y^0	-2.032D+00	1.225D+00
y^1	4.477D+01	5.760D-03
y^2	3.285D-01	1.092D-02
y^3	8.499D+00	-1.294D-03

(b)

Fig. 12 Nonparametric identification results for the Duffing oscillator; (*a*) Chebyshev coefficients; (*b*) denormalized power series coefficients

Downloaded 03 May 2010 to 171.66.16.245. Redistribution subject to ASME license or copyright; see http://www.asme.org/terms/Terms_Use.cfm

total error for $\eta = 0.10$. The high value of η reduces the error very fast: the plateau phase lasts for about ten iterations and the error is reduced to very low values in about 50 iterations, albeit in a very oscillatory manner. From Fig. 14(*c*) it is seen that the error reaches a minimum point several times but does not converge to any particular value: in a few iterations after reaching the minimum, the error jumps back to a maximum value (sometimes to a value which is even larger than the initial error).

For an explanation of such a behavior one has to take into account the shape of the error function: this is a quadratic function in the parameter space. For the application at hand, we use 216 adjustable weights (including the node biases), hence the error surface is a nonlinear surface in a 216-dimensional space. This surface contains many local minima, and it is precisely one of those local minima that the back propagation algorithm eventually converges to. However, if the value of η is too high, the algorithm bounces from one local minimum to another, resulting in a behavior similar to that of Fig. 14(*c*).

Before a qualitative interpretation of the final set of weights is given, it should be noted that the neural network contains a *distributed internal representation* of the system under identification (i.e., a representation which is not described by a few coefficients but which is distributed over the nodes and links of the hidden layers). Although the physical meaning of the input and output nodes is clear (i.e., displacement y and velocity $\dot{y}$ for input modes, and $g(y, \dot{y})$ for the output node), the physical meaning of the intermediate layer nodes is hidden due to the distributed nature of the system representation.

Item	Nonparametric Identification	Neural Network Identification
Assumptions regarding structure of system	None	None
Selection	Type of basis functions	Topology of network
Representation	Coefficients C_{ij} used	Weights W_{ij}^k
Order	Number of coefficients C_{ij} used	Number of layers and nodes
Identification ("Learning")	Determine optimum coefficients C_{ij} of doubly-indexed series to define restoring force surface	Train network to find optimum weights W_{ij}^k to reduce least-squares error
Prediction ("Generalization")	Use interpolation to predict an estimate of the restoring force g: $g(y,\dot{y}) = \sum_{i=0}^{n_1}\sum_{j=0}^{n_2} C_{ij}T_i(y')T_j(\dot{y}')$	Use interpolation to predict an estimate of g from input-output mapping: $g(y,\dot{y}) = N_3N_2N_1(y,\dot{y})$

Fig. 13 Analogy between the nonparametric identification approach and the neural network procedure in characterizing structure-unknown nonlinear systems

In Fig. 15 the optimal values of the weights and biases are shown in a set of self-explanatory plots. A comparison of these weight plots reveal that the set of weights connected to the displacement input y (column 1 of matrix W^1), is one order of magnitude larger than the set of weights connected to the velocity input $\dot{y}$ (column 2 of matrix W^2). This reflects the fact that the range of the y values is one order of magnitude smaller than the range of the $\dot{y}$ values (see Fig. 2). Since both the y and $\dot{y}$ terms have a significant contribution to the output $\hat{g}(y, \dot{y})$, the algorithm assigns larger weights to the smaller input so as to amplify its contribution to the final output. As

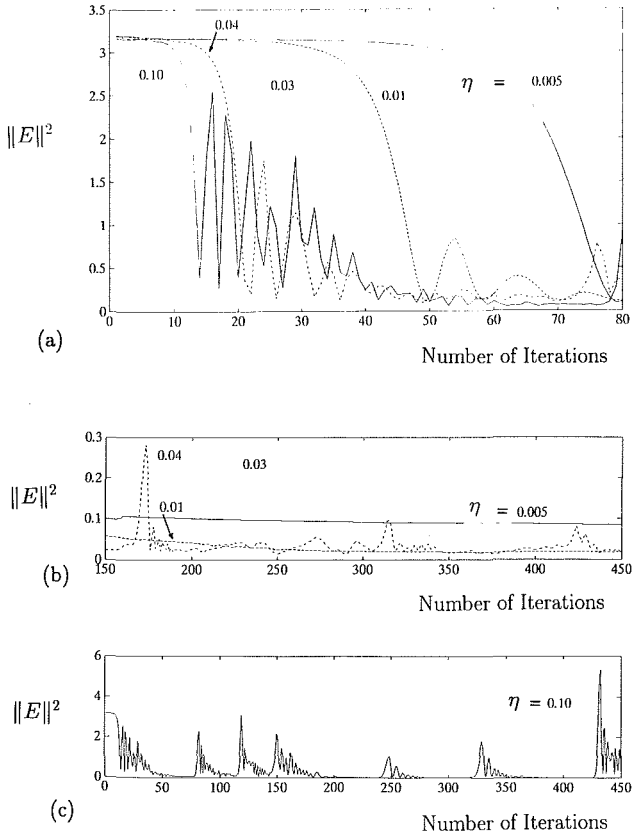


Fig. 14 Effects of learning rate η on the convergence rate; (*a*) comparison for the first 80 iterations ($\eta = 0.005, 0.01, 0.03, 0.04, 0.10$), (*b*) comparison over 450 iterations ($\eta = 0.005, 0.01, 0.03, 0.04$), (*c*) error variation for $\eta = 0.10$ over 450 iterations

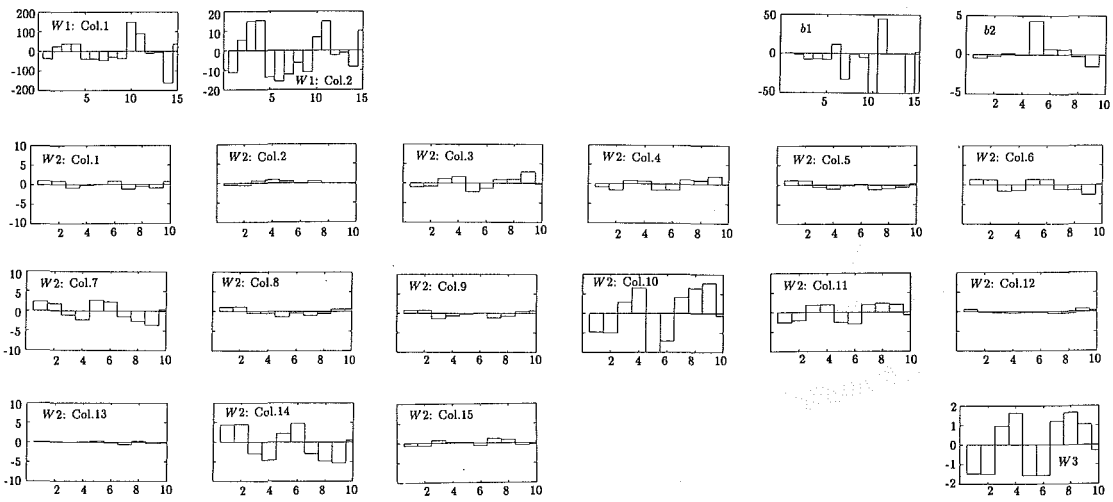


Fig. 15 Network weights and biases

Downloaded 03 May 2010 to 171.66.16.245. Redistribution subject to ASME license or copyright; see http://www.asme.org/terms/Terms_Use.cfm

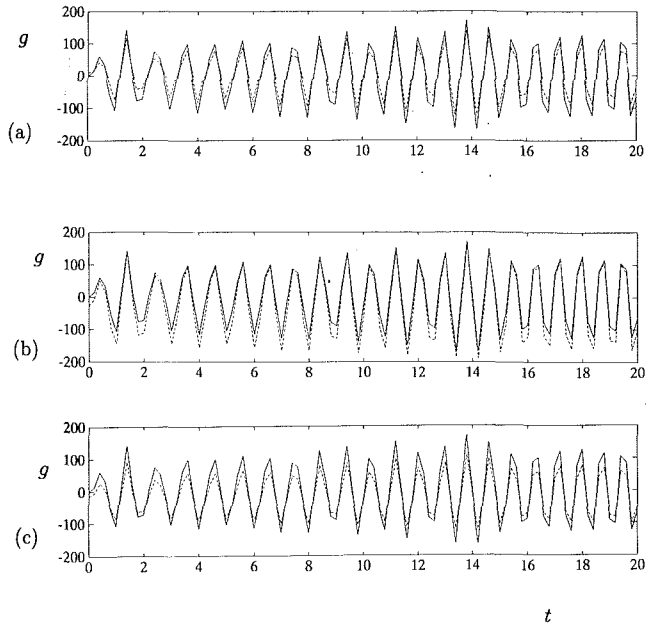


Fig. 16 Effects of severing network connections on performance. Solid line (——) equals exact response; dashed line (···) equals predictions of the neural net; (*a*) cutting off links corresponding to columns 1-5 of W^2, (*b*) cutting off links corresponding to columns 5-9 of bias b^1, (*c*) cutting off links corresponding to rows 1-3 of W^2

far as the weights of the hidden layers are concerned, no qualitative explanation of their values is readily available, since no clear physical meaning can be attached to the hidden units.

3.3 Fault Tolerance. An important issue concerning practical applications is the degree of fault tolerance of the neural network. It will be shown that the net is robust even when a significant portion of its has been "damaged." In order to investigate the network robustness, several connections between nodes were cut off and the network performance tested.

First of all, the connections going out of nodes 1 through 5 of the first hidden layer were severed. This corresponds to setting all the weights in columns 1 through 5 of matrix W^2 equal to zero (a total of 50 weights). These weights constitute a significant portion of the weight set (50 links were severed out of a total of 190 weight links). However, due to the distributed nature of the system representation, the neural network is inherently robust. The performance in predicting the value of the function $g(y, \dot{y})$ remains within acceptable limits as seen from Fig. 16(*a*).

Similar results are obtained if some of the bias terms are set equal to zero, or if other links are severed: In Fig. 16(*b*) the biases corresponding to nodes 5 through 9 of first hidden layer are set to zero and in Fig. 16(*c*) the links corresponding to rows one through three of matrix W^2 were cut off. The performance remains acceptable in both cases.

4 Summary and Conclusions

This exploratory study demonstrates that artificial neural networks can be used very effectively for the identification of the internal (restoring) forces of some typical nonlinear structural systems. It is shown that employing a three-layer net with two inputs, one output, and 15 and 10 nodes in the first and second hidden layers, respectively, is adequate to characterize the internal force in the damped Duffing oscillator of the demonstration example. Training of the net is performed under deterministic swept-sine excitation. The neural net is validated as a system identifier under stochastic excitation by using sequences of input vectors different than those used for training.

It is demonstrated that the neural network identification procedure uses the concepts of "learning" and "generalization" to accomplish essentially the same tasks that are performed in a qualitatively similar nonparametric identification procedure previously developed by the authors. It is also shown that the computational aspects of identification by neural networks involves several key issues related to the network size and topology, the training patterns and procedures, and parameters that influence the convergence criteria.

5 Acknowledgments

This study was supported in part by the National Science Foundation and by the Carpenters/Contractors Cooperation Committee, Inc.

References

Albus, J. S., 1975, "A New Approach to Manipulator Control: The Cerebellar Model Articulation Controller (CMAC)," ASME *Journal of Dynamic Systems, Measurement, and Control*, Vol. 97, pp. 220–227.

Aleksander, I., and Morton, H., 1990, *An Introduction to Neural Computing*, Chapman and Hall, London.

Grossberg, S., 1976, "Adaptive Pattern Recognition and Universal Recording: Part I, Parallel Development and Coding of Neural Feature Detectors," *Biol. Cybern.*, Vol. 23, pp. 121–134.

Hebb, D. O., 1949, *The Organization of Behaviour*, John Wiley and Sons, New York.

Hinton, G. E., Sejnowski, T. J., and Ackley, D., 1984, *Boltzmann Machines: Constraint Satisfaction Networks that Learn*, Tech. Rep. CMU CS-84, 111, Carnegie-Mellon University, Pittsburgh, PA.

Hopfield, J. J., 1982, "Neural Networks and Physical Systems with Emergent Collective Properties," *Proc. Nat. Acad. Sci. USA*, Vol. 79, pp. 2554–2558.

Khanna, T., 1990, *Foundations of Neural Networks*, Addison-Wesley, Reading, MA.

Kohonen, T., 1984, *Self Organization and Associative Memory*, Springer-Verlag, Heidelberg.

Lippmann, R. P., 1987, "An Introduction to Computing with Neural Nets," *IEEE ASSP Mag.*, Apr., pp. 4–22.

Masri, S. F., and Caughey, T. K., 1979, "A Nonparametric Identification Technique for Nonlinear Systems," ASME JOURNAL OF APPLIED MECHANICS, Vol. 46, No. 2, June, pp. 433–447.

McCulloch, W. S., and Pitts, W. H., 1943, "A Logical Calculus of the Ideas Imminent in Nervous Activity," *Bulletin of Mathematical Biophysics*, Vol. 5, pp. 115–133.

McLelland, J. L., and Rumelhart, D. E., 1986, *Parallel Distributed Processing*, Vol. 1, MIT Press, Cambridge, MA.

McLelland, J. L., and Rumelhart, D. E., 1987, *Explorations in Parallel Distributed Processing*, MIT Press, Cambridge, MA.

Mead, C., 1989, *Analog VLSI for Neural Systems*, Addison-Wesley, New York.

Minsky, M., and Papert, S., 1969, *Perceptrons: an Introduction to Computational Geometry*, MIT Press, Cambridge, MA.

Narendra, K. S., and Parthasarathy, K., 1990, "Identification and Control of Dynamical Systems Using Neural Networks," *IEEE Transactions of Neural Networks*, Vol. 1, No. 1, Mar., pp. 4–27.

Nelson, M. M., and Illingworth, W. T., 1991, *A Practical Guide to Neural Nets*, Addison-Wesley, Reading, MA.

Nguyen, D. H., and Widrow, B., 1990, "Neural Networks for Self Learning Control Systems," *IEEE Control Systems Magazine*, Vol. 10, No. 3, Apr., pp. 18–23.

Rosenblatt, F., 1962, *Principles of Neurodynamics: Perceptrons and the Theory of Brain Mechanisms*, Spartan Books, New York.

Werbos, P., 1974, "Beyond Regression: New Tools for Prediction and Analysis in the Behavioral Sciences," Ph.D. Thesis, Harvard University.

Widrow, B., 1962, "Generalization and Information Storage in Networks of ADALINE Neurons," *Self Organizing Systems*, G. T. Yovits, ed., Spartan Books, New York.

Downloaded 03 May 2010 to 171.66.16.245. Redistribution subject to ASME license or copyright; see http://www.asme.org/terms/Terms_Use.cfm

Vibrations of Sectorial Plates Having Corner Stress Singularities

A. W. Leissa
Department of Engineering Mechanics,
Fellow ASME.

O. G. McGee
Department of Civil Engineering.

C. S. Huang
Department of Engineering Mechanics.

Ohio State University,
Columbus, OH 43210

A procedure is presented for determining the free vibration frequencies and mode shapes of sectorial plates having re-entrant corners (i.e., vertex angles exceeding 180 degrees). No correct results for such problems have been found in the vast literature of plate vibrations. The procedure is applicable to sectorial plates having arbitrary (but continuous) boundary conditions (e.g., clamped, simply supported, or free) along the two radial edges and the circular edge. It is based upon the Ritz method, but utilizes two sets of admissible functions simultaneously. One set consists of algebraic-trigonometric polynomials. The other is the set of corner functions derived by Williams (1952) to deal with the bending stress singularities which may arise at the corner when the vertex angle becomes large. The method is demonstrated for sectorial plates having all edges simply supported, which yields the strongest singularity in a re-entrant corner. Frequencies are compared with those obtained from an analytical solution involving Bessel functions. It is shown that the latter solution is invalid for re-entrant corners. Analytical solutions are also obtained for annular sectorial plates having very small ratios of inner to outer boundary radii. These solutions are found to be consistent with those using polynomials and corner functions. Accurate fundamental frequency data is presented for simply supported sectorial plates having three values of Poisson's ratio (0, 0.3, 0.5) and the full range of vertex angles ($0 < \alpha \leq 360$ deg).

Introduction

The literature of free vibrations of plates is vast, with approximately 500 publications appearing before 1966 (Leissa, 1969) and at least 1500 since then. Relatively little is available for sectorial plates, consisting of two radial and one circular edge (see Fig. 1). A procedure for obtaining exact frequencies when the radial edges are both simply supported, with arbitrary conditions on the circular edge (e.g., clamped, simply supported, or free) is described in the monograph by Leissa (1969). This utilizes the well-known Bessel function solutions for complete circular plates, except that the functions are generally of non-integer order. An equivalent procedure was later used by Rubin (1975); however, the Frobenius method was employed to generate the radial functions, instead of using the Bessel functions. Previously, Westmann (1962) adopted a single-term approximation to the mode shape along with the Rayleigh method to obtain a crude estimate of the fundamental frequency when the radial sides are simply supported and the circular one is free.

A few vibration results are available for sectorial plates having both radial edges clamped. Ben-Amoz (1959) employed the Rayleigh-Ritz method to obtain the approximate fundamental frequency of the circular edge clamped, and Westmann (1962) did likewise for the circular edge free. Rubin (1975) also used a Kantorovich-like energy method to treat the completely clamped case. Bhattacharya and Bhowmic (1975) demonstrated the use of the Kantorovich method for all three cases when the circular boundary is either clamped, simply supported or free, and reported numerical results for the special case of the semicircular plate ($\alpha = 180$ deg). Experimental results were offered by Maruyama and Ichinomiya (1981) for completely

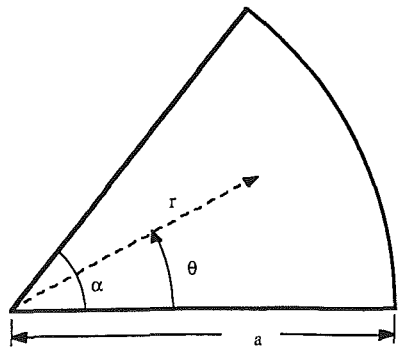


Fig. 1 Sectorial plate

Contributed by the Applied Mechanics Division of THE AMERICAN SOCIETY OF MECHANICAL ENGINEERS for publication in the ASME JOURNAL OF APPLIED MECHANICS.

Discussion on this paper should be addressed to the Technical Editor, Professor Lewis T. Wheeler, Department of Mechanical Engineering, University of Houston, Houston, TX 77204-4792, and will be accepted until four months after final publication of the paper itself in the ASME JOURNAL OF APPLIED MECHANICS.

Manuscript received by the ASME Applied Mechanics Division, June 26, 1991; final revision, Oct. 5, 1991. Associate Technical Editor: S. K. Datta.

Copyright © 1993 by ASME
Downloaded 03 May 2010 to 171.66.16.245. Redistribution subject to ASME license or copyright; see http://www.asme.org/terms/Terms_Use.cfm

Table 1 Characteristic equations for the eigenvalues λ_k of the corner functions W^*_{ck}

Edge conditions		Characteristic equation
$\theta=0$	$\theta=\alpha$	
s s	s s	$\cos\alpha\lambda = \mp\cos\alpha$
clamped	free	$\sin^2\alpha\lambda = \frac{4}{(3+\upsilon)(1-\upsilon)} - \left(\frac{1-\upsilon}{3+\upsilon}\right)\lambda^2\sin^2\alpha$
s s	free	$\sin 2\alpha\lambda = -\left(\frac{1-\upsilon}{3+\upsilon}\right)\lambda\sin 2\alpha$
clamped	s s	$\sin 2\alpha\lambda = \lambda\sin 2\alpha$
free	free	$\sin\alpha\lambda = \mp\left(\frac{1-\upsilon}{3+\upsilon}\right)\lambda\sin\alpha$
clamped	clamped	$\sin\alpha\lambda = \pm\lambda\sin\alpha$

clamped sectorial plates, determined by means of time-averaged holographic inferometry. Finally, one should not overlook the experimental nodal patterns obtained by Mary Waller (1952) for a completely free semi-circular plate.

In all of the previous research described above, no results are found for sectorial plates with included angles (α) exceeding 180 deg, that is, having corners which are re-entrant rather than salient. For such angles bending stress singularities exist, resulting from infinite bending moments, as was shown by Williams (1952) in his classic paper. Indeed, when the radial edges are both simply supported, the singularity exists for $\alpha > 90$ deg. These boundary conditions yield the strongest singularities.

In the present paper a procedure is presented for determining the free vibration frequencies and mode shapes of sectorial plates having arbitrary (but continuous) edge conditions. Using classical thin plate theory and the Ritz method, two sets of admissible transverse displacement functions are *simultaneously* employed; i.e., algebraic-trigonometric polynomials and the Williams corner functions. It will be shown that both sets of functions are typically needed to yield accurate results when the stress singularity exists at the vertex. The procedure is demonstrated for sectorial plates with radial edges simply supported, thereby obtaining the first known correct and accurate vibration data for sectorial plates having $\alpha > 180$ deg.

Method of Analysis

In terms of the polar coordinates (r, θ) shown in Fig. 1, the vibratory transverse displacement of the sectorial plate is $w = w(r, \theta, t)$, where t is time. For free vibrations, assuming

$$w(r, \theta, t) = W(r, \theta)\sin\omega t, \tag{1}$$

the maximum strain energy due to bending during the vibratory cycle is

$$V_{\max} = \frac{D}{2}\int\int_A [(\kappa_r+\kappa_\theta)^2 - 2(1-\nu)(\kappa_r\kappa_\theta - \kappa_{r\theta}^2)]dA \tag{2}$$

where $D = Eh^3/12(1-\nu^2)$ is the flexural rigidity and κ_r, κ_θ, and $\kappa_{r\theta}$ are the maximum bending and twisting curvatures:

$$\kappa_r = \frac{\partial^2 W}{\partial r^2},\ \kappa_\theta = \frac{1}{r}\frac{\partial W}{\partial r} + \frac{1}{r^2}\frac{\partial^2 W}{\partial\theta^2},\ \kappa_{r\theta} = \frac{\partial}{\partial r}\left(\frac{1}{r}\frac{\partial W}{\partial\theta}\right). \tag{3}$$

The maximum kinetic energy is

$$T_{\max} = \frac{\rho\omega^2}{2}\int_A\int W^2 dA \tag{4}$$

where ρ is the mass per unit area of the plate.

Displacement trial functions are assumed as the sum of two finite sets

$$W = W_p + W_c, \tag{5}$$

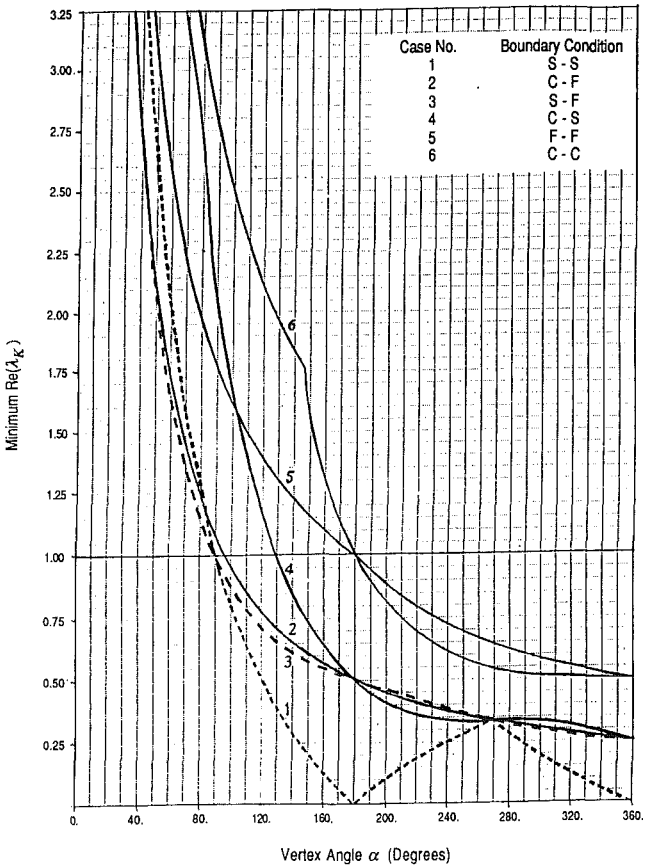


Fig. 2 Variation of minimum values of Re(λ_k) with vertex angle α

where W_p are algebraic-trigonometric polynomials and W_c are corner functions. The polynomials may be written as

$$W_p = G(r)\sum_m\sum_n A_{mn}r^m F_n(\theta) \tag{6}$$

where A_{mn} are undetermined coefficients, $F_n(\theta)$ are functions satisfying the geometric boundary conditions along $\theta = 0$ and $\theta = \alpha$, and

$$G(r) = \begin{cases} 1, \text{ for a free circular boundary} \\ a-r, \text{ for a simply supported circular boundary} \\ (a-r)^2, \text{ for a clamped circular boundary.} \end{cases} \tag{7}$$

Thus, W_p satisfies the geometric conditions on all the boundaries.

The corner functions may be written as

$$W_c = G(r)\sum_{k=1}^{K} B_k W^*_{ck} \tag{8}$$

where B_k are arbitrary coefficients, and W^*_{ck} are solutions of the biharmonic, static equilibrium equation for plate bending

$$\nabla^4 W^*_{ck} = 0. \tag{9}$$

The latter are written here in the form used by Williams (1952):

$$W^*_{ck} = r^{\lambda_k+1}[a_k\sin(\lambda_k+1)\theta + b_k\cos(\lambda_k+1)\theta + c_k\sin(\lambda_k-1)\theta + d_k\cos(\lambda_k-1)\theta]. \tag{10}$$

The values λ_k are the set of eigenvalues of the fourth-order characteristic determinant arising from applying the boundary conditions at $\theta = 0$ and $\theta = \alpha$. The eigenvector components b_k/a_k, c_k/a_k, and d_k/a_k are determined by back substitution of the λ_k into the boundary conditions. The characteristic equations yielding the roots λ_k are listed in Table 1. Generally, the roots are complex. Figure 2 is a plot of the minimum real parts

Downloaded 03 May 2010 to 171.66.16.245. Redistribution subject to ASME license or copyright; see http://www.asme.org/terms/Terms_Use.cfm

of λ_k arising from the characteristic equations, as presented by Williams (1952) for $0 < \alpha \leq 180$ deg, and extended here to the range 180 deg $< \alpha \leq 360$ deg so as to be useful for all angles. Inasmuch as the bending and twisting moments (per unit length) are

$$M_r = -D(\kappa_r + \nu\kappa_\theta),\ M_\theta = -D(\kappa_\theta + \nu\kappa_r),\ M_{r\theta} = -D(1-\nu)\kappa_{r\theta}, \tag{11}$$

it is clear from Eqs. (3) and (10) that the moments become infinite (i.e., singular) for the real part of $\lambda_k < 1$. In Fig. 2 it is seen that the moment singularities arise for $\alpha > 90$ deg in Cases 1 and 3, for $\alpha > 95$ deg in Case 2, for $\alpha > 128$ deg in Case 4, and for $\alpha > 180$ deg in Cases 5 and 6. Values of the real part of $\lambda_k < 0$ also exist, but are not used. For such values the slope $(\partial W/\partial r)$ becomes infinite at $r = 0$, and the strain energy integral (2) becomes unbounded. Use of the corner functions W_c in conjunction with the polynomials W_p permits proper representation of the corner stress singularities when they exist.

The free vibration problem is formulated by substituting Eqs. (6)–(10) into (2)–(5) and employing the minimizing equations.

$$\frac{\partial}{\partial A_{mn}}(V_{\max} - T_{\max}) = 0$$

$$\frac{\partial}{\partial B_k}(V_{\max} - T_{\max}) = 0 \tag{12}$$

This results in a set of homogeneous algebraic equations in the constants A_{mn} and B_k. Setting the determinant of the coefficient matrix equal to zero yields the eigenvalues, which are nondimensional frequency parameters. Eigenvectors and associated mode shapes are determined in the usual manner by substituting the eigenvalues back into the homogeneous equations. The frequencies are guaranteed to be upper bounds on the exact values.

The Simply Supported Sectorial Plate

The method described in the previous section will now be demonstrated for the sectorial plate having all edges simply supported. This problem is chosen partly because it yields the strongest singularities when $\alpha > 180$ deg, as may be seen from Fig. 2.

Using the coordinate system of Fig. 1, the axis $\theta = 0$ is a symmetry axis. Therefore, all free vibration modes are either symmetric or antisymmetric with respect to this axis.

For the symmetric modes the polynomials of Eqs. (5) and (6) are taken as

$$W_p = G(r) \sum_{m=2}^{M} \sum_{n=0}^{N} A_{mn} r^m \cos[(2n+1)\pi\theta/\alpha]. \tag{13}$$

For the antisymmetric modes they are

$$W_p = G(r) \sum_{m=2}^{M} \sum_{n=1}^{N} A_{mn} r^m \sin[(2n\pi\theta/\alpha]. \tag{14}$$

Here, $G(r)$ is the second of the three functions given in Eq. (7). Equations (13) and (14) then satisfy *all* the boundary conditions ($W = M_\theta = 0$) along the radial edges $\theta = \pm\alpha/2$, and only the geometric boundary condition ($W = 0$) along the circular edge $r = a$. Moreover, it has been shown that the functions given by Eqs. (13) and (14) are mathematically complete as M and N become sufficiently large (Huang, 1991). The index m begins with 2 in Eqs. (13) and (14) to eliminate possible singularities in the polynomials and to permit the strain energy function (2) to be integrable.

For the symmetric modes the corner functions of Eqs. (5), (8), and (10) become

$$W_c = G(r) \sum_{k=1}^{K} B_k r^{\lambda_k + 1} \times \left\{ \frac{\cos[(\lambda_k - 1)\alpha/2]}{\cos[(\lambda_k + 1)\alpha/2]} \cos(\lambda_k + 1)\theta - \cos(\lambda_k - 1)\theta \right\} \tag{15}$$

where the λ_k are the roots of the characteristic equation $\cos\alpha\lambda = -\cos\alpha$ (see Table 1) and $G(r)$ is again taken from Eq. (7). For the antisymmetric modes they are

$$W_c = G(r) \sum_{k=1}^{K} B_k r^{\lambda_k + 1} \times \left\{ \frac{\sin[(\lambda_k - 1)\alpha/2]}{\sin[(\lambda_k + 1)\alpha/2]} \sin(\lambda_k + 1)\theta - \sin(\lambda_k - 1)\theta \right\} \tag{16}$$

where now the λ_k are the roots of $\cos\alpha\lambda = \cos\alpha$.

The characteristic equations for the λ have closed form, exact solutions for the case when the radial edges are both simply supported; viz., for the symmetric modes

$$\lambda_p = \begin{cases} [(2p+1)\pi/\alpha] \pm 1, & \text{for } 0 \leq \alpha \leq 180 \text{ deg} \\ [(2p \pm 1)\pi/\alpha] + 1, & \text{for } 180 \text{ deg} \leq \alpha \leq 360 \text{ deg}, \end{cases} \tag{17}$$

where $p = 0, 1, 2, 3, \ldots$, and for the antisymmetric modes

$$\lambda_p = (2p\pi/\alpha) \pm 1, \text{ for all } \alpha, \tag{18}$$

where $p = 0, 1, 2, 3, \ldots$. The special case when $\lambda = 1$ yields a trivial solution for W_{ck}^* in Eq. (10), except for $\alpha = 90$ deg and 270 deg in the symmetric modes and $\alpha = 180$ deg in the antisymmetric modes.

Substituting Eqs. (13)–(18) in (2)–(5), and utilizing the minimizing Eqs. (12) yields the frequencies and mode shapes for both the symmetric and antisymmetric modes.

Analytical Solutions

Although the method described in the preceding sections may be used to obtain properly convergent solutions for sectorial plates having arbitrary boundary conditions, a more simple exact solution procedure was described by Leissa (1969) for plates having the radial edges simply supported.

The differential equation of motion for free vibrations is

$$D\nabla^4 W - \rho\omega^2 W = 0. \tag{19}$$

Its solution is

$$W(r, \theta) = [C_1 J_\mu(kr) + C_2 Y_\mu(kr) + C_3 I_\mu(kr) + C_4 K_\mu(kr)]\cos\mu\theta \tag{20}$$

where $k^2 = \omega\sqrt{\rho/D}$, and the J_μ, Y_μ, I_μ, and K_μ are standard and modified Bessel functions. This solution is also applicable to closed circular and annular plates. For such problems μ takes on integer values 0, 1, 2, ... In the case of a sectorial plate having the radial edges simply supported, the boundary conditions $W = M_\theta = 0$ are satisfied along $\theta = \pm\alpha/2$ by choosing $\mu = (2n+1)\pi/\alpha$, where $n = 0, 1, 2, \ldots$. Equation (20) then yields the symmetric modes. The antisymmetric modes are obtained by replacing $\cos\mu\theta$ by $\sin\mu\theta$, and setting $\mu = 2n\pi/\alpha$, with $n = 1, 2, \ldots$.

Because the Bessel functions Y_μ and K_μ become unbounded as $r \to 0$, it is traditional for closed circular plate problems to enforce the regularity conditions at $r = 0$ by setting $C_2 = C_4 = 0$ in Eq. (20). Satisfying boundary conditions at $r = a$ then yields a second-order characteristic determinant, the eigenvalues of which are nondimensional frequencies. This procedure may also be applied to the sectorial plate with simply supported radial edges. Setting $C_2 = C_4 = 0$, applying further the boundary conditions $W = M_r = 0$ along $r = a$, and expanding the resulting characteristic determinant yields the frequency equation

Downloaded 03 May 2010 to 171.66.16.245. Redistribution subject to ASME license or copyright; see http://www.asme.org/terms/Terms_Use.cfm

Table 2 Comparison between minimum values of $\lambda_1 + 1$ in the corner functions and μ in the analytic solution for sectorial plates with simply supported radial edges

α (degrees)	Smallest $\lambda_1 + 1$		Smallest μ	
	S	A	S	A
60	3.00	6.00	3.00	6.00
90	2.00	4.00	2.00	4.00
120	1.50	3.00	1.50	3.00
150	1.20	2.40	1.20	2.40
165	1.09	2.18	1.09	2.18
175	1.03	2.06	1.03	2.06
180	1.00	2.00	1.00	2.00
185	1.03	1.95	0.97	1.95
195	1.08	1.85	0.92	1.85
240	1.25	1.50	0.75	1.50
270	1.33	1.33	0.67	1.33
330	1.45	1.09	0.55	1.09
360	1.50	1.00	0.5	1.00

* S : symmetric modes,
A : antisymmetric modes.

$$\frac{J_{\mu+1}(\bar{\lambda})}{J_\mu(\bar{\lambda})}+\frac{I_{\mu+1}(\bar{\lambda})}{I_\mu(\bar{\lambda})}=\frac{2\bar{\lambda}}{1-\nu}, \tag{21}$$

where $\bar{\lambda} = ka$.

It is interesting and significant to compare the bending moments and stresses at the vertex ($r = 0$) of the simply supported sectorial plate when the present analytical solution is compared with the previously described Ritz solution. With $C_2 = C_4 = 0$ in Eq. (20), consider the power series expansions of the Bessel functions used (cf., Tranter, 1968):

$$J_\mu(kr)=\sum_{j=0,\ 1}^{\infty}\frac{(-1)^j(kr/2)^{\mu+2j}}{j!\Gamma(\mu+j+1)} \tag{22}$$

$$I_\mu(kr)=\sum_{j=0,\ 1}^{\infty}\frac{(kr/2)^{\mu+2j}}{j!\Gamma(\mu+j+1)} \tag{23}$$

where Γ is the gamma function and $\mu = (2n+1)\pi/\alpha$ for symmetric modes and $\mu = 2n\pi/\alpha$ for antisymmetric modes, as described above. The smallest degree term in r in the series occurs for $j = 0$, and is r^μ. Thus, considering Eqs. (3) and (11), stress singularities occur for $\mu < 2$. This corresponds to the situation when the smallest root (λ_1) used in the corner functions of Eqs. (15) and (16) become less than unity; that is, $\lambda_1 + 1 < 2$.

Table 2 lists the smallest values of $\lambda_1 + 1$ appearing in Eqs. (15) and (16) and the smallest values of μ arising in Eqs. (22) and (23), as determined by the vertex angle (α), for the symmetric and antisymmetric modes. Comparing the parameters $\lambda_1 + 1$ and μ, it is seen that they agree for antisymmetric modes over the entire range of α. However, for the symmetric modes they differ significantly for $\alpha > 180$ deg. This then raises the question: "Which solution represents the stress singularities properly for $\alpha > 180$ deg ?"

Because of the disagreement described above, another analytical solution will also be investigated. This is the problem of the *annular* sectorial plate (Fig. 3) having all boundaries simply supported. This configuration has an inner circular boundary of radius "*b*," as well as an outer one of radius "*a*." Its free vibration characteristics will be analyzed as the ratio *b/a* becomes very small.

The free vibration solution for the annular sectorial plate is obtained by using all terms of Eq. (20) for the symmetric modes, and the corresponding one with $\sin\mu\theta$ for antisymmetric modes. That is, all Bessel functions are retained, for the inner boundary has $b > 0$, and no singularities exist. The boundary conditions $W = M_r = 0$ are applied to $r = a$ and $r = b$, yielding a fourth-order determinant. The elements of the determinant involve the Bessel functions used in Eq. (20) and combinations of their first and second derivatives. This determinant was formulated by Vogel and Skinner (1965) for the closed annular plate, for which integer values of μ are used. The annular sectorial plate typically requires non-integer μ, as described above for the sectorial plate.

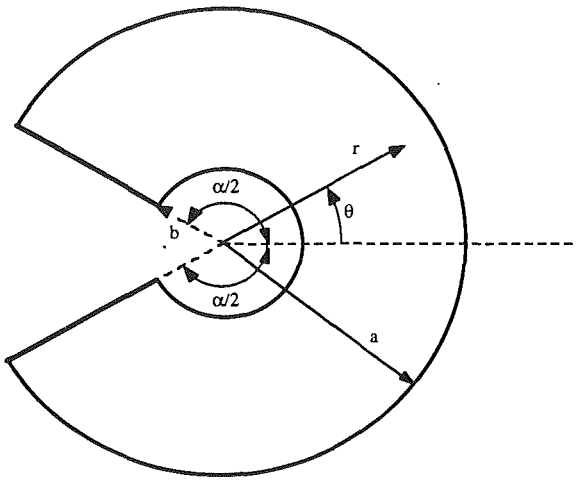


Fig. 3 Annular sectorial plate

Table 3 Convergence of frequency parameters $\omega a^2\sqrt{\rho/D}$ for simply supported sectorial plates ($\nu = 0.3$)

α (degrees)	Mode (n , s)	No. of corner functions	Total no. of terms in W_p 5	10	15	19	Analytical solutions*
120	(0 , 0)	0	19.5453	19.4596	19.4393	19.4332	19.4202
		1	19.4202	19.4202	19.4202	19.4202	
	(0 , 1)	0	59.3467	59.0583	58.9993	58.9815	58.9437
		1	58.9460	58.9437	58.9437	58.9437	
	(0 , 2)	0	120.800	118.403	118.286	118.250	118.176
		1	120.794	118.176	118.176	118.176	
	(0 , 3)	0	207.204	197.483	197.322	197.257	197.139
		1	207.140	197.147	197.139	197.139	
	(0 , 4)	0	763.787	296.322	296.112	295.920	295.839
		1	551.132	295.898	295.840	295.840	
165	(0 , 0)	0	64.2339	15.6693	15.5104	15.4435	14.8515
		1	14.8515	14.8515	14.8515	14.8515	
	(0 , 1)	0	212.078	52.0869	51.7246	51.5745	50.3284
		1	50.3307	50.3284	50.3284	50.3284	
	(0 , 2)	0	440.085	108.373	107.760	107.505	105.520
		1	106.948	105.520	105.520	105.520	
	(0 , 3)	0	772.391	184.471	183.623	183.226	180.445
		1	188.486	180.448	180.445	180.445	
	(0 , 4)	0	3044.36	280.480	279.302	278.592	275.107
		1	458.864	275.151	275.107	275.107	

* Indicates results obtained from equation (21).

Numerical Results

Table 3 presents a convergence study for the nondimensional frequencies $\omega a^2\sqrt{\rho/D}$ of the symmetric modes of two sectorial plates ($\alpha = 120$ deg and 165 deg) using the Ritz method described previously. In the present case with the two radial edges simply supported, the circumferential (θ) variation in Eq. (13) is found to be uncoupled; that is, the *summations* on *n* are not needed in Eq. (13). (All mode shapes for sectorial plates having both radial edges simply supported are found to have node lines which are radial and circular.) Results are given for

Downloaded 03 May 2010 to 171.66.16.245. Redistribution subject to ASME license or copyright; see http://www.asme.org/terms/Terms_Use.cfm

Table 4 Frequency parameters $\omega a^2\sqrt{\rho l D}$ for simply supported annular sectorial plates having very small b/a ratios (ν = 0.3)

α (degrees)	Mode (n , s)	Annular sectorial plate b/a 10^{-4}	10^{-5}	10^{-6}	10^{-8}	Sectorial plate* b/a=0
120	(0 , 0)	19.4210	19.4202	19.4202	19.4202	19.4202
	(0 , 1)	58.9461	58.9437	58.9437	58.9437	58.9437
	(0 , 2)	118.180	118.176	118.176	118.176	118.176
	(0 , 3)	197.147	197.140	197.139	197.139	197.139
	(0 , 4)	295.852	295.840	295.840	295.839	295.839
165	(0 , 0)	15.1125	15.0107	14.9514	14.8921	14.8515
	(0 , 1)	50.8615	50.6505	50.5295	50.4104	50.3284
	(0 , 2)	106.352	106.194	105.8305	105.647	105.520
	(0 , 3)	181.599	181.134	180.872	180.619	180.445
	(0 , 4)	276.603	275.996	275.657	275.330	275.107

* Indicates results from equation (21).

Table 5 Comparison of frequency parameters $\omega a^2\sqrt{\rho l D}$ for simply supported sectorial plates (ν = 0.3)

α (degrees)	Mode (n , s)	Ritz method Total no. of terms* 10	20	Annular sectorial plate solution b/a 10^{-6}	10^{-8}	Sectorial plate solutions+
195	(0 , 0)	14.0367	14.0367	14.1567	14.0977	13.1093
	(0 , 1)	48.6272	48.6272	48.8694	48.7395	46.9326
	(0 , 2)	102.921	102.921	103.295	103.093	100.468
	(0 , 3)	176.955	176.949	177.461	177.184	173.737
	(0 , 4)	271.620	270.714	271.371	271.014	266.743
270	(0 , 0)	14.4129	14.4129	14.4130	14.4129	10.5980
	(0 , 1)	49.0344	49.0344	49.0345	49.0344	41.9017
	(0 , 2)	103.328	103.328	103.328	103.328	92.9088
	(0 , 3)	177.362	177.356	177.357	177.356	163.648
	(0 , 4)	271.984	271.121	271.122	271.121	254.122
330	(0 , 0)	14.5467	14.5467	14.5467	14.5467	9.47492
	(0 , 1)	49.1807	49.1807	49.1807	49.1807	39.5899
	(0 , 2)	103.475	103.474	103.474	103.474	89.4021
	(0 , 3)	177.509	177.503	177.503	177.503	158.945
	(0 , 4)	272.118	271.268	271.268	271.268	248.225

* : One corner function is used with the polynomials.
\+ : Results obtained from equation (21).

modes having no radial node lines (n = 0) and s = 0, 1, 2, 3, 4 nodal circles. Frequencies are obtained using 5, 10, 15, and 19 polynomial terms (i.e., M = 6, 11, 16, and 20) in Eq. (13), and either zero or one corner functions in Eq. (15). These frequencies are compared with analytical solutions obtained from Eq. (21). Data shown is for a Poisson's ratio of ν = 0.3.

It is observed in Table 3 that, in general, if no corner functions are used convergence of the upper bound Ritz solutions is slow, particularly for the *lower* frequencies. On the other hand, adding a single corner function accelerates the convergence dramatically, especially as α approaches 180 deg. Thus, for example, using polynomials only, the frequency determinant of 19th order yields a fundamental (i.e., lowest) frequency parameter for the 165 deg plate (15.4435) that is 4.0 percent higher than the exact value (14.8515); moreover, it would take many more polynomial terms to obtain three significant figure agreement with the analytical solution. But, using an additional corner function yields six significant figure convergence with a determinant of only sixth order. Thus, although the polynomials do form a set of functions which are mathematically complete, thereby guaranteeing convergence to the exact frequencies as sufficient terms are taken, numerical computation limitations will prevent achieving accurate results unless convergence is accelerated by means of additional corner functions. Conversely, use of the corner functions alone would not yield correct solutions, for they do not form a complete function set.

Table 4 summarizes another study for the same plates of Table 3 (α = 120 deg and 165 deg, ν = 0.3), this time using the analytical solution for the *annular* sectorial plate described in the preceding section, with very small inside radii. Table 4 shows that, as the ratio of radii (b/a) approaches zero, the frequencies approach those of the sectorial plate. For α = 120 deg excellent agreement is seen for all five frequencies when $b/a = 10^{-4}$. However, for α = 165 deg, the agreement is not so good, especially for the fundamental frequency. A difference of 0.3 percent between the two fundamental frequencies is found for the extremely small value of $b/a = 10^{-8}$. Double precision (16 significant figure) calculations were used to obtain these accurate data.

In Table 5 data for plates having α > 180 deg are listed, arising from all three types of solutions. The most striking conclusion is that the converged data obtained from the Ritz solution and from the annular sectorial plate analytical solution agree, but the sectorial plate analytical solution yields different results. This latter solution does not properly represent the sectorial plate for α > 180 deg, for the Bessel functions which are singular at r = 0 (Y_μ and K_μ of Eq. (20)) are not used in it. It is also seen in Table 5 that the agreement between the Ritz solution and the annular sectorial plate analytical solution improves as the vertex angle increases beyond 180 deg.

The behavior of the Bessel functions and their coefficients in the eigenfunction (20) is exhibited in Table 6 for the fundamental mode shapes of two annular sectorial plates (ν = 0.3) with vanishingly small radii ratios (b/a). In the first case (α = 120 deg), the normalized eigenvector coefficients $C_2^* = C_2/C_1$ and $C_4^* = C_4/C_1$ are seen to vanish relative to C_1^* and C_3^* as b/a decreases. Thus, the sectorial plate analytical solution, which does not include C_2 and C_4, is valid. The singularity of the Y_μ and K_μ at $r = b$, and of their products with C_2^* and C_4^*, with decreasing b/a is also apparent from Table 6. In the second case (α = 270 deg), C_2^* and C_4^* do not vanish with decreasing b/a, but convergence to finite values two orders of magnitude larger than C_3^*. Furthermore, although the Y_μ and K_μ again become unbounded with vanishing b/a, as do the two products $C_2^* Y_\mu(kb)$ and $C_4^* K_\mu(kb)$, these products become the negatives of each other, and cancel each other out. Thus, the displacement $W(r, \theta)$ in Eq. (20) remains bounded at r = 0.

It is also interesting to note that, as α approaches 360 deg, the configuration results in a hinged crack (i.e., both radial edges simply supported). At α = 360 deg, the two edges become coincident, but no circumferential moment (M_θ) is transferred across the boundaries—both radial edges may be regarded as being attached to a single hinge. However, Table 7 shows that the fundamental frequency of a complete plate is much less than that of the 360 deg sectorial plate. While there is a loss of circumferential moment in the sectorial plate, the transverse displacement constraint along the radial hinge supplies considerable additional stiffness.

Variation in the nondimensional frequency parameter

Downloaded 03 May 2010 to 171.66.16.245. Redistribution subject to ASME license or copyright; see http://www.asme.org/terms/Terms_Use.cfm

Table 6 Terms of the eigenfunctions (20) for the fundamental mode shapes of two annular sectorial plates (α = 120 deg and 270 deg) with vanishingly small radii ratios (b/a)

Coefficient or function	$\alpha = 120^\circ$			$\alpha = 270^\circ$		
	$b/a=10^{-4}$	$b/a=10^{-6}$	$b/a=10^{-8}$	$b/a=10^{-4}$	$b/a=10^{-6}$	$b/a=10^{-8}$
C_1^*	1	1	1	1	1	1
C_2^*	$8.5235*10^{-5}$	$3.9588*10^{-7}$	$3.9588*10^{-7}$	$5.7400*10^{-1}$	$5.7383*10^{-1}$	$5.7382*10^{-1}$
C_3^*	$-2.6620*10^{-3}$	$-2.6622*10^{-3}$	$-2.6622*10^{-3}$	$-6.1193*10^{-3}$	$-6.1198*10^{-3}$	$-6.1199*10^{-3}$
C_4^*	$5.4262*10^{-5}$	$2.5203*10^{-7}$	$2.5203*10^{-7}$	$3.6542*10^{-1}$	$3.6531*10^{-1}$	$3.6530*10^{-1}$
J_μ(kb)	$2.4605*10^{-6}$	$2.4604*10^{-9}$	$2.4604*10^{-12}$	$3.6588*10^{-3}$	$1.6982*10^{-4}$	$7.8825*10^{-6}$
Y_μ(kb)	$-8.6246*10^{4}$	$-8.6248*10^{7}$	$-8.6248*10^{10}$	$-1.3050*10^{2}$	$-2.8115*10^{3}$	$-6.0573*10^{4}$
I_μ(kb)	$2.4605*10^{-6}$	$2.4604*10^{-9}$	$2.4604*10^{-12}$	$3.6588*10^{-3}$	$1.6982*10^{-4}$	$7.8825*10^{-6}$
K_μ(kb)	$1.3547*10^{5}$	$1.3548*10^{8}$	$1.3548*10^{11}$	$2.0498*10^{2}$	$4.4163*10^{3}$	$9.5147*10^{4}$
$C_1^*J_\mu$(kb)	$2.4605*10^{-6}$	$2.4604*10^{-9}$	$2.4604*10^{-12}$	$3.6588*10^{-3}$	$1.6982*10^{-4}$	$7.8825*10^{-6}$
$C_2^*Y_\mu$(kb)	$-7.3512*10^{0}$	$-3.4144*10^{1}$	$-3.4144*10^{4}$	$-7.4906*10^{1}$	$-1.6134*10^{3}$	$-3.4758*10^{4}$
$C_3^*I_\mu$(kb)	$-6.5497*10^{-9}$	$-6.5502*10^{-12}$	$-6.5502*10^{-15}$	$-2.2390*10^{-5}$	$-1.0393*10^{-6}$	$-4.8240*10^{-8}$
$C_4^*K_\mu$(kb)	$7.3512*10^{0}$	$3.4144*10^{1}$	$3.4144*10^{4}$	$7.4903*10^{1}$	$1.6134*10^{3}$	$3.4758*10^{4}$

Table 7 Fundamental frequency parameters $\omega a^2\sqrt{\rho/D}$ of simply supported sectorial plates

α (degrees)	υ			Max. percent difference in :	
	0	0.3	0.5	$\omega a^2\sqrt{\rho/D}$	ω
30	97.66	97.99	98.21	0.6	16.1
60	39.60	39.96	40.18	1.5	17.2
90	25.24	25.61	25.84	2.4	18.2
120	19.04	19.42	19.66	3.3	19.2
150	15.64	16.03	16.26	4.0	20.0
165	14.46	14.85	15.09	4.4	20.5
180	13.50	13.90	14.14	4.7	20.9
195	13.64	14.04	14.28	4.7	20.9
210	13.74	14.15	14.39	4.7	20.9
240	13.89	14.30	14.56	4.8	21.0
270	14.00	14.41	14.67	4.8	21.0
300	14.07	14.49	14.74	4.8	21.0
330	14.14	14.54	14.81	4.7	20.9
350	14.16	14.58	14.83	4.7	20.9
360	14.17	14.59	14.84	4.7	20.9
complete	4.444	4.935	5.078	14.3	31.9

$\omega a^2\sqrt{\rho/D}$ with ν is seen in Table 7 to be quite small for all α, with a maximum percent difference of 4.8. Moreover, the maximum percent difference remains virtually constant in the range (180 deg $\leq \alpha \leq$ 360 deg). The complete circular plate has considerably greater change in its fundamental frequency parameter due to variation in ν (14.3 percent). This is because the circumferential moment (M_θ) generated depends strongly upon ν. Because the frequency parameter contains $D = Eh^3/12(1-\nu^2)$, the maximum percent difference in ω due to varying ν is seen in Table 7 to be much greater.

The fundamental frequencies listed in Table 7 are for mode shapes which have only one circumferential half-wave (no radial nodal lines). For modes having one or more radial nodal lines, frequencies may be obtained from the relatively simple characteristic equation, Eq. (21). For such modes, simply supported edge conditions are duplicated along the radial nodal lines, and therefore the analytical solution represented by Eq. (21) is valid for all vertex angles ($0 < \alpha \leq 360$ deg). The extensive frequency data which is available for the higher modes of complete, simply supported circular plates for $\nu = 0$ (0.1) 0.5 (Leissa and Narita, 1980) may similarly be used for this purpose.

Concluding Remarks

A procedure has been developed for the free vibration analysis of sectorial plates. The procedure is based upon the well-known Ritz method, but utilizes two sets of admissible functions—algebraic-trigonometric polynomials and corner functions. The procedure was demonstrated for the plate having simply supported edges, where comparisons could be made with the results of two analytical solutions. Such analytical solutions do not exist for radial edges which are not both simply supported.

It has been shown that the relatively simple analytical solution for sectorial plates becomes invalid for vertex angles (α) exceeding 180 deg. This is because the stress singularity existing at the vertex ($r = 0$) for such angles is not properly accounted for. Thus, such solutions obtained for other boundary conditions used along the circular edge would also be invalid when $\alpha > 180$ deg.

Accurate results for the case of the radial edges both simply supported were obtained with only a single corner function added to the polynomials. However, using the procedure for sectorial plates having two *free* radial edges (i.e., the circular plate with a V-notch) has shown that additional corner functions must be used to obtain accurate results (Huang, 1991).

The first known, correct results for sectorial plates having re-entrant angles ($\alpha > 180$ deg) have been presented in Tables 5 and 6. These data may also be useful to measure the accuracy and corrections of other solution procedures, such as finite elements or finite differences, when they are applied to situations involving re-entrant corners.

Because of geometrical considerations, results were obtained for $0 < \alpha \leq 360$ deg. However, mathematical solutions could also be developed by the present procedures for $\alpha > 360$ deg. Frequencies obtained from such solutions could closely approximate the lowest (i.e., flexural mode) frequencies of thin, helical shells having small helix angles.

Downloaded 03 May 2010 to 171.66.16.245. Redistribution subject to ASME license or copyright; see http://www.asme.org/terms/Terms_Use.cfm

Finally, it should be mentioned that the Ritz procedure presented here, using both algebraic-trigonometric polynomials and corner functions, may also be used to determine the transverse deflections and bending stresses in sectorial plates having re-entrant corners, or the buckling loads and mode shapes of such plates.

References

Ben-Amoz, M., 1959, "Note on Deflections and Flexural Vibrations of Clamped Sectorial Plates," ASME JOURNAL OF APPLIED MECHANICS, Vol. 26, pp. 136–137.

Bhattacharya, A. P., and Bhowmic, K. N., 1975, "Free Vibration of a Sectorial Plate," *Journal of Sound and Vibration*, Vol. 41, No. 4, pp. 503–505.

Huang, C. S., 1991, "Singularities in Plate Vibration Problems," Ph.D. Dissertation, The Ohio State University.

Leissa, A. W., 1969, "Vibration of Plates," NASA SP-160, U.S. Government Printing Office.

Leissa, A. W., and Narita, Y., 1980, "Natural Frequencies of Simply Supported Circular Plates," *Journal of Sound and Vibration*, Vol. 70, No. 2, pp. 221–229.

Maruyama, K., and Ichinomiya, O., 1981, "Experimental Investigation of Free Vibrations of Clamped Sector Plates," *Journal of Sound and Vibration*, Vol. 74, No. 4, pp. 565–573.

Rubin, C., 1975, "Nodal Circles and Natural Frequencies for the Isotropic Wedge," *Journal of Sound and Vibration*, Vol. 39, No. 4, pp. 523–526.

Tranter, C. J., 1968, *Bessel Functions with Some Physical Applications*, The English Universities Press Ltd.

Vogel, S. M., and Skinner, D. W., 1965, "Natural Frequencies of Transversely Vibrating Uniform Annular Plates," ASME JOURNAL OF APPLIED MECHANICS, Vol. 62, pp. 926–931.

Waller, Mary D., 1952, "Vibrations of Free Plates, Line Symmetry, Corresponding Modes," *Proceedings of the Royal Society*, London, Vol. A211, pp. 265–276.

Westmann, R. A., 1962, "A Note on Free Vibrations of Triangular and Sector Plates," *Journal of the Aerospace Sciences*, Vol. 29, No. 9, pp. 1139–1140.

Williams, M. L., 1952, "Surface Stress Singularities Resulting from Various Boundary Conditions in Angular Plates Under Bending," *Proceedings of the First U.S. National Congress of Applied Mechanics*, pp. 325–329.

Downloaded 03 May 2010 to 171.66.16.245. Redistribution subject to ASME license or copyright; see http://www.asme.org/terms/Terms_Use.cfm

Stochastic Dynamics of Nonlinear Systems Driven by Non-normal Delta-Correlated Processes

Mario Di Paola
Professor.

Giovanni Falsone

Dipartimento di Ingegneria Strutturale & Geotecnica, DISEG, Universita di Palermo, Viale delle Scienze, I-90128 Palermo, Italy

In this paper, nonlinear systems subjected to external and parametric non-normal delta-correlated stochastic excitations are treated. A new interpretation of the stochastic differential calculus allows first a full explanation of the presence of the Wong-Zakai or Stratonovich correction terms in the Itô's differential rule. Then this rule is extended to take into account the non-normality of the input. The validity of this formulation is confirmed by experimental results obtained by Monte Carlo simulations.

Introduction

In many cases of engineering interest, it has become quite common to use stochastic processes to model loading such as those resulting from earthquakes, turbulent winds, or ocean waves. In these circumstances the structural response needs to be adequately evaluated in the probabilistic sense by means of the cumulants or the moments of any order of the response (see, e.g., Stratonovich (1963), Lin (1977)). In particular, for linear systems excited by normal input, the response process is also normal, and the moments or the cumulants up to the second order fully characterize the probability density function of both input and output processes. Fortunately, many practical problems involve processes which are approximately normal and the effect of the non-normality is often considered to be negligible, and this explains the popularity of the second-order analysis.

In some circumstances, however, the excitations are significantly non-normal, such as quadratic terms commonly used in fluid mechanics. In these cases, and also in the simpler case of linear systems, the response is non-normal and the probabilistic characterization of the response requires higher order moments.

For linear or nonlinear systems driven by parametric normal delta-correlated processes, the problem of finding the probabilistic characterization of the response can be faced by means of Itô's stochastic calculus (Itô, 1951) which, in connection with Itô's rule (Itô, 1961; Jazwinski, 1970; Arnold, 1973), allows the complete characterization of the response process. It can be obtained, for example, by means of the moment equation approach (Stratonovich, 1963; Lin, 1977; Ibrahim et al., 1985). The method consists first in converting the equation of motion into an Itô-type stochastic differential equation and then applying Itô's rule in evaluating the differential equations governing the response moments of any order. Unfortunately, this powerful approach fails when the input is non-normal.

Recently, Lutes (1986) and Lutes and Hu (1986) investigated the case of linear systems excited by non-normal delta-correlated of filtered processes by means of two methods which permit evaluation of the cumulants up to the fourth order of the response. These methods, however, do not seem to be easily extendible to nonlinear systems.

Roberts (1965) investigated the case of nonlinear systems excited by external trains of pulses—Poisson distributed in time. This kind of excitation can be considered as a particular non-normal delta-correlated process (see also Iwankievicz, 1990). In his work Roberts extended the Itô's differential calculus in order to take into account the non-normality of the input. However, no research works have been devoted to the more general case of nonlinear systems excited by parametric delta-correlated non-normal processes.

Probably this is due to the fact that, although Itô's differential calculus is now popular with people working in random vibration, some basic aspects of this calculus are not fully clear from a theoretical point of view. For example, recently To (1988), in a well-argued letter, raised the controversial question of dynamic systems involving parametric-type excitations. The controversy refers to the explanation of the presence of the so-called Wong-Zakai (1965) or Stratonovich (1966) correction term in Itô's stochastic differential equations. It was shown that the usual reason given by some authors (see, e.g., Ibrahim, 1985; Kozin, 1986) that the Wong-Zakai or Stratonovich correction term is required in converting ideal white noises into physical white noises is not a clear cut one in general, and To concludes that the presence of the Wong-Zakai or Stratonovich correction term is not self-evident. This explains the difficulty of extending the Itô's calculus to a more complicated type of excitation, such as a non-normal delta-correlated process.

In this paper a new interpretation of the Itô's differential calculus is given. For normal delta-correlated excitation, this

Contributed by the Applied Mechanics Division of THE AMERICAN SOCIETY OF MECHANICAL ENGINEERS for publication in the ASME JOURNAL OF APPLIED MECHANICS.

Discussion on this paper should be addressed to the Technical Editor, Professor Lewis T. Wheeler, Department of Mechanical Engineering, University of Houston, Houston, TX 77204-4792, and will be accepted until four months after final publication of the paper itself in the ASME JOURNAL OF APPLIED MECHANICS.

Manuscript received by the ASME Applied Mechanics Division, May 7, 1991; final revision, Aug. 17, 1992. Associate Technical Editor: P. S. Spanos.

Copyright © 1993 by ASME
Downloaded 03 May 2010 to 171.66.16.245. Redistribution subject to ASME license or copyright; see http://www.asme.org/terms/Terms_Use.cfm

interpretation allows one to obtain the classical Itô's differential rule explaining the presence of the Wong-Zakai or Stratonovich correction term. At the same time, it allows the extension to non-normal delta-correlated inputs, showing the necessity of the presence of new correction terms in the stochastic differential equation. Experimental results obtained by means of Monte Carlo simulation confirm the validity of the approach here presented.

Preliminary Concepts

For clarity's sake and with the aim of introducing appropriate symbologies, some preliminary concepts are briefly summarized in this section.

Let $X(t)$ be a stochastic process; its probabilistic description can be obtained by means of the knowledge of the infinite hierarchy of the joint probability density functions

$$p_{\mathbf{x}_s}(\mathbf{x}_s;\ \mathbf{t}_s),\quad s=1,\ 2,\ \cdots,\ \infty \tag{1}$$

where

$$\mathbf{X}_s^T=[X_1X_2\cdots X_s];\quad \mathbf{x}_s^T=[x_1x_2\cdots x_s];\quad \mathbf{t}_s^T=[t_1t_2\cdots t_s]. \tag{2}$$

In Eq. (2) the apex T means transpose and $X_k=X(t_k)$. The stochastic process $X(t)$ can be equivalently characterized by means of the knowledge of the characteristic functions $M_{\mathbf{X}_s}(\boldsymbol{\theta}_s;\ \mathbf{t}_s)$ which are related to the probability density functions by means of the Fourier transform operator, that is

$$M_{\mathbf{X}_s}(\boldsymbol{\theta}_s;\ \mathbf{t}_s)=\int_{-\infty}^{\infty}\cdots\int_{-\infty}^{\infty}\exp(-i\boldsymbol{\theta}_s^T\mathbf{x}_s)p_{\mathbf{x}_s}(\mathbf{x}_s;\ \mathbf{t}_s)dx_1dx_2\cdots dx_s \tag{3}$$

where i is the imaginary unit and $\boldsymbol{\theta}_s$ is an s-vector of the real parameter

$$\boldsymbol{\theta}_s^T=[\theta_1\theta_2\cdots\theta_s]. \tag{4}$$

A Taylor expansion of the characteristic function gives

$$M_{\mathbf{X}_s}(\boldsymbol{\theta}_s;\ \mathbf{t}_s)=1+\sum_{j=1}^{s}-i\theta_j m_1[X_j]+\frac{1}{2!}\sum_{j=1}^{s}\sum_{k=1}^{s}(-i)^2\theta_j\theta_k m_2[X_jX_k]+\cdots \tag{5}$$

where $m_r\,[X_1^pX_2^q\cdots X_s^l]$ with $p+q+\cdots+l=r$ is the moment of order r of the variable $X_1^pX_2^q\cdots X_s^l$, that is

$$m_r[X_1^pX_2^q\cdots X_s^l]=E[X_1^pX_2^q\cdots X_s^l]=\frac{1}{(-i)^r}\left[\frac{\partial^r}{\partial\theta_1^p\partial\theta_2^q\cdots\partial\theta_s^l}M_{\mathbf{X}_s}(\boldsymbol{\theta}_s;\ \mathbf{t}_s)\right]_{\boldsymbol{\theta}_s=\mathbf{0}} \tag{6}$$

where $E[\ ]$ means stochastic average. A different representation of the characteristic function can be made introducing the so-called cumulants $k_r[X_1^pX_2^q\cdots X_s^l]$, in the form

$$M_{\mathbf{X}_s}(\boldsymbol{\theta}_s;\ \mathbf{t}_s)=\exp\left(\sum_{j=1}^{s}-i\theta_j k_1[X_j]+\frac{1}{2!}\sum_{j=1}^{s}\sum_{k=1}^{s}(-i)^2\theta_j\theta_k k_2[X_jX_k]+\cdots\right) \tag{7}$$

where the cumulants can be obtained by the following relationship:

$$k_r[X_1^pX_2^q\cdots X_s^l]=\frac{1}{(-i)^r}\left[\frac{\partial^r}{\partial\theta_1^p\partial\theta_2^q\cdots\partial\theta_s^l}\ln M_{\mathbf{X}_s}(\boldsymbol{\theta}_s;\ \mathbf{t}_s)\right]_{\boldsymbol{\theta}_s=\mathbf{0}}$$

So it is clear that the probabilistic description of the process $X(t)$ can be obtained indifferently by means of the knowledge of its probability density functions, or of its characteristic functions, moments, or cumulants.

Many physical problems have small values of the higher order cumulants and, for normal processes, they are exactly zero for orders greater than two. For such processes, all higher moments can be obtained by the knowledge of only the first and second-order moments; thus, in this case, these quantities fully define the probabilistic description of the process.

In some circumstances we are concerned with quantities defined as

$$E_r[X;\ \mathbf{t}_r]=E[X_1X_2\cdots X_r], \tag{9}$$

that is one of the moments of order r defined in Eq. (6). If this quantity is known for every value of the time instants t_1, t_2, $\cdots$, t_r, then all possible moments of order r, $m_r\,[X_1^pX_2^q\cdots X_s^l]$ with $(p+q+\cdots l=r)$ can be easily computed by means of an appropriate choice of the time instants t_1, t_2, $\cdots$, t_r. For this reason it seems to be appropriate to introduce a new nomenclature for a moment of order r of the type given in Eq. (9) and it will be called "average at multiple times." The counterpart of $E_r[X;\ \mathbf{t}_r]$, in terms of cumulants is, following a nomenclature given by Stratonovich (1963), the correlation $C_r[X;\ \mathbf{t}_s]$. If the correlation is known as a function of the various instants t_1, t_2, $\cdots$, t_r, then all possible cumulants of order r, $k_r\,[X_1^pX_2^q\cdots X_s^l]$ can be easily evaluated. Relationships between averages at multiple times and correlations are available in the literature (Ibrahim, 1985).

If $X(t)$ is a strong stationary process of order r, then the average at multiple times and the correlations up to the rth order depend on the time differences t_1-t_2, t_1-t_3, $\cdots$ t_1-t_r instead of the time instants t_1, t_2, $\cdots$, t_r taken separately.

Delta-Correlated Processes

Stratonovich (1963) called a strong stationary random process $W(t)$ "delta-correlated" up to sth order if it is characterized by correlation functions made up of products of Dirac's delta functions, that is

$$C_r(W;\ \mathbf{t}_r)=q^{(r)}\delta(t_1-t_2)\delta(t_1-t_2)\cdots\delta(t_1-t_r),\qquad r=2,\ 3,\ \ldots,\ s \tag{10}$$

where $q^{(r)}$ are intensity coefficients. Setting $t_2=\cdots=t_r=t_1$ in Eq. (10), the correlation function $C_r(W;\ t_1,\ t_1,\ \cdots,\ t_1)$ coincides with the cumulant of order r of the random variable $W(t_1)$, extracted by the process $W(t)$ at the time instant t_1. So we see that at each instant a delta-correlated process has infinite cumulants values. Physical processes, of course, generally have finite cumulants, so they cannot be delta-correlated. There are situations, however, where it is useful to substitute a delta-correlated process for a physical process, with resulting mathematical simplifications. It has been shown (Lutes, 1986) that sometimes the output of a system is almost unchanged if the actual input is replaced by a delta-correlated process. This surely happens when the input is correlated only over very short time intervals.

Among delta-correlated processes, a special role is played by the normal zero-mean processes having only the coefficient q_2 different from zero. These processes are usually called "white noise," and this definition has been extended to all delta-correlated processes by Lutes and Hu (1986). Following Karlin and Taylor (1981) and Horstenke and Lefever (1984), a stationary white noise can be obtained by means of the following relationship:

$$W(t)=\frac{dL(t)}{dt} \tag{11}$$

in which $L(t)$ belongs to the class of processes with stationary independent increments (Levy processes). Following this definition, $W(t)$ can be called the "Levy white noise process." Strictly speaking, the definition given in Eq. (11) is invalid in the ordinary differential calculus because $L(t)$ is not differentiable everywhere. However, it can be made rigorous in the framework of the generalized theory of random processes (Gel'fand and Valenkin, 1964; Horstemke and Lefever, 1984;

Downloaded 03 May 2010 to 171.66.16.245. Redistribution subject to ASME license or copyright; see http://www.asme.org/terms/Terms_Use.cfm

Grigoriu, 1987). Alternatively one can interpret $W(t)dt$ as an increment of $L(t)$, that is

$$W(t)dt = dL(t). \tag{12}$$

In this way, setting $t_1 = t_2 = \cdots = t_r = t$ in Eq. (10) and using Eq. (12), it can be easily shown that an increment $dL(t)$ of the Levy process $L(t)$, connected with $W(t)$, delta correlated up to sth order, has cumulants which, at each time instant, are given in the form

$$k_1[dL(t)] = 0; \quad k_r[dL(t)] = q^{(r)}dt, \quad r = 2, 3, \cdots, s;$$
$$k_{s+p}[dL(t)] \approx 0, \quad p = 1, 2, \cdots \tag{13}$$

where $q^{(r)}$ are the same intensity coefficients defined in Eq. (10). Taking into account the relationships between moments and cumulants, it can be easily seen that, neglecting infinitesimals of higher order than dt, the moments of $dL(t)$ coincide with the cumulants, that is

$$m_r[dL(t)] = E[(dL(t))^r] = k_r[dL(t)]. \tag{14}$$

In the case of normal white noise processes, $L(t)$ coincides with the Wiener process and all the moments and the cumulants of order greater than two are zeros. This implies that an increment $dL(t)$ of the Wiener process is an infinitesimal one of order $(dt)^{1/2}$. While, for a general Levy process, the order of its increment $dL(t)$ cannot be established. These concepts will be extensively used in the next section.

Basic Concepts of Stochastic Differential Calculus

For clarity's sake, in this section some preliminary well-known concepts of stochastic differential calculus involving a first-order differential equation are summarized. An extension to multi-degree-of-freedom systems is reported in the Appendix. For more detailed discussions readers are referred, for example, to Jazwinski (1970), Arnold (1973), Horsthemke and Lefever (1984), and Ibrahim (1985).

The dynamical system to be considered is governed by the equation

$$\dot{Z} = A(Z, t) + G(Z, t)W(t) \tag{15}$$

where $W(t)$ is a zero-mean stationary normal white noise process, while $A(Z, t)$ and $G(Z, t)$ are deterministic functions depending on the process Z and the time t. Then, in general, Eq. (15) is the so-called differential equation driven by parametric-type excitations. If $G(Z, t)$ is independent of Z then the excitation is external.

The first step to obtain the probabilistic characterization of Z is to convert Eq. (15) into an Itô-type stochastic differential equation which has the form

$$dZ = f(Z, t)dt + G(Z, t)dL \tag{16}$$

where dL is an increment of a Wiener process characterized by

$$E[dL] = 0; \quad E[(dL)^2] = q^{(2)}dt; \quad E[(dL)^r] = 0, \quad r = 3, 4, \cdots. \tag{17}$$

In Eq. (16), $f(Z, t)$ is the so-called drift coefficient which takes into account the Wong-Zakai (1965) or Stratonovich (1966) correction term, that is

$$f(Z, t) = A(Z, t) + \frac{1}{2}\frac{\partial G(Z, t)}{\partial Z}G(Z, t)q^{(2)}. \tag{18}$$

Equation (16) is not a classical differential equation because in it a summation of infinitesimals of different orders appears (dL is of order $(dt)^{1/2}$), and it is so-called stochastic differential equation.

The second step consists of the application of the Itô's differential rule (Itô, 1961) that allows the complete characterization of the response process. In order to obtain this rule, we consider a scalar real-valued function $\phi(Z, t)$, continuously differentiable on t and twice differentiable on Z. The differential of $\phi(Z, t)$ can be obtained expanding $d\phi(Z, t)$ into a Taylor series and retaining the second term in dL (see, e.g., Jazwinski, 1973), that is

$$d\phi(Z, t) = \frac{\partial\phi(Z, t)}{\partial t}dt + \frac{\partial\phi(Z, t)}{\partial Z}dZ + \frac{1}{2}\frac{\partial^2\phi(Z, t)}{\partial Z^2}(dZ)^2. \tag{19}$$

Remembering that dZ is given in Eq. (16) and that, neglecting the infinitesimals of higher order than dt, the following relationship holds:

$$(dZ)^2 = G^2(Z, t)(dL)^2 = G^2(Z, t)q^{(2)}dt. \tag{20}$$

We obtain the classical Itô's differential rule in the form (with argument omitted)

$$d\phi = \frac{\partial\phi}{\partial t}dt + \frac{\partial\phi}{\partial Z}(df + GdL) + \frac{1}{2}\frac{\partial^2\phi}{\partial Z^2}G^2q^{(2)}dt. \tag{21}$$

Summarizing the usual approach for the mathematical treatment of the stochastic calculus of nonlinear systems excited by parametric normal white noises consists first in converting the given differential equation of motion into an Itô-type stochastic differential equation. This equation is obtained modifying the drift coefficient in order to take into account the Wong-Zakai or Stratonovich correction term. Then the Itô differential equation can be treated in the same way as any ordinary differential equation. However, the reason of the presence of Wong-Zakai or Stratonovich correction term, connected with the replacement of physical white noises into ideal white noises (Ibrahim, 1985; Yong and Lin, 1987), is not a clear-cut one (To, 1988). Moreover, using the above outlined approach, the extension of the Itô calculus to non-normal delta-correlated processes becomes a very serious problem. The questions are as follows: (1) is it possible to extend the Itô's rule to such processes and, if yes, (2) what are the new correction terms, like Wong-Zakai or Stratonovich ones, which take into account the non-normality of the input? This problem, following the above outlined method has no solution. This means that a new way has to be pursued in order to have arrived at an answer. In the next section a new formulation will be presented that, explaining the presence of the Wong-Zakai or Stratonovich correction term, allows a natural extension to the stochastic differential equations driven by non-normal delta-correlated processes.

A New Approach to the Stochastic Differential Calculus

The dynamical system to be considered is in the form

$$dZ = A(Z, t)dt + G(Z, t)dL \tag{22}$$

where $dL(t)/dt = W(t)$ is a zero-mean normal delta-correlated process and $L(t)$ is a Wiener process whose increments are characterized by the moments given in Eq. (17).

An increment of a scalar real-valued function $\phi(Z, t)$, continuously differentiable on t and twice differentiable on Z, can be expressed in the form (Picone and Fichera, 1975)

$$\Delta\phi(Z, t) = d\phi(Z, t) + \frac{1}{2!}d^2\phi(Z, t) + \frac{1}{3!}d^3\phi(Z, t) + \cdots. \tag{23}$$

From this equation we can observe that, for the presence of the additional terms $(1/2!)d^2\phi + (1/3!)d^3\phi + \cdots$, increments and differentials are quite different concepts, so that $\Delta\phi/dt \equiv \dot{\phi}$ is different from $d\phi/dt$. Using the rules of differentiation of composite functions, we obtain

$$d\phi(Z, t) = \frac{\partial\phi(Z, t)}{\partial t}dt + \frac{\partial\phi(Z, t)}{\partial Z}dZ \tag{24}$$

$$d^2\phi(Z, t) = \frac{\partial^2\phi(Z, t)}{\partial Z^2}(dZ)^2 + \frac{\partial\phi(Z, t)}{\partial Z}d^2Z. \tag{25}$$

Downloaded 03 May 2010 to 171.66.16.245. Redistribution subject to ASME license or copyright; see http://www.asme.org/terms/Terms_Use.cfm

Remembering that dZ has been defined in Eq. (22), we obtain for d^2Z the following expression:

$$d^2Z=\frac{\partial G(Z,\,t)}{\partial Z}G(Z,\,t)\,(dL)^2=\frac{\partial G(Z,\,t)}{\partial Z}G(Z,\,t)q^{(2)}dt \tag{26}$$

in which the Martingale property has been used (see, e.g., Jazwinski, 1973). It can be easily seen that in the case of normal delta-correlated input, higher order differentials than $d^2\phi(Z,\,t)$ are infinitesimals of higher order than dt. Hence, inserting Eq. (26) in (25) and Eqs. (24) and (25) in (23), we obtain Eq. (21). This means that expansion (23), in which dZ is given in Eq. (22), coincides with expansion (19), in which dZ is given in Eq. (16).

Setting $\phi(Z,\,t)=Z$ in Eq. (23) we obtain

$$\Delta Z=dZ+\frac{1}{2}d^2Z \tag{27}$$

which, taking Eqs. (22) and (26) into account, writes

$$\Delta Z=A(Z,\,t)dt+\frac{1}{2}\frac{\partial G(Z,\,t)}{\partial Z}G(Z,\,t)q^{(2)}dt+G(Z,\,t)dL. \tag{28}$$

Dividing for dt, Eq. (28) can be rewritten in the form

$$\dot{Z}=A(Z,\,t)+\frac{1}{2}\frac{\partial G(Z,\,t)}{\partial Z}G(Z,\,t)q^{(2)}+G(Z,\,t)W(t). \tag{29}$$

Comparing the latter equation with Eq. (22), it is easy to note that, for normal delta-correlated parametric excitation, the differential of the response process Z and the increment of Z are quite different concepts and they coincide only in the case of purely external excitations—that is when $d^2Z=0$ and then when the Wong-Zakai or Stratonovich correction term is zero.

To summarize, following expansion (23), an increment of a scalar real-valued function of Z and t is composed by two terms: the first one is given in Eq. (24) and the second one is given in Eq. (25). The latter is composed of two terms: the first one is present in both cases of purely external excitations and parametric ones. The second one, homogeneous to $\partial\phi/\partial Z$, appears only in the case of parametric excitations. On the other hand, in the case of parametric excitations starting from the classical Itô's rule (19), a term is not present and, in order to compensate for this one, an extra term (the Wong-Zakai or Stratonovich correction term) must be introduced in the drift coefficient to take into account the effect of the local irregularities of the process L. While, using Eq. (27), the presence of the Wang-Zakai or Stratonovich correction term is explained in a natural way: it is a term which compensates for the difference between the derivative of Z ($\Delta Z/dt=\dot{Z}$) and ratio dZ/dt. These two quantities coincide only when dealing with smooth parametric excitations or in the case of external excitations.

It is interesting to note that expansion (23), neglecting infinitesimals of higher order than dt, proves to be rewritten in the following form:

$$\Delta\phi(Z,\,t)=\frac{\partial\phi(Z,\,t)}{\partial t}dt+\frac{\partial\phi(Z,\,t)}{\partial Z}\Delta Z+\frac{1}{2}\frac{\partial^2\phi(Z,\,t)}{\partial Z^2}(\Delta Z)^2 \tag{30}$$

in which ΔZ is given in Eq. (28). Relationship (30) will hereafter be referred to as the "non-classical stochastic differential rule." Starting from Eqs. (23) or (30), the extension to the case of non-normal delta-correlated process is very simple as will be shown in the next section.

Extension to Non-normal Delta-Correlated Input

Let the dynamical system be given as

$$dZ=A(Z,\,t)dt+G(Z,\,t)dL \tag{31}$$

where $dL/dt=W(t)$ is a stationary delta-corrected process up to the sth order; this means that the moments of the increment dL of the Levy process L are given as

$$E[dL]=0;\quad E[(dL)^r]=q^{(r)}dt,\quad r=2,\,3,\,\cdots,\,s$$
$$E[(dL)^{s+k}]\approx 0,\quad k=1,\,2,\,\cdots. \tag{32}$$

In this case, an increment of a scalar real-valued function $\phi(Z,\,t)$, continuously differentiable on t and s times differentiable on Z, and neglecting infinitesimals of higher order than dt can be written in the form

$$\Delta\phi(Z,\,t)=d\phi(Z,\,t)+\frac{1}{2!}d^2\phi(Z,\,t)+\cdots+\frac{1}{s!}d^s\phi(Z,\,t). \tag{33}$$

Using the rules of differentiation of composite functions we obtain, for example, for the first four differentials of Z, the following relationships (with argument omitted):

$$d\phi=\frac{\partial\phi}{\partial t}+\frac{\partial\phi}{\partial Z}dZ \tag{34a}$$

$$d^2\phi=\frac{\partial^2\phi}{\partial Z^2}(dZ)^2+\frac{\partial\phi}{\partial Z}d^2Z \tag{34b}$$

$$d^3\phi=\frac{\partial^3\phi}{\partial Z^3}(dZ)^3+3\frac{\partial^2\phi}{\partial Z^2}dZd^2Z+\frac{\partial\phi}{\partial Z}d^3Z \tag{34c}$$

$$d^4\phi=\frac{\partial^4\phi}{\partial Z^4}(dZ)^4+6\frac{\partial^3\phi}{\partial Z^3}[d^2Z(dZ)^2]+\frac{\partial^2\phi}{\partial Z^2}[4d^3ZdZ+3(dZ)^2]+\frac{\partial\phi}{\partial Z}d^4Z \tag{34d}$$

where dZ is given in Eq. (31). Inserting Eqs. (34) into Eq. (33) we obtain, neglecting infinitesimals of higher order than dt, the increment of ϕ in the form

$$\Delta\phi=\frac{\partial\phi}{\partial t}dt+\frac{\partial\phi}{\partial Z}\Delta Z+\frac{1}{2}\frac{\partial^2\phi}{\partial Z^2}(\Delta Z)^2+\cdots+\frac{1}{s!}\frac{\partial^s\phi}{\partial Z^s}(\Delta Z)^s \tag{35}$$

where, according to Eq. (33), an increment of Z is given as

$$\Delta Z=dZ+\frac{1}{2}d^2Z+\cdots+\frac{1}{s!}d^sZ. \tag{36}$$

Equation (35) represents the extension of the nonclassical stochastic differential rule given in Eq. (30), in the case of non-normal delta-correlated input processes. Taking Eq. (31) into account and remembering the properties of dL, it can easily be seen that

$$(dZ)^r=G^r(Z,\,t)\,(dL)^r,\quad r=2,\,3,\,\cdots,\,s;$$
$$(dZ)^{s+p}\approx 0,\quad p=1,\,2,\,\cdots. \tag{37}$$

Moreover,

$$d^rZ=G^{(r)}(Z,\,t)\,(dL)^r,\quad r=2,\,3,\,\cdots,\,s;$$
$$d^{s+p}Z\approx 0,\quad p=1,\,2,\,\cdots \tag{38}$$

where

$$G^{(1)}(Z,\,t)=G(Z,\,t);\quad G^{(r)}(Z,\,t)=\frac{\partial G^{(r-1)}(Z,\,t)}{\partial Z}G(Z,\,t),$$
$$r=2,\,3,\,\cdots. \tag{39}$$

Then, an increment of Z can be written in the following explicit form:

$$\Delta Z=A(Z,\,t)dt+\sum_{j=1}^{s}\frac{G^{(j)}(Z,\,t)}{j!}(dL)^j. \tag{40}$$

From this equation we recognize that, when the input $W(t)$ is a non-normal delta-correlated process, new correction terms like the Wong-Zakai or Stratonovich ones must be considered in order to take into account the non-normality of the input process. For example, the new correction term in the case of

Downloaded 03 May 2010 to 171.66.16.245. Redistribution subject to ASME license or copyright; see http://www.asme.org/terms/Terms_Use.cfm

delta-correlated input processes up to the third order is (with argument omitted)

$$\frac{1}{2}G^{(2)}(dL)^2+\frac{1}{3!}G^{(3)}(dL)^3=\frac{1}{2}\frac{\partial G}{\partial Z}G(dL)^2 + \frac{1}{3!}\left[\frac{\partial^2 G}{\partial Z^2}G+\left(\frac{\partial G}{\partial Z}\right)^2\right]G(dL)^3. \quad (41)$$

It is easy to verify that the new correction term is the sum of the Wong-Zakai or Stratonovich correction one, and a term which is connected to the non-normality of the input.

In the simpler case of purely external excitation it is obvious that $\Delta Z \equiv dZ$ because all the correction terms in Eq. (40) are exactly zeros.

Probabilistic Characterization of the Response

In order to characterize the response process Z, the moments of any order of Z have to be evaluated. Then, setting $\phi(Z, t) = Z^r$ in Eq. (35), applying the stochastic average and dividing by dt, we obtain

$$\dot{m}_r[Z]=rE\left[Z^{r-1}\frac{\Delta Z}{dt}\right]+\frac{1}{2}r(r-1)E\left[Z^{r-2}\frac{(\Delta Z)^2}{dt}\right] + \cdots+\frac{1}{s!}r(r-1)\cdots(r-s+1)E\left[Z^{r-s}\frac{(\Delta Z)^s}{dt}\right] \quad (42)$$

where $m_r[Z]=E[Z^r]$, ΔZ is given in Eq. (40), and

$$(\Delta Z)^2=\sum_{j=1}^{s-1}\sum_{k=1}^{s-1}\frac{G^{(j)}G^{(k)}}{j!k!}(dL)^{j+k},\quad j+k=2,\ 3,\ \cdots,\ s \quad (43a)$$

$$(\Delta Z)^3=\sum_{j=1}^{s-2}\sum_{k=1}^{s-2}\sum_{l=1}^{s-2}\frac{G^{(j)}G^{(k)}G^{(l)}}{j!k!l!}(dL)^{j+k+l},\quad j+k+l=3,\ 4,\ \cdots,\ s \quad (43b)$$

$$\vdots$$

$$(\Delta Z)^s=G^s(dL)^s. \quad (43c)$$

Hence, Eq. (42) becomes

$$\dot{m}_r[Z]=rE[Z^{r-1}A]+r\sum_{j=2}^{s}\frac{1}{j!}E[Z^{r-1}G^{(j)}]q^{(j)} + \frac{1}{2!}r(r-1)\sum_{j=1}^{s-1}\sum_{k=1}^{s-1}\frac{1}{j!k!}E[Z^{r-2}G^{(j)}G^{(k)}]q^{(j+k)} + \cdots+\frac{1}{s!}r(r-1)(r-s+1)E[Z^{r-s}G^s]q^{(s)}. \quad (44)$$

In this equation use has been made of the fact that, according to the Itô's stochastic calculus, the following relationship holds:

$$E[g(Z)(dL)^r]=E[g(Z)]E[(dL)^r]=E[g(Z)]q^{(r)}dt \quad (45)$$

where $g(Z)$ is any scalar real-valued function of Z. Equation (44) represents the differential equation governing the response moments of any order of a nonlinear system excited by parametric non-normal delta-correlated excitations.

In the simpler case of non-linear systems driven by external non-normal delta-correlated process, that is when $G^{(j)}=0, j=2, 3, \cdots, s$, Eq. (44) reads:

$$\dot{m}_r[Z]=rE[Z^{r-1}A]+\frac{1}{2}r(r-1)m_{r-2}[Z]G^2q^{(2)} + \cdots+\frac{1}{s!}r(r-1)\cdots(r-s+1)m_{r-s}[Z]G^sq^{(s)}. \quad (46)$$

This equation proves to be equivalent to that one obtained by Roberts (1972) in the case in which the input is a train of Poisson distributed pulses.

When $A(Z, t)=A(t)$ the system is linear and it is easy to see that the equation governing the moments of order r of Z involves moments of order r and moments of lesser order than r. It follows that, starting from the knowledge of the first-order moment, one can obtain the second-order moment and so on. In the nonlinear case the problem of the probabilistic characterization of the response becomes more complicated; this happens because the averages at the right-hand side of Eqs. (44) and (46) have to be evaluated starting from the knowledge of the probability density function of Z, which in turn depends on the knowledge of all the moments. So only approximated solutions can be pursued by means of well-known truncation schemes (see, e.g., Wu and Lin, 1984; Ibrahim, 1985).

Monte Carlo Simulation

In order to verify the validity of the extension of Itô's rule presented in the previous section, the results obtained by solving differential Eqs. (44) are compared with the experimental ones obtained by means of a Monte Carlo simulation. For this purpose it is necessary to generate a process that can be approximated to a non-normal delta-correlated process.

Constructing a normal process, correlated in so short time intervals that can be considered as a normal delta-correlated process, is a problem solved in literature and available methods can be found (e.g., see, Clough-Penzien, 1975; Shinozuka, 1972). By contrast, constructing a non-Poisson process which can be approximated to a non-normal delta-correlated one, is more complicated. For this reason it has been necessary to carry out an "ad hoc" method which is presented here.

The basic idea consists of generating a segment of a stationary process in the form

$$Y(t)=\sum_{k=1}^{N}R_kw_k(t) \quad (47)$$

where R_k are independent random variables characterized by having zero mean and an assigned probability distribution and $w_k(t)$ is a window function defined as

$$w_k(t)=\begin{cases}1 & \text{for } t_k-\Delta t/2\le t\le t_k+\Delta t/2\\ 0 & \text{elsewhere.}\end{cases} \quad (48)$$

In this way the duration of the process $Y(t)$ is $T=N\Delta t$. It is easy to see that the process $Y(t)$ has zero mean and the second order correlation given by

$$E[Y(t_i)Y(t_j)]=\sum_{k=1}^{N}\sum_{l=1}^{N}E[R_kR_l]w_k(t_i)w_l(t_j) \quad (49)$$

For $k\neq l$ the various terms of the summation are zeros because $E[R_kR_l]=\delta_{kl}E[R^2]$ (δ_{kl} being the kronecker delta), in virtue of the independence of the random variables. So we can write

$$E[Y(t_i)Y(t_j)]=E[R^2]\sum_{k=1}^{N}w_k(t_i)w_k(t_j). \quad (50)$$

Taking into account Eq. (48), one can observe that the terms of the summation in Eq. (50) are different from zero only when $t_k-\Delta t/2\le t\le t_k+\Delta t/2$. It follows that

$$E[Y(t_i)Y(t_j)]=\begin{cases}E[R^2] & \text{for } |t_i-t_j|\le\Delta t\\ 0 & \text{elsewhere.}\end{cases} \quad (51)$$

So the process $Y(t)$ is correlated only in the time interval between $-\Delta t/2$ and $\Delta t/2$ and in this interval the correlation takes the constant value $E[R^2]$.

In order to obtain a process that can be approximated to a delta-correlated one up to the second order, the second-order moment of R has to be given in the form

$$E[R^2]=\frac{q^{(2)}}{\Delta t}. \quad (52)$$

Downloaded 03 May 2010 to 171.66.16.245. Redistribution subject to ASME license or copyright; see http://www.asme.org/terms/Terms_Use.cfm

In fact, in this way, when $\Delta t \to 0$ we can affirm that the following relationship holds at the limit:

$$E[Y(t_i)Y(t_j)] = q^{(2)}\delta(t_i - t_j) \tag{53}$$

and this ensures that $Y(t)$ is delta correlated up to the second order.

The correlation of third order of $Y(t)$ (that in this case coincides with the average at multiple times of the same order) is given in the form

$$E_3[Y(t_i)Y(t_j)Y(t_h)] = \sum_{k=1}^{N}\sum_{l=1}^{N}\sum_{m=1}^{N} E[R_k R_l R_m] w_k(t_i) w_l(t_j) w_m(t_h) \tag{54}$$

which, taking into account the properties of the random variables R_k, reduces in the form

$$E_3[Y(t_i)Y(t_j)Y(t_h)] = E[R^3]\sum_{k=1}^{N} w_k(t_i) w_k(t_j) w_k(t_h). \tag{55}$$

The terms in the summation in Eq. (55) are different from zero only when $t_k - \Delta t/2 \le t_i,\ t_j,\ t_h \le t_k + \Delta t/2$; it follows that

$$E_3[Y(t_i)Y(t_j)Y(t_h)] = \begin{cases} E[R^3] & \text{for } |t_i - t_j| \le \Delta t \text{ and } |t_i - t_h| \le \Delta t \\ 0 & \text{elsewhere.} \end{cases} \tag{56}$$

Equation (56) shows that the correlation of third order of $Y(t)$ is different from zero only in the time interval between $-\Delta t/2$ and $\Delta t/2$ and in this interval it takes the constant value $E[R^3]$. In order to obtain a process that can be approximated to a delta correlated one up the third order, $E[R^3]$ has to be given in the form

$$E[R^3] = \frac{q^{(3)}}{(\Delta t)^2}. \tag{57}$$

In fact, in this way, at the limit when $\Delta t \to 0$, since $t_j \to t_i$ and $t_h \to t_i$, the correlation of third order of $Y(t)$ becomes a product of Dirac's delta functions, that is

$$E_3[Y(t_i)Y(t_j)Y(t_h)] = q^{(3)}\delta(t_i - t_j)\delta(t_i - t_h). \tag{58}$$

A generalization of the concepts outlined above for obtaining delta-correlated processes of higher order is straightforward.

As a conclusion we can say that a random process, generated by means of Eq. (47), is delta correlated up to the sth order, at the limit when $\Delta t \to 0$, if the distribution of the random variable R is chosen in a such particular form that $E[R] = 0$, $E[R^2] = q^{(2)}/\Delta t, \cdots, E[R^s] = q^{(s)}/(\Delta t)^{s-1}$. For example, we assume a random variable with probability density function

$$p_R(r) = \begin{cases} \alpha/r^2 & \text{for } -a \le r \le -b \text{ and } b \le r \le a \\ 0 & \text{elsewhere} \end{cases} \tag{59}$$

where α is a normalization factor given by

$$\alpha = \frac{ab}{2(a-b)}. \tag{60}$$

Then the moments of R are

$$E[R^{2k+1}] = 0, \quad k = 0, 1, 2, \cdots \tag{61a}$$

$$E[R^2] = ab; \quad E[R^4] = \frac{ab}{3}(a^2 + ab + b^2); \quad E[R^6] = \frac{ab}{5}(a^4 + a^3 b + a^2 b^2 + ab^3 + b^4); \quad \cdots \tag{61b}$$

Setting $a = 1/\Delta t$ and $b = q^{(2)}$, for very small Δt, we have

$$E[R^2] = \frac{q^{(2)}}{\Delta t}; \quad E[R^4] \approx \frac{q^{(2)}}{3(\Delta t)^3}; \quad \cdots E[R^{2s}] \approx \frac{q^{(2)}}{(2s-1)(\Delta t)^{2s-1}} \tag{62}$$

This means that, starting from a distribution given in Eq. (59), at the limit when $\Delta t \to 0$, the process $Y(t)$ approaches to a delta correlated one up to the infinite order. In particular, it is easy to see that a random variable with this type of distribution can be obtained by the inversion of the random variable S having the following probability density function:

$$p_S(s) = \begin{cases} \alpha & \text{for } -1/b \le s \le -1/a \text{ and } 1/a \le s \le 1/b \\ 0 & \text{elsewhere.} \end{cases} \tag{63}$$

Numerical Example

The system studied in the numerical example is a quasi-linear one given in the form

$$dZ = -AZdt + Cdt + \beta Z dL; \quad A > 0 \tag{64}$$

where A, C, and β are constants. The system is considered at rest with probability one at the time $t = 0$. The choice of this particular system has been made because the moment equations connected with it do not constitute an infinite hierarchy; in this way the effects of the new correction terms which appear in Eq. (40) can be evidenced in a clear manner, without masking effects due to the closure schemes. The non-normal process dL is characterized by having moments

$$E[(dL)^{2r+1}] = 0, \quad r = 0, 1, 2\cdots; \qquad E[(dL)^{2r}] = q^{(2r)} = \frac{q^{(2)}}{(2r-1)}, \quad r = 1, 2, \cdots. \tag{65}$$

Moreover the coefficient β is chosen in such a way that the new correction terms of higher order make significant contributions and, at the same time, the influence of the non-normality of the process dL is significant up to the fourth order. Lastly, the coefficient A is chosen in such a way that we do not have stability problems. Considering that the input process is delta correlated up to the fourth order and, in this case, $G^{(r)} = \beta^r Z$, the equations of moments up to the third order of the response are

$$\dot{m}_1[Z] = \left(-A + \frac{1}{2}\beta^2 q^{(2)} + \frac{1}{24}\beta^4 q^{(4)}\right) m_1[Z] + C \tag{66a}$$

$$\dot{m}_2[Z] = \left(-2A + 2\beta^2 q^{(2)} + \frac{2}{3}\beta^4 q^{(4)}\right) m_2[Z] + 2C m_1[Z] \tag{66b}$$

$$\dot{m}_3[Z] = \left(-3A + \frac{9}{2}\beta^2 q^{(2)} + \frac{27}{8}\beta^4 q^{(4)}\right) m_3[Z] + 3C m_2[Z] \tag{66c}$$

In order to evidence the influence of the new correction terms of higher order we write the same equations obtained by setting $G^{(3)} = G^{(4)} = 0$, that is

$$\dot{m}_1[Z] = \left(-A + \frac{1}{2}\beta^2 q^{(2)}\right) m_1[Z] + C \tag{67a}$$

$$\dot{m}_2[Z] = \left(-2A + 2\beta^2 q^{(2)} + \frac{1}{4}\beta^4 q^{(4)}\right) m_2[Z] + 2C m_1[Z] \tag{67b}$$

$$\dot{m}_3[Z] = \left(-3A + \frac{9}{2}\beta^2 q^{(2)} + \frac{9}{4}\beta^4 q^{(4)}\right) m_3[Z] + 3C m_2[Z] \tag{67c}$$

The parameters chosen for the analysis are summarized in Table 1. In Figs. 1, 2, and 3, the solutions of Eqs. (66) and (67) are plotted versus time. Moreover, the solutions of Eqs. (67b) and (67c) are plotted letting $q^{(4)} = 0$, in order to evidence the influence of the non-normality of the input. The results are compared with those obtained adopting the Monte Carlo simulation procedure proposed in the previous section. The step selected for the analysis is $\Delta t = 0.05$ and the number of samples used for the simulations is also reported in Table 1. The very large number of samples is due to the fact that, increasing the order of moments, a greater and greater number of samples are necessary to achieve a good accuracy. Lastly, it is important to note that, due to the particular way of constructing a delta-correlated input process, when the equation of motion is integrated by means of any numerical method

Downloaded 03 May 2010 to 171.66.16.245. Redistribution subject to ASME license or copyright; see http://www.asme.org/terms/Terms_Use.cfm

Table 1 Parameters selected

Figs.	A	β	C	$q^{(2)}$	samples
1	7.0	2.5	1.0	1	10000
2	5.0	1.5	5.0	1	10000
3	3.5	1.0	5.5	1	50000

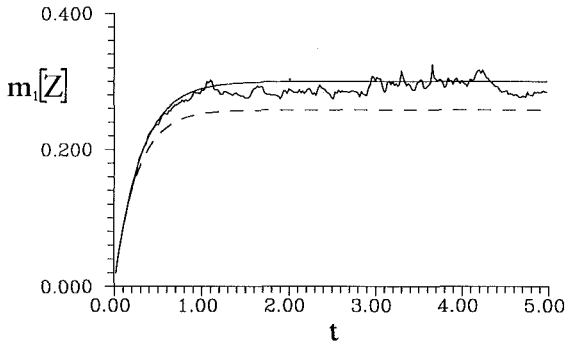


Fig. 1 Moment of first order ($m_1[Z]$); solid line: Eq. (66*a*); dashed line: Eq. (67*a*)

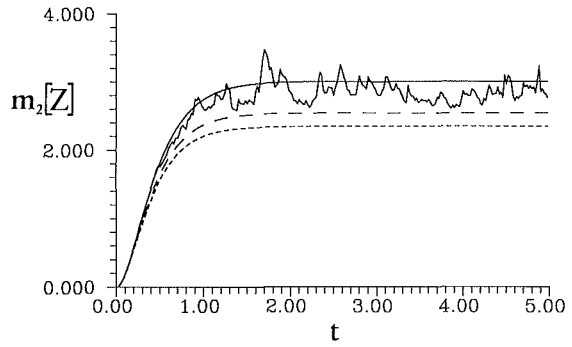


Fig. 2 Moment of second order ($m_2[Z]$); solid line: Eq. (66*b*); dashed line (— —): Eq. (67*b*); dashed line (···): normal response

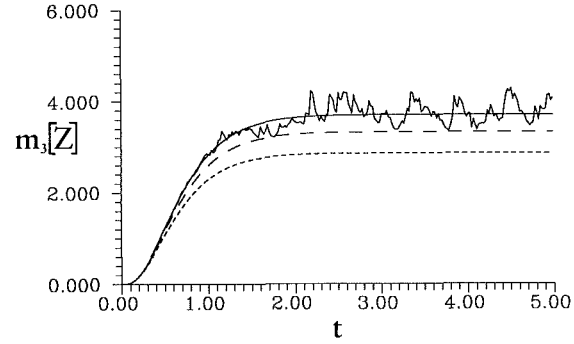


Fig. 3 Moment of third order ($m_3[Z]$); solid line: Eq. (66*c*); dashed line (— —): Eq. (67*c*); dashed line (···): normal response

(here a Runge-Kutta method has been employed), the value of input must be considered constant at each temporal step. This is due to the fact that, if we assume, for example, a linear input function at each temporal step, we obtain a nonzero probability of the input in the range $-b$, b and this produces unaccurate results.

From these figures we can observe that the influence of the new correction terms of higher order makes important contributions. Moreover, the comparison with the simulation results confirms the validity of the new interpretation of stochastic differential calculus.

Conclusions

In this paper a new interpretation of the stochastic differential calculus has been presented. Starting from a quite different Taylor expansion with respect to that one proposed in the Itô's differential rule, and here called nonclassical stochastic differential rule, the presence of the Wong-Zakai or Stratonovich correction term in the Itô stochastic differential equation is first explained. In this frame, the generalization of the nonclassical stochastic differential rule, in order to take into account the non-normality of the input process, has been straightforward. The basic idea of this new interpretation consists in evidencing the difference between the concepts of differential and of increment of the response process. These two concepts coincide when the input process is filtered or when it is purely external. On the contrary, when the system is excited by delta-correlated parametric excitations, the two concepts drastically differ from each other for the influence of the irregularities of the input process on the drift coefficient. In particular, if the input is a normal delta-correlated one, then this influence is marked by the Wong-Zakai or Stratonovich correction term. While, if the input is a non-normal delta-correlated one, the influence is marked by new correction terms which take into account the non-normality of the input.

A simple example, "ad hoc" constructed in order to evidence the influence of the various correction terms on the response, has been examined and the results obtained by means of Monte Carlo simulation confirm, in an equivocable manner, the validity of the theory presented.

References

Arnold, L., 1973, *Stochastic Differential Equations: Theory and Applications*, John Wiley and Sons, New York.

Clough, R. W., and Penzien, J., *Dynamic of Structures*, McGraw-Hill, New York.

Crandall, S. H., and Zhu, W. Q., 1983, "Random Vibration: A Survey of Recent Developments," ASME JOURNAL OF APPLIED MECHANICS, Vol. 50, pp. 953–962.

Gel'fand, I. M., and Vilenkin, N. Ya., 1964, *Generalized Functions*, Academic Press, New York.

Grigoriu, M., 1987, "White Noise Processes," *Journal of Engineering Mechanics*, Vol. 113, No. 5, ASCE, New York, pp. 757–765.

Horsthemke, W., and Lefever, R., 1984, *Noise-Induced Transitions: Theory and Applications in Physics, Chemistry and Biology*, Springer-Verlag, New York.

Ibrahim, R. A., 1985, *Parametric Random Vibration*, Research Studies Press, Letchworth, England.

Ibrahim, R. A., Soundararajan, A., and Heo, H., 1985, "Stochastic Response of Nonlinear Dynamic Systems Based on a Non-Gaussian Closure," ASME JOURNAL OF APPLIED MECHANICS, Vol. 52, pp. 965–970.

Itô, K., 1951, "On a Formula Concerning Stochastic Differential," *Nagoya Mathematical Journal*, Vol. 3, pp. 55–65.

Itô, K., 1961, *Lectures of Stochastic Processes*, Tata Institute Fundamental Research, Bombay, India.

Iwankiewicz, R., Nielsen, S. R. K., and Christensen, P. T., 1990, "Dynamic Response of Nonlinear Systems to Poisson Distributed Pulse Train: Markov Approach," *Nonlinear Structural Systems Under Random Condition*, edited by F. Casciati, I. Elishakoff, and J. B. Roberts, pp. 223–238.

Jazwinski, A. H., 1973, *Stochastic Process and Filtering Theory*, Academic Press, New York.

Lin, Y. K., 1967, *Probabilistic Theory of Structural Dynamics*, McGraw-Hill, New York.

Lutes, L. D., and Hu, S.-L. J., 1986, "Non-normal Stochastic Response of Linear Systems," *Journal of Engineering Mechanics*, Vol. 112, No. 2, ASCE, New York, pp. 127–141.

Lutes, L. D., 1986, "Cumulants of Stochastic Response for Linear Systems," *Journal of Engineering Mechanics*, Vol. 112, No. 10, ASCE, New York, pp. 1062–1075.

Picone, M., and Fichera, G., 1975, *Corso di analisi matematica*, Libreria eredi Virgilio Veschi, Roma (in Italian).

Roberts, J. B., 1972, "System Response to Random Impulses," *Journal of Sound and Vibration*, Vol. 24, pp. 23–34.

Roberts, J. B., 1984, "Techniques for Nonlinear Random Vibration Problems," *Shock Vibration Digest*, Vol. 16, No. 9, pp. 3–14.

Roberts, J. B., and Spanos, P. D., 1986, "Stochastic Averaging: An Approximate Method of Solving Random Vibration Problems," *International Journal of Nonlinear Mechanics*, Vol. 21, No. 2, pp. 111–134.

Shinozuka, M., 1972, "Monte Carlo Solution of Structural Dynamics," *International Journal of Computers and Structures*, Vol. 2, pp. 855–874.

Downloaded 03 May 2010 to 171.66.16.245. Redistribution subject to ASME license or copyright; see http://www.asme.org/terms/Terms_Use.cfm

Spanos, P. D., and Lutes, L. D., 1986, "A Primer of Random Vibration in Structural Engineering," *Shock Vibration Digest*, Vol. 18, No. 4, pp. 3–9.

Stratonovich, R. L., 1963, *Topics in the Theory of Random Noise*, Gordon and Breach, New York.

Stratonovich, R. L., 1966, "A New Form of Representing Stochastic Integrals and Equations," *J. SIAM Control*, Vol. 4, pp. 362–371.

To, C. W. S., 1988, "On the Dynamic System Disturbed by Random Parametric Excitation," *Journal of Sound and Vibration*, Vol. 123, pp. 387–390.

Wong, E., and Zakai, M., 1985, "On the Relation Between Ordinary and Stochastic Differential Equations," *International Journal of Engineering Sciences*, Vol. 3, pp. 213–229.

Wu, W. F., and Lin, Y. K., 1984, "Cumulant-Neglect Closure for Nonlinear Oscillators Under Random Parametric and External Excitations," *International Journal of Non-Linear Mechanics*, Vol. 19, No. 4, pp. 349–362.

Yong, Y., and Lin, Y. K., 1987, "Exact Stationary Response Solution for Second Order Nonlinear System Under Parametric and External White Noise Excitation," ASME JOURNAL OF APPLIED MECHANICS, Vol. 54, No. 6, pp. 414–418.

APPENDIX

Here the extension of Eq. (21) to the case of a multidimensional system will be treated. For the sake of compactness, the tensorial calculus will be used.

Let the dynamical system be given in the form

$$\mathbf{Z} = \mathbf{A}(\mathbf{Z}, t)\mathbf{Z} + \mathbf{G}(\mathbf{Z}, t)\mathbf{W}(t) \tag{A1}$$

where $\mathbf{Z}$ is an n-vector of state variables, $\mathbf{A}(\mathbf{Z}, t)$ and $\mathbf{G}(\mathbf{Z}, t)$ are deterministic matrices of order $n \times n$ and $n \times m$, respectively, whose elements are functions of $\mathbf{Z}$ and t, and $\mathbf{W}(t)$ is an m-vector of non-normal stochastic processes delta-correlated up to the sth order. The ith equation of the system (A1) can be written in the following differential form:

$$dZ_i = A_{il}(\mathbf{Z}, t)Z_l dt + G_{ir}(\mathbf{Z}, t)dL_r \tag{A2}$$

where the summation convention of the tensorial calculus has been adopted. The processes dL_r are characterized by the following moments:

$$E[dL_i(t)] = 0; \quad E[dL_i(t)dL_j(t)] = q_{ij}^{(2)}dt; \quad \cdots;$$
$$E[dL_i(t)dL_j(t)\cdots dL_k(t)] = q_{ij\cdots k}^{(s)}.$$

Let $\phi(\mathbf{Z}, t)$ be any scalar real-valued function of $\mathbf{Z}$ and t, continuously differentiable on t and s-times differentiable with respect to the various components of $\mathbf{Z}$; then an increment of $\phi(\mathbf{Z}, t)$ can be written in the form

$$\Delta\phi = \frac{\partial\phi}{\partial t}dt + \phi_{,i}\Delta Z_i + \frac{1}{2!}\phi_{,ij}\Delta Z_i\Delta Z_j + \cdots + \frac{1}{s!}\phi_{,ij\cdots k}\Delta Z_i\Delta Z_j\cdots\Delta Z_k \tag{A4}$$

where $\phi_{,i} = \partial\phi/\partial Z_i$, $\phi_{,ij} = \partial^2\phi/\partial Z_i\partial Z_j$, and so on. In Eq. (A4), ΔZ_i is given in the form

$$\Delta Z_i = dZ_i + \frac{1}{2!}d^2Z_i + \cdots + \frac{1}{s!}d^sZ_i. \tag{A5}$$

Neglecting infinitesimals of higher order than dt we obtain

$$\begin{aligned} d^2Z_i &= G_{iu,j}G_{jv}dL_u dL_v = G_{iuv}^{(2)}dL_u dL_v \\ &\cdots \\ d^sZ_i &= G_{iuv\cdots q}^{(s)}dL_u dL_v\cdots dL_q \end{aligned} \tag{A6}$$

where

$$G_{iuv\cdots pq}^{(s)} = G_{iuv\cdots p,j}^{(s-1)}G_{jp}. \tag{A7}$$

It follows that an increment of Z_i is given in the form

$$\Delta Z_i = A_{il}Z_l dt + G_{ir}dL_r + \frac{1}{2!}G_{iuv}^{(2)}dL_u dL_v + \cdots + \frac{1}{s!}G_{iuv\cdots q}^{(s)}dL_u dL_v\cdots dL_q \tag{A8}$$

in which the new correction terms are evidenced.

Inserting Eq. (A8) in Eq. (A4) we obtain the extension of the stochastic differential rule to multidimensional systems.

Downloaded 03 May 2010 to 171.66.16.245. Redistribution subject to ASME license or copyright; see http://www.asme.org/terms/Terms_Use.cfm

Random Vibrations of Externally Damped Viscoelastic Timoshenko Beams With General Boundary Conditions

M. P. Singh
Professor.

A. S. Abdelnaser
Graduate Student.

Department of Engineering Science and Mechanics,
Virginia Polytechnic Institute and State University,
Blacksburg, VA 24061-0219

A complex mode approach is presented to analyze an externally damped viscoelastic Timoshenko beam subjected to distributed loads. The eigenfunctions of the original and adjoint equations are used to decouple the equations. Any conventional or nonstandard boundary conditions at beam ends can be handled with equal ease. Numerical response results are presented for random loads with spatial and temporal correlations.

Introduction

The vibration analysis of Timoshenko beams has been of continued interest to engineers since the beginning of this century. There have been several studies dealing with the effects of the shear deformation and rotatory inertia on the beam frequencies as well as some notable studies dealing with the forced vibration analysis of Timoshenko beams with general boundary conditions. Dolph (1954), Anderson (1953), and Herrmann (1955) developed the orthogonality conditions which are essential relationships required to solve a forced vibration problem by the modal analysis approach. Explicit expressions for the frequency equations and characteristic functions were developed by Huang (1961) for beams with standard boundary conditions. A quite comprehensive account of the forced vibration analysis of undamped Timoshenko beams is also given by Leonard (1959).

There have also been some studies on the damped vibrations of Timoshenko beams. Relevant to this work are the studies by Samuels and Eringen (1958), Newman (1969), Lee (1960), Crandall and Yildiz (1962), Pan (1966), Banerjee and Kennedy (1985), and Elishakoff and Livshits (1989). Samuels and Eringen (1958) studied the random response of a simply-supported Timoshenko beam with transverse and rotational viscous damping terms and examined the boundedness of the response for delta-correlated loads. Newman (1959) and Lee (1960) considered damping in the beam through viscoelastic behavior in extensional strain. Newman used the Laplace transform technique to solve the problem of a cantilever beam whereas Lee solved the steady-state response of a cantilever beam subjected to a sinusoidal load.

Crandall and Yildiz (1962) examined the problem of a simply-supported Timoshenko beam with a quite general damping model. The model consisted of external dampings in the transverse and rotational motions and different viscoelastic damping parameters in the flexure and shear deformations. They examined the convergence characteristics of the mean square values of various response quantities of a simply-supported beam subjected to delta-correlated loads. The known eigenfunctions of a simple-supported beam were utilized to obtain the complex frequency response functions for various response quantities of interest. These frequency response functions could be conveniently used with the white-noise excitation to obtain the closed-form expressions for the mean-square response. Pan (1966) also analyzed a Timoshenko beam with viscoelastic material both in extension and shear. The material was assumed to be incompressible whereby the same viscoelastic operators could be used both for the flexural and shear deformations. However, beside the viscoelastic damping, no other external damping was considered in this study. This permitted the use of the normal modes and their orthogonality conditions to solve this viscoelastic forced vibration problem. The example problem of a simply-supported beam was presented. Banerjee and Kennedy (1985) analyzed a damped and axially loaded Timoshenko beam for random transverse loads. Only a special case of damping in the transverse and rotatory motions was considered which allowed them to use the orthogonality conditions of the undamped modes to decouple the modal equations. Elishakoff and Livshits (1989) have obtained the *closed-form* solution, but for an incomplete differential equation of a simply-supported beam with external damping. They neglected a total of eight terms from the complete Timoshenko beam differential equation; three out of these eight terms were the forcing function terms. They claimed, referring to an unpublished correspondence, that this incorrect equation was

Contributed by the Applied Mechanics Division of THE AMERICAN SOCIETY OF MECHANICAL ENGINEERS for publication in the ASME JOURNAL OF APPLIED MECHANICS.

Discussion on this paper should be addressed to the Technical Editor, Professor Lewis T. Wheeler, Department of Mechanical Engineering, University of Houston, Houston, TX 77204-4792, and will be accepted until four months after final publication of the paper itself in the ASME JOURNAL OF APPLIED MECHANICS.

Manuscript received by the ASME Applied Mechanics Division, Apr. 3, 1991; final revision, Oct. 18, 1991. Associate Technical Editor: P. D. Spanos.

Copyright © 1993 by ASME
Downloaded 03 May 2010 to 171.66.16.245. Redistribution subject to ASME license or copyright; see http://www.asme.org/terms/Terms_Use.cfm

"more consistent than the original Timoshenko equation." No definition of the consistency and no numerical results were, however, provided to substantiate their claim.

In this paper we present a general modal approach to solve the linear vibration problem of a uniform Timoshenko beam with external transverse and rotatory viscous dampings and different viscoelastic dampings in the flexural and shear deformations. With this approach, the beams with any boundary conditions can be as conveniently analyzed as a beam with simple supports. Using this approach, the numerical response results are obtained and reported for spatially and temporally correlated or uncorrelated transverse loads acting on a beam.

Analytical Formulation

The equations of motion of an externally damped uniform viscoelastic beam can be written in the following form:

$$-k\hat{A}\hat{G}(t)\left[\frac{\partial^2\hat{w}}{\partial\hat{x}^2}-\frac{\partial\psi}{\partial\hat{x}}\right]+\hat{c}_2\frac{\partial\hat{w}}{\partial\hat{t}}+\rho\hat{A}\frac{\partial^2\hat{w}}{\partial\hat{t}^2}=\hat{f} \tag{1}$$

$$-\hat{A}\hat{r}^2\hat{E}(t)\frac{\partial^2\psi}{\partial\hat{x}^2}-k\hat{A}\hat{G}(t)\left[\frac{\partial\hat{w}}{\partial\hat{x}}-\psi\right]+\hat{c}_3\frac{\partial\psi}{\partial\hat{t}}+\hat{A}\hat{r}^2\rho\frac{\partial^2\psi}{\partial\hat{t}^2}=0 \tag{2}$$

where

$\hat{w}$ = transverse deflection
ψ = angular rotation
$\hat{f}$ = external force per unit length
$\hat{A}$ = area of cross-sections
r = radius of gyration of cross-section
ρ = mass density
k = shear correction factors
$\hat{c}_2$ = linear viscous damping coefficient per unit length
$\hat{c}_3$ = rotational viscous damping per unit length.

$\hat{G}(t)$ and $\hat{E}(t)$, respectively, are the viscoelastic shear and Young's modulus. For the Voigt material they can be written as

$$E(t)=E^*\left[1+\hat{\xi}\frac{\partial}{\partial\hat{t}t}\right];\quad G(t)=G^*\left[1+\hat{\eta}\frac{\partial}{\partial\hat{t}}\right]. \tag{3}$$

To obtain the equations of motion in nondimensional form, we introduce the following nondimensional quantities:

$$x=\frac{\hat{x}}{L},\quad w=\frac{\hat{w}}{L},\quad G=\frac{G^*}{E^*};\quad t=\frac{\hat{t}}{T};\quad T=\left[\frac{L^2}{r}\right]\sqrt{\frac{\rho}{E^*}}, \tag{4}$$

and obtain

$$-P_2(t)\frac{\partial}{\partial x}\left[\frac{\partial w}{\partial x}-\psi\right]+gc_2\frac{\partial w}{\partial t}+g\frac{\partial^2 w}{\partial t^2}=gf \tag{5}$$

$$-P_1(t)\frac{\partial^2\psi}{\partial x^2}-\frac{P_2(t)}{g}\left[\frac{\partial w}{\partial x}-\psi\right]+Rc_3\frac{\partial\psi}{\partial t}+R\frac{\partial^2\psi}{\partial t^2}=0, \tag{6}$$

where L = length of the beam and

$$\left\{\begin{array}{c} P_1(t)=\left[1+\left(\frac{r}{L}\right)\xi\frac{\partial}{\partial t}\right];\quad P_2(t)=\left[1+\left(\frac{r}{L}\right)\eta\frac{\partial}{\partial t}\right] \\ \xi=L\hat{\xi}/(Tr),\quad \eta=L\hat{\eta}/(Tr),\quad R=(r/L)^2g=r^2E^*/(KG^*L^2) \\ c_2=\frac{L^2\hat{c}_2}{\hat{A}r\sqrt{E^*\rho}};\quad c_3=\frac{\hat{c}_3L^2}{\hat{A}r^3\sqrt{\rho E^*}},\quad F=\frac{\hat{f}L^3}{\hat{A}r^2E^*} \end{array}\right\} \tag{7}$$

Equations (5) and (6) are associated with appropriate boundary conditions which depend upon the support conditions at the ends of the beam.

The solution of a damped Timoshenko beam problem described in Eqs. (5) and (6) has not been reported for arbitrary values of ξ, η, c_2, and c_3, and generalized boundary conditions. The solution by Pan (1966) was for a special damping case in which $P_1(t)$ and $P_2(t)$ were identical and the terms associated with viscous damping c_2 and c_3 were absent. These special situations enabled him to use the orthogonality conditions of an undamped beam. These conditions corresponding to Eqs. (5) and (6) can be written as

$$\int_0^1 \cdot\,(w_m w_n+R\psi_m\psi_n)\,dx=\delta_{mn} \tag{8}$$

where w_m and ψ_m are the mth eigenfunctions for variables w and ψ of an undamped Timoshenko beam. It can be shown that the undamped eigenfunctions w_m and ψ_m can be used to decouple Eqs. (5) and (6) by the following transformation:

$$\begin{Bmatrix} w \\ \psi \end{Bmatrix}=\sum_{m=1}^{\infty}\begin{Bmatrix} w_m \\ \psi_m \end{Bmatrix}q_m(t), \tag{9}$$

if the following restrictions are satisfied by the viscoelastic and viscous damping parameters

$$\xi=\eta;\quad c_2=c_3. \tag{10}$$

If any of the two equalities in Eq. (10) is not satisfied, then the transformation in Eq. (9) will not decouple the equations of motion. Assuming that the conditions of Eq. (10) are satisfied, a decoupled equation for a principal coordinate can be obtained as

$$\ddot{q}_m+2\beta_m\omega_m\dot{q}_m+\omega_m^2q_m=\int_0^1 w_m f(x,\,t)\,dx \tag{11}$$

where a dot over a quantity denotes time differentiation, $\omega_m=m$th modal frequency, and

$$\beta_m=\frac{1}{2}\left[\frac{c_2}{\omega_m}+\left(\frac{r}{L}\right)\xi\omega_m\right]. \tag{12}$$

Equation (12) indicates that the modal damping ratio associated with the viscous damping coefficients c_2 and c_3 will decrease for higher modes whereas the ratio associated with the viscoelastic damping coefficients η and ξ will increase for the higher modes.

In a more general damping case where any of the two conditions in Eq. (10) is not satisfied, the forced vibration problem cannot be solved by the normal mode approach. However, it can still be solved by a complex mode approach. The situation here is similar to the case of a damped discrete dynamical system where it becomes necessary to employ the complex mode approach to solve the problem if the damping matrix of the system does not satisfy certain proportionality conditions (Foss, 1958; Singh, 1980; Fang and Wang, 1985). The application of the complex mode approach to an undamped beam problem can also be helpful, as it is quite convenient to develop the eigenfunctions for generalized beam boundary conditions. The approach also avoids the need of developing orthogonality conditions explicitly (Singh and Abdelnaser, 1990). Here we present a more general application of the complex mode approach to solve the forced vibration problem of a damped Timoshenko beam.

In this method, we write Eqs. (5) and (6) in the state form in the spatial domain as

$$[C_3]\frac{\partial}{\partial x}\{u\}+[C_2]\frac{\partial^2}{\partial t\,\partial x}\{u\}+[K]\{u\}+[C_1]\frac{\partial}{\partial t}\{u\}+[M]\frac{\partial^2}{\partial t^2}\{u\}=\{\hat{F}(x,\,t)\} \tag{13}$$

where

Downloaded 03 May 2010 to 171.66.16.245. Redistribution subject to ASME license or copyright; see http://www.asme.org/terms/Terms_Use.cfm

$$\{u\}^T=\{u_1,\ u_2,\ u_3,\ u_4\}=\left\{w,\ \psi,\ \frac{\partial w}{\partial x},\ \frac{\partial \psi}{\partial x}\right\};$$

$$\{\hat{F}(x,\ t)\}^T=\{0,\ 0,\ f(x,\ t),\ 0\}. \quad (14)$$

The matrices in Eq. (13) are (4×4) and their nonzero elements are defined as

$$\left.\begin{aligned} &C_2(3,\ 3)=-\bar{\eta};\ \ C_2(4,\ 4)=-\bar{\xi};\ \ C_1(3,\ 1)=gc_2\\ &C_1(3,\ 4)=\bar{\eta};\ \ C_1(4,\ 2)=(Rc_3+\bar{\eta}/g);\ \ C_1(4,\ 3)=-\bar{\eta}/g\\ &K(1,\ 3)=1;\ \ K(2,\ 4)=1;\ \ K(4,\ 2)=1/g;\ \ K(4,\ 3)=-1/g\\ &M(3,\ 1)=g;\ \ M(4,\ 2)=R;\ \ [C_3]=-[I] \end{aligned}\right\} \quad (15)$$

where now $\bar{\eta}=(r\eta/L)$, $\bar{\xi}=(r\xi/L)$ and $[I]$ is an identity matrix. All other elements of the matrices are zero.

We will first obtain the solution for the homogeneous part of Eq. (13). We examine a solution of the following form:

$$\{u\}=\{\bar{u}\}e^{\omega t} \quad (16)$$

where ω is, in general, a complex quantity. Substituting Eq. (16) into Eq. (13) we obtain

$$[C_3+\omega C_2]\{\bar{u}'\}+[K+\omega C_1+\omega^2 M]\{\bar{u}\}=0 \quad (17)$$

where a prime now denotes differentiation with respect to x. The solution of Eq. (17) can be written as

$$\{\bar{u}\}=\sum_{j=1}^{4} a_j\{\phi_j\}e^{\lambda_j x} \quad (18)$$

where λ_j and $\{\phi_j\}$ are the eigenvalues and eigenvectors obtained from

$$\lambda_j[C_3+\omega C_2]\{\phi_j\}=-[K+\omega C_1+\omega^2 M]\{\phi_j\}. \quad (19)$$

It is quite simple to solve Eq. (19) in closed form. The expression for λ_j, in terms of parameter ω is as follows:

$$\lambda=\pm\left[\frac{-b\pm\sqrt{b^2-4ac}}{2a}\right]^{1/2} \quad (20)$$

where

$$\left.\begin{aligned} a&=(1+\omega\bar{\eta})(1+\omega\bar{\xi})\\ b&=-\omega[(1+\omega\bar{\eta})(c_3+\omega)R+g(1+\omega\bar{\xi})(c_2+\omega)]\\ c&=\omega(c_2+\omega)\{1+\omega\bar{\eta}+\omega g R(c_3+\omega)\}. \end{aligned}\right\} \quad (21)$$

The elements of $\{\phi_j\}$ are

$$\phi_{j1}=\frac{(1+\omega\bar{\eta})}{\lambda_j^2(1+\bar{\eta}\omega)-\omega g(c_2+\omega)};$$

$$\phi_{j2}=\frac{1}{\lambda_j};\ \ \phi_{j3}=\lambda_j\phi_{j1};\ \ \phi_{j4}=1 \quad (22)$$

where ϕ_{jk} is the kth element of $\{\phi_j\}$.

The coefficients a_j in Eq. (18) are obtained so that the elements of $\{\bar{u}\}$ satisfy the boundary conditions of the beam. The satisfaction of these conditions will lead to a set of four homogeneous simultaneous equations as follows:

$$[\Delta]\{a\}=\{0\} \quad (23)$$

where a_j are the elements of $\{a\}$. The entries of $[\Delta]$ depend upon the end conditions. For example, for the case of a fixed-free beam, the elements of matrix $[\Delta]$ are

$$[\Delta]=\begin{bmatrix} \phi_{11} & \phi_{21} & \phi_{31} & \phi_{41}\\ \phi_{12} & \phi_{22} & \phi_{32} & \phi_{42}\\ (\phi_{12}-\phi_{13})e^{\lambda_1} & (\phi_{22}-\phi_{23})e^{\lambda_2} & (\phi_{32}-\phi_{33})e^{\lambda_3} & (\phi_{42}-\phi_{43})e^{\lambda_4}\\ \phi_{14}e^{\lambda_1} & \phi_{24}e^{\lambda_2} & \phi_{34}e^{\lambda_3} & \phi_{44}e^{\lambda_4} \end{bmatrix}. \quad (24)$$

For a nontrivial solution of Eq. (20),

$$|\Delta|=0. \quad (25)$$

Equation (25) provides the characteristic equation for the frequency parameter ω. There will be infinite possible solutions for ω which will occur either in the pairs of complex and conjugate for lower modes or have real values for the higher modes which could possibly become overdamped. For each ω_n, there is a set of a_{nj}, λ_{nj}, $\{\phi_{nj}\}$ and characteristic function $\{\bar{u}_n\}$, defined according to Eq. (18).

These eigenvalues and eigenfunctions by themselves are not quite adequate for modal decoupling of Eq. (13). To proceed further with the analysis, we introduce the state variables in the time domain as

$$\left[\frac{\partial u_1}{\partial t},\ \frac{\partial u_2}{\partial t},\ \frac{\partial u_3}{\partial t},\ \frac{\partial u_4}{\partial t}\right]=(u_5,\ u_6,\ u_7,\ u_8) \quad (26)$$

and write Eq. (13) as

$$[A_1]\{U'\}+[A_2]\{U\}+[A_3]\{\dot{U}\}=\{F(x,\ t)\} \quad (27)$$

where now

$$\{U\}^T=(\{u\},\ \{\dot{u}\})^T \quad (28)$$

$$\left.\begin{aligned} &[A_1]=\begin{bmatrix} C_3 & C_2\\ 0 & 0 \end{bmatrix};\ [A_2]=\begin{bmatrix} K & C_1\\ 0 & I \end{bmatrix};\ [A_3]=\begin{bmatrix} 0 & M\\ -I & 0 \end{bmatrix}\\ &\{F(x,\ t)\}^T=(\{\hat{F}(x,\ t)\},\ \{0\})^T \end{aligned}\right\}. \quad (29)$$

We assume the homogeneous solution of (27) to be

$$\{U\}=\{\bar{U}\}e^{\omega t}=\begin{Bmatrix} U_u\\ U_l \end{Bmatrix}e^{\omega t} \quad (30)$$

where $\{U_u\}$, and $\{U_l\}$, respectively, are the upper and lower parts of $\{\bar{U}\}$. $\{\bar{U}\}$, then, must satisfy

$$[A_1]\{\bar{U}'\}+[A_2+\omega A_3]\{\bar{U}\}=\{0\}. \quad (31)$$

Equation (31) is equivalent to two equations:

$$[C_3]\{U_u'\}+[C_2]\{U_l'\}+[K]\{U_u\}+[C_1]\{U_l\}+\omega[M]\{U_l\}=0 \quad (32)$$

$$\{U_l\}=\omega\{U_u\}. \quad (33)$$

Substituting (33) into Eq. (32), we obtain

$$[C_3+\omega C_2]\{U_u'\}+[K+\omega C_1+\omega^2 M]\{U_u\}=\{0\}. \quad (34)$$

Equations (17) and (34) are identical with the same boundary conditions. Thus, a solution $\{u_n\}$ of Eq. (17), given by Eqs. (18) corresponding to eigenvalue ω_n, also provides the upper part of $\{\bar{U}_n\}$. The lower part of $\{\bar{U}_n\}$ is obtained from Eq. (33). Thus, the eigenfunction of Eq. (27) is defined as

$$\{\bar{U}_n\}=\begin{bmatrix} \bar{u}_n\\ \omega_n\bar{u}_n \end{bmatrix}. \quad (35)$$

These eigenfunctions alone, however, are not sufficient to decouple the equation (27) into its modal equations. Since the homogeneous Eq. (31) is not self-adjoint, we also need to develop its adjoint equation and the corresponding biorthogonal eigenfunctions (Bisplinghoff and Ashley, 1962).

Following Ince (1956) or Nayfeh (1981), it is quite straightforward to show that the adjoint of Eq. (31) is

$$-[A_1]^T\{\bar{V}'\}+[A_2+\omega A_3]^T\{\bar{V}\}=\{0\} \quad (36)$$

and the boundary conditions on adjoint $\{V\}$ consistent with the boundary conditions on $\{\bar{U}\}$ are given by

$$\{\bar{U}\}^T[A_1]^T\{\bar{V}\}=0 \ \text{ at } \ x=0 \text{ and } 1. \quad (37)$$

For example, for the case of a fixed-free beam, the consistent boundary conditions on the elements of $\{\bar{U}\}$ and $\{\bar{V}\}$ are

Downloaded 03 May 2010 to 171.66.16.245. Redistribution subject to ASME license or copyright; see http://www.asme.org/terms/Terms_Use.cfm

$$\left.\begin{array}{lll} \text{At } x=0: & \overline{U}_1=\overline{U}_2=0; & \overline{V}_3=\overline{V}_4=0 \\ \text{At } x=1: & \overline{U}_4=0 \quad ; & \overline{V}_1=0 \\ & \overline{U}-\overline{U}_3=0\ ; & \overline{V}_2+\overline{V}_3 e=0 \end{array}\right\} \tag{38}$$

where $e=(1+\omega\bar{\eta})$.

Equation (36) is also equivalent to two sets of equations, expressed in terms of the upper and lower parts of $\{\overline{V}\}$ as

$$-[C_3]^T\{\overline{V}_u'\}+[K]^T\{\overline{V}_u\}-\omega\{\overline{V}_l\}=0 \tag{39}$$

$$-[C_2]^T\{\overline{V}_u'\}+[C_1]^T\{\overline{V}_u\}+\{\overline{V}_l\}+\omega[M]^T\{\overline{V}_u\}=0 \tag{40}$$

where the subscripts u and l indicate the upper and lower parts, respectively. Substituting for $\{\overline{V}_l\}$ from Eq. (40) into Eq. (39), we obtain an equation in terms of $\{\overline{V}_u\}$ alone as:

$$-[C_3+\omega C_2]^T\{\overline{V}_u'\}+[K+\omega C_1+\omega^2 M]^T\{\overline{V}_u\}=0 \tag{41}$$

It can be shown that Eq. (41) is the adjoint of Eq. (17). That is, it is not necessary to develop Eq. (36) to obtain Eq. (41); rather, the latter equation can be obtained from Eq. (17) directly. However, it is necessary to know Eq. (36), to develop the relationship between the upper and lower parts of $\{\overline{V}\}$. This relationship is provided by Eq. (39) or (40).

The solution of Eq. (41) can now be written as

$$\{\overline{V}_u\}=\sum_{j=1}^{4} b_j\{\psi_j\}e^{\mu_j x} \tag{42}$$

where the eigenvalues μ_j and eigenvectors $\{\psi_j\}$ are obtained from

$$\mu_j[C_3+\omega C_2]^T\{\psi_j\}=[K+\omega C_1+\omega^2 M]^T\{\psi_j\} \tag{43}$$

Comparing Eqs. (19) and (43), we note that

$$\mu_j=-\lambda_j \tag{44}$$

and the elements of the eigenvector $\{\psi_j\}$ are

$$\psi_{j1}=\frac{\psi(1+\omega\bar{\eta})\ (c_2+\omega)}{\{\mu^2(1+\omega\bar{\eta})-\omega g(c_2+\omega)\}};\quad \psi_{j2}=-\frac{R}{\mu}(c_3+\omega)\omega-\frac{(1+\omega\bar{\eta})}{\mu g}$$

$$\psi_{j3}=-\mu\psi_{j1}/[\omega-g(c_2+\omega)];\quad \psi_{j4}=1. \tag{45}$$

To obtain b_j in Eq. (42), we apply the boundary condition on the adjoint $\{\overline{V}\}$. This provides a set of four homogeneous simultaneous equations as

$$[\Gamma][b]=\{0\}. \tag{46}$$

The elements of $[\Gamma]$, of course, depend upon the boundary conditions. For example, for a fixed-free beam, the elements of $[\Gamma]$ are as follows:

$$[\Gamma]=\begin{bmatrix} \psi_{13} & \psi_{23} & \psi_{33} & \psi_{43} \\ \psi_{14} & \psi_{24} & \psi_{34} & \psi_{44} \\ (\psi_{12}+e\psi_{13})e^{-\lambda_1} & (\psi_{22}+e\psi_{23})e^{-\lambda_2} & (\psi_{32}+e\psi_{33})e^{-\lambda_3} & (\psi_{42}+e\psi_{43})e^{-\lambda_4} \\ \psi_{11}e^{-\lambda_1} & \psi_{21}e^{-\lambda_2} & \psi_{31}e^{-\lambda_3} & \psi_{41}e^{-\lambda_4} \end{bmatrix} \tag{47}$$

where ψ_{jk} is the kth element of $\{\psi_j\}$.

For a nontrivial solution of Eq. (46) the determinant of $[\Gamma]$ must be zero. This will provide the characteristic equation to solve for ω. However, if Eq. (25) has been solved for ψ_n, it is necessary to solve $|\Gamma|=0$ again. For each ω_n obtained from Eq. (25), the coefficients b_{nj} are obtained from Eq. (46). Equation (42), then defines the $\{\overline{V}_{nu}\}$, the upper part of the nth eigenfunction $\{\overline{V}_n\}$. The lower part is obtained from Eq. (40), which can also be written as

$$\{\overline{V}_{nl}\}=\sum_{j=1}^{4} b_{nj}e^{\mu_{nj}x}[T]\{\psi_{nj}\} \tag{48}$$

where

$$[T]=-[\lambda_{nj}C_2+C_1+\omega_n M]^T. \tag{49}$$

The complete adjoint eigenfunction is then defined as

$$\{\overline{V}_n\}=\sum_{j=1}^{4} b_{nj}e^{\mu_{nj}x}\begin{bmatrix} I \\ T \end{bmatrix}\{\psi_{nj}\}. \tag{50}$$

Orthogonality of Eigenfunctions

A very useful property of the adjoint eigenfunctions $\{\overline{U}_n\}$ and $\{\overline{V}_n\}$ is that they are biorthogonal. To show this, we write Eq. (31) for the nth eigenfunction and Eq. (36) for the mth eigenfunction as

$$[A_1]\{\overline{U}_n'\}+[A_2+\omega_n A_3]\{\overline{U}_n\}=\{0\} \tag{51}$$

$$-[A_1]^T\{\overline{V}_m'\}+[A_2+\omega_m A_3]^T\{\overline{V}_m\}=\{0\}. \tag{52}$$

Premultiplying Eq. (52) by $\{\overline{U}_n\}^T$ and integrating by parts, we obtain

$$-\{\overline{U}_n\}^T[A_1]^T\{\overline{V}_m\}\Big|_0^1+\int_0^1[\{\overline{U}_n'\}^T[A_1]^T\{\overline{V}_m\}+\{\overline{U}_n\}^T[A_2+\omega_m A_3]^T\{\overline{V}_m\}]dx=0. \tag{53}$$

According to Eq. (37), the boundary terms in Eq. (53) are zero. Transposing the scalars in Eq. (53), we obtain

$$\int_0^1[\{\overline{V}_m\}^T[A_1]\{\overline{U}_n'\}+\{\overline{V}_m\}^T[A_2+\omega_m A_3]\{\overline{U}_n\}]dx=0. \tag{54}$$

Premultiplying Eq. (51) by $\{\overline{V}_m\}^T$, integrating over the domain, and then subtracting the resulting equation from Eq. (54) we obtain

$$(\omega_m-\omega_n)\int_0^1\{\overline{V}_m\}^T[A_3]\{\overline{U}_n\}dx=0. \tag{55}$$

Equation (55) provides the required orthogonality condition. For $m=n$, we can use this condition to normalize the eigenfunctions. That is

$$\int_0^1\{\overline{V}_m\}^T[A_3]\{\overline{U}_n\}dx=\delta_{mn}, \tag{56}$$

where δ_{mn} is the Kronecker delta. Using (56) with Eq. (54), we obtain another form of orthogonality condition as

$$\int_0^1\{\overline{V}_m\}^T[[A_1]\{\overline{U}_n'\}+[A_2]\{\overline{U}_n\}]dx=-\omega_m\delta_{mn}. \tag{57}$$

Forced Vibration Problem

To solve Eqs. (5) and (6), we solve their state vector form, Eq. (27). We expand the solution in terms of the eigenfunctions as

$$\{U\}=\sum_{n=1}^{\infty}\{\overline{U}_n\}q_n(t) \tag{58}$$

where $q_n(t)$ are the time-dependent principal coordinates. Substituting Eq. (58) into Eq. (27), premultiplying by $\{\overline{V}_m\}^T$ followed by integration over the domain, we obtain

$$\sum_{n=1}^{\infty}\left[q_n(t)\int_0^1\{\overline{V}_m\}^T[[A_1]\{\overline{U}_n'\}+[A_2]\{\overline{U}_n\}]dx+\dot{q}_n(t)\int_0^1\{\overline{V}_m\}^T[A_3]\{\overline{U}_n\}dx\right]=\int_0^1\{\overline{V}_m\}^T\{F(x,t)\}dx. \tag{59}$$

Downloaded 03 May 2010 to 171.66.16.245. Redistribution subject to ASME license or copyright; see http://www.asme.org/terms/Terms_Use.cfm

Utilizing the orthogonality conditions in Eqs. (56) and (57), we obtain a decoupled equation for $q_m(t)$ as

$$\dot{q}_m(t) - \omega_m q_m(t) = \int_0^1 \overline{V}_{m3} f(x,t)\,dx \tag{60}$$

where $\overline{V}_{m3}$ is the third element of $\{\overline{V}_m\}$. The solution of Eq. (60) for the zero-start initial conditions can be written as

$$q_m(t) = \int_0^t e^{\omega_m(t-\tau)} \int_0^1 \overline{V}_{m3} f(x,\tau)\,dx\,d\tau. \tag{61}$$

Equations (58) and (61) define the time variation of the response. Any response quantity linearly related $\{u\}$ can also be written as

$$Q(x,\ t) = \sum_{n=1}^{\infty} \rho_n(x) q_n(t) \tag{62}$$

where $\rho_n(x)$ is the nth mode contribution to the response. For example, if the response quantity of interest is the shear force in the beam at any point x, then

$$\rho_n = kG^*\{U_{n3} - U_{n2} + \hat{\eta}\omega_n(U_{n3} - U_{n2})\} \tag{63}$$

Response for Random Load

We will now obtain the statistics of response $Q(x, t)$ for a temporally and spatially correlated or uncorrelated random load. For a zero-mean load process, the mean of $Q(x, t)$ will be zero. The autocorrelation function is then given by

$$E[Q(x_1,\ t_1)Q(x_2,\ t_2)] = \sum_{m=1}^{\infty}\sum_{n=1}^{\infty} \rho_m(x_1)\rho_n(x_2)E[q_m(t_1)q_n(t_2)] \tag{64}$$

where $E(,)$ denotes the ensemble expectation of $(,)$. We will obtain the correlation between the principal coordinates required in Eq. (64) in the frequency domain for a temporally stationary and spatially homogeneous distribution of the load. It can be easily shown that the stationary correlation function of the principal coordinates required in Eq. (64) is given by

$$E[q_m(t_1)q_n(t_2)] = \int_{-\infty}^{\infty} \exp\{i\omega(t_2 - t_1)\} H_m(\omega)H_n(-\omega) \times \int_0^1\int_0^1 \Phi_{ff}(\omega,\ y_1',\ y_2')\overline{V}_{m3}(y_{n3}'(y_2')\,dy_1'\,dy_2'\,d\omega \tag{65}$$

where $\Phi_{ff}\ (\omega,\ x_1,\ x_2)$ is the spectral density function of the load process and H_m is the steady-state frequency response function defined as

$$H_m = -\,(i\omega + \omega_m)^{-1}. \tag{66}$$

For calculating the mean-square value of a response quantity, the correlation of the principal coordinates at $t_1 = t_2 = t$ will be of interest. We will now define this for several stochastic models of the distributed load $f(x, t)$ which have been considered in the past.

One popular and analytically convenient, but physically unrealistic, model is the delta-correlated model in time and space. For such a model, the correlation function of the load $R_{ff}(x_1,\ t_1;\ x_2,\ t_2)$ is represented by

$$R_{ff}(x_1,\ t_1;\ x_2,\ t_2) = E[f(x_1,\ t_1)f(x_1,\ t_2)] = \sigma_0^2\delta(x_2 - x_1)\delta(t_2 - t_1). \tag{67}$$

For this model the correlation at $t_1 = t_2 = t$ in Eq. (65), denoted by $R_{q_mq_n}(t,\ t)$ becomes

$$R_{q_mq_n}(t,\ t) = I_{mn} \cdot J_{mn} \tag{68}$$

where

$$I_{mn} = \sigma_0^2(\omega_m + \omega_n)^{-1} \tag{69}$$

$$J_{mn} = \sum_j^4\sum_k^4 b_{mj}b_{nk}\psi_{mj3}\psi_{nk3}[1 - \exp\{-(\lambda_{mj} + \lambda_{nk})\}]/(\lambda_{mj} + \lambda_{nk}) \tag{70}$$

Similarly if the loading is uniform in space and delta correlated in time as

$$R_{ff}(x_1,\ t_1;\ x_2,\ t_2) = \sigma_0^2\delta(t_2 - t_1) \tag{71}$$

then the principal coordinate correlation is still given by Eq. (68), with J_{mn} defined as follows:

$$J_{mn} = \sum_j^4\sum_k^4 b_{mj}b_{nk}\psi_{mj3}\psi_{nk3} \times [1 - \exp(-\lambda_{mj})][1 - \exp(-\lambda_{nk})]/\lambda_{mj}\lambda_{nk}. \tag{72}$$

Yet another model which has also been commonly used is with the exponential correlations in the spatial and time domains as

$$R_{ff}(x_1,\ t_1;\ x_2,\ t_2) = \sigma_0^2\exp\{-\alpha|x_2 - x_1| - \beta|t_2 - t_1|\}. \tag{73}$$

For this model, $R_{q_mq_n}(t,\ t)$ is still defined by Eqs. (68), with I_{mn} and J_{mn} now defined as

$$I_{mn} = -\frac{\sigma_0^2\beta}{(\beta + \omega_n)}\left[\frac{1}{\beta(\beta - \omega_m)} + \frac{2}{(\beta - \omega_n)(\omega_n + \omega_m)}\right] \tag{74}$$

$$J_{mn} = \sum_j\sum_k b_{mj}b_{nk}\psi_{mj3}\psi_{nk3}[G_{mn} + G_{nm}] \tag{75}$$

with

$$G_{mn} = \frac{1}{(\alpha - \lambda_{nk})}\left\{\frac{1 - \exp(-\lambda_{mj} - \lambda_{nk})}{(\lambda_{mj} + \lambda_{nk})} - \frac{1 - \exp(-\alpha - \lambda_{mj})}{(\alpha + \lambda_{mj})}\right\}. \tag{76}$$

Similar expressions can also be obtained for many other load models. Some of these load models have been used to obtain the numerical results presented in the following section.

Numerical Results

As a numerical example, a rectangular beam with the following properties has been considered: $E^*/G^* = 2.6$, $\eta = \xi = 5 \times 10 - 3$, $C_2 = 0.5$ and $C_3 = 0.7$. When the load is exponentially correlated in time and space, the parameters α and β are taken to be 0.5 and 15, respectively. The length-to-depth ratio (L/d) of the beam will be changed to study its effect on the response. First we present the results obtained from the eigenvalue analysis of a fixed-fixed beam with $L/d = 7$. Using the complex eigenvalues obtained from the solution of the characteristic Eq. (25), the modal damping ratios defined as follows.

$$\beta_n = -\,\text{Real}(\omega_n)/|\omega_n| \tag{77}$$

are obtained and shown in Fig. 1 for different damping parameter values. Top part of the figure shows the contribution of the parameters c_2 and c_3 and the lower part the contribution of parameters η and ξ to the modal damping ratios. For the first few modes, the modal damping ratio due to c_2 decreases monotonically. A similar trend is also observed for c_3 except for the first two modes. The contributions due to η and ξ on the other hand increase with the mode. These trends, however, change dramatically as higher shear modes appear in the spectrum. For these higher modes, the effects of the parameters c_2 and c_3 as well as those of the η and ξ on the modal damping ratios are opposite of each other; that is, if the damping ratio of a mode for one of the parameters is large then it would be small for the other parameter. On the whole, the viscoelastic parameters η and ξ are seen to damp out the higher modes by providing rather high modal damping ratios. In fact for higher

Downloaded 03 May 2010 to 171.66.16.245. Redistribution subject to ASME license or copyright; see http://www.asme.org/terms/Terms_Use.cfm

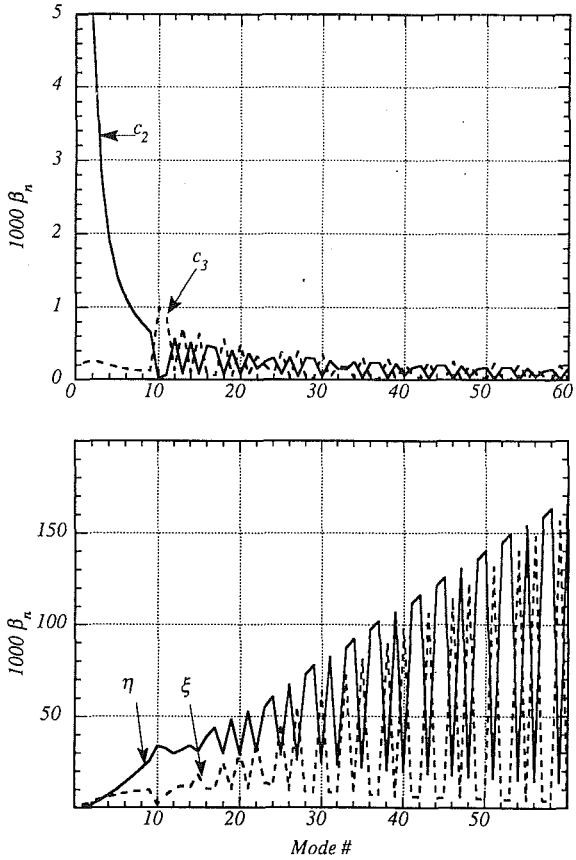


Fig. 1 Contributions of the parameters c_2, c_3, ξ, η to the modal damping ratios of a clamped-clamped beam.

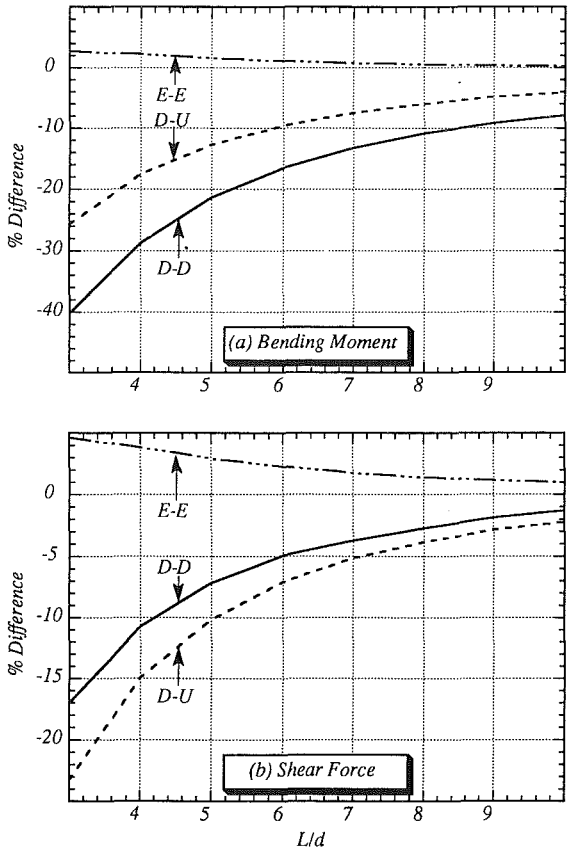


Fig. 3 Percent differences in the standard deviation responses calculated by Timoshenko and Euler-Bernoulli beam theories for different types of loads

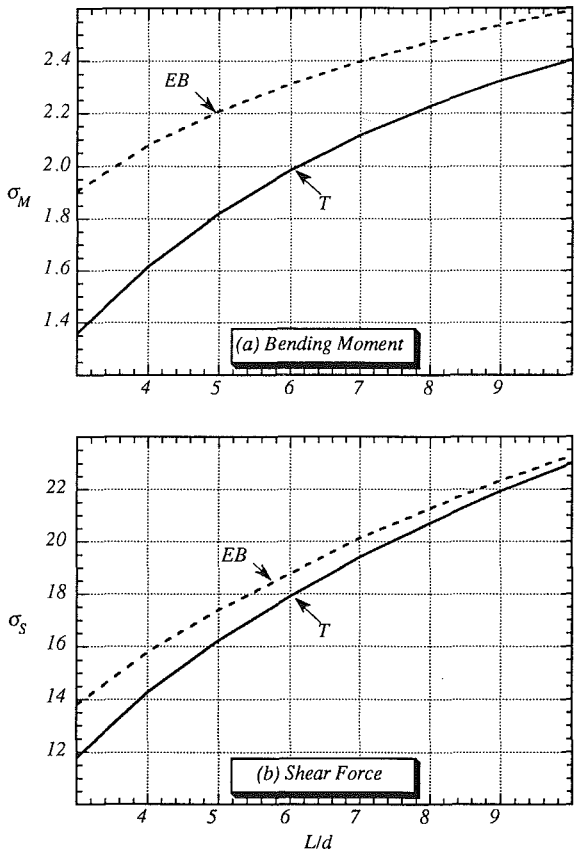


Fig. 2 Standard deviation of bending moment and shear force responses at the end of a clamped-clamped beam obtained by Timoshenko (*T*) and Euler-Bernoulli (*EB*) theories.

values of ξ and η, the higher modes can even be overdamped. It is also noted that a nonzero ξ implies the presence of a flexural strain-rate-dependent viscous damping as described by Clough and Penzien (1975).

Figure 2 compares the standard deviation of the nondimensional bending moment and shear force responses obtained at the end of a clamped-clamped beam, by the Timoshenko and Euler-Bernoulli beam theories. The bending moment, M, and shear forces, S, have been nondimensionalized as: $M = (\hat{M}L/E^*Ar^2)$ and $S = (\hat{S}L^2/E^*Ar^2)$, where the quantities with hats are dimensional quantities. For these results, the loading was delta-correlated in time and along the beam. The beams are damped with c_2, c_3, and ξ. The viscoelastic shear damping coefficient η is taken to be equal to ξ in the Timoshenko beam theory to be consistent with the Euler-Bernoulli beam where this parameter does not appear. It is seen that the difference in the response results obtained by the two theories can be large, thus showing the effect of the shear deformation and rotatory inertia. Although here we show some results for some small L/d ratios, we admit that the applicability of the Timoshenko beam model for such cases can be argued.

It is relevant to mention here that except for a simply-supported case, the undamped normal modes can not be used to solve the forced vibration problem of even a uniform Euler-Bernoulli beam if the rotatory damping is present, that is, if c_3 is nonzero. Thus to solve the damped Euler-Bernoulli problems considered in this paper, an adjoint eigenfunction approach similar to the approach presented above for the Timoshenko beam was developed and used for the numerical results presented in Fig. 2 as well as the following three figures. The details of this approach for the Euler-Bernoulli beam are, however, omitted here.

Figure 3 shows, for a clamped-clamped beam, the percent

Downloaded 03 May 2010 to 171.66.16.245. Redistribution subject to ASME license or copyright; see http://www.asme.org/terms/Terms_Use.cfm

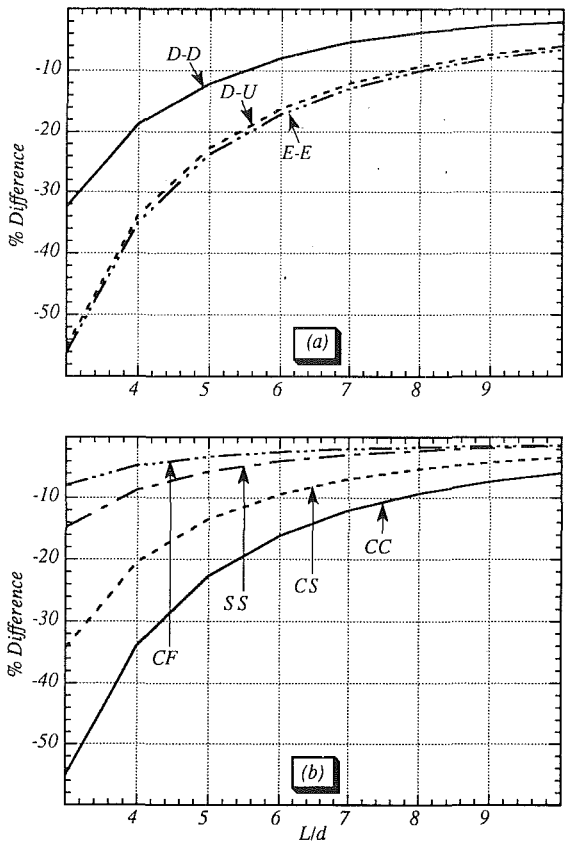


Fig. 4 Percent difference in the standard deviation responses calculated by Timoshenko and Euler-Bernoulli beam theories for beams with different end conditions

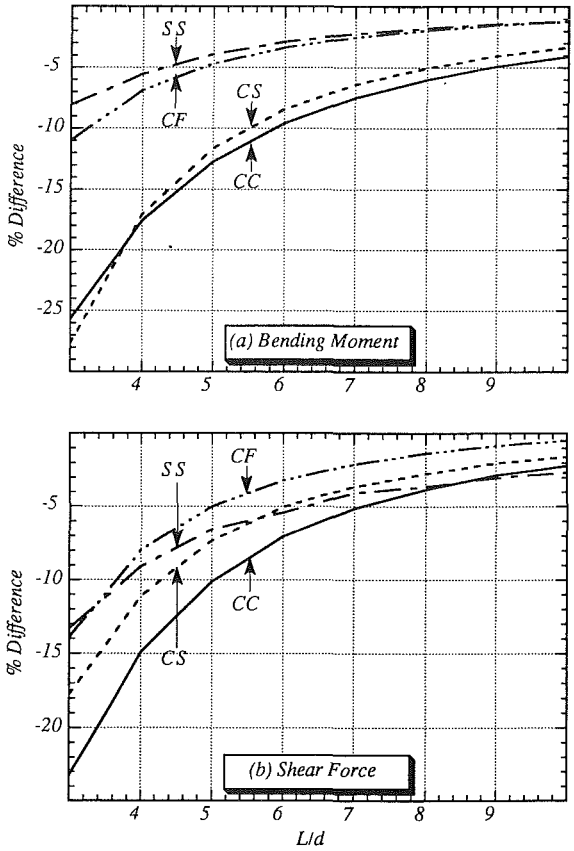


Fig. 5 Percent differences in the crossing rates calculated for Timoshenko and Euler-Bernoulli beams for (*a*) clamped-clamped beam with different types of loads; (*b*) beams with different end conditions and delta correlated in time and uniform in space load

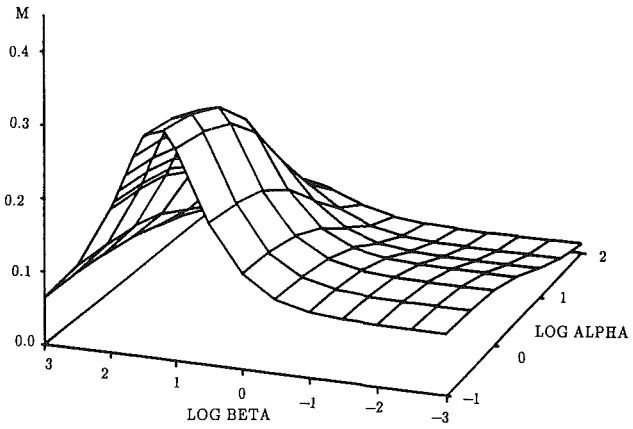


Fig. 6 Bending moment and standard deviation at the end of a clamped-clamped beam for different parameters of the exponentially correlated load

difference in the bending moment and shear force standard deviation values calculated according to the Timoshenko and Euler-Bernoulli beam theories for three different types of loading defined by Eqs. (67), (71), and (73). In the figure these loadings are denoted by DD—delta correlated in space and time, DU—delta correlated in time and uniform in space and EE—exponentially correlated in time and space. The difference is calculated by assuming the Timoshenko beam result to be the base result. The difference is seen to depend, not only on the beam characteristics, but also on the characteristics of the load. The loads with higher energies in the higher end of their spectrum, which could excite the higher shear modes, would tend to cause a larger difference in the response calculated by the Euler-Bernoulli and Timoshenko theories. Thus, the errors for the loads with delta correlated inputs in time are seen to be larger than the errors for the exponentially correlated load. Depending upon what parameters are chosen for the exponentially correlated input, the error can be positive or negative; that is, the Timoshenko beam response can be greater or smaller than the Euler-Bernoulli beam response. Figure 4 shows the effect of the end conditions on the magnitude of the difference in the bending moment and shear force responses for delta-correlated load in time and space. The end conditions considered are: clamped-clamped (CC), clamped-simply supported (CS), clamped-free (CF) and simply supported on both ends (SS). Clearly the beams with most constraints, the responses of which are most affected by the higher modes, are more sensitive to the shear deformation and rotatory inertia effects. Figure 5 shows the shear deformation and rotatory inertia effect on the zero-crossing rates of the maximum displacement response. Figure 5(*a*) is for a fixed-fixed beam but for different types of load. Figure 5(*b*), on the other hand, is for the load with uniform distribution in space and delta correlated in time, but for beams with different end conditions. The zero crossing rate was defined as

$$\nu_0 = \frac{1}{2\pi}\sqrt{E[\dot{w}^2]/E[w^2]} \tag{78}$$

where the mean square values for the displacement and velocity required in this equation are calculated according to Eq. (65). It is noted that the magnitudes of the differences in this response quantity are larger than those shown in previous figures. This has some implications in the reliability calculations.

Figure 6 shows the results of varying the parameters α and β of the load model in Eq. (73) on the response for a clamped-

Downloaded 03 May 2010 to 171.66.16.245. Redistribution subject to ASME license or copyright; see http://www.asme.org/terms/Terms_Use.cfm

clamped Timoshenko beam. Clearly, there are certain optimum values of the temporal and spatial decay parameters in this load model which tend to produce a maximum response for the beam model used in this study.

Concluding Remarks

The forced vibration problem of a damped Timoshenko beam can only be solved by using the undamped modes if transverse and rotational damping coefficients as well as the viscoelastic operators for extensional and shear deformations satisfy certain conditions. In other situations it is necessary to use the damped eigenfunctions and their adjoint biorthogonal eigenfunctions, if the response by a modal approach is desired. An approach is presented to obtain these sets of biorthogonal eigenfunctions. The approach is general and can be used with any conventional or unconventional boundary conditions with equal ease. The approach is used to obtain the random response of a beam subjected to temporally and spatially correlated random loads. The characteristics of various damping parameters and their effect on the response is numerically examined. The effect of the shear deformations and rotatory inertia on various response quantities of beams with different boundary conditions subjected to various random load models is also examined.

Acknowledgments

This work is financially supported in part by the National Science Foundation through research grant no. BCS-8822864 with S. C. Liu as its Program Director. This support is gratefully acknowledged.

References

Anderson, R. A., 1953, "Flexural Vibrations in Uniform Beams According to the Timoshenko Theory," ASME JOURNAL OF APPLIED MECHANICS, Vol. 20, pp. 504–510.

Banerjee, J. R., and Kennedy, D., 1985, "Response of an Axially Loaded Timoshenko Beam to Random Loads," *Journal of Sound and Vibration*, Vol. 101, No. 4, pp. 481–487.

Bisplinghoff, R. L., and Ashley, H., 0000, *Principles of Aeroelasticity*, Dover Publications, New York.

Clough, R. W., and Penzien, J., 1975, *Structural Dynamics*, McGraw-Hill, New York.

Crandall, S. H., and Yildiz, A., 1962, "Random Vibration of Beams," ASME JOURNAL OF APPLIED MECHANICS, Vol. 29, pp. 267–275.

Dolph, C. L., 1954, "On the Timoshenko Theory of Transverse Beam Vibrations," *Quarterly of Applied Mathematics*, Vol. 12, pp. 175–187.

Elishakoff, I., and Livshits, D., 1989, "Some Closed-Form Solutions in Random Vibration of Bresse-Timoshenko Beams," *Probabilistic Engineering Mechanics*, Vol. 4, No. 1, pp. 49–54.

Fang, T., and Wang, Z.-N., 1985, "Complex Modal Analysis of Random Vibrations," *AIAA Journal*, Vol. 24, pp. 342–344.

Foss, K. A., 1958, "Coordinates which Decouple the Equations of Motion of Damped Linear Dynamic Systems," ASME JOURNAL OF APPLIED MECHANICS, Vol. 25, pp. 31–364.

Herrmann, G., 1955, "Forced Motion of Timoshenko Beams," ASME JOURNAL OF APPLIED MECHANICS, Vol. 22, pp. 53–56.

Huang, T. C., 1961, "The Effect of Rotatory Inertia and Shear Deformation on the Frequency and Normal Mode Equations of a Uniform Beam with Simple End Conditions," ASME JOURNAL OF APPLIED MECHANICS, Vol. 28, pp. 579–584.

Ince, E. L., 1956, *Ordinary Differential Equations*, Dover Publications, New York.

Lee, H. C., 1960, "Forced Lateral Vibration of a Uniform Cantilever Beam with Internal and External Damping," ASME JOURNAL OF APPLIED MECHANICS, Vol. 27, pp. 551–556.

Lin, Y. K., 1976, *Probabilistic Theory of Structural Dynamics*, Krieger, New York.

Nayfeh, A. H., 1981, *Introduction to Perturbation Techniques*, John Wiley, New York.

Newmann, M. K., 1959, "Viscous Damping in Flexural Vibrations of Bars," ASME JOURNAL OF APPLIED MECHANICS, Vol. 26, pp. 367–376.

Pan, H., 1966, "Vibration of Viscoelastic Timoshenko Beam," *ASCE Journal of the Engineering Mechanics Division*, Vol. 92, pp. 213–234.

Samuels, J. C., and Eringen, A. C., 0000, "Response of a Simply Supported Timoshenko Beam to a Purely Random Gaussian Process," ASME JOURNAL OF APPLIED MECHANICS, Vol. 25, pp. 496–500.

Singh, M. P., 1980, "Seismic Response by SRSS for Non-Proportional Damping," *ASCE Journal of the Engineering Mechanics Division*, Vol. 106, pp. 1405–1419.

Singh, M. P., and Abdelnaser, A. S., 1990, "Random Vibration of Timoshenko Beams with Generalized Boundary Conditions," Second Int. Conference on Stochastic Structural Dynamics, May 10–12, Boca Raton.

Downloaded 03 May 2010 to 171.66.16.245. Redistribution subject to ASME license or copyright; see http://www.asme.org/terms/Terms_Use.cfm

Axisymmetric Bending of Generally Laminated Cylindrical Shells

Victor Birman
Engineering Education Center,
University of Missouri-Rolla,
St. Louis, MO 63121
Mem. ASME

Nonlinear bending deformations of generally laminated circular cylindrical shells subjected to an axisymmetric radial pressure, axial loading, and torsion are considered. Deformations of such shells are axisymmetric, i.e., while cross-sections can rotate about the shell axis, they remain circular and all derivatives with respect to the circumferential coordinate are equal to zero. In this case a nonlinear term is included into the axial strain only. Excluding this strain from the equilibrium equations, one can reduce the analysis to integration of a system of linear differential equations. In the first part of the paper the solution based on Love's first approximation and Donnell's theories is shown for thin shells. While out-of-surface boundary conditions can be arbitrary, several combinations of in-surface conditions are discussed. The second part of the paper outlines the approach to the solution for shear-deformable geometrically nonlinear shells. First-order shear-deformation theory is used in the analysis. The approach is based on exclusion of the nonlinear term (axial strain) and subsequent solution of linear differential equations of equilibrium by the operational method. This approach can be also used for an analysis of thin, generally laminated cylindrical shells.

Introduction

A rapid advance of composite structures constantly brings new problems to the attention of researchers. Some of these problems are related to geometrically nonlinear response of shells manufactured from composite materials.

A general theory of geometrically linear arbitrary laminated shells was presented by Ambartsumian (1974). This theory can be extended to include geometric nonlinearities. However, the recent comprehensive review of Noor and Burton (1990) illustrates that very little research has been done on bending of geometrically nonlinear generally laminated shells. Grigorenko et al. (1983) reported the results of a numerical analysis of geometrically nonlinear generally laminated shells of revolution. It was shown that such shells can experience significant circumferential displacements under an axisymmetric normal pressure. However, exact or closed-form analytical solutions for geometrically nonlinear generally laminated shells have not been published.

A combination of shear deformability and geometric nonlinearities is usually considered unpractical for isotropic structures. The situation can be different for composites due to their relatively low transverse shear moduli. An interest to shear deformable, geometrically nonlinear composite structures has mostly been limited to plates (Stein, 1989; Chia, 1988; Librescu and Stein, 1991). Theories for composite shells have also been developed. Stein (1986) used trigonometric series representation of displacements through the thickness to derive a two-dimensional theory of shear deformable, geometrically nonlinear cylindrical shells. Schmidt and Reddy (1988) published a consistent first-order shear deformation theory with small strains and moderate rotations. Anastasiadis and Simitses (1990) developed a third-order shear deformation theory for geometrically nonlinear imperfect cylindrical shells subjected to hydrostatic pressure, axial compression, and in-surface shear. In the general case the governing equations obtained for any of the theories cited above are very complex. Therefore, it can be expected that future solutions will concentrate on finite element or finite difference procedures.

It is necessary to mention here the pioneering work of Reissner and Wan (1971) who formulated the problem of rotationally symmetric stresses and strains in anisotropic elastic shells of revolution. Their solution was based on uncoupled systems of equilibrium and compatibility differential equations developed for geometrically linear polar-orthotropic shells in the earlier paper (Reissner and Wan, 1969). The authors analyzed generally anisotropic shells and showed that the problem could be reduced to two simultaneous second-order differential equations.

In the present paper the methods of exact solution for nonlinear bending of generally laminated thin and shear-deformable cylindrical shells subjected to an axisymmetric loading and torsion are outlined. Numerous applications can be treated as particular cases of the problem considered in the paper.

Analysis of Thin Geometrically Nonlinear Shells

Equilibrium equations of cylindrical shells are

Contributed by the Applied Mechanics Division of THE AMERICAN SOCIETY OF MECHANICAL ENGINEERS for publication in the ASME JOURNAL OF APPLIED MECHANICS.

Discussion on this paper should be addressed to the Technical Editor, Professor Lewis T. Wheeler, Department of Mechanical Engineering, University of Houston, Houston, TX 77204-4792, and will be accepted until four months after final publication of the paper itself in the ASME JOURNAL OF APPLIED MECHANICS.

Manuscript received by the ASME Applied Mechanics Division, May 3, 1991; final revision, Dec. 2, 1991. Associate Technical Editor: J. G. Simmonds.

 Copyright © 1993 by ASME

Downloaded 03 May 2010 to 171.66.16.245. Redistribution subject to ASME license or copyright; see http://www.asme.org/terms/Terms_Use.cfm

$$N_{x,x}+N_{xy,y}=0$$

$$N_{xy,x}+N_{y,y}+n\frac{M_{xy,x}+M_{y,y}}{R}=0$$

$$M_{x,xx}+2M_{xy,xy}+M_{y,yy}-\frac{N_y}{R}+\underline{(N_xw_{,x}+N_{xy}w_{,y})_{,x}}+\underline{(N_{xy}w_{,x}+N_yw_{,y})_{,y}}=-q, \quad (1)$$

where N_i and M_i $(i=x, y, xy)$ denote stress resultants and stress couples, respectively; q is a pressure, positive when acting in the outward direction; R is the middle surface radius; x and y are the axial and circumferential coordinates; w is a radial defection positive in the outward direction; and n is a tracer indicating the shell theory used in the analysis. If the underlined nonlinear terms in the third Eq. (1) are omitted and $n=1$, equations of equilibrium reduce to those of Love's first approximation theory. If $n=0$, linearized equations correspond to Donnell's shell theory. The load q being axisymmetric, deformations are the same for all middle surface points of a given cross-section. Therefore, all derivatives with respect to the circumferential coordinate vanish, although cross-sections can rotate about the shell axis; i.e., circumferential displacements should not be disregarded in a general case. Accordingly, equilibrium equations become

$$N_{x,x}=0$$

$$N_{xy,x}+n\frac{M_{xy,x}}{R}=0$$

$$M_{x,xx}-\frac{N_y}{R}+(N_xw_{,x})_{,x}=-q. \quad (2)$$

The vector of stress resultants and stress couples is given by

$$\begin{Bmatrix} N \\ M \end{Bmatrix}=\begin{bmatrix} A & B \\ B & D \end{bmatrix}\begin{Bmatrix} \epsilon \\ \kappa \end{Bmatrix} \quad (3)$$

where A, B, and D are 3×3 matrices of extensional, coupling, and bending stiffnesses. If the shell is generally laminated, none of the elements of these matrices is equal to zero.

The strains and changes of curvature and twist are

$$\begin{Bmatrix} \epsilon \\ \kappa \end{Bmatrix}=\begin{Bmatrix} \epsilon_x \\ \epsilon_y \\ \epsilon_{xy} \\ \kappa_x \\ \kappa_y \\ \kappa_{xy} \end{Bmatrix}=\begin{Bmatrix} u_{,x}+1/2\,w_{,x}^2 \\ w/R \\ v_{,x} \\ -w_{,xx} \\ 0 \\ nv_{,x}/R \end{Bmatrix} \quad (4)$$

where u and v denote the axial and circumferential displacements, respectively.

The substitution of stress resultants and stress couples in terms of ϵ_x, w and v into the first two Eqs. (2) yields

$$\begin{bmatrix} A_{11} & \left(A_{16}+\frac{n}{R}B_{16}\right) \\ \left(A_{16}+\frac{n}{R}B_{16}\right) & \left(A_{66}+\frac{n}{R}\left(2B_{66}+\frac{D_{66}}{R}\right)\right) \end{bmatrix}\begin{Bmatrix} \epsilon_x \\ v_{,x} \end{Bmatrix}=\begin{Bmatrix} C_0 \\ C_0' \end{Bmatrix}$$

$$-\begin{Bmatrix} \frac{A_{12}}{R} \\ \frac{1}{R}\left(A_{26}+\frac{n}{R}B_{26}\right) \end{Bmatrix}w+\begin{Bmatrix} B_{11} \\ B_{16}+\frac{n}{R}D_{16} \end{Bmatrix}w_{,xx} \quad (5)$$

where C_0 and C_0' are constants of integration.

As follows from Eqs. (5),

$$\epsilon_x=k_1+k_2w+k_3w_{,xx}$$
$$v_{,x}=k_4+k_5w+k_6w_{,xx}. \quad (6)$$

The coefficients k_i can be easily evaluated. Upon the substitution of Eqs. (3) and (6), the third Eq. (2) yields

$$k_7w_{,xxxx}+k_8w_{,xx}+k_9w=-p \quad (7)$$

where

$$k_7=\left(B_{16}+\frac{n}{R}D_{16}\right)k_6+B_{11}k_3-D_{11}$$

$$k_8=B_{11}k_2+\frac{2B_{12}}{R}+\left(B_{16}+\frac{n}{R}D_{16}\right)k_5-\frac{A_{12}}{R}k_3-\frac{1}{R}\left(A_{16}+\frac{n}{R}B_{16}\right)k_6+C_0$$

$$k_9=-\frac{A_{12}}{R}k_2-\frac{A_{22}}{R^2}-\frac{1}{R}\left(A_{26}+\frac{n}{R}B_{26}\right)k_5$$

$$p=q-\frac{A_{12}}{R}k_1-\frac{1}{R}\left(A_{26}+\frac{n}{R}B_{26}\right)k_4. \quad (8)$$

The integral of Eq. (7) includes four constants of integration multiplied by odd and even functions of the axial coordinate

$$w=\sum_{i=1}^{4}C_if_i(x)+w_p, \quad (19)$$

where C_i are constants, $f_1(x)$ and $f_2(x)$ are even functions of x, $f_3(x)$ and $f_4(x)$ are odd functions, $x=0$ corresponds to the shell midspan, and w_p is a particular integral of Eq. (7) corresponding to a given pressure distribution $q(x)$.

There are no limitations on out-of-surface boundary conditions when using the present method. Solutions for different in-surface boundary conditions are discussed as follows:

(1) prescribed in-surface stress resultants at the ends of the shell; Donnell's shell theory.

In this case, $N_x=N_x^0$, $N_{xy}=N_{xy}^0$ at $x=\pm L/2$, L being the shell length (superscripts "0" indicate prescribed values). In addition, $n=0$. It is observed that $C_0=N_x^0$, $C_0'=N_{xy}^0$. Four constants of integration C_i $(i=1\text{–}4)$ are determined from four out-of-surface boundary conditions. The solution is particularly simple, if the pressure $q(x)$ is symmetric about the midspan since then $C_3=C_4=0$ and two remaining constants are obtained from the conditions at one of the ends.

(2) prescribed in-surface stress resultants at the ends of the shell; Love's first approximation shell theory $(n=1)$.

Obviously, $C_0=N_x^0$. There are five unknown constants of integration: C_0', C_i. If $q(x)$ is symmetric about the midspan, $C_3=C_4=0$ and the values of C_0', C_1, and C_2 are determined from two out-of-surface boundary conditions and the condition $N_{xy}=N_{xy}^0$ at one of the ends.

Note that the functions $f_i(x)$ include trigonometric and hyperbolic functions. Therefore, according to the second Eq. (6), if $q(x)$ and w are symmetric with respect to $x=0$, v is antisymmetric with respect to the midspan.

(3) prescribed axial load and circumferential displacement: $N=N_x^0$, $v=v^0$.

For both shell theories considered here, $C_0=N_x^0$ and

$$v=\int v_{,x}dx+C_5 \quad (10)$$

where C_5 is a constant of integration, $v_{,x}$ is given in terms of w by the second Eq. (6).

Six constants C_0', C_i $(i=1\text{–}4)$ and C_5 are determined from six boundary conditions: two out-of-surface conditions and $v=v^0$ at each end.

(4) prescribed in-surface shear load and axial displacement; Donnell's shell theory.

Downloaded 03 May 2010 to 171.66.16.245. Redistribution subject to ASME license or copyright; see http://www.asme.org/terms/Terms_Use.cfm

In this case $C_0' = N_{xy}^0$. The axial displacement is determined from

$$u = \int \left(\epsilon_x - \frac{1}{2} w_{,x}^2 \right) dx + C_6 \tag{11}$$

where C_6 is a constant and ϵ_x is expressed in terms of w via the first Eq. (6).

The constants of integration C_0, C_i ($i = 1$–4) and C_6 are obtained from six boundary conditions: two out-of-surface conditions and $u = u^0$ at each end.

Note that the right side of Eq. (11) includes products $C_i C_j$ ($i, j = 1$–4). Therefore, if geometric nonlinearity cannot be neglected, a system of algebraic equations obtained from the boundary conditions is nonlinear.

If Love's first approximation theory is used, an additional constant C_0' has to be determined (it was equal to N_{xy}^0 when $n = 0$). The corresponding boundary conditions are $N_{xy} = N_{xy}^0$ where N_{xy} is expressed in terms of displacements using Eqs. (3), (4) and (6). If the load $q(x)$ is symmetric about $x = 0$, five constants of integration have to be determined; i.e., C_0, C_0', C_1, C_2, and C_6. Note that since $w(x)$ is an even function, N_{xy} is also even. Therefore, the boundary conditions for N_{xy} at $x = \pm L/2$ coincide. Then five boundary conditions can be used to determine the constants, i.e., two out-of-surface boundary conditions and $N = N_{xy}^0$ at any end and $u = u^0$ at $x = \pm L/2$.

(5) prescribed in surface displacements: $u = u^0$, $v = v^0$. A solution employing either Love's or Donnell's theory includes eight constants of integration: C_0, C_0', C_i ($i = 1$–4), C_5, and C_6. These constants can be obtained from eight boundary conditions at the ends of the shell. A system of algebraic equations corresponding to boundary conditions is nonlinear as in the previous case.

If the loading is symmetric with respect to the midspan and in-surface displacements are odd functions of the axial coordinate, the nonzero constants of integration C_0, C_0', C_1, and C_2 can be evaluated from four boundary conditions at any end of the shell. Note that the stresses are identical in linear and nonlinear problems, if the axial boundary conditions are $N_x = N_x^0$ (cases 1-3). This is due to a combination of axial symmetry and a lack of restraints in the x-direction. However, even in these cases axial displacements depend on nonlinear contributions.

Analysis of Shear-Deformable Geometrically Nonlinear Shells

Equations of equilibrium of generally laminated shear-deformable cylindrical shells subjected to an axisymmetric load are presented here for the first-order shear deformation theory (Bert and Kumar, 1982):

$$\begin{aligned} &N_{x,x} = 0 \\ &N_{xy,x} + n\frac{Q_y}{R} = 0 \\ &Q_{x,x} - \frac{N_y}{R} + (N_x w_{,x})_{,x} = -q \\ &Q_x = M_{x,x} \\ &Q_y = M_{xy,x}. \end{aligned} \tag{12}$$

In Eqs. (12), Q_x and Q_y are transverse shear stress resultants:

$$\begin{Bmatrix} Q_x \\ Q_y \end{Bmatrix} = \begin{bmatrix} A_{55} & A_{45} \\ A_{45} & A_{44} \end{bmatrix} \begin{Bmatrix} \psi_x + w_{,x} \\ \psi_y - n\dfrac{v}{R} \end{Bmatrix} \tag{13}$$

where ψ_x and ψ_y represent rotations of an element perpendicular to the undeformed middle surface. The following strain-displacement relations in Eqs. (4) are modified:

$$\begin{aligned} \kappa_x &= \psi_{x,x} \\ \kappa_{xy} &= \psi_{y,x} \end{aligned} \tag{14}$$

An axial strain ϵ_x is excluded from the equations of equilibrium using the first Eq. (12):

$$\epsilon_x = \left(C_0 - A_{12}\frac{w}{R} - A_{16} v_{,x} - B_{11}\psi_{x,x} - B_{16}\psi_{y,x} \right) \Big/ A_{11}, \tag{15}$$

C_0 being a constant of integration.

Now the remaining Eqs. (12) can be written in terms of displacements w and v and rotations as

$$\begin{bmatrix} \mathcal{L}_{11} & \mathcal{L}_{12} & \mathcal{L}_{13} & \mathcal{L}_{14} \\ \mathcal{L}_{21} & \mathcal{L}_{22} & \mathcal{L}_{23} & \mathcal{L}_{24} \\ \mathcal{L}_{31} & \mathcal{L}_{32} & \mathcal{L}_{33} & \mathcal{L}_{34} \\ \mathcal{L}_{41} & \mathcal{L}_{42} & \mathcal{L}_{43} & \mathcal{L}_{44} \end{bmatrix} \begin{Bmatrix} \psi_x \\ \psi_y \\ \mathrm{w} \\ \mathrm{v} \end{Bmatrix} = \begin{Bmatrix} 0 \\ -\bar{p} \\ 0 \\ 0 \end{Bmatrix} \tag{16}$$

where linear differential operators $\mathcal{L}_{ij}$ and $\bar{p}$ are given in the Appendix.

The solution of a system of linear differential equations with constant coefficients presented in the form (16) can be obtained by the operational method (Wylie, 1960). For example, such an approach was used for integration of governing equations for isotropic shells by Philin (1975).

Particular integrals of the system of Eqs. (16) are determined from

$$\begin{Bmatrix} \psi_x \\ \psi_y \\ w \\ v \end{Bmatrix}_p = \frac{[M]}{\det(\mathcal{L}_{ij})} \begin{Bmatrix} 0 \\ -\bar{p} \\ 0 \\ 0 \end{Bmatrix} \tag{17}$$

where $[M]$ is a transpose of a matrix of cofactors of the determinant $\det(\mathcal{L}_{ij})$.

Denote

$$P = -\frac{\bar{p}}{\det(\mathcal{L}_{ij})}. \tag{18}$$

If P is determined, particular integrals (17) can be evaluated.

According to Eq. (18), P is a solution of the equation

$$\det(\mathcal{L}_{ij}) P = -\bar{p}. \tag{19}$$

This is an eight-order ordinary differential equation. If $\bar{p} = \bar{p}(x)$ is a Fourier series, the solution of the nonhomogeneous equation (19) can be immediately obtained.

Complimentary integrals of the system of Eqs. (16) can be evaluated in the form

$$\begin{Bmatrix} \psi_x \\ \psi_y \\ w \\ v \end{Bmatrix} = \begin{Bmatrix} A_1 \\ A_2 \\ A_3 \\ A_4 \end{Bmatrix} e^{mx} \tag{20}$$

where A_j are constants and m is determined from the equation

$$\det(\mathcal{L}_{ij}(m)) = 0. \tag{21}$$

In Eq. (21), differentiations are replaced with the corresponding powers of m in the operators $\mathcal{L}_{ij}(m)$. Each root of Eq. (21) corresponds to a vector A_j ($j = 1$–4) determined from the system of four homogeneous algebraic equations

$$\mathcal{L}_{ij}(m) A_j = 0, \tag{22}$$

$\mathcal{L}_{ij}(m)$ being a 4×4 matrix of coefficients. Obviously, vectors A_j are determined to within a scalar factor. The number of these unknown factors is equal to the number of roots of Eq. (21), i.e., eight, and their values must be specified from the boundary conditions.

Notably, the solution of Eqs. (16) provides displacements and rotations rather than their derivatives. Therefore, four boundary conditions at each end can be arbitrary.

Downloaded 03 May 2010 to 171.66.16.245. Redistribution subject to ASME license or copyright; see http://www.asme.org/terms/Terms_Use.cfm

Table 1 Difference between nondimensional deflections calculated using Love's and Donnell's theories (percent)

L/R	1.0	2.0	4.0	6.0	8.0
R=0.25m	0.128	0.282	0.253	0.252	0.251
R=1.0m	0.103	0.074	0.067	0.064	0.064

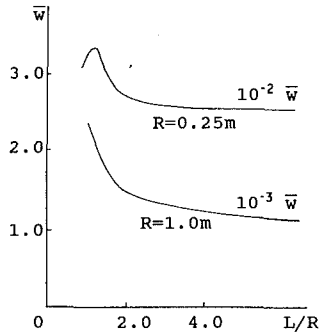


Fig. 1 Nondimensional deflections of generally laminated shells (properties as in Example 5.1 of Agarwal and Broutman (1980)); $\bar{w} = wQ_{11}/qR$ where Q_{11} is the reduced stiffness of the material in the fiber direction

The fifth condition is either $N_x = N_x^0$ or $u = u^0$. In the former case, $C_0 = N_x^0$ and there are eight boundary conditions to evaluate eight constants of integration. In the latter case, axial displacements are determined from Eq. (11) where ϵ_x is substituted from Eq. (15). This results in ten constants of integration and ten boundary conditions.

In the conclusion of this paragraph, the present approach is applied to thin geometrically nonlinear shells.

The first Eq. (2) yields

$$\epsilon_x = \left[C_0 - A_{12}\frac{w}{R} - \left(A_{16} + \frac{n}{R}B_{16}\right) v_{,x} + B_{11} w_{,xx} \right] \Big/ A_{11}. \quad (23)$$

Then the remaining Eqs. (2) are represented in the form

$$\begin{bmatrix} \bar{\mathfrak{L}}_{11} & \bar{\mathfrak{L}}_{12} \\ \bar{\mathfrak{L}}_{21} & \bar{\mathfrak{L}}_{22} \end{bmatrix} \begin{Bmatrix} w \\ v \end{Bmatrix} = \begin{Bmatrix} 0 \\ -\bar{p} \end{Bmatrix}. \quad (24)$$

The operators $\bar{\mathfrak{L}}_{ij}$ are presented in the Appendix. The expression for $\bar{p}$ coincides with that in Eqs. (16).

The solution is similar to that discussed above for the system of Eqs. (16).

Numerical Examples

Maximum radial deflections of thin-walled shells obtained using Love's and Donnell's theories were compared to estimate the accuracy of a relatively simple latter theory. The results are presented in Table 1 for generally laminated shells (all extensional, coupling, and bending stiffnesses are present), with the properties from Example 5.1 of the book of Agarwal and Broutman (1980). The shell's ends were clamped, free in the axial direction and restrained in the circumferential direction.

The comparison of results in Table 1 illustrates that discrepancies between the theories remain small. This conclusion is in agreement with the results obtained by Bert and Reddy (1982) who showed that Donnell's theory is reliable, if the shell is thin ($R/h \geq 20$), and the condition is satisfied in the present example.

Nondimensional deflection-to-pressure ratios are shown as functions of length-to-radius ratios in Fig. 1. These ratios decrease when the length of the shell increases. On the other hand, in short shells with $L/R \leq 0.5$–1.0, deflections can increase with the length. Similar behavior was found for beams on an elastic foundation, isotropic cylindrical shells subjected

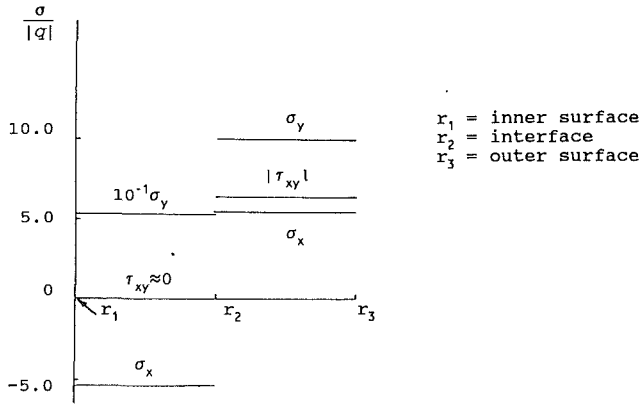


Fig. 2 Distribution of stresses proportional to pressure through the shell thickness at the midsection, $N_x^0 = 0$

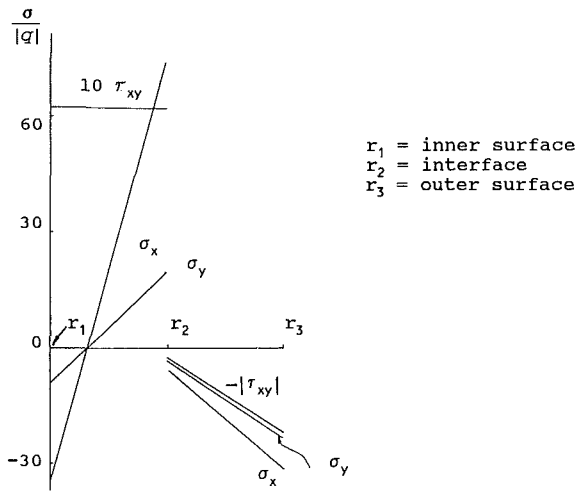


Fig. 3 Distribution of stresses proportional to pressure through the shell thickness at the end cross-sections, $N_x^0 = 0$

to concentrated loading (Caladine, 1983), and composite cylindrical shells undergoing thermal bending (Birman, 1991).

In other examples, a clamped shell composed of an internal steel layer and external multilayered angle-ply graphite/epoxy coating was considered. The thicknesses of steel and composite were equal, if not indicated otherwise, the lamination angle was ±45 deg.

The properties of materials were

1 steel (ASTM-36)
$E = 200$ GPa, $G = 79$ GPa, and
2 composite (Thornel 300 graphite-epoxy, fiber volume fraction 63 percent)
$E_L = 159$ GPa, $E_T = 10.9$ GPa, $\nu_{LT} = 0.38$, $G_{LT} = 6.4$ GPa.

Here the subscripts indicate directions along (L) and across (T) the fibers.

The geometry of the shell was $L = 3$ m, $R = 0.3$ m, $h = 0.01$ m (total thickness).

First, the shell was subject to an axisymmetric internal pressure. Distributions of the stresses through the thickness are shown in Figs. 2, 3 for the midsection and the end cross-section, respectively. It appears that the stresses within the steel layer are practically independent of the thickness coordinate at the midsection. Within composite layers, the axial stresses are also practically constant at the midsection while the shear stress alters its sign depending on the sign of the lamination angle.

At the clamped end, the axial stresses change as linear functions of the thickness coordinate within both steel and com-

Downloaded 03 May 2010 to 171.66.16.245. Redistribution subject to ASME license or copyright; see http://www.asme.org/terms/Terms_Use.cfm

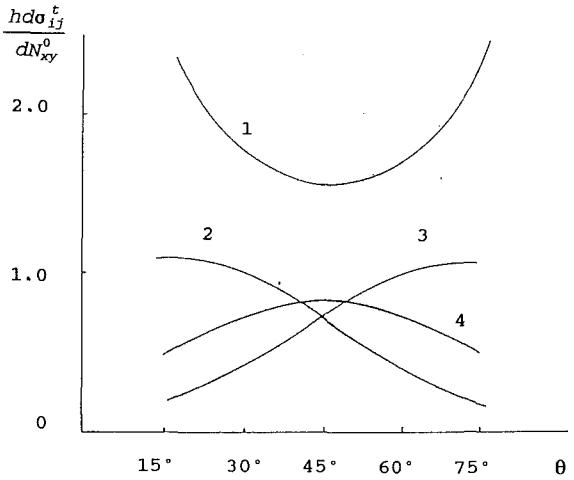


Fig. 4 Stress rates $[h\,(d\sigma_{ij}^t/dN_{xy}^0)]$ as functions of the lamination angle; $\bar{h}_{st}=0.25$. Curve 1: steel, τ_{xy}^t. Curves 2-4: composite $|\sigma_x^t|$, $|\sigma_y^t|$, τ_{xy}^t, respectively.

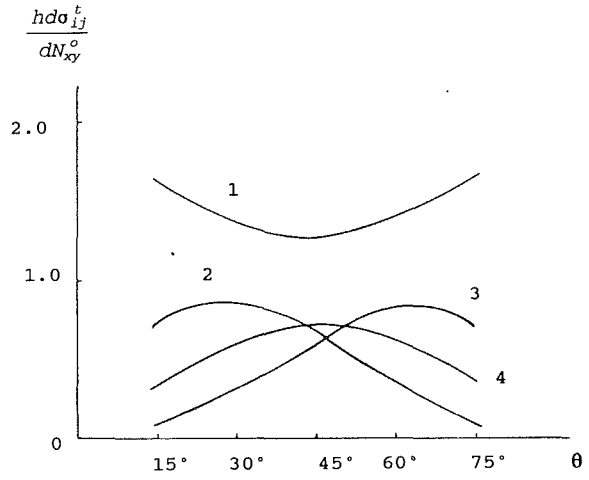


Fig. 5 Stress rates $[h\,(d\sigma_{ij}^t/dN_{xy}^0)]$ as functions of the lamination angle; $\bar{h}_{st}=0.50$. Curve 1: steel, τ_{xy}^t. Curves 2-4: composite, $|\sigma_x^t|$, $|\sigma_y^t|$, τ_{xy}^t, respectively.

posite layers. The sign of the shear stresses in composite layers changes depending on the lamination angle.

Torsion due to shearing stress resultants applied at the end cross-sections results in circumferential displacements, shearing stresses in the steel layer, and both axial as well as shearing stresses in angle-ply composite layers. It is convenient to represent the effect of the shear stress resultants by the rate of stress increase, i.e., $[(d\sigma_{ij}^t/dN_{xy}^0)h]$ where σ_{ij}^t is a stress component proportional to torsion. These stress rates were calculated for three different ratios $\bar{h}_{st}$ (ratio of the thickness of steel to the thickness of composite) in Figs. 4–6. Various lamination angles are considered in these figures to establish their effect on the stress rates. As follows from Figs. 4–6, the largest rate of the shearing stress τ_{xy}^t in steel corresponds to extreme lamination angles while the smallest rate is achieved at the angles ± 45 deg. In the contrary, the shearing stresses in composites increase at the highest rate at the lamination angle ± 45 deg and at the smallest rate if lamination approaches the cross-ply case. The stresses σ_x^t and σ_y^t have the largest rates of increase at ± 30 deg and ± 60 deg, respectively, while their smallest rates are obtained in arrangements approaching cross-ply lamination. All stress rates decrease in shells with relatively thicker steel layers.

Conclusions

The paper presents an outline of an exact solution for nonlinear bending of generally laminated thin and shear-deformable cylindrical shells. Nonlinear extensions of Love's first approximation and Donnell's theories are used, while the first-order shear deformation theory is employed to include transverse shearing deformations into the analysis. Loads can include an axisymmetric pressure, axial tension or compression, and torsion. Deformations of each cross-section are independent of the circumferential coordinate, although circumferential displacements are present.

The method of solution discussed in the paper is based on an exclusion of the only nonlinear element of the strain tensor (ϵ_x) from the equations of equilibrium. Then the solution is reduced to integration of linear differential equations. Geometric nonlinearity reappears in the analysis only if axial displacements have to be evaluated. The stresses are independent of geometric nonlinearity, if the value of an axial stress resultant acting on the shell ends is prescribed. Geometric nonlinearity affects the stresses only if the boundary conditions in the axial direction include a prescribed value of the corresponding displacement.

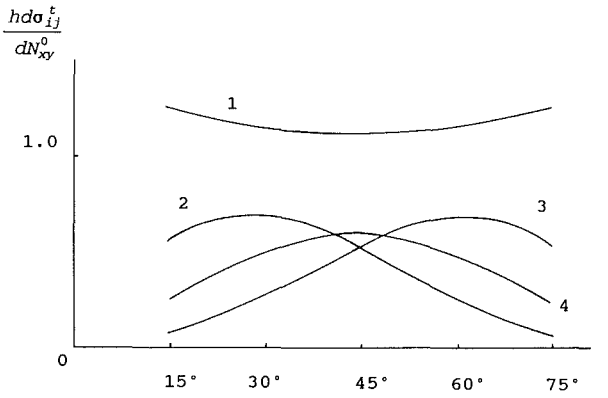


Fig. 6 Stress rates $[h\,(d\sigma_{ij}^t/dN_{xy}^0)]$ as functions of the laminations angle; $\bar{h}_{st}=0.75$. Curve 1: steel, τ_{xy}^t. Curves 2-4: composite, $|\sigma_x^t|$, $|\sigma_y^t|$, τ_{xy}^t, respectively.

Acknowledgment

The author is grateful to Prof. Eric Reissner of the University of California, San Diego, for calling his attention to the first results in the area of generally anisotropic shells (Reissner and Wan, 1971).

References

Agarwal, B. D., and Broutman, L. J., 1980, *Analysis and Performance of Fiber Composites*, John Wiley and Sons, New York, pp. 152–155.

Ambartsumian, S. A., 1974, *General Theory of Anisotropic Shells*, Nauka Publishers, Moscow, pp. 162–205 (in Russian).

Anastasiadis, J. S., and Simitses, G. J., 1990, "A Higher Order Shell Theory for Cylindrical Laminates," *Developments in Theoretical and Applied Mechanics*, Vol. 15, S. V. Hanagud, M. P. Kamat, and C. D. Ueng, eds., Georgia Institute of Technology, Atlanta, GA, pp. 803–810.

Bert, C. W., and Kumar, M., 1982, "Vibration of Cylindrical Shells of Bimodulus Composite Materials," *Journal of Sound and Vibration*, Vol. 81, pp. 107–121.

Bert, C. W., and Reddy, V. S., 1982, "Cylindrical Shells of Bimodulus Composite Materials," *ASCE Journal of Engineering Mechanics*, Vol. 108, pp. 675–688.

Birman, V., 1991, "Thermal Bending of Shear-Deformable Orthotropic Cylindrical Shells Reinforced by Cylindrically-Orthotropic Rings," *International Journal of Solids and Structures*, Vol. 28, pp. 819–830.

Caladine, C. R., 1983, *Theory of Shell Structures*, Cambridge University Press, Cambridge, pp. 278–307.

Chia, C.-Y., 1988, "Geometrically Nonlinear Behavior of Composite Plates: A Review," ASME *Applied Mechanics Reviews*, Vol. 41, pp. 439–451.

Grigorenko, Ya. M., Vasilenko, A. T., and Kryukow, N. N., 1983, "Numerical Solution of Nonlinear Problems of the Axisymmetric Deformation of Laminar Anisotropic Shells of Revolution," *Mekhanika Kompozitnykh Ma-*

Downloaded 03 May 2010 to 171.66.16.245. Redistribution subject to ASME license or copyright; see http://www.asme.org/terms/Terms_Use.cfm

terialov, Vol. 19, pp. 1023–1028 (in Russian); English translation: *Mechanics of Composite Materials*, 1984, Vol. 19, pp. 746–751.

Librescu, L., and Stein, M., 1991, "A Geometrically Nonlinear Theory of Transversely Isotropic Laminated Composite Plates and its Use in the Post-Buckling Analysis," *Thin-Walled Structures*, Vol. 11, pp. 177–201.

Noor, A. K., and Burton, W. S., 1990, "Assessment of Computational Models for Multilayered Composite Shells," ASME *Applied Mechanics Reviews*, Vol. 43, pp. 67–97.

Philin, A. P., 1975, *Elements of Theory of Shells*, Stroyizdat, Leningrad, pp. 229–235 (in Russian).

Reissner, E., and Wan, F. Y. M., 1969, "Rotationally Symmetric Stress and Strain in Shells of Revolution," *Studies in Applied Mathematics*, Vol. 48, pp. 1–17.

Reissner, E., and Wan, F. Y. M., 1971, "On Rotationally Symmetric Stress and Strain in Anisotropic Shells of Revolution," *Studies in Applied Mathematics*, Vol. 50, pp. 391–394.

Schmidt, R., and Reddy, J. N., 1988, "A Refined Small Strain and Moderate Rotation Theory of Elastic Anisotropic Shells," ASME JOURNAL OF APPLIED MECHANICS, Vol. 55, pp. 611–617.

Stein, M., 1986, "Nonlinear Theory for Plates and Shells Including the Effects of Transverse Shearing," *AIAA Journal*, Vol. 24, pp. 1537–1544.

Stein, M., 1989, "Effects of Transverse Shearing Flexibility on Postbuckling of Plates in Shear," *AIAA Journal*, Vol. 27, pp. 652–655.

Wylie, C. R., Jr., 1960, *Advanced Engineering Mathematics*, McGraw-Hill, New York, pp. 114–129.

APPENDIX

1 Linear differential operators $\mathcal{L}_{ij}$ and $\bar{p}$ in Eqs. (16)

$$\mathcal{L}_{11}=\mathcal{L}_{34}=\left(B_{16}-\frac{B_{11}A_{16}}{A_{11}}\right)\frac{d^2}{dx^2}+\frac{n}{R}A_{45}$$

$$\mathcal{L}_{12}=\mathcal{L}_{44}=\left(B_{66}-\frac{B_{16}A_{16}}{A_{11}}\right)\frac{d^2}{dx^2}+\frac{n}{R}A_{44}$$

$$\mathcal{L}_{13}=-\mathcal{L}_{24}=\frac{1}{R}\left(A_{26}+nA_{45}-\frac{A_{12}A_{16}}{A_{11}}\right)\frac{d}{dx}$$

$$\mathcal{L}_{14}=\left(A_{66}-\frac{A_{16}^2}{A_{11}}\right)\frac{d^2}{dx^2}-\frac{n}{R^2}A_{44}$$

$$\mathcal{L}_{21}=\left[\frac{1}{R}\left(\frac{B_{11}A_{12}}{A_{11}}-B_{12}\right)+A_{55}\right]\frac{d}{dx}$$

$$\mathcal{L}_{22}=-\mathcal{L}_{43}=\left[\frac{1}{R}\left(\frac{B_{16}A_{12}}{A_{11}}-B_{26}\right)+A_{45}\right]\frac{d}{dx}$$

$$\mathcal{L}_{23}=A_{55}\frac{d^2}{dx^2}+\frac{1}{R^2}\left(\frac{A_{12}^2}{A_{11}}-A_{22}\right)$$

$$\mathcal{L}_{31}=\left(D_{11}-\frac{B_{11}^2}{A_{11}}\right)\frac{d^2}{dx^2}-A_{55}$$

$$\mathcal{L}_{32}=\mathcal{L}_{41}=\left(D_{16}-\frac{B_{16}B_{11}}{A_{11}}\right)\frac{d^2}{dx^2}-A_{45}$$

$$\mathcal{L}_{33}=-\left[\frac{1}{R}\left(\frac{A_{12}B_{11}}{A_{11}}-B_{12}\right)+A_{55}\right]\frac{d}{dx}$$

$$\mathcal{L}_{42}=\left(D_{66}-\frac{B_{16}^2}{A_{11}}\right)\frac{d^2}{dx^2}-A_{44}$$

$$\bar{p}=q-\frac{A_{12}}{A_{11}R}C_0$$

where C_0 is a constant of integration.

2 Linear differential operators $\bar{\mathcal{L}}_{ij}$ in Eqs. (24):

$$\bar{\mathcal{L}}_{11}=\frac{1}{A_{11}}\left(A_{16}+\frac{n}{R}B_{16}\right)\left(B_{11}\frac{d^3}{dx^3}-\frac{A_{12}}{R}\frac{d}{dx}\right)-\left(B_{16}+\frac{n}{R}D_{16}\right)\frac{d^2}{dx^2}+\frac{1}{R}\left(A_{26}+\frac{n}{R}B_{26}\right)$$

$$\bar{\mathcal{L}}_{12}=-\frac{1}{A_{11}}\left(A_{16}+\frac{n}{R}B_{16}\right)^2\frac{d^2}{dx^2}+\left[A_{66}+\frac{n}{R}\left(2B_{66}+\frac{D_{66}}{R}\right)\right]\frac{d}{dx}$$

$$\bar{\mathcal{L}}_{21}=-\left(D_{11}-\frac{B_{11}^2}{A_{11}}\right)\frac{d^4}{dx^4}+\left[\frac{2}{A_{11}R}\left(B_{12}A_{11}-A_{12}B_{11}\right)+C_0\right]\frac{d^2}{dx^2}+\frac{A_{12}^2-A_{11}A_{22}}{A_{11}R^2}$$

$$\bar{\mathcal{L}}_{22}=\left[-\frac{B_{11}}{A_{11}}\left(A_{16}+\frac{n}{R}B_{16}\right)+B_{16}+\frac{n}{R}D_{16}\right]\frac{d^3}{dx^3}+\frac{1}{R}\left[\frac{A_{12}}{A_{11}}\left(A_{16}+\frac{n}{R}B_{16}\right)-A_{26}-\frac{n}{R}B_{26}\right]\frac{d}{dx}.$$

Downloaded 03 May 2010 to 171.66.16.245. Redistribution subject to ASME license or copyright; see http://www.asme.org/terms/Terms_Use.cfm

Amruthur S. Ramamurthy
Professor,
Civil Engineering Department,
Concordia University,
Montreal H3G 1M8, Canada
Mem. ASME

Ngoc-Diep Vo
Graduate Student,
Civil Engineering Department,
Concordia University
Montreal, H3G 1M8, Canada

Application of Dressler Theory to Weir Flow

The curvilinear flow past a circular-crested weir is analyzed with the help of Dressler equations. Specifically, the lower range of the depth over the weir crest is considered in the analysis, so that the shallow depth model could be adopted. The weir discharge coefficient is determined as a function of the total head of the approach flow and the crest radius. The weir discharge coefficient obtained on the basis of Dressler theory is verified with the help of present and previous experimental data.

Introduction

Circular-crested weirs (Fig. 1) are used in the field for flow measurement and regulation. The simplest form of such a weir consists of a circular crest *BCE* of radius R set tangentially to an upstream face *DB* and perpendicular to the direction of flow (Fig. 2). They have a high discharge coefficient C_d compared to sharp-crested weirs. The discharge equation can be written as follows (Bos, 1978):

$$q = C_d \frac{2}{3}\sqrt{\frac{2}{3}\, g\, H_1^{1.5}}. \tag{1}$$

Here, q = the discharge/unit crest length, g = the acceleration due to gravity and H_1 = the total head of the approaching flow reckoned above the crest level. Escande and Sananes (1959) showed that suction of the crest boundary layer increases C_d. Jaeger (1956) and Sananes (1957) related the minimum crest surface pressure head $(P/\gamma)_{\min}$ with the parameter H_1/R, the crest flow depth Y_2 and the streamline curvature $1/r$. Here, γ denotes the specific weight of water. Bos (1978) has compiled existing test data to relate C_d and H_1/R of circular-crested weirs for which the downstream slope $\beta = 45$ deg. For flow over circular-crested weirs ($H_1/R \leq 1.0$), Matthew (1963) outlined a simple theory which clearly explains the influence of streamline geometry, surface tension, and viscosity on C_d. Cassidy (1965) presented ideal fluid flow models of circular-crested weirs and standard spillways. A rational procedure to pass the maximum flood flow over the standard spillway with a specified minimum crest pressure was proposed by Cassidy (1970). Sinniger and Hager (1985) have reported an interesting experimental study of both gated and ungated standard spillways. Circular-crested weirs and sharp-crested weirs were studied by Sarginson (1972) who determined the influence of surface tension on C_d, adopting the theory of Jaeger (1956). Based on ideal flow theory, Dressler (1978) derived governing equations for shallow, two-dimensional flow over a curved channel floor of radius $1/k$ for which the flow depth normal to the floor is N. His theory is applicable when the local shallowness parameter kN is in the range $-0.85 \leq kN \leq 0.50$. Negative values of kN refer to the convex profiles such as spillways. For flowover spillway crests, Sivakumaran et al. (1981, 1983) stated that Dressler equations yield accurate crest pressure data in the range $-2.0 \leq kN \leq 0.54$.

In the present study, Dressler equations are adapted to determine the weir characteristics such as the velocity distribution at the crest section and the weir discharge coefficient C_d. These results are verified using past and present test data for three types of circular-crested weirs. Further, the dimensionless water surface profiles and the angular locations of the point of nappe separation are also reported, in the range $H_1/R \leq 2.28$ or $-1.6 \leq kN$, where the shallow depth model is applicable.

Theoretical Considerations

The following assumptions are made in the development of the model for circular-crested weirs based on Dressler theory (Figs. 1 and 2): (1) The approach flow is steady, two-dimensional, and subcritical; (2) the effects of fluid properties such as surface tension and viscosity on the weir flow characteristics are not significant; (3) and for the accelerating flow on the

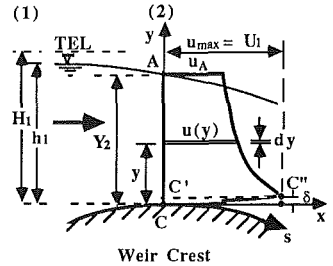


Fig. 1 Flow past a circular-crested weir

Contributed by the Applied Mechanics Division of THE AMERICAN SOCIETY OF MECHANICAL ENGINEERS for publication in the ASME JOURNAL OF APPLIED MECHANICS.

Discussion on this paper should be addressed to the Technical Editor, Professor Lewis T. Wheeler, Department of Mechanical Engineering, University of Houston, Houston, TX 77204-4792, and will be accepted until four months after final publication of the paper itself in the ASME JOURNAL OF APPLIED MECHANICS.

Manuscript received by the ASME Applied Mechanics Division, May 14, 1991; final revision, Feb. 21, 1992. Associate Technical Editor: K. R. Sreenivasan.

 Copyright © 1993 by ASME

Downloaded 03 May 2010 to 171.66.16.245. Redistribution subject to ASME license or copyright; see http://www.asme.org/terms/Terms_Use.cfm

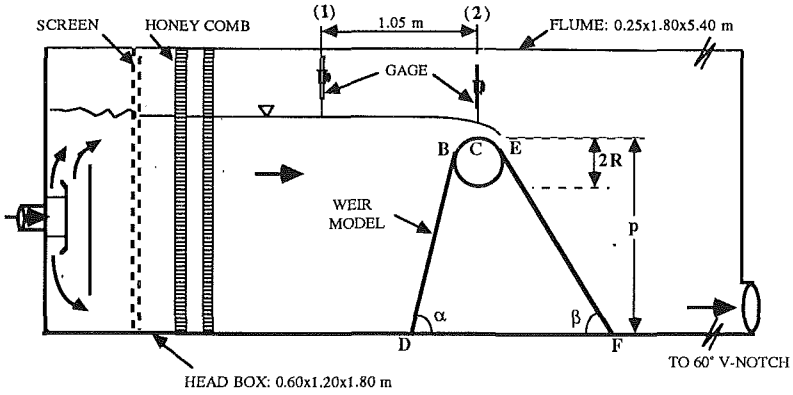


Fig. 2 Circular-crested weir and test set-up

crest surface upstream of C (Fig. 1), the crest boundary layer thickness δ is negligibly small compared to Y_2 and H_1. Typically, δ/H_1 is of the order of 0.02.

Following the procedures outlined by Dressler (1978) and Sivakumaran et al. (1981, 1983), the equation for a steady flow rate of q per unit crest length of the weir may be written as

$$q = U_1 R \ln\left(1+\frac{Y_2}{R}\right) \tag{2}$$

where $U_1 = \sqrt{2g(H_1-(P/\gamma)_{cr})}$ is the maximum velocity at the crest for ideal flow. For this flow, the horizontal velocity u at a depth y over the crest C can be expressed as follows (Dressler, 1978):

$$u = \frac{U_1}{\left(1+\frac{y}{R}\right)}. \tag{3}$$

In real flows over a circular-crested weir, the maximum velocity U_1 is not at the crest but at the edge of the thin boundary layer (assumption 3). As such, for $\delta \le y \le Y_2$ the horizontal velocity component u (Fig. 1) is given by

$$u \cong \frac{U_1}{1+\frac{(y-\delta)}{(R+\delta)}}. \tag{4}$$

The converging flow over the weir in the region ($y \ge \delta$) excluding the crest boundary layer is irrotational and hence, the total head is constant along the section AC'. At C' where $y = \delta$, $u = U_1$, using assumption 3 and applying the energy equation between sections 1 and 2 (Fig. 2) gives us

$$H_1 = \delta + \frac{U_1^2}{2g} + \left[\left(\frac{P}{\gamma}\right)_{cr} - \frac{dP}{\gamma dy}\delta\right] \approx \frac{U_1^2}{2g} + \left(\frac{P}{\gamma}\right)_{cr}. \tag{5}$$

Hence, rewriting Eq. (5),

$$U_1 \approx \sqrt{2g\left(H_1 - \left(\frac{P}{\gamma}\right)_{cr}\right)}. \tag{6}$$

For flow over the weir crest, for which δ is extremely small ($\delta/H_1 \ll 1$, $\delta/R \ll 1$), the normalized velocity profile can be written as

$$\frac{u}{U_1} = \frac{1}{\left(1+\frac{y}{R}\right)}. \tag{7}$$

Alternatively, u can also be normalized by $U = \sqrt{2gH_1}$. Hence, using Eq. (6),

$$\frac{u}{U} = \frac{\left[1-\left(\frac{P}{\gamma H_1}\right)_{cr}\right]^{0.5}}{\left(1+\frac{y}{R}\right)}. \tag{8}$$

Using Eqs. (2) and (6) in Eq. (1) and simplifying, C_d can be expressed as follows:

$$C_d = \frac{3\sqrt{3}}{2}\left[1-\left(\frac{P}{\gamma H_1}\right)_{cr}\right]^{0.5} \frac{\ln\left(1+\frac{Y_2}{R}\right)}{\left[\frac{H_1}{R}\right]}. \tag{9}$$

Tests were mainly conducted to verify the above expression for C_d for $0 < H_1/R \le 2.28$, which is in the practical range of application and where Dressler theory is applicable.

Nomenclature

C_d = coefficient of discharge
g = acceleration due to gravity
h = piezometric head, flow depth above crest level
H = total head reckoned above crest level
k = curvature ($k = 1/r$)
N = flow depth normal to bed
p = weir height
P = pressure
q = discharge per unit width
r = radial distance, radius of curvature
R = radius of crest circular weir
TEL = total energy line
s = distance along curved bed, s-direction
u = horizontal velocity component
U = reference velocity ($U = \sqrt{2gH_1}$)
U_1 = maximum velocity at crest, ideal flow ($U_1 = \sqrt{2g(H_1-(P/\gamma)_{cr})}$)
x = x-direction, horizontal distance
y = y-direction, vertical distance, depth from bed
Y = total flow depth
α = upstream slope angle
β = downstream slope angle
δ = boundary layer thickness
γ = specific weight of water
θ = angular position, q-direction

Subscripts

1 = approach section 1, index
2 = downstream section 2, index
cr = at weir crest
D = design
Pm = minimum pressure

Downloaded 03 May 2010 to 171.66.16.245. Redistribution subject to ASME license or copyright; see http://www.asme.org/terms/Terms_Use.cfm

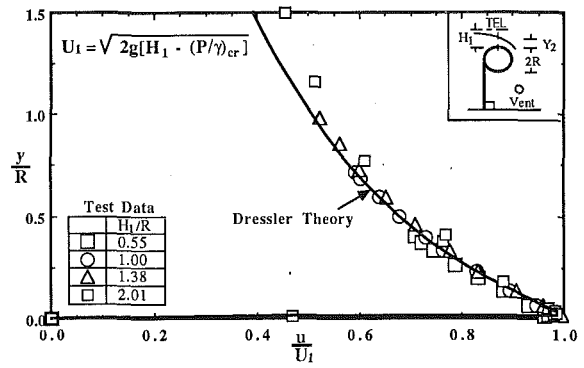


Fig. 3(*a*) Variation of y/R with u/U_1 (α = 90 deg, no *D/S* slope-ventilated)

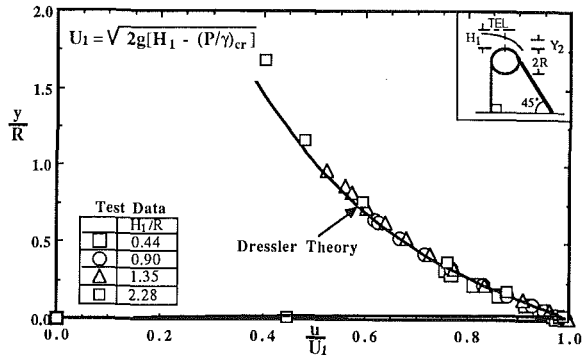


Fig. 3(*b*) Variation of y/R with u/U_1 (α = 90 deg, β = 45 deg)

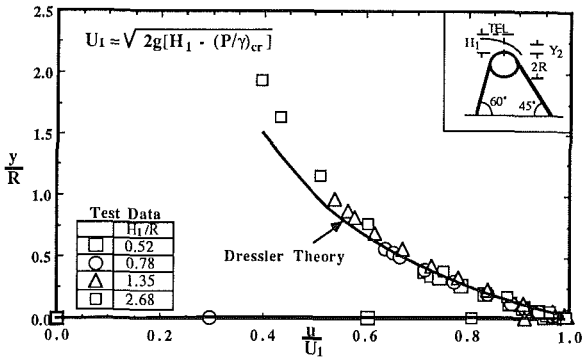


Fig. 3(*c*) Variation of y/R with u/U_1 (α = 60 deg, β = 45 deg)

Fig. 3 Experimental velocity distribution at crest section—(0.44 ≤ H_1/R ≤ 2.68)

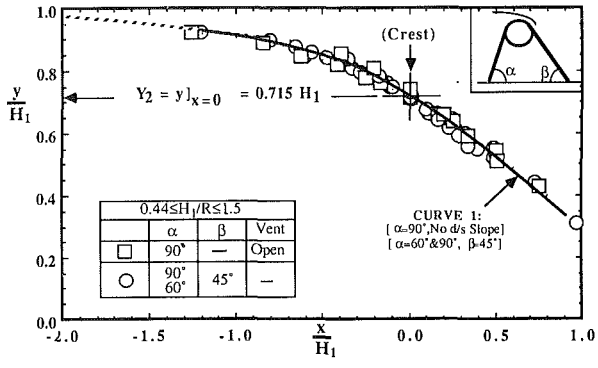


Fig. 4(*a*) Water surface profiles over weir crest (0.44 ≤ H_1/R ≤ 2.28)

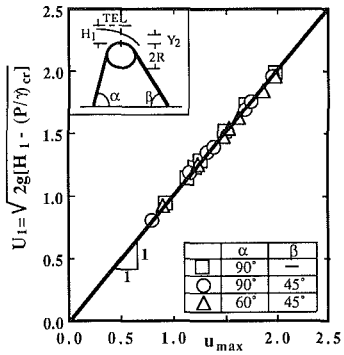


Fig. 4(*b*) Predicted and measured values of maximum velocity

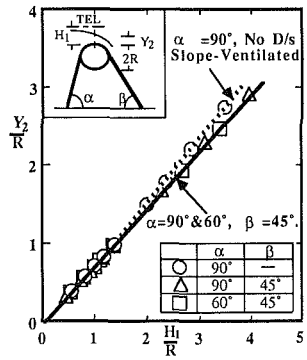


Fig. 4(*c*) Variation of Y_2/R with H_1/R (0.44 ≤ H_1/R ≤ 4.0)

Experimental Set-up and Procedure

Machined plexiglass weir models were set in a smooth stainless steel flume (Fig. 2). The test section was 0.25 m wide, 1.80 m high, and 2.50 m long. The side walls were equipped with transparent windows for flow visualization. Sufficient stilling arrangements were provided to obtain smooth flow without large-scale turbulence. For the weir without the downstream slope, a ventilation duct provided full aeration of the nappe in some cases.

All models were equipped with sufficient pressure taps of diameter 0.0005 m to record the pressure distribution along the center line of the weir models. On the vertical weir face, pressure taps were spaced at every 0.050 m. On the weir crest, they were spaced at 5-deg intervals. The pressure head was measured to the nearest 0.0005 m. The flow depth upstream of the weir (Fig. 2) and the water surface profiles over the weir crest were measured by point gages to the nearest 0.0003 m. The flow rate was measured using a standard 60-deg V-notch. The maximum error in the estimation of the discharge was three percent. A Helium-Neon Laser Doppler Velocimeter (LDV) TSI System 9100-3 was used to determine the horizontal velocity distribution above their weir crest. The velocity in the potential core of an axisymmetrical jet of diameter of 0.0125 m was used to verify (Balachandar, 1990) the velocity calibration data supplied by the LDV manufacturer (TSI). This verification indicated that the accuracy of velocity measurement was close to 0.5 percent.

Discussion of Result

Flow Characteristics. Figs 3(*a*), (*b*), and 3(*c*) show the selected velocity profiles for the three weir models in the range $0.44 \le H_1/R \le 2.28$. Here, the depth y and the horizontal velocity u are normalized by R and $U_1 = \sqrt{2g(H_1 - (P/\gamma)_{cr})}$, respectively. Experimental velocity distributions agree very well with the theoretical profiles (Eq. (3)) for the flow up to $Y_2/R \le 1.0$. One can recall that Dressler (1978) recommended the use of his equations for $Y_2/R \le 0.85$ for a convex bed. $Y_2/R = 1.0$ approximately corresponds to $H_1/R = 1.40$. Figure 4(*a*) shows the water surface profiles for the three weirs in the range $0.44 \le H_1/R \le 2.28$. The total head H_1 was used to normalize the depth h above the crest and the horizontal distance x (Fig. 1). Figure 4(*a*) shows that the water surface profiles for all the three weirs merge into the

Downloaded 03 May 2010 to 171.66.16.245. Redistribution subject to ASME license or copyright; see http://www.asme.org/terms/Terms_Use.cfm

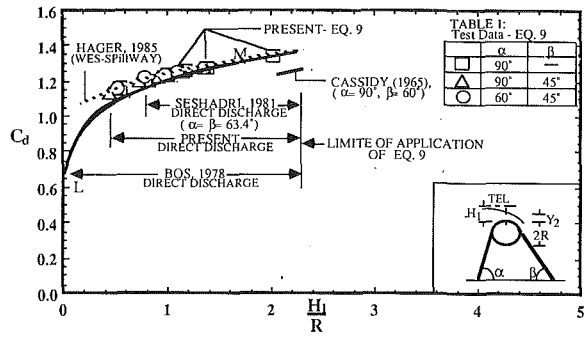


Fig. 5(*a*) Variation of C_d with H_1/R – ($0.44 \leq H_1/R \leq 2.28$)

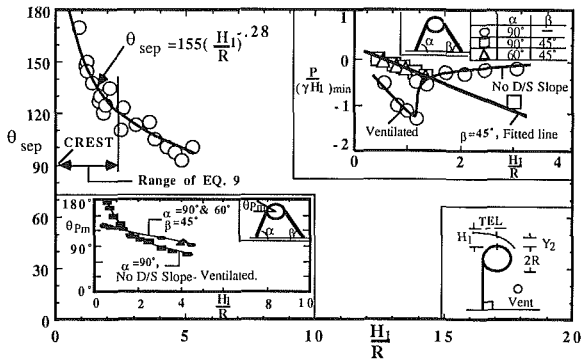


Fig. 5(*b*) Point of separation on crest surface (visual observations)—(α = 90 deg, no *D/S* slope—ventilated). Upper insert: variation of minimum pressures with H_1/R (all weirs). Lower insert: points of minimum pressures over crest surface (all weirs).

same average curve, and the mean flow depth at the crest $Y_2 = 0.715\ H_1$.

Range of Applicability of Dressler Equations. As H_1/R is increased from low values, the center of curvature of the segment of the surface profile above the crest C (Fig. 1) begins to drift away from the center of the circular crest surface. When H_1/R is large ($H_1/R > 1.4$), the center of curvature of the streamlines between C' and A (Fig. 1), will be very far from the center of the crest surface. Consequently, the formulation of Eq. (3) which implies that the crest surface and the streamlines above it are concentric (Fig. 1), begins to be strongly violated. Hence, the limit to obtain the accurate velocity distribution from Dressler theory appears to be $H_1/R \leq 1.4$, which is nearly the same as $Y_2/R \leq 1.0$. Figure 4(*b*) provides a comparison between the predicted maximum velocity U_1 (Eq. (6)) and the measured maximum velocity u_{max} at the weir crest. At the crest, the variation of the dimensionless flow depths Y_2/R with H_1/R is given in Fig. 4(*c*). This relationship is almost linear and identical for all the weirs up to $H_1/R = 1.4$.

Discharge Coefficient C_d. Equation (9) based on Dressler theory was used to compute C_d for the weirs. Figure 5(*a*) shows these data points plotted as a function of H_1/R. The solid line LM in this figure denotes the average relationship between C_d based on Eq. (1) (direct discharge measurement) of the present and existing (Seshadri, 1981; Bos, 1978) studies. Figure 5(*a*) also provides a comparison of the present results with the existing ideal flow model of Cassidy (1965) for circular-crested weirs which, like Dressler's model, excludes effects due to boundary layer growth and flow separation. Hager (1985) has presented the values of C_d for standard spillways as a function of h_1/h_D (dashed line, Fig. 5(*a*)). To qualitatively compare the present results with the results of Hager (1985), a scale factor = 1.5 was used to account for the fact that the crest pressure is atmospheric for standard spillways at $h_1/h_D = 1.0$ and for circular-crested weirs at $H_1/R = 1.5$.

In the range of $H_1/R \leq 2.28$ or $Y_2/R \leq 1.6$, for all the weirs, the variations of C_d with H_1/R based on Eq. (9) (Dressler theory) and Eq. (1) (direct discharge measurement) agree very well. Hence, the model based on Dressler theory appears to be valid in a larger range of H_1/R for C_d than for the velocity distribution. This, in part, can be traced to the fact that the velocity distributions refers to the detailed flow structure, while C_d refers to the gross flow characteristic.

Nappe Separation and Minimum Pressure. Figure 5(*b*) shows the results of visual observation of the point of nappe separation from the crest surface for the weir with $\alpha = 90$ deg, no downstream slope and a ventilated nappe. The minimum pressure $(P/\gamma H_1)_{min}$ and its angular location recorded on the crest surface of all the three weirs are given in the upper and lower inserts of Fig. 5(*b*), respectively. They indicate that the dependence of these parameters on H_1/R is essentially the same for the two weirs with the downstream slope $\beta = 45$ deg. In this regard, their behavior differs significantly from the weir with $\alpha = 90$ deg and with no downstream slope and a ventilated nappe. Further, the minimum pressure data needed for the determination of cavitation potential on the weir crest surface are important only for the two weirs with a downstream slope, since $(P/\gamma H_1)_{min}$ continues to drop as H_1/R increases. For these two weirs, the lower insert of Fig. 5(*b*) shows that the angular locations of the points of minimum pressure occur downstream of the crest ($\theta = 90$ deg) for the entire recorded data range.

Summary and Conclusions

Dressler equations can be adapted to formulate the model for curvilinear flow past circular-crested weirs. The water surface profiles for all the three weirs tested are very similar for $H_1/R \leq 2.28$. For the prediction of the velocity distribution over the weir crest, the Y_2/R range of applicability of Dressler theory appears to be 1.0. However, the predicted values of C_d based on this model agree well with C_d determined from direct discharge measurements, in the range $H_1/R \leq 2.28$ or $Y_2/R \leq 1.6$. This corresponds to $-1.6 \leq kN$ (Convex bed).

References

Balachandar, R., 1990, "Characteristics of Separated Flows Including Cavitation Effects," Ph.D. Thesis, Concordia University, Montreal, Quebec, Canada, Mar.

Bos, M. G., 1978, "Discharge Measurement Structures," Publ. 20, ILRI, The Netherlands.

Cassidy, J. J., 1965, "Irrotational Flow over Spillways of Finite Height," *J. of the Engineering Mechanics Div.*, ASCE, Vol. 91, No. 6, pp. 155–173.

Cassidy, J. J., 1970, "Designing Spillway Crests for High Head Operation," *J. Hyd. Div.*, ASCE, Vol. 96, No. 3, pp. 745–753.

Dressler, R. F., 1978, "New Nonlinear Shallow Flow Equations with Curvature," *J. Hyd. Res., IAHR*, Vol. 16, No. 3, pp. 205–222.

Escande, L., and Sananes, F., 1959, "Étude des Seuils Déversants à Fente Aspiratrice (Weirs with Suction Slots)," *La Houille Blanche*, Vol. 14, No. Spl B, pp. 892–902.

Jaeger, C., 1956, *Engineering Fluid Mechanics*, Blackie, London.

Matthew, G. D., 1963, "On the Influence of Curvature, Surface Tension and Viscosity on Flow Over Round-Crested Weirs," *Proc. of the Inst. of CE*, ASCE, Vol. 25, pp. 511–524.

Sananes, M. F., 1957, "Étude des Seuils Déversants à Fente Aspiratrice," *IAHR, 7th Gen. Meet. Trans., Lisbon*, Vol. II, pp. D24.1–D24.23.

Sarginson, E. J., 1972, "The Influence of Surface Tension on Weir Flow," *J. of Hyd. Res.*, Vol. 10, pp. 431–446.

Seshadri, S., 1981, "Flow Characteristics of Hydrofoil Weirs, Hydrofoil Topped Weirs and Streamlined Triangular Profiles Weirs," Ph.D. Thesis, Indian Institute of Science, Nov.

Sinniger, R., and Hager, W. H., 1985, "Flood Control by Gated Spillways," *Commission Internationale des Grands barrages, 15e Congrès des barrages, Lausanne*, Q.59, R.9, pp. 121–149.

Sivakumaran, N. S., Hosking, R. J., and Tingsanchali, T., 1981, "Steady Shallow Flow Over a Spillway," *J. of Fl. Mech.*, Vol. 111, pp. 411–420.

Sivakumaran, N. S., Tingsanchali, T., and Hosking, R. J., 1983, "Steady Shallow Flow OVer Curved Beds," *J. of Fl. Mech.*, Vol. 128, pp. 469–487.

Downloaded 03 May 2010 to 171.66.16.245. Redistribution subject to ASME license or copyright; see http://www.asme.org/terms/Terms_Use.cfm

Chaotic Vibrations of Beams: Numerical Solution of Partial Differential Equations

N. S. Abhyankar[1]
Assistant Professor,
Department of Aerospace and Mechanical Engineering,
Syracuse University,
Syracuse, NY 13244
Mem. ASME

E. K. Hall, II[2]
Graduate Student.

S. V. Hanagud
Professor,
Mem. ASME.

School of Aerospace Engineering,
Georgia Institute of Technology,
Atlanta, GA 30332

The objective of this paper is to examine the utility of direct, numerical solution procedures, such as finite difference or finite element methods, for partial differential equations in chaotic dynamics. In the past, procedures for solving such equations to detect chaos have utilized Galerkin approximations which reduce the partial differential equations to a set of truncated, nonlinear ordinary differential equations. This paper will demonstrate that a finite difference solution is equivalent to a Galerkin solution, and that the finite difference method is more powerful in that it may be applied to problems for which the Galerkin approximations would be difficult, if not impossible to use. In particular, a nonlinear partial differential equation which models a slender, Euler-Bernoulli beam in compression is solved to investigate chaotic motions under periodic transverse forcing. The equation, cast as a system of first-order partial differential equations is directly solved by an explicit finite difference scheme. The numerical solutions are shown to be the same as the solutions of an ordinary differential equation approximating the first mode vibration of the buckled beam. Then rigid stops of finite length are incorporated into the model to demonstrate a problem in which the Galerkin procedure is not applicable. The finite difference method, however, can be used to study the stop problem with prescribed restrictions over a selected subdomain of the beam. Results obtained are briefly discussed. The end result is a more general solution technique applicable to problems in chaotic dynamics.

Introduction

Researchers, during the last two decades, have been intrigued by the existence of aperiodic or randomlike responses resulting from periodic inputs to nonlinear, deterministic dynamical systems. The wealth of new problems which developed from these observations has led to a new branch of study termed chaotic dynamics. The so-called chaotic responses have been observed in a wide range of problems involving both iterated mappings and nonlinear ordinary differential equations which model physical phenomena. The problems have also come from a wide range of fields including engineering mechanics, fluid mechanics, biological sciences, chemistry, and plasma physics. As such, there have been papers and entire books written about the characteristics of chaotic systems. Helleman (1980), Pippard (1982), Abraham and Shaw (1982), Garrido (1982), and Moon (1986, 1987) are just a few references which provide good general information about chaotic systems.

In structural mechanics, the first evidence of chaotic vibration in a buckled beam was recorded in the work of Tseng and Dugundji (1971). They solved the problem of a fixed, buckled beam in a two mode approximation by the harmonic balancing method. The beam was excited at the base without any transverse loading, and their observation of aperiodic responses to periodic excitation was verified with experimentation. Later, Holmes (1979) presented a study of the most basic model for a buckled beam, Duffing's equation. He also found chaotic responses, and his work laid the foundation for much of the subsequent chaos studies in structural mechanics. Moon and Holmes (1983), and Moon and Shaw (1983) next reported chaotic behavior in problems involving a cantilever beam with magnetic attractors at its free end, and involving a cantilever beam with a stop restricting the motion of its free end. A further extention was completed by Dowell (1982) when he predicted chaos in the flutter of a buckled plate governed by an autonomous system of ordinary differential equations.

At the present time, almost all studies pertaining to chaos have been restricted to the solution of simple iterated mappings and ordinary differential equations. Moore, Toomre, Knobloch, and Weiss (1983) were the first to solve a partial differential equation exhibiting chaotic behavior directly in their

[1]Currently at Phillips Laboratory, Edwards Air Force Base.
[2]Currently at The Aerospace Corporation, Los Angeles, CA 90009-2957.

Contributed by the Applied Mechanics Division of THE AMERICAN SOCIETY OF MECHANICAL ENGINEERS for publication in the ASME JOURNAL OF APPLIED MECHANICS.

Discussion on this paper should be addressed to the Technical Editor, Professor Lewis T. Wheeler, Department of Mechanical Engineering, University of Houston, Houston, TX 77204-4792, and will be accepted until four months after final publication of the paper itself in the ASME JOURNAL OF APPLIED MECHANICS.

Manuscript received by the ASME Applied Mechanics Division, Dec. 13, 1988; final revision, Mar. 7, 1991. Associate Technical Editor: D. J. Inman.

Copyright © 1993 by ASME
Downloaded 03 May 2010 to 171.66.16.245. Redistribution subject to ASME license or copyright; see http://www.asme.org/terms/Terms_Use.cfm

study of a thermosolutal convection problem. In structural mechanics, a similar study has not been completed. Thus, the purpose of this paper is to discuss the general advantages and disadvantages of direct, numerical solution procedures in chaotic dynamics and demonstrate their utility in nonlinear structural mechanics problems. These goals will be accomplished through solutions of an approximate model for a Euler-Bernoulli beam, simply supported on both ends and subjected to an axial load as well as a transverse forcing function. This model has previously received considerable attention including a study by Holmes and Marsden (1981) in which the mathematical aspects of the problem were analyzed from the point of view of averaging procedures, Lyapunov stability, and an extension of Melnikov theory. This paper, however, describes the first direct numerical solution of the buckled beam partial differential equation model.

Motivation

Prior to studying the buckled beam problem, it is wise to justify the investigation of direct solutions of partial differential equations in chaos studies. When a beam oscillates chaotically, its motion has a frequency content much like that of white noise. Energy is spread out over most of the spectrum and accordingly the time variation of the motion is very complex. For problems in which the deformation of the beam is restricted to one or two modes, the complex motion can be easily found using separable solutions. If the motion is a combination of several modes, however, a separable solution can quickly become very difficult. Attempts to simplify the procedure by approximating a multimode motion using a small number of modes can lead to significant errors because of the sensitivity of chaotic systems to small parameter changes. Tang and Dowell (1988), for example, have shown that neglecting higher modes can lead to significant errors in estimates of chaotic motion thresholds. Thus any solution method which would inherently include higher modes could provide improved accuracy. Such a solution method would be even more valuable in problems in which a Galerkin-type solution would be prohibitively complex such as in problems with either time dependent boundary conditions or deformations which can not be described by a linear combination of a finite number of modes. In these problems, the assumed modes of the separable solution would have to be changed many times as the solution proceded, and in many cases it would be impossible to predict when a change would be required. A numerical solution of the partial differential equation, on the other hand, would theoretically account for all of the infinite number of modes which comprise the transverse motion of a continuous beam. In practice, the discretization process restricts the number of modes because of finite resolution, but the restrictions are not as severe as in a Galerkin procedure. So a finite difference or finite element method can be expected to be more generally applicable in chaotic dynamics.

In addition to the greater generality, such numerical methods have several other advantages over traditional methods. First, the development of an algorithm is much simpler than performing a Galerkin approximation since integrations are not required. Second, after the original development of the numerical algorithm, changing the boundary conditions on the beam is a relatively simple process requiring only slight modifications of the algorithm. Similarly, forcing functions and even stops are easily implemented and either could have discrete or continuous distributions along the length of the beam. Third, the effects of different types of damping and material nonlinearities can be studied, provided the mathematical nature of the damping and nonlinearities do not cause considerable departure from beam theory. Fourth, the accuracy of a solution can be estimated beforehand by just knowing the discretization. Finally, the methods are computationally efficient because of the possible use of parallel computing.

Despite the advantages, there are some problems which may occur due to the numerical aspects of the solution procedure. For example, the consistency, accuracy, and stability of the routine must be insured, and the effects of truncation errors must be minimized. In addition, computational effort and post-processing of the computed information in studies of chaotic behavior may be unmanageable. There is also the possibility of numerically induced errors in the solutions involving chaotic motion as has been discussed by Tongue (1987). If these potential problems are appropriately addressed, however, an efficient and accurate direct solution procedure can be developed.

With these concepts in mind, an explicit, stable finite difference solution to the partial differential equation governing the buckled beam problem is used in this paper. The same partial differential equation is also solved by reducing it to an infinite set of ordinary differential equations using the method of weighted residuals. The solution of the ordinary differential equation representing the first mode vibration of the beam is then compared to the numerical solution. Specific parameter values are chosen so that the ordinary differential equation reduces to the Duffing's type ordinary differential equation studied by Holmes (1979) thus allowing further verification and comparison. Finally, rigid stops of finite length are added to the beam problem to demonstrate the advantages of the finite difference technique in connection with a problem with time-dependent boundary conditions.

Formulation

Consider the beam system represented graphically in Fig. 1(*a*) where w is the transverse displacement of the beam from the base line, w_B is the displacement of the base, and f is a transverse time-dependent forcing function. The beam is assumed to be compressed initially by an axial load P and then fixed in its compressed position. In this situation, the motion of the beam can be approximated by a modified Euler-Bernoulli beam equation,

$$\rho A \frac{\partial^2 w}{\partial t^2} + c \frac{\partial w}{\partial t} + EI \frac{\partial^4 w}{\partial x^4} - N \frac{\partial^2 w}{\partial x^2} = f - \rho A \frac{\partial^2 w_B}{\partial t^2}, \qquad (1)$$

where linear viscous damping has been assumed. In general, excitation arises due to the external distributed loading $f(x, t)$ and the base excitation $w_B(t)$. The total axial force, N, consists of the applied force at the ends of the beam and the contribution from membrane stretching,

$$N = -P + \frac{EA(2K)}{2L} \int_0^L \left(\frac{\partial w}{\partial x}\right)^2 dx.$$

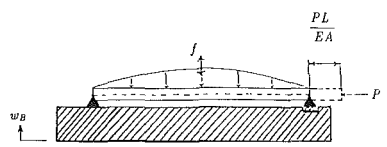


Fig. 1(*a*) Simply-supported beam, sinusoidal loading

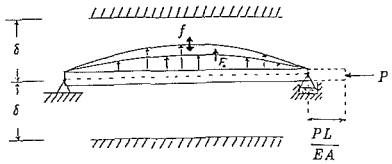


Fig. 1(*b*) Beam with constant load and rigid stops added

Fig. 1 Two cases of a simply-supported beam

Downloaded 03 May 2010 to 171.66.16.245. Redistribution subject to ASME license or copyright; see http://www.asme.org/terms/Terms_Use.cfm

Equation (1) can be nondimensionalized by using the following nondimensional parameters:

$$\tilde{t}=\frac{t}{L^2}\sqrt{\frac{EI}{\rho A}} \quad \tilde{x}=\frac{x}{L}$$

$$\tilde{w}=\frac{w}{r} \quad r=\sqrt{\frac{I}{A}}$$

$$\tilde{w}_B=\frac{w_B}{r} \quad \tilde{c}=\frac{cL^2}{\sqrt{\rho AEI}}$$

$$\tilde{\Gamma}=\frac{PL^2}{EI} \quad \tilde{N}=\frac{NL^2}{EI}$$

$$\tilde{f}=\frac{fL^4}{EIr}.$$

Substituting these parameters in Eq. (1), and neglecting the tildes for simplicity, the governing partial differential equation becomes

$$\ddot{w}+w''''+c\dot{w}-Nw''=f-\ddot{w}_B \tag{2}$$

with

$$N=-\Gamma+K\int_0^l (w')^2dx.$$

Here K is a proportionality constant and has a value equal to one half for the nondimensional variables given. Also note that the overdots represent partial differentiation with respect to nondimensional time and primes represent partial differentiation with respect to nondimensional position.

The case of static deflection of the beam is governed by Eq. (2) when all of the time dependence is removed, and reduces to an eigenvalue problem. The solution of this problem when Γ is greater than the critical load of the beam reveals that the beam has a straight equilibrium position which is unstable, and two buckled equilibrium positions which are stable. It will be seen that the respective repulsion and attraction of the three equilibrium positions create the appropriate environment for chaos to occur.

Next note that the nondimensional moment-curvature relationship can be written as

$$M=w''.$$

For application of the finite difference method, it is convenient to use this equation as a state variable definition and transform the governing partial differential equation into a set of partial differential equations which are all first order in the time derivatives and second order in the spatial derivatives. The resulting equations are

$$\frac{\partial \dot{w}}{\partial t}=-M''-c\dot{w}+NM+f-\ddot{w}_B \tag{3}$$

$$\frac{\partial M}{\partial t}=(\dot{w})'' \tag{4}$$

$$\frac{\partial w}{\partial t}=\dot{w} \tag{5}$$

In addition to aiding in the numerical solution of the governing equation, this transformation allows the physical variables such as moment and velocity to be monitored.

Ordinary Differential Equation Formulation. Partial differential equations are often reduced to ordinary differential equations to extract physical, but approximate information about a system. Such a reduction of Eq. (2) can be made by Galerkin's procedure. In this procedure, the solution of the partial differential equation is assumed to be separable into amplitudes and mode shapes. An important criteria is that the displacement functions chosen must satisfy all the essential and natural boundary conditions. Initially, the deflection of the beam can be written in series form as

$$w(x,\,t)=\sum_{n=1}^{\infty} q_n(t)\phi_n(x)$$

where q_n represents the amplitude and ϕ_n the mode shape of the nth mode of the beam. Then using ϕ_m as a normalized weighting function, the ordinary differential equation governing the mth mode of vibration becomes

$$\ddot{q}_m+c\dot{q}_m+\sum_{n=1}^{\infty} q_nA_{nm}=\int_0^1 (f-\ddot{w}_B)\phi_m dx \tag{6}$$

where

$$A_{nm}=\int_0^1 \phi_n''''\phi_m dx+\Gamma\int_0^1 \phi_n''\phi_m dx$$
$$-K\left[\int_0^1\left(\sum_{k=1}^{\infty} q_k\phi_k'\right)\left(\sum_{l=1}^{\infty} q_l\phi_l'\right)dx\right]\int_0^1 \phi_n''\phi_m dx.$$

For the stated simply-supported beam, $\phi_m = \sin m\pi x$ satisfies all of the boundary conditions and thus is an appropriate weighting function. Substituting into Eq. (6), an ordinary differential equation is obtained.

$$\ddot{q}_m+c\dot{q}_m+q_m\left[m^4\pi^4-m^2\pi^2\Gamma+\frac{m^2\pi^2K}{2}\sum_{n=1}^{\infty} n^2\pi^2q_n^2\right]$$
$$=F_m(t)+\frac{2\ddot{w}_B[(-1)^m-1]}{m\pi} \quad \text{for } m=1,\,2,\,3,\,\ldots\,\infty \tag{7}$$

In this equation,

$$F_m=2\int_0^1 f\sin m\pi x dx$$

and is a generalized mth mode force amplitude and depends on the type of loading $f(x,\,t)$. Many simplifications of this model could be studied. In the case of base excitation, all of the symmetric, or odd, modes would be excited. Holmes (1979) has discussed and analyzed a Duffing's type of equation corresponding to only single mode vibration due to a sinusoidally distributed loading with cosine time variation. In this case, $F_1 = A\cos\omega t$ and all other F_m's are zero. With this loading, the higher modes do not contribute and the beam vibrates only in the first mode. However, there are many problems in which the higher modes are important. For example, Holmes and Marsden (1981) considered the general case in which base excitation gives rise to multimode vibration. A similar problem will be addressed later when examining the advantages of a partial differential equation solution.

Numerical Solution of a Partial Differential Equation

Equation (1) governing the vibration of a beam including the effect of nonlinear stretching is an integrodifferential equation. Direct central differencing of the derivatives in (1) leads to a finite difference scheme which is second-order accurate in the variable w (Ames, 1977). However, physically identifiable variables such as displacement, velocity, and moment are of interest in any real problem, and thus Eqs. (3)–(5) are more appropriate to solve. This choice is also governed by the benefits of lower-order derivatives in the equations of motion as well as in the boundary conditions. Additionally, there are a wider variety of available difference procedures for the lower order problem, and it allows a simpler stability analysis and more convenient handling of variables at different time levels.

An appropriate difference scheme for Eqs. (3)–(4) is given by

Downloaded 03 May 2010 to 171.66.16.245. Redistribution subject to ASME license or copyright; see http://www.asme.org/terms/Terms_Use.cfm

$$\dot{w}_i^{n+1} = \dot{w}_i^n - \frac{\Delta t}{\Delta x^2}\,(M_{i+1} - 2M_i + M_{i-1})^n + \Delta t(-c\dot{w}_i^n + NM_i^n + f_i - \ddot{w}_{B_i}^n) \quad (8)$$

$$M_i^{n+1} = M_i^n + \frac{\Delta t}{\Delta x^2}\,(\dot{w}_{i+1} - 2\dot{w}_i + \dot{w}_{i-1})^{n+1}. \quad (9)$$

It can be observed that Eq. (8) has a forward time derivative approximation, and that once $\dot{w}_i$ is found at the $n + 1$th time level, this value can be substituted into Eq. (9) to evaluate the new M_i. The scheme is stable because of the combination of the forward and backward time substitutions; otherwise, it is unstable. Equations (8) and (9) together are exactly equivalent to centered differencing of Eq. (1). The only difference is that the displacement should be evaluated separately. Although Eqs. (8)–(9) satisfy first-order accuracy in $\dot{w}$ and M, second-order accuracy for the displacement w can be obtained by averaging velocities

$$w_i^{n+1} = w_i^n + \frac{\Delta t}{2}\,[\dot{w}_i^{n+1} + \dot{w}_i^n]. \quad (10)$$

There are instances in which this averaging, used purely to get second-order accuracy, turns out to be unstable in the sense of von Neumann stability analysis. An example of this is found in flutter or in feedback control systems in which the forcing function, f, or the base excitation, w_B, is displacement dependent. Without averaging, only first-order displacement accuracy is achieved for a stable solution.

The source of nonlinearity in the beam equation is the membrane stretching term in the axial force N. Its value greatly affects the final solution and thus is required to be as accurate as possible. Evaluation of the integral in a finite difference procedure is done as a summation. Integration schemes such as trapezoidal, rectangle, midpoint, and Simpson's are commonly used. Belz (1966) had integrated the membrane stretching term by an approximation which did not resemble any of these schemes. However, his results were found to be in error because the slopes at the boundaries were effectively ignored. For the present study, Simpson's rule has been used. Accordingly, the expression for the axial force, N, is given by

$$N = \frac{K}{3\Delta x}\left[.5(w_2^2 + w_p^2) + .25\sum_{j=2}^{p}(w_{j+1} - w_{j-1})^2 + 2\sum_{j=2}^{p+1}(w_j - w_{j-1})^2\right] - \Gamma$$

where the beam of nondimensional length equal to unity has been divided into p meshes by $p + 1$ mesh points. Computationally, the value of N is evaluated separately at each time-step. Note that this expression is dependent upon the boundary conditions of the problem. For example, if the beam was fixed at $x = 0$, the w_2 term would be zero.

The explicit nature of the scheme (8)–(10) restricts the time-step required to achieve numerical stability. The stability criteria is given by

$$\Delta t \le \frac{\Delta x^2}{2}.$$

This is based on the local linearization in which the axial force N, at any particular instant of time, is assumed to be constant. Since the time-step is dependent on the square of the mesh size Δx, a large number of time-steps are required to reach a steady state. An unconditionally stable, implicit difference scheme in which large time-steps are allowed could also be used to solve Eq. (1). However, implicit schemes require iteration procedures which may eventually consume the same amount of computer time to achieve the same accuracy as an explicit scheme which is much easier to implement and can be incorporated in a parallel computational scheme.

Results and Discussion

The explicit finite difference routine given in Eqs. (8)–(10) was used to solve the stated beam vibration problem. Two possible cases were considered, and they are demonstrated graphically as Fig. 1. In the first case, a beam was assumed to be compressed with an axial load greater than its Euler buckling load and then fixed in simple supports that restricted axial motion. A transverse, sinusoidal load distribution of the form $f = F\sin\pi x\cos\omega t$ was then assumed. For this loading, the steady-state motion of the beam is composed of only its first mode and thus this case is well suited for a comparison between the partial differential equation and ordinary differential equation solutions, which should be identical. Parameter values used for this study were the same as those used by Holmes (1979), and with the present nondimensionalizations they were equal to $c = 1$, $K = 0.50$, and $\Gamma = 10.88281625$. The stability condition was taken to be $\Delta t = 0.99\Delta x^2/2$.

The beam in the given configuration has three equilibrium positions. Identifying these positions by the displacement of the midpoint of the beam, Q, there is a saddle point at $Q = 0$ and two sinks at $Q = \pm\sqrt{2(\Gamma - \pi^2)/(K\pi^2)}$. For small load amplitudes, the beam oscillates about one of the sinks where the initial conditions determine which of them. As the load increases the oscillations progress through a series of period doubling bifurcations. Then, as analyzed by Holmes (1979), the forcing amplitude reaches a critical value where the minimum value of Q approaches the saddle point and the motion develops into movement about all three equilibrium points, although in an unspecified manner. For loads above this critical value, the steady state of the beam passes through a variety of motions including period-doubling cascades, transient and fully developed chaos, and even three-period motion. After this transitional region, the forcing amplitude reaches a level at which the beam moves periodically about all three equilibrium positions.

In Figs. 2 and 3 the progression of motion predicted by the ordinary differential equation and the partial differential equation solutions are compared using phase plane plots of $\dot{Q}$ versus Q. (Note that the ordinary differential equation was solved using an integration routine, RKINIT, found in the Mathematical Science Library, MSFLIB.) The values of the amplitude, F, were chosen so that the oscillations gradually changed through the above series of steady-state motions. The corresponding bifurcation plots are given as Figs. 4(*a*)–4(*c*). The bifurcation plots consist of the values of the response amplitude at which the phase plane trajectories cross the zero velocity axis; the number of points thus corresponded to double the response periodicity. For all of the plots, it was verified that transients had died out prior to the construction of the graphs.

The results from the ordinary differential equation and the partial differential equation in Figs. 2 and 3 matched very accurately. The individual trajectories generally are similar, but more importantly, the two solutions predict the transitions and period doubling points at the same values of F. The results in Fig. 4(*c*) indicate that the results are even closer when $\Delta x = 0.05$. Further discretization, however, did not show any appreciable differences. Considering that halving the mesh size increases the number of iterations almost fourfold, it was decided that for practical purposes $\Delta x = 0.1$ yielded adequate accuracy. With some verification that the direct partial differential equation solution yielded the same results as a traditional approximate ordinary differential equation solution, an example where the partial differential equation solution would have an advantage over the well-studied ordinary differential equation solutions was considered.

In the second case, a sinusoidally distributed, constant transverse load and stops of finite length were added to the beam model (Fig. 1(*b*)). Because of the stops, the sinks were moved to $Q = \pm\delta$ where δ was the position of the stop, chosen to

Downloaded 03 May 2010 to 171.66.16.245. Redistribution subject to ASME license or copyright; see http://www.asme.org/terms/Terms_Use.cfm

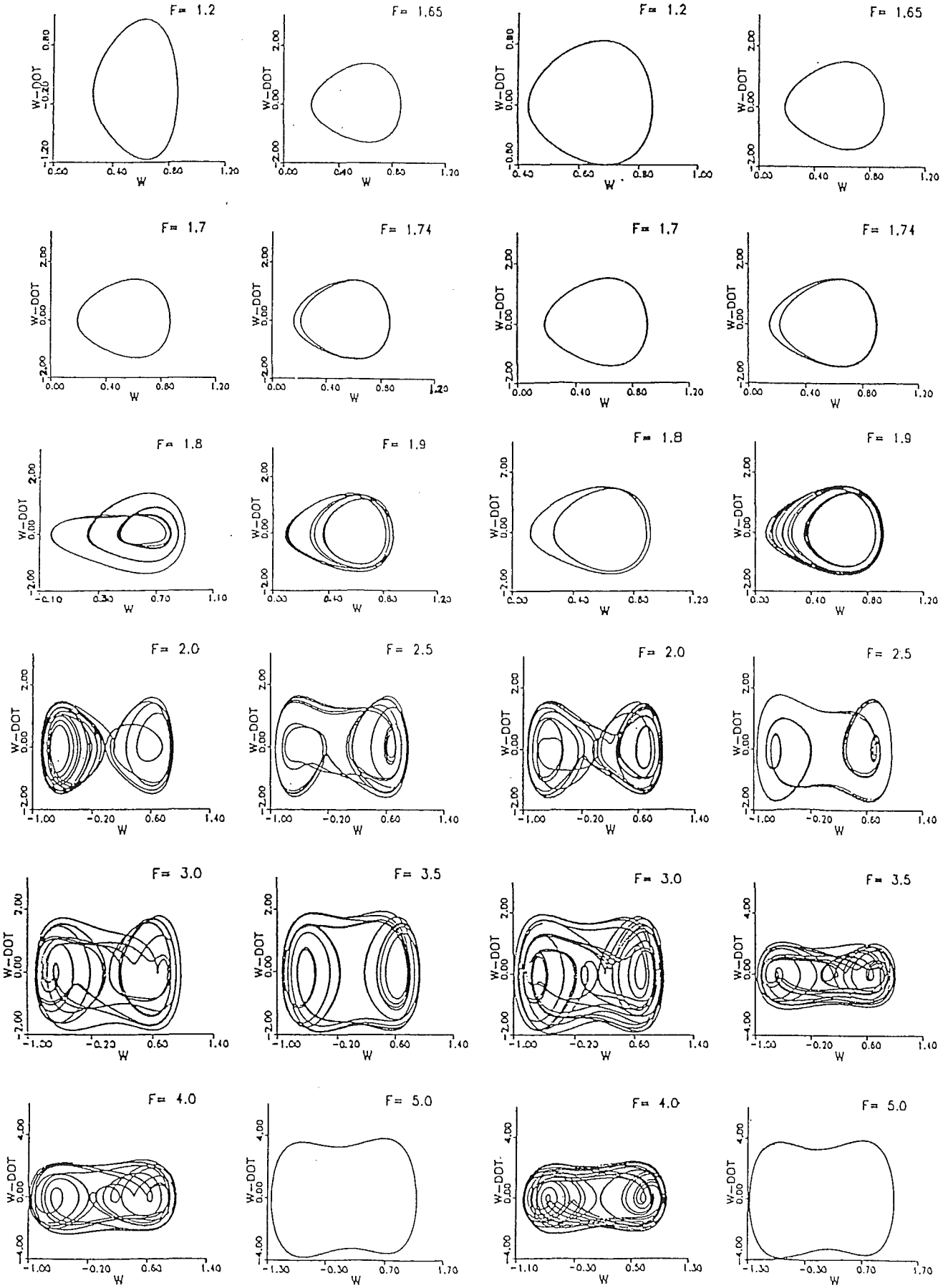


Fig. 2 Phase plane trajectories for a sequence of forcing amplitudes: ordinary differential equation solution of a single-mode buckled beam vibration

Fig. 3 Phase plane trajectories for a sequence of forcing amplitudes: partial differential equation solution of a single-mode buckled beam vibration

Downloaded 03 May 2010 to 171.66.16.245. Redistribution subject to ASME license or copyright; see http://www.asme.org/terms/Terms_Use.cfm

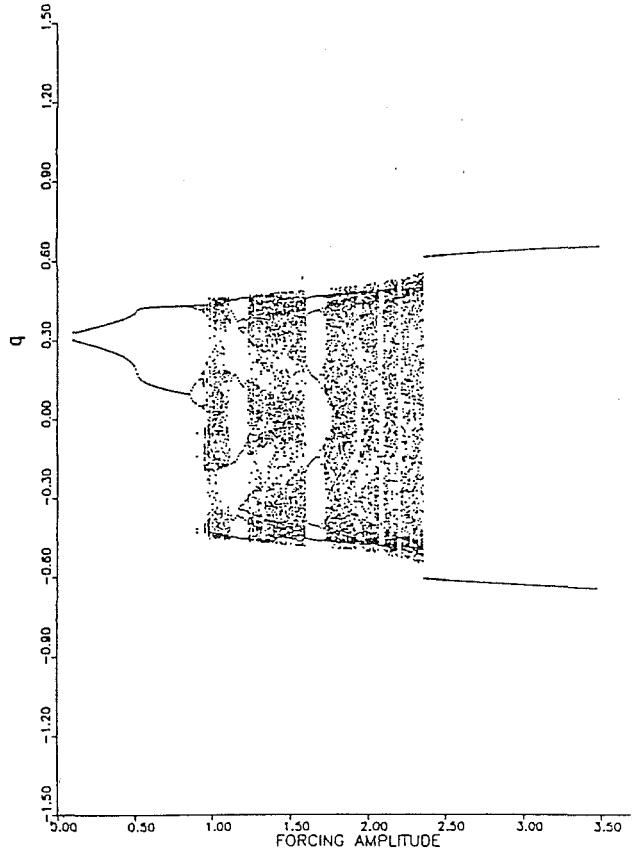


Fig. 4(*a*) Solution of the ordinary differential equation

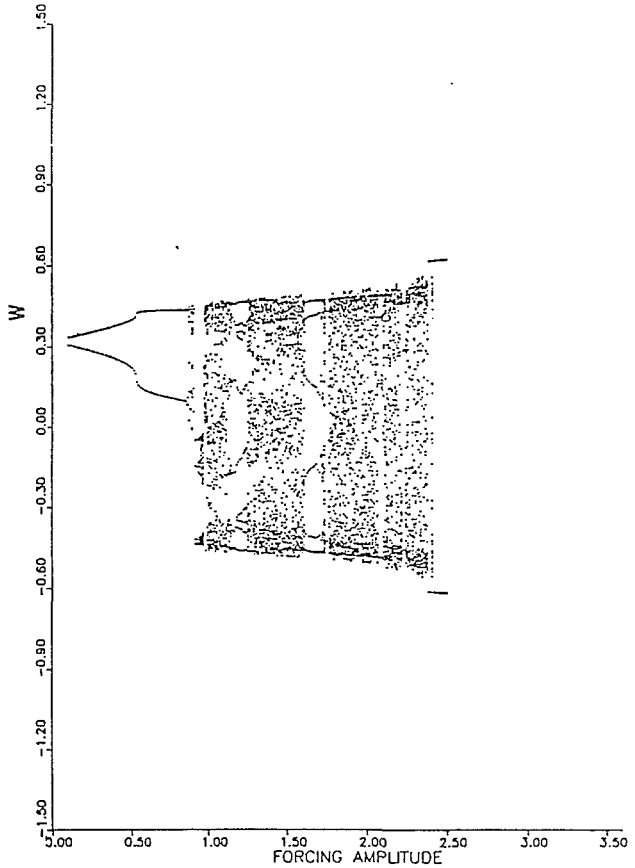


Fig. 4(*c*) Solution of the partial differential equation with $\Delta x = 0.05$

Fig. 4 Bifurcation diagram (zero velocity crossings)

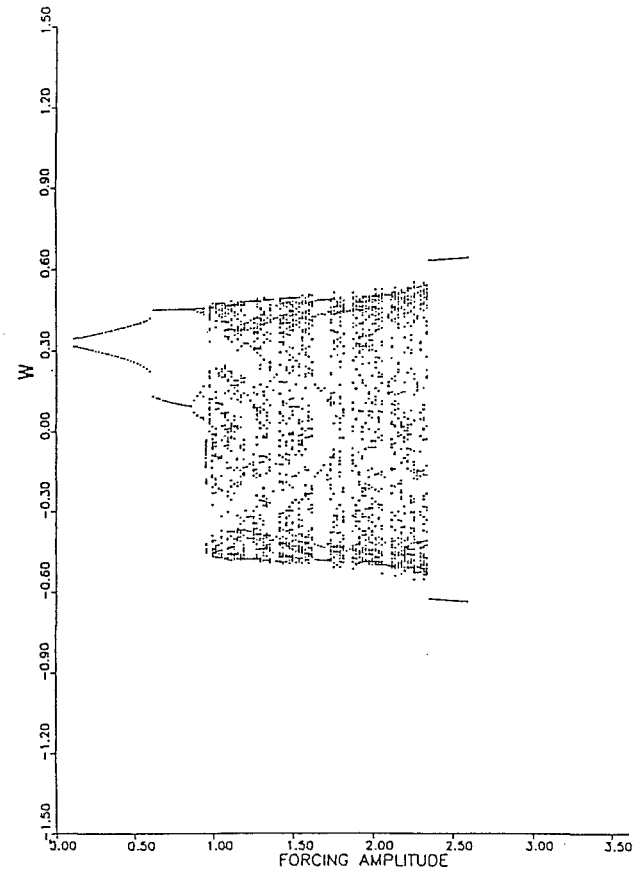


Fig. 4(*b*) Solution of the partial differential equation with $\Delta x = 0.1$

be smaller than the deflection in the original stable equilibrium position. Now when the beam was disturbed toward the $Q = \delta$ stop, the constant load and the axial load worked to press the beam against the stop. Then as the magnitude of the oscillating load changed, more or less of the beam came in contact with the stop. Thus as the beam vibrated, three different types of modes were possible: one in which the beam was not in contact with a stop, one in which the beam was just touching a stop, and a third in which a finite portion of the beam was forced flat against a stop. With the possibility of the mode shape having a flat section, a complete set of functions could not be found which could accurately describe the mode shape of the beam for all times. In addition, if the beam was in contact with a stop, the problem became that of two beams with a continuity requirement and a new set of boundary conditions at the stop. Without an adequate description of the changing mode shape of the beam and with the time dependent boundary conditions, a Galerkin procedure was not easily applicable to this problem.

The finite difference procedure, on the other hand, could solve this problem with only the addition of a few lines of code. Starting from the assumption of elastic contact with the stop, all that was required was a check to insure that the deflection of the beam was not greater than the height of either of the stops. Restricting the points of the beam predicted to be in contact with the stop, the kinetic energy of the beam prior to impact is transferred into strain energy due to an increase in curvature of the beam at the point of contact. Eventually, enough strain energy is built up in the beam to predict that the beam moves away from the stop, and thus the restraints are relaxed and the solution would proceed as before. The one difference between the solution of the first problem and that of the stop problem was in the stability analysis where

Downloaded 03 May 2010 to 171.66.16.245. Redistribution subject to ASME license or copyright; see http://www.asme.org/terms/Terms_Use.cfm

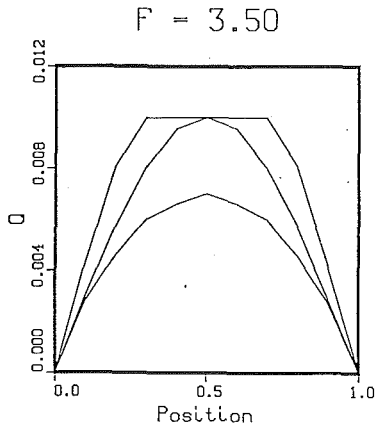


Fig. 5 Mode shapes for stop problem with $F = 3.5$ and a constant sinusoidally distributed load with magnitude $F_o = 3.0$

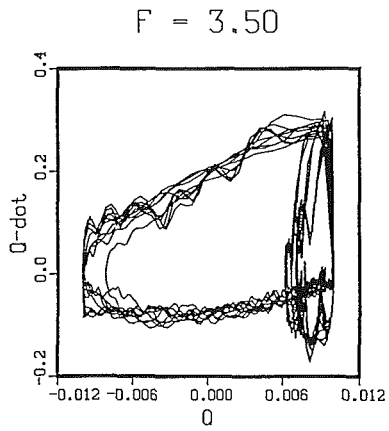


Fig. 6 Phase plane plot for a chaotic trajectory

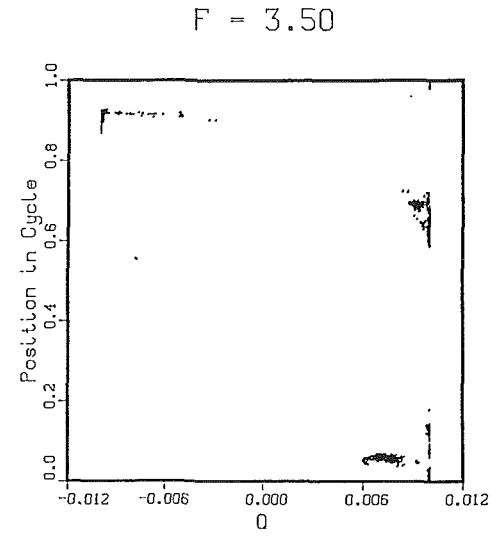


Fig. 7 Zero velocity Poincaré plot for a chaotic trajectory

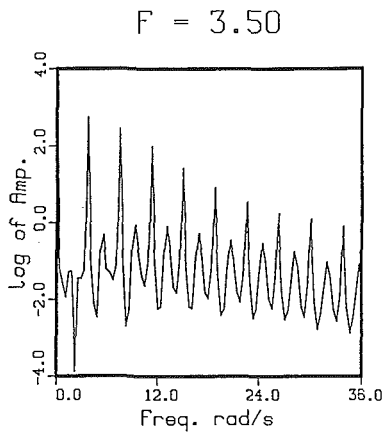


Fig. 8 Frequency response plot for a chaotic trajectory

the nonlinear boundary conditions required a smaller time-step for accurate results.

To demonstrate the utility of the finite difference method, a sample problem was solved. Parameter values were the same as in the first case, and δ was chosen to be 0.01. The sinusoidally distributed constant load had an amplitude of 3.0, and the oscillating load again had magnitude F. For $F = 3.5$, all three types of mode shapes were observed. Here 11 nodes were used in the discretization, and during the motion up to three nodes came in contact with one of the stops. In Fig. 5 are some examples of the different deformation modes which the beam experienced as the oscillating load varied through its cycle. The time dependence of Q was equally complicated due to the influence of higher modes. Both periodic and chaotic motions were observed as the oscillating load amplitude was varied. Phase plane, Poincaré, and frequency response plots for a chaotic motion are in Fig. 6–8.

When the beam strikes a stop, many of its higher modes are excited and thus its resulting motion is a combination of many modes. In addition to the complex spatial variations in the response, the time history of the motion never settled down into a repeatable pattern. Accordingly, the phase plane plot in Fig. 6 is very jagged, and the zero velocity points in Fig. 7 are quite numerous and occur at many positions of the forcing cycle. However, the zero velocity points are restricted to certain regions of the phase space and they appear to lie on a strange attractor. The finite difference solution, not depending on the mode of deformation, can easily pick up this very complex and erratic motion. The frequency plot in Fig. 8 further demonstrates the higher frequency content of the motion with the larger peaks representing the appearance of multiples of the driving frequency. However, it also emphasizes the chaotic nature of the motion as the spectrum is rather broad. Thus, this problem is a good example of a chaotic system whose accurate analysis can only be completed by direct numerical solution procedures.

Conclusions

In conclusion, a simply-supported buckled beam governed by a Euler-Bernoulli beam equation with transverse loading and nonlinear membrane stretching effect has been studied. By using a stable, explicit finite difference scheme to solve the governing partial differential equation it has been demonstrated that various problems are easily handled. The solution technique theoretically accounts for the infinite dimensional analysis of the beam and has been compared favorably to traditional ordinary differential equation solution techniques. In problems solvable by both methods, the two techniques yielded similar results. However, it is possible to find physically meaningful problems in which the numerical solution of the partial differential equation is the only feasible solution technique available. Furthermore, the solution technique developed here can be applied to beams of various boundary conditions and forcing functions without much trouble, and thus proves to be a powerful tool in nonlinear dynamics and chaos studies. It is expected that other numerical methods like the finite element methods commonly used in structural mechanics will yield similar results.

Downloaded 03 May 2010 to 171.66.16.245. Redistribution subject to ASME license or copyright; see http://www.asme.org/terms/Terms_Use.cfm

Acknowledgments

Authors greatly acknowledge the support of the Air Force Office of Scientific Research, Bolling AFB DC, and the U.S. Army, Contract #DAAL03-88-C-0003, to create a Center of Excellence in Rotary Wing Aircraft Technology.

References

Abhyankar, N. S., 1986, "Studies in Nonlinear Structural Dynamics: Chaotic Behavior and Poynting Effect," Ph.D. Thesis, School of Aerospace Engineering, Georgia Institute of Technology, Atlanta, GA.

Abraham, R. H., and Shaw, C. D., 1982, *Dynamics: The Geometry of Behavior Part I: Periodic Behavior, Part II: Chaotic Behavior, Part III: Global Behavior, Part IV: Bifurcational Behavior*, Aerial Press, Santa Cruz, CA.

Ames, W. F., 1977, *Numerical Method for Partial Differential Equations*, 2nd ed., Academic Press, New York.

Belz, D. J., 1966, "A Numerical Study of Nonlinear Vibrations Induce by Correlated Random Loads," *Int. J. Nonlinear Mechanics*, Vol. 1, pp. 139–145.

Dowell, E. H., 1982, "Flutter of a Buckled Plate as an Example of Chaotic Motion of a Deterministic Autonomous System," *J. Sound and Vibration*, Vol. 85, pp. 333–344.

Garrido, L., 1983, *Dynamical Systems and Chaos*, Proceedings of the Sitges Conference on Statistical Mechanics, Barcelona, Spain, Sept. 1982, Springer-Verlag, Berlin.

Helleman, R., ed., 1980, *Nonlinear Dynamics*, Annals of N.Y. Academy of Sciences, Vol. 357.

Holmes, P. J., 1979, "A Nonlinear Oscillator with a Strange Attractor," *Philosophical Transactions of the Royal Society, London*, Vol. A292, pp. 419–448.

Holmes, P. J., and Marsden, J., 1981, "A Partial Differential Equation with Infinitely Many Periodic Orbits: Chaotic Oscillations of a Forced Beam," *Arch. Rat. Mech. Anal.*, Vol. 76, pp. 135–166.

Moon, F. C., 1986, "New Research Directions for Chaotic Phenomena in Solid Mechanics," *Perspectives in Nonlinear Dynamics*, R. Cawley and Shlesinger eds., World Scientific Publisher, Singapore.

Moon, F. C., 1987, *Chaotic Vibrations: An Introduction for Applied Scientists and Engineers*, John Wiley and Sons, New York.

Moon, F. C., and Holmes, P. J., 1983, "Strange Attractors and Chaos in Nonlinear Systems," ASME JOURNAL OF APPLIED MECHANICS, Vol. 50, pp. 1021–1032.

Moon, F. C., and Shaw, S. W., 1983, "Chaotic Vibrations of a Beam with Nonlinear Boundary Conditions," *Int. J. Nonlinear Mechanics*, Vol. 18, pp. 465–477.

Moore, D. R., Toomre, J., Knobloch, E., and Weiss, N. O., 1983, "Period Doubling Chaos in Partial Differential Equations for Thermosolutal Convection," *Nature*, Vol. 303, pp. 663–667.

Pipard, Sir Brian, 1982, "Instability and Chaos: Physical Models of Everyday Life," *Interdisciplinary Science Reviews*, Vol. 7, No. 2, pp. 92–101.

Shaw, S. W., 1985, "The Dynamics of a Harmonically Excited System Having Rigid Amplitude Constraints: Part I—Subharmonic Motions and Local Bifurcations; Part II—Chaotic Motions and Global Bifurcations," ASME JOURNAL OF APPLIED MECHANICS, Vol. 52, pp. 453–465.

Tang, D. M., and Dowell, E. H., 1988, "On the Threshold Force for Chaotic Motions for a Forced Buckled Beam," ASME JOURNAL OF APPLIED MECHANICS, Vol. 55, pp. 190–196.

Thompson, J. M. T., and Stewart, H. B., 1986, *Nonlinear Dynamics and Chaos*, John Wiley and Sons, New York.

Thompson, J. M. T., and Ghaffari, R., 1983, "Complex Dynamics of Bilinear Systems with Bifurcational Instabilities Leading to Chaos," *Collapse: The Buckling of Structures in Theory and Practice*, IUTAM Symposium.

Tongue, B. H., 1987, "Characteristics of Numerical Simulations of Chaotic Systems," ASME JOURNAL OF APPLIED MECHANICS, Vol. 54, pp. 695–699.

Tseng, W. Y., and Dugundji, J., 1971, "Nonlinear Vibrations of a Buckled Beam Under Harmonic Excitation," ASME JOURNAL OF APPLIED MECHANICS, pp. 467–476.

Downloaded 03 May 2010 to 171.66.16.245. Redistribution subject to ASME license or copyright; see http://www.asme.org/terms/Terms_Use.cfm

An Analysis of Crack Trapping by Residual Stresses in Brittle Solids

A. F. Bower

M. Ortiz

Division of Engineering,
Brown University,
Providence, RI 02912

The residual stress distribution in a brittle polycrystalline solid may have a significant influence on its toughness. Grains in a state of residual compression are less likely to be fractured by a growing crack and may trap the crack front or be left behind as bridging particles (Evans et al., 1977). This paper estimates the toughness enhancement due to intergranular residual stresses, using a three-dimensional model. The residual stress is approximated as a doubly sinusoidal distribution acting perpendicular to the plane of an initially straight semi-infinite crack. An incremental perturbation method developed by Bower and Ortiz (1990) for solving three-dimensional crack problems is extended here to cracks loaded by nonuniform remote stresses. It is used to calculate the shape of the semi-infinite crack as it propagates through the doubly sinusoidal residual stress. It is shown that the local regions of compression may trap the crack front and give rise to some transient toughening. In addition, if the residual stress exceeds a critical magnitude, pinning particles may be left in the crack wake. However, for practical values of residual stress and grain size, the predicted toughness enhancement is insignificant. Furthermore, the analysis cannot account for the large bridging zones observed in experiments. It is concluded that the R-curve behavior and bridging particles observed in monolithic ceramics are caused by mechanisms other than residual stresses acting perpendicular to the crack plane.

1 Introduction

The toughness of a brittle material may be significantly improved by the presence of small quantities of tough particles. Two mechanisms are responsible. The particles may trap the front of a crack propagating through the matrix, causing it to bow out between them. In addition, they may be left behind in the wake of the crack, pinning its faces and carrying part of the load. Several theoretical models have been developed to predict the toughness enhancement in composite materials such as particle or fiber reinforced ceramics. The effects of crack bridging may be estimated using a simple two-dimensional model, in which the bridging zone is approximated by a distribution of pressure $p(\delta)$ acting on the crack flanks. The relationship between p and the crack opening displacement δ is determined by the properties and volume fraction of the second-phase particles: for ductile particles, appropriate expressions have been given by Budiansky (1986) and Budiansky, Amazigo, and Evans (1988). The influence of frictionally constrained fibers has been modeled by Budiansky et al. (1986), Budiansky and Amazigo (1989), and Sigl and Evans (1989), among others. It is less straightforward to estimate the toughness enhancement due to crack trapping, since this requires a three-dimensional analysis. The behavior of a semi-infinite crack bypassing a single row of particles was investigated by Fares (1989), Gao and Rice (1989), and Bower and Ortiz (1990). More recently, Bower and Ortiz (1991) developed a full three-dimensional model which includes the effects of both crack trapping and bridging. These analyses predict substantial improvements in toughness: increases of 10–20 times the matrix toughness have been estimated for a brittle material reinforced by ductile particles, and 2–4 times for a fiber-reinforced solid. The predictions are in good agreement with experimental measurements by Mendelson and Fine (1974) and Krstic et al. (1981).

Crack trapping and bridging are also believed to be important toughening mechanisms in monolithic ceramics and rocks. Swanson et al. (1987), and Vekinis et al. (1990) have observed bridging particles in the wake of cracks propagating through Alumina. Vekinis and co-workers also measured a substantial increase toughness as the bridging zone developed. This toughness enhancement is difficult to estimate theoretically, since the source of the particles is not clear. It is possible to apply the models developed for composite materials, if the properties of the particles are regarded as adjustable parameters, which are determined by fitting the theory to experimental measurements. This approach was used successfully by Bower and Ortiz (1991) to predict the R-curve behavior observed in Alumina by Vekinis et al. (1990). However, it would be more satisfactory to account for the mechanisms responsible for forming the pinning particles.

Contributed by the Applied Mechanics Division of THE AMERICAN SOCIETY OF MECHANICAL ENGINEERS for publication in the ASME JOURNAL OF APPLIED MECHANICS.

Discussion on this paper should be addressed to the Technical Editor, Professor Lewis T. Wheeler, Department of Mechanical Engineering, University of Houston, Houston, TX 77204-4792, and will be accepted until four months after final publication of the paper itself in the ASME JOURNAL OF APPLIED MECHANICS.

Manuscript received by the ASME Applied Mechanics Division, May 22, 1991; final revision, Dec. 30, 1991. Associate Technical Editor: R. M. McMeeking.

Copyright © 1993 by ASME

Downloaded 03 May 2010 to 171.66.16.245. Redistribution subject to ASME license or copyright; see http://www.asme.org/terms/Terms_Use.cfm

Evans et al. (1977) have suggested that bridging particles in ceramics may be attributed to the action of intergranular residual stresses. Substantial residual stresses may be set up in polycrystalline ceramics during manufacture, due to the thermal and elastic anisotropy of the grains: stresses of the order 70–150 MPa have been measured experimentally (Blendell and Coble, 1982) and stresses of a similar magnitude have been predicted theoretically (Ortiz and Molinari, 1988; Ortiz and Suresh, 1990). According to Evans and co-workers, grains in a state of residual compression are less likely to be fractured by a growing crack and may be left behind as bridging particles. They pointed out that compressive grains may be thought of as regions of increased toughness, and have proposed an expression relating the magnitude of the compressive stress and the grain size to the equivalent toughness of the particles.

This paper investigates the influence of intergranular residual stresses on the effective toughness of a brittle polycrystalline solid, using a three-dimensional model. The problem to be solved is illustrated in Fig. 1. We consider an unbounded elastic body containing a semi-infinite crack on the plane $x_3 = 0$. The crack front is initially straight and parallel to the x_2-axis, at a position $x_1 = a$. The solid is elastically homogeneous and isotropic, and is assumed to be ideally brittle with a fracture toughness K_c^{mat}. It is subjected to remote loads, which set up a uniform distribution of mode I stress intensity $K(s) = K^\infty$ along the crack front. In addition, the solid contains a distribution of self-equilibrating residual stress. For simplicity, we consider only the component of residual stress acting perpendicular to the plane of the crack, which is approximated by

$$\sigma_{33}(x_1,x_2) = \sigma_r \cos(2\pi x_1/L_1)\cos(2\pi x_2/L_2). \tag{1}$$

Here, σ_r is the magnitude of the residual stress, and the wavelengths L_1 and L_2 are assumed to be of the order of the grain size. Thus, the $x_3 = 0$ plane is subjected to equi-distant regions of alternating tension and compression. The residual stress induces only mode I stress intensities, so the crack is not deflected from its initial plane, but once the crack starts to advance, its front does not remain straight. The compressive zones tend to trap the crack front, while the tensile regions accelerate growth. We seek to calculate the crack shape and the variation in remote stress, parameterized by K^∞, as the crack propagates through the solid.

Some qualitative predictions may be made without analysis. Since the residual stress field is self-equilibrating, the *average* effective toughness is given by $K^\infty = K_c^{\text{mat}}$. In other words, if a large area of material is fractured, the strengthening effect of the compressive zones exactly cancels the weakening due to tensile regions. However, the residual stress gives rise to some *transient* toughening. The crack front will initially propagate rapidly through tensile regions, and will adopt a configuration such that the entire crack front is subjected to compressive loading. In order for the crack to bypass the compressive zones, it is necessary to increase the remote load so that $K^\infty > K_c^{\text{mat}}$. The overall behavior of the solid is determined by the boundary conditions. If displacements are prescribed at infinity, the remote load fluctuates about the mean value $K^\infty = K_c^{\text{mat}}$. Under conditions of prescribed remote stress, the load must be increased to its maximum value so as to bypass the first set of compressive zones. Thereafter, the crack propagates rapidly through the intervening tensile regions, radiating energy in the form of elastic waves. Here, we assume remote displacement boundary conditions, and the possibility of dynamic crack growth is not considered.

A rigorous analysis of the problem in hand is not trivial. It is necessary to calculate stress intensity factors for an arbitrarily shaped crack under nonuniform loading. In addition, the shape of the crack is not known a priori, and must be determined as part of the solution. A suitable approach to solving problems of this nature has been devised by Rice (1985, 1989) and Gao and Rice (1986, 1987), who found a method for calculating the change in stress intensity factor caused by a small change in the geometry of a crack. Bower and Ortiz (1990) recently followed a suggestion by Rice (1989) to extend the method to arbitrarily large changes in crack shape. By applying a succession of small perturbations to a crack of some convenient initial geometry and updating the stress intensity factors at each step, it is possible to find stress intensities for any arbitrarily shaped crack. This approach has two advantages over alternative numerical methods. First, the solution only involves evaluating two one-dimensional integrals around the crack front, and secondly, it is straightforward to find a change in crack shape consistent with a prescribed change in stress intensity factor.

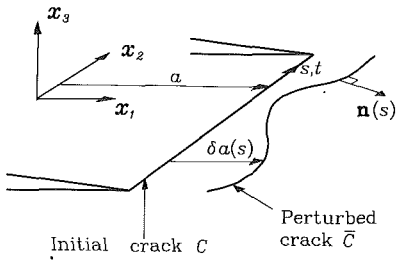


Fig. 1 Semi-infinite crack with a wavy front, showing notation and sign convention

Bower and Ortiz (1990) were only able to apply the incremental perturbation method to conditions where the crack was subjected to uniform remote stresses. It is extended here to arbitrary loading, and used to investigate the propagation of a semi-infinite crack through a doubly sinusoidal residual stress field. The analysis shows that residual stresses can give rise to some transient toughening in the solid, and may also lead to the formation of bridging particles in the crack wake, as suggested by Evans et al. (1977). However, for realistic values of residual stress and grain size, the toughening is extremely small, and no bridging particles are likely to be formed. It therefore appears that the crack bridging and R-curve behavior observed in monolithic ceramics is due to mechanisms other than crack trapping by intergranular residual stresses.

2 Theory

We begin by describing a method for calculating stress intensity factors on a planar crack with an arbitrarily shaped front. The procedure is based on work by Rice (1985, 1989) and Gao and Rice (1986, 1987), who devised a linear perturbation scheme to find the variation in stress intensity factor due to small changes in crack geometry. Bower and Ortiz (1990, 1991) have used this approach as the basis of a numerical method for calculating stress intensity factors for three-dimensional cracks. Their analysis considered only the special case of cracks subjected to a uniform distribution of remote stress: it is extended here to arbitrary mode I loading.

Consider an infinite solid, containing an arbitrarily shaped crack which lies in the (x_1, x_2) plane, as illustrated in Fig. 1. The shape of the crack front C is specified by its parametric equation $\mathbf{z}(s)$. The crack is subjected to a distribution of remote stress, acting in the x_3 direction, which induces a mode I stress intensity factor $K(s)$ on the crack front. Assume that the stress intensity factor at a point s on the crack front due to a pair of unit wedging forces acting on the crack faces at ξ is given by $H(\xi, s)$, where H is the crack face weight function. The stress intensity factor due to the remote stress distribution can therefore be calculated by integrating the weight function over the crack faces

$$K(s) = \int_\Omega H(\xi,s)p(\xi)d\xi_1 d\xi_2, \quad [\xi \in \Omega]. \tag{2}$$

Downloaded 03 May 2010 to 171.66.16.245. Redistribution subject to ASME license or copyright; see http://www.asme.org/terms/Terms_Use.cfm

where $p(\xi)$ is the distribution of stress in the uncracked solid, and Ω is the area bounded by the crack front. It is convenient at this point to define an additional influence function D for the crack, given by

$$D(t, s) = \lim_{\epsilon \to 0} \sqrt{\frac{\pi^3}{2}} \frac{H(\mathbf{z}(t) - \epsilon \mathbf{n}(t), s)}{\sqrt{\epsilon}}, \tag{3}$$

where $\mathbf{z}(t)$ is the position vector of a point t on the crack front, and $\mathbf{n}(t)$ is a unit vector in the crack plane, pointing in a direction normal to C at t. The influence function D can be seen to be the limiting stress intensity factor as a pair of square-root singular point loads approach the crack front: its significance is discussed in Bower and Ortiz (1990).

Now, imagine allowing the crack front to advance by a small increment $\delta a(s)\mathbf{n}(s)$, so that the crack occupies a new configuration $\overline{C}$, given by

$$\overline{\mathbf{z}}(s) = \mathbf{z}(s) + \delta a(s)\mathbf{n}(s). \tag{4}$$

The stress intensity factor for the perturbed geometry becomes

$$\overline{K}(s) = K(s) + \delta K(s), \tag{5}$$

and we wish to calculate δK at some point $s = t$ to first order in $\delta a(s)$. Following Rice (1985, 1989), $\overline{C}$ is reached in two stages. First, we translate the crack by a distance $\delta a(t)\mathbf{n}(t)$ to a reference configuration C^{ref}, while leaving its shape unchanged. The weight function H is invariant under translation, so (2) shows that the stress intensity factor on C^{ref} is

$$K^{\text{ref}}(t) = \int_{\Omega^{\text{ref}}} H(\xi,t)p(\xi - \delta a(t)\mathbf{n}(t))d\xi_1 d\xi_2, \quad [\xi \in \Phi^{\text{ref}}]. \tag{6}$$

Expanding to first order in $\delta a(t)$ shows that

$$K^{\text{ref}}(t) = K(t) + \delta a(t) \int_{\Omega} H(\xi,t) \frac{\partial p(\xi)}{\partial \xi} \cdot \mathbf{n}(t) d\xi_1 d\xi_2, \quad [\xi \in \Omega]. \tag{7}$$

Next, the crack is perturbed from C^{ref} by an amount

$$\delta a^{\text{ref}}(s) = \delta a(s) - \mathbf{n}(s) \cdot \mathbf{n}(t) \delta a(t), \tag{8}$$

so that the combined translation and perturbation reaches $\overline{C}$. Rice (1985, 1989) has shown that the change in stress intensity factor due to this perturbation is

$$\delta K(t) = \frac{1}{2\pi} \int_C K^{\text{ref}}(s) D(s,t) \delta a^{\text{ref}}(s) ds, \tag{9}$$

so that, combining (7) and (9) and discarding second order terms, we find

$$\overline{K}(t) = K(t) + \delta a(t) \int_{\Omega} H(\xi,t) \frac{\partial p(\xi)}{\partial \xi} \cdot \mathbf{n}(t) d\xi_1 d\xi_2 + \frac{1}{2\pi} \int_C K(s) D(s,t) [\delta a(s) - \mathbf{n}(s) \cdot \mathbf{n}(t) \delta a(t)] ds + \mathcal{O}(\delta a^2). \tag{10}$$

The process of dividing $\delta a(s)$ into a sequence of translation and perturbation appears cumbersome, but is necessary to ensure that the second integral in (10) be well defined. Rice (1989) has shown that $D(s, t)$ contains a singularity of order $(t - s)^{-2}$ as $s \to t$. The reference configuration C^{ref} is chosen so that when the crack is perturbed from C^{ref} to $\overline{C}$, $\delta a^{\text{ref}}(s) \to 0$ as $s \to t$. The integral around the crack front in (10) may then be shown to exist as a principal value, provided that $d\delta a^{\text{ref}}(s)/ds$ is Hölder continuous at $s = t$.

Equation (10) extends the results given by Rice (1985) to take into account the effects of non-uniform remote loading. For the particular case of a uniform remote stress field, $\partial p(\xi)/\partial \xi = 0$, so the first integral vanishes, and (10) is then identical to equations given in Rice (1985, 1989).

Bower and Ortiz (1990) have developed a numerical method, based on (10), for solving three-dimensional crack problems. They considered only uniform remote loading, with $\partial p(\xi)/\partial \xi = 0$. In this case, stress intensity factors may be calculated for any arbitrarily shaped crack, by applying a succession of small perturbations to a crack with some convenient initial geometry. After each perturbation, $K(s)$ may be updated by evaluating the integral in (10), provided that $D(s,t)$ can be found. In practice, exact expressions for D are known only for circular and semi-infinite cracks. However, the change in D due to small changes in the shape of a crack may be calculated: Bower and Ortiz (1990, 1991) have shown that

$$\begin{aligned}\delta D(s,t) = \frac{1}{2\pi} \int_C D(\lambda,t) D(s,\lambda) \\ \times \left\{ \delta a(\lambda) - \frac{[\mathbf{z}(s) - \mathbf{z}(t)] \cdot [\mathbf{z}(\lambda) - \mathbf{z}(t)]}{[\mathbf{z}(t) - \mathbf{z}(s)] \cdot [\mathbf{z}(t) - \mathbf{z}(s)]} \mathbf{n}(\lambda) \cdot \mathbf{n}(s) \delta a(s) \right. \\ \left. - \frac{[\mathbf{z}(t) - \mathbf{z}(s)] \cdot [\mathbf{z}(\lambda) - \mathbf{z}(s)]}{[\mathbf{z}(t) - \mathbf{z}(s)] \cdot [\mathbf{z}(t) - \mathbf{z}(s)]} \mathbf{n}(\lambda) \cdot \mathbf{n}(t) \delta a(t) \right\} d\lambda \\ - \frac{\delta a(s)}{2\pi} \int_C D(\lambda,t) D(s,\lambda) \frac{[\mathbf{z}(\lambda) - \mathbf{z}(t)] \wedge [\mathbf{z}(s) - \mathbf{z}(t)] \cdot \mathbf{k}}{[\mathbf{z}(t) - \mathbf{z}(s)] \cdot [\mathbf{z}(t) - \mathbf{z}(s)]} \\ \times \mathbf{n}(\lambda) \wedge \mathbf{n}(s) \cdot \mathbf{k} d\lambda \\ - \frac{\delta a(t)}{2\pi} \int_C D(\lambda,t) D(s,\lambda) \frac{[\mathbf{z}(\lambda) - \mathbf{z}(s)] \wedge [\mathbf{z}(t) - \mathbf{z}(s)] \cdot \mathbf{k}}{[\mathbf{z}(s) - \mathbf{z}(t)] \cdot [\mathbf{z}(s) - \mathbf{z}(t)]} \\ \times \mathbf{n}(\lambda) \wedge \mathbf{n}(t) \cdot \mathbf{k} d\lambda \\ - 2D(s,t) \frac{[\delta a(t)\mathbf{n}(t) - \delta a(s)\mathbf{n}(s)] \cdot [\mathbf{z}(t) - \mathbf{z}(s)]}{[\mathbf{z}(t) - \mathbf{z}(s)] \cdot [\mathbf{z}(t) - \mathbf{z}(s)]} + \mathcal{O}(\delta a^2).\end{aligned} \tag{11}$$

Here, $\wedge$ denotes a vector product, and $\mathbf{k}$ is a unit vector in a direction perpendicular to the plane of the crack. Thus, the changes in both K and D due to advancing the crack by δa may be found. By applying a succession of perturbations to a crack of some convenient initial geometry such as a circular or half-plane crack, stress intensity factors may be found for any arbitrarily shaped three-dimensional crack. For a uniform remote stress, the procedure only involves evaluating two one-dimensional integrals, so this method has many advantages over alternative techniques. To date, the incremental perturbation method has only been applied to situations where the remote stress is uniform, so that $\partial p(\xi)/\partial \xi = 0$. It is extended in the next section to arbitrary remote stress.

2.1 Perturbation Method for Arbitrary Remote Stress. At first sight it appears that if the remote stress is nonuniform, the main advantages of the incremental perturbation method are lost, since it becomes necessary to evaluate an integral over the crack faces during each perturbation in geometry. However, it is shown below that it is possible to reduce the first integral in (10) to a hierarchy of equations involving only the crack front, by expanding $p(\xi)$ in Taylor or Fourier series. This simple extension allows the incremental perturbation method to be used to find stress intensity factors for arbitrarily shaped cracks under any remote loading.

(*a*) *Polynomial Expansion of Remote Stress.* We begin by introducing the notation

$$K_\alpha(s) = \int_{\Omega} H(s,\xi) p_{,\alpha}(\xi) d\xi \tag{12}$$

where

Downloaded 03 May 2010 to 171.66.16.245. Redistribution subject to ASME license or copyright; see http://www.asme.org/terms/Terms_Use.cfm

$$p_{,\alpha}=\frac{\partial p}{\partial x_\alpha} \quad [\alpha=1,2]. \tag{13}$$

Equation (10) may therefore be rewritten as

$$\overline{K}(s)=K(s)+\delta a(s)n_\alpha(s)K_\alpha(s) + \frac{1}{2\pi}\int_C D(s,t)K(t)\delta a^{\text{ref}}(t)dt, \tag{14}$$

where n_α are the components of $\mathbf{n}$, and δa^{ref} is given in (8). Comparison of Eqs. (12) and (2) shows that $K_\alpha(s)$ can be regarded, for each value of α, as the stress intensity factor induced by a distribution of normal stress equal to $p_{,\alpha}(\mathbf{x})$. Therefore, $K_\alpha(s)$ can be updated in exactly the same manner as $K(s)$, i.e.,

$$\delta K_\alpha(s)=\delta a(s)n_\beta(s)K_{\alpha\beta}(s) + \frac{1}{2\pi}\int_C D(s,t)K_\alpha(t)\delta a^{\text{ref}}(t)dt, \tag{15}$$

where

$$K_{\alpha\beta}(s)=\int_\Omega H(s,\xi)p_{,\alpha\beta}(\xi)d\xi. \tag{16}$$

Proceeding inductively, it follows that a hierachy of stress intensity like functions may be defined by

$$K_{\alpha_1\ldots\alpha_k}(s)=\int_\Omega H(s,\xi)p_{,\alpha_1\ldots\alpha_k}(\xi)d\xi_1d\xi_2, \quad (\alpha_k=1,2), \tag{17}$$

and each function may be updated using the recurrence relation

$$\delta K_{\alpha_1\ldots\alpha_k}(s)=\delta a(s)n_{\alpha_{k+1}}(s)K_{\alpha_1\ldots\alpha_k\alpha_{k+1}}(s) + \frac{1}{2\pi}\int_C D(s,t)K_{\alpha_1\ldots\alpha_k}(t)\delta a^{\text{ref}}(t)dt. \tag{18}$$

If $p(\mathbf{x})$ is a polynomial of order m, then

$$K_{\alpha_1\ldots\alpha_{m+1}}(s)=0, \tag{19}$$

and the hierarchy can be truncated at the mth term. Special cases are those of a constant pressure, which requires only one term in the hierarchy; of a linear pressure, which requires two terms; of a quadratic pressure, which requires three terms, and so on.

Equations (17), (18), and (11) allow the incremental perturbation method described in the previous section to be applied to nonuniform remote loading. The solution begins with a crack of some convenient reference geometry, for which the crack face weight function $H(\xi, s)$ is known. Two suitable examples are a circular crack, or a half-plane crack. The remote stress is approximated by a polynomial of degree n, and Eq. (17) is used to set up each $K_{\alpha_1\ldots\alpha_{n+1}}(s)$. Stress intensity factors may then be found for any other crack in the same plane by advancing the crack front in a succession of small steps until the required geometry is reached. At each increment, the hierarchy of $K_{\alpha_1\ldots\alpha_{n+1}}$ is updated using (18), and the influence function D is updated using (11). This procedure only involves evaluating one-dimensional integrals around the crack front.

(b) Fourier Expansion of Remote Stress. Equation (10) may also be reduced to one-dimensional integrals by taking Fourier transforms of the remote stress. To this end, let $\hat{K}(s, \lambda)$ be the distribution of stress intensity factors due to stresses of the form $p(\xi) = \exp(i\lambda \cdot \xi)$, where λ is the wave number vector and $i = \sqrt{-1}$. Explicitly,

$$\hat{K}(s,\lambda)=\int_\Omega H(s,\xi)\exp(i\lambda\cdot\xi)d\xi_1d\xi_2. \tag{20}$$

Using the notation introduced in the preceding section, define

$$\hat{K}_\alpha(s,\lambda)=i\lambda_\alpha\int_\Omega H(s,\xi)\exp(i\lambda\cdot\xi)d\xi_1d\xi_2=i\lambda_\alpha\hat{K}(s,\lambda). \tag{21}$$

Therefore, from the general result (10) we obtain the following remarkably simple expression:

$$\delta\hat{K}(s,\lambda)=\delta a(s)i\lambda_\alpha n_\alpha(s)\hat{K}(s,\lambda) + \frac{1}{2\pi}\int_C D(s,t)\hat{K}(t,\lambda)\delta a^{\text{ref}}(t)dt. \tag{22}$$

Consider now an arbitrary distribution of stress defined by its Fourier representation

$$p(\mathbf{x})=\int\int \hat{p}(\lambda)\exp(i\lambda\cdot\mathbf{x})d\lambda_1d\lambda_2. \tag{23}$$

By superposition, it follows that

$$K(s)=\int\int \hat{p}(\lambda)\hat{K}(s,\lambda)d\lambda_1d\lambda_2, \tag{24}$$

so that the change in stress intensity factor on the crack front due to the perturbation in geometry is found to be

$$\delta K(s)=\int\int \hat{p}(\lambda)\delta\hat{K}(s,\lambda)d\lambda_1d\lambda_2, \tag{25}$$

where $\delta\hat{K}(s, \lambda)$ is given by (22).

Thus, each Fourier component may be updated following a perturbation in crack geometry by evaluating an integral around the crack front. Remarkably, each Fourier component may be updated independently of the rest. The Fourier expansion method is most useful when $\hat{p}(\lambda)$ can be approximated by a finite number of components. If, in addition $p(\mathbf{x})$ is periodic, then fast Fourier transform techniques can be used.

(c) Semi-Infinite Crack in a Doubly Sinusoidal Stress Field. In this paper, we investigate the propagation of a semi-infinite crack through a doubly sinusoidal residual stress field. In principle, it would be possible to approximate the residual stress using a Taylor or Fourier series, and update the stress intensities using the procedure described in the preceding sections. However, it proves more convenient to derive directly expressions analogous to (18) and (22) for a doubly sinusoidal stress.

We therefore consider a semi-infinite crack, which occupies the region ($x_1 < a$, $x_3 = 0$), Fig. 1, and is loaded by the residual stress field given in (1). For the straight crack, the residual stress induces a stress intensity factor

$$K^{\text{res}}(s)=\int_{-\infty}^{a}\int_{-\infty}^{+\infty} H(a-x_1,s-x_2)\sigma_r\cos(2\pi x_1/L_1) \times\cos(2\pi x_2/L_2)dx_2dx_1. \tag{26}$$

Here,

$$H(\xi_1,\xi_2)=\sqrt{\frac{2\xi_1}{\pi^3}}\frac{1}{\xi_1^2+\xi_2^2} \tag{27}$$

is the crack face weight function for a half-plane crack. The change in $K^{\text{res}}(s)$ due to advancing the crack by δa is given by (10). The result may be simplified by defining the following stress intensity factor like functions on the crack front:

$$K_1(s)=-\frac{2\pi}{L_1}\int_{-\infty}^{a}\int_{-\infty}^{+\infty} H(a-x_1,\,s-x_2)\sigma_r \times\sin(2\pi x_1/L_1)\cos(2\pi x_2/L_2)dx_2dx_1 \tag{28}$$

$$K_2(s)=-\frac{2\pi}{L_2}\int_{-\infty}^{a}\int_{-\infty}^{+\infty} H(a-x_1,\,s-x_2)\sigma_r \times\cos(2\pi x_1/L_1)\sin(2\pi x_2/L_2)dx_2dx_1 \tag{29}$$

$$K_{12}(s)=\frac{4\pi^2}{L_1L_2}\int_{-\infty}^{a}\int_{-\infty}^{+\infty} H(a-x_1,\,s-x_2)\sigma_r \times\sin(2\pi x_1/L_1)\sin(2\pi x_2/L_2)dx_2dx_1, \tag{30}$$

so that the expression for $\delta K^{\text{res}}(s)$ may be written

Downloaded 03 May 2010 to 171.66.16.245. Redistribution subject to ASME license or copyright; see http://www.asme.org/terms/Terms_Use.cfm

$$\delta K^{\text{res}}(s) = (n_1(s)K_1(s) + n_2(s)K_2(s))\delta a(s) + \frac{1}{2\pi}\int_{-\infty}^{+\infty} K^{\text{res}}(t)D(t,s)\delta a^{\text{ref}}(t)dt. \quad (31)$$

Since the residual stress field is periodic with wavelength L_2 in the x_2 direction, it may be assumed that the crack front also remains periodic. Consequently, the integral in (31) may be reduced to one wavelength of the crack front, by writing

$$\delta K^{\text{res}}(s) = (n_1(s)K_1(s) + n_2(s)K_2(s))\delta a(s) + \frac{1}{2\pi}\int_0^c K^{\text{res}}(t)\mathbf{D}(t,s)\delta a^{\text{ref}}(t)dt, \quad (32)$$

where c is the arc length of one period of the crack front, and

$$\mathbf{D}(s,t) = \sum_{m=-\infty}^{\infty} D(s+mc, t). \quad (33)$$

In addition, each $K_{\alpha\beta}$ may be updated as follows:

$$\delta K_1(s) = (-n_1(s)\lambda_2^2 K^{\text{res}}(s) + n_2(s)K_{12}(s))\delta a(s) + \frac{1}{2\pi}\int_0^c K_1(t)\mathbf{D}(t,s)\delta a^{\text{ref}}(t)dt \quad (34)$$

$$\delta K_2(s) = (n_1(s)K_{12}(s) - n_2(s)\lambda_1^2 K^{\text{res}}(s))\delta a(s) + \frac{1}{2\pi}\int_0^c K_2(t)\mathbf{D}(t,s)\delta a^{\text{ref}}(t)dt \quad (35)$$

$$\delta K_{12}(s) = -(n_1(s)\lambda_1^2 K_2(s) + n_2(s)\lambda_2^2 K_1(s))\delta a(s) + \frac{1}{2\pi}\int_0^c K_{12}(t)\mathbf{D}(t,s)\delta a^{\text{ref}}(t)dt, \quad (36)$$

where $\lambda_1 = 2\pi/L_1$ and $\lambda_2 = 2\pi/L_2$. The influence functions $D(t, s)$ and $\mathbf{D}(s, t)$ for the straight crack may be found using (3) and (27), and are given by

$$D(t,s) = \frac{1}{(t-s)^2} \quad (37)$$

$$\mathbf{D}(t,s) = \frac{1}{(c/\pi)^2 \sin^2 \pi(t-s)/c}. \quad (38)$$

The results enable stress intensity factors to be found for a planar semi-infinite crack with an arbitrarily shaped periodic front. Each $K_{\alpha\beta}$ may be evaluated in closed form for the straight crack, and are found to be

$$K^{\text{res}}(s) = A\cos(2\pi a/L_1 - \theta)\cos(2\pi s/L_2), \quad (39)$$

$$K_1(s) = -\frac{2\pi}{L_1} A\sin(2\pi a/L_1 - \theta)\cos(2\pi s/L_2), \quad (40)$$

$$K_2(s) = -\frac{2\pi}{L_2} A\cos(2\pi a/L_1 - \theta)\sin(2\pi s/L_2), \quad (41)$$

$$K_{12}(s) = \frac{4\pi^2}{L_1 L_2} A\sin(2\pi a/L_1 - \theta)\sin(2\pi s/L_2), \quad (42)$$

$$A = \frac{\sigma_r}{\sqrt{\pi}} \frac{\sqrt{L_1 L_2}}{(L_1^2 + L_2^2)^{1/4}}, \quad \theta = \frac{1}{2}\tan^{-1}(L_2/L_1). \quad (43)$$

2.2 Application to Crack Trapping by Residual Stresses. Finally, we may apply the procedure developed in the preceding sections to investigate crack growth through a doubly sinusoidal stress field. We now assume that the half-plane crack shown in Fig. 1 is subjected to a combination of a uniform remote stress, together with the residual stress distribution given in (1). The crack front is initially straight, and is at a position $a = 5L_1/16$. The remote load therefore induces a uniform stress intensity factor $K^{\text{load}}(s) = K^{\infty}$, while Eq. (37) shows that initially $K^{\text{res}}(s) = 0$. When K^{∞} reaches the toughness of the material K_c^{mat}, the crack starts to propagate. Thereafter, the shape of the crack is determined from the condition that $K(s) \le K_c^{\text{mat}}$ over its entire front. The crack shape is calculated here by applying a succession of small perturbations to the crack front, and calculating the crack advance consistent with the fracture criterion at each step. This condition leads to an integral equation for $\delta a(s)$

$$0 = \delta K^{\text{load}}(s) + \delta K^{\text{res}}(s) \quad (44)$$

$$= \frac{\delta K^{\infty}}{K^{\infty}} K^{\text{load}}(s) + (n_1(s)K_1(s) + n_2(s)K_2(s))\delta a(s) + \frac{1}{2\pi}\int_0^c (K^{\text{load}}(t) + K^{\text{res}}(t))\mathbf{D}(t,s) \times (\delta a(t) - \mathbf{n}(s)\cdot\mathbf{n}(t)\delta a(s))dt. \quad (45)$$

Here, the first term represents the change in $K(s)$ due to an increment in the remote load, and the remaining terms give δK due to changing the crack shape. The values of K_1 and K_2 for the straight crack are given in Eqs. (39) to (42), while $\mathbf{D}$ is given in (38). In principle, it would be possible to specify an increment in remote load δK^{∞}, and then use (45) to calculate the corresponding change in crack shape. However, this causes numerical difficulties when the crack is propagating under decreasing remote load. It is preferable to leave δK^{∞} as an unknown, and enforce an additional constraint on the maximum crack advance. Here, we have set $\delta a_{\max} = L_1/500$.

The solution of (45) is complicated by the possibility that parts of the crack front may be trapped by compressive residual stress, and may arrest. Over arrested zones, it is necessary to enforce the "no healing" constraint, $\delta a(s) = 0$. The positions of the arrested regions are not known a priori, and must be determined by iteration. Here, we use the following procedure. Each increment is begun with a suitable guess for the new arrested regions, and (45) is used to determine the corresponding crack advance. The solution is then checked to ensure that $\delta a(s) \ge 0$ over the entire crack front: if a negative crack advance is found at any point, that part of the crack is subsequently assumed to arrest. In addition, the condition that $K(s) \le K_c^{\text{mat}}$ is checked over arrested portions: if this requirement is violated, the appropriate point is allowed to advance. A solution is found to (45) with the new approximation to the crack configuration, and the iteration is continued until successive approximations for the arrested zones agree.

Once a suitable solution has been found, K^{load} is updated using

$$\delta K^{\text{load}}(s) = \frac{\partial K^{\infty}}{K^{\infty}} K^{\text{load}}(s) + \frac{1}{2\pi}\int_0^c K^{\text{load}}(t)\mathbf{D}(t,s) \times (\delta a(t) - \mathbf{n}(s)\cdot\mathbf{n}(t)\delta a(s))dt, \quad (46)$$

while the change in K^{res} and each $K_{\alpha\beta}$ are calculated from (39) to (41). Finally, D is updated using (11). This process is repeated to progressively march the crack front through the residual stress field.

A suitable numerical method for solving the integral Eq. (45) is described in detail by Bower and Ortiz (1990), and will only be briefly summarized here. One wavelength of the crack front is divided into m elements, with three nodes s_{2k-2}, s_{2k-1} and s_{2k} on the kth element. In addition, $2m - 1$ collocation points are defined, such that $s_j < t_j < s_{j-1}$. The geometry of the crack front is specified in terms of the coordinates of each node and collocation point, and the crack advance is approximated using Hermitian interpolation between values of $\delta a(s_{2k})$ and $d\delta a(s_{2k})/ds$ for $k = 1, 2 \ldots m$. The variation of K^{load}; K^{res} and each $K_{\alpha\beta}$ is approximated by means of a Lagrangian interpolation between nodal values. Similarly, to approximate the weight function $\mathbf{D}$, we write

Downloaded 03 May 2010 to 171.66.16.245. Redistribution subject to ASME license or copyright; see http://www.asme.org/terms/Terms_Use.cfm

$$\mathbf{D}(s,t)=\frac{\mathbf{d}(s,t)\,(\sinh 2\pi\gamma)/(2\pi\gamma)}{(L_2/\pi)^2(\sin^2\pi\eta+\sinh^2\pi\gamma)}, \tag{47}$$

$$\gamma=(z_1(s)-z_1(t))/L_2;\quad \eta=(z_2(s)-z_2(t))/L_2,$$

and use three point Lagrangian interpolation between nodal values to approximate the function **d**. The integrand in (46) may then be expressed in terms of nodal values of δa by means of the adopted interpolation functions. As a result, the integrals may be evaluated explicitly, and the integral equation may be written in the linear form:

$$0=\frac{\delta K^\infty}{K^\infty}K(t_j)+\sum_{i=0}^{m}W_i(t_j)\delta a(s_{2i})+V_i(t_j)\delta a'(s_{2i}), \tag{48}$$

where W_i and V_i are integration weights depending on the current crack configuration. These functions are given in Bower and Ortiz (1990). Equation (48) may then be solved for the nodal values of δa and $\delta a'$. Subsequently, the numerical approximation to **D** must be updated: an appropriate procedure is described in Bower and Ortiz (1990). A 24 element mesh was used in all the numerical simulations reported below.

3 Results and Discussion

The toughening effect of the residual stress distribution can be expressed in terms of two dimensionless groups

$$\frac{K_c^{\text{eff}}}{K_c^{\text{mat}}}=F\left(\frac{\sigma_r\sqrt{L_1L_2}}{K_c^{\text{mat}}(L_1^2+L_2^2)^{1/4}},\ \frac{L_1}{L_2}\right). \tag{49}$$

For the particular case $L_1/L_2 = 0$, the toughening may be calculated exactly. The residual stress then varies sinusoidally in a direction perpendicular to the crack front, but is uniform in the x_2-direction. The crack front remains straight, so that the remote load induces a uniform stress intensity of magnitude $K^{\text{load}} = K^\infty$, while K due to the residual stress is

$$K^{\text{res}}(s)=\frac{\sigma_r\sqrt{L_1}}{\sqrt{\pi}}\cos(2\pi a/L_1-\pi/4). \tag{50}$$

Applying the fracture criterion $K^{\text{load}} + K^{\text{res}} = K_c^{\text{mat}}$ gives the variation of the remote load as a function of the position of the crack front a

$$\frac{K^\infty}{K_c^{\text{mat}}}=1-\frac{\sigma_r\sqrt{L_1}}{\sqrt{\pi}\,K_c^{\text{mat}}}\cos(2\pi a/L_1-\pi/4). \tag{51}$$

This result confirms the qualitative prediction of the influence of residual stress made in the introduction. The average energy release rate is unchanged but the load fluctuates about the mean. In order for unstable fracture to occur, it is necessary to increase K^∞ to its maximum value. If the effective toughness of the solid is taken as the maximum value of K^∞, then we find that

$$K_c^{\text{eff}}=K_c^{\text{mat}}+\sigma_r\sqrt{L_1/\pi}. \tag{52}$$

Evans et al. (1977) used a similar model to estimate the toughness enhancement, but assumed a square wave variation of residual stress instead of the sinusoid used here. Their analysis also gives $K_c^{\text{eff}} - K_c^{\text{mat}} = \alpha\sigma_r\sqrt{L_1}$, but the value of α they predict is twice that in (52).

For values of $L_1/L_2 > 0$, the toughening must be calculated numerically. In practice, the wavelengths L_1 and L_2 are both likely to be of the order of the grain size of the material, so detailed computations will only be presented here for $L_1 = L_2 = L$. Predicted crack shapes are shown in Fig. 2 for three values of $\sigma_r\sqrt{L}/K_c^{\text{mat}}$. Only one wavelength of the crack front has been plotted in each case, since the crack front has been constrained to remain periodic with wavelength L in the x_2-direction. The sequence of crack shapes also repeats every half wavelength in the x_1-direction. The positions of maximum tensile and compressive stress are also marked on Fig. 2 for reference. The behavior of the crack during propagation is governed by the magnitude of the residual stress and grain size. For values of $\sigma_r\sqrt{L}/K_c^{\text{mat}}$ less than 0.85, the crack front remains almost straight, and no crack arrest is observed. As expected, regions of the crack which propagate through tensile zones tend to bow out ahead of regions in compression. For $\sigma_r\sqrt{L}/K_c^{\text{mat}} > 0.85$, the residual stresses are sufficient to arrest parts of the crack front, as shown in Fig. 2(*b*). If $\sigma_r\sqrt{L}/K_c^{\text{mat}}$

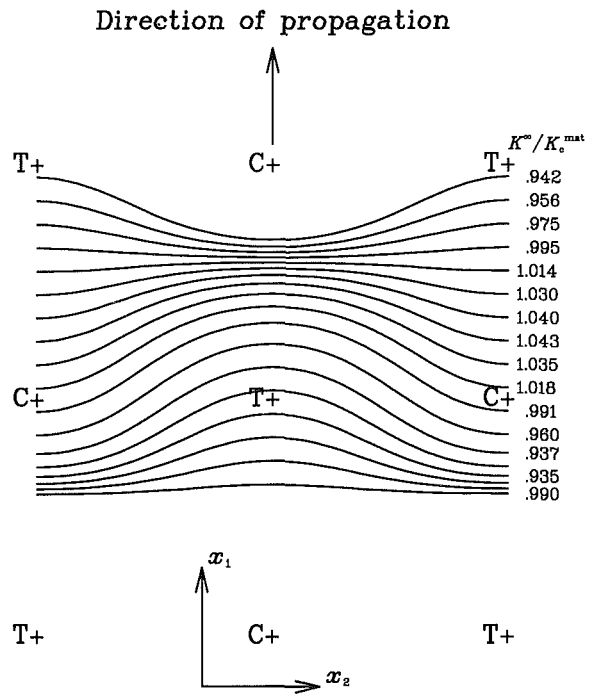


Fig. 2(*a*) Successive crack front profiles for a crack propagating through doubly sinusoidal stress. Residual stress amplitude $\sigma_r\sqrt{L}/K_c^{\text{mat}} = 0.71$. Points marked T and C correspond to locations of maximum tension and compression.

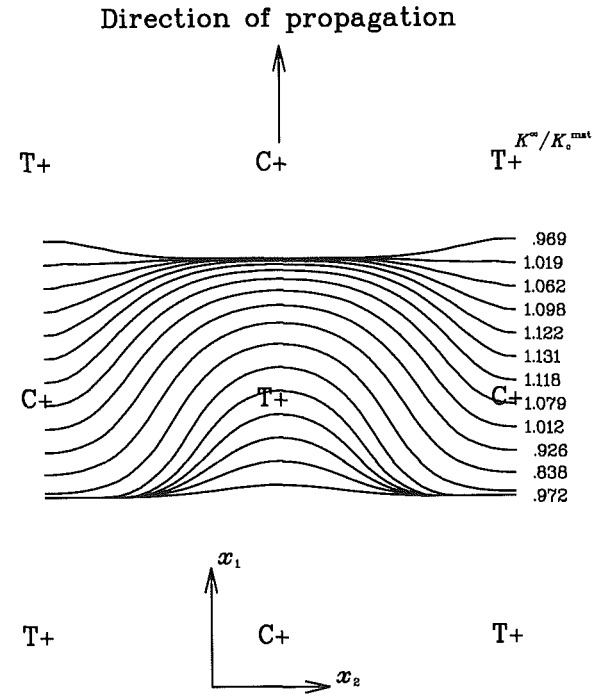


Fig. 2(*b*) Successive crack front profiles for a crack propagating through doubly sinusoidal stress. Residual stress amplitude $\sigma_r\sqrt{L}/K_c^{\text{mat}} = 1.41$. Points marked T and C correspond to locations of maximum tension and compression.

Downloaded 03 May 2010 to 171.66.16.245. Redistribution subject to ASME license or copyright; see http://www.asme.org/terms/Terms_Use.cfm

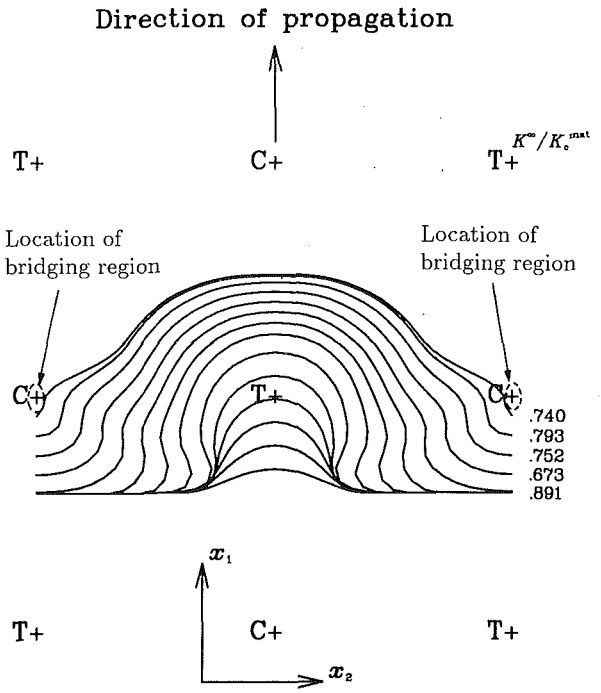


Fig. 2(c) Successive crack front profiles for a crack propagating through doubly sinusoidal stress. Residual stress amplitude $\sigma_r\sqrt{L}/K_c^{mat} = 2.3$. Points marked T and C correspond to locations of maximum tension and compression.

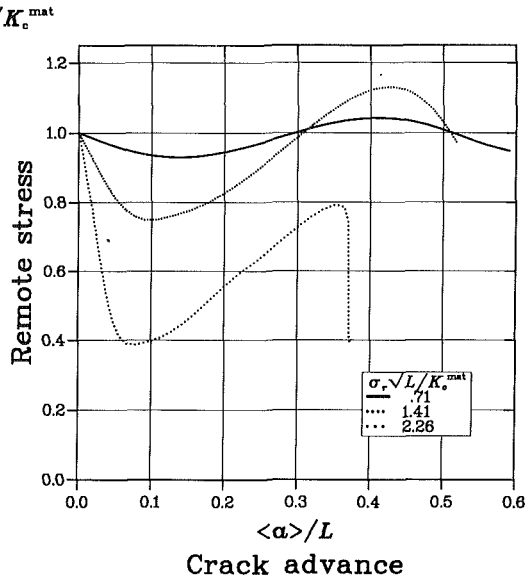


Fig. 3 Variation of remote stress with average crack advance for the cracks shown in Fig. 2

exceeds 2.1, then the compressive stress completely pins small regions of the crack, so that parts of the crack front on the far side of the pinned region join up leaving a small bridging particle in the crack wake. This behavior is illustrated in Fig. 2(c). The result confirms that residual stresses acting perpendicular to the crack plane may be responsible for the formation of pinning particles, as suggested by Evans et al. (1977). There are some numerical difficulties associated with applying the perturbation method to a situation where two points on a crack front coalesce (Bower and Ortiz, 1991), so Fig. 2(c) only shows the sequence of crack fronts up to the formation of the first row of pinning particles. This is not a serious restriction, for it is shown below that for practical values of σ_r and L, bridging particles are unlikely to be formed.

It should be recognized that while the crack is propagating into tensile zones under decreasing remote stress, its shape is not necessarily unique. A detailed study of the stability and uniqueness of the crack shape has not been attempted, but it is possible to make some qualitative predictions. Rice (1985) has discussed the stability of a straight, semi-infinite crack propagating into a region of increasing stress. In his analysis, he assumes that the stress is uniform in the x_2-direction but increases in a direction perpendicular to the crack front. If the crack remains straight, the stress intensity factor increases at a constant rate $\partial K^\infty/\partial a = \eta$. Rice showed that if the crack is perturbed slightly from its straight configuration, there exists a critical wavelength $c_{crit} = \pi K^\infty/\eta$ above which perturbations tend to grow. This criterion may be used to estimate conditions for stability of a crack subjected to a doubly sinusoidal stress of wavelength L. The stress intensity induced by the residual stress is given in Eq. (37), and its gradient $\partial K^{res}/\partial a = K_1(s)$ is given in (39). The critical wavelength of unstable perturbations is thus of the order

$$c_{crit} \approx \frac{K_c^{mat}\sqrt{L}\sqrt{\pi}}{2^{3/4}\sigma_r}. \tag{53}$$

Here, the crack is constrained to remain periodic, so the wavelength of any unstable perturbations cannot exceed L. Putting $c_{crit} = L$ shows that instabilities may form if

$$\frac{\sigma_r\sqrt{L}}{K_c^{mat}} > \frac{\sqrt{\pi}}{2^{3/4}}. \tag{54}$$

In the numerical simulations, the onset of crack arrest is observed to occur at a similar magnitude of residual stress.

The variation of remote stress intensity factor is plotted in Fig. 3, for the three values of $\sigma_r\sqrt{L}/K_c^{mat}$ used in the simulations shown in Fig. 2. The load is shown as a function of $\langle a\rangle/L$, where $\langle a\rangle$ is the average crack advanced, calculated using the area swept by one wavelength of the crack front. For $\sigma_r\sqrt{L}/K_c^{mat} = 2.3$, results are shown only up to the formation of the first row of pinning particles: the remote stress drops sharply as the crack joins up on itself, and never exceeds K_c^{mat}. If the analysis were continued beyond this point, the constraining effect of the pinning particles in the crack wake would increase the remote stress above K_c^{mat}. In the remaining cases, the load fluctuates about a mean value, such that the average energy release rate is equal to the toughness of the matrix. The maximum value of K^∞ may be interpreted as the effective toughness of the brittle solid, since it would be necessary to increase the remote stress beyond the maximum value to produce unstable fracture.

The effective toughness has been plotted as a function of the dimensionless residual stress amplitude in Fig. 4. The result for $L_1/L_2 = 0$, given in Eq. (4), is also shown for comparison. Only a small increase in toughness is caused by the residual stress distribution considered here. Using practical values of $\sigma_r = 150\ \mathrm{NMm}^{-2}$; $L = 10\ \mu\mathrm{m}$; $K_c^{mat} = 5\ \mathrm{MNm}^{-3/2}$ gives $\sigma_r\sqrt{L}/K_c^{mat} = 0.095$: the corresponding toughness enhancement is $K_c^{eff}/K_c^{mat} = 1.005$. Furthermore, the analysis predicts that no pinning particles are formed under these conditions. However, in practice bridging particles have been observed up to 1000 grain diameters behind the crack front, and a toughness increase of up to 30 percent has been measured as the bridging zone is established (Vekinis et al., 1990). It therefore appears that the crack bridging and R-curve behavior observed in monolithic ceramics must be attributed to mechanisms other than residual stresses acting perpendicular to the crack plane.

The results presented here should not be taken as an indication that intergranular residual stresses have no influence on the fracture of brittle materials. Our analysis has considered only stresses acting perpendicular to the crack plane: residual

Downloaded 03 May 2010 to 171.66.16.245. Redistribution subject to ASME license or copyright; see http://www.asme.org/terms/Terms_Use.cfm

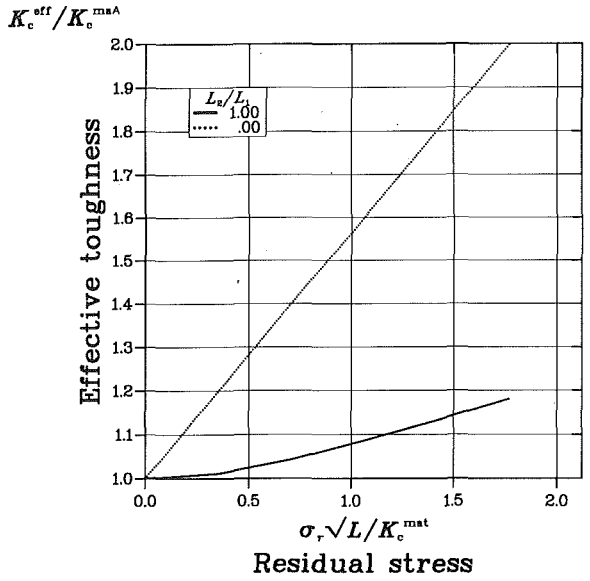


Fig. 4 Variation of effective toughness with residual stress amplitude

shear stresses may also contribute to the formation of bridging particles and cause some toughening, by deflecting the crack around grains. In addition, toughening is known to be caused by the energy dissipated by friction forces as grains are pulled out in the crack wake (Vekinis et al., 1990). Residual stresses acting parallel to the crack plane have a strong influence on this process, since the friction forces are caused in part by local compressive stresses acting between a grain and the surrounding matrix. A more detailed model of this process has been given by Bower and Ortiz (1991).

4 Summary and Conclusions

The toughening enhancement due to residual stresses in a polycrystalline ceramic has been estimated, using a theoretical model. The residual stress was idealized as a doubly sinusoidal distribution, amplitude σ_r, and wavelength L, acting perpendicular to the plane of an initially straight semi-infinite crack. Only mode I stress intensities are induced by this stress, so the crack is not deflected from its initial plane. However, regions of compressive stress trap the crack front, causing it to bow out between them. The crack shape has been calculated for a range of residual stress amplitudes, using an incremental perturbation method developed by Bower and Ortiz (1990), suitably extended to account for nonuniform remote stresses. It has been shown that some transient toughening is produced by the residual stresses. Furthermore, if the stress amplitude exceeds $\sigma_r\sqrt{L}/K_c^{\text{mat}} = 2.1$, pinning particles are left behind in the crack wake. These results confirm the predictions of Evans et al. (1977).

However, for values of residual stress and grain size representative of a typical ceramic, the predicted toughness enhancement is less than one percent. Furthermore, no pinning particles are formed. It is concluded that the R-curve behavior and bridging particles observed in monolithic ceramics are not caused by residual stresses acting perpendicular to the crack plane.

References

Blendell, J. E., and Coble, R. L., 1982, "Measurement of Stress Due to Thermal Expansion Anisotropy in Al_2O_3," *J. Am. Ceram. Soc.*, Vol. 65, No. 3, pp. 174–183.

Bower, A. F., and Ortiz, M., 1990, "Solution of Three-Dimensional Crack Problems by a Finite Perturbation Method," *Journal of the Mechanics and Physics of Solids*, Vol. 38, No. 4, pp. 443–480.

Bower, A. F., and Ortiz, M., 1991, "A Three-Dimensional Analysis of Crack Trapping and Bridging by Tough Particles," *Journal of the Mechanics and Physics of Solids*, Vol. 39, No. 6, pp. 815–858.

Budiansky, B., 1986, "Micromechanics II," *Proc. 10th National U.S. Congress of Applied Mechanics*, P. J. Lamb, ed., Austin, Texas, pp. 25–32.

Budiansky, B., and Amazigo, J. C., 1989, "Toughening by Aligned, Frictionally Constrained Fibres," *Journal of the Mechanics and Physics of Solids*, Vol. 37, No. 1, pp. 93–109.

Budiansky, B., Amazigo, J. C., and Evans, A. G., 1988, "Small Scale Crack Bridging and the Fracture Toughness of Particulate Reinforced Ceramics," *Journal of the Mechanics and Physics of Solids*, Vol. 36, No. 2, pp. 167–187.

Budiansky, B., Hutchinson, J., and Evans, A. G., 1986, "Matrix Fracture in Fibre Reinforced Ceramics," *Journal of the Mechanics and Physics of Solids*, Vol. 34, pp. 167–189.

Evans, A. G., Heuer, A. H., and Porter, D. L., 1977, "The Fracture Toughness of Ceramics," *Advances in Research on the Strength and Fracture of Materials, ICF4*, D.M.R. Taplin, ed.

Fares, N., 1989, "Crack Fronts Trapped by Arrays of Obstacles: Numerical Solutions Based on Surface Integral Representation," ASME JOURNAL OF APPLIED MECHANICS, Vol. 56, pp. 837–843.

Gao, H., and Rice, J. R., 1986, "Shear Stress Intensity Factors for a Planar Crack with Slightly Curved Front," ASME JOURNAL OF APPLIED MECHANICS, Vol. 53, pp. 774–778.

Gao, H., and Rice, J. R., 1987, "Somewhat Circular Tensile Cracks," *International Journal of Fracture*, Vol. 33, pp. 115–174.

Gao, H., and Rice, J. R., 1989, "A First-Order Perturbation Analysis of Crack Trapping by Arrays of Obstacles," ASME JOURNAL OF APPLIED MECHANICS, Vol. 56, pp. 828–836.

Krstic, V. V., Nicholson, P. S., and Hoagland, R. G., 1981, "Toughening of Glasses by Metallic Particles," *Journal of the American Ceramics Society*, Vol. 64, No. 9, pp. 499–503.

Mendelson, M. I., and Fine, M. F., 1974, "Enhancement of Fracture Properties of Wustite by Precipitation," *Journal of the American Ceramics Society*, Vol. 57, No. 4, pp. 154–159.

Ortiz, M., and Molinari, A., 1988, "Microstructural Thermal Stresses in Ceramic Materials," *Journal of the Mechanics and Physics of Solids*, Vol. 36, pp. 385–400.

Ortiz, M., and Suresh, S., 1993, "Residual Stresses in Ceramics due to Thermal and Elastic Anisotropy: Statistical Properties and Microfracture," ASME JOURNAL OF APPLIED MECHANICS, in press.

Rice, J. R., 1985, "First Order Variation in Elastic Fields due to Variation in Location of a Planar Crack Front," ASME JOURNAL OF APPLIED MECHANICS, Vol. 52, pp. 571–579.

Rice, J. R., 1989, "Weight Function Theory for Three-Dimensional Elastic Crack Analysis," *Fracture Mechanics: Perspectives and Directions (Twentieth Symposium), ASTM-STP-1020*, R. P. Wei and R. P. Gangloff, eds., American Society Testing and Materials, Philadelphia, pp. 29–57.

Sigl, L. S., and Evans, A. G., 1989, "Effects of Residual Stress and Frictional Sliding on Cracking and Pull Out in Brittle Matrix Composites," *Mechanics of Materials*, Vol. 8, pp. 1–12.

Swanson, P. L., Fairbanks, C. J., Lawn, B. R., Mai, Y. W., and Hockey, B. J., 1987, "Crack Interface Grain Bridging as a Fracture Resistance Mechanism in Ceramics I: Experimental Study on Alumina," *Journal of the American Ceramics Society*, Vol. 70, No. 4, pp. 279–289.

Vekinis, G., Ashby, M. F., and Beaumont, P. W. R., 1990, "R-Curve Behavior of Al_2O_3 Ceramics," *Acta Metall.*, Vol. 38, No. 6, pp. 1151–1162.

Downloaded 03 May 2010 to 171.66.16.245. Redistribution subject to ASME license or copyright; see http://www.asme.org/terms/Terms_Use.cfm

General Crack-Tip Fields for Stationary and Steadily Growing Interface Cracks in Anisotropic Bimaterials[1]

X. Deng
Department of Mechanical Engineering,
University of South Carolina,
Columbia, SC 29208
Assoc. Mem. ASME

This study builds upon some recent results in the literature regarding the asymptotic behavior of bimaterial interface cracks, and gives the general form, both oscillatory and nonoscillatory, of the crack-tip stress and displacement fields for stationary and steadily growing interface cracks in anisotropic bimaterials, which are equivalent to complete Williams-type series expansions. Special cases, such as cracks in homogeneous anisotropic materials and interface cracks with decoupled antiplane shear and in-plane deformations, are discussed briefly. Explicit series expansions of the stress and displacement fields in crack-tip polar coordinates are derived for both stationary and steadily propagating interface cracks in isotropic bimaterials.

1 Introduction

Much progress has recently been made in the analysis of interface cracks in dissimilar anisotropic materials, an excellent exposition of which can be found in Suo (1990). Concepts evolved for interface cracks in dissimilar isotropic solids, as distilled in Rice (1988), have been generalized in a unified fashion (Ting, 1986, 1990; Qu and Bassani, 1989; Wu, 1990; Suo, 1990), which is made possible by complex function representations of stress and deformation fields in general anisotropic materials (Eshelby et al., 1953; Lekhnitskii, 1963; Stroh, 1958, 1962). With some modifications, this unified approach was carried out not long ago by Wu (1991) and Yang et al. (1991) for steadily growing interface cracks, which was also studied by Aminpour et al. (Aminpour, 1986; Aminpour and Holsapple, 1990) using an equivalent formulation developed from Lekhnitskii's theory (Lekhnitskii, 1963).

In this paper, the author extends the results of previous studies to obtain general crack-tip fields for stationary and steadily growing interface cracks in anisotropic bimaterials, which are equivalent to complete Williams-type series expansions (Williams, 1957). The nonsingular higher-order terms in these solutions have applications in areas such as multiterm fracture criteria and boundary layer analyses, interpretation of experimental measurements in regions not dominated by the singular terms, evaluation of stress intensity factors from far-field numerical data such as finite element results, etc. For transient crack propagation, the current results must be modified as is done for isotropic homogeneous materials by Freund and Rosakis (1992).

The method of analytic continuation is adopted in this study. The particular procedure used follows that of Rice (1988) for isotropic bimaterials, and builds upon the unified approach for anisotropic dissimilar materials developed in Suo (1990) and Yang et al. (1991).

In Section 2 of this paper, the problem and Stroh formalism (Stroh, 1958, 1962) are outlined. Then in Section 3, we derive general expressions for the complete crack-tip fields in dissimilar anisotropic materials, which contain the common oscillatory features for interface cracks. Section 4 gives the complete crack-tip fields when condition for nonoscillatory behavior exists, such as in the case of anisotropic homogeneous materials. Section 5 discusses briefly some special cases such as antiplane shear and in-plane deformations when they can be decoupled from each other. Finally, steady dynamic crack growth along the interface of two dissimilar isotropic materials will be studied in Section 6. Explicit expressions of the complete near-tip stress and displacement fields for stationary and steadily growing interface cracks in dissimilar isotropic materials will be given in the Appendix.

In the sequel, unless stated otherwise, boldfaced lower case letters will be used to denote vectors, and boldfaced upper case letters to denote tensors and matrices. Roman indices will have range 1 to 3, and Greek indices, range 1 and 2. Repeated indices imply summation, and indices following a comma mean differentiation. A bar over a quantity denotes the complex conjugate of that quantity. Standard matrix and vector operations will be assumed throughout, and conventional symbols for the inverse of matrices and transpose of matrices and vectors will be used. Most notations follow those in Suo (1990) and Yang et al. (1991).

[1]This is an abridged version of a detailed report, which is available from the author upon request.

Contributed by the Applied Mechanics Division of THE AMERICAN SOCIETY OF MECHANICAL ENGINEERS for publication in the ASME JOURNAL OF APPLIED MECHANICS.

Discussion on this paper should be addressed to the Technical Editor, Professor Lewis T. Wheeler, Department of Mechanical Engineering, University of Houston, Houston, TX 77204-4792, and will be accepted until four months after final publication of the paper itself in the ASME JOURNAL OF APPLIED MECHANICS.

Manuscript received by the ASME Applied Mechanics Division, May 22, 1991; final revision, Jan. 21, 1992. Associate Technical Editor: C. F. Shih.

Copyright © 1993 by ASME
Downloaded 03 May 2010 to 171.66.16.245. Redistribution subject to ASME license or copyright; see http://www.asme.org/terms/Terms_Use.cfm

2 The Problem and Stroh Formalism

For the purpose of asymptotic analysis, consider a semi-infinite crack along the interface of two dissimilar elastic anisotropic half-planes. Let (x_1, x_2, x_3) be a rectangular coordinate system with its origin at the crack tip, such that the traction-free crack surfaces and the interface of the two materials lie in the x_1-x_3 plane. Denote the top and bottom half-planes, respectively, by R_1 (occupied by material 1) and R_2 (occupied by material 2). Two types of interface cracks will be studied here: stationary cracks and steadily growing cracks. For a steadily growing crack, it is assumed that the crack-tip coordinate system translates (relative to an inertia frame) with the crack tip along the interface at a constant speed v. The stationary crack problem is recovered by setting $v = 0$.

According to the Stroh formalism (Stroh, 1962), the stress and displacement fields for each half-plane of the present problem can be expressed in terms of three arbitrary analytic functions $f_1(z_1)$, $f_2(z_2)$, and $f_3(z_3)$, where $z_i = x_1 + p_i x_2$ $(i = 1, 2, 3)$, as

$$\mathbf{u} = 2\mathrm{Re}[\mathbf{A}\mathbf{f}(z)]$$
$$\mathbf{t} = 2\mathrm{Re}[\mathbf{L}\mathbf{f}'(z)]$$
$$\mathbf{s} = -2\mathrm{Re}[\mathbf{L}\boldsymbol{\Gamma}\mathbf{f}'(z) - \rho v^2 \mathbf{A}\mathbf{f}'(z)] \tag{1}$$

which hold for both coupled and uncoupled in-plane and antiplane deformations, where vector $\mathbf{f}(z)$ has components f_i with the understanding that z is to be replaced for f_i by z_i, and $\mathbf{f}'(z)$ is formed by the derivative of f_i with respect to its argument. (This convention also is used later.) The symbol Re[ ] denotes the real part of the content in [ ]. $\mathbf{u}$ is the displacement vector, and $\mathbf{t}$ and $\mathbf{s}$ are the stress vectors with stress components σ_{2i} and σ_{1i}, respectively. And $\mathbf{A}$, $\mathbf{L}$, and $\boldsymbol{\Gamma}$ are matrices related to the following eigenvalue problem:

$P(p)\mathbf{a} = 0$ with

$$P_{ik} = (\mathbf{C}_{i\alpha k\beta} - \rho v^2 \delta_{ik}\delta_{1\alpha}\delta_{1\beta})(\delta_{1\alpha} + p\delta_{2\alpha})(\delta_{1\beta} + p\delta_{2\beta}) \tag{2}$$

where p and $\mathbf{a}$ are, respectively, the eigenvalue and eigenvector; $\mathbf{C}$, the material's 4th order stiffness tensor; δ, the Kronecker delta; ρ, the material's mass density. There are six complex eigenvalues and p_i are those with positive imaginary parts. Now $\mathbf{A}$ has $\mathbf{a}_i$, associated with p_i, as its ith column; $\boldsymbol{\Gamma}$ is diagonal with p_i as its ith diagonal term; and $\mathbf{L}$ has components

$$\mathbf{L}_{ij} = (\mathbf{C}_{i\alpha k\beta} - \rho v^2 \delta_{ik}\delta_{1\alpha}\delta_{1\beta})\delta_{2\alpha}(\delta_{1\beta} + p_j\delta_{2\beta})\mathbf{A}_{kj} \quad \text{(no sum over } j\text{)}. \tag{3}$$

To simplify derivations in the subsequent sections, a vector of analytic functions, $\mathbf{h}(z)$, and a positive definite hermitian matrix, $\mathbf{B}$, which were introduced by Suo (1990), will be adopted here, which are

$$\mathbf{h}(z) = \mathbf{L}\mathbf{f}(z), \quad \mathbf{B} = i\mathbf{A}\mathbf{L}^{-1} \tag{4}$$

where $i = \sqrt{-1}$. Hence, once a solution for $\mathbf{h}(z)$ is obtained, $\mathbf{f}(z)$ can be solved from Eq. (4), which then can be substituted into Eq. (1), with the argument z replaced by z_i for the ith component, f_i, of the vector $\mathbf{f}(z)$, to obtain the final solution for stress and displacements.

In the following, whenever necessary, explicit subscripts 1 and 2 will be used to signify quantities for the top and bottom half-planes, respectively. The crack speed will be assumed to be smaller than c_R, the smaller of the Rayleigh wave speeds of the top and bottom materials. For clarity, x will be used in place of x_1, and y in place of x_2.

3 Oscillatory Solution

Recall that we are looking for near-tip fields of an interface crack, and accordingly we have assumed that the crack is traction-free and semi-infinite, and lies along the negative x-axis, and that the interface lies along the positive x-axis. With the complex representation of the stress and displacement fields in Eq. (1), the only conditions of concern here are the traction-free conditions along the crack surfaces and the continuity conditions of tractions and displacements along the interface. As a result of the above conditions, which are manipulated with the method of analytic continuation (for details, see Deng, 1991), the problem is reduced to solving the following nonhomogeneous Hilbert problem:

$$\overline{\mathbf{H}}\mathbf{h}_1'(x)^+ + \mathbf{H}\mathbf{h}_1'(x)^- = 2(\mathrm{Re}\mathbf{B}_2)\mathbf{g}(x), \quad -\infty < x < 0 \tag{5}$$

where superscripts + and − mean that the x-axis is approached, respectively, from the top and the bottom of the axis; $\mathbf{H} = \mathbf{B}_1 + \overline{\mathbf{B}}_2$, a Hermitian matrix defined in Suo (1990); $\mathbf{g}(z)$, a vector composed of entire functions and satisfies the relation $\mathbf{g}(z) = -\overline{\mathbf{g}}(z)$ (here $\overline{\mathbf{g}}(z)$ denotes the complex conjugate of $\mathbf{g}(\bar{z})$; this convention also is used later). It can be shown that the general solution for Eq. (5) is given by

$$\mathbf{h}_1'(z) = \frac{e^{\pi\epsilon}\zeta(z)z^{i\epsilon}\mathbf{w} + e^{-\pi\epsilon}\overline{\zeta}(z)z^{-i\epsilon}\overline{\mathbf{w}}}{2(2\pi z)^{1/2}\cosh\pi\epsilon} + \frac{\zeta_3(z)\mathbf{w}_3}{2(2\pi z)^{1/2}} + [I + (\mathrm{Re}\mathbf{B}_2)^{-1}\mathrm{Re}\mathbf{B}_1]^{-1}\mathbf{g}(z) \tag{6}$$

where $\zeta(z)$ and $\zeta_3(z)$ are entire functions, and $\zeta_3(z) = \overline{\zeta}_3(z)$ (that is, $\zeta_3(z)$ is real valued if z is replaced by a real variable), and their values at $z = 0$, $\zeta(0)$ and $\zeta_3(0)$ are, respectively, the stress intensity factors K, complex, and K_3, real, as defined in Suo (1990). The oscillation index ϵ has the same form as that given by Ting (1986)

$$\epsilon = \frac{1}{2\pi}\ln\frac{1-\beta}{1+\beta}, \quad \beta = -\sqrt{-\frac{1}{2}\mathrm{tr}[\mathrm{Im}\mathbf{H})(\mathrm{Re}\mathbf{H})^{-1}]^2} \tag{7}$$

where β is a generalization of one of the Dundurs' parameters (Dundurs, 1969). Vectors $\mathbf{w}$, $\overline{\mathbf{w}}$, and $\mathbf{w}_3$ (a real vector), are eigenvectors associated with eigenvalues ϵ, $-\epsilon$, and 0, respectively, of the following eigenvalue problem:

$$\overline{\mathbf{H}}\mathbf{w} = e^{2\pi\epsilon}\mathbf{H}\mathbf{w}. \tag{8}$$

The general solution for $\mathbf{h}_2'(z)$ can be obtained from Eq. (6) by setting $\pi\epsilon$ to $-\pi\epsilon$ and switching $\mathbf{B}_1$ and $\mathbf{B}_2$. From the relation $\mathbf{g}(z) = -\overline{\mathbf{g}}(z)$ observed earlier (that is, it is purely imaginary if z is replaced by a real variable), the vector $\mathbf{g}(z)$ can be expressed in terms of vectors $\mathbf{w}$, $\overline{\mathbf{w}}$, and $\mathbf{w}_3$, as follows:

$$\mathbf{g}(z) = \xi(z)\mathbf{w} - \overline{\xi}(z)\overline{\mathbf{w}} + i\xi_3(z)\mathbf{w}_3 \tag{9}$$

where $\xi(z)$ and $\xi_3(z)$ are entire functions, and $\xi_3(z) = \overline{\xi}_3(z)$.

Equation (6) and its counterpart for $\mathbf{h}_2'(z)$ can be integrated with respect to z to give expressions for $\mathbf{h}_1(z)$ and $\mathbf{h}_2(z)$, which, together with expressions in Eqs. (4) and (1), form the general solution of the near-tip stress and displacement fields for stationary and steadily growing interface cracks in general dissimilar anisotropic materials. For stationary interface cracks in isotropic bimaterials, such a general solution has been given by Rice (1988) for in-plane deformations. Since functions $\zeta(z)$, $\zeta_3(z)$, $\xi(z)$, and $\xi_3(z)$ are analytic everywhere, they can be expanded into Taylor series at $z = 0$ as

$$\zeta(z) = \sum_{n=0}^{\infty} a_n z^n, \quad \zeta_3(z) = \sum_{n=0}^{\infty} b_n z^n$$
$$\xi(z) = \sum_{n=0}^{\infty} c_n z^n, \quad \xi_3(z) = \sum_{n=0}^{\infty} d_n z^n \tag{10}$$

where coefficients a_n and c_n are complex numbers; b_n and d_n, real numbers; and $a_0 = K$, $b_0 = K_3$, representing the stress intensity factors. If Eq. (10) is substituted into Eqs. (9) and (6) and its counterpart for $\mathbf{h}_2'(z)$, and subsequently into Eq. (1), a complete Williams-type series expansions of the near-tip fields will be generated, from which explicit expressions of the stress and displacement fields in terms of crack-tip polar coordinates r and θ can be derived. To be concise, such explicit

Downloaded 03 May 2010 to 171.66.16.245. Redistribution subject to ASME license or copyright; see http://www.asme.org/terms/Terms_Use.cfm

expressions will be derived only for stationary and steadily growing interface cracks in dissimilar isotropic materials, which will be given in the Appendix.

It is the author's experience (Deng, 1992) that when the oscillation index ϵ is not zero, the one-term eigenexpansion technique developed by Williams (1957) will not always yield a solution, in which case two-term eigenexpansion must be used. That is, a solution of the form $\mathbf{h}(z)$ or $\mathbf{h}'(z) = \mathbf{a}z^{\lambda} + \mathbf{b}\bar{z}^{\lambda}$ must be sought explicitly at the very beginning, where λ is an unknown complex eigenvalue, and $\mathbf{a}$ and $\mathbf{b}$, the corresponding complex eigenvectors.

4 Nonoscillatory Solution

The oscillatory behavior of the crack-tip fields represented in Eqs. (6) will disappear if the oscillation index ϵ, or equivalently, the generalized Dundurs parameter β is zero, which has been shown (Ting, 1986; Qu and Bassani, 1989) to correspond to cases where the hermitian matrix $\mathbf{H}$ is real. Since derivations of Section 3 can be carried over without much modification, the Hilbert problem in Section 3 can be reduced here to

$$\mathbf{h}_1'(x)^+ + \mathbf{h}_1'(x)^- = 2[I + (\mathrm{Re}\mathbf{B}_2)^{-1}\mathrm{Re}\mathbf{B}_1]^{-1}\mathbf{g}(z) \tag{11}$$

which has the following general solution, representing the nonoscillatory interface crack-tip fields in dissimilar anisotropic bimaterials

$$\mathbf{h}_1'(z) = \frac{1}{2}(2\pi z)^{-1/2}\zeta(z) + [I + (\mathrm{Re}\mathbf{B}_2)^{-1}\mathrm{Re}\mathbf{B}_1]^{-1}\mathbf{g}(z)$$

$$\mathbf{h}_2'(z) = \frac{1}{2}(2\pi z)^{-1/2}\zeta(z) + [I + (\mathrm{Re}\mathbf{B}_1)^{-1}\mathrm{Re}\mathbf{B}_2]^{-1}\mathbf{g}(z). \tag{12}$$

When the top and bottom materials are identical, the bimaterial becomes homogeneous, for which Eq. (12) is simplified to

$$\mathbf{h}_1'(z) = \mathbf{h}_2'(z) = \frac{1}{2}(2\pi z)^{-1/2}\zeta(z) + \frac{1}{2}\mathbf{g}(z). \tag{13}$$

This general solution of crack-tip fields in homogeneous anisotropic materials is an extension of previous work in the literature regarding the singular behavior of such fields (Sih et al., 1965, 1968; Hoenig, 1982; Wu, 1989).

5 Decoupled Antiplane Shear and In-Plane Deformation

Antiplane shear and in-plane deformation can be decoupled if the x-y plane is a material symmetry plane. In this case, those components of the stiffness tensor $\mathbf{C}_{ijkl}$ with $ijkl$ containing odd numbers of 3 will be identically zero. Separate solutions for antiplane shear and in-plane deformation can be readily obtained following the procedures developed in previous sections.

Antiplane Shear. The nonzero displacement and stress components are u_3 and $\sigma_{3\alpha}$ ($\alpha = 1, 2$), which, for crack velocity v smaller than c_R, the Rayleigh wave speed, can be represented in terms of one analytic function $f(z)$, where $z = x + p_3 y$, as

$$u_3 = 2\mathrm{Re}[f(z)], \quad \sigma_{32} = 2\mathrm{Re}[Lf'(z)],$$
$$\sigma_{31} = -2\mathrm{Re}[(Lp_3 - \rho v^2)f'(z)] \tag{14}$$

where complex numbers p_3 and L are related to the components of the stiffness tensor $\mathbf{C}$ by

$$p_3 = -\mathbf{C}_{3132}/\mathbf{C}_{3232} + i[\mathbf{C}_{3232}(\mathbf{C}_{3131} - \rho v^2) - \mathbf{C}_{3132}^2]^{1/2}/\mathbf{C}_{3232}$$
$$L = i[\mathbf{C}_{3232}(\mathbf{C}_{3131} - \rho v^2) - \mathbf{C}_{3132}^2]^{1/2}$$
$$c_R = [(\mathbf{C}_{3232}\mathbf{C}_{3131} - \mathbf{C}_{3132}^2)/\rho\mathbf{C}_{3232}]^{1/2}. \tag{15}$$

The general solution of the interface crack-tip fields for the top material is

$$[Lf'(z)]_1 = \frac{\zeta(z)}{2(2\pi z)^{1/2}} + \frac{ig(z)}{1 + B_1/B_2} \tag{16}$$

where $B_1 = i/L_1$ and $B_2 = i/L_2$, and $\zeta(z)$ and $g(z)$ are entire functions satisfying $\zeta(z) = \bar{\zeta}(z)$ and $g(z) = \bar{g}(z)$. The counterpart solution for the bottom material can be obtained from Eq. (16) by exchanging B_1 and B_2. The stress intensity factor K_{III} for the singular term is given by $\zeta(0)$.

In-Plane Deformation. The nonzero displacement and stress components are u_α, $\sigma_{\alpha\beta}$ ($\alpha, \beta = 1, 2$), and σ_{33} in plane strain or ϵ_{33} in plane stress. Discussions in Sections 2 through 4 regarding the representation of the stress and displacement fields, and the general oscillatory and nonoscillatory interface crack-tip fields can be carried over here, if all vectors and matrices are replaced by their two-dimensional counterparts and all quantities with subscript 3 eliminated. Explicit expressions can be found in Yang et al. (1991) of $\mathbf{A}$, $\mathbf{L}$, $\mathbf{B}$, etc., under conditions that both materials are orthotropic with principal axes along x and y.

6 Steady Crack Growth in Dissimilar Isotropic Media

In this section the top and bottom materials are assumed to be isotropic but generally dissimilar. The stiffness tensor for each material becomes $C_{ijkl} = \lambda\delta_{ij}\delta_{kl} + \mu(\delta_{ik}\delta_{jl} + \delta_{il}\delta_{jk})$, where λ and μ are Lamé constants which are different for the two materials. In the following, attention will be directed to plane strain and plane stress, since here in-plane deformation can always be decoupled from antiplane shear which was treated separately in the preceding section.

Expressions for quantities such as eigenvalues p_1, p_2, generalized Dundurs' parameter β, vector $\mathbf{w}$, and matrices $\mathbf{A}$, $\mathbf{L}$, and $\mathbf{B}$ have been derived from their general definitions by Yang et al. (1991) (see also Wu, 1989, 1991). Note that expressions for $\mathbf{A}$, $\mathbf{L}$, and $\mathbf{B}$ also can be readily obtained from a complex function representation formulated by Rodak (1956), which are given later in Eqs. (17) and (18). Substitutions of these expressions into the two-dimensional counterparts of Eqs. (1) and (6) etc. will yield the desired general solution for the interface crack-tip fields. Presented in the following is the solution rearranged in a relatively simple format, which uses Radok's complex function representation for the stresses and displacements:

$$\sigma_{xx} = -\mathrm{Re}[(1 + 2\alpha_l^2 - \alpha_s^2)\varphi'(z_l) + 2\alpha_s\psi'(z_s)]$$
$$\sigma_{yy} = \mathrm{Re}[(1 + \alpha_s^2)\varphi'(z_l) + 2\alpha_s\psi'(z_s)]$$
$$\sigma_{xy} = \mathrm{Im}[2\alpha_l\varphi'(z_l) + (1 + \alpha_s^2)\psi'(z_s)] \tag{17}$$
$$u_x = -\mathrm{Re}[\varphi(z_l) + \alpha_s\psi(z_s)]/\mu$$
$$u_y = \mathrm{Im}[\alpha_l\varphi(z_l) + \psi(z_s)]/\mu \tag{18}$$

where the complex variables z_l and z_s, and constant α_l and α_s are defined as

$$z_l = x + i\alpha_l y \equiv r_l e^{i\theta_l}, \quad z_s = x + i\alpha_s y \equiv r_s e^{i\theta_s}$$
$$\alpha_l = \sqrt{1 - (v/c_l)^2}, \quad \alpha_s = \sqrt{1 - (v/c_s)^2}. \tag{19}$$

The longitudinal and shear wave speeds, c_l and c_s, respectively, are related to the mass density ρ, shear modulus μ, and Poisson's ratio ν, of the materials through

$$c_s = \sqrt{\mu/\rho}, \quad c_l = \sqrt{(k+1)/(k-1)}c_s \tag{20}$$

where $k = (3 - \nu)/(1 + \nu)$ for plane stress and $(3 - 4\nu)$ for plane strain. The analytic complex functions in Eqs. (17) and (18) are related to those in Eq. (1) through $\varphi = -2\mu f_1$ and $\psi = i2\mu f_2$. The general solution for $\varphi(z_l)$ and $\psi(z_s)$ for the top half-plane as derived from Eq. (6) are given by

Downloaded 03 May 2010 to 171.66.16.245. Redistribution subject to ASME license or copyright; see http://www.asme.org/terms/Terms_Use.cfm

$$\varphi'(z_l)=\frac{[2\alpha_s\eta-(1+\alpha_s^2)]e^{\pi\epsilon}\zeta(z_l)z_l^{i\epsilon}}{2D(2\pi z_l)^{1/2}\cosh\pi\epsilon}-\frac{[2\alpha_s\eta+(1+\alpha_s^2)]e^{-\pi\epsilon}\bar{\zeta}(z_l)z_l^{-i\epsilon}}{2D(2\pi z_l)^{1/2}\cosh\pi\epsilon}+\frac{[2\alpha_s\eta(1+\omega_l)-(1+\alpha_s^2)(1+\omega_s)]\xi(z_l)}{D(1+\omega_l)(1+\omega_s)}+\frac{[2\alpha_s\eta(1+\omega_l)+(1+\alpha_s^2)(1+\omega_s)]\bar{\xi}(z_l)}{D(1+\omega_l)(1+\omega_s)} \quad (21)$$

$$\psi'(z_s)=\frac{[2\alpha_l-\eta(1+\alpha_s^2)]e^{\pi\epsilon}\zeta(z_s)z_s^{i\epsilon}}{2D(2\pi z_s)^{1/2}\cosh\pi\epsilon}+\frac{[2\alpha_l+\eta(1+\alpha_s^2)]e^{-\pi\epsilon}\bar{\zeta}(z_s)z_s^{-i\epsilon}}{2D(2\pi z_s)^{1/2}\cosh\pi\epsilon}+\frac{[2\alpha_l(1+\omega_s)-\eta(1+\alpha_s^2)(1+\omega_l)]\xi(z_s)}{D(1+\omega_l)(1+\omega_s)}-\frac{[2\alpha_l(1+\omega_s)+\eta(1+\alpha_s^2)(1+\omega_l)]\bar{\xi}(z_s)}{D(1+\omega_l)(1+\omega_s)} \quad (22)$$

where the constant D is given by $D = 4\alpha_l\alpha_s - (1 + \alpha_s^2)^2$, which is a function of the crack speed v. The Rayleigh wave speed c_R is the smallest nonzero root of $D(v) = 0$. The oscillation index ϵ is given in terms of generalized Dundurs' parameter β in Eq. (7). In order to define concisely the mismatch parameter β, η, ω_l, and ω_s, the following intermediate constants are defined first:

$$P=\frac{2\alpha_l\alpha_s-(1+\alpha_s^2)}{\mu D},\quad Q=\frac{\alpha_s(1-\alpha_s^2)}{\mu D},\quad R=\frac{\alpha_l(1-\alpha_s^2)}{\mu D}. \quad (23)$$

Then the mismatch parameters can be defined by

$$\beta=\frac{P_1-P_2}{\sqrt{(R_1+R_2)(Q_1+Q_2)}},\quad \eta=\sqrt{\frac{R_1+R_2}{Q_1+Q_2}} \quad (24)$$

$$\omega_s=\frac{Q_1}{Q_2},\quad \omega_l=\frac{R_1}{R_2} \quad (25)$$

In the above equations, subscripts 1 and 2 refer to quantities for the top and bottom half-planes, respectively. The general solution for the bottom half-plane can be obtained from that for the top half-plane by changing $\pi\epsilon$ to $-\pi\epsilon$, ω_l to ω_l^{-1}, and ω_s to ω_s^{-1}. The complex functions ζ and ξ are entire functions and can be expanded into complex power series as expressed in Eq. (10), where the first term, i.e., the constant term, equals the complex stress intensity factor K. Series expansions of the stresses and displacements in terms of crack-tip polar coordinates r and θ can be derived from Eqs. (17) and (18), which will be given in the Appendix.

Acknowledgments

The author would like to thank Prof. Michael Sutton for helpful discussions. This work is partially supported by a research start-up grant from the College of Engineering of the University of South Carolina, Columbia, and by a grant from the University of South Carolina Research and Productive Scholarship Fund.

References

Aminpour, M. A., 1986, "Finite Element Analysis of Propagating Interface Cracks in Composites," Ph.D. Dissertation, Department of Aeronautics and Astronautics, University of Washington.

Aminpour, M. A., and Holsapple, K. A., 1990, "Near-Field Solutions for Propagating Cracks at the Interface of Dissimilar Anisotropic Elastic Materials," *Engineering Fracture Mechanics*, Vol. 36, pp. 93–103.

Deng, X., 1992, "Complete Complex Series Expansions of Near-Tip Fields for Steadily Growing Interface Cracks in Dissimilar Isotropic Materials," *Engineering Fracture Mechanics*, Vol. 42, pp. 237–242.

Deng, X., 1991, "General Crack Tip Fields for Stationary and Steadily Growing Interface Cracks in Anisotropic Bimaterials," MECH Report 91-2, Department of Mechanical Engineering, University of South Carolina, Columbia, SC.

Dundurs, J., 1969, "Edge-Bonded Dissimilar Orthogonal Elastic Wedges Under Normal and Shear Loading," ASME JOURNAL OF APPLIED MECHANICS, Vol. 36, pp. 650–652.

Eshelby, J. D., Read, W. T., and Shockley, W., 1953, "Anisotropic Elasticity with Applications to Dislocation Theory," *Acta Metall.*, Vol. 1, pp. 251—259.

Freund, L. B., and Rosakis, A. J., 1992, "The Structure of the Near Tip Field During Transient Elastodynamic Crack Growth," *J. Mech. Phys. Solids*, Vol. 40, pp. 699–719.

Hoenig, A., 1982, "Near-Tip Behavior of a Crack in a Plane Anisotropic Elastic Body," *Engineering Fracture Mechanics*, Vol. 3, pp. 393–403.

Lekhnitskii, S. G., 1963, *Theory of Elasticity of an Anisotropic Body*, Holden-Day, Inc., San Francisco.

Qu, J., and Bassani, J. L., 1989, "Cracks on Bimaterial and Bicrystal Interfaces," *J. Mech. Phys. Solids*, Vol. 37, pp. 417–433.

Radok, J. R. M., 1956, "On the Solution of Problems of Dynamic Plane Elasticity," *Quarterly of Applied Mathematics*, Vol. 14, pp. 289–298.

Rice, J. R., 1988, "Elastic Fracture Mechanics Concepts for Interfacial Cracks," ASME JOURNAL OF APPLIED MECHANICS, Vol. 55, pp. 98–103.

Sih, G. C., and Liebowitz, H., 1968, "Mathematical Theories of Brittle Fracture," *Fracture*, Vol. 2, H. Liebowitz, ed., Academic Press, New York.

Sih, G. C., Paris, P. C., and Irwin, G. R., 1965, "On Cracks in Rectilinearly Anisotropic Bodies," *Int. J. Fracture Mech.*, Vol. 1, pp. 189–202.

Stroh, A. N., 1958, "Dislocations and Cracks in Anisotropic Elasticity," *Phil. Mag.*, Vol. 3, pp. 625–646.

Stroh, A. N., 1962, "Steady State Problems in Anisotropic Elasticity," *J. of Mathematics and Physics*, Vol. 41, pp. 77–103.

Suo, Z., 1990, "Singularities, Interfaces and Cracks in Dissimilar Anisotropic Media," *Proc. Royal Soc. Lond.*, Vol. A427, pp. 331–358.

Ting, T. C. T., 1986, "Explicit Solution and Invariance of the Singularities at an Interface Crack in Anisotropic Composites," *Int. J. Solids Structures*, Vol. 22, pp. 965–983.

Ting, T. C. T., 1990, "Interface Cracks in Anisotropic Bimaterials," *J. Mech. Phys. Solids*, Vol. 38, pp. 505–513.

Williams, M. L., 1957, "On the Stress Distribution at the Base of a Stationary Crack," ASME JOURNAL OF APPLIED MECHANICS, Vol. 24, pp. 109–114.

Wu, K. C., 1989, "On the Crack-Tip Fields of a Dynamically Propagating Crack in an Anisotropic Elastic Solid," *Int. J. Fracture*, Vol. 41, pp. 253–266.

Wu, K. C., 1990, "Stress Intensity Factor and Energy Release Rate for Interfacial Cracks Between Dissimilar Anisotropic Materials," ASME JOURNAL OF APPLIED MECHANICS, Vol. 57, pp. 882–886.

Wu, K. C., 1991, "Explicit Crack-Tip Fields of an Extending Interface Crack in an Anisotropic Bimaterial," *Int. J. Solids Structures*, Vol. 27, pp. 455–466.

Yang, W., Suo, Z., and Shih, C. F., 1991, "Mechanics of Dynamic Debonding," *Proc. Royal Soc. Lond.*, Vol. 33, pp. 679–697.

APPENDIX

Complete Interface Crack-Tip Fields in Dissimilar Isotropic Media

In terms of the crack-tip polar coordinates r and θ, where θ is measured counterclockwise from the positive x-axis, the complete series expansions of the stress and displacement fields near the tip of an interface crack, stationary or steadily growing, can be written as

$$\sigma(r,\theta)=\sum_{n=0}^{\infty} r^{\frac{n-1}{2}}\left\{\frac{\mathrm{Re}(\eta_n^I k_n r^{i\epsilon_n})}{\sqrt{2\pi}}\hat{\sigma}_n^I(\theta)+\frac{\mathrm{Im}(\eta_n^{II} k_n r^{i\epsilon_n})}{\sqrt{2\pi}}\hat{\sigma}_n^{II}(\theta)+\frac{k_{3n}}{\sqrt{2\pi}}\hat{\sigma}_n^{III}(\theta)\right\} \quad (26)$$

$$\mathbf{u}(r,\theta)=\sum_{n=0}^{\infty} r^{\frac{n+1}{2}}\left\{\frac{\mathrm{Re}(\eta_n^I k_n r^{i\epsilon_n})}{\sqrt{2\pi}}\hat{\mathbf{u}}_n^I(\theta)+\frac{\mathrm{Im}(\eta_n^{II} k_n r^{i\epsilon_n})}{\sqrt{2\pi}}\hat{\mathbf{u}}_n^{II}(\theta)+\frac{k_{3n}}{\sqrt{2\pi}}\hat{\mathbf{u}}_n^{III}(\theta)\right\} \quad (27)$$

where $\epsilon_n = \epsilon$, $\eta_n^I = 1$, and $\eta_n^{II} = \eta$ when $n = 0, 2, 4, \ldots$, and $\epsilon_n = 0$, $\eta_n^I = \eta$, and $\eta_n^{II} = 1$ when $n = 1, 3, 5, \ldots$. The terms corresponding to $n = 0$ give the oscillatory singular crack-tip fields, with stress intensity factors $k_0 = K$, complex, and $k_{30} = K_3$, real. In the above and thereafter, definitions for most parameters, such as ϵ and η ($\eta = 1$ for stationary interface cracks), can be found in the main text. It can be verified that if k_n is written as $k_n = k_n^I/\eta_n^I + ik_n^{II}/\eta_n^{II}$, then when the bimaterial becomes homogeneous (hence $\epsilon = 0$), k_n^I, k_n^{II}, and

Downloaded 03 May 2010 to 171.66.16.245. Redistribution subject to ASME license or copyright; see http://www.asme.org/terms/Terms_Use.cfm

the angular functions in Eqs. (26) and (27) with superscripts *I* and *II* will reduce to those for classic mode *I* and mode *II* problems. Also in Eq. (26) and (27) superscript *III* denotes the antiplane shear mode. In the following, expressions for the hatted functions will be given only for the top half-plane ($0 \le \theta \le \pi$), from which those for the bottom half-plane ($-\pi \le \theta \le 0$) can be derived by changing a few parameters which will be specified later.

Steadily Growing Interface Cracks. To make the expressions compact, four functions of θ, with explicit dependence on parameters n, ϵ, and η, will be defined as follows:

$$C_l(n,\epsilon,\eta) = -\gamma_l^{(n-1)/2} e^{\epsilon(\pi-\theta_l)}[2\alpha_s\eta - (1+\alpha_s^2)]\cos\left(\frac{n-1}{2}\theta_l + \epsilon\ln\gamma_l\right)$$

$$S_l(n,\epsilon,\eta) = \gamma_l^{(n-1)/2} e^{\epsilon(\pi-\theta_l)}[2\alpha_s\eta - (1+\alpha_s^2)]\sin\left(\frac{n-1}{2}\theta_l + \epsilon\ln\gamma_l\right)$$

$$C_s(n,\epsilon,\eta) = -\gamma_s^{(n-1)/2} e^{\epsilon(\pi-\theta_s)}[2\alpha_l - \eta(1+\alpha_s^2)]\cos\left(\frac{n-1}{2}\theta_s + \epsilon\ln\gamma_s\right)$$

$$S_s(n,\epsilon,\eta) = \gamma_s^{(n-1)/2} e^{\epsilon(\pi-\theta_s)}[2\alpha_l - \eta(1+\alpha_s^2)]\sin\left(\frac{n-1}{2}\theta_s + \epsilon\ln\gamma_s\right) \quad (28)$$

where θ_β, γ_β ($\beta = l, s$) are determined from

$$\tan\theta_\beta = \alpha_\beta\tan\theta, \quad \gamma_\beta = \sqrt{\cos^2\theta + \alpha_\beta^2\sin^2\theta} \quad (\beta = l, s) \quad (29)$$

When $n = 0, 2, 4, \ldots$

$$\hat{u}^{II}_{xn}(\theta) = \frac{1}{\eta\mu D[(n+1)^2+4\epsilon^2]\cosh\pi\epsilon} \times \{(n+1)[S_l(n+2,\epsilon,\eta) - S_l(n+2,-\epsilon,-\eta)] + 2\epsilon[C_l(n+2,\epsilon,\eta) + C_l(n+2,-\epsilon,-\eta)] + \alpha_s(n+1)[S_s(n+2,\epsilon,\eta) - S_s(n+2,-\epsilon,-\eta)] + 2\alpha_s\epsilon[C_s(n+2,\epsilon,\eta) + C_s(n+2,-\epsilon,-\eta)]\} \quad (35)$$

$$\hat{u}^{II}_{yn}(\theta) = \frac{1}{\eta\mu D[(n+1)^2+4\epsilon^2]\cosh\pi\epsilon}\{\alpha_l(n+1)[-C_l(n+2,\epsilon,\eta) + C_l(n+2,-\epsilon,-\eta)] + 2\alpha_l\epsilon[S_l(n+2,\epsilon,\eta) + S_l(n+2,-\epsilon,-\eta)] + (n+1)[-C_s(n+2,\epsilon,\eta) + C_s(n+2,-\epsilon,-\eta)] + 2\epsilon[S_s(n+2,\epsilon,\eta) + S_s(n+2,-\epsilon,-\eta)]\} \quad (36)$$

$$\hat{u}^{III}_{3n}(\theta) = \frac{2}{\mu\alpha_s(n+1)}\gamma_s^{\frac{n+1}{2}}\sin\frac{n+1}{2}\theta_s. \quad (37)$$

When $n = 1, 3, 5, \ldots$

$$[\hat{\sigma}^I_{xxn}(\theta) \quad \hat{\sigma}^I_{yyn}(\theta) \quad \hat{\sigma}^I_{xyn}(\theta)]^T = \frac{1+\alpha_s^2}{D(1+\omega_s)} \times \begin{Bmatrix} -\frac{\alpha_s(1+2\alpha_l^2-\alpha_s^2)}{1+\alpha_s^2}\gamma_l^{\frac{n-1}{2}}\cos\frac{n-1}{2}\theta_l + \alpha_s\gamma_s^{\frac{n-1}{2}}\cos\frac{n-1}{2}\theta_s \\ \alpha_s\gamma_l^{\frac{n-1}{2}}\cos\frac{n-1}{2}\theta_l - \alpha_s\gamma_s^{\frac{n-1}{2}}\cos\frac{n-1}{2}\theta_s \\ \frac{2\alpha_s\alpha_l}{1+\alpha_s^2}\gamma_l^{\frac{n-1}{2}}\sin\frac{n-1}{2}\theta_l - \frac{1+\alpha_s^2}{2}\gamma_s^{\frac{n-1}{2}}\sin\frac{n-1}{2}\theta_s \end{Bmatrix} \quad (38)$$

$$[\hat{\sigma}^I_{xxn}(\theta) \quad \hat{\sigma}^I_{yyn}(\theta) \quad \hat{\sigma}^I_{xyn}(\theta)]^T = \frac{1}{2D\cosh\pi\epsilon}\begin{Bmatrix} (1+2\alpha_l^2-\alpha_s^2)[C_l(n,\epsilon,\eta) + C_l(n,-\epsilon,-\eta)] + 2\alpha_s[C_s(n,\epsilon,\eta) + C_s(n,-\epsilon,-\eta)] \\ -(1+\alpha_s^2)[C_l(n,\epsilon,\eta) + C_l(n,-\epsilon,-\eta)] - 2\alpha_s[C_s(n,\epsilon,\eta) + C_s(n,-\epsilon,-\eta)] \\ 2\alpha_l[S_l(n,\epsilon,\eta) + S_l(n,-\epsilon,-\eta)] + (1+\alpha_s^2)[S_s(n,\epsilon,\eta) + S_s(n,-\epsilon,-\eta)] \end{Bmatrix} \quad (30)$$

$$[\hat{\sigma}^{II}_{xxn}(\theta) \quad \hat{\sigma}^{II}_{yyn}(\theta) \quad \hat{\sigma}^{II}_{xyn}(\theta)]^T = \frac{1}{2\eta D\cosh\pi\epsilon}\begin{Bmatrix} (1+2\alpha_l^2-\alpha_s^2)[S_l(n,\epsilon,\eta) - S_l(n,-\epsilon,-\eta)] + 2\alpha_s[S_s(n,\epsilon,\eta) - S_s(n,-\epsilon,-\eta)] \\ (1+\alpha_s^2)[-S_l(n,\epsilon,\eta) + S_l(n,-\epsilon,-\eta)] + 2\alpha_s[-S_s(n,\epsilon,\eta) + S_s(n,-\epsilon,-\eta)] \\ 2\alpha_l[-C_l(n,\epsilon,\eta) + C_l(n,-\epsilon,-\eta)] + (1+\alpha_s^2)[-C_s(n,\epsilon,\eta) + C_s(n,-\epsilon,-\eta)] \end{Bmatrix} \quad (31)$$

$$\begin{Bmatrix} \hat{\sigma}^{III}_{x3n}(\theta) \\ \hat{\sigma}^{III}_{y3n}(\theta) \end{Bmatrix} = \gamma_s^{\frac{n-1}{2}}\begin{Bmatrix} \frac{1}{\alpha_s}\sin\frac{n-1}{2}\theta_s \\ \cos\frac{n-1}{2}\theta_s \end{Bmatrix} \quad (32)$$

$$\hat{u}^I_{xn}(\theta) = \frac{1}{\mu D[(n+1)^2+4\epsilon^2]\cosh\pi\epsilon} \times \{(n+1)[C_l(n+2,\epsilon,\eta) + C_l(n+2,-\epsilon,-\eta)] - 2\epsilon[S_l(n+2,\epsilon,\eta) - S_l(n+2,-\epsilon,-\eta)] + \alpha_s(n+1) \times [C_s(n+2,\epsilon,\eta) + C_s(n+2,-\epsilon,-\eta)] - 2\alpha_s\epsilon[S_s(n+2,\epsilon,\eta) - S_s(n+2,-\epsilon,-\eta)]\} \quad (33)$$

$$\hat{u}^I_{yn}(\theta) = \frac{1}{\mu D[(n+1)^2+4\epsilon^2]\cosh\pi\epsilon} \times \{\alpha_l(n+1)[S_l(n+2,\epsilon,\eta) + S_l(n+2,-\epsilon,-\eta)] - 2\alpha_l\epsilon[-C_l(n+2,\epsilon,\eta) + C_l(n+2,-\epsilon,-\eta)] + (n+1)[S_s(n+2,\epsilon,\eta) + S_s(n+2,-\epsilon,-\eta)] - 2\epsilon[-C_s(n+2,\epsilon,\eta) + C_s(n+2,-\epsilon,-\eta)]\} \quad (34)$$

$$[\hat{\sigma}^{II}_{xxn}(\theta) \quad \hat{\sigma}^{II}_{yyn}(\theta) \quad \hat{\sigma}^{II}_{xyn}(\theta)]^T = \frac{1+\alpha_s^2}{D(1+\omega_l)} \times \begin{Bmatrix} -\frac{1+2\alpha_l^2-\alpha_s^2}{2}\gamma_l^{\frac{n-1}{2}}\sin\frac{n-1}{2}\theta_l + \frac{2\alpha_s\alpha_l}{1+\alpha_s^2}\gamma_s^{\frac{n-1}{2}}\sin\frac{n-1}{2}\theta_s \\ \frac{1+\alpha_s^2}{2}\gamma_l^{\frac{n-1}{2}}\sin\frac{n-1}{2}\theta_l - \frac{2\alpha_s\alpha_l}{1+\alpha_s^2}\gamma_s^{\frac{n-1}{2}}\sin\frac{n-1}{2}\theta_s \\ -\alpha_l\gamma_l^{\frac{n-1}{2}}\cos\frac{n-1}{2}\theta_l + \alpha_l\gamma_s^{\frac{n-1}{2}}\cos\frac{n-1}{2}\theta_s \end{Bmatrix} \quad (39)$$

$$\begin{Bmatrix} \sigma^{III}_{x3n}(\theta) \\ \hat{\sigma}^{III}_{y3n}(\theta) \end{Bmatrix} = \frac{\omega_3}{1+\omega_3}\gamma_s^{\frac{n-1}{2}}\begin{Bmatrix} \frac{1}{\alpha_s}\cos\frac{n-1}{2}\theta_s \\ -\sin\frac{n-1}{2}\theta_s \end{Bmatrix} \quad (40)$$

Downloaded 03 May 2010 to 171.66.16.245. Redistribution subject to ASME license or copyright; see http://www.asme.org/terms/Terms_Use.cfm

$$[\hat{u}^I_{xn}(\theta) \quad \hat{u}^I_{yn}(\theta)]^T = \frac{1+\alpha_s^2}{\mu D(n+1)(1+\omega_s)} \times \begin{Bmatrix} -\dfrac{2\alpha_s}{1+\alpha_s^2}\,\overline{\gamma_l^{\,2}}^{\frac{n+1}{2}} \cos\dfrac{n+1}{2}\theta_l + \alpha_s\overline{\gamma_s^{\,2}}^{\frac{n+1}{2}} \cos\dfrac{n+1}{2}\theta_s \\ \dfrac{2\alpha_s\alpha_l}{1+\alpha_s^2}\,\overline{\gamma_l^{\,2}}^{\frac{n+1}{2}} \sin\dfrac{n+1}{2}\theta_l - \overline{\gamma_s^{\,2}}^{\frac{n+1}{2}} \sin\dfrac{n+1}{2}\theta_s \end{Bmatrix} \tag{41}$$

$$[\hat{u}^{II}_{xn}(\theta) \quad \hat{u}^{II}_{yn}(\theta)]^T = \frac{1+\alpha_s^2}{\mu D(n+1)(1+\omega_l)} \times \begin{Bmatrix} -\overline{\gamma_l^{\,2}}^{\frac{n+1}{2}} \sin\dfrac{n+1}{2}\theta_l + \dfrac{2\alpha_s\alpha_l}{1+\alpha_s^2}\,\overline{\gamma_s^{\,2}}^{\frac{n+1}{2}} \sin\dfrac{n+1}{2}\theta_s \\ -\alpha_l\overline{\gamma_l^{\,2}}^{\frac{n+1}{2}} \cos\dfrac{n+1}{2}\theta_l + \dfrac{2\alpha_l}{1+\alpha_s^2}\,\overline{\gamma_s^{\,2}}^{\frac{n+1}{2}} \cos\dfrac{n+1}{2}\theta_s \end{Bmatrix}. \tag{42}$$

$$\hat{u}^{III}_{3n}(\theta) = \frac{2\omega_3}{\mu\alpha_s(n+1)(1+\omega_3)}\,\overline{\gamma_s^{\,2}}^{\frac{n+1}{2}} \cos\frac{n+1}{2}\theta_s \tag{43}$$

where $\omega_3 = (\mu\alpha_s)_1/(\mu\alpha_s)_2$.

To obtain the counterpart expressions of stress and displacement components for the bottom half-plane, simply change π to $-\pi$ in Eq. (28), and change ω_s, ω_l, and ω_3, respectively, to ω_s^{-1}, ω_l^{-1}, and ω_3^{-1} in Eqs. (38) through (43).

Stationary Interface Cracks. In this case, $\eta = 1$ and the oscillation index ϵ is given by

$$\epsilon = \frac{1}{2\pi} \ln\frac{\mu_2 k_1 + \mu_1}{\mu_1 k_2 + \mu_2} \tag{44}$$

where the generic k for each material depends on the Poisson's ratio through $k = (3 - \nu)/(1 + \nu)$ for plane stress and $k = (3 - 4\nu)$ for plane strain. The expressions of the angular functions in Eqs. (26) and (27) for the top half-plane can be written as follows: when $n = 0, 2, 4, \ldots$

$$[\hat{\sigma}^I_{xxn}(\theta) \quad \hat{\sigma}^I_{yyn}(\theta) \quad \hat{\sigma}^I_{xyn}(\theta)]^T = \frac{1}{\cosh\pi\epsilon} \times \begin{Bmatrix} -[\sinh\epsilon(\pi-\theta) - e^{-\epsilon(\pi-\theta)}]\cos\dfrac{n-1}{2}\theta - \dfrac{1}{2}e^{-\epsilon(\pi-\theta)}\sin\theta\left[(n-1)\sin\dfrac{n-3}{2}\theta - 2\epsilon\cos\dfrac{n-3}{2}\theta\right] \\ [\sinh\epsilon(\pi-\theta) + e^{-\epsilon(\pi-\theta)}]\cos\dfrac{n-1}{2}\theta + \dfrac{1}{2}e^{-\epsilon(\pi-\theta)}\sin\theta\left[(n-1)\sin\dfrac{n-3}{2}\theta - 2\epsilon\cos\dfrac{n-3}{2}\theta\right] \\ \sinh\epsilon(\pi-\theta)\sin\dfrac{n-1}{2}\theta - \dfrac{1}{2}e^{-\epsilon(\pi-\theta)}\sin\theta\left[(n-1)\cos\dfrac{n-3}{2}\theta + 2\epsilon\sin\dfrac{n-3}{2}\theta\right] \end{Bmatrix} \tag{45}$$

$$[\hat{\sigma}^{II}_{xxn}(\theta) \quad \hat{\sigma}^{II}_{yyn}(\theta) \quad \hat{\sigma}^{II}_{xyn}(\theta)]^T = \frac{1}{\cosh\pi\epsilon} \begin{Bmatrix} [\cosh\epsilon(\pi-\theta) + e^{-\epsilon(\pi-\theta)}]\sin\dfrac{n-1}{2}\theta + \dfrac{1}{2}e^{-\epsilon(\pi-\theta)}\sin\theta\left[(n-1)\cos\dfrac{n-3}{2}\theta + 2\epsilon\sin\dfrac{n-3}{2}\theta\right] \\ -[\cosh\epsilon(\pi-\theta) - e^{-\epsilon(\pi-\theta)}]\sin\dfrac{n-1}{2}\theta - \dfrac{1}{2}e^{-\epsilon(\pi-\theta)}\sin\theta\left[(n-1)\cos\dfrac{n-3}{2}\theta + 2\epsilon\sin\dfrac{n-3}{2}\theta\right] \\ \cosh\epsilon(\pi-\theta)\cos\dfrac{n-1}{2}\theta - \dfrac{1}{2}e^{-\epsilon(\pi-\theta)}\sin\theta\left[(n-1)\sin\dfrac{n-3}{2}\theta - 2\epsilon\cos\dfrac{n-3}{2}\theta\right] \end{Bmatrix} \tag{46}$$

$$\begin{Bmatrix} \hat{\sigma}^{III}_{x3n}(\theta) \\ \hat{\sigma}^{III}_{y3n}(\theta) \end{Bmatrix} = \begin{Bmatrix} \sin\dfrac{n-1}{2}\theta \\ \cos\dfrac{n-1}{2}\theta \end{Bmatrix} \tag{47}$$

$$\hat{u}^I_{xn}(\theta) = -\frac{1}{\mu[(n+1)^2+4\epsilon^2]\cosh\pi\epsilon}\left\{(n+1)\left[\sinh\epsilon(\pi-\theta) - \frac{k-1}{2}e^{-\epsilon(\pi-\theta)}\right]\cos\frac{n+1}{2}\theta + \frac{1}{2}[(n+1)^2+4\epsilon^2]e^{-\epsilon(\pi-\theta)}\sin\theta\sin\frac{n-1}{2}\theta + 2\epsilon\left[\cosh\epsilon(\pi-\theta) + \frac{k-1}{2}e^{-\epsilon(\pi-\theta)}\right]\sin\frac{n+1}{2}\theta\right\} \tag{48}$$

$$\hat{u}^I_{yn}(\theta) = \frac{1}{\mu[(n+1)^2+4\epsilon^2]\cosh\pi\epsilon}\left\{(n+1)\left[\cosh\epsilon(\pi-\theta) + \frac{k-1}{2}e^{-\epsilon(\pi-\theta)}\right]\sin\frac{n+1}{2}\theta - \frac{1}{2}[(n+1)^2+4\epsilon^2]e^{-\epsilon(\pi-\theta)}\sin\theta\cos\frac{n-1}{2}\theta - 2\epsilon\left[\sinh\epsilon(\pi-\theta) - \frac{k-1}{2}e^{-\epsilon(\pi-\theta)}\right]\cos\frac{n+1}{2}\theta\right\} \tag{49}$$

Downloaded 03 May 2010 to 171.66.16.245. Redistribution subject to ASME license or copyright; see http://www.asme.org/terms/Terms_Use.cfm

$$\hat{u}^{II}_{xn}(\theta)=\frac{1}{\mu[(n+1)^2+4\epsilon^2]\cosh\pi\epsilon}\left\{(n+1)\left[\cosh\epsilon(\pi-\theta)+\frac{k-1}{2}e^{-\epsilon(\pi-\theta)}\right]\sin\frac{n+1}{2}\theta+\frac{1}{2}[(n+1)^2+4\epsilon^2]e^{-\epsilon(\pi-\theta)}\sin\theta\cos\frac{n-1}{2}\theta\right.$$
$$\left.-2\epsilon\left[\sinh\epsilon(\pi-\theta)-\frac{k-1}{2}e^{-\epsilon(\pi-\theta)}\right]\cos\frac{n+1}{2}\theta\right\} \quad (50)$$

$$\hat{u}^{II}_{yn}(\theta)=\frac{1}{\mu[(n+1)^2+4\epsilon^2]\cosh\pi\epsilon}\left\{(n+1)\left[\sinh\epsilon(\pi-\theta)-\frac{k-1}{2}e^{-\epsilon(\pi-\theta)}\right]\cos\frac{n+1}{2}\theta-\frac{1}{2}[(n+1)^2+4\epsilon^2]e^{-\epsilon(\pi-\theta)}\sin\theta\sin\frac{n-1}{2}\theta\right.$$
$$\left.+2\epsilon\left[\cosh\epsilon(\pi-\theta)+\frac{k-1}{2}e^{-\epsilon(\pi-\theta)}\right]\sin\frac{n+1}{2}\theta\right\} \quad (51)$$

$$\hat{u}^{III}_{3n}(\theta)=\frac{2}{\mu(n+1)}\sin\frac{n+1}{2}\theta. \quad (52)$$

When $n=1, 3, 5, \ldots$

$$\begin{Bmatrix}\sigma^{I}_{xxn}(\theta)\\ \sigma^{I}_{yyn}(\theta)\\ \sigma^{I}_{xyn}(\theta)\end{Bmatrix}=\frac{1}{1+\omega}\begin{Bmatrix}4\cos\frac{n-1}{2}\theta-(n-1)\sin\theta\sin\frac{n-3}{2}\theta\\ (n-1)\sin\theta\sin\frac{n-3}{2}\theta\\ -2\sin\frac{n-1}{2}\theta-(n-1)\sin\theta\cos\frac{n-3}{2}\theta\end{Bmatrix} \quad (53)$$

$$\begin{Bmatrix}\sigma^{II}_{xxn}(\theta)\\ \sigma^{II}_{yyn}(\theta)\\ \sigma^{II}_{xyn}(\theta)\end{Bmatrix}=\frac{1}{1+\omega}\begin{Bmatrix}2\sin\frac{n-1}{2}\theta+(n-1)\sin\theta\cos\frac{n-3}{2}\theta\\ 2\sin\frac{n-1}{2}\theta-(n-1)\sin\theta\cos\frac{n-3}{2}\theta\\ -(n-1)\sin\theta\sin\frac{n-3}{2}\theta\end{Bmatrix} \quad (54)$$

$$\begin{Bmatrix}\hat{\sigma}^{III}_{x3n}(\theta)\\ \hat{\sigma}^{III}_{y3n}(\theta)\end{Bmatrix}=\frac{\omega_3}{1+\omega_3}\begin{Bmatrix}\cos\frac{n-1}{2}\theta\\ -\sin\frac{n-1}{2}\theta\end{Bmatrix} \quad (55)$$

$$\begin{Bmatrix}u^{I}_{xn}(\theta)\\ u^{I}_{yn}(\theta)\end{Bmatrix}=\frac{1}{\mu(n+1)(1+\omega)}\times\begin{Bmatrix}(k+1)\cos\frac{n+1}{2}\theta-(n+1)\sin\theta\sin\frac{n-1}{2}\theta\\ (k-1)\sin\frac{n+1}{2}\theta-(n+1)\sin\theta\cos\frac{n-1}{2}\theta\end{Bmatrix} \quad (56)$$

$$\begin{Bmatrix}u^{II}_{xn}(\theta)\\ u^{II}_{yn}(\theta)\end{Bmatrix}=\frac{1}{\mu(n+1)(1+\omega)}\times\begin{Bmatrix}(k-1)\sin\frac{n+1}{2}\theta+(n+1)\sin\theta\cos\frac{n-1}{2}\theta\\ -(k+1)\cos\frac{n+1}{2}\theta-(n+1)\sin\theta\sin\frac{n-1}{2}\theta\end{Bmatrix} \quad (57)$$

$$\hat{u}^{III}_{3n}(\theta)=\frac{2\omega_3}{\mu(n+1)(1+\omega_3)}\cos\frac{n+1}{2}\theta \quad (58)$$

where $\omega = (k_1 + 1)\mu_2/(k_2 + 1)\mu_1$ and $\omega_3 = \mu_1/\mu_2$.

Counterpart expressions of the crack-tip stress and displacement fields for the bottom half-plane can be obtained simply by changing π to $-\pi$, ω to ω^{-1}, and ω_3 to ω_3^{-1} in Eqs. (45) through (58).

Downloaded 03 May 2010 to 171.66.16.245. Redistribution subject to ASME license or copyright; see http://www.asme.org/terms/Terms_Use.cfm

A Simple Continuum Model of Creep in a Fiber Composite Beam

J. T. Evans
Department of Mechanical, Materials and Manufacturing Engineering, University of Newcastle-upon-Tyne, Newcastle-upon-Tyne NE1 7RU, England

A simple linear model of creep of a fiber composite beam treated as a continuum is presented. The model predicts that the displacement of a tip-loaded cantilever is linear with time but that the surface tensile stress increases approximately with the square root of time. The increase in tensile stress is in line with the prediction of stress channelling in the theory of ideal fiber-reinforced materials. The results are discussed in relation to some previous experimental observations and a generalization of the model which might be of value in life-time prediction is suggested.

1 Introduction

Experimental observations of bending deformation by creep in metal-matrix, continuous fiber composite beams have recently been reported (Evans, 1988; Evans et al., 1990). Creep occurs at temperatures where the matrix softens but where the fibers are still hard and although the deformation is nominally in bending, the behavior of the material is very different to that of a monolithic material. When an inelastic shape change is imposed on the composite, the deformation is accommodated by shear in the matrix in directions constrained to be parallel to the fiber directions. The constraints arise because the fiber lengths can change only a little during deformation. When this is taken to the limit, the concept of an *ideal fiber-reinforced material* (IFRM) arises (Adkins and Rivlin, 1956; Mulhearn et al., 1967; Pipkin and Rogers 1971a,b; Spencer, 1972; Rogers, 1981), in which the material is treated as a continuum having the property of being inextensible in the fiber directions. The kinematic constraints that inextensibility places on the deformation were systematically investigated by Pipkin and Rogers (1971a,b). Interestingly, the constraints make the solution for the stresses relatively simple compared to other inelastic, large strain problems but an important feature of IFRM behavior is the occurrence of stress singularities after deformation. For instance, tensile stresses are infinite in the surface layers of an IFRM beam which has undergone plastic deformation. The concentration of stress in this way has been termed stress channelling (Everstine and Pipkin, 1979; Rogers, 1981) and its appearance has been associated with the breakdown of St. Venant's principle in an IFRM. The stress distribution in an IFRM beam is shown schematically in Fig. 1, contrasted with the stress distribution in an isotropic elastic beam.

In practice, deformation by creep of a fiber composite beam in bending involves an evolution in behavior, where the material starts out as mildly orthotropic elastic but proceeds to develop characteristics which foreshadow the IFRM limit as deformation develops. Deformation without catastrophic fracture has been observed in some of the experiments, but this poses a problem in linking the observations with the IFRM model because of the surface stress singularities which feature in the latter. The experimental observations suggest that the evolution of the stress distribution might be gradual, allowing large-scale deformation to occur before the maximum stress has grown too large. This point is investigated in the present work using a simple linear continuum model to deduce the change in stress distribution which occurs with time and deformation.

2 A Simplified Continuum Model

In order to model deformation of a fiber composite in bending we draw on the elegant analysis of Hu et al. (1985) of the elastic deformation of orthotropic beams. Consider a simple

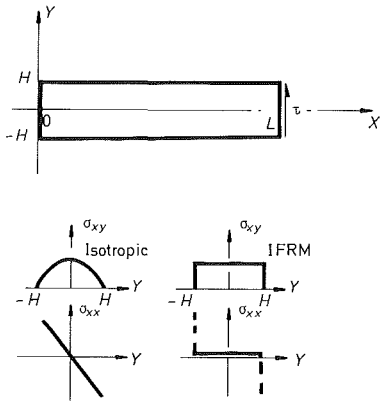


Fig. 1 Tip-loaded cantilever beam and schematic illustration of the stress distributions in an isotropic elastic and IFRM material

Contributed by the Applied Mechanics Division of THE AMERICAN SOCIETY OF MECHANICAL ENGINEERS for publication in the ASME JOURNAL OF APPLIED MECHANICS.

Discussion on this paper should be addressed to the Technical Editor, Prof. Lewis T. Wheeler, Department of Mechanical Engineering, University of Houston, Houston, TX 77204-4792, and will be accepted until four months after final publication of the paper itself in the ASME JOURNAL OF APPLIED MECHANICS.

Manuscript received by the ASME Applied Mechanics Division, Sept. 5, 1991; final revision, Feb. 26, 1992. Associate Technical Editor: G. J. Dvorak.

Copyright © 1993 by ASME
Downloaded 03 May 2010 to 171.66.16.245. Redistribution subject to ASME license or copyright; see http://www.asme.org/terms/Terms_Use.cfm

cantilever length L, height $2H$ with the X-axis passing through the neutral axis as in Fig. 1 and loaded with the shear traction τ at $X = L$ with a consequent displacement $V(x)$ parallel to the Y-axis. The infinitesimal strain formulation is assumed, and although this is a restriction in that some of the interesting features of the curvature of parts of the beam (Evans, 1988) is not modeled, the important feature of stress channelling is retained. Continuous fibers parallel to the x-axis are considered to be embedded in a matrix which can be soft enough to deform by creep. In line with the previous theoretical work, the distinction between fibers and matrix is not made explicit in the model. Instead, the beam is considered to be a continuum with attributes which model the presence of the fibers, i.e., the beam has Young's modulus E parallel to the fibers in the x-direction and a shear modulus μ which is regarded as being independently variable. In fact, the Young's modulus is determined by the rule of mixtures and is dominated by the properties of the fibers at high volume fractions. Consequently we do not expect much change in E if the matrix softens. In contrast, μ strongly reflects the properties of the matrix and will fall proportionately if the matrix is softened by some means. The composite also has the capacity to deform permanently in shear because of deformation in the matrix. To model this we envisage the following constitutive relation affecting only the shear stress σ_{xy} and strain e_{xy}

$$\frac{\dot{\sigma}_{xy}}{\mu} + A\sigma_{xy} = 2\dot{e}_{xy}, \tag{1}$$

where the dots represent differentiation with respect to time t and A is a constant with the dimensions of inverse viscosity. The constitutive relation in (1) is typical of a viscoelastic fluid, but it could also be taken to represent diffusional creep at high temperatures by the Herring-Nabarro or Coble mechanisms (Nabarro, 1948; Herring, 1950; Coble, 1963; Frost and Ashby, 1972). Equation (1) can be written in integral form

$$\bar{\sigma}_{xy} = 2\bar{\mu}\bar{e}_{xy} \tag{2}$$

where the bar denotes the Laplace transform[1], s is the transformed time and $\bar{\mu}$ is given below. According to the well-known *correspondence principle* (e.g., Lee, 1955; Pipkin, 1979), the time-dependent solution can be obtained by substituting the Laplace-transformed quantities into the conventional, elastic solution. In the present case these are

$$\begin{aligned} \bar{\tau} &= \tau/s, \\ \bar{E} &= E, \\ \bar{\mu} &= \mu s/(s+\mu A), \\ \bar{\epsilon} &= \epsilon\sqrt{s/(s+\mu A)}, \end{aligned} \tag{3}$$

where ϵ is the anisotropy ratio defined by

$$\epsilon = \sqrt{\mu/E}. \tag{4}$$

The elastic solution for a beam in cantilever bending is now examined with a view to using this method.

As a first step we seek an elastic solution for a beam composed of a material with the properties described above, i.e., the shear and Young's moduli (μ and E) are independently variable and the properties are characterized by the anisotropy ratio ϵ (Pipkin, 1979; Hu et al., 1985). An approximate first-order solution is given by the Timoshenko beam, which is now shown to be adequate for calculating the displacements but inadequate for the stresses. In order to simplify the analysis the following dimensionless variables are introduced:

$$\begin{aligned} x &= X/H, \\ y &= Y/H, \\ l &= L/H, \\ v(x) &= V(x)/L. \end{aligned} \tag{5}$$

The displacement of the tip of the beam $v^T(l)$ and the two stresses σ^T_{xx} and σ^T_{xy} for the Timoshenko beam are given by the expressions

$$\begin{aligned} v^T(l) &= kl\tau/\mu + l^3\tau/E, \\ \sigma^T_{xx} &= -3\tau y(l-x), \\ \sigma^T_{xy} &= \frac{3}{2}\tau(1-y^2), \end{aligned} \tag{6}$$

in which k is a shear factor of the order of unity. It is clear by inspection of (2), (3), and (6) that the displacement of a Timoshenko beam with the properties defined by (2) is time dependent but that the stresses are not because the elastic constants do not enter into the latter two expressions. This conclusion is at variance with the assumption stated above, that the stresses in the beam move towards the IFRM limit as the shear component of the deformation increases. The discrepancy arises because the Timoshenko beam does not correctly incorporate the end boundary conditions. A higher order approximation was given by Hu et al. (1985) in the form of additional terms (denoted here by the superscripts e) superimposed on the Timoshenko solution, i.e.,

$$\begin{aligned} v(l) &= v^T(l) + v^e(l), \\ \sigma_{xx} &= \sigma^T_{xx} + \sigma^e_{xx}, \\ \sigma_{xy} &= \sigma^T_{xy} + \sigma^e_{xy}. \end{aligned} \tag{7}$$

Expressions for the correction terms have been given by Hu et al. in the form

$$\begin{aligned} v^e(l) &= -(2\tau)/(\mu\epsilon)S_1(l, \epsilon), \\ \sigma^e_{xx} &= -(2\tau/\epsilon)S_2(x, y, l, \epsilon), \\ \sigma^e_{xy} &= 2\tau S_3(x, y, l, \epsilon), \end{aligned} \tag{8}$$

where S_1, S_2, and S_3 represent the infinite series shown in the Appendix. This solution more accurately describes the stresses in the beam although this is at the expense of introducing a singularity at $x = 0$, $y = \pm h$, where the series for σ^e_{xx} fails to converge.

The elastic solution given by (6), (7), and (8) can now be used to obtain the time-dependent solution by substituting the transformed constants in (3). In principle, the solution is completed by finding the inverse Laplace transform of the expressions for $v(l)$, σ_{xx}, and σ_{xy}. Unfortunately, this is not easy to do analytically in the present case because of the infinite series in the correction terms in (8). However, there are two additional approximations which can be made to produce a useful result. These are:

(i) the correction $v^e(l)$ of the Timoshenko displacement is always very small (Hu et al., 1985) and can be ignored for cases of interest. Inversion of the Laplace-transformed expression is then routine and gives

$$v(l) = v_0 + k\tau At, \tag{9}$$

where v_0 is the initial displacement at $t = 0$. Thus the displacement is linear in time, directly reflecting the behavior of the matrix.

(ii) The transform of σ^e_{xx} is

[1] e.g., $\bar{\sigma}_{xy} = \int_0^\infty \sigma_{xy} e^{-st} dt$

Downloaded 03 May 2010 to 171.66.16.245. Redistribution subject to ASME license or copyright; see http://www.asme.org/terms/Terms_Use.cfm

Table 1 Constants obtained from the curve fit (Eq. (14))

y	K	p
1	5.047	0.531
0.99	4.908	0.430

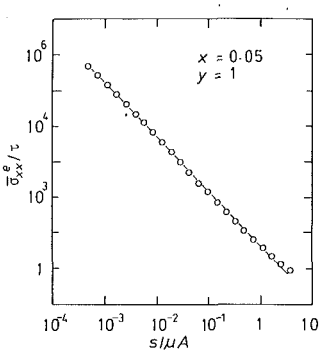


Fig. 2 Logarithmic plot of the transformed tensile stress σ^e_{xx} versus transformed time s, $x = 0.05$, $y = 1$

$$\bar{\sigma}^e_{xx} = -2\tau \frac{\sqrt{s+A}}{s^{3/2}} S_2(x, y, l, \epsilon). \tag{10}$$

The tensile stress near the surface of the beam at $y = \pm 1$ is of the most interest because the IFRM analysis shows a singularity on the boundary layer. But as shown below, the stress in this region can be represented in the form

$$\sigma_{xx} = \sigma^T_{xx} + K(\mu A t)^p \tag{11}$$

for large t and small x, where $p \approx 1/2$ at $y = 1$. Numerical estimates of σ_{xx} are made below, but an interesting conclusion follows from these approximations: the stress in a deforming beam increases at a slower rate than the displacement. Specifically, we deduce that at large times

$$v(l) \propto t, \quad \sigma_{xx} \propto t^{1/2}. \tag{12}$$

This is important in practice because it indicates the possibility that the approach towards the IFRM limit which accompanies creep deformation is relatively gentle with regard to the development of stress channelling. In other words, the simple analytical model indicates that a large displacement might occur without the intervention of catastrophic fracture. This is in qualitative agreement with experimental observation since large bending deformations have been produced in creep of composite beams while avoiding catastrophic fracture (Evans, 1988; Evans et al., 1990). The results of the numerical calculations are discussed in the next section.

3 Results

The deformation of a beam with ratio $L/H = 5$ and $\epsilon = 0.5$ was investigated. The estimates reported in the Appendix imply that $\bar{\sigma}^e_{xx}$ behaves as a negative power of s at small s (large t) when $y \approx 1$, i.e., we take the relation between $\bar{\sigma}^e_{xx}$ and s to be of the following form:

$$\bar{\sigma}^e_{xx} \simeq K_1 \left[\frac{s}{\mu A}\right]^{-\nu}. \tag{13}$$

The inverse transform of Eq. (13) is then

$$\sigma^e_{xx} = K(\mu A t)^p, \tag{14}$$

where $p = 1 - \nu$, $K = K_1/\Gamma(1 + p)$ and Γ is the gamma function. Values of K and p were obtained by plotting calculated values of $\bar{\sigma}^e_{xx}$ against s. An example is shown in Fig. 2, where $\bar{\sigma}^e_{xx}$ evaluated at $y = 1$ is shown as a function of s on logarithmic scales. A reasonable fit to a power-law relation was obtained by this method and values of K and p at the points $x = 0.05$, $y = 0.99$, and $y = 1$ are given in Table 1. Pronounced stress channelling develops as deformation proceeds as illustrated in Fig. 3 where σ_{xx}/τ at points near the surface is shown as a function of dimensionless time, $\mu A t$. The stress at a point on the surface diverges increasingly from that just below the surface with increasing time.

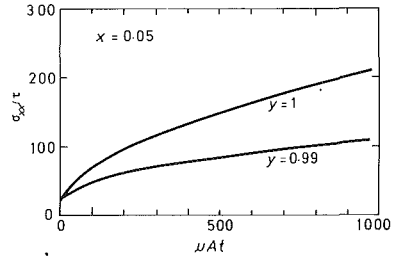


Fig. 3 Curves illustrating the development of stress channelling with time. Dimensionless tensile stress at $x = 0.05$, $y = 1$ and $y = 0.99$ as a function of dimensionless time $\mu A t$.

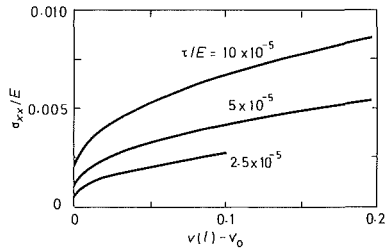


Fig. 4 Tensile stress at $x = 0.05$, $y = 0.99$ as a function of the time-dependent displacement, showing the effect of varying applied shear traction τ

Finally, since the displacement increases linearly with time (Eq. (9)), stress channelling can also be represented as a function of deformation. Figure 4, for instance, shows the effect of loading on the relation between σ_{xx} and displacement. As expected, the stress increases with increasing deformation but at a rate which depends on the applied shear traction. Thus large tensile stresses will develop after a displacement of between 10 to 20 percent of the beam length in a metal-matrix composite because a large load is required to produce observable deformation in a finite time. In contrast, large deformations with low stresses can be attained in a composite with a matrix with the viscosity typical of that of a viscous liquid (e.g., an uncured prepreg or a thermoplastic-matrix composite at a temperature near the melting point of the matrix) because the load required to produce the deformation will be small.

4 Discussion

The model shows that creep in a fiber composite in bending can be understood in a simply way. The stiff fibers, which do not soften at the temperature of testing remain largely unchanged in length as deformation occurs so that the creep deflection is produced by shear rather than tensile extension and compression of the fibers. As discussed by Pipkin and Rogers (1979a,b), a wide range of deformed shapes are possible with this form of deformation. In the IFRM model, fibers are assumed to infinitesimally thin although capable of supporting a tensile force. In practice, fibers with diameters in the range 10 to 20 μm behave in a way which closely approximates to the IFRM assumptions and metal matrix composites, for example, can be bent into a circular form by a combination of

Downloaded 03 May 2010 to 171.66.16.245. Redistribution subject to ASME license or copyright; see http://www.asme.org/terms/Terms_Use.cfm

shear deformation by creep in the matrix and individual bending of the fibers. An example is given in Fig. 5 which shows a metal-matrix composite after creep deformation at 300°C; to all intents and purposes the fibers have remained unstretched although they have slipped past one another following permanent shear deformation in the matrix. The ease of shear deformation largely reflects the properties of the matrix, which has here been characterized by a simple constitutive equation of the type shown in (1). The creep deflection of the tip-loaded cantilever in Fig. 1 can thus be understood in very simple terms, but the change in stress distribution which accompanies deformation is more complicated. It can be explained on the theory developed by Pipkin and his co-workers (Pipkin, 1979; Everstine and Pipkin, 1979; Hu et al., 1985). This shows that the conventional (Timoshenko) expressions for the stresses are perturbed by the end corrections. Normally end corrections are not considered to be of great importance in beam bending because of the operation of St. Venant's principle. With increasing anisotropy (reduction in ϵ) St. Venant's principle begins to break down and the so-called end corrections begin to influence the general behavior of the beam. The effect is equivalent in some ways to an expansion of the y-axis or an effective shortening of the beam (Pipkin, 1979). On the other hand, as was discussed by Hu et al. (1985), there are generally no great practical consequences in cases of elastic deformation, even for a material as anisotropic as carbon fiber reinforced polymer. A much larger effect accompanies creep in the matrix as could happen in metal-matrix or thermoplastic-matrix composites at elevated temperatures. As the creep deformation increases the end-affected regions expand until finally the whole beam is influenced. The expansion is associated with a flattening out of the shear stress distribution in the y-direction and concentration of tensile stress in the surface layers of the beam. These changes foreshadow the stress distributions which obtain in the limit of IFRM behavior, where the material is assumed to be inextensible in the fiber directions.

The present model predicts that the tensile stresses in a deforming beam rise more slowly with time than the deflection. This in line with the experimental observation that detectable deformation can be achieved before the stress is large enough to produce catastrophic fracture (Evans, 1988; Evans et al., 1990). More generally though, the pronounced increase in the concentration of stress at the surface is likely to produce time-dependent fracture. Since most engineering components are subjected to bending moments in service, an extension of the present model might be useful in the life prediction of fiber composites at elevated temperatures. This cannot be realistically considered on the basis of the present model because of its extreme simplicity particularly in view of the fact that a linear constitutive Eq. (2) is assumed. To go beyond this point requires generalization to constitutive equation of the power-law type which can only be undertaken with finite element modeling (Wang, 1991).

5 Summary

(1) A simple, linear model of creep in a fiber composite beam treated as a continuum has been presented.

(2) The model predicts that the displacement of the beam increases linearly with time at a rate proportional to the applied load.

(3) The model shows the development of stress channelling with time, as is expected from previous work, but the stress is found to increase at a slower rate than the displacement. This observation suggests that significant deformation might occur without fracture in some circumstances.

(4) A generalization of the model to include a nonlinear constitutive law might be useful in the life prediction of composites at elevated temperatures.

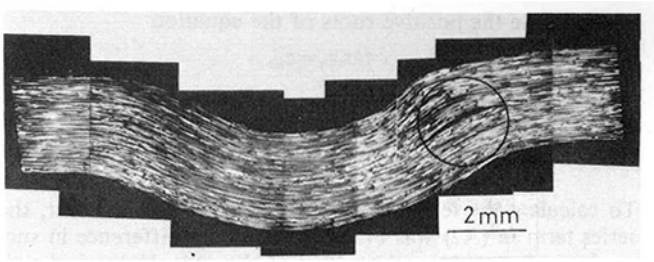


Fig. 5 A magnesium alloy-alumina fiber composite bent to a circular form by creep at 300°C. The fibers remain sensibly inextensible during deformation.

Acknowledgments

The author wishes to acknowledge useful discussion and advice given by H. W. Chandler and N. S. Clarke in the preparation of this work.

References

Adkins, J. E., and Rivlin, R. S., 1956, "Large Elastic Deformations of Isotropic Materials X. Reinforcement by Inextensible Cords," *Phil. Trans. R. Soc.*, Vol. A248, pp. 201–223.

Coble, R. L., 1963, "A Model for Boundary Diffusion Controlled Creep in Polycrystalline Materials," *J. Appl. Phys.*, Vol. 34, pp. 1679–1685.

Evans, J. T., 1988, "Bending Deformation of Metal-Matrix Fibre Composites at Elevated Temperatures," *Scripta Metall.*, Vol. 22, pp. 1223–1226.

Evans, J. T., Wang Ningyun and Chandler, W. H., 1990, "Creep of Fibre Composite Beams in Bending," *Acta Metall. Mater.*, Vol. 38, pp. 1565–1572.

Everstine, G. C., and Pipkin, A. C., 1979, "Boundary Layers in Fiber-Reinforced Materials," ASME Journal of Applied Mechanics, Vol. 40, pp. 518–522.

Frost, H. J., and Ashby, M. F., 1972, *Deformation Mechanism Maps*, Pergamon Press.

Herring, C., 1950, "Diffusional Viscosity of a Polycrystalline Solid," *J. Appl. Phys.*, Vol. 21, pp. 437–445.

Hu, M. Z, Kolsky, H., and Pipkin, A. C., 1985, "Bending Theory for Fiber-Reinforced Beams," *J. Composite Mater.*, Vol. 19, pp. 235–249.

Lee, E. H., 1955, "Stress Analysis for Visco-Elastic Bodies," *Quart. Appl. Math.*, Vol. 13, pp. 183–190.

Mulhearn, J. F., Rogers, T. G., and Spencer, A. J. M., 1967, "A Continuum Model for Fibre-Reinforced Plastic Materials," *Proc. Royal Soc.*, Vol. A301, pp. 473–492.

Nabarro, F. R. N., 1948, "Deformation of Crystals by the Motion of Single Ions," *Report on a Conference on the Strength of Solids*, The Physical Society, London.

Pipkin, A. C., 1979a, *Lectures on Viscoelasticity Theory*, Springer-Verlag, New York.

Pipkin, A. C., 1979b, "Stress Analysis for Fiber-Reinforced Materials," *Advances in Applied Mechanics*, Vol. 19, pp. 1–51.

Pipkin, A. C., and Rogers, T. G., 1971a, "Plane Deformations of Incompressible Fiber-Reinforced Materials," ASME Journal of Applied Mechanics, Vol. 38, pp. 634–640.

Pipkin, A. C., and Rogers, T. G., 1971b, "A Mixed Boundary Value Problem for Fibre-Reinforced Materials," *Quart. Appl. Math.*, Vol. 29, pp. 151–155.

Rogers, T. G., 1981, "Finite Deformation of Fibre-Reinforced Materials," *Continuum Theory of the Mechanics of Fibre-Reinforced Composites* (ed. A. J. M. Spencer ed., Springer, Berlin, p. 33.

Spencer, A. J. M., 1972, "Deformation of Fibre-Reinforced Materials," *Oxford Science Research Papers*, Clarendon Press, Oxford.

Wang Ningyun, 1991, "Deformation of Composite Materials," Ph.D. Thesis, University of Newcastle-upon-Tyne, Newcastle upon Tyne U.K.

APPENDIX

The expressions for the power series in Eq. (8) (Hu et al., 1985) are

$$S_1 = \sum_{n=1}^{\infty} z_n^{-3} \tanh(z_n l\epsilon), \tag{A1}$$

$$S_2 = \sum_{n=1}^{\infty} c_n z_n \frac{\sinh(z_n \epsilon[l-x])}{\cosh(z_n l\epsilon)} \sin(z_n y), \tag{A2}$$

$$S_3 = \sum_{n=1}^{\infty} c_n z_n \frac{\cosh(z_n \epsilon[l-x])}{\cosh(z_n l\epsilon)} [\cos(z_n y) - \cos z_n], \tag{A3}$$

Downloaded 03 May 2010 to 171.66.16.245. Redistribution subject to ASME license or copyright; see http://www.asme.org/terms/Terms_Use.cfm

where z_n are the positive roots of the equation

$$\tan z_n = z_n, \tag{A4}$$

and the c_n are given by

$$c_n = \frac{1}{z_n^2 \sin z_n}. \tag{A5}$$

To calculate the tensile stress using Eq. (10) in the text, the series term in (A2) was evaluated until the difference in successive terms was less than 10^{-5} of the sum. Numerical estimates show that at $y \approx 1$ the variation in σ_{xx}^e with s is dominated by the term $(s + A)^{1/2} s^{-3/2}$, with the series term S_2 varying only slowly with s. Treating the series as constant, inversion of (11) gives

$$\sigma_{xx}^e \propto \exp\left(-\frac{1}{2}\mu A t\right)\left[(1+\mu A t) I_0\left(\frac{1}{2}\mu A t\right) + \mu A t I_1\left(\frac{1}{2}\mu A t\right)\right] \tag{A6}$$

where I_0 and I_1 are the modified Bessel functions of zero and first order, respectively. At large t, (A6) can be further simplified with

$$\sigma_{xx}^e \propto 2\sqrt{\frac{\mu A t}{\pi}}\left[1 + \frac{1}{4\mu A t} + \frac{1}{32(\mu A t)^2} + \ldots\right]. \tag{A7}$$

Thus at large t, σ_{xx}^e is approximately proportional to $t^{1/2}$.

Downloaded 03 May 2010 to 171.66.16.245. Redistribution subject to ASME license or copyright; see http://www.asme.org/terms/Terms_Use.cfm

Buckling of Thick Orthotropic Cylindrical Shells Under External Pressure

G. A. Kardomateas
Associate Professor,
School of Aerospace Engineering,
Georgia Institute of Technology,
Atlanta, GA 30332-0150
Mem. ASME

An elasticity solution to the problem of buckling of orthotropic cylindrical shells subjected to external pressure is presented. In this context, the structure is considered a three-dimensional body. The results show that the shell theory predictions can produce nonconservative results on the critical load of composite shells with moderately thick construction. The solution provides a means of accurately assessing the limitations of shell theories in predicting stability loss.

Introduction

A class of important structural applications of fiber-reinforced composite materials involves the configuration of laminated shells. Although thin plate construction has been the thrust of the initial applications, much attention is now being paid to configurations classified as moderately thick shell structures. Such designs can be used in components in the aircraft and automobile industries, as well as in the marine industry. Moreover, composite laminates have been considered in space vehicles in the form of circular cylindrical shells as a primary load carrying structure.

In these light-weight shell structures, loss of stability is of primary concern. This subject has been researched to-date through the application of the cylindrical shell theory (e.g., Simitses, Shaw, and Sheinman, 1985). However, previous work (Pagano and Whitney, 1970; Pagano, 1971) has shown that considerable care must be exercised in applying thin shell theory formulations to predict the response of composite cylinders. Besides the anisotropy, composite shells have one other important distinguishing feature, namely extensional-to-shear modulus ratio much larger than that of their metal counterparts.

In order to more accurately account for the aforementioned effects, various modifications in the classical theory of laminated shells have generally been performed (Whitney and Sun, 1974; Librescu, 1975; Reddy and Liu, 1985; see also Noor and Burton, 1990 for a review of shear deformation theories). These higher-order shell theories can be applied to buckling problems with the potential of improved predictions for the critical load (Anastasiadis, 1990).

However, there has not yet been any effort to produce a solution based on three-dimensional elasticity to the problem of buckling of composite shell structures, against which results from various shell theories could be compared.

Towards this objective, this work presents an elasticity solution to the problem of buckling of composite cylindrical orthotropic shells subjected to external pressure. Numerical results for an example case of a fiber-reinforced hollow cylinder under external pressure are derived and compared with shell theory predictions. These results can be used to assess the accuracy of the classical shell theory and the existing improved shell theories for moderately thick construction.

Formulation

At the critical load there are two possible infinitely close positions of equilibrium. Denote by u_0, v_0, w_0 the r, θ, and z components of the displacement corresponding to the primary position. A perturbed position is denoted by

$$u = u_0 + \alpha u_1; \quad v = v_0 + \alpha v_1; \quad w = w_0 + \alpha w_1, \tag{1}$$

where α is an infinitesimally small quantity. Here, $\alpha u_1(r, \theta, z)$, $\alpha v_1(r, \theta, z)$, $\alpha w_1(r, \theta, z)$ are the displacements to which the points of the body must be subjected to shift them from the initial position of equilibrium to the new equilibrium position. The functions $u_1(r, \theta, z)$, $v_1(r, \theta, z)$, $w_1(r, \theta, z)$ are assumed finite and α is an infinitesimally small quantity independent of r, θ, z.

The nonlinear strain displacement equations are

$$\epsilon_{rr} = \frac{\partial u}{\partial r} + \frac{1}{2}\left[\left(\frac{\partial u}{\partial r}\right)^2 + \left(\frac{\partial v}{\partial r}\right)^2 + \left(\frac{\partial w}{\partial r}\right)^2\right], \tag{2a}$$

$$\epsilon_{\theta\theta} = \frac{1}{r}\frac{\partial v}{\partial \theta} + \frac{u}{r} + \frac{1}{2}\left[\left(\frac{1}{r}\frac{\partial u}{\partial \theta} - \frac{v}{r}\right)^2 + \left(\frac{1}{r}\frac{\partial v}{\partial \theta} + \frac{u}{r}\right)^2 + \left(\frac{1}{r}\frac{\partial w}{\partial \theta}\right)^2\right], \tag{2b}$$

$$\epsilon_{zz} = \frac{\partial w}{\partial z} + \frac{1}{2}\left[\left(\frac{\partial u}{\partial z}\right)^2 + \left(\frac{\partial v}{\partial z}\right)^2 + \left(\frac{\partial w}{\partial z}\right)^2\right], \tag{2c}$$

Contributed by the Applied Mechanics Division of THE AMERICAN SOCIETY OF MECHANICAL ENGINEERS for publication in the ASME JOURNAL OF APPLIED MECHANICS.

Discussion on this paper should be addressed to the Technical Editor, Professor Lewis T. Wheeler, Department of Mechanical Engineering, University of Houston, Houston, TX 77204-4792, and will be accepted until four months after final publication of the paper itself in the ASME JOURNAL OF APPLIED MECHANICS.

Manuscript received by the ASME Applied Mechanics Division, Sept. 12, 1991; final revision, Jan. 27, 1992. Associate Technical Editor: F. Y. M. Wan.

Copyright © 1993 by ASME
Downloaded 03 May 2010 to 171.66.16.245. Redistribution subject to ASME license or copyright; see http://www.asme.org/terms/Terms_Use.cfm

$$\gamma_{r\theta}=\frac{1}{r}\frac{\partial u}{\partial \theta}+\frac{\partial v}{\partial r}-\frac{v}{r}+\left[\frac{\partial u}{\partial r}\left(\frac{1}{r}\frac{\partial u}{\partial \theta}-\frac{v}{r}\right)+\frac{\partial v}{\partial r}\left(\frac{1}{r}\frac{\partial v}{\partial \theta}+\frac{u}{r}\right)+\frac{1}{r}\frac{\partial w}{\partial r}\frac{\partial w}{\partial \theta}\right], \quad (2d)$$

$$\gamma_{rz}=\frac{\partial u}{\partial z}+\frac{\partial w}{\partial r}+\left(\frac{\partial u}{\partial r}\frac{\partial u}{\partial z}+\frac{\partial v}{\partial r}\frac{\partial v}{\partial z}+\frac{\partial w}{\partial r}\frac{\partial w}{\partial z}\right), \quad (2e)$$

$$\gamma_{\theta z}=\frac{\partial v}{\partial z}+\frac{1}{r}\frac{\partial w}{\partial \theta}+\left[\frac{\partial u}{\partial z}\left(\frac{1}{r}\frac{\partial u}{\partial \theta}-\frac{v}{r}\right)+\frac{\partial v}{\partial z}\left(\frac{1}{r}\frac{\partial v}{\partial \theta}+\frac{u}{r}\right)+\frac{1}{r}\frac{\partial w}{\partial \theta}\frac{\partial w}{\partial z}\right]. \quad (2f)$$

Substituting (1) into (2) we find the strain components in the perturbed configuration:

$$\epsilon_{rr}=\epsilon_{rr}^0+\alpha\epsilon_{rr}'+\alpha^2\epsilon_{rr}'' \qquad \gamma_{r\theta}=\gamma_{r\theta}^0+\alpha\gamma_{r\theta}'+\alpha^2\gamma_{r\theta}'', \quad (3a)$$

$$\epsilon_{\theta\theta}=\epsilon_{\theta\theta}^0+\alpha\epsilon_{\theta\theta}'+\alpha^2\epsilon_{\theta\theta}'' \qquad \gamma_{rz}=\gamma_{rz}^0+\alpha\gamma_{rz}'+\alpha^2\gamma_{rz}'', \quad (3b)$$

$$\epsilon_{zz}=\epsilon_{zz}^0+\alpha\epsilon_{zz}'+\alpha^2\epsilon_{zz}'' \qquad \gamma_{\theta z}=\gamma_{\theta z}^0+\alpha\gamma_{\theta z}'+\alpha^2\gamma_{\theta z}'', \quad (3c)$$

where ϵ_{ij}^0 are the values of the strain components in the initial position of equilibrium, ϵ_{ij}' are the strain quantities corresponding to the linear terms, and ϵ_{ij}'' are the ones corresponding to the quadratic terms. These strain quantities are given explicitly in terms of the displacements u_0, v_0, w_0 and u_1, v_1, w_1 in Appendix B.

The stress-strain relations for the orthotropic body are

$$\begin{bmatrix}\sigma_{rr}\\ \sigma_{\theta\theta}\\ \sigma_{zz}\\ \tau_{\theta z}\\ \tau_{rz}\\ \tau_{r\theta}\end{bmatrix}=\begin{bmatrix}c_{11}&c_{12}&c_{13}&0&0&0\\ c_{12}&c_{22}&c_{23}&0&0&0\\ c_{13}&c_{23}&c_{33}&0&0&0\\ 0&0&0&c_{44}&0&0\\ 0&0&0&0&c_{55}&0\\ 0&0&0&0&0&c_{66}\end{bmatrix}\begin{bmatrix}\epsilon_{rr}\\ \epsilon_{\theta\theta}\\ \epsilon_{zz}\\ \gamma_{\theta z}\\ \gamma_{rz}\\ \gamma_{r\theta}\end{bmatrix}, \quad (4)$$

where c_{ij} are the stiffness constants (we have used the notation $1 \equiv r$, $2 \equiv \theta$, $3 \equiv z$). Substituting (3) into (4) we get the stresses as

$$\sigma_{rr}=\sigma_{rr}^0+\alpha\sigma_{rr}'+\alpha^2\sigma_{rr}'' \qquad \tau_{r\theta}=\tau_{r\theta}^0+\alpha\tau_{r\theta}'+\alpha^2\tau_{r\theta}'', \quad (5a)$$

$$\sigma_{\theta\theta}=\sigma_{\theta\theta}^0+\alpha\sigma_{\theta\theta}'+\alpha^2\epsilon_{\theta\theta}'' \qquad \tau_{rz}=\tau_{rz}^0+\alpha\tau_{rz}'+\alpha^2\tau_{rz}'', \quad (5b)$$

$$\sigma_{zz}=\sigma_{zz}^0+\alpha\sigma_{zz}'+\alpha^2\sigma_{zz}'' \qquad \tau_{\theta z}=\tau_{\theta z}^0+\alpha\tau_{\theta z}'+\alpha^2\tau_{\theta z}'', \quad (5c)$$

where σ_{ij}^0, σ_{ij}', σ_{ij}'', are expressed in terms of ϵ_{ij}^0, ϵ_{ij}', ϵ_{ij}'', respectively, in the same manner as Eqs. (4) for σ_{ij} in terms of ϵ_{ij}.

In the following we shall keep in (5) and (3) terms up to α, i.e., we neglect the terms which contain α^2.

Governing Equations. The equations of equilibrium are taken in terms of the second Piola-Kirchhoff stress tensor $\mathbf{\Sigma}$ the form

$$\operatorname{div}(\mathbf{\Sigma}\cdot\mathbf{F}^{\mathrm{T}})=0, \quad (6a)$$

where $\mathbf{F}$ is the deformation gradient defined by

$$\mathbf{F}=\mathbf{I}+\operatorname{grad} V, \quad (6b)$$

where V is the displacement vector and $\mathbf{I}$ is the identity tensor.

Notice that the strain tensor is defined by

$$\mathbf{E}=\frac{1}{2}(\mathbf{F}^{\mathrm{T}}\cdot\mathbf{F}-\mathbf{I}). \quad (6c)$$

More specifically, in terms of the linear strains,

$$e_{rr}=\frac{\partial u}{\partial r}, \quad e_{\theta\theta}=\frac{1}{r}\frac{\partial v}{\partial \theta}+\frac{u}{r}, \quad e_{zz}=\frac{\partial w}{\partial z}, \quad (7a)$$

$$e_{r\theta}=\frac{1}{r}\frac{\partial u}{\partial \theta}+\frac{\partial v}{\partial r}-\frac{v}{r}, \quad e_{rz}=\frac{\partial u}{\partial z}+\frac{\partial w}{\partial r}, \quad e_{\theta z}=\frac{\partial v}{\partial z}+\frac{1}{r}\frac{\partial w}{\partial \theta}, \quad (7b)$$

and the linear rotations,

$$2\omega_r=\frac{1}{r}\frac{\partial w}{\partial \theta}-\frac{\partial v}{\partial z}, \quad 2\omega_\theta=\frac{\partial u}{\partial z}-\frac{\partial w}{\partial r}, \quad 2\omega_z=\frac{\partial v}{\partial r}+\frac{v}{r}-\frac{1}{r}\frac{\partial u}{\partial \theta}, \quad (7c)$$

the deformation gradient $\mathbf{F}$ is

$$\mathbf{F}=\begin{bmatrix}1+e_{rr}&\frac{1}{2}e_{r\theta}-\omega_z&\frac{1}{2}e_{rz}+\omega_\theta\\ \frac{1}{2}e_{r\theta}+\omega_z&1+e_{\theta\theta}&\frac{1}{2}e_{\theta z}-\omega_r\\ \frac{1}{2}e_{rz}-\omega_\theta&\frac{1}{2}e_{\theta z}+\omega_r&1+e_{zz}\end{bmatrix} \quad (8)$$

and the equilibrium Eq. (6a) gives

$$\frac{\partial}{\partial r}\left[\sigma_{rr}(1+e_{rr})+\tau_{r\theta}\left(\frac{1}{2}e_{r\theta}-\omega_z\right)+\tau_{rz}\left(\frac{1}{2}e_{rz}+\omega_\theta\right)\right]+\frac{1}{r}\frac{\partial}{\partial \theta}\left[\tau_{r\theta}(1+e_{rr})+\sigma_{\theta\theta}\left(\frac{1}{2}e_{r\theta}-\omega_z\right)+\tau_{\theta z}\left(\frac{1}{2}e_{rz}+\omega_\theta\right)\right]+\frac{\partial}{\partial z}\left[\tau_{rz}(1+e_{rr})+\tau_{\theta z}\left(\frac{1}{2}e_{r\theta}-\omega_z\right)+\sigma_{zz}\left(\frac{1}{2}e_{rz}+\omega_\theta\right)\right]+\frac{1}{r}\left[\sigma_{rr}(1+e_{rr})-\sigma_{\theta\theta}(1+e_{\theta\theta})+\tau_{rz}\left(\frac{1}{2}e_{rz}+\omega_\theta\right)-\tau_{\theta z}\left(\frac{1}{2}e_{\theta z}-\omega_r\right)-2\tau_{r\theta}\omega_z\right]=0, \quad (9a)$$

$$\frac{1}{r}\frac{\partial}{\partial \theta}\left[\tau_{r\theta}\left(\frac{1}{2}e_{r\theta}+\omega_z\right)+\sigma_{\theta\theta}(1+e_{\theta\theta})+\tau_{\theta z}\left(\frac{1}{2}e_{\theta z}-\omega_r\right)\right]+\frac{\partial}{\partial z}\left[\tau_{rz}\left(\frac{1}{2}e_{r\theta}+\omega_z\right)+\tau_{\theta z}(1+e_{\theta\theta})+\sigma_{zz}\left(\frac{1}{2}e_{\theta z}-\omega_r\right)\right]+\frac{\partial}{\partial r}\left[\sigma_{rr}\left(\frac{1}{2}e_{r\theta}+\omega_z\right)+\tau_{r\theta}(1+e_{\theta\theta})+\tau_{rz}\left(\frac{1}{2}e_{\theta z}-\omega_r\right)\right]+\frac{1}{r}\left[\sigma_{rr}\left(\frac{1}{2}e_{r\theta}+\omega_z\right)+\sigma_{\theta\theta}\left(\frac{1}{2}e_{r\theta}-\omega_z\right)+\tau_{rz}\left(\frac{1}{2}e_{\theta z}-\omega_r\right)+\tau_{\theta z}\left(\frac{1}{2}e_{rz}+\omega_\theta\right)+\tau_{r\theta}(2+e_{rr}+e_{\theta\theta})\right]=0, \quad (9b)$$

$$\frac{\partial}{\partial z}\left[\tau_{rz}\left(\frac{1}{2}e_{rz}-\omega_\theta\right)+\tau_{\theta z}\left(\frac{1}{2}e_{\theta z}+\omega_r\right)+\sigma_{zz}(1+e_{zz})\right]+\frac{\partial}{\partial r}\left[\sigma_{rr}\left(\frac{1}{2}e_{rz}-\omega_\theta\right)+\tau_{r\theta}\left(\frac{1}{2}e_{\theta z}+\omega_r\right)+\tau_{rz}(1+e_{zz})\right]+\frac{1}{r}\frac{\partial}{\partial \theta}\left[\tau_{r\theta}\left(\frac{1}{2}e_{rz}-\omega_\theta\right)+\sigma_{\theta\theta}\left(\frac{1}{2}e_{\theta z}+\omega_r\right)+\tau_{\theta z}(1+e_{zz})\right]+\frac{1}{r}\left[\sigma_{rr}\left(\frac{1}{2}e_{rz}-\omega_\theta\right)+\tau_{r\theta}\left(\frac{1}{2}e_{\theta z}+\omega_r\right)+\tau_{rz}(1+e_{zz})\right]=0. \quad (9c)$$

Introducing the linear strains and rotations in the form (3), e.g., $e_{rr}=e_{rr}^0+\alpha e_{rr}'$, $\omega_z=\omega_z^0+\alpha\omega_z'$, as well as the stresses from (5) and keeping up to α^1 terms, we obtain a set of equations for the perturbed state in terms of the e_{ij}^0, ω_j^0 and e_{ij}', ω_j'. Notice that in addition to the notations we adopted earlier, e_{ij}^0 and ω_j^0 are the values of e_{ij} and ω_j for $u = u_0$, $v = v_0$ and $w = w_0$ and e_{ij}' and ω_j' are the values for $u = u_1$, $v = v_1$ and $w = w_1$.

Since the displacements u_0, v_0, w_0, correspond to positions of equilibrium, there must exist also equations of the form (9) with the zero superscript, which are obtained by referring (6a) to the initial position of equilibrium.

Downloaded 03 May 2010 to 171.66.16.245. Redistribution subject to ASME license or copyright; see http://www.asme.org/terms/Terms_Use.cfm

Thus, after subtracting the equilibrium equations at the perturbed and initial positions, we arrive at a system of homogeneous differential equations which are linear in the derivatives of u_1, v_1 and w_1 with respect to r, θ, z. This follows from the fact that σ'_{ij}, e'_{ij}, ω'_j appear linearly in the equation, and are themselves, in virtue of (7), linear functions of these derivatives. The system of equations, corresponding to (9), at the initial position of equilibrium, is, on the other hand, nonlinear in the derivatives of u_0, v_0, w_0. However, if we make the additional assumption to neglect the terms that have e^0_{ij} and ω^0_j as coefficients, i.e., terms $e^0_{ij}\sigma^0_{ij}$ and $\omega^0_j\sigma^0_{ij}$, we can use the linear classical equilibrium equations to solve for the initial position of equilibrium.

Moreover, if we make the assumption to neglect the terms that have e^0_{ij} and ω^0_j as coefficients, i.e., terms $e^0_{ij}\sigma'_{ij}$ and $\omega^0_j\sigma'_{ij}$ and furthermore, since a characteristic feature of stability problems is the shift from positions with small rotations to positions with rotations substantially exceeding the strains, if we neglect the terms $e'_{ij}\sigma^0_{ij}$ thus keeping only the $\omega'_j\sigma^0_{ij}$ terms, we obtain the following buckling equations:

$$\frac{\partial}{\partial r}(\sigma'_{rr}-\tau^0_{r\theta}\omega'_z+\tau^0_{rz}\omega'_\theta)+\frac{1}{r}\frac{\partial}{\partial\theta}(\tau'_{r\theta}-\sigma^0_{\theta\theta}\omega'_z+\tau^0_{\theta z}\omega'_\theta)+\frac{\partial}{\partial z}(\tau'_{rz}-\tau^0_{\theta z}\omega'_z+\sigma^0_{zz}\omega'_\theta)+\frac{1}{r}(\sigma'_{rr}-\sigma'_{\theta\theta}+\tau^0_{rz}\omega'_\theta+\tau^0_{\theta z}\omega'_r-2\tau^0_{r\theta}\omega'_z)=0, \quad (10a)$$

$$\frac{\partial}{\partial r}(\tau'_{r\theta}+\sigma^0_{rr}\omega'_z-\tau^0_{rz}\omega'_r)+\frac{1}{r}\frac{\partial}{\partial\theta}(\sigma'_{\theta\theta}+\tau^0_{r\theta}\omega'_z-\tau^0_{\theta z}\omega'_r)+\frac{\partial}{\partial z}(\tau'_{\theta z}+\tau^0_{rz}\omega'_z-\sigma^0_{zz}\omega'_r)+\frac{1}{r}(2\tau'_{r\theta}+\sigma^0_{rr}\omega'_z-\sigma^0_{\theta\theta}\omega'_z+\tau^0_{\theta z}\omega'_\theta-\tau^0_{rz}\omega'_r)=0, \quad (10b)$$

$$\frac{\partial}{\partial r}(\tau'_{rz}-\sigma^0_{rr}\omega'_\theta+\tau^0_{r\theta}\omega'_r)+\frac{1}{r}\frac{\partial}{\partial\theta}(\tau'_{\theta z}-\tau^0_{r\theta}\omega'_\theta+\sigma^0_{\theta\theta}\omega'_r)+\frac{\partial}{\partial z}(\sigma'_{zz}-\tau^0_{rz}\omega'_\theta+\tau^0_{\theta z}\omega'_r)+\frac{1}{r}(\tau'_{rz}-\sigma^0_{rr}\omega'_\theta+\tau^0_{r\theta}\omega'_r)=0. \quad (10c)$$

Boundary Conditions. The boundary conditions associated with (6a) can be expressed as

$$(\mathbf{F}\cdot\Sigma^{\mathrm{T}})\cdot\hat{n}=t(V), \quad (11)$$

where t is the traction vector on the surface which has outward unit normal $\hat{n}=(l, m, n)$ before any deformation. The traction vector t depends on the displacement field $V=(u, v, w)$. Indeed, because of the hydrostatic pressure loading, the magnitude of the surface load remains invariant under deformation, but its direction changes (since hydrostatic pressure is always directed along the normal to the surface on which it acts).

This gives

$$\left[\sigma_{rr}(1+e_{rr})+\tau_{r\theta}\left(\frac{1}{2}e_{r\theta}-\omega_z\right)+\tau_{rz}\left(\frac{1}{2}e_{rz}+\omega_\theta\right)\right]l+\left[\tau_{r\theta}(1+e_{rr})+\sigma_{\theta\theta}\left(\frac{1}{2}e_{r\theta}-\omega_z\right)+\tau_{\theta z}\left(\frac{1}{2}e_{rz}+\omega_\theta\right)\right]m+\left[\tau_{rz}(1+e_{rr})+\tau_{\theta z}\left(\frac{1}{2}e_{r\theta}-\omega_z\right)+\sigma_{zz}\left(\frac{1}{2}e_{rz}+\omega_\theta\right)\right]n=t_r, \quad (12a)$$

$$\left[\sigma_{rr}\left(\frac{1}{2}e_{r\theta}+\omega_z\right)+\tau_{r\theta}(1+e_{\theta\theta})+\tau_{rz}\left(\frac{1}{2}e_{\theta z}-\omega_r\right)\right]l+\left[\tau_{r\theta}\left(\frac{1}{2}e_{r\theta}+\omega_z\right)+\sigma_{\theta\theta}(1+e_{\theta\theta})+\tau_{\theta z}\left(\frac{1}{2}e_{\theta z}-\omega_r\right)\right]m+\left[\tau_{rz}\left(\frac{1}{2}e_{r\theta}+\omega_z\right)+\tau_{\theta z}(1+e_{\theta\theta})+\sigma_{zz}\left(\frac{1}{2}e_{\theta z}-\omega_r\right)\right]n=t_\theta, \quad (12b)$$

$$\left[\sigma_{rr}\left(\frac{1}{2}e_{rz}-\omega_\theta\right)+\tau_{r\theta}\left(\frac{1}{2}e_{\theta z}+\omega_r\right)+\tau_{rz}(1+e_{zz})\right]l+\left[\tau_{r\theta}\left(\frac{1}{2}e_{rz}-\omega_\theta\right)+\sigma_{\theta\theta}\left(\frac{1}{2}e_{\theta z}+\omega_r\right)+\tau_{\theta z}(1+e_{zz})\right]m+\left[\tau_{rz}\left(\frac{1}{2}e_{rz}-\omega_\theta\right)+\tau_{\theta z}\left(\frac{1}{2}e_{\theta z}+\omega_r\right)+\sigma_{zz}(1+e_{zz})\right]n=t_z. \quad (12c)$$

If we write these equations for the initial and the perturbed equilibrium position and then subtract them and use the previous arguments on the relative magnitudes of the rotations ω'_j we obtain

$$(\sigma'_{rr}-\tau^0_{r\theta}\omega'_z+\tau^0_{rz}\omega'_\theta)l+(\tau'_{r\theta}-\sigma^0_{\theta\theta}\omega'_z+\tau^0_{\theta z}\omega'_\theta)m+(\tau'_{rz}-\tau^0_{\theta z}\omega'_z+\sigma^0_{zz}\omega'_\theta)n=\lim_{\alpha\to 0}\left\{\frac{1}{\alpha}[t_r(V_0+\alpha V_1)-t_r(V_0)]\right\}, \quad (13a)$$

$$(\tau'_{r\theta}+\sigma^0_{rr}\omega'_z-\tau^0_{rz}\omega'_r)l+(\sigma'_{\theta\theta}+\tau^0_{r\theta}\omega'_z-\tau^0_{\theta z}\omega'_r)m+(\tau'_{\theta z}+\tau^0_{rz}\omega'_z-\sigma^0_{zz}\omega'_r)n=\lim_{\alpha\to 0}\left\{\frac{1}{\alpha}[t_\theta(V_0+\alpha V_1)-t_\theta(V_0)]\right\}, \quad (13b)$$

$$(\tau'_{rz}+\tau^0_{r\theta}\omega'_r-\sigma^0_{rr}\omega'_\theta)l+(\tau'_{\theta z}+\sigma^0_{\theta\theta}\omega'_r-\tau^0_{r\theta}\omega'_\theta)m+(\sigma'_{zz}+\tau^0_{\theta z}\omega'_r-\tau^0_{rz}\omega'_\theta)n=\lim_{\alpha\to 0}\left\{\frac{1}{\alpha}[t_z(V_0+\alpha V_1)-t_z(V_0)]\right\}. \quad (13c)$$

Let $\hat{n}^0$ and $\hat{n}^1$ denote the normal unit vectors to the bounding surface at the initial and perturbed positions of equilibrium, respectively. Before any deformation, this vector is $\hat{n}=(l, m, n)$. For external pressure p loading at the initial position

$$t_r(V_0)=-p\cos(\hat{n}^0,\hat{r}); \quad t_\theta(V_0)=-p\cos(\hat{n}^0,\hat{\theta}); \quad t_z(V_0)=-p\cos(\hat{n}^0,\hat{z}), \quad (14a)$$

and at the perturbed position

$$t_r(V_0+\alpha V_1)=-p\cos(\hat{n}^1,\hat{r}); \quad t_\theta(V_0+\alpha V_1)=-p\cos(\hat{n}^1,\hat{\theta}); \quad t_z(V_0+\alpha V_1)=-p\cos(\hat{n}^1,\hat{z}). \quad (14b)$$

But in terms of the deformation gradient

$$\mathbf{F}^{0,1}\cdot\hat{n}=(1+E^{0,1}_n)\hat{n}^{0,1}, \quad (15)$$

where E^0_n, E^1_n is the relative elongation normal to the bounding surface at the initial and perturbed equilibrium positions, respectively. More explicitly,

$$\cos(\hat{n}^0,\hat{r})=\frac{1}{1+E^0_n}\left[(1+e^0_{rr})l+\left(\frac{1}{2}e^0_{r\theta}-\omega^0_z\right)m+\left(\frac{1}{2}e^0_{rz}+\omega^0_\theta\right)n\right], \quad (16a)$$

Downloaded 03 May 2010 to 171.66.16.245. Redistribution subject to ASME license or copyright; see http://www.asme.org/terms/Terms_Use.cfm

$$\cos(\hat{n}^0,\hat{\theta})=\frac{1}{1+E_n^0}\left[\left(\frac{1}{2}e_{r\theta}^0+\omega_z^0\right)l+(1+e_{\theta\theta}^0)m+\left(\frac{1}{2}e_{\theta z}^0-\omega_r^0\right)n\right], \quad (16b)$$

$$\cos(\hat{n}^0,\hat{z})=\frac{1}{1+E_n^0}\left[\left(\frac{1}{2}e_{rz}^0-\omega_\theta^0\right)l+\left(\frac{1}{2}e_{\theta z}^0+\omega_r^0\right)m+(1+e_{zz}^0)n\right]. \quad (16c)$$

Similar expressions hold true for the perturbed state. For example,

$$\cos(\hat{n}^1,\hat{r})=\frac{1}{1+E_n^1}\left\{(1+e_{rr}^0+\alpha e_{rr}')l+\left[\left(\frac{1}{2}e_{r\theta}^0-\omega_z^0\right)+\alpha\left(\frac{1}{2}e_{r\theta}'-\omega_z'\right)\right]m+\left[\left(\frac{1}{2}e_{rz}^0+\omega_\theta^0\right)+\alpha\left(\frac{1}{2}e_{rz}'+\omega_\theta'\right)\right]n\right\}. \quad (17)$$

The assumption of small strains allows neglecting E_n^0 and E_n^1 in comparison with unity. Substituting into the expressions (14) for the tractions in terms of the pressure and subtracting the initial and perturbed state and using the same arguments on the magnitude of rotations to neglect e_{ij}' in comparison with ω_k', we arrive at the following expressions:

$$t_r(V_0+\alpha V_1)-t_r(V_0)=p\alpha(\omega_z'm-\omega_\theta'n), \quad (18a)$$

$$t_\theta(V_0+\alpha V_1)-t_\theta(V_0)=-p\alpha(\omega_z'l-\omega_r'n), \quad (18b)$$

$$t_z(V_0+\alpha V_1)-t_z(V_0)=p\alpha(\omega_\theta'l-\omega_r'm). \quad (18c)$$

And in lieu of (13) for the lateral surfaces, i.e., for $m = n = 0$ and $l = 1$,

$$\sigma_{rr}'-\tau_{r\theta}^0\omega_z'+\tau_{rz}^0\omega_\theta'=0, \quad (19a)$$

$$\tau_{r\theta}'+\sigma_{rr}^0\omega_z'-\tau_{rz}^0\omega_r'=-p\omega_z', \quad (19b)$$

$$\tau_{rz}'+\tau_{r\theta}^0\omega_r'-\sigma_{rr}^0\omega_\theta'=p\omega_\theta'. \quad (19c)$$

Prebuckling State. The problem at hand is that of a hollow cylinder rigidly fixed at its ends and deformed by uniformly distributed external pressure p (Fig. 1). The axially symmetric distribution of external forces produces stresses identical to all cross-sections and dependent only on the radial coordinate r. In this manner the forces at the ends are distributed identically over both surfaces and reduce to equal and opposite resultant forces and moments. Let R_1 be the internal and R_2 the external radius and set $c = R_1/R_2$. Lekhnitskii (1963) gave the stress field as follows:

$$\sigma_{rr}^0=-\frac{p}{1-c^{2k}}\left(\frac{r}{R_2}\right)^{k-1}+\frac{pc^{k-1}}{1-c^{2k}}c^{k+1}\left(\frac{R_2}{r}\right)^{k+1}, \quad (20a)$$

$$\sigma_{\theta\theta}^0=-\frac{p}{1-c^{2k}}k\left(\frac{r}{R_2}\right)^{k-1}-\frac{pc^{k-1}}{1-c^{2k}}kc^{k+1}\left(\frac{R_2}{r}\right)^{k+1}, \quad (20b)$$

$$\sigma_{zz}^0=\frac{p}{(1-c^{2k})a_{33}}(a_{13}+a_{23}k)\left(\frac{r}{R_2}\right)^{k-1}-\frac{pc^{k-1}}{(1-c^{2k})a_{33}}(a_{13}-a_{23}k)c^{k+1}\left(\frac{R_2}{r}\right)^{k+1}, \quad (20c)$$

$$\tau_{r\theta}^0=\tau_{rz}^0=\tau_{\theta z}^0=0. \quad (20d)$$

Equations (4) for the orthotropic constitutive behavior, where c_{ij} are the stiffness constants as well as the inverse relationship where a_{ij} are the compliance constants have been used, i.e.,

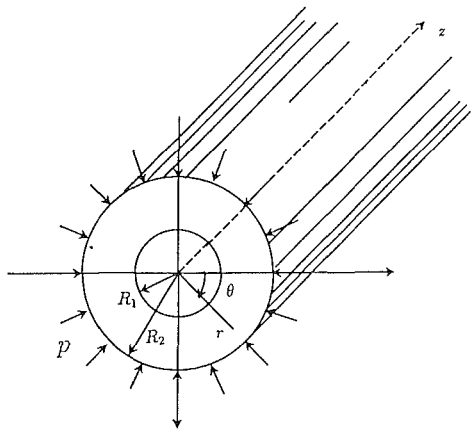


Fig. 1 Hollow cylinder under external pressure

$$\begin{bmatrix}\epsilon_{rr}\\ \epsilon_{\theta\theta}\\ \epsilon_{zz}\\ \gamma_{\theta z}\\ \gamma_{rz}\\ \gamma_{r\theta}\end{bmatrix}=\begin{bmatrix}a_{11}&a_{12}&a_{13}&0&0&0\\ a_{12}&a_{22}&a_{23}&0&0&0\\ a_{13}&a_{23}&a_{33}&0&0&0\\ 0&0&0&a_{44}&0&0\\ 0&0&0&0&a_{55}&0\\ 0&0&0&0&0&a_{66}\end{bmatrix}\begin{bmatrix}\sigma_{rr}\\ \sigma_{\theta\theta}\\ \sigma_{zz}\\ \tau_{\theta z}\\ \tau_{rz}\\ \tau_{r\theta}\end{bmatrix}. \quad (20e)$$

Since the rotations at the initial position of equilibrium are either zero or of the same order as the strains, the classical linear elasticity equilibrium and strain-displacement equations can ordinarily be applied to the initial position of equilibrium. Hence, integration of the above stress field through linear strain-displacement relations (Eqs. (7)) gives

$$u_0(r)=D_1pr^k+D_2pr^{-k}, \quad v_0=w_0=0, \quad (21)$$

where

$$k=\sqrt{\frac{a_{11}a_{33}-a_{13}^2}{a_{22}a_{33}-a_{33}^2}}=\sqrt{\frac{c_{22}}{c_{11}}}, \quad (22)$$

$$D_1=-\frac{1}{(1-c^{2k})kR_2^{k-1}}\left[a_{11}+a_{12}k-\frac{a_{13}}{a_{33}}(a_{13}+a_{23}k)\right]=-\frac{1}{(c_{11}k+c_{12})(1-c^{2k})R_2^{k-1}}, \quad (23a)$$

$$D_2=-\frac{c^{k-1}R_1^{k+1}}{(1-c^{2k})k}\left[a_{11}-a_{12}k-\frac{a_{13}}{a_{33}}(a_{13}-a_{23}k)\right]=\frac{c^{k-1}R_1^{k+1}}{(-c_{11}k+c_{12})(1-c^{2k})}. \quad (23b)$$

Perturbed State. In the perturbed position we seek plane equilibrium modes as follows:

$$u_1(r,\theta)=A_n(r)\cos n\theta;$$
$$v_1(r,\theta)=B_n(r)\sin n\theta; \quad w_1(r,\theta)=0. \quad (24)$$

Substituting in (7) we obtain

$$\epsilon_{rr}^0=kp(C_1r^{k-1}-C_2r^{-k-1}); \quad \epsilon_{\theta\theta}^0=p(C_1r^{k-1}+C_2r^{-k-1}), \quad (25a)$$

$$\epsilon_{zz}^0=\gamma_{\theta z}^0=\gamma_{rz}^0=\gamma_{r\theta}^0=0. \quad (25b)$$

The first-order strains are given in Appendix B. However, let us examine the expression for ϵ_{rr}':

$$\epsilon_{rr}'=(1+e_{rr}^0)\frac{\partial u_1}{\partial r}+\left(\frac{1}{2}e_{r\theta}^0+\omega_z^0\right)\frac{\partial v_1}{\partial r}+\left(\frac{1}{2}e_{rz}^0-\omega_\theta^0\right)\frac{\partial w_1}{\partial r}.$$

Since all terms multiplied by e_{ij}^0 or ω_j^0, can be neglected based on the arguments made previously, $\epsilon_{rr}' = \partial u_1/\partial r = e_{rr}'$. It turns

Downloaded 03 May 2010 to 171.66.16.245. Redistribution subject to ASME license or copyright; see http://www.asme.org/terms/Terms_Use.cfm

out that we can use for the first-order strains the very much simpler linear strains e'_{ij}, i.e., $\epsilon'_{ij} = e'_{ij}$. Therefore,

$$\epsilon'_{rr} = e'_{rr} = A'_n(r)\cos n\theta, \tag{26a}$$

$$\epsilon'_{\theta\theta} = e'_{\theta\theta} = \frac{A_n(r) + nB_n(r)}{r}\cos n\theta, \tag{26b}$$

$$\gamma'_{r\theta} = e'_{r\theta} = \left[B'_n(r) - \frac{B_n(r) + nA_n(r)}{r}\right]\sin n\theta, \tag{26c}$$

$$\epsilon'_{zz} = \gamma'_{\theta z} = \gamma'_{rz} = 0, \tag{26d}$$

and the first-order rotations are

$$2\omega'_z = \left[B'_n(r) + \frac{B_n(r) + nA_n(r)}{r}\right]\sin n\theta, \tag{26e}$$

$$\omega'_\theta = \omega'_r = 0. \tag{26f}$$

Denote $A_n^{(i)}(r)$, $B_n^{(i)}(r)$ the ith derivative of $A_n(r)$, $B_n(r)$, respectively, with the notation $A_n^{(0)}(r) = A_n(r)$ and $B_n^{(0)}(r) = B_n(r)$. Substituting in (10) and using (4) and (5), e.g., $\sigma'_{rr} = c_{11}\epsilon'_{rr} + c_{12}\epsilon'_{\theta\theta}$, we obtain the following two linear homogeneous ordinary differential equations of the second order for $A_n(r)$, $B_n(r)$:

$$\sum_{i=0}^{2} A_n^{(i)}(r)\,(d_{i0}r^{i-2} + d_{i1}pr^{k-3+i} + d_{i2}pr^{-k-3+i}) + \sum_{i=0}^{1} B_n^{(i)}(r)\,(q_{i0}r^{i-2} + q_{i1}pr^{k-3+i} + q_{i2}pr^{-k-3+i}) = 0, \quad R_1 \le r \le R_2 \tag{27a}$$

$$\sum_{i=0}^{2} B_n^{(i)}(r)\,(b_{i0}r^{i-2} + b_{i1}pr^{k-3+i} + b_{i2}pr^{-k-3+i}) + \sum_{i=0}^{1} A_n^{(i)}(r)\,(f_{i0}r^{i-2} + f_{i1}pr^{k-3+i} + f_{i2}pr^{-k-3+i}) = 0, \quad R_1 \le r \le R_2 \tag{27b}$$

The boundary conditions (19) are written as follows:

$$A'_n(R_j)c_{11} + [A_n(R_j) + nB_n(R_j)]\frac{c_{12}}{R_j} = 0, \quad j = 1,2 \tag{28a}$$

$$B'_n(R_j)\left[\left(c_{66} + \frac{p_j}{2}\right) + h_{01}pR_j^{k-1} + h_{02}pR_j^{-k-1}\right] + [B_n(R_j) + nA_n(R_j)]\left[\left(-c_{66} + \frac{p_j}{2}\right)\frac{1}{R_j} + h_{01}pR_j^{k-2} + h_{02}pR_j^{-k-2}\right] = 0, \quad j = 1,2 \tag{28b}$$

where $p_j = p$ for $j = 2$, i.e., $r = R_2$ (outside boundary), and $p_j = 0$ for $j = 1$, i.e., $r = R_1$ (inside boundary).

The constants d_{ij}, q_{ij}, b_{ij}, f_{ij}, h_{ij} in the above equations are given in Appendix A and depend on the material stiffness coefficients c_{ij} and the constants n and k.

Equations (27)–(28) constitute an eigenvalue problem for differential equations, with p the parameter, which can be solved by standard numerical methods (two-point boundary value problem). The relaxation method was used to obtain results which are discussed in the following. The minimum eigenvalue is obtained for $n = 2$. An equally spaced mesh of 241 points was used to derive the results. The procedure is highly efficient with rapid convergence. An investigation of the convergence showed that essentially the same results were produced with even three times as many mesh points.

Results and Discussion

As an illustrative example, the critical pressure was determined for a composite circular cylinder of inner radius $R_1 = 1$ m. The moduli in GN/m^2 and Poisson's ratios used (typical for a glass/epoxy material) are listed below, where 1 is the radial (r), 2 is the circumferential (θ), and 3 the axial (z) direction: $E_1 = 14.0$, $E_2 = 57.0$, $E_3 = 14.0$, $G_{12} = 5.7$, $G_{23} = 5.7$, $G_{31} = 5.0$, $\nu_{12} = 0.068$, $\nu_{23} = 0.277$, $\nu_{31} = 0.400$.

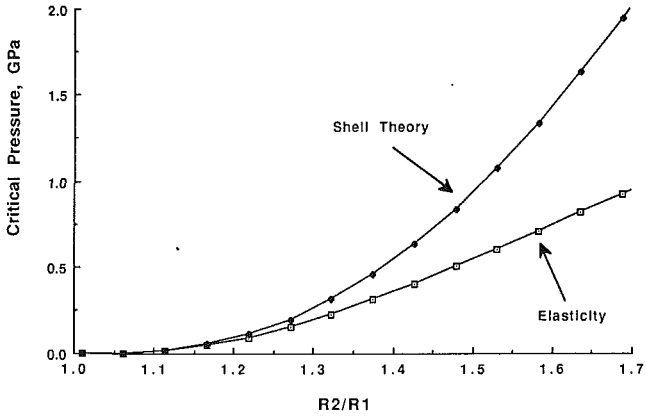


Fig. 2 Critical pressure, p_{cr} versus ratio of outside/inside radius, R_2/R_1. Comparison of the three-dimensional elasticity and the shell theory predictions.

Figure 2 shows the critical pressure as a function of the ratio of outside versus inside radius R_2/R_1. The elasticity solution is compared with the predictions of classical shell theory (e.g., Ambartsumyan, 1961). It is seen that the buckling load predicted by shell theory is 33 percent higher than the elasticity solution for $R_2/R_1 = 1.3$, it is 70 percent higher than the elasticity solution for $R_2/R_1 = 1.5$ and is more than two times the elasticity solution for $R_2/R_1 = 1.65$.

The direct expression for the critical pressure from classical shell theory is

$$p_{cr,sh} = \frac{E_2}{(1 - \nu_{23}\nu_{32})}(n^2 - 1)\frac{h^3}{12R^3} \tag{29a}$$

where $R = (R_1 + R_2)/2$ is the mid-surface radius, and $h = R_2 - R_1$ is the shell thickness.

The previous value can be found by using the Donnell nonlinear shell theory equations (Brush and Almroth, 1975) and seeking the buckled shapes in the form (24) where $A_n(r) = A_n$, i.e., it is now a constant instead of function of r, and $B_n(r) = B_n + (r - R)\beta$ with B_n being a constant, i.e., it admits a linear variation through the thickness. Since $\beta = (v_1 - u_{1,\theta})/R$, the latter can also be written in the form $B_n(r) = B_n + (r - R)(B_n + n)/R$.

As a consequence, we obtain the following shell theory buckling equations:

$$u_{1,\theta} + v_{1,\theta\theta} - \frac{h^2}{12R^2}(u_{1,\theta\theta\theta} - v_{1,\theta\theta}) = 0, \tag{29b}$$

$$\frac{h^2}{12R^2}(u_{1,\theta\theta\theta\theta} - v_{1,\theta\theta\theta}) + (u_1 + v_{1,\theta}) - \frac{pR(1 - \nu_{23}\nu_{32})}{E_2 h}(v_{1,\theta} - u_{1,\theta\theta}) = 0. \tag{29c}$$

Substituting the displacements from (24) and using the previous expressions for $A_n(r)$ and $B_n(r)$ results in the eigenvalue (29a) and the "eigenvectors" given by

$$A_n = 1; \quad B_n = -\left(1 + \frac{h^2}{12R^2}n^2\right)\Big/\left[n\left(1 + \frac{h^2}{12R^2}\right)\right]. \tag{29e}$$

Figures 3 and 4 show the variation of $A_n(r)$ and $B_n(r)$, which define the eigenfunctions, for $R_2/R_1 = 1.5$, as derived from the present elasticity solution, and in comparison with the shell theory assumptions of constant $A_n(r)$ and linear $B_n(r)$.

Downloaded 03 May 2010 to 171.66.16.245. Redistribution subject to ASME license or copyright; see http://www.asme.org/terms/Terms_Use.cfm

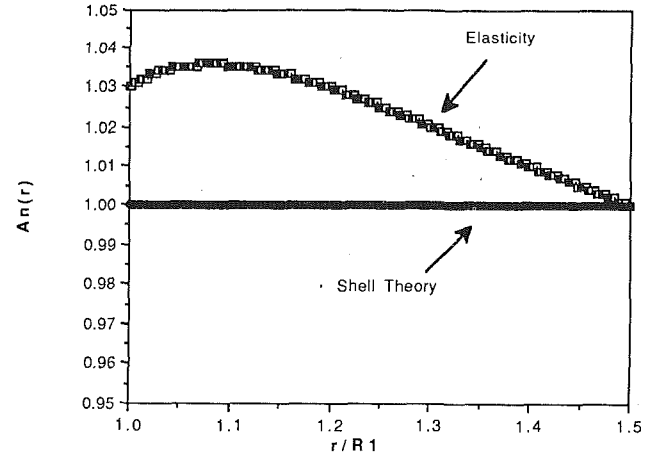


Fig. 3 "Eigenfunction" $A_n(r)$ versus normalized radial distance r/R_1. A unit value at the outside boundary has arbitrarily been set.

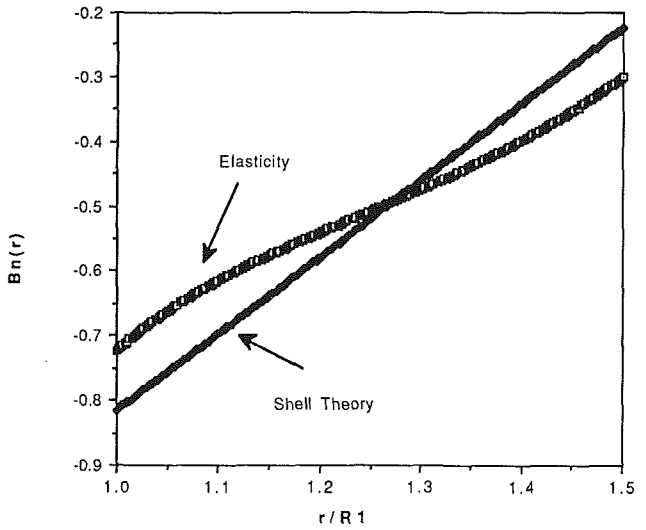


Fig. 4 "Eigenfunction" $B_n(r)$ versus normalized radial distance r/R_1.

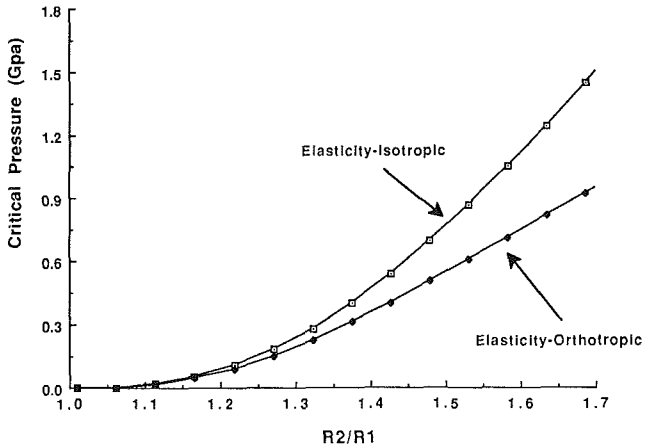


Fig. 5 Critical pressure, p_{cr} versus ratio of outside/inside radius, R_2/R_1, for the orthotropic case, and the isotropic one with $E = E_2$; i.e., the modulus along the periphery and Poisson's ratio $\nu = 0.3$

These values have been normalized by assigning a unit value for A_n at the outside boundary $r = R_2$.

Finally, Fig. 5 shows the effect of material constants by presenting a comparison of the critical load for the orthotropic case with the previously given moduli and Poisson's ratios, and the corresponding one by assuming isotropic material with modulus $E = E_2$, i.e., the modulus along the periphery, and Poisson's ratio $\nu = 0.3$. It is seen that the orthotropy results in significantly lower critical load with increased thickness. For example, at $R_2/R_1 = 1.5$, the isotropic material has 40 percent higher critical load than the orthotropic case. Naturally, the reduction in critical load can be qualitatively attributed to the reduced shear and radial stiffness of the orthotropic material.

Table 1 Critical pressure, $p_{cr}R_2^3/(E_2h^3)$

Orthotropic, moduli in GN/m^2: $E_2 = 57$, $E_1 = E_3 = 14$, $G_{31} = 5.0$, $G_{12} = G_{23} = 5.7$
Poisson's ratios: $\nu_{12} = 0.068$, $\nu_{23} = 0.277$, $\nu_{31} = 0.400$

R_2/R_1	Elasticity	Shell[1]	Percentage Increase
1.10	0.2728	0.2930	7.4
1.15	0.2768	0.3119	12.7
1.20	0.2784	0.3308	18.8
1.25	0.2780	0.3495	25.7
1.30	0.2762	0.3681	33.3
1.35	0.2733	0.3864	41.4
1.40	0.2696	0.4046	50.1

[1]from Eq. (29a) with $n = 2$

The comparison of our elasticity solution was performed with the Donnell shell theory. It has been known (Danielson and Simmonds, 1969) that the Donnell shell theory can produce in some instances inaccurate results (such as for long tude behavior), as opposed to the more elaborate Flügge theory that provides more accurate predictions. However, for the problem under consideration, due to the assumed two-dimensional buckling modes (i.e., no z component of the displacement field, and no z-dependence of the r and θ displacement components), both the Flügge and Donnell equations would give the same critical load. Indeed, the buckling equations for the Flügge shell theory (see, e.g., Simmonds, 1966) would be: the Eq. (29b) without the term $h^2/12R^2\ (u_{1,\theta\theta\theta} - v_{1,\theta\theta})$, and the Eq. (29$c$) with the first term being $h^2/12R^2\ (u_{1,\theta\theta\theta\theta} + 2u_{1,\theta\theta} + u_1)$ instead of $h^2/12R^2\ (u_{1,\theta\theta\theta\theta} - v_{1,\theta\theta\theta})$. Substitution of the buckling modes (24) gives the same critical load, Eq. (29a), as the Donnell shell theory. Future work will consider the more complete problem of buckling of cylindrical shells of finite length under axial compression and external pressure, in the context of the present elasticity formulation; in this case the differences among the various shell theories are expected to surface.

It should also be noted that although the equilibrium approach was employed in the present formulation, a variational approach could also be applied. In this case, we can use the principle of virtual displacements by considering virtual displacements of the form $\alpha\delta u_1$, $\alpha\delta v_1$, and $\alpha\delta w_1$. The internal virtual work, which is essentially a volume integral of the product of stresses and strains in (3) and (5), can be written in the form $\delta W_i = \delta W_i^{(0)} + \alpha\delta W_i^{(1)} + \alpha^2\delta W_i^{(2)}$, and the same is true for the external virtual work δW_e due to the applied pressure. Finally, we would obtain the variational formulation in the form of $\delta W_i^{(2)} = \delta W_e^{(2)}$. Such an approach is expected to lead to similar results as the present direct equilibrium approach.

For a more specific comparison of the results for a range of radii ratios that would probably constitute practically moderately thick-to-thick shell construction, Table 1 shows the critical load derived by the present elasticity formulation and the shell theory predictions for orthotropic material and for ratios of outside over inside radius ranging from 1.10 to 1.40. A similar comparison is performed for the isotropic case in Table 2.

From the results presented previously, it can be concluded that predictions of stability loss in composite thick structures can be quite nonconservative if classical approaches are used. Specifically, the previous example showed that the critical load predicted by shell theory is higher than the three-dimensional

Downloaded 03 May 2010 to 171.66.16.245. Redistribution subject to ASME license or copyright; see http://www.asme.org/terms/Terms_Use.cfm

Table 2 Critical pressure, $p_{cr}R_2^3/(E_2h^3)$

Isotropic, $E = E_2 = 57$ GN/m^2, $\nu = 0.3$

R_2/R_1	Elasticity	Shell[2]	Percentage Increase
1.10	0.2999	0.3159	5.3
1.15	0.3109	0.3363	8.2
1.20	0.3209	0.3567	11.2
1.25	0.3301	0.3769	14.2
1.30	0.3384	0.3969	17.3
1.35	0.3459	0.4167	20.5
1.40	0.3528	0.4363	23.7

[2]from Eq. (29*a*) with $n = 2$

elasticity predictions by more than a factor of two for a ratio of outside over inside radius greater than about 1.6. The present formulation and solution provide a means of accurately assessing the limitations of shell theories in predicting stability loss when the applications involve orthotropy and moderately thick construction. Further work is needed to assess the accuracy of improved higher-order shell theory predictions on the critical load in comparison to the elasticity ones. A comparison of these theories to the classical shell theory has already been performed by Anastasiadis (1990).

Acknowledgment

The financial support of the Office of Naval Research, Mechanics Division, Grant N00014-91-J-1892, and the interest and encouragement of the Project Monitor, Dr. Y. Rajapakse, are both gratefully acknowledged.

References

Ambartsumyan, S. A., 1961, "Theory of Anisotropic Shells," NASA Technical Translation N64-22801-N64-22808.

Anastasiadis, J. S., 1990, "Stability of Cylindrical Laminates by Higher Order Shear Deformable Theories," Ph.D. Thesis, School of Aerospace Engineering, Georgia Institute of Technology, Atlanta, GA.

Brush, D. O., and Almroth, B. O., 1975, *Buckling of Bars, Plates, and Shells*, McGraw-Hill, New York.

Danielson, D. A., and Simmonds, J. G., 1969, "Accurate Buckling Equations for Arbitrary and Cylindrical Elastic Shells," *Int. J. Eng. Sci.*, Vol. 7, pp. 459–468.

Lekhnitskii, S. G., 1963, *Theory of Elasticity of an Anisotropic Elastic Body*, Holden Day, San Francisco; also Mir Publishers, Moscow, 1981.

Librescu, L., 1975, *Elastostatics and Kinetics of Anisotropic and Heterogeneous Shell-Type Structures*, Nordhoff International, Leyden.

Noor, A. K., and Burton, W. S., 1990, "Assessment of Computational Models for Multilayered Composite Shells," ASME *Appl. Mech. Rev.*, Vol. 43, No. 4, pp.67–97.

Pagano, N. J., and Whitney, J. M., 1970, "Geometric Design of Composite Cylindrical Characterization Specimens," *Journal of Composite Materials*, Vol. 4, p. 360.

Pagano, N. J., 1971, "Stress Gradients in Laminated Composite Cylinders," *Journal of Composite Materials*, Vol. 4, p. 260.

Reddy, J. N., and Liu, C. F., 1985, "A Higher-Order Shear Deformation Theory of Laminated Elastic Shells," *Int. J. Eng. Sci.*, Vol. 23, No. 3, pp. 319–330.

Simitses, G. J., Shaw, D., and Sheinman, I., 1985, "Stability of Cylindrical Shells by Various Nonlinear Shell Theories," *ZAMM, Z. Angew. Math. u. Mech.*, Vol. 65, No. 3, pp. 159–166.

Simmonds, J. G., 1966, "A Set of Simple, Accurate Equations for Circular Cylindrical Elastic Shells," *Int. J. Solids Structures*, Vol. 2, pp. 525–541.

Whitney, J. M., and Sun, C. T., 1974, "A Refined Theory for Laminated Anisotropic Cylindrical Shells," ASME JOURNAL OF APPLIED MECHANICS, Vol. 41, No. 2, pp. 471–476.

APPENDIX A

Define the constants C_1 and C_2 (to simplify the σ_{ij}^0 expressions) as follows:

$$C_1 = -\frac{1}{(1-c^{2k})R_2^{k-1}}; \quad C_2 = \frac{c^{2k}R_2^{k+1}}{(1-c^{2k})}, \tag{A1}$$

where $c = R_1/R_2$. Furthermore, k is defined in (22) and c_{ij} are the stiffness constants from (4).

The coefficients of the first differential Eq. (27*a*) are

$$d_{20} = c_{11}; \quad d_{21} = d_{22} = 0, \quad d_{10} = c_{11}; \quad d_{11} = d_{12} = 0, \tag{A2}$$

$$d_{00} = -(c_{22} + c_{66}n^2); \quad d_{01} = -\frac{kn^2}{2}C_1; \quad d_{02} = \frac{kn^2}{2}C_2, \tag{A3}$$

$$q_{00} = -n(c_{22} + c_{66}); \quad q_{01} = -\frac{kn}{2}C_1; \quad q_{02} = \frac{kn}{2}C_2, \tag{A4}$$

$$q_{10} = n(c_{12} + c_{66}); \quad q_{11} = -\frac{kn}{2}C_1; \quad q_{12} = \frac{kn}{2}C_2. \tag{A5}$$

The coefficients of the second differential Eq. (27*b*) are given as follows:

$$b_{20} = c_{66}; \quad b_{21} = \frac{1}{2}C_1; \quad b_{22} = \frac{1}{2}C_2, \tag{B1}$$

$$b_{10} = c_{66}; \quad b_{11} = \frac{1}{2}C_1; \quad b_{12} = \frac{1}{2}C_2, \tag{B2}$$

$$b_{00} = -(c_{22}n^2 + c_{66}); \quad b_{01} = -\frac{1}{2}C_1, \quad b_{02} = -\frac{1}{2}C_2, \tag{B3}$$

$$f_{00} = -n(c_{22} + c_{66}); \quad f_{01} = -\frac{n}{2}C_1, \quad f_{02} = -\frac{n}{2}C_2, \tag{B4}$$

$$f_{10} = -n(c_{12} + c_{66}); \quad f_{11} = \frac{n}{2}C_1, \quad f_{12} = \frac{n}{2}C_2. \tag{B5}$$

Finally, the coefficients of the second boundary condition (28b) are

$$h_{01} = \frac{1}{2}C_1; \quad h_{02} = \frac{1}{2}C_2. \tag{C2}$$

APPENDIX B

The strain components in the initial position of equilibrium are

$$\epsilon_{rr}^0 = \frac{\partial u_0}{\partial r} + \frac{1}{2}\left[\left(\frac{\partial u_0}{\partial r}\right)^2 + \left(\frac{\partial v_0}{\partial r}\right)^2 + \left(\frac{\partial w_0}{\partial r}\right)^2\right], \tag{D1a}$$

$$\epsilon_{\theta\theta}^0 = \frac{1}{r}\frac{\partial v_0}{\partial \theta} + \frac{u_0}{r} + \frac{1}{2}\left[\left(\frac{1}{r}\frac{\partial u_0}{\partial \theta} - \frac{v_0}{r}\right)^2 + \left(\frac{1}{r}\frac{\partial v_0}{\partial \theta} + \frac{u_0}{r}\right)^2 + \left(\frac{1}{r}\frac{\partial w_0}{\partial \theta}\right)^2\right], \tag{D1b}$$

$$\epsilon_{zz}^0 = \frac{\partial w_0}{\partial z} + \frac{1}{2}\left[\left(\frac{\partial u_0}{\partial z}\right)^2 + \left(\frac{\partial v_0}{\partial z}\right)^2 + \left(\frac{\partial w_0}{\partial z}\right)^2\right], \tag{D1c}$$

$$\gamma_{r\theta}^0 = \frac{1}{r}\frac{\partial u_0}{\partial \theta} + \frac{\partial v_0}{\partial r} - \frac{v_0}{r} + \left[\frac{\partial u_0}{\partial r}\left(\frac{1}{r}\frac{\partial u_0}{\partial \theta} - \frac{v_0}{r}\right) + \frac{\partial v_0}{\partial r}\left(\frac{1}{r}\frac{\partial v_0}{\partial \theta} + \frac{u_0}{r}\right) + \frac{1}{r}\frac{\partial w_0}{\partial r}\frac{\partial w_0}{\partial \theta}\right], \tag{D1d}$$

$$\gamma_{rz}^0 = \frac{\partial u_0}{\partial z} + \frac{\partial w_0}{\partial r} + \left(\frac{\partial u_0}{\partial r}\frac{\partial u_0}{\partial z} + \frac{\partial v_0}{\partial r}\frac{\partial v_0}{\partial z} + \frac{\partial w_0}{\partial r}\frac{\partial w_0}{\partial z}\right), \tag{D1e}$$

$$\gamma_{\theta z}^0 = \frac{\partial v_0}{\partial z} + \frac{1}{r}\frac{\partial w_0}{\partial \theta} + \left[\frac{\partial u_0}{\partial z}\left(\frac{1}{r}\frac{\partial u_0}{\partial \theta} - \frac{v_0}{r}\right) + \frac{\partial v_0}{\partial z}\left(\frac{1}{r}\frac{\partial v_0}{\partial \theta} + \frac{u_0}{r}\right) + \frac{1}{r}\frac{\partial w_0}{\partial \theta}\frac{\partial w_0}{\partial z}\right]. \tag{D1f}$$

Downloaded 03 May 2010 to 171.66.16.245. Redistribution subject to ASME license or copyright; see http://www.asme.org/terms/Terms_Use.cfm

The strain components associated with the linear terms (corresponding to the perturbed position of equilibrium) are

$$\epsilon'_{rr}=\frac{\partial u_1}{\partial r}+\frac{\partial u_0}{\partial r}\frac{\partial u_1}{\partial r}+\frac{\partial v_0}{\partial r}\frac{\partial v_1}{\partial r}+\frac{\partial w_0}{\partial r}\frac{\partial w_1}{\partial r}, \tag{D2a}$$

$$\epsilon'_{\theta\theta}=\frac{1}{r}\frac{\partial v_1}{\partial\theta}+\frac{u_1}{r}+\left(\frac{1}{r}\frac{\partial u_0}{\partial\theta}-\frac{v_0}{r}\right)\left(\frac{1}{r}\frac{\partial u_1}{\partial\theta}-\frac{v_1}{r}\right)+\left(\frac{1}{r}\frac{\partial v_0}{\partial\theta}+\frac{u_0}{r}\right)\left(\frac{1}{r}\frac{\partial v_1}{\partial\theta}+\frac{u_1}{r}\right)+\frac{1}{r^2}\frac{\partial w_0}{\partial\theta}\frac{\partial w_1}{\partial\theta}, \tag{D2b}$$

$$\epsilon'_{zz}=\frac{\partial w_1}{\partial z}+\frac{\partial u_0}{\partial z}\frac{\partial u_1}{\partial z}+\frac{\partial v_0}{\partial z}\frac{\partial v_1}{\partial z}+\frac{\partial w_0}{\partial z}\frac{\partial w_1}{\partial z}, \tag{D2c}$$

$$\gamma'_{r\theta}=\frac{1}{r}\frac{\partial u_1}{\partial\theta}+\frac{\partial v_1}{\partial r}-\frac{v_1}{r}+\frac{\partial u_1}{\partial r}\left(\frac{1}{r}\frac{\partial u_0}{\partial\theta}-\frac{v_0}{r}\right)+\frac{\partial u_0}{\partial r}\left(\frac{1}{r}\frac{\partial u_1}{\partial\theta}-\frac{v_1}{r}\right)+\frac{\partial v_1}{\partial r}\left(\frac{1}{r}\frac{\partial v_0}{\partial\theta}+\frac{u_0}{r}\right)+\frac{\partial v_0}{\partial r}\left(\frac{1}{r}\frac{\partial v_1}{\partial\theta}+\frac{u_1}{r}\right)+\frac{1}{r}\frac{\partial w_1}{\partial r}\frac{\partial w_0}{\partial\theta}+\frac{1}{r}\frac{\partial w_0}{\partial r}\frac{\partial w_1}{\partial\theta}, \tag{D2d}$$

$$\gamma'_{rz}=\frac{\partial u_1}{\partial z}+\frac{\partial w_1}{\partial r}+\frac{\partial u_0}{\partial r}\frac{\partial u_1}{\partial z}+\frac{\partial u_1}{\partial r}\frac{\partial u_0}{\partial z}+\frac{\partial v_0}{\partial r}\frac{\partial v_1}{\partial z}+\frac{\partial v_1}{\partial r}\frac{\partial v_0}{\partial z}+\frac{\partial w_0}{\partial r}\frac{\partial w_1}{\partial z}+\frac{\partial w_1}{\partial r}\frac{\partial w_0}{\partial z}, \tag{D2e}$$

$$\gamma'_{\theta z}=\frac{\partial v_1}{\partial z}+\frac{1}{r}\frac{\partial w_1}{\partial\theta}+\frac{\partial u_1}{\partial z}\left(\frac{1}{r}\frac{\partial u_0}{\partial\theta}-\frac{v_0}{r}\right)+\frac{\partial u_0}{\partial z}\left(\frac{1}{r}\frac{\partial u_1}{\partial\theta}-\frac{v_1}{r}\right)+\frac{\partial v_1}{\partial z}\left(\frac{1}{r}\frac{\partial v_0}{\partial\theta}+\frac{u_0}{r}\right)+\frac{\partial v_0}{\partial z}\left(\frac{1}{r}\frac{\partial v_1}{\partial\theta}+\frac{u_1}{r}\right)+\frac{1}{r}\frac{\partial w_0}{\partial\theta}\frac{\partial w_1}{\partial z}+\frac{1}{r}\frac{\partial w_1}{\partial\theta}\frac{\partial w_0}{\partial z}. \tag{D2f}$$

The strain quantities corresponding to the quadratic terms (associated with the initial post-buckling behavior) are:

$$\epsilon''_{rr}=\frac{1}{2}\left[\left(\frac{\partial u_1}{\partial r}\right)^2+\left(\frac{\partial v_1}{\partial r}\right)^2+\left(\frac{\partial w_1}{\partial r}\right)^2\right], \tag{D3a}$$

$$\epsilon''_{\theta\theta}=\frac{1}{2}\left[\left(\frac{1}{r}\frac{\partial u_1}{\partial\theta}-\frac{v_1}{r}\right)^2+\left(\frac{1}{r}\frac{\partial v_1}{\partial\theta}+\frac{u_1}{r}\right)^2+\left(\frac{1}{r}\frac{\partial w_1}{\partial\theta}\right)^2\right], \tag{D3b}$$

$$\epsilon''_{zz}=\frac{1}{2}\left[\left(\frac{\partial u_1}{\partial z}\right)^2+\left(\frac{\partial v_1}{\partial z}\right)^2+\left(\frac{\partial w_1}{\partial z}\right)^2\right], \tag{D3c}$$

$$\gamma''_{r\theta}=\frac{\partial u_1}{\partial r}\left(\frac{1}{r}\frac{\partial u_1}{\partial\theta}-\frac{v_1}{r}\right)+\frac{\partial v_1}{\partial r}\left(\frac{1}{r}\frac{\partial v_1}{\partial\theta}+\frac{u_1}{r}\right)+\frac{1}{r}\frac{\partial w_1}{\partial r}\frac{\partial w_1}{\partial\theta}, \tag{D3d}$$

$$\gamma''_{rz}=\frac{\partial u_1}{\partial r}\frac{\partial u_1}{\partial z}+\frac{\partial v_1}{\partial r}\frac{\partial v_1}{\partial z}+\frac{\partial w_1}{\partial r}\frac{\partial w_1}{\partial z}, \tag{D3e}$$

$$\gamma''_{\theta z}=\frac{\partial u_1}{\partial z}\left(\frac{1}{r}\frac{\partial u_1}{\partial\theta}-\frac{v_1}{r}\right)+\frac{\partial v_1}{\partial z}\left(\frac{1}{r}\frac{\partial v_1}{\partial\theta}+\frac{u_1}{r}\right)+\frac{1}{r}\frac{\partial w_1}{\partial\theta}\frac{\partial w_1}{\partial z}. \tag{D3f}$$

Downloaded 03 May 2010 to 171.66.16.245. Redistribution subject to ASME license or copyright; see http://www.asme.org/terms/Terms_Use.cfm

Journal of Applied Mechanics

Brief Notes

A Brief Note is a short paper that presents a specific solution of technical interest in mechanics but which does not necessarily contain new general methods or results. A Brief Note should not exceed 1500 words *or equivalent* (a typical one-column figure or table is equivalent to 250 words; a one line equation to 30 words). Brief Notes will be subject to the usual review procedures prior to publication. After approval such Notes will be published as soon as possible. The Notes should be submitted to the Technical Editor of the JOURNAL OF APPLIED MECHANICS. Discussions on the Brief Notes should be addressed to the Editorial Department, ASME, United Engineering Center, 345 East 47th Street, New York, N. Y. 10017, or to the Technical Editor of the JOURNAL OF APPLIED MECHANICS. Discussions on Brief Notes appearing in this issue will be accepted until two months after publication. Readers who need more time to prepare a Discussion should request an extension of the deadline from the Editorial Department.

Stress Concentration due to the Interaction Between Two Imperfectly Bonded Fibers in a Continuous Fiber Composite

D. Kouris[1]

1 Introduction

One of the common modes of failure of intermetallic composites is attributed to the presence of interfacial cracking.

The loss of interfacial integrity is a consequence of the inherent differences between the thermoelastic properties of the matrix/fiber system as well as its chemical reactivity.

In an effort to evaluate the local stress state due to thermal residual strains, Kouris and Tsuchida (1991) obtained an analytical solution for a pair of fibers, under plane-strain conditions. The fiber cross-sections were modeled by circular inhomogeneities that sustain uniform eigenstrains, proportional to the mismatch of the coefficients of thermal expansion. It was found that the relative distance between fibers (volume fraction) has a considerable effect on the stress concentration, which cannot be accounted for by means of an "average" approach.

The problem of an infinite thin plate with two circular inclusions, perfectly bonded to the plate, has been considered by Shioya (1971). Under conditions of generalized plane stress, the solution has been obtained on the basis of Airy's stress functions by utilizing bipolar coordinates and a perturbation method.

In the present study, an analytical solution is obtained for a pair of fibers embeeded in a linear elastic matrix under remote tension. The plane-strain formulation is based upon a displacement approach and the effects of he condition of the interface are examined. The results focus on the stress state of the matrix along the interface.

[1]Mechanical and Aerospace Engineering Department, Arizona State University, Tempe, AZ 85287-6106. Assoc. Mem. ASME.

Manuscript received by the ASME Applied Mechanics Division, Feb. 14, 1991; final revision, Sept. 10, 1991. Associate Technical Editor: G. J. Dvorak.

2 Analytical Approach

The geometry of the boundary value problem under consideration is shown in Fig 1. The cross-sections of the two continuous fibers are modeled by two circular inhomogeneities (plane strain) and the transverse remote tension is indicated by T_x and T_y.

In the absence of the fibers, the uniform stress field is described by

$$
\begin{aligned}
2Gu_r &= \frac{1}{4}(\kappa-1)\, r(T_x+T_y)+\frac{1}{2} r(T_x-T_y)\cos 2\theta,\\
2Gu_\theta &= \frac{1}{2} r(T_y-T_{xx})\sin 2\theta,\\
\sigma_r &= \frac{1}{2}(T_x+T_y)+\frac{1}{2}(T_x-T_y)\cos 2\theta,\\
\sigma_\theta &= \frac{1}{2}(T_x+T_y)+\frac{1}{2}(T_y-T_x)\cos 2\theta, \text{ and}\\
\tau_{r\theta} &= \frac{1}{2}(T_y-T_x)\sin 2\theta,
\end{aligned}
\tag{1}
$$

in terms of polar coordinates, where $\kappa = 3-4\nu$.

The centers O_1, O_2 of the fiber cross-sections coincide with the origins of the Cartesian coordinates (x_1, y_1) and (x_2, y_2). If we assume that the central distance is equal to unity then

$$x_1 = x_2 + 1,\ y_1 = y_2 \tag{2}$$

and

$$x_i = r_i\cos\theta_i,\ y_i = r_i\sin\theta_i \quad (i=1, 2).$$

The displacement vector u can be expressed as the sum of the vectors corresponding to the O_1 and O_2 coordinate systems. Therefore,

$$u = u_1 + u_2. \tag{3}$$

Due to the applied mechanical loading, the far-field boundary conditions require that the nonzero stresses σ_{xx} and σ_{yy} at infinity, are equal to the external load T_{xx} and T_y, respectively.

In order to account for the imperfect bond between the fibers and the matrix, and spring-type thin layer along the interface is considered. Such a model allows for displacement discontinuities along the interface, while tractions remain continuous. The thin layer provides a viable alternative to the "three phase" approach and has been utilized by a number of researchers (Lene and Leguillon, 1982; Benveniste, 1984; Jasiuk et al., 1991; among others).

Copyright © 1993 by ASME
Downloaded 03 May 2010 to 171.66.16.245. Redistribution subject to ASME license or copyright; see http://www.asme.org/terms/Terms_Use.cfm

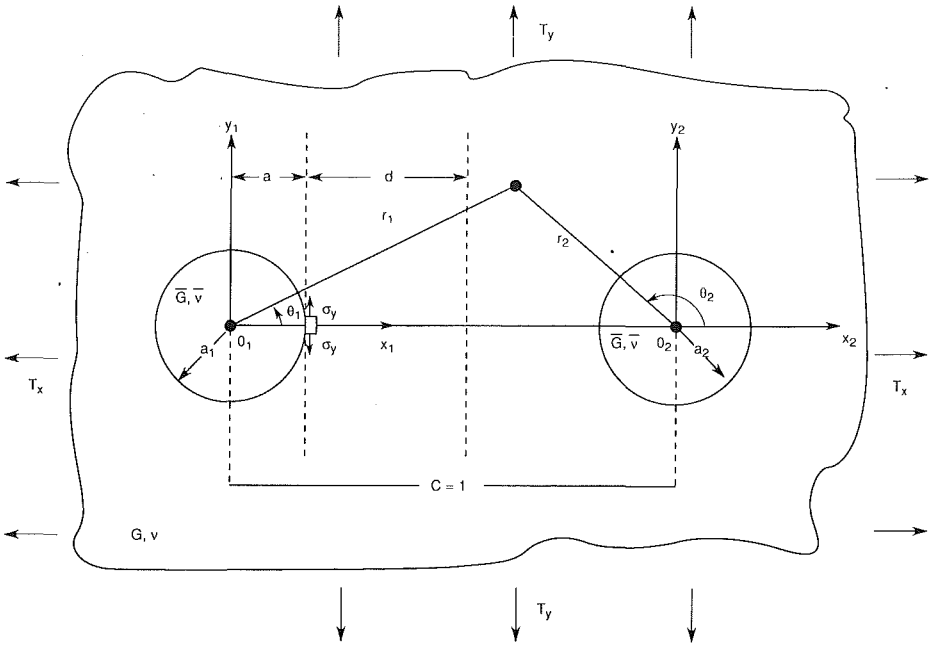


Fig. 1 Geometry of the problem

Based on the model described above, the boundary conditions along the circular interfaces ($r_i = a_i$) are

$$u_r = \bar{u}_r,\ [u_\theta] = \lambda \frac{a}{2G} \bar{\tau}_{r\theta},\ \sigma_r = \bar{\sigma}_r, \text{ and } \tau_{r\theta} = \bar{\tau}_{r\theta} \tag{4}$$

where $[u_\theta] = u_\theta - \bar{u}_\theta$. Here, the quantities with a bar refer to the inhomogeneities; in addition, G and a denote the shear moduli of the matrix and the radius of the fiber cross-section, respectively. The constant of proportionality λ indicates the degree of interfacial integrity; $\lambda \to 0$ corresponds to perfect bonding, while when $\lambda \to \infty$, conditions of perfect slip are obtained (the interface does not sustain any shear tractions).

In order to account for the disturbance due to the presence of the inhomogeneities, we utilize the Papkovich-Neuber displacement formulation. Consequently, the displacement fields u_1 and u_2 are

$$2Gu_i = \text{grad}\ [\varphi_{0i} + x_i\, \varphi_{1i} + y_i\, \varphi_{2i}] - 4(1-\nu)\ [\varphi_{1i},\ \varphi_{2i}],\ (i = 1,\ 2) \tag{5}$$

where φ_{0i}, φ_{1i}, and φ_{2i} are arbitrary harmonic functions.

For the problem under consideration, the potentials chosen are: for the matrix ($r_i > a_i$)

$$\begin{cases} \varphi_{0i} = p_0 \left[F_0^i \log \rho_i + \sum_{n=1}^{\infty} A_n^i\, \rho_i^{-n} \cos n\theta_i \right] \\ \varphi_{1i} = p_0 \sum_{n=1}^{\infty} B_n^i \rho_i^{-n} \cos n\theta_i \quad \varphi_{2i} \equiv 0 \end{cases} \tag{I}$$

and for the two inhomogeneities ($r_i < a_i$)

$$\begin{cases} \varphi_{0i} = p_0 \sum_{n=1}^{\infty} \bar{A}_n^i\, \rho_i^n \cos n\theta_i \\ \varphi_{1i} = p_0 \sum_{n=1}^{\infty} \bar{B}_n^i \rho_i^n \cos n\theta_i \quad \varphi_{2i} \equiv 0 \end{cases} \tag{II}$$

where $\rho_i = r_i/c$ and $p_0 = T$. The central distance c is taken to be equal to unity and T is equal to T_x or T_y.

Using the potential functions [I] and [II], we can derive stresses and displacements in the matrix and the inhomogeneities; with the addition of the uniform field described in (1), what remain to be determined are the values of the coefficients F_0^i, A_n^i, B_n^i, $\bar{A}_n^i$ and $\bar{B}_n^i$. This can be accomplished by enforcing the boundary conditions (4) along the interface of the inclusions.

Using the transformation formulas that have been given in Kouris and Tsuchida (1991), the requirement for continuity of the normal stress along the interface of the cross-section of the first fiber ($r_1 = a_1$) is expressed by:

$$\begin{aligned} \sigma_r = \bar{\sigma}_r \Rightarrow & -F_0^1 \frac{1}{a_1^2} + \sum_{n=1}^{\infty} A_n^1 \frac{n(n+1)}{a_1^{n+2}} \cos n\theta_1 \\ & + \frac{1}{2} \sum_{n=2}^{\infty} B_{n-1}^1 \frac{(n-1)(n+2)}{a_1^n} \cos n\theta_1 \\ & + \frac{1}{2} \sum_{n=0}^{\infty} B_{n+1}^1 \frac{n(n+1)(n+1+\kappa)}{a_1^{n+2}} \cos n\theta_1 \\ & - F_0^2 \sum_{n=1}^{\infty} (n-1)\, a_1^{n-2} \cos n\theta_1 \\ & + \sum_{n=0}^{\infty} \sum_{m=1}^{\infty} (-1)^m\, (A_m^2 - B_m^2)\, W_n^m\, n(n-1)\, a_1^{n-2} \cos n\theta_1 \\ & + \frac{1}{2} \sum_{n=1}^{\infty} \sum_{m=1}^{\infty} (-1)^m\, B_m^2\, W_{n-1}^m\, a_1^{n-2} \\ & (n-1) \times (n-1-\kappa) \cos n\theta_1 \\ & + \frac{1}{2} \sum_{n=0}^{\infty} \sum_{m=1}^{\infty} (-1)^m\, B_m^2\, W_{n+1}^m\, a_1^n\, (n+1)\, (n-2) \cos n\theta_1 \\ & - \sum_{n=1}^{\infty} \bar{A}_n^1\, n(n-1)\, a_1^{n-2} \cos n\theta_1 \\ & - \frac{1}{2} \sum_{n=2}^{\infty} \bar{B}_{n-1}^1\, (n-1)\, (n-1-\bar{\kappa})\, a_1^{n-2} \cos n\theta_1 \end{aligned}$$

Downloaded 03 May 2010 to 171.66.16.245. Redistribution subject to ASME license or copyright; see http://www.asme.org/terms/Terms_Use.cfm

$$-\frac{1}{2}\sum_{n=0}^{\infty}\overline{B}^1_{n+1}\,(n+1)\,(n-2)\,a_1^n\cos n\theta_1$$

$$-\frac{1}{2}(1+t)-\frac{1}{2}(1-t)\cos 2\theta_1, \quad (6)$$

where $t=T_y/T_x$ $(0<t<1)$ and $W_n^m=(m+n-1)!/(m-1)!n!$.

Similar expressions are obtained for the remaining boundary conditions given in (4).

Using the same procedure, we can enforce the boundary conditions along the interface of the second circular inhomogeneity. However, since the fiber cross-sections are identical and due to the symmetry of the problem, we only have to satisfy the boundary conditions along one of the interfaces; the other will be satisfied automatically.

Utilizing the symmetry relations

$$A_n^1=(-1)^n A_n^2=A_n,\ B_n^1=(-1)^{n+1}B_n^2=B_n, \quad (7)$$
$$\overline{A}_n^1=(-1)^n\overline{A}_n^2=\overline{A}_n,\ \overline{B}_n^1=(-1)^{n+1}\overline{B}_n^2=\overline{B}_n,\ a_1=a_2=a,$$

we can express the condition (6) as follows:

$$-F_0\frac{1}{a_2}\delta_n^{(0)}+A_n\frac{n(n+1)}{a^{n+2}}+\frac{1}{2}B_{n-1}\frac{(n-1)(n+2)}{a^n}$$
$$+\frac{1}{2}B_{n+1}\frac{(n+1)(n+1+\kappa)}{a^{n+2}}$$
$$-F_0\,(n-1)\,a^{n-2}+\sum_{m=1}^{\infty}(A_m+B_m)\,W_n^m\,n(n-1)\,a^{n-2}$$
$$-\frac{1}{2}\sum_{m=1}^{\infty}B_m\,W_{n-1}^m\,(n-1)(n-1-\kappa)\,a^{n-2}$$
$$-\frac{1}{2}\sum_{m=1}^{\infty}B_m\,W_{n+1}^m\,(n+1)(n-2)\,a^n-\overline{A}_n\,n(n-1)\,a^{n-2}$$
$$-\frac{1}{2}\overline{B}_{n-1}\,(n-1)\,(n-1-\overline{\kappa})\,a^{n-2}-\overline{B}_{n+1}\,(n+1)\,(n-2)\,a^n$$
$$=-\frac{1}{2}(1+t)\,\delta_n^{(0)}-\frac{1}{2}(1-t)\,\delta_n^{(2)}\quad(n=0,1,2,\ldots) \quad (8)$$

where $\delta_n^{(i)}$ denotes Kronecker's delta.

3 Results and Discussion

The linear system of equations consisting of (8) and the remaining boundary conditions is solved for the unknown coefficients F_0, A_n, B_n, $\overline{A}_n$, and $\overline{B}_n$. The series solution requires no more than 15 terms to ensure matching of the boundary conditions up to the three significant figures, and its convergence is numerically evident. After evalulating the series coefficients, stresses and displacements in the matrix and the fiber cross-sections can be determined.

In order to illustrate the effects of the fiber/matrix shear moduli ratio $\Gamma(\Gamma=\overline{G}/G)$ and the fiber/fiber distance on the stress concentration, the external load has been taken as $p_0=T_x=T_y$ $(t=1)$.

In a number of studies that investigate effective properties of composites, the "single fiber" solution is utilized in order to obtained global properties, in an average sense. Such an approach, however, may be quite inaccurate in predicting the local stress field, which is essential from a fracture point of view. Figure 2 indicates the variation of the matrix interfacial stress σ_y/p_0 (at the central line) versus the normalized fiber distance d/a; the shear moduli ratio is taken equal to 2, 5, and 10 and $\nu=\overline{\nu}=0.3$.

If we denote with an asterisk (*) the values of σ_y/p_0 that are obtained from superposition of the single fiber solution, we

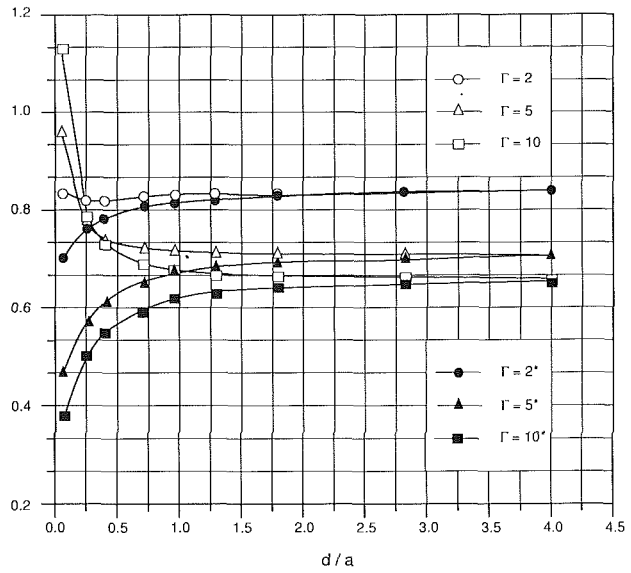


Fig. 2 Distribution of σ_y/p_0 at the interface versus the fiber distance; comparison between the exact and approximate solutions

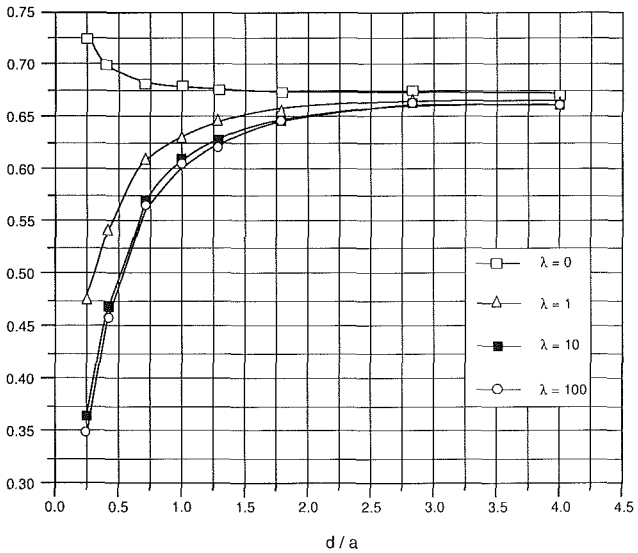


Fig. 3 Effect of the incoherent interface on the distribution of σ_y/p_0 for a Ti_3Al/SCS6 system

can observe that they are in error; such an error becomes significant with increasing Γ (stiffer fibers) when the fibers approach each other (high volume fraction). It is expected, however, that as the fiber distance increases, the differences between the exact and approximate solutions tend towards zero.

Another aspect of the problem relates to the effect of incoherent interfaces. As a example, we consider a Ti_3Al/SiC (SCS6) composite with the following properties: (a) Ti_3Al (matrix) $-G=30$GPa and $\nu=0.25$ (b) SCS6 (fibers) $-\overline{G}=154$GPa and $\overline{\nu}=0.17$.

The distribution of σ_y/p_0 versus the fiber distance, is shown in Fig. 3; here $\lambda=0$ corresponds to the condition of perfect bond, while $\lambda=100$ indicates perfect sliding. As the fiber distance decreases, a weak interfacial bond causes a considerable relaxation of the matrix stress and, therefore, enhances the fracture toughness. However, if the fibers are far apart, the degree of the interfacial integrity has no effect on the stress concentration.

Downloaded 03 May 2010 to 171.66.16.245. Redistribution subject to ASME license or copyright; see http://www.asme.org/terms/Terms_Use.cfm

Acknowledgment

This work has been supported by the Air Force Office of Scientific Research through the University Research Initiative Award AFOSR90-0235.

References

Benveniste, Y., 1984, "On the Effect of Debonding on the Overall Behavior of Composite Materials," *Mechanics of Materials*, Vol. 3, pp. 349-358.

Jasiuk, I., Chen, J., and Thrope, M. F., 1989, "Elastic Moduli of Composites with Rigid Sliding Inclusions," *Journal of Mechanics and Physics of Solids*, to appear.

Kouris, D., and Tsuchida, E., 1991, "On the Elastic Interaction between two Fibers in a Continuous Fiber Composite under Thermal Loading," *Mechanics of Materials*, Vol. 12, pp. 131-146.

Lene, F., and Leguillon, D., 1982, "Homogeneized Constitutive Law for a Partially Cohesive Composite Material," *Int. Journal of Solids and Structures*, Vol. 18, No. 5, pp. 443-458.

Shioya, S., 1971, "On the Tension of an Infinite Thin Plate Containing a Pair of Circular Inclusions," *Bulletin of the JSME*, Vol. 14, No. 68, pp. 117-126.

A Superposition Method for One-Dimensional Axially Symmetric Elastic Waves

Zhang Xiangzhou[2]

Introduction

Responses of an elastic, infinite medium containing a cylindrical, circular cavity to axially symmetric dynamic loading is of fundamental interest in elastodynamics. The geometry, loading, and mathematical formulation involved in the responses are simple. Nevertheless, this problem is very difficult to solve analytically. As indicated in standard reference books, the integral in the solution of the problem is "extremely difficult" to evaluate, and there is "an essential difficulty" inherent in this kind of wave propagation (Eringen and Suhubi, 1975); the solution and its derivation are "not simple" (Miklowitz, 1978); the problem is "much more difficult to analyze" (Achenbach, 1976); and so on. Therefore, an analytic solution method, which can solve the problem effectively, still appears to be desirable.

In this Note, a superposition method, based on Lamb's formal solution, is developed to treat the problem. Numerical examples demonstrate that the method is able to solve the axially symmetric wave propagation problem accurately and neatly.

Basic Solutions for the Radial Motion Problem

A cross-section of a linearly elastic, infinite medium containing a cylindrical, circular cavity is depicted in Fig. 1. The medium is at rest initially and then undergoes a radial motion due to an axially symmetric, normal traction $g(t)$ suddenly applied on its circumferential boundary. As is well known (Achenbach, 1976), the radial displacement u and the normal stresses σ_r, σ_θ, and σ_z developed in the medium should be sought via the following basic equation and conditions:

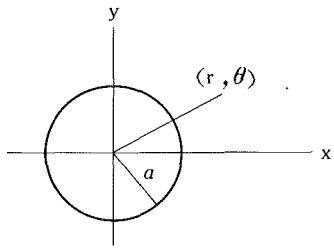


Fig. 1 Geometry of the problem

$$\frac{\partial^2\varphi}{\partial r^2}+\frac{1}{r}\frac{\partial\varphi}{\partial r}=\frac{1}{c_1^2}\frac{\partial^2\varphi}{\partial t^2} \tag{1}$$

$$c_1t<a,\quad u=0,\quad \partial u/\partial t=0 \tag{2a,b}$$

$$c_1t>a,\quad r=a,\quad \sigma_r=g(t) \tag{3}$$

$$r\to\infty,\quad u\to 0,\quad \partial u/\partial t\to 0 \tag{4a,b}$$

$$u=\frac{\partial\varphi}{\partial r},\quad \sigma_r=\lambda\left(\frac{\partial u}{\partial r}+\frac{u}{r}\right)+2\mu\frac{\partial u}{\partial r} \tag{5a,b}$$

$$\sigma_\theta=\lambda\left(\frac{\partial u}{\partial r}+\frac{u}{r}\right)+2\mu\frac{u}{r},\quad \sigma_z=\lambda\left(\frac{\partial u}{\partial r}+\frac{u}{r}\right) \tag{6a,b}$$

where λ and μ stand for Lame constants and c_1 represents the longitudinal wave speed of the material. Equations (5b) and (6a,b) are for plane-strain state. For plane stress, λ in Eqs. (5b), (6a) should be replaced by $2\lambda\mu/(\lambda+2\mu)$ and $\sigma_z=0$.

Lamb provided a formal solution to Eq. (1). It reads (Eringen and Suhubi, 1975; Lamb, 1902):

$$\varphi(r,t)=\begin{cases}0, & c_1t<r \qquad (7a)\\ \displaystyle\int_0^{\cosh^{-1}c_1t/r} f(c_1t-r\cosh u)du, & c_1t>r. \qquad (7b)\end{cases}$$

Subsequent to Eqs. (7a,b), the following expressions for u and $\partial u/\partial r$ can be obtained directly:

$$u(r,t)=\begin{cases}0, & c_1t<r \qquad (8a)\\ \displaystyle-\int^{\cosh^{-1}c_1t/r}\cosh u f'(c_1t-r\cosh u)du & \\ -f(0)c_1t/[r(c_1^2t^2-r^2)^{1/2}], & c_1t>r. \qquad (8b)\end{cases}$$

$$\frac{\partial u}{\partial r}=\begin{cases}0, & c_1t<r \qquad (9a)\\ \displaystyle\int_0^{\cosh^{-1}c_1t/r}\cosh^2 u f''(c_1t-r\cosh u)du+\frac{f'(0)c_1^2t^2}{r^2(c_1^2t^2-r^2)^{1/2}} & \\ \displaystyle+\frac{f(0)c_1t}{(c_1^2t^2-r^2)^{1/2}}\left(\frac{1}{r^2}-\frac{1}{c_1^2t^2-r^2}\right), & c_1t>r \qquad (9b)\end{cases}$$

where $f'(x)=df(x)/dx$.

The displacement and stresses in the medium are developed for $t>a/c_1$. However, our main concern lies within the prime stage of the dynamic response, that is, within a certain interval of t, $[a/c_1, T]$, with T being a sufficiently large number. Within the interval, any continuous function $f(c_1t-r)$ in Eq. (7b) can be expanded into the following form:

$$f(c_2t-r)=a_0+a_1(c_1t-r)+a_2(c_1t-r)^2+\cdots+a_n(c_1t-r)^n+\cdots. \tag{10}$$

Denoting φ, u and $\partial u/\partial r$ derived from the term $a_n(c_1t-r)^n$ in the above formula with $a_n=1$ by σ_n, u_n and $(\partial u/\partial r)_n$,

[2]Department of Aircraft Engineering, Northwestern Polytechnical University, Xian, 710072, China.

Manuscript received by the ASME Applied Mechanics Division, Jan. 1, 1991; final revision, Oct. 17, 1991. Associate Technical Editor: S. K. Datta.

Downloaded 03 May 2010 to 171.66.16.245. Redistribution subject to ASME license or copyright; see http://www.asme.org/terms/Terms_Use.cfm

Acknowledgment

This work has been supported by the Air Force Office of Scientific Research through the University Research Initiative Award AFOSR90-0235.

References

Benveniste, Y., 1984, "On the Effect of Debonding on the Overall Behavior of Composite Materials," *Mechanics of Materials*, Vol. 3, pp. 349-358.

Jasiuk, I., Chen, J., and Thrope, M. F., 1989, "Elastic Moduli of Composites with Rigid Sliding Inclusions," *Journal of Mechanics and Physics of Solids*, to appear.

Kouris, D., and Tsuchida, E., 1991, "On the Elastic Interaction between two Fibers in a Continuous Fiber Composite under Thermal Loading," *Mechanics of Materials*, Vol. 12, pp. 131-146.

Lene, F., and Leguillon, D., 1982, "Homogeneized Constitutive Law for a Partially Cohesive Composite Material," *Int. Journal of Solids and Structures*, Vol. 18, No. 5, pp. 443-458.

Shioya, S., 1971, "On the Tension of an Infinite Thin Plate Containing a Pair of Circular Inclusions," *Bulletin of the JSME*, Vol. 14, No. 68, pp. 117-126.

A Superposition Method for One-Dimensional Axially Symmetric Elastic Waves

Zhang Xiangzhou[2]

Introduction

Responses of an elastic, infinite medium containing a cylindrical, circular cavity to axially symmetric dynamic loading is of fundamental interest in elastodynamics. The geometry, loading, and mathematical formulation involved in the responses are simple. Nevertheless, this problem is very difficult to solve analytically. As indicated in standard reference books, the integral in the solution of the problem is "extremely difficult" to evaluate, and there is "an essential difficulty" inherent in this kind of wave propagation (Eringen and Suhubi, 1975); the solution and its derivation are "not simple" (Miklowitz, 1978); the problem is "much more difficult to analyze" (Achenbach, 1976); and so on. Therefore, an analytic solution method, which can solve the problem effectively, still appears to be desirable.

In this Note, a superposition method, based on Lamb's formal solution, is developed to treat the problem. Numerical examples demonstrate that the method is able to solve the axially symmetric wave propagation problem accurately and neatly.

Basic Solutions for the Radial Motion Problem

A cross-section of a linearly elastic, infinite medium containing a cylindrical, circular cavity is depicted in Fig. 1. The medium is at rest initially and then undergoes a radial motion due to an axially symmetric, normal traction $g(t)$ suddenly applied on its circumferential boundary. As is well known (Achenbach, 1976), the radial displacement u and the normal stresses σ_r, σ_θ, and σ_z developed in the medium should be sought via the following basic equation and conditions:

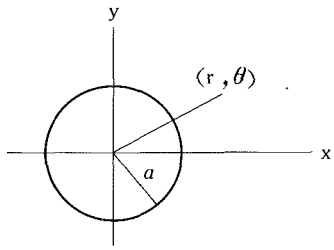


Fig. 1 Geometry of the problem

$$\frac{\partial^2\varphi}{\partial r^2}+\frac{1}{r}\frac{\partial\varphi}{\partial r}=\frac{1}{c_1^2}\frac{\partial^2\varphi}{\partial t^2} \tag{1}$$

$$c_1t<a,\quad u=0,\quad \partial u/\partial t=0 \tag{2a,b}$$

$$c_1t>a,\quad r=a,\quad \sigma_r=g(t) \tag{3}$$

$$r\to\infty,\quad u\to 0,\quad \partial u/\partial t\to 0 \tag{4a,b}$$

$$u=\frac{\partial\varphi}{\partial r},\quad \sigma_r=\lambda\left(\frac{\partial u}{\partial r}+\frac{u}{r}\right)+2\mu\frac{\partial u}{\partial r} \tag{5a,b}$$

$$\sigma_\theta=\lambda\left(\frac{\partial u}{\partial r}+\frac{u}{r}\right)+2\mu\frac{u}{r},\quad \sigma_z=\lambda\left(\frac{\partial u}{\partial r}+\frac{u}{r}\right) \tag{6a,b}$$

where λ and μ stand for Lame constants and c_1 represents the longitudinal wave speed of the material. Equations (5b) and (6a,b) are for plane-strain state. For plane stress, λ in Eqs. (5b), (6a) should be replaced by $2\lambda\mu/(\lambda+2\mu)$ and $\sigma_z=0$.

Lamb provided a formal solution to Eq. (1). It reads (Eringen and Suhubi, 1975; Lamb, 1902):

$$\varphi(r,t)=\begin{cases}0, & c_1t<r \qquad (7a)\\ \displaystyle\int_0^{\cosh^{-1}c_1t/r} f(c_1t-r\cosh u)du, & c_1t>r. \qquad (7b)\end{cases}$$

Subsequent to Eqs. (7a,b), the following expressions for u and $\partial u/\partial r$ can be obtained directly:

$$u(r,t)=\begin{cases}0, & c_1t<r \qquad (8a)\\ \displaystyle-\int^{\cosh^{-1}c_1t/r}\cosh u f'(c_1t-r\cosh u)du & \\ -f(0)c_1t/[r(c_1^2t^2-r^2)^{1/2}], & c_1t>r. \qquad (8b)\end{cases}$$

$$\frac{\partial u}{\partial r}=\begin{cases}0, & c_1t<r \qquad (9a)\\ \displaystyle\int_0^{\cosh^{-1}c_1t/r}\cosh^2 u f''(c_1t-r\cosh u)du+\frac{f'(0)c_1^2t^2}{r^2(c_1^2t^2-r^2)^{1/2}} & \\ \displaystyle+\frac{f(0)c_1t}{(c_1^2t^2-r^2)^{1/2}}\left(\frac{1}{r^2}-\frac{1}{c_1^2t^2-r^2}\right), & c_1t>r \qquad (9b)\end{cases}$$

where $f'(x)=df(x)/dx$.

The displacement and stresses in the medium are developed for $t>a/c_1$. However, our main concern lies within the prime stage of the dynamic response, that is, within a certain interval of t, $[a/c_1, T]$, with T being a sufficiently large number. Within the interval, any continuous function $f(c_1t-r)$ in Eq. (7b) can be expanded into the following form:

$$f(c_2t-r)=a_0+a_1(c_1t-r)+a_2(c_1t-r)^2+\cdots+a_n(c_1t-r)^n+\cdots. \tag{10}$$

Denoting φ, u and $\partial u/\partial r$ derived from the term $a_n(c_1t-r)^n$ in the above formula with $a_n=1$ by σ_n, u_n and $(\partial u/\partial r)_n$,

[2]Department of Aircraft Engineering, Northwestern Polytechnical University, Xian, 710072, China.

Manuscript received by the ASME Applied Mechanics Division, Jan. 1, 1991; final revision, Oct. 17, 1991. Associate Technical Editor: S. K. Datta.

Copyright © 1993 by ASME
Downloaded 03 May 2010 to 171.66.16.245. Redistribution subject to ASME license or copyright; see http://www.asme.org/terms/Terms_Use.cfm

respectively; φ_0, u_o, $(\partial u/\partial r)_0$, φ_1, u_1, $(\partial u/\partial r)_1$ can be worked out and written as follows for $c_1 t > r$:

$$\varphi_0 = \cosh^{-1} c_1 t/r, \quad u_0 = -c_1 t/(r\sqrt{c_1^2 t^2 - r^2}) \qquad (11a,b)$$

$$\left(\frac{\partial u}{\partial r}\right)_0 = \frac{c_1 t}{\sqrt{c_1^2 t^2 - r^2}} \left(\frac{1}{r^2} - \frac{1}{c_1^2 t^2 - r^2}\right) \qquad (12)$$

$$\varphi_1 = c_1 t \cosh^{-1} \frac{c_1 t}{r} - \sqrt{c_1^2 t^2 - r^2} \qquad (13)$$

$$u_1 = -\frac{\sqrt{c_1^2 t^2 - r^2}}{r}, \quad \left(\frac{\partial u}{\partial r}\right)_1 = \frac{c_1^2 t^2}{r^2 \sqrt{c_1^2 t^2 - r^2}}. \qquad (14a,b)$$

From Eqs. (11)–(14) it is seen that φ_0 and φ_1 represent strong disturbances producing infinite displacement and (or) stress discontinuities on the wave front. For $n > 2$, φ_n, u_n and $(\partial u/\partial r)_n$ can be found from the following recurrence formulas:

$$\varphi_n = [(2n-1)c_1 t \varphi_{n-1} + (n-1)(r^2 - c_1^2 t^2)\varphi_{n-2}]/n \qquad (15)$$

$$u_n = n(\varphi_n - c_1 t \varphi_{n-1})/r \qquad (16)$$

$$\left(\frac{\partial u}{\partial r}\right)_n = n(n-1)(\varphi_n - 2c_1 t \varphi_{n-1} + c_1^2 t^2 \varphi_{n-2})/r^2. \qquad (17)$$

It can be seen that Eqs. (16) and (17) give a complete group of u_n and $(\partial u/\partial r)_n$ that are continuous across the wave front.

To simulate some idealized physical process, for instance one that induced by a step load, solutions having finite jumps of stresses on the wave front are also of interest. One basic type of such solutions can be constructed from the disturbance $f(c_1 t - r) = \varphi_{3/2} = (c_1 t - r)^{3/2}$. The displacement and the displacement gradient corresponding to this form of disturbance can be obtained from Eqs. (8) and (9) using some quadrature formulas contained in standard reference books (Gradshteyn and Ryzhik, 1980). For $c_1 t > r$, the results are

$$u_{3/2} = -\frac{c_1 t}{r}\sqrt{c_1 t + r}E(\alpha) + \sqrt{c_1 t + r}F(\alpha) \qquad (18)$$

$$\left(\frac{\partial u}{\partial r}\right)_{3/2} = \frac{c_1 t}{r^2}\sqrt{c_1 t + r}E(\alpha) + \frac{1 - 2c_1 t/r}{2\sqrt{c_1 t + r}}F(\alpha) \qquad (19)$$

where $\alpha = \sqrt{(c_1 t - r)/(c_1 t + r)}$, $F(\alpha)$ and $E(\alpha)$ stand for the complete elliptic integrals of the first and second kinds, respectively.

Equation (18) shows that the displacement vanishes on the wave front and is therefore continuous. On the other hand, as indicated in Eq. (19), across the wave front, $(\partial u/\partial r)_{3/2}$ undergoes a jump of finite magnitude $3\sqrt{2\pi}/8r^{1/2}$. The jump decays as $r^{-1/2}$ during propagation, a fact that is consistent with the known result about the wave front approximation (Miklowitz, 1978).

The basic solutions for the axially symmetric wave propagation, φ_n, u_n, $(\partial n/\partial r)_n$ $(n = 0, 1, 2, \cdots)$ and $\varphi_{3/2}$, $u_{3/2}$, $(\partial u/\partial r)_{3/2}$ are now prepared. By the use of these solutions and Eqs. (7), the solution of a particular problem of dynamic response, prescribed by Eqs. (1–6), is reduced to the solution of the following integro-differential equation

$$(\lambda + 2\mu)\int_0^{\cosh^{-1} c_1 t/a} \cosh^2 u f''(c_1 t - a\cosh u)du - \frac{\lambda}{a}\int_0^{\cosh^{-1} c_1 t/a} \cosh u f'(c_1 t - a\cosh u)du = g(t), \quad c_1 t > a \qquad (20)$$

which is an alternative form of the primary boundary condition (3). Equation (20) applies to the plane-strain state. For the plane-stress state, the constant λ in the equation should be substituted by $2\lambda\mu/(\lambda + 2\mu)$. The solution of Eq. (20) will be discussed in the following section.

Example and Discussion

In this section, an example of radial motion is treated and is used to demonstrate that the axially symmetric wave propagation problem can accurately and neatly be solved via the solving of the integro-differential Eq. (20) with the basic solutions developed in the preceding section.

In the example, the radial motion is developed under the plane-stress state and the problem is prescribed by Eqs. (1)–(6) with $a = 1$, $\lambda/[2(\lambda + \mu)] = 0.3$ and $g(t) = H(t - c_1^{-1})$, where $H(\tau)$ denotes the Heaviside unit step function.

To solve the problem, the basic solutions φ_2, φ_3, $\varphi_{3/2}$, and their derivatives will be used. Writing σ_r corresponding to φ_k $(k = 2, 3, 3/2)$ with σ_{rk}, the expressions for the radial stress σ_r on the boundary $r = a = 1$ is written as follows:

$$\text{for } c_1 t < 1, \quad \sigma_r(1,t) = 0 \qquad (21)$$

$$\text{for } c_1 t > 1, \quad \sigma_r(1,t) = \sigma_{r3/2}(1,t)/\sigma_{r3/2}(1,1/c_1) + a_1\sigma_{r2}(1,t) + b_1\sigma_{r3}(1,t) + a_2\sigma_{r2}(1,t-\Delta t) + b_2\sigma_{r3}(1,t-\Delta t) + \sum_{i=3}^{N}[a_i\sigma_{r2}(1,t-(i-1)\Delta t) + b_i\sigma_{r3}(1,t-(i-1)\Delta t)]. \qquad (22)$$

In the preceding formula, Δt represents a definite time interval and it is prescribed that $\sigma_{rk} = 0$ for $t < c_1^{-1}$. At the initiation moment $c_1 t = 1$, the value of the first term is unity and those of the other terms are respectively zero. The boundary condition $\sigma_r(1, t) = H(t - c_1^{-1})$ is exactly satisfied at $c_1 t = 1$ by these terms. For $t > c_1^{-1}$, the sum of the first three terms will deviate from $H(t - c_1^{-1})$. However, the deviation can be suppressed by imposing the following requirements on $\sigma_r(1, t)$:

$$a_1\sigma_{r2}(1,c_1^{-1} + \Delta t/2) + b_1\sigma_{r3}(1,c_1^{-1} + \Delta t/2) = 1 - \sigma_{r3/2}(1,c_1^{-1} + \Delta t/2)/\sigma_{r3/2}(1,c_1^{-1}) \qquad (23)$$

$$a_1\sigma_{r2}(1,c_1^{-1} + \Delta t) + b_1\sigma_{r3}(1,c_1^{-1} + \Delta t) = 1 - \sigma_{r3/2}(1,c_1^{-1} + \Delta t)/\sigma_{r3/2}(1,c_1^{-1}) \qquad (24)$$

which means that $\sigma_r(1, t) = 1$ at $t = 1/c_1 + \Delta t/2$, $1/c_1 + \Delta t$. Consequently, the boundary condition $\sigma_r(1, t) = H(t - 1/c_1)$ is satisfied at $t = 1/c_1 + \Delta t/2$, $1/c_1 + \Delta t$ as well. For an instant within the time interval $[1/c_1, 1/c_1 + \Delta t]$ other than the above three instants, the boundary condition is not satisfied exactly, in general, but the deviation will be tiny, provided Δt is small.

To guarantee that $\sigma_r(1, t) = H(t - 1/c_1)$ is exactly valid at $t = 1/c_1 + 3\Delta t/2$, $1/c_1 2\Delta t$, two additional terms with factors a_2 and b_2 must be added to the right-hand side of Eq. (22). Similarly, the factors a_2 and b_2 should be determined from the following equations:

$$a_2\sigma_{r2}(1,c_1^{-1} + \Delta t/2) + b_2\sigma_{r3}(1,c_1^{-1} + \Delta t/2) = 1 - \sigma_{r3/2}(1,c_1^{-1} + 3\Delta t/2)/\sigma_{r3/2}(1,c_1^{-1}) - a_1\sigma_{r2}(1,c_1^{-1} + 3\Delta t/2) - b_1\sigma_{r3}(1,c_1^{-1} + 3\Delta t/2) \qquad (25)$$

$$a_2\sigma_{r2}(1,c_1^{-1} + \Delta t) + b_2\sigma_{r3}(1,c_1^{-1} + \Delta t) = 1 - \sigma_{r3/2}(1,c_1^{-1} + 2\Delta t)/\sigma_{r3/2}(1,c_1^{-1}) - a_1\sigma_{r2}(1,c_1^{-1} + 2\Delta t) - b_1\sigma_{r3}(3,c_1^{-1} + 2\Delta t). \qquad (26)$$

Similar steps should be carried on until $t = 1/c_1 + N\Delta t$ is reached, with N being a sufficiently large integer. These subsequent steps bring about the summation term on the right-hand side of Eq. (22).

In this example, the integro-differential Eq. (20) takes the form of

$$\int_0^{\cosh^{-1} c_1 t/a}\left[\frac{4\mu(\lambda+\mu)\cosh^2 u}{(\lambda+2\mu)}f''(c_1 t - a\cosh u) - \frac{2\lambda\mu\cosh u}{a(\lambda+2\mu)}f'(c_1 t - a\cosh u)\right]du = H(t - c_1^{-1}), \quad c_1 t > a, a = 1. \qquad (27)$$

Downloaded 03 May 2010 to 171.66.16.245. Redistribution subject to ASME license or copyright; see http://www.asme.org/terms/Terms_Use.cfm

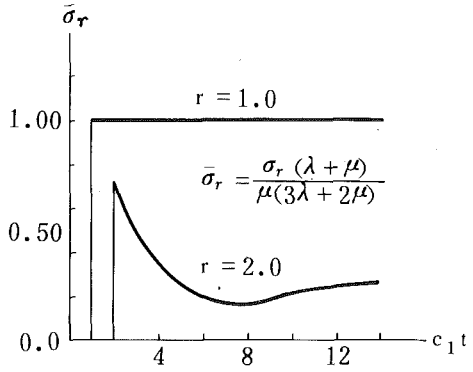


Fig. 2 Numerical values of radial stress

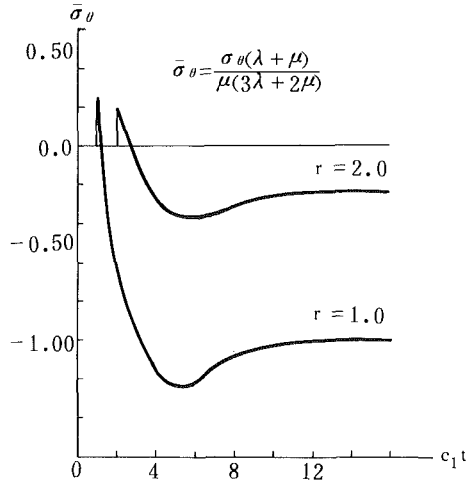


Fig. 3 Numerical values of tangential stress

It is seen that Eqs. (21) and (22) satisfy the above equation almost exactly within the interval $[1/c_1, 1/c_1 + N\Delta t]$. At points $t = 1/c_1 + j\Delta t$, $1/c_1 + j\Delta t - \Delta t/2$, $j = 0, 1, 2, \cdots, N$, the satisfying is rigorous.

Accurate values of displacement and stresses in this example can easily be computed from the solution. Using $c_1\Delta t = 1$, which is a fairly large number in this example, numerical values of radial and tangential stresses in the medium have been evaluated and shown by curves in Fig. 2 and Fig. 3, respectively. The results agree very well with those obtained by others (Chou and Koenig, 1966).

Rotary shear and axial shear are two other forms of one-dimensional axially symmetric elastic waves. They have been treated by the same method developed in this Note with favorable results. It is not necessary to present the results here, owing to their close similarity in mathematical formulation to the radial motion problem.

References

Achenbach, J. D., 1976, *Wave Propagation in Elastic Solids*, North Holland, Amsterdam.

Chou, P. C., and Koenig, H. A., 1966, "A Unified Approach to Cylindrical and Spherical Elastic Waves by Method of Characteristics," ASME JOURNAL OF APPLIED MECHANICS, Vol. 88, pp. 159-167.

Eringen, A. C., and Suhubi, E. S., 1975, *Elastodynamics*, Vol. 2: *Linear Theory*, Academic Press, New York.

Gradshteyn, I. S., and Ryzhik, I. M., 1980, *Tables of Integrals, Series, and Products*, Academic Press, New York.

Lamb, H., 1902, "On Wave Propagation in Two-Dimensions," *Proc. London Math. Soc.*, Vol. 35, pp. 141-161.

Miklowitz, J., 1978, *Elastic Waves and Waveguides*, North Holland, Amsterdam.

Transverse Vibration of Solid Circular Plates Continuous Over Multiple Concentric Annular Supports

K. M. Liew[3] and K. Y. Lam[4]

1 Introduction

A survey from the literature reveals that only a limited amount of research work has been done on ring-supported circular plates during the past few decades (Bodine, 1959; Kunukkasseril and Swamidas, 1974). The drawback may be due to the difficulty in forming a simple and adequate deflection function which can be applied to the entire plate domain, such that it satisfies the boundary conditions at the ring supports and also the plate periphery. The aim of the present work is to develop an accurate and efficient numerical model based on a set of orthogonal plate functions (details can be found in Liew and Lam, 1991) and to study the free vibration of multiple ring-supported circular plate.

2 Method of Analysis

The expression for the strain energy of a plate in bending is given by

$$V=\frac{1}{2}D\int\int_R\left\{\left[\frac{\partial^2 W}{\partial x^2}\right]^2+2\nu\left[\frac{\partial^2 W}{\partial x^2}\frac{\partial^2 W}{\partial y^2}\right]+\left[\frac{\partial^2 W}{\partial y^2}\right]^2+2(1-\nu)\left[\frac{\partial^2 W}{\partial x\partial y}\right]^2\right\}dxdy \quad (1)$$

where $D = Eh^3/12(1-\nu^2)$, E is the Young's modulus, h is the plate thickness, and ν is the Poisson's ratio.

To find the least upper bound on the frequency, minimization is needed, with respect to the undetermined coefficients C_i,

$$\frac{\partial V}{\partial C_i}-\frac{1}{2}\rho h\omega^2\frac{\partial}{\partial C_i}\left[\int\int_R W^2(x,y)dxdy\right]=0, \quad (2)$$

which leads to the governing eigenvalue equation

$$\Sigma[K_{ij}-\lambda M_{ij}]C_i=0;\ i,j=1,2,\ \ldots,m \quad (3)$$

where

$$K_{ij}=P_{ij}+Q_{ij}+\nu(R_{ij}+S_{ij})+2(1-\nu)T_{ij} \quad (4)$$

$$M_{ij}=\int\int_R\phi_i(x,y)\phi_j(x,y)dxdy \quad (5)$$

$$P_{ij}=\int\int_R\frac{\partial^2\phi_i(x,y)}{\partial x^2}\frac{\partial^2\phi_j(x,y)}{\partial x^2}dxdy \quad (6)$$

$$Q_{ij}=\int\int_R\frac{\partial^2\phi_i(x,y)}{\partial y^2}\frac{\partial^2\phi_j(x,y)}{\partial y^2}dxdy \quad (7)$$

$$R_{ij}=\int\int_R\frac{\partial^2\phi_i(x,y)}{\partial y^2}\frac{\partial^2\phi_j(x,y)}{\partial x^2}dxdy \quad (8)$$

[3]Lecturer, School of Mechanical and Production Engineering, Nanyang Technological University, Singapore 2263, Republic of Singapore.

[4]Senior Lecturer, Department of Mechanical and Production Engineering, National University of Singapore, Singapore 0511, Republic of Singapore. Mem. ASME.

Manuscript received by the ASME Applied Mechanics Division, May 25, 1990; final revision, May 31, 1991. Associate Technical Editor: D. J. Inman.

Downloaded 03 May 2010 to 171.66.16.245. Redistribution subject to ASME license or copyright; see http://www.asme.org/terms/Terms_Use.cfm

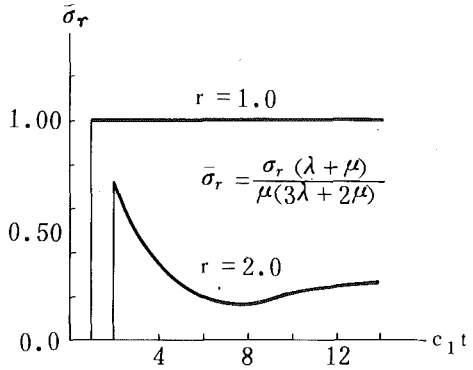


Fig. 2 Numerical values of radial stress

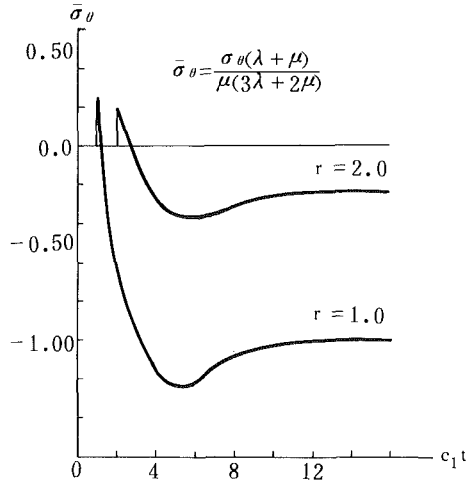


Fig. 3 Numerical values of tangential stress

It is seen that Eqs. (21) and (22) satisfy the above equation almost exactly within the interval $[1/c_1, 1/c_1 + N\Delta t]$. At points $t = 1/c_1 + j\Delta t$, $1/c_1 + j\Delta t - \Delta t/2$, $j = 0, 1, 2, \cdots, N$, the satisfying is rigorous.

Accurate values of displacement and stresses in this example can easily be computed from the solution. Using $c_1\Delta t = 1$, which is a fairly large number in this example, numerical values of radial and tangential stresses in the medium have been evaluated and shown by curves in Fig. 2 and Fig. 3, respectively. The results agree very well with those obtained by others (Chou and Koenig, 1966).

Rotary shear and axial shear are two other forms of one-dimensional axially symmetric elastic waves. They have been treated by the same method developed in this Note with favorable results. It is not necessary to present the results here, owing to their close similarity in mathematical formulation to the radial motion problem.

References

Achenbach, J. D., 1976, *Wave Propagation in Elastic Solids*, North Holland, Amsterdam.

Chou, P. C., and Koenig, H. A., 1966, "A Unified Approach to Cylindrical and Spherical Elastic Waves by Method of Characteristics," ASME JOURNAL OF APPLIED MECHANICS, Vol. 88, pp. 159-167.

Eringen, A. C., and Suhubi, E. S., 1975, *Elastodynamics*, Vol. 2: *Linear Theory*, Academic Press, New York.

Gradshteyn, I. S., and Ryzhik, I. M., 1980, *Tables of Integrals, Series, and Products*, Academic Press, New York.

Lamb, H., 1902, "On Wave Propagation in Two-Dimensions," *Proc. London Math. Soc.*, Vol. 35, pp. 141-161.

Miklowitz, J., 1978, *Elastic Waves and Waveguides*, North Holland, Amsterdam.

Transverse Vibration of Solid Circular Plates Continuous Over Multiple Concentric Annular Supports

K. M. Liew[3] and K. Y. Lam[4]

1 Introduction

A survey from the literature reveals that only a limited amount of research work has been done on ring-supported circular plates during the past few decades (Bodine, 1959; Kunukkasseril and Swamidas, 1974). The drawback may be due to the difficulty in forming a simple and adequate deflection function which can be applied to the entire plate domain, such that it satisfies the boundary conditions at the ring supports and also the plate periphery. The aim of the present work is to develop an accurate and efficient numerical model based on a set of orthogonal plate functions (details can be found in Liew and Lam, 1991) and to study the free vibration of multiple ring-supported circular plate.

2 Method of Analysis

The expression for the strain energy of a plate in bending is given by

$$V=\frac{1}{2}D\int\int_R\left\{\left[\frac{\partial^2 W}{\partial x^2}\right]^2+2\nu\left[\frac{\partial^2 W}{\partial x^2}\frac{\partial^2 W}{\partial y^2}\right]+\left[\frac{\partial^2 W}{\partial y^2}\right]^2+2(1-\nu)\left[\frac{\partial^2 W}{\partial x\partial y}\right]^2\right\}dxdy \quad (1)$$

where $D = Eh^3/12(1-\nu^2)$, E is the Young's modulus, h is the plate thickness, and ν is the Poisson's ratio.

To find the least upper bound on the frequency, minimization is needed, with respect to the undetermined coefficients C_i,

$$\frac{\partial V}{\partial C_i}-\frac{1}{2}\rho h\omega^2\frac{\partial}{\partial C_i}\left[\int\int_R W^2(x,y)dxdy\right]=0, \quad (2)$$

which leads to the governing eigenvalue equation

$$\Sigma[K_{ij}-\lambda M_{ij}]C_i=0;\ i,j=1,2,\ \ldots,m \quad (3)$$

where

$$K_{ij}=P_{ij}+Q_{ij}+\nu(R_{ij}+S_{ij})+2(1-\nu)T_{ij} \quad (4)$$

$$M_{ij}=\int\int_R\phi_i(x,y)\phi_j(x,y)dxdy \quad (5)$$

$$P_{ij}=\int\int_R\frac{\partial^2\phi_i(x,y)}{\partial x^2}\frac{\partial^2\phi_j(x,y)}{\partial x^2}dxdy \quad (6)$$

$$Q_{ij}=\int\int_R\frac{\partial^2\phi_i(x,y)}{\partial y^2}\frac{\partial^2\phi_j(x,y)}{\partial y^2}dxdy \quad (7)$$

$$R_{ij}=\int\int_R\frac{\partial^2\phi_i(x,y)}{\partial y^2}\frac{\partial^2\phi_j(x,y)}{\partial x^2}dxdy \quad (8)$$

[3]Lecturer, School of Mechanical and Production Engineering, Nanyang Technological University, Singapore 2263, Republic of Singapore.

[4]Senior Lecturer, Department of Mechanical and Production Engineering, National University of Singapore, Singapore 0511, Republic of Singapore. Mem. ASME.

Manuscript received by the ASME Applied Mechanics Division, May 25, 1990; final revision, May 31, 1991. Associate Technical Editor: D. J. Inman.

Copyright © 1993 by ASME

Downloaded 03 May 2010 to 171.66.16.245. Redistribution subject to ASME license or copyright; see http://www.asme.org/terms/Terms_Use.cfm

$$S_{ij}=\int\int_R \frac{\partial^2\phi_i(x,y)}{\partial x^2}\frac{\partial^2\phi_j(x,y)}{\partial y^2}\,dxdy \tag{9}$$

$$T_{ij}=\int\int_R \frac{\partial^2\phi_i(x,y)}{\partial x\partial y}\frac{\partial^2\phi_j(x,y)}{\partial x\partial y}\,dxdy \tag{10}$$

$$\lambda=\rho h\omega^2 a^4/D. \tag{11}$$

The eigenvalue Eq. (3) can be solved by expressing the deflection in terms of a set of two-dimensional orthogonal plate functions $\phi_i(\xi, \eta)$ given by

$$W(\xi,\eta)=\sum_{i=1}^{m} C_i\phi_i(\xi,\eta) \tag{12}$$

where $\xi = x/a$, $\eta = y/a$, and C_i are the undetermined coefficients.

The plate functions $\phi_i(\xi, \eta)$ are constructed such that each member in the set satisfies the geometrical boundary conditions of the plate and are generated through a recurrence formula. Further details on the constructions of $\phi_i(\xi, \eta)$ and the generation of the recurrence formula can be found in Liew and Lam (1991).

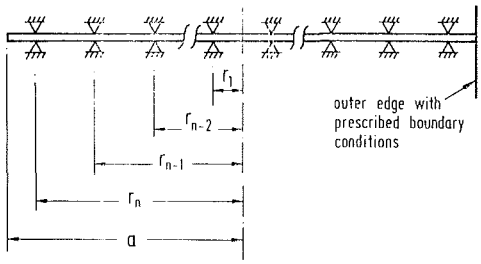


Fig. 1 Geometry of a continuous plate with *n* ring supports

3 Practical Applictions

Several examples are solved to demonstrate the accuracy and the applicability of the proposed method. Poisson's ratio $\nu = 0.30$ is used for all examples. The eigenvalues obtained for the examples are expressed in terms of nondimensional frequency parameters given by

$$\sqrt{\lambda''}=(\rho h\omega^2 a^4/D)^{1/2} \tag{13}$$

First we consider a solid circular plate of radius a with only constraint at the plate periphery. The results obtained by the present approach, using 60 terms in the deflection series, are given in Table 1 together with the published values. For the simply-supported circular plate a good agreement, with the results obtained by Leissa and Narita (exact values, 1980), and Kim and Dickinson (1989), is observed. The first six frequency parameters for the fully clamped circular plate are compared with those values presented by Kim and Dickinson (1989) and Carrington (exact values, 1925), again good agreement is obtained.

Next, the present approach is applied to anayze a multiple-ring supported circular plate. The analysis is carried out for the circular plate which is continuous over two annular rings located at: (i) $r_1/a = 1/4$ and at $r_2/a = 1/2$, or, (ii) $r_1/a = 1/2$ and at $r_2/a = 3/4$. The plate structure, with support conditions, is studied at the circumferential periphery—completely free or simply supported. The plate functions formed for the problem, according to the proposed method, satisfy the geometrical boundary conditions of the two rings and the prescribed constraints at the circumferential periphery. Since no results are available for comparison, convergence studies are carried out

Table 1 Comparison of frequency parameters $(\rho h\omega^2 a^4/D)^{1/2}$ for the circular plate

Source of results	Mode sequence number					
	1	2	3	4	5	6
(i) Simply supported						
Present	4.9352	13.8982	13.8982	25.6138	25.6138	29.7241
Leissa and Narita	4.9352	13.8982	13.8982	25.6133	25.6133	29.7200
Kim and Dickinson	4.9352	13.8982	13.8982	25.6133	25.6133	29.7200
(ii) Fully clamped						
Present	10.2160	21.2601	21.2601	34.8786	34.8786	39.7712
Kim and Dickinson	10.2158	21.260	21.260	34.877	34.877	39.771
Carrington	10.2158	21.26	21.26	34.88	34.88	39.771

Table 2 Frequency parameters $(\rho h\omega^2 a^4/D)^{1/2}$ for the solid circular plate on two annular supports

r_1/a	r_2/a	No. of terms, m	Mode sequence number					
			1	2	3	4	5	6
(i) Completely Free								
1/4	1/2	50	25.7213	28.3179	28.3179	33.6016	33.6016	47.4219
		60	25.6851	28.3181	28.3181	33.5674	33.5674	41.4115
		70	25.6651	28.2681	28.2681	33.5674	33.5674	41.3921
1/2	3/4	50	10.4840	11.5635	11.5635	14.9882	14.9882	16.9300
		60	10.4691	10.8165	10.8165	13.6289	13.6289	16.7542
		70	10.2807	10.6217	10.6217	13.3263	13.3263	16.2987
(ii) Simply Supported								
1/4	1/2		57.3223	64.5287	64.5287	76.4586	76.4586	89.1623
1/2	3/4		50.6657	51.0105	51.0105	55.4187	55.4187	63.3039

Downloaded 03 May 2010 to 171.66.16.245. Redistribution subject to ASME license or copyright; see http://www.asme.org/terms/Terms_Use.cfm

for the circular plate with free periphery. The results are given in Table 2. It can be seen from the study that satisfactory results are obtained by using 70 terms in the deflection series. The same number of terms are used to obtain results for the circular plates with simply-supported periphery as shown in Table 2.

4 Conclusions

An accurate numerical approach has been proposed for solving free vibration of circular plates continuous over multiple-ring supports of arbitrary radii. By using a set of orthogonally generated plate functions as the admissible function in the Rayleigh-Ritz method, the natural frequencies of the plates are obtained. The set of orthogonal plate functions is generated to satisfy the zero lateral displacement and the continuity of normal slope at the supports, and it also satisfies the geometrical boundary conditions at the plate periphery. The accuracy of the proposed method has been demonstrated by considering several examples for which known solutions exist. Comparison of the obtained frequency parameters with those existing in the literature showed that the proposed method gives very accurate results. Moreover, the present approach can be further extended to study bending and buckling problems where the energy expressions are known.

References

Bodine, R. Y., 1959, "The Fundamental Frequency of a Thin, Flat, Circular Plate Simply Supported Along a Circle of Arbitrary Radius," ASME JOURNAL OF APPLIED MECHANICS, Vol. E26, pp. 666-668.

Carrington, H., 1925, "The Frequencies of Vibration of Flat Circular Plates Fixed at the Circumference," *Philosophical Magazine*, Vol. 50, pp. 1261-1264.

Kim, C. S., and Dickinson, S. M., 1989, "On the Lateral Vibration of Thin Annular and Circular Composite Plates Subject to Certain Complicating Effects," *Journal of Sound and Vibration*, Vol. 130, pp. 363-377.

Kunukkasseril, V. X., and Swamidas, A. S. J., 1974, "Vibration of Continuous Circular Plates," *International Journal of Solids and Structures*, Vol. 10, pp. 603-619.

Leissa, A. W., and Narita, Y., 1980, "Natural Frequencies of Simply Supported Circular Plates," *Journal of Sound and Vibration*, Vol. 70, pp. 221-229.

Liew, K. M., and Lam, K. Y., 1991, "A Rayleigh-Ritz Approach to Transverse Vibration of Isotropic and Anisotropic Trapezoidal Plates Using Orthogonal Plate Functions," *International Journal of Solids and Structures*, Vol. 27, pp. 189-203.

A Bilinear Variational Principle Governing Longitudinal Vibration of Rods With Frequency-Dependent Material Damping

George A. Lesieutre[5]

The equations governing the longitudinal vibration of rods with frequency-dependent material damping are developed as the Euler equations of a bilinear variational principle. Frequency-dependent material damping and modulus are accommodated through the introduction of an augmenting thermodynamic field that interacts with the mechanical displacement field. These two primary dependent fields are supplemented with two corresponding adjoint fields for the purpose of addressing nonconservative system behavior. The variational function is nearly symmetric in the primary and adjoint variables, a formulation which may be particularly useful in computational simulation of system behavior using finite elements. The augmenting thermodynamic field is found to be effectively internal—no boundary conditions involve it alone.

Introduction

Real engineering structures are not elastic. However, the structural designer has few physically based tools for the analysis of damped structures that can be used to evaluate the performance of candidate designs—conventional models of dissipation such as viscous damping and hysteretic damping, while mathematically simple, are of limited utility in describing the behavior of real materials. In particular, the characteristic frequency dependence of material damping and modulus are not well modeled by conventional time-domain techniques. Viscoelastic models, while capable of capturing this behavior, are not widely used in design, perhaps because of the slowness to accommodate them within the conventional framework of modern structural analysis, i.e., the finite element method.

Recent work has addressed the development of a physically motivated modeling method fully compatible with current computational structural analysis techniques (Lesieutre and Mingori, 1990). Its key feature is the introduction of one or more augmenting thermodynamic fields (ATF) to interact with the usual displacement field of continuum structural dynamics. Finite elements for structures made from one-dimensional members (rods and beams) have been developed and the retention of characteristic frequency dependence has been verified.

The equations that describe the behavior of such dissipative, nonconservative systems are generally nonselfadjoint and are not derivable using standard variational principles. However, suitable bilinear functionals may sometimes be found for such systems (Leipholz, 1972). The following section describes the derivation of the governing equations for longitudinal vibration of rods with ATF damping using such a bilinear variational functional.

Theory

Consider the case of one-dimensional motion, corresponding to longitudinal vibration of a rod. Frequency-dependent damping and modulus are assumed to be due to an unspecified microstructural mechanism, the scalar relaxation of which is driven by a local departure from thermodynamic equilibrium. This mechanism is modeled via the introduction of a single augmenting thermodynamic field (ATF), effectively resulting in a continuum version of the standard anelastic solid.

For clarity of presentation, this discussion is limited to autonomous linear deformation of a uniform rod of length L (with constant cross-sectional area, A; constant unrelaxed modulus of elasticity E_u; and constant density, ρ). The reference location of a mass particle along the rod axis is denoted by "x," the longitudinal mechanical displacement of a mass particle by $u(x)$, and the longitudinal normal strain by $\epsilon(x) = u'(x)$. A single scalar augmenting thermodynamic field, $\xi(x)$, is also introduced, with the inverse of the relaxation time at constant strain given by the material property B.

The fields which are thermodynamically conjugate to $\epsilon(x)$ and $\xi(x)$ are the stress, $\sigma(x)$, and the affinity, $A(x)$. The affinity can be interpreted as a thermodynamic "force" driving the augmenting field towards equilibrium. The material property κ describes the strength of the coupling of the two dependent fields, $u(x)$ and $\xi(x)$. In the absence of coupling of the two fields, increments of stress and strain are proportional, with

[5]Assistant Professor of Aerospace Engineering, The Pennsylvania State University, University Park, PA 16802.

Contributed by the Applied Mechanics Division of THE AMERICAN SOCIETY OF MECHANICAL ENGINEERS for publication in the ASME JOURNAL OF APPLIED MECHANICS.

Manuscript received by the ASME Applied Mechanics Division, Mar. 19, 1991; final revision, Nov. 18, 1992. Associate Technical Editor: P. D. Spanos.

Downloaded 03 May 2010 to 171.66.16.245. Redistribution subject to ASME license or copyright; see http://www.asme.org/terms/Terms_Use.cfm

for the circular plate with free periphery. The results are given in Table 2. It can be seen from the study that satisfactory results are obtained by using 70 terms in the deflection series. The same number of terms are used to obtain results for the circular plates with simply-supported periphery as shown in Table 2.

4 Conclusions

An accurate numerical approach has been proposed for solving free vibration of circular plates continuous over multiple-ring supports of arbitrary radii. By using a set of orthogonally generated plate functions as the admissible function in the Rayleigh-Ritz method, the natural frequencies of the plates are obtained. The set of orthogonal plate functions is generated to satisfy the zero lateral displacement and the continuity of normal slope at the supports, and it also satisfies the geometrical boundary conditions at the plate periphery. The accuracy of the proposed method has been demonstrated by considering several examples for which known solutions exist. Comparison of the obtained frequency parameters with those existing in the literature showed that the proposed method gives very accurate results. Moreover, the present approach can be further extended to study bending and buckling problems where the energy expressions are known.

References

Bodine, R. Y., 1959, "The Fundamental Frequency of a Thin, Flat, Circular Plate Simply Supported Along a Circle of Arbitrary Radius," ASME JOURNAL OF APPLIED MECHANICS, Vol. E26, pp. 666-668.

Carrington, H., 1925, "The Frequencies of Vibration of Flat Circular Plates Fixed at the Circumference," *Philosophical Magazine*, Vol. 50, pp. 1261-1264.

Kim, C. S., and Dickinson, S. M., 1989, "On the Lateral Vibration of Thin Annular and Circular Composite Plates Subject to Certain Complicating Effects," *Journal of Sound and Vibration*, Vol. 130, pp. 363-377.

Kunukkasseril, V. X., and Swamidas, A. S. J., 1974, "Vibration of Continuous Circular Plates," *International Journal of Solids and Structures*, Vol. 10, pp. 603-619.

Leissa, A. W., and Narita, Y., 1980, "Natural Frequencies of Simply Supported Circular Plates," *Journal of Sound and Vibration*, Vol. 70, pp. 221-229.

Liew, K. M., and Lam, K. Y., 1991, "A Rayleigh-Ritz Approach to Transverse Vibration of Isotropic and Anisotropic Trapezoidal Plates Using Orthogonal Plate Functions," *International Journal of Solids and Structures*, Vol. 27, pp. 189-203.

A Bilinear Variational Principle Governing Longitudinal Vibration of Rods With Frequency-Dependent Material Damping

George A. Lesieutre[5]

The equations governing the longitudinal vibration of rods with frequency-dependent material damping are developed as the Euler equations of a bilinear variational principle. Frequency-dependent material damping and modulus are accommodated through the introduction of an augmenting thermodynamic field that interacts with the mechanical displacement field. These two primary dependent fields are supplemented with two corresponding adjoint fields for the purpose of addressing nonconservative system behavior. The variational function is nearly symmetric in the primary and adjoint variables, a formulation which may be particularly useful in computational simulation of system behavior using finite elements. The augmenting thermodynamic field is found to be effectively internal—no boundary conditions involve it alone.

Introduction

Real engineering structures are not elastic. However, the structural designer has few physically based tools for the analysis of damped structures that can be used to evaluate the performance of candidate designs—conventional models of dissipation such as viscous damping and hysteretic damping, while mathematically simple, are of limited utility in describing the behavior of real materials. In particular, the characteristic frequency dependence of material damping and modulus are not well modeled by conventional time-domain techniques. Viscoelastic models, while capable of capturing this behavior, are not widely used in design, perhaps because of the slowness to accommodate them within the conventional framework of modern structural analysis, i.e., the finite element method.

Recent work has addressed the development of a physically motivated modeling method fully compatible with current computational structural analysis techniques (Lesieutre and Mingori, 1990). Its key feature is the introduction of one or more augmenting thermodynamic fields (ATF) to interact with the usual displacement field of continuum structural dynamics. Finite elements for structures made from one-dimensional members (rods and beams) have been developed and the retention of characteristic frequency dependence has been verified.

The equations that describe the behavior of such dissipative, nonconservative systems are generally nonselfadjoint and are not derivable using standard variational principles. However, suitable bilinear functionals may sometimes be found for such systems (Leipholz, 1972). The following section describes the derivation of the governing equations for longitudinal vibration of rods with ATF damping using such a bilinear variational functional.

Theory

Consider the case of one-dimensional motion, corresponding to longitudinal vibration of a rod. Frequency-dependent damping and modulus are assumed to be due to an unspecified microstructural mechanism, the scalar relaxation of which is driven by a local departure from thermodynamic equilibrium. This mechanism is modeled via the introduction of a single augmenting thermodynamic field (ATF), effectively resulting in a continuum version of the standard anelastic solid.

For clarity of presentation, this discussion is limited to autonomous linear deformation of a uniform rod of length L (with constant cross-sectional area, A; constant unrelaxed modulus of elasticity E_u; and constant density, ρ). The reference location of a mass particle along the rod axis is denoted by "x," the longitudinal mechanical displacement of a mass particle by $u(x)$, and the longitudinal normal strain by $\epsilon(x) = u'(x)$. A single scalar augmenting thermodynamic field, $\xi(x)$, is also introduced, with the inverse of the relaxation time at constant strain given by the material property B.

The fields which are thermodynamically conjugate to $\epsilon(x)$ and $\xi(x)$ are the stress, $\sigma(x)$, and the affinity, $A(x)$. The affinity can be interpreted as a thermodynamic "force" driving the augmenting field towards equilibrium. The material property κ describes the strength of the coupling of the two dependent fields, $u(x)$ and $\xi(x)$. In the absence of coupling of the two fields, increments of stress and strain are proportional, with

[5]Assistant Professor of Aerospace Engineering, The Pennsylvania State University, University Park, PA 16802.

Contributed by the Applied Mechanics Division of THE AMERICAN SOCIETY OF MECHANICAL ENGINEERS for publication in the ASME JOURNAL OF APPLIED MECHANICS.

Manuscript received by the ASME Applied Mechanics Division, Mar. 19, 1991; final revision, Nov. 18, 1992. Associate Technical Editor: P. D. Spanos.

Copyright © 1993 by ASME
Downloaded 03 May 2010 to 171.66.16.245. Redistribution subject to ASME license or copyright; see http://www.asme.org/terms/Terms_Use.cfm

E_u the relating constant. Analogously, in the absence of coupling, α is the material property that relates changes in A to those in ξ.

Material constitutive equations may be found from thermodynamic considerations (using the Helmholtz free-energy density) as

$$\sigma = E_u u' - \kappa\xi \tag{1a}$$

$$A = \kappa u' - \alpha\xi. \tag{1b}$$

The elastic one-dimensional stress-strain constitutive relation is seen to be augmented by an additional term in ξ, in a manner similar to that of one-dimensional thermoelasticity.

The following bilinear variational principle for this coupled-field problem generates a set of governing PDE and boundary conditions, along with corresponding adjoint equations:

$$\delta H = 0 \tag{2}$$

where

$$H = \int_{t_1}^{t_2}\int_0^L \left\{ \rho\dot{u}\dot{v} - E_u u' v' + \alpha\xi z + \kappa(\xi v' - z u') + \frac{1}{2}\frac{\alpha}{\beta}(\dot{\xi}z - \dot{z}\xi) \right\} dx dt. \tag{3}$$

In this nearly symmetric functional, $v(x)$ is a field adjoint to $u(x)$ and $z(x)$ is a field adjoint to $\xi(x)$.

Using integration by parts, the variation of H may be expressed as the sum of independent and arbitrary variations $\delta u(x, t)$, $\delta v(x, t)$, $\delta\xi(x, t)$ and $\delta z(x, t)$, leading to four governing differential equations and sets of boundary conditions:

$$\int_{t_1}^{t_2}\int_0^L \{-\rho\ddot{u} + E_u u'' - \kappa\xi'\}\delta v dx dt + \int_0^L \rho\dot{u}\delta v|_{t_1}^{t_2} dx - \int_{t_1}^{t_2} \sigma\delta v|_0^L dt = 0 \tag{4a}$$

$$\int_{t_1}^{t_2}\int_0^L \{-\rho\ddot{v} + E_u v'' + \kappa z'\}\delta u dx dt + \int_0^L \rho\dot{v}\delta u|_{t_1}^{t_2} dx + \int_{t_1}^{t_2} \sigma_{\text{adj}}\delta u|_0^L dt = 0 \tag{4b}$$

$$\int_{t_1}^{t_2}\int_0^L \left\{\frac{\alpha}{B}\dot{\xi} + \alpha\xi - \kappa u'\right\}\delta z dx dt - \int_0^L \frac{1}{2}\frac{\alpha}{B}\xi\delta z|_{t_1}^{t_2} dx = 0 \tag{4c}$$

$$\int_{t_1}^{t_2}\int_0^L \left\{-\frac{\alpha}{B}\dot{z} + \alpha z + \kappa v'\right\}\delta\xi dx dt + \int_0^L \frac{1}{2}\frac{\alpha}{B} z\delta\xi|_{t_1}^{t_2} dx = 0 \tag{4d}$$

where the adjoint stress, σ_{adj}, is given by (compare to (1a)):

$$\sigma_{\text{adj}} = -E_u v' - \kappa z. \tag{5}$$

The terms multiplying the variations δv and δz yield two coupled partial differential equations (PDE) that govern the temporal evolution of the primary dependent fields $u(x)$ and $\xi(x)$—these are the same equations that result from consideration of momentum balance:

$$\rho\ddot{u} - E_u u'' = -\kappa\xi' \tag{6a}$$

$$\dot{\xi} + B\xi = \left(\frac{B\kappa}{\alpha}\right)u' \tag{6b}$$

as well as boundary conditions (BC):

$$\sigma(0)\delta v(0) = 0 \quad \text{and} \quad \sigma(L)\delta v(L) = 0. \tag{7}$$

As for elastic rods, there are natural and geometrical BC—either the stress or the adjoint displacement must be specified at each end of the rod. Note that the natural BC for stress involves both the strain, $u'(x)$, and the augmenting field, $\xi(x)$ (again, see (1a)).

In addition, it is assumed that the kinematic variations are everywhere zero at the endpoints of an unspecified time interval. These conditions are similar to those usually associated with Hamilton's principle:

$$\delta v(x, t_1) = \delta v(x, t_2) = 0 \tag{8a}$$

$$\delta z(x, t_1) = \delta z(x, t_2) = 0. \tag{8b}$$

Consideration of the terms multiplying the other two variations, δu and $\delta\xi$, leads to the PDE and BC that govern the evolution of the adjoint fields $v(x)$ and $z(x)$. Initial conditions for the adjoint fields may be addressed following the approach of Shen (1984). The displacement field, $u(x)$, and its adjoint, $v(x)$, are found to satisfy identical geometrical boundary conditions. Because there are no explicit constraints on the augmenting field, $\xi(x)$, or its adjoint, $z(x)$, they are effectively internal fields.

Solutions to linear, nonselfadjoint eigenvalue boundary problems corresponding to longitudinal vibration of a rod have been previously obtained by Lesieutre and Mingori (1990) using the finite element method. Finite elements were developed by direct application of the method of weighted residuals to the governing equations. An alternate approach might employ hybrid Galerkin's equations as discussed by Leipholz (1972), using the subject bilinear variational principle.

Summary

A bilinear variational principle that generates the equations governing longitudinal vibration of rods with frequency-dependent material damping has been developed. The variational functional is nearly symmetric in the primary and adjoint variables, a formulation which may be particularly useful in approximate analysis of system behavior using the finite element method. Augmenting thermodynamic fields, introduced to preserve the characteristic frequency dependence of material properties, are found to be effectively internal fields.

References

Leipholz, H., 1972, "On a Stability Theory of Non-Selfadjoint Mechanical Systems," *Acta Mechanica*, Vol. 14, pp. 283–295.

Lesieutre, G. A., and Mingori, D. L., 1990, "Finite Element Modeling of Frequency-Dependent Material Damping using Augmenting Thermodynamic Fields," *Journal of Guidance, Control and Dynamics*, Vol. 13, pp. 1040–1050.

Shen, C. N., 1984, "Variational Principle for Penetrator Dynamics using Bilinear Functional and Adjoint Formulation," *Transactions of the Army Conference on Applied Mathematics and Computing* 2nd ed. pp. 185–197.

Elastic-Plastic Tip Field for a Stationary Crack in a Reinforced Thin Sheet

P. Ståhle[6]

A class of plane stress problems for incompressible materials is studied. The class concerns problems for unidirectionally reinforced thin sheets under quasi-static loading conditions.

[6]Department of Technology, Uppsala University, S-751 21, Uppsala, Sweden.

Contributed by the Applied Mechanics Division of THE AMERICAN SOCIETY OF MECHANICAL ENGINEERS for publication in the ASME JOURNAL OF APPLIED MECHANICS. Manuscript received by the Applied Mechanics Division, Jan. 25, 1991; final revision, Dec. 11, 1991. Associate Technical Editor: C. F. Shih.

Downloaded 03 May 2010 to 171.66.16.245. Redistribution subject to ASME license or copyright; see http://www.asme.org/terms/Terms_Use.cfm

E_u the relating constant. Analogously, in the absence of coupling, α is the material property that relates changes in A to those in ξ.

Material constitutive equations may be found from thermodynamic considerations (using the Helmholtz free-energy density) as

$$\sigma = E_u u' - \kappa\xi \tag{1a}$$

$$A = \kappa u' - \alpha\xi. \tag{1b}$$

The elastic one-dimensional stress-strain constitutive relation is seen to be augmented by an additional term in ξ, in a manner similar to that of one-dimensional thermoelasticity.

The following bilinear variational principle for this coupled-field problem generates a set of governing PDE and boundary conditions, along with corresponding adjoint equations:

$$\delta H = 0 \tag{2}$$

where

$$H = \int_{t_1}^{t_2}\int_0^L \left\{\rho\dot{u}\dot{v} - E_u u' v' + \alpha\xi z + \kappa(\xi v' - z u') + \frac{1}{2}\frac{\alpha}{\beta}(\dot{\xi}z - \dot{z}\xi)\right\} dx dt. \tag{3}$$

In this nearly symmetric functional, $v(x)$ is a field adjoint to $u(x)$ and $z(x)$ is a field adjoint to $\xi(x)$.

Using integration by parts, the variation of H may be expressed as the sum of independent and arbitrary variations $\delta u(x, t)$, $\delta v(x, t)$, $\delta\xi(x, t)$ and $\delta z(x, t)$, leading to four governing differential equations and sets of boundary conditions:

$$\int_{t_1}^{t_2}\int_0^L \{-\rho\ddot{u} + E_u u'' - \kappa\xi'\}\delta v dx dt + \int_0^L \rho\dot{u}\delta v|_{t_1}^{t_2} dx - \int_{t_1}^{t_2} \sigma\delta v|_0^L dt = 0 \tag{4a}$$

$$\int_{t_1}^{t_2}\int_0^L \{-\rho\ddot{v} + E_u v'' + \kappa z'\}\delta u dx dt + \int_0^L \rho\dot{v}\delta u|_{t_1}^{t_2} dx + \int_{t_1}^{t_2} \sigma_{\text{adj}}\delta u|_0^L dt = 0 \tag{4b}$$

$$\int_{t_1}^{t_2}\int_0^L \left\{\frac{\alpha}{B}\dot{\xi} + \alpha\xi - \kappa u'\right\}\delta z dx dt - \int_0^L \frac{1}{2}\frac{\alpha}{B}\xi\delta z|_{t_1}^{t_2} dx = 0 \tag{4c}$$

$$\int_{t_1}^{t_2}\int_0^L \left\{-\frac{\alpha}{B}\dot{z} + \alpha z + \kappa v'\right\}\delta\xi dx dt + \int_0^L \frac{1}{2}\frac{\alpha}{B} z\delta\xi|_{t_1}^{t_2} dx = 0 \tag{4d}$$

where the adjoint stress, σ_{adj}, is given by (compare to (1a)):

$$\sigma_{\text{adj}} = -E_u v' - \kappa z. \tag{5}$$

The terms multiplying the variations δv and δz yield two coupled partial differential equations (PDE) that govern the temporal evolution of the primary dependent fields $u(x)$ and $\xi(x)$—these are the same equations that result from consideration of momentum balance:

$$\rho\ddot{u} - E_u u'' = -\kappa\xi' \tag{6a}$$

$$\dot{\xi} + B\xi = \left(\frac{B\kappa}{\alpha}\right)u' \tag{6b}$$

as well as boundary conditions (BC):

$$\sigma(0)\delta v(0) = 0 \quad \text{and} \quad \sigma(L)\delta v(L) = 0. \tag{7}$$

As for elastic rods, there are natural and geometrical BC—either the stress or the adjoint displacement must be specified at each end of the rod. Note that the natural BC for stress involves both the strain, $u'(x)$, and the augmenting field, $\xi(x)$ (again, see (1a)).

In addition, it is assumed that the kinematic variations are everywhere zero at the endpoints of an unspecified time interval. These conditions are similar to those usually associated with Hamilton's principle:

$$\delta v(x, t_1) = \delta v(x, t_2) = 0 \tag{8a}$$

$$\delta z(x, t_1) = \delta z(x, t_2) = 0. \tag{8b}$$

Consideration of the terms multiplying the other two variations, δu and $\delta\xi$, leads to the PDE and BC that govern the evolution of the adjoint fields $v(x)$ and $z(x)$. Initial conditions for the adjoint fields may be addressed following the approach of Shen (1984). The displacement field, $u(x)$, and its adjoint, $v(x)$, are found to satisfy identical geometrical boundary conditions. Because there are no explicit constraints on the augmenting field, $\xi(x)$, or its adjoint, $z(x)$, they are effectively internal fields.

Solutions to linear, nonselfadjoint eigenvalue boundary problems corresponding to longitudinal vibration of a rod have been previously obtained by Lesieutre and Mingori (1990) using the finite element method. Finite elements were developed by direct application of the method of weighted residuals to the governing equations. An alternate approach might employ hybrid Galerkin's equations as discussed by Leipholz (1972), using the subject bilinear variational principle.

Summary

A bilinear variational principle that generates the equations governing longitudinal vibration of rods with frequency-dependent material damping has been developed. The variational functional is nearly symmetric in the primary and adjoint variables, a formulation which may be particularly useful in approximate analysis of system behavior using the finite element method. Augmenting thermodynamic fields, introduced to preserve the characteristic frequency dependence of material properties, are found to be effectively internal fields.

References

Leipholz, H., 1972, "On a Stability Theory of Non-Selfadjoint Mechanical Systems," *Acta Mechanica*, Vol. 14, pp. 283–295.

Lesieutre, G. A., and Mingori, D. L., 1990, "Finite Element Modeling of Frequency-Dependent Material Damping using Augmenting Thermodynamic Fields," *Journal of Guidance, Control and Dynamics*, Vol. 13, pp. 1040–1050.

Shen, C. N., 1984, "Variational Principle for Penetrator Dynamics using Bilinear Functional and Adjoint Formulation," *Transactions of the Army Conference on Applied Mathematics and Computing* 2nd ed. pp. 185–197.

Elastic-Plastic Tip Field for a Stationary Crack in a Reinforced Thin Sheet

P. Ståhle[6]

A class of plane stress problems for incompressible materials is studied. The class concerns problems for unidirectionally reinforced thin sheets under quasi-static loading conditions.

[6]Department of Technology, Uppsala University, S-751 21, Uppsala, Sweden.

Contributed by the Applied Mechanics Division of THE AMERICAN SOCIETY OF MECHANICAL ENGINEERS for publication in the ASME JOURNAL OF APPLIED MECHANICS. Manuscript received by the Applied Mechanics Division, Jan. 25, 1991; final revision, Dec. 11, 1991. Associate Technical Editor: C. F. Shih.

Copyright © 1993 by ASME
Downloaded 03 May 2010 to 171.66.16.245. Redistribution subject to ASME license or copyright; see http://www.asme.org/terms/Terms_Use.cfm

An incremental theory of plasticity and an isotropic yield condition is assumed. It is demonstrated how a corresponding antiplane strain problem can be identified. Thus solutions are readily found to a variety of problems. A stationary crack in a perfectly plastic material is chosen for demonstration. Small-scale yielding is assumed but solutions for, e.g., large-scale of yielding or hardening materials are also easily obtained.

Introduction

Stationary mode III is one of the few elastic plastic boundary value crack problems that can be solved analytically. For this case, however, quite a few different solutions have been obtained, e.g., for different scales of yielding and different materials (Hult and McClintock, 1956; Rice, 1968). A simplifying circumstance when mode III is concerned is that it is a case of antiplane strain and thus only one displacement component is nonzero. In many cases of interest another remarkable condition makes analytical solutions possible to obtain. This is that proportional loading often prevails in the plastic zone. It is remarkable since the loading immediately outside the plastic zone may be far from proportional.

This paper deals with a class of plane stress problems for which similar simplifications, as for antiplane strain, can be made. The class includes unidirectionally reinforced thin sheets of incompressible elastic-plastic materials. The reinforcement has to be rigidly bonded in one direction and fully flexible perpendicular to that.

Several applications can be thought of. Figure 1 shows the principal structure of a cooler, composed of a thin sheet, supported by parallel ridges. These are welded to a rigid foundation. The ridges are assumed to be sufficiently flexible to be regarded as perfectly free, perpendicular to their surface (the y-direction in the figure), and stiff enough to be regarded as rigidly founded in the direction along the edges (the x-direction). Another application could be a sheet reinforced with thin fibers which are practically inextensible. Each fiber must be rigidly bonded in at least one point along its length.

With access to antiplane strain solutions, it is here demonstrated how corresponding plane stress problems can be solved. An analogy between plane stress and antiplane strain is used (Ståhle, 1986). The method is demonstrated for a simple case of a reinforced perfectly plastic sheet with a crack. A solution to the corresponding mode III problem was given by Hult and McClintock (1956).

The Method

A problem for a sheet subjected to in-plane loading is considered. The sheet is assumed to be sufficiently thin so that plane stress can be assumed. It is further assumed to be free of residual stresses in its unloaded state. The material is incompressible and the plastic behavior is governed by an isotropic incremental theory. Young's modulus is E and the flow stress is σ_f. The sheet is further assumed to be unidirectionally reinforced or supported so that the displacements vanish in one in-plane direction. A coordinate system is introduced with the x-axis along this direction. The sheet is defined by the planes $|z| \leq \pm h/2$. Neither buckling nor necking is considered. Thus, the only relevant nonzero displacement is v in the y direction. The nonvanishing strain components reduce to

$$\epsilon_y = \frac{\partial v}{\partial y}, \tag{1}$$

and

$$\gamma_{xy} = \frac{\partial v}{\partial x}. \tag{2}$$

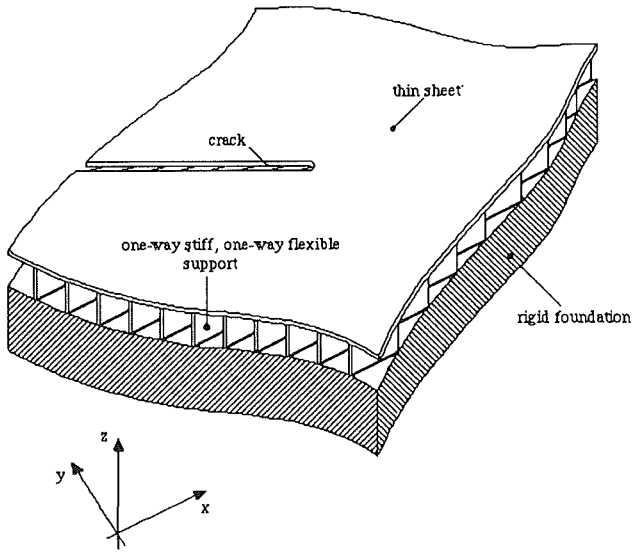


Fig. 1 The principal structure of a cooler

The strain component ϵ_x vanishes. Further, γ_{xz} and γ_{yz} are supposed to be negligibly small and ϵ_z does not enter the analysis.

Equilibrium requires that

$$\frac{\partial \tau_{xy}}{\partial x} + \frac{\partial \sigma_y}{\partial y} = 0. \tag{3}$$

A second equation of equilibrium defines the reaction forces in the x direction and is irrelevant in the present analysis. The constitutive relationship between stress and strain increments is for the incompressible material, given as follows:

$$d\epsilon_x = \frac{1}{E}\left(d\sigma_x - \frac{d\sigma_y}{2}\right) + \frac{d\lambda}{3}(2\sigma_x - \sigma_y), \tag{4}$$

$$d\epsilon_y = \frac{1}{E}\left(d\sigma_y - \frac{d\sigma_x}{2}\right) + \frac{d\lambda}{3}(2\sigma_y - \sigma_x) \tag{5}$$

$$d\gamma_{xy} = \frac{3d\tau_{xy}}{E} + 2d\lambda\tau_{xy}, \tag{6}$$

where

$$d\lambda = 0 \text{ for } \sigma_e < \sigma_f \text{ or } \sigma_e = \sigma_f \text{ and } d\sigma_e < 0. \tag{7}$$

At plasticity, $d\lambda$ may be a function of both stress and strain. The constrained displacements in the x direction imply that $d\epsilon_x = 0$ and thus the constitutive relation (4) provides the following:

$$\sigma_x = \frac{\sigma_y}{2}. \tag{8}$$

Insertion into (5) gives

$$d\epsilon_y = \frac{1}{4}\left(\frac{3d\sigma_y}{E} + 2d\sigma_y\right). \tag{9}$$

The effective stress for any isotropic yield condition is given by

$$\sigma_e = 3^{1/2}\left(\frac{\sigma_y^2}{4} + \tau_{xy}^2\right)^{1/2}. \tag{10}$$

One notes the resemblance with the governing equations for antiplane strain. By making the following changes of denotation in Eqs. (1)–(3), (6), (9), and (10),

Downloaded 03 May 2010 to 171.66.16.245. Redistribution subject to ASME license or copyright; see http://www.asme.org/terms/Terms_Use.cfm

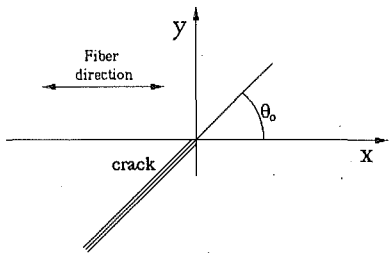


Fig. 2 Definition of the coordinate system for the plane stress problem

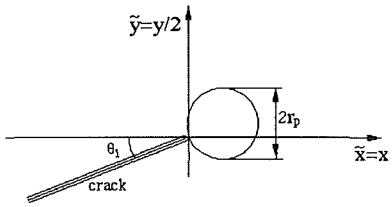


Fig. 3 Definition of the coordinate system for the antiplane strain problem

$$\tau_{xy} \rightarrow \tau_{xz},$$

$$\sigma_y \rightarrow 2\tau_{yz},$$

$$\gamma_{xy} \rightarrow \gamma_{xz},$$

$$\epsilon_y \rightarrow \gamma_{yz}/2,$$

$$v \rightarrow w$$

and

$$y \rightarrow 2y, \tag{11}$$

the equations for antiplane strain are readily obtained. The consequence is that a variety of solutions for antiplane strain can be immediately applied to corresponding plane stress situations.

A Simple Example

A large thin fiber-reinforced sheet is selected for the analysis. Apart from the requirements specified in the previous section, the sheet contains a crack that is large compared to the thickness of the sheet. The fibers are assumed to continue unbroken through the crack. This means that the crack is free to open only perpendicularly to the fiber direction. The material is assumed to be elastic-perfectly plastic. An isotropic yield criterion and associated flow rule are adopted. The yield stress is σ_Y.

The vicinity of one crack tip is studied. A coordinate system is attached to tip (see Fig. 2). The x-axis is chosen to be parallel with the fiber direction. The crack occupies the region

$$0<r<2a,\ \theta=\pm\pi+\theta_o, \tag{12}$$

where $r = (x^2 + y^2)^{1/2}$ and $\theta = \tan^{-1}(y/x)$ represent a polar coordinate system attached to the crack tip.

A small-scale yielding is assumed. The stress σ_∞ at a large distance from the crack is chosen to be uniaxial and perpendicular to the crack plane. In the x, y coordinate system the stresses are given by

$$\sigma_y=\sigma_\infty\cos^2(\theta_o),\ \text{and}\ \tau_{xy}=\sigma_\infty\sin(\theta_o)\cos(\theta_o). \tag{13}$$

First, let us recapitulate the properties of the corresponding mode III solution by Hult and McClintock (1956). They deal with sharp notches with different opening angles. The limiting case of a very shallow notch, i.e., a crack, was also treated. It should be noted that the general solution for an arbitrary notch angle also provide a solution for the general plane stress problem of the same kind.

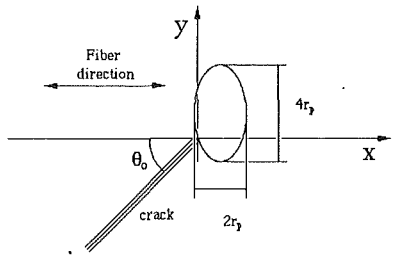


Fig. 4 The shape of the plastic zone for the plane stress case

Only one characteristic feature is discussed here in any detail, namely the shape of the plastic zone which in the mode III assumes the shape of a circle with the radius, say r_p. Its center is at the distance r_p straight ahead of the crack tip.

We introduce a coordinate system $\tilde{x}$ and $\tilde{y}$ defined by

$$x=\tilde{x}\ \text{and}\ y=2\tilde{y}. \tag{14}$$

In these coordinates the crack (see Fig. 3) is situated at

$$\frac{\tilde{y}}{\tilde{x}}=\frac{\tan(\theta_o)}{2}\ \text{with}\ \tilde{x}>0\ \text{and}\ \tilde{y}>0. \tag{15}$$

The parametric description of the circular elastic plastic boundary is as follows:

$$[\tilde{x}-r_p\cos(\theta_1)]^2+[\tilde{y}-r_p\sin(\theta_1)]^2=r_p^2 \tag{16}$$

where $\theta_1 = \tan^{-1}[\tan(\theta_o)/2]$. The radius is given by the remote load. We have

$$r_p=\frac{3}{2\pi}\left(\frac{K_{III}}{\sigma_Y}\right)^2, \tag{17}$$

where the stress intensity factor K_{III} is defined by the load at a large distance from the crack as follows:

$$K_{III}=\tau_\infty(\pi a)^{1/2}. \tag{18}$$

τ_∞ is the limiting shear stress at large distances from the crack. This is given by

$$\tau_\infty=\lim_{\tilde{x}^2+\tilde{y}^2\to\infty}[\tau_{\tilde{y}\tilde{z}}\cos(\theta_1)+\tau_{\tilde{x}\tilde{z}}\sin(\theta_1)]$$

$$=\frac{\sigma_y}{2}\cos(\theta_1)+\tau_{xy}\sin(\theta_1). \tag{19}$$

Insertion of (13) and (19) into (17) and (18) gives

$$r_p=\frac{3a\cos^2(\theta_o)}{2[1+3\cos^2(\theta_o)]}\left(\frac{\sigma_\infty}{\sigma_Y}\right)^2. \tag{20}$$

According to (11), the shape of the plastic zone for the plane stress problem for the reinforced sheet is immediately found by substituting

$$\tilde{x}=x\ \text{and}\ \tilde{y}=y/2 \tag{21}$$

into (16). One obtains the following elliptic shape for the plane stress plastic zone (see Fig. 4)

$$[x-2q\cos(\theta_0)]^2+\left[\frac{y}{2}-q\sin(\theta_0)\right]^2=r_p^2, \tag{22}$$

where

$$q=r_p[1+3\cos^2(\theta_o)]^{-1/2}. \tag{23}$$

The minor half-axis of the ellipse is r_p and the major half-axis is $2r_p$. In accordance with the mode III case, the displacement within the plastic zone is constant along straight lines in a fan arrangement centered at the crack tip. Thus, it is obvious

Downloaded 03 May 2010 to 171.66.16.245. Redistribution subject to ASME license or copyright; see http://www.asme.org/terms/Terms_Use.cfm

that the plastic strain is singular and of the order of $1/r$ in the vicinity of the crack tip. Since the strain at the elastic plastic boundary is constant, the strain at a constant distance from the crack tip becomes proportional to the distance to the elastic plastic boundary $\rho_p(\theta)$, i.e.,

$$\gamma_{r\theta} = \text{const}\,\frac{\rho_p(\theta)}{r}. \tag{24}$$

Thus, the largest strain at a constant radius is found where $\rho_p(\theta)$ assumes its maximum. For mode III, this occurs at $\theta = 0$. For plane stress, one immediately notes from Fig. 4 that the direction forms a blunter angle to the fiber direction than the crack itself does. The maximum can be found through differentiation of the relation (22), by putting $dr = 2(xdx + ydy) = 0$. For instance, for a crack parallel with the fibers, the maximum is found at $\theta = \tan^{-1}(4 \times 2^{1/2})$ which is around 79.9 deg, whereas a local minimum is found straight ahead of the crack tip.

Conclusions

The simplifications of anti-plane strain is retained for a specific class of plane stress problems, for which the displacement is constrained in an arbitrary direction. Available mode III solutions to quasi-static rate-independent problems for incompressible materials are easily transformed to solutions for corresponding plane stress problems.

The case of a stationary crack, remotely subjected to mode I loading conditions, is solved. An interesting deviation from the corresponding mode III problem is found, namely that a strain maximum in the vicinity of the crack tip does not occur straight ahead of the crack tip. Instead it is found at a blunter angle towards the fiber direction.

References

Hult, J. A., and McClintock, F. A., 1956, *Proc. of the 9th Congress of Applied Mechanics*, Vol. 8, Brüssels, p. 51.

Rice, J. R., 1968, *Fracture II*, Academic Press, New York, p. 191.

Ståhle, P., 1986, *Int. Journ. for Num. Meth. in Engin.*, Vol. 23, p. 1847.

An Approximate Solution of a Coupled Differential Equation With Variable Parameter

L. Cveticanin[7]

1 Introduction

Numerous real physical problems are described by a system of two nonlinear coupled differential equations with variable parameter. Usually the parameter is time dependent. This parameter may be mass, length, rigidity, coefficient of friction, material property, etc. The mathematical model is

$$\ddot{z} + \omega^2(\tau) z^3 + \epsilon f(z, \dot{z}, \bar{z}, \dot{\bar{z}}), \tag{1}$$

where $z = x + iy$ is a complex function, x, y are deflections in two perpendicular directions, $i = \sqrt{-1}$ is an imaginary unit, $\bar{z}$ is a complex conjugate function of the z, $(\dot{}) = d/dt$, ϵ is a small positive parameter, $\tau = \epsilon t$, and f is an arbitrary function of its arguments. Since ϵ is small, ϵ is a "slow time". Parameter ω is a function of slow time. The nonlinearity in the system is strong.

This type of model corresponds to a rotor with variable mass (see Cveticanin and Zlokolica, 1987). The rotors with variable mass are the fundamental working elements of a lot of machines in cable, paper, textile industry, etc. Due to strong nonlinearity and mass variation, severe vibration occurs. The vibrations represent a "side effect" to pure rotational motion of the rotor. They are harmful and unwilling. Because of this it is necessary that it is obtained and eliminated. The aim of this paper is to obtain an analytical solution for (1). This solution will make it possible to analyze the influence of the nonlinearity and variable parameter on the behavior of the system.

In this Note the analytical procedure for solving Eq. (1) is based on the method of Bogolubov-Mitropolski (BM) (see Bogolubov and Mitropolski, 1963). For $\epsilon = 0$ and $\tau = \tau_0 = \text{const}$, the solution of the generating equation is denoted.

According to the results of Mickens and Oyedeji (1985) and Yuste and Bejarano (1986), as well as Cveticanin (1991), the solution with Jacobi elliptic functions, instead of circular functions, is introduced. The trial solution of (1) has the same form as the generating one, but the amplitude and phase are time dependent.

2 The Generating Solution

If $\epsilon = 0$ and $\tau = \tau_0 = \text{const}$, the generating equation for (1) is

$$\ddot{z} + \omega^2(\tau_0) z^3 = 0. \tag{2}$$

The exact solution in terms of elliptic functions is

$$z = A\,(cn\Omega t - \theta, k^2) + isn\,(\Omega t - \theta, k^2)) \equiv A\,(cn + isn), \tag{3a}$$

where cn and sn are Jacobi elliptic functions defined by Abramowitz and Stegun (1972), and

$$\Omega = A\omega(\tau_0), \tag{3b}$$

$$k^2 = 2 = \text{const}. \tag{3c}$$

Ω is the frequency, k is the constant parameter, and A and θ are constant values.

3 Approximate Solution

The method of Bogolubov-Mitropolski is adopted for solving Eq. (1). The trial solution is assumed in the form of the generating solution (3).

Let us assume the approximate solution of Eq. (1) in the form

$$\begin{aligned} z = A(t)\,(cn(\psi(t), k^2 = 2) + isn(\psi(t), k^2 = 2) + \epsilon z_1(A, \psi, \tau), \\ + \epsilon z_2(A, \psi, \tau) + \epsilon^3 \ldots \\ \equiv A(t)\,(cn + isn) + \sum_i \epsilon^i z_i(A, \psi, \tau) \end{aligned} \tag{4a}$$

where

[7]Associate Professor, Faculty of Technical Sciences, V. Vlahovica 3, 21000, Novi Sad, Yugoslavia.

Contributed by the Applied Mechanics Division of THE AMERICAN SOCIETY OF MECHANICAL ENGINEERS, for publication in the ASME JOURNAL OF APPLIED MECHANICS.

Manuscript received by the ASME Applied Mechanics Division, Apr. 19, 1991; final revision, Sept. 30, 1991. Associate Technical Editor: D. J. Inman.

Downloaded 03 May 2010 to 171.66.16.245. Redistribution subject to ASME license or copyright; see http://www.asme.org/terms/Terms_Use.cfm

that the plastic strain is singular and of the order of $1/r$ in the vicinity of the crack tip. Since the strain at the elastic plastic boundary is constant, the strain at a constant distance from the crack tip becomes proportional to the distance to the elastic plastic boundary $\rho_p(\theta)$, i.e.,

$$\gamma_{r\theta} = \text{const}\,\frac{\rho_p(\theta)}{r}. \tag{24}$$

Thus, the largest strain at a constant radius is found where $\rho_p(\theta)$ assumes its maximum. For mode III, this occurs at $\theta = 0$. For plane stress, one immediately notes from Fig. 4 that the direction forms a blunter angle to the fiber direction than the crack itself does. The maximum can be found through differentiation of the relation (22), by putting $dr = 2(xdx + ydy) = 0$. For instance, for a crack parallel with the fibers, the maximum is found at $\theta = \tan^{-1}(4 \times 2^{1/2})$ which is around 79.9 deg, whereas a local minimum is found straight ahead of the crack tip.

Conclusions

The simplifications of anti-plane strain is retained for a specific class of plane stress problems, for which the displacement is constrained in an arbitrary direction. Available mode III solutions to quasi-static rate-independent problems for incompressible materials are easily transformed to solutions for corresponding plane stress problems.

The case of a stationary crack, remotely subjected to mode I loading conditions, is solved. An interesting deviation from the corresponding mode III problem is found, namely that a strain maximum in the vicinity of the crack tip does not occur straight ahead of the crack tip. Instead it is found at a blunter angle towards the fiber direction.

References

Hult, J. A., and McClintock, F. A., 1956, *Proc. of the 9th Congress of Applied Mechanics*, Vol. 8, Brüssels, p. 51.

Rice, J. R., 1968, *Fracture II*, Academic Press, New York, p. 191.

Ståhle, P., 1986, *Int. Journ. for Num. Meth. in Engin.*, Vol. 23, p. 1847.

An Approximate Solution of a Coupled Differential Equation With Variable Parameter

L. Cveticanin[7]

1 Introduction

Numerous real physical problems are described by a system of two nonlinear coupled differential equations with variable parameter. Usually the parameter is time dependent. This parameter may be mass, length, rigidity, coefficient of friction, material property, etc. The mathematical model is

$$\ddot{z} + \omega^2(\tau) z^3 + \epsilon f(z, \dot{z}, \bar{z}, \dot{\bar{z}}), \tag{1}$$

where $z = x + iy$ is a complex function, x, y are deflections in two perpendicular directions, $i = \sqrt{-1}$ is an imaginary unit, $\bar{z}$ is a complex conjugate function of the z, $(\dot{}) = d/dt$, ϵ is a small positive parameter, $\tau = \epsilon t$, and f is an arbitrary function of its arguments. Since ϵ is small, ϵ is a "slow time". Parameter ω is a function of slow time. The nonlinearity in the system is strong.

This type of model corresponds to a rotor with variable mass (see Cveticanin and Zlokolica, 1987). The rotors with variable mass are the fundamental working elements of a lot of machines in cable, paper, textile industry, etc. Due to strong nonlinearity and mass variation, severe vibration occurs. The vibrations represent a "side effect" to pure rotational motion of the rotor. They are harmful and unwilling. Because of this it is necessary that it is obtained and eliminated. The aim of this paper is to obtain an analytical solution for (1). This solution will make it possible to analyze the influence of the nonlinearity and variable parameter on the behavior of the system.

In this Note the analytical procedure for solving Eq. (1) is based on the method of Bogolubov-Mitropolski (BM) (see Bogolubov and Mitropolski, 1963). For $\epsilon = 0$ and $\tau = \tau_0 = \text{const}$, the solution of the generating equation is denoted.

According to the results of Mickens and Oyedeji (1985) and Yuste and Bejarano (1986), as well as Cveticanin (1991), the solution with Jacobi elliptic functions, instead of circular functions, is introduced. The trial solution of (1) has the same form as the generating one, but the amplitude and phase are time dependent.

2 The Generating Solution

If $\epsilon = 0$ and $\tau = \tau_0 = \text{const}$, the generating equation for (1) is

$$\ddot{z} + \omega^2(\tau_0) z^3 = 0. \tag{2}$$

The exact solution in terms of elliptic functions is

$$z = A\,(cn\Omega t - \theta, k^2) + isn\,(\Omega t - \theta, k^2)) \equiv A\,(cn + isn), \tag{3a}$$

where cn and sn are Jacobi elliptic functions defined by Abramowitz and Stegun (1972), and

$$\Omega = A\omega(\tau_0), \tag{3b}$$

$$k^2 = 2 = \text{const}. \tag{3c}$$

Ω is the frequency, k is the constant parameter, and A and θ are constant values.

3 Approximate Solution

The method of Bogolubov-Mitropolski is adopted for solving Eq. (1). The trial solution is assumed in the form of the generating solution (3).

Let us assume the approximate solution of Eq. (1) in the form

$$\begin{aligned} z = A(t)\,(cn(\psi(t), k^2 = 2) + isn(\psi(t), k^2 = 2) + \epsilon z_1(A, \psi, \tau), \\ + \epsilon z_2(A, \psi, \tau) + \epsilon^3 \ldots \\ \equiv A(t)\,(cn + isn) + \sum_i \epsilon^i z_i(A, \psi, \tau) \end{aligned} \tag{4a}$$

where

[7]Associate Professor, Faculty of Technical Sciences, V. Vlahovica 3, 21000, Novi Sad, Yugoslavia.

Contributed by the Applied Mechanics Division of THE AMERICAN SOCIETY OF MECHANICAL ENGINEERS, for publication in the ASME JOURNAL OF APPLIED MECHANICS.

Manuscript received by the ASME Applied Mechanics Division, Apr. 19, 1991; final revision, Sept. 30, 1991. Associate Technical Editor: D. J. Inman.

Copyright © 1993 by ASME

Downloaded 03 May 2010 to 171.66.16.245. Redistribution subject to ASME license or copyright; see http://www.asme.org/terms/Terms_Use.cfm

$$dA/dt = \epsilon A_1(A, \tau) + \epsilon^2 A_2(A, \tau) + \epsilon^3 \ldots = \sum_i \epsilon^i A_i(A, \tau), \quad (4b)$$

$$d\psi/dt = \Omega(A, \tau) + \epsilon B_1(A, \tau) + \epsilon^2 B_2(A, \tau) + \ldots \equiv \Omega(A, \tau) + \sum_i \epsilon^i B_i(A, \tau), \quad (4c)$$

and A_i, B_i, z_i are unknown functions. The first and the second time derivatives of the Eq. (4) are obtained.

When substituting the relations (4) into Eq. (1) and equating the terms with the same order of the small parameter ϵ, the following will result:

$$\epsilon^0: A\Omega^2(cn_{\psi\psi} + isn_{\psi\psi}) + \omega^2(\tau)A^3(cn + isn)^3 = 0 \quad (5a)$$

$$\epsilon^1: \Omega^2(d^2z_1/d\psi^2) + 3\omega^2(\tau)A^2z_1(cn + isn)^2 = -(2A_1\Omega + A((\partial\Omega/\partial t)A_1 + \partial\Omega/\partial\tau))(cn_\psi + isn_\psi) - 2AB_1\Omega(cn_{\psi\psi} + isn_{\psi\psi}) + f_1(A, \psi) \quad (5b)$$

$$\epsilon^2: \Omega^2(d^2z_2/d\psi^2) + 3\omega^2(\tau)A^2z_2(cn + isn)^2 = -(2A_2\Omega + A(\partial\Omega/\partial t)A_2)(cn_\psi + isn_\psi) - 2AB_2\Omega(cn_{\psi\psi} + isn_{\psi\psi}) + f_2(A, \psi) \quad (5c)$$

where

$$f_1 = f(A(cn + isn), A\Omega(cn_\psi + isn_\psi), A(cn - isn), A\Omega(cn_\psi - isn_\psi)) \quad (6a)$$

$$f_2 = -3\omega^2(\tau)Az_1^2(cn + isn) - (A_1(\partial A_1/\partial A) + \partial A/\partial\tau)(\mathrm{cn} + \mathrm{isn}) - 2(A_1B_1 + AA_1(\partial B_1/\partial A) + \mathrm{A}(\partial \mathrm{B}_1/\partial\tau))(\mathrm{cn}_\psi + \mathrm{isn}_\psi) - \mathrm{AB}_1^2(\mathrm{cn}_{\psi\psi} + \mathrm{isn}_{\psi\psi}) - 2\Omega(A_1(d^2z_1/dAd\psi) + B_1(d^2z_1/d\psi^2 + \partial^2z_1/(\partial\psi\partial\tau))) - (dz_1/d\psi)((d\Omega/dA)A_1 + \partial\Omega/\partial\tau) + f(A(cn + isn), A\Omega(cn_\psi + isn_\psi), A(cn - isn), A\Omega(cn_\psi - isn_\psi))z_1 + f'(A(cn + isn), A\Omega(cn_\psi + isn_\psi), A(cn - isn), A\Omega(cn_\psi - isn_\psi))A(cn + isn). \quad (6b)$$

Equation (5*a*) is identically satisfied.

Byard and Friedman (1971) give the derivatives of the elliptic functions

$$cn_\psi + isn_\psi = idn(cn + isn) \quad (7a)$$

$$cn_{\psi\psi} + isn_{\psi\psi} = -(dn^2 + ik^2sncn)(cn + isn). \quad (7b)$$

Substituting (7) into (5) and (6) and separating real and imaginary parts, it follows that

$$\mathrm{Re}: -2AB_1\Omega dn^2 = \mathrm{Re}(f_1(cn - isn)), \quad (8a)$$

$$\mathrm{Im}: (2A_1\Omega + A((\partial\Omega/\partial A)A_1 + \partial\Omega/\partial\tau)dn - 2AB_1\Omega k^2sncn = \mathrm{Im}(f_1(cn - isn)), \quad (8b)$$

and

$$\mathrm{Re}: -2AB_i\Omega dn^2 = \mathrm{Re}(f_1(cn - isn)), \quad (9a)$$

$$\mathrm{Im}: (2\Omega + A(\partial\Omega/\partial A))A_i dn - 2AB_i\Omega k^2sncn = \mathrm{Im}(f_i(cn - isn)) \quad (9b)$$

where $i = 2, 3, \ldots$.

The functions A_1, B_1, and A_i, B_i (for $i = 2, 3, \ldots$) are obtained by using the averaging method. The averaging is over the Jacobi elliptic function period, $4K(k^2)$, where $K(k^2)$ is the complete elliptic integral of the first kind.

Then the following is obtained:

$$(2\Omega A_1 + A(A_1(\partial\Omega/\partial A) + \partial\Omega/\partial\tau))\langle dn^2\rangle - 2B_1A\Omega k^2\langle sncndn\rangle = \langle dn\mathrm{Im}(f(cn - isn))\rangle, \quad (10a)$$

$$2\Omega AB_1\langle dn^2\rangle = -\langle \mathrm{Re}(f(cn - isn))\rangle, \quad (10b)$$

and

$$A_i(2\Omega + A(\partial\Omega/\partial A))\langle dn^2\rangle - 2B_iA\Omega k^2\langle sncndn\rangle = \langle dn\mathrm{Im}(f(cn - isn))\rangle, \quad (11a)$$

$$2\omega AB_i\langle dn^2\rangle = -\langle \mathrm{Re}(f(cn - isn))\rangle, \quad (11b)$$

for $i = 1, 2, \ldots$, where $\langle(\ldots)\rangle = (1/4K(k^2))\int_0^{4K}(\ldots)d\psi$ is the averaged value of $(\ldots)$.

The averaged values of the elliptic functions are (see Byard and Friedman, 1971) $\langle sncndn\rangle = 0$, and $\langle dn^2\rangle = E(2)/K(2)$ and the unknown functions are

$$A_1 = (\langle dn\mathrm{Im}(f_1(cn - isn))\rangle - A(\partial\Omega/\partial\tau)(E(2)/K(2))/(2\Omega + A(\partial\Omega/\partial A))(E(2)/K(2))) \quad (12a)$$

$$B_1 = -\langle \mathrm{Re}(f_1(cn - isn))\rangle/(2\Omega A\langle dn^2\rangle) \quad (12b)$$

and

$$A_i = K(2)\langle dn\mathrm{Im}(f_i(cn - isn))\rangle/(E(2)(2\Omega + A(\partial\Omega/\partial A))), \quad (13a)$$

$$B_i = -K(2)\langle \mathrm{Re}(f_i(cn - isn))\rangle/(2E(2)\Omega A), \quad (13b)$$

$i = 2, 3, \ldots$, where $E(2) = (E(1/2) - K(1/2)/2)/\sqrt{2}$ and $K(2) = K(1/2)/(2\sqrt{2})$.

Now, substituting (12) and (13) into Eqs. (4) and integrating the so-obtained differential equations, the amplitude and phase of the motion are obtained.

4 Solution in the First Approximation

It is sometimes enough to find the solution in the first approximation. The trial solution is then

$$z = A(t)(cn(\psi(t), k^2 = 2) + isn(\psi(t), k^2 = 2) \quad (14)$$

where the amplitude and phase variation in the first approximation is

$$dA/dt = \epsilon A_1(A, \tau), \quad d\psi(t)/dt = \Omega(A, \tau) + \epsilon B_1(A, \tau). \quad (15)$$

The functions $A(t)$, $\psi(t)$, and $\Omega(t)$ are time dependent. However, the task of finding the solution $z(t)$ of (1) is transformed into the problem of finding these three functions. In accordance with Eqs. (12) and (15), the amplitude and phase varying in slow time (in the first approximation) is obtained from the following:

$$dA/d\tau = (\langle dn\mathrm{Im}(f_1(cn - isn))\rangle/(3A\omega(\tau)(E(2)/K(2))) - A(d\omega(\tau)/d\tau)/(3\omega(\tau)) \quad (16a)$$

$$d\theta/d\tau = \epsilon K(2)\langle \mathrm{Re}(f(cn - isn))\rangle/(2E(2)A^2\omega(\tau)), \quad (16b)$$

where

$$\psi(t) = \int_0^t \omega(s)ds - \theta(t). \quad (16c)$$

5 Numeric Solution

Equation (1) can be written in the form of the following four differential equations of the first order:

$$\dot{x} = u, \ \dot{u} = -\omega^2(\tau)x(x^2 - 3y^2) + \epsilon\mathrm{Re}(f(x, y, u, v)), \quad \dot{y} = v, \ \dot{v} = \omega^2(\tau)y(y^2 - 3x^2) + \epsilon\mathrm{Im}(f(x, y, u, v)). \quad (17)$$

They can be solved by applying the Runge-Kutta numeric method. The initial conditions for $t = 0$ are

$$x_0 = A_0cn\theta_0, \ y_0 = A_0sn\theta_0, \ u_0 = -A_0^2\omega(\tau_0)sn\theta_0dn\theta_0, \quad v_0 = A_0^2\omega(\tau_0)cn\theta_0dn\theta_0. \quad (18)$$

Downloaded 03 May 2010 to 171.66.16.245. Redistribution subject to ASME license or copyright; see http://www.asme.org/terms/Terms_Use.cfm

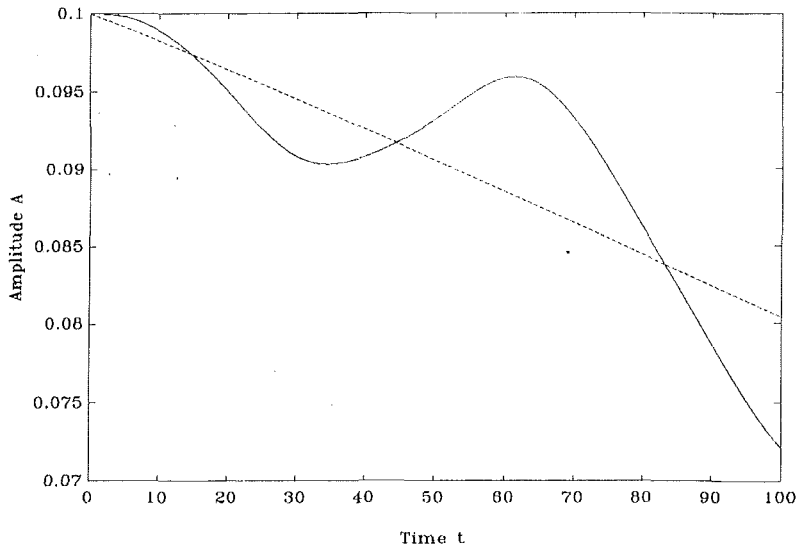


Fig. 1 Amplitude-time diagram of a cubic rotor system with linear damping ——— numerical solution; · · · · analytical solution

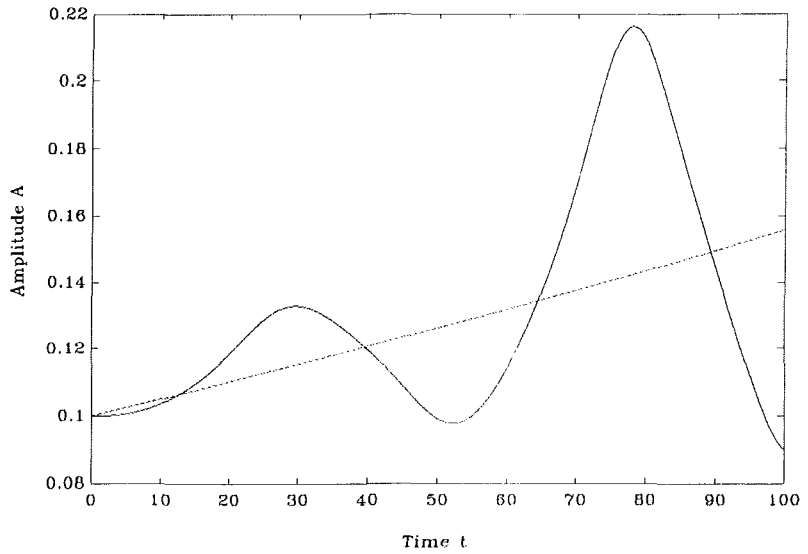


Fig. 2 Amplitude-time diagram of a cubic rotor system with nonlinear hydrodynamic force ——— numerical solution; · · · · analytical solution

6 Examples

The method developed in this paper is applied to some particular problems. So, the vibrations of the rotor on which a thin band is winding up will be considered. The rotor is modeled as a shaft-disk system. The shaft is supported by two bearings. In the middle of the shaft a disk is settled. The mass of the disk is varied due to spooling up of the band. The mass variation is after Bessonov (1967)

$$m(t) = m_0 + R_0 h L \rho \Omega t, \tag{19}$$

where m_0 is the mass of the disk without the band, R_0 is the radius of the disk without the band, ρ is the density of the band material, h is the thickness of the band, L is the width of the band, Ω is the angular velocity of the rotor, and t is time. Mass of the shaft is negligible in comparison to disk. To describe the motion of rotor's center the following dimensionless parameters $\epsilon = R_0 h L \rho \Omega$, $\tau = \epsilon T$, $z = Z/l$, $m(\tau) = 1 + \tau$, where $Z = X + iY$ is the complex deflection of mass center, l is the length of the shaft are introduced. The mathematical model of lateral vibrations has the form (1) (see, Cveticanin, 1984, 1986, 1991) and

$$\omega^2(\tau) = 1/(1+\tau). \tag{20}$$

(a) Cubic Rotor System With Linear Damping. Often a damping force acts in the real rotor systems. If a small linear damping acts, the differential equation of motion is

$$\ddot{z} + \omega^2(\tau) z^3 = -\epsilon \dot{z}. \tag{21}$$

The real and imaginary parts of the function $f(cn - isn)$ are

$$\mathrm{Re}(f(cn - isn)) = 0, \quad \mathrm{Im}(f(cn - isn)) = -\Omega A dn, \tag{22}$$

and the solution in the first approximation (16) is given by

$$A = A_0 \exp(-\epsilon t/3)(\omega(\tau_0)/\omega(\tau))^{1/3}, \quad \theta = \theta_0. \tag{23}$$

Downloaded 03 May 2010 to 171.66.16.245. Redistribution subject to ASME license or copyright; see http://www.asme.org/terms/Terms_Use.cfm

For the parameter value $\epsilon = 0.01$ and initial conditions $\tau_0 = 0, A_0 = 0.1, \theta_0 = 0$, the amplitude-time diagrams are plotted in Fig. 1. Both numerical and analytical results are obtained. The solutions are compared showing a good agreement. It is obvious that the result obtained by this Bogolubov-Mitropolski method is an averaged value of the numeric solution.

Solution (23) can be discussed. The deflection of a rotor's center has a tendency of decrease. The parameter of mass variation tends to increase the deflection. It means, for higher amount of band is winding up the rotor's center deflects more. At the same time the damping decreases the vibrations. As a result, in spite of small damping, the vibration decreases. For higher values of the damping coefficient ϵ, the vibrations decrease faster.

(b) Cubic Rotor System With Nonlinear Hydrodynamic Force. The mathematical model of the cubic two-dimensional rotor system with nonlinear hydrodynamic force (see Tondl, 1979) is

$$\ddot{z} + \omega^2(\tau) z^3 = \epsilon \dot{z}(1 - z\bar{z}). \tag{24}$$

Also, the approximate analytical solution of the problem is obtained by application of the previous method. The relation

$$f(cn - isn) = idnA\Omega(1 - A^2) \tag{25}$$

has only an imaginary part, and for that reason the amplitude is time dependent while the angle is constant, i.e.,

$$A = A_0\sqrt{3}\exp(-\epsilon t/3)(\epsilon t + 1)^{-1/6} \times (2A_0^2\epsilon \int_0^t \exp(-2\epsilon t/3)dt/(\epsilon t + 1)^{1/3} - 3)^{-1/2},$$
$$\theta = \theta_0. \tag{26}$$

The exact numerical and approximate analytic solutions are compared (Fig. 2) for $\epsilon = 0.01$ and initial conditions $t = 0$, $A_0 = 0.1$, $\theta_0 = 0$. They are in good agreement and the amplitude of vibration increases due to the mass variation and nonlinear damping property.

7 Conclusion

In this paper, the Bogolubov-Mitropolski procedure is extended for solving a system of two coupled differential equations which can be simplified with a complex function. The parameters are time dependent and the equation has a strong nonlinear cubic term.

The solutions of a generic equation are Jacobi elliptic functions, and the trial solution of the perturbed equation has an argument which is a function of slow time. This method obtains the amplitude and phase variation and the solution is in good agreement with the numerical result. The analytical solution represents the averaged value of the exact numerical solution and the analytical solution in the first approximation is enough for an accurate discussion of the behavior of the system. It makes it possible for an engineer to define the influence of the parameters on the real system.

Acknowledgment

Research was supported by the SF of AP Vojvodina and VANU.

References

Abramowitz, M., and Stegun, I. A., 1972, *Handbook of Mathematical Functions*, Dover, New York.

Bessonov, A. P., 1967, *Osnovji dinamiki mehanizmov s peremennoj massoj zvenjev*, Nauka, Moscow.

Bogolubov, P. P., and Mitropolski, Ju. A., 1963, *Assimptoticheskie metodi v teorii nelinejnih kolebanij*, Fiz.mat.giz., Moscow.

Byard, P. D., and Friedman, M. D., 1971, *Handbook of Elliptic Integrals for Engineers and Scientists*, Springer-Verlag, Berlin.

Cveticanin, L., 1984, "Vibrations of a Textile Machine Rotor," *J. Sound and Vibrations*, Vol. 97, pp. 181–187.

Cveticanin, L., 1986, "The Vibrations of a Textile Machine Rotor with Nonlinear Characteristics," *Mechanism and Machine Theory*, Vol. 21, pp. 29–32.

Cveticanin, L., and Zlokolica, M., 1987, "The Vibrations of the Rotor for the Case of Winding Up of the Band with Constant Velocity," *Rotor Dynamics*, Pergamon Press, pp. 1815–1819.

Cveticanin, L. J., 1991, "The Oscillations of a Textile Machine Rotor on Which the Textile is Wound Up," *Mechanism and Machine Theory*, Vol. 26, pp. 253–260.

Cveticanin, L., 1992, "An Approximate Solution for Cubic Coupled Differential Equations," *Facta Universitatis*, Vol. 1, pp. 177–186.

Mickens, R. E., and Oyedeji, K., 1985, "Construction of Approximate Analytical Solutions to a New Class of Nonlinear Oscillator Equation," *J. Sound and Vibration*, Vol. 102, pp. 579–582.

Tondl, A., 1979, *Avtokolebanija mehanicheskih sistem*, Mir, Moscow.

Yuste, S. B., and Bejarano, J. D., 1986, "Construction of Approximate Analytical Solutions to a New Class of Nonlinear Oscillator Equations," *J. Sound and Vibration*, Vol. 110, pp. 347–350.

Response of a Fiber Composite Laminate to a Time-Varying Surface Line Load

E. Rhian Green[8]

A symmetric cross-ply laminated plate consisting of four layers of a fiber-reinforced composite material is subjected to a time varying line load on its upper surface. The response at points remote from the application of the line load on both upper and lower surfaces of the plate is determined. Two different pulses are considered, namely a square pulse and a half-sine pulse. The significant parameter governing the nature of the response is the duration of the pulse.

1 Introduction

Theoretical predictions of the response due to a surface impact on a composite laminated plate have previously been reported by Green (1991a, b). These papers include both displacement and stress variations at various positions within the plate. The impact was assumed to be a delta function line load acting normally to the upper surface of the plate. However, in the attempt to validate the analytical results with experimental data, it has been necessary to consider different impact time histories which could be reproduced in the laboratory. Two impulses have been investigated, namely a square pulse and a half-sine pulse. The purpose of the present paper is to show how the response varies with the impulse producing the propagating stress wave.

The laminated plate consists of four layers of a fiber-rein-

[8]Department of Engineering, The University of Leicester, Leicester, LE1 7RH, England.

Contributed by the Applied Mechanics Division of THE AMERICAN SOCIETY OF MECHANICAL ENGINEERS for publication in the ASME JOURNAL OF APPLIED MECHANICS.

Manuscript received by the ASME Applied Mechanics Division, Apr. 19, 1991; final revision, Oct. 10, 1991. Associate Technical Editor: S. K. Datta.

Downloaded 03 May 2010 to 171.66.16.245. Redistribution subject to ASME license or copyright; see http://www.asme.org/terms/Terms_Use.cfm

For the parameter value $\epsilon = 0.01$ and initial conditions $\tau_0 = 0, A_0 = 0.1, \theta_0 = 0$, the amplitude-time diagrams are plotted in Fig. 1. Both numerical and analytical results are obtained. The solutions are compared showing a good agreement. It is obvious that the result obtained by this Bogolubov-Mitropolski method is an averaged value of the numeric solution.

Solution (23) can be discussed. The deflection of a rotor's center has a tendency of decrease. The parameter of mass variation tends to increase the deflection. It means, for higher amount of band is winding up the rotor's center deflects more. At the same time the damping decreases the vibrations. As a result, in spite of small damping, the vibration decreases. For higher values of the damping coefficient ϵ, the vibrations decrease faster.

(b) Cubic Rotor System With Nonlinear Hydrodynamic Force. The mathematical model of the cubic two-dimensional rotor system with nonlinear hydrodynamic force (see Tondl, 1979) is

$$\ddot{z} + \omega^2(\tau) z^3 = \epsilon \dot{z}(1 - z\bar{z}). \tag{24}$$

Also, the approximate analytical solution of the problem is obtained by application of the previous method. The relation

$$f(cn - isn) = idnA\Omega(1 - A^2) \tag{25}$$

has only an imaginary part, and for that reason the amplitude is time dependent while the angle is constant, i.e.,

$$A = A_0\sqrt{3}\exp(-\epsilon t/3)(\epsilon t + 1)^{-1/6} \times (2A_0^2\epsilon \int_0^t \exp(-2\epsilon t/3)dt/(\epsilon t + 1)^{1/3} - 3)^{-1/2},$$
$$\theta = \theta_0. \tag{26}$$

The exact numerical and approximate analytic solutions are compared (Fig. 2) for $\epsilon = 0.01$ and initial conditions $t = 0$, $A_0 = 0.1$, $\theta_0 = 0$. They are in good agreement and the amplitude of vibration increases due to the mass variation and nonlinear damping property.

7 Conclusion

In this paper, the Bogolubov-Mitropolski procedure is extended for solving a system of two coupled differential equations which can be simplified with a complex function. The parameters are time dependent and the equation has a strong nonlinear cubic term.

The solutions of a generic equation are Jacobi elliptic functions, and the trial solution of the perturbed equation has an argument which is a function of slow time. This method obtains the amplitude and phase variation and the solution is in good agreement with the numerical result. The analytical solution represents the averaged value of the exact numerical solution and the analytical solution in the first approximation is enough for an accurate discussion of the behavior of the system. It makes it possible for an engineer to define the influence of the parameters on the real system.

Acknowledgment

Research was supported by the SF of AP Vojvodina and VANU.

References

Abramowitz, M., and Stegun, I. A., 1972, *Handbook of Mathematical Functions*, Dover, New York.

Bessonov, A. P., 1967, *Osnovji dinamiki mehanizmov s peremennoj massoj zvenjev*, Nauka, Moscow.

Bogolubov, P. P., and Mitropolski, Ju. A., 1963, *Assimptoticheskie metodi v teorii nelinejnih kolebanij*, Fiz.mat.giz., Moscow.

Byard, P. D., and Friedman, M. D., 1971, *Handbook of Elliptic Integrals for Engineers and Scientists*, Springer-Verlag, Berlin.

Cveticanin, L., 1984, "Vibrations of a Textile Machine Rotor," *J. Sound and Vibrations*, Vol. 97, pp. 181–187.

Cveticanin, L., 1986, "The Vibrations of a Textile Machine Rotor with Nonlinear Characteristics," *Mechanism and Machine Theory*, Vol. 21, pp. 29–32.

Cveticanin, L., and Zlokolica, M., 1987, "The Vibrations of the Rotor for the Case of Winding Up of the Band with Constant Velocity," *Rotor Dynamics*, Pergamon Press, pp. 1815–1819.

Cveticanin, L. J., 1991, "The Oscillations of a Textile Machine Rotor on Which the Textile is Wound Up," *Mechanism and Machine Theory*, Vol. 26, pp. 253–260.

Cveticanin, L., 1992, "An Approximate Solution for Cubic Coupled Differential Equations," *Facta Universitatis*, Vol. 1, pp. 177–186.

Mickens, R. E., and Oyedeji, K., 1985, "Construction of Approximate Analytical Solutions to a New Class of Nonlinear Oscillator Equation," *J. Sound and Vibration*, Vol. 102, pp. 579–582.

Tondl, A., 1979, *Avtokolebanija mehanicheskih sistem*, Mir, Moscow.

Yuste, S. B., and Bejarano, J. D., 1986, "Construction of Approximate Analytical Solutions to a New Class of Nonlinear Oscillator Equations," *J. Sound and Vibration*, Vol. 110, pp. 347–350.

Response of a Fiber Composite Laminate to a Time-Varying Surface Line Load

E. Rhian Green[8]

A symmetric cross-ply laminated plate consisting of four layers of a fiber-reinforced composite material is subjected to a time varying line load on its upper surface. The response at points remote from the application of the line load on both upper and lower surfaces of the plate is determined. Two different pulses are considered, namely a square pulse and a half-sine pulse. The significant parameter governing the nature of the response is the duration of the pulse.

1 Introduction

Theoretical predictions of the response due to a surface impact on a composite laminated plate have previously been reported by Green (1991a, b). These papers include both displacement and stress variations at various positions within the plate. The impact was assumed to be a delta function line load acting normally to the upper surface of the plate. However, in the attempt to validate the analytical results with experimental data, it has been necessary to consider different impact time histories which could be reproduced in the laboratory. Two impulses have been investigated, namely a square pulse and a half-sine pulse. The purpose of the present paper is to show how the response varies with the impulse producing the propagating stress wave.

The laminated plate consists of four layers of a fiber-rein-

[8]Department of Engineering, The University of Leicester, Leicester, LE1 7RH, England.

Contributed by the Applied Mechanics Division of THE AMERICAN SOCIETY OF MECHANICAL ENGINEERS for publication in the ASME JOURNAL OF APPLIED MECHANICS.

Manuscript received by the ASME Applied Mechanics Division, Apr. 19, 1991; final revision, Oct. 10, 1991. Associate Technical Editor: S. K. Datta.

Copyright © 1993 by ASME
Downloaded 03 May 2010 to 171.66.16.245. Redistribution subject to ASME license or copyright; see http://www.asme.org/terms/Terms_Use.cfm

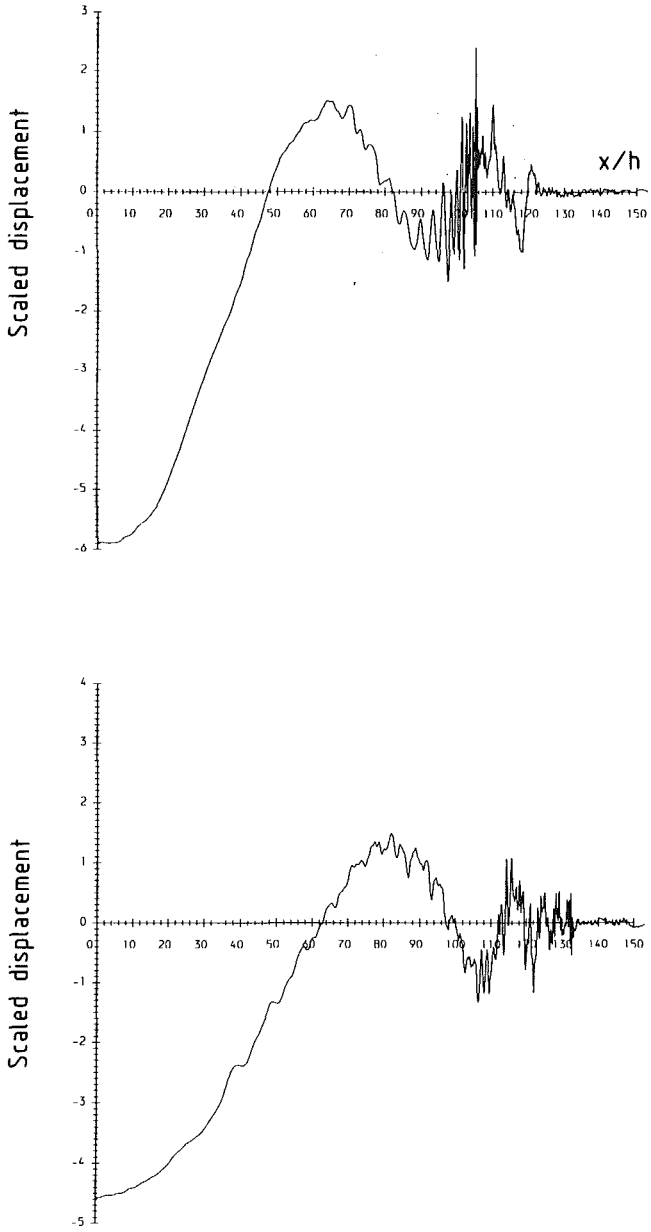


Fig. 1 Delta function impulse. Upper surface normal displacement at $T = 200$; $\gamma = 30$ deg (top) and $\gamma = 60$ deg (bottom).

forced material, each of depth h but of infinite lateral extent. The material is modeled as a homogeneous, transversely isotropic, elastic continuum with the axis of transverse isotropy being parallel to the fibers and in the plane of the lamina. The layers are perfectly bonded in a symmetric cross-ply configuration. The upper surface of the laminate is subjected to a line load impact, along a line making an angle $\pi/2 - \gamma$ with the core fiber direction. The lower surface is kept traction-free. The resulting plane wave disturbance will travel in the plate along the direction normal to the line load, that is, at an angle γ to the core fibers.

The procedure involves setting up the full three-dimensional equations of elasticity in each layer and solving them subject to the perfect bonding conditions at the interfaces and the prescribed loading conditions on the outer surfaces. It will be shown that the crucial parameter governing the response of the plate is the duration of the pulse. The response due to a square or half-sine pulse of very short duration is almost indistinguishable from that of the delta function impact, whereas some of the interesting features become less significant and eventually disappear as the time span of the pulse is increased. The detailed derivation of the solution to the basic problem obtained by transform techniques is reported by Green (1991a). In particular, the upper surface normal displacement is expressed by Eq. (4.12) which has the general form given by

$$u_1(x_1, x, t) = \frac{1}{2\pi} \sum_{j=1}^{20} \int_0^{20} \{R(x_1, k, s) e^{st} e^{ikx} dk\}_{s = \pm i\omega_j(k)} \quad (1)$$

where k and s are transform parameters, t is time, x is the in-plane spatial coordinate, and x_1 is the normal coordinate. $w_j(k)$ $(j = 1, 2, \ldots)$ are the roots of the dispersion equation for plane harmonic waves propagating in an identical plate under traction-free conditions. Here, the residue R differs from that in the previously cited equation by a factor $G_i(s)$, $(i = 1, 2)$, of the Laplace transform of the source function. These factors are given by

$$G_1(s) = \frac{1}{sR}(1 - e^{-sR}) \quad (2)$$

$$G_2(s) = \frac{1 + e^{-sR}}{2(1 + s^2R^2/\pi^2)} \quad (3)$$

where R is the parameter governing the duration of the pulse.

Discussion

The results quoted are for a typical carbon fiber-epoxy resin unidirectional composite with the ratio of the modulus along the fibers to that orthogonal to the fibers of the order of 25. The material constants are the same as those used by Green (1991a).

Here, a set of curves showing the variation of the displacement u_1 normal to the plate as a function of the propagation distance x/h from the line of impact is presented. These results relate to two values of γ, namely 30 deg and 60 deg, and to one instant of time $T = 200$, where $T = ct/h$, and c is the speed of a longitudinal wave travelling transverse to the fibers. Attention is restricted to the response of the outer surfaces.

Figure 1 shows the variation of the normal displacement of the upper surface for $\gamma = 30$ deg and 60 deg, respectively, after a delta function impulse. The large amplitude oscillation which indicates the presence of a surface wave at $\gamma = 30$ deg is consistent with the theory which predicts that such a wave exists in this particular four-ply plate whenever γ is less than 47.3 deg.

Figures 2 and 3 show the variation in the normal displacement of the upper surface for the two other time histories considered. In each case, a is at $\gamma = 30$ deg and b is at $\gamma = 60$ deg. Since it is intended to show the significance of the duration of the impact, results are shown for three values of R. These are (i) $R = 0.1$ which defines a pulse of very short duration, (ii) $R = 1$, and (iii) $R = 10$ which gives a very long pulse.

One striking feature is the extremely close similarity between the response to the delta function impulse and the response to a square or half-sine pulse of very short duration. (Figures 1 (top), 2(a(i)), 3(a(i)) for $\gamma = 30$ deg and Figs. 1 (bottom), 2(b(i)), and 3(b(i)) for $\gamma = 60$ deg.) Both pulses will in the limit yield the delta function and in that sense it is not surprising that responses to pulses of very short duration closely resemble that of the delta function.

Another striking feature is brought out by comparing the results for a given shape pulse for different values of R, say Figs. 2(a(i–iii)). As the duration of the pulse increases, the high-frequency oscillations become less significant and have disappeared completely when $R = 10$. When the pulse spans a relatively long period of time, no high-frequency motion is set up and the ensuing disturbance is that due to the low-

Downloaded 03 May 2010 to 171.66.16.245. Redistribution subject to ASME license or copyright; see http://www.asme.org/terms/Terms_Use.cfm

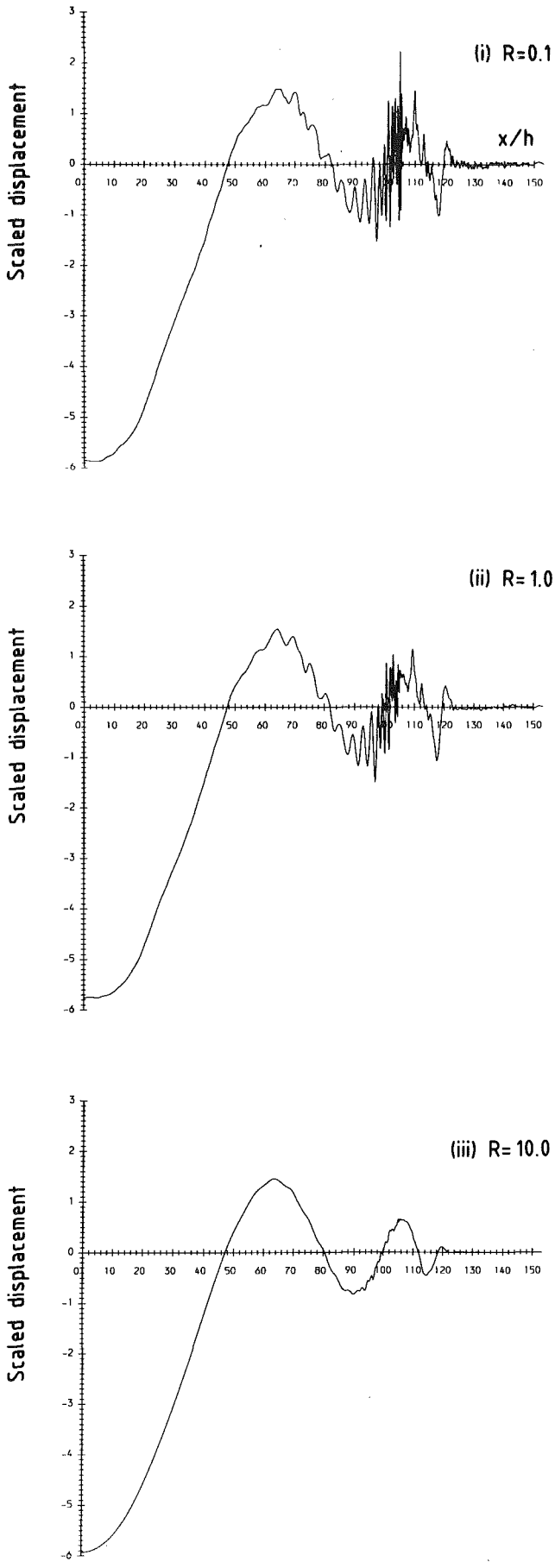


Fig. 2(*a*) Square pulse. Upper surface normal displacement at $T = 200$, $\gamma = 30$ deg.

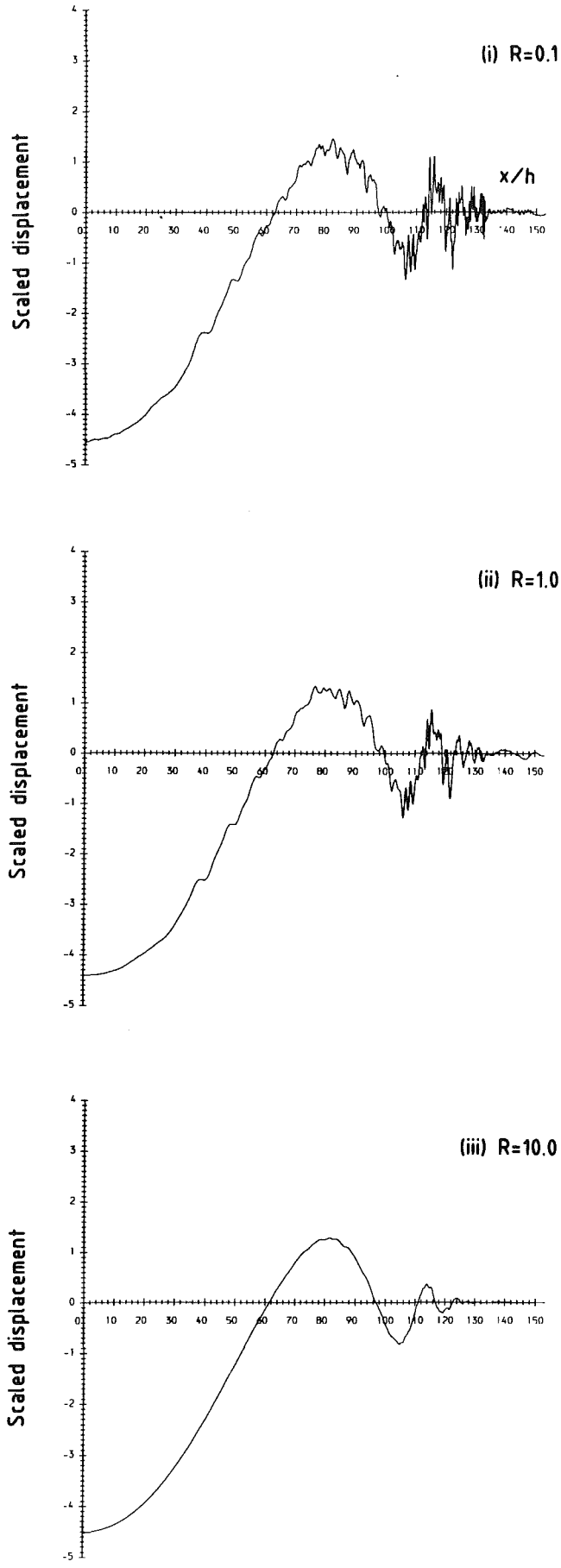


Fig. 2(*b*) Square pulse. Upper surface normal displacement at $T = 200$, $\gamma = 60$ deg.

Downloaded 03 May 2010 to 171.66.16.245. Redistribution subject to ASME license or copyright; see http://www.asme.org/terms/Terms_Use.cfm

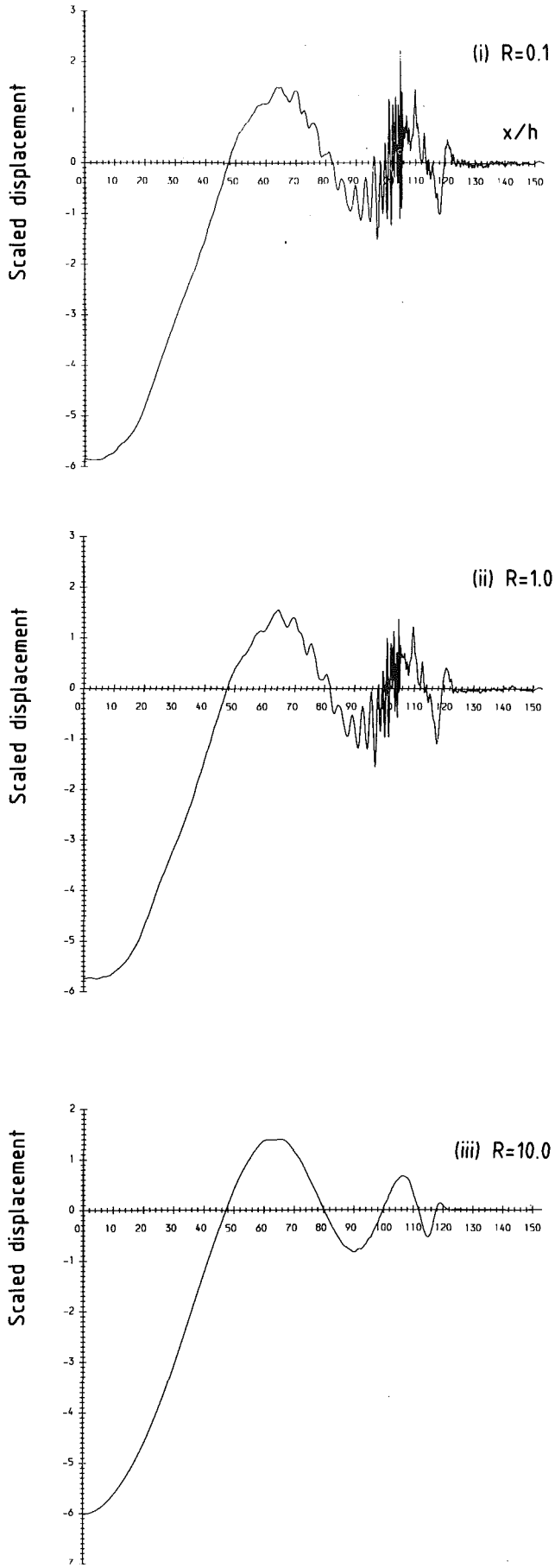


Fig. 3(*a*) Half sine pulse. Upper surface normal displacement at T = 200, γ = 30 deg.

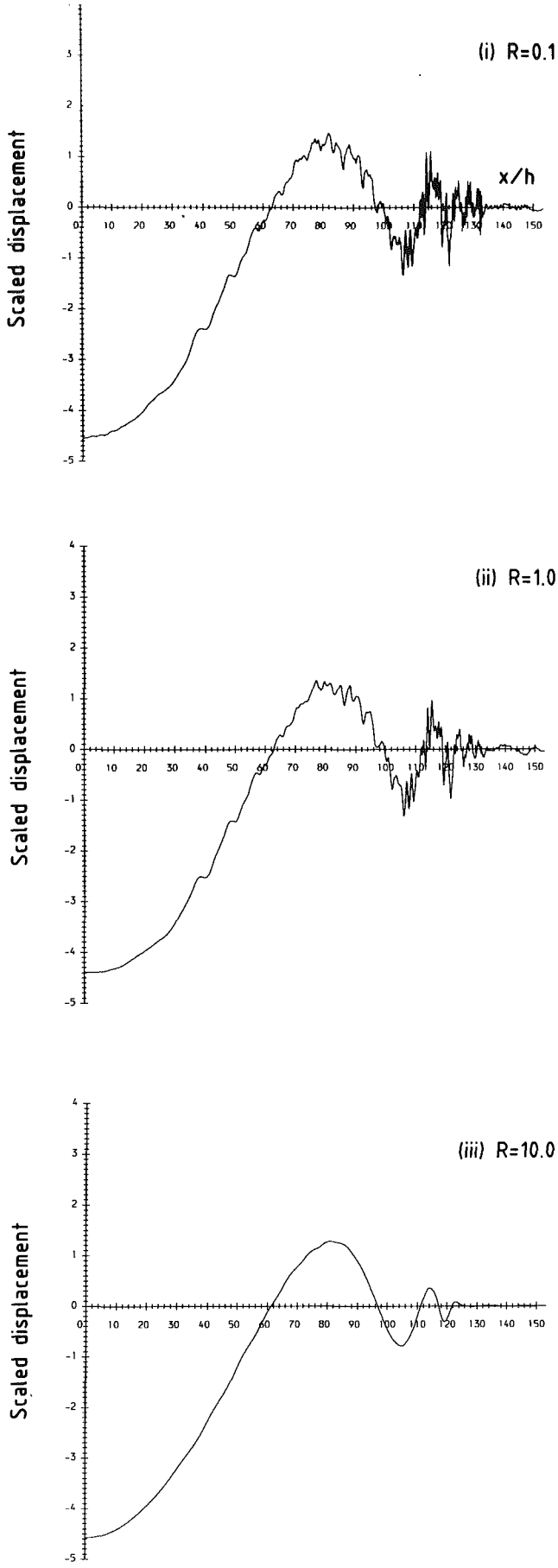


Fig. 3(*b*) Half-sine pulse. Upper surface normal displacement at T = 200, γ = 60 deg.

Downloaded 03 May 2010 to 171.66.16.245. Redistribution subject to ASME license or copyright; see http://www.asme.org/terms/Terms_Use.cfm

frequency content of the delta function impulse. This behavior is independent of the angle of propagation and the shape of the pulse.

Acknowledgment

I am grateful to the NATO Collaborative Research Grant 0243/89 for financial support of this work.

References

Green, E. Rhian, 1991, "Transient Impact Response of a Fibre Composite Laminate," *Acta Mech.*, Vol. 86, pp. 153-165.

Green, E. Rhian, 1991, "Interfacial Response of a Fibre Composite Laminate to a Surface Impact," *Proc. of 1st Int. Conf. on Mathematical and Numerical Aspects of Wave Propagation Phenomena*, Strasbourg.

Evaluation of a Complex Stress Intensity Factor of Interface Cracks: A Perturbation Approach

C. Y. Hui[9] and Y. C. Chen[9]

This Note presents a perturbation method of calculating the complex stress intensity factor K of infinitely sharp cracks lying on a bimaterial interface. The small parameter ϵ in our problem is the oscillatory index defined by

$$\epsilon = (1/2\pi)\ln[(1-\beta)/(1+\beta)] \tag{1}$$

where $\beta = [\mu_1(\kappa_2 - 1) - \mu_2(\kappa_1 - 1)]/[\mu_1(\kappa_2 + 1) + \mu_2(\kappa_1 + 1)]$ is one of Dundur's parameters. The subscripts 1 and 2 refer to the two materials, $\kappa = 3 - 4\nu$ for plane strain and $(3 - \nu)/(1 + \nu)$ for plane stress, ν is the Poisson's ratio, and μ is the shear modulus. As pointed out by Rice (1988) and Suo (1989), typical values of ϵ are quite small, e.g., its absolute value does not exceed 0.175.

Figure 1(*a*) shows a semi-infinite plane strain or plane stress crack lying along the negative x-axis, that is loaded by equal and opposite traction $\sigma_{yy} + i\sigma_{xy} = -T(x)$ on the crack face. The complex stress intensity K is given by Suo (1989):

$$K = A_1 \int_0^\infty [f(t)]^{-1/2} T(-t)\exp[-i\epsilon \ln f(t)]dt \tag{2a}$$

where $f(t) = t$ and $A_1 = (2/\pi)^{1/2}\cosh(\pi\epsilon)$.

Figure 1(*b*) shows an interface crack of length $2a$ in the interior of a bimaterial plate joined along the x-axis. The crack is loaded by equal and opposite traction $\sigma_{xx} + i\sigma_{xy} = -T(x)$ on the crack face. The complex stress intensity K at the right crack tip is given by Suo (1989):

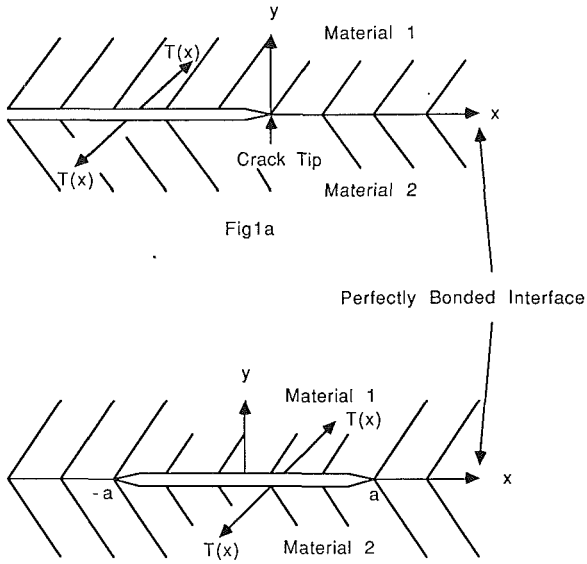


Fig. 1(*a*) A semi-infinite crack loaded by a distributed traction $T(x)$ along the crack faces; the traction vector T is shown only at one point. (*b*) A finite crack of length $2a$ loaded by a distributed traction $T(x)$ along the crack faces; the traction vector T is shown only at one point.

$$K = A_2 \int_{-1}^{1-} [f(t)]^{1/2} T(at)\exp[i\epsilon \ln f(t)]dt \tag{2b}$$

where $A_2 = (a/\pi)^{1/2}(2a)^{-i\epsilon}\cosh(\pi\epsilon)$ and $f(t) = (1 + t)/(1 - t)$ for this case.

The main results of this Note are

$$K \cong A_1 \sum_{n=0}^{\infty} \frac{1}{n!} \int_0^\infty [f(t)]^{-1/2} T(-t)[-i\epsilon \ln f(t)]^n dt \tag{3a}$$

and

$$K \cong A_2 \sum_{n=0}^{\infty} \frac{1}{n!} \int_{-1}^{1} [f(t)]^{1/2}\, T(at)[i\epsilon \ln f(t)]^n dt \tag{3b}$$

for K in Fig. 1(*a*) and Fig. 1(*b*), respectively, i.e., K can be obtained by expanding $\exp[i\epsilon \ln f(t)]$ into a power series in $[i\epsilon \ln f(t)]$ and integrating term by term. The above perturbation series are accurate to all order in ϵ with the possible exception of exponentially small terms on the order of $O(\exp(-\lambda/|\epsilon|))$ where $\lambda > 0$. Furthermore, for continuous $T(t)$ we will show that the perturbation series converge if $|\epsilon| < 1/2$.

The difficulty lies in the fact that the series expansion

$$\exp[i\epsilon \ln f(t)] = \sum_{n=0}^{\infty} \frac{1}{n!} [i\epsilon \ln f(t)]^n \tag{4}$$

with $f(t) = (1 + t)/(1 - t)$ is not uniformly convergent in $(-1, 1)$. Furthermore, convergence in the perturbation sense is not satisfied in $(-1, 1)$. Indeed, convergence in the perturbation sense requires

$$|\epsilon \ln f(x)| << 1 \tag{5}$$

which is violated near the crack tip where rapid oscillation occurs. The region near the crack tip where (5) is violated can be estimated by setting $|\epsilon \ln f(x)| \approx 1$ and is found to be of order $O(\exp(-1/|\epsilon|))$ for sufficiently small $|\epsilon|$.

The proof of (3*b*) is as follows.

Let $\delta = \exp(-|\epsilon|^{-p})$ where p satisfies $0 < p < 1$. Let $f(t) = (1 + t)/(1 - t)$, $h(t, \epsilon) = \exp[i\epsilon \ln f(t)]$, and $g(t, \epsilon) = T(at)\,[f(t)]^{1/2}\, h(t, \epsilon)$. Consider the integral

[9]Department of Theoretical and Applied Mechanics, Cornell University, Ithaca, NY 14853.

Contributed by the Applied Mechanics Division of THE AMERICAN SOCIETY OF MECHANICAL ENGINEERS for publication in the ASME JOURNAL OF APPLIED MECHANICS. Manuscript received by the ASME Applied Mechanics Division, Aug. 1, 1990; final revision, Dec. 30, 1991. Associate Technical Editor: C. F. Shih.

Downloaded 03 May 2010 to 171.66.16.245. Redistribution subject to ASME license or copyright; see http://www.asme.org/terms/Terms_Use.cfm

frequency content of the delta function impulse. This behavior is independent of the angle of propagation and the shape of the pulse.

Acknowledgment

I am grateful to the NATO Collaborative Research Grant 0243/89 for financial support of this work.

References

Green, E. Rhian, 1991, "Transient Impact Response of a Fibre Composite Laminate," *Acta Mech.*, Vol. 86, pp. 153-165.

Green, E. Rhian, 1991, "Interfacial Response of a Fibre Composite Laminate to a Surface Impact," *Proc. of 1st Int. Conf. on Mathematical and Numerical Aspects of Wave Propagation Phenomena*, Strasbourg.

Evaluation of a Complex Stress Intensity Factor of Interface Cracks: A Perturbation Approach

C. Y. Hui[9] and Y. C. Chen[9]

This Note presents a perturbation method of calculating the complex stress intensity factor K of infinitely sharp cracks lying on a bimaterial interface. The small parameter ϵ in our problem is the oscillatory index defined by

$$\epsilon = (1/2\pi)\ln[(1-\beta)/(1+\beta)] \tag{1}$$

where $\beta = [\mu_1(\kappa_2 - 1) - \mu_2(\kappa_1 - 1)]/[\mu_1(\kappa_2 + 1) + \mu_2(\kappa_1 + 1)]$ is one of Dundur's parameters. The subscripts 1 and 2 refer to the two materials, $\kappa = 3 - 4\nu$ for plane strain and $(3 - \nu)/(1 + \nu)$ for plane stress, ν is the Poisson's ratio, and μ is the shear modulus. As pointed out by Rice (1988) and Suo (1989), typical values of ϵ are quite small, e.g., its absolute value does not exceed 0.175.

Figure 1(*a*) shows a semi-infinite plane strain or plane stress crack lying along the negative x-axis, that is loaded by equal and opposite traction $\sigma_{yy} + i\sigma_{xy} = -T(x)$ on the crack face. The complex stress intensity K is given by Suo (1989):

$$K = A_1 \int_0^\infty [f(t)]^{-1/2} T(-t)\exp[-i\epsilon\ln f(t)]dt \tag{2a}$$

where $f(t) = t$ and $A_1 = (2/\pi)^{1/2}\cosh(\pi\epsilon)$.

Figure 1(*b*) shows an interface crack of length $2a$ in the interior of a bimaterial plate joined along the x-axis. The crack is loaded by equal and opposite traction $\sigma_{xx} + i\sigma_{xy} = -T(x)$ on the crack face. The complex stress intensity K at the right crack tip is given by Suo (1989):

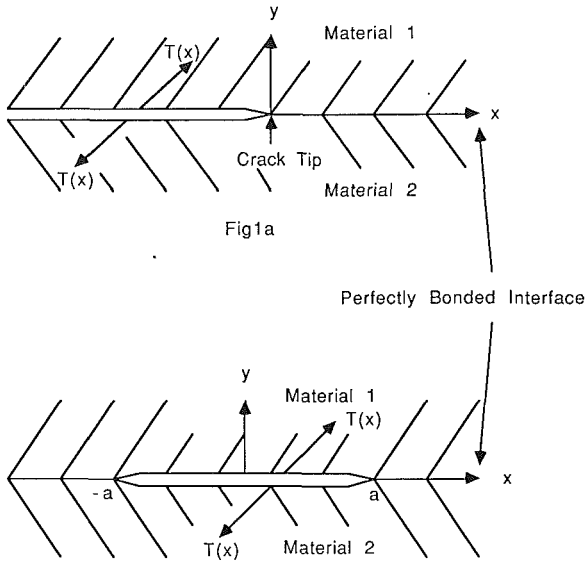


Fig. 1(*a*) A semi-infinite crack loaded by a distributed traction $T(x)$ along the crack faces; the traction vector T is shown only at one point. (*b*) A finite crack of length $2a$ loaded by a distributed traction $T(x)$ along the crack faces; the traction vector T is shown only at one point.

$$K = A_2 \int_{-1}^{1-} [f(t)]^{1/2} T(at)\exp[i\epsilon\ln f(t)]dt \tag{2b}$$

where $A_2 = (a/\pi)^{1/2}(2a)^{-i\epsilon}\cosh(\pi\epsilon)$ and $f(t) = (1 + t)/(1 - t)$ for this case.

The main results of this Note are

$$K \cong A_1 \sum_{n=0}^{\infty} \frac{1}{n!} \int_0^\infty [f(t)]^{-1/2} T(-t)[-i\epsilon\ln f(t)]^n dt \tag{3a}$$

and

$$K \cong A_2 \sum_{n=0}^{\infty} \frac{1}{n!} \int_{-1}^{1} [f(t)]^{1/2}\, T(at)[i\epsilon\ln f(t)]^n dt \tag{3b}$$

for K in Fig. 1(*a*) and Fig. 1(*b*), respectively, i.e., K can be obtained by expanding $\exp[i\epsilon\ln f(t)]$ into a power series in $[i\epsilon\ln f(t)]$ and integrating term by term. The above perturbation series are accurate to all order in ϵ with the possible exception of exponentially small terms on the order of $O(\exp(-\lambda/|\epsilon|))$ where $\lambda > 0$. Furthermore, for continuous $T(t)$ we will show that the perturbation series converge if $|\epsilon| < 1/2$.

The difficulty lies in the fact that the series expansion

$$\exp[i\epsilon\ln f(t)] = \sum_{n=0}^{\infty} \frac{1}{n!} [i\epsilon\ln f(t)]^n \tag{4}$$

with $f(t) = (1 + t)/(1 - t)$ is not uniformly convergent in $(-1, 1)$. Furthermore, convergence in the perturbation sense is not satisfied in $(-1, 1)$. Indeed, convergence in the perturbation sense requires

$$|\epsilon\ln f(x)| << 1 \tag{5}$$

which is violated near the crack tip where rapid oscillation occurs. The region near the crack tip where (5) is violated can be estimated by setting $|\epsilon\ln f(x)| \approx 1$ and is found to be of order $O(\exp(-1/|\epsilon|))$ for sufficiently small $|\epsilon|$.

The proof of (3*b*) is as follows.

Let $\delta = \exp(-|\epsilon|^{-p})$ where p satisfies $0 < p < 1$. Let $f(t) = (1 + t)/(1 - t)$, $h(t, \epsilon) = \exp[i\epsilon\ln f(t)]$, and $g(t, \epsilon) = T(at)\,[f(t)]^{1/2}\,h(t, \epsilon)$. Consider the integral

[9]Department of Theoretical and Applied Mechanics, Cornell University, Ithaca, NY 14853.

Contributed by the Applied Mechanics Division of THE AMERICAN SOCIETY OF MECHANICAL ENGINEERS for publication in the ASME JOURNAL OF APPLIED MECHANICS. Manuscript received by the ASME Applied Mechanics Division, Aug. 1, 1990; final revision, Dec. 30, 1991. Associate Technical Editor: C. F. Shih.

Copyright © 1993 by ASME
Downloaded 03 May 2010 to 171.66.16.245. Redistribution subject to ASME license or copyright; see http://www.asme.org/terms/Terms_Use.cfm

$$I=\int_{-1}^{1} g(t,\epsilon)dt$$

which can be written as the sum of three integrals I_1, I_2, and I_3 defined by

$$I_1=\int_{-1}^{-1+\delta} g(t,\epsilon)dt,\ I_2=\int_{-1+\delta}^{1-\delta} g(t,\epsilon)dt,\ I_3=\int_{1-\delta}^{1} g(t,\epsilon)dt.$$

The function $h(t,\epsilon)$ can be expanded into a power series in $\Omega = [-1+\delta, 1-\delta]$, i.e.,

$$h(t,\epsilon)=\sum_{n=0}^{\infty}\frac{1}{n!}[i\epsilon\ln f(t)]^n \tag{6}$$

By the definition of δ, the series expansion of $g(t,\epsilon)$ in Ω is a perturbation series since

$$|\epsilon\ln f(t)|=O(|\epsilon|^{1-p})<<1 \quad \text{for all } t \text{ in } \Omega. \tag{7}$$

Multiplying (6) by $T(at)[f(t)]^{1/2}$ and integrating term by term in a perturbation series for I_2, i.e.,

$$I_2=\sum_{n=0}^{\infty}\frac{1}{n!}\int_{-1+\delta}^{1-\delta} T(at)[f(t)]^{1/2}[i\epsilon\ln f(t)]^n dt. \tag{8}$$

To estimate the contributions of I_1 and I_3 to I, we note that

$$|I_3|\le\int_{1-\delta}^{1}|T(at)|[f(t)]^{1/2}dt$$

$$<4[\max|T|]\exp(-|\epsilon|^{-p}/2), \tag{9}$$

if the maximum of $|T|$ exists (e.g., if T is continuous). If $T(x)$ has, near $x=a$, an integrable singularity of the form

$$T(x)\approx A(a-x)^{-q} \quad 0<q<1/2$$

where A is some complex constant, then (9) should be replaced by

$$I_3=O(\exp[-(1/2-q)/|\epsilon|^p]). \tag{10}$$

A similar estimate can be found for I_1. These results show that the contributions of I_1 and I_3 to I are exponentially small as $\epsilon\to 0$. Finally, (3b) is obtained by observing that each term in the perturbation series given by (8) can be replaced by

$$\frac{1}{n!}\int_{-1}^{1} T(at)[f(t)]^{1/2}|i\epsilon\ln f(t)]^n dt. \tag{11}$$

By the same argument leading to (9), this replacement introduces only exponentially small errors as $\epsilon\to 0$. Equations (2b) and (8), combining with the above analysis, give us (3b).

The proof of (3a) follows in exactly the same manner and will not be repeated here.

Note that if we set $T(at)=(1+|t|)^{-2}$, the integral (3b) can be evaluated exactly, i.e.,

$$K=A_2\sum_{n=0}^{\infty}[(2i\epsilon)^n+(-2i\epsilon/3)^n/3]. \tag{12}$$

This series converges to the exact solution $K=A_2[1/(1-2i\epsilon)+1/(3+2i\epsilon)]$ only if $|\epsilon|<1/2$! Indeed, the convergence of the series given by (2a) and (2b) to the exact solution is not a coincidence but is guaranteed if $T(x)$ is continuous. To prove this statement, we use Lebegue's theorem of dominated convergence (Widom, 1969). This theorem states that if a sequence of measurable functions $\{h_k\}$ in an interval E is uniformly bounded almost everywhere ($a.e$) by an integrable function ψ in E and converges to a function $h(a.e)$ in E, then

$$\int_E h_k(t)dt\to\int_E h(t)dt \quad k\to\infty \tag{13}$$

The proof of the convergence of (3b) is as follows:

Let

$$h_k=\sum_{n=0}^{k}\frac{1}{n!}[f(t)]^{1/2}T(at)[i\epsilon\ln f(t)]^n$$

$$h=[f(t)]^{i\epsilon+1/2}T(at).$$

Then $h_k\to h$ as $k\to\infty$. Let

$$\varphi(t)=[(t)]^{1/2+|\epsilon|\mathrm{sgn}(t)}|T(at)|.$$

For $|\epsilon|<1/2$,

$$\int_{-1}^{1}\varphi(t)dt<\infty,$$

i.e., φ is integrable on $[-1,1]$. Furthermore,

$$|h_k|\le[f(t)]^{1/2}|T(at)|\sum_{n=0}^{\infty}\frac{1}{n!}[|\epsilon|\mathrm{sgn}(t)\ln f(t)]^n$$

$$=[f(t)]^{1/2}|T(at)|\exp[|\epsilon|\mathrm{sgn}(t)\ln f(t)]$$

$$=\varphi(t)$$

for all t in $(-1,1)$. By Lebesgue's theorem of dominated convergence we have

$$\int_E h_k(t)dt\to\int_E h(t)dt \quad k\to\infty,$$

where $E=[-1,1]$. This shows that the right-hand side of (3b) converges to the right-hand side of (2b) if $|\epsilon|<1/2$. The proof for the convergence of (3a) is similar if one assumes that $T(x)$ is absolutely integrable.

Conclusion

We have found a perturbation series for the complex stress intensity factor for two important interface crack configurations in terms of the oscillation parameter ϵ. The first term of the perturbation series gives the complex stress intensity factor when the two materials have identical elastic modulus. When the traction on the crack faces is continuous, it is found that the perturbation series converges to the exact solution if $|\epsilon|<1/2$. When the traction has singularity of order less than $r^{-1/2}$ near a crack tip, where r is the distance measured from the tip, the perturbation series may not converge but is usage introduces at most exponentially small errors. Our analysis shows that the contribution of rapid oscillation near the crack tip to the complex stress intensity factor is insignificant. For typical values of ϵ, two terms of the perturbation series will give an error of less than one percent.

Acknowledgment

C. Y. Hui acknowledges partial support from the Material Science Center at Cornell University, which is funded by the National Science Foundation (DMR-MRL program). He also acknowledges partial support from E. I. Dupont de Nemours and Co. Inc., Y. C. Chen acknowledges the partial support from Mathematical Sciences Institute at Cornell University.

References

Rice, J. R., 1988, "Elastic Fracture Concepts for Interfacial Cracks," ASME Journal of Applied Mechanics, Vol. 32, pp. 418-423.

Suo, Z., 1989, "Singularities Interacting With Interfaces and Cracks," *Int. J. Solids Structures*, Vol. 25, pp. 1133-1142.

Widom, H,. 1969, *Lectures on Measure and Integration*, p. 34, (Van Nostrand Mathematical Studies, No. 20), Van Nostrand Reinhold, New York, p. 34.

Downloaded 03 May 2010 to 171.66.16.245. Redistribution subject to ASME license or copyright; see http://www.asme.org/terms/Terms_Use.cfm

Dynamic Crack Propagation in a Linearly Viscous Body

S. J. Fariborz[10]

Introduction

The growth of a semi-infinite crack in a viscoelastic body has been the subject of several investigations, e.g., Willis (1967) and Atkinson and List (1972). In these analyses, a closed-form solution may be obtained only along the line of crack advance near the crack tip. Moreover, the solutions are restricted to the requirement that displacement must decay exponentially far from the crack tip.

In this Note, the steady-state, dynamic growth of a semi-infinite crack in an elastic/linearly viscous (Maxwell) material under conditions of antiplane strain (Mode III) is studied. The differential operator form of the constitutive relations is considered, and the governing equation is formulated in terms of the displacement. This equation is converted to a Helmholtz equation which is solved by means of the Kontorovich-Lebedev transformation. There is no need to assume exponentially decaying behavior of the displacement field. The analysis allows the determination of the closed-form solution for displacement in the entire half-plane and the dominant terms of the stress field in the region near the crack tip.

Analysis

We consider a semi-infinite growing crack located on the horizontal axis X_1 (Fig. 1). The crack propagates from right to left with a known constant velocity v. The constitutive behavior is taken to be that for a Maxwell material. Under conditions of antiplane strain, the only nonzero component of the displacement vector is the out-of-plane component $W(X_1, X_2)$. Consequently, the only nonvanishing components of the stress tensor are σ_{13} and σ_{23}. In differential operator representation, the constitutive equations are

$$\left(\frac{1}{2}\right)\frac{\partial^2 W}{\partial X_1 \partial t}=\left(\frac{1}{2\mu}\right)\frac{\partial \sigma_{13}}{\partial t}+C\sigma_{13}$$
$$\left(\frac{1}{2}\right)\frac{\partial^2 W}{\partial X_2 \partial t}=\left(\frac{1}{2\mu}\right)\frac{\partial \sigma_{23}}{\partial t}+C\sigma_{23} \tag{1}$$

where μ is the elastic shear modulus and C is a material constant. The only equation of motion not identically satisfied is

$$\frac{\partial \sigma_{13}}{\partial X_1}+\frac{\partial \sigma_{23}}{\partial X_2}-\rho\frac{\partial^2 W}{\partial t^2}=0 \tag{2}$$

where ρ is the mass density of the material. Assuming steady-state crack growth, the use of the Galilean transformation, $x_1 = X_1 + vt$, $x_2 = X_2$ eliminates the dependency on the time variable t. Equations (1) and (2) in the moving coordinate system (x_1, x_2), where the origin is located at the tip of the crack, are

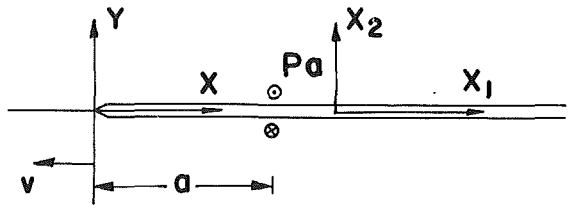


Fig. 1

$$\frac{\partial \sigma_{13}}{\partial x_1}+\frac{\partial \sigma_{23}}{\partial x_2}-(\rho v^2)\frac{\partial^2 W}{\partial x_1^2}=0$$
$$\left(\frac{v}{2}\right)\frac{\partial^2 W}{\partial x_1^2}-\left(\frac{v}{2\mu}\right)\frac{\partial \sigma_{13}}{\partial x_1}-C\alpha_{13}=0$$
$$\left(\frac{v}{2}\right)\frac{\partial^2 W}{\partial x_1 \partial x_2}-\left(\frac{v}{2\mu}\right)\frac{\partial \sigma_{23}}{\partial x_1}-C\alpha_{23}=0. \tag{3}$$

In order to render the problem time invariant under the Galilean transformation, it is assumed that the applied traction on the crack faces follows behind the advancing crack so as to remain fixed with respect to the crack tip. Hence, the applied traction is taken as $\sigma_{23}(x_1, 0) = F(x_1)$; $x_1 > 0$. The symmetry of the problem with respect to the x_1-axis yields the remaining boundary data

$$W(x_1, 0)=0; \qquad x_1<0$$
$$\sigma_{13}(x_1, 0)=0; \qquad x_1<0. \tag{4}$$

Finally, the self-equilibrating nature of the loading leads to

$$(W, \sigma_{13}, \sigma_{23})\to 0 \text{ as } (x_1^2+x_2^2)^{1/2}\to\infty. \tag{5}$$

We introduce the following nondimensional variables

$$\tau_x=\sigma_{13}/\mu, \qquad \tau_y=\sigma_{23}/\mu \qquad w=2\mu CW/C_1, \quad \epsilon v/C_1,$$
$$x=2\mu Cx_1/C_1, \qquad y=2\mu Cx_2/C_1, \qquad f(x)=F(X_1)/\mu$$

where $C_1 = (\mu/\rho)^{1/2}$ is the characteristic elastic shear wave velocity for the material and ϵ is the Mach number into Eqs. (3). This follows:

$$\frac{\partial \tau_x}{\partial x}+\frac{\partial \tau_y}{\partial y}-(\epsilon^2)\frac{\partial^2 w}{\partial^2 w}=0$$
$$\epsilon\frac{\partial^2 w}{\partial x^2}-\epsilon\frac{\partial \tau_x}{\partial x}-\tau_x=0$$
$$\epsilon\frac{\partial^2 w}{\partial x \partial y}-\epsilon\frac{\partial \tau_y}{\partial x}-\tau_y=0. \tag{8}$$

The boundary data associated with the above equations become

$$\tau_y(x, 0)=f(x); \quad x>0$$
$$w(x, 0)=0; \qquad x<0$$
$$\tau_x(x, 0)=0; \qquad x<0. \tag{7}$$

Elimination of the stress components in Eqs. (6) yields the differential equation governing the displacement field

$$\frac{\partial}{\partial x}\left[(1-\epsilon^2)\frac{\partial^2 w}{\partial x^2}+\frac{\partial^2 w}{\partial y^2}+\frac{\partial^2 w}{\partial y^2}-\epsilon\frac{\partial w}{\partial x}\right]=0. \tag{8}$$

We integrate the above equation with respect to x and make use of the limit condition (5) to arrive at

$$(1-\epsilon^2)\frac{\partial^2 w}{\partial x^2}+\frac{\partial^2 w}{\partial y^2}-\epsilon\frac{\partial w}{\partial x}=0. \tag{9}$$

The speed of crack propagation is assumed to be subsonic, i.e., $\epsilon < 1$.

We now introduce a new set of independent variables

$$X=x/(1-\epsilon^2)^{1/2}, \quad Y=y$$

and write Eq. (9) as

[10]Department of Mechanical Engineering and Mechanics, Lehigh University, Bethlehem, PA 18015. Assoc. Mem. ASME.

Contributed by the Applied Mechanics Division of THE AMERICAN SOCIETY OF MECHANICAL ENGINEERS for publication in the ASME JOURNAL OF APPLIED MECHANICS.

Manuscript received by the ASME Applied Mechanics Division, Sept. 4, 1987; final revision, Jan. 17, 1992. Associate Technical Editor: W. G. Knauss.

Copyright © 1993 by ASME
Downloaded 03 May 2010 to 171.66.16.245. Redistribution subject to ASME license or copyright; see http://www.asme.org/terms/Terms_Use.cfm

$$\frac{\partial^2 w}{\partial X^2}+\frac{\partial^2 w}{\partial Y^2}-\frac{\epsilon}{(1-\epsilon^2)^{1/2}}\frac{\partial w}{\partial X}=0. \tag{10}$$

Utilizing the transformation

$$\Phi(X, Y)=w(X, Y)\exp(-\lambda X) \tag{11}$$

where $\lambda = \epsilon/2(1-\epsilon^2)^{1/2}$, we obtain the Helmholtz equation

$$\frac{\partial^2 \Phi}{\partial X^2}+\frac{\partial^2 \Phi}{\partial Y^2}-\lambda^2\Phi=0. \tag{12}$$

Equation (12) in polar coordinates may be expressed as

$$\frac{\partial^2 \Phi}{\partial r^2}+\frac{1}{r}\frac{\partial \Phi}{\partial r}+\frac{1}{r^2}\frac{\partial^2 \Phi}{\partial \theta^2}-\lambda^2\Phi=0 \tag{13}$$

with $r^2 = X^2 + Y^2$. We now derive the boundary data for this equation. The second of the boundary data (7) and Eq. (11) imply that

$$\Phi(r, \pi)=0. \tag{14}$$

From the last of Eqs. (6), Eq. (11) and the first of boundary data (7) we have

$$\frac{1}{r}\frac{\partial \Phi(r, 0)}{\partial \theta}=\left[f(r)-\frac{1}{2\lambda}\int_r^\infty f(\xi)d\xi\right]\exp(-\lambda r). \tag{15}$$

The stress component $(\tau_x, \tau_y) = 0\,(r^{-1/2})$ as $r \to 0$, consequently $w(r, \theta) = 0(r^{1/2})$ as $r \to 0$. In the region near the crack tip, the first and the second terms of the last of Eqs. (6) must balance each other. From this observation we conclude that only the first term on the right-hand side of the boundary data (15), the term which corresponds to the derivative of τ_y, must yield the dominant term of displacement field.

The Helmholtz Eq. (13) in the half-plane may be solved by employing the Kontorowich-Levedev transformation, (Davies, 1978)

$$F(\nu, \theta)=\int_0^\infty \frac{1}{r}\Phi(r, \theta)K_\nu(\lambda r)dr \tag{16}$$

where $K_\nu(x)$ is the modified Bessel function of the second kind of order ν. The inversion formula for this transformation is

$$\Phi(r, \theta)=\frac{1}{\pi i}\int_{\gamma-i\infty}^{\gamma+i\infty}\nu F(\nu, \theta)I_\nu(\lambda r)d\nu \tag{17}$$

in which $I_\nu(x)$ is the modified Bessel function of the first kind of order ν. Application of transformation (16) on Eq. (13), in conjunction with integration by parts, gives

$$\frac{d^2F}{d\theta^2}+\nu^2F=0. \tag{18}$$

In the derivation of Eq. (18) we have required that $[\Phi(r, \theta)K_\nu(\lambda r)] \to 0$ as $r \to 0$. The solution of Eq. (18) is readily found to be

$$F(\nu, \theta)=A(\nu)\cos(\nu\theta)+B(\nu)\sin(\nu\theta). \tag{19}$$

From the boundary condition (14) and Eq. (16), we then obtain

$$F(\nu, \theta)=A(\nu)\frac{\sin(\nu(\pi-\theta))}{\sin(\nu\pi)}. \tag{20}$$

To make the mathematical analysis more tractable, we assume that the applied traction on the crack flanks is

$$f(r)=P\delta\left(\frac{r-a}{a}\right) \tag{21}$$

where $a = 2\mu C\bar{a}/C_1(1-\epsilon^2)^{1/2}$, $\bar{a}$ is the distance between the crack tip and point force, and $\delta(x)$ is the Dirac delta function. It is worth noting that the solution of this problem may be used as the Green's function for the case of general applied traction. The boundary data (15), in view of Eqs. (16) and (21), after integration by parts, become

$$\frac{dF(\nu, 0)}{d\theta}=aP\left\{K_\nu(\lambda a)\exp(-\lambda a)-\frac{a}{2\lambda}\int_0^1 K_\nu(\lambda a\xi)\exp(-\lambda a\xi)d\xi\right\}. \tag{22}$$

From the substitution of Eq. (20) into (22) we get

$$A(\nu)=-\frac{aP\sin(\nu\pi)}{\nu\cos(\nu\pi)}\left\{K_\nu(\lambda a)\exp(-\lambda a)-\frac{a}{2\lambda}\int_0^1 K_\nu(\lambda a\xi)\exp(-\lambda a\xi)d\xi\right\}. \tag{23}$$

Equation (17) by virtue of (20) and (23) yields

$$\Phi(r, \theta)=\frac{aP}{\pi i}\int_{\alpha-i\infty}^{\alpha+i\infty}K_\nu(\lambda a)\exp(-\lambda a)\frac{\sin(\nu(\theta-\pi))}{\cos(\nu\pi)}I_\nu(\lambda r)d\nu - \frac{a^2P}{2\lambda\pi i}\int_{\beta-i\infty}^{\beta+i\infty}\frac{\sin(\nu(\theta-\pi))}{\cos(\nu\pi)}I_\nu(\lambda r)\int_0^1 K_\nu(\lambda a\xi)\exp(-\lambda a\xi)d\xi d\nu. \tag{24}$$

The above integration must be carried out in two different regions, $r < a$ and $r > a$. As was mentioned before, the first term on the right-hand side of Eq. (24) ought to produce the leading solution near the crack tip. Therefore, we choose the Bromwich lines, $0 \le \alpha < 1/2$ and $1/2 < \beta < 3/2$ and complete the contours of integration by a semicircular arc in the right side of the real axis. Using the properties of the asymptotic behavior of the modified Bessel functions with larger orders (Abromowitz and Stegun, 1970), it may be verified that when the radius of this arc $|\nu| \to \infty$, $K_\nu(y)I_\nu(x) = o(\nu^{-1})$ provided that $x/y < 1$. Utilizing the standard formula

$$I_\nu(x)-I_{-\nu}(x)=\frac{2\sin(\nu\pi)}{\pi}K_\nu(x), \tag{25}$$

Eq. (24) in both regions $r < a$ and $r > a$ can be written such that the contribution to the integral along the semicircle tends to zero as the radius approaches infinity (Turner, 1956). The residues of the integrand at the singular points give

$$\Phi(r, \theta)= -\frac{2aP}{\pi}\sum_{n=0}^{\infty}\exp(-\lambda a)K_{n+1/2}(\lambda a)I_{n+1/2}(\lambda r)\cos[(n+1/2)\theta] + \frac{a^2P}{\lambda\pi}\sum_{n=1}^{\infty}\{I_{n+1/2}(\lambda r)\int_{r/a}^1 K_{n+1/2}(\lambda a\xi)\exp(-\lambda a\xi)d\xi + K_{n+1/2}(\lambda r)\int_0^{r/a} I_{n+1/2}(\lambda a\xi)\exp(-\lambda a\xi)d\xi\}\cos[(n+1/2)\theta]; \quad r<a \tag{26}$$

$$\Phi(r, \theta)= -\frac{2aP}{\pi}\exp(-\lambda a)\sum_{n=0}^{\infty}I_{n+1/2}(\lambda a)K_{n+1/2}(\lambda r)\cos[(n+1/2)\theta] + \frac{a^2P}{\lambda\pi}\sum_{n=1}^{\infty}K_{n+1/2}(\lambda r)\cos[(n+1/2)\theta] \times\int_0^1 I_{n+1/2}(\lambda a\xi)\exp(-\lambda a\xi)d\xi; \quad r>a. \tag{27}$$

From Eq. (11), the displacement field in the half-plane then becomes

$$w(r, \theta)=-\frac{2aP}{\pi}\exp[\lambda(r\cos\theta-a)] \times\sum_{n=0}^{\infty}K_{n+1/2}(\lambda a)I_{n+1/2}(\lambda r)\cos[(n+1/2)\theta]$$

Downloaded 03 May 2010 to 171.66.16.245. Redistribution subject to ASME license or copyright; see http://www.asme.org/terms/Terms_Use.cfm

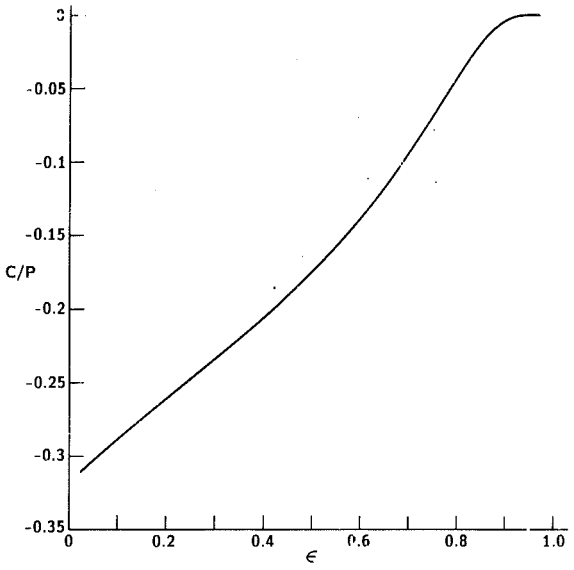


Fig. 2

$$+\frac{a^2P}{\lambda\pi}\exp(\lambda r\cos\theta)\sum_{n=1}^{\infty}\{I_{n+1/2}(\lambda r)\int_{r/a}^{1}K_{n+1/2}(\lambda a\xi)\exp(-\lambda a\xi)d\xi + K_{n+1/2}(\lambda r)\int_{0}^{r/a}I_{n+1/2}(\lambda a\xi)\exp(-\lambda a\xi)d\xi\}\cos[(n+1/2)\theta];\quad r<a \qquad (28)$$

$$w(r,\theta)=-\frac{2aP}{\pi}\exp[\lambda(r\cos\theta-a)]\times\sum_{n=0}^{\infty}I_{n+1/2}(\lambda a)K_{n+1/2}(\lambda/r)\cos[(n+1/2)\theta] +\frac{a^2P}{\lambda\pi}\exp(\lambda r\cos\theta)\sum_{n=1}^{\infty}K_{n+1/2}(\lambda r)\cos[(n+1/2)\theta]\times\int_{0}^{1}I_{n+/1/2}(\lambda a\xi)\exp(-\lambda a\xi)d\xi;\quad r>a. \qquad (29)$$

Equations (28) and (29) show that the continuity of displacement along semicircle $r = a$ is satisfied. Nevertheless, as might be expected, the series at the point of load singularity, $w(a, 0)$, is divergent. Furthermore, we may observe from Eq. (29) that the displacement decays exponentially in the far field except on the crack flanks were $w(r, 0) = 0(r^{-1/2})$ as $r \to \infty$.

The stress components are the solutions of the last two of Eqs. (6)

$$\tau_x=(1-\epsilon^2)^{-1/2}\exp(-X/2\lambda)\int_{-\infty}^{X}\exp(\xi/2\lambda)\frac{\partial^2 w(\xi,Y)}{\partial^2\xi}d\xi \qquad (30)$$

$$\tau_y=\exp(-X/2\lambda)\int_{-\infty}^{X}\exp(\xi/2\lambda)\frac{\partial^2 w(\xi,Y)}{\partial\xi\partial Y}d\xi. \qquad (31)$$

An application of integration by parts gives the leading term in the asymptotic expansion of stress fields in the region near the crack tip

$$\tau_x=[(1-\epsilon^2)^{-1/2}]\frac{\partial W(X,Y)}{\partial X} \qquad (32)$$

$$\tau_y=\frac{\partial W(X,Y)}{\partial y}. \qquad (33)$$

Substitution of the first term of the series solution (28) into the above expressions leads to

$$\tau_x=C(1-\epsilon^2)^{1/2}\exp(\lambda r\cos\theta)\cos(\theta/2)/r^{1/2} \qquad (34)$$

$$\tau_y=(C)\exp(\lambda r\cos\theta)\sin(\theta/2)/r^{1/2} \qquad (35)$$

where the stress intensity factor

$$C=-(aP/\pi)(2\lambda/\pi)^{1/2}K_{1/2}(\lambda a)\exp(-\lambda a).$$

Taking the limit of the above equation as $\epsilon \to 0$, we obtain the stress intensity factor corresponding to quasi-static crack propagation $C = -P\sqrt{a/\pi}$. The plot of C/P versus ϵ with $\tilde{a} = a(1-\epsilon^2)^{1/2} = 1$ where $\tilde{a} = a(1-\epsilon^2)^{1/2}$, is shown in Fig. 2.

Acknowledgment

The author is grateful to Prof. T. J. Delph of Lehigh University for his helpful suggestions.

References

Abromowitz, M., and Stegun, I. A., 1970, *Handbook of Mathematical Functions*, Dover, New York, pp. 377–378.

Atkinson, C., and List, R. D., 1972, "A Moving Crack in a Viscoelastic Solid," *Int. J. Engng. Sci.*, Vol. 10, pp. 309–322.

Davies, B., 1978, *Integral Transforms and Their Applications*, Springer-Verlag, New York, pp. 276–283.

Turner, R. D., 1956, "The Diffraction of a Cylindrical Pulse by a Half-Plane," *Quart. Appl. Math.*, Vol. 14, pp. 63–73.

Willis, J. R., 1967, "Crack Propagation in Viscoelastic Media," *J. Mech. Phys. Solids*, Vol. 15, pp. 229–240.

Shear Flow Over a Periodically Heated Plate

C. Y. Wang[11]

Introduction and Formulation

In forced convection, the boundary is often assumed to have uniform temperature or uniform flux. In practice, however, the boundary temperature may be spatially periodic due to uneven heating by spaced heating elements. This Note investigates the effect on temperature distribution due to such unevenness.

Let $y = 0$ be the solid boundary which is heated to a temperature $T = T_0 + T_1 \cos \lambda x$. Let $U(y)$ be the parallel flow across the surface. The energy equation is

$$U(y)T_x=a(T_{xx}+T_{yy}) \qquad (1)$$

where (x, y) are Cartesian coordinates and a is the diffusivity. Since Eq. (1) is linear, one can separate the effect of the periodic temperature from the mean temperature T_0. Also, we assume the flow is a linear shear flow $U = Ay$ where A is constant. This velocity profile is exact for Couette flow and is a good approximation for any viscous flow near a solid boundary. Our problem becomes

$$AyT_x=a(T_{xx}+T_{yy}) \qquad (2)$$

$$T|_{y=0}=T_1\cos\lambda x,\quad T|_{y=\infty}=0. \qquad (3)$$

[11]Department of Mathematics, Michigan State University, East Lansing, MI 48824-1027. Mem. ASME.

Contributed by the Applied Mechanics Division of THE AMERICAN SOCIETY OF MECHANICAL ENGINEERS for publication in the ASME JOURNAL OF APPLIED MECHANICS.

Manuscript received by the ASME Applied Mechanics Division, Dec. 18, 1990; final revision, Feb. 10, 1992. Associate Technical Editor: K. R. Sreenivasan.

Downloaded 03 May 2010 to 171.66.16.245. Redistribution subject to ASME license or copyright; see http://www.asme.org/terms/Terms_Use.cfm

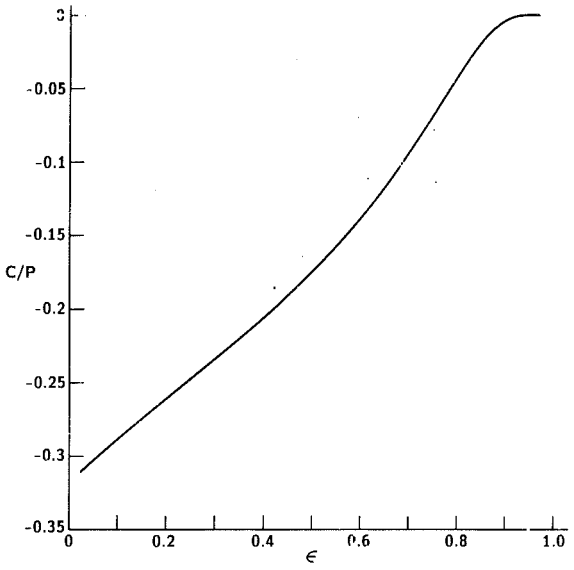


Fig. 2

$$+\frac{a^2P}{\lambda\pi}\exp(\lambda r\cos\theta)\sum_{n=1}^{\infty}\{I_{n+1/2}(\lambda r)\int_{r/a}^{1}K_{n+1/2}(\lambda a\xi)\exp(-\lambda a\xi)d\xi + K_{n+1/2}(\lambda r)\int_{0}^{r/a}I_{n+1/2}(\lambda a\xi)\exp(-\lambda a\xi)d\xi\}\cos[(n+1/2)\theta]; \quad r<a \qquad (28)$$

$$w(r,\theta)=-\frac{2aP}{\pi}\exp[\lambda(r\cos\theta-a)]\times\sum_{n=0}^{\infty}I_{n+1/2}(\lambda a)K_{n+1/2}(\lambda/r)\cos[(n+1/2)\theta] +\frac{a^2P}{\lambda\pi}\exp(\lambda r\cos\theta)\sum_{n=1}^{\infty}K_{n+1/2}(\lambda r)\cos[(n+1/2)\theta]\times\int_{0}^{1}I_{n+/1/2}(\lambda a\xi)\exp(-\lambda a\xi)d\xi; \quad r>a. \qquad (29)$$

Equations (28) and (29) show that the continuity of displacement along semicircle $r = a$ is satisfied. Nevertheless, as might be expected, the series at the point of load singularity, $w(a, 0)$, is divergent. Furthermore, we may observe from Eq. (29) that the displacement decays exponentially in the far field except on the crack flanks were $w(r, 0) = 0(r^{-1/2})$ as $r \to \infty$.

The stress components are the solutions of the last two of Eqs. (6)

$$\tau_x=(1-\epsilon^2)^{-1/2}\exp(-X/2\lambda)\int_{-\infty}^{X}\exp(\xi/2\lambda)\frac{\partial^2 w(\xi, Y)}{\partial^2\xi}d\xi \qquad (30)$$

$$\tau_y=\exp(-X/2\lambda)\int_{-\infty}^{X}\exp(\xi/2\lambda)\frac{\partial^2 w(\xi, Y)}{\partial\xi\partial Y}d\xi. \qquad (31)$$

An application of integration by parts gives the leading term in the asymptotic expansion of stress fields in the region near the crack tip

$$\tau_x=[(1-\epsilon^2)^{-1/2}]\frac{\partial W(X, Y)}{\partial X} \qquad (32)$$

$$\tau_y=\frac{\partial W(X, Y)}{\partial y}. \qquad (33)$$

Substitution of the first term of the series solution (28) into the above expressions leads to

$$\tau_x=C(1-\epsilon^2)^{1/2}\exp(\lambda r\cos\theta)\cos(\theta/2)/r^{1/2} \qquad (34)$$

$$\tau_y=(C)\exp(\lambda r\cos\theta)\sin(\theta/2)/r^{1/2} \qquad (35)$$

where the stress intensity factor

$$C=-(aP/\pi)(2\lambda/\pi)^{1/2}K_{1/2}(\lambda a)\exp(-\lambda a).$$

Taking the limit of the above equation as $\epsilon \to 0$, we obtain the stress intensity factor corresponding to quasi-static crack propagation $C = -P\sqrt{a/\pi}$. The plot of C/P versus ϵ with $\tilde{a} = a(1-\epsilon^2)^{1/2} = 1$ where $\tilde{a} = a(1-\epsilon^2)^{1/2}$, is shown in Fig. 2.

Acknowledgment

The author is grateful to Prof. T. J. Delph of Lehigh University for his helpful suggestions.

References

Abromowitz, M., and Stegun, I. A., 1970, *Handbook of Mathematical Functions*, Dover, New York, pp. 377–378.

Atkinson, C., and List, R. D., 1972, "A Moving Crack in a Viscoelastic Solid," *Int. J. Engng. Sci.*, Vol. 10, pp. 309–322.

Davies, B., 1978, *Integral Transforms and Their Applications*, Springer-Verlag, New York, pp. 276–283.

Turner, R. D., 1956, "The Diffraction of a Cylindrical Pulse by a Half-Plane," *Quart. Appl. Math.*, Vol. 14, pp. 63–73.

Willis, J. R., 1967, "Crack Propagation in Viscoelastic Media," *J. Mech. Phys. Solids*, Vol. 15, pp. 229–240.

Shear Flow Over a Periodically Heated Plate

C. Y. Wang[11]

Introduction and Formulation

In forced convection, the boundary is often assumed to have uniform temperature or uniform flux. In practice, however, the boundary temperature may be spatially periodic due to uneven heating by spaced heating elements. This Note investigates the effect on temperature distribution due to such unevenness.

Let $y = 0$ be the solid boundary which is heated to a temperature $T = T_0 + T_1 \cos \lambda x$. Let $U(y)$ be the parallel flow across the surface. The energy equation is

$$U(y)T_x=a(T_{xx}+T_{yy}) \qquad (1)$$

where (x, y) are Cartesian coordinates and a is the diffusivity. Since Eq. (1) is linear, one can separate the effect of the periodic temperature from the mean temperature T_0. Also, we assume the flow is a linear shear flow $U = Ay$ where A is constant. This velocity profile is exact for Couette flow and is a good approximation for any viscous flow near a solid boundary. Our problem becomes

$$AyT_x=a(T_{xx}+T_{yy}) \qquad (2)$$

$$T|_{y=0}=T_1\cos\lambda x, \quad T|_{y=\infty}=0. \qquad (3)$$

[11]Department of Mathematics, Michigan State University, East Lansing, MI 48824-1027. Mem. ASME.

Contributed by the Applied Mechanics Division of THE AMERICAN SOCIETY OF MECHANICAL ENGINEERS for publication in the ASME JOURNAL OF APPLIED MECHANICS.

Manuscript received by the ASME Applied Mechanics Division, Dec. 18, 1990; final revision, Feb. 10, 1992. Associate Technical Editor: K. R. Sreenivasan.

Copyright © 1993 by ASME
Downloaded 03 May 2010 to 171.66.16.245. Redistribution subject to ASME license or copyright; see http://www.asme.org/terms/Terms_Use.cfm

Normalize as follows:

$$\eta \equiv \lambda y, \quad \xi \equiv \lambda x, \quad \tau(\xi, \eta) \equiv T/T_1. \tag{4}$$

Equations (2), (3) become the complex ordinary differential equation

$$f''(\eta) - (1 + \alpha\eta i) f = 0 \tag{5}$$

$$f(0) = 1, \quad f(\infty) = 0 \tag{6}$$

where

$$\tau = \mathrm{Re}\, e^{i\xi} f(\eta) \tag{7}$$

and $\alpha \equiv A/(\lambda^2 a)$ is an important nondimensional parameter signifying the relative importance of shear flow to diffusion.

The Exact Solution

Let

$$\zeta \equiv (\alpha i)^{1/3}\eta + (\alpha i)^{-2/3}, \quad f(\eta) = F(\zeta) \tag{8}$$

Equation (5) becomes the Airy equation

$$F''(\zeta) - \zeta F = 0 \tag{9}$$

$$F((\alpha i)^{-2/3}) = 1, \quad F(\infty) = 0. \tag{10}$$

The solution is

$$F = \frac{A_i(\zeta)}{A_i((\alpha i)^{-2/3})} \tag{11}$$

where A_i, B_i are the Airy functions. Due to the complex argument ζ, this form of the solution is very difficult to evaluate, even numerically. The gradient at the boundary is

$$f'(0) = (\alpha i)^{1/3} F'((\alpha i)^{-2/3}) = (\alpha i)^{1/3} \frac{A_i'((\alpha i)^{-2/3})}{A_i((\alpha i)^{-2/3})}. \tag{12}$$

Using the identity (Abramowitz and Stegun, 1965)

$$A_i(ze^{2\pi i/3}) = \frac{1}{2} e^{\pi i/3}[A_i(z) - iB_i(z)] \tag{13}$$

we find

$$A_i(ze^{-\pi i/3}) = \frac{1}{2} e^{\pi i/3}[A_i(-z) - iB_i(-z)]. \tag{14}$$

The derivative is

$$A_i'(ze^{-\pi i/3}) = \frac{1}{2} e^{-\pi i/3}[A_i'(-z) - iB_i'(-z)]. \tag{15}$$

Now set $z = \alpha^{-2/3} \equiv \beta$, and Eq. (12) becomes

$$\begin{aligned} f'(0) &= -i\alpha^{1/3} \frac{A_i'(-\beta) - iB_i'(-\beta)}{A_i(-\beta) - iB_i(-\beta)} \\ &= -\alpha^{1/3}[A_i^2(-\beta) + B_i^2(-\beta)]^{-1} \\ &\quad \left\{\frac{1}{\pi} + [A_i(-\beta)A_i'(-\beta) + B_i(-\beta)B_i'(-\beta)]i\right\} \end{aligned} \tag{16}$$

where we have used a simplifying Wronskian identity. The arguments of the Airy functions are now real. Set

$$f'(0) \equiv b(\alpha) + c(\alpha)i. \tag{17}$$

Using tables of Airy functions, the real and imaginary parts of $f'(0)$ can be evaluated. In particular, $b(0) = -1$ and $c(0) = 0$, b, c, $\sim \alpha^{1/3}$ as $\alpha \to \infty$.

The local heat transfer per area is

$$\begin{aligned} q &= -k \left.\frac{\partial T}{\partial y}\right|_0 = -kT_1\lambda \mathrm{Re}[e^{i\xi} f'(0)] \\ &= -kT_1\lambda\sqrt{b^2 + c^2}\cos\left(\xi + \tan^{-1}\frac{c}{b}\right) \end{aligned} \tag{18}$$

where k is the thermal conductivity. The normalized amplitude $\sqrt{b^2 + c^2}$ and the phase shift $-\tan^{-1}(c/b)$ are plotted in Fig. 1. We see that local heat transfer increases with convection rate nonlinearly. Also, the location of the maximum heat transfer coincide with that of the maximum temperature when $\alpha = 0$, but is shifted upstream when $\alpha \neq 0$.

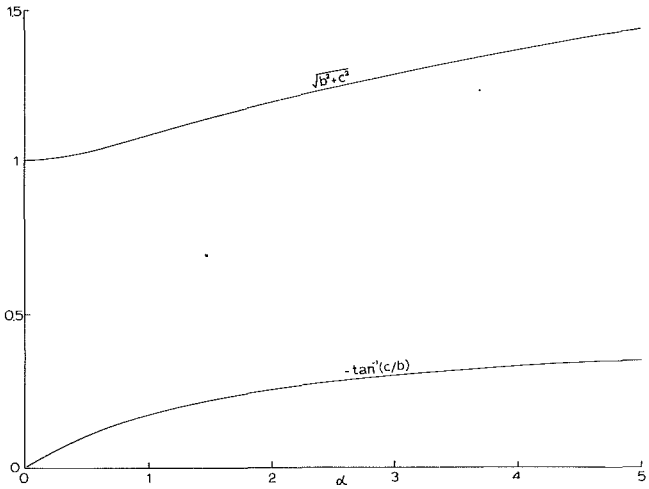


Fig. 1 Amplitude and phase of local heat transfer

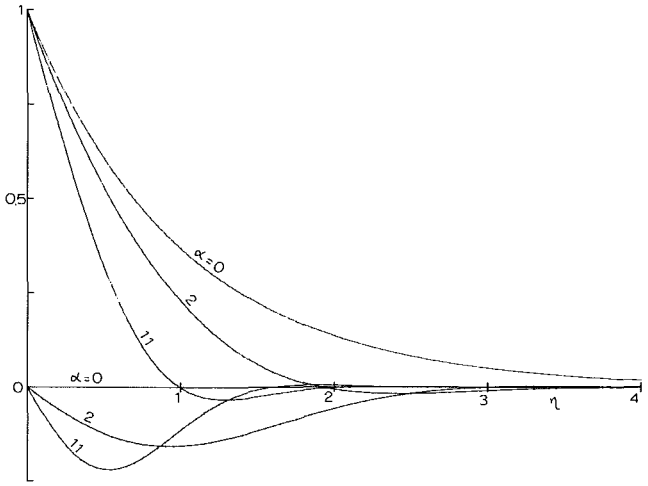


Fig. 2 The real and imaginary parts of $f(\eta)$. Top $g(\eta)$, bottom $h(\eta)$.

Temperature Distribution

Since the exact solution involving $A_i((\alpha i)^{1/3}\eta + (\alpha i)^{-2/3})$ is inconvenient to evaluate, perhaps it is better to solve the problem by the following method. Let

$$f(\eta) = g(\eta) + ih(\eta) \tag{19}$$

where g and h are real functions. Equations (5), (6) become

$$g'' = g - \alpha\eta h \tag{20}$$

$$h'' = h + \alpha\eta g \tag{21}$$

$$g(0) = 1, \quad h(0) = 0 \tag{22}$$

$$g(\infty) = h(\infty) = 0. \tag{23}$$

This two-point boundary value problem is as difficult as before. However, from Eqs. (16), (17) we find the initial values can be exactly evaluated.

$$g'(0) = b(\alpha), \quad h'(0) = c(\alpha) \tag{24}$$

Thus it is easy to integrate Eqs. (20)–(24) numerically as an initial value problem. We used the Runge-Kutta-Fehlberg algorithm with $\Delta\eta = 0.1$, obtaining at least five digit accuracy. The results are shown in Fig. 2 for some α values. For $\alpha = 0$,

Downloaded 03 May 2010 to 171.66.16.245. Redistribution subject to ASME license or copyright; see http://www.asme.org/terms/Terms_Use.cfm

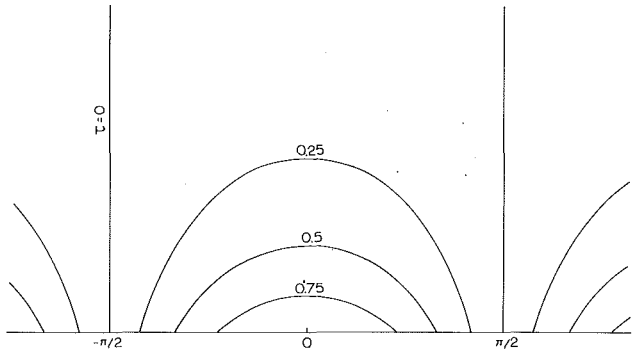


Fig. 3 Isotherms for $\alpha = 0$

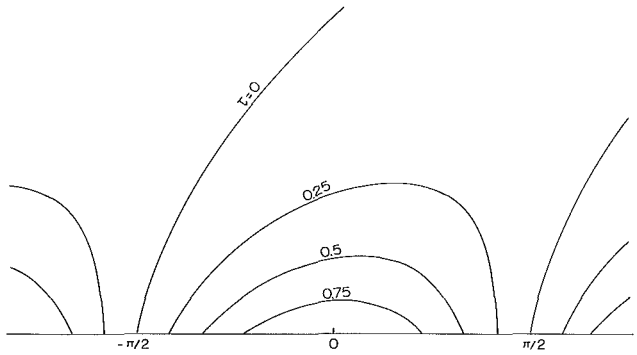


Fig. 4 Isotherms for $\alpha = 1$

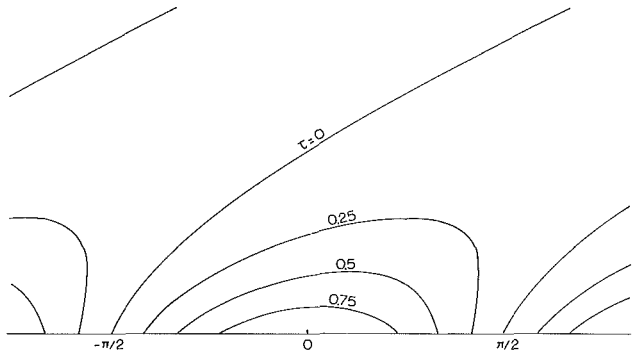


Fig. 5 Isotherms for $\alpha = 5$

the exact solution is $g = \exp(-\eta)$, $h = 0$. As shear or α is increased, both g and h functions show oscillatory decay. The thermal boundary layer thickness is also decreased.

The normalized temperature is given by Eq. (7),

$$\tau = g(\eta)\cos\xi - h(\eta)\sin\xi. \tag{25}$$

Figure 3 shows the isotherms for $\alpha = 0$ when convection is absent. The temperature is symmetric about $\xi = 0$ and is 2π periodic. Figure 4 shows the effect of shear flow ($\alpha = 1$) which is from left to right. The isotherms are swept downstream thus destroying the symmetry. For higher α (Fig. 5), the isotherms become more skewed. In this case the location of highest local heat transfer shifted left to $\xi = -0.33$.

Discussion

Superposed periodicity in boundary temperature is sometimes unavoidable. Although such periodicity does not affect total heat transfer, local thermal characteristics are altered. The isotherms become periodic and skewed. The locations of maximum heat transfer shift upstream. These influences could become important when detailed local measurements are required.

Since Eq. (18) shows a periodic local heat transfer, our results apply as well to the case of the given periodic boundary flux. The maximum temperature is then shifted downstream with similar isotherm characteristics.

References

Abramowitz, M., and Stegun, I. A., eds., 1965, *Handbook of Mathematical Functions*, Dover, New York.

Initiation of an Interface Crack Under Mixed-Mode Loading

P. A. Foltyn[12] and K. Ravi-Chandar[12,13]

The compact tension shear specimen is proposed as a simple experimental configuration suitable for the determination of the variation of the interfacial fracture toughness as a function of the loading mixity. The suitability of this specimen is demonstrated on a model system of diffusion bonded PMMA.

1 Introduction

The applicability of LEFM concepts to interface fracture phenomena and the importance of interfaces in composites and multilayered structures, such as microelectronic devices, have generated enormous interest in theoretical and experimental analysis of interface cracks. While a number of early experiments in the area of adhesively bonded joints used LEFM concepts from monolithic materials, the recent availability of analyses for bi-material crack problems has led to new interpretation of experimental observations. A detailed survey of many aspects of cracking in interfaces under mixed-mode loading can be found in the review article by Hutchinson and Suo (1991). Identifying the mixity of the loading (between the crack opening and sliding modes) as the key parameter in determining the details of the fracture process, experimental configurations have been designed to determine the "interfacial fracture toughness" as a function of the mixity (Charalambides et al., 1989); these admit a limited range of mode mix. The bi-axial loading device and strip specimen used by Liechti and Chai (1991) permits fine control of the mode mix over the complete range of interest. A simple configuration—called the compact tension shear (CTS) specimen—that has been used in mixed-mode experiments on monolithic materials (Buchholz (1987) and Mahajan and Ravi-Chandar (1989)) is suggested here to investigate the interface fracture toughness; this configuration enables the variation of the mode mixity over the complete range of interest in coarse increments but inexpensively. The use of this configuration to examine interfacial toughness is demonstrated by applying the method to a diffusion bond in a PMMA specimen.

[12]Department of Mechanical Engineering, University of Houston, Houston, TX 77204-4792.

[13]Assoc. Mem. ASME.

Contributed by the Applied Mechanics Division of THE AMERICAN SOCIETY OF MECHANICAL ENGINEERS for publication in the ASME JOURNAL OF APPLIED MECHANICS.

Manuscript received by the ASME Applied Mechanics Division, Mar. 1, 1991; final revision, Jan. 6, 1992. Associate Technical Editor: R. L. Huston.

Downloaded 03 May 2010 to 171.66.16.245. Redistribution subject to ASME license or copyright; see http://www.asme.org/terms/Terms_Use.cfm

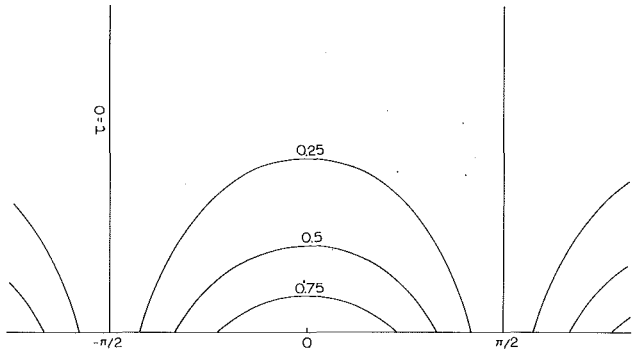


Fig. 3 Isotherms for $\alpha = 0$

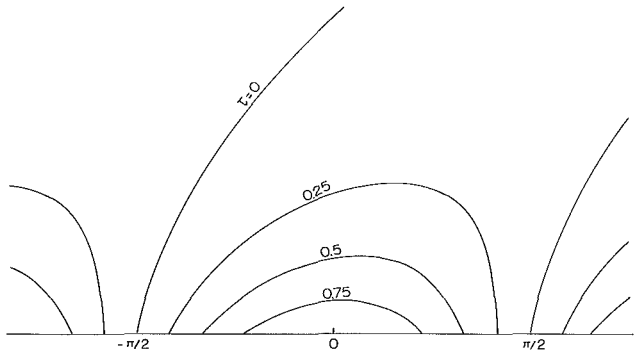


Fig. 4 Isotherms for $\alpha = 1$

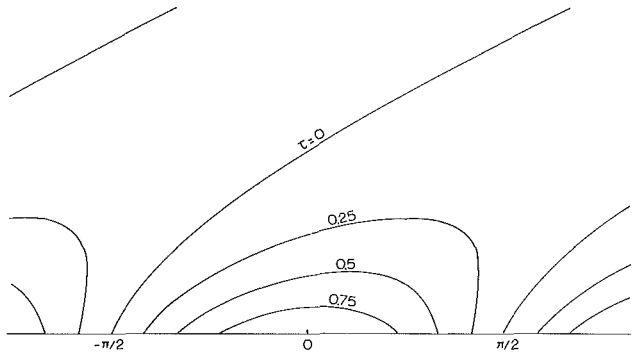


Fig. 5 Isotherms for $\alpha = 5$

the exact solution is $g = \exp(-\eta)$, $h = 0$. As shear or α is increased, both g and h functions show oscillatory decay. The thermal boundary layer thickness is also decreased.

The normalized temperature is given by Eq. (7),

$$\tau = g(\eta)\cos\xi - h(\eta)\sin\xi. \tag{25}$$

Figure 3 shows the isotherms for $\alpha = 0$ when convection is absent. The temperature is symmetric about $\xi = 0$ and is 2π periodic. Figure 4 shows the effect of shear flow ($\alpha = 1$) which is from left to right. The isotherms are swept downstream thus destroying the symmetry. For higher α (Fig. 5), the isotherms become more skewed. In this case the location of highest local heat transfer shifted left to $\xi = -0.33$.

Discussion

Superposed periodicity in boundary temperature is sometimes unavoidable. Although such periodicity does not affect total heat transfer, local thermal characteristics are altered. The isotherms become periodic and skewed. The locations of maximum heat transfer shift upstream. These influences could become important when detailed local measurements are required.

Since Eq. (18) shows a periodic local heat transfer, our results apply as well to the case of the given periodic boundary flux. The maximum temperature is then shifted downstream with similar isotherm characteristics.

References

Abramowitz, M., and Stegun, I. A., eds., 1965, *Handbook of Mathematical Functions*, Dover, New York.

Initiation of an Interface Crack Under Mixed-Mode Loading

P. A. Foltyn[12] and K. Ravi-Chandar[12,13]

The compact tension shear specimen is proposed as a simple experimental configuration suitable for the determination of the variation of the interfacial fracture toughness as a function of the loading mixity. The suitability of this specimen is demonstrated on a model system of diffusion bonded PMMA.

1 Introduction

The applicability of LEFM concepts to interface fracture phenomena and the importance of interfaces in composites and multilayered structures, such as microelectronic devices, have generated enormous interest in theoretical and experimental analysis of interface cracks. While a number of early experiments in the area of adhesively bonded joints used LEFM concepts from monolithic materials, the recent availability of analyses for bi-material crack problems has led to new interpretation of experimental observations. A detailed survey of many aspects of cracking in interfaces under mixed-mode loading can be found in the review article by Hutchinson and Suo (1991). Identifying the mixity of the loading (between the crack opening and sliding modes) as the key parameter in determining the details of the fracture process, experimental configurations have been designed to determine the "interfacial fracture toughness" as a function of the mixity (Charalambides et al., 1989); these admit a limited range of mode mix. The bi-axial loading device and strip specimen used by Liechti and Chai (1991) permits fine control of the mode mix over the complete range of interest. A simple configuration—called the compact tension shear (CTS) specimen—that has been used in mixed-mode experiments on monolithic materials (Buchholz (1987) and Mahajan and Ravi-Chandar (1989)) is suggested here to investigate the interface fracture toughness; this configuration enables the variation of the mode mixity over the complete range of interest in coarse increments but inexpensively. The use of this configuration to examine interfacial toughness is demonstrated by applying the method to a diffusion bond in a PMMA specimen.

[12]Department of Mechanical Engineering, University of Houston, Houston, TX 77204-4792.

[13]Assoc. Mem. ASME.

Contributed by the Applied Mechanics Division of THE AMERICAN SOCIETY OF MECHANICAL ENGINEERS for publication in the ASME JOURNAL OF APPLIED MECHANICS.

Manuscript received by the ASME Applied Mechanics Division, Mar. 1, 1991; final revision, Jan. 6, 1992. Associate Technical Editor: R. L. Huston.

Copyright © 1993 by ASME
Downloaded 03 May 2010 to 171.66.16.245. Redistribution subject to ASME license or copyright; see http://www.asme.org/terms/Terms_Use.cfm

Under the mixed-mode loading, the interface crack may not always extend along the interface; thus the interface fracture toughness can be determined only for those mode mixities for which crack extension is along the interface. He and Hutchinson (1989) provide a detailed analysis of the kinking of a crack from an interface and their results are summarized below. Considering a crack in an interface under arbitrary mixed-mode loading, they computed the energy release rate, G_0, for crack propagation along the interface and the energy release rate, $G_M(\omega)$, for crack propagation out of the interface at the arbitrary angle ω. Kinking was presumed to occur at an angle $\hat{\omega}$ when $G_M(\hat{\omega}) > G_0$ and $G_M(\hat{\omega}) \geq G_{MC}$, where G_{MC} is the energy release rate required for cohesive fracture of the monolithic material. From this analysis, they determined whether kinking would occur, and if so, at what angle. A major conclusion was reached indicating that an interface crack will be trapped along the interface, regardless of the mode mixity, $\gamma = \arctan(K_2/K_1)$, if the energy for cohesive fracture in the matrix, G_{MC}, is at least 2.5 times the energy for interface fracture, G_{0C} (for $\alpha = 0.75$ (α is the first Dundurs' parameter); they also provide a plot of the variation of this ratio with α). This result is based on the assumption that the energy for interface crack growth, G_{0C}, is independent of γ. Variation of G_{0C} with γ as well as the variation of β (the second Dundurs' parameter) will affect the conclusions, but only quantitatively,—i.e., the ratio G_{MC}/G_{0C} above which the crack is trapped will be smaller or higher; qualitatively the behavior described above would be expected. In general, the energy required for crack extension along the interface G_{0C} will depend on γ; Evans and Hutchinson (1989) have provided a surface roughness induced shielding model for the dependence of G_{0C} on γ. Using the CTS specimen, the variation of G_{0C} with γ is examined for a diffusion bond in PMMA.

2 Specimen Design for Interface Fracture

In the present investigation, two PMMA plates were diffusion bonded to create the interface specimens. The two plate surfaces were wetted with acetone and pressed firmly together until full contact was achieved along the length of the two surfaces. This pressure was maintained for ten minutes using a clamping device. The bonded specimens were then subjected to an annealing process at a temperature of 96°C. It was found that if two machine-cut polished surfaces were wetted with acetone and pressed together, crazing would develop on the two contacted surfaces. This could be due to residual stresses introduced on the specimen through the machining process. However, when two fractured pieces were subsequently wetted with acetone and pressed together, the two surfaces did not craze, but rather, a bond was created which was optically transparent to the eye.

The CTS specimen first introduced by Buchholz et al. (1987) has been successfully used in mixed-mode fracture study by Mahajan and Ravi-Chandar (1989). Figure 1 shows a sketch of the configuration of the CTS specimen. These grips can vary the loading angle from 0 deg (Mode-I) to 90 deg (Mode-II) in 15 deg increments. Buchholz et al. (1987) performed a finite element analysis of the CTS specimen to determine the variation of K_I and K_{II} with the angle of loading. In their analysis, the crack length was one half of the specimen width. For our specimens where the crack length was only 0.2 of the specimen width we had to obtain a calibration of the variation of K_I and K_{II} with the loading angle. The calibration was performed by loading the specimen at various loading angles and determining the values of K_I and K_{II} using the method of caustics. When analyzing the caustic measurements, the K-field caustic analysis for monolithic materials was used which is justified since in this study, the interface was between two similar materials bonded through a diffusion process. The calibration results are plotted in Fig. 2. This plot allows us to

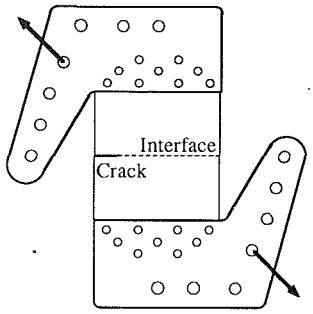


Fig. 1 Compact tension shear specimen

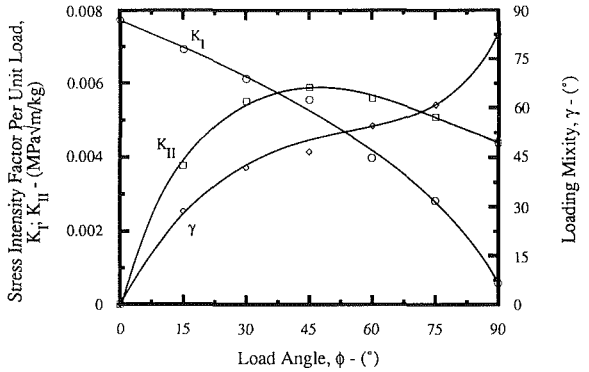


Fig. 2 Variation of the stress intensity factor and loading mixity with the loading angle

determine K_I, K_{II} and γ for each loading angle. Thus, in the experiments the peak load corresponding to a loading angle is determined and then K_I, K_{II} and γ at crack growth initiation are obtained from the calibration curve. Note, however, that if routine fracture toughness tests are to be performed, the variation of the stress intensity factors with crack length and loading angle can be computed and cataloged and only the peak load at failure needs to be measured in the experiments; the method of caustics was used in the present investigation because it was easier than a finite element analysis.

3 Interfacial Crack Initiation Under Mixed-Mode Loading

The CTS specimens with the diffusion bonded interface were loaded in an Instron testing machine to failure at different loading angles, while monitoring the peak load. It was found that the crack growth beyond initiation was dynamic; a high-speed camera was used to follow the dynamic crack and these results will be reported elsewhere. For loading angles (not mixities) less than 30 deg, the crack was trapped in the interface; for loading angles >60 deg, a kinked crack was initiated. For the loading angle of 45 deg, the crack initially ran along the interface for about 6 mm and then kinked out. From the peak loads and the calibration curve, the critical stress intensity factors at initiation were determined. The onset of interface crack initiation under mixed-mode loading could be displayed in terms of a K_I-K_{II} interaction curve as shown in Fig. 3. Note that the points (○) represents crack growth along the interface while (⊙) represent kinked cracking. The corresponding interaction curve for the monolithic material (PMMA), which coincides well with the maximum tangential stress criterion, is also shown in this figure. It can be seen that the toughness of the interface crack increases sharply as the loading mixity, γ, approaches $\approx$ 50 deg. For larger γ, crack growth along the interface is not favored; the crack kinks out of the interface; the kink/trap boundary is roughly at $\gamma \approx 50$ deg. To show

Downloaded 03 May 2010 to 171.66.16.245. Redistribution subject to ASME license or copyright; see http://www.asme.org/terms/Terms_Use.cfm

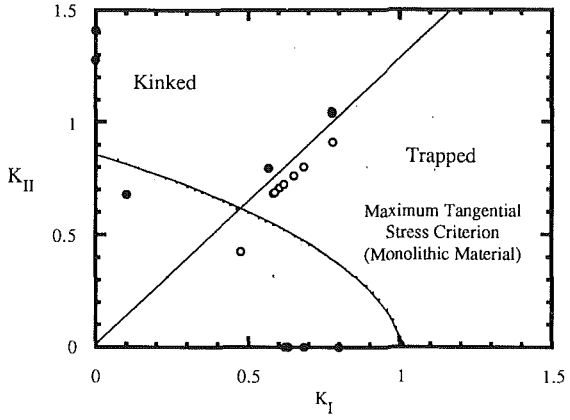


Fig. 3 K_I -K_{II} interaction curve

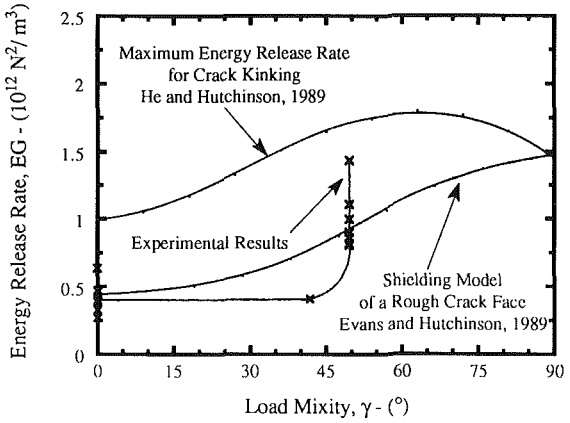


Fig. 4 Energy release rate as a function of loading mixity

clearly the dependence of interface strength on γ, the same data could also be represented as the variation of the energy release ($EG = [K_I^2 + K_{II}^2]$ for propagation along the interface) required to extend an interface crack as a function of the loading mixity, γ, as shown in Fig. 4. Thus, the CTS configuration is seen to be suitable for the evaluation of the interfacial fracture toughness and its variation with γ.

The maximum energy release rate (for a kinked crack) for a given γ, based on the results of He and Hutchinson (1989), is also plotted in Fig. 4. From this figure, it is evident that the energy required to sustain crack growth along the interface increases sharply with γ, to such an extent that energetically, kinking is favored for γ greater than some critical value. When the loading mixity reaches this critical value ($\approx$ 50 deg), the energy release required for interface crack propagation approaches the maximum energy release available from a kinked crack, thus facilitating kinked crack growth as observed in the experiments for $\gamma > 50$ deg. Evans and Hutchinson (1989), proposed a model for the dependence of G_{0C} on γ using a surface roughness model. Neglecting friction, they arrived at a model where the governing parameter in increasing the toughness is $\alpha_0 \approx 0.1\ (EH/G_0)/(1 - \nu^2)$, where E is the modulus of elasticity and H is the height of the surface roughness. Assuming $H = 0.1\ \mu$m, α_0 can be calculated as 0.4. Evaluating the amount of roughness induced toughening, (using Eq. (40) from Evans and Hutchinson), the predicted toughening is shown in Fig. 4 along with the experimentally measured values of EG. It is possible to investigate experimentally the effect of the variation in toughening with α_0 by changing the interface toughness at zero mixity G_0 (by altering the healing) and this is under investigation. The disagreement between the roughness induced shielding model and the experiments indicates that perhaps some other mechanism, such as near-tip plasticity, might play a role in determining the interface fracture energy.

4 Conclusion

The CTS specimen was investigated and shown to be a possible configuration for the evaluation of the variation of the interface fracture toughness with the mixity γ. For our investigation, a diffusion bond was created to form the interface in a PMMA specimen. Under mixed-mode conditions, it was determined that the interface fracture energy increases significantly with the loading mixity, γ. In all cases, whether the crack propagated along the interface or kinked from it, crack growth was dynamic, even under quasi-static loading. In the experimental study of interface crack extension, a dynamic analysis, such as through high-speed photography, becomes necessary.

References

Buchholz, F. G., Pirro, P. J. M., Richard H. A., and Dreyer, K. H., 1987, *Proceedings, Fourth International Conference on Numerical Methods in Fracture Mechanics*, A. R. Luxmore et al., eds., Pineridge Press, Swansea, UK.

Charalambides, P. G., Lund, J., Evans, A. G., and McMeeking, R. M., 1989, "A Test Specimen for Determining the Fracture Resistance of Bimaterial Interfaces," ASME JOURNAL OF APPLIED MECHANICS, Vol. 56, pp. 77–82.

Evans, A. G., and Hutchinson, J. W., 1989, "Effects of Non-Planarity on the Mixed-Mode Fracture Resistance of Bimaterial Interfaces," *Acta Metallurgica*, Vol. 37, pp. 909–916.

He, M-Y., and Hutchinson, J. W., 1989, "Kinking of a Crack Out of an Interface," ASME JOURNAL OF APPLIED MECHANICS, Vol. 56, pp. 270–278.

Hutchinson, J. W., and Suo, Z., 1991, "Mixed-Mode Cracking in Layered Materials," *Advances in Applied Mechanics*, Vol. 28, Academic Press, New York.

Liechti, K. M., and Chai, Y-S., 1991, "Biaxial Loading Experiments for Determining Interfacial Fracture Toughness," ASME JOURNAL OF APPLIED MECHANICS, in press.

Mahajan, R. V., and Ravi-Chandar, K., 1989, "An Experimental Investigation of Mixed-Mode Fracture," *International Journal of Fracture*, Vol. 41, pp. 235–252.

Boundary Layer Phenomena in Large Deflection, Small Strain Plate Theory

L. J. Berg[14]

Boundary layers exist at the edges of thin plates undergoing large deformations because the interior of the plate must assume a developable shape. The developable shape is sometimes incompatible with the force and moment resultants prescribed at the plate's boundary, in particular when the edge of the plate is stress free. A boundary layer solution is presented which describes the shape of a boundary layer in a plate undergoing large deflections. The boundary layer is a slight perturbation of the interior shape which allows the appropriate boundary conditions to be satisfied. Since developable shells are applicable to a plane, the boundary layer is also appropriate for arbitrary developable shells.

[14]ADSTAR, IBM Corporation, Rochester, MN 55901-7829.

Contributed by the Applied Mechanics Division of THE AMERICAN SOCIETY OF MECHANICAL ENGINEERS for publication in the ASME JOURNAL OF APPLIED MECHANICS.

Manuscript received by the ASME Applied Mechanics Division, Mar. 14, 1991; final revision, Dec. 30, 1991. Associate Technical Editor: J. G. Simonds.

Downloaded 03 May 2010 to 171.66.16.245. Redistribution subject to ASME license or copyright; see http://www.asme.org/terms/Terms_Use.cfm

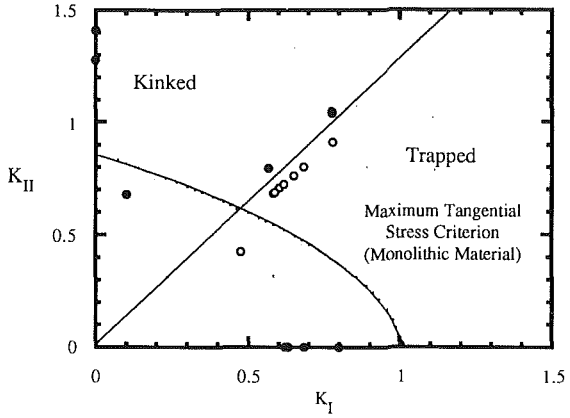


Fig. 3 K_I -K_{II} interaction curve

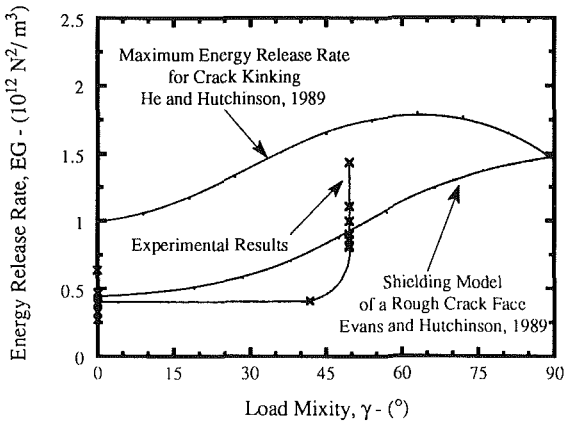


Fig. 4 Energy release rate as a function of loading mixity

clearly the dependence of interface strength on γ, the same data could also be represented as the variation of the energy release ($EG = [K_I^2 + K_{II}^2]$ for propagation along the interface) required to extend an interface crack as a function of the loading mixity, γ, as shown in Fig. 4. Thus, the CTS configuration is seen to be suitable for the evaluation of the interfacial fracture toughness and its variation with γ.

The maximum energy release rate (for a kinked crack) for a given γ, based on the results of He and Hutchinson (1989), is also plotted in Fig. 4. From this figure, it is evident that the energy required to sustain crack growth along the interface increases sharply with γ, to such an extent that energetically, kinking is favored for γ greater than some critical value. When the loading mixity reaches this critical value ($\approx$ 50 deg), the energy release required for interface crack propagation approaches the maximum energy release available from a kinked crack, thus facilitating kinked crack growth as observed in the experiments for $\gamma > 50$ deg. Evans and Hutchinson (1989), proposed a model for the dependence of G_{0C} on γ using a surface roughness model. Neglecting friction, they arrived at a model where the governing parameter in increasing the toughness is $\alpha_0 \approx 0.1\ (EH/G_0)/(1 - \nu^2)$, where E is the modulus of elasticity and H is the height of the surface roughness. Assuming $H = 0.1\ \mu$m, α_0 can be calculated as 0.4. Evaluating the amount of roughness induced toughening, (using Eq. (40) from Evans and Hutchinson), the predicted toughening is shown in Fig. 4 along with the experimentally measured values of EG. It is possible to investigate experimentally the effect of the variation in toughening with α_0 by changing the interface toughness at zero mixity G_0 (by altering the healing) and this is under investigation. The disagreement between the roughness induced shielding model and the experiments indicates that perhaps some other mechanism, such as near-tip plasticity, might play a role in determining the interface fracture energy.

4 Conclusion

The CTS specimen was investigated and shown to be a possible configuration for the evaluation of the variation of the interface fracture toughness with the mixity γ. For our investigation, a diffusion bond was created to form the interface in a PMMA specimen. Under mixed-mode conditions, it was determined that the interface fracture energy increases significantly with the loading mixity, γ. In all cases, whether the crack propagated along the interface or kinked from it, crack growth was dynamic, even under quasi-static loading. In the experimental study of interface crack extension, a dynamic analysis, such as through high-speed photography, becomes necessary.

References

Buchholz, F. G., Pirro, P. J. M., Richard H. A., and Dreyer, K. H., 1987, *Proceedings, Fourth International Conference on Numerical Methods in Fracture Mechanics*, A. R. Luxmore et al., eds., Pineridge Press, Swansea, UK.

Charalambides, P. G., Lund, J., Evans, A. G., and McMeeking, R. M., 1989, "A Test Specimen for Determining the Fracture Resistance of Bimaterial Interfaces," ASME JOURNAL OF APPLIED MECHANICS, Vol. 56, pp. 77–82.

Evans, A. G., and Hutchinson, J. W., 1989, "Effects of Non-Planarity on the Mixed-Mode Fracture Resistance of Bimaterial Interfaces," *Acta Metallurgica*, Vol. 37, pp. 909–916.

He, M-Y., and Hutchinson, J. W., 1989, "Kinking of a Crack Out of an Interface," ASME JOURNAL OF APPLIED MECHANICS, Vol. 56, pp. 270–278.

Hutchinson, J. W., and Suo, Z., 1991, "Mixed-Mode Cracking in Layered Materials," *Advances in Applied Mechanics*, Vol. 28, Academic Press, New York.

Liechti, K. M., and Chai, Y-S., 1991, "Biaxial Loading Experiments for Determining Interfacial Fracture Toughness," ASME JOURNAL OF APPLIED MECHANICS, in press.

Mahajan, R. V., and Ravi-Chandar, K., 1989, "An Experimental Investigation of Mixed-Mode Fracture," *International Journal of Fracture*, Vol. 41, pp. 235–252.

Boundary Layer Phenomena in Large Deflection, Small Strain Plate Theory

L. J. Berg[14]

Boundary layers exist at the edges of thin plates undergoing large deformations because the interior of the plate must assume a developable shape. The developable shape is sometimes incompatible with the force and moment resultants prescribed at the plate's boundary, in particular when the edge of the plate is stress free. A boundary layer solution is presented which describes the shape of a boundary layer in a plate undergoing large deflections. The boundary layer is a slight perturbation of the interior shape which allows the appropriate boundary conditions to be satisfied. Since developable shells are applicable to a plane, the boundary layer is also appropriate for arbitrary developable shells.

[14]ADSTAR, IBM Corporation, Rochester, MN 55901-7829.

Contributed by the Applied Mechanics Division of THE AMERICAN SOCIETY OF MECHANICAL ENGINEERS for publication in the ASME JOURNAL OF APPLIED MECHANICS.

Manuscript received by the ASME Applied Mechanics Division, Mar. 14, 1991; final revision, Dec. 30, 1991. Associate Technical Editor: J. G. Simonds.

Copyright © 1993 by ASME
Downloaded 03 May 2010 to 171.66.16.245. Redistribution subject to ASME license or copyright; see http://www.asme.org/terms/Terms_Use.cfm

Introduction

Large deflection, small strain plate theories are available which describe the shape of a thin plate when it is bent by forces large enough that the deflections are on the order of the plate's lateral dimensions (Berg and Johnson, 1989; Berg, 1991). These plate theories prescribe that, to lowest order, the plate assumes a developable shape. The boundary layer is discussed in detail for plates undergoing finite deflections in Fung and Wittrick (1955). The nature of this boundary layer is investigated here in the more general case of plates undergoing large elastic deflections.

The boundary layer analysis in Fung and Wittrick (1955) is based on the von Karman equations for finite deflection of plates. Ashwell (1963) presents an analysis of boundary layers in plates undergoing large deflections. Ashwell proposed that the boundary layer be replaced by a fictitious edge beam. The purpose of the edge beam is to apply loads to the plate to force it to be developable right up to its edge. Because the beam is very small, its stiffness has no effect on the shape assumed by the plate. Equilibrium equations for the edge beam give relations between the loads required on the plate and the internal forces and couples in the beam.

Ashwell (1963) used scaling arguments to show that two of the three edge beam couple components were negligible. Six beam equilibrium equations in three unknown force components and one unknown couple component left two independent relations to be used as plate boundary conditions. These boundary conditions were used by Simmonds and Libai (1979a, 1979b) in their large deflection plate formulation.

Kinematics

Consider a thin rectangular plate whose thickness h is much smaller than its lateral extent. The plate is flat in the undeformed (reference) state, and its midsurface is assumed to be in the X_1-X_2 plane of a rectangular cartesian coordinate system. The third coordinate, X_3, is perpendicular to the flat undeformed plate. The edges of the plate are aligned with the X_1 and X_2-axes.

The displacement of the plate is assumed to be large. All three components of displacement will potentially be the same size, but will be presumed limited by boundary conditions prohibiting rigid body translation. The plate is allowed to rotate through large angles.

The midsurface of the plate will have a typical lateral extent L,which is much larger than the thickness h. The ratio h/L defines the geometric scaling factor $\epsilon = h/L$, $X_1 = O(L)$, $X_2 = O(L)$, $X_3 = O(\epsilon L)$. Dimensionless coordinates are

$$\xi_1 = \frac{X_1}{L},\ \xi_2 = \frac{X_2}{L},\ \xi_3 = \frac{X_3}{\epsilon L},\ \xi_i = O(1). \tag{1}$$

Near the edge of the plate, the length scales L and h are not appropriate. Some variables will change over lengths intermediate between L and h. The length scale $\sqrt{hL} = \sqrt{\epsilon}\, L$ can be shown to be appropriate. The assumed asymptotic expansion for displacements used in Berg (1991) will also be used here, but will be modified to include half integer powers in ϵ.

$$u_i(\xi_j,\epsilon) = L(u_i^0(\xi_j) + \epsilon^{1/2} v_i^0(\xi_j) + \epsilon^1 u_i^1(\xi_j) + \epsilon^{3/2} v_i^1(\xi_j) + \cdots)$$

$$u_i^n = O(1),\ v_i^n = O(1),\ n = 0,1,2,\ \ldots$$

Standard order symbols are used and refer to limits as ϵ approaches zero. Ordinary rectangular cartesian tensor notation is used. Latin indices will take on the values 1, 2, and 3, while Green indices will taken on the values 1 and 2. Summation is assumed over repeated indices, both Latin and Greek.

The independent variables ξ_i in (1) are appropriate for the interior of the plate. An independent variable which is scaled by $\sqrt{hL}$ is required in the boundary layer, $\eta(\xi_2) = \sqrt{\epsilon}\, \xi_2$. Because ξ_1 and ξ_2 are parallel to the edges of the plate, η is a coordinate directed into the plate parallel to the ξ_2-axis. The coordinates ξ_i and η are known as slow and fast variables, respectively. Using a chain rule, the derivative of u_i can be written as

$$\frac{\partial u_i}{\partial \xi_2} + \frac{\partial u_i}{\partial \eta}\frac{\partial \eta}{\partial \xi_2} = \frac{\partial u_i}{\partial \xi_2} + \frac{1}{\sqrt{\epsilon}}\frac{\partial u_i}{\partial \eta}.$$

The following derivative notation will be used:

$$\frac{\partial(\bullet)}{\partial \xi_i} = (\bullet)_{,i},\ \frac{\partial(\bullet)}{\partial \eta} = (\bullet)_{,\eta}.$$

The subscript η will be an exception to the subscript rule stated earlier. It will never be used as an index representing the 1 or 2-coordinate direction.

As in Berg (1991), one can substitute the displacement expansion into strain displacement relations to obtain an expansion for the strain components

$$E_{ij} = \epsilon^{-2} E_{ij}^{-2} + \epsilon^{-3/2} E_{ij}^{-3/2} + \cdots. \tag{2}$$

Since most engineering materials can only undergo very small strains, it is assumed that the strains are always small, both in the interior and in the boundary layer, $E_{ij} = O(\epsilon)$.

Several of the lowest order terms in (2) will be required to vanish as a result of the strain scaling assumption. This gives rise to relations among displacement gradients, some of which can be integrated. The integrations are straightforward, and give rise to displacements in the form

$$\frac{u_i}{L} = U_i^0(\xi_\alpha) + \epsilon\{\tilde{U}_i^1(\xi_\alpha,\eta) + \xi_3 \bar{u}_i^1(\xi_\alpha)\} + \epsilon^{3/2}\{\tilde{V}_i^1(\xi_\alpha,\eta) + \xi_3 \bar{v}_i^1(\xi_\alpha,\eta)\} + O(\epsilon^2).$$

A tilde indicates an unknown η-dependence; an overbar indicates a coefficient of a term linear in ξ_3.

Next, consider a set of unit vectors $\mathbf{e}_i$ aligned with the coordinate axes X_i. These vectors will be rotated into a second set of base vectors $\mathbf{h}_i$ in the deformed plate. The base vectors $\mathbf{h}_i$ are taken to be the lowest order approximation to the mapping of the $\mathbf{e}_i$ vectors onto the deformed configuration. They are orthonormal (Berg, 1991). The first few strain components can be written in terms of $\mathbf{h}_i$

$$\begin{aligned} E_{ij}^0 &= \mathbf{h}_i \cdot \mathbf{h}_j - \delta_{ij} = 0 \\ E_{11}^{1/2} &= 0 \\ E_{22}^{1/2} &= \mathbf{h}_2 \cdot \tilde{\mathbf{U}}_{,\eta}^1 = 0 \\ 2E_{12}^{1/2} &= \mathbf{h}_1 \cdot \tilde{\mathbf{U}}_{,\eta}^1 = 0. \end{aligned} \tag{3}$$

From (3) it is seen that $\tilde{\mathbf{U}}_{,\eta}^1$ has nonzero components only in the direction normal to the deformed plate. This is assumed *a priori* in von Karman plate theory.

The next order strains can be written in terms of a membrane term and a bending term

$$E_{ij}^1 = e_{ij}^1 + \xi_3 \kappa_{ij}^1. \tag{4}$$

The displacements can be written using components referred to either $\mathbf{e}$ or $\mathbf{h}$. In particular, $U_i e_i = W_i h_i$. With this, part of (4), written out, is

$$e_{11}^1 = \mathbf{h}_1 \cdot \tilde{\mathbf{U}}_{,1}^1 = W_{1,1}^1 + \kappa_{11}^1 \tilde{W}_3^1. \tag{5}$$

Equilibrium

The equations of equilibrium for the plate, referred to the reference coordinate system, are

Downloaded 03 May 2010 to 171.66.16.245. Redistribution subject to ASME license or copyright; see http://www.asme.org/terms/Terms_Use.cfm

$$\frac{\partial P_{ik}}{\partial X_i}+b_k=0 \tag{6}$$

where P is the Piola-Kirchhoff stress tensor of the first kind and **b** is a vector of body force components. The stress components and body forces are assumed to have the following representation

$$P_{ij}=\tau(P^0_{ij}+\epsilon^{1/2}P^{1/2}_{ij}+\epsilon P^1_{ij}+\cdots)$$

$$b_i=\frac{\tau}{L}\,(b^0_i+\epsilon^{1/2}b^{1/2}_i+\epsilon b^1_i+\cdots) \tag{7}$$

where τ is a load scaling parameter. It is shown in Berg (1991) that it is consistent to take

$$P^0_{3i}=0. \tag{8}$$

When (7) and (8) are substituted into (6), and the second Piola-Kirchhoff stress T is used, a sequence of equilibrium equations results:

$$P^{1/2}_{3k,3}+T^0_{2j,\eta}F^0_{kj}=0 \tag{9}$$

$$P^1_{3k,3}+T^0_{2j,\eta}F^{1/2}_{kj}+T^0_{2j}F^{1/2}_{kj,\eta}+T^{1/2}_{2j,\eta}F^0_{kj}+T^0_{\alpha j,\alpha}F^0_{kj}+T^0_{\alpha j}F^0_{kj,\alpha}+b^0_k=0 \tag{10}$$

etc.

Next, introduce force and moment resultants

$$\int_{-1/2}^{1/2}(1,\xi_3)T^n_{ij}d\xi_3=(N^n_{ij},\,M^n_{ij}),\ 2n=0,1,2,\ldots$$

$$\int_{-1/2}^{1/2}P^n_{3k,3}+b^n_k d\xi_3=\gamma^n_k,\ 2n=1,2,3,\ldots \tag{11}$$

$$\int_{-1/2}^{1/2}\xi_3 b^n_k d\xi_3=0,\ 2n=0,1,2,\ldots$$

$$\int_{-1/2}^{1/2}\xi_3 P^{1/2}_{3k,3}d\xi_3=P^{1/2}_{3k+}-N^{1/2}_{3\alpha}F^0_{k\alpha}-N^{1/2}_{33}F^0_{k3}. \tag{12}$$

The surface pressure loads and body forces are indistinguishable in this theory (Berg, 1991), as is seen in (11). The body force vector is assumed to have no body couple component in (12).

The lowest order force equilibrium equations, referred to the deformed basis, are

$$N^0_{2\alpha,\eta}=0. \tag{13}$$

The third equation, equilibrium normal to the plate, is satisfied automatically as a result of the scalings used in (7) and (8). The load expansions in (7) are general. However, the surface loads in the interior problem contain no half-integer powers of ϵ, so it is inconsistent to keep them in the boundary layer. The lowest order moment equilibrium equations result from multiplying (9) by ξ_3, integrating, and using the deformed basis,

$$M^0_{2\alpha,\eta}=N^{1/2}_{\alpha 3},\ N^{1/2}_{33}=0. \tag{14}$$

The transverse component, referred to the deformed basis, of the next order force equilibrium Eq. (10) is

$$M^0_{22,\eta\eta}-N^0_{\alpha\beta}\kappa^1_{\alpha\beta}+\gamma^0_k F^0_{k3}=0. \tag{15}$$

Boundary Layer

Consider the problem originally solved in Fung and Wittrick (1955), but without the restriction of finite deflections. In particular, consider a strip bent by some combination of forces and couples applied at its ends. The part of the strip away from the ends appears in Fig. 1. The surface loads and body forces are assumed to vanish, $\gamma^0_i=0$. The lowest order equilibrium equations imply

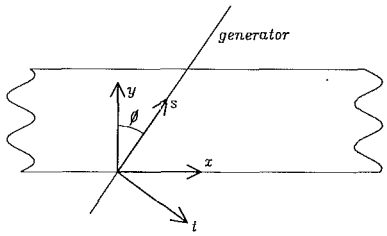


Fig. 1 Coordinate system geometry

$$N^0_{\alpha\beta}=0 \tag{16}$$

in the interior. More generally, $N^0_{\alpha\beta}=N^0_{\alpha\beta}(\eta)$ in the boundary layer. With this, (13) can be integrated, along with the stress-free condition on $\eta=0$, to give

$$N^0_{12}=N^0_{22}=0 \tag{17}$$

in the boundary layer. Equation (15) can also be simplified

$$M^0_{22,\eta\eta}-N^0_{11}\kappa^1_{11}=0. \tag{18}$$

Equation (17) implies a plane (membrane) stress state in the boundary layer, so with (5) and (16), (18) takes the form

$$\tilde{W}^1_{3,\eta\eta\eta\eta}+\frac{A}{D}\,(\kappa^1_{11})^2\tilde{W}^1_3=0$$

where a linear homogeneous constitutive law has been used, and A and D are the scaled membrane and bending stiffnesses, respectively. This is precisely the form derived by Fung and Wittrick (1955) where they assumed that the deflections were restricted to be only finite. This equation can be integrated to give

$$\tilde{W}^1_3=\sqrt{\frac{D}{A}}\,(\nu+\tan^2\phi)e^{-\alpha\eta}(\cos\alpha\eta-\sin\alpha\eta) \tag{19}$$

where ν is Poisson's ratio, ϕ is shown on Fig. 1, and $\alpha^4=(\kappa^1_{11})^2A/4D$.

This boundary layer is interesting in that its amplitude, modulated by a decaying sinusoid, is independent of any loading or deformation parameters. As soon as the plate is bent, even the slightest amount, the boundary layer leaps into existence and the edge of the plate is deformed to its full extent. The length scale α, on the other hand, depends on the interior curvature. As the plate is bent further, the boundary layer grows towards the interior. It is easy to show that the unscaled transverse displacement is $O(h)$, exactly as in Fung and Wittrick (1955).

Of special interest are the boundary layer forces and couple introduced by Ashwell (1963) in a fictitious edge beam. By scaling arguments, Ashwell argues that two in-plane moment components are negligible. This leaves three force components and a moment normal to the deformed plate which can be potentially nonzero in the edge beam.

With (19), we can evaluate the forces and couple introduced by Ashwell (1963) and used by Simmonds and Libai (1979a, 1979b) and by Darmon and Benson (1985, 1986). The in-plane force, parallel to the plate's edge, is

$$\int_0^\infty N^0_{11}(\eta)d\eta=\int_0^\infty A\kappa^1_{11}\tilde{W}^1_3 d\eta=0 \tag{20}$$

which implies that the net force in the boundary layer, and hence in the edge beam, vanishes; the stresses are self-equilibrating. The in-plane force, perpendicular to the plate's edge, is

$$\int_0^\infty N^0_{12}d\eta=0 \tag{21}$$

Downloaded 03 May 2010 to 171.66.16.245. Redistribution subject to ASME license or copyright; see http://www.asme.org/terms/Terms_Use.cfm

using (17). The transverse component of the force is

$$\int_0^\infty N_{13}^{1/2} d\eta = \int_0^\infty M_{12,\eta}^0 d\eta = \int_0^\infty D(1-\nu)\kappa_{12,\eta}^1 d\eta = 0. \quad (22)$$

Finally, the fictitious edge beam couple component normal to the deformed plate is

$$\int_0^\infty \eta N_{11}^0 d\eta = D(\nu + \tan^2\phi).$$

Just as with the displacement, this component of moment leaps into existence as soon as the plate is bent. It appears then, that at this order of approximation, one need not include the force component effects of Ashwell's edge beam. Only the normal couple is significant.

Discussion

Darmon (1989) indicates that as part of his solution to the Simmonds and Libai plate equations, the edge forces were noted to be very much smaller than the applied plate loads. This is in good agreement with (20)–(22). Simmonds and Libai also discovered that the normal couple component is independent of load using Ashwell's edge beam equilibrium equations. They argue that for small loads and nearly flat plates, the linear theory holds sway and that the constraint of inextensibility prohibits a continuous transition from linear to nonlinear theories. The assumed displacement and strain scaling assumptions are not as restrictive as they perhaps should be for very small deflections. Consequently, the theory presented here is not valid for very nearly flat plates. The boundary layer and moment which appears with finite amplitude for infinitesimal bending is not accurately characterized for very nearly flat plates, so there is no inconsistency.

It is somewhat remarkable that the shape of the boundary layer is the same in finite and large deflection linearly elastic plate theories. The von Karman theory is "nonlinear enough" to encompass all of the effects of the large deformation boundary layer to the order considered here. This can be seen in (3) and (5) where the same kinematics as in the von Karman plate theory are adequate in describing the large deflection boundary layer. Higher order plate theories considered in Berg (1991) may indeed have more complicated boundary layers.

Acknowledgments

Thanks are due to Pierre Darmon for discussions regarding the results of his numerical simulation (Darmon and Benson (1985, 1986)). I would also like to thank the reviewers for their insightful and useful comments.

References

Ashwell, D. G., 1963, "The Boundary Layer in the Bending of Inextensible Plates and Shells," *Quarterly Journal of Mechanics and Applied Mathematics*, Vol. 16, Pt. 2, pp. 179–191.

Berg, L. J., 1991, "Asymptotic Variational Methods in Large Deflection Small Strain Plate Theory," *International Journal of Solids and Structures*, Vol. 27, No. 11, pp. 1401–1417.

Berg, L. J., and Johnson, M. W., 1989, "Large Deflection Small Strain Plate Theory: Application to the Analysis of Cellulosic Structures," *Mechanics of Cellulosic and Polymeric Materials*, R. W. Perkins, ed., ASME AMD-Vol. 99, MD-Vol. 13, pp. 95–103.

Darmon, P., 1989, private communication.

Darmon, P., and Benson, R. C., 1985, "Large Inextensional Deformation of Thin Orthotropic Cantilevered Plates With Distributed Loads," ASME Journal of Applied Mechanics, Vol. 52, pp. 385–388.

Darmon, P., and Benson, R. C., 1986, "Numerical Solution to an Inextensible Plate Theory With Experimental Results," ASME Journal of Applied Mechanics, Vol. 53, pp. 886–890.

Fung, Y. C., and Wittrick, W. H., 1955, "A Boundary Layer Phenomenon in the Large Deflexion of Thin Plates," *Quarterly Journal of Mechanics and Applied Mathmatics*, Vol. 8, Pt. 2, pp. 191–210.

Simmonds, J. G., and Libai, A., 1979a, "Exact Equations for the Inextensional Deformation of Cantilevered Plates," ASME Journal of Applied Mechanics, Vol. 46, pp. 631–636.

Simmonds, J. G., and Libai, A., 1979b, "Alternate Exact Equations for the Inextensional Deformation of Arbitrary, Quadrilateral, and Triangular Plates," ASME Journal of Applied Mechanics, Vol. 46, pp. 895–900.

On the Approximation of a Deflection Curve by Force Actuators

K. Natarajan[15], G. A. Dumont[16,17], and M. S. Davies[17]

In this paper we discuss a method of approximating a deflection curve of a simple beam by means of a given number of equi-spaced force actuators subject to constraints on the bending moment. The deflection curve is assumed to be specified at a number of equi-spaced points greater than the number of actuators. The method developed minimizes the approximation error in an integral squared sense. The method is applied to an example of approximation of a deflection curve of the slice lip on a paper machine headbox for the control of basis weight of paper.

1 Introduction

The problem discussed in this paper arose out of a study on the manipulation of the slice lip of a headbox on a paper machine for the control of basis weight (Natarajan et al., 1988). Basis weight of paper is its weight per unit area. It is controlled by a set of N force actuators positioned on the lip with a uniform spacing. Vertical movement of the slice lip, by developing adequate force in the actuators, causes a change in the opening between the lip and the apron of the headbox. As it flows out of the headbox onto the wire, the material spreads on the web as waves propagate across the machine (Wahren, 1986). The combination of the slice lip deflection and of this water wave effect causes a change in basis weight profile. Although the lip can be modeled as a simple beam (Balakrishnan and McFarlin, 1985), no water wave effect model has so far been developed, and thus it will not be taken into account in this paper.

Basis weight is measured at N_m equi-spaced points along the width of the paper by a scanning sensor. From the measurements, the deflections at the corresponding N_m points on the lip can be computed. With N_m actuators located on the lip the desired deflections can be exactly achieved. The deflection curve so achieved is termed the desired deflection curve. How-

[15]Department of Electrical Engineering, Lakehead University, Thunder Bay, ON, Canada.

[16]Department of Electrical Engineering, University of British Columbia, Vancouver, BC, Canada.

[17]To whom all correspondence should be addressed. Send to Professor G. A. Dumont, Pulp and Paper Centre, 2385 East Mall, University of British Columbia, Vancouver, BC V6T 1Z4, Canada.

Contributed by the Applied Mechanics Division of The American Society of Mechanical Engineers for publication in the ASME Journal of Applied Mechanics.

Manuscript received by the ASME Applied Mechanics Division, Apr. 10, 1991; final revision, Aug. 29, 1991. Associate Technical Editor: D. J. Inman.

Downloaded 03 May 2010 to 171.66.16.245. Redistribution subject to ASME license or copyright; see http://www.asme.org/terms/Terms_Use.cfm

using (17). The transverse component of the force is

$$\int_0^\infty N_{13}^{1/2} d\eta = \int_0^\infty M_{12,\eta}^0 d\eta = \int_0^\infty D(1-\nu)\kappa_{12,\eta}^1 d\eta = 0. \quad (22)$$

Finally, the fictitious edge beam couple component normal to the deformed plate is

$$\int_0^\infty \eta N_{11}^0 d\eta = D(\nu + \tan^2\phi).$$

Just as with the displacement, this component of moment leaps into existence as soon as the plate is bent. It appears then, that at this order of approximation, one need not include the force component effects of Ashwell's edge beam. Only the normal couple is significant.

Discussion

Darmon (1989) indicates that as part of his solution to the Simmonds and Libai plate equations, the edge forces were noted to be very much smaller than the applied plate loads. This is in good agreement with (20)–(22). Simmonds and Libai also discovered that the normal couple component is independent of load using Ashwell's edge beam equilibrium equations. They argue that for small loads and nearly flat plates, the linear theory holds sway and that the constraint of inextensibility prohibits a continuous transition from linear to nonlinear theories. The assumed displacement and strain scaling assumptions are not as restrictive as they perhaps should be for very small deflections. Consequently, the theory presented here is not valid for very nearly flat plates. The boundary layer and moment which appears with finite amplitude for infinitesimal bending is not accurately characterized for very nearly flat plates, so there is no inconsistency.

It is somewhat remarkable that the shape of the boundary layer is the same in finite and large deflection linearly elastic plate theories. The von Karman theory is "nonlinear enough" to encompass all of the effects of the large deformation boundary layer to the order considered here. This can be seen in (3) and (5) where the same kinematics as in the von Karman plate theory are adequate in describing the large deflection boundary layer. Higher order plate theories considered in Berg (1991) may indeed have more complicated boundary layers.

Acknowledgments

Thanks are due to Pierre Darmon for discussions regarding the results of his numerical simulation (Darmon and Benson (1985, 1986)). I would also like to thank the reviewers for their insightful and useful comments.

References

Ashwell, D. G., 1963, "The Boundary Layer in the Bending of Inextensible Plates and Shells," *Quarterly Journal of Mechanics and Applied Mathematics*, Vol. 16, Pt. 2, pp. 179–191.

Berg, L. J., 1991, "Asymptotic Variational Methods in Large Deflection Small Strain Plate Theory," *International Journal of Solids and Structures*, Vol. 27, No. 11, pp. 1401–1417.

Berg, L. J., and Johnson, M. W., 1989, "Large Deflection Small Strain Plate Theory: Application to the Analysis of Cellulosic Structures," *Mechanics of Cellulosic and Polymeric Materials*, R. W. Perkins, ed., ASME AMD-Vol. 99, MD-Vol. 13, pp. 95–103.

Darmon, P., 1989, private communication.

Darmon, P., and Benson, R. C., 1985, "Large Inextensional Deformation of Thin Orthotropic Cantilevered Plates With Distributed Loads," ASME Journal of Applied Mechanics, Vol. 52, pp. 385–388.

Darmon, P., and Benson, R. C., 1986, "Numerical Solution to an Inextensible Plate Theory With Experimental Results," ASME Journal of Applied Mechanics, Vol. 53, pp. 886–890.

Fung, Y. C., and Wittrick, W. H., 1955, "A Boundary Layer Phenomenon in the Large Deflexion of Thin Plates," *Quarterly Journal of Mechanics and Applied Mathmatics*, Vol. 8, Pt. 2, pp. 191–210.

Simmonds, J. G., and Libai, A., 1979a, "Exact Equations for the Inextensional Deformation of Cantilevered Plates," ASME Journal of Applied Mechanics, Vol. 46, pp. 631–636.

Simmonds, J. G., and Libai, A., 1979b, "Alternate Exact Equations for the Inextensional Deformation of Arbitrary, Quadrilateral, and Triangular Plates," ASME Journal of Applied Mechanics, Vol. 46, pp. 895–900.

On the Approximation of a Deflection Curve by Force Actuators

K. Natarajan[15], G. A. Dumont[16,17], and M. S. Davies[17]

In this paper we discuss a method of approximating a deflection curve of a simple beam by means of a given number of equi-spaced force actuators subject to constraints on the bending moment. The deflection curve is assumed to be specified at a number of equi-spaced points greater than the number of actuators. The method developed minimizes the approximation error in an integral squared sense. The method is applied to an example of approximation of a deflection curve of the slice lip on a paper machine headbox for the control of basis weight of paper.

1 Introduction

The problem discussed in this paper arose out of a study on the manipulation of the slice lip of a headbox on a paper machine for the control of basis weight (Natarajan et al., 1988). Basis weight of paper is its weight per unit area. It is controlled by a set of N force actuators positioned on the lip with a uniform spacing. Vertical movement of the slice lip, by developing adequate force in the actuators, causes a change in the opening between the lip and the apron of the headbox. As it flows out of the headbox onto the wire, the material spreads on the web as waves propagate across the machine (Wahren, 1986). The combination of the slice lip deflection and of this water wave effect causes a change in basis weight profile. Although the lip can be modeled as a simple beam (Balakrishnan and McFarlin, 1985), no water wave effect model has so far been developed, and thus it will not be taken into account in this paper.

Basis weight is measured at N_m equi-spaced points along the width of the paper by a scanning sensor. From the measurements, the deflections at the corresponding N_m points on the lip can be computed. With N_m actuators located on the lip the desired deflections can be exactly achieved. The deflection curve so achieved is termed the desired deflection curve. How-

[15]Department of Electrical Engineering, Lakehead University, Thunder Bay, ON, Canada.

[16]Department of Electrical Engineering, University of British Columbia, Vancouver, BC, Canada.

[17]To whom all correspondence should be addressed. Send to Professor G. A. Dumont, Pulp and Paper Centre, 2385 East Mall, University of British Columbia, Vancouver, BC V6T 1Z4, Canada.

Contributed by the Applied Mechanics Division of The American Society of Mechanical Engineers for publication in the ASME Journal of Applied Mechanics.

Manuscript received by the ASME Applied Mechanics Division, Apr. 10, 1991; final revision, Aug. 29, 1991. Associate Technical Editor: D. J. Inman.

Copyright © 1993 by ASME

Downloaded 03 May 2010 to 171.66.16.245. Redistribution subject to ASME license or copyright; see http://www.asme.org/terms/Terms_Use.cfm

ever, the number of actuators N available on the lip is usually less than the number of measurement points N_m. Also, there are constraints on the force producing capability of the actuators and the bending moment or shear force that can be borne safely by the lip. The various constraints can be transformed into constraints on the bending moment by a worst-case analysis (Natarajan et al., 1988).

In this Note, we discuss the optimal approximation of the desired deflection curve by the N actuators without exceeding the constraints on the bending moment applied to the lip. The optimality criterion is an integral squared error criterion. The integral involved in the criterion is approximated numerically. In Section 2, we discuss the preliminaries and assumptions and show how to set up the approximation problem, assuming that there are N_m actuators on the lip. In Section 3, we discuss the reduction from the assumed N_m actuators to the available N actuators through the notion of actuator failures. We apply the method to an example in Section 4 and conclude the paper in Section 5.

2 Preliminaries

For more details on the method for calculating the moments, including a sketch of the beam and the sign convention, see Natarajan et al. (1989). The slice lip is modeled as a simple beam with uniform cross-section. The forces acting on the lip are assumed to act in a plane containing the neutral axis and perpendicular to the breadth of the lip. With the sign conventions, notations and frame of reference of Popov (1978), the deflection of the lip is assumed to be governed by

$$EI\frac{d^2y}{dx^2}=M(x). \tag{1}$$

The actuators are capable of only applying force (no moment). It is assumed that the lip is always supported by an actuator at either end. This assumption can be relaxed. The assumption of end support and the equilibrium of the lip imply that (L is the length of the lip)

$$M(0)=M(L)=0. \tag{2}$$

If (x_k, M_k), $k = 0, 1, \ldots, (N_m - 1)$ are N_m values of position of the actuator and corresponding bending moment with the x_k such that $0 = x_0 < x_1 < \ldots < x_{(N_m-1)} = L$, then the deflection of the lip y at a point x on the lip can be expressed by

$$y(x)=\sum_{k=1}^{N_m-1} V_k(x-x_{k-1})^3-\sum_{k=1}^{N_m-1} V_k(x-x_k)^3+C_1x+C_2 \tag{3}$$

where

$\langle\theta\rangle$ is the singularity function of the argument θ and evaluates to θ if $\theta > 0$, else to 0;

V_k is the negative of the shear force in the section of the beam between x_{k-1} and x_k and is given by

$$V_k=(M_k-M_{k-1})/\{6EI(x_k-x_{k-1})\}; \text{ and} \tag{4}$$

C_1, C_2 are constants determined using (3) and the values of $y(0)$ and $y(L)$ as

$$C_1=\left(\frac{y(L)-y(0)}{L}\right)-\frac{1}{L}\left(\sum_{k=1}^{N_m-1} V_k(L-x_{k-1})^3-\sum_{k=1}^{N_m-1} V_k(L-x_k)^3\right) \tag{5}$$

$$C_2=y(0). \tag{6}$$

From the deflections specified at the N_m equi-spaced points x_k, $k = 0, 1, \ldots, (N_m - 1)$, the moments M_k can be obtained by using cubic B-splines (Natarajan, et al., 1988, 1989) or by the method of Balakrishnan and McFarlin (1985). Since the deflections are computed from basis weight measurements, the computed moments M_k can exceed constraints. We shall use the adjective unconstrained in referring to these moments.

2.1 Posing the Optimization Problem. In this subsection, we discuss how to pose the optimization problem with constraints on the moments assuming that N_m equi-spaced actuators are available on the lip.

When the unconstrained moment M_k is changed by δM_k, $k \in \{1, 2, \ldots, (N_m - 2)\}$ then the corresponding change in $y(x)$ is given without any approximation (since higher order derivatives are zero) by (7). Note that no changes to M_0 and M_{N_m} can be made as equilibrium of the lip demands that these moments be identically zero.

$$\delta y(x)=\sum_{k=1}^{(N_m-2)}\frac{\partial y(x)}{\partial M_k}\delta M_k \tag{7}$$

The changes (errors) $\delta y(x)$ at q equi-spaced points on the lip are given by

$$\delta y=\frac{1}{EI}A_q\delta M \tag{8}$$

where ($'$ denotes transpose)

$$\delta y=[\delta y(x_1), \delta y(x_2), \ldots, \delta y(x_q)]' \tag{9}$$

$$\delta M=[\delta M_1, \delta M_2, \ldots, \delta M_{(N_m-2)}]' \tag{10}$$

and A_q is a $q \times (N_m - 2)$ matrix with the j, k element obtained by evaluating at x_j the partial derivative (with EI factored out) of (3), taking into account (4, 5), with respect to M_k.

From (8), the sum of the squared errors at the q points is

$$\delta y'\delta y=\sum_{j=1}^{q}\delta y(x_j)^2=\delta M'Q\delta M \tag{11}$$

where

$$Q=\frac{1}{(EI)^2}A_q'A_q. \tag{12}$$

If (11) is multiplied on both sides by the spacing between the q points, we get an approximation to the integral of the squared error of the deflections of the lip due to the changes in the $(N_m - 2)$ moments. The approximation improves as q increases. Henceforth in this Note, the minimization criterion considered is the minimization (with q chosen *a priori*) of (11) subject to constraints on the bending moment to be applied to the lip. The constraints can be described by

$$|M^c| \le M_{\max} \tag{13}$$

where $M^c = M + \delta M$ is the constrained moment vector to be applied to the lip.

The minimization problem posed here is of the quadratic programming (QP) type and has been well studied in the literature (Osborne, 1985).

If the end deflections are to be used as variables in the minimization of the L^2 norm, then in (7), δy_0 and δy_L and the corresponding partial derivatives enter. Further modifications for this case should be obvious and are available in Natarajan et al. (1988).

3 Reduction From N_m To N Actuators

We initially discuss the case when the spacing between the N actuators on the lip is an integer multiple of the spacing between the N_m actuators assumed available on the lip in Section 2. The problem of reduction can then be treated by declaring that the $N_m - N$ actuators "in-between" have failed,

Downloaded 03 May 2010 to 171.66.16.245. Redistribution subject to ASME license or copyright; see http://www.asme.org/terms/Terms_Use.cfm

i.e., cannot develop any force. This mode of failure of the actuators implies that the bending moment diagram cannot change slope at a failed actuator. The value of the bending moment at the location of a failed actuator can be obtained by linear interpolation using the moments at, and the known distances to, the nearest unfailed actuators on either side of the failed actuator. From this observation, it can be verified that M^c of Section 2 is given by

$$M^c = TM_r^c \tag{14}$$

where

M_r^c is the constrained moment vector consisting of the final moments to be applied at the unfailed actuator locations, and

T is a sparse linear transformation of size $N_m \times N$ whose elements involve ratios of distances to and between the unfailed actuators. Since we know *a priori* which actuators are going to be declared to have failed, T can be precomputed before the optimization is carried out.

Using (14) and the definition of M^c given immediately after (13), in (11) we obtain

$$\delta y' \delta y = M_r^{c\prime} T' QTM_r^c - 2\{M' QT\}M_r^c + M' QM. \tag{15}$$

Henceforth $M_{\max}$ will denote the constraint vector on M_r^c. Introducing the vectors p, c, and the matrix Q_2 defined in (16, 17, 18), the minimization problem can be brought into the standard quadratic programming (QP) format given in (19). The term independent of p has been omitted in (19) as it plays no further part in the minimization.

$$p = M_{\max} + M_r^c \tag{16}$$

$$Q_2 = T' QT \tag{17}$$

$$c = -2Q_2 M_{\max} - 2T' QM \tag{18}$$

$$\text{Minimize } \{p' Q_2 p + c' p\} \text{ subject to } 0 \le p \le 2M_{\max}. \tag{19}$$

A complete Fortran code for solving the QP problem by Lemke's method (Osborne, 1985) is available in Ravindran (1972). This code with the modification suggested in Proll (1974) is used in the example requiring QP solution in this paper.

The spacing h between the N actuators on the slice lip is rarely an integer multiple of the spacing h_m between the N_m measurement points. Hence, a further refinement is now discussed. Let S_{N_m} and S_N denote the sets of points on the lip spaced at intervals h_m and h, respectively. We introduce a hypothetical set of N_s actuators on the lip where N_s is the cardinality of the set S_{N_s} given by

$$S_{N_s} = S_{N_m} \cup (S_N - S_{N_m}). \tag{20}$$

In order that the deflection curve with N_s actuators match the desired deflection curve (set up from the deflections at locations in S_{N_m}), the force in the actuators located at positions in $(S_N - S_{N_m})$ must be zero. Since the unconstrained moments at locations in S_{N_m} are known, the unconstrained moments at the locations in $(S_N - S_{N_m})$ can be computed by linear interpolation from the value of the moments in S_{N_m} and the distances between points in $(S_N - S_{N_m})$ and S_{N_m}. Thus, the initial unconstrained moment vector at the set of N_s actuators can be computed. The problem of reduction from N_s actuators to N actuators can then be treated as at the beginning of this section and the optimization problem can be similarly set up. The only modification to be remembered is that the spacings between the N_s actuators although known *a priori* are not uniform.

Table 1 Computation times for the example

Computational Stage	Time in seconds	Type of computation
Solve for 58 unconstrained moments by cubic B-splines	0.29	on-line
Interpolation of moments at points in $S_N - S_{N_m}$	0.17	on-line
Compute $\frac{1}{EI}A_q$, a 501 × 85 matrix	4.51	off-line
Compute $Q = \frac{1}{(EI)^2}A_q' A_q$	23.28	off-line
Generate T	0.02	on-line
Compute QT and Q_2	2.09	on-line
Compute c	0.13	on-line
Solve QP	8.61	on-line

4 An Example

From actual basis weight measurements by a scanning sensor on a paper machine, filtered basis weight profile deviations were obtained at $N_m = 58$ equi-spaced points across an $L = 5$m width. The profile deviations were converted to deflections at the N_m points by using the proportionality constant (1 mil deflection produces 0.25 lb/1000 ft^2 change in basis weight profile). The number of equi-spaced actuators available on the lip is $N = 29$. The constraint on the absolute value of the moments at the N locations is 1660 Nm. We seek an optimal approximation to the (unconstrained) desired deflection curve.

For the data of this problem, $N_s = 85$. All computations were done on a μVax-II (0.3 Mflops) in double precision Fortran. The computation time for the various stages are shown in Table 1. In the table, computations which have to be done whenever there is a change in the desired deflection curve are termed "on-line." Computations that depend only on the physical constants and geometry of measurements and actuator locations and have to be done only once for a given paper machine are termed "off-line." From the table, we observe that the total time for on-line computations for this example is 11.31 s. The total time for on-line and off-line computations is 39.1 s. The current generation of personal computers have Mflop ratings similar to the μVax used. Thus, from a computational point of view, the method requires a modest time for computations. The computation times reported are to be compared with the (scan) time of 60s for the profile to be measured at the 58 points by the scanning sensor. Figure 1 and Fig. 2 show the unconstrained (desired) and optimal constrained (approximate) deflection curves and corresponding moments, respectively.

5 Conclusion

In this paper we considered the optimal approximation of a desired deflection curve by a set of N uniformly spaced actuators on the beam. The approximation is done subject to constraints on the bending moment applied to the beam. From the example worked out in this paper, it is seen that the computational time involved for a practical problem is within the

Downloaded 03 May 2010 to 171.66.16.245. Redistribution subject to ASME license or copyright; see http://www.asme.org/terms/Terms_Use.cfm

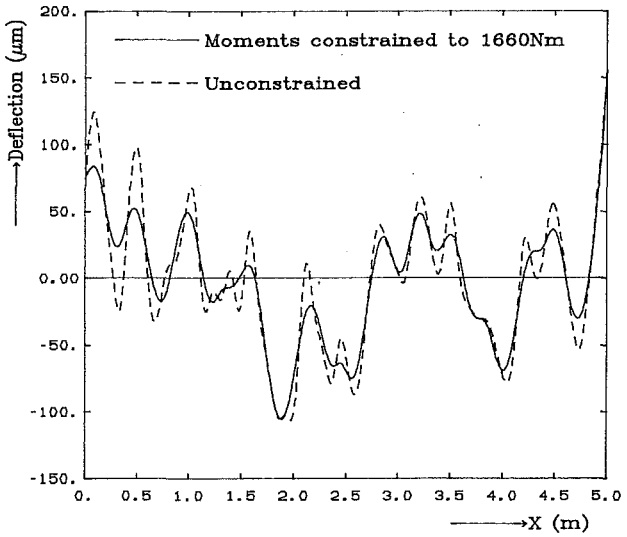


Fig. 1 Desired deflection curve (N_m = 58) and its optimal approximation (N = 29, M_{max} = 1660 Nm)

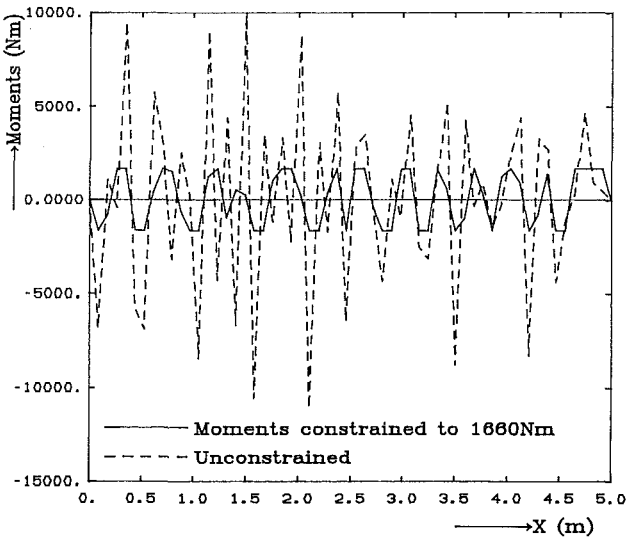


Fig. 2 Bending moment distribution for the curves of Fig. 1

reach of modern personal computers. As mentioned earlier, the water wave effect (Wahren, 1986) has not been taken into account in this work and this aspect should be investigated. It is expected that the integration of this aspect with the method discussed in this paper would be of significant value to the paper-making industry.

References

Balakrishnan, R., and McFarlin, D., 1985, "The Application of a Model of the Slice Lip as an Elastic Beam for Weight Profile Control," *TAPPI Process Control Symposium*, pp. 105–109.

Natarajan, K., Dumont, G. A., and Davies, M. S., 1988, "On the Manipulation of the Slice Lip for the Control of Basis Weight," PGRL Report, Pulp and Paper Research Institute of Canada, Pointe Claire, P.Q., Canada.

Natarajan, K., Dumont, G. A., and Davies, M. S., 1989, "On the Approximation of a Deflection Curve by Force Actuators With Variable Spacing," ASME Journal of Applied Mechanics, Vol. 56, pp. 865–867.

Osborne, M. R., 1985, *Finite Algorithms in Optimization and Data Analysis*, John Wiley and Sons, Ltd.

Popov, E. P., 1978, *Introduction to Mechanics of Solids*, Prentice-Hall, Englewood Cliffs, NJ.

Proll, L. G., 1974, "Remark on Algorithm 431 [H]," *ACM Communications*, Vol. 17, No. 10, p. 590.

Ravindran, A., 1972, "Algorithm 431 [H]: A Computer Routine for Quadratic and Linear Programming Problems," *ACM Communications*, Vol. 15, No. 9, pp. 818–820.

Wahren, D., 1986, "Recent Highlights in Paper Technology," *TAPPI Journal*, Vol. 69, No. 3, pp. 36–45.

Further Results on Iterative Approaches to the Determination of the Response of Nonclassically Damped Systems

Firdaus E. Udwadia[18]

Iterative schemes for obtaining the response of nonclassically damped dynamic systems have been shown to converge when the damping matrix possesses certain specific characteristics. This paper extends those previous results which pertain to symmetric, positive-definite damping matrices. The paper considers a more general decomposition of the damping matrix, and extends the applicability of these iterative methods to all *positive definite, symmetric damping matrices. This decomposition is governed by a parameter* α. *Conditions on* α *under which convergence is guaranteed are provided. Estimates of* α *which yield the fastest asymptotic convergence as well as estimates of the value of this asymptotic rate of convergence are also provided.*

1 Introduction

The iterative solution of linear nonclassically damped systems is an area which is rather new and which promises to yield considerable insight into the dynamics of linear classically damped systems. Udwadia and Esfandiari (1990) proposed an iterative scheme in which at each iteration the system can be thought of as being decoupled. They showed that such a scheme converges to the exact response of the coupled equations of motions when the damping matrices satisfy certain conditions.

For ease of presentation, the notation that will be used throughout this paper will be consistent with that in the 1990 paper of Udwadia and Esfandiari.

Specifically they considered the "reduced," coupled system given by (see Udwadia and Esfandiari, 1990, for details) the equation

$$\ddot{z}+F\dot{z}+\Lambda z=h(t);\ z(t_o)=z_o,\ \dot{z}(t_o)=\dot{z}_o,\ t\in(t_o,\ T], \quad (1)$$

where the matrix Λ is an $N \times N$ diagonal matrix of positive elements and F is the reduced $N \times N$ damping matrix, which, in general, is a full matrix. By splitting the matrix F as $D + B$, where the matrix D is a diagonal matrix whose diagonal entries are the same as those of F, they proposed the following iterative scheme:

[18]Professor of Mechanical Engineering, Civil Engineering and Decision Systems, University of Southern California, Los Angeles, CA 90089-1453. Mem. ASME.

Contributed by the Applied Mechanics Division of The American Society of Mechanical Engineers for publication in the ASME Journal of Applied Mechanics.

Manuscript received by the Applied Mechanics Division, June 26, 1991; final revision, Oct. 24, 1991. Associate Technical Editor: D. J. Inman.

Downloaded 03 May 2010 to 171.66.16.245. Redistribution subject to ASME license or copyright; see http://www.asme.org/terms/Terms_Use.cfm

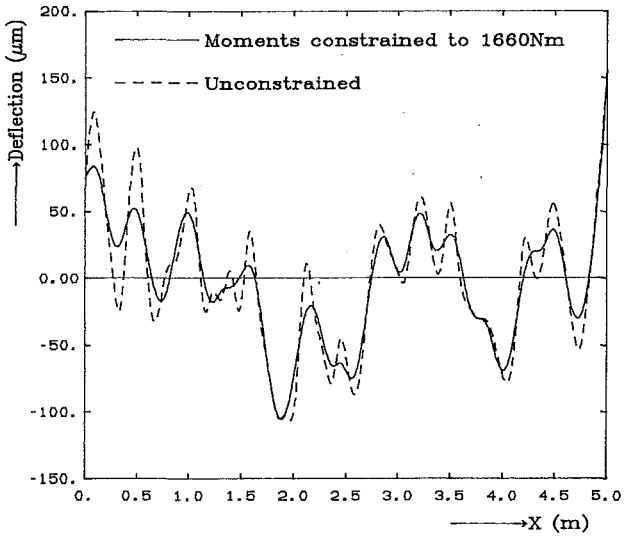


Fig. 1 Desired deflection curve (N_m = 58) and its optimal approximation (N = 29, M_{max} = 1660 Nm)

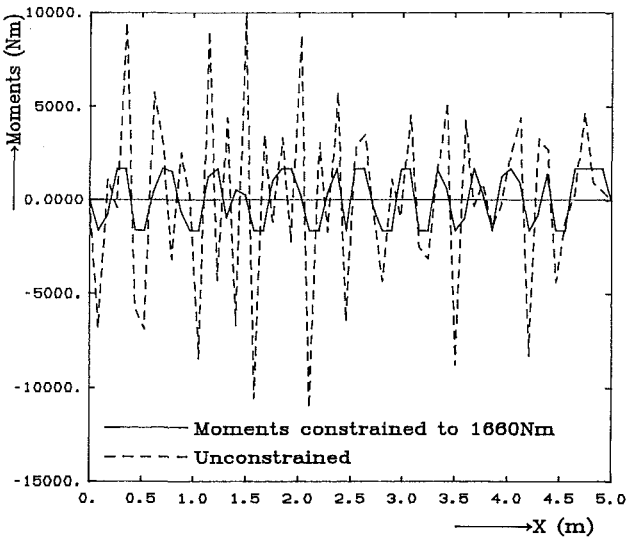


Fig. 2 Bending moment distribution for the curves of Fig. 1

reach of modern personal computers. As mentioned earlier, the water wave effect (Wahren, 1986) has not been taken into account in this work and this aspect should be investigated. It is expected that the integration of this aspect with the method discussed in this paper would be of significant value to the paper-making industry.

References

Balakrishnan, R., and McFarlin, D., 1985, "The Application of a Model of the Slice Lip as an Elastic Beam for Weight Profile Control," *TAPPI Process Control Symposium*, pp. 105–109.

Natarajan, K., Dumont, G. A., and Davies, M. S., 1988, "On the Manipulation of the Slice Lip for the Control of Basis Weight," PGRL Report, Pulp and Paper Research Institute of Canada, Pointe Claire, P.Q., Canada.

Natarajan, K., Dumont, G. A., and Davies, M. S., 1989, "On the Approximation of a Deflection Curve by Force Actuators With Variable Spacing," ASME Journal of Applied Mechanics, Vol. 56, pp. 865–867.

Osborne, M. R., 1985, *Finite Algorithms in Optimization and Data Analysis*, John Wiley and Sons, Ltd.

Popov, E. P., 1978, *Introduction to Mechanics of Solids*, Prentice-Hall, Englewood Cliffs, NJ.

Proll, L. G., 1974, "Remark on Algorithm 431 [H]," *ACM Communications*, Vol. 17, No. 10, p. 590.

Ravindran, A., 1972, "Algorithm 431 [H]: A Computer Routine for Quadratic and Linear Programming Problems," *ACM Communications*, Vol. 15, No. 9, pp. 818–820.

Wahren, D., 1986, "Recent Highlights in Paper Technology," *TAPPI Journal*, Vol. 69, No. 3, pp. 36–45.

Further Results on Iterative Approaches to the Determination of the Response of Nonclassically Damped Systems

Firdaus E. Udwadia[18]

Iterative schemes for obtaining the response of nonclassically damped dynamic systems have been shown to converge when the damping matrix possesses certain specific characteristics. This paper extends those previous results which pertain to symmetric, positive-definite damping matrices. The paper considers a more general decomposition of the damping matrix, and extends the applicability of these iterative methods to all *positive definite, symmetric damping matrices. This decomposition is governed by a parameter* α. *Conditions on* α *under which convergence is guaranteed are provided. Estimates of* α *which yield the fastest asymptotic convergence as well as estimates of the value of this asymptotic rate of convergence are also provided.*

1 Introduction

The iterative solution of linear nonclassically damped systems is an area which is rather new and which promises to yield considerable insight into the dynamics of linear classically damped systems. Udwadia and Esfandiari (1990) proposed an iterative scheme in which at each iteration the system can be thought of as being decoupled. They showed that such a scheme converges to the exact response of the coupled equations of motions when the damping matrices satisfy certain conditions.

For ease of presentation, the notation that will be used throughout this paper will be consistent with that in the 1990 paper of Udwadia and Esfandiari.

Specifically they considered the "reduced," coupled system given by (see Udwadia and Esfandiari, 1990, for details) the equation

$$\ddot{z}+F\dot{z}+\Lambda z=h(t);\ z(t_o)=z_o,\ \dot{z}(t_o)=\dot{z}_o,\ t\in(t_o,\ T], \quad (1)$$

where the matrix Λ is an $N \times N$ diagonal matrix of positive elements and F is the reduced $N \times N$ damping matrix, which, in general, is a full matrix. By splitting the matrix F as $D + B$, where the matrix D is a diagonal matrix whose diagonal entries are the same as those of F, they proposed the following iterative scheme:

[18]Professor of Mechanical Engineering, Civil Engineering and Decision Systems, University of Southern California, Los Angeles, CA 90089-1453. Mem. ASME.

Contributed by the Applied Mechanics Division of The American Society of Mechanical Engineers for publication in the ASME Journal of Applied Mechanics.

Manuscript received by the Applied Mechanics Division, June 26, 1991; final revision, Oct. 24, 1991. Associate Technical Editor: D. J. Inman.

Copyright © 1993 by ASME
Downloaded 03 May 2010 to 171.66.16.245. Redistribution subject to ASME license or copyright; see http://www.asme.org/terms/Terms_Use.cfm

$$\ddot{u}^{(n)}(t)+D\dot{u}^{(n)}(t)+\Lambda u^{(n)}(t)=h(t)+(D-F)\dot{u}^{(n-1)}(t) \quad (2a)$$

with

$$u^{(n)}(t_o)=z_o,\ n=0,1,2,\ \ldots, \quad (2b)$$

$$\dot{u}^{(n)}(t_o)=\dot{z}_o,\ n=1,2,\ \ldots,\ \text{and}, \quad (2c)$$

$$\dot{u}^{(o)}(t)=0,\ t\in(t_o,\ T], \quad (2d)$$

where the superscript 'n'' indicates the respective quantities at the nth iteration. They solved the *coupled* system of Eqs. (1) by considering the iterative scheme comprised of equations (2*a*), (2*b*), (2*c*), and (2*d*) where each iteration required the solution of an uncoupled system of equations. The right-hand side of (2*a*) was referred to by them as the "pseudo-force."

They showed that $u^{(n)}(t) \to z(t)$ almost everywhere (a.e.): (1) when the matrix F is strictly diagonally dominant, or (2) when F is a positive-definite symmetric matrix and the eigenvalues of $D^{-1}F$ are less than 2.

In this paper we extend the convergence results pertaining to the situation where the matrix F is positive definite and symmetric, but not necessarily diagonally dominant. Some of these results were first developed in Udwadia (1989); we show that by a slight variation of the previous iterative method we can guarantee convergence, thereby removing the restriction that the eigenvalues of $D^{-1}F$ be less than 2.

2 The Iterative Scheme

The matrix F was decomposed in the form (Udwadia and Esfandiari, 1990):

$$F=D+B. \quad (3a)$$

This led Eq. (1) to be recast into the iterative form given in Eq. (2*a*).

Here, we propose a slight variant to the scheme (3*a*), and decompose the matrix F now as

$$F=\alpha D+\{B+(1-\alpha)D\} := D_1+E, \quad (3b)$$

where D is again a diagonal matrix whose entries are the diagonal entries of matrix F. The parameter α is, an as yet unknown, positive scalar, $D_1 = \alpha D$, and $E = B + (1 - \alpha)D$. We use the same iterative scheme as in (2) except that the matrix D_1 replaces the matrix D now in Eq. (2*a*). Thus, Eq. (2*a*) is replaced by

$$\ddot{u}^{(n)}(t)+D_1\dot{u}^{(n)}(t)+\Lambda u^{(n)}(t)=h(t)+(D_1-F)\dot{u}^{(n-1)}(t) \quad (2'a)$$

The new iterative scheme is now constituted by Eqs. (2′*a*), (2*b*), (2*c*), and (2*d*).

3 Convergence of the Variant Scheme for Symmetric, Positive-definite Damping Matrices

Since scheme (3*b*) is obtained from (3*a*) by replacing D by D_1 and B by E, several of the results obtained in Udwadia and Esfandiari (1990) remain valid when the matrices D and B are replaced by D_1 and E, respectively. Also, the proofs of these results can be obtained by a direct replacement of D by D_1 and B by E in the earlier proofs. Therefore, for the sake of brevity, we simply state the results here and for those proofs which follow *mutatis mutandis*, we refer the reader to their 1990 paper. We note that since F is symmetric, E is also symmetric.

We denote $S(\omega) = [\omega(\omega A)^{-1}E]$, where $\omega A = -\omega D_1 + i\omega G$. The matrix G is defined by the relation $\omega G = \text{Diag}\,\{\omega^2 - \lambda_1, \omega^2 - \lambda_2, \ldots, \omega^2 - \lambda_N\}$, where λ_i are the diagonal elements of Λ (for details, see Udwadia and Esfandiari (1990)).

Theorem 1: $u^{(n)}(t) \to z(t)$ almost everywhere (a.e.) if and only if $S(\omega)$ is quasi-nilpotent, i.e., $\{S(\omega)\}^n \to 0$, for all $\omega \in \mathbf{R}$, as $n \to \infty$.

This condition is equivalent to the spectral radius of $S(\omega)$, denoted $\rho_S(\omega)$, being less than unity for all $\omega \in \mathbf{R}$.

Proof: See Udwadia and Esfandiari (1990).

We now give the following results:

Lemma 1: $\rho_S(\omega) := \rho_{A^{-1}E}(\omega) \le \rho_{D_1^{-1}E}$.

Proof: Similar to Lemma 3 in Udwadia and Esfandiari (1990) when D is replaced by D_1 and B by E. ■

Lemma 2: The eigenvalues of
(a) $D_1^{-1}E$ are all real, and those of
(b) $D_1^{-1}F$ are all real and positive and identical to those of $F' = D_1^{-1/2}FD_1^{-1/2}$.

Proof: (a) Since the eigenvalues of $D_1^{-1}E$ and $D_1^{-1/2}ED_1^{-1/2}$ are identical, the result follows. (b) It is obvious that the eigenvalues of $D_1^{-1}F$ are identical to those of $D_1^{-1/2}FD_1^{-1/2}$. Since F is positive definite, the result follows. ■

Lemma 3: $\rho_{D_1^{-1}E} < 1$ if and only if every eigenvalue, μ, of $D_1^{-1}F$ is such that $0 < \mu < 2$, i.e., $\rho_{D_1^{-1}E} < 1 \Leftrightarrow \rho_{D_1^{-1}F} < 2$.

Proof: (Similar to the proofs of Lemmas 4 and 5 in Udwadia and Esfandiari (1990), again replacing D by D_1 and B by E.) We provide here, however, a more straightforward proof.

We start by noting Lemma 2. Let λ be an eigenvalue of $D_1^{-1}E$ and y the corresponding eigenvector. Then, since $E = F - D_1$, we get

$$D_1^{-1}Fy=(\lambda+1)y. \quad (4)$$

Thus, the eigenvalue $\mu = \lambda + 1$. Since $\rho_{D_1^{-1}E} < 1$, we have, for any eigenvalue λ, $|\lambda| < 1$, and therefore for all μ, $\mu < 2$. The converse can be similarly proved. ■

Theorem 2: The iterative scheme represented by equations (2′*a*), (2*b*), (2*c*), and (2*d*) converges for all values of the scalar, α, for which

$$\alpha > \left[\frac{\rho_{D^{-1}F}}{2}\right] = \frac{\lambda_{\max}(D^{-1}F)}{2}. \quad (5)$$

Proof: We have shown that $\rho_{D_1^{-1}E} < 1 \Leftrightarrow \rho_{D_1^{-1}F} < 2$. But since $D_1^{-1} = (1/\alpha)D^{-1}$, $\rho_{D_1^{-1}F} = \rho_{D^{-1}F}/\alpha$. Thus, we have $\rho_{D_1^{-1}F} < 2$, whenever $\alpha > \lambda_{\max}(D^{-1}F)/2$. Hence, we have shown that when the scalar α satisfies relation (5), $\rho_{D_1^{-1}E} < 1$, and by Theorem 1 and Lemma 1, the result follows. ■

We next provide an estimate of the spectral radius of $D^{-1}F$ which does not need any eigenvalue computations.

Lemma 4: $\rho_{D^{-1}F} < N$, where N is the dimension of the square matrix F.

Proof: We note that the eigenvalues λ of $D^{-1}F$ are identical to those of $\hat{F} := D^{-1/2}FD^{-1/2}$. But the elements of $\hat{F}$ are given by

$$[\hat{F}]_{i,j}=\begin{cases}1, & i=j\\ \dfrac{f_{ij}}{\sqrt{f_{ii}f_{jj}}}, & i\neq j\end{cases} \quad \text{where } [F]_{ij}=f_{ij}. \quad (6)$$

Downloaded 03 May 2010 to 171.66.16.245. Redistribution subject to ASME license or copyright; see http://www.asme.org/terms/Terms_Use.cfm

Since the matrix F is positive definite, the modulus of each of its off-diagonal elements (see Eq. (6)), is less than or equal to unity. Using Gerschgorin's Theorem (Noble, 1969), we then find that for any eigenvalue λ of $D^{-1}F$, $|\lambda - 1| < N - 1$. Using Lemma 2(b) again, we obtain the result.

Theorem 3: The iterative scheme of equations (2′a), (2b), (2c), and (2d) converges for *all* symmetric, positive-definite damping matrices, F, for all $\alpha > N/2$.

Proof: Using Theorem 2 and Lemma 4, the result is obvious. ■

The rate of convergence of the iterative scheme defined by equations (2′a), (2b), (2c), and (2d) depends on the spectral radius of the matrix $S(\omega)$; the smaller this spectral radius, the faster the asymptotic convergence. This spectral radius is controlled by the value of the parameter α. In Theorem 3 we provide a value of α which requires no eigenvalue computations and assures convergence; yet, this convergence may be very slow.

Lemma 1 shows that the spectral radius of $S(\omega)$ is always less than or equal to the spectral radius of $D_1^{-1}E$. We now present a result related to the optimal value of the parameter α so that the spectral radius of the matrix, $D_1^{-1}E$, is a minimum. However, the determination of this value of α, requires a knowledge of, or an estimate of, the highest and lowest eigenvalues of $D^{-1}F$.

Lemma 5. The spectral radius of the matrix $D_1^{-1}E$ is a minimum when the parameter α is given by (Udwadia, 1992),

$$\alpha_{\text{opt}} = \frac{\lambda_{\max}(D^{-1}F) + \lambda_{\min}(D^{-1}F)}{2}. \tag{8}$$

The spectral radius for this value of α, i.e., $\alpha = \alpha_{\text{opt}}$ is

$$\min_{\alpha} \rho_{D_1^{-1}E} := \kappa = \frac{\lambda_{\max}(D^{-1}F) - \lambda_{\min}(D^{-1}F)}{\lambda_{\max}(D^{-1}F) + \lambda_{min}(D^{-1}F)}. \tag{9}$$

Proof: We note that

$$\lambda_i(D_1^{-1}E) = \lambda_i(D_1^{-1}F - I) = \lambda_i(D_1^{-1}F) - 1 = \frac{\lambda_i(D^{-1}F)}{\alpha} - 1, \tag{10}$$

where by $\lambda_i(*)$ we mean the ith eigenvalue of "$*$". The value of α that causes $\rho(D_1^{-1}E)$ to be a minimum therefore requires us to find α such that we minimize

$$\min_{\alpha} \rho_{D_1^{-1}E} := \operatorname{Min}_{\alpha} \left\{ \operatorname{Max}_{\forall i} \left| \frac{\lambda_i(D^{-1}F)}{\alpha} - 1 \right| \right\}. \tag{11}$$

This minimization can be geometrically thought of as a "rescaling" of the eigenvalues $\lambda_i(D^{-1}F)$ by a constant α such that the rescaled, extreme-outliers among them lie "closest" to unity. Noting that the eigenvalues of $D^{-1}F$ are always positive, this can be achieved uniquely by placing unity at the center of the rescaled interval over which these eigenvalues span. This requires that we satisfy the following condition:

$$\frac{\lambda_{\max}(D^{-1}F)}{\alpha_{\text{opt}}} - 1 = 1 - \frac{\lambda_{\min}(D^{-1}F)}{\alpha_{\text{opt}}}. \tag{12}$$

From this relation, the result in Eq. (8) follows. We note in passing that α_{opt} always satisfies relation (5).

Again, looking at it geometrically, for $\alpha = \alpha_{\text{opt}}$ the spectral radius is obtained as

$$\rho_{D_1^{-1}E} = \operatorname{Max}_{\forall i} \left| \frac{\lambda_i(D^{-1}F)}{\alpha_{\text{opt}}} - 1 \right|. \tag{13}$$

The maximum of the right-hand side, because of our rescaling, will occur for both $\lambda_i(D^{-1}F) = \lambda_{\max}(D^{-1}F)$, and $\lambda_i(D^{-1}F) = \lambda_{\min}(D^{-1}F)$. Using these values in Eq. (13) we obtain the result given in Eq. (9). ■

Thus, the smallest spectral radius of $D_1^{-1}E$ occurs for $\alpha = \alpha_{\text{opt}}$, where α_{opt} is the arithmetic mean of the highest and lowest eigenvalues of $D^{-1}F$. The value of this spectral radius, κ, by Eq. (9), is always less than unity.

Theorem 4: For a given positive-definite symmetric damping matrix F, when the parameter α defining the matrix D_1 in the iterative scheme given by (2′a), (2b), (2c), (2d), and 3(b) is chosen to be α_{opt}, where α_{opt} is given by Eq. (8), then the spectral radius of the matrix $S(\omega)$ satisfies the relation

$$\rho_S(\omega) \le \kappa < 1, \tag{14}$$

where the parameter κ is defined in Eq. (9).

Proof: The result follows from Lemma 1 and Lemma 5. ■

We observe that the determination of both the parameters α_{opt} and κ in the above theorem relies on a determination of the highest and lowest eigenvalues of $D^{-1/2}FD^{-1/2}$. Good estimates of these two parameters can be obtained with little computational effort even for large-order matrices, F, because reliable *estimates* of the highest and lowest eigenvalues of $D^{-1/2}FD^{-1/2}$ can be found very efficiently. For example, one could use the conjugate gradient method to obtain a much lower dimensional tri-diagonal matrix from which estimates of the lowest and highest eigenvalues, and thence estimates of α_{opt} and κ, can be rapidly determined.

We observe from Lemmas 1 and 5 that the value of κ in Eq. (9) appears to be the *lowest upper bound* value of $\rho_S(\omega)$ which is independent of ω; it is in this sense that α_{opt} may be thought of as an *estimate* of the optimal value of α for fastest convergence of the iterative scheme suggested by Eqs. (2′a), (2b), (2c), and (2d).

4 Numerical Examples

In this section we present two numerical examples of the results developed in this paper.

Example 1: Consider the reduced damping matrix, F, given by

$$F = \begin{bmatrix} 0.3 & 0.2 & 0.3 & 0.4 & 0.2 \\ 0.2 & 1.0 & 1.0 & 0.2 & 0.3 \\ 0.3 & 1.0 & 1.5 & 0.4 & 0.2 \\ 0.4 & 0.2 & 0.4 & 1.0 & 0.1 \\ 0.2 & 0.3 & 0.2 & 0.1 & 0.5 \end{bmatrix}.$$

The spectral radius $\rho_{D^{-1}F} = 2.713$. The smallest eigenvalue of $D^{-1}F$ is 0.1167. Thus, by Lemma 1, the standard iterative method may fail to converge. However, the scheme proposed herein will assuredly converge, according to Theorem 2, for all $\alpha > 1.357$. We note, however, that application of Theorem 2 requires knowledge of the largest eigenvalue of $D^{-1}F$. The estimate provided by Theorems 3 which avoids such eigenvalue computations yields $\alpha > 2.5$. The value of α_{opt} is found, using Lemma 5, to be 1.415.

In Fig. 1, the spectral radii of $D_1^{-1}E$ (solid line), and $D_1^{-1}F$ (dashed line) are plotted versus the parameter $\beta = \alpha/\rho_{D^{-1}F}$. We note that when β has a value of 0.5, the spectral radius of $D_1^{-1}E$ is unity. With increasing β, the spectral radius of $D_1^{-1}E$ decreases and then increases, as expected, back to unity as $\beta \to \infty$. On the other hand, the spectral radius of $D_1^{-1}F$ (dashed line) is seen to monotonically decrease with increasing β, again as expected. The value of β when the spectral radius of $D_1^{-1}E$

Downloaded 03 May 2010 to 171.66.16.245. Redistribution subject to ASME license or copyright; see http://www.asme.org/terms/Terms_Use.cfm

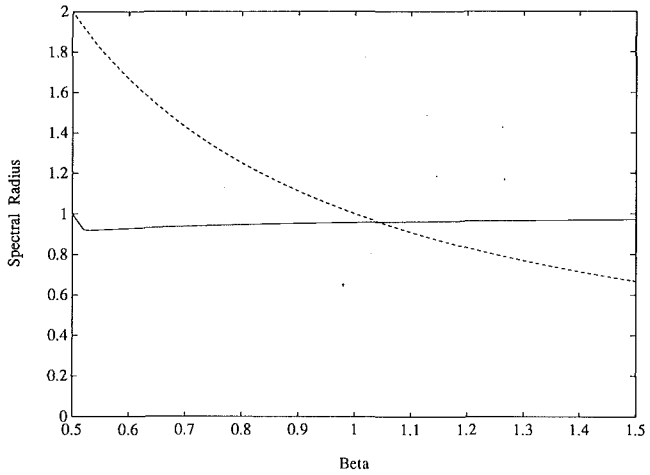


Fig. 1 The spectral radii, $\rho_{D_1^{-1}E}$ and $\rho_{D_1^{-1}F}$, as functions of β. The radius, $\rho_{D_1^{-1}F}$, shown in the dashed line, monotonically decreases with increasing β, while $\rho_{D_1^{-1}E}$, shown in the solid line, reduces first and then asymptotically approaches unity for large values of β. The optimal value of β for which $\rho_{D_1^{-1}E}$ is a minimum is 0.5215.

is a minimum is obtained, using Lemma 5, as 0.5215; the spectral radius, κ, for this value of β is found, by Eq. (9), to be 0.9174. The numerical computations performed show that this optimal value of β, as also the spectral radius corresponding to this value of β, are both correctly predicted by Lemma 5.

Example 2. Consider the three degree-of-freedom system described by Eq. (1) with the following parameter values:

(a) $\Lambda = \text{Diag}\{20, 25, 20\}$,
(b) $z_0 = [1,1,1]^T$, $\dot{z}_0 = [0, 0, 0]^T$,
(c) $h = (t) = [2\text{Sin}\sqrt{20t}, -2\text{Sin}\sqrt{20t}, 2\text{Sin}\sqrt{20t}]^T$ and,

(d) $$F = \begin{bmatrix} 0.4 & 0.3 & 0.1 \\ 0.3 & 0.6 & 0.45 \\ 0.1 & 0.45 & 0.5 \end{bmatrix}$$

The matrix F is symmetric and positive definite. However, $\rho_{D^{-1}F} = 2.1391$. This spectral radius being greater than 2, the iterative scheme proposed in Udwadia and Esfandiari (1990) would not be guaranteed to converge. The variant scheme proposed in this paper requires that the value of α must, according to Theorem 2, be greater than 1.0695 to ensure convergence. By Theorem 4 the optimal value α_{opt}, is, 1.1067. Figure 2 shows the results for the iterative scheme proposed in this paper for $\alpha = 1.1067\ (= \alpha_{\text{opt}})$. The fourth-order Runge-Kutta method (with a time step of 0.01 time units) is used to compare results. The normalized error at the nth iteration $N_i^{(n)}$, in the ith component of the displacement is defined as

$$N_i^{(n)} = \frac{RMS \text{ of } \{z_i^{RK}(t) - u_i^{(n)}(t)\}}{RMS \text{ of } z_i^{RK}(t)}$$

where $z_i^{RK}(t)$ is the ith component determined by the Runge-Kutta scheme and $u_i^{(n)}(t)$ is the ith component of the response obtained at the nth iteration. Figure 2(a) shows the normalized error plotted versus the iteration number for each component of the displacement. The actual *RMS* values of the three components determined from Runge-Kutta integration are also shown. The normalized errors at the eighth iteration for the three displacement components are 0.00038, 0.00046, and 0.00146, respectively. Figure 2(b) shows the second component of the displacement response obtained by the Runge-Kutta integration (referred to in the plot as "exact") and compares it with that obtained by the iterative approach at the first, fourth, and eighth iterations. With the scales used in the plot, the response at the eighth iteration is virtually indistinguishable from the Runge-Kutta results. Figures 3(a) and 3(b) show similar results with $\alpha = 2.2134$, a value of α approximately twice its optimal value. The first, fourth, and tenth iteration results are plotted along with the Runge-Kutta results. The tenth iteration result is virtually indistinguishable from the "exact" response. The plots show that convergence now requires a larger number of iterations. The normalized errors in the three displacement components at the end of the tenth iteration are now 0.00237, 0.00237, and 0.00479, respectively.

Udwadia and Esfandiari (1990) have given a comparison of the number of multiplications needed by the Runge-Kutta method, and those needed by the iterative scheme described by Eqs. (2′a), (2b), (2c), and (2d). They conclude that the iterative scheme is computationally superior when it converges in less than about 16 iterations. In the example shown, this is the case for both values of α, though, as expected, the convergence is much improved when $\alpha = \alpha_{\text{opt}}$.

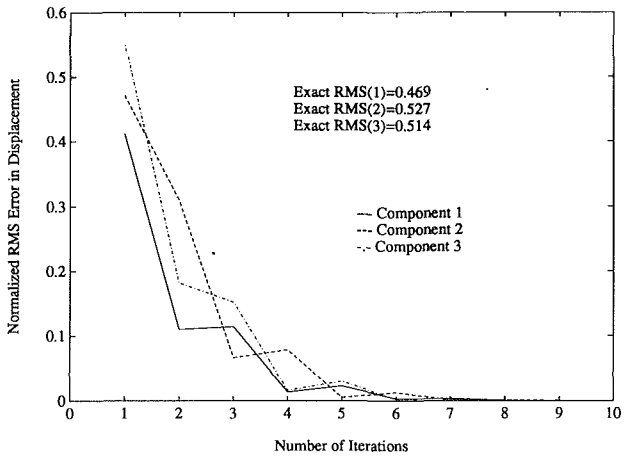


Fig. 2(a) Normalized error versus iteration number showing rate of convergence of the scheme for $\alpha = \alpha_{\text{opt}}$

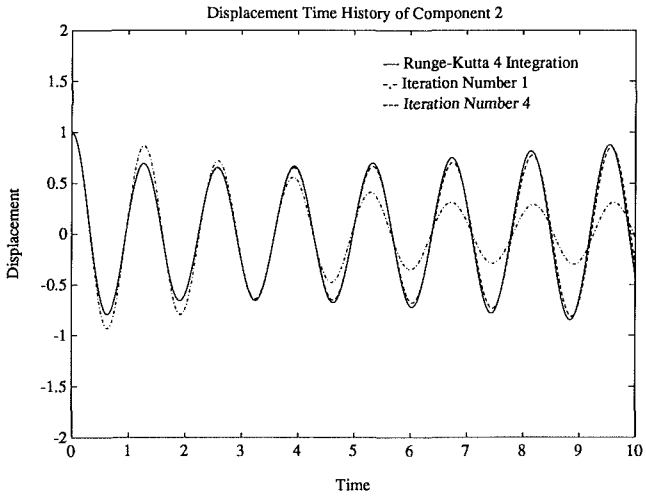


Fig. 2(b) Time histories of the second component of the response for $\alpha = \alpha_{\text{opt}}$

Downloaded 03 May 2010 to 171.66.16.245. Redistribution subject to ASME license or copyright; see http://www.asme.org/terms/Terms_Use.cfm

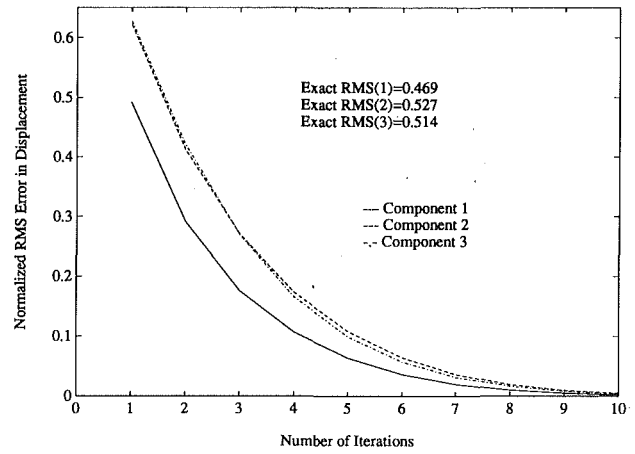


Fig. 3(*a*) Normalized error versus iteration number showing a slower rate of convergence of the scheme for $\alpha = 2\alpha_{opt}$

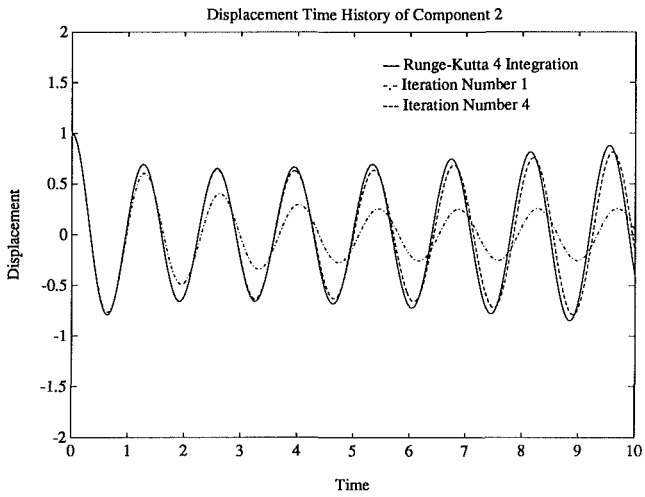


Fig. 3(*b*) Time histories of the second component of the response for $\alpha = 2\alpha_{opt}$

5 Conclusions

We have used in this paper a slight variant, namely relation (3*b*), of the original decomposition of the matrix F used in Udwadia and Esfandiari (1990), to create an iterative scheme for the determination of the response of nonclassically damped dynamic systems. The iterative scheme so generated is analytically studied, and it is shown to converge to the exact response of the coupled nonclassically damped system almost everywhere (a.e.) for *all* damping matrices which are positive definite and symmetric, provided the parameter α is appropriately chosen. This generalization of our previous result thus makes a larger class of damping matrices amenable to the iterative approach. Estimates of the parameter α which yield the highest asymptotic rate of convergence have also been provided along with estimates of these rates of convergence.

Acknowledgments

The author thanks Mr. Ravi Kumar for performing the computations presented in Figs. 2 and 3.

References

Noble, B., 1969, *Applied Linear Algebra*, Prentice-Hall, Englewood Cliffs, NJ.

Udwadia, F. E., 1989, "Some Analytical Results on the Iterative Approaches to the Determination of the Response of Nonclassically Damped Systems With Symmetric, Positive Definite Damping Matrices," University of Southern California Report, Department of Mechanical Engineering, Los Angeles, CA.

Udwadia, F. E., and Esfandiari, R., 1990, "Nonclassically Damped Dynamic Systems: An Iterative Approach," ASME JOURNAL OF APPLIED MECHANICS, Vol. 57, pp. 423–433.

Udwadia, F. E., 1992, "Some Convergence Results Related to the JOR Iterative Method for Symmetric, Positive-Definite Matrices," *Applied Mathematics and Computation*, Vol. 47, No. 1, pp. 37–45.

On the Interaction of Torsion and Bending in Rotating Shafts

C. Nataraj[19]

The problem of torsional and transverse deformations of a shaft rotating at a constant speed is considered. The displacements are expressed in a perturbation series in terms of a small parameter. Energy expressions are derived to each order and Hamilton's principle is applied to obtain the equations of motion and the boundary conditions governing the displacement functions of different orders. It is clearly shown that the interaction of torsion and transverse vibration occurs at second order. Previous work reporting results of torsional vibration caused at a frequency equal to twice the rotational speed due to this interaction is confirmed.

Introduction

The interaction of torsional and flexural vibration in rotating shafts has been subjected to some study in the past. Some early results can be found in Tondl (1965), in which he considered a turbogenerator shaft with a synchronizing moment.

Broniarek (1968) showed that torsional vibrations can be caused by parametric excitation due to transverse vibrations. Gasch et al. (1979) obtained a quasi-static torsional response due to coupling which was a first approximation result. Kellenberger (1980) considered the effect of a harmonic torque upon transverse vibration. Bernasconi (1987) analyzed the cause of a $2X$ torsional vibration induced by transverse vibration and correctly traces it to the gyroscopic effect.

The objective of this paper is to derive accurate expressions for the energy terms and to obtain the relevant equations and boundary conditions using a perturbation approach to show clearly the level and extent of interaction between torsion and flexure.

Mathematical Development

Coordinate Systems. Let $OXYZ$ be a fixed coordinate system (relative to the shaft housing), considered here to be an inertial frame of reference. An element of the shaft is considered to be a disk of infinitesimal thickness and is located with the aid of several displacements and rotations.

[19]Department of Mechanical Engineering, Villanova University, Villanova, PA 19085-1681. Assoc. Mem. ASME.

Contributed by the Applied Mechanics Division of THE AMERICAN SOCIETY OF MECHANICAL ENGINEERS for publication in the ASME JOURNAL OF APPLIED MECHANICS.

Manuscript received by the ASME Applied Mechanics Division, Jan. 25, 1991; final revision, Feb. 7, 1992. Associate Technical Editor: A. K. Noor.

Downloaded 03 May 2010 to 171.66.16.245. Redistribution subject to ASME license or copyright; see http://www.asme.org/terms/Terms_Use.cfm

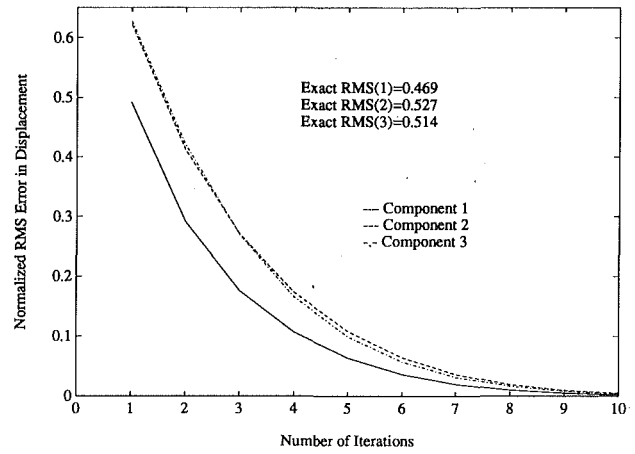


Fig. 3(*a*) Normalized error versus iteration number showing a slower rate of convergence of the scheme for $\alpha = 2\alpha_{opt}$

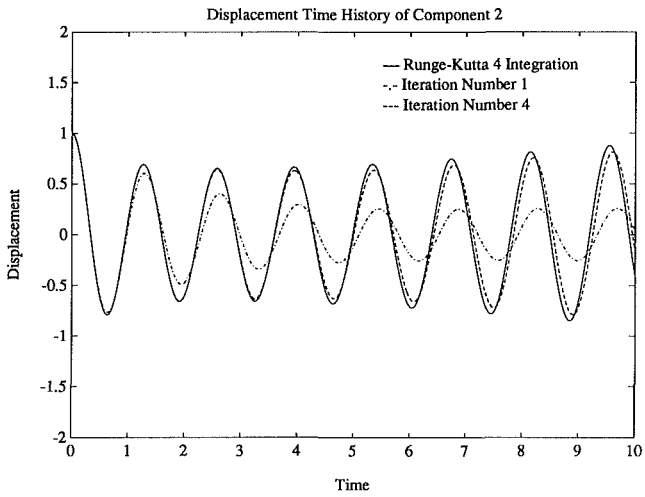


Fig. 3(*b*) Time histories of the second component of the response for $\alpha = 2\alpha_{opt}$

5 Conclusions

We have used in this paper a slight variant, namely relation (3*b*), of the original decomposition of the matrix F used in Udwadia and Esfandiari (1990), to create an iterative scheme for the determination of the response of nonclassically damped dynamic systems. The iterative scheme so generated is analytically studied, and it is shown to converge to the exact response of the coupled nonclassically damped system almost everywhere (a.e.) for *all* damping matrices which are positive definite and symmetric, provided the parameter α is appropriately chosen. This generalization of our previous result thus makes a larger class of damping matrices amenable to the iterative approach. Estimates of the parameter α which yield the highest asymptotic rate of convergence have also been provided along with estimates of these rates of convergence.

Acknowledgments

The author thanks Mr. Ravi Kumar for performing the computations presented in Figs. 2 and 3.

References

Noble, B., 1969, *Applied Linear Algebra*, Prentice-Hall, Englewood Cliffs, NJ.

Udwadia, F. E., 1989, "Some Analytical Results on the Iterative Approaches to the Determination of the Response of Nonclassically Damped Systems With Symmetric, Positive Definite Damping Matrices," University of Southern California Report, Department of Mechanical Engineering, Los Angeles, CA.

Udwadia, F. E., and Esfandiari, R., 1990, "Nonclassically Damped Dynamic Systems: An Iterative Approach," ASME JOURNAL OF APPLIED MECHANICS, Vol. 57, pp. 423–433.

Udwadia, F. E., 1992, "Some Convergence Results Related to the JOR Iterative Method for Symmetric, Positive-Definite Matrices," *Applied Mathematics and Computation*, Vol. 47, No. 1, pp. 37–45.

On the Interaction of Torsion and Bending in Rotating Shafts

C. Nataraj[19]

The problem of torsional and transverse deformations of a shaft rotating at a constant speed is considered. The displacements are expressed in a perturbation series in terms of a small parameter. Energy expressions are derived to each order and Hamilton's principle is applied to obtain the equations of motion and the boundary conditions governing the displacement functions of different orders. It is clearly shown that the interaction of torsion and transverse vibration occurs at second order. Previous work reporting results of torsional vibration caused at a frequency equal to twice the rotational speed due to this interaction is confirmed.

Introduction

The interaction of torsional and flexural vibration in rotating shafts has been subjected to some study in the past. Some early results can be found in Tondl (1965), in which he considered a turbogenerator shaft with a synchronizing moment.

Broniarek (1968) showed that torsional vibrations can be caused by parametric excitation due to transverse vibrations. Gasch et al. (1979) obtained a quasi-static torsional response due to coupling which was a first approximation result. Kellenberger (1980) considered the effect of a harmonic torque upon transverse vibration. Bernasconi (1987) analyzed the cause of a $2X$ torsional vibration induced by transverse vibration and correctly traces it to the gyroscopic effect.

The objective of this paper is to derive accurate expressions for the energy terms and to obtain the relevant equations and boundary conditions using a perturbation approach to show clearly the level and extent of interaction between torsion and flexure.

Mathematical Development

Coordinate Systems. Let $OXYZ$ be a fixed coordinate system (relative to the shaft housing), considered here to be an inertial frame of reference. An element of the shaft is considered to be a disk of infinitesimal thickness and is located with the aid of several displacements and rotations.

[19]Department of Mechanical Engineering, Villanova University, Villanova, PA 19085-1681. Assoc. Mem. ASME.

Contributed by the Applied Mechanics Division of THE AMERICAN SOCIETY OF MECHANICAL ENGINEERS for publication in the ASME JOURNAL OF APPLIED MECHANICS.

Manuscript received by the ASME Applied Mechanics Division, Jan. 25, 1991; final revision, Feb. 7, 1992. Associate Technical Editor: A. K. Noor.

Copyright © 1993 by ASME
Downloaded 03 May 2010 to 171.66.16.245. Redistribution subject to ASME license or copyright; see http://www.asme.org/terms/Terms_Use.cfm

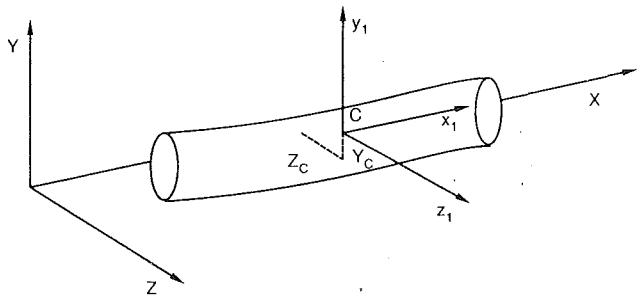


Fig. 1 Coordinate systems

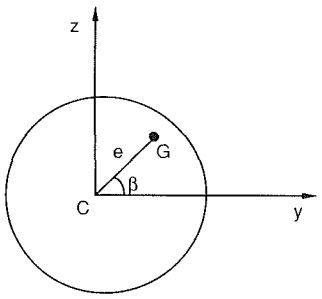


Fig. 2 A cross-section of the shaft

The geometric center, C, of the disk is located by the axial location, X_C, and the transverse displacements, Y_C, and Z_C (Fig. 1). Also shown in the figure is the set of axes $Cx_1y_1z_1$ which is fixed to the geometric center of the disk, and is hence translating with respect to the axes $OXYZ$ such that it is always parallel to it.

Next, a sequence of Euler angle rotations, ψ, θ, and ϕ are specified in order to locate every point of the infinitesimal disk in space. It should be noted that the angle ϕ essentially consists of the rigid-body rotation and the torsional vibration of the shaft. Hence, in subsequent analysis, ψ and θ can be considered to be small, but not ϕ.

Small Deformation Approximations. It is assumed in this analysis that the unbalance eccentricity is small; that both the torsional and transverse deformations are small and of the same order; and that the rotor spins with a constant angular velocity.

Hence, using a small quantity, $\epsilon \ll 1$, all the displacement coordinates can be expressed in the form of a straightforward expansion as shown by example of Y_c:

$$Y_c = \epsilon Y_1 + \epsilon^2 Y_1 + \cdots. \tag{1}$$

Note that the ϕ expansion contains a zeroth-order term, which corresponds to the rigid-body rotation of the shaft; ϕ_1, ϕ_2, etc., are the torsional deformation coordinates. Hence,

$$\phi = \phi_0 + \epsilon\phi_1 + \epsilon^2\phi_2 + \cdots \tag{2}$$

where $\dot{\phi}_0 = \Omega$, the constant rotational speed of the shaft.

The unbalance eccentricity and the axial torque are also expressed in similar series. Note that the zeroth-order term should be omitted from the torque series, which is consistent with the assumption that the rotational speed Ω is constant.

Kinematics. The angular velocity of the xyz frame relative to the reference frame $x_1y_1z_1$ expressed in body-fixed coordinates xyz is of the standard type (Greenwood, 1965), and is hence not given here.

With reference to Fig. 2, note that C is the geometric center, G is the mass center, e is the unbalance eccentricity at any position along the length of the shaft, and β is the unbalance phase. The velocity of the mass center with respect to the fixed frame is then

$$\begin{aligned}\mathbf{V}_G = {} & [\dot{Y}_C \sin\psi\cos\theta - \dot{Z}_C \sin\theta + e\dot{\theta}\sin(\phi+\beta) \\ & - e\dot{\psi}\cos\theta\cos(\phi+\beta)]\mathbf{i} \\ & + [\dot{Y}_C(\cos\psi\cos\phi + \sin\psi\sin\theta\sin\phi) \\ & + \dot{Z}_C\cos\theta\sin\phi - e(\dot{\phi} - \dot{\psi}\sin\theta)\sin\beta]\mathbf{j} \\ & + [\dot{Y}_C(-\cos\psi\sin\phi + \sin\psi\sin\theta\cos\phi) \\ & + \dot{Z}_C\cos\theta\cos\phi + e(\dot{\phi} - \dot{\psi}\sin\theta)\cos\beta]\mathbf{k} \end{aligned} \tag{3}$$

Energy Expressions. The kinetic energy of the shaft per unit length is given by

$$\hat{T} = \frac{1}{2} m V_G^2 + \frac{1}{2} I_p \omega_x^2 + \frac{1}{2} I_d(\omega_y^2 + \omega_z^2) \tag{4}$$

where, I_p and I_d are the polar and diametral moments of inertia (per unit length), respectively, and m is the mass per unit length of the shaft.

With standard assumptions of linear elasticity and neglecting shear, the potential energy per unit length is given by

$$\hat{U} = \frac{1}{2} GJ(\phi')^2 + \frac{1}{2} EI[(Y_c'')^2 + (Z_c'')^2] \tag{5}$$

where GJ and EI are the torsional and flexural rigidities of the shaft, respectively, and the primes denote derivatives with respect to the axial coordinate.

The virtual work due to the axial torque $T(x, t)$ per unit length is found to be

$$\delta\hat{W}_e = -T\sin\theta\,\delta\psi + T\,\delta\phi. \tag{6}$$

Substituting for the velocities and using the perturbation series for the deformations, the energy expressions can be written to different orders. The detailed expressions are omitted here to conserve space.

Equations of Motion. When the generalized Hamilton's principle is applied to the energy expressions obtained earlier and some kinematical constraints are imposed, partial differential equations associated with each coordinate are obtained. Separating terms of different order, the equations governing the displacement at each order can be obtained.

At $O(\epsilon)$, the transverse and torsional deformations are completely decoupled from each other (in the equations of motion as well as in the boundary conditions) and can be solved independently; i.e., within the framework of the assumptions of this analysis, torsional motion can not induce transverse motion and vice versa at this order. The individual differential equations along with their respective boundary conditions are fairly standard and can be solved easily.

The equations of motion at $O(\epsilon^2)$, however, display an interaction between the two motions and are given as follows:

$$\begin{aligned}(EIY_2'')'' + m\ddot{Y}_2 - (I_d\ddot{Y}_2')' - (I_p\Omega\dot{Z}_2')' = {} & (I_p\dot{\phi}_1 Z_1')' + (I_p\dot{\phi}_1\dot{Z}_1')' \\ & + \frac{\partial}{\partial t}[me_2\Omega\sin(\phi_0+\beta)] + \frac{\partial}{\partial t}[me_1\Omega\phi_1\cos(\phi_0+\beta)] \\ & + \frac{\partial}{\partial t}[me_1\dot{\phi}_1\sin(\phi_0+\beta)] - (T_1Z_1')' \end{aligned} \tag{7}$$

$$\begin{aligned}(EIZ_2'')'' + m\ddot{Z}_2 - (I_d\ddot{Z}_2')' + (I_p\Omega\dot{Y}_2')' = {} & -(I_p\dot{\phi}_1 Y_1')' \\ & - \frac{\partial}{\partial t}[me_2\Omega\cos(\phi_0+\beta)] + \frac{\partial}{\partial t}[me_1\Omega\phi_1\sin(\phi_0+\beta)] \\ & - \frac{\partial}{\partial t}[me_1\dot{\phi}_1\cos(\phi_0+\beta)] \end{aligned} \tag{8}$$

$$\begin{aligned}(GJ\phi_2')' - I_p\ddot{\phi}_2 = {} & I_p\frac{\partial}{\partial t}(\dot{Y}_1'Z_1') \\ & - me_1[\ddot{Y}_1\sin(\phi_0+\beta) - \ddot{Z}_1\cos(\phi_0+\beta)] + T_2. \end{aligned} \tag{9}$$

Downloaded 03 May 2010 to 171.66.16.245. Redistribution subject to ASME license or copyright; see http://www.asme.org/terms/Terms_Use.cfm

The associated boundary conditions also display interaction and are not listed here in the interest of brevity. In the above equations the torsional vibration ϕ_1 appears as a forcing term on the right-hand side of the transverse vibrational equations, and the transverse coordinates Y_1 and Z_1 appear in the torsional equation. Hence, it is clear that there is an interaction between the two motions at this order (and at higher orders).

Example

In order to better understand the mode of interaction between torsion and flexure, a simple example of a uniform circular shaft which is simply supported at both ends is considered. It will be assumed that the torque fluctuations are zero.

At $O(\epsilon)$, the unbalance response can be obtained by eigenfunction expansion in the form

$$Y_1(x, t) = \sum_{n=1}^{\infty} A_n \sin \frac{n\pi x}{l} \cos(\Omega t + \beta)$$

$$Z_1(x, t) = \sum_{n=1}^{\infty} A_n \sin \frac{n\pi x}{l} \sin(\Omega t + \beta) \tag{10}$$

where A_n is the amplitude of response in each mode. The torsion equation is homogeneous and can be solved easily to yield the eigenmodes.

The equations to the next order, $O(\epsilon^2)$, show an interaction between torsional and flexural motions as noted in the previous section. In the sequel, the torsional motion will be considered first, and using the results obtained, the effect on flexural vibration will be discussed.

The torsion equation for the case of the simple uniform shaft fixed at both ends simplifies to the following form, using the solution for Y_1 and Z_1.

$$GJ\phi_2'' - I_p\ddot{\phi}_2 =$$

$$-I_p\Omega^2\left[\sum_m \sum_n A_m A_n \frac{nm\pi^2}{l^2} \cos \frac{m\pi x}{l} \cos \frac{n\pi x}{l}\right] \sin[2(\Omega t + \beta)] \tag{11}$$

The solution to the above equation is found to be

$$\phi_2(x, t) = \left[\sum_k \frac{1}{-1 + \left(\frac{\delta_k}{2\Omega}\right)^2} \frac{F_k}{4} \sin \frac{k\pi x}{l}\right] \sin[2(\Omega t + \beta)] \tag{12}$$

where the kth modal generalized force (F_k) is due to the interaction with flexural motion and is given by

$$F_k = \frac{2}{l} \sum_m \sum_n A_m A_n \frac{mn\pi^2}{l^2} \int_0^l \sin \frac{k\pi x}{l} \cos \frac{m\pi x}{l} \cos \frac{n\pi x}{l}\, dx. \tag{13}$$

It is clear that a torsional motion at twice the rate of spin is caused due to the flexural motion. Hence, when the spin speed Ω is close to one half of any of the torsional natural frequencies (δ_k), resonance can occur.

Other Interaction Effects. Careful examination of the differential equations and their boundary conditions presented earlier yields several interesting results. Without explicit solution (like the one carried out in the previous section), one can make some general observations.

If the torque on the shaft is assumed to be constant such that T_1 is zero, then the first-order terms act as synchronous excitation on the second order for flexural vibration. Hence, the response of the rotor in flexure would be different in magnitude if the second order effect were included, but would still have a single frequency component, namely the spin speed of the rotor.

In practice, the torque on the rotor can vary with a frequency equal to the spin speed, or sometimes at twice the spin speed (Rao, 1983). If the torque varies with a frequency equal to the spin speed, $T_1 \sim e^{i\Omega t}$. Then, the torsional vibration to the first order exhibits the same frequency, and the flexural vibration (to the second order) will contain both Ω and 2Ω components. This is a case of flexural vibration induced by torsional vibration and is the counterpart of the example presented in the previous section.

If the torque varies at twice the spin speed, it follows that the torsional vibration at first order has the same frequency (2Ω), and the flexural vibration at second order can exhibit a response with Ω and 3Ω components.

In a practical situation, the presence of such higher frequency components in both torsional and flexural response is not only possible but is in fact frequently observed. The preceding analysis attempts to provide a clear explanation for such phenomena.

Conclusion

The problem of torsional and transverse deformations of a shaft rotating at a constant speed is considered. The displacements are expressed in a perturbation series in terms of a small parameter. Energy expressions are derived to each order and Hamilton's principle is applied to obtain the equations of motion and the boundary conditions governing the displacement functions of different orders.

A simple example of a uniform simply supported rotor is considered and it is clearly shown that the interaction of torsional and transverse vibration occurs at second order which confirms previously observed results. It is also shown that, with the help of the equatins derived, it is possible to determine further intreaction effects without carrying out a detailed solution. Some of the higher frequency components of vibration observed in practical rotating shafts can be explained by the model discussed.

References

Bernasconi, O., 1987, "Bisynchronous Torsional Vibrations in Rotating Shafts," ASME JOURNAL OF APPLIED MECHANICS, Vol. 54, pp. 893–897.

Broniarek, C., 1968, "Investigation of the Coupled Flexural-Torsional Vibration of Rotors with Continuous Parameters," *Zagadninia Drgan Nieliniowych*, No. 9, pp. 169–228.

Gasch, R., Market, R., and Pfützner, H., 1979, "Acceleration of Unbalanced Rotors through the Critical Speeds," *Journal of Sound and Vibration*, Vol. 63, No. 3, pp. 393–409.

Greenwood, D. T., 1965, *Principles of Dynamics*, Prentice-Hall, Englewood Cliffs, NJ.

Kellenberger, W., 1980, "Résonances Combinées Forcées de l'Arbre Tournant-Couplage de Flexion et Torsion," *Revue Brown-Bovery*, Vol. 2-80, pp. 117–121.

Rao, J. S., 1983, *Rotor Dynamics*, Wiley Eastern Ltd., New Delhi.

Tondl, A., 1965, *Some Problems of Rotor Dynamics*, Chapman and Hall, London.

Negativism: A Nonlinear Version

T. M. Atanackovic[20] and Dj. S. Djukic[20]

Introduction

Consider an elastic system that is in equilibrium under the

[20] Professor, University of Novi Sad, 21000 Novi Sad, Yugoslavia.

Contributed by the Applied Mechanics Division of THE AMERICAN SOCIETY OF MECHANICAL ENGINEERS for publication in the ASME JOURNAL OF APPLIED MECHANICS.

Manuscript received by the ASME Applied Mechanics Division, July 5, 1991; final revision, Feb. 28, 1992. Associate Technical Editor: D. J. Inman.

Downloaded 03 May 2010 to 171.66.16.245. Redistribution subject to ASME license or copyright; see http://www.asme.org/terms/Terms_Use.cfm

The associated boundary conditions also display interaction and are not listed here in the interest of brevity. In the above equations the torsional vibration ϕ_1 appears as a forcing term on the right-hand side of the transverse vibrational equations, and the transverse coordinates Y_1 and Z_1 appear in the torsional equation. Hence, it is clear that there is an interaction between the two motions at this order (and at higher orders).

Example

In order to better understand the mode of interaction between torsion and flexure, a simple example of a uniform circular shaft which is simply supported at both ends is considered. It will be assumed that the torque fluctuations are zero.

At $O(\epsilon)$, the unbalance response can be obtained by eigenfunction expansion in the form

$$Y_1(x, t) = \sum_{n=1}^{\infty} A_n \sin \frac{n\pi x}{l} \cos(\Omega t + \beta)$$

$$Z_1(x, t) = \sum_{n=1}^{\infty} A_n \sin \frac{n\pi x}{l} \sin(\Omega t + \beta) \tag{10}$$

where A_n is the amplitude of response in each mode. The torsion equation is homogeneous and can be solved easily to yield the eigenmodes.

The equations to the next order, $O(\epsilon^2)$, show an interaction between torsional and flexural motions as noted in the previous section. In the sequel, the torsional motion will be considered first, and using the results obtained, the effect on flexural vibration will be discussed.

The torsion equation for the case of the simple uniform shaft fixed at both ends simplifies to the following form, using the solution for Y_1 and Z_1.

$$GJ\phi_2'' - I_p\ddot{\phi}_2 =$$

$$-I_p\Omega^2\left[\sum_m \sum_n A_m A_n \frac{nm\pi^2}{l^2} \cos \frac{m\pi x}{l} \cos \frac{n\pi x}{l}\right] \sin[2(\Omega t + \beta)] \tag{11}$$

The solution to the above equation is found to be

$$\phi_2(x, t) = \left[\sum_k \frac{1}{-1 + \left(\frac{\delta_k}{2\Omega}\right)^2} \frac{F_k}{4} \sin \frac{k\pi x}{l}\right] \sin[2(\Omega t + \beta)] \tag{12}$$

where the kth modal generalized force (F_k) is due to the interaction with flexural motion and is given by

$$F_k = \frac{2}{l} \sum_m \sum_n A_m A_n \frac{mn\pi^2}{l^2} \int_0^l \sin \frac{k\pi x}{l} \cos \frac{m\pi x}{l} \cos \frac{n\pi x}{l}\, dx. \tag{13}$$

It is clear that a torsional motion at twice the rate of spin is caused due to the flexural motion. Hence, when the spin speed Ω is close to one half of any of the torsional natural frequencies (δ_k), resonance can occur.

Other Interaction Effects. Careful examination of the differential equations and their boundary conditions presented earlier yields several interesting results. Without explicit solution (like the one carried out in the previous section), one can make some general observations.

If the torque on the shaft is assumed to be constant such that T_1 is zero, then the first-order terms act as synchronous excitation on the second order for flexural vibration. Hence, the response of the rotor in flexure would be different in magnitude if the second order effect were included, but would still have a single frequency component, namely the spin speed of the rotor.

In practice, the torque on the rotor can vary with a frequency equal to the spin speed, or sometimes at twice the spin speed (Rao, 1983). If the torque varies with a frequency equal to the spin speed, $T_1 \sim e^{i\Omega t}$. Then, the torsional vibration to the first order exhibits the same frequency, and the flexural vibration (to the second order) will contain both Ω and 2Ω components. This is a case of flexural vibration induced by torsional vibration and is the counterpart of the example presented in the previous section.

If the torque varies at twice the spin speed, it follows that the torsional vibration at first order has the same frequency (2Ω), and the flexural vibration at second order can exhibit a response with Ω and 3Ω components.

In a practical situation, the presence of such higher frequency components in both torsional and flexural response is not only possible but is in fact frequently observed. The preceding analysis attempts to provide a clear explanation for such phenomena.

Conclusion

The problem of torsional and transverse deformations of a shaft rotating at a constant speed is considered. The displacements are expressed in a perturbation series in terms of a small parameter. Energy expressions are derived to each order and Hamilton's principle is applied to obtain the equations of motion and the boundary conditions governing the displacement functions of different orders.

A simple example of a uniform simply supported rotor is considered and it is clearly shown that the interaction of torsional and transverse vibration occurs at second order which confirms previously observed results. It is also shown that, with the help of the equatins derived, it is possible to determine further intreaction effects without carrying out a detailed solution. Some of the higher frequency components of vibration observed in practical rotating shafts can be explained by the model discussed.

References

Bernasconi, O., 1987, "Bisynchronous Torsional Vibrations in Rotating Shafts," ASME JOURNAL OF APPLIED MECHANICS, Vol. 54, pp. 893–897.

Broniarek, C., 1968, "Investigation of the Coupled Flexural-Torsional Vibration of Rotors with Continuous Parameters," *Zagadninia Drgan Nieliniowych*, No. 9, pp. 169–228.

Gasch, R., Market, R., and Pfützner, H., 1979, "Acceleration of Unbalanced Rotors through the Critical Speeds," *Journal of Sound and Vibration*, Vol. 63, No. 3, pp. 393–409.

Greenwood, D. T., 1965, *Principles of Dynamics*, Prentice-Hall, Englewood Cliffs, NJ.

Kellenberger, W., 1980, "Résonances Combinées Forcées de l'Arbre Tournant-Couplage de Flexion et Torsion," *Revue Brown-Bovery*, Vol. 2-80, pp. 117–121.

Rao, J. S., 1983, *Rotor Dynamics*, Wiley Eastern Ltd., New Delhi.

Tondl, A., 1965, *Some Problems of Rotor Dynamics*, Chapman and Hall, London.

Negativism: A Nonlinear Version

T. M. Atanackovic[20] and Dj. S. Djukic[20]

Introduction

Consider an elastic system that is in equilibrium under the

[20] Professor, University of Novi Sad, 21000 Novi Sad, Yugoslavia.

Contributed by the Applied Mechanics Division of THE AMERICAN SOCIETY OF MECHANICAL ENGINEERS for publication in the ASME JOURNAL OF APPLIED MECHANICS.

Manuscript received by the ASME Applied Mechanics Division, July 5, 1991; final revision, Feb. 28, 1992. Associate Technical Editor: D. J. Inman.

Copyright © 1993 by ASME
Downloaded 03 May 2010 to 171.66.16.245. Redistribution subject to ASME license or copyright; see http://www.asme.org/terms/Terms_Use.cfm

action of a given system of forces. Let κ_o be the equilibrium configuration of the body.

Suppose that an arbitrary point of the system, say D, an additional (concentrated) force $\mathbf{Q}$ is applied and that the system takes a new equilibrium configuration, say κ_1. In Feodosiev (1990) the following interesting question was posed: Is it possible to have a system for which the point of application of the force $\mathbf{Q}$, that is the point D, displaces in the direction *opposite* to the direction of the force $\mathbf{Q}$ while the system changes its configuration from κ_o and κ_1? If such a system exists, then it is said that it exhibits a *negativism* (a term borrowed from psychiatry). Otherwise, if the point D displaces in the direction of $\mathbf{Q}$, the system is called normal. In Panovko and Gubanova (1979) an example of a system exhibiting negativism is analyzed. It consists of a rod built in at one end and free at the other. The rod is loaded by a concentrated (compressive) follower-type force and a couple. In Feodosiev (1990) a more interesting example shown in Fig. 1 is analyzed. It consists of an elastic rod of length L, built in at the point O and free at the point B. At B a rigid rod of the length $L/2$ is fixed and an extensional follower-type force $\mathbf{P}$ is applied. This system has a unique equilibrium configuration (in which the axis of the elastic rod remains straight and coincides with the rigid rod) for all values of $\mathbf{P}$. Now, if a concentrated force $\mathbf{Q}$ is applied at the end of the rigid rod (point D), then the new equilibrium configuration could belong to the one of two classes: one in which point D is displaced to the left (shown in Fig. 1-*b*) and one in which point D displaces to the right (shown in Fig. 1-*c*). If $\mathbf{P}$ is such that the point D displaces in the direction of the force $\mathbf{Q}$ (case b), the system is normal, while in the case when the point D displaces in the direction opposite to the $\mathbf{Q}$, the system exhibits negativism. The additional force $\mathbf{Q}$ during deformation remains parallel to its initial direction. The y-coordinate of the point D, after the application of $\mathbf{Q}$, depends on $\mathbf{P}$ and $\mathbf{Q}$ so that we could write

$$y_D = f(P, Q). \tag{1}$$

Then, the negativistic behavior is characterized by

$$y_D > 0. \tag{2}$$

In Feodosiev (1990) the critical value of $\mathbf{P}$, denoted by $\overline{\mathbf{P}}_{cr}$ was determined so that for $\mathbf{P} > \overline{\mathbf{P}}_{cr}$ the condition (2) is satisfied. This value, however, corresponds to the limiting case when $\mathbf{Q}$ approaches to zero (although this was not explicitly stated in Feodosiev (1990)).

We note that the central difference between the system treated in Feodosiev (1990) and here and the system presented in Panovko and Gubanova (1979) is that here the rod OB is loaded by extensional force so that the negativistic behavior cannot be connected with the loss of stability (buckling). Also, if we in the system treated here reduce the force $\mathbf{Q}$ at the point B, the so-obtained system differs from the system of Panovko and Gubanova (1979) in two details. First, the reduced system has a horizontal force of intensity $\mathbf{Q}$ at the point B, and secondly, the intensity of applied couple is a function of deformation.

In the analysis that follows we propose to determine the critical value of $\mathbf{P}$ that separates normal from negativistic behavior *for any value of* $\mathbf{Q}$. Thus, we shall determine

$$\mathbf{P}_{cr} = \mathbf{P}_{cr}(\mathbf{Q}). \tag{3}$$

We shall show that the critical value $\mathbf{P}_{cr}$ determined in Feodosiev (1990) corresponds to the limit in (3) when $\mathbf{Q} \to 0$, that is

$$\overline{\mathbf{P}}_{cr} = \lim_{\mathbf{Q}\to 0} \mathbf{P}_{cr}(\mathbf{Q}). \tag{4}$$

Also, by numerical integration of the equilibrium equations, we shall determine the deformed shape of the system shown in Fig. 1 for few values of parameters.

Our analysis is based on the classical Euler elastica theory.

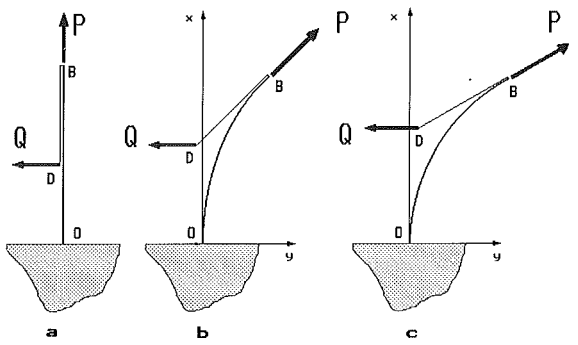


Fig. 1 Coordinate system and load configuration

Analysis

The equilibrium equations for the system shown in Fig. 1-*c* could be written in nondimensional form as

$$\begin{aligned} \dot{\mathfrak{M}} &= [\lambda \sin \vartheta(1) - \beta]\cos\vartheta - \lambda \cos\vartheta(1)\sin\vartheta; \\ \dot{\vartheta} &= -\mathfrak{M}; \\ \dot{\alpha} &= \cos\vartheta; \\ \dot{y} &= \sin\vartheta, \end{aligned} \tag{5}$$

where $(\dot{\cdot}) = d/dt\,(\cdot)$ and the following non-dimensional quantities are used:

$$\lambda = \frac{\mathbf{P}L^2}{EI};\quad \beta = \frac{\mathbf{Q}L^2}{EI};\quad \mathfrak{M} = \frac{ML}{EI};\quad \alpha = \frac{x}{L};\quad y = \frac{y}{L};\quad t = \frac{s}{L}. \tag{6}$$

In (6), EI is the bending rigidity, M is the bending moment in an arbitrary cross-section, and s is the arc length measured along the rod axis from point 0. Also in (5) we used ϑ to denote the angle between tangent to the rod axis and x-axis. The boundary conditions corresponding to the rod in Fig. 1 are

$$\begin{aligned} &\mathfrak{M}(1) + \frac{\beta}{2}\cos\vartheta(1) = 0; \\ &\vartheta(0) = 0; \\ &\alpha(0) = 0; \\ &y(0) = 0. \end{aligned} \tag{7}$$

The solution to (5), (7) determines the shape of the rod. Using the fact that BD is rigid we get

$$y_D = \alpha(1) - \frac{1}{2}\sin\vartheta(1). \tag{8}$$

If (5), (7) is solved then from (8) we can conclude whether the behavior of the system is normal or negativistic.

(i) Solution of (5), (7) and critical value of λ for small β. To solve the boundary value problem (5), (7) for small β we note that for $\beta = 0$ the solution to (5), (7) reads

$$\mathfrak{M}_0 = 0;\quad \vartheta_0 = 0;\quad \alpha_0 = t;\quad y_0 = 0, \tag{9}$$

so that (8) gives

$$y_{OD} = 0. \tag{10}$$

Assuming that solution of (5), (7) is an analytic function of β we get (Nayfeh, 1981)

$$\begin{aligned} &\mathfrak{M} = \mathfrak{M}_0 + \sum_{i=1}^{\infty} \beta^i \mathfrak{M}_i;\quad \vartheta = \vartheta_0 + \sum_{i=1}^{\infty} \beta^i \vartheta_i; \\ &\alpha = \alpha_0 + \sum_{i=1}^{\infty} \beta^i \alpha_i;\qquad y = y_0 + \sum_{i=1}^{\infty} \beta^i y_i, \end{aligned} \tag{11}$$

and

Downloaded 03 May 2010 to 171.66.16.245. Redistribution subject to ASME license or copyright; see http://www.asme.org/terms/Terms_Use.cfm

$$y_D = y_{OD} + \sum_{i=1}^{\infty} \beta^i y_{iD}, \tag{12}$$

and substituting into (5), (7) we show the first-order terms as

$$\begin{aligned} \dot{\mathfrak{M}}_1 &= [\lambda \vartheta_1(1) - \beta] - \lambda \vartheta_1; \\ \dot{\vartheta}_1 &= -\mathfrak{M}_1 \\ \dot{\alpha}_1 &= 1; \\ \dot{y}_1 &= \vartheta_1, \end{aligned} \tag{13}$$

with the following boundary conditions

$$\begin{aligned} \mathfrak{M}_1(1) + \frac{\beta}{2} &= 0; \\ \vartheta_1(0) &= 0; \\ \alpha_1(0) &= 0; \\ y_1(0) &= 0. \end{aligned} \tag{14}$$

The solution to (13), (14) reads

$$\begin{aligned} \mathfrak{M}_1 &= -\left[\vartheta(1) - \frac{\beta}{\lambda}\right]\{-\lambda^{1/2}\sinh(\lambda^{1/2}t)\} \\ &\quad - \left\{\left[\vartheta(1) - \frac{\beta}{\lambda}\right]\mathrm{th}(\lambda^{1/2}) + \frac{\beta}{2\lambda^{1/2}}\cosh(\lambda^{1/2})\right\}\lambda^{1/2}\cosh(\lambda^{1/2}t); \\ \vartheta_1 &= \left[\vartheta(1) - \frac{\beta}{\lambda}\right]\{1 - \cosh(\lambda^{1/2}t)\} \\ &\quad + \left\{\left[\vartheta(1) - \frac{\beta}{\lambda}\right]\mathrm{th}(\lambda^{1/2}) + \frac{\beta}{2\lambda^{1/2}\cosh(\lambda^{1/2})}\right\}\sinh(\lambda^{1/2}t); \\ \alpha_1 &= 0; \\ y_1 &= \left[\vartheta(1) - \frac{\beta}{\lambda}\right]\left\{t - \frac{1}{\lambda^{1/2}}\sinh(\lambda^{1/2}t)\right\} + \left\{\left[\vartheta(1) - \frac{\beta}{\lambda}\right]\mathrm{th}(\lambda^{1/2})\right. \\ &\quad \left. + \frac{\beta}{2\lambda^{1/2}\cosh(\lambda^{1/2})}\right\}\frac{1}{\lambda^{1/2}}[\cosh(\lambda^{1/2}t) - 1], \end{aligned} \tag{15}$$

where

$$\vartheta(1) = \frac{\beta}{\lambda}[1 - \cosh(\lambda^{1/2})] + \frac{\beta}{2\lambda^{1/2}}\sinh(\lambda^{1/2}). \tag{16}$$

Using (9) and (15) in (12) we get

$$\begin{aligned} y_D &= \beta\left\{\left[\frac{\sinh(\lambda^{1/2})}{2\lambda^{1/2}} - \frac{\cosh(\lambda^{1/2})}{\lambda}\right]\left[1 - \frac{\sinh(\lambda^{1/2})}{\lambda^{1/2}}\right]\right. \\ &\quad + \left[\frac{\cosh(\lambda^{1/2})}{2\lambda^{1/2}} - \frac{\sinh(\lambda^{1/2})}{\lambda}\right]\frac{1}{\lambda^{1/2}}[\cosh(\lambda^{1/2}) - 1] + \\ &\quad \left. - \frac{1}{2}\left[\frac{1 - \cosh(\lambda^{1/2})}{\lambda} + \frac{\sinh(\lambda^{1/2})}{2\lambda^{1/2}}\right]\right\} + 0(\beta^2). \end{aligned} \tag{17}$$

Now for $\beta \to 0$ the sign of y_D is determined by the sign of the expression in parenthesis in Eq. (17). Setting this expression to zero, we get $\lambda_{cr} = 5.769153$ so that

$$\mathbf{P}_{cr} = 5.7569153\frac{EI}{L^2} \tag{18}$$

and is in agreement with Feodosiev (1990).

(ii) Solution of (5), (7) and Critical Value of λ for Arbitrary β. The nonlinear boundary value problem (5), (7) has two parameters β and λ. For given β the critical value of λ is determined from the condition that $y_D = 0$. The problem is solved numerically and the critical values of λ for $\beta \in [0, 10]$ are presented in Fig. 2.

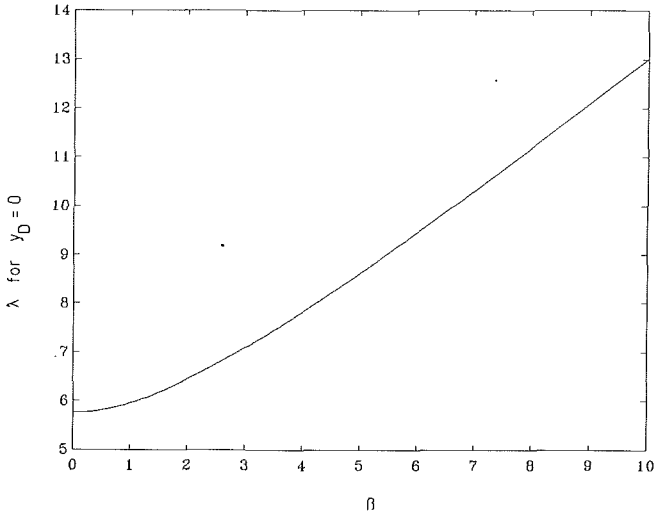


Fig. 2 The values of P_{cr} for different β

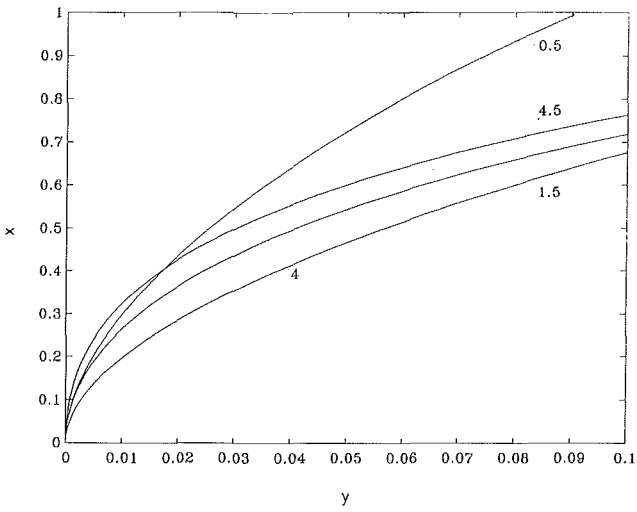


Fig. 3 The shape of the deformed rod

In Fig. 3 the shape of the rod, which is obtained by numerical integration of the two-point boundary problem (5), (7), is shown for $\lambda = 6.5$ and a few values of β.

Conclusions

We analyzed equilibrium configurations of a mechanical system shown in Fig. 1 that could exhibit negativism. That is, if a force **Q** is applied at the point D, the point D displaces in the direction opposite to the direction of force **Q**. We showed that the value of **P** that separates normal from negativistic behavior depends on the value of **Q**. Note that the unusual negativistic behavior in the example analyzed here cannot be connected with the loss of stability, since the system loaded by **P** has stable equilibrium configuration, described by (8), for any value of **P**. If the system exhibits negativism the work of the force **Q** is negative. This work and the work needed to deform elastic rod OB is performed by the nonconservative force **P**.

Acknowledgment

Research was supported by VANU, Novi Sad.

Downloaded 03 May 2010 to 171.66.16.245. Redistribution subject to ASME license or copyright; see http://www.asme.org/terms/Terms_Use.cfm

References

Feodosiev, V. I., 1990, "Once More About Negativism," *Proc. of the Academy of Sci. of the U.S.S.R.: Mechanics of Solid Body*, Vol. 6, p. 167.

Nayfeh, A. H., 1981, *Introduction to Perturbation Techniques*, John Wiley and Sons, New York.

Panovko, J. G., and Gubanova, I. I., 1979, *Stability and Vibration of Elastic Systems*, Nauka, Moscow.

Compound Infinitesimal Mechanisms

E. N. Kuznetsov[21]

Introduction

A system with infinitesimal mobility (an infinitesimal mechanism) is a system allowing virtual displacements but no kinematic displacements. Complete information on the kinematic properties of a system is contained in a set of simultaneous constraint equations,

$$F^i(X_1,\ldots,X_n,\ldots,X_N)=0, \quad i=1,2,\ldots,C, \tag{1}$$

with at least one known solution, $X_n = X_n^0$, taken as a reference geometric configuration. The C constraint functions F^i relate the N generalized coordinates X_n to the invariant geometric parameters of the system (member sizes, linear and angular distances, etc.). If the solution to the constraint equations is isolated, the system lacks kinematic mobility: it has a unique geometric configuration but may possess virtual (infinitesimal) mobility. It is assumed that F^i can be expanded into power series at the solution point $X_n = X_n^0$:

$$F_n^i x_n + (1/2!)F_{mn}^i x_m x_n + \ldots = 0, \quad m,n=1,2,\ldots,N, \tag{2}$$

where x_n are infinitesimal increments of the respective coordinates (virtual displacements) and a repeated subscript denotes summation over the indicated range.

The linear terms of the expansion appear in the linearized constraint equations

$$F_n^i x_n = 0, \tag{3}$$

where the first derivatives,

$$F_n^i = \partial F^i / \partial X_{n|0}, \tag{4}$$

are the elements of the constraint function Jacobian matrix at X_n^0. The matrix rank r being less than C indicates constraint dependence. Its statical consequence is the existence of virtual self-stress, i.e., the statical possibility of initial forces.

The issue of infinitesimal mobility has been investigated mostly for systems with one degree of singularity, $D = C - r = 1$. In this case a necessary and sufficient condition for a first-order infinitesimal mechanism allows two equivalent implementations (Kuznetsov, 1991). The first is a matrix test establishing the existence of a positive-definite combination of the C quadratic forms in (2) subject to linear equations (3). The second seeks a definite combination of the C reduced forms obtained by eliminating, with the aid of (3), $N - r$ dependent displacements. The existence of such a linear combination, signifying the statical possibility of a stable virtual self-stress, is a statical criterion of immobility.

When considering multiple singularity ($D > 1$), two distinct classes of systems are encountered: systems with all of the constraints mutually dependent, and those containing independent constraints as well. The two classes, referred to as complex and compound systems, respectively, are characterized by overlapping and nonoverlapping subsystem self-stress patterns. For a complex system, the statical criterion of immobility is valid. Accordingly, its analysis requires a search for a definite linear combination Q of the reduced quadratic forms Q_d engendered by the D independent self-stress patterns.

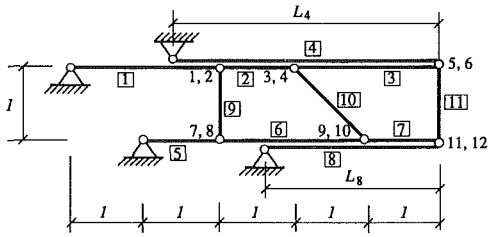


Fig. 1 Underconstrained compound system with two singular subsystems (N = 12, C = 11, D = 2)

What sets compound systems apart is the presence of independent constraints (like the vertical and inclined bars in the system in Fig. 1). Independent constraints cannot counteract, hence, cannot develop initial forces, thus ruling out a comprehensive self-stress pattern, i.e., one involving all bars of the system. As a result, the self-stress patterns of D singular subsystems in a compound system do not overlap and, as shown below, this renders the statical criterion of immobility only sufficient, thus creating an entirely new situation.

Assessing kinematic mobility of compound systems requires either an analysis of D simultaneous complete quadratic forms subject to the pertinent linearized constraint equations or a more convenient analysis of D reduced quadratic forms. A condition for immobility formulated by Kötter (1912) was definiteness of one of the reduced forms subject to zero values for the rest of them. This amounts to verifying the absence of a nontrivial set of virtual displacements that turns all D forms Q_d into zero simultaneously. Then, and only then, the system is kinematically immobile and possesses just first-order virtual mobility.

In this light, it is not difficult to see that the existence of a sign-definite combination Q of reduced quadratic forms Q_d as a condition for first-order infinitesimal mobility is only sufficient (Calladine and Pellegrino, 1992). For the system considered in the quoted paper, a definite combination of the reduced quadratic forms does not exist at *any* length of bar 6 within $0 < L \leq 3$; yet the system *is* a first-order infinitesimal mechanism, except for $L = 1$ and $L = 3$, where it degenerates into mixed-order mechanisms. (Depending on the perturbation mode, the order is first or second at $L = 1$ and first or third at $L = 3$.)

Analysis of Compound Systems

It is assumed, without a loss of generality, that among the D reduced quadratic forms there are no semi-definite and, the more so, definite ones; their presence would only downsize the problem by decreasing the number of independent displacements (in the case of a definite form—all the way to zero, thereby solving the problem).

With this assumption in mind, the following geometric interpretation illustrates the possible situations and facilitates a numerical realization of the analysis. In the space of independent virtual displacements x_s, an indefinite quadratic form Q_d describes a hypersurface (multidimensional convex cone) representing the domain of second-order virtual displacements of the dth singular subsystem. If the intersection of all the D cones is not confined to their common vertex, it constitutes

[21]Professor, Department of General Engineering, University of Illinois, Urbana, IL 61801. Mem. ASME.

Contributed by the Applied Mechanics Division of THE AMERICAN SOCIETY OF MECHANICAL ENGINEERS for publication in the ASME JOURNAL OF APPLIED MECHANICS.

Manuscript received by the ASME Applied Mechanics Division, Sept. 5, 1991; final revision, Feb. 14, 1992. Associate Technical Editor: D. J. Inman.

Downloaded 03 May 2010 to 171.66.16.245. Redistribution subject to ASME license or copyright; see http://www.asme.org/terms/Terms_Use.cfm

References

Feodosiev, V. I., 1990, "Once More About Negativism," *Proc. of the Academy of Sci. of the U.S.S.R.: Mechanics of Solid Body*, Vol. 6, p. 167.

Nayfeh, A. H., 1981, *Introduction to Perturbation Techniques*, John Wiley and Sons, New York.

Panovko, J. G., and Gubanova, I. I., 1979, *Stability and Vibration of Elastic Systems*, Nauka, Moscow.

Compound Infinitesimal Mechanisms

E. N. Kuznetsov[21]

Introduction

A system with infinitesimal mobility (an infinitesimal mechanism) is a system allowing virtual displacements but no kinematic displacements. Complete information on the kinematic properties of a system is contained in a set of simultaneous constraint equations,

$$F^i(X_1,\ldots,X_n,\ldots,X_N)=0, \quad i=1,2,\ldots,C, \tag{1}$$

with at least one known solution, $X_n = X_n^0$, taken as a reference geometric configuration. The C constraint functions F^i relate the N generalized coordinates X_n to the invariant geometric parameters of the system (member sizes, linear and angular distances, etc.). If the solution to the constraint equations is isolated, the system lacks kinematic mobility: it has a unique geometric configuration but may possess virtual (infinitesimal) mobility. It is assumed that F^i can be expanded into power series at the solution point $X_n = X_n^0$:

$$F_n^i x_n + (1/2!)F_{mn}^i x_m x_n + \ldots = 0, \quad m,n=1,2,\ldots,N, \tag{2}$$

where x_n are infinitesimal increments of the respective coordinates (virtual displacements) and a repeated subscript denotes summation over the indicated range.

The linear terms of the expansion appear in the linearized constraint equations

$$F_n^i x_n = 0, \tag{3}$$

where the first derivatives,

$$F_n^i = \partial F^i / \partial X_{n|0}, \tag{4}$$

are the elements of the constraint function Jacobian matrix at X_n^0. The matrix rank r being less than C indicates constraint dependence. Its statical consequence is the existence of virtual self-stress, i.e., the statical possibility of initial forces.

The issue of infinitesimal mobility has been investigated mostly for systems with one degree of singularity, $D = C - r = 1$. In this case a necessary and sufficient condition for a first-order infinitesimal mechanism allows two equivalent implementations (Kuznetsov, 1991). The first is a matrix test establishing the existence of a positive-definite combination of the C quadratic forms in (2) subject to linear equations (3). The second seeks a definite combination of the C reduced forms obtained by eliminating, with the aid of (3), $N - r$ dependent displacements. The existence of such a linear combination, signifying the statical possibility of a stable virtual self-stress, is a statical criterion of immobility.

When considering multiple singularity ($D > 1$), two distinct classes of systems are encountered: systems with all of the constraints mutually dependent, and those containing independent constraints as well. The two classes, referred to as complex and compound systems, respectively, are characterized by overlapping and nonoverlapping subsystem self-stress patterns. For a complex system, the statical criterion of immobility is valid. Accordingly, its analysis requires a search for a definite linear combination Q of the reduced quadratic forms Q_d engendered by the D independent self-stress patterns.

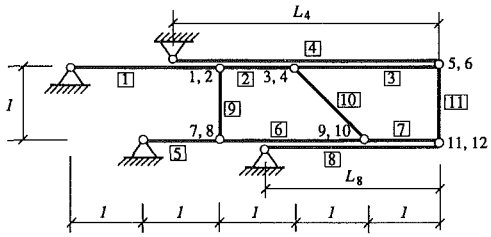


Fig. 1 Underconstrained compound system with two singular subsystems (N = 12, C = 11, D = 2)

What sets compound systems apart is the presence of independent constraints (like the vertical and inclined bars in the system in Fig. 1). Independent constraints cannot counteract, hence, cannot develop initial forces, thus ruling out a comprehensive self-stress pattern, i.e., one involving all bars of the system. As a result, the self-stress patterns of D singular subsystems in a compound system do not overlap and, as shown below, this renders the statical criterion of immobility only sufficient, thus creating an entirely new situation.

Assessing kinematic mobility of compound systems requires either an analysis of D simultaneous complete quadratic forms subject to the pertinent linearized constraint equations or a more convenient analysis of D reduced quadratic forms. A condition for immobility formulated by Kötter (1912) was definiteness of one of the reduced forms subject to zero values for the rest of them. This amounts to verifying the absence of a nontrivial set of virtual displacements that turns all D forms Q_d into zero simultaneously. Then, and only then, the system is kinematically immobile and possesses just first-order virtual mobility.

In this light, it is not difficult to see that the existence of a sign-definite combination Q of reduced quadratic forms Q_d as a condition for first-order infinitesimal mobility is only sufficient (Calladine and Pellegrino, 1992). For the system considered in the quoted paper, a definite combination of the reduced quadratic forms does not exist at *any* length of bar 6 within $0 < L \leq 3$; yet the system *is* a first-order infinitesimal mechanism, except for $L = 1$ and $L = 3$, where it degenerates into mixed-order mechanisms. (Depending on the perturbation mode, the order is first or second at $L = 1$ and first or third at $L = 3$.)

Analysis of Compound Systems

It is assumed, without a loss of generality, that among the D reduced quadratic forms there are no semi-definite and, the more so, definite ones; their presence would only downsize the problem by decreasing the number of independent displacements (in the case of a definite form—all the way to zero, thereby solving the problem).

With this assumption in mind, the following geometric interpretation illustrates the possible situations and facilitates a numerical realization of the analysis. In the space of independent virtual displacements x_s, an indefinite quadratic form Q_d describes a hypersurface (multidimensional convex cone) representing the domain of second-order virtual displacements of the dth singular subsystem. If the intersection of all the D cones is not confined to their common vertex, it constitutes

[21]Professor, Department of General Engineering, University of Illinois, Urbana, IL 61801. Mem. ASME.

Contributed by the Applied Mechanics Division of THE AMERICAN SOCIETY OF MECHANICAL ENGINEERS for publication in the ASME JOURNAL OF APPLIED MECHANICS.

Manuscript received by the ASME Applied Mechanics Division, Sept. 5, 1991; final revision, Feb. 14, 1992. Associate Technical Editor: D. J. Inman.

Copyright © 1993 by ASME

Downloaded 03 May 2010 to 171.66.16.245. Redistribution subject to ASME license or copyright; see http://www.asme.org/terms/Terms_Use.cfm

the domain of nontrivial second-order virtual displacements shared by all of the singular subsystems of the system. The existence of such a domain indicates second-order virtual mobility, meaning that the original constraint equations are compatible at least to the second order. The dimension of the feasible domain determines the number of independent second-order virtual displacements. Thus, for a compound system to possess second- (and, perhaps, higher-) order virtual mobility, all of the D cones must share at least one generator.

Taking advantage of this geometric interpretation and the properties of conical surfaces, the problem of locating the intersection of several cones with a common vertex can be simplified and solved as follows. In the displacement space, it is always possible to find a hyperplane whose intersection with one of the cones is a closed manifold (in a three-dimensional space this is an ellipse, as opposed to any other conic). After such a plane, along with the resulting intersection, is identified, the entire analysis can be confined to this plane, thereby reducing the problem size. The next task is to determine sequentially the intersections of the plane with the remaining cones. This process continues as long as each new intersection has common elements with *all* of the preceeding ones. As soon as this condition is violated (in particular, a cone is found that is not intersected by the plane), the problem is solved: the last examined cone does not share a generator with all of the previous ones, hence, the subsystem domains of second-order virtual displacements are incompatible. The conclusion is that the constraint equations are compatible only to the first order and the system is a first-order compound infinitesimal mechanism.

On the other hand, if the process is successfully completed and a generator shared by all D cones is found, the constraint equations are compatible to at least the second order. If all the cones *intersect* (i.e., no two of them are just *touching*) the system has finite (kinematic) mobility; if, however, touching cones are present, the system may possess only second- or higher-order virtual mobility, and further analysis is required which calls for the construction and evaluation of the constraint discontinuity form (Kuznetsov, 1991).

It is convenient at this point to illustrate the analysis with a simple example.

Example

The planar compound system in Fig. 1 involves two singular subsystems, each comprised of four horizontal bars. The bar lengths, shown to scale, are either 1, or 2, except for the bottom bar with $L_8 = 3.7$ and the upper bar of the yet unspecified length L_4. The two subsystems are connected by the vertical bars 9 and 11 of length 1 and an inclined bar 10 as shown. The numbers at pins identify coordinates, with the origin of the coordinate system at the upper left support; for example, the position of the first pin is given by (X_1, X_2). The constraint equations of the system are

$$
\begin{aligned}
&[1]\ X_1^1 + X_2^2 = 2^2\\
&[2]\ (X_3 - X_1)^2 + (X_4 - X_2)^2 = 1^2\\
&[3]\ (X_5 - X_3)^2 + (X_6 - X_4)^2 = 2^2\\
&[4]\ (X_5 - 5 + L_4)^2 + X_6^2 = L_4^2\\
&[5]\ (X_7 - 1)^2 + (X_8 - 1)^2 = 1^2\\
&[6]\ (X_9 - X_7)^2 + (X_{10} - X_8)^2 = 2^2\\
&[7]\ (X_{11} - X_9)^2 + (X_{12} - X_{10})^2 = 1^2\\
&[8]\ (X_{11} - 5 + L_8)^2 + (X_{12} - 1)^2 = L_8^2\\
&[9]\ (X_7 - X_1)^2 + (X_8 - X_2)^2 = 1^2\\
&[10]\ (X_9 - X_3)^2 + (X_{10} - X_4)^2 = 2\\
&[11]\ (X_{11} - X_5)^2 + (X_{12} - X_6)^2 = 1^2.
\end{aligned}
\tag{5}
$$

In the given configuration (with the first support as the coordinate origin),

$$
\begin{aligned}
&X_1 = X_7 = 2,\ X_2 = X_4 = X_6 = 0,\ X_3 = 3,\\
&X_5 = 5,\ X_8 = X_{10} = X_{12} = 1,\ X_9 = 4,\ X_{11} = 5.
\end{aligned}
\tag{6}
$$

The system is topologically inadequate (its 11 bars are insufficient for geometric invariance) and is in a geometrically singular configuration. Upon deriving the linearized constraint Eq. (3), the Jacobian matrix rank is found to be 9. Solving the obtained equations with virtual displacements x_2, x_4, and x_6 as independent (i.e., arbitrary) yields

$$
\begin{aligned}
&x_8 = x_2,\ x_{10} = x_4,\ x_{12} = x_6,\\
&x_1 = x_3 = x_5 = x_7 = x_9 = x_{11} = 0.
\end{aligned}
\tag{7}
$$

By transposing the constraint Jacobian matrix, the matrix of equilibrium equations in 11 unknown generalized constraint reactions Λ_i obtained. In the absence of external loads the equations allow two independent nontrivial solutions describing self-stress in the two singular subsystems:

$$
\begin{aligned}
&\Lambda_1/L_1 = \Lambda_2/L_2 = \Lambda_3/L_3 = -\Lambda_4/L_4 = \Lambda^{(1)},\\
&\Lambda_5 = \ldots = \Lambda_8 = 0,\ \Lambda_9 = \ldots = \Lambda_{11} = 0,\\
&\Lambda_1 = \ldots = \Lambda_4 = 0,\ \Lambda_5/L_5 = \Lambda_6/L_6 = \Lambda_7/L_7 = -\Lambda_8/L_8 = \Lambda^{(2)},\\
&\Lambda_9 = \ldots = \Lambda_{11} = 0.
\end{aligned}
\tag{8}
$$

Since constraint functions for pin-bar systems are homogeneous quadratic, the corresponding quadratic forms in their power series expansions are obtained simply by replacing the coordinates (capital letters) by their infinitesimal increments, i.e., virtual displacements (lowercase letters). The sum of these quadratic forms weighed by the respective generalized constraint reactions Λ_i is the complete quadratic form for a singular subsystem. Eliminating the dependent displacements with the aid of (7) and omitting the constants $\Lambda_{(1)}$ and $\Lambda_{(2)}$ leads to the reduced quadratic forms for the two subsystems:

$$Q_1 = x_2^2/2 + (x_4 - x_2)^2 + (x_6 - x_4)^2/2 - x_6^2/L_4, \tag{9}$$

$$Q_2 = x_2^2 + (x_4 - x_2)^2/2 + (x_6 - x_4)^2/2 - x^6/L_8. \tag{10}$$

The fact that the forms are indefinite has both statical and kinematic implications. On the statical side, it means that self-stress in each singular subsystem is only virtual, i.e., unstable and physically unrealizable; in spite of being statically indeterminate, neither subsystem can be prestressed. As to kinematics, an indefinite form mutually relates the subsystem displacements which were independent in the first-order analysis. Thus, taken separately, each subsystem is unprestressable and kinematically mobile; the question is, what are the resulting statical and kinematic properties of the system as a whole.

First of all, note that at $0 < L_4 < 5$ a definite combination of forms (9) and (10) does not exist. Were it to exist, the system would be prestressable and, according to the statical criterion of immobility, would be an infinitesimal mechanism. For instance, this takes place outside of the indicated range for L_4; in this case form (9) becomes definite, thereby assuring the existence of a definite linear combination of the two forms. (In fact, the first subsystem alone, being immobile, immobilizes the entire system.) As to the system in consideration, the verdict on its mobility requires further analysis which will be conducted taking advantage of the above geometric interpretation.

In the space of independent virtual displacements x_2, x_4, and x_6, equations $Q_1 = 0$ and $Q_2 = 0$ describe two elliptical cones with a common vertex at the coordinate origin. The mutual position of the cones allows for three possible patterns, each resulting in a different outcome with regard to the type of the system mobility.

(1) The vertex is the only common point of the cones, so that the trivial solution $x_2 = x_4 = x_6 = 0$ of the simultaneous quadratic equations is isolated. The system is kinematically

Downloaded 03 May 2010 to 171.66.16.245. Redistribution subject to ASME license or copyright; see http://www.asme.org/terms/Terms_Use.cfm

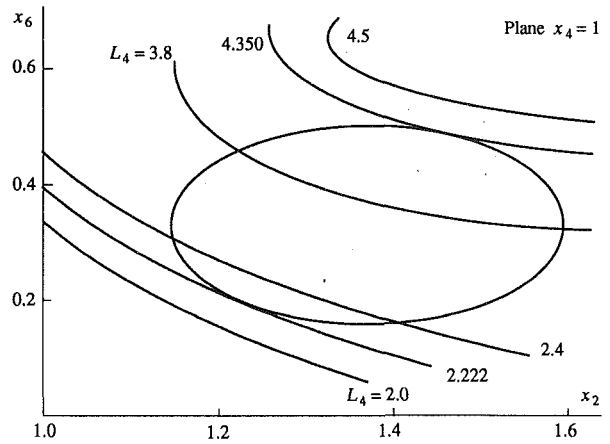


Fig. 2 Intersection patterns in the plane $x_4 = 1$ representing the loci of the subsystem displacements

immobile and possesses only first-order virtual mobility; it is a first-order compound infinitesimal mechanism with three virtual degrees-of-freedom and no kinematic ones.

(2) The two cones touch along a generator, thus determining the displacement ratio and the corresponding direction of compatible displacements of the two subsystems. This outcome is inconclusive in that it only identifies a second-order virtual displacement, but leaves the question on kinematic mobility unresolved. At this stage it is only clear that the constraints are compatible to at least the second order and a higher-order analysis is required for evaluating the system mobility.

(3) The cones intersect along two generators, thereby determining two directions (displacement ratios) along which the displacements of the two singular subsystems are compatible. With these displacements possible, the system is kinematically mobile, it is a finite mechanism with one kinematic degree-of-freedom in each to the two distinct deformation modes characterized by the two displacement ratios.

All three of the described situations are observed in the course of varying the length L_4 in the example system. As discussed above, the problem size is reduced by switching to a plane intersecting one of the cones over an ellipse. A suitable plane is given by $x_4 = 1$; introducing this into (9) and (10) and setting the resulting forms to zero yields

$$q_1 = 3x_2^2/2 - 2x_2 + 3/2 - x_6 + (1/2 - 1/L_4)x_6^2 = 0, \quad (11)$$

$$q_2 = 3x_2^2/2 - x_2 + 3/2 - 2x_6 + (1 - 1/3.7)x_6^2 = 0. \quad (12)$$

The length $L_8 = 3.7$ has been chosen such that the graph of Eq. (12), defining the displacement domain for the second subsystem, is a relatively small ellipse (Fig. 2). This enables the curve given by (11) to be shifted relative to the ellipse by changing L_4. At $L_4 = 2$ the curve is a parabola not intersecting the ellipse, which produces outcome (1). With an increasing L_4, (11) becomes an ellipse that first touches (12) (outcome 2); intersects it (3); again touches it (2) and, finally, disengages once again (1).

Note in conclusion that unprestressable compound infinitesimal mechanisms, along with the only class of unprestressable systems with infinitesimal mobility—even-order mechanisms—would require perfect geometric precision for their implementation. A slight deviation from the nominal bar lengths, while not precluding the possibility of assembling these systems, would restore them to one of the two generic types—geometrically invariant (with an ill-conditioned stiffness matrix) or variant (with a very small domain of finite displacements).

Conclusions

(1) Prestressability, i.e., the existence of stable virtual self-stress, as a statical criterion of immobility in underconstrained systems, is only sufficient. All even-order infinitesimal mechanisms and some compound infinitesimal mechanisms are unprestressable, yet kinematically immobile.

(2) The class of unprestressable systems with *first-order* infinitesimal mobility is confined to compound infinitesimal mechanisms. Remarkably, these include some topologically inadequate underconstrained systems (i.e., ones, with the number of constraints *smaller* than the total number of degrees-of-freedom, $C < N$).

(3) Capitalizing on a geometric interpretation of indefinite quadratic forms as convex conical surfaces, analysis of compound mechanisms reduces to finding the common intersection of several cones with one (hyper)plane in the space of virtual displacements.

References

Calladine, C. R., and Pellegrino, S., 1992, "Further Remarks on First-Order Infinitesimal Mechanisms," *Int. J. Solids Structures*, Vol. 29, pp. 2119–2122.

Kötter, E., 1912, "Uber die Moglichkeit, n Punkte in der Ebene oder im Raume...," *Festchrift Heinrich Muller-Breslau*, Kroner, Leipzig, p. 61.

Kuznetsov, E. N., 1991, *Underconstrained Structural Systems*, Springer-Verlag, New York.

A Beam Theory for Laminated Composites and Application to Torsion Problems

Bhavani V. Sankar[22]

A theory for laminated composite beams is derived from the shear deformable laminated plate theory. The displacement field in the beam is derived by retaining the first-order terms in the Taylor series expansion for the plate midplane deformations in the width coordinate. The displacements in the beam are expressed in terms of three deflections, three rotations, and one warping term. The equilibrium equations are assumed to be satisfied in an average sense over the width of the beam. This introduces a new set of force and moment resultants for the beam. The principle of minimum potential energy is applied to derive the equilibrium equations and boundary conditions. A closed-form solution is derived for the problem of torsion of a specially orthotropic laminated beam.

Derivation of a Composite Beam Theory

Consider a laminated composite beam shown in Fig. 1. The midplane displacements u_0, v_0, w_0, and rotations ψ_x and ψ_y can be expanded in the form of a Taylor series in y. Retaining only the first-order terms in y, we obtain

[22]Associate Professor, Department of Aerospace Engineering, Mechanics and Engineering Science, University of Florida, Gainesville, FL 32611-2031. Mem. ASME.

Contributed by the Applied Mechanics Division of THE AMERICAN SOCIETY OF MECHANICAL ENGINEERS for publication in the JOURNAL OF APPLIED MECHANICS.

Manuscript received by the ASME Applied Mechanics Division, Nov. 26, 1991; final revision, Feb. 21, 1992. Associate Technical Editor: S. K. Datta.

Downloaded 03 May 2010 to 171.66.16.245. Redistribution subject to ASME license or copyright; see http://www.asme.org/terms/Terms_Use.cfm

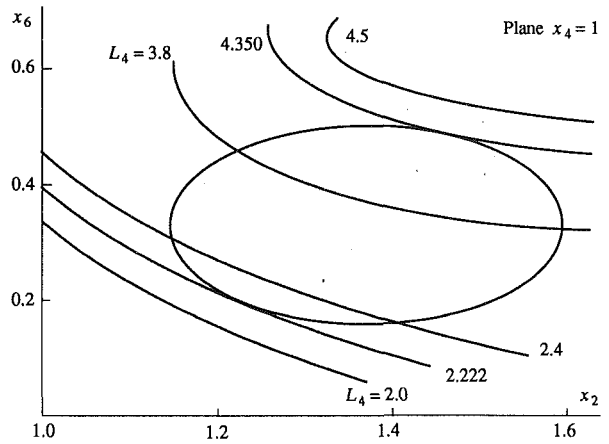


Fig. 2 Intersection patterns in the plane $x_4 = 1$ representing the loci of the subsystem displacements

immobile and possesses only first-order virtual mobility; it is a first-order compound infinitesimal mechanism with three virtual degrees-of-freedom and no kinematic ones.

(2) The two cones touch along a generator, thus determining the displacement ratio and the corresponding direction of compatible displacements of the two subsystems. This outcome is inconclusive in that it only identifies a second-order virtual displacement, but leaves the question on kinematic mobility unresolved. At this stage it is only clear that the constraints are compatible to at least the second order and a higher-order analysis is required for evaluating the system mobility.

(3) The cones intersect along two generators, thereby determining two directions (displacement ratios) along which the displacements of the two singular subsystems are compatible. With these displacements possible, the system is kinematically mobile, it is a finite mechanism with one kinematic degree-of-freedom in each to the two distinct deformation modes characterized by the two displacement ratios.

All three of the described situations are observed in the course of varying the length L_4 in the example system. As discussed above, the problem size is reduced by switching to a plane intersecting one of the cones over an ellipse. A suitable plane is given by $x_4 = 1$; introducing this into (9) and (10) and setting the resulting forms to zero yields

$$q_1 = 3x_2^2/2 - 2x_2 + 3/2 - x_6 + (1/2 - 1/L_4)x_6^2 = 0, \quad (11)$$

$$q_2 = 3x_2^2/2 - x_2 + 3/2 - 2x_6 + (1 - 1/3.7)x_6^2 = 0. \quad (12)$$

The length $L_8 = 3.7$ has been chosen such that the graph of Eq. (12), defining the displacement domain for the second subsystem, is a relatively small ellipse (Fig. 2). This enables the curve given by (11) to be shifted relative to the ellipse by changing L_4. At $L_4 = 2$ the curve is a parabola not intersecting the ellipse, which produces outcome (1). With an increasing L_4, (11) becomes an ellipse that first touches (12) (outcome 2); intersects it (3); again touches it (2) and, finally, disengages once again (1).

Note in conclusion that unprestressable compound infinitesimal mechanisms, along with the only class of unprestressable systems with infinitesimal mobility—even-order mechanisms—would require perfect geometric precision for their implementation. A slight deviation from the nominal bar lengths, while not precluding the possibility of assembling these systems, would restore them to one of the two generic types—geometrically invariant (with an ill-conditioned stiffness matrix) or variant (with a very small domain of finite displacements).

Conclusions

(1) Prestressability, i.e., the existence of stable virtual self-stress, as a statical criterion of immobility in underconstrained systems, is only sufficient. All even-order infinitesimal mechanisms and some compound infinitesimal mechanisms are unprestressable, yet kinematically immobile.

(2) The class of unprestressable systems with *first-order* infinitesimal mobility is confined to compound infinitesimal mechanisms. Remarkably, these include some topologically inadequate underconstrained systems (i.e., ones, with the number of constraints *smaller* than the total number of degrees-of-freedom, $C < N$).

(3) Capitalizing on a geometric interpretation of indefinite quadratic forms as convex conical surfaces, analysis of compound mechanisms reduces to finding the common intersection of several cones with one (hyper)plane in the space of virtual displacements.

References

Calladine, C. R., and Pellegrino, S., 1992, "Further Remarks on First-Order Infinitesimal Mechanisms," *Int. J. Solids Structures*, Vol. 29, pp. 2119–2122.

Kötter, E., 1912, "Uber die Moglichkeit, n Punkte in der Ebene oder im Raume...," *Festchrift Heinrich Muller-Breslau*, Kroner, Leipzig, p. 61.

Kuznetsov, E. N., 1991, *Underconstrained Structural Systems*, Springer-Verlag, New York.

A Beam Theory for Laminated Composites and Application to Torsion Problems

Bhavani V. Sankar[22]

A theory for laminated composite beams is derived from the shear deformable laminated plate theory. The displacement field in the beam is derived by retaining the first-order terms in the Taylor series expansion for the plate midplane deformations in the width coordinate. The displacements in the beam are expressed in terms of three deflections, three rotations, and one warping term. The equilibrium equations are assumed to be satisfied in an average sense over the width of the beam. This introduces a new set of force and moment resultants for the beam. The principle of minimum potential energy is applied to derive the equilibrium equations and boundary conditions. A closed-form solution is derived for the problem of torsion of a specially orthotropic laminated beam.

Derivation of a Composite Beam Theory

Consider a laminated composite beam shown in Fig. 1. The midplane displacements u_0, v_0, w_0, and rotations ψ_x and ψ_y can be expanded in the form of a Taylor series in y. Retaining only the first-order terms in y, we obtain

[22]Associate Professor, Department of Aerospace Engineering, Mechanics and Engineering Science, University of Florida, Gainesville, FL 32611-2031. Mem. ASME.

Contributed by the Applied Mechanics Division of THE AMERICAN SOCIETY OF MECHANICAL ENGINEERS for publication in the JOURNAL OF APPLIED MECHANICS.

Manuscript received by the ASME Applied Mechanics Division, Nov. 26, 1991; final revision, Feb. 21, 1992. Associate Technical Editor: S. K. Datta.

Copyright © 1993 by ASME
Downloaded 03 May 2010 to 171.66.16.245. Redistribution subject to ASME license or copyright; see http://www.asme.org/terms/Terms_Use.cfm

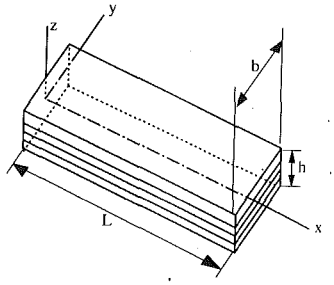


Fig. 1 Laminated composite beam

$$u_0(x,y) = U(x) + yF(x) \tag{1}$$

$$v_0(x,y) = V(x) + yG(x) \tag{2}$$

$$w_0(x,y) = W(x) + y\theta(x) \tag{3}$$

$$\psi_x(x,y) = \phi(x) + y\alpha(x) \tag{4}$$

$$\psi_y(x,y) = \Psi(x) + yH(x). \tag{5}$$

The terms U, V, and W are displacements of points on the longitudinal axis of the beam (x-axis). Similarly, ϕ and Ψ are rotations along the x-axis. From the above kinematic assumptions the expressions for normal strain ϵ_{yy} and shear strain γ_{yz} take the form

$$\epsilon_{yy} = G + zH \tag{6}$$

$$\gamma_{yz} = \Psi + yH + \theta. \tag{7}$$

We will further assume that the normal strain ϵ_{yy} and shear strain γ_{yz} vanish. This can be accomplished by setting $G = 0$, $H = 0$, and $\Psi = -\theta$. These assumptions, along with the plate theory assumption $\epsilon_{zz} = 0$, imply that beam cross-sections normal to the x-axis do not undergo andy in-plane deformations. From the assumed displacement the midplane deformations $\mathbf{E}$ can be expressed as

$$\mathbf{E} = \overline{\mathbf{E}} + y\hat{\mathbf{E}} \tag{8}$$

where

$$\mathbf{E}^T = [u_{0,x}\, v_{0,y}\, (u_{0,x} + v_{0x})\, \psi_{x,x}\, \psi_{y,y}\, (\psi_{x,y} + \psi_{y,x})\, (\psi_y + w_{,y})\, (\psi_x + w_{,x})] \tag{9}$$

$$\overline{\mathbf{E}}^T = [U'\ \ 0\ \ (V' + F)\ \ \phi'\ \ 0\ \ (a - \theta')\ \ 0\ \ (\phi + W')] \tag{10}$$

$$\hat{\mathbf{E}}^T = [F'\ \ 0\ \ 0\ \ a'\ \ 0\ \ 0\ \ 0\ \ (a + \theta')] \tag{11}$$

and a prime denotes differentiation with respect to x. From (8) the constitutive relations $\mathbf{F} = \mathbf{CE}$ become

$$\mathbf{F} = C(\overline{\mathbf{E}} + y\hat{\mathbf{E}}) \tag{12}$$

where $\mathbf{F}$ is the vector of force and moment resultants and $\mathbf{C}$ is the laminate stiffness given by (Whitney, 1987)

$$\mathbf{F}^T = [N_x\ N_y\ N_{xy}\ M_x\ M_y\ M_{xy}\ V_y\ V_x] \tag{13}$$

$$\mathbf{C} = \begin{bmatrix} \mathbf{A} & \mathbf{B} & 0 \\ \mathbf{B} & \mathbf{D} & 0 \\ 0 & 0 & \mathbf{K} \end{bmatrix}. \tag{14}$$

A new set of force and moment resultants for the beam are defined as follows:

$$\overline{\mathbf{F}}(x) = \int_{-b/2}^{+b/2} \mathbf{F}(x,y)\, dy \tag{15}$$

$$\hat{\mathbf{F}}(x) = \int_{-b/2}^{+b/2} y\mathbf{F}(x,y)\, dy. \tag{16}$$

Then the laminate constitutive relations (12) take the form

$$\overline{\mathbf{F}} = b\mathbf{C}\overline{\mathbf{E}} \tag{17}$$

$$\hat{\mathbf{F}} = \left(\frac{b^3}{12}\right)\mathbf{C}\hat{\mathbf{E}}. \tag{18}$$

In deriving (17) and (18), $\mathbf{C}$ is assumed to be constant along y. Explicit forms of the laminate constitutive relations are presented in the following four expressions (19)–(22) as they will be used in the next section:

$$\begin{Bmatrix} \overline{N}_x \\ \overline{N}_{xy} \\ \overline{M}_x \\ \overline{M}_{xy} \end{Bmatrix} = b \begin{bmatrix} A_{11} & A_{16} & B_{11} & B_{16} \\ A_{16} & A_{66} & B_{16} & B_{66} \\ B_{11} & B_{16} & D_{11} & D_{16} \\ B_{16} & B_{66} & D_{16} & D_{66} \end{bmatrix} \begin{Bmatrix} U' \\ V' + F \\ \phi' \\ a - \theta' \end{Bmatrix} \tag{19}$$

$$\overline{V}_x = b\kappa^2 A_{55}(\phi + W') \tag{20}$$

$$\begin{Bmatrix} \hat{N}_x \\ \hat{M}_x \end{Bmatrix} = \left(\frac{b^3}{12}\right) \begin{bmatrix} A_{11} & B_{11} \\ B_{11} & D_{11} \end{bmatrix} \begin{Bmatrix} F' \\ a' \end{Bmatrix} \tag{21}$$

$$\hat{V}_x = \left(\frac{b^3}{12}\right)\kappa^2 A_{55}(a + \theta') \tag{22}$$

where the bar and hat accents associate the resultants in the obvious way. In Eqs. (20) and (22) κ^2 is the shear correction factor. The strain energy per unit area of the laminate, Φ_L, can be derived as

$$\Phi_L = \frac{1}{2}\mathbf{E}^T\mathbf{CE}. \tag{23}$$

From Eqs. (8) and (23) the strain energy per unit length of the beam, Φ_B, can be derived as

$$\Phi_B = \int_{-b/2}^{+b/2} \Phi_L\, dy = \left(\frac{1}{2}\right)\left(b\overline{\mathbf{E}}^T\mathbf{C}\overline{\mathbf{E}} + \left(\frac{b^3}{12}\right)\hat{\mathbf{E}}^T\mathbf{C}\hat{\mathbf{E}}\right). \tag{24}$$

The principle of minimum potential energy (Reddy, 1984) is applied to derive the equations of equilibrium and the boundary conditions. For the purpose of illustration we will consider only transvers loading, $q(x,y)$, in the z-direction acting on the beam surface. The equilibrium equations and boundary conditions are:

Variable	Equilibrium Equations	Boundary Conditions	
δU:	$\dfrac{d\overline{N}_x}{dx} = 0$	$\overline{N}_x \delta U = 0$	(25)
δV:	$\dfrac{d\overline{N}_{xy}}{dx} = 0$	$\overline{N}_{xy}\delta V = 0$	(26)
δW:	$\dfrac{d\overline{V}_x}{dx} + \overline{q} = 0$	$\overline{V}_x \delta w = 0$	(27)
δF:	$\overline{N}_{xy} - \dfrac{d\hat{N}_x}{dx} = 0$	$\hat{N}_x \delta F = 0$	(28)
$\delta\theta$:	$\dfrac{d}{dx}(\hat{V}_x - \overline{M}_{xy}) + \hat{q} = 0$	$(\hat{V}_x - \overline{M}_{xy})\delta\theta = 0$	(29)
$\delta\phi$:	$\overline{V}_x - \dfrac{d\overline{M}_x}{dx} = 0$	$\overline{M}_x \delta\phi = 0$	(30)
δa:	$\dfrac{d\hat{M}_x}{dx} = \hat{V}_x + \overline{M}_{xy}$	$\hat{M}_x \delta a = 0.$	(31)

In (27) and (29), $\overline{q}$ and $\hat{q}$ are given by

$$\overline{q}(x) = \int_{-b/2}^{+b/2} q(x,y)\, dy \tag{32}$$

Downloaded 03 May 2010 to 171.66.16.245. Redistribution subject to ASME license or copyright; see http://www.asme.org/terms/Terms_Use.cfm

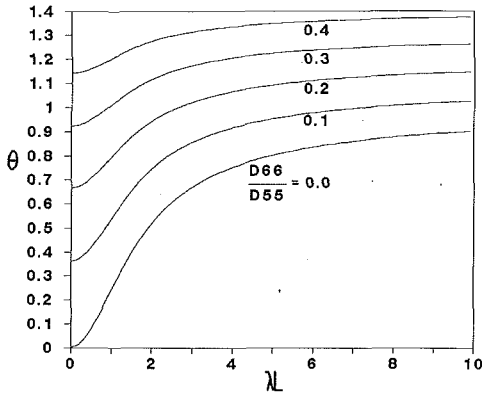


Fig. 2 Nondimensional tip rotation θ (Eq. (36))

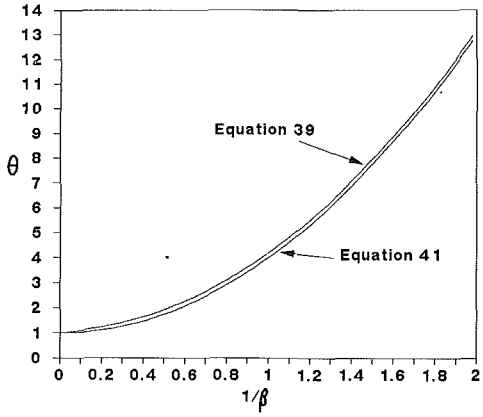


Fig. 3 Nondimensional tip rotation θ for long beams

$$\hat{q} = \int_{-b/2}^{+b/2} yq(x,y)dy. \tag{33}$$

The solution to the problem of a cantilever beam sujected to end loads is derived in Sankar (1991).

Torsion of Specially Orthotropic Laminated Beams

For specially orthotropic beams, $\mathbf{B} = \mathbf{0}$, $A_{16} = A_{26} = D_{16} = D_{26} = 0$. We assume that an end torque T is the only external force acting on the beam. The solution for the angle of twist is (Sankar, 1991)

$$\theta(x) = \frac{T}{D'_{66}}x - \left(\frac{D'^2_{55}T}{4D_{55}D_{66}D'_{66}}\right) \times \left(\frac{\sinh\lambda x}{\lambda} - x - \frac{\tanh\lambda L}{\lambda}(\cosh\lambda x - 1)\right) \tag{34}$$

where $D_{55} = (b^2/12)\kappa^2 A_{55}$, $D'_{55} = (D_{55} - D_{66})$ and $D'_{66} = (D_{66} + D_{55})$.

For the purpose of comparison with available results we will introduce a nondimensional tip rotation Θ defined as

$$\Theta = \frac{4bD_{66}\theta(L)}{TL}. \tag{35}$$

Then from (34) and (35) the solution for the tip rotation takes the form

$$\Theta = 1 + \frac{D_{66}}{D_{55}} - \frac{\left(1 - \frac{D_{66}}{D_{55}}\right)^2}{\left(1 + \frac{D_{66}}{D_{55}}\right)}\frac{\tanh\lambda L}{\lambda L}. \tag{36}$$

In the above result, the first term on the right-hand side corresponds to the classical theory solution for isotropic beams. The shear deformation effects are reflected in the second and third terms. The third term represents the effect of the restrained end $x = 0$, where warping is prevented, i.e., $\alpha(0) = 0$. In Fig. 2, Θ is plotted as a function of λL for various values of (D_{66}/D_{55}). It may be seen that the restrained end effects are felt only for $\lambda L < 10$. Further, the restrained end effects are less pronounced as the ratio of the shear stiffness coefficients (D_{66}/D_{55}) increases. The effect of transverse shear flexibility $(1/D_{55})$ is to increase the angle of twist significantly.

We will compare our results with two available results. If we ignore the shear deformation, i.e., let $D_{55} \to \infty$ in Eq. (36), we will obtain

$$\Theta = 1 + \frac{\tanh\lambda L}{\lambda L}, \tag{37}$$

which is identical to the result for an isotropic beam (Boresi, Sidebottom, Seely, and Smith, 1978). If we ignore the restrained end effects by letting $\lambda L \to \infty$ in result (36), then we obtain

$$\theta = 1 + \frac{D_{66}}{D_{55}}. \tag{38}$$

The above results can be compared with that of (Tsai, Daniel, and Yaniv, 1990) for a 0 deg unidirectional composite beam. Let us denote their result by Θ_1. In their notation

$$\Theta_1 = \left(1 - \frac{\tanh\beta}{\beta}\right) - 1 \tag{39}$$

where

$$\beta = \left(\frac{b}{2h}\right)\sqrt{10\frac{G_{13}}{G_{12}}}. \tag{40}$$

In the same notation, result (38) obtained in the present study can be written as

$$\Theta = 1 + \frac{3}{\beta^2}. \tag{41}$$

In deriving (39) and (41) the shear correction factor κ^2 is assumed to be 5/6. The two results, Θ and Θ_1, are compared for some practical range of $1/\beta$ in Fig. 3. The agreement is quite good. The maximum difference is about 11 percent which occurs at $1/\beta \simeq 0.288$. It is interesting to note that

$$\lim_{\beta\to 0}\beta^2\left(1 - \frac{\tanh\beta}{\beta}\right)^{-1} = 3 = \lim_{\beta\to 0}\beta^2\left(1 + \frac{3}{\beta^2}\right) \tag{42}$$

so that $(\Theta/\Theta_1) \to 1$ as $1/\beta \to \infty$.

Acknowledgments

This research was supported by a grant from the Technology Research and Development Authority of the State of Florida. The author is thankful to Dr. Peter Mataga for many helpful discussions.

References

Boresi, A. P., and Sidebottom, O. M., Selly, F. B., and Smith, J. O., 1978, *Advanced Mechanics of Materials*, John Wiley and Sons, New York, pp. 242–249.

Reddy, J. N., 1984, *Energy and Variational Methods in Applied Mechanics*, John Wiley and Sons, New York.

Sankar, B. V., 1991, "A Beam of Laminated Composites and Application to

Downloaded 03 May 2010 to 171.66.16.245. Redistribution subject to ASME license or copyright; see http://www.asme.org/terms/Terms_Use.cfm

Torsion Problems," Report AeMES TR-91-1-01, 231 University of Florida, Ganinesville, FL.

Tsai, C.-L, Daniel, I. M., and Yaniv, G., 1990, "Torsional Response of Rectangular Composite Laminates," ASME JOURNAL OF APPLIED MECHANICS, Vol. 57, pp. 383-387.

Whitney, J. M., 1987, *Structural Analysis of Laminated Anisotropic Plates*, Technomic, Lancaster, PA.

Fjortoft's Theorem for a Parallel Flow With a Free Surface

John P. McHugh[23]

1 Introduction

The stability of inviscid parallel flows has been intensively studied in the past. The theory is reviewed by Drazin and Howard (1966), Drazin and Reid (1981), and Craik (1985). Several comprehensive and important theorems which have been proven for flows between rigid boundaries are Rayleigh's theorem, Fjortoft's theorem, and Howard's semicircle theorem. Rayleigh's theorem and Howard's theorem have been extended to include a free surface by Yih (1972). Yih (1972) also found a variety of results concerning the neutral modes. The equivalent to Fjortoft's theorem for a parallel flow with a free surface is presented in this Note.

2 Basic Equations

The flow is considered to be inviscid and incompressible. All variables are assumed to be the sum of a primary flow and a disturbance quantity, and the primary flow is a parallel flow, $U(y)$. The equation governing stability is Rayleigh's equation,

$$\phi'' - \alpha^2\phi - \frac{U''}{U-c}\phi = 0, \tag{1}$$

where ϕ is the stream function, α is the wave number, c is the wave speed, and the prime denotes differentiation.

The free-surface boundary condition is

$$\phi'' - \left(\frac{U'}{U-c} + \frac{1}{F^2(U-c)^2}\right)\phi = 0, \tag{2}$$

which holds on the mean free surface. Equations (1) and (2) have been made nondimensional using the depth of the layer, d, as the length scale, and the velocity range, ΔU, i.e., the difference between the maximum and minimum values of U, as the velocity scale. The Froude number is $F = \Delta U/\sqrt{gd}$. Equation (2) appears in Yih (1972) (Eq. (11) in Yih's paper) in dimensional form.

The boundary condition on the flat rigid bottom is

$$\phi = 0. \tag{3}$$

3 Derivation of the Theorem

The coordinate system is chosen to be moving with the velocity of the primary flow at the free surface. In this way, the value of U is zero at the free surface. The difference between this case and a primary velocity profile with a nonzero value at the free surface is merely a Galilean transformation by the amount U_f, where U_f is the primary velocity at the free surface.

Multiply (1) by the conjugate of ϕ, denoted by ϕ^*, and integrate over the domain, integrating the first term in (1) by parts, to obtain

$$\int \phi'\phi'^* dy + \alpha^2 \int \phi\phi^* dy + \int \frac{U''\phi\phi^*}{U-c} dy = \phi_f^*\phi_f', \tag{4}$$

where again the subscript f refers to the value on the free surface. The term on the right-hand side of (4) contains ϕ_f', which is evaluated using the free-surface boundary condition. Equation (4) then becomes

$$J_1 + \int \frac{U''\phi\phi^*}{U-c} dy = \left(-\frac{U_f'}{c} + \frac{1}{F^2c^2}\right)\phi_f^*\phi_f, \tag{5}$$

where J_1 is the sum of the first two terms in (4). Note that U does not appear in the right-hand side of (5), since $U_f = 0$. The imaginary part of (5) is

$$c_i \int \frac{U''|\phi|^2}{(U-c_r)^2 + (c_i)^2} dy = c_i\left(\frac{U_f'}{c_r^2+c_i^2} - \frac{1}{F^2}\frac{2c_r}{[c_r^2+c_i^2]^2}\right)|\phi_f|^2, \tag{6}$$

where c_r and c_i are the real and imaginary parts of c, respectively. For unstable flows, c_i cannot be zero, and the remaining terms in (6) must balance.

The real part of (5) is

$$J_1 + \int \frac{U''|\phi|^2(U-c_r)}{(U-c_r)^2 + (c_i)^2} dy = \left(\frac{c_r U_f'}{c_r^2+c_i^2} + \frac{1}{F^2}\frac{c_r^2-c_i^2}{[c_r^2+c_i^2]^2}\right)|\phi_f|^2, \tag{7}$$

The integral on the left-hand side of (7) may be split into two integrals. One of the new integrals is the negative of the left-hand side of Eq. (6), and may be replaced by the right-hand side of (6). After some cancellation and rearranging, (7) reduces to

$$J_1 + \int \frac{UU''|\phi|^2}{(U-c_r)^2 + (c_i)^2} dy = -\frac{1}{F^2}\frac{|\phi_f|^2}{c_r^2+c_i^2}. \tag{8}$$

The right-hand side of (8) without the negative sign is assigned the value J_2, and it can be seen from (8) that J_2 is positive definite. Equation (8) becomes

$$J_1 + J_2 + \int \frac{UU''|\phi|^2}{(U-c_r)^2 + (c_i)^2} dy = 0. \tag{9}$$

The important conclusion from (9) may now be explained as follows. Since the sum of J_1 and J_2 is positive definite, then the integral must be negative definite. Since the integrand other than $U''U$ is positive definite, then the product $U''U$ must be negative somewhere in the domain of flow for instability. Note that this conclusion is necessary for instability, but not sufficient. A velocity profile may obey (9) and still be stable.

The coordinate system could be chosen so that the value of U at the free surface, U_f, is not zero. The conclusion would then be that $U''(U-U_f)$ must be negative somewhere in the domain of flow. Consider monotonic velocity profiles, for which the quantity $U-U_f$ is either negative or positive throughout. The above result implies that U'' and $U-U_f$ must have opposite sign for instability.

This version of Fjortoft's theorem with monotonic profiles distinguishes between flows which are driven by a shear force, such as wind on the free surface, and flows driven by a pressure gradient or body force.[24] The shear driven flows may be unstable while the others cannot. This result implies that the

[23]Department of Mechanical Engineering, University of New Hampshire, Durham, New Hampshire 03824-3591. Assoc. Mem. ASME.

Contributed by the Applied Mechanics Division of THE AMERICAN SOCIETY OF MECHANICAL ENGINEERS for publication in the ASME JOURNAL OF APPLIED MECHANICS.

Manuscript received by the ASME Applied Mechanics Division, Oct. 15, 1991; final revision, Mar. 6, 1992. Associate Technical Editor: T. R. Akylas.

[24]Noted by a referee.

Downloaded 03 May 2010 to 171.66.16.245. Redistribution subject to ASME license or copyright; see http://www.asme.org/terms/Terms_Use.cfm

Torsion Problems," Report AeMES TR-91-1-01, 231 University of Florida, Ganinesville, FL.

Tsai, C.-L, Daniel, I. M., and Yaniv, G., 1990, "Torsional Response of Rectangular Composite Laminates," ASME JOURNAL OF APPLIED MECHANICS, Vol. 57, pp. 383-387.

Whitney, J. M., 1987, *Structural Analysis of Laminated Anisotropic Plates*, Technomic, Lancaster, PA.

Fjortoft's Theorem for a Parallel Flow With a Free Surface

John P. McHugh[23]

1 Introduction

The stability of inviscid parallel flows has been intensively studied in the past. The theory is reviewed by Drazin and Howard (1966), Drazin and Reid (1981), and Craik (1985). Several comprehensive and important theorems which have been proven for flows between rigid boundaries are Rayleigh's theorem, Fjortoft's theorem, and Howard's semicircle theorem. Rayleigh's theorem and Howard's theorem have been extended to include a free surface by Yih (1972). Yih (1972) also found a variety of results concerning the neutral modes. The equivalent to Fjortoft's theorem for a parallel flow with a free surface is presented in this Note.

2 Basic Equations

The flow is considered to be inviscid and incompressible. All variables are assumed to be the sum of a primary flow and a disturbance quantity, and the primary flow is a parallel flow, $U(y)$. The equation governing stability is Rayleigh's equation,

$$\phi'' - \alpha^2\phi - \frac{U''}{U-c}\phi = 0, \tag{1}$$

where ϕ is the stream function, α is the wave number, c is the wave speed, and the prime denotes differentiation.

The free-surface boundary condition is

$$\phi'' - \left(\frac{U'}{U-c} + \frac{1}{F^2(U-c)^2}\right)\phi = 0, \tag{2}$$

which holds on the mean free surface. Equations (1) and (2) have been made nondimensional using the depth of the layer, d, as the length scale, and the velocity range, ΔU, i.e., the difference between the maximum and minimum values of U, as the velocity scale. The Froude number is $F = \Delta U/\sqrt{gd}$. Equation (2) appears in Yih (1972) (Eq. (11) in Yih's paper) in dimensional form.

The boundary condition on the flat rigid bottom is

$$\phi = 0. \tag{3}$$

3 Derivation of the Theorem

The coordinate system is chosen to be moving with the velocity of the primary flow at the free surface. In this way, the value of U is zero at the free surface. The difference between this case and a primary velocity profile with a nonzero value at the free surface is merely a Galilean transformation by the amount U_f, where U_f is the primary velocity at the free surface.

Multiply (1) by the conjugate of ϕ, denoted by ϕ^*, and integrate over the domain, integrating the first term in (1) by parts, to obtain

$$\int \phi'\phi'^* dy + \alpha^2 \int \phi\phi^* dy + \int \frac{U''\phi\phi^*}{U-c} dy = \phi_f^*\phi_f', \tag{4}$$

where again the subscript f refers to the value on the free surface. The term on the right-hand side of (4) contains ϕ_f', which is evaluated using the free-surface boundary condition. Equation (4) then becomes

$$J_1 + \int \frac{U''\phi\phi^*}{U-c} dy = \left(-\frac{U_f'}{c} + \frac{1}{F^2c^2}\right)\phi_f^*\phi_f, \tag{5}$$

where J_1 is the sum of the first two terms in (4). Note that U does not appear in the right-hand side of (5), since $U_f = 0$. The imaginary part of (5) is

$$c_i \int \frac{U''|\phi|^2}{(U-c_r)^2 + (c_i)^2} dy = c_i\left(\frac{U_f'}{c_r^2 + c_i^2} - \frac{1}{F^2}\frac{2c_r}{[c_r^2 + c_i^2]^2}\right)|\phi_f|^2, \tag{6}$$

where c_r and c_i are the real and imaginary parts of c, respectively. For unstable flows, c_i cannot be zero, and the remaining terms in (6) must balance.

The real part of (5) is

$$J_1 + \int \frac{U''|\phi|^2(U-c_r)}{(U-c_r)^2 + (c_i)^2} dy = \left(\frac{c_r U_f'}{c_r^2 + c_i^2} + \frac{1}{F^2}\frac{c_r^2 - c_i^2}{[c_r^2 + c_i^2]^2}\right)|\phi_f|^2, \tag{7}$$

The integral on the left-hand side of (7) may be split into two integrals. One of the new integrals is the negative of the left-hand side of Eq. (6), and may be replaced by the right-hand side of (6). After some cancellation and rearranging, (7) reduces to

$$J_1 + \int \frac{UU''|\phi|^2}{(U-c_r)^2 + (c_i)^2} dy = -\frac{1}{F^2}\frac{|\phi_f|^2}{c_r^2 + c_i^2}. \tag{8}$$

The right-hand side of (8) without the negative sign is assigned the value J_2, and it can be seen from (8) that J_2 is positive definite. Equation (8) becomes

$$J_1 + J_2 + \int \frac{UU''|\phi|^2}{(U-c_r)^2 + (c_i)^2} dy = 0. \tag{9}$$

The important conclusion from (9) may now be explained as follows. Since the sum of J_1 and J_2 is positive definite, then the integral must be negative definite. Since the integrand other than $U''U$ is positive definite, then the product $U''U$ must be negative somewhere in the domain of flow for instability. Note that this conclusion is necessary for instability, but not sufficient. A velocity profile may obey (9) and still be stable.

The coordinate system could be chosen so that the value of U at the free surface, U_f, is not zero. The conclusion would then be that $U''(U-U_f)$ must be negative somewhere in the domain of flow. Consider monotonic velocity profiles, for which the quantity $U-U_f$ is either negative or positive throughout. The above result implies that U'' and $U-U_f$ must have opposite sign for instability.

This version of Fjortoft's theorem with monotonic profiles distinguishes between flows which are driven by a shear force, such as wind on the free surface, and flows driven by a pressure gradient or body force.[24] The shear driven flows may be unstable while the others cannot. This result implies that the

[23]Department of Mechanical Engineering, University of New Hampshire, Durham, New Hampshire 03824-3591. Assoc. Mem. ASME.

Contributed by the Applied Mechanics Division of THE AMERICAN SOCIETY OF MECHANICAL ENGINEERS for publication in the ASME JOURNAL OF APPLIED MECHANICS.

Manuscript received by the ASME Applied Mechanics Division, Oct. 15, 1991; final revision, Mar. 6, 1992. Associate Technical Editor: T. R. Akylas.

[24]Noted by a referee.

Copyright © 1993 by ASME
Downloaded 03 May 2010 to 171.66.16.245. Redistribution subject to ASME license or copyright; see http://www.asme.org/terms/Terms_Use.cfm

unstable modes, which grow into visible surface waves, are created by wind and not by subsurface phenomena.

Fjortoft's theorem with rigid boundaries states that $U''(U-U_s)$ must change sign in the fluid domain, where U_s is the value of velocity at the point of inflection. Flows with a free surface are not required to have a point of inflection in the velocity profile for instability. The presence of U_f in Fjortoft's theorem instead of U_s shows that the free surface acts as a point of inflection. The fluid can be thought to behave as if there is another layer of fluid above the free surface, and the velocity profile in the imaginary upper layer is such that the free surface is a point of inflection. In this way, a parallel flow without a point of inflection may be unstable, if one boundary is free.

Acknowledgments

Thanks to Lawrence Morland for his helpful suggestions.

References

Craik, A. D. D., 1985, *Wave Interactions and Fluid Flows*, Cambridge University Press, Cambridge, U.K.

Drazin, P. G., and Howard, L. N., 1966, "Hydrodynamic Stability of Parallel Flow of Inviscid Fluid," *Advances in Applied Mechanics*, Vol. 9, pp. 1–89.

Drazin, P. G., and Reid, W. H., 1981, *Hydrodynamic Stability*, Cambridge University Press, Cambridge, U.K.

Yih, C. S., 1972, "Surface Waves in Flowing Water," *Journal of Fluid Mechanics*, Vol. 51, pp. 209–220.

Downloaded 03 May 2010 to 171.66.16.245. Redistribution subject to ASME license or copyright; see http://www.asme.org/terms/Terms_Use.cfm

Journal of Applied Mechanics

Discussion

Effect of Accuracy Loss in Classical Shell Theory[1]

Robert Schmidt.[2] Even though many of the multitudinous theories of shells are seriously deficient when applied to the solution of certain problems, the authors' first example, chosen to demonstrate a deficiency, fails to do so, i.e., it fails to confirm their statement that the "... classical shell theory does not yield correct values of displacements in some shell problems." This failure is due to the inconsistencies in their reasoning. They first present an exact solution of the axisymmetric plane-strain elasticity problem of a tube compressed by gas pressure P, Eqs. (1) to (4). Then they use this exact solution to formulate certain boundary conditions for a semicircular shell (half the tube) and obtain Eqs. (7), viz., $N = PR$ and $M = -Ph^2/12$ at $\theta = \pm\pi/2$, from the exact expressions

$$N = PR\left(1+\frac{h}{2R}\right),$$

$$M = \frac{P(4R^2-h^2)^2}{32Rh}\left(\ln\frac{2R-h}{2R+h}+\frac{4Rh}{4R^2-h^2}\right)$$

after neglecting terms of order h/R in comparison with unity, as required by the authors' definition of the "classical" theory of shells. Those approximate boundary conditions, used within the "classical" theory, lead to the authors' Eqs. (11), which are quite different from the exact elasticity results of Eqs. (4) and hence seem to support the authors' contention.

Now, let us integrate the first of Eqs. (6), and obtain $RN + M =$ constant. The substitution of $N = PR$ and $M = -Ph^2/12$ from Eq. (8) into the foregoing equation yields

$$PR^2\left(1-\frac{h^2}{12R^2}\right) = \text{constant},$$

where the (moment) term $h^2/12R^2$ must be negligible in comparison with unity, in view of the authors' hypothesis that $h/R << 1$. This implies that the authors' boundary conditions $N = PR$ and $M = -Ph^2/12$ should be replaced by $N = PR$ and $M = 0$, as is usually done for such a problem in the theories of thin shells, tubes, and arches. The latter boundary conditions, when used in the classical shell theory employed by the authors, lead to Eqs. (4), i.e., to the correct values of displacements.

Much more serious repercussions are sometimes encountered in the analysis of the initial post-buckling behavior based on well-accepted nonlinear theories of shells. For example, Sanders's (1963) shell equations have been respectively applied by Rehfield (1972) and Dym (1973) to the post-buckling analyses of rings and circular arches subjected to external gas pressure P. Rehfield's calculations predicted an imperfection-sensitive behavior while Sills and Budiansky (1978) and Schmidt (1979) arrived at a contrary conclusion via a very accurate theory. In the case of a two-hinged circular arch (for which 2α is the central angle and β is the rotation of the crown), the following values of the ratio $P_2/P_0 \equiv P_2/P_{cr}$ in the expression

$$\frac{P-P_0}{P_0} = \frac{P_2}{P_0}\beta^2 + \frac{P_4}{P_0}\beta^4 + \ldots$$

have been calculated (Schmidt, 1981) by means of a very accurate and the Sanders theories, respectively, -1.594 and -2.002 for $\alpha = 30$ deg, -0.3870, and -0.8347 for $\alpha = 45$ deg, $+0.0927$, and -0.3945 for $\alpha = 60$ deg, $+0.7813$, and -0.0221 for $\alpha = 90$ deg (the ratio P_2/P_0 characterizes the initial post-buckling behavior and the negative values correspond to the imperfection sensitive behavior). Thus, we see that some shell theories do not yield even qualitatively correct results.

References

Dym, C. L., 1973, "Buckling and Postbuckling Behavior of Steep Compressible Arches," *International Journal of Solids and Structures*, Vol. 9, No. 1, pp. 129–140.

Rehfield, L. W., 1972, "Initial Postbuckling of Circular Rings Under Pressure Loads," *AIAA Journal*, Vol. 10, No. 10, pp. 1358–1359.

Sanders, J. L., Jr., 1963, "Nonlinear Theories for Thin Shells," *Quarterly of Applied Mathematics*, Vol. 21, No. 1, pp. 21–36.

Schmidt, R., 1979, "A Critical Study of Postbuckling Analyses of Uniformly Compressed Rings," *Zeitschrift für angewandte Mathematik und Mechanik*, Vol. 59, No. 10, pp. 581–582.

Schmidt, R., 1981, "Approximate and Exact Analyses of Initial Postbuckling Behavior of Two-Hinged Circular Arch Subjected to External Normal Pressure Load," *Industrial Mathematics*, Vol. 31, Part 2, pp. 79–84.

Sills, L. B., and Budiansky, B., 1978, "Postbuckling Ring Analysis," ASME Journal of Applied Mechanics, Vol. 45, No. 1, pp. 208–210.

Author's Closure[3]**.** The inconsistency in Professor Schmidt's argument is in the conclusion that neglecting the moment in the equation $RN + M =$ const. implies the replacement of boundary condition $M = -Ph^2/12$ by $M = 0$. There is a general rule of asymptotical analysis: one can neglect a small term if there is a much greater term in the same equation. Therefore, one really can neglect the moment in the equation $RN + M =$ const. since $N \sim PR$, $M \sim Ph^2$ and $h << R$. However, replacement of the boundary condition $M = -Ph^2/12$ by $M = 0$ is incorrect, because moment M has the order of Ph^2, and there is not any term in the boundary condition which is much greater than Ph^2. By the way, the impossibility to change the moment boundary condition from asymptotical reasonings is clearly seen from the fact that the

[1]By V. Berdichevsky and V. Misyura and published in the June 1992 issue of the ASME Journal of Applied Mechanics, Vol. 59, pp. S217–S223.

[2]Professor of Engineering Mechanics, College of Engineering and Science, University of Detroit, Detroit, MI 48221. Mem. ASME.

[3]Victor Berdichevsky, Professor of Mechanics, School of Aerospace Engineering, Georgia Institute of Technology.

Copyright © 1993 by ASME
Downloaded 03 May 2010 to 171.66.16.245. Redistribution subject to ASME license or copyright; see http://www.asme.org/terms/Terms_Use.cfm

suggested change leads to a change in the displacements of order unity. One can change the boundary condition $M = -Ph^2/12$ by $M = 0$ if moment M were big and had the order PR^2. However, this is not our case: we have considered shell deformations caused by small moments.

The onset of finite displacements under action of small moments is the substance of the effect of accuracy loss which we have discussed. This effect becomes pronounced if the shell admits infinitesimally small bending (as cylindrical shells do). In principle, the effect of accuracy loss of classical shell theory might be responsible for discrepancies in the theoretical predictions of post-buckling behavior of rings and arches, mentioned by Professor Schmidt. However, careful analysis is needed in order to find a real cause.

In conclusion, I must add that I cannot share Professor Schmidt's point of view that "many of the multitudinous theories of shells are seriously deficient when applied to the solution of certain problems." Classical shell theory works perfectly if it is applied to the problems for which it was designed. To avoid "deficiencies," one needs to bear in mind all the constraints posed by accepted assumptions and to make necessary improvements if these assumptions are violated.

On Cauchy's Mean Rotation[4]

R. Rösel.[5] It is much easier to arrive at the authors' conclusions by using Mohr's circle in the *complex* plane, as shown below. To a real matrix

$$\mathbf{F} = \begin{pmatrix} a & c \\ d & b \end{pmatrix}$$

we associate the two complex numbers

$$\Phi = a + c + i(c - d), \quad \Theta = -a + b + i(c + d);$$

we call this the *Kolosov* representation of the matrix, since it gives the Kolosov functions when applied to the plane stress tensor. Let in the complex plane $\Phi/2$ be the center, $|\Theta|/2$ the radius of a circle, the *complex Mohr* circle of matrix $\mathbf{F}$. I have not seen this idea proposed anywhere, although it is very helpful in several respects. It turns out that this circle is oriented upside down as compared to the generalized Mohr's circle as introduced by Means (1983), or, that we take the transpose of matrix $\mathbf{F}$: the point is that in the complex plane the above convention is the "natural" one, as is also our convention regarding vectors introduced below.

We note in passing that the eigenvalues of $\mathbf{F}$ are the intersections of the circle with the real axis, if they are real, or else two complex conjugate points on the vertical through the center, which form a *harmonic double ratio* with the highest and lowest point on the circle: this projective property is true also in the case of real eigenvalues, it is thus the general interpretation.

As usual in flow mechanics, to a vector $N = \{N_1, N_2\}$ we associate the complex number $N = N_1 - iN_2$, or $N = |N|\exp\langle -i\nu\rangle$; then to $n = \mathbf{F}N$ there corresponds $n = (\Phi N - \Theta\bar{N})/2$. Let $\mathbf{f}$: $n/N = (\Phi - \Theta\bar{N}/N)/2 = (\Phi N - \Theta \exp\langle 2i\nu\rangle)/2$, so that $n = \mathbf{f}N$.

To a plane deformation field $w(x, y) = \{u, v\}$ there corresponds the complex number $w(z, \bar{z}) = u - iv$ and the plane deformation gradient

$$\mathbf{F} = \begin{pmatrix} \partial u/\partial x & \partial u/\partial y \\ \partial v/\partial x & \partial v/\partial y \end{pmatrix},$$

and thus the functions

$$\Phi = 2\partial w/\partial \bar{z}, \quad \Theta = -2\partial w/\partial z.$$

In this interpretation, let $N = dX/|dX|$, $n = dx$, where dX, dx are any line element before and after deformation; the "rotation angle" between them is arg(**f**). The *unit* vectors N are now mapped, as $0 \le \nu < 2\pi$, onto the circle (oriented counterclockwise)

$$\overline{\mathfrak{D}_\nu}(w) = \partial w/\partial \bar{z} + (\partial w/\partial z)\exp\langle 2i\nu\rangle,$$

where $\overline{\mathfrak{D}_\nu}(w)$ is the *directional derivative w.r.t.* $\bar{z}$ *of* w *in the direction* ν as in Herold (1988),

$$\overline{\mathfrak{D}_\nu}(w) := \lim_{\substack{z \to 0 \\ \arg(z) = \nu}} \frac{w(z)}{\bar{z}}.$$

We thus have the natural property that the center $\partial w/\partial \bar{z}$ of the circle is the mean of the directional derivatives, the angle $\arg(\partial w/\partial \bar{z})$ is *Cauchy's mean rotation angle*. It is well defined if and only if the origin of the complex plane is outside the circle. This means that the circle may not cut the real axis at two points on opposite sides of the origin, i.e., the eigenvalues should be complex (in which case they are conjugate) or have the same sign, if they are real. In either case their product $\det(\mathbf{F}) \ge 0$, and this is obviously true for a deformation gradient.

References

Means, W. D., 1983, "Application of the Mohr-Circle Construction to Problems of Inhomogeneous Deformation," *J. Structural Geology*, Vol. 5, pp. 279–286.

Herold, H., 1988, "Über die partielle Differentiation nach z und $\bar{z}$," *Zeitschrift angewandte Math. und Mech.*, Vol. 68, pp. 389–391.

Authors' Closure[6]**.** In the discussion by Rösel, a graceful interpretation of the deformation rotation circle, introduced in our paper, in terms of the complex Mohr circle is proposed. Some additional properties of the deformation rotation circle (or, equivalently, the complex Mohr circle) are provided. However, we note that the association between the complex Mohr circle and deformation rotation angle is evident, as illustrated by Rösel, with respect to only a plane finite deformation but not a spatial finite deformation as analyzed in our paper.

To a plane finite deformation, the formula of Cauchy's mean rotation angle can very easily be derived. Denote by $\mathbf{F}$ the deformation gradient, $\mathbf{F} = \mathbf{QU}$ the right polar decomposition of $\mathbf{F}$ where $\mathbf{Q}$ is the finite rotation tensor and $\mathbf{U} = \sqrt{\mathbf{F}^T\mathbf{F}}$ the right stretch tensor, Θ the rotation angle of $\mathbf{Q}$, and $\mathbf{N}_1$ and $\mathbf{N}_2$ the two principal directions of $\mathbf{U}$. Here, the notation that the superscripts T and -1 indicate transpose and inverse, respectively, and the prefixes det and tr mean determinant and trace, respectively, is employed. First, we should point out that the Cauchy's mean rotation angle to a plane finite deformation is just the Θ. From the geometric sense of a rotation tensor $\mathbf{Q}$ and a positive definite symmetric tensor $\mathbf{U}$, it is clear that for any angle φ, $0 \le \varphi \le \pi$, the mean value of the two deformation angles of directions

$$\cos\varphi\,\mathbf{N}_1 + \sin\varphi\,\mathbf{N}_2 \quad \text{and} \quad \cos\varphi\,\mathbf{N}_1 - \sin\varphi\,\mathbf{N}_2$$

is equal to Θ. Thus, the mean value of deformation angles of all directions on the deformation plane is just the finite rotation angle Θ. The above geometric explanation was proposed by Zheng and Xiong (1988). Secondly, from the following identity to a plane finite deformation

$$\mathbf{Q} = \mathbf{FU}^{-1} = (\det \mathbf{U})^{-1}[(\operatorname{tr} \mathbf{U})\mathbf{F} - \mathbf{FU}] \quad \text{or}$$

$$\mathbf{Q}[(\det \mathbf{U})\mathbf{I} + \mathbf{F}^T\mathbf{F}] = (\operatorname{tr} \mathbf{U})\mathbf{F},$$

[4]By Q. S. Zheng and K. C. Hwang and published in the June 1992 issue of the ASME JOURNAL OF APPLIED MECHANICS, Vol. 59, pp. 405–410.

[5]Paul Scherrer Institut, 5232 Villigen PSI, Switzerland.

[6]Closure prepared by Q.-S. Zheng, Department of Mathematical Models in Materials Science, Technical University Aachen, D-5100 Aachen, Germany.

Copyright © 1993 by ASME
Downloaded 03 May 2010 to 171.66.16.245. Redistribution subject to ASME license or copyright; see http://www.asme.org/terms/Terms_Use.cfm

where **I** is the plane second-order identity tensor, one can easily obtain the following well-known representation of Θ in the Cartesian coordinate component form

$$\tan\Theta=\frac{Q_{21}-Q_{12}}{Q_{11}+Q_{22}}=\frac{F_{21}-F_{12}}{F_{11}+F_{22}}.$$

References

Zheng, Q.-S. and Xiong, Z.-H., 1988, "On the Decompositions of the Deformation Gradient in Plane Problems," *J. Jiangxi Polytechnic Univ.*, Vol. 10, No. 3, pp. 8–21 (in Chinese).

The Complementary Potentials of Elasticity, Extremal Properties, and Associated Functionals[7]

W. T. Koiter[8]. The main body of the present paper is a repetition of the author's 1978 publication, mentioned in the list of references. A significant new element is the statement that the complementary energy functional attains a relative *maximum* as a consequence of the minimum property of the potential energy functional in a state of stable equilibrium. This conclusion, however, is obviously incompatible with Castigliano's famous theorem in the *linear* theory of elastic structures where the complementary energy functional exhibits an *absolute minimum* for the actual stress distribution. A similar contradiction occurs in the nonlinear theory of elasticity in the case of so-called semilinear isotropic materials (also sometimes called John's harmonic or quasi-linear materials). Whenever the sums of all three pairs of principal Jaumann stresses are positive, the complementary energy functional attains a proper relative *minimum*.

The author starts his discussion of the energy functionals by means of a primitive functional P, his Eq. (11), which may be reduced to the sum of the potential and complementary energy functionals. The arguments in these functionals are, respectively, the kinematically admissible displacement fields and the statically admissible stress distributions. Since P and its first variation are both zero for all admissible states, the author argues effectively that the second variations of the potential and complementary energies must be opposite in sign. In a state of stable equilibrium, the positive definite character of the second variation of the potential energy would thus entail a negative definite second variation of the complementary energy—hence the author's statement that this energy would exhibit a maximum in the actual state of stress.

The basic error in the author's argument above is that it overlooks the fact that the potential and complementary functionals operate in completely different spaces. In the case of the potential energy, it is the space of all kinematically admissible displacement fields, and in the case of the complementary energy, it is the space of all statically admissible stress distributions. The zero values of the primitive functional P (11) and its first variation are consequences of the stationary property of the potential and complementary energies, each considered as a functional of its own argument, the admissible displacement field, and the admissible stress distribution, respectively. The positive character of the second variation of the potential energy is ensured in a case of stable equilibrium, but no similar general statement can be made for the second variation of the complementary energy. On the other hand, in the linear theory Castigliano's minimum property of the complementary energy must be recovered when all prescribed loads and displacements tend to zero. As mentioned above, a similar minimum property for the complementary energy holds true for so-called semilinear materials under certain restrictions on the stresses.

Author's Closure[9]

The author is grateful to Professor Koiter for his comments which raise several relevant questions: the distinctions between the present and earlier paper (1978), the conditions for an extremum of the complementary potential, and the correlation with the Castigliano-Crotti theorem of linear elasticity.

The author's earlier paper adopted a different philosophical viewpoint and formulation. Previously (Wempner, 1978), to couch the complementary variational criteria in a more general context, the author showed that the complementary potentials might be viewed as constituents of a general functional:

$$P(\mathbf{R},\ \mathbf{T}^i)=P_w(\mathbf{R})+P_c(\mathbf{T}^i). \tag{1a}$$

The functional P is independent of the medium. Thus the stationarity with respect to position ($\mathbf{R}$) and stress ($\mathbf{T}^i$) of their respective potentials might be viewed as special cases of the *principles* of *virtual* displacement and stress, which render P stationary. In the formulation of the complementary potentials the author followed Fraeijs de Veubeke and employed components of the engineering strain (h_{ij}) and Jaumann stress (T^{ij}). In the present paper the author adopted the *definition* of the complementary potential:

$$P_c(\mathbf{T}^i)\equiv P(\mathbf{R},\ \mathbf{T}^i)-P_w(\mathbf{R}). \tag{1b}$$

Thus, one has the interesting analogy between the transformation of functionals and functions, to wit, the complementary densities:

$$\overline{W}_c(T^{ij})\equiv T^{ij}h_{ij}-\overline{W}_w(h_{ij}). \tag{2}$$

The first terms on the right sides of (1*b*) and (2) are independent of the medium. An objective of the later paper is the formulation in terms of the Cauchy-Green strain (γ_{ij}) and the Kirchhoff-Trefftz stress (S^{ij}). In the latter formulation an essential issue is the distinction between the geometrical and statical variations. Specifically, when the stress is referred to the stretched and rotated basis ($\mathbf{T}^i = S^{ij}\mathbf{G}_j$), the variation of stress ($\dot{\mathbf{T}}^i = \dot{S}^{ij}\mathbf{G}_j$) does not imply a variation of basis ($\dot{\mathbf{G}}_j$) which is kinematical.

Only geometrically admissible states are considered throughout; $\mathbf{R}$ and $\mathbf{R}_{,i}$ are continuous and $\mathbf{R}$ is invariable on a_v. To rupture, fold, or tear the body from its moorings would be meaningless. If the variations of stress are statically admissible then $P = 0$ and

$$P_c(\mathbf{T}^{ij})=-P_w(\mathbf{R}). \tag{3}$$

As in the variations of the functional P, the stationary conditions of P_w enforce equilibrium and those of P_c necessitate geometrical continuity. These are necessary conditions for an extrema. The question then concerns the higher-order variation(s) at such stationary "points."

Typically an adjacent state of equilibrium is accompanied by an increment of loading (variation of T^i on a_t). Indeed, in linear elastostatics a unique state exists. Typically at a bifurcation point (buckling) an adjacent state exists at the prevailing load. Then, a geometrically and statically admissible variation exists, viz. an eigenfunction. At such points, there exists an

[7]By Gerald Wempner and published in the Sept. 1992 issue of the ASME JOURNAL OF APPLIED MECHANICS, Vol. 59, pp. 568–571.

[8]Prof. W. T. Koiter, Laboratory for Engineering Mechanics, Delft University of Technology, Makelweg 2, 2628 CD Delft, The Netherlands.

[9]Gerald Wempner, Professor Emeritus, Georgia Institute of Technology, Atlanta, GA 30332.

Copyright © 1993 by ASME
Downloaded 03 May 2010 to 171.66.16.245. Redistribution subject to ASME license or copyright; see http://www.asme.org/terms/Terms_Use.cfm

infinity of geometrically admissible variations which render P_w stationary. It may be a *relative* minimum or maximum. Pursuit and resolution of the question serves to ascertain the practical matter of stability; indeed, the important questions were largely resolved by Koiter's monumental dissertation (1945). If such a state is stable, e.g., a simple column, then P_w is a relative minimum for every geometrically admissible variation (including the statically admissible variation - eigenfunction); then P_c is a *relative* maximum under the stated conditions. The statically and geometrically admissible variation(s), eigenfunction(s), lies in a subspace of the geometrically admissible variations.

As Professor Koiter has noted, the potential is a *relative* minimum in a state of stable equilibrium. If the material is linear, then the density is a positive definite quadratic form in the strain. The actual behavior depends on the components employed: Jaumann stress and engineering strain, or Kirchhoff-Trefftz and Cauchy-Green strain. If the linearity is displayed with respect to the former, then in accordance with (2),

$$\overline{W}_w = \frac{1}{2} C^{ijkl} h_{ij} h_{kl} = \frac{1}{2} C^{-1}_{ijkl} T^{ij} T^{kl} = \overline{W}_c.$$

Here, C^{ijkl} and C^{-1}_{ijkl} denote components of the stiffness and inverse, respectively. The relevant terms of Eq. (3) follow:

$$\overline{P}_c(T^{ij}) = -\int_v \frac{1}{2} C^{-1}_{ijkl} T^{ij} T^{kl} dv. \tag{4}$$

It appears that the definition (1*b*) has caused an unfortunate misunderstanding, specifically, the negative sign in (3) and (4). The latter exhibits an absolute maximum as opposed to a minimum if defined otherwise. Our choice was prompted by the mechanics, as cited above (Eq. (1*a*)).

In their review of energetical principles, Oravas and McLean (1966) allude to "Born's Principle" wherein a transformation—"converts a minimal principle [minimum potential] into a maximal principle, in which the constraint conditions [compatibility] of the variational principle become the natural conditions of the reciprocal [complementary] variational principle." Regrettably, the writer has not had the opportunity to review Born's dissertation (1906), though it appears likely that it embodies the essentials of the present article.

It is generally difficult to obtain the stress-strain equations of nonlinear materials, and most unlikely that one could invert them. In practice, the relations are obtained *and* implemented, mechanically and computationally, by incremental procedures. However, the stationary and extremal conditions involve only behavior in a neighborhood of an existing state, so that these conditions *might* be investigated with an adequate expansion.

References

Born, M., 1960, "Untersuchungen über der stabilität der elastichen, Linie in Ebene und Raum under verschiedenen Grenzbedingungen," dissertation, Gottingen.

Koiter, W. T., 1945, "Over der Stabiliteit van het Elastisch Evenwicht," dissertation, Delft.

Orvas, G. AE., and McLean, L., 1966, "Historical Development of Energetical Principles in Elastomechanics, Part II," *Applied Mechanics Reviews*, Vol. 19, ASME, New York.

Wempner, G., 1978, *Complementary Theorems of Solid Mechanics*, S. Nemat-Nasser, ed., Pergamon Press, New York.

Downloaded 03 May 2010 to 171.66.16.245. Redistribution subject to ASME license or copyright; see http://www.asme.org/terms/Terms_Use.cfm

Journal of Applied Mechanics

Book Review

Three-Dimensional Elastic Bodies in Rolling Contact, by J. J. Kalker, Dordrecht, The Netherlands, 1990. 314 pages.

REVIEWED BY K. L. JOHNSON[1]

The traction, braking, guidance, and stability of wheeled vehicles is governed by the distribution of friction forces in the small area of contact between the wheel and the surface on which it rolls. The behavior is far from simple, since the contact area is almost invariably divided into regions of "stick" and regions of "slip" whose disposition is unknown at the outset.

Professor Kalker has devoted his professional life to a study in depth of this problem in contact mechanics. He has brought the rigor of his mathematical calling to the subject, while aiming to provide working numerical programs for engineers needing to apply the results of his researches. For many years his doctoral dissertation: "On the rolling contact of two elastic bodies in the presence of dry friction" (1967) provided the standard reference on the subject. The present volume greatly extends the scope of the dissertation and will become a reference work for many years to come. Although the principal technological application of this field of research lies with wheeled vehicles, the approach is not specific to vehicle technology and important applications can be found in other areas such as rolling contact bearings.

In Chapters 1 and 2, the problem is stated and modelled; the question of numerical methods of solution is discussed. Chapter 3 is devoted to the "simplified" or "elastic foundation" model of contact, in which the elastic displacement of any point in the contact is a linear function of the traction *at that point only*. Kalker rightly emphasizes the value of this approach to obtain quick solutions of reasonable accuracy to a wide variety of steady and transient problems. A rapid, efficient program is developed.

In general, non-Hertzian contact problems the shape of the contact area is not known in advance. Kalker has followed the approach of Duvaut and Lions in developing a variational theory of frictional contact. This has the advantage of being soundly based upon theorems of existence and uniqueness, while lending itself for implementation to the well-developed methods of numerical optimization. This forms the basis of his most comprehensive programs which will handle static as well as rolling problems. Although slow in operation, they can be implemented on a personal computer.

Chapter 5 includes the results of a wide variety of problems which have been computed using the author's programs. This chapter includes some new results relating to rolling with combined creepage and spin, transient rolling contact, and to the unloading of a static contact between dissimilar elastic spheres.

The treatment is (understandably) restricted to homogeneous, isotropic elastic bodies, hence its direct application is to rail vehicles. Nevertheless the concepts discussed are equally applicable to road vehicles with pneumatic tires. As the author comments, ". . . the automotive tire is perhaps the supreme challenge of continuum rolling theory".

The author has a rather cryptic style in which mathematical symbolism plays a large part and which some will not find easy reading. But the fact that the author's theories and programs are used by the majority of the world's railways shows that the effort is rewarding.

[1]Professor, University Engineering Department, Cambridge University, Cambridge, CB2 1PZ, England.

Copyright © 1993 by ASME
Downloaded 03 May 2010 to 171.66.16.245. Redistribution subject to ASME license or copyright; see http://www.asme.org/terms/Terms_Use.cfm